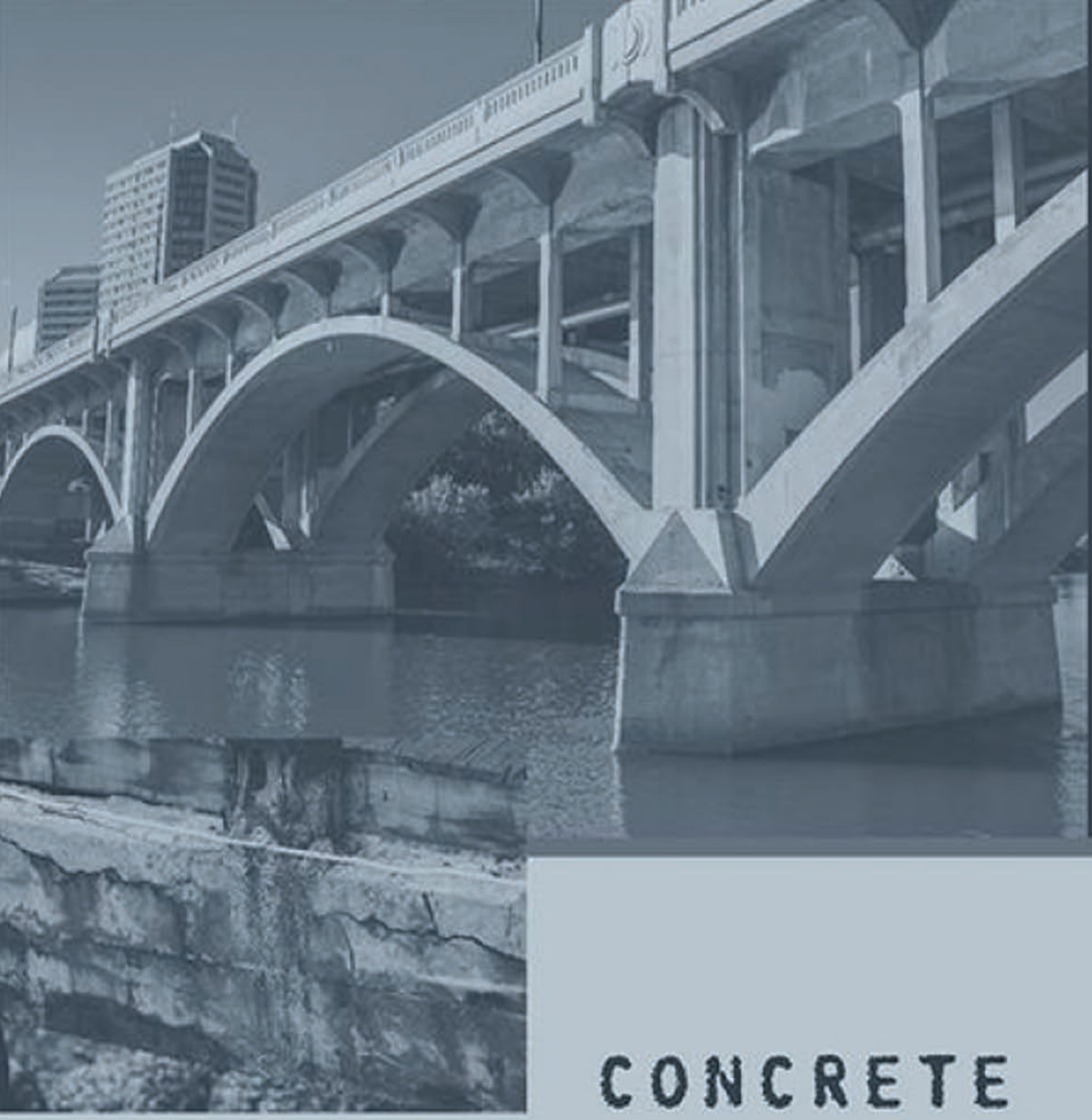

CONCRETE SOLUTIONS

Michael G. Grantham
Ioanna Papayianni
Kosmas Sideris

EDITORS

CRC Press
Taylor & Francis Group
A BALKEMA BOOK



Taylor & Francis
Taylor & Francis Group
http://taylorandfrancis.com

PROCEEDINGS OF CONCRETE SOLUTIONS, 6TH INTERNATIONAL CONFERENCE ON CONCRETE REPAIR, THESSALONIKI, GREECE, 20–23 JUNE 2016

Concrete Solutions

Editors

Michael G. Grantham
Concrete Solutions, Margate, Kent, UK
Sandberg LLP, London, UK

Ioanna Papayianni
Laboratory of Building Materials, Department of Civil Engineering, Aristotle University of Thessaloniki, Greece

Kosmas Sideris
Department of Civil Engineering, Democritus University of Thrace, Xanthi, Thrace, Greece

CRC Press
Taylor & Francis Group
Boca Raton London New York Leiden

CRC Press is an imprint of the
Taylor & Francis Group, an **informa** business

A BALKEMA BOOK

CRC Press/Balkema is an imprint of the Taylor & Francis Group, an informa business

© 2016 Taylor & Francis Group, London, UK

Typeset by MPS Limited, Chennai, India
Printed and bound in Great Britain and the USA

All rights reserved. No part of this publication or the information contained herein may be reproduced, stored in a retrieval system, or transmitted in any form or by any means, electronic, mechanical, by photocopying, recording or otherwise, without written prior permission from the publishers.

Although all care is taken to ensure integrity and the quality of this publication and the information herein, no responsibility is assumed by the publishers nor the author for any damage to the property or persons as a result of operation or use of this publication and/or the information contained herein.

Published by: CRC Press/Balkema
P.O. Box 11320, 2301 EH Leiden, The Netherlands
e-mail: Pub.NL@taylorandfrancis.com
www.crcpress.com – www.taylorandfrancis.com

ISBN: 978-1-138-03008-4 (Hbk)
ISBN: 978-1-315-31560-7 (eBook PDF)

Concrete Solutions – Grantham et al. (Eds.)
© 2016 Taylor & Francis Group, London, ISBN 978-1-138-03008-4

Table of contents

Preface XI
Sponsors XIII

Case studies

Protection of a pier structure using an alternative combined electrochemical approach 3
R. Brueckner, C. Atkins, R. Merola & P. Lambert

Analysis of adaptation of reinforced concrete structures from early 20th century to the needs of modern requirements – a case study 9
G. Dmochowski & P. Berkowski

Application of a surface-applied cathodic protection system on a light weight concrete bridge – Part I: Condition assessment, intervention options and trial investigations 13
J.J.W. Gulikers, R.G. Giorgini & A.J. van den Hondel

What are the benefits of corrosion monitoring in concrete structures from an owner's perspective? 19
J.J.W. Gulikers

Modern techniques and concrete technology used to conserve a unique heritage breakwater 25
S. Hold

WWII German concrete defence walls in Jersey, Channel Islands 33
S. Hold

Micropiling a bridge in construction in the motorway M-410 in Madrid (Spain) 43
C. Jurado Cabañes

Road bridge decks sealing, joints and pavement practice, the Greek motorway experience 49
A. Kokkalis & P. Panetsos

Corrosion propagation phase in reinforced concrete facades 55
A. Köliö & J. Lahdensivu

ASR possibilities in Finnish concrete bridges 61
J. Lahdensivu, A. Köliö & D. Husaini

Survey of the largest prefabricated concrete structure of Spain 65
A. Lozano, M. Alonso, F. Álvarez, J.J. Del Coz

Management strategy for localized concrete maintenance on the Rion-Antirion Bridge 73
I.C. Papantoniou, P. Corbett, A. Stathopoulos-Vlamis & P. Papanikolas

Focused, non-destructive repair of tunnel walls with electrochemical chloride extraction 81
U. Schneck

NDT and diagnostic study of corrosion damaged RC structures to enhance their service life – case studies 87
S. Sharma, A. Pahuja, B.S. Rao, N.S. Adarsh Kumar & A. Sharma

Design of repair works in underground structures located in fine-grained soil 95
A. Shilin & A. Schukina

Various stages of protection of concrete roads 99
S.N. Tolmachov, O.A. Belichenko & H.V. Brazhnyk

Analysis of the failure of a track slab concrete 105
Z. Yi, H. Li, H. Jin & Y. Xie

Electrochemical repair

Electrochemical re-alkalisation, chloride extraction and alkali-silica reaction in concrete 113
P.F.G. Banfill

Acid damage to anode mortar when using cathodic protection 121
P.M. Chess

The flow of ions through concrete structures 125
P.M. Chess

Impressed Current Cathodic Protection (ICCP) on reinforced concrete drilled piles buried in soil, Fürth, Germany 131
H. Esteves & S. Mayer

Assessment of the throwing power generated by a surface applied galvanic cathodic protection system on a light weight concrete bridge deck soffit 135
R.G. Giorgini, H. van den Hondel & J.J.W. Gulikers

The durability of reference electrodes in reinforced concrete applications 143
P.M. Chess, O. Klinghoffer & B. Kofoed

An investigation into impressed current cathodic protection systems in Australian wharfs 149
P. Nicholls & D.W. Law

Prevention of incipient anodes induced by patch repair by a novel type of discrete galvanic zinc anodes 157
W. Schwarz, M. Bakalli & M. Donadio

Application of a surface-applied cathodic protection system on a light weight concrete bridge – Part II: Developments in time of the effectiveness by potential decay values and current densities 165
A.J. van den Hondel, R.G. Giorgini & J.J.W. Gulikers

NDT and diagnosis of problems

3D localization of the reinforcement in reinforced concrete slab by using GPR 175
K. Agred, G. Klysz & J.P. Balayssac

Determination of the electrical resistivity of concrete structures using electrical impedance tomography 181
A. Asgharzadeh, K. Reichling & M. Raupach

NDT for damage diagnosis in shear-critical concrete beams using external PZTs and a new wireless monitoring system (WiAMS) 187
M.E. Voutetaki, N.A. Papadopoulos, C.E. Chalioris & C.P. Providakis

Effect of stirrups on reinforcement corrosion measurements in concrete 195
C.-T. Chen, C.-J. Li & T.-P. Chang

Reinforced concrete NDT research and practice in Turkey: A gap analysis 201
O. Gunes, C. Sengul, C. Colak & M. Asan

In-situ methods of detecting steel corrosion using permanent and non-electronic systems 207
T. Juraschek & O. Weichold

Influence of the reinforcement on concrete resistivity with a new measurement technique 213
A.Q. Nguyen, G. Klysz, F. Deby & J.P. Balayssac

Injection quality of steel cable ducts evaluated by NDT 221
C.G. Petersen

Non-destructive testing of joints in precast element structures 229
C.G. Petersen & H.D.O. Recillas

Development of electrically conductive resins for the on-site fabrication of sensors for corrosion detection and risk assessment in reinforced concrete 235
P.B. Sassmann & O. Weichold

Frequency dependency of concrete resistance measurements 239
A.-M. Thoresen, K. Hornbostel & M.R. Geiker

Patch repair

An experimental investigation into the effects of water and binder-related parameters on restrained shrinkage cracking in concrete patch repair mortars 247
P.A. Arito, H. Beushausen & M.G. Alexander

Strength recovery of concrete repaired using normal and rapid hardening repair mortars 253
A. Badr & S. Ioannou

Development of new types of repair materials by imparting thixotropic properties 259
H. Fujiwara, M. Maruoka, T. Kawato, T. Sugawara, K. Yoshikawa, T. Abe, S. Takemoto & H. Kasahara

Microwave system for *in-situ* curing of concrete repair 267
P.S. Mangat, K. Grigoriadis, S. Abubakri, A. Javaid & C. Zhao

Temperature development in microwave cured repair materials 273
P.S. Mangat, K. Grigoriadis & S. Abubakri

Sustainable and effective self-leveling mortars 281
I. Papayianni, E. Anastasiou, P. Avramidis & P. Chatziagorastou

The effect of binding system of mortars on chloride ion penetration 287
I. Papayianni, M. Papachristoforou & F. Kesikidou

Bonding properties of magnesium phosphate cement-based repair materials 293
C. Shi, N. Yang, L. Chong, Z. Wu & J. Yang

Effectiveness of different repair materials and methods used for the repair of chloride corroded reinforced concrete structures 301
K.K. Sideris, E. Manikas & A. Michalakopoulos

Analytical investigation of bond between ECC matrix and steel reinforcement 305
S.P. Tastani

Flexural response of corroded reinforced concrete beams: Experiments and finite element analyses 311
G.G. Triantafyllou, T.C. Rousakis & A.I. Karabinis

Performance of rapid repair mortars with sulfate aluminium cement and Portland cement 317
J. Yuan, W. Yang, X. Cai & Q. Li

Early-age cracking resistance of repair cement mortar with copolymer powder and fibers 325
W. Yang, X. Cai, Y. Ge, J. Yuan & D. Zhou

Repair and preservation of heritage structures, Roman cement

Historical and structural aspects of the durability and maintenance of a reinforced concrete market hall building from the early 20th century 335
P. Berkowski & M. Kosior-Kazberuk

Restoration of historical heritage in Russia: The age of architectural concrete 345
V.R. Falikman & V.V. Deniskin

The survey of a historical building from the beginning of the previous century. Evaluation of mechanical characteristics of the load bearing system 353
I. Papayianni, V. Pachta & A. Milosi

Repair of fire damage

Study on the effect of firing heating on FRC with various types and content 363
D. Choumanidis, P. Nomikos, A. Sofianos, E. Badogiannis & E. Papadimitriou

Investigation, assessment and repair of a fire-damaged reinforced concrete structure 369
A. Elenas & K.K. Sideris

Innovative materials for passive fire protection of concrete 373
K.M. Sakkas, P. Nomikos, A. Sofianos & D. Panias

Risk management

Application of carbon nanotubes in structural health monitoring of steel-reinforced concrete 381
P.H.P. Lagason, O.V.M. Antonio & S.A.P. Peñeda

Service life modelling

Chloride threshold values for corrosion in concrete – a myth? 391
U.M. Angst & B. Elsener

Durability design of reinforced concrete structures – service life estimation 397
S. Demis & V.G. Papadakis

Service life estimation of cracked and healed concrete in marine environment 409
M. Maes & N. De Belie

Propagation of pitting corrosion of steel in concrete: Conceptual models for local cross section loss 417
R.B. Polder, U.M. Angst, J. Pacheco & W.H.A. Peelen

Influence of crack width on the initial corrosion of surfaces exposed to high chloride 423
M. Schneider, E. Baumgartner, P. Druml & F. Pruckner

The "Predicted Performance Curve" (PPC): A new structural performance deterioration model for concrete infrastructure 429
N. Semaan & T. Zayed

Service life design of concrete structures using probabilistic modelling tools: Statistical analysis of input parameters 437
I.P. Sfikas & J.P. Ingham

Strengthening materials and techniques/Repair with composites

Assessment of strengthening techniques of reinforced concrete elements rehabilitated with composites 449
D.V. Achillopoulou, A.N. Kiziridou, G.A. Papachatzakis & A.I. Karabinis

Experimental analysis for the development of an Ultra High Performance Fiber Reinforced Concrete (UHPFRC) 467
A.L. Mina, M.F. Petrou & K.G. Trezos

Bond performance of the deep embedment shear strengthening method 471
M. Caro, Y. Jemaa, S. Dirar & A. Quinn

Shear strengthening of reinforced concrete T-beams with EB-FRP sheets 479
C.E. Chalioris & C.A. Argiriou

Flexural and cracking behaviour of concrete beams reinforced with FRP bars 487
C.E. Chalioris, P.K. Kosmidou, T.A. Panagiotopoulos & C.G. Karayannis

Fatigue design of RC beams strengthened in flexure with FRP laminates 493
B. Charalambidi, T.C. Rousakis & A.I. Karabinis

Evaluation of the mechanical behavior of FRC with different types of fibre, through Barcelona and bending testing 499
D. Choumanidis, P. Nomikos, A. Sofianos, E. Badogiannis & E. Papadimitriou

Improving the ductility of FRP strengthened unidirectional RC slabs via hybrid CFRP/BFRP reinforcing 505
T. Donchev, D. Petkova & A. Pavlovic

Stress field analysis of reinforced concrete slab with central cutout strengthened using FRP laminates 511
L. Vasiliadis, I. Kavvadias, I. Litina & K. Bantilas

Pullout behavior of single steel fiber with different strengths of concrete 517
M.I. Khan & W. Abbass

FRP confinement of high-aspect ratio concrete columns 525
C.S. Kolyvas, T.C. Triantafillou & A.I. Bernakos

Durability restoration of cementitious composites via micro encapsulated mineral repair agents 531
C. Litina, A. Kanellopoulos & A. Al-Tabbaa

Cyclic response of large lightly reinforced concrete walls made of plain and fibre concrete 539
C.G.R. Mircea, A. Faur, A. Harcsa, M. Mulea & C. Baera

Differences in losses of prestress between steel and FRP reinforcement 547
M. Mirshekari, T. Donchev, D. Petkova & M. Limbachiya

Use of 3D microscopy in the analysis of FRP strengthened concrete 553
D. Petkova, T. Donchev & D. Wertheim

CFRP-steel hybrid retrofitting of steel-concrete composite structures 557
M. Subhani, R. Al-Ameri & M.I. Kabir

Bacteria-based self-healing mortar: A comparison of two studies 565
E. Tziviloglou, V. Wiktor, H.M. Jonkers & E. Schlangen

Some considerations on precipitation rate of calcium carbonate in bio-based materials used for concrete repair 571
K. Kawaai, I. Ujike, S. Yamamoto & P.Y. Putri

Study on tensile bearing behavior of nodes in CFRP grid 579
B. Wang, K. Uji, V.D. Tran, A. Ueno & K. Ohno

Resistance to fatigue of self-healed concrete based on encapsulated polymer precursors 585
J. Feiteira, V. Couvreur, E. Gruyaert & N. De Belie

Surface protection methods and materials

Concrete protection with hydrophobic impregnation – importance of correct specifications 591
M. Donadio & N. Anagnostopoulos

Development of chloride induced reinforcement corrosion in cracked concrete after application of a surface protection system 595
F. Hiemer, S. Keßler & C. Gehlen

An investigation of the surface properties of air-cured microconcretes developed with controlled permeability formwork liners using destructive and non-destructive methods 603
A.S. Marinos, M.S. Katsiotis, G. Batis, M. Beazi-Katsioti, J.L. Gallias & V. Kaloidas

Durable surface repair of waterway engineering structures with sprayed textile reinforced concrete 613
C. Morales Cruz & M. Raupach

Sustainable repair

An engineering example of energy saving renovation of external wall of original building with lightweight insulation composite panel 621
Y. Shi, Y. Zhang, J. Shi, S. Yang & W. Liu

Production of durable concretes using EAF slag aggregates 625
K.K. Sideris, A. Chatzopoulos & Ch. Tassos

Author index 631



Taylor & Francis
Taylor & Francis Group
http://taylorandfrancis.com

Concrete Solutions – Grantham et al. (Eds.)
© 2016 Taylor & Francis Group, London, ISBN 978-1-138-03008-4

Preface

The Concrete Solutions series of international conferences on concrete repair began in 2003 with a conference held in St. Malo, France in association with INSA Rennes. Subsequent conferences have seen us partnering with the University of Padua in 2009, with TU Dresden in 2011 and with Queen's University Belfast in 2014. 2016 sees us in Thessaloniki, partnering with both Aristotle University of Thessaloniki (AUTH) and Democritus University of Thrace (DUTH) and brings together delegates from some 30 countries to discuss the latest advances and technologies in concrete repair.

Strengthening and retrofitting are major themes this time, with NDT and electrochemical repair following closely. Some interesting theoretical approaches have been taken and some challenging papers are presented concerning the "state of the art" and do we really understand and approach such topics as corrosion monitoring correctly.

This book is an essential reference work for those working in the concrete repair field, from Engineers to Architects and from Students to Clients.

The next conference in the series will be held in 2019 in Istanbul.



Taylor & Francis
Taylor & Francis Group
http://taylorandfrancis.com

Concrete Solutions – Grantham et al. (Eds.)
© 2016 Taylor & Francis Group, London, ISBN 978-1-138-03008-4

Sponsors



Concrete Solutions 2016 is sponsored by the following

Democritus University of Thrace

Democritus University of Thrace (DUTH) was established in July 1973 by Legislative Decree No. 87 of 27 July 1973, and started operating during the academic year 1974–1975. It was named "Democritus" in honour of the ancient Greek philosopher Democritus, who hailed from the town of Abdera in Thrace.

The administration of DUTH is headquartered in Komotini, which is the capital city of the Administrative Region of Eastern Macedonia and Thrace. The University is currently operating eight Faculties and nineteen Schools in four cities of Thrace – eight in Komotini, five in Xanthi, four in Alexandroupolis and two in Orestiada. Overall, more than 15,000 students are studying at DUTH at undergraduate and post-graduate level.

The University plays an important role in strengthening the national and cultural identity of the region of Thrace, and contributes to the high level of education in Greece. Relying on the quality of teaching and research level, DUTH has secured a place among the best Greek Universities.

Portable Test Equipment

Proceq, founded 60 years ago, manufactures high-quality portable testing instruments for the non-destructive testing of material properties of metal, concrete, rock, paper and composites. Proceq designs and manufactures its products in Switzerland and with its in-house Research and Development team continues to bring products to the market that set new standards for the industry. The Swiss company with subsidiaries in North and South America, United Kingdom, Russia, the Middle East, China and Singapore provides its international customers with excellent local support. Proceq is part of the Tectus Group.

The Institute of Concrete Technology

The Institute of Concrete Technology – The Institute aims to promote concrete technology as a recognised engineering discipline and to consolidate the professional status of practising concrete technologists around the world. The Institute offers designatory letters TechICT, AfflICT, AMICT, MICT, or FICT to appropriately qualified individuals, either by the highly regarded Institute's own examinations or via an alternative qualifications route. More information can be found at http://ict.concrete.org.uk/

Germann Instruments

Germann Instruments, are the leading manufacturer of advanced state-of-the-art Non-Destructive Testing Equipment for evaluating concrete structures. We are committed to advancing knowledge as well as bringing new technology to market. Germann Instruments is the developer of the most accurate test systems for measuring the in-place compressive strength of concrete, the LOK-Test and the CAPO-Test. Germann Instruments was the first to bring to market the DOCter Impact-Echo and the s'MASH Impulse Response systems for non-destructive investigation of concrete structures.

Germann Instruments offers a complete range of products for corrosion evaluation, analysis of chlorides, and service life estimation. We, as well, are the only producer of a portable concrete rheometer and the Air Void Analyzer for fresh concrete.

Hilti offers products, systems and services that have leading-edge technology and provide professional customers in the construction and energy sectors with innovative solutions that feature outstanding added value.

Active in more than 120 countries, Hilti not only operates production facilities and R&D centers, but is also involved in various international technology partnerships. Hilti stands for exceptional innovations, the highest quality and direct customer relationships. We are committed in developing innovative systems for rehabilitation and strengthening of existing main concrete elements.

In addition to standard products we can meet your unique applications in the following areas:

Anchoring, Drilling, Diamond Coring, Chemicals and highly accurate measuring and detection systems Ferroscan PS250 and PS1000.

Through our engineering services we manage to support every construction project, offering with our complete portfolio the best and less invasive solution for each application.



Ed Zublin AG

The roots of Ed. Züblin AG lie in Strasbourg in Alsace, where the company was founded by Swiss engineer Eduard Züblin in 1898. Today, Züblin is headquartered in Stuttgart and, with some 13,000 employees and an annual construction output volume of € 3.1 billion, is one of Germany's leading construction companies. For more than 110 years, Züblin has been successfully realising challenging construction projects nationally and internationally and is the German market leader in building construction and civil engineering. The company's range of services includes all construction related tasks – from complex turnkey construction to civil engineering, bridge building and tunnelling to public private partnerships.

Züblin places great importance on its cooperation with clients and subcontractors in the realisation of building construction projects. The Züblin teamconcept, a partnering model with some 15 years of experience on the market, guarantees high standards of quality at an early stage, on time and within budget constraints.



Sika Hellas

Sika AG, was established in 1910 located in Switzerland. Nowadays, Sika is a global player in specialty chemicals for construction and Industry, holding a leading position in the development and production of systems and products for bonding, sealing, damping, reinforcing and protecting in the building sector and the mottor vehicle industry. Sika has subsidiaries in 90 countries around the world and manufactures in over 160 factories. Approximately 17.000 employees.

SIKA HELLAS Sika Hellas was founded in 1995. Since then, it has managed to be the first choice of the Greek engineers providing the most innovative and specialized solutions in the specific construction field. The launch of innovative products and applications, with certified quality and excellent technical support, are key features of its corporate identity. Its reputation in solving the most demanding technical challenges makes it a key-player in the implementation of the most of prominent projects. Through close cooperation with technical and commercial collaborators throughout the Greek territory, Sika Hellas has achieved conveying this state-of-the-art technology even in the most distant site.



The special anodes manufacturing division is specialised in the manufacturing and distribution of both sacrificial and impressed current anodes for steel in concrete throughout the world under our own brand names.

Our product range:

- ZLA Zinc Layer Anode: A surface applied zinc foil with ion-conductive adhesive.
- ZDA: A zinc discrete concrete embeddable anode.
- RollAnode: A zinc discrete anode for pre-drilled holes.
- Snap-on anode: A zinc discrete anode designed for precast concrete.
- CorrAnode: A discrete ICCP MMO-Ti anode with dia 10 mm × max 1 mtr L for pre-drilled holes.
- And titanium accessories for CP systems.

NORDIA SA

NORDIA S.A. is a Hellenic group of companies dedicated in producing high quality, safe and user friendly building materials. Under the MARMOLINE brand name we are producing innovative dry mix mortars, adhesives, thermal insulation systems, and mortars for the repair and protection of concrete structures. Since 1998, when Marmoline was founded, we have provided many big construction sites in Athens with our products. Now we are also expanding abroad, opening a significant path to China and Australia.

We place particular emphasis in delivering applicator friendly and final user safe products for building "kind to the environment" residential and commercial constructions. We continuously reduce our footprint to the environment, saving energy, water and resources, modernizing our management methods and improving our knowledge and skills.

MARMOLINE's vision aims to confront two current challenges:

- Support the need of society for maximum energy efficiency and environmental protection
- Satisfy people's need for comfortable, relaxed, care-free living in their homes, offices and commercial buildings.

Case studies



Taylor & Francis
Taylor & Francis Group
http://taylorandfrancis.com

Concrete Solutions – Grantham et al. (Eds.)
© 2016 Taylor & Francis Group, London, ISBN 978-1-138-03008-4

Protection of a pier structure using an alternative combined electrochemical approach

R. Brueckner
Mott MacDonald, Bristol, UK

C. Atkins, R. Merola & P. Lambert
Mott MacDonald, Altrincham, UK

ABSTRACT: The pier structure was constructed in 1877 to serve ferries to the mainland of the UK and, due to popular demand, a new station platform was built on the pier in the 1930's. The pier structure with its railway station is still in operation and is required to operate for a significant time. Major refurbishment works were necessary to protect the submerged iron and steelwork and the exposed reinforced concrete elements from deterioration.

The pier structure has suffered from severe corrosion of the reinforcement and the steelwork in the marine environment. Spalling and delamination of concrete and significant section loss of the steel elements were identified. Cathodic Protection (CP) was selected as the most appropriate repair, when considering the condition of the structure, its location in a marine environment over a site of special scientific interest, access restraints and the fact that repair works had to be carried out on an operating structure. This was combined with conventional concrete repair to reinstate spalled areas.

Marine anodes were to be used to protect steelwork up to mid tide. It was considered that the same system may be able to protect steelwork in concrete above this level. This would increase the working window and reduce the extent of anode installation in the concrete. The amount of work could be reduced by 20% and the productive working time increased by 55% with an end product that provided the required protection to the client. The paper discusses approach taken to identify the alternative method, the challenges experienced and the effectiveness of the alternative approach based on initial tests and on monitoring results.

1 INTRODUCTION

Ryde Pier is England's oldest seaside pier. Measuring 681m, it still features a timber-planked promenade and has carried pedestrians and vehicles since it was built in 1814. A second tramway pier opened five years later, while in 1880 a third pier was opened alongside the first two, providing a direct steam railway link to the pier-head. In 1895 a concert pavilion was constructed at the pier-head and over the next sixteen years the original wooden piles were replaced in cast iron. The pier head was remodelled in the 1930s using concrete.

In 2009 an outline repair specification was produced for the pier involving two cathodic protection systems. One to protect the steelwork, one to protect the reinforced concrete. For the concrete system the outline design required work down to 1 m below the average tide level. This would involve cutting into the concrete, installing anodes and grouting them in place, which would be a difficult process due to the surrounding tidal environment. Access to this level would be required for prolonged periods and would need to be robust enough to cope with being submerged regularly.

For the iron and steelwork system the outline design used conventional marine anodes placed on the sea bed. These protected up to mid tide level. It was considered that it may be possible to use the marine anodes to protect the concrete above mid tide level and a trial was undertaken. After a detailed interpretation of the results it was confirmed it would work to at least 1 m above mid tide. The concrete needed protecting to 1 m below mid tide level, so installation of anodes at 0.5 m below mid tide level would be required. After demonstrating that the system could protect to 1 m above mid-tide level using marine anodes, the concrete anodes could actually be installed in the concrete at 1.5 m above mid-tide level. This removed the requirement to install anodes into and below the horizontal bracing on the pier. This approach also eliminated the need to carry out significant work below mid-tide, so access could be simplified.

Raising the level of anode installation saved 600 m of chasing, anode installation, wiring and grouting

operations. This was approximately 20% of the total length of anode on the project, but more significantly was also the most difficult to install. From an installation point of view, it was estimated productive time would increase by 55%. In addition the area most likely to be affected by the weather was removed, reducing the risk to the programme.

The system was commissioned in 2013, with one year of monitoring demonstrating that it worked successfully. This paper presents subsequent monitoring data and discusses protection criteria.

2 RESULTS

The instant-off data with respect to time is presented in the following tables. There are gaps in the data that are the result of difficulties in downloading the data files and therefore only the most recent potentials are stated. The system collects depolarisation data monthly and this can be seen as spikes in the data that depolarised, typically the data from the deck soffit and upper beams.

2.1 *Protection criteria:*

Protection criteria are required contractually to demonstrate that the design and installation functions correctly. The relevant standard for reinforced concrete is BS EN ISO 12696 2012, that quotes in Section 8.6 three criteria.

"For any structure, any representative steel in concrete location shall meet any one of the criteria given in items a) to c):

a) an "Instantaneous OFF" potential more negative than −720 mV with respect to Ag/AgCl/0,5 M KCl; or
b) a potential decay over a maximum of 24 h of at least 100 mV from "Instantaneous OFF"; or
c) a potential decay over an extended period (typically 24 h or longer) of at least 150 mV from the instant off subject to a continuing decay and the use of reference electrodes (not potential decay probes) for the measurement extended beyond 24 h"

2.2 *Zone 1*

The pre-energisation potentials, and most recent measured potentials (mV vs Ag/AgCl/0.5 mKCl) for zone 1 are presented in table 1.

Prior to energization, all potentials measured ranged between −321 mV and −434 mV. The reference electrode installed in the beam below the deck was unstable. It was expected that the potentials at or below 1 m above mean tide level would tend towards significantly negative values indicative of reduced oxygen availability combined with polarisation from the marine anodes. In this case the only reference electrode that did not do this was installed in the soffit of the deck. The electrode at 2 m indicated a more negative potential than that at +1 m above mean tide level.

Table 1. Zone 1 Reference Electrode Potentials.

Location	Pre-energisation Potential mV	Potential measured 20/12/15 mV	Approximate negative shift mV
Deck Soffit	−397	−477	80
Beam +1 mOD	−434	−619	185
Col +2 mOD	−321	−843	522
Beam Below Deck	−522	−578	56

Table 2. Zone 2 Reference Electrode Potentials.

Location	Pre-energisation Potential mV	Potential measured 20/12/15 mV	Approximate negative shift mV
Deck Soffit	−339	−475	136
Beam +1 mOD	−305	−795	490
Col +1 mOD	−464	−833	369
Beam Below Deck	−356	−488	132

Table 3. Zone 3 Reference Electrode Potentials.

Location	Pre-energisation Potential mV	Potential measured 20/12/15 mV	Approximate negative shift mV
Deck Soffit	−375	−506	131
Col +1 mOD	−217	−426	209
Beam +1 mOD	−269	−701	432
Beam Below Deck	−226	−476	250

2.3 *Zone 2*

The pre-energisation potentials, and most recent measured potentials (mV vs Ag/AgCl/0.5 mKCl) for zone 2 are presented in table 2.

Prior to energization, the potentials ranged from −305 to −464 mV. From the above data, electrodes at +1 mOD indicated protection. Values from the reference electrode in the deck soffit initially showed significantly negative readings, but were more positive in December 2015. The beam below deck level was more negative than would be expected. Depolarisations of the electrodes at the deck soffit and at the beam below deck level have indicated protection in the past.

2.4 *Zone 3*

The pre-energisation potentials, and most recent measured potentials (mV vs Ag/AgCl/0.5 mKCl) for zone 3 are presented in table 3.

Pre-energisation readings ranged from −217 mV to −375 mV. In the above data, the column at +1 mOD was more positive than the deck soffit, and showed

Table 4. Zone 4 Reference Electrode Potentials.

Location	Pre-energisation Potential mV	Potential measured 20/12/15 mV	Approximate negative shift mV
Beam Below Deck	−249	−389	140
Beam +1 mOD	−476	−537	61
Col +1 mOD	−363	−668	305
Deck Soffit	−299	−387	88

Table 5. Zone 5 Reference Electrode Potentials.

Location	Pre-energisation Potential mV	Potential measured 20/12/15 mV	Approximate negative shift mV*
Beam +1 mOD	−300	−911	611
Beam below deck	−337	−259	(−78)
Col +1 mOD	−507	−634	127
Deck Soffit	−358	−249	(−109)

*values in brackets signify a positive shift

significant variability in measured potential. The beam at +1 mOD was significantly negative. Depolarisations of the electrodes at the deck soffit and at the beam below deck level have indicated protection in the past.

2.5 *Zone 4*

The pre-energisation potentials, and most recent measured potentials (mV vs Ag/AGCl/0.5 mKCl) for zone 4 are presented in table 4:

The pre energisation potentials ranged from −249 to −476 mV. The beam at +1mOD is not sufficiently negative to indicate protection but the depolarisation data confirms 100 mV decay was achieved. The deck soffit and beam potentials are relatively consistent.

2.6 *Zone 5*

The pre-energisation potentials, and most recent measured potentials (mV vs Ag/AgCl/0.5 mKCl) for zone 5 are presented in table 5:

Significant negative potentials were found at +1 mOD. For the column, the potential did not achieve the −720 mV criteria but was indicative of low oxygen and trending in a negative direction. The beams below deck and the deck soffit potentials that show a positive difference on the two dates shown did not exhibit a significant trend in polarization.

3 DISCUSSION

On this structure, when the system was energised all potentials shifted in a negative direction. Over the first twelve months, one or more of the protection criteria were achieved at each reference electrode, and so in accordance with BS EN ISO 12696, the structure is protected.

The protection criteria within BS EN ISO 12696 Section 8.6 sound clear and straightforward, however there are also a large number of informative notes that accompany the above.

NOTE 4 states:

"Criteria, a), b) and c) are not necessarily supported by theoretical considerations but are a non-exhaustive, practical series of criteria to indicate adequate polarization which will lead to the maintenance or re-establishment of protective conditions for the steel within the concrete."

NOTE 7 states:

"The criteria given in items b) and c) above may be invalidated by variations in temperature, and moisture content. Such variations, themselves, can be the cause of significant changes in steel/concrete potentials."

NOTE 8 states:

"For structures, such as buried, immersed or coated structures, where oxygen availability within the concrete is limited, the criteria given in items b) and c) above may not be practical due to the very slow rate of depolarization, as detailed in 8.5, Note 2. Similarly, as detailed in the paragraph below Note 2 in 8.5, potential shift measurement may not be equivalent to potential decay over a limited time period and changes in the "natural" or "as found" due to oxygen depletion can lead to serious errors in assessment of potential shift."

Section 8.5 Note 2 states:

"For buried (particularly those buried in wet conditions or impermeable clays) and immersed structures and for atmospherically exposed structures that incorporate a surface coating that limits oxygen availability within the concrete, potential decay may be very slow and may extend to weeks. In the extreme, oxygen availability at the steel may not be sufficient to maintain passivity of the steel/concrete interface and the potential may "rest" at a relatively negative value. In these conditions potential decay may not be a practical protection criterion."

The subsequent paragraph that is not a note and is therefore mandatory rather than informative, states:

"Potential shift (see 8.4, Note 1) may be equivalent to potential decay but only if the initial potential ("natural" or "as found" from which the potential shift is measured) is determined immediately before energizing the cathodic protection system and if this value is not affected by stray current. Particular caution should be exercised if potential shift measurements are used as a protection criterion on buried, immersed, water saturated or coated structures as the "natural" or "as found" potential may be subject to very significant negative potential changes as oxygen is depleted within the concrete. Negative potential shifts of 200 mV to 300 mV are quite possible due to oxygen depletion without the application of cathodic protection. "

Annex A2 provides further information on protection criteria. It states:

"In older structures with corroding steel, cathodic protection is part of the rehabilitation concept and

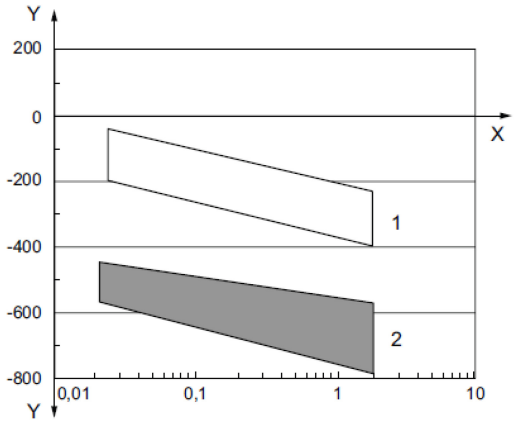

Figure 1. Figure A2 from BS EN ISO 12696 2012 showing values of E Pit (denoted 1) and E Prot (denoted 2) measured on steels buried in sand covered with saturated calcium hydroxide solution, from Pedeferri (1996). Potentials are expressed in mV vs Ag/AgCl/0.5 MKCl, the X axis is chloride concentration in mols/l.

is aimed to decrease the corrosion rate of the steel from significant to negligible values. For this purpose, the steel/concrete potential should be lowered (made more negative) to values in the range of the protection potential E_{prot}. The corrosion potential E_{corr} and the protection potential E_{prot} are dependent upon environmental conditions (chloride content, pH at local anodic sites, temperature, oxygen content, humidity). Based on the complex interaction of these factors and also practical experience, the definition of one precise protection potential is impossible and also unnecessary for cathodic protection of steel in concrete. It is this complex interaction of factors that dictates that a range of criteria are properly required for cathodic protection of steel in concrete, as is reflected in 8.6." Figure 1 presents the accompanying figure.

To convert between moles per litre to a mass of chloride by mass of cement it is necessary to make a series of assumptions. For a 14% cement content, 0.4% chloride by mass of cement equals 0.056% chloride by mass of concrete. This is 0.56mg of chloride per gram of concrete, which in turn is 0.016 millimoles of chloride per gram of concrete. Assuming a density of 2400 kg/m^3 for concrete this gives 38 moles of chloride per cubic meter of concrete. If the porosity is assumed to be 20%, this is 38Moles of chloride per 200 litres of pore water, which is approximately 0.2 M/l. 1 M/l is approximately 2% chloride by mass of cement.

A large proportion of area 2 in the figure above is more positive than −720 mV. There is a need for a degree of conservatism in criteria in standards so this is not unexpected. The reference quoted in BS EN ISO 12696 is Pedeferri (1996), however this figure is taken from earlier work (Cigna 1981) and it has not been possible to obtain this at this time.

Pedeferri states that with potentials in the range (E_{pit} to E_{prot}) corrosion will not initiate but, if initiated, it can propagate. Nevertheless when the potential of corroding steel is taken in this range, the potential differences between cathodic and anodic areas are reduced and thus the current exchanged between them and the active zones are reduced. Consequently, the corrosion rate of the active zones (which is mainly connected with the functioning of these active-passive couples) is reduced. This suggests that a significant reduction in corrosion rate is achieved above E_{prot}.

Pourbaix (1974) states that it may be sufficient to prevent the pits and crevices from growing by placing the metal in a state of perfect passivation, which he stated was about −400 mV on the standard hydrogen scale (SHE) for iron and steels. −400 mV SHE is equivalent to −641 mV vs Ag/AgCl/0.5 MKCl. This falls within the range that Pedeferri proposed for protection, but is obviously significantly more positive than −720 mV.

BS EN 12954 "Cathodic protection of buried or immersed metallic structures — General principles and application for pipelines" also includes protection criteria for a range of metals. These are all quoted to the nearest 0.05 V vs the Copper/Copper Sulphate (Sat) reference Electrode. For steel in concrete it suggests −0.75 V. The correction to the Normal Hydrogen Scale states a difference of 0.32 V. The protection criteria for steel in concrete is therefore −0.43 VNHE or −0.67 V Ag/AgCl/0.5 MKCl, which is again more positive than that quoted in BS EN ISO 12696.

For the purposes of a contract the figure of −720 mV vs Ag/AgCl/0.5 M KCl is applied, as it is codified but based on Pedeferri, Pourbaix and BS EN 12954 protection is achieved at values significantly more positive than this. Whilst it is a requirement to have protection criteria such that they are conservative, −720 mVvs Ag/AgCl/0.5 M KCl may be too conservative. It is additionally worth noting that although equipment and reference electrodes are available that provide readings in 0.1 mV or finer, Pourbaix's work generally quotes to the nearest 0.1 V, BS EN 12954 quotes to the nearest 50 mV, Pedeferri's work too is to the nearest 50 mV. A certain amount of common sense is required in application of −720 mV, however as it can be used within a contract, this may well exclude this option. −719 mV is more positive than −720 mV and therefore does not meet the criterion in BS EN ISO 12696.

BS EN 12696 cl 8.5 Note 2 states that a lack of oxygen results in a slow depolarisation. Historically on this structure if potentials are more negative than around −600 mV little depolarisation is noted over a 24 hour period. Potentials more negative than −600 mV appear to indicate slow depolarisations and hence a low level of oxygen availability. This falls within Pedeferri's proposed range of potentials for protection. It is considered that for the tidal exposed elements on this structure protection has been achieved at −600 mV and BS EN 12696 is conservative. Additional polarisation beyond this to achieve values more negative than −720 mV vs Ag/AgCl/0.5 M KCl is unlikely to provide increased corrosion protection.

4 CONCLUSIONS

The use of marine anodes to protect concrete above mid tide level was demonstrated via a trial and was successful. Protection was achieved at +1 mOD, which limited the anode installation down to a level of +1.5 mOD.

It is considered that for this structure, polarisation of the steel more negative than −600 mV would provide little additional corrosion protection. A significant negative shift has been achieved from the pre energisation potentials accompanied with a slow depolarisation.

REFERENCES

BS EN ISO 12696 2012 “Cathodic Protection of Steel in Concrete”, Pub BSI

BS EN 12954 (2001) Cathodic protection of buried or immersed metallic structures — General principles and application for pipelines” pub BSI.

Cigna, R. Fumei Sulla protezione catodica dei ferri nel calcestruzzo. Ind. It. Cemento, 1981, 9

Pedeferri, P., Cathodic Protection and Cathodic Prevention, Construction and Building Materials, Vol. 10, No. 5, pp. 391–402, 1996

Pourbaix M, Corrosion Science 1974 v14 pp25 to 82



Taylor & Francis
Taylor & Francis Group
http://taylorandfrancis.com

Concrete Solutions – Grantham et al. (Eds.)
© 2016 Taylor & Francis Group, London, ISBN 978-1-138-03008-4

Analysis of adaptation of reinforced concrete structures from early 20th century to the needs of modern requirements – a case study

G. Dmochowski & P. Berkowski
Wrocław University of Technology, Wrocław, Poland

ABSTRACT: This work highlights the problems connected to defining the bearing capacity and possibility of further usage of the reinforced concrete floors constructed in different type of buildings erected in the beginning of the 20th century, and which are in use to this day. In this case, proper evaluation of the static scheme, size of the elements, type and the amount of reinforcement bars, as well as definition of concrete class are the main issues. Material parameters, provided by the research, may often be different from the historical data found in literature, which does not necessarily mean that they are incorrect, but require extensive verification. These problems are presented in the example of two historical buildings situated in Wroclaw, which fulfil different utility functions. The first one is an industrial storage hall and the second one is a former customs building, in later times used as police headquarters.

1 INTRODUCTION

Reinforced concrete structures built in the early 20th century are now over 100 years old. Based on general guidelines concerning service lifetime of such buildings they are now nearly at the end of their service. However, most of them are still in use, often differently to the original purpose. In most cases, excluding structures damaged during the war, these buildings remain in a relatively good technical condition. Local concrete losses, carbonation, corrosion of concrete cover and reinforcement bars are the man visible defects.

Numerous research indicate that in most cases the used concrete was of a fairly poor quality, which can be compared to the current classes ranging from C7,5/C10 to C10/C15 and for rebar smooth steel with design strength of 150 MPa was used. To meet the requirements for further use (especially concerning new and higher service loads) every construction must be checked due to material properties and recalculated, then eventually undergo the process of strengthening and protection.

Due to the fire resistance requirements and the overall poor concrete quality these aims cannot usually be achieved with the use of modern techniques, as for example carbon strips or sheets. Structures must be confined to the alternation of static schemes, cross-section increase or additional structural support application, in connection to providing proper thickness and tightness of concrete slabs.

Some problems connected with these actions are presented in two examples: the first is the cellar floor slab with binders in one of the industrial halls and the second is a multi-storey public service building with concrete floor slabs.

2 INDUSTRIAL STORAGE FACILITY

In this instance the building is located within the area of the Wroclaw's Technological Park. It is an old German, standalone industrial hall, built, according to the archive data, in 1940. It is of rectangular shape, possesses two over ground storeys and a full basement complex (Fig. 1).

The main load bearing structure at basement level is comprised of the outer brick walls, reinforced concrete columns and floor slabs over, steel pillars and fragmental masonry ceiling over the steel beams at the ground floor and steel roof with skylight above the first storey (Fig. 2). This hall was partially expanded after the war, increasing its area of both the ground and first floors. The building is currently unused.

The construction of the floor over the basement is post-and-beam type, with main beams situated every 6 m. Main beams are situated perpendicularly to the longitudinal walls, have six spans and cants near the columns. The cross-section of the main beams is 37×75 cm and columns 50×50 cm. Perpendicularly to the main beams are situated the secondary ones with size 30×60 cm. Based on the conducted outcrops, it was determined that the slab is 24 cm thick and covered with 5.5 cm of concrete flooring.

The bottom of the slab is covered with plaster that has thickness varying from 1.5 to 2.0 cm. Thanks to the outcrops it was possible to ascertain the occurrence of smooth steel reinforcement with 3.0 cm concrete cover for the lower layer and 7.0 to 10.0 cm for the upper layer.

Main beams have lower reinforcement at central spans 2ø18 mm + 5ø22 mm (Fig. 3), at outside spans



Figure 1. General view of old industrial hall.



Figure 2. View of main RC bearing structure in basement.



Figure 3. Rebar of main beam in basement floor.

6ø22 mm and upper reinforcement over the columns – 4ø22 mm. The floor slab from the lower side is reinforced with steel mesh ø10 mm every 16.5 × 16.5 cm (Fig. 4) and the upper reinforcement over the beams is ø10 mm every 10 cm (Fig. 5). The main column reinforcement comprises of 8ø18 mm placed all-round, connected with stirrups ø8 mm every 21 cm (Fig. 6).



Figure 4. Bottom reinforcement of floor slab.



Figure 5. Upper reinforcement of floor slab.



Figure 6. Reinforcement of main pillars.

The conducted research was supposed to answer the following questions:

– what is the highest, possible imposed load, with the expected 700 kg/m^2;
– is it possible to use vehicle loading on the floor (forklift);
– does the ceiling possess two-hour fire resistance?

In general, the technical state of the basement's ceiling was deemed sufficient. No significant damage nor excessive displacements were found. However many losses of concrete cover were noticed upon the lower

part of the ceiling. It was also noted that reinforcing bars of the lower layer were corroded although the bars in the upper layer were free of corrosion.

It is clear that over the extended period of usage, theconcrete cover suffered from carbonation and no longer serves its protective purpose.

Based on the conducted, non invasive research it was assumed that the concrete in the slab above the basement corresponds with concrete classes from C10 to C12.5. According to Czapliñski (2009) and taking the age of the construction into consideration it was determined that post-German is so called "commercial steel" with design strength 150 MPa (Ahnert & Krause 1991). No additional research upon the steel was conducted on the premise that its parameters were sufficiently covered in the historical literature.

Based on the static calculation it was determined that the carrying capacity of the floor is equal to 500 kg/m^2 and can be additionally encumbered with a heavy forklift while simultaneously reducing the carrying capacity of the floor to 200 kg/m^2. These values matched anticipated results, despite different expectations. There was no need to validate calculations any further, while additionally proving that:

– in view of the lower layer concrete cover, but also its poor technical condition, the ceiling's fire resistance had to be determined as REI60 (one hour);
– it would be possible to improve the ceiling's fire resistance by creating a new spray on its lower surface that would increase the thickness of the concrete cover of the bars, by the use of nano concrete plaster as an example. This would have to be connected to the repair or adding additional protection to the existing concrete cover. If done properly, this could result in an increase of the fire resistance to REI120.
– it is possible to increase the overall carrying capacity of the ceiling by removing the 5.5 cm thick concrete flooring and replacing it with a layer of reinforced concrete connected to the ceiling's slab by the means of steel connectors. It was estimated that this would increase the overall carrying capacity of the ceiling by 40%.
– in view of carbonation of the lower layer concrete cover it would be wise to consider its total renovation, consisting of reinforcement or adding additional protection to the existing cover. Alternatively it is possible to remove the existing concrete cover and replacing it with a new one, made according to one of the concrete repair systems.

3 PUBLIC SERVICE BUILDING

The building described is located in central Wroclaw and it was built at the beginning of the 20th century. Historical data indicates that it was completed in 1909. Before the war, it was a main customs office and was used as a police barracks in later times.



Figure 7. General view of former customs office building.



Figure 8. View of the floor structure over the basement.

The building is "U" shaped with the shorter, front façade facing the street. It consists of four over ground storeys (ground floor and three upper floors), unusable attic and basement under the outer parts of "U" wings (Fig. 7). The building's entire construction layout is longitudinal, with corridors situated on the sides of the inner yard.

The building's construction is traditional: it has masonry brick foundations and main support walls made entirely out of bricks (Fig. 8). The described building has concrete wired floors, a wooden trusswork with a queen-post structure covered with ceramic tiles. The building is currently unused.

The conducted research was supposed to answer only one question:

– are existing ceilings capable of withstanding the weight of office or residential usage?

It was determined that the floor slabs over the rooms are made from concrete, reinforced with smooth steel mesh ø8 mm every 12 × 12 cm (Fig. 9). Over the corridors, slabs are reinforced with steel strips 2 × 30 mm every 12 cm. The slab's thickness varies, from 10 to 12 cm in the corridors and 16 to 20 cm in rooms.

The overall technical condition of the floors is sufficient. However, numerous cracks were found on the slabs above corridors, especially on the ground and the first floor. The second floor has undergone a renovation process and the cracks are not visible. This damage



Figure 9. Bottom reinforcement in floor slab over the basement.



Figure 10. Twisted band-iron reinforcement in floor slab.

was caused by the corrosion of steel plates, and their weak adherence to the concrete and weak resistance to twisting (Fig. 10).

In almost every unrepaired slab, cracks are visible on the corners (Fig. 11). This is a typical kind of damage for thin reinforced concrete slabs, that lack upper reinforcing. Such reinforcements were indeed not found while conducting outcrops or using a rebar detector.

The historical data does not indicate the initial creation of any additional flooring beyond a thin finishing layer. It was added to the second and third floors in later years to even floor height between rooms and corridors and simultaneously add additional weight.

Based on the non invasive research it was determined that the concrete corresponds to the modern C15-C17.5 classes (PN-EN 206:2014), which highly exceeds initial expectations.

Based on research by Czapliński (2009) and by taking the age of the building into consideration, it was determined that post-German reinforcing steel is a so called "commercial steel" with design strength of 150 MPa (Ahnert & Krause 1991).

In the conducted static and resistance calculations it was proved that the carrying capacity of the ceiling is barely 50 k/m^2, that said, it does not even allow



Figure 11. Typical crack in corner of floor slabs.

for creation of any additional finishing layers. However, the building is known to have been used as a police barracks, which would suggest higher possible loadings. Based on that it was decided to acquire samples and then evaluate the resistance of the reinforcing steel. It was surprising that the resistance of this steel was above 500 MPa, in contradiction to both the data available in the literature (Ahnert & Krause 1991) and the personal experience of the authors of this work (Berkowski & Dmochowski 2015). After correcting the calculations it was determined that most ceilings, under few restrictions, can be adapted for further usage after changing the building's main function.

4 FINAL REMARKS

Any effort to use old reinforced concrete structural elements in renovated historic buildings requires evaluation of their bearing capacity, which is always preceded by identification of the static schemes, concrete class and both resistance and type of the reinforcing steel. It requires execution of numerous on-site examination holes and both destructive and non destructive tests.

The data concerning types and kinds of constructions from the beginning of the 20th century, despite their extensive diagnosis in literature, cannot be treated as definitive, without additional verifications, however in most cases, to the knowledge of the authors, they often meet with reality.

REFERENCES

Ahnert, R., Krause, K. H. 1991. *Typische Baukonstruktionen von 1860 bis 1960. Zur Beaurteilung der vorhandenen Baussubstanz, Band 1*. Berlin: Verlag für Bauwesen (in German).

Czapliński, K. 2009. *Products from old iron alloys*. Wrocław: Arkady (in Polish).

Berkowski, P., Dmochowski, G. 2015. Structural problems of reconstruction of blocked buildings of fire station from the 40s of the twentieth century. *Materiały Budowlane* 11:113–114 (in Polish).

PN-EN 206:2014. Concrete. Specification, performance, production and conformity.

Concrete Solutions – Grantham et al. (Eds.)
© 2016 Taylor & Francis Group, London, ISBN 978-1-138-03008-4

Application of a surface-applied cathodic protection system on a light weight concrete bridge – Part I: Condition assessment, intervention options and trial investigations

J.J.W. Gulikers
Ministry of Infrastructure and the Environment, Rijkswaterstaat-GPO, Utrecht, The Netherlands

R.G. Giorgini
CorrPre Engineering, Reeuwijk, The Netherlands

A.J. van den Hondel
Vogel Cathodic Protection, Zwijndrecht, The Netherlands

ABSTRACT: During regular inspections performed in 2011 a significant amount of hollow-sounding areas were detected over the full length of a cantilever of a box girder bridge. Being the first in a triptych, this paper will discuss the investigations that were performed for condition assessment, the evaluation of the results obtained, and the available practical options to bring the structure in an acceptable serviceable condition. Finally, the solution considered to be the most economical and practical, i.e. the application of galvanic cathodic protection, is described in more detail.

1 INTRODUCTION

During regular inspections performed in 2011 a significant amount of hollow-sounding areas were detected over the full length of a cantilever of a box girder bridge. In the first inspection report the cause was described as 'unknown'. This situation resulted in a number of detailed technical inspections in order to assess the nature, extent and cause of these hollow areas. The information thus obtained would help in the decision process on the measures to be taken for effective and efficient long-term management.

This paper constitutes part 1 of a triptych which will mainly focus on the condition assessment of the bridge, discuss the possible methods of intervention and provide details on the trial exercise with the proposed galvanic cathodic protection. Part 2 addresses practical issues regarding the execution of the galvanic protection system whereas Part 3 discusses in more detail the issue of the so-called throwing power.

2 DESCRIPTION OF THE BRIDGE

The Neerbossche bridge built in 1982 is located west of Nijmegen and spans the Maas-Waal canal. The structure consists of two twin bridges, referred to as the northern and the southern bridge, see Figure 1 for a cross section and major dimensions. Both box girder bridges are post-tensioned in the longitudinal direction with the main span composed of 31 lightweight concrete segments of 3.40 m length. In the horizontal part of the cantilevers 6 post-tensioned steel cables are employed as transverse prestressing. The low-density concrete for the segments was achieved using expanded clay as lightweight aggregate.

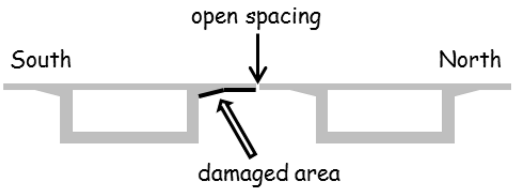

Figure 1. Cross section of the Neerbossche bridge indicating the damaged area and the open spacing between the northern and southern bridge.

In compliance with the then prevailing codes (VB 1974) the required minimum cover depth to the reinforcing steel for structural slab-like elements exposed to aggressive exposure conditions amounted to 25 mm. However, for lightweight concrete /structures the minimum cover depth should amount to at least 35 mm. It should be noted that at that time, i.e. 1982, the design service life was not explicitly specified in terms of years.

Between both bridges an open spacing of 60 mm width is present over the full length. The detailing of this spacing is such that run-off water will flow to the underside of the cantilever of the southern bridge

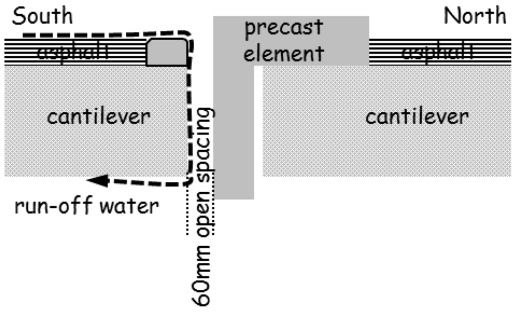

Figure 2. Detail of the open spacing between the northern and southern bridge.

whereas the underside of the northern bridge is sheltered from rain and run-off water by a precast concrete element attached to the deck of the northern bridge. A detailed sketch of the spacing is shown in Figure 2.

A regular condition assessment in 2011, i.e. at an age of 29 years, performed by visual inspection revealed the presence of large areas of delaminated concrete cover at the soffit of one of the cantilevers of the southern bridge. In view of the possible adverse consequences regarding load-bearing capacity, and taking into account the relatively young age, the local authority of Rijkswaterstaat considered it wise to execute more in-depth investigations in the short term to assess the nature and extent of the damage, as well as to find the major cause in order to develop the most economical and effective maintenance strategy for the next decades.

3 TECHNICAL INSPECTIONS

As the visual inspection in 2011 had identified the presence of significant tracks of leakage and taking into account the frequent use of de-icing salts during winter periods, it was likely that chloride-induced corrosion of the reinforcement steel was the primary cause of the extensive delamination observed on the soffit of the southern bridge. Thereupon, in September-October 2012 additional inspections (Boutz 2012a, 2012b and 2012c) were performed to find factual evidence for this reasoning. Stages 1 and 3 were focused on the condition of the soffit of the bridge, whereas in stage 2 the condition of the top side of the bridge deck was assessed. These investigations involved both destructive and non-destructive methods aimed at the detection of areas suspected of reinforcement corrosion.

For the bridge soffit, half-cell potential mapping and electrical resistance measurements were employed to detect corroding spots and areas with high moisture content, respectively. Numerous spots in the cantilever suspect of corrosion could thus be identified whereas the resistance measurements clearly indicated that large concrete areas were very moist.

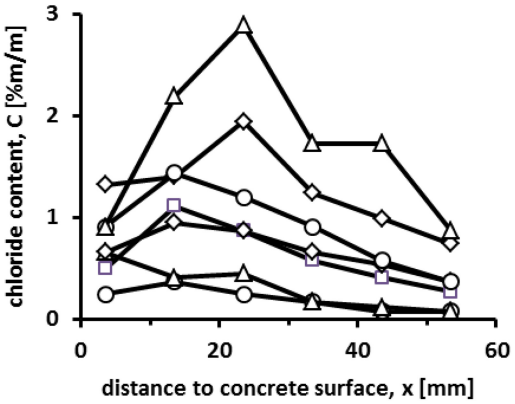

Figure 3. Variation in chloride profiles measured in the bridge soffit.

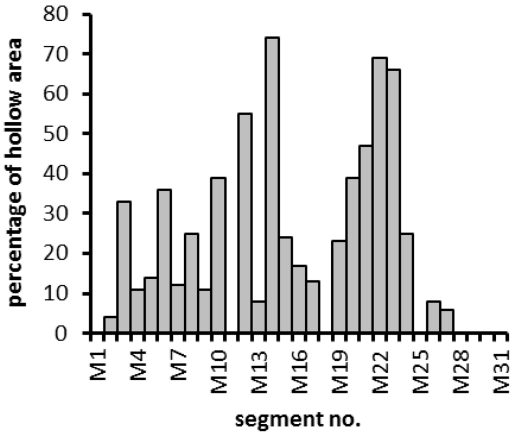

Figure 4. Percentage of delaminated surface area per segment.

At several suspect locations the cover was chipped off as to have a visual impression on the nature and depth of the corrosion attack. The appearance of the pits was considered characteristic for chloride-induced reinforcement corrosion.

In addition, a limited number of powder samples were taken so as to quantify the chloride profiles and in particular the chloride content at the level of the reinforcing steel. The results obtained revealed the presence of chlorides with contents ranging from insignificant to values far in excess of 1% (by mass of cement). Figure 3 shows the significant variation in chloride profiles obtained on the bridge soffit (Boutz 2012a, Boutz 2012b, Boutz 2012c).

In order to have a reliable estimate on the concrete surface area to be repaired, the delaminated concrete surface area was approximated by tapping, see Figure 4. The total surface area thus characterised to be delaminated added up to 44 m^2.

In view of the relatively young age of this bridge, the poor accessibility and the localised nature of the

damage, the local asset owner asked for an effective and durable solution for at least 25 years, preferably maintenance-free. With this objective and boundary conditions in mind several intervention methods were evaluated.

4 INTERVENTION OPTIONS

In view of the poor accessibility the local asset owner imposed a largely maintenance-free service life of 25 years. In addition, the original dimensions of the bridge had to be maintained not only due to aesthetical reasons but also to prevent an increase of dead weight resulting in discussions on the load bearing capacity.

For all parties involved it was evident from the beginning that, independent of the eventual solution to be chosen, it was essential to eliminate the prime source of chloride contamination of the soffit. This would be achieved simply by closing the open spacing between the two parallel bridges preventing access of run-off water from the bridge deck. In addition, it was clear that any spalled and loose concrete surface areas had to be repaired.

The least invasive and most economical option, at least in the short term, is not to intervene and adopt a "wait and see" approach until significant damage has occurred warranting the need for intervention. However, in the longer term this approach may result in an uncontrolled situation as most of the corrosion attack may proceed largely unnoticed for visual inspection, particularly when bearing in mind that inspection will have to be performed at a large distance, i.e. from the banks of the canal using binoculars. In addition, it was noted that, over time, significant loss of both steel and concrete cross sectional area may develop, leading to an unacceptable risk regarding structural safety. This risk was considered high since chloride penetration in 2011 had already advanced locally to depths beyond the embedded reinforcing steel.

Thus the major task to be addressed in all repair options would be to inhibit the corrosion process already taking place and, in addition, how to prevent future depassivation of the reinforcing steel. The latter problem was considered realistic in view of the significant amounts of chloride that were already present in the cover zone and beyond. Although exposure to external chlorides was virtually impossible after having closed the spacing, redistribution of penetrated chlorides in the undamaged areas could possibly result in an increase of the chloride content at the level of the steel reinforcement in the course of time, in excess of the critical chloride content. Moreover, it was acknowledged that there is a future risk of reinforcement corrosion developing in concrete adjacent to the patched areas due to potential differences arising from repassivation of the steel in the repaired areas. Due to this formation of incipient anodes, patch repairing is not usually adequate to stop further deterioration in the presence of chloride attack (Broomfield, 1997).

A simple, practical and relatively cheap solution would be to replace all spalled and loose concrete areas by repair mortar or shotcrete, thereby restoring passivity. In order to lower the corrosion rate, in addition a hydrophobic treatment or a coating should have to be applied on the complete concrete surface to prevent the concrete to be in direct contact with running water. As a result, the moisture content of the cover zone will gradually decrease to such an extent that the electrolytic pathway in the corrosion circuit will prove to be too resistive to sustain the corrosion process to an appreciable rate. However, it may take more than a decade to achieve such a 'dry' situation and meanwhile corrosion may still proceed at a significant rate. As porous lightweight aggregates have been used in the concrete mix it is likely that a significant amount of water will be contained in the aggregate particles acting as a water reservoir. In addition, the top surface of the bridge deck may show to be the weakest link regarding water ingress. For this option it is therefore essential to waterproof the deck surface to prevent rapid ingress of water by capillary suction. With respect to long-term cost it has to be borne in mind that both hydrophobic treatment and coating have to be re-applied every 5 to 10 years (Christodoulou et al.2014, Dai et al. 2010). Taking into account the fact that the soffit of the bridge is sheltered from direct rain, snow and hail and that the spacing between the bridges will be closed, the application of neither a coating nor a hydrophobic treatment is considered to have any beneficial effect.

A further non-invasive measure in combination with patch repair was to apply a so-called migrating corrosion inhibitor on the concrete surface. This chemical agent is expected to penetrate the concrete cover and upon reaching the reinforcing steel it will intervene in the electrochemical reactions of the corrosion process. However, the effectiveness of such surface-applied inhibitors has not yet been proven to work in practice, particularly in the long term. At present no reliable, preferably non-destructive, method is available to clearly demonstrate on site that inhibitors will result in a significant reduction of the corrosion rate in real structures (Ormellese et al. 2006, Söylev et al., 2007). Moreover, if such a method would be available, it would necessitate frequent monitoring and inevitably lead to additional cost.

The most drastic option was to remove all chloride-contaminated concrete and replace this by shotcrete. However, taking into account the observed chloride penetration depth, this would imply that over large areas, the concrete cross section of the cantilever would be significantly reduced. Due to this temporary reduction it was anticipated that the load-bearing capacity would be seriously impaired. Consequently, this option would require complex and costly structural provisions during the repair period to guarantee the load-bearing capacity. Moreover, from a sustainability point of view, several arguments were raised as this option would result into the removal of significant amounts of structurally sound concrete.

Lastly, patch repairs combined with cathodic protection was suggested as an interesting option. In view of the widespread occurrence of reinforcement corrosion a cathodic protection system covering the complete soffit surface area is considered to be most effective and efficient. Both an impressed current or a galvanic system are available to achieve sufficient corrosion protection. However, for several reasons an impressed current system is considered less attractive. Such a system requires the use of long cabling, sensors and placement of electronic equipment to frequently control, monitor and adjust its input and output. The asset owner will thus be confronted with planning of these monitoring activities and annual costs. In addition he will be faced with the risk of vandalism of the equipment and the resulting malfunctioning of the protection system which is likely to remain unnoticed for several months. Taking into account these 'undesirable events' inherent to an impressed current system it was anticipated that the application of a galvanic cathodic protection system, combined with patch repairing, would be the most appropriate option.

5 TRIAL APPLICATION OF GALVANIC CATHODIC PROTECTION

The proprietary zinc sheet anode is intended to cover the complete concrete surface. In order to act as an anode the zinc is provided with an ion conductive adhesive which simultaneously acts as an ion conductor, an adhesive, an activator as well as a storage for the non-soluble zinc salts. The protection current is generated through the continuous dissolution of zinc into the ion-conductive adhesive, resulting in the release of negatively charged electrons which are fed to the reinforcement through direct metallic contact between the zinc and the embedded reinforcing steel. This electronic contact can either be made through external wiring or through metallic pins.

In view of the nature of the prevailing exposure conditions, the presence of lightweight concrete and the deep chloride ingress several questions emerged on the long-term effectiveness of such a galvanic system.

With respect to lightweight concrete its electrical resistivity may be significantly different from 'conventional' normal weight concrete and this may affect the magnitude of the current output as well as the spatial distribution of the protection current over the reinforcing steel. If the concrete resistivity would appear to be low then this would result in a reduced overall electrical resistance of the galvanic circuit. Consequently, a higher current output would be generated resulting in a higher zinc consumption rate. Information on the actual zinc consumption rate is required to determine the zinc layer thickness to achieve the required 25 year operational service life of the cathodic protection system.

In view of the deep chloride penetration it was anticipated that not only the first layer of reinforcing steel would need protection current, but also the second layer embedded at greater depth. As the driving voltage of a galvanic system is relatively small (in most situations involving corroding steel the driving voltage is significantly less than 1 V), the so-called throwing power in depth as well as in lateral direction will be limited. Thus quantitative information on the throwing power in a lateral direction is considered relevant to determine the borders of the concrete area which should be covered with zinc sheet to achieve sufficient protection of corroding reinforcing steel embedded in neighbouring non-covered concrete areas, see Figure 5. Based on results obtained in 2002 with a similar zinc sheet anode a pronounced attenuation of protection current in the lateral direction was observed and it was concluded that steel embedded at a greater distance than 200 mm to the border of the concrete area covered with zinc sheet will not be sufficiently protected against corrosion.

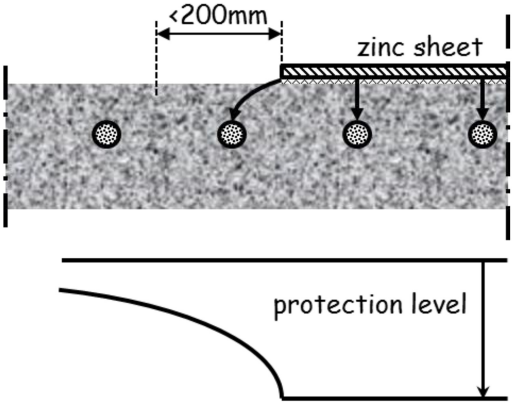

Figure 5. Schematic presentation of the throwing power.

6 CONCLUDING REMARKS

Initially it was envisaged to perform the trial during a period of no more than 6 months, however due to some delays in the tendering stage, the trial eventually lasted nearly 1 year. Based on the results of the trial it was concluded that for this situation encountered at the Neerbossche bridge:

- The throwing power of the zinc sheet in a lateral direction is limited to less than 10 cm;
- The second layer of reinforcing steel becomes sufficiently protected;
- The zinc consumption rate is such that the standard layer thickness can be used for a service life of 25 years.

Following these conclusions, the concrete surface area to be covered with zinc sheet was enlarged so as to include neighbouring concrete surfaces which were less suspect of reinforcement corrosion. The decision

to enlarge the zinc-covered surface area was considered wise as the throwing power in a lateral direction was very limited. Moreover, the poor accessibility would make it a costly business to apply additional zinc sheet at a later stage.

The zinc consumption rate was such that a standard thickness could be used provided the complete concrete surface area was covered with zinc sheet, i.e. without a spacing between neighbouring strips. This decision was also supported by the fact that covering 50% of the concrete surface with zinc would lead to doubling the zinc thickness so as to achieve a service life of 25 years. Furthermore, using zinc sheet with a smaller width would lead to additional costs for cutting and application on the concrete surface.

Eventually, the zinc strips used for the investigations were left unchanged after the trial, whereas the remaining segments were completely covered with zinc sheet using the standard width and thickness. The measurements on the trial section (2 segments) will continue so as to obtain information on the long term performance of galvanic cathodic protection.

REFERENCES

Boutz, M. 2012a. Investigations on cavities in the cantilever of the Neerbossche bridge – Results of stage 1 Investigations on the soffit of the bridge. Interim Report of SGS INTRON, Sittard (in Dutch).

Boutz, M. 2012b. Investigations on cavities in the cantilever of the Neerbossche bridge – Results of stage 2 Investigation on the top surface of the bridge deck. Interim Report of SGS INTRON, Sittard (in Dutch).

Boutz, M. 2012c. Investigations on cavities in the cantilever of the Neerbossche bridge – Results of stage 3 Investigation on the soffit of the bridge deck. Final Report of SGS INTRON, Sittard (in Dutch).

Broomfield, J. 1997. Corrosion of steel in concrete – Understanding, investigation and repair. London: E&FN Spon.

Christodoulou, C. Tiplady, H., Goodier, C.I. & Austin, S.A. Performance of silane impregnants for the protection of reinforced concrete. In Mike Grantham et al. (eds) *Concrete Solutions 2014. Proceedings of Concrete Solutions, the 5th Int. Conf. on Concrete Repair*, Belfast, 1–3 September 2014. Boca Raton, Fl: CRC Press.

Dai, J.-G., Akira, Y., Wittmann, F.H., Yokota, H. & Zhang, P. 2010. Water repellent surface impregnation for extension of service life of reinforced concrete structures in marine environments: The role of cracks. *Cement & Concrete Composites* 32: 101–109.

Ormellese, M., Berra, M., Bolzoni, F. & Pastore, T. 2006. Corrosion inhibitors for chlorides induced corrosion in reinforced concrete structures. *Cement and Concrete Research* 36: 536–547.

Söylev, T.A., McNally, C. & Richardson, M. 2007. Effectiveness of amino alcohol-based surface-applied corrosion inhibitors in chloride-contaminated concrete. *Cement and Concrete Research* 37: 972–977.

Netherlands Normalisation Institute 1984. Regulations for concrete VB 1974/1984 NEN 3880 – Part G Lightweight concrete – Additional clauses. Delft: NNI (in Dutch).



Taylor & Francis
Taylor & Francis Group
http://taylorandfrancis.com

Concrete Solutions – Grantham et al. (Eds.)
© 2016 Taylor & Francis Group, London, ISBN 978-1-138-03008-4

What are the benefits of corrosion monitoring in concrete structures from an owner's perspective?

J.J.W. Gulikers
Ministry of Infrastructure and the Environment, Rijkswaterstaat-GPO, Utrecht, The Netherlands

ABSTRACT: During the last decades developments have been made regarding the use of corrosion monitoring to gain reliable information on the actual behavior of a structure during its operational service life and have the possibility to perform timely interventions before significant damage occurs. However, until now little information has been published on the experience with these sensors in real structures.

In order to identify possible difficulties, pitfalls and shortcomings in the interpretation of the results a numerical simulation of an ideal case has been performed. In view of the high variability in prevailing exposure conditions, cover depth and concrete cover quality it is concluded that a probabilistic approach will be more suitable for a correct interpretation. However, this will also necessitate major investments by the asset owner regarding the amount of sensors needed and in the long term for managing the process. Consequently, it is considered questionable if corrosion monitoring of concrete structures will eventually provide a practical and cost-effective tool to support management and maintenance of concrete structures.

1 INTRODUCTION

The current codes present a deemed-to-satisfy approach to address durability in the design stage of new structures by introducing limiting values for water to cement ratio, cement content, crack width and cover depth. Apparently, the engineering community considers these provisions practical, effective and efficient to warrant sufficiently durable concrete structures with limited maintenance without major repair being necessary during the anticipated working life, following the definition of design working life given in EN 1992-1-1 and EN 1990. In fact, these provisions are based on local 'expert opinion' and practical experience rather than on a transparent rational approach. As the "deemed-to-satisfy provisions" vary considerably between European countries, serious doubt can be expressed on the validity of the current deemed-to-satisfy approach.

In practice it is common for an asset owner to plan interventions only after visual inspections have clearly evidenced major signs of distress, e.g. cracking and spalling. However, a structure may then be degraded to such an extent that substantial costly and time-consuming repair activities are necessary. In view of this adverse impact it has been suggested that the use of permanent monitoring systems could prove to be an economical solution to follow a structures condition over time as the results obtained could be used as a reliable basis for cost-effective maintenance management.

Among all deterioration mechanisms, corrosion of the reinforcing steel is considered the most prominent threat to long-term durability of concrete structures, affecting both their serviceability and load-bearing capacity. It is therefore not a surprise that since the 1990's, several monitoring systems have been developed to provide quantitative information on the position of the 'depassivation front' within the cover zone. Such systems involve probes representing reinforcing steel which are embedded within the cover zone, either at one fixed depth or at a range of depths with a fixed interval. As these probes are embedded at a shallower depth, they can serve as an early warning system for onset of corrosion of the reinforcing steel. The information thus obtained over time can be employed by engineers to compare the actual behavior with that anticipated during design, to determine the rate of deterioration, to optimize the timing of maintenance and to warn of an impending failure (Buenfeld et al. 2008).

Apart from concerns over accuracy, stability and durability of monitoring sensors, amongst others, there are also serious concerns on the interpretation of the data obtained over time and the eventual benefits with regard to maintenance from the point of view of the asset owner. This paper will focus on the difficulties in data interpretation and their consequences for reliable service life prediction of reinforced concrete structures.

2 CONCEPTUAL BACKGROUNDS

With regard to reinforcement corrosion it has become common to distinguish between two consecutive stages in the service life of a concrete structure, i.e. the initiation stage and the propagation stage, see Figure 1

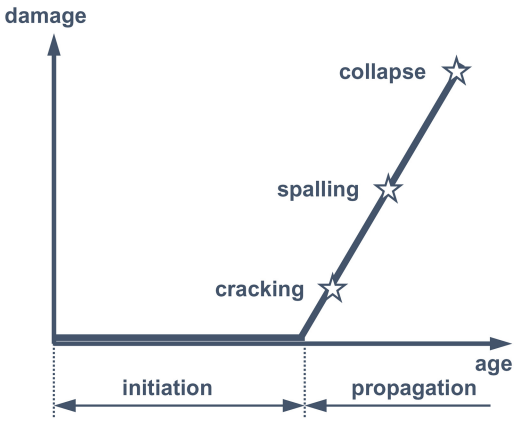

Figure 1. Conceptual service life model for a concrete structure with respect to reinforcement corrosion according to Tuutti (1982).

(Tuutti 1982). The common assumption is that the definition of the design working life reflects the initiation stage, at the instant that onset of corrosion occurs.

During the initiation stage, the gradual ingress of deleterious substances from the prevailing exposure environment into the concrete cover will take place largely unnoticed, until cracking and spalling due to corroding reinforcement occurs. However, under certain conditions, such visible signs of distress may not appear and debonding and loss of steel cross section may then have advanced to such an extent that the structural integrity of the concrete component is seriously impaired.

Consequently, during the last 2 decades, monitoring has become a major research activity as to develop embeddable sensors providing real time condition information which may serve as an early warning system for reinforcement corrosion. Logically, these sensors will be installed in the concrete cover at depths less than the actual concrete cover thickness to reveal the position of the depassivation front over time. Such information can then be used to allow for a reliable prediction of the time to onset of corrosion of the steel reinforcement. Ideally, in case the predicted time to corrosion onset is significantly less than the required design service life, timely and appropriate preventive actions can then be undertaken before serious cracking and spalling will occur. Such a preventive maintenance may thus prove to be very efficient as the corresponding measures may remain simple and cheap.

In practice, several types of corrosion sensors are available and it is known that some concrete structures of major importance have already been equipped with such sensors for more than 2 decades, e.g. the Storebaelt Tunnel in Denmark and the Green Heart Tunnel in the Netherlands. However, so far, only little information has been published on the actual performance of such corrosion sensors embedded in real structures under real exposure conditions as well as on the measured data and the interpretation regarding

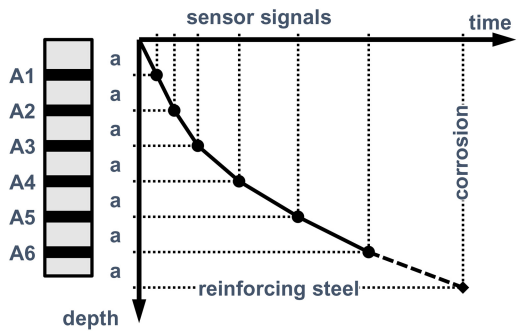

Figure 2. Conceptual model to predict the time-to-corrosion of reinforcing steel using an embedded anode ladder (Raupach & Schiessl 2001).

service life prediction and maintenance. Most information published in literature merely describes the theoretical backgrounds and the working principle of the sensor and presents a simple conceptual model for the prediction of corrosion onset based on qualitative or laboratory results obtained with these sensors (Duffó and Farina 2009, McCarter & Vennesland 2004, Raupach & Schiessl 2001, Gehlen & Dauberschmidt 2007), see Figure 2.

Surprisingly, in the literature, no realistic case studies are elaborated to explain how the prediction of onset of reinforcement corrosion should be accomplished or how the use of sensors could be incorporated in an overall maintenance strategy.

It should be noted that this paper will not discuss the validity of the working principle of corrosion sensors but will focus only on the usefulness of the results obtained to allow for a reliable prediction of onset of corrosion as well as on several practical aspects concerning installation in new structures and execution of the measurements over time during the operational life of a structure.

3 THEORETICAL BACKGROUNDS

In order to allow for a proper interpretation of the results obtained from permanent corrosion monitoring and for a prediction of onset of reinforcement corrosion it is necessary to translate the conceptual model presented in Figure 2 into a suitable mathematical model.

Depassivation of reinforcing steel may occur either due to the presence of an amount of chlorides exceeding the chloride threshold level for corrosion initiation or as a result of carbonation. For simplicity, this paper will focus only on depassivation resulting from chloride ingress, although the reasoning is also applicable to carbonation-induced corrosion.

As a result of continuous or frequent exposure to a saline environment, chloride ions will penetrate the concrete cover and in the course of time the chloride content at the level of the reinforcing steel may reach a threshold level, C_{crit}. Thereupon, onset of corrosion

will occur and the rate of the subsequent corrosion process is to a large extent dependent on the moisture content of the surrounding concrete as to allow for ionic transport. The position of the depassivation front, i.e. the depth at which the chloride content $C = C_{crit}$, will move deeper as time passes by. By embedding pieces of steel, similar to the reinforcing steel, at known depth levels within the concrete cover, the position of the depassivation front, x_{dep}, can then be monitored over time, generally through periodic measurements, e.g. of the corrosion potential or the macrocell current. Under most exposure conditions, the transition of steel from a passive to an active state is accompanied by a drop in potential towards more negative values as well as a significant reduction of the so-called polarization resistance. The combination of both changes will result in a significant increase of the macrocell current when the steel is coupled with a more noble metal. In practice, measurement of the potential over time is straightforward and the easiest. The potential will be measured as a potential difference between a reference electrode having a stable potential and an embedded steel section without any interference of the electrochemical processes.

In engineering practice chloride ingress into the concrete cover is commonly modelled through the following mathematical expression, based on a differential equation commonly known as Fick's second law of diffusion [1, 2]:

$$C(x,t) = C_s - (C_s - C_i) \cdot \mathrm{erf}\left(\frac{x}{2\sqrt{D_a \cdot t}}\right) \quad (1)$$

where $C(x,t)$ = chloride content at depth x and age t [%m/m]; C_s = surface chloride content [%m/m]; C_i = initial chloride content [%m/m]; x = distance to the exposed concrete surface [m]; D_a = apparent chloride diffusion coefficient [m^2/yr]; t = age (exposure time) [yr]; and erf = error function.

Calculations based on Equation 1 will either yield the chloride profile, i.e. the spatial distribution of penetrated chlorides in depth, at a certain point in time, see Figure 3, or the development of the chloride content at a specific depth x as a function of time.

Generally, the apparent chloride diffusion coefficient is considered to be dependent on concrete age according to (fib 2006):

$$D_a(t) = D_a(t_{ref}) \cdot \left(\frac{t_{ref}}{t}\right)^n \quad (2)$$

where $D_a(t)$ = apparent chloride diffusion coefficient at age t [m^2/yr]; $D_a(t_{ref})$ = apparent chloride diffusion coefficient at reference age t_{ref} [m^2/yr]; t_{ref} = reference concrete age [yr]; and n = ageing factor ($0.0 < n < 1.0$) [-].

With respect to onset of corrosion, the development over time of the chloride content at the level of the reinforcing steel is of major importance, i.e. the chloride content at a distance $x = c_{st}$. Onset of corrosion is considered to occur at the instant that at a depth $x = c_{st}$ the chloride content reaches the corrosion threshold level, C_{crit}.

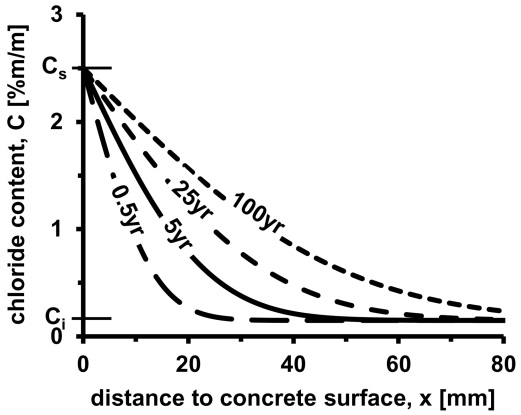

Figure 3. Chloride profiles calculated according to Equation 1 for ages t = 0.5, 5, 25, and 100 yr.

For the mathematical treatment and the interpretation of results obtained from corrosion sensors in the cover zone it is useful to introduce the existence of a depassivation front, where the chloride content $C(x_{dep}) = C_{crit}$. Based on Equation 1, a mathematical expression for the movement of such a depassivation front can be derived, given by:

$$x_{dep} = 2\sqrt{D_a \cdot t} \cdot \mathrm{inverf}\left(\frac{C_s - C_{crit}}{C_s - C_i}\right) \quad (3)$$

where inverf = inverse error function.

Introduction of the time-dependency of D_a according to Equation 2 then will result into:

$$x_{dep} = 2 \cdot \mathrm{inverf}\left(\frac{C_s - C_{crit}}{C_s - C_i}\right) \cdot \sqrt{D_a(t_{ref}) \cdot (t_{ref})^n} \cdot t^{\frac{1-n}{2}} \quad (4)$$

If C_s, C_{crit}, C_i, $D_a(t_{ref})$, t_{ref} and n are assumed to be constant, Equation 4 can be simplified to:

$$x_{dep} = A \cdot t^{\varphi} \quad (5)$$

where A = factor reflecting the locally prevailing exposure conditions and the quality of the concrete cover; and φ = factor reflecting the ageing effect on concrete transport properties.

According to Equation 5, the movement of the depassivation front will follow a power law, see Figure 4. For a constant value of $D_a(t)$, i.e. for n = 0.0, the depassivation front will advance according to a square root of time law. Generally, this situation will result in the most conservative prediction. In contrast, for n = 1.0 over time the depassivation front will remain fixed at a specific depth: $x_{dep} = A$.

In practice, the magnitude of the parameters included in Equation 4 can only be quantified through destructive testing, involving extraction of concrete cores from the structure under investigation and determination of the chloride profile in a laboratory, followed by regression analysis to arrive at values for the

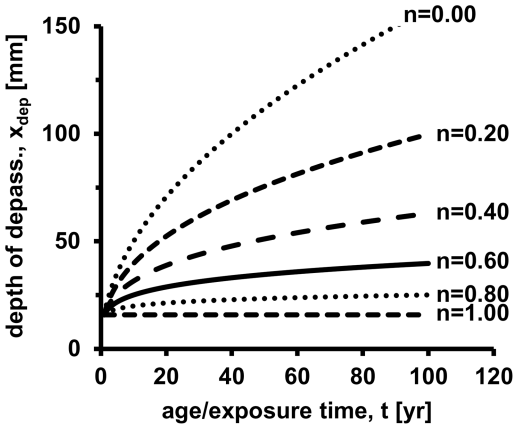

Figure 4. Development of the depassivation depth over time for different levels of the ageing factor, n.

model parameters C_s, C_i and $D_a(t)$. However, the quantification of the ageing factor n will only be possible when $D_a(t)$ is determined for at least two distinctly different ages. In addition, this procedure does not allow obtaining reliable information on the critical chloride content, C_{crit}. It should be borne in mind that in practice, concrete coring to determine chloride ingress profiles and derive values for $D_a(t)$, C_s and C_i is rarely performed on structures at an age where there are no clear signs of deterioration due to reinforcement corrosion. For an asset owner, there is mostly no clear objective incentive to evaluate a reinforced concrete structure's condition at a relatively young age by destructive means, i.e. coring.

The common lack of performance data of a structure at a relatively young age as well as the disadvantages involved in destructive testing can be largely overcome through the use of corrosion probes embedded in the concrete cover, i.e. at a depth less than the actual concrete cover on the reinforcing steel. When these probes have a similar electrochemical behavior of the reinforcing steel the time-dependent position of the depassivation front can then be detected through periodic measurements of their electrochemical behavior, however without the need to have reliable quantitative information on either C_s, C_i, $D_a(t)$, n and C_{crit}.

If corrosion probes are installed at different depths in the cover zone, the magnitude of both A and φ can then easily be derived by applying Equation 5. Let corrosion probe 1 be embedded at depth c_{p1} and probe 2 at depth c_{p2}, then it follows that:

$$\varphi = \frac{\ln\left(\frac{c_{p1}}{c_{p2}}\right)}{\ln\left(\frac{t_{dep,p1}}{t_{dep,p2}}\right)} \quad (6)$$

and thus:

$$A = \frac{c_{p1}}{(t_{dep,p1})^{\varphi}} \quad (7)$$

where $t_{dep,pi}$ signifies the time of depassivation for corrosion probe i being embedded at depth c_{pi}.

Once this information on φ and A is available the time to onset of corrosion of the reinforcing steel, embedded at depth $x = c_{st}$, can easily be predicted through re-arrangement of Equation 5:

$$t_{dep,st} = \left(\frac{c_{rst}}{A}\right)^{\frac{1}{\varphi}} \quad (8)$$

As an alternative Equations 7 and 8 can be combined resulting into the simple expression:

$$t_{dep,st} = t_{dep,pi} \cdot \left(\frac{c_{st}}{c_{pi}}\right)^{\frac{1}{\varphi}} \quad (9)$$

According to this line of reasoning, in a reinforced concrete structure, only 2 probes embedded at 2 different depths would be required to allow for a reliable prediction of corrosion onset of the reinforcing steel being embedded at a greater depth than both probes. If only one corrosion probe is used, then the ageing factor has to be estimated based on the type of cement and the prevailing exposure conditions, in particular regarding wetting and drying, or a conservative approach can be adopted by using $\varphi = 0.5$, corresponding to an age factor $n = 0.0$.

In summary, the approach with embedding corrosion probes for prediction of corrosion onset of the reinforcing steel, essentially involves the following 6 steps:

1. Embedment during construction of 2 corrosion probes each at a different but known depth, c_{p1} and c_{p2}, respectively, in the cover zone with $c_{p1} < c_{p2} < c_{st}$;
2. Periodic measurement over time of the development of the electrochemical condition of both corrosion probes;
3. Determination of the time to depassivation of corrosion probe p1 having the shallowest cover depth (c_{p1}): $t_{dep,p1}$;
4. Determination of the time to depassivation of corrosion probe p2 embedded at a depth c_{p2}, at a level between corrosion probe p1 and the reinforcing steel ($x_{p1} < x_{p2} < c_{st}$): $t_{dep,p2}$;
5. Calculation of the power factor φ (Equation 6) and the constant A (Equation 7);
6. Prediction of the time to corrosion onset of the reinforcing steel, $t_{dep,st}$ using either Equation 8 or Equation 9.

4 ELABORATED NUMERICAL SIMULATION OF AN IDEAL CASE STUDY

The application of corrosion probes and the interpretation of the measurement results will be exemplified by a simple numerical case study reflecting an ideal situation in practice as to clarify the theory as well as to identify the assumptions, pitfalls and shortcomings. It

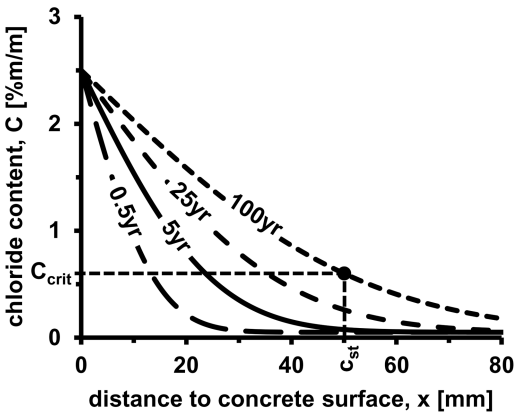

Figure 5. Ideal chloride profiles for the given input values of the model parameters calculated according to Equations 1 and 2.

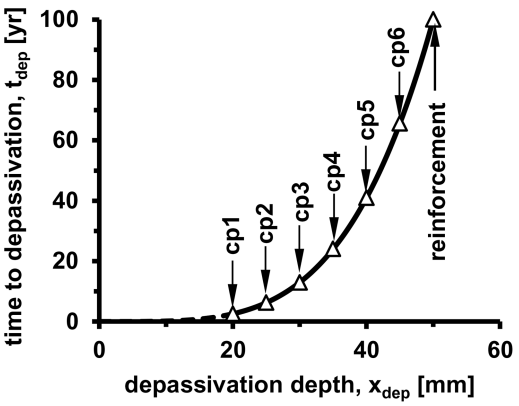

Figure 6. Development of the depassivation time, $t_{dep,pi}$, for corrosion probes embedded at depths $c_{pi} = 20, 25, 30, 35, 40,$ and 45 mm.

is thus assumed that Equation 1 combined with given input values correctly and accurately predicts chloride ingress over time and time to onset of corrosion.

The case study considers a concrete structure exposed to a marine environment, e.g. concrete elements in the splash zone. For the model parameters the following input values are used: $C_s = 2.5\%$; $C_i = 0.05\%$; $C_{crit} = 0.6\%$; $c_{st} = 50$ mm, $n = 0.50$; $D_a(t_{ref}) = 84.72$ mm^2/yr and $t_{ref} = 1$ yr. Note that the values for C_s, C_i and C_{crit} are expressed by mass of cement. The value for the ageing factor n reflects the use of blast furnace slag cement for concrete exposed to a high humidity environment. With these parameter values the chloride content at $x = c_{st} = 50$ mm will then amount to $C_{crit} = 0.60\%$ at $t = 100$ yr. Figure 5 shows the resulting chloride profiles for this ideal case calculated for $t = 0.5$, 5, 25 and 100 yr. Note that according to the mathematical model at an age 0.5yr the depassivation front has already advanced to a depth of 13.3 mm whereas for $t = 5$ yr the front has reached a depth of 23.6 mm.

Using these parameter values the factors φ and A are easily calculated yielding $\varphi = 0.25$ and $A = 15.81$ mm^2 yr$^{-0.5}$. If only one corrosion probe would be used which is embedded at a depth c_p, then no information on the ageing effect, reflected in the parameter n, could be derived from the results. Consequently, the time to depassivation, $t_{dep,p}$ obtained for this single depth would have to be used for a prediction of time to onset of corrosion of the reinforcing steel, $t_{dep,st}$.

Now assume that a series of 6 corrosion probes are embedded at a range of depths with an interval of 5 mm. As chloride ingress in the near-surface zone is known not to obey the diffusion equation, i.e. Equation 1, due to effects like capillary suction and washing out by rain water, the first probe will be embedded at a depth of 20 mm whereas the deepest probe will be located at a depth of 45 mm, i.e. at a depth 5 mm less than that of the reinforcing steel. As the cover depths are exactly known for each probe the time to depassivation can easily be calculated, see Figure 6.

For corrosion probe p1, having a cover depth $c_{p1} = 20$ mm, the time to depassivation is calculated to be $t_{dep,p1} = 2.56$ yr, whereas for the next corrosion probe with a cover $c_{p2} = 25$ mm, $t_{dep,p2} = 6.25$ yr. However, at an age of 2.56 yr only $t_{dep,p1}$ will be known and a conservative prediction based on $n = 0.0$ would then result into $t_{dep,p2} = 4.0$ yr whereas for the reinforcing steel it is estimated that $t_{dep,st} = 16$ yr. These predicted values are significantly less than the actual values for both $t_{dep,p1}$ and $t_{dep,st}$ and consequently the time to depassivation of the reinforcing steel will be seriously underestimated.

For a specific area, it may be assumed that both C_s and C_i will not change over time, however, for a specific area, different levels of critical chloride content C_{crit} may apply for the individual corrosion probes. This may then result in erroneous conclusions regarding the advancement of the depassivation front. Consider the situation that multiple corrosion probes are located in the same area but embedded at a range of depths. Assume that, for all corrosion probes, a similar value for C_s as well as a similar value for C_i applies. Figure 7 shows the impact of the critical chloride content, $C_{crit,pi}$ on the depassivation time of the individual corrosion probes, $t_{dep,pi}$.

If C_{crit} increases with depth, then a lower value for φ and correspondingly a higher value for the ageing factor n will be derived. Figure 8 shows the apparent effect of a different C_{crit}-value for corrosion probe p5 (embedded at $c_{p5} = 40$ mm) as compared to p4 (embedded at a depth of $c_{p4} = 35$ mm) on the ageing factor.

It should be noted that values for $n > 1.0$ imply that according to Equation 1 the depassivation front retracts over time to lesser depths. This confusing situation will occur when $t_{dep,pi+1} < t_{dep,pi}$. In this example this applies to $C_{crit,p5} < 0.454\%$ while maintaining $C_{crit,p4} = 0.60\%$, resulting into $t_{dep,p5} < 24.01$ yr ($= t_{dep,p4}$).

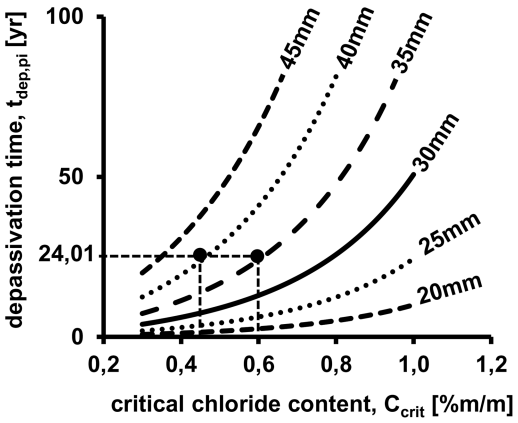

Figure 7. Development of the depassivation time, $t_{dep,pi}$, for corrosion probes embedded at $c_{pi} = 20$, 25, 30, 35, 40, and 45 mm as a function of critical chloride content, C_{crit}.

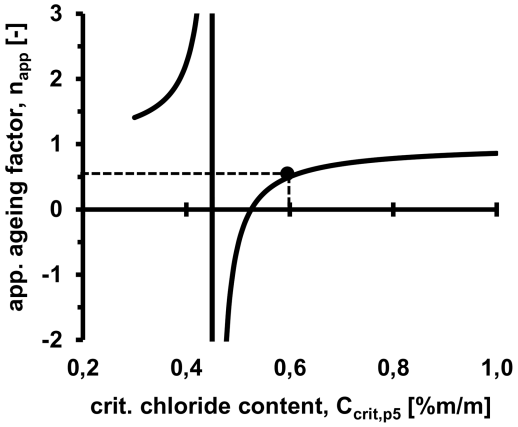

Figure 8. Impact of the critical chloride content of corrosion probe 5, $C_{crit,p5}$, on the calculated apparent ageing factor n based on $t_{dep,p4}$ ($c_{p4} = 35$ mm) and $t_{dep,p5}$ ($c_{p5} = 40$ mm).

5 DISCUSSION AND CONCLUDING REMARKS

The limited number of examples provided in the numerical case study has already clearly shown that major pitfalls will occur in the interpretation of the results obtained by corrosion monitoring. Users should therefore be aware that intelligent (corrosion) monitoring is at an early stage of development and that it's use will require expert specialist expertise both in initiating and managing the process and in carrying out the work (Buenfeld et al. 2007).

The case study has also indicated that in view of the significant spatial variability of the prevailing exposure conditions and the concrete quality of the cover depth, a high number of corrosion probes will be needed to give representative information on the condition of a structure. As corrosion sensors can be relatively expensive, this will lead to substantial costs for the asset owner. Consequently, corrosion sensors are considered to be appropriate only for larger structures or sites in severe environments.

In view of the high spatial variability of both concrete cover quality, cover depth and exposure conditions a probabilistic approach seems to be more appropriate for the analysis of the results. However, such an approach requires more expert knowledge.

In practice the asset owner should be aware that there is a serious risk that the contractor will devote more and special care to the concrete areas where corrosion probes are embedded. Consequently, the results obtained with the corrosion monitoring systems will indicate a much longer service life. Consequently, this monitoring data is not considered to be representative for the actual condition of the concrete structure.

Not only costs in installation are involved but also costs due to periodic monitoring and the analysis of the results obtained. These costs are often not mentioned by the supplier of the corrosion monitoring system. Moreover, the asset owner should be aware that the use of corrosion monitoring will be a long term operation covering several decades. Information obtained in the short term for corrosion probes embedded at a depth less than 30mm can prove to be quite unreliable regarding prediction of time to corrosion of the reinforcement.

In view of the anticipated high costs for corrosion monitoring and the doubts on maintenance and management of the monitoring system to keep it in a serviceable condition on the long term, for the asset owner it will be more cost-effective and attractive from a maintenance point of view to spent the money on high quality control on site during execution and if needed on additional measures, e.g. the use of stainless steel to warrant a largely maintenance-free service life of concrete structures.

REFERENCES

Buenfeld, N.R., Davies, R.D. Karimi, A. & Gilbertson, A.L. 2008. Intelligent monitoring of concrete structures. CIRIAC661. London: CIRIA.

Duffó, G.S. & Farina, S.B. 2009. Development of an embeddable sensor to monitor the corrosion process of new and existing concrete structures. *Construction and Building Materials* 23: 2746–2751.

fib 2006. Model code for service life design. *fib* bulletin 34. Lausanne: *fib*.

Gehlen, C & Dauberschmidt, C. 2007. Condition control of existing structures by performance testing. In V. Baroghel-Bouny (ed.), *Performance based evaluation and indicators for concrete durability; Proc.. intern. workshop, Madrid, 19–21 March 2006*. Bagneux: RILEM.

McCarter, W.J. & Vennesland, Ø. 2004. Sensor systems for use in reinforced concrete structures. *Construction and Building Materials* 18: 351–358.

Raupach, M. & Schiessl, P. 2001. Macrocell sensor systems for monitoring of the corrosion risk of the reinforcement in concrete structures. *NDT&E International* 34: 435–442.

Tuutti, K. 1982. Corrosion of steel in concrete. CBI research fo 4 · 82. Stockholm: Swedish Cement and Concrete Research Institute.

Concrete Solutions – Grantham et al. (Eds.)
© 2016 Taylor & Francis Group, London, ISBN 978-1-138-03008-4

Modern techniques and concrete technology used to conserve a unique heritage breakwater

S. Hold
Independent Consultant

ABSTRACT: The channel island of Jersey has one major commercial port which is not only vital for the island's daily supplies but also the main port of entry for tourist trade. St Helier Harbour is protected from the south-westerly prevailing wind and waves by Hermitage Breakwater, construction of which was started in 1874. The ravages of time appeared to have not unduly damaged the structure but recently the Island's engineers had been monitoring the breakwater and became concerned over its deteriorating condition. The damage to the surface protection of the precast blocks and joints on this south-west facing section of the wall of the pre-1887 construction was seen to have significantly deteriorated after the early 2014 storms. Using petrography from concrete core samples it was found that at depth in the section some of the cement had not hydrated which meant that the blocks, once they had sustained surface damage had a residual capacity, when coming in to contact with sea water as the outer concrete was worn away and therefore had self-annealing properties.

1 THE HISTORY AND SIGNIFICANCE OF THE BREAKWATER

The breakwater from Elizabeth Castle to Hermitage Rock and then beyond out to the Plate Rock was a concept in the 1850s for the construction of a grand harbour in St. Helier, Jersey.

Previous large scale breakwaters in the Channel Islands and in particular Jersey, such as St. Cathe-rine's, had utilised dressed quarried stone mass gran-ite blocks for outer walls with a soft inner core of secondary material. The initial engineering design for Hermitage Breakwater entailed constructing blocks of concrete and aggregate cast in pits in the ground. The blocks were of a similar form and shape to the mass granite blocks used prior to this but, by using this method, regular geometry and lower costs were achieved (Figure 3).

The location of the breakwater and harbour proved to be in an extremely vulnerable part of the southern Jersey coast and the arm of the harbour from the La Collette rocks was abandoned early in construction (Figures 1 and 4). The main sheltering arm from the Hermitage Rock out to the Plate Rock was started in 1856, utilising the external block wall and 'soft core' method but braced by having a series of cross walls forming cells filled with loose core material.

The method proved very difficult out from Hermitage rock as the water level deepened and exposure to the south-west prevailing weather and swells increased (Figure 4).

In 1876 the block and cross wall cell method was abandoned and a new design of solid blocks, referred to as 'slice block', was constructed and built end over end. This method used tessellated blocks slid down one over other forming a 'solid' mass breakwater formed



Figure 1. Hermitage breakwater and St Helier Harbour.



Figure 2. SW face of pre 1876 Hermitage Breakwater.

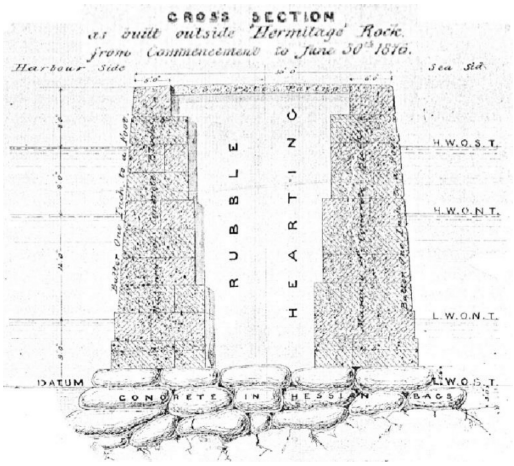

Figure 3. Original cross wall design 1850s.

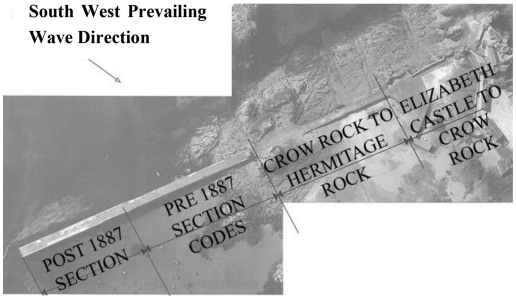

Figure 4. Elizabeth Castle, Hermitage rock and the pre 1876 and post 1876 length of breakwater.

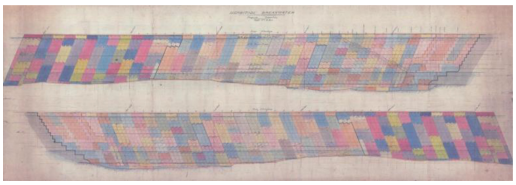

Figure 5. A construction record of the slice block method.



Figure 6. End of blocks and start of slice blocks.

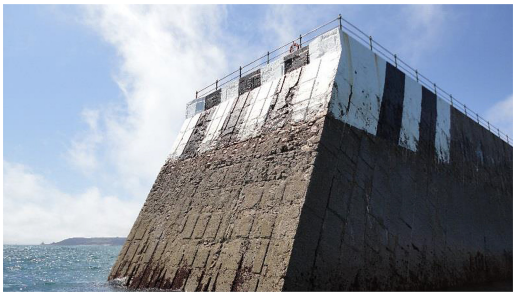

Figure 7. Tessellated end of slice block construction.

with granite outer facing blocks for added durability (Figures 5, 6 and 7).

However, even using this new, solid and more robust construction method, it was still not possible to complete the full breakwater out to Plate Rock and the project was abandoned in 1880.

The significance of the Hermitage breakwater in the modern era is that it provides essential shelter to the whole of the modern current St. Helier Harbour complex and has stood the test of time, reducing swells and wave impacts from the south-west (Figure 1).

2 ARCHIVE CONSTRUCTION INFORMATION

Research was undertaken in 2005 to locate historical information which revealed the methods described in the previous paragraphs. Such sources were the Maritime Museum, Société Jersiaise and other historical archives. Interestingly, also discovered were the progress notes and drawings from the time of construction which show a dramatic slowing up of the pre- 1876 cross wall method as progress gets further away from Hermitage rocks (Figure 8). The plan and enlarged plan show the process becoming slower and slower and it is then understandable that better progress is made using the different solid tessellated 'slice block' arrangement.

It is not exactly known, or recorded, why this new method was halted some 200m from Plate Rock but the inference is that once again conditions in this location proved far too aggressive for even the new 'slice block' construction method.

3 HEALTH CHECK SURVEY

The Transport & Technical Services Department (T&TS) in Jersey required in 2005 that a 'health check' to be carried out upon Hermitage Breakwater. This was to be undertaken at low tide/high tide to record the structural conditions at that time. T&TS had over many years been carrying out 'a little maintenance often' and the 2005 survey proved that this approach had enabled such an important, significant heritage

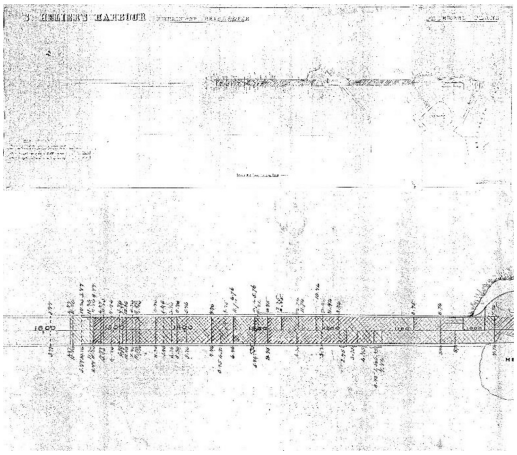

Figure 8. Site progress drawing from 1876 showing halted method.



Figure 9. Surface loss 2005.

structure to be well maintained with little, other than surface defects being identified (Figure 11).

The 2005 survey was updated in 2013 and some further deterioration of the pre-1876 block surfaces and joints was observed (Figures 9 and 10). These were noteworthy because wave energy impact on air pockets formed at the opening of perpendicular and bed joints would produce large 'exploding' forces locally in the



Figure 10. Pockets at block joints from 2013 survey.

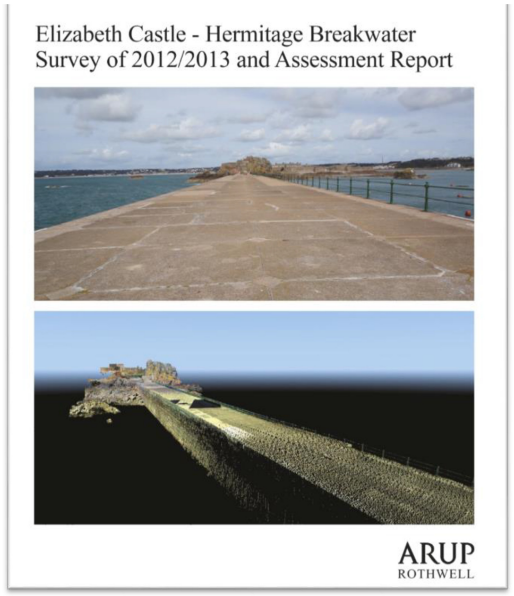

Figure 11. Survey report, LiDAR model of 2013.

concrete around the opening of the joints. As the holes become larger wave impact would in turn accelerate the deterioration. In 2014 an underwater survey found little or no deterioration below low water but it was observed that there were one or two loose, or unused, 'slice blocks' at the base end of the breakwater, which were preventing, or acting against, scour in this 11.5 m tidal environment.

In 2013 a digital asset register was set up to record the current condition of the structure and in particular the deterioration of the blocks from Hermitage out to the post-1876 section (Figures 11 and 12). The storms of February and March 2014 were of such a magnitude that they constituted a 'trigger event' and therefore the 2013/14 survey was updated in the specific area of most abrasion damage in and around the south-west part of Hermitage Breakwater of the pre-1876 section.

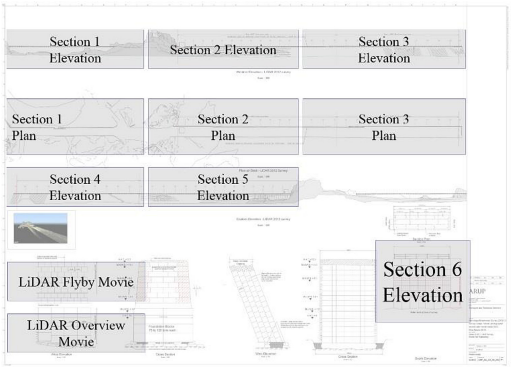

Figure 12. Digital asset form of monitoring the breakwater.

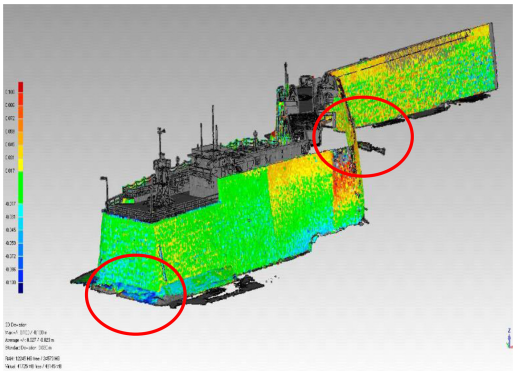

Figure 13. Gore Pier LiDAR models superimposed identity movements of masonry.

This survey showed that the pockets that were identified in 2013 had also become larger and some new pockets were discovered using a drone survey. A more detailed investigation was then instructed in terms of obtaining intrusive data information of the condition and make-up of the blocks and the core material behind them in the pre-1876 sections.

4 PRODUCTION OF THE DATA ASSET MANAGEMENT SYSTEM

The data monitoring system is basically a 'layered' information map of the structure recorded at a specific time (Figure 12). The structure itself is very large but by homing in on specific photographed areas, the current condition can be 'benchmarked' so that in the future, either visually or by photographs or drones, the individual blocks can be assessed over time to track deterioration. The call up of information includes a LiDAR flythrough, virtual model and production of accurate geometry drawings from the LiDAR model that act now as a benchmark for future monitoring.

5 FUTURE MONITORING USING LIDAR MODEL OVERLAYS

The principle of monitoring mass masonry heritage breakwaters in Jersey has been established; in particular for Gorey Pier. Here localised movements of areas of this irregular maritime heritage granite wall structure were assessed after 'trigger events'. The original LiDAR model from 2009 had superimposed another LiDAR model of 2011 and discrepancies of areas of movement were identified as well as their magnitude (Figure 13). Just as importantly, areas that had not moved during the trigger event were also identified thus allowing the owners to focus only upon repair elements or areas that had been identified as susceptible. In this way, the LiDAR monitoring model set up for Hermitage Breakwater in 2014 forms the benchmark for similar future monitoring of the breakwater



Figure 14. Loss of surface and other pockets at joints.

geometry together with the digital asset photographs which record the rate of specific areas of deterioration.

6 THE TRIGGER EVENTS IN MARCH 2014

This specifically identified that more joints had lost material at the junction between perpendicular and horizontal bed joints of the precast concrete large aggregate blocks forming outer walls. The surface 'crust' of concrete in many areas had also been abraded away exposing the large aggregate and cement matrix (Figure 14). More worryingly, the detailed study from the LiDAR model and the drone survey indicated that some areas not identified in previous monitoring in 2005 and 2013 had been formed. The newly identified openings had become enlarged in areas beyond normal visual data gathering range but were observable from the drone survey (Figure 6).

Similar heritage marine structures in Jersey had been given a reinforced concrete overlay protection to prolong their life in use. At St. Ouen's sea wall for



Figure 15. St. Ouen's sea wall Atlantic waves impact from S.W.





Figure 16. St Ouen's sea wall overlay.

example an abrasion resistant 5 km length of armour reinforced concrete had been overlaid on the WWII concrete defence wall in 2006. This provides protection against the aggressive Atlantic environment and the gravel and rocks on the beach causing the abrasion (Figures 15 and 16).

Another similar overlay protection was used in Jersey at the foundations of the St. Helier Marina where the same blocks originally produced for Hermitage Breakwater pre-1876, which had not been used, were then used to provide the foundations for the North Quay (Figure 17).

Although in the marina they were less susceptible to deterioration, in 2013 it was necessary to overlay the loose and degrading concrete and these blocks had overlay protection applied. The formwork was indented to give the appearance of blocks for aesthetic reasons (Figure 17).

Therefore, the original design for protecting the vulnerable area of the south-westerly hermitage breakwater was a similar overlay concept (Figure 18). This was discussed with Heritage consultants and Planners who felt that it would be necessary for such a significant heritage structure to have the concrete overlay protection of the same colour and visual effect as the original 1876 concrete and aggregates.

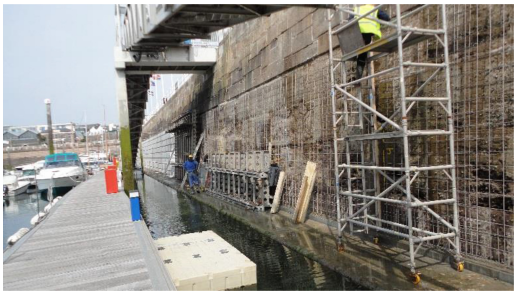

Figure 17. Concrete overlay on marina block foundation left over from the Hermitage construction.

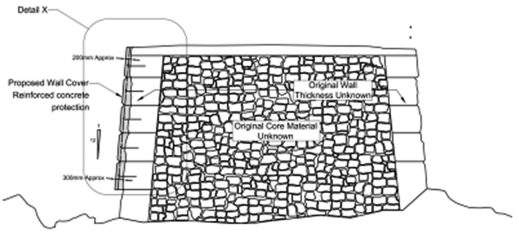

Figure 18. Overlay concept at Hermitage pre 1876 blocks.

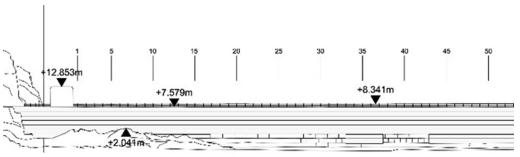

Figure 19. Extent of overlay envisaged.

To achieve this, it was then necessary to obtain samples of the Hermitage concrete facing blocks. It was also necessary to determine the actual thickness and constituent materials together with the strength of these blocks so cores were taken though the blocks (Figure 20). Only archive drawings were available from the construction era (Figure 3) so it was not clear if the soft core material inside the crosswalls had deteriorated or had been washed out.

7 THE SITE INVESTIGATION AND TAKING CORES

Two horizontal concrete cores were taken in the area to be overlaid to identify the mix, type of aggregate and the reasons for the deterioration of the concrete blocks

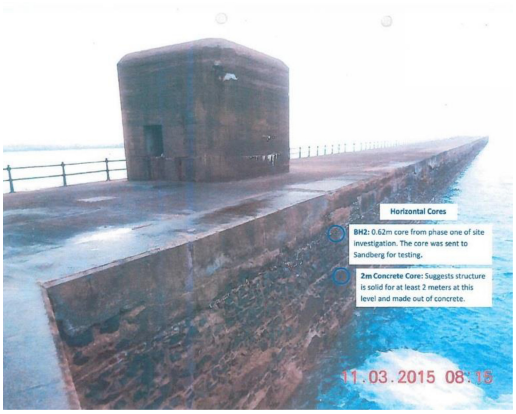

Figure 20. Location.

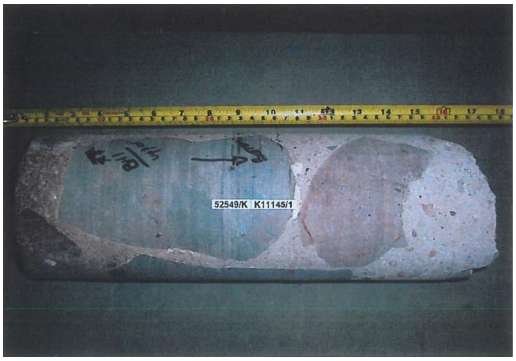

Figure 21. Scale and length of core 1. Note size of aggregate.



Figure 22. Scale and length of core 2. Note size of aggregate.

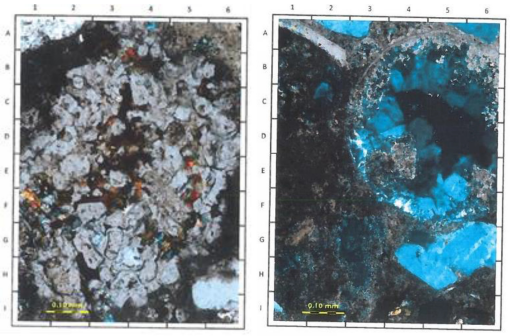

Figure 23. Petrographic slides used to determine concrete constituents at different depths.

surface (Figure 20 is location, figures 21 and 22 the cores).

It was discovered using petrography at incremental depths (Figure 23) from the cores that as the depth of section progressed, hydration had not taken place in the large grain size early Portland cement matrix around some of the large aggregates. This means that parts of the cement matrix within the body of the blocks had not reacted to form concrete. This was possibly due to no contact, or limited contact, with water during the original casting process by hand. The implications were that if successive layers of cement matrix are being degraded by abrasion and salt attack from the sea then hydration will take place once the new layer comes in contact with the sea water. Therefore in this context, there is a 'self-annealing' mechanism available to the overall thickness of the blocks. Small pilot hole drilling was also carried out to determine the thickness of the blocks and the depth down to the soft core from the deck concrete level. These investigations showed that there had been no core loss due to 'wash out' (where core material is washed out through open joints) and the core fill was formed from sand and rock fragments mixed.

8 PROTECTION SOLUTION SCALED DOWN

There then became a reduced level of concern for the concrete blocks to protect them against a breach in a storm and rapid loss of loose core fill from within the cells. However, the pockets or voids at joints were still providing air entrapment possibilities and under wave pressure still needed to be dealt with. Therefore, as an alternative to the full scale concrete overlay concepts, a design to repair the damaged pockets was produced (Figures 23 and 24). In this way, significant savings were made for the long term maintenance of the structure. As part of this exercise it was necessary, to analyse what tension against 'pull out' of the pocket repairs was required. The general wave load exposure was assessed as 26 kN/m^2 but local pressure developed by breaking waves in the pockets could be as much as 320 kN/m^2 (Figure 26).

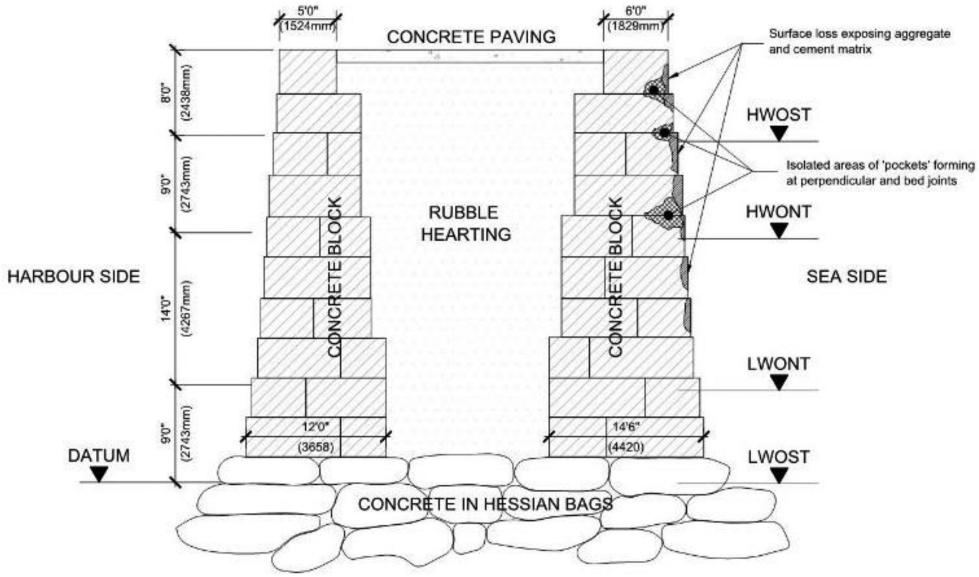

Figure 24. Existing damage.

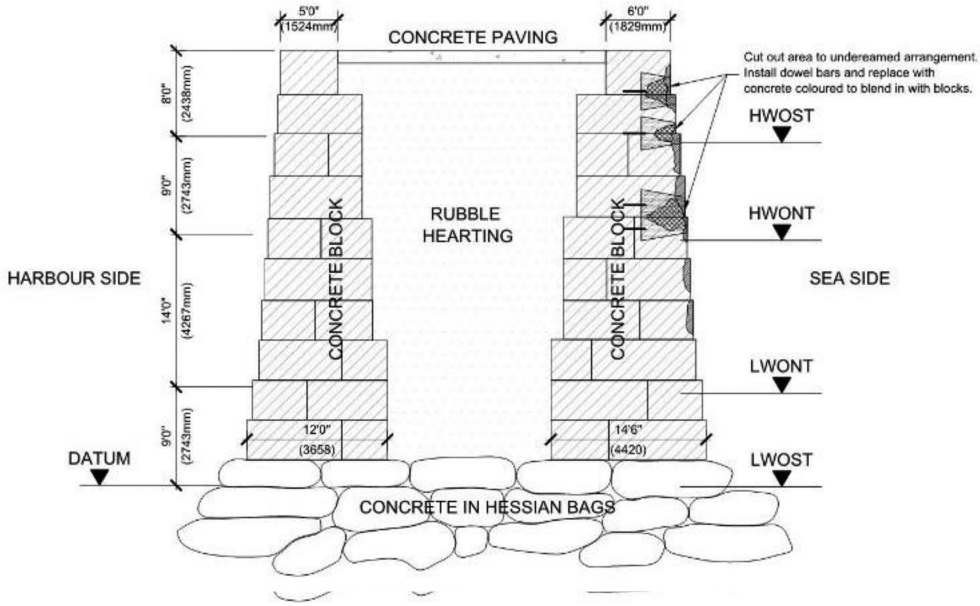

Figure 25. Repair pocket only solution.

9 FUTURE MONITORING

The Breakwater, as can be seen in the photographs (Figures 1 and 2), has protected the harbour of St. Helier for over 120 years. It has suffered a few abrasions and some impact damage in that period but remains a robust marine breakwater. However, the advent of sea-level rise inevitably means that, in the not too distant future, significant storm waves are likely to pass directly over the Breakwater and thus threaten St. Helier Harbour itself (Figures 27 and 28). The monitoring set up in 2014 will be a benchmark for future data gathering in order to determine when major intervention will be necessary to both protect and raise this magnificent Heritage marine engineering structure.

The effects of future wave overtopping will lead to significant waves rolling over the breakwater and reaching St. Helier Port (Figure 28).

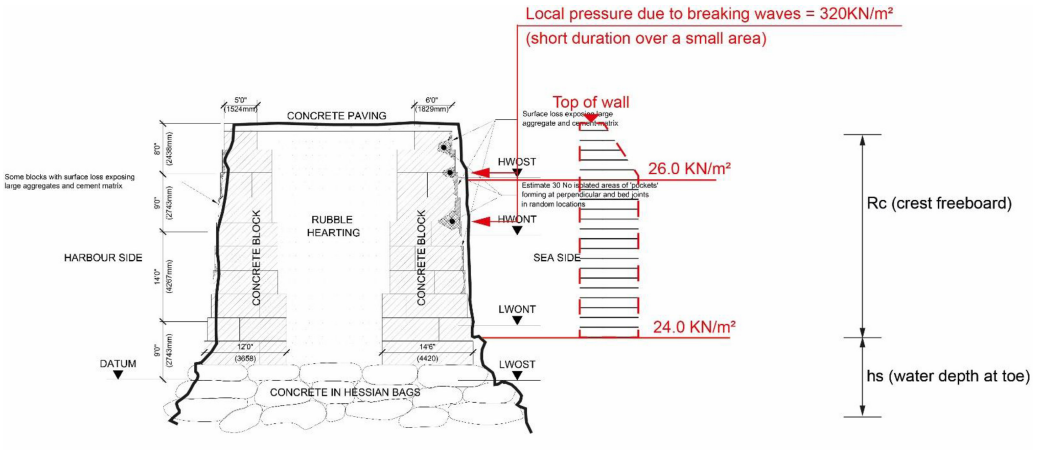

Figure 26. Estimate of wave loadings.

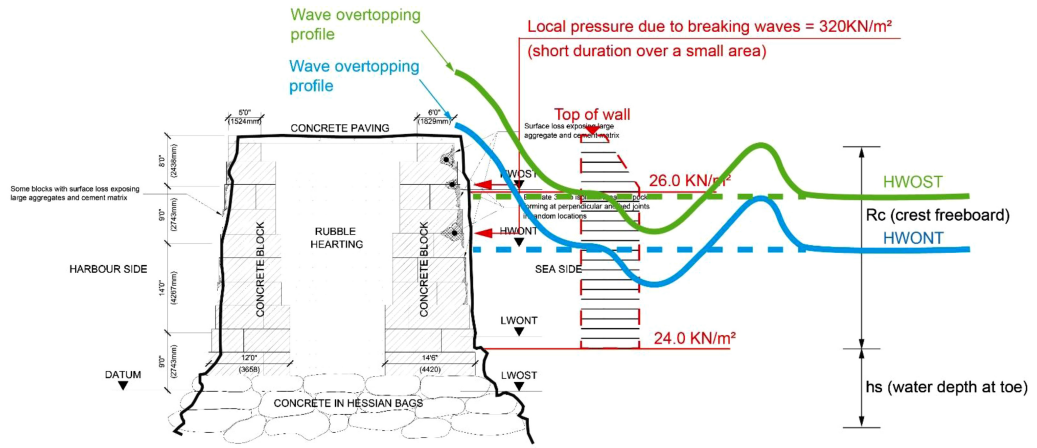

Figure 27. Predicted wave overtopping.



Figure 28. Hermitage breakwater in background under water in 2008.

ACKNOWLEDGEMENTS

With thanks to the States of Jersey Transport and Technical Services engineers Kevin Armstrong, Mick Johnson and Jamie Mason.

REFERENCES

Goda, Y. (ed.) World Scientific. *Random seas and design of maritime structures, advanced series on ocean engineering* – Volume 15.

Hold, S. 2009. *Repair of St. Catherine's Breakwater Roundhead*. ICE 2009 Proceedings

Muller, Dr G., Alsop, W., Bruce, T., Kartenhaus, A., Pearce, A. and Sutherland, J. 2007 *The occurrence and effect of wave impacts*, Proc I.C.E., Maritime Engineering 160pp: 167–173, Thomas Telford.

Muller, Dr G. and Wolters, G. 2005. ICE Proceedings Coastlines, Structure and Breakwaters 2005. *Failure Mechanism for Blockwork Breakwaters*.

Maritime Museum

Overtopping Manual – http://www.overtopping-manual.com/calculation-tool.html

Sociéte Jersiaise

Concrete Solutions – Grantham et al. (Eds.)
© 2016 Taylor & Francis Group, London, ISBN 978-1-138-03008-4

WWII German concrete defence walls in Jersey, Channel Islands

S. Hold
Independent Consultant

ABSTRACT: In the early part of WWII the German occupation of the Channel Islands led to a series of protective sea defence walls being constructed. In the sense of sea defence, the word is not correct; the Military Commander of the regime in Jersey in 1940, LtGen Graf Von Schmettow, ordered that all large flat beaches around the island of Jersey be protected from tank landings. Nine walls were constructed in a short time in very difficult circumstances. They were large mass concrete structures twice as high as the width, with a projection, or overhang at the top, to stop tanks climbing such walls and they were reinforced on the surface to resist tank shell blasts. Today the walls suffer overtopping that causes wash out of material from behind, posing a threat to structural integrity, as well as inland flooding in some areas. Modern concrete technology has revealed some interesting properties.

1 INTRODUCTION AND BACKGROUND

The Channel Islands of Jersey and Guernsey are close to the coast of Normandy on the north coast of France. During the Second World War the German conquest of Europe included overrunning and taking control of the Channel Islands in which Jersey is the southernmost land in the British Isles and the only part of the U.K. that was subject to German occupation. The occupation itself was from 1940 to 1945 and the military engineering in such a time of strife was a considerable achievement. The island of Jersey sits in the Channel but faces the onslaught of the western Atlantic and the associated storms and wave threats. The German defence walls have had several remedial projects in their lifetime, one as early as 1946, then after successive high tides and severe storms in 1974 and again in 1990, severe overtopping and flooding had damaged housing behind some of the beach defence walls.

Today's engineering problems at these walls are related to extremely high tides and wave overtopping linked to the removal of beach sand from in front of the walls. Recent and current phenomena such as sea level rise, increasing storm severity and duration has resulted in further beach sand movements that have once again brought matters to a head for the island's WWII concrete wall defences. Several of these defences have in recent years and currently required another round of repair and intervention to prolong and enhance their usefulness to the Island's infrastructure. This paper discusses the background of the investigations in recent years and survey methods that have been used to assess the integrity of the walls. The paper also describes some of the remedial and structural enhancement works that have been carried out.



Figure 1. The strategic location of Jersey in WWII.

2 HISTORY OF THE WALLS

The coast and bays of the island of Jersey have been the subject of protection and enhancement since 1790. Then, in around the 1880s sea walls of mass granite were constructed between the Martello Towers because of the threats, as seen in that period from the French during the Napoleonic wars (Figure 4). During World War II, the German military commander of the island of Jersey, General Lieutenant Graf von Schmettow, ordered many coastal strong points to be constructed on the island, together with several anti-tank landing walls. These military defence walls around the island

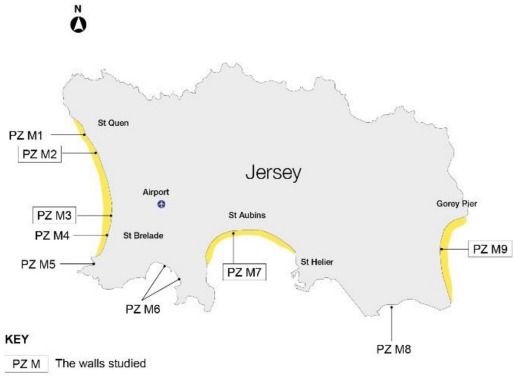

Figure 2. The location of the nine Panzer Mauern.

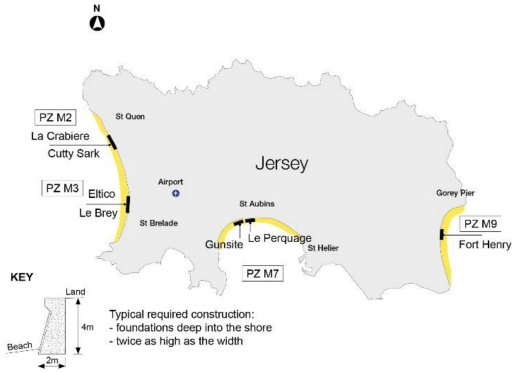

Figure 3. Construction concept and concrete walls studied.



Figure 4a. 1880s Granite sea wall at St. Ouens.



Figure 4b. PzM2 at St Ouens Bay – flat sandy beach.

were primarily to deter tank landings and in particular along the flat sandy beaches which are quite numerous in Jersey (Figure 2 and 4b). Von Schmettow instructed nine walls (Panzer Mauern, now referred to as PzM's) to be built and the word Panzer Mauer approximately translates to 'armour wall' and all of these civil engineering feats that are proving to be important today were constructed under extremely difficult circumstances from 1940 to 1945 using forced labour and slave labour.

A designation of the walls was given working in an anti-clockwise direction around Jersey, starting at the north end of St. Ouens Bay working south, where five of these walls were constructed and were identified as PzM1 to PzM5 (Figure 3). These walls in St Ouens Bay, which is 5 km long, were all approximately 5 m high (Figure 5). The western end of St Brelades Bay wall, PzM6, was also constructed 5 m high. Facing more southerly, the St. Aubin's Bay has a continuous section of wall that was constructed approximately 3 m high, PzM7. However, this wall in some areas has some higher lengths but generally reduces to 3m in height in several locations that were made smaller in order to save cement during a time of blockading which caused a crisis of supply.

In St. Clements Bay, PzM8 began construction but was soon halted in 1942 because it became apparent that the very rocky approaches to this bay precluded seaborne invasion with landing craft and tanks etc. Moving further around the coast eastwards to Grouville Bay, PzM9 from Fort Henry to Fort William was constructed and had remained, until recent times undamaged like the St. Aubins bay walls was only just over 3 m high. Large amounts of beach sand were extracted for the construction of this and the other seawalls and local Jersey residents pointed out at the time that the depletion of sand in Grouville Bay was resulting in flooding. In modern times, the culprit of beach sand migration in Grouville Bay can also be attributed to the current problems at the wall and the northern German WWII gun emplacement area of PzM9 close to Fort Henry.

Von Schmettow's construction brief was that these walls were to be "founded deep into the sea shore, 3 m high with a height to breadth ratio of 2:1" (Figure 5). They were also to be constructed generally with an overhang at the top which we, in modern times, refer to as a 're-curve' for reflecting waves but it is not clear whether this was intended at that time or simply as an anti-climbing measure for the wall.



Figure 5. The WWII concrete projection (re-curve at top of wall to further prevent tank climbing. St. Ouens PzM2.

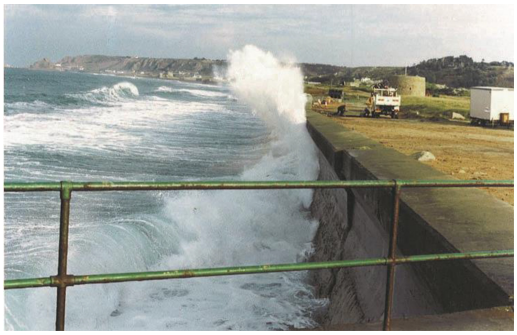

Figure 6. The very aggressive wave environment at St Ouens PzM2.

3 THE NEED FOR INTERVENTIONS

The significant storms, overtopping and flooding in 1974 and again in 1990 meant that large lengths of wall bases became exposed and the stability of the walls was threatened due to washout and loss of material from behind the wall (Figure 6). The loss of material was from underneath the exposed bases of the concrete walls when the beach sand was removed.

A remedial measure of inserting sheet piles at the toe of the wall with a capping beam in front of the damaged areas was carried out in 1990 at PzM2, PzM3 and PzM6 and has been subsequently used in many other sea wall locations on the island experiencing beach sand migration.





Figure 7. The 'armour' concrete placed on PzM2 in 2006 to arrest erosion.



Figure 8. Concrete armour protection against gravel and rocks.

The shingle banks in St. Ouens Bay also caused large scale abrasion damage to PzM2 and PzM3 and the States of Jersey Engineers trialled many concepts for overcladding the surface of the WWII concrete with hard wearing high strength concrete to provide abrasion resistance against the shingle and rocks that were mixed up in the turbulent Atlantic waves that pound the



Figure 9. Gunsite Café wall at the slipway. Note recurve to the west of the slip and rounded top to the east. PzM7.

walls (Figures 6 and 8) Panels of hard wearing spray concrete with fibres and various other additives were trialled but did not achieve the level of success required to combat the very large forces generated from the Atlantic waves. To assess options for protecting these sections of wall in St. Ouens Bay, a feasibility study was carried out in 2004 which resulted in the selection of an option that provided an 'armoured' concrete overlay to the abraded and damaged areas of PzM2 and PzM3 (Figure 8). The chosen solution of remedial overlay works was undertaken by the States of Jersey engineers in 2006.

Recently at the location in St. Aubins Bay, referred to as the Gun Site Café PzM7 (which has a gun site and bunker embedded into the defence wall that has been turned into a café), has been the subject of an in depth study because of wave overtopping in this area of the wall results in significant flooding behind including the roundabout area leading to the airport (Figure 9). Lastly, in relatively recent times, significant washout after the March 2015 storms was experienced at PzM9 in the location close to Fort Henry where once again the base of the wall became exposed by migration of beach sand from in front of the wall (Figure 10). The resultant loss of material from behind the wall led to the rotation seawards of the north gun emplacement bunker constructed as a separate structure behind the concrete sea wall. Archive research shows that, unlike at the Gunsite café and the other seawalls, the bunkers at Fort Henry were constructed before and separately to the sea wall.

4 ENGINEERING DATA FROM THE ST. OUENS OVERLAY WORK AT PZM2 AND PZM3

Two sections of the defence walls at St. Ouens bay PzM2 and PzM3 were the subjects in recent years of detailed technical investigations into the integrity of the WWII concrete. In October 2004 as part of a major feasibility study core samples were taken from the wall at various heights which were then assessed by the



Figure 10. Wash out from behind Fort Henry concrete wall PzM9.

BRE (Building Research Establishment) Microscopy Unit to examine the concrete and its present day strength and capacity for overlaying with a toughened armour protective layer (Figures 11 and 12).

In addition to corroding surface reinforcement (placed as anti-tank shell resistance and not structural) the existing eroding concrete surfaces were significantly deteriorating, so a stronger concrete with a robust wearing surface was designed for the overlay of the existing WWII concrete.

Engineering analysis was undertaken for both static and dynamic load cases to assess what was happening and once again the 'culprit' for the distress was identified as the free flow of water from behind the wall in the areas which were overtopped.

The flow of water and material from below the wall needed to be 'cut off' by the sheet pile and capping beam method.

In terms of details of the concrete, the BRE's assessment of the cores taken through the wall at top, middle and bottom levels of the 5 m high wall provided significant detailed information and found that:

– Generally sound material was used.
– The integrity of the surface would be satisfactory, once the anti-tank shell blast reinforcement, was removed, and the fresh surface was deemed suitable to add layers of protecting hard panels of reinforced concrete.



Figure 11. Core locations at St. Ouens PzM2.



Figure 12. Trial pit excavated behind PzM2 at core hole locations.

– There would however be a need for the limited removal of weak surface concrete together with the corroding reinforcement and surface preparation.

The BRE's conclusion was that "the concrete had a moderately dense, apparently strong formation with adequate voidage and capillary porosity to absorb the small amounts of ASR gel being produced. (Alcali – silicate Reaction, ASR, is an expansive degradation mechanism when elements of certain Jersey aggregates react with water and alkaline cements in the concrete). The limited compaction during construction and the voids were not deemed detrimental to the concrete's long term durability and the limited removal of the surface concrete would then facilitate the ability to overlay it with a harder material." (Figure 13.)

The overtopping and water behind such a length of wall and cutting off drainage from beneath the wall has not presented problems since the works were undertaken in 2006.

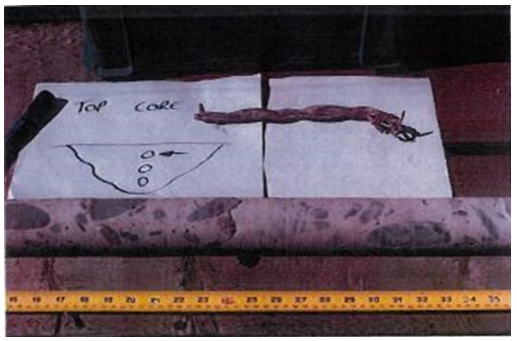

Figure 13. St. Ouens concrete core-top. See Figure 11.



Figure 14. St Ouens overlay constructed in 2006.

It can be seen that the protective layer against wave impact and abrasion with the high strength overlay concrete has performed well with lessons learned about bonding, early heating and shrinkage cracking of strong concrete mixes together with, the use of stainless steel reinforcement all provided a steep learning curve for the implementation of such a large overlay project. The overlay of armour concrete is still performing well today (Figure 14).

5 GUN SITE CAFÉ TO LE PERQUAGE CAR PARK PZM7

Another area of WWII wall studied was as part of a flood assessment for the inundation problems regularly experienced at the roundabout at the confluence of roads behind the seafront location at the bottom of Beaumont Hill (one of the main roads that lead to the airport from the island capital St. Helier). Large amounts of overtopping water in this part of St. Aubins Bay at PzM7, referred to as the Gun Site Café with the gun site 'built into' the wall forms part of the beach defences here. This wall varies in height from East of Le Perquage Car Park and in terms of archive research

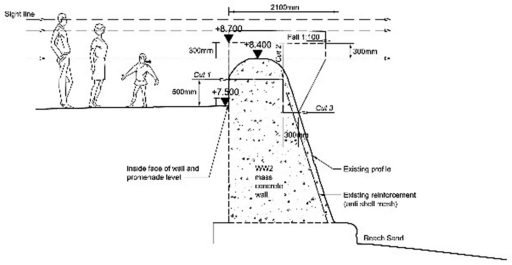

Figure 15. Existing profile of Gunsite Café Wall PzM7.



Figure 16. Gunsite Café wall. Inclined face and rounded top.

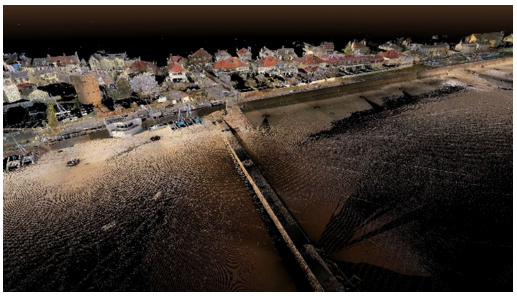

Figure 17. Gunsite café and slipway and PzM7 wall area from LiDAR model.



Figure 18. Wave overtopping at Gunsite Café wall (Figure 16).

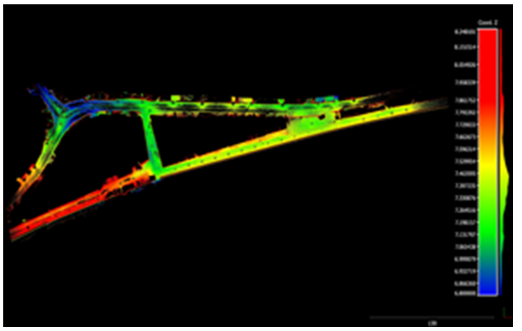

Figure 19. Blue indicates lowest point on LiDAR model scale of the wall and roads behind.

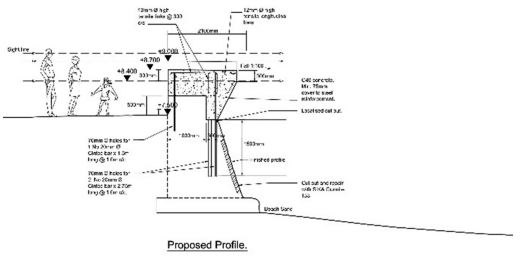

Figure 20. Raised new profile of WWII wall with re-curve.

the varying heights of the wall were due, according to the records to the lack of availability of cement.

However, the overtopping near the Gunsite cafe causing the flooding here has taken place for many years as a result of the wall not only being not high enough but also it does not have the 'outward recurve' at the top of the wall that the other German seawall defences have (see Figures 9, 15 and 16). The troubled area of the flood study sea wall also has a rounded top as well as inwardly sloping geometry which not only allows, but encourages a 'run up' and further overtopping from breaking waves (Figure 18).

Use of modern techniques to study the area of the wall using a LiDAR survey and making digital models (Figure 19) have iteratively allowed a solution to be arrived at which raises the level of the wall with a sympathetic addition of reinforced concrete section at the top with a recurve shaped to look like the WWII anti-tank profile (Figures 9 and 20). The additional height and mass of the new concrete was designed to structurally and visually tie in to the existing wall which was showing significant signs of deterioration and required large scale concrete repairs. The LiDAR



Figure 21. Extracted core from Gunsite Café wall PzM7.



Figure 22. East of Le Perquage core location H2 still in PzM7.

survey allowed accurate drawings and contour mapping of the whole area to assess the most viable options for geometry and to assess the anti-flooding benefits to be gained (Figure 19).

Similarly to the St. Ouens wall, core samples were taken from this wall and evaluated by Sandberg Ltd's laboratory (Figure 21). There were two elements of testing required from these cores; one was to test the integrity of the samples in tension in order to establish the 'pull out' capacity of the mass concrete. This was necessary to find the tying forces necessary to be able to add a further section of reinforced concrete onto the top of the mass concrete wall that would be able to resist the large wave impacts and upward forces on the recurve imparted at the new top of wall. The second part of the investigation of the concrete cores was a petrographic analysis. This established the characteristics of the existing concrete so that the new concrete addition that would increase the height of the wall would perform satisfactorily and in a similar manner to the stitching on of armour protection as at the St. Ouens sea wall. The Sandberg Ltd analysis of three cores taken in February 2015 from the Gun Site Cafe wall show that all the aggregates and cement matrix of the cores were consistent and unsurprisingly similar to the mix at St. Ouens:

– There was a Meta-argillite and salacious marine sand.
– The aggregate of the concrete was also dense and robust with little evidence of weakening.
– The rock types did have the potential for ASR in all three cores which could react with the alkaline in the cements paste

It was not surprising to find that only Portland cement was used and the mix had no additives because additives are a modern day phenomenon. The binder content and voidage was greater in one of the cores showing the variant in workability. (It was recorded in the archive literature that actions by the prisoners and forced labour gangs deliberately tried to sabotage the concrete while it was being constructed. Not using enough cement, leaving voids and putting wood, debris and other materials in the concrete during casting.) Compressive strength of the concrete was identified as originally of 40 to 50 N/mm^2 and the tensile strength capability for adding on top a significant concrete section with a re-curve was 1.15 to 2.55 N/mm^2. A note was made by Sandberg that the Portland cement used does not resemble the particles of modern Portland cement but it must be remembered that the 1940s to 1945 variety was much coarser grained than modern cements.

As found in some areas of the St. Ouens wall, the core evidence also showed some areas of poor compaction and mixing together with a variable water cement ratio of 0.45 to 0.55 close to the surface but within a section of the concrete the w/c was 0.55 to 0.60 at depth.

The current design for raising the height of the wall now includes a re-curve shaped like the WWII anti-tank climbing geometry to further reduce the current overtopping (Figure 20).

For the cores taken from this wall east of Le Perquage car park similar concrete was used but a much larger capacity was found for producing an AAR reaction (Figure 22). The horizontal cracking of the mass concrete wall and opening up here as well as the white leachate staining are indications of this expansive reaction (Figures 23 and 24). The cores from this part of the wall identify the different 'layers' of concrete poured and the variations in density and aggregate mix as the archives confirm that there was a difficulty in obtaining cement because of the blockade. Despite the variability of the mass concrete, the conclusion was that this mass concrete too could take an overlay, but needed to be repaired and also had the potential for being raised.

6 FORT HENRY SEAWALL IN GROUVILLE BAY PZM9

At this wall a different problem was encountered but with similar root cause. At the location of the



Figure 23. Horizontal crack, lifting potential.

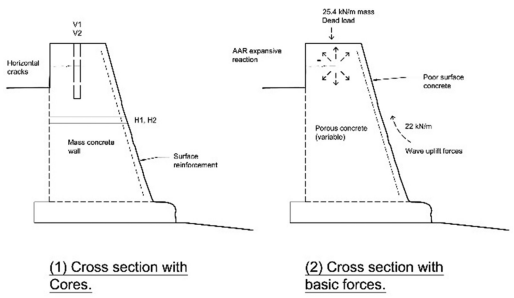

Figure 24. Cross section of MzM7 – East of Le Perquage Car Park.

Napoleonic Fort Henry and between two large WWII gun emplacement bunkers behind the sea wall there was a need to assess the damage and excessive wash out being sustained to the fill behind the wall (Figures 10 and 25). This was related to both overtopping of waves at high tide and wave action during storms removing beach sand from in front of the wall further east along the beach. Major settlements and washout from behind the wall had occurred at several high tides and storms in recent years, resulting in significant washout which had also taken material from underneath the northern WWII bunker as well from beneath the wall. This situation was monitored by the States of Jersey engineers and after another overtopping event in March 2015 the northern bunker was seen to have rotated significantly towards the seawall. The two gun emplacement bunkers here, unusually, had not been built into the wall as the other German defence bunkers and strong points were (Figure 30).

Desk study research identified that the bunkers were constructed and placed well before the wall was built.

The wall was constructed very quickly and used a railway system on land and on the beach for rapidly moving large quantities of materials to construct the wall (Figure 26). However, as these two gun emplacement bunkers are large, heavy independent structures separate to the wall there were engineering concerns

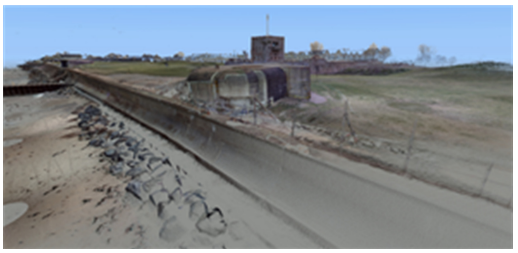

Figure 25. Wash out at Fort Henry and LiDAR survey of area – PzM9 (see Figure 10).

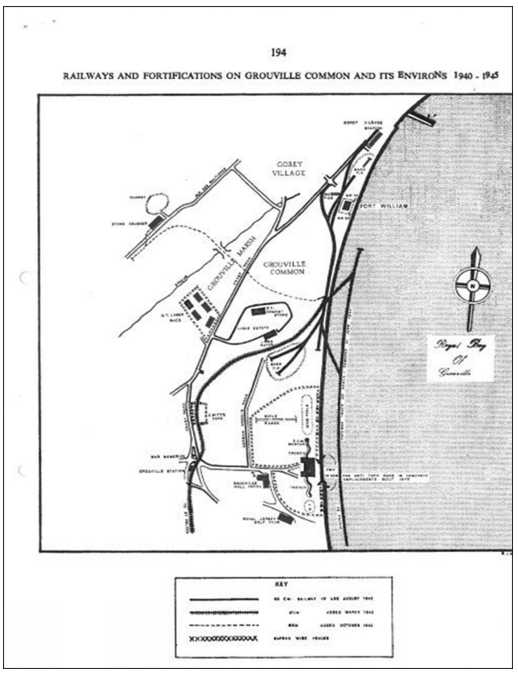

Figure 26. WWII Rail track on beach to provide sand for wall construction.

about the heavy concrete northern bunker rotating towards the sea wall because of the wash out of material from beneath it (Figure 27). If the rotation of the bunker toward the wall makes contact with the back of the sea wall this would impart a large additional point load pressure locally on the back of the mass concrete wall considerably increasing the overall outward loads (Figure 30).

The work on the Gun Site Café project i.e. PzM7, found that the optimum level currently for the top of a sea defence wall around the cost of Jersey should be approximately 9 m A.O.D. However, at Fort Henry, similar to Gun Site café, the top level of the WWII wall is also only 8.50 m and therefore the area behind this wall also suffers from severe overtopping.

Significant material losses in previous years to the area around the north bunker had resulted in the Jersey



Figure 27. Water flowing from beneath wall and sand migration up the beach.



Figure 28. Site Investigation at northern bunker rotation.



Figure 29. Sheet pile and capping beam repair.

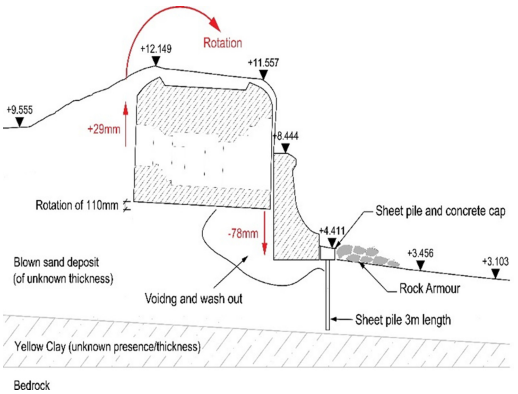

Figure 30. Cross section drawing of sheet piles and support to north bunker at Fort Henry PzM9.

Golf club pumping concrete beneath the bunker into the voids that became visible under and around the bunker (Figure 10). However, this adhoc reaction to the voiding beneath the bunker had not arrested the movements that took place in March 2015.

An intrusive site investigation was carried out in April 2015 based upon the desk study research and with further helpful localised information supplied by the golf club (Figure 28). At the same time the States of Jersey Engineers Department were installing the standard protection to the toe of the wall formed from sheet pile cut off with a capping beam tied into the WWII old concrete wall above (Figures 29 and 30).

In addition, to reduce further movement of sand along the beach rock armour was placed in front of the wall in the area between the two bunkers. The area of the wall was also surveyed using a drone and then locally a LiDAR survey was carried out to produce an accurate data record of what was happening around the northern bunker after the March 2015 storm (Figure. 25). This model data also enabled accurate drawings of the geometry and levels in around the bunker and if the wall to be produced.

The bunker and wall showed further signs of movement during the following monitoring period so remedial solution options were required to provide stability of the wall and protection of the fill behind the wall. The solutions included providing a run-off apron of concrete at the top of the wall and groins on the each between the two bunkers to stop further beach sand migration (Figure 30).

Conventional survey monitoring data also shows the rotation of rear part of the bunker was vertically upwards 21 mm and the front corner of the bunker closest to the wall settled downwards 78 mm, together showing a significant amount of rotation of the northern bunker. The wall itself in a localised area showed some settlement during the recent period of monitoring which is still ongoing (Figure 30).

7 LESSONS LEARNT

Physically and engineering wise the current sea defences in Jersey have greatly benefitted from the construction of these walls built during the WWII period. There are many areas and tales from archives relating to inconsistency and sabotage by the prisoners and forced labourers which to a certain extent provide an explanation for areas of inconsistency and, by modern standards, unsatisfactory sea defence concrete. However, a lesson that could be taken from this



Figure 31. Recent failure of a 1970s concrete wall at what would have been PzM8.

legacy of mass concrete defence walls around the flat beaches of the island is that if the planned wall in St. Clements Bay at Le Bourg was constructed, i.e. PzM8, then a significant amount of property is likely to have been saved from flooding in 1990 and again during the recent wall failure due to the storm surge and high tides of 2013 (Figure 31). Shortly after work began on PzM8, it was realised that a beach landing in this bay was unlikely because of the reef and rocks on the beach and as a military beach defence it was never built.

However, the investigation work and enhancement concrete overlay works at St. Ouens sea wall and the raising of the wall levels with a re-curve at Gun Site sea wall have meant that the basic inherent qualities of these mass concrete defence infrastructure walls has been found to be still be capable of structural function. They continue to work as sea defence but our recent studies and intervention and remedial work has also enabled them to be better understood and conserved thus protecting the Heritage aspects of Jersey's historic WWII concrete legacy.

REFERENCES

CI Occupation Society (Jersey) Ltd
Ginns, M. Anti-Tank walls on Jersey
Société Jersiaise

With thanks to: Armstrong, K; Johnson, M. and Mason, J. of Jersey Engineers Transport and Technical Services and Iles, K. of Arup (research, archive research and site investigations)

Concrete Solutions – Grantham et al. (Eds.)
© 2016 Taylor & Francis Group, London, ISBN 978-1-138-03008-4

Micropiling a bridge in construction in the motorway M-410 in Madrid (Spain)

C. Jurado Cabañes
Polytechnic University of Madrid/Ingecal Ingenieros, S. L., Madrid, Spain

ABSTRACT: The new highway M-410 in Madrid was constructed in the year 2007. This motorway near to Parla city crosses the road from Madrid to Toledo. To solve this crossing three bridges were constructed with deep foundations. On the two lateral bridges, called PS-18 and PS-19, after constructing the piles and the deck-slab resting on the soil, it was necessary to remove the earth under the concrete slab to make two lateral roads, but before this sonic tests were conducted in each pile and two boreholes which showed that the earth at the level of the bottom of the piles, was sandy and with a great water flow, so it was was impossible to retire the earth under the concrete deck-slab, because the piles were not correctly founded. To solution of this pathology was the construction of two sheets of deep micropiles at each abutment of the bridges.

1 INTRODUCTION

1.1 During the year 2007 a new highway called M-410 which surrounds the city along the south has been constructed in the village of Parla near to Madrid, the capital city of Spain (Fig. 1),

1.2 The new highway M-410 belongs to the project of construction, of a part of a net of infrastructures along the south zone of Madrid named REDSUR, and this consists of a highway of 25 kilometres, for the connection of the radial highways N-IV and N-V.

REDSUR comprises 81 new kilometres of highways and infrastructures, surrounding Madrid along their south side, that connects 16 cities and the cost of the works was 272 million Euros (Fig. 2).

The project was divided in 10 actuations and was finished in 2007 and the phase which is the subject of this paper, was the actuation number 2, to connect the villages of Arroyomolinos and Valdemoro.

REDSUR will improve the communications of 1.3 million people going to and from Madrid, who live in the southwest region, which supports a very heavy traffic of vehicles between 20,000 and 60,000 every day and whose roads have remained saturated during recent years. Near to Parla village this new motorway M-410 crosses the existing one A-42, which connects Madrid with Toledo (Fig. 3).

2 THE BRIDGES PS-18 AND PS-19

The bridges PS-18 and PS-19 are two symmetrical bridges with respect t the motorway A-42, with abutments constituted with sheet piles of 1.00 meter



Figure 1. Situation of Parla near Madrid.

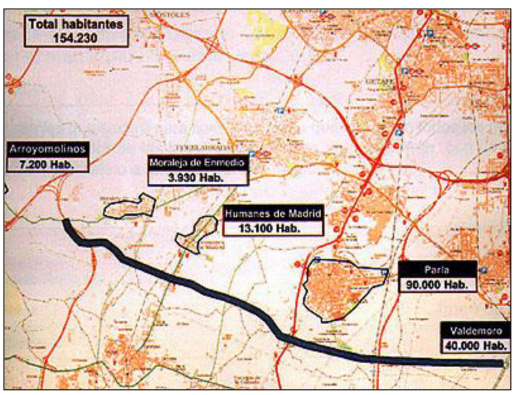

Figure 2. Plan of REDSUR actuation on the South of Madrid.

diameter and 13.00 meters long, separated 1.25 m in order to form one discharge arch between two piles, to permit the excavation under the bridge forming a hollow of 5.50 meter high, that could be covered with a reinforced concrete wall (Fig. 4).

3 THE PATHOLOGY DETECTED

In September 2007, sonic tests were conducted in each of the 22 piles of every structure, detecting that important anomalies existed on the bottom of the piles of both bridges. We recommended a thorough detail study of the pathology, to discover if these anomalies, could affect the structural behaviour of the bridges. The bridges should be opened to the traffic in January 2008.

As a consequence of this, four new boreholes and four penetrometer tests, each one at every abutment of the bridges, were made, discovering the existence of a cap of granular material with a strong flow of water, that had produced a washing of the concrete at the base of the piles (fig. 5).

In these conditions it was prudent to consider only the friction load of the piles, discarding the tip resistant



Figure 3. Situation of new the bridges over the motorway A-42 which connects Madrid with Toledo.



Figure 5. Sandy material under the bottom of one of the piles.

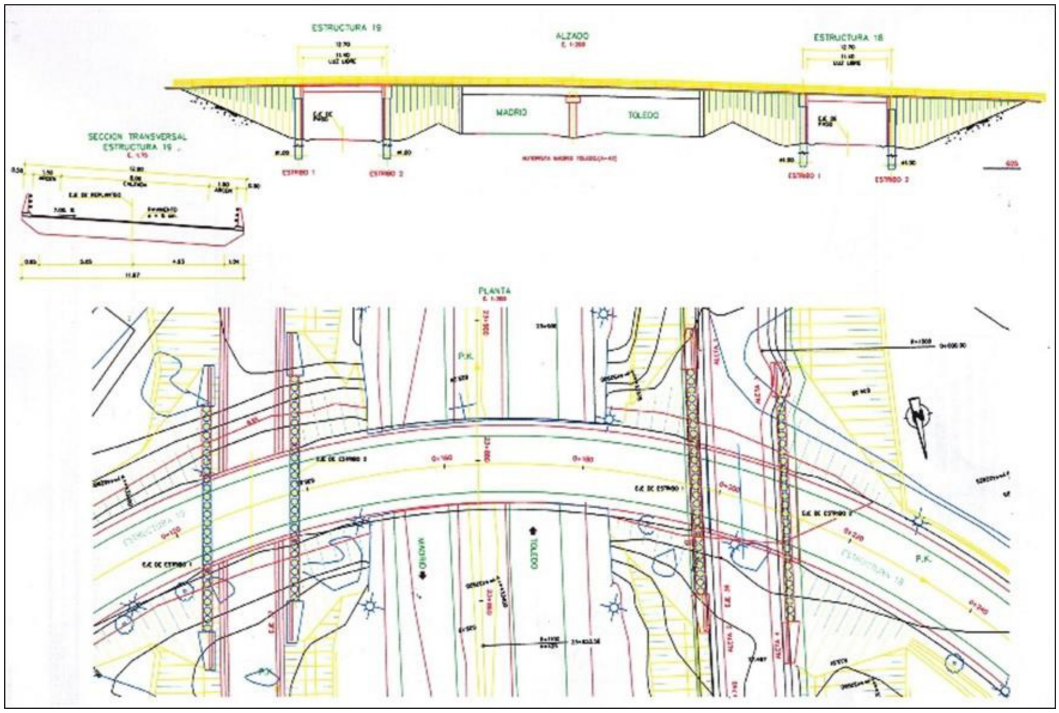

Figure 4. Plan of situation of bridges PS-18 and PS-19.

load, since we were not able to know what percentage of this last load could be useful. So for safety, it was decided to design a new system of foundation, that would allow the load to be resisted at the top of the piles, discarding completely the influence of the tip and considering only the friction resistance of the piles.

4 THE REPAIR OPTIONS

To repair the pathology two options were studied:

A. To perforate the interior of the piles and withdraw the low detritus on the bottom, subsequently injecting mortar that replaced the detritus. This would allow the complete restoration of the admissible tip load resistance for the piles.
B. To discard totally the capacity of the tip load resistance of the piles, considering only the friction resistance, which was not affected by the mentioned anomalies in the bottom, studying a supplementary system that was capable to resist the rest of the load.

The two bridges have at each abutment 11 piles of 1.00 m diameter. and 13.00 meters in length, tied on the top by a concrete tied beam, with a transversal section of 1.30 m width and 2.11 m height.

For the first option it was necessary to make three drilled holes in each of the 44 meters of piles, so this implies the accomplishment of $3 \times 44 = 132$ meters of drilling in concrete. The operative procedure would consist of injecting water through one hole and extracting the detritus through the other two, until the rejection was turning out to be clean water. Later closing two drilled holes, cement mortar would be injected through the third one with pressure, until it was overflowing, which would indicate that the hole had been refilled completely at the bottom of the pile and the three drilled holes. This system however presented the uncertainty, that if the bottom of the piles were located in a constant cap of granular material with a significant flow of water, much of the cement injection and mortar could get lost across the above mentioned cap and not return for the other two drilled holes. And there were indications, which showed that an underground flow of water existed at this depth. On the other hand, still supposing that this was not taking place, the accomplishment of 132 meters of drills and the later operations, would require an extraordinarily long time, not being able to conclude the works, before the time foreseen to open the bridges to traffic, in January 2008.

5 THE GEOTECHNICAL CAMPAIGN

The geotechnical characteristics of site can be seen in Figure 7. The geotechnical campaign showed the existence of four layers:

A. Superficial landfill corresponding to the package of road works with a thickness of 2.00 m.
B. Landfill of terrace with a thickness of 7.00 m. and a friction resistance for piles of $r_f = 3.36\ t/m^2$.
C1. Mioceno Sustratum. Coarse sandy very dense soil with a thickness of 7.00 m., a friction resistance for piles of $r_f = 9.00\ t/m^2$ and tip resistance of $r_p = 900\ t/m^2$.
C2. Substratum Mioceno. Coarse clayey very hard, soil which corresponded to the low substratum with a thickness until the end of the tested area.

6 THE ADOPTED REPAIR SOLUTION

Finally the adopted solution to solve the pathology detected consisted of the construction of two sheet micropiles of 200 mm diameter and 18 m length, inclined 15° with the vertical, outside the abutment of each bridge, in order to avoid the area of the bottom of the concrete piles, going 4.00 meters below the zone of the water flow, to situate the influence zones of the tip of micropile away from the saturated area, so the active and passive zone of micropiles were in healthy clays (figure 8).

Since the friction resistance load of the existing piles was intact, it was only necessary that each sheet of micropiles must resist the tip load resistance of the piles at every abutment.

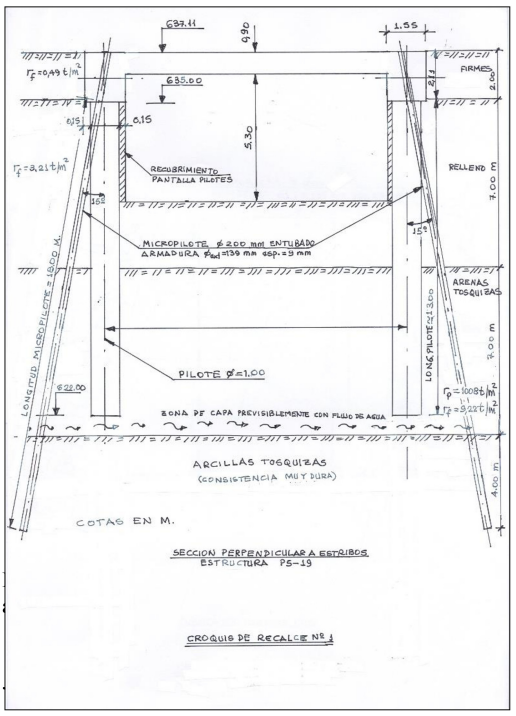

Figure 6. Solution adopted for the rehabilitation of PS-18 and PS-19.

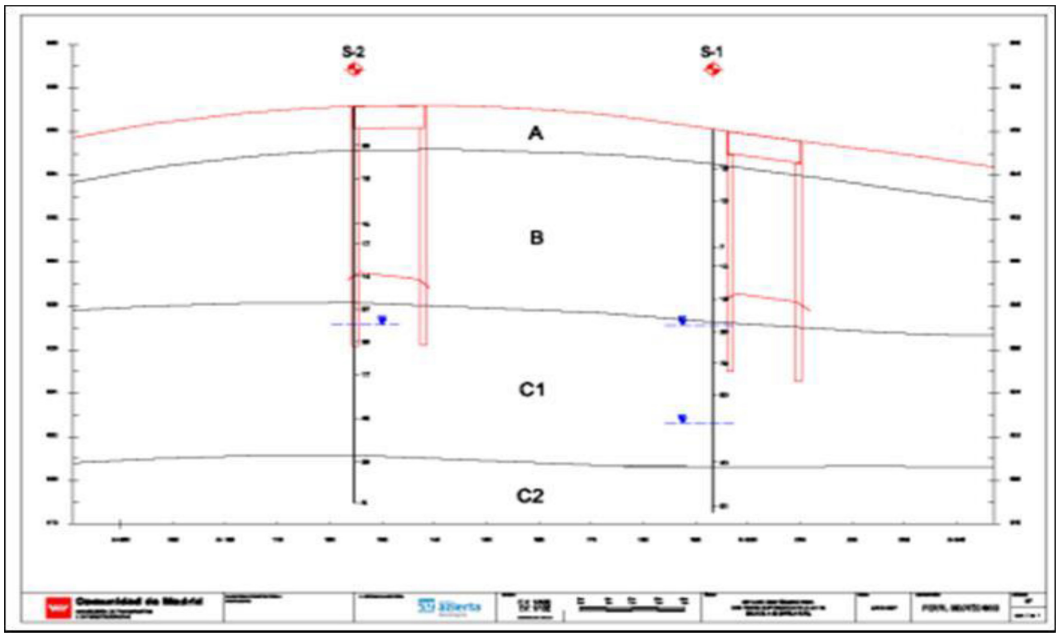

Figure 7. Geotechnical profile of the site.

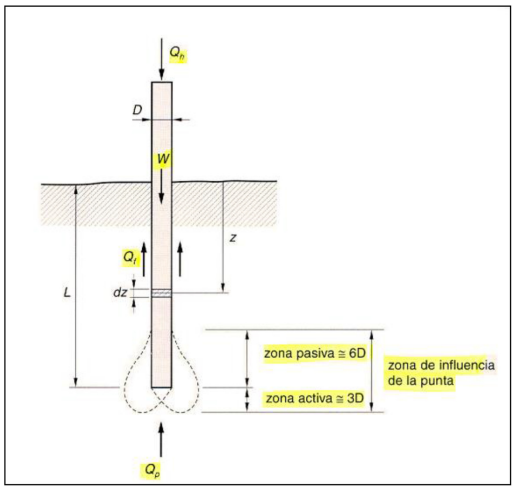

Figure 8. Active and passive zones of one pile.

Making the necessary calculations and discarding the tip load resistance of the existing piles, each new micropile might absorb $N_{p,Ed} = 736{,}96$ kN.

Discarding as is usual, the tip resistance of the micropiles and considering only the friction resistance, which is a supplementary security, and using four new micropiles at each abutment, every new micropile could resist $R_{fc,d} = 738{,}43$ kN, that is:

$$R_{fc,d} = 738,43 \text{ kN} > N_{p,Ed} = 736,96 \text{ kN}$$

Figure 9 shows the plan of the disposition of the existing piles and the new micropiles at each bridge.

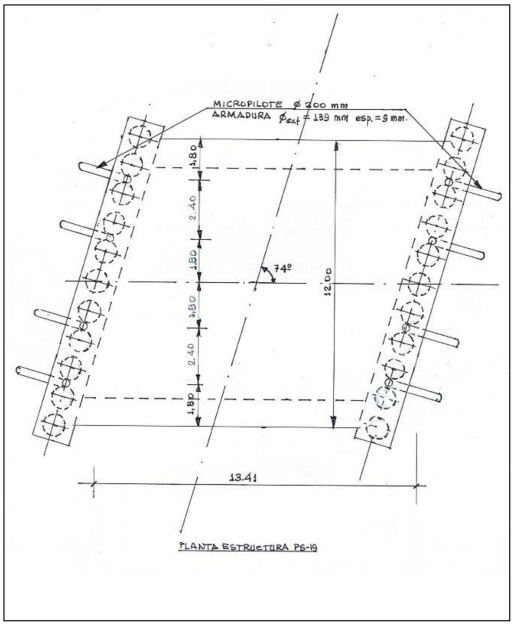

Figure 9. Plan of the existing piles and the new micropiles.

In this way, the existing piles resist part of the loads by friction resistance and the rest of the loads which must support the bridge are resisted by the friction resistance of the micropiles, avoiding the transmission of loads to the level of the water flow.

Figure 10 shows a transversal section of the micropiles and Figure 11 shows the micropiling work

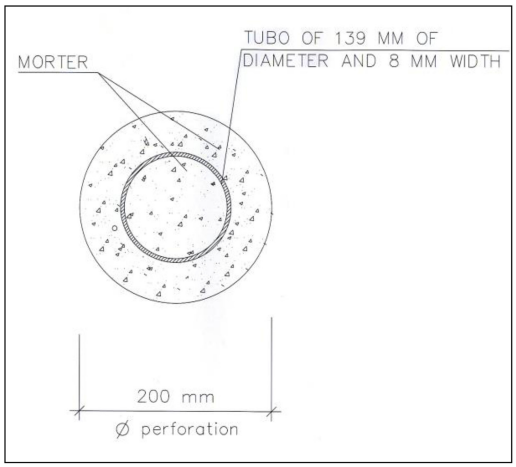

Figure 10. Transversal section of micropiles.



Figure 11. Micropiling Work on PS-18.

on bridge PS-18. Also it was necessary to design an element of connection between the existing tie beams of each abutment and the new micropiles.

For this, connectors were designed consisting of reinforced bars welded to the tube of the micropiles (Figs. 12 and 13)

7 CONCLUSIONS

The works were completed between December 2007 and January 2008 without any problems and the bridges were inaugurated on time, by the Mayor of the city of Madrid, at the end of January 2008.

By this system all the load was transmitted from the longitudinal beams at the level of the deck to the soil by the micropiles and the existing piles remain as a reserve of strength for the two bridges.

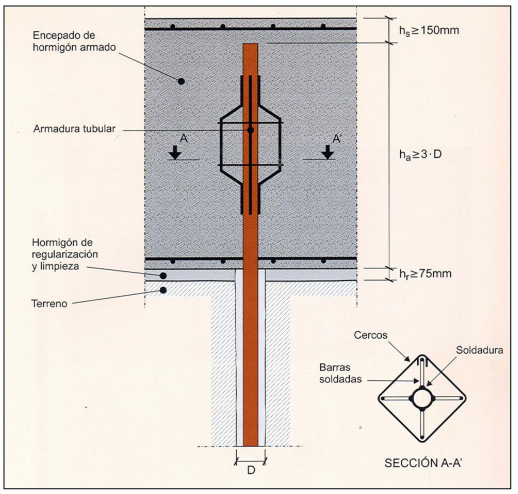

Figure 12. Connection between the existing structure and the new micropiles.



Figure 13. Connectors designed to transmit the loads to the micropiles.

REFERENCES

Escario, V. *Geotechnical Synthesis of the Soils in Madrid*. Ministerio de Trasportes y Comunicaciones. (1985).
Eurocode 1. *"Bases of project and actions in structures"*.
Eurocode 2. *"Project of structures of reinforced concrete"*.
Eurocode 3. *"Project of structures of steel"*.
Jiménez Montoya, P. García Meseguer, A.. Morán, Cabré, F *Reinforced Concrete*. 14ª edición. Ed. Gustavo Gili.
Spanish Ministry of Civil Works. *"Instruction on the actions to consider in the project of bridges of highway. IAP-98"*.
Spanish Ministry of Civil Works. *"Norm of seismic construction: General part and Building Construction"*. NCSE–O2 (Real Decreto 997/2002).
Spanish Ministry of Civil Works. "*Spanish rules relative to the actions to consider in the project of roadway bridges"*.



Taylor & Francis
Taylor & Francis Group
http://taylorandfrancis.com

Concrete Solutions – Grantham et al. (Eds.)
© 2016 Taylor & Francis Group, London, ISBN 978-1-138-03008-4

Road bridge decks sealing, joints and pavement practice, the Greek motorway experience

A. Kokkalis
Department of Civil Engineering, Democritus University of Thrace, Xanthi, Greece

P. Panetsos
Structural Maintenance of Egnatia Odos S.A., Thessaloniki, Greece

ABSTRACT: The Greek motorway network totals some 2,500 km crossing a rather mountainous terrain. A great number of bridges have been constructed along them. The standard construction bridge deck pavement practice is to lay 10 cm asphalt over a bituminized waterproofing membrane. Most Greek motorway bridge pavements have been trafficked for 5 to 25 years carrying 1 to 20 million Standard Axles, whilst they have been exposed to a variety of adverse weather conditions. The mountainous nature of the terrain means that the bridge geometry comprises many tight curves and steep slopes (for motorway standards). This means that there is a high need for repeated braking for heavy vehicles along downgrade bridges. Also centrifugal forces act along bridge horizontal turns. Thus, high horizontal shear strains apply to the bridge pavements and, in conjunction with reduced shear strength due to the existence of the watertight membrane, may cause a variety of wear and pavement damage. That wear has been observed as pot holes, shoveling, raveling or other types of shear failure, mostly appearing to downgrade decks in comparison to their twin upgrade decks of a bridge as well as to bridge decks in comparison to their adjacent embankments. Concrete bridge expansion joints are also a particularly vulnerable bridge construction element, affecting greatly maintenance operations. In this paper, an attempt is made to present and classify the extended experience concerning waterproofing, pavement surfacing behavior of bridge decks, as well as expansion joint decay which has been gathered along the Greek motorway network, especially along Egnatia Odos during the last 5–20 years of operation, together with a scientific documentation of the observed damage and decay.

1 CONCRETE BRIDGES ON GREEK MOTORWAYS

During the last 20 years an extensive motorway construction project has been taking place in Greece. A snapshot of the project progress in 2010 is illustrated in Fig. 1. Black lines show already completed and trafficked motorways, yielding a total of approximately 2,500 km, whilst, almost 500 km are under construction. Unfortunately, the severe economic crisis wracking Greece for the last 5 years, has radically retarded work progress. Egnatia Odos is the most famous completed motorway being a 680 km long 2-lane dual expressway crossing the western and northern Greece. PAThE is a 780 km long 2-lane dual expressway being the most important in Greece in terms of traffic volumes crossing south to northern Greece. Peloponnese and the western Ionian motorways complete the picture.

Greece is a rather mountainous country, so hundreds of motorway kilometers, particularly along Egnatia Odos, have been constructed in mountainous terrain (Fig. 2). The diverse terrain together with frequently imposed strict environmental terms, led to the construction of a great number of bridges (instead of high embankments) summing a total length of 150 km (single decks).



Figure 1. The Greek motorway network, black lines show completed sections.

Actually, more than 400 bridges, longer than 100m, have been or are under construction. Approximately 2–3% of the motorway length runs over bridges, corresponding to about 10% of the total motorway's construction cost.



Figure 2. A long dual deck bridge constructed at Egnatia Odos, mountain Pindos area.



Figure 3. Concrete spalling due to steel corrosion, due to water ingress.

2 WATERPROOFING PRACTICES AT MOTORWAY BRIDGE PAVEMENTS

Reinforcing steel (rebar) in bridges is particularly susceptible to corrosion. Because of the porous nature of concrete, moisture and winter road deicing treatment can seep into the concrete, reaching the rebar within. Exposed to these corrosive elements, the rebar will begin to develop rust corrosion products that are 2–10 times more voluminous than the original steel pieces (Kepler *et al*., 2000, Park *et al.,* 2008). As these corrosion products continue to build, stress on the surrounding concrete increases until the surface begins to crack and spall (Fig. 3). This may weaken and damage the stability of the bridge structure.

Winter motorway deicing is a common practice in mountainous motorway sections. The exposure of the decks to deicers is a primary cause of corrosion-related distress. Hence, a practice to inhibit water ingress is imperative.

Generally, the service life of a deck is dependent on the exposure conditions, the concrete permeability, the concrete cover, and the rebar. The life-cycle of typical motorway bridge extends to 100 years and rebar corrosion is, probably, the most important factor diminishing bridge life. Stipulating the risk of future corrosion is necessary so that the best repair or preventive strategy can be implemented.

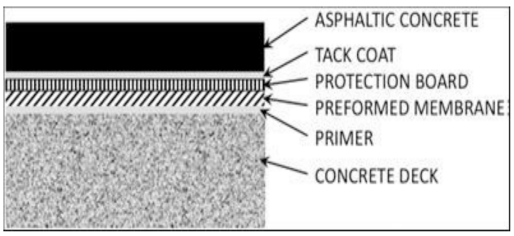

Figure 4. Typical components of concrete deck waterproofing.

In deicing environments, asphalt pavement overlays should not be placed directly on the deck concrete without a membrane, as the asphalt pavement may be cracked and hold chloride-laden water against the concrete surface causing accelerated corrosion and deterioration that is difficult to identify until serious problems develop. Waterproofing systems are designed to keep water off the bridge deck upper surface. Various types of waterproofing membranes are used in bridge deck protection. A waterproofing membrane is defined as a thin impermeable material acting as a barrier to protect the deck concrete from the penetration of moisture and deicing salts (NCHRP, 2012). Whilst deck membranes are applied to protect the underlying deck, they require a traffic bearing layer, usually a double hot-mix asphalt concrete wearing material, to protect the membrane itself from damage (Fig. 4). Obviously, the long-term performance of membrane systems is strongly affected by the integrity of the asphalt overlay. Other components are used to improve adhesion of the membrane to the deck. Inadequate performance by any component can result in poor overall performance.

Outlining the typical waterproofing practice applied to Greek motorway bridge decks, first the concrete deck surface should be at least three to four weeks old before starting any relevant work. The deck surface must be sound, dry, clean and free of protrusions and rough edges. Abrasive blasting may be used to remove any contamination, avoiding the use of water to clean the deck, as the surface must be dry before the primer is applied. The surface may also be cleaned with brooms, vacuum, or compressed air to remove any loose material and dust before applying the membrane system. Common practice is to first apply a primer coat over the deck to enhance the bond between the concrete deck and the membrane. Typically, the membrane is provided in roll form and is installed by merely rolling out the membrane in strips, as suggested in Figure 5. The membrane may be cut to fit as necessary to ensure that it is coextensive with the deck surface. The placement of preformed membranes should begin on the low point of the deck and provide adequate lap between adjacent strips. This permits water to drain without accumulating against the seams. The width of the horizontal overlaps should be at least 20 cm



Figure 5. Laying waterproofing membranes over a concrete bridge.

and that of the longitudinal overlaps should be at least 10 cm.

Once a course of the membrane has been laid out and fitted in place, it is heated to a temperature of approximately 90°C to form a tight integument which is highly waterproof and tightly secured to the deck. While the membrane is still in this heated condition, it is pressed down, preferably by means of a hand roller to ensure that all air bubbles are rolled out from between the deck and the membrane before the material has cooled. When installing the membrane, ambient temperature should preferably be at least 2˚ C, in order to allow the membrane to be properly heated and to retain heat long enough for the membrane to be rolled to remove air bubbles.

A minimum and maximum time should be specified between membrane application and the first layer of the asphalt overlay placement. The minimum time allows for the membrane to cure properly and depends on the manufacturer's recommendations. The maximum time reduces the length of time that the membrane is exposed to potential damage. Normal values range from 1 to 2 days. A tack coat is first used to enhance the bond between the membrane and the overlay to come.

Bridge deck pavements are extensively used both to protect the bridge deck against moisture and to provide good ride quality and skid resistance. According to OSMEO (2002) an asphalt 5 cm course is put directly on the tack coat above the waterproofing membrane and is normally an A260 (Highways Agency, 2009) asphalt base course layer. In case the waterproofing membrane is susceptible to damage by the overlaid coarser aggregates of the base course, a 20mm thick sand asphalt protective layer is recommended to be placed or finer aggregates should be preferred for minimal puncture potential. The temperature of the asphalt should not exceed 170°C degrees at pouring. During compacting the temperature should not exceed 150 degrees. Only vehicles involved with the asphalt courses should be permitted to the bridge deck area, since it is the contractor's responsibility not to damage the membrane. Then, over the base layer, a 5 cm A265 wearing course is laid. Finally, a 2.5 cm antiskid layer is laid, typical for motorways. Overall some 12 cm of asphalt layers cover and protect the waterproofing membrane of the bridge decks. This thickness is the typical thickness of protective pavement layers on concrete bridge decks in most European countries.

Membranes may include liquid applied acrylics, urethanes, neoprenes, vinyls, rubberized asphalts, silicones and preformed membranes such as rubberized asphalts, neoprenes and butyl rubbers, and ethylene propylene rubbers. The usual type of waterproofing membranes along the Greek motorway decks are hot applied rubberized or bituminized asphalt membranes according to AASHTO, (2010). In a few cases (Kristallopigi, Metsovitis and Grevenitikos bridges, Egnatia Odos), an acrylic membrane has also been applied.

In Europe using waterproofing membranes for bridge deck moisture protection is the most common practice. However, it should be mentioned that in many US States hot-dip galvanized rebar is used to eliminate the risk of spalling, because the zinc corrosion products are less voluminous and migrate away from the bar into the matrix of the concrete. The migration alleviates the potential for increased pressure, thus eliminating the risk of spalling (NCHRP, 2008 & 2012).

3 JOINT PRACTICE IN MOTORWAY BRIDGES

It is well known that the effectiveness of bridge joints is very important to the life expectancy of concrete bridges. Bridge expansion joints are used to accommodate horizontal/longitudinal and, to a lesser degree, vertical movements within bridge structures. More than 5.000 expansion joints have been constructed during the last 15 years along Greek motorways. They have been designed to accommodate movements, on average, of 50mm. A typical picture of a bridge joint along Egnatia Odos is shown in Figure 6. Finger joints have also extensively been used. Traffic durability, smooth transition, water sealing, speed and convenience of installation are the main characteristics sought by a typical concrete bridge joint (Austroroads, 2012). They can also be replaced without the need for excavation and should guarantee short lane closure time or even allow partial traffic flow during maintenance operations. To meet bridge deck skews is also a high requirement, since, due to the Greek mountainous terrain curved and skewed bridges make the rule.

4 DISTRESS AND DAMAGE IN WATERPROOFING STRUCTURES AND JOINTS IN MOTORWAY BRIDGES

Most Greek motorway bridge pavements have been trafficked for 5 to 25 years. Traffic volumes vary considerably along motorway sections, being heavier in the proximity of the capital, Athens, as well as in the Thessaloniki area. Actually, along the motorways, one



Figure 6. A typical expansion joint at a concrete bridge.



Figure 7. Pot holes and raveling appeared at a downgrade bridge deck in Egnatia motorway.

can meet a bridge carrying light traffic (almost one million Standard Axles (SA)) and another one carrying more than twenty million SA. Obviously, the number of SA being carried has a direct effect on the distress and damage induced to the overlay waterproofing structure of the bridge decks, as well as to the condition of the joints and their cumulative relative movement. It should be mentioned that, even in bridge decks trafficked only by two million SA, a number of (premature) failures have been observed.

A typical bridge in a mountainous terrain is usually exposed to a variety of adverse weather conditions. Deck winter temperatures are ∼1°C lower than the surrounding surfaces. Deck moisture exposure too, especially over rivers and ravines, is markedly greater. Hence, water freezing and thawing cycles are more severe in deck pavements.

Also, the mountainous nature of the terrain implies that the road alignment, hence the bridge alignment as well, comprises many tight curves and steep gradients (for motorway standards). This practically means that there is a high need for consecutive braking for heavy vehicles along downgrade bridges. Plus, high centrifugal forces develop along bridges at tight horizontal curves (as tight horizontal curves are considered the minimum ones corresponding to the design speed Ve or even to (Ve+10) km/h). Thus, high horizontal shear strains apply and upset bridge pavements. Also, as seen in Figure 4, the structure of the (relatively thinner compared with the adjacent pavements) deck pavements include a potential slippage surface (membrane). The bond strength between the waterproofing membrane and the concrete deck or the overlay has always been a matter of research (FHWA, 2001, Nicholls *et al.,* 2007). High horizontal stresses in combination with the adverse weather may cause a variety of wear and pavement damage such as cracking, pot holes, shoveling, raveling (Fig. 7) or other types of shear failure.

Such deterioration reduces service life of the bridge system and increases repair and rehabilitation costs. It is worth mentioning that this damage is systematically more extended and severe at downgrade decks in comparison to their twin upgrade deck of the bridge. The only sound explanation should be the additional effect of the horizontal repeated braking forces of the heavy goods vehicles along downgrades. Also, that pavement wear appears in greater frequency and severity along bridges than to adjacent similar embankment sections. The only sound explanation for that is the detrimental effect of the membrane slippage surface.

Although several types of defects have been observed within waterproofing systems, the four predominant ones are:

– lack of adhesion between the waterproofing membrane and the concrete deck,
– lack of adhesion between the waterproofing membrane and the asphalt surface,
– moisture penetration through the membrane and
– pot holes, raveling and similar local failures in the overlay pavement generally appearing more frequently than the adjacent pavements.

The typical degradation mechanism is the accumulation of water above the membrane in the bottom portion of the asphaltic concrete. This phenomenon, combined with freezing and thawing cycles and repeated hydraulic pressure from traffic, weakens both the asphalt layers as well as the bond between the asphaltic concrete and the membrane (NCHRP, 2012). Hence, damage to the asphalt overlay itself, both induces membrane deterioration risks bond deterioration.

Many attempts have been made to solve the bridge deck waterproofing problem but none of these has been entirely successful from the standpoints of effectiveness, cost, ease of installation and durability. Various coatings have been employed but have not provided a durable, fully waterproofed layer over the entire surface and for a long period of time. Various sheet materials have also been utilized but these have been difficult to install and have not bonded well to the deck and also frequently form air pockets when entrained moisture becomes heated during warm periods (Nicholls *et al*., 2007). Generally, waterproofing bituminized membranes protected by asphalt overlays were found to be quite efficient and particularly cost-effective in preventing salt intrusion into the underlying deck. When properly constructed, they can prevent salt infiltration, but their service life depended on the rate at which the membrane deteriorated. In any

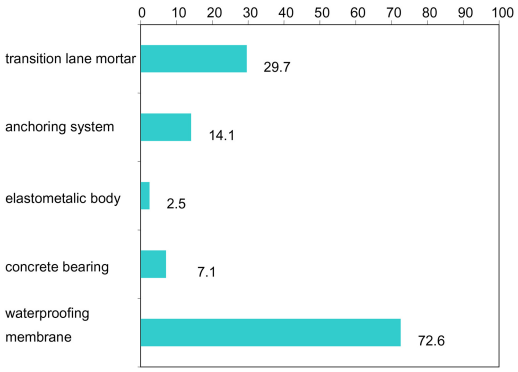

Diagram 1. Damage statistics (%) of the expansion joints failure type along Egnatia Odos bridges.

case, after 15 years of service, membranes are expected to have been deteriorated and to have exhausted their design life as a result of ageing and traffic fatigue.

Fatigue cracking is also a primary mode of distress in bridge deck pavements and directly affects the durability of the asphalt overlay and the whole waterproofing structure. Fatigue cracking, in conjunction with moisture ingress, typically reduces the stiffness of the asphalt mixture and the adhesive bond between the asphalt layer and the bridge deck. Several studies have been conducted to assess the fatigue cracking potential of mixtures in bridge deck pavements (Park *et al*., 2008). As mentioned, moisture been trapped within the deck or in the inner face between the deck and the membrane may expand when frozen, causing the asphalt to lift and crack. Air blistering underneath the membrane also has a similar result. Blistering will also result in puncturing of the membrane by the coarse aggregates of the base asphalt course. Hence, the waterproofing structure will experience maintenance problems resulting in water leakage passing through the asphalt into the concrete deck. If the highway has been salted, the leaks can result in rapid rusting of rebars, deck plates and other ferrous metal parts.

As far as bridge expansion joints are concerned, a procedure for their assessment has been established at Greek motorway Egnatia Odos. It is based on monitoring joint functionality, recording their picture and measuring the displacements.

A statistical evaluation of the inspection findings of the bridge expansion joints along Egnatia Odos has been conducted. All relevant findings gained by that detailed inspection are recorded in an electronic database (inventory) and their analysis is carried out in order to gain useful results regarding the time, the extent and the type of damage that takes place in the bridge expansion joints. In Diagram 1, the various types of damage observed have been recorded. Loss of the water proofing membrane happened at 72nd may facilitate damage of the joint anchoring system (14.1%). Actually, a correlation of $R = 0.6$ has been found.



Figure 8. Transition mortar failure along an expansion joint.

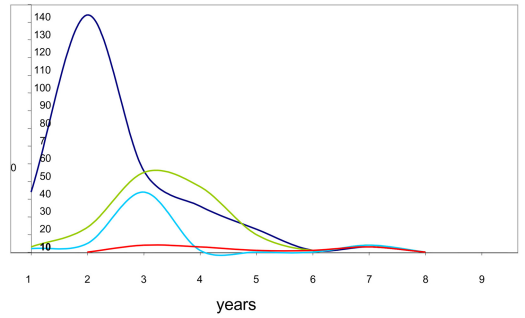

Diagram 2. Number of expansion joints failures observed (transmission mortar, anchoring system, concrete bearing and body failure) along years of operation.

In Diagram 2, the distribution of the time elapsed since the installation of the expansion joints, in respect of the various types of damage observed, is depicted. The diagram has been based on empirical deterioration data of almost 10 km of bridge expansion joints. Thus, their representative maintenance life cycle can be estimated. Damage has been classified to a 9-degree severance scale from a fully operative joint to one needing immediate repair. Transmission lane mortar failure (Fig. 8) has proved to be the first damage to appear. The mortar receives direct dynamic strains by the stronger metal body, which cause its fracture. To replace the mortar is an easy and quick maintenance operation. After 3–4 years, on average, joint anchoring systems and concrete bearing surfaces fail, needing heavier maintenance operations involving lane closures. In general, a well-constructed concrete bridge expansion joint is not expected to last more than 5 years. Damage observed is consecutive with those in similar evaluation studies (Ni *et al*., 2007).

5 DISCUSSION AND CONCLUSIONS

Greek Motorways have accumulated extended experience in using asphalt pavements and bituminized membranes to waterproof bridge decks. That experience is generally in accordance with that gathered

by other Highway Agencies. An extended presentation of the issue is made by NCHRP (2008 & 2012). More specifically, the combined experience shows that asphalt concrete overlays with a waterproofing bituminized membrane have, more or less, the advantages of:

- low cost,
- desired service life,
- ease and speed of installation,
- familiarity with the product and the method,
- availability and
- improved rideability of the surface,

and the disadvantages of:

- spalling and deterioration of concrete deck below the membrane,
- certain installation or other problems resulting in water getting trapped underneath the membrane,
- lack of adhesion between the waterproofing membrane and the concrete deck and horizontal shear failure at the membrane,
- voids under the membrane and membrane blistering resulting in punctured waterproofing membranes,
- difficulty of removal,
- underlying deck cannot be seen or inspected and effectiveness of membrane is unknown,
- necessity for lane closure during maintenance and
- shoving of the membrane over time.

Along Greek motorways, the waterproofing bridge structure lifespan observed has been, on average, 15 years. Generally, waterproofing membranes are not expected to last much longer than the asphalt wearing surface. However, one resurfacing of the asphalt overlay should be always taken into account. To achieve this, the initial asphalt thickness has either to be sufficient to allow the top surface to be milled without damaging the membrane, or the milling depth should be shallower.

That 15 years lifespan is consistent with similar evaluation studies. Extensive research in US (NCHRP, 2008 & 2012) determine the expected lifespan of the membrane-overlay system as 12–19 years, on average 15 years, when installed on new bridge decks and anywhere between 6 and 19 years when installed on existing bridge decks.

As far as the cost is concerned, a typical bituminized fabric costs about 10 €/m^2 at today's prices whilst the acrylic membrane cost typically reaches 40 €/m^2. Taking into account both the asphalt concrete overlay and the bituminized membrane, the mean installed waterproofing structure cost amounts to about 50 €/m^2. It should be mentioned that, in a relevant evaluation study, Kepler *et al.,* (2000) compared the life cycle costs of 33 different corrosion protection systems and concluded that the use of hot rubberized asphalt membrane was the second-lowest cost strategy. However, spending for the membrane itself 40 €/m^2, instead of 10 €/m^2 (acrylic ones instead of bituminized ones) may mean a fourfold cost for that specific item, a 70% increase in cost for the whole waterproofing structure (membrane-overlay pavement), but, actually, only an approximately 2–3% increase for the total cost of the bridge.

Unlike the 15 year waterproofing bridge structure lifespan, a typical bridge expansion joint is expected to last 1/3 of that time. The underlying waterproofing membrane is again the most usual damage, although not having the gravity of a similar deck membrane damage, mainly because it can be easily replaced. What also requires frequent action is the replacement of the transition lane mortar, the fragility and disintegration of which directly affects vehicle movement evenness as well as the stability of the joint itself.

REFERENCES

AASHTO 2010. Bridge construction specifications. 3rd edition, *AASHTO*, Washington D. C.

Austroroads 2012. Design rules for bridge bearings and expansion joints. *AP-R405-12*. Sydney, Australia.

FHWA 2001. Long term pavement performance. Test method for determining the creep compliance, resilient modulus and strength of asphalt material using the indirect tensile test device. *FHWA* Version 1.1, LTPP Test Protocol.

Highways Agency 2009. Design Manual for Road & Bridges, Vol. 7 Pavement Design and Maintenance.

Kepler, J. L., D. Darwin & C. E. Locke 2000. Evaluation of corrosion protection methods for reinforced concrete highway structures. SM Report No. 58, *University of Kansas Center for Research*, Lawrence, 222p.

NCHRP 2008. Guidelines for selection of bridge deck overlays, sealers and treatments. Project 20-07, Task 234, *Transportation Research Board*.

NCHRP, 2012. Waterproofing membranes for concrete bridge decks. *Transportation Research Board Synthesis 425*.

Ni, Y., X. Hua, K. Wong and J. Ko 2007. Assessment of bridge expansion joints using long-term displacement and temperature measurement, *Journal of Performance ao Contructed Facilities*, Vol. 21, Issue 2.

Nicholls, J. C., R. W. Jordan, K. E. Hassan, J. T. Williams & A. S. M. Badr 2007. Asphalt surfacing to bridge decks. 4th *International Conf. Bituminous Mixtures and Pavements*, Thessaloniki, 19–20 April, Greece.

OSMEO (Greek acronym for Guidelines for the Design of Transportation Works), 2002. *Greek Ministry of Public Works*, 3rd edition, 1st Volume, Greece.

Park H. M., J. Y. Choi, H. L. Lee & E. Young. 2008. Performance evaluation of a high durability asphalt binder and a high durability asphalt mixture for bridge deck pavements. *Construction Technology*, *Elsevier Ltd*.

Zimmerman, J.M., Olson, S.A, & Schultz, A. E. 2007. Determining economic strategies for repair and replacement of low slump overlays of bridge decks. Minneapolis, *Minnesota Department of Transportation, MN/RC-2007-14*.

Concrete Solutions – Grantham et al. (Eds.)
© 2016 Taylor & Francis Group, London, ISBN 978-1-138-03008-4

Corrosion propagation phase in reinforced concrete facades

A. Köliö & J. Lahdensivu
Tampere University of Technology, Tampere, Finland

ABSTRACT: There is a rising national concern in Finland on increasing maintenance needs of the existing building stock. Active corrosion was studied as an extension to the service life of concrete facade panels in Nordic climate. The objective was to contribute to the knowledge on the corrosion propagation phase in these structures under actual long term weather exposure and to generate data for its modelling purposes. The project combined statistical analysis of a large database of condition investigation data to the more in-depth analysis of twelve case-study buildings and field measurement data on reinforcement corrosion. Corrosion rate was tied to weather parameters representing the geographical location of the buildings by a time series analysis with corresponding weather data. Although carbonation resistance remains as the primary factor in ensuring proper service life, it was found that the modelling of active corrosion may provide a considerable extension to it.

1 INTRODUCTION

Reinforcement corrosion affects concrete structures basically either by cracking of concrete cover caused by corrosion products or by reduction of effective steel cross-section. However, cracking is typically the first sign of corrosion damage visible to the structure's surface. Before visible cracking occurs the structure has gone through an initiation phase and a propagation phase until crack formation. Both phases can be analysed as separate entities or combined to form a holistic view of the structure's lifetime for service life design purposes.

The majority of the existing concrete facades in Finland have been built at a time when service life design practice was not yet established; whereas today, a service life requirement of 50 years is commonly set based on the initiation phase i.e. carbonation resistance of the structure (Concrete association 2012). This strategy provides additional safety since no damage at all has happened yet at the chosen end of service life. In addition, in new construction, carbonation can be fairly easily accounted for by engineering concrete composition and reinforcement cover depths accordingly. Concerning existing buildings, a problem is formed since these properties are already fixed.

Concerning reinforced concrete service life, the most used concept is the division of the service life into an initiation phase and a propagation phase as first introduced by Tuutti (1982). This dual phase model illustrates that the principal requirement for corrosion of steel in concrete is the de-passivation of the reinforcing steel (in the initiation phase). The de-passivation happens via carbonation of the surrounding concrete or locally by the ingress of chlorides.

Subsequent to initiation, is the propagation phase where the reinforcement is corroded generating ferrous oxides i.e. rust (Tuutti 1982). The rate of corrosion, as well as the type of corrosion products formed, is influenced by the corrosion environment, namely temperature, moisture and pH and their fluctuation (Page 1988; Andrade and Castillo 2003). Available limits for the end of service life are e.g. cracking/spalling, critical deflection or collapse (Li 2004).

In existing structures, the concrete quality has been weaker and therefore the initiation phase is in many cases already passed. This makes the assessment of the residual service life of these structures problematic in two ways: (i) the residual service life is, by definition, zero even though no damage at all has happened, (ii) there are no methods available to evaluate the residual service life since existing methods are based on initiation.

This research entity was focused on the service life design and maintenance strategies of existing concrete facades in Finland. Service life extension is gained by defining the end of service life in a new way and reliably modelling the corrosion propagation phase.

2 RESEARCH MATERIAL AND METHODS

The propagation of corrosion on concrete facades in Finnish environmental conditions was studied by a series of field and laboratory studies conducted on twelve residential concrete buildings located in different parts of southern Finland. The studies were conducted in connection to the normal condition assessment practice of these buildings. In addition, the response of corrosion rates in concrete facades to an outdoor environment was analysed based on long term (25 months) field measurements on concrete facades under natural conditions. The experimental

results were contrasted to statistical information on 947 case-study buildings.

2.1 *Characterization studies on case buildings*

The type and critical amount of corrosion products to form visual damage were studied by electron microscopy and X-ray diffractometry on concrete and reinforcement samples. The samples were taken from existing concrete facades on visually damaged locations. The research material was gathered from 12 buildings chosen to be consistent with the larger statistical data. The buildings were located in the southern parts of Finland and their construction years ranged from 1971 to 1984. In all 27 sample cores of 50 mm diameter were drilled from the outer layer of the facade panels directly on visually observable corrosion cracks or spalls.

The length of the active corrosion phase was calculated by subtracting from the total age of the samples the time of initiation determined by carbonation depth measurements. The reinforcing bars trapped inside the carbonated layer of concrete were extracted from the core samples and subjected to electron microscopic studies.

Cross sections of the reinforcing steel samples were prepared by moulding into resin followed by mechanical grinding and polishing (without water to avoid dissolution of rust). The cross-sectional samples were characterized with a scanning electron microscope (SEM, ULTRAplus, Zeiss) equipped with an energy dispersive spectrometer (EDS, INCA Energy 350 analyzator with INCAx-act detector, Oxford Instruments). The overall thickness of corrosion products was measured from the SEM images of the samples by utilizing an image analysis software (imageJ).

EDS analyses were performed on the samples to study the elemental composition of the rust layer. Later on, scraped rust powder from 12 samples was studied with an X-ray diffractometer (XRD, Empyrean, PANanalytical) to analyze compounds of the corrosion products.

2.2 *Corrosion monitoring*

Long term corrosion current density measurements based on linear polarisation resistance were conducted in 2000–2002 on concrete facades and balconies of residential buildings in two locations in Finland: an inland location at Fysiikanpolku 5, Tampere, built in 1978 and a coastal area at Joupinrinne 4, Espoo, built in 1978 (Mattila 2003). The instrumented structures were, in both measurement sites, facing southern directions: at Fysiikanpolku southeast (154 degrees from north, clockwise) and at Joupinrinne 4 southwest (223 degrees from north, clockwise). This data was combined with long term weather observation data corresponding to the same time period.

The weather observation data was collected for this study by the Finnish Meteorological Institute (FMI) and it was then further refined to form four weather parameters: Temperature (T, [°C]), relative humidity (RH, [%]), amount of wind-driven rain on the measured wall surface (I_{WA}, [mm]), amount of direct and diffuse solar radiation on the measured wall surface (RAD, [kJ/m^2]). The data was obtained from observation stations nearest to the case buildings with a time resolution of three hours. Multi linear regression analysis was finally used to determine the partial influence of single or a sequence of weather parameters to the observed corrosion current density.

Table 1. Material for the statistical analysis.

Parameter	Brushed painted concrete facades	Exposed aggregate concrete facades	Concrete balcony slab
Age of the structure [a]	9–43	7–37	7–52
Visual ratings [number of observations]	250	193	331
Carbonation coefficient [number of samples]	1 285	849	884
Reinforcement cover depth [number of measurements]	60 640	104 958	12 957

2.3 *Statistical condition investigation database*

Concrete facades of buildings in Finland have been subject to condition investigations since the late 1980s and data measured by standardised procedures (desk studies, visual observation and rating, field measurements, laboratory analyses) has been produced in the majority of these assessments (Lahdensivu et al. 2013). A database has been collected from condition assessments conducted by various professional engineers during 1992–2006. The database includes the condition assessment information of 947 buildings built 1965–1995. (Lahdensivu 2012). Typically, the same building has not yet been subjected to assessment more than once. This means that each building in the database represents an individual case.

In regard of reinforcement corrosion, the investigated structures have been subjected to thorough cover depth mapping, carbonation depth and chloride content measurements and visual inspection during the condition assessment (Table 1).

The specified concrete grade used in facade panels was equivalent to a C20/25 from 1965 until 1989. The cement type used in these precast panels was mostly CEM I ordinary Portland cement. The concrete composition realized during construction has not been analysed in connection with the condition assessments and is therefore not known precisely.

3 RESULTS AND DISCUSSION

3.1 *Statistical analysis of the service life*

The age at which visual corrosion damage is generally observed in concrete facades was studied using

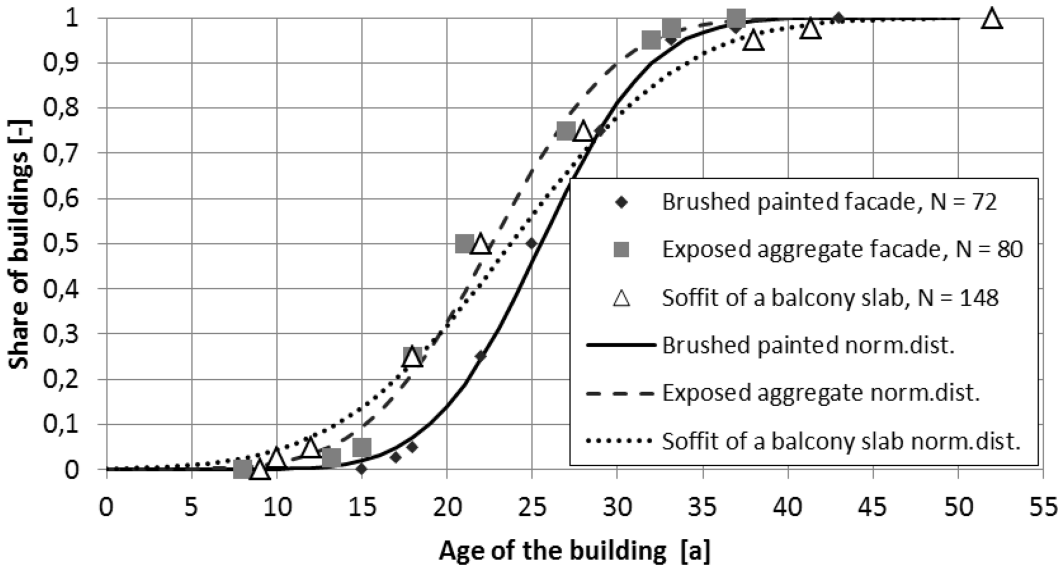

Figure 1. A statistical model for the evolution of corrosion damage on concrete facades.

visual damage ratings given in condition assessments. This damage rating was used together with the age of buildings to study the time it has taken for corrosion damage to emerged (Fig. 1).

The first visual damage had occurred after 15 years from construction in brushed and painted concrete facades and after 8 years in exposed aggregate facades. In balcony slabs, first damage was observed after 9 years. By median, visual corrosion damage had formed on concrete facades after 21 to 25 years from construction (exposed aggregate and brushed painted respectively). The generation of corrosion related damage has thereby been quite fast in these structures. Corrosion damage seems to be a problem especially with the small concrete cover depth cases where both initiation and active corrosion is fast. The statistical analysis is discussed in more detail in (Köliö et al. 2014).

3.2 *The critical extent of corrosion*

The age of the studied concrete structures was on average 38.8 years. Contrasting to the statistical information (Fig. 1) reveals that the damage has in these cases been quite far advanced in order to be visually observable. The average time under active corrosion was, for the cracked locations, 26.0 years (n = 15) and for spalled locations 33.1 years (n = 13). In the studied structures, the main reason for the damage to emerge in the studied time span as cracking or spalling was the concrete cover depth in relation to the rebar diameter, i.e. the cover/diameter ratio. It should also be noted that for all of the samples, corrosion had initiated quite fast (by average 12.6 years) which indicates that both concrete resistance against carbonation was poor and the environmental conditions favorable to carbonation.

The SEM analysis confirmed that corrosion products form layers of different composition around the steel. The corrosion products also contained veins of highly dense rust and veins of, presumably, residue of concrete pore water. Also particles that were trapped inside the rust were observed.

The outer rust layer contained typically less iron and on the other hand more oxygen and various other elements than inner and single layers. In the inner rust layer the amount of iron was higher and the layer was composed more strictly of pure iron oxides. Particles that were entrapped in the rust were mainly composed of calcium, silicon, and oxygen. These constituents originate from the calcium-silicate-hydrate (CSH) and the pore water of concrete. The study suggests that the more porous corrosion products responsible for the most volume increase are located on the outer circumference near the concrete interface.

Mainly Goethite, Feroxyhyte and Lepidocrocite corrosion products were identified in the majority of the samples by comparing the X-ray diffraction patterns to literature and powder diffraction files (Legodi and de Waal 2006, Drits et al. 1993, PDF 00-060-0344, PDF 01-079-1971). However, more sophisticated methods could be used to study the heterogeneity of the rust in more detail.

Corrosion products associated with carbonation initiated corrosion on the studied concrete facade panels were mostly hydroxide type rust with a unit volume of roughly 3 times the volume of iron (Jaffer and Hansson 2009). Taking the determined relative volume of the rust layer into account, the required corrosion penetration to initiate visually observable cracks in the studied facade panels was on average 53.6 μm (total range 14.5–90.4) with a corresponding rust thickness of 111.7 μm. The large scatter associated with rust

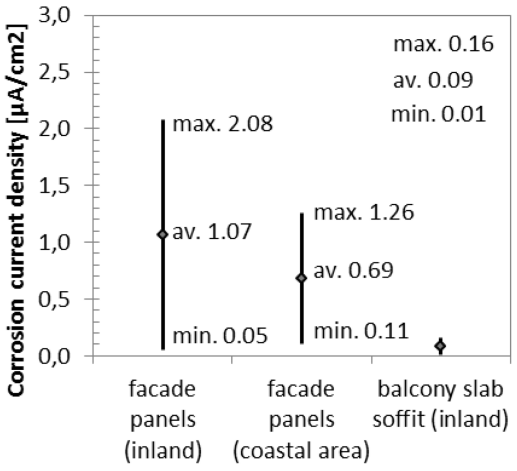

Figure 2. Monthly averaged corrosion current densities in facade structures in inland and in coastal area of Finland.

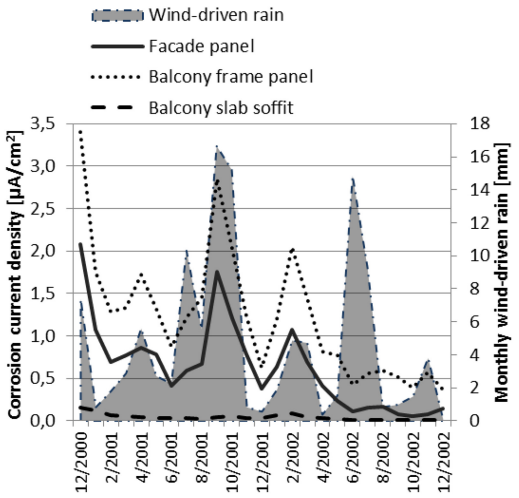

Figure 3. Comparison of the monthly wind driven rain amount on the structure to the observed corrosion rate in inland (Fysiikanpolku 5).

thicknesses should, however, also be taken into account in practical application of the limit state. The analysis on the extent of corrosion is discussed in more detail in (Köliö et al. 2015).

3.3 *Corrosion rate*

The corrosion rate monitoring data visualizes that the consecutive years have been different regarding the corrosive environmental conditions. Measured corrosion current densities show high scatter but are in general rather high (Fig. 2).

An initial presumption that corrosion rates will be higher on sites located in coastal regions was not visible during the measurement period. The wind-driven rain amounts on the structures have during the monitoring period been 47% higher inland than in the coastal region. Inherently, the corrosion rates have been 11–18% higher inland than in the coastal region. This observation stresses the importance of the micro climate around the building along with the geographical location in regard of degradation rate. In the bottom surface of the slab, the shelter from wetting is shown clearly as negligible corrosion rates.

In a regression analysis between corrosion rate and weather parameters all seasons showed high correlation between wind-driven rain and corrosion rate (Figs. 3 and 4). However, correlation was low in summer season at Fysiikanpolku 5 site due to the rain event at 6-7/2002 and in spring at Joupinrinne 4 site due to a non-captured rise in corrosion rate at 4/2001.

A multi-linear regression model for corrosion rate was created based on the correlation results of single weather parameters. The model was composed of linear relationship equations (Eq. 1) for every season utilizing monthly averaged weather parameters of temperature (T, °C), relative humidity (RH, %), wind-driven rain (I_{WA}, mm) and solar radiation (RAD, kJ/m^2). The choice of parameters to the equation was made by optimizing the parameter composition in regard of the total correlation to corrosion rate (coefficient of determination) as well as choosing a composition of parameters where the effect of single weather parameters is of the suitable form (negative/positive).

Table 2 shows the parameters and coefficients that can be applied in modelling reinforcement corrosion rate in concrete facades together with monthly weather data.

$$y = \beta_0 + \beta_1 \cdot x_1 + (\beta_2 \cdot x_2 + \beta_3 \cdot x_3 + \beta_4 \cdot x_4) + \nu \qquad (1)$$

where y = the dependent variable (corrosion current density); β_0 = interception term; β_1, x_1 = coefficient and parameter of the first weather parameter; β_2, x_2 = coefficient and parameter of the second weather parameter (optional); β_3, x_3 = coefficient and parameter of the third weather parameter (optional); β_4, x_4 = coefficient and parameter of the fourth weather parameter (optional); and ν = error term.

The corrosion initiation phase normally in the existing painted concrete facades and painted balcony frame panels is on average 20 years. (However, significantly faster and slower initiation may occur, too!) Taking this average behaviour into account and utilizing a 30-year weather data for the propagation phase, the concrete service life can be illustrated as combined initiation and propagation for both locations (Figs. 5 and 6).

The average long term corrosion rate, after initiation, was, for concrete facades 1.2 μA/cm^2 inland and 1.7 μA/cm^2 in coastal areas. For balcony frames the average corrosion rate was 2.0 μA/cm^2 inland and 2.8 μA/cm^2 in coastal areas. Even though corrosion rates were lower in the coastal area than inland during the actual monitoring period (Fig. 2) the long term corrosion rate level was still the opposite. The two studied facades were, however, very exposed to driving rain which leads to considerably high corrosion rates.

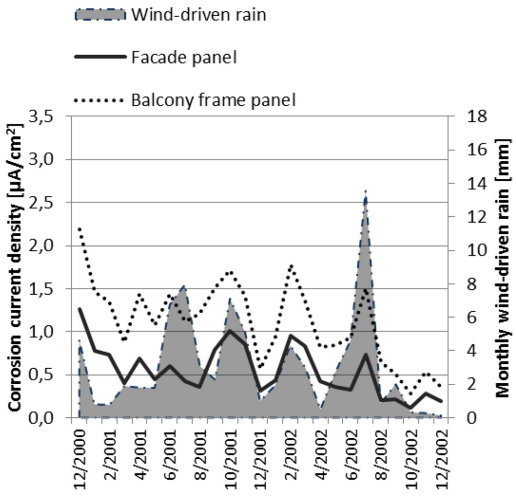

Figure 4. Comparison of the monthly wind driven rain amount on the structure to the observed corrosion rate in coastal area (Joupinrinne 4).

Table 2. Regression models for reinforcement in facade panels (with heat flux) and balcony frame panels (cold structures).

Season	R squared	Parameter	Coefficient, facades	Coefficient, balcony frames
Spring	0.45	β_3, (I_{WA})	0.035	0.126
		β_4, (RAD)	−0.0008	−0.0007
		β_0 (intercept)	1.913	2.091
Summer	0.95	β_2, (RH)	0.011	0.065
		β_3, (I_{WA})	0.037	0.047
		β_4, (RAD)	−0.0006	−0.0007
		β_0 (intercept)	0.562	−2.749
Autumn	0.69	β_3, (I_{WA})	0.084	0.122
		β_0 (intercept)	0.112	0.472
Winter	0.79	β_1, (T)	0.068	0.101
		β_3, (I_{WA})	0.134	0.235
		β_0 (intercept)	0.857	1.420

4 CONCLUSIONS

The research project confirmed that using the active corrosion phase, rather than defining service life by the initiation phase, can provide a considerable extension to the service life of concrete facade panels in Nordic climate. This extension can be from ten to even 30 years based on the case studies.

The occurrence of visual damage is a natural way of judging the service life of these structures since all of the renovation and maintenance decisions are made based on investigations which are usually commissioned because of these visual signs. Corrosion induced damage occurred on the studied structures commonly on the lap splicing locations of rebars, in the edges and window openings of the panels and in locations with pronounced moisture load due to poorly

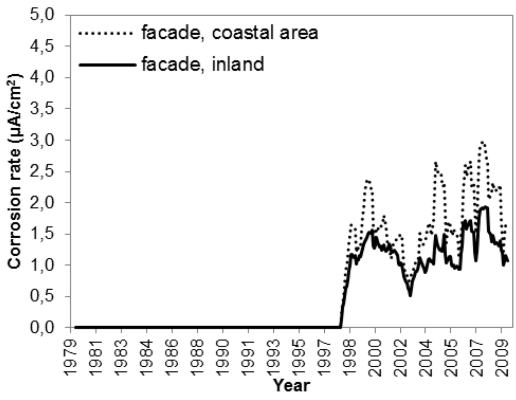

Figure 5. The average case of combined initiation and propagation in concrete facades.

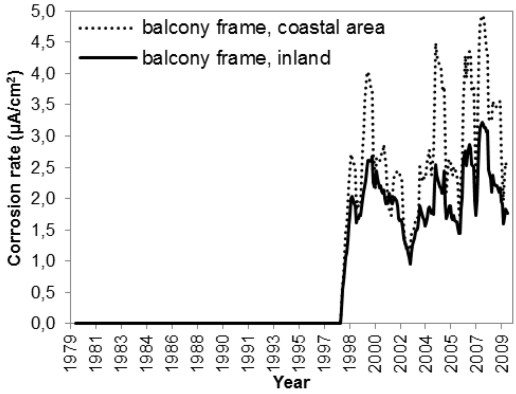

Figure 6. The average case of combined initiation and propagation in concrete balconies.

functioning flashings and rain water runoff control. If the ratio of concrete cover to reinforcement diameter was small (below 1.5) corrosion related damage had emerged as spalling. If the ratio was well over 1.5, the damage more probably emerged as cracking.

One of the objectives was to determine critical parameters that can be used in service life design concerning the active corrosion phase especially. These factors included critical corrosion penetration in regard of visual damage and the corrosion rate. The general corrosion rate for these structures can be regarded as high after initiation. Thus, the average extension to service life during the active corrosion phase can be approximately 1–6 years in the most severe cases. This extension to service life is considered relatively minor. However, these structures, which are facing southern directions, are subjected to the most severe weather. In structures more sheltered from wind-driven rain due to location, orientation or obstruction factors, the extension in service life can be remarkably higher.

A simple linear active corrosion phase model until visual damage on the concrete surface was proposed,

defined by the onset by carbonation, an angle coefficient of corrosion rate and a defined limit state. Corrosion rate was modelled dependent from outdoor environment parameters as a constantly changing variable over time. A limit state for corrosion until visual damage i.e. critical corrosion penetration of 15–90 μm (depending greatly on reinforcement cover/diameter-ratio and the corrosion environment) was proposed for thin concrete facade panels.

The ability to model or forecast corrosion rates on concrete facades will enhance the capability of property owners to react to upcoming repair needs. This kind of model would be able to predict the residual service life of a certain structure, but it could also be used in creating renovation strategies for a larger building stock by revealing the order of importance or the urgency of single renovation projects. Such a tool could also be used in moving towards a predictive upkeep of realty and the confidence of making long term contracts between property owners, renovation engineers and contractors.

REFERENCES

Andrade, C., Castillo, A. 2003. *Evolution of reinforcement corrosion due to climatic variations*. Materials and Structures 54, pp. 379–386.

Concrete Association of Finland. 2012. BY 50 Concrete Code 2012. Helsinki, The Concrete Association of Finland. (in Finnish).

Drits, V.A., Sakharov, B.A., Manceau, A. 1993. *Structure of feroxyhite as determined by simulation of x-ray diffraction curves*. Clay Minerals 28(1993). pp. 209–222.

Jaffer, S.J., Hansson, C.M. 2009. *Chloride-induced corrosion products of steel in cracked.concrete subjected to different loading conditions.* Cement and Concrete Research 39(2009). pp. 116–125.

Köliö, A., Pakkala, T.A., Annila, P.J., Lahdensivu, J., Pentti, M. 2014. *Possibilities to validate design models for corrosion in carbonated concrete using condition assessment data.* Engineering Structures 75:539–549.

Köliö, A., Honkanen, M., Lahdensivu, J., Vippola, M., Pentti, M. 2015. *Corrosion products of carbonation induced corrosion in existing reinforced concrete facades.* Cement and Concrete Research, 78(2015). pp. 200–207.

Lahdensivu, J. 2012. *Durability Properties and Actual Degradation of Finnish Concrete Facades and Balconies*. Tampere University of Technology, TUT Publ. 1028.

Lahdensivu, J., Varjonen, S., Pakkala, T., Köliö, A. 2013. *Systematic condition assessment of concrete facades and balconies exposed to outdoor climate.* Int. J. of Sustainable Building Technology and Urban Development, 4:3(2013). pp. 199–209.

Legodi, M.A., de Waal, D. 2006. *The preparation of magnetite, goethite, hematite and maghemite of pigment quality from mill scale iron waste.* Dyes and Pigments 74(2007). pp. 161–168.

Li C.Q. 2004. *Reliability service life prediction of corrosion affected concrete structures*. ASCE Journal of Structural Engineering 2004:130(10). pp. 1570–1577.

Mattila, J. 2003. *On the durability of cement-based patch repairs on Finnish concrete facades and balconies*. Tampere University of technology, TUT Publ. 450, 111 p.

Page, C. L. 1988. *Basic Principles of Corrosion*. In: Schiessl, P. (editor). Corrosion of Steel in Concrete. London, Chapman and Hall. pp. 3–21.

Tuutti, K. 1982. *Corrosion of steel in concrete.* Stockholm. Swedish Cement and Concrete Research Institute. CBI Research 4:82. 304 p.

Concrete Solutions – Grantham et al. (Eds.)
© 2016 Taylor & Francis Group, London, ISBN 978-1-138-03008-4

ASR possibilities in Finnish concrete bridges

J. Lahdensivu, A. Köliö & D. Husaini
Tampere University of Technology, Tampere, Finland

ABSTRACT: In Central Europe and Scandinavia, Alkali-Aggregate Reaction (AAR) typically occurs in massive concrete structures like bridges and dams. Despite having similar geology to Sweden, Finland has been considered as an AAR free country. The scope of this study was to find out existence of alkali-silica reaction (ASR) in Finnish bridges and how the age of the bridge as well as aggregate type has affected occurrence of ASR. The research material consists of 97 condition assessment reports from concrete bridges made between 1912 and 1999. ASR was found in 27 bridges, which is 27.8% of all studied bridges. 16 of those bridges which were built in 1970's, which is 59% of all found cases in this research material. In all there were 38 bridges made in the 1970's and the ASR share of those was 42.1%. Bridges made in the 1960's were the second largest with 33 bridges. ASR was detected in six of them, which corresponds to 22% of found cases and 17.6% of all investigated bridges from the 1960's.

1 INTRODUCTION

The Finnish Road Administration manages approximately 14 700 bridges in Finland and cities and towns manage approximately same amount of similar bridges, which together means app. 30 000 bridges in Finland. In different periods, several different materials have been used to construct bridges, including stone, wood, steel and concrete. Finnish bridges are for the most part quite young – over 95 % have been built after 1950. The largest number of bridges were built in the 1960s and '70s. The most prevalent building material has been concrete. Reinforced and prestressed concrete bridges account for 67 % of the bridge stock (Finnish Transport Agency 2010). Moreover, the decks and substructures of steel bridges as well as the substructures of wooden bridges are also primarily of concrete which means that concrete structures' share of the structures of the bridge stock is even larger.

The bridge stock in Finland is under a regular inspection system. Each bridge will be inspected visually at five year intervals. The system provides up-to-date data on the condition of bridges which allows determining the technical repair needs of various structural members of bridges in the future and the required financing. The management system is based on data depicting the condition of and damage to bridges compiled in the Bridge Register, in connection with bridge inspections as well as administrative, road-specific, road and traffic volume data, data on the structure and dimensions of bridges, and data on bridge fixtures and equipment. Based on visual inspection, systematic condition assessment will be ordered to the bridge before any repair activities (Finnish Transport Agency, 2013).

In Central Europe and Scandinavia, Alkali-Aggregate Reaction (AAR) typically occurs in massive concrete structures like bridges and dams (Punkki and Suominen 1994). Despite similar geology to Sweden, Finland has been considered as an AAR free country (Richardson 2002). The scope of this study was to find out the existence of alkali-silica reaction (ASR) in Finnish bridges and how the age of the bridge as well as the aggregate type has affected occurrence of ASR.

2 ALKALI-AGGREGATE REACTIONS

The alkali-aggregate reaction is an expansion reaction of the aggregate of concrete caused by the alkalinity of hydrated cement, which may disintegrate concrete. The existence of AAR was first discovered in USA in the 1940's, and it is generally divided into three types according to the reacting aggregate: alkali-silicate reaction, alkali-carbonate reaction and alkali-silica reaction (Gjørv 2009). All AARs require reactive aggregate, a sufficient amount of alkali ions in the hydrated cement, and a minimum relative humidity of concrete of 80% (Punkki and Suominen 1994).

The alkali-silica reaction (ASR) is the most general form of AAR. For the alkali-silicate reaction to take place, the pore water must contain dissolved sodium and potassium alkalis, and the aggregate must contain minerals that have low resistance to alkalinity. The gel produced by the reaction absorbs much water from its surroundings, which causes its volume to grow leading to internal pressure within the pore system. As the building pressure exceeds the tensile strength of concrete, cracks form in the concrete structure allowing

the relatively soft gel to extrude through them (Neville 1995).

The alkali-silicate reaction is similar to ASR: the reaction mechanism is similar, but there are some differences in the physical and chemical form of gel and other reaction products. The disintegration process of concrete is remarkable slower than in ASR, so the reaction is usually called also slow or delayed alkali-silica reaction (Pyy et al. 2012).

The alkali-carbonate reaction is affected by the alkalinity of some limestones and cement and produces a swelling clay-like substance. The gel that forms at high humidity swells about 4% by volume creating pressure within the pore system of the concrete. The cracking of concrete generates a cracking pattern and leads to a loss of bond between the aggregate and the cement paste (Neville 1995).

AAR generally means slow deterioration of concrete. The degradation rate is influenced by prevailing conditions as well as the quality of aggregate and cement. In the case of siliceous rocks, AAR develops sooner, in 2–5 years, whereas with slower reacting rocks, like sandstone and limestone, the reaction may take 10–20 years to develop.

AAR has been reported to occur also with highly stable rocks such as granite, quartzite and sandstone (Gjørv 2009). With blended cements like BFS and PFA, AAR is less common since fewer reacting alkalis are generally involved than with OPC (Punkki and Suominen 1994).

A concrete structure suffering from AAR typically exhibits discolouration due to surface moisture, irregular pattern cracking, swelling and oozing of a gel-like reaction product from the cracks (Neville 1995). The damage from AAR resembles the cracking caused by freeze-thaw attack and often coincides with it (Punkki and Suominen 1994). The most significant difference between AAR and freeze-thaw damage is the pattern of cracking, which in the case of freeze-thaw damage is most intensive close to the outer surface and loses intensiveness with depth. AAR cracking begins deeper inside the concrete and produces a more regular cracking pattern across the entire concrete structure (Rønning 2001). In load bearing structures, like bridge deck, the crack pattern can be modified by stress. However, AAR and freeze-thaw damage could occur at the same time and, therefore, the real reason for damage might be unfocused.

3 RESEARCH MATERIAL

The research material consists of 97 condition assessment reports from concrete bridges made between 1912 and 1999, see Fig. 1. The condition assessments were carried out during 2001-2014. All studied bridges were situated in south or south-west Finland.

The basic aim of the condition assessment is to produce information about the factors affecting the condition and the performance of the structure and consequently about the need and the options for repair

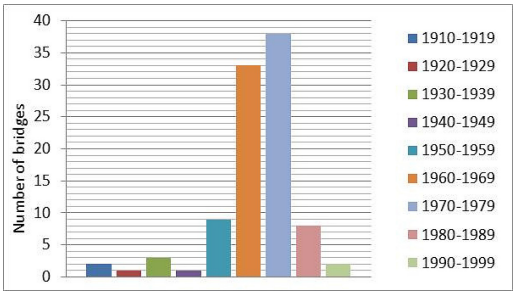

Figure 1. Age distribution of studied bridges.

Table 1. Number of bridges and ASR cases in different decades.

		ASR detected		
Decade	Number of bridges	Number of bridges	share from detected cases [%]	share from all bridges in the decade [%]
1910	2	0	0	0
1920	1	0	0	0
1930	3	1	3.7	33.3
1940	1	0	0	0
1950	9	0	0	0
1960	33	6	22.2	18.2
1970	38	16	59.3	42.1
1980	8	3	11.1	37.5
1990	2	1	3.7	50.0

for the owner of the building or structure. Damage to structures, its degree and extent, due to various degradation phenomena can be determined by a comprehensive systematic condition assessment (Condition assessment manual for bridges 2013 and Lahdensivu et al. 2013).

In this study, the most important information from the condition assessment reports was:

– situation of bridge
– age of the bridge when ASR was detected
– thin-section analyses (cement type, reactive aggregate) – number of samples was 97 and tensile strength of concrete – number of samples was 33.

4 RESULTS AND DISCUSSION

4.1 *Occurrence of ASR*

Alkali-silica reaction was found in 27 bridges, which is 27.8% of all studied bridges. The situation of found ASR cases is shown in the map, see Fig. 2. Most of the cases were in Helsinki (6), Vantaa (5) and Turku (3) while other localities had only one or two cases. The ASR cases found are in the same area in south and south-west Finland to those bridges where ASR wasn't detected.

The ASR was detected in 16 bridges which were built in the 1970's. This is 59 % of all found cases in



Figure 2. Found ASR cases. All studied bridges were situated in south and south-west Finland.

this research material. The age of those bridges varied between 31 and 44 years, while the average was 38.6 years. In all there were 38 bridges made in the 1970's and the ASR share of those was 42.1 %. Bridges made in the 1960's were the second largest with the number of 33 bridges. ASR was detected in six of them, which corresponds to 22 % of found cases and 17.6 % of all investigated bridges from the 1960's, see Table 1. The age of the 1960's bridges in which ASR was detected varied between 43 and 52 years and the average was 46 years.

Eight bridges were built in the 1980's and ASR was detected in three of them, which is 11 % of all ASR findings. It was 37.5 % of all bridges made in the 1980's, but the number of bridges was rather small for reliable statistical analysis. In the research material there were nine bridges from the 1950's but no ASR was detected from those.

4.2 *Initiation time for ASR*

Condition assessments of bridges were carried out to determine the repair needs of the bridges, not for finding out especially about ASR. However, it is still possible to estimate roughly the initiation period of ASR from the age of the bridge when ASR was detected.

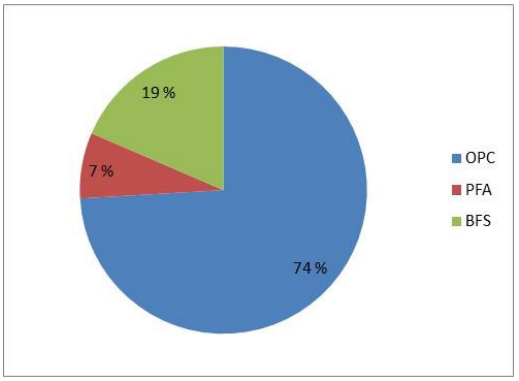

Figure 3. Distribution of cement types in cases where ASR was detected (n = 27).

According to condition assessment reports, ASR was detected only in thin-section analyses, no visual damage was detected. The initiation time for thin-section detectable ASR varied between 22 and 77 years in this study. The mean initiation time was 42 years while the standard deviation was 7.5 years. The initiation time for ASR might be some years shorter, because this was random sampling and condition assessment was made for another purpose than looking for ASR. All in all, it may be stated that ASR has a relatively long initiation time in Finnish concrete bridges compared to the literature.

4.3 *Cement type in ASR cases*

The cement type was detected from thin-section analyses. The most common cement type in Finnish bridges was Portland cement (OPC) with a share of 77% of bridges in this study. The second was blast furnace slag (BFS) with an 8% share and third pulverized fly ash (PFA) with a 5% share. In nine per cent of cases the cement type was unknown or it wasn't reported.

In bridges where ASR was detected, the cement type was, in 20 cases, OPC, see Fig. 3. It must be noticed that in Finland in blended cements BFS and PFA less than 50% of binder is something other than Portland cement. Obviously dissolved sodium and potassium alkalis originate from Portland cement.

The concrete grade in superstructures used to be equivalent to a modern C20/25 or C25/30 until the 1970's. Since the beginning of the 1980's the concrete grade has been at least equivalent to C30/37. According to Finnish concrete codes, the cement content in concrete has been usually 300 kg/m^3 at least.

The alkali content of cement should be determined for estimating the possibility of ASR. Alkalinity of Portland clinker consists of sodium and potassium. Alkali content of cement and can be determined as the Na_2O equivalent:

$$Na_2O_{EQ} = (Na_2O\ \% + 0.658\ K_2O\ \%) \quad (1)$$

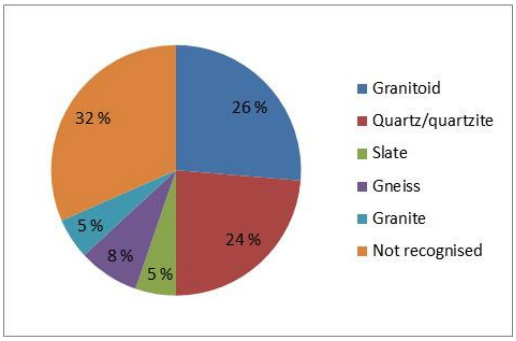

Figure 4. Distribution of reactive aggregates (n = 38).

According to some European standards Na_2O_{EQ} should be less than 0.60% (BS 4027, DIN 1164-10 and NBN B 12-109). Na_2O equivalent in mostly used Finnish cement types varies between 0.80% and 1.35%.

4.4 *Reactive aggregate*

Reactive aggregate was detected from thin-section analyses. Two most common reactive aggregate types were granitic rocks (26%) and quartzite (24%). In 32% of cases, reactive aggregate wasn't recognised or reported, see Fig. 4.

All those reported reactive aggregate occur typically in Finnish bedrock and natural rock material. However, those aggregates have been rated relatively stable aggregates in the literature, which explains why occurrence of ASR has taken round 40 years.

5 CONCLUSIONS

The research material comprised 97 condition assessment reports from concrete bridges made between 1912 and 1999 and 27 ASR cases were found. It means that Finland also has AAR problems in existing concrete bridges. Reported reactive aggregates were granitic rocks and quartzite, which occur typically in Finnish bedrock and natural rock material. However, those aggregates have been rated relatively stable aggregates in the literature, which explains why the initiation time of ASR has taken round 40 years.

During autumn and winter time, the relative humidity in outdoor air in Finland is typically 90% or higher. This will keep relative humidity in concrete bridges at a high level most time of the year, too. Despite relatively stable aggregates, this high relative humidity together with high alkalinity Portland cement in concrete makes the probability of ASR in Finnish concrete bridges very high, because the Finnish bridge stock has been mostly built in the 1960s and '70s.

REFERENCES

BS 4027. 1996. *Sulfate-resisting Portland Cement*. British Standards Institution.

Finnish Transport Agency *Condition assessment manual for bridges.* 2013., Guidelines of the Finnish Transport Agency 26/2013. Helsinki. 142 p. (in Finnish).

DIN 1164-10. 2008. *Zement mit besonderen Eigenschaften.* German Standards.

Gjørv, O. E. 2009. *Durability design of concrete structures in severe environments*. Taylor & Francis. 220 p.

Lahdensivu, J., Varjonen, S., Pakkala & T., Köliö, A. 2013. *Systematic condition assessment of concrete facades and balconies exposed to outdoor climate*. Int. J. of Sustainable Building Technology & Urban Development. Vol. 4:3 pp. 199–209.

NBN B 12-109. 1993. Cement – *Low alkali limited cement*. Netherland Standards.

Neville, A. 1995. *Properties of concrete*. Essex. Longman Group. 844 p.

Punkki, J. & Suominen, V. 1994. *Alkali aggregate reaction in Norway – and in Finland?* Betoni 2/1994. Helsinki. Suomen Betonitieto Oy. s. 30-32 (in Finnish).

Pyy, H., Holt, E. & Ferreira, M. 2012. *Prestudy on alkali aggregate reaction and its existing in Finland.* VTT. Helsinki. Report VTT-CR-00554-12/FI. 27 s. (in Finnish).

Richardson, M. G., 2002. *Fundamentals of durable reinforced concrete*. London. Spon Press. 260 p.

Finnish Transport Agency *Road bridges of Finnish Transport Agency. Structure, service level and condition of bridge stock.* 2010. Helsinki. Finnish Transport Agency, Statistics of the Finnish Transport Agency 3/2010. 90 p. (in Finnish).

Rønning, T. 2001. *Freeze-thaw resistance of concrete. Effect of curing conditions, moisture exchange and materials.* Doctoral thesis. Trondheim. NTNU. 416 p.

Concrete Solutions – Grantham et al. (Eds.)
© 2016 Taylor & Francis Group, London, ISBN 978-1-138-03008-4

Survey of the largest prefabricated concrete structure of Spain

A. Lozano, M. Alonso, F. Álvarez & J.J. Del Coz
Construction Engineering Area, University of Oviedo, Asturias, Spain

ABSTRACT: Recently two Spanish companies got a contract for the construction of twenty foundation structures for an offshore wind farm that should be installed in the North Sea. The manufacture of these elements requires a considerable area of industrial land, and that is why they rented two of the old naves of the steel factory "Ensidesa", a very unique structure, the biggest in our country, with a high degree of prefabrication and a very advanced design for its time (early 50s). The paper describes the current state of these huge naves, including the results of NDT and Destructive Tests (DT) performed on their concrete, after 50 years of construction and major maintenance problems, especially if we consider the aggressiveness environment of the steel plant.

1 INTRODUCTION

1.1 *Historical background*

In September 1945 the Industrial National Institute (INI) contracted the London engineering company "H.A. Brassert & Company Limited", to identify the most suitable place for the implementation of two steel factories in the north of Spain: one would be located in Asturias and the other one in Leon.

The report submitted by the British consulting firm, known as the "John Miles Report" recommended the construction of just a single factory. The chosen place was the village of Avilés (Asturias).

Later, in the month of June 1950, the "National Steel Company (Ensidesa)" was created. In subsequent years the factory was designed and its construction began immediately. The project engineer was Mr. Carlos Fernández Casado and the construction company "Huarte & Cia, S.A."

In 1956 the civil work was almost completed and the strategic lines of the corporation defined: 700,000 tons of steel in the form of rolled products should be manufactured to supply the national processing industry.

The plant, which employed 21,000 people and had an area of 191,000 m^2, was finished in 1959. It was distributed in seven parallel naves of almost one kilometer length; six of 30.2 m span and the last one with 20.0 m span. This means a huge industrial building of 950 meters long and 201 meters wide.

The structure of the naves was organized in longitudinal frames, with pillars at distances between 13–14 m. The whole structure, except for the pillars, was prefabricated on site.

After many years of continuous production, several vicissitudes, problems and privatizations, the production was significantly reduced and finally the industry was dismantled.

In the 1990s, after two conversions, the merging of major Spanish steel companies took place. ENSIDESA, AHV and AHM became the "Integral Steel Corporation". Later it changed its name to "CSI Steel Corporation". Once privatized, it was renamed as "Aceralia."

In 2001 "Aceralia", Luxembourg steelmaker "Arbed" and French brand "Usinor" formed the first global steel company by production volume: "Arcelor". In 2006 it merged with "Mittal Steel", the second world company by volume. This Indian company remains the current owner.

1.2 *Aim and main object*

During last years the naves were dedicated exclusively to storage steel coils. However, when two of these buildings were rented (naves n° 6 and 7), the owners needed to undertake various configuration changes to locate the new machinery and equipment.

Moreover, after more than fifty years since its construction, the buildings had various problems arising from a significant lack of maintenance.

Previous studies carried out to determine the state of the structure are described in the paper, including the instructions related to its reinforcing and structural consolidation, in order to ensure its waterproofing conditions and safety.

2 DESCRIPTION OF THE STRUCTURE

2.1 *Plant organization*

The old steel factory of "Ensidesa" consists of seven buildings covering an area of 905.5 m long and 201.2 m wide. Six of these naves are 30.2 m span and the other one 20.0 m.



Figure 1. Current state of nave n° 7, now with no activity.



Figure 2. Pillars, Pratt beams and the bracing system.

2.2 *Structural organization*

Except for their span, all naves are identical. The plant is divided into horizontal frames, responsible for supporting the gravitational actions and part of the wind and earthquake actions; and vertical porticos receiving them; and together with the crane beams' actions, are lead to ground through the foundation piles.

Besides, porticos are braced longitudinally through those intermediate beams and also with the skylights in the upper level. This means that the superstructure is composed of horizontal and vertical frames, braced together by the crane beams and the skylights.

All elements were made of reinforced concrete, and prefabricated on site.

The described structure is complemented with some triangulated prestressed concrete beams. They were also cast on site. Figure 1 shows the inner part of nave n° 7.

2.3 *Horizontal frames*

Their separation is 13–16 m, so that there are two types of porticos corresponding to such lengths, although both are of the same type. They are made with Pratt beams (Wikipedia, 2016) and ribbed slabs. The first ones are triangulated structures, used for medium and large spans. As is usual, diagonals absorb traction stresses and vertical elements, the compression ones.

At the time, they were prefabricated in inverted position in order to facilitate their extraction from the mould. Its cross section adopts a truncated pyramid shape.

2.4 *Vertical frames*

They consist of variable inertia pillars and three hinge arches. The section of the pillars is 220 × 120 cm at startup, and it is reduced in the upper part to form the short brackets that support the rail beams and the facade at intermediate levels; arches are placed at the end.

These arches, articulated in the keystone and springers have a section of 60 × 25 cm. Their tensile component is absorbed by beams of 50 × 25 cm placed at the ends thirds and a heavily armed brace (6 Ø 35 + 6 Ø 32) in the center.

The skylights are placed between the arches and the bracing elements. One important feature of these skylights is that in this position they transversely embrace the arches. They were prefabricated on the horizontal plane, allowing the reuse of the molds.

These elements and the Pratt beams can be seen in Fig. 2.

2.5 *Rail beams*

These elements, projected as beams with null moment points, were responsible for receiving the big loads of the powerful crane bridges. That is, as continuous beams jointed at points of zero bending moment, with cantilever supports. They were cast together with the pillars. On the contrary, as it was discovered during the inspection, the central section was lightened by the use of prefabricated beams of 150 × 36 cm, with double T sections at the ends and rectangular in braces. Just here the interior space was filled with concrete to improve their shear behavior, despite the existence of bent bars of Ø 32.

2.6 *Roof*

Finally, the roof plates were only 4 cm thick and were reinforced with 3 Ø 7 per meter.

3 DEFECTS AND DAMAGES

Before performing non-destructive testing on concrete components, a visual inspection of the naves n° 6–7 was carried out in order to determine the elements on which to perform the non-invasive tests.

At the same time, information that could estimate the degree of deterioration of some of the structural components (especially the ones due to the exposure to the aggressive environment of the steel factory), were collected.

3.1 *Pillars*

These elements had very big concrete and steel bars sections. Besides, their implementation had been carried out carefully. They had no cracks, hollows, imperfections or similar defects related to poor vibration. Also the verticality and flatness of their surfaces was perfect.

In fact, damage associated with corrosion of the reinforcement bars was not visible, despite the time elapsed and the lack of maintenance during the last years.

The careful execution and the provision of adequate cover to the reinforcement (at least for the standards of that time), were determined in the first inspection. This factor undoubtedly influenced the general good condition of the reinforcement bars.

As for the concrete composition, a large diameter of the aggregates was observed, exceeding 25 mm in many zones. In any case, at least outwardly, the concrete quality could be described as acceptable.

Unfortunately, in certain expansion joints affected by lack of maintenance or areas where there were failures in the roof covering, the steel bars were seriously damaged by corrosion. In these zones, leaks had caused leaching and dissolution of the calcium components of the cement.

Logically this situation remains on the outside, where in certain locations, the same defects and damage due to water exposition are more obvious.

3.2 *Rail beams*

As in the previous case, the beams of the crane bridges were visually in good condition, with generous resistant sections and short lengths, especially if we consider the great height of the elements.

There was no evidence of failures by mechanical action or fatigue: the few visible cracks were related to the corrosion of the reinforcement the due to carbonation and the action of water. In any case, the damage suffered so far by these concrete elements was quite low, especially when taking into account the significant leaks of the deck and from the facades, as well as the lack of maintenance of the installation (Figure 2).

In terms of composition, the situation was similar to the pillars: there were a large amount of bars, large diameter of the aggregates and an abundance of fines.

Likewise, it must be mentioned that, as for the pillars, cover to the steel reinforcement was generally greater than 40 mm. This data could be applied to the edges of the beams but not the soffits, since it would not be possible to have separators for a reinforcement of such weight. In any case, no corrosion or cracks were visible, which denotes a really neat prefabrication on site, especially considering the age of the structure.

3.3 *Arches*

These were undoubtedly the elements most severely affected by the action of weather agents and pollutants existing in the atmosphere. At the time of inspection, all the arches showed an advanced stage of corrosion, especially on the intrados. In fact, most of the concrete covering was detached and some of the bars had completely disappeared (Fig 3 and 4).



Figure 3. Arches of the roof system.



Figure 4. High level of corrosion in main bars and stirrups.

The degree of oxidation was such that a great part of the cover had spalled, promoting and accelerating the deterioration of the steel.

In summary it can be said that both the main bars and the stirrup damage undoubtedly needed reinforcement intervention and replacement of the concrete cover, due to the carbonation combined with the water ingress and consequent increase of the volume of the bars.

3.4 *Roof beams*

On the contrary, the triangulated structures receiving the cover were in perfect condition. No damage or defects worthy of mention were detected during the inspections. In fact, not even signs of corrosion of reinforcement were apparent, despite their situation (Fig. 5).

In principle, the type and composition of the steel was unknown, but perhaps their good behavior against corrosion, was related to their carbon content.



Figure 5. Roof beams were in very good condition.

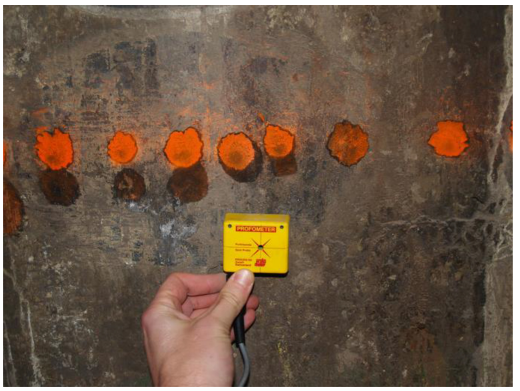

Figure 6. Rebar detector measuring the concrete covering.

3.5 *Roof covering*

While this element could not be inspected because of the difficulty of access, evidence of the dissolution of calcium cement components, the whitish spots and corrosion evidence visible from the intrados surface, suggested that the roof presented important sealing defects.

Also it was also important to reflect the performance of an incorrect construction practice, which moreover is unfortunately common: the application of polyurethane foam on the lower surface of the roof, probably in order to reduce water seepage. Indeed, such actions not only fail to fully solve the problem, but in certain cases (open cell materials) favor the retention of water in the foam and thus carbonation and steel corrosion.

4 PATHOLOGICAL STUDY: ND/D TESTS

4.1 *ND Tests*

Taking into account the need to adapt the existing structure to the loads and actions of the new bridge cranes, it was necessary to know, with some approximation, the mechanical properties of the materials, as a prelude to the calculation and verification of the structure.

Despite the apparent quality of the construction and especially the expertise of its designer Don Carlos Fernandez Casado, the fact is that there was no reliable data on the concrete compressive strength and the yield strength of the steel bars, especially when the naves were built over fifty years ago.

According to these premises, the following tests were defined:

– First, the determination of the progress of carbonation due to its influence on the increase of the surface resistance of the concrete and its importance in relation to reinforcement corrosion. The test was carried out according to UNE 112011: 2011 “Corrosion of concrete reinforcement steel. Determination of the carbonation depth for in – service concrete”
– To complement the above test, the determination of the position of the bars and their cover (Fig. 6), were determined using a rebar detector and verification of the results was obtained through DT’s.
– Schmidt hammer tests, carried out according to UNE – EN 12504-2: 2013 “Testing concrete in structures – Part 2: Non-destructive testing – Determination of rebound number”.
– Study of ultrasonic of pulse velocity and concrete compaction. Test performed according to UNE – EN 12504-4: 2006 “Testing concrete in structures – Part 4: Determination of ultrasonic pulse velocity”.

The minimum concrete elements to be analyzed were six pillars and two rail beams. Depending on the variability of results, the number of tests could be increased as required.

4.2 *D Tests*

After performing nondestructive testing, extractions of core samples of the concrete were made on five of the structural components where the NDT was carried out.

The procedure followed to get the specimens was performed according to UNE 12504 – 1:2009 “Testing concrete in structures – Part 1: Cored specimens – Taking, examining and testing in compression” (Fig. 7).

The rest of the tests were performed using the UNE 112-011:2011 “Corrosion in concrete reinforcement steel. Determination of carbonation depth for in-service concrete” and UNE-EN 12390-3:2009 “Testing hardened concrete – Part 3: Compressive strength of test specimens”.

It was decided not to do more core extractions because the results obtained were very uniform and quite similar to those obtained through non-invasive tests.

For the steel it was mandatory to determine the mechanical characteristics of the bars. The tests were performed according to UNE-EN ISO 6892-1:2010 “Metallic materials – Tensile testing – Part 1: Method of test at room temperature” and UNE-36097:1981 “Hot rolled plain bars for the reinforcement of concrete. Characteristics”.



Figure 7. Extraction of concrete cores.

Table 1. NDT/DT performed in pillars and beams.

Concrete tests	Min. value	Max. value
Carbonation (mm)	7	18.5
Concrete cover (mm)	14	22
Schmidt hammer (Mpa)	18	32
Ultrasonic pulse (m/s)	4167	4545
Compression test (Mpa)	18.5	28.4

4.3 *Results*

Use of NDT and DT methods allowed the extrapolation of the results to the rest of the structural elements with a certain confidence level. This procedure enables to analyze the results related to the concrete tests and the comparison between data collected in both types of surveys.

The most important information related to concrete tests is given in Table 1.

In this case, five tests were carried out in different pillars and beams. Figure 8 shows one of the graphs obtained by testing the steel bars.

Table 2 includes the results of the DT carried out on the steel specimens.

5 CONCLUSIONS

The combined analysis of the results of non-destructive testing and data obtained from extraction and compression tests of the concrete specimens concludes that during the construction of the structures of this industrial plant, the cement and aggregates had pretty good quality; and the prefabrication on site of their concrete elements was made carefully. It is thus explained that the finishing of the prefabricated elements, their appearance and compactness reach a more than acceptable standard for the time of the construction.

Table 2. DT performed in the reinforcement bars.

Test N°	Ø mm	T. Stress MPa	T. Strength MPa	Elong. %
1	16	253.60	409.00	48.11
2	16	283.70	445.30	48.72
3	18	282.60	375.40	48.12
4	16	312.60	483.40	51.50
5	18	227.20	334.10	57.33

6 CONCLUSIONS ABOUT NAVES N° 6–7

The values of the concrete cover, depth of carbonation, compaction and compressive strength obtained through NDT/DT were considered sufficiently reliable for the final analysis of the structure.

According to this information, the following conclusions were made:

1) The design, dimensions, prefabrication and assembly of the concrete elements of the structure denote comprehensive expertise and a very careful execution.
2) Concrete had always more than acceptable quality and even sometimes could be described as very good (by contemporary standards). The values obtained for their characteristic strength were around 20.0 N/mm^2 (20.0 MPa).
3) Concrete cover was generally acceptable, though it is assumed that in the bottoms of the beams the thickness was not correct, because of the impossibility to place separators under the heavy weight of the bars.
4) In this regard, the reinforcement, composed of plain bars and a large amount of steel, had remained in a more than acceptable state with minimal corrosion despite the time elapsed, the lack of maintenance and aggressive industrial atmosphere where the naves are located.
5) Only certain zones affected by leaks from the deck and especially those located near the expansion joints were affected by water. In these cases there was significant damage due to the carbonation of concrete and steel corrosion.
6) The arches on the outside also had important problems due to carbonation and corrosion, and a large amount of the bars had completely disappeared (Fig. 9). The repair and rehabilitation of these elements was considered compulsory.
   The problem is even more important if it is considered that the actions over these arches are significant and according to the engineering, the

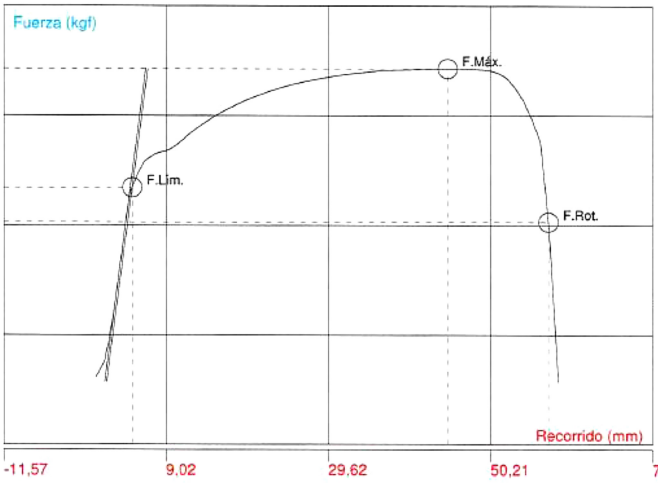

Fecha del último ensayo :
10-04-2015

Parámetros del ensayo

Sección nominal	201,06	mm²
Longitud base	120	mm
Inicio de cálculo	30,0	%
Final de cálculo	60,0	%
Límite elástico	0,2	%

Dimensiones de la probeta

Tipo de probeta	Redonda	
Diámetro	16,0	mm

Figure 8. Information related to test n° 1.



Figure 9. Main bars of the arches had almost disappeared.

section of the bars was not too large. This is the reason why their reinforcement should be performed first, at the same time as the following intervention.

7) Distances between stirrups were correct, and always below 35 cm; at least on the elements included in this scope.
8) No cracks were observed or mass loss and fractures that indicate some kind of failure by overloads inside the nave. Little damage was caused by the increase of the volume of steel bars due to the corrosion process.
9) The ultrasonic pulse test showed that the central section of the rail beams was lightened by the use of two elements of 150 × 36 cm, with double T sections at the ends, and rectangular in the connections with the pillars. Here the inner space of 23 cm had been filled with concrete to improve shear resistance, despite the existence of bent bars of Ø 32.
10) It will be necessary to act on the roofs, in order to ensure their continued waterproofing and stop the deterioration of the concrete elements.
11) Regarding the cover, it was considered advisable to remove the polyurethane foam applied to the lower surface as soon as possible.

7 RECOMMENDATIONS

7.1 *Porticos*

It was undoubtedly necessary to act on the pillars and beams that had suffered a reduction in their bearing capacity due to corrosion of the bars. In this case these areas were mostly restricted to the elements close to the expansion joints and near areas with localized sealing defects.

The reinforcing procedure is well known so it is considered that further explanations are not necessary.

7.2 *Arches*

They were the most damaged parts, and unfortunately also the most complex to be reinforced, due to the difficulty of access.

For these reasons the following procedure was proposed:

a) As in the pillars and beams, first of all, damaged concrete and rusted steel have to be mechanically cleaned and the surface prepared.
b) Then the accurate amount of steel should be defined, according to the damage and the new specific actions considered in the project.
c) The reinforcement of the arches was performed using two pieces of polyester and fiber glass placed around each arch as the formwork. From the bottom thereof, by pumping, they were filled with self-compacting concrete (SCC).



Figure 10. Polyurethane foam over the intrados of the roof.

SCC is similar to conventional concrete, but its fluidity and cohesion avoid the need for vibration, even with a large amount of steel. Pumping from the bottom of the formwork also ensures filling of the mould. This procedure, especially with complex elements and difficult access (as in this case), reduces the formation of air bubbles trapped between the wall of the formwork, and the mass of concrete.

The use of aggregates with a maximum size of 10–12 mm is mandatory.

7.3 *Concrete roof*

All damage was due to the continuous action of UV rays and rainwater, so a waterproofing system must be properly designed, considering not only the high rainfall of the region but the aggressive environment and the pollution as well.

To reduce times and facilitate implementation on a surface with a complex, reduced thickness profile, and a high number of singular points (the meetings of the arches and cables with the covering are hardly treatable areas with prefabricated sheets), the use of liquid waterproofing systems or hybrid polyurea polyurethane coating is highly recommended.

At the same time, it is advisable to remove the polyurethane foam of the roof (Fig. 10), because open cell insulating materials only retain moisture, instead of avoiding the action of water.

Finally, with regard to the safety of workers operating in the nave, it is advisable to place a safety net for collecting the possible detachment of the thin layer of concrete that forms the roof.

REFERENCES

ACI 214-02 (2002). *Evaluation of strength test results of concrete.*

Calavera, J. et al (2001). *Evaluación resistente de estructuras de hormigón armado.* Madrid: Intemac.

Chen, W. (1982). *Plasticity in reinforced concrete*. New York: McGraw-Hill Book Company.

Dirección General de Arquitectura (1947). *Sistemas especiales de forjados para la edificación.* Madrid: Vega Imp.

El-Reedi, M. (2013). *Concrete and steel construction: quality control and assurance*. Rotterdam: Balkema.

Heckroodt, R. (2002). *Guide to the deterioration and failure of building materials*. London: T. Thelford.

Hostalet, F. (1994). *Strength evaluation of in-situ hardened concrete.* Madrid: Intemac.

Ministerio de Fomento (2008). *Instrucción de hormigón estructural EHE.08*. Madrid: Servicio de publicaciones del Ministerio de fomento.

Lozano, A. et al (2003). *Diseño, cálculo, construcción y patología de los forjados según EFHE, EHE y EA 95*. Consultores técnicos de construcción: Gijón.

Mackenzie, W. (2013). Examples in structural analysis. Rotterdam: Balkema.

Moaveny, S. (2007). *Finite element analysis: theory and applications with ANSYS*. Prentice Hall; New York.

Petersons, N. (1980). *Recommendations for estimation of quality of concrete in finished structures.* Bulletin RILEM n° 24 November–December 1971.

Richardson, M. G. (2002). *Fundamentals of durable reinforced concrete*. London: Spon Press.

Breysse, D. et al (2015). Comparing investigation approaches and ndt methodologies for concrete strength estimation. An internal benchmarck. International. *Symposiu Non Destructive Testing in Civil Engineering.* Bundesanstalt für Materialforschung una prüfung (BAM); Berlin.

Shah, A. A. (2014). Ultrasonic non destructive testing techniques for diagnosing concrete damage. Concrete Solutions: 587–590. Leiden: CRC Press/Balkema.

UNE – EN 12504-2: 2013 "Testing concrete in structures – Part 2: Non-destructive testing – Determination of rebound number".

UNE – EN 12504-4: 2006 "Testing concrete in structures – Part 4: Determination of ultrasonic pulse velocity".

UNE 12504 – 1:2009 "Testing concrete in structures – Part 1: Cored specimens – Taking, examining and testing in compression".

UNE 112011:2011 "Corrosion of concrete reinforcement steel. Determination of the carbonation depth of in-service concrete".

UNE-EN ISO 6892-1:2010 "Metallic materials – Tensile testing – Part 1: Method of test at room temperature".

UNE-36097:1981 "Hot rolled plain bars for the reinforcement of concrete. Characteristics".

UNE-EN 1504:2005" Products and systems for the protection and repair of concrete structures – Definitions, requirements, quality control and evaluation of conformity – Part 2: Surface protection systems for concrete".

Wikipedia – Details of the Pratt truss beamhttps://en.wikipedia.org/wiki/Truss_bridge#Pratt_truss, accessed march 2016.



Taylor & Francis
Taylor & Francis Group
http://taylorandfrancis.com

Concrete Solutions – Grantham et al. (Eds.)
© 2016 Taylor & Francis Group, London, ISBN 978-1-138-03008-4

Management strategy for localized concrete maintenance on the Rion-Antirion Bridge

I.C. Papantoniou, P. Corbett, A. Stathopoulos-Vlamis & P. Papanikolas
GEFYRA SA (the Concessionaire of the Rion-Antirrion Bridge "Charilaos Trikoupis", Greece)

ABSTRACT: A considerable factor which reflects directly on the total life cycle cost of a structure such as the Rion-Antirion Bridge is the maintenance cost. A rational maintenance strategy has to ensure the continuous fulfillment of technical, aesthetic and environmental performance criteria of the structure while prioritizing the safety and minimum disturbance of the user, together with the minimization of total life cycle cost. This paper presents the strategy for the management of concrete defects affecting the local durability and also describes the preventive actions adopted. More specifically this study describes the treatment of findings from their identification through the scheduled visual monitoring campaigns until their recording on completion of the maintenance works. Examples of the processes which are related to these treatments will be addressed such as defect evaluation, integration of international norms in the repair selection and continuous training of personnel. Finally, in order to monitor and evaluate the performance of each concrete repair, a newly adopted practical coding system which describes not only the utilized repair material, based on defects characteristics, but also the repair methodology is presented.

1 INTRODUCTION

1.1 *Scope*

The main commitment and responsibility of a road infrastructure Concessionaire is to provide and guarantee to the public 24 hour undisturbed services acting at the same time in the context of technical, economic, environmental and aesthetic efficiency. Especially in a bridge where concrete areas are located over the carriageway, even localized concrete durability defects require special attention and treatment since additional safety and economic issues are raised. Consequently, an integrated defect management system is necessary in order to formalize and coordinate the actions which aim to provide optimum technical solutions. The present contribution illustrates the basic points of the management strategy of localized concrete defects from the Concessionaire's point of view. Although the number and the severity of defects is limited, the Concessionaire has already set a detailed maintenance strategy.

After the brief technical description of the bridge, the outline of the maintenance strategy and a more detailed presentation of each one of the key points follows. Also an illustrative example for the decision making process for preventive maintenance is presented. The contribution closes with the conclusions.

2 TECHNICAL DESCRIPTION OF THE PROJECT

2.1 *General*

The Rion Antirion Bridge is a four span cabled stayed bridge with total length equal to 2252 m which started operating in 2004 after 7 years for the financing, design and construction stage. Figure 1 depicts the general layout of the Bridge while Figure 2 exhibits the terminology of the concrete structural elements of the bridge. The four piers (M1 to M4) are founded in the sea bed of the Corinthian gulf. The foundation depth varies from 48 to 65 m from the Mean Sea Level. The diameter of the footings is equal to 90 m (M1, M2, M3)/80 m (M4) and the highest point (M3) of the Bridge measures 227 m from the sea bed. The continuous and fully suspended bridge deck is a steel concrete composite structure. In total 61600 m of cables were used for the suspension of the bridge.

In the extremities of the main bridge two expansion joints undertake the longitudinal displacements of the bridge (thermal or seismic) in both service and ultimate conditions. For the Ultimate Limit State condition the expansion joint is designed to undertake opening/closing at the level of +2810/−2200 mm while in the Serviceability Limit State the respective values are +1260/−1100 mm. Also transversal displacements can be compensated at the level of ±2.60 m

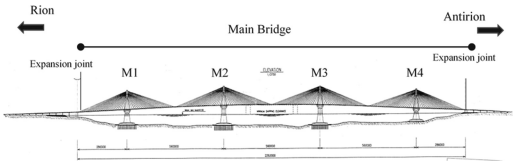

Figure 1. Illustration of Rion-Antirion Bridge.

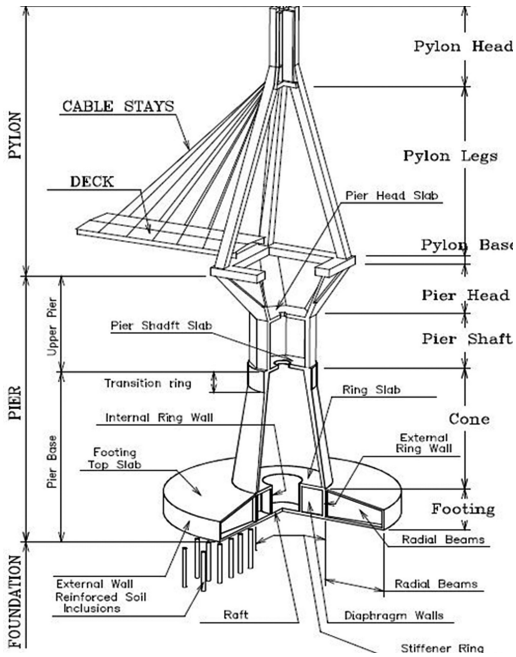

Figure 2. Terminology for Pier and Pylon structural elements.

in Ultimate Limit State conditions. Four dampers with capacity 3500 kN and one fuse/damper with capacity 10500 kN in each pier ensure the seismic energy dissipation and the partial transverse restraint of the suspended deck.

2.2 *Design specifications*

The bridge is designed in order to withstand:

- Earthquake with a return period of 2000 yrs or 5% possibility of exceedance in 120 yrs (operational life)
- Tectonic movements of 2 m in all directions between adjacent piers
- Aerodynamic stability at a wind speed of 266 km/h
- Ship collision of 180000 DWT (bulk)/85000 DWT full loaded approaching at a speed of 16 knots.

2.3 *Concrete elements & durability design*

In total 312517 m^3 of reinforced concrete spread in a surface of 190000 m^2 were used for the construction of Rion-Antirion Bridge. As described in detail in technical papers dedicated to the subject (Harikiopoulou – Cordova et al. 2003, Cussigh et al. 2010) the strategy of the concrete durability approach to protect the steel reinforcement relied mainly on a proper definition of the exposure zones, selection of appropriate concrete covers for each zone, and a proper characterization and evaluation of the concrete itself. The lower concrete strength class which was used for the construction was C45/55 while the highest was C60/75. The higher concrete class was utilized in the Pylon structure. The actual minimum concrete cover is equal to 50 mm for the immersed zone (below Mean Sea Level-5 m) and the externally exposed substructure (MSL + 10 m). The higher actual minimum cover is met in the splash zone located in the area –5 m < MSL < +10 m and is equal to 75 mm. Apart from conventional reinforced concrete elements, external and internal prestressing is applied in the Pylon head and Pylon Base region respectively.

3 OUTLINE OF THE PROCEDURE

The followed maintenance strategy could be described as a cyclic three component process where the outcome of the one feeds the next. Figure 3 illustrates this process.

The first group of actions is monitoring. Three types of monitoring are performed: visual monitoring, material monitoring, structural health (instrumented) monitoring (as described in detail in the relevant technical paper Papanikolas et al. 2011) including periodic geometry control. For concrete elements, the predominant tool for the identification of defects & irregularities is the performance of visual inspections. The importance of defect detection on concrete, except to record local degradations of concrete durability, is to identify potential performance degradation of a structural elements or equipment. It can also be the starting point for further investigation through alternative monitoring methods (e.g. specific tests for chloride penetration depth).

The second group of actions is a two-step procedure. The first step is the analysis of inspection data. The analysis synthesizes all the obtained data relating to a structure (or part of a structure) from visual monitoring and specific instrumented inspection. The scope of the analysis is to evaluate the structural condition of the concrete elements and point out issues requiring immediate action thus limiting the possibility of an unexpected local failure or fast degradation of structural performance. In addition the type and the urgency for further follow-up is determined. Also the repair or preventive maintenance methodology is proposed. The second step is an overview of all the results of the analysis from all structures in order to prioritize and schedule further inspection and maintenance works for the entire asset.

The third group of actions comprises all the necessary actions for the performance of maintenance.

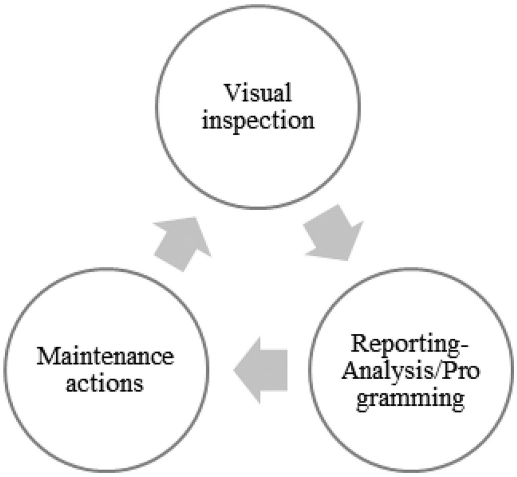

Figure 3. Basic steps of the maintenance strategy.

It initiates by the final determination of repair methodology including material evaluation tests and continues with the maintenance actions; the cost control of the repair works finishes with the verification of the repairs by the visual inspection team. The following paragraphs describe in more detail the performance of visual monitoring and maintenance processes.

4 VISUAL MONITORING

4.1 *Inspection of concrete elements*

The frequency of inspection is defined by the Inspection and maintenance Manual (IMM) based on a risk analysis and review of construction data by designers and construction engineers. Generally, a complete visual inspection is performed every four years on the majority of concrete structural elements of the bridge. The inspection is performed both in the internal and external concrete faces. Most are performed through internal resources: a team of civil engineers dedicated to Visual Monitoring. For external areas where the access technique requires particular skills & methods (e.g. rope access works, divers) the inspection is performed through specialized service providers with experience also on other major projects.

4.2 *Inspection procedure*

During the inspection the personnel check for irregularities in the concrete elements. The inspection is performed with the support of inspection software. The software incorporates a suitable defect library, drawings of each inspected element and inspection checklists. When a defect is identified, the inspector selects the respective defect from the defect database, assigns a photo and positions the defect in the drawing. Also the inspectors assign characteristics values of the defect (e.g. dimensions) in the respective field. If the

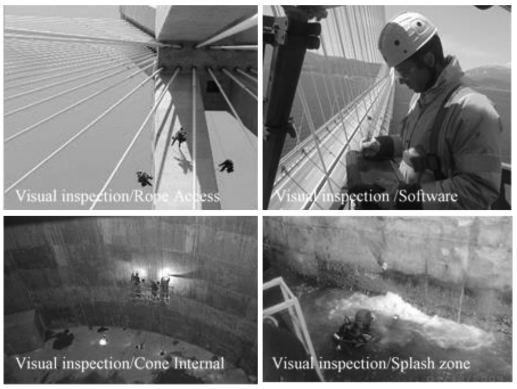

Figure 4. Inspection on the bridge.

defect is already registered from a previous inspection, then the inspector iterates-updates the status of the defect by assigning a new photo and changing any other characteristic value. The direct photo comparison facilitates the characterization of the defects as "Stable" or "Evolutive". In cases where repairs have been performed, the inspector inactivates the defect. Inactivation reason is also the decision for termination of the follow –up in case that is assessed that there is no such reason. All the registered defects are stored in the global defects database which is the full defect record of the project since the end of construction.

For inspections performed by the Rope Access team and divers, operations on the electronic database in the course of inspection are impractical. The inspections are performed on specially prepared inspection sheets. After the end of inspection, all the data is handed to the VM engineers in order to integrate the information in the software as in a regular inspection campaign.

4.3 *Commonly met defects*

This paragraph presents the defects which are commonly met by the visual inspection team during the scheduled inspection of concrete. As a whole, in relation with the project's size, the quantity & magnitude of the defects is limited. They are mostly related to local durability degradations: the presence of exposed steel, the presence of water infiltration and the presence of cracks with limited opening value. Figure 7 illustrates some of these defects.

4.3.1 *Exposed steel defects*

The main differentiation point is the origin of these defects. Consequently, the inspectors have to clarify if this finding is a part of a steel rebar with structural contribution or if it is a steel insert left from construction. The most commonly met steel insert is the one presented in Figure 7. In case of exposed steel rebar, the exposed length and the actual cover are recorded in order to facilitate follow up. Also a cover meter measurement is performed in order to identify any neighboring low–cover areas. If low cover areas are observed, then half–cell potential measurements can

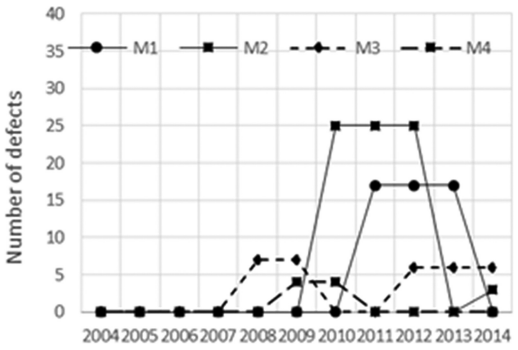

Figure 5. Number of exposed steel defects of footing structures.

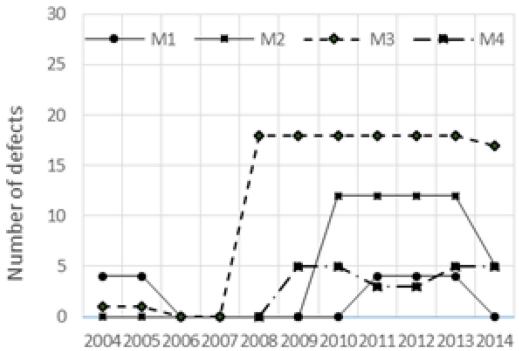

Figure 6. Humidity trace defects in the footing structure.

be performed. Regarding the steel inserts, only the dimensions are registered. Figure 5 illustrates the number of registered exposed steel defects in the footing structures of the bridge. The drops in the number of registered defects indicate maintenance actions. After two cycles of inspections it is assessed that this number will not be increased significantly. It has to be noted that 17% of the total number of exposed steel defects correspond to steel inclusion defects. The total number of exposed steel defects in the whole structure was 117 at the time of writing.

4.3.2 *Cracks*

The importance of crack recording is of great importance, since the presence of cracking could be a sign for the degradation of the structural performance of the structural elements especially for the prestressed elements. Also, in terms of durability the presence of cracks could lead to water infiltration and chloride ingress.

The main recording criterion for a crack is the crack opening, which is 0.3 mm for conventional reinforced elements and 0.1 mm for prestressed ones. Also, independently of the crack opening value, the crack is recorded if wet traces-water infiltration is presented. The inspectors record the direction of the cracks, the length and the crack opening. Up to date the number of registered crack defects is very limited and none of the crack defects is related to the performance of the prestressing action.

4.3.3 *Humidity traces*

These defects are related to the presence of humidity-water infiltration. In many cases the presence of steel–inserts leads to these defects. Figure 6 illustrates the number of registered humidity trace defects in the footing structure. The great foundation depth contributes to the development of these defects. From technical point of view the repair of these defects is a challenge. Up to date the maintenance team utilizes waterproofing mortars with good results.

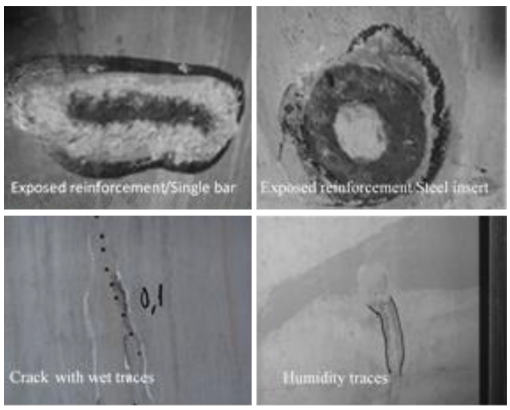

Figure 7. Commonly met defects on the elements of the bridge.

5 MAINTENANCE

5.1 *Selection criteria*

The main selection criteria for the determination of repair methodology are given in Figure 8. The Engineering team takes into account these criteria and decides repair methodology to be followed. Considering the inelastic cost factor related to access, this means in most of the cases, the cost of the repair material is negligible. Treatments which are performed by the Rope Access Team or negative telescopic bridge inspection platform exhibit higher cost. Consequently the demand for the effectiveness of the repair methodology in terms of minimization of repair sessions, complexity of materials and the maximum achievable durability becomes stricter.

5.2 *Repair methodology*

The suitable repair methodology is selected from a pool of available methodologies which have been issued in order to organize in detail the technical information and the actions that have to be performed in order to treat the commonly met defects. The terminology and the majority of selected materials comply

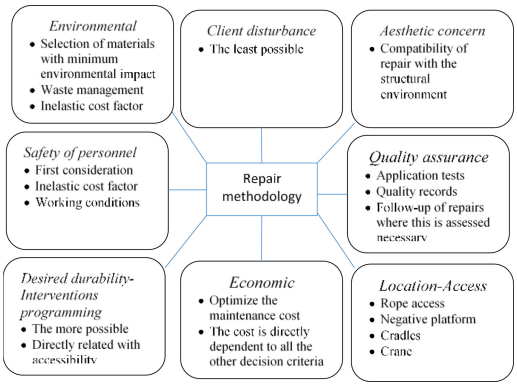

Figure 8. Selection criteria taken into consideration.

with EN 1504. Each methodology is written in a card form (Repair Card). The information is given as a step procedure in order to facilitate the personnel during execution of works and preparation. Also the information related to the necessary tooling and personal protection equipment is given. Finally, for each repair card, the respective quality control form which the personnel have to complete during the execution of works is produced. Data such as the consumption of each material, the mix–analogies and the achieved level of concrete surface roughness are completed by the personnel. The characterization of concrete is performed according to ICRI No. 310.2R-2013. The Repair Cards are organized according to the related defect type.

5.3 *Recording and cost control*

In-house developed software facilitates the recording and cost control of maintenance actions. More specifically the preparatory actions, the progress of maintenance actions, quality control records, material consumptions and economic data such as man-days and material costs are recorded. This information facilitates not only the follow-up of the maintenance campaign but also the time and economic scheduling of relevant maintenance campaigns.

5.4 *Evaluation of repair methodologies & quality control*

Although the applied materials are well proven as effective, the special characteristics or conditions, which are mostly location related, indicate the necessity for the evaluation of effectiveness of the repair methods in terms of applicability, durability and productivity. The evaluation of repair methodologies is performed by two means. Firstly by the performance of specific trial tests and small scale trial applications and secondly from the long term follow-up of the repairs where the actual durability of the repair is evaluated. The follow-up of repairs is carried out mainly in the course of the scheduled visual monitoring or by specialized follow-up campaigns depending on the criticality of the application.



Figure 9. Application area.

The above strategy in conjunction with the use of repair cards and the quality control forms satisfies the quality control demands and increases the effectiveness of the application. The visual monitoring team provide a second level of quality control through verification of the repairs, update of the status of defects in the global database and also recording of the followed repair methodology.

Finally one of the most important issues which enhances the effectiveness of the materials is the continuous training of personnel. The Concessionaire invests in the training of personnel. Before the application of a new material, or the adoption of a new application methodology, the personnel is trained sufficiently. Often, due to the considerable cost of access and practical difficulties to have on site supervision, this training is performed on mock-ups to preview all relevant parameters with the relevant technicians.

6 ILLUSTRATIVE EXAMPLE

6.1 *Scope of application*

The present paragraph illustrates a typical example for the decision making processes, the evaluation and finally the application of a material for the protection against water (mainly) and chloride ingress of a concrete area.

More specifically the under protection area acts as a cap for the prestressing anchorage zone of the tendons which run in the perimeter of the Pylon Square Base.

Visual monitoring which was performed in 2008 revealed some thin cracking on the concrete covers (2nd phase concrete to protect the anchorages). Also cracks were observed in the construction joint between the concrete cap and the neighboring concrete. The inspection was extended to all piers for an overview of the situation on this critical zone. Figure 10 depicts the findings from visual monitoring. Analysis recommended preventive maintenance for the protection of the anchorage area against water and chloride ingress both in vertical and horizontal surfaces.

It has to be noted that regarding chloride ingress the risk is not high since the results from chloride penetration tests which were performed in the splash zone (nearly 30 m below the application area) exhibit low penetration level. The analysis presented in Cussigh et al. 2010 confirms also this hypothesis. The extra protection in the area will keep the chloride concentration level low. Provided that the application aims to the prevention of water ingress further reduction

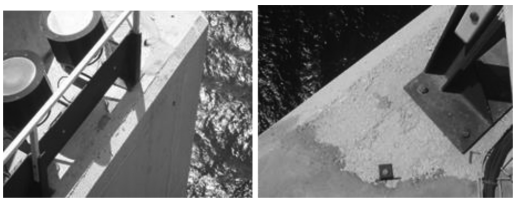

Figure 10. Findings on the region.

Table 1. Summary Table for selection criteria.

Selection criteria	Hydrophobic Impr.	Membrane
Access means	Rope Access Team	
Surface preparation	+	
Environmental impact	+	
Applicable over cracks	+ (<0.3 mm)	++
Number of visits	+ (3)	>3
Aesthetic effect	++	–
UV durability	++	+
Durability of application	++	+
Test evaluation needed	Yes	No
Cost of material	Equivalent	
Cost of application	++	–

* + Stands for better,++ for much better, – Worst.

of risk will be achieved. Additionally no low cover or steel rebar corrosion defects have been observed up to date in the area.

6.2 *Selection of material*

The norms of EN1504 were followed for the selection of protection materials. For the top surface a cementitious waterproofing mortar was selected while for the vertical surfaces two treatments were candidate for the application. The first was the application of a waterproofing polyurethane membrane and the second was to achieve a water repellent surface by hydrophobic impregnation. The following table summarizes the main selection criteria that were taken into account and their appraisal.

From Table 1, the selected repair application was hydrophobic impregnation.

6.3 *Test evaluation and application*

For the hydrophobic material two were the main queries for the final approval.

- Whether the hydrophobic material could penetrate through the dense concrete structure (C50/60) in order to achieve a durable protection system. Also the applied quantity had to be determined.
- The appropriateness of the application means in terms of applicability and productivity.

For this reason, the Maintenance team in cooperation with the Engineering team of the material's supplier deployed a test evaluation plan. There were two target performance criteria. The first criterion was to achieve

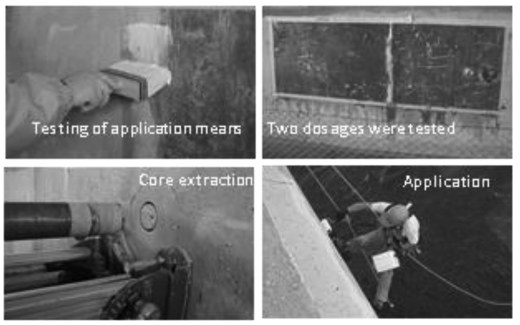

Figure 11. Application of material with Rope Access team.

a penetration depth greater than 5 mm and a water uptake less than 0.1 kg/(m^2x $h^{0.5}$)

Two quantities (500 g/m^2 and 700 g/m^2) were applied in an easily accessible test area which was constructed with the same concrete mix design as that of the actual application area. The evaluation of performance in the high density concrete was performed in samples that were taken by the extraction of cores from the test application area. The performance parameters were determined according to EN 14630 & EN 1062-3. Both applied quantities reached the target. Finally, a quantity equal to 600 g/m^2 was applied.

6.4 *Application and quality control*

Regarding the application means, although an airless spray would allow the highest material economy, it was rejected since the high wind would not allow controlled application. Also comparing with the application by brush, the application with roller was characterized as more productive.

The application area was divided into vertical panels of 1 m corresponding to the rope access technician's most ergonomic movement. Carefully weighed doses of material were issued for each panel to control the application. The complete treatment was applied in two coats. Before the application of material the substrate humidity level and the concrete surface temperature were measured. The readings were recorded in the quality control forms which were issued for hydrophobic impregnation applications. Additional care was addressed to the sequence of faces to respect the maximum substrate temperature (depending on sun exposure).

The material was applied in all the Pylons from the rope access team in the summer of 2014 after preliminary pressure cleaning. The total application area was equal to 476 sq.m. The result is aesthetically and technically compliant with the objectives. Application records and cost control data were archived for future reference.

6.5 *Follow-up*

The visual monitoring continues every 4 years. Even if they are now protected, the thin cracks are still

visible to the inspectors, so they remain under regular monitoring. Any evolution will be recorded. Material monitoring will provide data for when the application needs to be renewed.

7 DISCUSSION-CONCLUSIONS

This contribution highlighted the context within which the Concessionaire of the Rion - Antirion Bridge performs technical management for the maintenance of the structure. The management concept is based on the triptych Monitoring-Analysis-Maintenance. Furthermore, the Maintenance is generally "preventive Maintenance" and related to localized restoration of durability because of the high quality of the initial construction. The high quality concept in the repair interventions is the one that will compress the long-term maintenance cost.

Regarding the concrete structural elements of the bridge, visual monitoring is the main tool for the identification of localized defects. The use of inspection software in all the inspections facilitates the traceability and the follow-up of the defects. Also the performance of inspections from in–house personnel increases the effectiveness of these inspections since, in order to perform such inspections, a deep knowledge of the structure is required. For the same reason, the performance of analysis internally enhances the effectiveness of the reports. The training of staff is proven to be effective in terms of safety, productivity & quality assurance.

The implementation of Repair Cards is a very useful tool for the formalization of repair methodologies, the quality assurance and the follow-up –evaluation of repairs.

The adopted terminology and philosophy introduced from EN 1504 facilitates the selection of repair materials.

Until today the frequency of inspections on the concrete elements has proven sufficient since no sudden failures or significant defects have been observed in the bridge. Also the durability of the performed repairs has been sufficient. This fact verifies the efficiency of the adopted technical solutions.

The presented adopted strategy is evaluated continuously from comparison of previous years productivity and economic data. The maintenance software has been proven to be a useful tool.

Although all the presented approach is systematic, further improvement in terms of productivity is expected after the implementation of the Integrated Management System procedure (with certification according to ISO 9001), where all the presented actions are described in a practical and detailed way. Full implementation is expected at the end of 2016.

REFERENCES

Cussigh et al. 2010, "Rion – Antirion Bridge project – concrete durability towards corrosion risk", *3rd fib* international congress, Washington DC USA.

EN 1504 Products and systems for the protection and repair of concrete structures. Definitions, requirements, quality control and evaluation of conformity.

EN 14630 Products and systems for the protection and repair of concrete structures Test methods Determination of carbonation depth in hardened concrete by the phenolphthalein method.

EN 1062-3 Paints and varnishes. Coating materials and coating systems for exterior masonry and concrete. Determination of liquid water permeability.

Harikiopoulou – Cordova et al. 2003, "Concrete Durability towards corrosion risk – Protection strategy applied on the Rion-Antirion Bridge Project", Concrete Conference, Technical Chamber of Greece, Kos

ICRI No. 310.2R-2013. "Selecting and Specifying Concrete Surface Preparation for Sealers, Coatings, Polymer Overlays, and Concrete Repair".

Papanikolas et al. 2011, "The structural health monitoring system of Rion Antirion Bridge "Charilaos Trikoupis", IBSBI 2011, October 13–15, 2011, Athens, Greece.



Taylor & Francis
Taylor & Francis Group
http://taylorandfrancis.com

Concrete Solutions – Grantham et al. (Eds.)
© 2016 Taylor & Francis Group, London, ISBN 978-1-138-03008-4

Focused, non-destructive repair of tunnel walls with electrochemical chloride extraction

U. Schneck
CITec Concrete Improvement Technologies GmbH, Germany

ABSTRACT: Some side wall sections of a highway tunnel had accumulated large amounts of chloride after 10 years of service, but, due to the high concrete cover, the reinforcement was not affected by increased corrosion activity. With the help of a rapid, non-destructive resistivity measurement and sufficient backup from chloride testing, the likelihood of future corrosion attack within a total suspect wall area of 1,500 m^2 could be limited to 400 m^2. A non-destructive electrochemical chloride extraction was executed prior to the coating and surface protection of the concrete as an instant-off treatment. In total, 11 kg chloride could be removed from the application areas. Partly the treatment has been done under traffic, so the long application times did not affect other maintenance actions on the related surfaces.

1 INTRODUCTION

In a divided 2 × 2 lane highway tunnel, considerable amounts of chloride contamination had accumulated in the side walls of a right-angled section after 10 years of service. There, a different concrete composition had been used than for the longer tubular section. Although the concrete cover ranged between 60 and 80 mm, and chloride had not yet reached the reinforcement, the durability against corrosion could not be guaranteed in a long-term forecast: initial chloride tests gave values up to 2.5% until 40 mm depth and 1.7% in 60 mm depth (related to the cement mass). A coating of the concrete surface, which was the most cost effective repair, risked enclosing too much chloride in certain parts of the walls. Basically, the coating had to be supported by other maintenance methods – either cathodic protection or chloride extraction.



Figure 1. View on the tunnel entrance.

2 CONDITION SURVEY AND REPAIR SPECIFICATION

The test methods that have been used for the condition survey are described in detail in Reichling et al (2013). According to Broomfield (Broomfield et al 2013) "the condition survey should provide sound information about wall areas with increased chloride content within the splash zone (bottom to +1.80 m). It was unlikely to have a general or evenly increased chloride distribution, and intensive dust sampling would have caused too much effort and damage to the concrete. So the electrical surface resistivity was planned to give the necessary knowledge, backed up by additional, but small numbers of dust samples of the concrete and chloride analysis.

Potential mapping could not be very helpful in this case, because no corrosion elements had been triggered yet by chloride. But to delay the survey until corrosion had started was not considered a useful alternative; the maintenance and repair effort would be significantly higher then.

The site measurements consisted of the following investigations (done in this order):

- definition of a grid overlay on 60 × 60 cm on the wall surfaces from +0.00 to +1.80 m
- combined potential- and surface resistivity measurement



Figure 2. Right-angled tunnel section with chloride accumulation in the side walls.

– drill samples in layers of 2-4-6-8 cm depth for chloride and humidity analysis in areas with a low concrete resistivity (and at higher resistivity values for counter checks)
– scanning of the concrete cover in the dust sampling locations
– (supporting visual inspection of reinforcement in suspect areas).

As can be seen in fig. 8 top graphic, the potential plot showed a slight shift from values about −50 mV vs. CSE to −250 mV down the measured wall section from top to bottom. This did not change basically along the investigated tunnel length. With the known chloride profile from the previous investigation (taken at random), a first interpretation on site seemed to be a correlation with an increasing water content in the bottom area of the wall.

The surface resistivity plot (see fig. 8 bottom graphic) showed a higher portion of low resistivity readings within the measured surface. This measurement needs good conditions (clean, even concrete surface and no large aggregates on top to place all four Wenner pins on cement paste), and this was possible on the investigated concrete. The resistivity values appeared instantly, were stable and reproducible. So the measurement results indicated that the resistivity could be a reliable basis for further testing.

According to this, drilled samples were taken from concrete areas with low resistivity readings, mainly $<100\ \Omega$m, but also from areas between 100 and 500 Ωm. The table in fig. 9 shows, that the surface resistivity correlated quite well with the chloride concentration in the concrete. It could be stated that obviously in concrete areas with a surface resistivity less than 100 Ωm a considerably increased chloride content could be expected, and that readings $>100\ \Omega$m indicated uncritical chloride ingress – considering the high concrete cover.

The table in fig. 9 is a representative collection of project data from the whole investigated surface and in 90% of all sampling locations the above interpretation was true. So it could be considered to be a solid basis for finding chloride containing areas and evaluating feasible maintenance strategies.

The water content varied between 2 and 4% on the concrete surface, but the average water content within the outer 4 cm (which influences the resistivity) was quite constantly ranging between 2.5 and 3.2%. Therefore, different resistivity readings could be correlated with different chloride content.

With the help of a rapid, non-destructive resistivity measurement and sufficient backup from chloride testing, the likelihood of future corrosion attack within a total suspect wall area of 1,500 m^2 could be limited to 400 m^2. The sub-areas were ranging from 20 to 120 m^2. In this case, an electrochemical chloride extraction could be done, prior to the coating and surface protection of the concrete, as an instant-off treatment to provide the most economical maintenance strategy."

3 ELECTROCHEMICAL CHLORIDE EXTRACTION

Basic considerations about ECE, its merits, limitations, beneficial application scenarios and an introduction to the specific ECE system used in this project can be found in (Schneck, 2009). The pre-manufactured and re-usable electrodes had a size of 60 × 60 × 2 cm and contained besides the Ti-MMO mesh anode an ion exchange resin that is meant to buffer the pH value inside the electrode and on the concrete surface as well as to adsorb the chloride and to prevent chlorine evolution. The exchanger capacity per electrode is sufficient for a usual treatment stage (ca. 4 to 8 weeks); otherwise a chloride measurement unit (Schneck et al 2006) will signal possible saturation and trigger an automated termination of the respective group of electrodes along with a notification for the operator.

In the case of the tunnel walls, a mounting system was needed to attach up to 300 single electrodes per application step, quickly and tightly to the tunnel wall and to allow flexible wiring. It was also important to permit regular check-up on proper attachment between electrodes and switch boxes and other maintenance, as well as wetting and temporary removal of some electrodes on request of other companies that needed access to the concrete surface. The electrode arrangement can be seen in figures 3, 4 and 5, showing also the wetting system with barrels of tap water, a pump and "micro-drop" gardening hoses.

The entire ECE application was divided into 6 sub areas with sizes between 20 and 86 m^2. In each sub area the single electrodes were combined into groups of between 8 and 17 m^2. This way, all electrical data could be specified and measured in detail.

The treatment times had to be extended for up to 10 weeks per sub-area, as the large concrete cover reduced the strength of the electrical field by at least 50% – compared to (usual) applications at a cover of ca. 30 to 40 mm. Partly the treatment was done under traffic, so the long application times did not affect the use of



Figure 3. View on the electrode arrays on the tunnel wall.

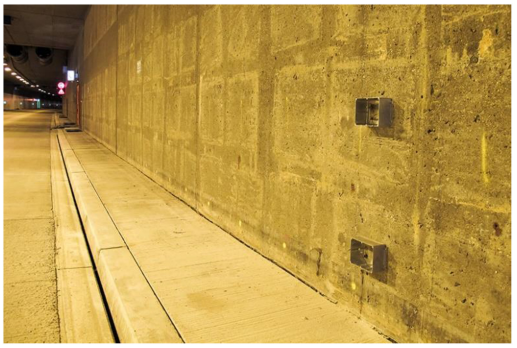

Figure 6. Passive monitoring boxes.



Figure 4. Control unit with central high current power supply.



Figure 7. View inside a monitoring box with connectors to the reinforcement, a counter electrode and a drill hole for a reference cell.



Figure 5. Water supply with tap water barrels and pump.

the tunnel and other maintenance actions on the related surfaces.

Figure 10 shows chloride profiles on selected sampling locations before and after the ECE treatment. It can be seen that a good desalination effect could be achieved: Initial maximum chloride contents of up to 3.9 % in 0–2 cm and 2.1% in 0–8 cm depth were reduced to 1.0% in 0–2 cm and 0.5% on average at 0–8 cm. The removal effect ranged between 23 and 86%, depending on the initial amount of chloride (always higher efficiency at higher chloride contents).

Despite the long treatment times and the applied voltage of 40 V, the impressed charge stayed low to moderate (ranging between 71 and 566 Ah/m^2 of rebar surface across the electrode groups). An example of the charge accumulation can be seen in fig. 11.

As analysed from the regeneration solutions of the electrodes, in total, 14.6 kg chloride was removed from the application areas, which corresponds to ca. 23 kg of NaCl from de-icing salts – on average ca. 60 g/m^2.

4 LONG-TERM CORROSION SURVEILLANCE

For a long-term survey of the rehabilitation result, monitoring boxes with stainless counter electrodes and drill holes for mounting of reference electrodes were installed according to figures 6 and 7.

The locations for the monitoring boxes were selected on coordinates with some known residual

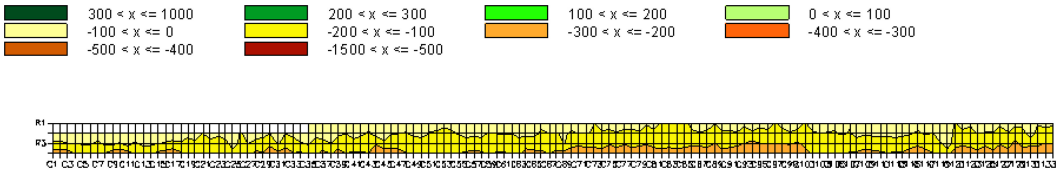

Röhre West - Ostseite/C / EM100810A
Inspection Report Open Circuit Potential [mV], Electrode: saturated Copper-Copper Sulphate

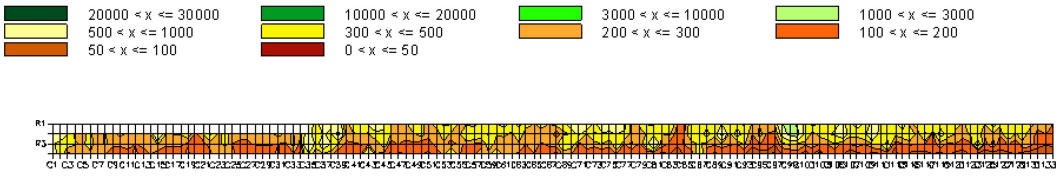

Röhre West - Ostseite/C / EM100810A
Inspection Report Surface Resistivity [Ohmm]

Figure 8. Contour plots of potentials (top) and surface resistivities (bottom) of parts of the tunnel wall.

Cell	R3C81 R: 1,2.. 1,8 C: 48,0.. 48,6	R4C14 R: 1,8.. 2,4 C: 7,8.. 8,4	R4C33 R: 1,8.. 2,4 C: 19,2.. 19,8	R4C68 R: 1,8.. 2,4 C: 40,2.. 40,8	R4C82 R: 1,8.. 2,4 C: 48,6.. 49,2	R4C129 R: 1,8.. 2,4 C: 76,8.. 77,4	R4C130 R: 1,8.. 2,4 C: 77,4.. 78,0	R4C133 R: 1,8.. 2,4 C: 79,2.. 79,8
Concrete Cover [mm]	55	68	70	54	76			76
Potential [mV vs. CSE]	-161	-365	-220	-165	-274	-292	-257	-229
Surface Resistivity [Ohmm]	250	21	17	187	22	40	67	109
Chloride Content [% Cement] at level [mm] 20, 40, 60, 80, 100	0,86 0,35 0,01 0,02 --	3,25 1,02 0,02 0,02 --	3,85 1,59 0,06 0,02 --	0,72 0,03 0,02 0,02 --	2,85 0,75 0,02 0,03 --	2,45 1,58 0,48 0,09 --	3,92 2,54 1,71 0,34 --	0,63 0,16 0,01 0,01 --
Concrete Humidity [%] at level [mm] 20, 40, 60, 80, 100	2,08 2,90 3,06 [illegible]2 --	[illegible]42 2,75 [illegible] 2,99 --	[illegible]52 3,19 2,18 2,90 --	2,56 2,93 3,98 3,33 --	[illegible]6 2,78 2,85 2,91 --			2,25 2,61 2,92 3,87 --
Carbonation 1 [mm]								
Carbonation 2 [mm]								
Surface Strength (Rebound)								
Concrete Strength [N/mm2]								
Delamination								
Info	Cl 11 RW 322-O	Cl 4 RW 318-W	Cl 6 RW 319-W B1224	Cl 9 RW 314-O	Cl 2 RW 314-W	P CC RW 325-W B1219	P CC RW 325-O	Cl 8 RW 309-O

Figure 9. Data table showing multiple corrosion relevant data on certain test locations including bar graph displays of chloride and water contents in sampling layers of 0–2, 2–4, 4–6 and 6–8 cm depth. Note the correlation between surface resistivity and surface chloride content: increased chloride ingress at resistivity readings $<100\ \Omega$m.

chloride after the termination of the ECE. This allows enhanced corrosion measurements (impedance, galvanostatic pulse measurements, LPR or Tafel polarisation) at any time under the surface protection, but does not require permanent data recording. With the help of these measurements, not only possible changes in the corrosion behaviour, but also re-distribution effects of chloride and concrete moisture can be traced.

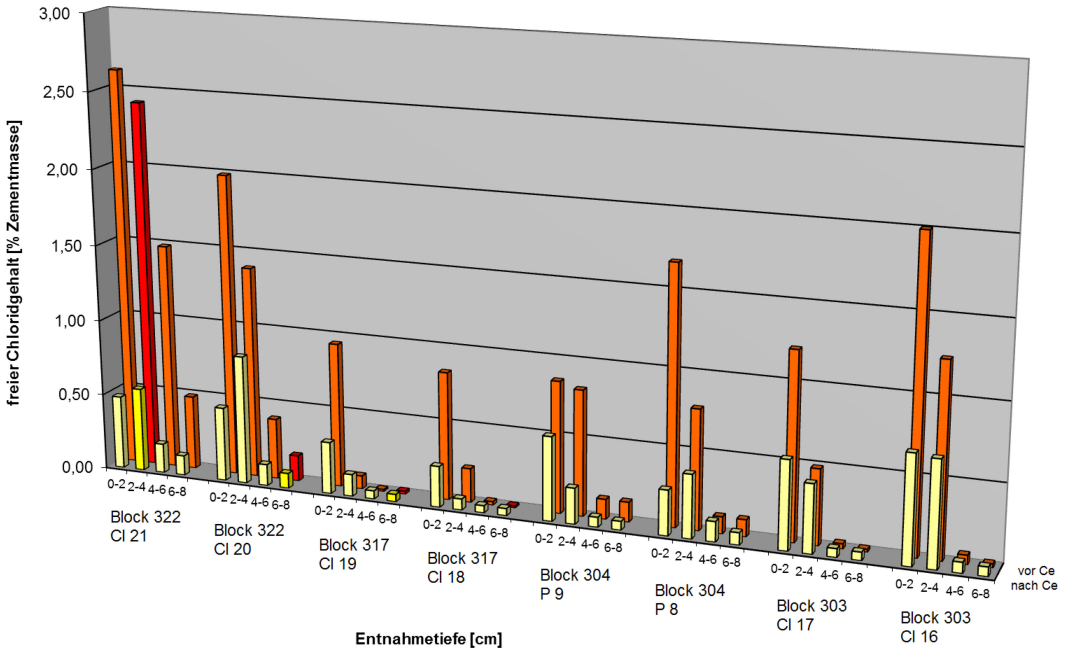

Figure 10. Chloride profiles (free chloride content – analysed from water soluble chloride, related to the cement mass) on selected sampling location before and after the ECE application of about 10 weeks.

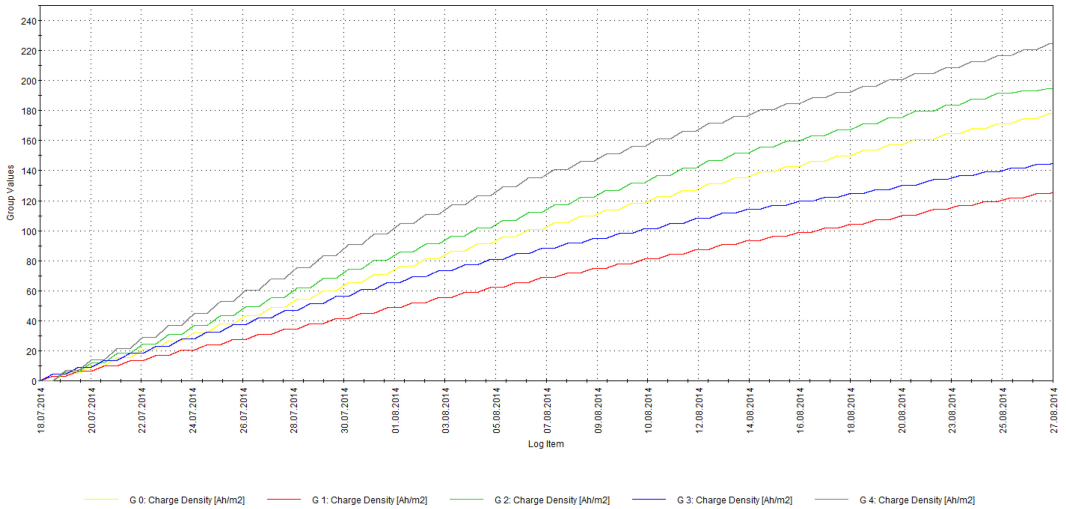

Figure 11. Development of impressed charge densities for several groups of electrodes during the ECE application as recorded by the ECE control software [Ah/m^2 rebar surface].

5 CONCLUSIONS

Within the condition survey, the surface resistivity measurements appeared to be very useful and important, as with these data and the correlation to dust samples and their moisture and chloride contents, the areas affected by chloride could be made visible on the concrete surface with good reliability. As rebar corrosion had not yet been initiated or just in very limited areas, the potential survey could not provide useful information for assessing chloride affected concrete areas.

ECE can be adapted very exactly to local conditions of chloride contamination and corrosion activity – at least with the specific system used in this project. With such a tailored solution, the treatment cost can be kept

as low as possible, and the slim layout permits the ECE application to run for extended periods and under traffic.

The amount of impressed charge remained rather low, which was caused by the large concrete cover thickness and the resulting increased concrete resistance. Under the given circumstances, this was no problem as the passivity around the reinforcement had not been harmed substantially. So the requirements of DIN CEN TS 14038-2 (DIN, 2011), to achieve impressed charges between 1,000 and 2,000 Ah/m^2, could not be met. The high polarisation resistances on the still passive reinforcement limited the impressing of charge considerably, but an additional alkalisation, which is normally intended to obtain during an ECE, was not necessary here.

The desalination effect on the sampling locations was convincing – especially in comparison to the amount of removed chloride analysed from the electrode regeneration. Residual chloride can be tolerated by experience (see also Schneck 2009), and in the close to the rebar vicinity almost all chloride could be removed. Re-distributional effects theoretically may cause a slight increase there, but experiences from other projects rather suggest a continued migration of chlorides towards the concrete surface – forced by water migration after the intensive wetting during the ECE treatment. New or repeated chloride ingress from de-icing salts should be safely prevented by the surface protection system (applied after the ECE) for several years.

REFERENCES

Broomfield, J., Fischer, J., Mietz, J, Schneck, U. 2013. Case Studies. *Materials and Corrosion 2 (2013)*, 147–160

DIN CEN/TS 14038-2, 2011. *Elektrochemische Realkalisierung und Chloridextraktionsbehandlungen für Stahlbeton – Teil 2: Chloridextraktion*. Berlin: Beuth Verlag GmbH

Reichling, K., Raupach, M., Broomfield, J., Gulikers, J., l'Hostis, V., Kessler, S., Osterminski, K., Pepenar, I., Schneck, U., Sergi, G., Taché, G. 2013. Full surface inspection methods regarding reinforcement corrosion of concrete structures. *Materials and Corrosion 2 (2013)*, 116–127

Schneck, U., Grünzig, H., Vonau, W., Herrmann, S., Berthold, F. 2006. Chloride measuring unit for the improvement of security and performance of electrochemical chloride extraction. In M. Grantham (ed): *2nd International Concrete Solutions Conference, Proc., St. Malo, 2006*. Watford: BRE Press

Schneck, U. 2009. Long term behaviour of box girder sections with residual chloride after the application of ECE. In M. Grantham (ed): *3rd International Concrete Solutions Conference, Proc., Padova, 2009*. Rotterdam: Balkema

Schneck, U. 2011. Non-destructive diagnosis and repair of 300 concrete columns beneath a shopping mall under full operation. In M. Grantham (ed): *4th International Concrete Solutions Conference, Proc., Dresden, 2011*. Rotterdam: Balkema

Concrete Solutions – Grantham et al. (Eds.)
© 2016 Taylor & Francis Group, London, ISBN 978-1-138-03008-4

NDT and diagnostic study of corrosion damaged RC structures to enhance their service life – case studies

Satish Sharma, Ashwani Pahuja, B.S. Rao, N.S. Adarsh Kumar & Ankit Sharma
National Council for Cement and Building Materials, India

ABSTRACT: Concrete structures in service deteriorate slowly either due to ageing or due to durability problems caused by exposure conditions. The deterioration of structures generally appears in the form of cracking. Freeze thaw, alkali-silica reaction, abrasion, carbonation and chloride diffusion into the cover concrete leading to corrosion of reinforcing bars in RC structures are well known and globally recognized causes of cracking & spalling of concrete in service structures. Large amounts of energy and materials, in addition to financial resources, are wasted when structures deteriorate. To determine the cause of damage and to carry out repair & restoration to enhance the service life, NDT and related diagnostic study are carried out.

This paper highlights the NDT and diagnostic studies of a distressed 37-year-old service building located in a semi-arid region and another service structure located near the sea shore in India. This paper highlights the field and laboratory studies carried out using non-destructive and partially destructive testing techniques. The investigation included visual survey, compressive strength, ultrasonic pulse velocity testing, carbonation and chloride measurement. Estimation of corrosion using half-cell potential testing was also done. The study reported was done on selected RC members of each structure. Data interpretation of the test results and service life of the structure is briefly given.

Based on the visual inspection and analysis of the test data, the indigenously available repair and strengthening measures to restore the service life of the structure are described, covering application of anti-corrosive treatment, epoxy grouting, bond coat, polymer modified mortar as per ACI Committee Report, an anti-carbonation protective coating, unidirectional Glass Fibre Reinforcement Polymer (GFRP) wrapping technique using epoxy saturant is summarized in this paper.

1 INTRODUCTION

Concrete construction is generally expected to give trouble free service throughout its intended design life. However, these expectations are not realized in many constructions because of structural deficiency, material deterioration, unanticipated over loadings or physical damage. The deterioration of structures is a time dependent process caused by several factors such as plastic deformations, interaction with the environment, initial design and construction flaws and accidents like fire and earthquake. It is a crucial problem to have the correct assessment of concrete strength to enhance the life of the structure. If the cause of deterioration is predicted and a proper assessment of the structure is made, it may be economically viable to repair the distressed structure and prolong its life.

Today engineers & technologists all over the world are concerned about the structural problems of RC structures and are looking for enhancing the service life of existing structures. In this paper In-situ non-destructive Evaluation in the field and laboratory test on representative samples from different structural elements of the structures is reported. The field assessment included the quality assessment of hardened concrete in structure using Ultrasonic Pulse Velocity technique (IS: 13311-1992 Part-I), study of concrete cover and carbonation and corrosion status using half cell potential technique (ASTM C 876). Evaluating equivalent cube compressive strength and chemical composition of concrete powder sample is also reported. Apart from field & lab study, this paper also highlights the different methodologies adopted for repair, restoration & strengthening of distressed RC elements of the service structures.

2 LITERATURE SURVEY OF ASSESSMENT, REPAIR & RESTORATION OF CONCRETE STRUCTURES

Extensive research on the complex phenomenon of deterioration of concrete in service and premature durability issues has been reported around the globe. P.E. Gratten-Bellew studied the microstructure investigation of deteriorated Portland Cement Concretes (Gratten-Bellew, 1996). D.C.K. Tay et. al. reported the insitu investigation of the strength of deteriorated concrete (Tay, 1996). Predictive models for deterioration of concrete structures have been studied by P.A.M. Basheer et. al. (Basheer, 1996). Kenneth C. Hover covered special problems in evaluating the safety of concrete bridges and concrete bridge components (Hover, 1996). A wide range of repair options

to repair and rehabilitate damaged reinforced concrete structures has been reported by John Broomfield (Broomfield, 2010). John Bickley et. al. investigated the Issues related to performance based specifications for concrete (Bickley, 2010). Odd E. Gjorv et. al. carried out a study on the advances in durability design and performance based specifications (Gjorv, 2010).

A study on the present and future perspective on maintenance and repair systems for concrete structures has been reported by Toyoaki Mit Agawa (Agawa, 2015). H. Mihashi et. al. worked for the Establishment of JCI Special Technical Committee on the Great East Japan earthquake disaster and its activity plan (Mihashi, 2015). Satish Sharma et al. reported the distress assessment, repair and strengthening of RC members of a turbo generator foundation of the Anpara thermal power station at Uttar Pradesh (India) (Sharma, 2015). A case study on non-destructive evaluation and repair and strengthening of a corrosion distressed RC structure was done by Satish Sharma et.al (Sharma, 2015). A study on quantities and durability of concrete for revetment in Gunkanjima Island after long term service has been done by Yoshikazu Akira et. al. (Akira, 2015). Ryoichi Tanaka et al. studied the soundness of historical concrete revetments at Gunkanjima Island in Japan (Tanaka, 2015). Rahmita Sari Bintirafdinal et al. reported deterioration evaluation and life-extension strategy of a 77-year-old concrete structure exposed to the Indonesian marine Environment (Bintirafdinal, 2015). Roberto Torrent et al. studied site testing of air permeability as an indicator for carbonation rate in old structures (Torrent, 2015). A study on the Influence of construction work conditions on the relationship between concrete carbonation rate and the air permeability of surface concrete was done by Kazuaki Nishimura et al. (Nishimura, 2015). Haixue Liao studied corrosion control of reinforced concrete in corrosive environments (Liao, 2015). Hirozo Mihashi worked on JCI Guidelines for assessment of Existing concrete structures 2014 (Mihashi, 2015).

3 INVESTIGATION ON A 37 YEAR OLD SERVICE BUILDING LOCATED IN A SEMI ARID REGION OF INDIA

The typical plan of a service building located in a semi-arid region of India is shown in fig 1. It was a framed structure and was constructed in the year 1977. As per the drawings, the grade of concrete used at the time of construction was M20. The main objective was to investigate the cause and extent of damage that has occurred due to ageing and environmental influence, using the methodology described in the paper.

(a) Visual survey:

During the visual survey, distress in the form of vertical cracks, spalling of concrete and exposure of corroded reinforcement was observed at different locations on external RC Columns and RC beams as shown in fig. 2 & 3. No signs of cracks and spalling of concrete were

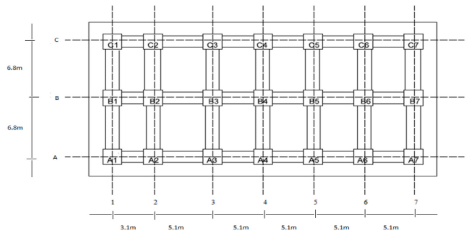

Figure 1. Typical plan of service building located in semi-arid region of India.



Figure 2. Vertical crack & spalling of concrete in RC Columns located in semi-arid region.



Figure 3. Shows distress in an RC Beam located in semi-arid region.

observed in the inner RC columns, beams and slabs. All the chajjahs were found to be severely damaged with exposed corroded reinforcing bars with 10-30% diameter reduction as shown in fig. 4.

(b) Field investigation

The field study included ultrasonic pulse velocity testing, carbonation measurement and a corrosion study. The study reported was done on selected RC members of the structure. The test results obtained are shown in Table 1.

(c) Laboratory investigation

The Laboratory study included determination of equivalent cube compressive strength from the cores extracted and chloride content. The study reported was done on selected RC members of the structure. The test results obtained are shown in Table 2.

(d) Service life prediction

The service life here is defined as the assumed period for which a structure, or part of it, is to be used for its intended purpose with anticipated maintenance, but without major repair being necessary. According to ISO: 16204-2012, the carbonation is proportional to the square root of age in years i.e. $C = K.t^{1/2}$, where C is carbonation depth in mm, 'K' is carbonation coefficient and t is time in years. From the data obtained on carbonation depth, the carbonation co-efficient 'K' has been worked out and is shown in Table 3.

Based on the carbonation depth and k value obtained in RC Columns/beams/slabs, the cause of corrosion was found to be carbonation. With the help of K_{avg} calculated below and using the equation $C = K.t^{1/2}$, it was found that the remaining service life of the structure was substantially reduced and hence there was a need to prolong the life of the structure through major repair.



Figure 4. Shows spalling of concrete in RC Chajjahs (overhanging roof element) located in semi-arid region with dia of corroded bar reduced to 10–30%.

4 TEST RESULTS AND DISCUSSION OF SERVICE BUILDING LOCATED IN SEMI ARID REGION OF INDIA

The test results were analyzed to work out the cause and extent of damage and find out the suitable specifications for repair. Based on Ultrasonic Pulse Velocity testing done on representative samples by random sampling technique on RC Columns, RC Beams and RC Slabs, the overall quality of concrete was graded as 'Good' as shown in Table 1. The test results of concrete cores, as shown in Table 2, indicate that the equivalent cube compressive strength values for the RC Columns/beams/slabs was found to meet the specified characteristic compressive strength of 20 MPa. Based on the half-cell potential measurement done as per ASTM C876, 90% corrosion probability was suggested in RC Columns whereas corrosion was uncertain in RC beams & RC slabs. The value of average depth of carbonation was found to be 45 mm against the measured average depth of cover of 40 mm for RC Columns, 45 mm against average value of 25 mm in case of RC beams and 38 mm against 30 mm average measured cover depth in RC Slab as shown in Table-3. Carbonation was found to reach beyond the cover of concrete. Hence the cause of damage for distress in structure was found to be carbonation. Chloride

Table 1. Test results of field investigation done on different RC members located in semi-arid region.

RC Members	Range of UPV values (km/s)	Avg. Concrete Cover (mm)	Depth of Carbonation (mm)	Corrosion status as per ASTM C 876
RC Column	3.51 to 3.72	40 (38 to 43)	40 to 50	90% probability
RC Beam	3.57 to 3.76	25 (23 to 27)	40 to 50	Uncertain
RC Slab	–	20 (18 to 22)	25 to 50	Uncertain

Table 2. Test results of laboratory investigation done on different RC members located in semi-arid region.

RC Members	Average Equivalent Cube Compressive strength (MPa)	Chloride content in cover zone (kg/m^3)
RC Column	27	0.10 to 0.12
RC Beam	24	0.10 to 0.24
RC Slab	24	0.50 to 0.98

Table 3. Carbonation co-efficient of different RC members located in semi-arid region.

RC Members	Age (Years)	Avg. measured concrete cover (mm)	Avg. Depth of Carbonation (mm)	Carbonation Coefficient 'K'	Average Carbonation Coefficient 'K_{avg}'
RC Column	37	40	45	7.40	7.01
RC Beam	37	25	45	7.40	
RC Slab	37	20	38	6.25	

was not the cause of corrosion as it was within the specified value.

5 INVESTIGATION ON 15 YEAR OLD RC COLUMNS OF STEAM TURBINE GENERATOR (STG) LOCATED IN A POWER HOUSE NEAR THE SEA SHORE IN INDIA

The typical layout plan of RC Columns located in the power house is shown in fig 1. The subject RC structure wassituated at a distance less than 1 kilometre from the seashore and was constructed in the year 1999.As per the drawings, the grade of concrete used at the time of construction was M30. The main objective was to investigate the cause and extent of damage that had occurred due to ageing, using the methodology discussed in the paper.

(e) Visual survey:

During the visual survey, distress in the form of vertical cracks, spalling of concrete and exposure of corroded reinforcement was observed at different locations in the RC Columns as shown in fig. 6 & 7. Only two faces of two RC Columns were found distressed due to abrasion/erosion of concrete surface due to constant splashes of sea water leakage from pipes adjoining the RC Columns. The samples of water leaking from the pipe were taken for chemical analysis which is shown in Table-5.

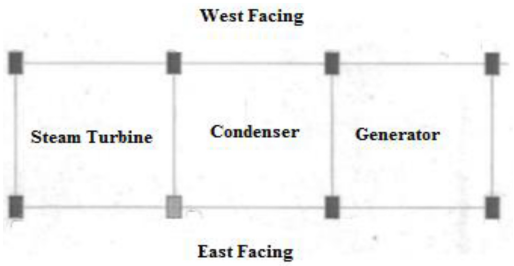

Figure 5. Typical plan of RC Columns located in power house near sea shore in India.



Figure 6. Shows vertical crack and abrasion of concrete surface in RC Column located in power house near sea shore.

(f) Investigations on RC columns of steam turbine generator (STG)

Quality of concrete as obtained by UPV testing as per IS 13311-1992 (part 1) carried out on RC Columns has indicated Good grading. Compressive strength of concrete in RC Columns as assessed as per IS 516 & IS 456, is found to be meeting the specifications of M30 grade of concrete. The results of chloride content on concrete powder samples extracted by drilling cores of 60mm diameter from three different depths of cover concrete (0–20 mm, 20–40 mm & 40–60 mm) are shown in Table 4. The chloride content of the concrete core powder of one of the RC Columns obtained



Figure 7. Shows horizontal crack and abrasion of concrete surface in RC Column located in power house near sea shore.

Table 4. Test results of laboratory investigation done on 30 MPa RC Columns located in power house near sea shore having avg. concrete cover of 60 mm.

	Results of chemical analysis		
Location	Depth (mm)	Chloride content (Kg/m^3)	pH
Columns B-2	0–20	6.24	8.61
	20–40	6.72	11.39
	40–60	6.00	12.47
Columns D-2	0–20	9.84	12.83
	20–40	9.36	12.69
	40–60	10.32	12.82
Columns C-3	0–20	11.28	12.83
	20–40	9.60	12.56
	40–60	1.58	12.76
Columns F-2	0–20	15.60	12.28
	20–40	1.46	12.20
	40–60	10.80	12.81
Columns B-2	0–20	0.38	8.82
	20–40	0.34	8.78
	40–60	1.82	11.24
Columns C-2	0–20	1.13	11.34
	20–40	0.34	12.59
	40–60	0.46	12.78
Columns F-3	0–20	6.24	8.61
	20–40	6.72	11.39
	40–60	6.00	12.47

(As per Indian Standard code IS 456:2000, specified limit of chloride is 0.6 Kg/m^3 of concrete which is equivalent to 0.15% by mass of cement)

after grinding in layers by profiling was determined at the NCB laboratory and is shown in Fig 8.

(g) Test results of water samples

The average results of chemical analysis of a water samples taken from leaking water from the pipes adjoining the RC columns indicates that Chloride content, sulphate content, organic matter & inorganic matter were exceeding the permissible limits as per Codal provisions specified in IS :456-2000 as shown in Table 5.

(h) Effect of chloride diffusion on service life of structure

Chloride diffusion has led to the chances of corrosion of reinforcing bars of RC Columns. The alkaline environment of concrete forming a passive film on the surface of the embedded steel is disrupted which may lead to the corrosion of rebar. In this case, there was no reduction in diameter of reinforcing bars.

Table 5. Test results of Water Sample.

Sl. No.	Content	Test Results	Permissible limit as per IS 456-2000
1	pH	8.41	6 (min.)
2	Sulphate (SO3)	2421 mg/l	400 mg/l (max.)
3	Chloride (Cl)	23750 mg/l	500 mg/l (max.)
4	Inorganic Matter	36900 mg/l	3000 mg/l (max.)
5	Organic Matter	2318 mg/l	200 mg/l (max.)
6	Suspended Matter	12 mg/l	2000 mg/l (max.)

6 TEST RESULTS AND DISCUSSION OF RC COLUMNS LOCATED NEAR SEA SHORE

The test results were analyzed to work out the cause and extent of damage and find out the suitable specifications for repair. The test results of concrete cores indicate that the equivalent cube compressive strength values for RC Columns were found to meet the specified characteristic compressive strength of 30 MPa. The likely cause of damage in the structure was found to be the chloride content which was found to be greater than the specified value. The reinforcement was not found to be damaged with the penetration of chloride in the concrete cover. High level of chloride content upto the reinforcement has enhanced the chances of corrosion of reinforcing bars of RC Columns.

7 REPAIR AND STRENGTHENING MEASURES

In the present investigations, the distress in the RC structural members of a service building in a semi-arid region was caused by carbonation of cover concrete leading to reinforcing bar corrosion and distress in the RC columns of the STG building near the sea shore was caused due to chloride diffusion. To carry out repair & restoration of these affected RC members, a systematic procedure for repair is suggested in Table 6.

Table 6. Repair and restoration measures.

RC Members of Service Building in semi arid region	RC Columns of STG near sea shore
1. Removal of all soft and loose concrete from the visible distressed portion and chipping using light hammer (2lb hammer) 2. Grouting with high molecular weight indigenously available low viscosity epoxy grout to fill the cracked portion & to fill the voids. 3. Cleaning of rust from corroded reinforcing steel and providing additional steel bars wherever required to compensate for corrosion losses followed by anticorrosive treatment. 4. Applying two component epoxy bond coat conforming to specifications of ASTM C 881 – 13 TYPE II to ensure the effective bond of old substrate obtained after chisel cutting of cover concrete and new concrete. 5. Applying the Polymer Modified Mortar (PMM) to build the profile of structural members in damaged cover portion as per ACI Committee report (ACI 548.3 R-03). 6. Strengthening of distressed RC members using indigenously available nonmetallic composite fiber wrapping system. 7. Applying protective coating on surface of RC Columns/ beams/slabs to protect from the further corrosion to reinforcing bars.	1. Removal of all soft and loose concrete from the visible distressed portion and chipping using light hammer (2lb hammer) 2. Cleaning of rust wherever required followed by anticorrosive treatment. 3. Applying two component epoxy bond coat conforming to specifications of ASTM C 881 – 13 TYPE II to ensure the effective bond of old substrate obtained after chisel cutting of cover concrete and new concrete. 4. Applying the Polymer Modified Mortar (PMM) to build the profile of structural members in damaged cover portion as per ACI Committee report (ACI 548.3 R-03). 5. Strengthening of distressed RC Columns using indigenously available nonmetallic composite fiber wrapping system. 6. Applying protective coating on surface of RC Columns to protect from the further corrosion to reinforcing bars.

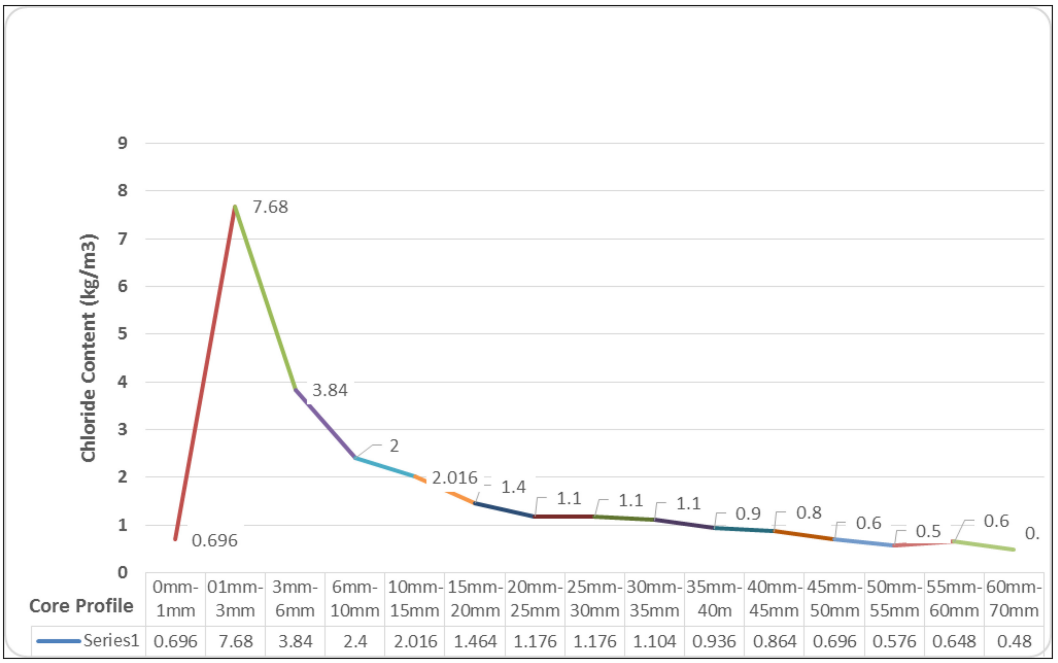

Figure 8. Test results of chloride content of RC Column located in power house near sea shore obtained after profiling.

8 CONCLUSIONS

- Environmental influence into cover concrete exposed to rain & other seasonal influence of environment for 37 years caused by carbonation, has led to the deterioration of concrete in the service building.
- Chloride diffusion has led to the chances of corrosion of reinforcing bars of RC Columns of STG. The chloride has entered from outside sea water leaking from pipes.
- Keeping in view the excessive distress of cover concrete caused by carbonation in the 37 year old service building and chloride penetration in the 15 year old RC columns of the STG in the power house, suitable remedial and strengthening measures to arrest the corrosion are suggested.

ACKNOWLEDGEMENT

This paper pertains to R&D work carried out by the Construction, Development and Research Centre at the National Council for Cement and Building Materials. The Authors acknowledge the contribution of the staff of the institute in carrying out the work. The paper is published with the permission of the Director General of the Council who is also the co-author of this paper.

REFERENCES

ACI 548.3 R-03. Polymer Modified Concrete

Agawa, Toyoaki Mit. 2015. Present and future perspective on maintenance and repair system for concrete structures, International Conference on the regeneration and conservation of concrete structures, Nagasaki, Japan, June 1–2, 2015.

Akira, Yoshikazu, Habuchi, Takashi, Sakai, Takahiro Sasaki, kenji and Kiyomiya, Samu. 2015. A study on Quantities and Durability of concrete for revetment in Gunkanjima Island after long term service, International Conference on the regeneration and conservation of concrete structures, Nagasaki, Japan, June 1–2, 2015.

ASTM C876: Standard Test Method for Half-Cell Potentials of Uncoated Reinforcing Steel in Concrete.

ASTM C1059: Standard Specification for Latex Agents for Bonding Fresh To Hardened Concrete

ASTM C 881: Standard Specification for Epoxy-Resin-Base Bonding Systems for Concrete.

Basheer, P.A.M., Chidiac, S.E., and Long, A.E. 1996. Predictive models for deterioration of concrete structures, Construction and Building materials, Vol. 10, No. 1, 1996.

Bickley,John, Hooton, R.D. and Hover, K.C. 2010 Issues related to performance based specifications for concrete, Chapter 12, Concrete Durability

Bintirafdinal, Rahmita Sari, Hamada, Hindenaori,Sagawa, Yasutaka,Yamamoto, Daisuke, Sumargo. 2015. Deterioration evaluation and life-extension strategy of 77 year old concrete structure exposed to Indonesian marine Environment, International Conference on the regeneration and conservation of concrete structures, Nagasaki, Japan, June 1-2, 2015.

Broomfield, John. 2010. Repair methods, Chapter 11, Concrete Durability.

Gjorv, Odd E. 2010. Advances in durability design and performance based specifications, Chapter 13, Concrete Durability

Gratten-Bellew, P.E. 1996. Microstructure investigation of deteriorated Portland Cement Concretes, Construction and Building materials, Vol. 10, No. 1, 1996.

Hover, Kenneth C. 1996. Special problems in evaluating the safety of concrete bridges and concrete bridge components, Construction and Building materials, Vol. 10, No. 1, 1996.

IS: 13311 – 1992 (Part II): Non Destructive Testing of Concrete – Methods of Test, Part – II Rebound Hammer

IS: 13311 – 1992 (Part I): Non Destructive Testing of Concrete – Methods of Test, Part – I Ultrasonic Pulse Velocity

IS: 516-1959: Methods of tests for strength of concrete

IS: 456 – 2000: Indian Standard for Plain and Reinforced Concrete – Code of Practice

ISO: 16204: 2012: Durability – Service life design of concrete structures.

Liao, Haixue. 2015. Corrosion control of reinforced concrete in corrosive environment, International Conference on the regeneration and conservation of concrete structures, Nagasaki, Japan, June 1–2, 2015.

Mihashi, Hirozo. 2015. JCI Guidelines for assessment of Existing concrete structures 2014, International Conference on the regeneration and conservation of concrete structures, Nagasaki, Japan, June 1–2, 2015.

Mihashi, H., Establishment of JCI Special Technical Committee on the Great East Japan Earthquake Disaster and its Activity Plan.

Nishimura, Kazuaki, kato, Yoshitaka and Mita, Katsuya. 2015. Influence of construction work condition on the relationship between concrete carbonation rate and the air permeability of surface concrete, International Conference on the regeneration and conservation of concrete structures, Nagasaki, Japan, June 1-2, 2015.

Sharma, Satish, Arora, V.V., and N.S., Adarsh Kumar. 2014. Non destructive evaluation and repair and strengthening of corrosion distressed RC structure – a case study, ICDC, Dec 2014, New Delhi, India.

Sharma, Satish and Arora, V.V. 2015. Distress Assessment, Repair and Strengthening of RC members of Turbo Generator Foundation of Anpara Thermal Power Station at Uttar Pradesh (India), International Conference on the regeneration and conservation of concrete structures, Nagasaki, Japan, June 1–2, 2015.

Tanaka, Ryoichi, Naitou, Hideharu, Sano, Kiyofumi, Harada, Tetsuo and Kiyomiya, Osamu. 2015. Soundness of Histrical Concrete revetment Gunkanjima Island in Japan, International Conference on the regeneration and conservation of concrete structures, Nagasaki, Japan, June 1–2, 2015.

Tay, D.C.K. and Tam, C.T. 1996. In situ investigation of the strength of deteriorated concrete, Construction and Building materials, Vol. 10, No. 1, 1996.

Torrent, Roberto, and Kei-Ichi. 2015. Site testing of Air Permeability as indicator for Carbonation rate in old structures, International Conference on the regeneration and conservation of concrete structures, Nagasaki, Japan, June 1–2, 2015.



Taylor & Francis
Taylor & Francis Group
http://taylorandfrancis.com

Concrete Solutions – Grantham et al. (Eds.)
© 2016 Taylor & Francis Group, London, ISBN 978-1-138-03008-4

Design of repair works in underground structures located in fine-grained soil

A. Shilin
ZAO "Triada-Holding", Moscow, Russia

A. Schukina
National University of Science and Technology MISiS, Moscow, Russia
ZAO "Triada-Holding", Moscow, Russia

ABSTRACT: A vast selection of products and techniques for repair of underground structures available nowadays make the issue of surrounding soil stabilization and consolidation more and more acute as structural stability and durability fully depend on their state.

Analysis of practical experience shows that to merely observe the existing norms and repair work regulations is not enough. It is essential to take hydrogeological factors into account which influence greatly the state of any underground structure; otherwise it will not be possible either to make a safe design or to perform a high-quality repair. Major problems are caused by fine-grained soils: they are easily subject to suffosion, and become unstable up to liquefaction when saturated with water.

To be able to study in detail soil behavior when injected with different materials, we carried out a comprehensive test program varying grain size and permeability of soil, both in the lab and on site.

Overall analysis of the test results allowed us to explore soil behavior mechanisms after consolidation with various injection materials.

1 INTRODUCTION

In modern construction practice, subterranean structures constitute a substantial part of both industrial facilities and civil buildings.

At the same time, extensive development of subsurface space results in a rapid growth of technically unique underground projects.

In other words, the construction industry is facing a lot of challenging engineering tasks, often involving high risks; thus, reliable design and planning become centerpieces of successful project solutions.

Underground structures of buildings operate under difficult hydro- and geological conditions, often surrounded by highly unstable soils and underground water. High water levels exert excessive pressure on structures which impairs their durability and operational safety. Besides, underground structural elements are subject to substantial static and dynamic loading.

A considerable number of repair and rehabilitation projects implemented by our company in the course of the last 5 years showed that selection of particular techniques and grouts is defined basically by component interaction within the "underground structure – surrounding soil" system, as well as various engineering, geological, technical and economic conditions, such as:

- aim of the job (e.g. protection, repair, rehabilitation, etc.);
- state of the structure as well as at the contact between the structure and the surrounding soil, soil parameters;
- site geology (to adjust working technique and sequence);
- general term of a project and working hours, if the job has to be done in facilities under operation;
- parametric requirements (both structure and soil);
- availability of grouts, tools and equipment, qualified personnel;
- cost of works and subsequent operation.

Quite often both protection and repair are required to provide reliable operation of structural parts of buildings located below ground. Integrated engineering solutions are used in many cases. Frequently injection works gain an advantage over other techniques (Karol 2003), as they allow to:

- modify surrounding soil parameters, i.e. increase their carrying capacity and impermeability (soil strengthening, sealing curtains, etc.)
- eliminate water leaks and suffosion.

Due to the fact that quite often underground structures to be repaired are located in loose fine-grained soils with variable water level, designers and contractors have to find novel solutions and techniques, which are not covered by the existing standards and regulations. Moreover, quite often they have to do it when a job has been already underway, and this definitely creates some difficulties, for example,

increases expenses and working period, causes new defects, etc.

Hence, efficient design and work planning become most essential; of course, it should be backed up by theoretical studies, normative documents, laboratory researches, which include among others:

- detailed in-situ inspection of structures /geological survey;
- experimenting with injection grouts in the lab and subsequent fine-tuning prior to trial application on site;
- outlining complete working procedure at the trial site;
- trial site application;
- adjusting grout composition and injection technique with regard to the test application results.

Only when this stage is finalized, can we start with design engineering. This approach is very important for projects, the operation of which cannot be stopped or interrupted, such as metro lines.

2 LABORATORY TESTING MODEL SET FOR EXPERIMENTAL STUDIES

2.1 *Description of laboratory test model set*

To be able to study the injection process of different grouts in fine-grained sands, a testing model set was developed (Fig.1), based on the requirements of EN 1504-5:2013 and the respective draft standard of the CIS standards system. The testing model set is an adequate physical model that can be used for reconstructing physical and mechanical properties of soil, including grain size distribution, porosity, density, moisture content, coefficient of filtration.

Its working principle is based on similarity of hydrodynamic laws of fluid motion and incorporates also practical know-how of injection works.

The testing model set was manufactured with regard of:

- geometrical model-prototype relationship which was set randomly (theory of stationary physical fields similarity implies that similar physical processes can take place only in geometrically similar systems) (Nasonov 1978);
- observance of similarity criteria equality; for this purpose, sands with typical grain size distribution as well as common injection grouts were chosen to be used in our testing model set.

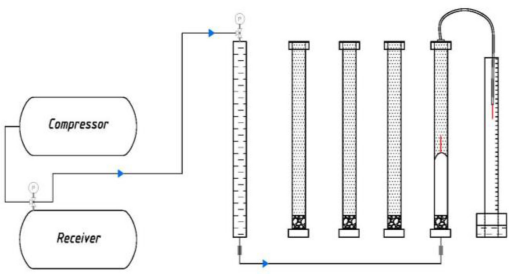

Figure 1. Layout of the laboratory test model set.

Our model allowed to "play" with soil and injection grout properties, parameters of injections. While testing in the lab, similarity criteria were fully observed, thus reconstructing geometry and nature of injection process.

The set consisted of a pump with a receiver and a pressure gage, a tube for an injection grout and water, and plexiglass tubes (500 mm high; ø 400 mm) filled with samples of soil to be tested compacted to a required degree.

To facilitate visual checking, there were scale marks on a transparent tube wall: they were used to monitor and record injection grout spread.

Injections were performed by an excessive pressure produced by a compressor as well as the head of the injected grout. Pressure was checked with the help of the pressure gage.

As we were interested primarily in injecting into water-saturated compacted fine-grained soils to impregnate them to the depth up to 20 m, our trial injections were carried out with the pressure of up to 0.5 MPa.

2.2 *Injection grouts*

Three injection grouts were selected for trial application: polyurethane-based (grout I), gelacryl-based (grout II), micro-fine cement-based (grout III).

The aim of the job was to evaluate penetrability of grouts with different bases and composition into soils with different grain size distribution.

The basic parameters of the injection grouts are given in Tables 1–3.

2.3 *Soils at test application*

For test application we investigated water-saturated fine-grained sands compacted to various degrees. Natural grain size distribution of the sands was quite uniform, that's why we had to prepare samples combining different sand types with more diverse grain sizes, to be able to model different site conditions.

It should be noted that selection of the respective grouts was one of the major issues of injection process modeling. A wide range of physical and mechanical

Table 1. Basic parameters of grout I.

Parameter	Value
Viscosity at 25°C	25–35 MPa · s
Density	1120 kg/m^3
Density when cured	
Compression strength	11,6 MPa
Gel time	≈15 min.

Table 2. Basic parameters of grout II.

Parameter	Value
Component I	
Viscosity at 25°C	15–20 MPa · s
Density	1170 kg/m^3
Content of solids	≈45%
Catalyst	
Content	≈85%
Initiator	
Density	≈1,9 kg/dm^3
Elongation at break	300%
Gel time	≈15 min.

Table 3. Basic parameters of grout III.

Parameter	Value
Density	≈2900 kg/dm^3
d_{95}	≈23.4 μm
d_{95}	≈13.8 μm
Specific surface area (Blaine test)	≈9000 cm^2/Ω
Compression test	≈11 MPa

properties of fine-grained sands could hardly be reconstructed if only one type of raw material was taken. It was explained by quite a big spread of parametric values which in its turn happened due to their natural inhomogeneity as well as measurement inaccuracy.

Generally, similarity of the following parameters should be observed when modeling: grain size distribution, moisture content, density, coefficient of filtration.

The process of production of injection grouts also affected reliability and representativeness of test results.

Fine- and medium-size water-saturated sands were to be strengthened. Content of dust-like and clay particles was from several fractions of percent up to 20%.

Grain size distribution of sands is shown in Figures 2–3.

A special mode of compaction was developed to provide similar (in terms of density and physical/technical parameters) sand samples.

When samples were ready, an injection grout was mixed and its parameters were measured.

Then the grout was injected under the set pressure. In the course of injection the following parameters were monitored: injection pressure, grout consumption, penetration time.

2.4 *Preparation and testing*

Prior to testing, a sand sample was put into the tube and compacted to the required degree (structural density was modeled up to the depth of 20 m).

After injection, several samples were stored for a set period of time (for 1, 3, 7, 28 days) under

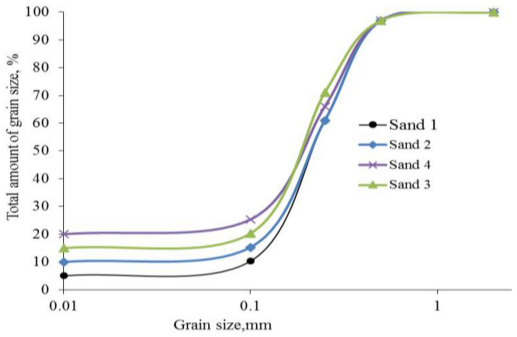

Figure 2. Grain size distribution of fine sands.

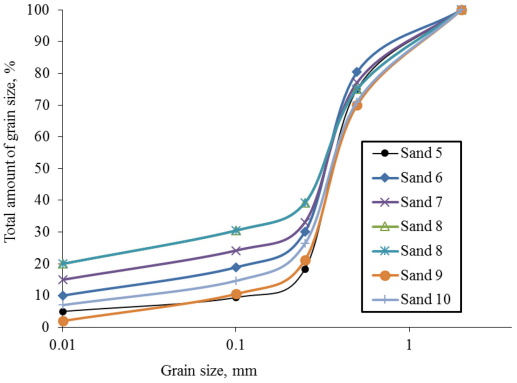

Figure 3. Grain size distribution of medium-size sands.

conditions (soil temperature/moisture content) close to those which were expected on site.

Then, in accordance with the existing standards, cylinder samples of injected soil were taken and tested to determine its compression strength, density, water permeability, etc.

The results obtained with the help of the testing set were used for design analysis of the area to be injected, grout consumption, injection pressure, grout extent radius.

2.5 *Test results*

Our tests showed that for all sand samples prepared by mixing different sand types, injection grout penetrability went down as the content of dust-like and clay particles was increased.

The relationship between the injection pressure and percentage of dust-like and clay particles was nonlinear.

If the grout was injected at 30 kPa into fine- and medium-size sands with a 5% content of dust-like and clay particles, the grout extent radius was much less when compared to a similar sand mix with only 1% of dust-like and clay particles. Further increase of injection pressure up to 50 kPa stopped grout extent abruptly.

Increase of dust-like and clay particles from 5 to 10% demanded increase of injection pressure, which in its turn terminated grout extent.

When the content of dust-like and clay particles was 15% and more, grout penetrated for 1/10 of the injection pipe length (appr. 5 cm).

This effect could be explained by a new mechanism of grout extent termination which differed from the known earlier rheological blockade and filtration (Axelsson & Gustafson, 2007). It was named "suction effect": dust-like and clay particles blocked transfer of water squeezed from soil pores by the pressure of the injection grout, thus terminating grout extent.

We tried to "by-pass" the suction effect in the following way: we changed the conditions of grout penetration changing injection pressure and/or chemical properties of the grout.

It should be noted though that if the content of dust-like and clay particles was as much as 15–20%, neither of the aforementioned tricks worked.

Thus we came to the conclusion that in fine and medium-size sand with the content of dust-like and clay particles of 15–20%, injections could not be performed.

Of course in real site conditions, the presence of fine soil particles is inevitable, so in each particular case a detailed lab and site testing shall be accomplished prior to the start of a full-scale injection work.

3 IN–SITU TESTS

For further research and testing of the injection process into fine-grained sands, we developed and manufactured a large-scale physical model set providing the required criteria similarity.

The test set included a cast in-situ reinforced concrete pit sized 4×15 m in plane and 5 m high. The pit was filled by sands to be tested, each layer being compacted to their natural density value.

After the filling-in was finished, several sleeve pipes (tubes a manchette) were installed to the full depth of the pit to perform injections.

Relationships obtained at the small-scale test set were used – with regard to the similarity factor – to set basic injection parameters, which were re-calculated respectively based on the actual size of the large-scale test set.

During the whole working cycle, injection pressure, grout consumption and injection time up to the grout run-out were monitored continuously.

Grout extent within the soil was checked by ultrasonic probing between injection holes.

On the 7th day after the injection, the pit was excavated, samples were taken and the results were recorded.

At the large-scale test set we tested low-viscous grouts I and II. Due to the abrupt increase of injection pressure the suction effect could be observed there. Figures 4-5 shows the sand soil injected by grout I and II, respectively.



Figure 4. Soil after injection of grout I, II.

4 CONCLUSIONS

- An experimental system to study injections of grouts with different composition into fine-grained soils was developed, manufactured, and tested. It can be used for design and planning both by new construction and also for repair and rehabilitation works as it provides similarity of all physical and mechanical parameters and processes.
- The data obtained was processed and analyzed in accordance with the aim of the research. Comparison of the results obtained at the small-scale (lab) and large-scale (pit) test sets allowed the formulation of basic mechanisms of the process as well as relationships between different variables that could be compared as non-dimensional values.
- The test series allowed the discovery of a new mechanism of grout extent determination in water-saturated fine-grained soils, a so-called "suction effect"; it shall be accounted for while performing injections in such type of soils.
- It was established that due to the suction effect, injections were impossible in fine- and medium-size sands if they contained 20% of dust-like and clay particles. The situation could be improved by changing grout penetration conditions as well as chemical properties of grouts.

REFERENCES

Axelsson M. & Gustafson G. 2007. Grouting with high water/solid-ratios – literature and laboratory study. *Report No. 2007:5.* Department of Civil and Environmental Engineering, Division of GeoEngineering, Chalmers University of Technology: Göteborg

Karol, R. 2003. *Chemical Grouting and Soil Stabilization: Third Edition, Revised and Expanded.* Basel: Marcel Dekker, Inc.

Nasonov, *Process modelling in rock*. 1978.
Moscow, Nedra (in Russian)

Nasonov, I.D., Shilin A.A. & Schukina A.B. 2014. Studying injections into loose soil in underground construction. *Transport Construction* (12): 20–23 (in Russian)

Concrete Solutions – Grantham et al. (Eds.)
© 2016 Taylor & Francis Group, London, ISBN 978-1-138-03008-4

Various stages of protection of concrete roads

S.N. Tolmachov, O.A. Belichenko & H.V. Brazhnyk
Kharkov National Automobile and Highway University, Kharkov, Ukraine

ABSTRACT: Concrete roads have to work under difficult conditions. They are exposed to temperature, humidity, and mechanical stress. In these circumstances, the concrete durability may be reduced. There are two ways to increase the resistance of concrete under the action of aggressive factors. The first concrete protection is carried out at the stage of selection of materials. In this case, you can protect the concrete, if you use high-quality aggregates. In addition, an important role is played by the use of modern chemical and mineral additives. After the choice of materials, the selection of concrete in order to achieve maximum density is also important. If all of these requirements have been met, the road concrete is protected.

The second stage of protection is applied when the concrete exploit. It is used when the surface of the concrete has begun to deteriorate. The concrete surface can be impregnated with a special compound. This protection is also used when you want to increase the service life of the road concrete.

1 INTRODUCTION

Concrete roads have to work under difficult conditions. They are: temperature, humidity and mechanical stresses. Under these conditions the concrete durability may be reduced.

The concrete durability depends on internal and external factors. Internal factors are a cement and fillers for concrete. The higher their quality, the higher the concrete durability is. The external factors include the conditions of hardening and maintenance of the concrete. The proper choice of fillers can provide the required durability of the road concrete. The most important index of concrete durability is concrete freeze-thaw resistance, particularly under the simultaneous influence of temperature and salt solutions.

I.M. Grushko considered that the main cause of concrete destruction because of simultaneous influence of freezing and salt solutions is a crystallization of ice and salt hydrates at a depth of 10...12 mm from the concrete surface (Gruschko & Kireeva, 1978). This often happens in the case of removing the ice from the surface of concrete pavement with chemical agents. In one case, the destruction appears as a separation of a thin film solution. In another case, the surface layer of concrete is removed together with a pieces of a large sized filler. Solutions of chlorides, nitrates, ammonia, alcohols and other solutions destroy concrete the most severely.

Among the causes of freeze-thaw and salt concrete destruction, Powers allocates the following (Powers, 1966):

1. The hydraulic pressure that occurs in the voids and capillaries of concrete under the influence of freezing water.
2. The pressure from ice crystallization in the voids of concrete.

Osmotic pressure (Vlasov, 1963) and the pressure of salt crystallization in the voids of concrete (Tolmachov, 2010) are also active in addition to the two factors mentioned.

Increasing freeze-thaw and salt resistance of concrete can be achieved by improving the density of the cement paste. In addition, it is possible to introduce into the concrete air-entraining additives. These additives will help to increase the air content in the concrete mix from 1...2 to 4...6%. Such air bubbles increase the plasticity of the concrete mix and improve freeze-thaw resistance and salt resistance of concrete, but the concrete strength will be reduced. Therefore, it is necessary to use other ways to increase the density and impermeability of concrete.

For increasing the resistance of concrete under the influence of aggressive factors two methods of protection are used. Primary protection of concrete is fulfilled at the stage of concrete mix design and concrete production. The principles of primary protection are known as following ones:

1. Using high quality fillers (silica sand, gravel).
2. A correct choice of cement (CEM I 42,5N).
3. An application of modern chemical and mineral additives.
4. To observe technologies of concrete production, transportation, compaction, sealing and curing.

Table 1. Particle-size distribution of silica sand.

	Sieve mesh, mm						
	2.5	1.25	0.63	0.315	0.16	0.071	<0.071
Silica sand 1		0.4	4.1	37.8	49.5	7.6	0.6
Silica sand 2	7.7	10.7	23.7	36.5	15.2	3.5	27

Table 2. Particle-size distribution of screenings.

	Sieve mesh, mm							
	5	2.5	1.25	0.63	0.315	0.16	0.071	<0.071
Screenings	12.0	20.7	9.9	16.7	14.3	8.5	5.9	3.0

Secondary protection of road concrete is used at the stage of its exploitation. It is used when the concrete surface has begun to deteriorate and, for protection, the concrete surface is impregnated with a special compound. This protection is also used when it is necessary to increase the service life of the road concrete.

When choosing a primary or secondary concrete protection it is necessary to state the value of the work from the economic side. If durability can be achieved using only primary protection, secondary protection is meaningless.

Therefore, the aim of this work is to determine the need for using different methods for concrete protection.

2 MATERIALS AND METHODS FOR EXPERIMENTS

Cement, silica sand (tab. 1), screenings (tab. 2) and gravel fractions 5–10 mm and 10–20 mm were used in experiments.

For this research, cement CEM I 42,5N was used. The beginning of cement setting – 1 h 45 min, the end of cement setting – 4 h 30 min, cement brand – M 500 (compression strength after 28 days was 50 MPa).

Gravel fractions 5–10 mm and 10–20 mm were used.

The FM21 superplasticizer (BASF firm, Germany) and the air-entraining additive LP 71 of the same firm were used for this research.

FM21 is a sulfonated melamine derivative. It is produced as a dark brown liquid with a density of 1140 ± 30 kg/m^3. The recommended amount is 0.1–2.3% of cement weight.

For secondary concrete protection protective waterproofing and sealing additives (impregnating liquids) Silol and CONWISOL S-60 (tab. 3) were used.

Silol additive is a liquid solution of siloxanes in organic solvent. After coating the concrete surface the solution penetrates into the voids and creates a siloxane film. The film prevents water and gas penetration into the concrete and reinforces it.

Table 3. Properties of impregnating additives.

No	Additives	Density, kg/m^3 ±20	Consumption, kg/m^2
1	CONWISOL S-60	790	0.20–0.80
2	Silol	960	0.20–0.30

Table 4. Concrete mix.

	kg/m^3	
Components of concrete	C1	C2
Cement	380	380
Silica sand	560	560
Gravel 5–10 mm	536	536
Gravel 10–20 mm	804	804
Superplasticizer FM21	2.66	2.66
Air-entraining additive LP 71	–	0.38
Water, kg/m^3	166.6	166.6

CONWISOL S-60 additive is a transparent hydrophobic solution based on polimetilgidrogensilana. Due to the low molecular weight, the solution penetrates easily into the concrete. CONWISOL S-60 reacts with the cement forming a silicone polymer.

The concrete mix is given in Table 4.

Studies of concrete freeze-thaw resistance were carried out on samples with the dimensions $70 \times 70 \times 70$ mm and pre-saturated with a 5% solution of NaCl. Thereafter the samples were frozen and kept at -18°C for 1.5 hours. Then the samples were thawed in 5% NaCl solution at a temperature of $+18$°C for 1.5 hours. This was one cycle of the thawing and freezing test. Prior to testing and after 100, 200, 300 and 400

Table 5. Influence of curing conditions on the mortar porosity.

Curing conditions	Total porosity,%	Capillary voids quantity, %			
		Less than 510^{-9} m	$5{\cdot}10^{-9}$ to 10^{-7} m	10^{-7} to 10^{-6} m	More than 10^{6} m
In air	17.4	15.0	20.6	25.7	38.7
In water	16.6	17.8	40.2	30.5	11.5

Table 6. Properties of concrete B 40 compacted with vibrating.

Additive for impregnation/ Number of concrete	Density, kg/m^3		Water uptake, W, %		Compression strength, R, MPa	
	C1	C2	C1	C2	C1	C2
Without impregnation			2.34	2.7		
CONWISOL S-60	2453	2405	1.12	1.5	52.6	47.4
Silol			1.07	1.6		

cycles of thawing and freezing test, the compressive strength of the concrete samples was determined. The ratio of compressive strength after a specified number of cycles to compressive strength before testing is a coefficient of freeze-thaw resistance. It should not be less than 0.95.

3 EXPERIMENTAL STUDIES

It is known that the structure of concrete depends on the conditions of curing. If the concrete or mortar hardens in water, they absorb moisture. In this case, they will form the microvoids and microcapillaries. Such voids are uniformly distributed in the concrete volume. Under these conditions of curing, the capillary porosity of concrete decreases (tab. 5).

According to Usherov-Marshak et al (2002) (tab. 5) in mortar that hardens in water, a number of capillary voids with radius larger than 1 micron (10^{-6} m) is 3.4 times less than in mortar that hardens in air. It is known that voids with radius greater than 1 micron reduce freeze-thaw resistance of concrete and mortars. The number of microcapillaries in solutions that harden in water (with radius less than 10^{-7} m) decreases by a factor of two.

Research conducted at the University of Construction and Architecture and Automobile and Highway University from Kharkiv, have shown that the radii of the voids in the cement paste, hardening in different conditions can be very different. With the help of thermoporometry it has been found that in cement paste hardening in water, the average void radii decrease by 7 times, compared with cement paste hardening in air. Average radii of voids in the cement paste which have been hardened in air and impregnated with compositions such as CONWISOL S-60 or Silol type decrease by 3.5 times. The hardening temperature of all samples was +30°C.

It is known that when reducing the average radii of voids, the basic properties of concrete increase. To confirm this, we have carried out research on strength, permeability to water and freeze-thaw-resistance of concrete. Two groups of samples were made: control ones without protection additives and samples with the surface covered with the protective solution additives. All concrete samples were preincubated for 12 hours in the chamber for heat and humidity treatment at the temperature of +80°C. After that, the dry surface of the samples was treated by spraying protective compounds CONWISOL S-60 and Silol. The properties of concrete were measured after 28 days.

Studies of concrete properties (tab. 6) showed that the density and strength of concrete composition C2 were smaller than those of composition C1. Water uptake was respectively greater. It can be explained with an increased content of air entrainment in composition C2. The water uptake of concrete samples which had been processed with impregnating additives was 2 times lower. Such a significant reduction of water uptake confirms the protective capacity of impregnating additives. At the same time, the strength of concrete with and without protective additives was identical.

Further studies were focused on the influence of impregnating additives on the main indicator of durability – the freeze-thaw resistance (tab. 7). Analysis of the table shows that the freeze-thaw resistance of concrete composition C1, which contains superplasticizer, corresponded to the mark F 200. The C2 composition, which contained an air-entraining agent and superplasticizer had a higher mark of freeze-thaw resistance – F 300. The coefficient of freeze-thaw resistance of all concrete compositions studied continuously decreased after 100 test cycles. This indicates a constant decrease of freeze-thaw resistance of concrete and means that the ability of concrete to resist freeze-thaw cycles with the number of test cycles was steadily falling. The coefficient of freeze-thaw resistance of concrete samples which had been impregnated with protective additives

Table 7. Freeze-thaw resistance of concrete B 40 compacted with vibrating.

	Coefficient of freeze-thaw resistance after a number of cycles							
	100		200		300		400	
Additive for impregnation	C1	C2	C1	C2	C1	C2	C1	C2
Without impregnation	1.01	1.06	0.95	1.00	0.91	0.95		0.82
CONWISOL S-60	1.01	1.02	0.99	1.01	0.96	1.0	0.85	0.95
Silol	1.03	1.02	0.99	1.03	0.95	0.99	0.88	0.96



Figure 1. The sample after 300 test cycles.



Figure 2. The sample after 400 test cycles.

varied slightly during 300 test cycles. The coefficient of freeze-thaw resistance of concrete with or without an air entraining admixture was the same. But after 300 cycles of the test, destruction of the protective surface layer of concrete had taken place. This leads to the penetration of corrosive fluids into the concrete and facilitates its further frosty-salt destruction, as shown in Figs. 1, 2.

Before 300 cycles the sample surface remained unchanged (Fig. 1). Loosening and partial destruction of the upper layer of the sample (Fig. 2) had taken place after 300 cycles. Studies have shown that weight loss of samples as a result of the destruction amounted to 1.5...2.1%. With such destruction, the protective ability of impregnating additives disappears and concrete cannot resist the effects of freezing and thawing. Therefore, the 400 test cycle shows a strong decline of the freeze-thaw resistance coefficient. But the mark of freeze-thaw resistance of concrete composition C2 was higher than concrete composition C1. This is explained with the presence of air-entraining agents in the composition.

Compaction of concrete products is produced not only with vibration, but also with pressing. In this case, the amount of water in the concrete is considerably smaller. This can reduce the strength of the concrete, but can increase its durability. The C1 concrete composition was used for our study.

Table 8. Properties of concrete B30 compacted with pressing.

Additive for impregnation	Water uptake, W, %	Compression strength, R, MPa
Without impregnation	2.95	41.3
CONWISOL S-60	0.87	42.4
Silol	0.91	40.8

In the case when the concrete is compacted with pressing, an air-entraining additive does not exhibit its properties, so it is not applicable. The density of concrete compacted with compression was 2380 kg/m^3. Properties of such concrete are shown in Table 8.

Water uptake in pressed concretes is greater than in concrete compacted with vibration by 26%. Therefore, application of impregnating additives leads to reducing water absorption by 3.2–3.4 times.

This is more than in concretes compacted with vibration. The strength of pressed concretes with and

Table 9. Freeze-thaw resistance concrete B30 compacted with pressing.

Additive for impregnation	Coefficient of freeze-thaw resistance after a number of cycles			
	100	200	300	400
Without impregnation	1.01	0.98	0.96	0.93
CONWISOL S-60	1.02	1.10	1.04	0.99
Silol	1.03	1.06	1.02	0.98

without impregnating additives was the same. The compressive strength of the pressed concretes was lower than those concretes compacted with vibration and the cement flow rate was the same.

Further studies of freeze-thaw resistance of concretes have shown that a slow decline of the freeze-thaw resistance coefficient has been observed in concrete without impregnating additives. But in this case the mark of freeze-thaw resistance increased almost to F 400. The coefficient of freeze-thaw resistance after 400 cycles of the test is insignificantly less compared with the limiting value of 0.95.

The use of impregnating compositions changes the nature of resistance to freezing and thawing of such concretes. It is rather like a wave – at the beginning (up to 200 cycles) an increase in the coefficient of freeze-thaw resistance occurs, and in the future- a smooth decrease.

The studies have shown that the application of primary and secondary concrete protection helps to ensure the necessary design marks of concrete considering strength and freeze-thaw resistance. For example, in the Ukraine conditions it is the F 200 mark. In the case of using a combination of protection methods, durability of concretes is increased substantially.

4 CONCLUSIONS

- It has been found that the introduction of air entraining additives as a method of concrete primary protection improves their freeze-thaw resistance, irrespective of the impregnating composition application.
- It has been shown that the use of impregnating additives as a method of secondary protection, does not alter concrete strength, but allows to reduce concrete water uptake and thereby to increase their freeze-thaw resistance.
- A correct selection of the composition as a primary method of concrete protection compacted with pressing provides high density and frost resistance without applying any impregnation.
- The use of impregnating materials for concretes which are compacted with pressing can significantly increase the frost resistance of road concretes comparing with concretes without impregnation.
- For necessity to provide a fixed value of concrete mark considering strength and freeze-thaw resistance, methods for primary protection are adequate – a correct composition selection and the provision of appropriate chemical additives.

REFERENCES

Gruschko I.M. & Kireeva E.B. 1978. The durability of concrete joint action with the environment and mechanical stress, *Auto. road and dor. bud. of. "Rep. mizhvid. scientific-technical. coll."* 23: 64–68.

Powers T.C. 1966. The mechanism of Frost Action in Concrete. *Cement, Lime, Grevel*: 5. 143–148, 181–185.

Tolmachov S.N. & Kondratjeva I.G. & MatyaschA.V. 2010. Investigation of the mechanism of destruction of frosty road concrete. *Concrete and reinforced concrete in Ukraine*: 2: 18–22.

Tudorie Gheorghe & Pasnicu Alexendru. Coroziunea si degradarea betonului din suprastructura podurilor de sosea in conditii de exploatereIO 1991. *Rev.transp.: Auto, drumuri, navig.* 3–4: 65–69.

Usherov-Marshak A. & Zlatkovsky O. & Sopov V. 2002. Calorimetric study of frost attack during cement hardening. *Journal of thermal analysis and calorimetry*: V. 68: 1: 223–230.

Vlasov O.E. 1963. Equilibrium of a multi-component and multi-phase capillary system. *The durability of fencing and building structures (the physical basis):* 6–11. Russcha: Moskow.



Taylor & Francis
Taylor & Francis Group
http://taylorandfrancis.com

Concrete Solutions – Grantham et al. (Eds.)
© 2016 Taylor & Francis Group, London, ISBN 978-1-138-03008-4

Analysis of the failure of a track slab concrete

Zhonglai Yi, Huajian Li, Hao Jin & Yongjiang Xie
China Academy of Railway Sciences, Beijing, China

ABSTRACT: A few pieces of track slab showed serious cracking failure after serving five years. The appearance was similar to the alkali aggregate reaction, with map cracking. In this paper, the cause of the failure of the track slab concrete was studied. Core samples were drilled from the cracked track slab. The residual expansion rates of the core samples were tested. X-Ray Diffraction, Scanning Electron Microscope, TG-DTA and Optical Microscope Analysis were used. The results show that some periclase minerals were mingled in the track slab concrete aggregate. Brucite was generated when the periclase absorbed water. The volume expansion leads to the cracking failure of the track slab concrete.

1 INTRODUCTION

Track slab is an important part of a ballastless track structure. Steel rails are fixed on the track slab through rail fasteners. The track slabs bear the train load and transfer the load form the rail and fasteners to the substructure. The track slabs are factory prefabricated from prestressed concrete.

A few pieces of track slab showed serious cracking failure after serving five years. After the field survey, the following characteristics of the track slab damage could be found: Firstly, the crack appearance was similar to the alkali aggregate reaction, with characteristic map cracking. Secondly, the surface concrete at the position of the crack failure had bulged. The cracks were typical of expansion cracking, as shown in Fig. 1. Thirdly, the failure had developed from the surface to the centre. The cracking failure were on the concrete slab surface when the damage first appeared. Lastly, at the center position of failure, some special yellow or white aggregate could be found, as shown in Fig. 2.



Figure 1. Map crack of the track slab.

In order to analyse the failure of the track slab concrete, some core samples were drilled from the track slab. The residual expansion rates of the core samples were tested. X-Ray Diffraction, Scanning Electron Microscope, TG-DTA and Optical Microscope Analysis were used.

2 EXPERIMENTAL

2.1 *Residual expansion rate test method*

Core samples with Ψ50 mm diameter drilled from the track slab were cut and measuring heads were installed. The prepared core samples were cured in 80°, 1 mol/L NaOH solution. The length of the core samples were tested at different ages to test the residual expansion rate.

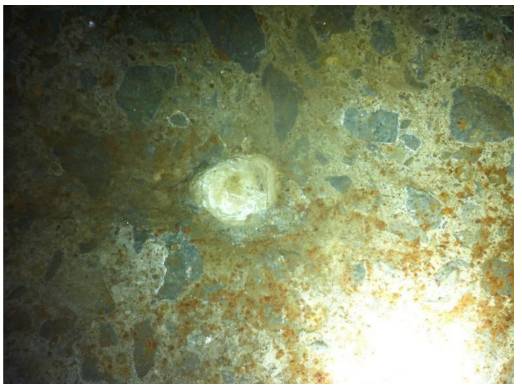

Figure 2. The special aggregate at the center position of failure.

2.2 *Petrographic analysis method*

The special aggregates chiselled from the failed concrete were made into petrographic thin slices. A polarizing microscope was used to analyse the petrographies of the special aggregate.

2.3 *Component analysis method*

Powder X-ray Diffraction (XRD) was used to analyse the component the aggregates. The XRD analysis was conducted on a Rigaku D/max 2550 spectrometer using Cu Kα radiation (40 kV, 200 mA) at a scanning rate of 8°/min from 5° to 80°.

2.4 *Thermal analysis method*

A thermal analyser with Thermogravimetry (TG) and Differential Scanning Calorimetry (DSC) system were used.

2.5 *Morphology analysis method*

A Scanning Electron Microscope (SEM) combined with energy dispersive spectrum analysis were used to observed the microstructure and element composition of the special aggregates.

3 RESULTS AND DISCUSSION

3.1 *Residual expansion rate*

Three core samples were tested for residual expansion rate. The test results are shown in Table 1. A dramatic results can be seen in Table 1. Two core samples were fractured just when cured in high temperature and high alkali environment for 3 days. The core sample's fracture status is shown in Fig. 3 and Fig. 4. From Fig. 3 and Fig. 4, it can be seen that there are some white or yellow aggregates at the failure positions. In Fig. 4, three radial cracks appeared around the white aggregate. Obviously, the white aggregate is the direct cause of the cracking of concrete. This phenomenon matched with the field track slab concrete damage situation. Some special yellow or white aggregates could be found at the center position of failure.

For the core sample without fracture, the residual expansion rates were significantly increased with the increase of curing age. The 35 day expansion rate reached 0.273%. These expansion rate values are higher than reported values of the relevant literature (Berra M, et al. 2005; Criaud A, et al. 1994).

3.2 *Petrographic analysis*

Petrographic images of two selected representative samples were observed by optical microscope. The analysis results are shown in table 2–table 3 and Fig. 5–Fig. 6.

From the petrographic analysis results, it can be seen that those special aggregates belong to the periclase. Mineral class. Part of the aggregates were hydrated and brucite had been generated.

Table 1. Residual expansion rate of core samples (%).

age	1-1	1-2	1-3
1d	0.185	0.011	0.116
3d	fracture	0.015	fracture
5d		0.022	
7d		0.022	
10d		0.044	
14d		0.065	
22d		0.131	
28d		0.207	
35d		0.273	



Figure 3. Core samples fracture status (1-1#).



Figure 4. Core samples fracture status (1-3#).

3.3 *Component analysis*

Powder X-ray Diffraction (XRD) were used to analysis the component the special aggregates chiselled form the failure concrete. The test results are shown in Fig. 7.

It can be seen that the main components of all the special aggregates are periclase (MgO style) and brucite ($Mg(OH)_2$). The diffraction peaks of periclase are higher, showing that the periclase content was higher. For different samples, the diffraction peak intensity of brucite is different. The brucite diffraction peaks intensity of 4#, 5# samples are relatively high,

Table 2. Petrographic analysis results of special aggregates (1#).

Rock name	Serpentinized periclase	
Structure type	residual replacement and pseudomorphic replacement structure	
mineral constituent	content	mineral composition and characteristic
periclase	25%	similar equiaxial granular, particle size of +/−0.1 mm, colorless ~ pale yellowish green. Most periclase showed serpentinization or brucitization. It only has the crystal form illusion of periclase.
serpentine	70%	Colorless, blade shape – a product of periclase alteration, belong to layered silicate minerals.
brucite	5%	Fawn, scaly, diameter of 0.01 mm, periclase alteration products.

Table 3. Petrographic analysis results of special aggregates (2#).

Rock name	periclase	
Structure type	granoblastic texture	
mineral constituent	content	mineral composition and characteristics
periclase	91%	Yellow-green, similar equiaxial granular, diameter 0.1 mm±, orthometric protuberant, complete extinction in orthogonal mirror, there was a slight serpentinization.
serpentine	7%	Colorless, blade shape., distribution in some periclase edge, is periclase alteration minerals
magnetite	2%	xenomorphic granular, particle size of 0.02 mm, black non-transparent

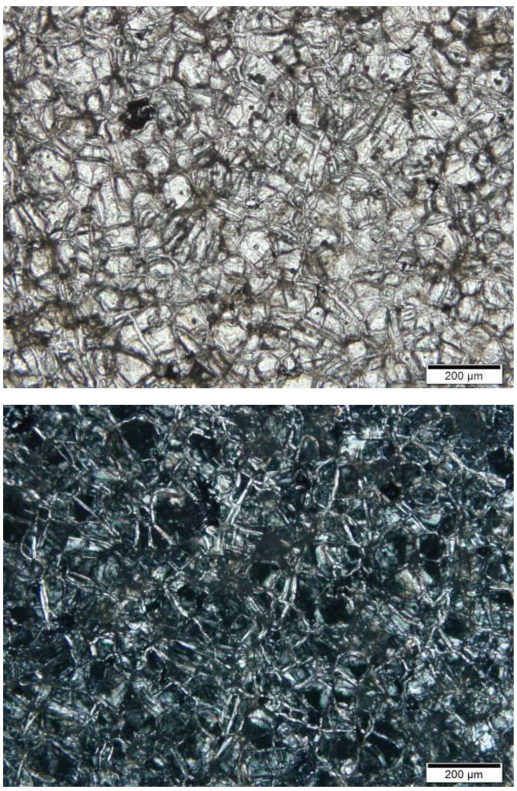

Figure 5. Optical microscope analysis of special aggregate (1#).

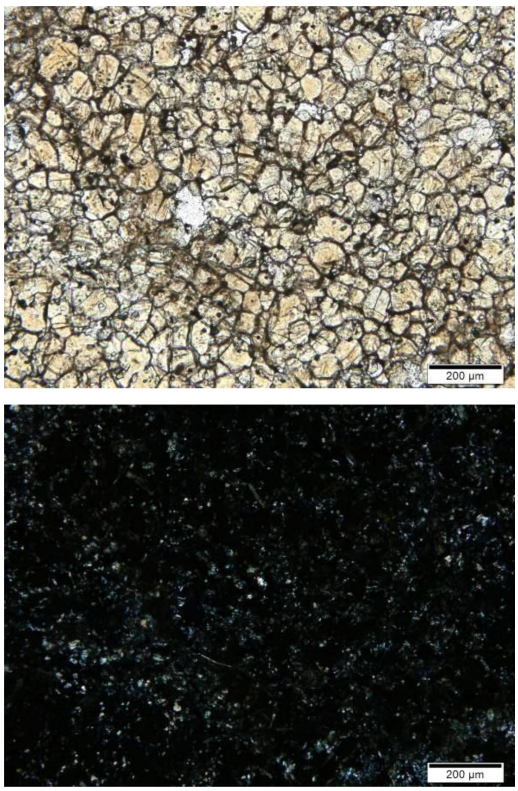

Figure 6. Optical microscope analysis of special aggregate (2#).

showing that the brucite content of 4#, 5# samples was relatively high. The brucite diffraction peaks intensity of 1#, 6# samples are relatively low, showing that the brucite content of 1#, 6# samples was relatively low.

XRD analysis shows that the special aggregates were periclase. Most of the periclase aggregates were partial hydrated to brucite with different degrees.

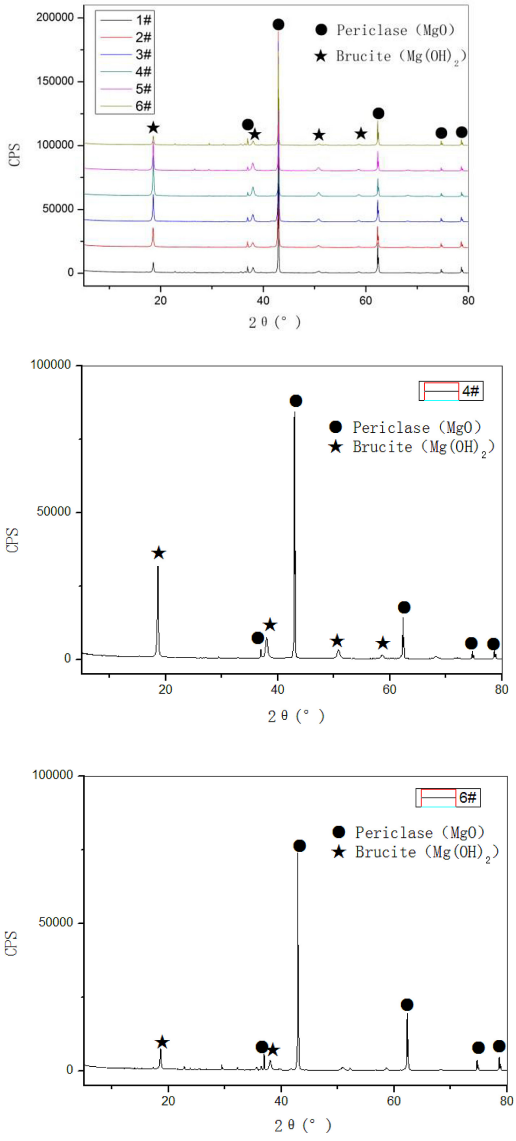

Figure 7. XRD analysis of special aggregates.

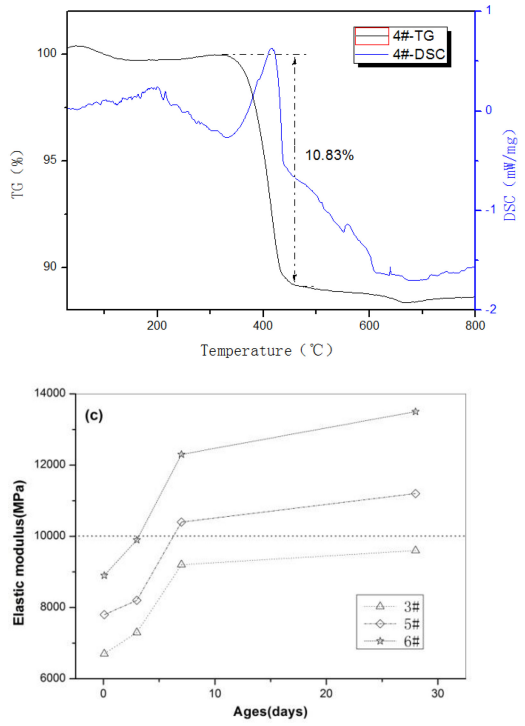

Figure 8. TG-DSC analysis results of special aggregates.

3.4 *Thermal analysis*

For the special aggregate, thermal analysis (TG-DSC) was done at the same time. Combined with XRD analysis, the composition of the special aggregate can be confirmed. Typical TG-DSC curves are shown in Fig. 8.

From Fig. 8, it can be seen that 4# and 6# samples have an endothermic peak at about 400°C. This endothermic peak is the decomposition reaction of brucite around 400°C. At the same time, there is an obvious weight loss on the thermogravimetric curve. The weight loss of 4# sample is 10.83%, and the weight loss of the 6# sample is only 3.46%. Combined with XRD analysis, this is due to the different hydation degree of periclase of the 4# and 6#samples. The brucite content of the samples were different.

From TG-DSC thermal analysis, it can be confirmed that the special aggregate had different contents of brucite.

3.5 *Morphology analysis*

Scanning Electron Microscopy (SEM) combined with energy dispersive spectrum analysis were used to observe the microstructure of special aggregate and element composition. Spectrum analysis results are shown in Fig. 9. SEM morphology analysis results are shown in Fig. 10.

Fig. 9 shows that the special aggregate was composed of rounded particles. The energy spectrum analysis shows that the main composition elements of the special aggregate were Mg and O. This is consistent with the XRD analysis results. It is reconfirmed that the special aggregate composition was periclase.

For Fig. 10, at low magnification, it can be seen clearly that this kind of special aggregate was composed of rounded shape or circular particles which is the characteristic morphology of periclase. The particle size was about 20–40 microns. Many microcrystalline flakes can be seen at high magnification. The flake forming microcrystalline material can even be seen in some places (Fig. 8(g)). The microcrystalline flake structure is the typical morphology of brucite.

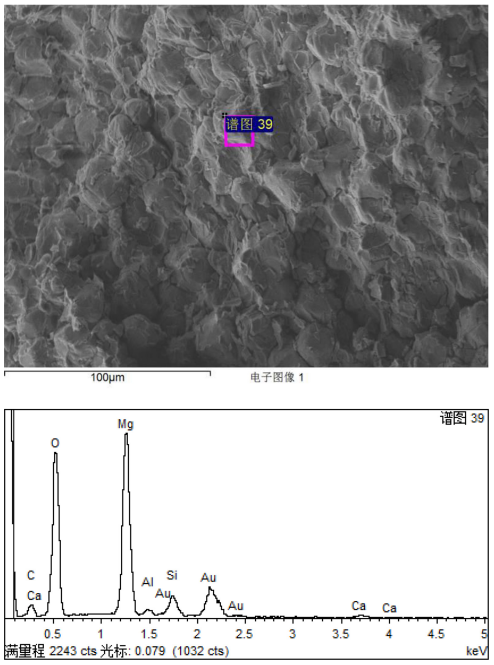

Figure 9. Energy spectrum analysis of special aggregates.

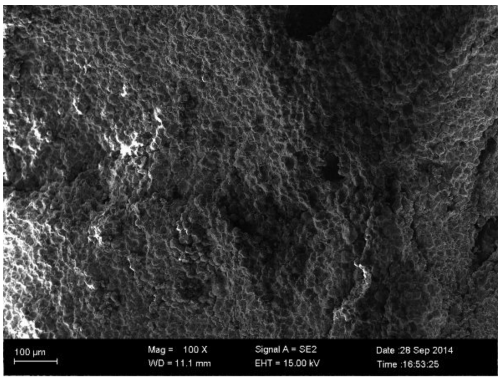

(a) ×100

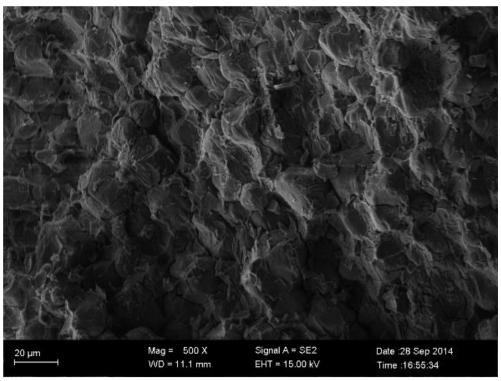

(b) ×500

Figure 10. SEM analysis of special aggregates.

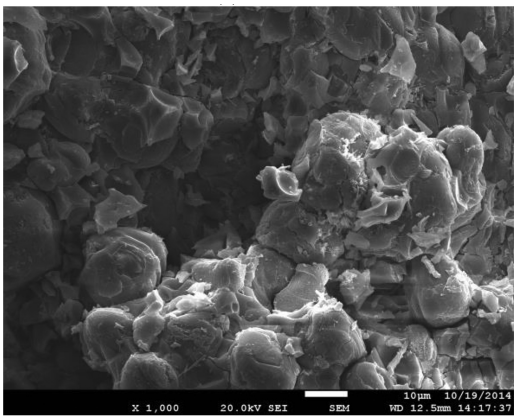

(c) ×1000

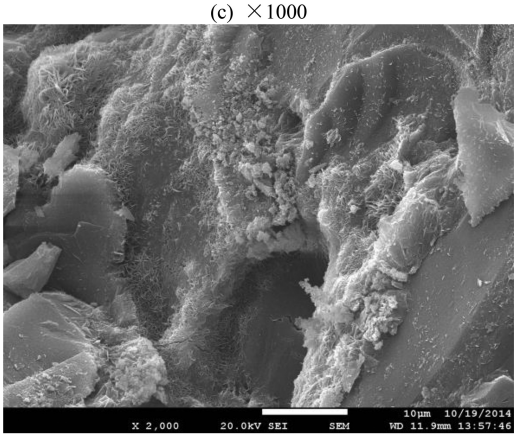

(d) ×2000

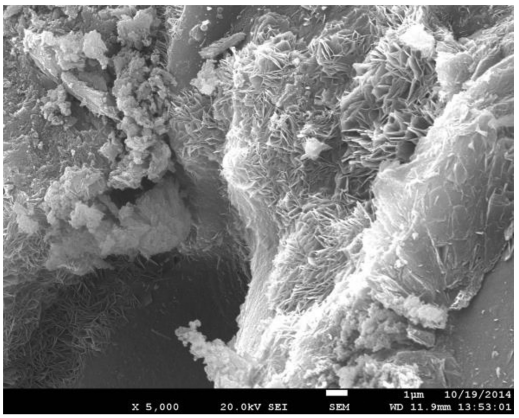

(e) ×5000

Figure 10. Continued.

3.6 *Failure mechanism analysis*

From the above analysis, it can be seen that the special aggregate was periclase. Part of the aggregate was hydrated to brucite. The hydration reaction equation of periclase is shown as following.

$$MgO+H_2O=Mg(OH)_2 \quad (1)$$

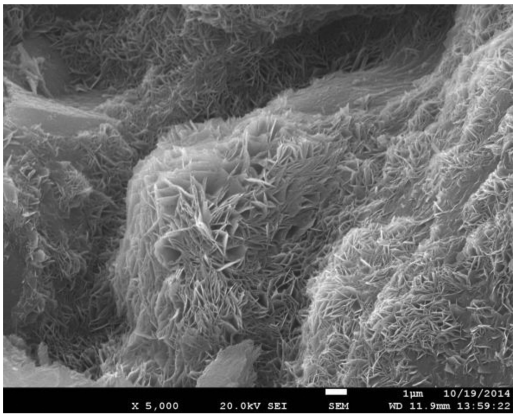

(f) ×5000

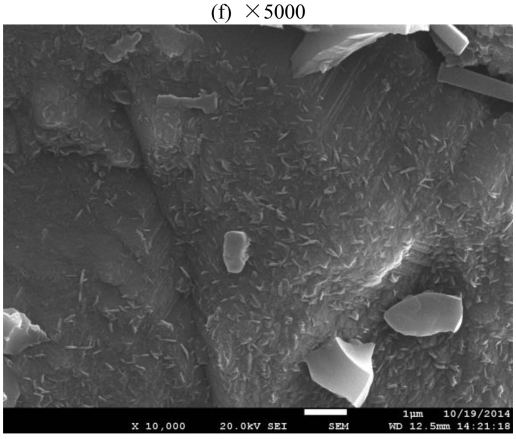

(g) ×10000

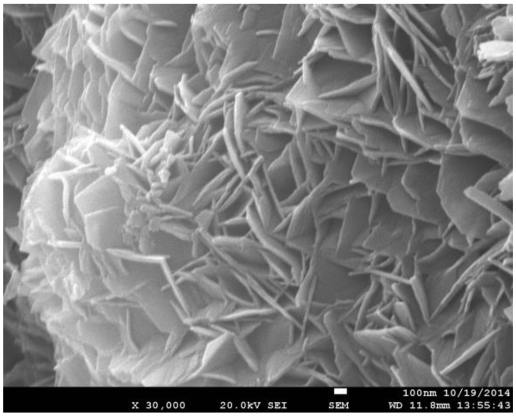

(h) ×20000

Figure 10. Continued.

The periclase hydration reaction is very slow. In the presence of water, periclase hydates slowly and generates brucite ($Mg(OH)_2$) as microcrystalline flakes. The solid phase volume increases to 212.6% when periclase hydrates to brucite (Mucahit Sutcu, et al. 2009). The volume expansion had led to the expansion and cracking of the concrete.

4 CONCLUSIONS

- The aggregates of the failure track slab concrete were mixed with some periclase aggregates.
- Periclase aggregates had hydrated slowly and generated brucite ($Mg(OH)_2$) microcrystalline flakes. The volume expansion was the main cause leading to the cracking failure of the track slab concrete.

ACKNOWLEDGEMENT

This work was financially supported by the National Natural Science Foundation of China (51308546).

REFERENCES

Berra M., Mangialardi T., Paolini A. Use of an ultra-accelerated concrete prism expansion test for alkali-silica reactivity assessment [J]. Magazine of Concrete Research, 2005, 57(1): 39–48

Criaud A., Defosse C., Andrei V. An accelerated method for evaluation of ASR risks of actual concrete compositions [A]. Third CANMET/ACI International Conference on Durability of Concrete [C]. France: 1994. 687–712

Mucahit Sutcu, Sedat Akkurt, Salih Okur. Influence of crystallographic orientation on hydration of MgO single crystals [J]. Ceramics International, 2009, 35: 2571–2576

Electrochemical repair



Taylor & Francis
Taylor & Francis Group
http://taylorandfrancis.com

Concrete Solutions – Grantham et al. (Eds.)
© 2016 Taylor & Francis Group, London, ISBN 978-1-138-03008-4

Electrochemical re-alkalisation, chloride extraction and alkali-silica reaction in concrete

P.F.G. Banfill
Heriot-Watt University, Edinburgh, UK

ABSTRACT: Concrete made with potentially reactive aggregate was artificially contaminated with chloride (two levels) or artificially carbonated (two levels) or both in combination. These nine combinations were either left untreated or electrochemically treated by realkalisation and/or chloride extraction and then subjected for one year to the conditions of 38°C and high relative humidity that are known to promote alkali-silica reaction. Expansion measurements, pore solution analysis and microscopy confirmed that ASR is unlikely to be a problem in realkalised carbonated concrete because the hydroxyl ion concentration does not reach the level needed to initiate the reaction. However, ASR is potentially significant in concrete treated by chloride removal: observed expansion increased tenfold. In chloride contaminated concrete, increasing carbonation progressively reduces the expansion, although it may still be unacceptably high in partially carbonated concrete.

1 INTRODUCTION

Re-alkalisation and chloride extraction have maintained a significant share of the world market for concrete repair, and are attractive because they treat the causes of reinforcement corrosion (carbonation and chloride contamination) rather than just the symptoms (cracking, spalling and delamination). Used in conjunction with local patch repairs, where necessary, re-alkalisation re-establishes alkaline conditions in the cover zone and chloride extraction reduces the chloride concentration. These beneficial effects are counterbalanced by the increased risk of Alkali-Silica Reaction (ASR) resulting from the higher concentrations of alkali metal and hydroxyl ions. However, while Al-Kadhimi et al (1996a) found that re-alkalisation decreased ASR expansion, Page & Yu (1995) showed that there exists a pessimum amount of charge passed in the chloride extraction treatment at which expansion is greatest. This paper describes hitherto unpublished experimental work from a project completed in 1997 which aimed to resolve this disagreement in the observed ASR of concrete.

2 A MECHANISTIC MODEL FOR ASR IN ELECTROCHEMICAL TREATMENTS

In amorphous or glassy silica the Si-OH groups react with hydroxyl ions at low concentrations while in more stable silica the Si-O-Si bridging groups react at higher concentrations. In both cases the product of reaction is alkali-silica gel, a poorly defined colloidal isotropic coagulate with exceptional swelling capacity which may cause expansion and cracking in moist conditions. Formation of the gel is only possible if sodium and hydroxyl ions are present at sufficiently high concentration. Calcium hydroxide acts as a reserve of hydroxyl ions, feeding the reaction. The extent of reaction and consequent expansion depends on the alkali/silica ratio with a pessimum value in the range 0.01–0.05. Once formed, the alkali-silica gel imbibes water and swells because of the osmotic potential developed by the sodium ion concentration gradient between the gel and the matrix. Finally, if the rate of reaction is high, silica will diffuse out and react with calcium hydroxide to form calcium silicate hydrate near the reactive grain which means that calcium hydroxide increases the rate of expansion. All this shows that calcium hydroxide is very important (Wang & Gillott, 1991) and suggests that its absence in carbonated and re-alkalised concrete will reduce expansion.

When concrete is carbonated, the pH is reduced and the hydroxyl concentration falls below the threshold value. Calcium and alkali hydroxide are converted to calcium and alkali carbonate and the lime/silica ratio in the calcium silicate hydrate is reduced below 1.4 thus increasing the sorption capacity for alkali (Durand et al. 1990). The cement matrix is densified, reducing the mobility of water and ions. All this reduces ASR, but when the concrete is re-alkalised the ingress of sodium ions and the production of hydroxyl ions by electrolysis at the reinforcement increases reactivity again and this may offset the lack of calcium hydroxide.

The role of chloride in alkali-silica reaction in contaminated concrete depends on its origin. External contamination by sodium chloride increases the sodium concentration in the gel and the matrix, increases ionic strength and compresses the double layer around calcium silicate hydrate releasing hydroxyl ion into solution and this increases

Table 1. Degrees of ASR expected to result from electrochemical treatment.

Condition of concrete	Reference, uncarbonated	Partially carbonated, not reaching the steel	Fully carbonated, up to and beyond the steel
Reference, uncontaminated with chloride	1. reaction at pessimum level	2. moderate increase in reaction and expansion	3. no reaction
Partially contaminated with chloride, not reaching the steel	4. large increase in reaction, moderate expansion	5. large increase in reaction, moderate expansion	6. no reaction
Fully contaminated with chloride, up to and beyond the steel	7. large increase in reaction, moderate expansion	8. large increase in reaction, moderate expansion	9. no reaction

alkali-silica reactivity (Chatterji et al. 1986). External contamination by calcium chloride causes calcium hydroxide to dissolve and leach out of the concrete decreasing alkali-silica reactivity (Chatterji 1979). Internal contamination by cast-in sodium or calcium chloride accelerates hydration leading to more calcium hydroxide and a denser, more rigid, microstructure, less able to accommodate swelling which is therefore more destructive. Some of the chloride is bound as Friedel's salt which also releases calcium hydroxide. Thus greater alkali-silica reactivity results.

Based upon these considerations nine possible scenarios can be identified for electrochemically treated concrete in a real structure and these are expected to give rise to different degrees of alkali-silica reactivity and expansion, as summarised in Table 1. In Table 1 it is assumed that in every case chloride contaminated concrete is electrochemically treated with saturated calcium hydroxide electrolyte and that uncontaminated but carbonated concrete is re-alkalised with sodium carbonate solution.

The disparity in the observed reactivity between re-alkalisation and chloride removal can be explained on this hypothetical model because Page et al studied cases 1, 4 and 7 whereas Al-Kadhimi et al studied cases 1 and 3. The aim of this investigation was to validate this model experimentally.

3 EXPERIMENTAL WORK

3.1 *Preliminaries: preparing specimens*

Following Al-Kadhimi et al (1996b) fully carbonated specimens were produced by air curing for 28 days then stored in the laboratory air until the relative humidity within a cavity drilled in the concrete had dropped to 70% and finally exposed to high pressure carbon dioxide in a hyperbaric chamber. Partial carbonation was achieved by immersing specimens 10 mm deep in water, waiting until the penetration front had reached about 80 mm then coating the saturated surfaces with a rubberised masking lacquer (Hi-Tek Micro Super XP2000 Masking Lacquer) leaving the top face open (the lacquer adheres well even to wet concrete). The specimen was then exposed to a carbon dioxide pressure which steadily increased from 3 to 8 atmospheres over 6–8 hours.

Reliable penetration of chloride to about 20 mm was achieved in less than 2 hours partial immersion in 10 mm of 1 M sodium chloride solution. Full contamination was achieved by immersion in salt solution for 48 hours.

The specimens required for the work were prepared using the above procedures either individually or in combination – carbonation followed by chloride contamination.

3.2 *Materials and mixes*

In the light of experience outlined in BRE Digest 330 (Anon, 1996), and because below the concrete used in this work had a cement content of only 300 kg/m^3 the alkali content was increased to 6 kg/m^3 as follows. The portland cement contained 1.14% Na_2O eq so an additional 2.58 kg/m^3 of sodium and potassium sulfate were added, in proportions 27.5:72.5 by weight. Sulfate was used in preference to hydroxide because the latter affects the hydration process and alters the alkalinity of the concrete and this could have interfered with the electrochemical treatments. The alkali reactive aggregate was Thames Valley sand, used at 30% by total weight of aggregate, in conjunction with carboniferous limestone coarse aggregate. Expressed as kg/m^3 the concrete consisted of 300 cement, 210 water, 720 sand and 1080 coarse aggregate.

3.3 *Specimens*

Sketched in Figure 1, 280 × 75 × 75 mm concrete prisms were cast containing an embedded 18/8 stainless steel plate 270 × 65 mm perforated to give a good key to the concrete and located at 10 mm nominal depth from the top (as cast) surface, i.e. 60–65 mm from the treated face when set up for electrochemical treatment. The plate was smaller than the prism to ensure that current flow occurred through the concrete and not along the surface. The plate was electrically wired with a self-tapping screw.

3.4 *Electrochemical treatment*

Before treatment, any masking lacquer used was peeled off and the specimens partially or fully saturated with water using a vacuum/ saturation chamber. The saturation process for partially contaminated specimens was carefully controlled to prevent chloride

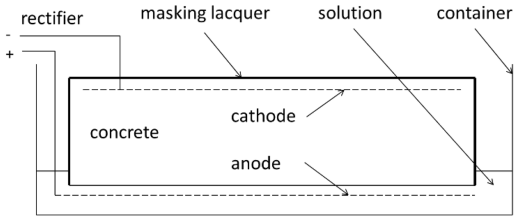

Figure 1. Schematic of electrochemical treatment apparatus.

being washed out of the specimen by excessive soaking and to ensure that the specimen is saturated with water in the bottom part (around the cathode) and salt solution in the top part (the cover zone below the anode face). Specimens were then recoated with masking lacquer on all except the anode face of the prism. Each specimen was set up in a bath of the appropriate electrolyte solution with the embedded cathode connected to one terminal of a transformer/rectifier and a titanium mesh anode located in the solution and connected to the other terminal. (Figure 1) The current was maintained at 2.5 A/m^2 by continuous adjustment of a simple bridge circuit as the electrical resistance of the specimens changed during treatment. Electrolyte was replenished with solution as necessary. The total charge for re-alkalisation of the specimens was 840 Ah/m^2 (about 2 weeks) and for chloride removal was 2940 Ah/m^2 (about 8 weeks). For comparison it can be noted that Page & Yu (1995) found the pessimum charge for ASR to be 2000–5000 Ah/m^2. The total charge for re-alkalisation is rather high compared to industrial practice because the cathode is deeper than the steel would be in most real concrete.

The electrolyte used in the treatment depended upon the nature of the specimen. Re-alkalisation of partially or fully carbonated specimens used 1 M sodium carbonate. Chloride removal used saturated calcium hydroxide solution irrespective of the degree of carbonation.

3.5 *After electrochemical treatment*

All masking lacquer was removed and specimens transferred to a controlled environment chamber to permit the ASR to develop. All specimens were stored at 100% relative humidity and 38 deg C for 12 months (Anon, 1993). Expansion was measured on 3 specimens for each set of treatment conditions at monthly intervals using a demec gauge between points 200 mm apart. ASR expansion was found to be greatest on the cathode face (because of the production of hydroxyl there) and all results are based on the average of the measurements on the cathode face for the 3 specimens. An extra prism was stored alongside the others and cut into sections for chemical analysis at the start and after 6 and 12 months' exposure.

3.6 *Chemical analysis*

Pore solution was expressed from the concrete using a device made to a design developed from that of Barneyback & Diamond (1981), permitting a larger amount of sample to be pressed (about 500 g of roughly broken concrete from which the coarse particles have been removed) and making the apparatus more operator friendly in use. The sodium, potassium, sulphate, hydroxyl and chloride content of the extracted pore solution were determined. The metal ions were determined directly by atomic absorption spectrophotometry and sulfate indirectly by measurement of the barium content remaining after reaction of the solution with barium chloride. Chloride content was determined by potentiometric titration and hydroxyl by acid-base titration.

3.7 *Microscopical analysis*

Thin sections were prepared from slices of concrete about 100 × 60 mm and 10 mm thick and examined with a Zeiss petrological microscope. Sections were examined for potentially reactive lithologies in the aggregate, for evidence of reaction (cracking and presence of gel) and for evidence of paste recrystallization.

4 RESULTS AND DISCUSSION

4.1 *Alkali-silica expansion*

Figure 2 shows the trend of expansion for the untreated specimens and vindicates the selection of experimental mixes and conditions for the work. The expansion of the reference specimens increased to a plateau level of about 0.1 mm/m over the first 20–30 weeks, remaining stable up to the end of the experiment at 55 weeks. This level is a good compromise between being high enough to confirm that reaction has taken place, but not so high as to mask the anticipated effects of the treatments. The measured expansions should be compared to the ASTM acceptance level of 1 mm/m (Anon, 1985), below which no problems in service are expected. Fully carbonated concrete expanded much less than the reference prisms because of the reduction in hydroxyl content, but partial carbonation had no effect since the carbonated zone is only about 20 mm thick and does not reach the cathode where most of the expansive reaction occurs. Partially and fully chloride contaminated concrete expanded much more than the reference prisms (Table 2), confirming the well known catalytic effect of chloride ion on ASR (Idorn & Roy, 1986). Introducing chloride ion into carbonated concrete reduced the expansion because the resulting production of calcium chloride from calcium carbonate reduces the availability of hydroxide in solution (Chatterji, 1979).

After electrochemical treatment the trends of expansion over time were similar to the untreated concrete and the level of the final expansions only will be discussed (Table 2). The carbonated concrete expanded about the same as the reference prisms because the treatment does not raise the hydroxyl concentration to the threshold for expansion. All chloride contaminated

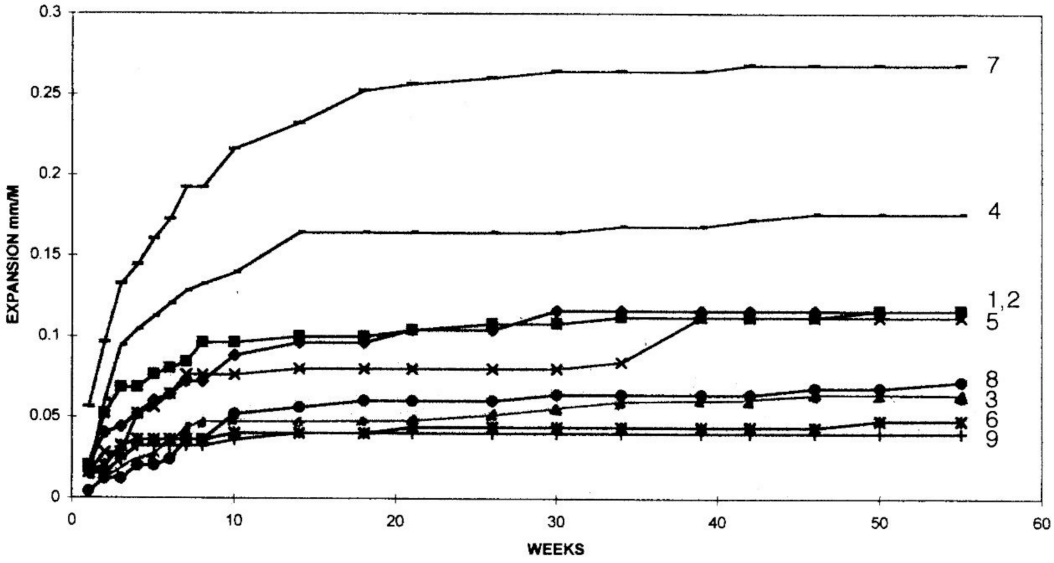

Figure 2. ASR expansion of untreated concrete. Numbers denote the different cases in Table 1.

Table 2. ASR expansion after one year (mm/m).

	Reference		Partially carbonated		Fully carbonated	
Concrete condition	Untreated	Treated	Untreated	Treated	Untreated	Treated
Reference	0.11	0.11	0.11	0.16	0.06	0.06
Partially chloride contaminated	0.17	1.4	0.11	0.31	0.05	0.18
Fully chloride contaminated	0.26	1.01	0.06	0.68	0.04	0.14

concrete expanded more after treatment than the corresponding untreated concrete. The increase was slight for chloride contaminated fully carbonated concrete but considerable for chloride contaminated partially carbonated concrete. This is due either to the extra sodium ions present in chloride contaminated concrete or to the higher concentration of hydroxyl ions generated as a result of the longer period of polarisation used for treating the chloride contaminated specimens. Partially and fully chloride contaminated uncarbonated concrete expanded up to 10 times the reference prisms, confirming that chloride removal is the treatment most likely to produce problems with ASR in sensitive concrete.

4.2 *Chemical analysis*

From the analysis of pore solutions from untreated specimens, carbonated concrete showed the expected reduction in initial hydroxyl content (Table 3) together with a slight increase in sulphate (Table 4), reflecting the effect of carbon dioxide on the hydrated cement. In the same way chloride contamination increased the sodium and chloride content (Table 5–6) with insignificant changes in potassium, sulphate and hydroxyl levels. The sodium and chloride concentrations reached in carbonated specimens were somewhat lower, reflecting the lower absorption of these specimens.

Table 3. Initial untreated hydroxyl content (mM/L).

	Reference	Partially carbonated	Fully carbonated
Reference	11.5	1.6	3.1
Partially contaminated	10.4	6.8	–
Fully contaminated	9.4	4.4	–

The electrochemical treatment had a consistent effect neither on the sodium content (Table 7) nor on the potassium content, slightly reduced the sulphate content (Table 8), considerably reduced the chloride content (Table 9) and slightly raised the hydroxyl content (Table 10). These features are consistent with the known behaviour of electrochemically treated concrete.

During exposure of the various specimens to the accelerated ASR conditions the sodium and potassium content of the pore solution decreased (Figure 3–4). In general potassium decreased in the first six months and

Table 4. Initial untreated sulphate content (mg/mL).

	Reference	Partially carbonated	Fully carbonated
Reference	10.7	13.9	12.1
Partially contaminated	11.2	10.2	11.2
Fully contaminated	7.9	6.6	11.2

Table 5. Initial untreated sodium content (mg/mL).

	Reference	Partially carbonated	Fully carbonated
Reference	17.1	17	23.7
Partially contaminated	22.9	20.9	20.7
Fully contaminated	30.6	20.1	16.1

Table 6. Initial untreated chloride content (mg/mL).

	Reference	Partially carbonated	Fully carbonated
Reference	0.08	–	–
Partially contaminated	1.77	–	2.67
Fully contaminated	3.28	1.14	2.94

Table 7. Initial treated sodium content (mg/mL).

	Reference	Partially carbonated	Fully carbonated
Reference	17.1	34.1	21.5
Partially contaminated	21.9	18.5	16.6
Fully contaminated	33.9	21.7	21.3

Table 8. Initial treated sulphate content (mg/mL).

	Reference	Partially carbonated	Fully carbonated
Reference	10.7	2	18.5
Partially contaminated	10.2	8.9	4.8
Fully contaminated	7	8.9	7.5

Table 9. Initial treated chloride content (mg/mL).

	Reference	Partially carbonated	Fully carbonated
Reference	0.08	–	–
Partially contaminated	0.56	–	0.29
Fully contaminated	1.17	0.21	0.57

Table 10. Initial treated hydroxyl content (mM/L).

	Reference	Partially carbonated	Fully carbonated
Reference	11.5	17.9	12.42
Partially contaminated	–	3.5	1.9
Fully contaminated	18.7	7.2	1.4

remained roughly constant thereafter while sodium decreased at an accelerating rate with considerable reductions by twelve months. These are consistent with the trends in the ASR expansion where the expansion stopped between six and twelve months as a result of the depletion of the supply of free alkali metal ions in solution. There was no significant trend of chloride content with time during ASR, with the correlation between expansion and chloride content confirming its catalytic effect on the reaction. The hydroxyl content of all the uncarbonated specimens, cases 1, 4 and 7, (and also some carbonated treated specimens, cases 2 and 3) stayed high throughout storage (Figure 5) with the greater ASR expansions of these specimens (Table 2) confirming that it remained above the threshold concentration.

4.3 *Microscopical examination*

Chert, metaquartzite and recrystallized sandstone and siltstone were identified from all thin sections, with occasional silicified limestone, greywacke and schist. These are the origin of the observed ASR expansion. Figure 6 shows a cracked chert grain containing gel, extending into the paste, in a treated sample of case 4, which showed high expansion (Table 2). This sample also showed extensive paste recrystallization, as exemplified by Figure 7, which shows ettringite in a parting between aggregate and paste. Figure 8 shows gel in a crack associated with a recrystallized sandstone particle containing strained quartz, in a treated sample of case 8, which showed high expansion (Table 2). These are all typical features of ASR.

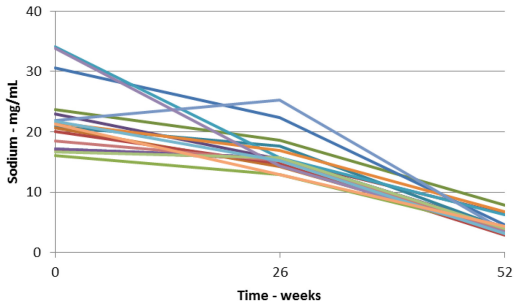

Figure 3. Variation of sodium content with time of ASR.

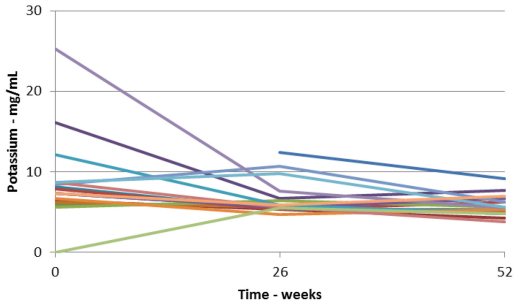

Figure 4. Variation of potassium content with time of ASR.

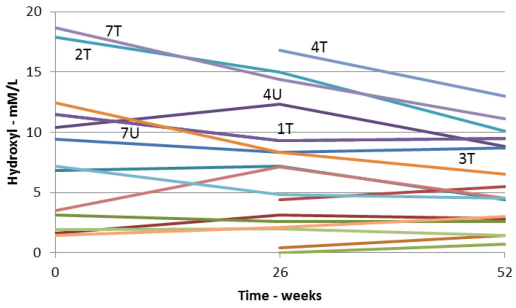

Figure 5. Variation of hydroxyl content with time of ASR. Numbers denote the different cases in table 1, U – untreated, T – treated.

5 GENERAL DISCUSSION

It must be emphasised that these results have been obtained under accelerated laboratory testing conditions of high water/cement ratio and alkali content and with higher treatment current densities than are typical in industrial practice. These conditions were necessary in order to achieve expansions within the project period. Also, the use of embedded stainless steel as the cathode means that none of the impressed charge is consumed in reducing the oxide film that would be present on mild steel in field concrete. Nevertheless they have clearly shown a direct comparison between the effects of re-alkalisation and chloride removal on ASR in sensitive concrete, and confirm the conflicting results reported in the literature as a real effect. The

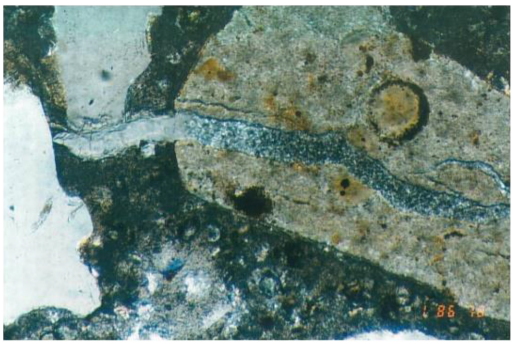

Figure 6. A gel filled crack in treated case 4. Field width 0.5 mm.

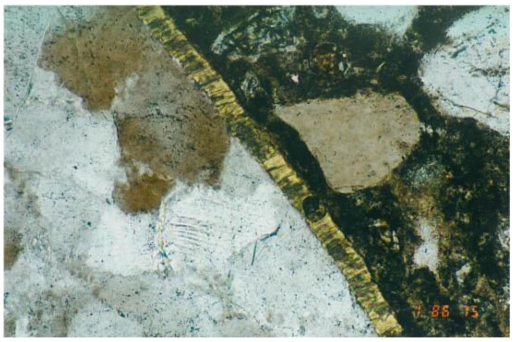

Figure 7. Ettringite developed at an aggregate surface in treated case 4. Field width 0.5 mm.

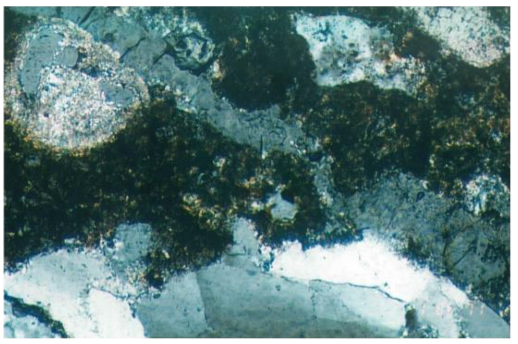

Figure 8. A gel filled crack in treated case 8. Field width 0.5 mm.

results support the mechanistic model summarised in section 2 and confirm the effects predicted in table 1.

Alkali silica reaction is unlikely to be a problem in re-alkalised carbonated concrete because the hydroxyl concentration in the concrete never reaches the threshold level needed to initiate the reaction and expansion is negligible.

ASR is a potentially significant problem in concrete treated by chloride removal since residual chloride can catalyse the reaction and the hydroxyl concentration is above the threshold level. Observed expansion is increased about tenfold.

In chloride contaminated concrete, increasing carbonation progressively reduces the ASR expansion, but the expansion with partially carbonated concrete may still be unacceptably high. In general when chloride is present ASR expansion increases considerably.

6 CONCLUSIONS

Accelerated ASR expansion measurements under laboratory conditions suggest that re-alkalisation will not provoke ASR but that electrochemical chloride removal could potentially promote expansion in sensitive concrete. These findings would need to be confirmed in the field.

ACKNOWLEDGEMENTS

I thank Talib Al-Kadhimi, Claire Robbie and David Woodward for their experimental work, David Oldham for provision of facilities and Geomaterials Research Services (now part of Sandberg LLP) for microscopical analysis. The work was funded by the Engineering and Physical Sciences Research Council under grants GR/K80853/1 and GR/K80860/1.

REFERENCES

Al-Kadhimi, T.K.H. & Banfill, P.F.G. 1996a. The effect of electrochemical re-alkalisation on alkali-silica expansion in concrete, in A. Shayan (ed.) *Alkali-Aggregate Reaction in Concrete*, Proceedings of 10th International Conference, Melbourne, 637–644.

Al-Kadhimi, T.K.H., Banfill, P.F.G., Bungey, J.H. & Millard, S.G. 1996b. An accelerated carbonation procedure for studies of concrete, *Advances in Cement Research*, 8: 47–59.

Anon 1985. Standard test method for potential alkali reactivity of cement-aggregate combination (mortar bar method), ASTM standard C227-81, *Annual Book of ASTM standards*, vol 04.02: 156–161. Philadelphia: ASTM.

Anon 1996. *Alkali-silica reaction in concrete*, Watford: Building Research Establishment. Digest 330.

Anon 1993. *The diagnosis of alkali-silica reaction*, Crowthorne: British Cement Association, Publication 45.042.

Barneyback, R.S. & Diamond, S. 1981. Expression and analysis of pore fluids from hardened cement pastes and mortars, *Cement and Concrete Research*, 11: 279–285.

Chatterji, S. 1979. Role of $Ca(OH)_2$ in the breakdown of portland cement concrete due to alkali-silica reaction, *Cement and Concrete Research*, 9: 185–188.

Chatterji, S., Jensen, A.D., Thaulow, N. & Christensen, P. 1986. Studies of alkali-silica reaction Part 3: mechanism by which NaCl and $Ca(OH)_2$ affect the reaction, *Cement and Concrete Research*, 16: 246–254.

Durand, B., Berard, J. & Roux, R. 1990. Alkali-silica reaction: the relation between pore solution characteristics and expansion test results, *Cement and Concrete Research*, 20: 419–428.

Idorn, G.M., Roy, D.M. 1986. Opportunities with alkalies in concrete testing, research and engineering practice, in V.H. Dodson (ed) *Alkalies in Concrete*, Philadelphia: ASTM STP-930: 5–15.

Page, C.L., & Yu, S.W. 1995. Potential effects of electrochemical desalination of concrete on alkali-silica reaction, *Magazine of Concrete Research*, 47: 23–31.

Wang, H. & Gillott, J.E. 1991. The mechanism of alkali-silica reaction and the role of calcium hydroxide, *Cement and Concrete Research*, 21: 647–654.



Taylor & Francis
Taylor & Francis Group
http://taylorandfrancis.com

Concrete Solutions – Grantham et al. (Eds.)
© 2016 Taylor & Francis Group, London, ISBN 978-1-138-03008-4

Acid damage to anode mortar when using cathodic protection

P. M. Chess
FORCE Technology/CP International

ABSTRACT: Cathodic Protection (CP) of reinforced concrete structures has become increasingly common and is now being routinely installed on many projects around the world. The most popular cathodic protection systems have their anodes placed either on the surface of the concrete, in slots or in holes. Generally, the couplant to electrolytically connect the primary anode to the concrete substrate is a cementitious grout, mortar or sprayed concrete. This hydraulic material is often based on Ordinary Portland Cement (OPC). When current is passed at the anode, acid is generated and this could cause damage to the cementitious couplant. Because of this there are, in several standards such as EN 12696, current density limitations placed on the anode. This limitation has profound implications on the economics of CP as it could increase the number of anodes required by a factor of four or more. The purpose of this paper is to explore what is happening in the CP process particularly at the primary anode side, examine data from various sources and comment on whether these current limitations are sensible.

Keywords: Cathodic protection, reinforced concrete, acid, current limitations

1 INTRODUCTION

Cathodic Protection (CP) of reinforced concrete structures has become increasingly common and is now being routinely installed on many projects around the world. The most popular cathodic protection systems have their anodes placed either on the surface of the concrete, in slots or in holes. Generally, the couplant to electrolytically connect the primary anode to the concrete substrate is a cementitious grout, mortar or sprayed concrete. This hydraulic material is often based on Ordinary Portland Cement (OPC now referred to as CEM1). When current is passed at the anode, acid is generated and this could cause damage to the cementituous couplant. Because of this there are in several standards, such as EN 12696current density limitations placed on the anode. This limitation has profound implications on the economics of CP as it could increase the number of anodes required by a factor of four or more. The purpose of this paper is to explore what is happening in the CP process particularly at the primary anode side, examine data from various sources and comment on whether these current limitations are sensible.

1.1 *Mortar degradation*

Cathodic protection is applied to reinforced concrete structures to stop corrosion of the steel reinforcement, and is often the only economically viable repair option. To accomplish this an electrical charge (which is carried through the electrolyte as ions) is passed between an assembly of anodes through the concrete and onto the steel. This converts the reinforcing steel, which could previously be oxidising (losing electrons) into a net receiver of these electrons. This changes parts of the steel previously corroding from being an anode into a cathode, hence the name CP. The current passes between an anode, which is energised with a low voltage DC current, through the electrolytic medium (the cementitious couplant and then the parent concrete) and on to the reinforcement. This electrolytic medium is not electronically conductive but is ionically conductive. Thus, the charge is carried by ions. The net effect is to cause a deficit of electrons at the anode surface and a surplus of electrons at the steel reinforcement surface. By this mechanism, the corrosion activity is displaced from the surface of the steel to that of the applied (impressed current) anode which is designed to be corrosion resistant.

CP has been successfully used for hundreds of years on ships where the high conductivity of the seawater made it easy to pass the current through this medium. Cathodic protection came ashore over a hundred years ago to protect steel in the ground and this was found to be easily achievable despite the lower conductance of the soil electrolyte compared to seawater. The reason for success was aided by the fact that the volume of the soil around the protected object is large so the actual electrical resistance diminishes. CP of reinforced concrete was first tried by the Americans in the late fifties (Stratfull 1959) and it had expanded to preventing further corrosion of reinforced concrete bridge decks in the late 1960's and early 1970's. They found that the

high resistance and limited cover depths of the concrete placed significant limits on the output of an anode and its current spread. They also found that, over a certain current density, damage may occur (Bennett 1993) to the concrete or couplant mortar adjacent to the primary anode. Researchers first noticed this problem in site observations of impressed current slotted systems on bridge decks and undertook limited laboratory experimentation with a Mixed Metal Oxide (MMO) ribbon anode cast into the concrete. Research by Bennett 1993 (provided the data that was used as the basis for the anode current density limitations in the present European standard EN ISO 12696 (). This research was based on MMO ribbons cut into slots in the concrete surface, an arrangement that is known for its uneven dispersion of current. The testing looked for any signs along the ribbons length for cementitious softening or discolouration. This effect was found to occur at an applied current density of more than 110 mA/m^2 of anode surface area.

1.2 *Summary of Danish, Norwegian and American grout testing results*

Three cementitious grouts of slightly different compositions (designated A, B and C) were tested at CP International in Denmark (Gronvold 1998 at extreme current densities for 6 months indoors. The test rig had durAnode 2 MMO discrete anodes embedded in a test mortar tube of 12mm diameter in a saltwater bath. This test was at an anode current density of 1,600 mA/m^2. At the conclusion of the test; specimen group A had minor damage, specimen group B had some damage and specimen group C was destroyed.

A purpose built outdoor test facility was constructed at CP International to allow detailed measurement of impressed current anodes performance and current spread. This had a water storage tank cast into the top of the structure so high anode currents (700 mA/m^2) could be passed at normal voltages (4–5 V). These trials were run for up to eight years with core examinations showing limited or no acid damage at the interface between the special grout (this had fine particles to give good flow characteristics, ionic conduction enhancers and was based on the Group A grout above) and the MMO coated titanium tube (Gronvold 1996).

An early test (Gronvold 1998) of acidification at extremely high anode current densities was made in the mid 1990's. Here the couplant was graphite, which is electronically conductive, directly linked with the parent concrete. The anode test was at 4,000 mA/m^2 at a DC voltage of between 60 and 70 V for one year. The anode to concrete interface was examined by the Laboratory of the Danish Road Authority. They found that about 2–3 mm of the concrete abutting the graphite was acidified but no concrete material was missing. The researcher (F Gronvold) found on this and other tests that the critical condition is to have no voids against the primary anode surface which can fill with water.

A Norwegian Highways Authority trial (1997) made an evaluation of acid damage to the anode interface. Its conclusion was that *durAnode3* MMO anodes with special grout suffered little or no acid damage over an operating period of eight years at 450 mA/m^2. This finding has been replicated on literally hundreds of systems around the world some of which have been operating for more than 25 years at this or slightly lower anode current densities.

Testing of Elgard discrete anodes by J. E. Bennett Consultants (the same person who did the original experiments) in Ohio, USA for Eltech's range of MMO discrete anodes was begun in 1996. Anode current densities of between 387 and 775 mA /m^2 were used and the anodes and surrounding mortar autopsied after 235, 404 or 570 days under current. The removed core was split and the anode and surrounding grout examined for damage. The damage being looked for was Anode Reaction Product (ARP), which is a softening and discolouration of the cement paste. It should be noted that this ARP does not mean that the anode had stopped functioning but merely that the appearance and structure of the grout had changed. Table 1 below has been compiled using the data from two reports (Bennett 2007 and 2008) detailing this project.

From Table 1 it can be read that at an anode current density of 387 mA/m^2 all the anodes inspected showed minimal damage to the cementitious grout. At 516 mA/m^2 some mortars showed significant damage and some did not. At 775 mA/m^2 there was some damage to one mortar and little to another. There was no correlation between the time that the current had been passed and the amount of damage. There were very significant differences in performance between mortars at the same current density.

It should be noted that ARP was noted on the inside surface of the anode in certain autopsied anodes (The anode is perforated and hollow so mortar was on the inside and outside of the anode).

This implies that a significant proportion of the current was provided from the inside surface of the anode. The grout used was Sika 223. Some of these samples had lithium nitrate added to the grout to improve the acid resistance and this is documented in the table with a Y for yes and N for no.

In the overall conclusions, it was stated that there was no significant difference in ARP formation between standard grout and the grout containing added lithium chloride.

1.3 *Calculation of acid formation at the primary anode*

As current is passed there will be acid formation at the interface between the primary anode and the electrolyte. This acid could react with the alkaline calcium hydroxide compound predominately in the grout causing acid damage.

Assuming the anode reaction is

$$H_2O \rightarrow O_2 + H^+ + e^- \quad (1)$$

Table 1. Evaluation of Grout Damage.

Anode No	$LiNO_3$ added to mortar	Current (mA/m^2)	Time (days)	ARP outside	ARP inside	Overall condition
1	N	387	235	None	None	Excellent
6	Y	387	235	20%	none	Good
7	N	387	235	None	None	excellent
10	Y	516	235	Extensive	Extensive	Poor
3	N	387	404	Less than 20 %	Significant	Excellent
11	Y	387	404	None	None	Excellent
9	Y	516	404	None	Significant	Excellent
5	Y	775	404	20 %	Significant	Good
2	N	387	570	30 %	significant	Good
4	Y	387	570	None	None	Excellent
12	Y	387	570	Less than 20 %	None	Excellent
8	N	516	570	None	None	Excellent
13	Y	775	570	Extensive	Extensive	Fair

Using a 12 mm diameter hole of 100 mm the following calculation can be made;

Vol. of material in hole $= \pi\ (0.6)^2$ cm $\times$ 10 cm $=$ 11.31 cm^3

Mass of ribbon is 738 gms for 26 m length

Titanium density is 4.51 gms/cm^3

Volume of titanium in 100 mm hole is thus $=$ $(738/260)/4.51 = 0.63\ cm^3$

With complete filling of the hole amount of grout is $= 11.31 - 0.63 = 10.7\ cm^3$

Grout has a set specific density of 2.10 then the mass of cementitious material in the hole can be calculated $= 10.7 \times 2.10 = 22.5$ gms

The amount of alkali in the form of Ca(OH)2 in the grout is assumed to be 19%

Molar weight of $Ca(OH)_2 = 74$ g so the 100 mm length hole $= 22.5/74 \times 0.19 = 0.058$ mole

Operating at 450 mA/m^2, computes to an output of 2.39 mA for a 100 mm length.

The number of amp hours available in the alkali $= 0.058 \times 26.8$ amp hours $= 1.55$ amp hours

Assuming a 50% electrochemical efficiency then at 2.39 mA output all the cement paste will be consumed in $= (1.55 \times 1{,}000/2.39) = 1/0.5 = 1{,}292$ hours $= 54$ days.

1.4 *Comparison between predicted and actual anode mortar degradation*

The acidification predicted by the electrochemical calculations above did not occur in any of the practical trials of the mortars outlined above. Further, at some of the trials extremely high levels of current output were introduced and no, or little, discernible damage was noted after several years of testing. This suggest that the calculation for anode cement degeneration is an over simplification of a complex process. This finding was confirmed (Bertolini 2013) by other research who used colour –pH indicators to indicate that acidification around the anode had occurred. The amount of acidification they had expected in accordance with Faraday's law (the same calculation as used above) did not occur. The actual amount of acid was about 10% of the level predicted. It was suggested that the hydroxyl ions produced at the cathode migrated to the anode and neutralised the acid. Further research work is described in (Bertolini, 2013) where thin sections of the anode/mortar interface were taken and studied using a light microscope and a scanning electron microscope. In this study, it was suggested that there could be other mechanisms than the hydroxyl migration, which caused the acid damage to be less than predicted. Further tests were done on cathodic protection system anodes, which had passed current at 20 mA/m^2 for up to 6 years. Again there was less acid formation than that calculated and it was stated that there were certain processes which are insufficiently understood. In conclusion, it stated that 'acid formation at the anode, at least at moderate current densities, is not critical for the service life of CP systems. However, it may be relevant for (unintended) local high current densities.

It appears significant that in different trials described above (in Gronvold 1996 and Bennett 2008) at identical current densities we are getting diverging outcomes (small damage or destruction of sample) for no immediately obvious reason.

During the trials it was noted that in certain circumstances, anodes were producing chlorine gas on a continuous basis, gas, which could be smelt, seen (a greenish yellow gas) and analysed. This took place at the low voltages (say 3 to 5 volts) and current used in the CP of reinforced concrete. The discharge of chlorine means that the oxygen producing reaction of $H_2O = O_2 + H^+ +$ electrons has not occurred and the alternative of $Cl^- = Cl_2 +$ electrons – has. Of course, both reactions can occur simultaneously. It also means that the chloride has moved from the concrete through the mortar (which is chloride free) and onto the primary anode interface. This chlorine producing reaction gives much less acidification than the water reduction reaction (10). If this alternative reaction is occurring, there must be a plentiful resupply of chloride ions from the surrounding matrix. This can only

occur if the surrounding concrete is chloride contaminated and this may account for the large difference in behaviour of certain specimens under the same experimental conditions, i.e. if the oxygen production occurs there will be a large amount of acidity produced, which will damage the cement paste, whereas if chlorine gas is produced, there will be less damage. It is more fully covered in another paper by Chess 2016) but any voidage where there is grout missing is likely to prevent electro-osmosis of the chloride. If this voidage is beside the primary anode this would see a reduction in pH in these locations as the oxygen reaction is favoured. This could explain the disparity in the test results.

Which reaction occurs at the anode depends on several factors, which have not been fully explored but will include the anode type. For example RuO_2 favours oxygen production while IrO_2 favours chlorine production. The MMO ribbon commonly used for CP in concrete is an IrO_2/TaO_2 mix, which favours chlorine production (Shrier 1998. The ratio of the oxygen to chlorine reaction probably depends on the relative concentrations of the water or chloride and the potential difference at the anode to grout interface. If the oxygen evolution reaction occurs, there is a much greater drop in pH then if the chlorine reaction occurs.

2 CONCLUSIONS

Despite the rise in importance of electrochemical techniques for the renovation of reinforced concrete structures surprisingly little fundamental research has been undertaken on anode couplant durability.

Commercial companies have been selling discrete CP anodes with claimed long-term durability with current densities at multiple times more than that defined in the EN ISO 12696.

Looking at the available trial data it appears that this approach can be justified with two important caveats. Firstly, the higher current limits only apply when the surrounding concrete is chloride contaminated and secondly this output limit is along the anodes length so that only anodes with a balanced output should be treated this way. This means that anodes such as ribbon in slots should keep their existing current limitation while discrete anodes with current balancing technology can operate at more than 400 mA/m^2.

REFERENCES

Bennett et al. 1993. SHRP –S-372, Cathodic protection of concrete bridges: a manual of practice: 28

Bennett. J et al. 2007. NACE paper: Testing of Stargard discrete anodes for concrete

Bennett. J. 2008. Eltech discrete anode tests 570 day autopsy and operational report

Bertolini et al. 2013. Corrosion of steel in concrete, second edition: 372.

Chess. P. 2016. The flow of ions through concrete., Proceedings of Concrete Solutions Conference, Thessaloniki, June 2016. CRC Press

Danish Road Authority report. 1994

EN ISO 12696. 2012. Cathodic protection of steel in concrete. British Standards Institute, London, UK

Gronvold. F. 1996. Gronvold & Karnov internal trial document.

Gronvold. F. 1998. Gronvold & Karnov internal trial document

Shrier L et al.1998. Corrosion. 10: 66

Shrier L et al. 1998. Corrosion, 10: 67.

Stratfull, R. 1959. Corrosion, Vol 15. No 6:65.

Videm K. May 28, 1997. Norwegian Highways Authority (Statensvegvesen)

Concrete Solutions – Grantham et al. (Eds.)
© 2016 Taylor & Francis Group, London, ISBN 978-1-138-03008-4

The flow of ions through concrete structures

P.M. Chess
FORCE Technology/CP International

ABSTRACT: Modern structures in aggressive environments are increasingly being engineered to achieve a life expectancy based on the impenetrability of the concrete to chloride ions. These predictions are commonly based on Fick's laws of diffusion, but it is possible that there is a much quicker transport mechanism in hardened concrete. Some evidence for this is provided by the fact that it has been known for many years that the application of an external DC current can dramatically alter the rate that ions, such as chloride, can move through concrete and this technique is used to make rapid assessments of the likely permeability of concrete samples.

In the last few decades electrochemical treatment of reinforced concrete such as electrochemical chloride removal and Impressed Current Cathodic Protection (ICCP) of reinforced concrete structures have become increasingly commonplace and are now being routinely installed on many projects around the world. In both of these processes there are significant flows of ions at far higher rates then would be predicted by diffusion calculations.

The purpose of this paper is to assess the nature of these ionic flows and propose a possible mechanism. Further an estimate of the sort of time scale of this type of flow in a normal reinforced concrete structure is developed. Finally it is suggested how experiments can be performed to find whether there is a significant movement mechanism in a normal hardened reinforced concrete structure.

Keywords: Life expectancy, chloride permeability, ionic flows

1 INTRODUCTION

Modern structures in aggressive environments are increasingly being engineered to achieve a life expectancy based on the impenetrability of the concrete to chloride ions. These predictions are commonly based on Fick's law of diffusion, but it may be possible that there is a much quicker transport mechanism in hardened concrete. Some evidence for this is provided by the fact that it has been known for many years that the application of an external DC current can dramatically alter the rate that ions, such as chloride, can move through concrete and this technique is used to make rapid assessments of the likely permeability of concrete samples.

In the last few decades electrochemical treatment of reinforced concrete such as electrochemical chloride removal and Impressed Current Cathodic Protection (ICCP) of reinforced concrete structures have become increasingly popular and are now being routinely installed on many projects around the world. In both of these processes there are significant flows of ions at far higher rates then would be predicted by diffusion calculations.

The purpose of this paper is to assess the nature of these ionic flows and propose a possible mechanism. Further an estimate of a time scale for this type of flow in a normal reinforced concrete structure is developed. Finally it is suggested how experiments can be performed to find whether there is a significant movement mechanism in a normal hardened reinforced concrete structure.

1.1 *Water movement in concrete*

If looked at in isolation with a permeability of 4.6×10^{-11} m^2s^{-1} (Hall and Hoff 2002) or lower for hardened cement paste or sand cement mortars then the possibility of significant water movement through a concrete matrix appears remote.

If we take a further look at published data (Hall and Hoff 2002 we find that with a combination of factors 'that the quantities of water flowing under the action of capillarity and evaporation are prodigious'. The particular circumstances described are commonly called rising damp. It is a dynamic interplay between the upward flow of water within a ground supported structure and evaporative loss of water from the exposed surfaces of that structure. This is one way water can move through concrete much quicker than is generally quoted.

When ICCP is applied to a reinforced concrete structure, the steel reinforcement becomes a cathode. The anode surface becomes drier because of the breakdown of water molecules. The cathode becomes more alkaline because of the production of hydroxyl ions. It is widely reported that the cathode becomes wetter as current is passed, presumably water molecules

from the surrounding concrete are being brought to the steel surface. This is possibly some form of electro-migration.

1.2 *Electro-osmotic flow and electrophoresis*

Reuss in 1809) demonstrated that water could be made to flow through porous clay diaphragms through the application of an electric field. The observed mobility of the water was due to the fact that the clay particles acquire a surface charge when in contact with an electrolyte. Water is not electrically neutral and is a polar molecule. This means there is a small net negative charge near the oxygen atom and partial positive charges near the hydrogen atoms. So when there is a net charge the water molecules align themselves in a polarised way. This causes an inner layer of bound water to attach to the clay particle and then an outer layer, which is free to move. This is the so-called electrical double layer. Many materials including concrete display the same behaviour as the clay particles. The immobile surface charge surrounding the concrete particle in turn attracts a cloud of free ions of the opposite sign creating a thin (typically 1 to 10 nm) Debye layer next to it. The thickness of this electric double layer (EDL) is determined by a balance between the intensity of the thermal (Brownian) fluctuations and the strength of the electrostatic attraction to the substrate. In the presence of an external electrical field, the fluid in this charged double layer acquires a momentum, which is then transmitted to adjacent layers through the effect of viscosity. In this outer layer, the water can flow taking dissolved salts along with it.

Reuss also showed that unbonded clay particles can be made to flow when the electrical current was applied and this phenomenon is now called electrophoresis. This is particles of solid matter which are small enough to be contained in this mobile layer and not physically attached to the solid (such as concrete) structure will move when a potential difference is applied.

Commonly both electrophoresis and electro-osmosis occur simultaneously.

In the case of concrete, calcium hydroxide within the pore water is sparingly soluble between 1.4 and 1.7 grams per kg of water and will be transported towards the anode along with the water flow so there will be a little bit of re-alkalisation with water movement. Chloride is very soluble in water with 350 grams per litre for sodium chloride, 350 grams for potassium chloride and 750 grams for calcium chloride, so we could expect, in chloride contaminated concrete, that if water flows there will be an associated large movement of chloride.

It has been found practically that the rate of flow of ions is directly linked to the size of the electric field applied. This is unusual in that in most electrochemical processes there is a logarithmic relationship. It could be that this points to the double layer getting wider as the potential is increased giving a greater flow rate. This however is contradicted by a hypothesis laid out by Hudson (Chess 1998) which is discussed later in this paper.

1.3 *Ionic movement in water and concrete*

We know from experimentation that most ions (chlorides, sulphates, calcium, sodium) travel at roughly the same speed, whatever their size, with two exceptions (Barrow 1973). These are H^+ which is 6 times faster than a typical ion and OH^-, which is 3 times faster. This is probably due to a proton transfer mechanism. In aqueous solutions at a potential of 1,000 V m^{-1} it will take a typical ion 30 minutes to travel 1 meter. If we used the above data (assuming it is proportional) to more represent a typical CP set up i.e. 5 volts and an anode to cathode distance of 50mm then it can be calculated that it takes 5 hours for the typical cation to reach the anode. Of course, the H^+ and OH^- will be predicted to arrive a lot faster in an aqueous solution. It appears reasonable to assume that the same movement ratios exist in hardened concrete for the abovementioned ions, but this is contradicted by data presented later in this paper. In an aqueous solution the double layer movement mechanism previously described does not occur.

When concrete sets, the hydrated cement consists of the solid products of hydration plus the water, which is held physically or is adsorbed on the large surface area of the cement hydrates. This water is called gel water and is located between the solid products of hydration in gel pores.

The solid products of hydration occupy a smaller volume then the original solid and thus there are residual spaces in the structure, which are called capillary pores. These can be empty or full of water and are about 1,000 nm in width (Neville 1995).

The capillary pores are big enough to allow the double layer conduction described above to occur but the tortuosity of the pores will account for a considerably slower transport for the ions. This tortuosity is, for the calculations later in this paper, directly related to resistance when an attempt is made to compare different data sets.

1.4 *Ionic flow of lithium ions*

Research was undertaken to see if lithium based compounds could be injected into hardened concrete in order to prevent ongoing alkali silica reactions (ASR) occurring in the concrete. The set up (7) was to have a reservoir of lithium nitrate on the surface of the concrete specimens, a primary anode of MMO coated titanium and the reinforcement as a cathode. The cover depth was 50 mm. Unfortunately, the driving voltage was not defined. What was found after 300 days was that the lithium had penetrated only 25 mm from the surface but the sodium and potassium ions had been moved inwards to a much greater depth of over 60 mm in from the surface. This finding accorded well the result that the ASR had been increased by this infusion process, as the increased alkalinity at the cathode would promote this reaction. It is worth noting the ionic mobility of different anions seems to vary greatly and this will be discussed in more detail later in the paper.

1.5 *Chloride movement in desalination*

Desalination of reinforced concrete was practised as a repair technique commonly in the 1990's and the first decade of the twenty first century but has become less common as CP has become more popular. It consists of putting a temporary anode on the surface of the chloride-contaminated structure and applying a potential of between 40 and 50V DC between this anode and the steel reinforcement cathode, which acts as the cathode. In the Burlington skyway trial (Broomfield, 2007in Canada they removed about 80% of the chloride above the first layer of reinforcement and 55% between the first and second layer of reinforcement within a treatment time of 55 days. Various other projects have shown that between 50 and 90% of the chloride can be removed from the concrete.

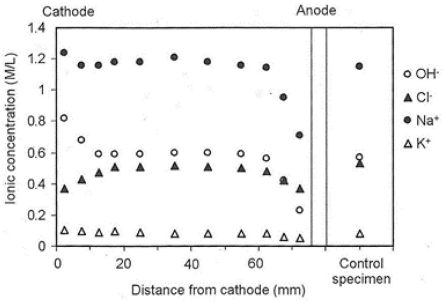

Figure 20.2 Profiles of ionic concentration measured between an anode and a cathode embedded in cement paste after one month of circulating current (average current density 350 mA/m^2) obtained by maintaining a potential of the cathode at –850 mV SCE [28].

Figure 1. Graph showing variation of ionic concentration with distance from the cathode (after Sergi and Page 1995).

1.6 *Re-alkalisation*

This electrochemical technique has also fallen out of favour compared to other procedures. It consisted of putting an alkaline solution on the surface of the concrete (typically sodium carbonate) and applying a temporary anode at between 10 and 40 volts DC. It was found that in some conditions electro-osmosis did occur and in others, it did not (Chess 1998)). Electro-osmosis was seen to occur when the concrete was not contaminated with chlorides and was also un-carbonated. When there was significant, contamination by chloride salts the water flow and hence injection of the sodium carbonate was reduced by more than a factor of three. This meant that the time taken to realkalise the cathode was increased from one to three weeks. It was theorised by Hudson (Chess 1998) that this reduction in flow was caused by a reduction in size of the double layer due to the chloride improving the electrolytic conductance of the solution.

Interestingly, Miller (2015) reported that 'uncarbonated concrete cannot sustain significant electro-osmosis' which is a different conclusion to that stated above. Further evidence of the unpredictability of electro-osmosis is described by Millar, 2015() with different investigators coming to different conclusions about the presence or absence of this water flow. In one test described, it was shown that the electro-osmotic flow of water direction was reversed in alkaline mortar compared to carbonated mortar. This uncertainty certainly needs further investigation.

1.7 *Concentration profiles of ions before and after cathodic protection*

Work by Page (Bertolini, 2013 looking at the profiles of four ions varied after a CP circuit was made for a month at a high current density of 350 mA/m^2. The graph of the data is shown in Fig 1. This shows that there is significant movement of certain ions over the time-period compared to the control specimen where no electrical field had been applied. This is on the right hand side of the figure. The movement of ions is most pronounced in the 10 mm closest to the anode and the 10 mm closest to the cathode. The largest movement is of hydroxyl ions with a halving of its concentration at the anode and an increase by approximately 50% at the cathode. The movement rate of the sodium ions almost matches that of the hydroxyl ions.

The anions (K+ and Na+) behave very differently, with the sodium being removed from the anode and congregating at the cathode. The potassium ions distribution has not been affected by the imposition of the electrical field. Both these cations chloride salts have virtually identical solubility in water.

2 DISCUSSION

It is apparent that ions can flow through concrete and that their mobility is affected by the application of an electrical current. It has been attempted in this paper to take data from several different sources to try and understand what is happening when a potential difference is applied between an anode and a cathode.

Using the aqueous solution data, it was calculated that it would take 5 hours at 5 volts for the ions to be moved 50mm. It is reasonable to assume that in this case the water is not being moved; as there is no double layer effect possible.

For the lithium trial in hardened concrete by Bentivegna 2012, it took 300 days for the movement of 25 mm by lithium ions though the calcium and sodium ions seemed more mobile. No voltage was specified so we will not take this data further.

For the desalination works, again in hardened concrete, movement of almost all of the chloride between the anode and cathode, occurred in 55 days at 45 volts.

For the re-alkalisation the average voltage was 25 volts with movement in either 7 days or 21 days depending on whether electro-osmosis occurred.

In an attempt to compare the above data, the driving voltage has been commoned and an estimate of the relative resistance made.

Using a typical resistivity of seawater of 30 ohm.cm (NACE handbook 2002) and a typical resistivity of 10,000 ohm.cm (Broomfield 2007) of chloride contaminated hardened concrete then the concrete is 333 times more resistive then the seawater. Taking the aqueous solution data and converting it into the same driving voltage of 50 volts, the movement of ions can be calculated-

0.21 day/10 (for 50 volts instead of 5) $\times$ 333 (increased resistance) = 7 days.

Using the desalination data, the chloride moved in 49 days at a common 50 volts.

For the re-alkalisation data if you use the same 50 V driving voltage, the movement is in either 3.5 days or 10.5 days.

The re-alkalisation data shows a much faster transport of ions then the other data. This can partially be accounted for by the much higher transfer rates of the hydrogen and hydroxide ion (six times and three times faster respectively) than the chloride ions.

With the re-alkalisation data, it also shows that in certain circumstances, you can get very much higher flow rates of ions. This is probably related to electro-osmosis of the pore water.

If there is significant, electro-osmosis, the water will be moved. The direction of travel is a moot point. But if the cathode (the steel reinforcement) gets wetter when CP is applied, which is normally the case, this will speed up the transport of anions (those with a positive charge such as Ca^{++} and Na^{+} and H^{+}) and reduce the rate at which the Cl^{-} and OH^{-} gets to the anode. This may have an important consequence in reducing the acidification of the anode.

If you reduced the driving voltage to the potential difference which can be seen in potential mapping of hardened concrete, which is something of the order of 300 mV, then adapting the desalination data there would be a chloride ion movement of 50mm in 22 years. This of course assumes that the mechanism is the same and the transfer rate is proportionate.

2.1 *Future experimentation*

There are several unknowns, which this paper has highlighted. The first is, does the enhanced flow of ions have a direct relationship with the potential difference even at small values such as 0.5 volt? At this low level, is this mechanism significant to the movement of ions in hardened concrete?

The second significant unknown is, when and where is electro-osmosis occurring, and what effect does this have on ionic flows?

The third unknown outlined here is that the flow rate of ions in reinforced concrete under an electrical field is not complying with the flow rates observed in normal aqueous solutions and seems to be selective. This would appear to have critical durability implications and it would be sensible to obtain some data on the relative performances of the different types of cement commonly available.

To look at the first point, a series of experiments could be based on the rapid chloride migration test AASHTO TP64 and could be carried out at voltages from 0.2 to 60 V DC

For the second evaluation, a series of concrete specimens could be constructed of varying compositions such as carbonated, uncarbonated and chloride contaminated and tested at various potential difference levels. A low technology way would be to measure the moisture levels by relative humidity sensors in voids in the samples.

The most elegant way to undertake research on this topic would be by laser induced breakdown spectroscopy (LIBS) as described in (Wilsch et al, 2014) and operated at the BAM institute in Berlin.

3 CONCLUSIONS

The application of a current does change the transport rate of ions in concrete and this has been widely used in electrochemical techniques for the rehabilitation of damaged concrete structures. For some reason it has not been considered that this may be an important mechanism for the movement of ions in concrete which does not have external current flows caused by electrical interference or electrochemical treatments. If this is the case then it would have profound implications on the durability of reinforced concrete which is a topic of extreme commercial importance.

Presently there is significant uncertainty on the mechanism of this ionic flow with some ideas for why this may be occurring but little or no research to back this up.

There appears to be certain circumstances where electro-osmosis can occur and this should be investigated so that a clearer understanding of this phenomenon is obtained. The flow rates when this process appears are of the order of four times the normal so this topic is clearly of great interest to ensure durability.

The way that ions are moving in concrete does not appear to follow the rules established in aqueous electrochemistry and the reasons for this difference also merits further investigation.

REFERENCES

Barrow G. 1973. *Physical Chemistry. Third edition*. Page 638 McGraw Hill

Bentivegna, A.F. Giannini E.R. & Folliard K.J. "Use of electrochemical migration to mitigate alkali-silica reaction in large scale concrete structures." *Proceedings of Concrete Solutions – 4th International Conference on Concrete Repair, Dresden, 2011.* CRC press.

Bertolini L et al, 2013. *Corrosion of steel in concrete*. Second edition. page 395. Wiley VCH

Broomfield J. 2007. *Corrosion of steel in concrete*. Second edition: page 68. Taylor and Francis

Broomfield J. 2007. *Corrosion of steel in concrete*. Second edition: page 193. Taylor and Francis

Chess P. 1998. *Cathodic protection of steel in concrete*. First edition: page154. Spon press

Chess P. 1998. *Cathodic protection of steel in concrete*. First edition: page 155. Spon press

Hall C & Hoff W. 2012. *Water transport in brick, stone and concrete:* Page 77. Spon press

Hall C & Hoff W. 2012 *Water transport in brick, stone and concrete:* Page 265. Spon press

Millar S et al. 2015. *Proceedings of 4th International Conference on Concrete repair rehabilitation and retrofitting*. Leipzig. Page 59. CRC Press

Neville A, 1995. *Properties of concrete*, Fourth edition: 483. Longman

NACE corrosion engineers reference book. 2002 third edition: page 163. NACE press

Neville A, 1995. *Properties of concrete*, Fourth edition:page 483. Longman

Norecon Task T2. April 2004. *Repair methods – a review*: page 23.

Reuss F. 1809 *Mem Soc Imperiale Naturulists de Moscow* 2. Edition 327 F.

Sergi G & Page C. 21-23 November 1995. *Advances in electrochemical rehabilitation techniques for reinforced concrete.* UK Corrosion paper 95.

Wilsch, G. Eichler, T, Millar, S and Schaurich, D. Laser induced breakdown spectroscopy (LIBS) – alternative to wet chemistry and micro-XRF . *Proceedings of 5th International Conference on Concrete Repair, Belfast, 2014.* CRC Press pp744–748.



Taylor & Francis
Taylor & Francis Group
http://taylorandfrancis.com

Concrete Solutions – Grantham et al. (Eds.)
© 2016 Taylor & Francis Group, London, ISBN 978-1-138-03008-4

Impressed Current Cathodic Protection (ICCP) on reinforced concrete drilled piles buried in soil, Fürth, Germany

H. Esteves & S. Mayer
Ed. Züblin AG, Essen, Germany

1 INTRODUCTION

Today, new constructions in the transportation industries are commonly designed for a lifespan of 100 years. Some bridges like the Great Belt Bridge as a fixed link between Central Europe and Scandinavia have been built to last for at least 120 years.

With lifespans of 100 years and more, durability aspects become a key parameter in design and execution and strongly affect the chances whether a structure stays in service during the expected time. In this case study, a CP system on drilled piles is presented as a solution to fulfill the 100 years specified by the client – without undertaking any measures on the inadequate concrete cover of the piles below ground level.

2 CATHODIC PROTECTION ON BURIED DRILLED PILES – PREPARATION

2.1 *Situation*

The noise protection wall in this structure runs on the left and right hand sides of the railway route and consists of drilled piles of reinforced concrete as a foundation and wall socket, partly buried in soil. On top of the piles, beams of reinforced concrete bear elements of steel which represent the upper part of the noise protection wall.

Since the railway route was already under traffic at the time when the inadequate concrete cover was observed, there was no option to reconstruct the piles without shutting down railway traffic, a scenario which was impossible for the client. In agreement with the client and his specialists, CP was seen as the only option to achieve the 100 years lifespan in a reasonable way.

The installation of the CP system to the buried part of the piles is divided into eight batches and a number of 1,389 piles, stretching a total length of 1,600 meters. Different diameters of the piles and varying soil compositions demanded an individual design of the CP system, based on measurements and on parameters given from the layout of the piles. Finally, a concept for power supply of 36 protection zones and a monitoring system was produced, strictly in line with the demands of Deutsche Bahn for communication standard, cables, cabinets and safety equipment.

2.2 *Pre-investigations, on site measurements and field test*

In order to create a properly designed CP system, it was essential to analyze concrete quality, concrete resistivity, continuity of the reinforcement and the spreading resistance in the soil. In addition, a field test was executed to evaluate the calculated design parameters, the resistance of the buried anodes and the influences from adjacent lines as well as from railway traffic. Under testing, measuring coupons gave an idea of macro element currents and protection current density.

2.3 *Continuity of reinforcement*

A requirement under CP application is continuity of the reinforcement in a structure. This way, the entire reinforcement cage is defined as cathode and no stray currents will damage any rebar under impact of the CP. Using a DC voltmeter instrument, continuity between two uncovered rebar spots can be detected. With reference to DIN ISO EN 12696: 2012-05, continuity is approved if the value is constant and the resistance is $\leq 1\ \Omega$, including polarity reversal at the instrument. More measuring points give a more stable statement about continuity. In case effective continuity is not present, continuity must be generated by welding or wire connection.

2.4 *Soil resistivity and spreading resistance of anode*

Anode dimensions and spacing between the anodes significantly depend on soil resistivity and soil characteristics. Using a four point Wenner probe and pins in the ground surface connected with the device, soil resistivity in various depths were recorded in all treated batches along the railway route.

Based on the soil resistivity and the dimensions of the anode used in the test, it is possible to calculate

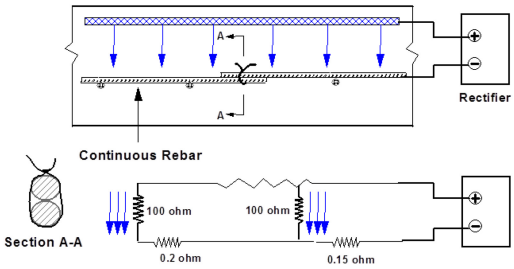

Figure 1. Continuity between two rebars can be detected using a DC voltmeter. Continuity confirmed if R ≤ 1 Ω.

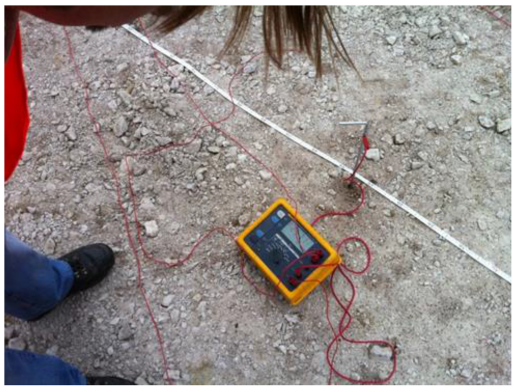

Figure 2. Soil resistivity measurements using a 4-pole earth ground tester.

Table 1. Example of examination location with soil resistivity from 1 m below ground level up to 11 m depth, 1 m steps.

Low Level (m)	Mean specific ground resistance [Ωm]	Low Level (m)	Mean specific ground resistance [Ωm]
1	239	7	99
2	168	8	96
3	131	9	97
4	106	10	92
5	107	11	89
6	100		

the approximate spreading resistance of the anode as given in equation (1) below:

$$R_y \approx \frac{0.4 * \rho}{L} * \log\frac{2 * L}{d} * \sqrt{\frac{4 * t + 3 * L}{4 * t + L}} \quad (1)$$

where ρ = soil resistivity; t = depth of earth cover; L = total length of anode in coke embedment; d = anode diameter with coke embedment

With respect to the equation above it becomes clear that greater anode dimensions reduce the spreading resistance of the anode.



Figure 3. Tubular anode of 1 m length.

Table 2. Data for tubular anode of 1 m length.

Measuring Element	Stream Entry (Current) Density (mA/cm^2)	Macro Element Power (mA/cm^2)
Measuring Coupon 1/1 v	+20	−7 (−28)
Measuring Coupon 1/10v	+5	−4 (−7)
Measuring Coupon 1/1n	−7	−48 (−182)
Measuring Coupon 1/1 On	+2	−18 (−52)
Measuring Coupon 2/10v	+5	−6 (−17)
Measuring Coupon 2/1n	−12	−42 (−102)
Measuring Coupon 2/10n	−2	−12 (−26)
Measuring Coupon 3/10v	+4	−4 (−13)
Measuring Coupon 3/10n	−8	−20 (−39)
Measuring Coupon 4/10v	+2	−14 (−32)
Measuring Coupon 4/1n	−4	−36 (−118)
Measuring Coupon 4/10n	−2	−16 (−41)

2.5 *Design current density*

During the field test, measuring coupons were installed with the target to monitor both macro element currents as well as current ingress under CP treatment. Placing measuring coupons on different spots around a drill pile, the bundle of recorded data gives an idea of how intense corrosion progress is (see Table 2, right column) and how much current might be necessary to create a CP system which gives full protection to the buried pile sections. Under CP application, current ingress and current emission at each coupon were detected (see Table 2, column in the middle).

3 CONCEPT AND FULL-SCALE SET-UP

3.1 *CP system set-up*

Special tubular MMO anodes were typically installed in vertical holes with an anode to anode distance of up to 10 m and in depths of 4 to 10 m below ground level. All anodes lay in an axle which runs parallel to the wall between the railway track and wall. At some

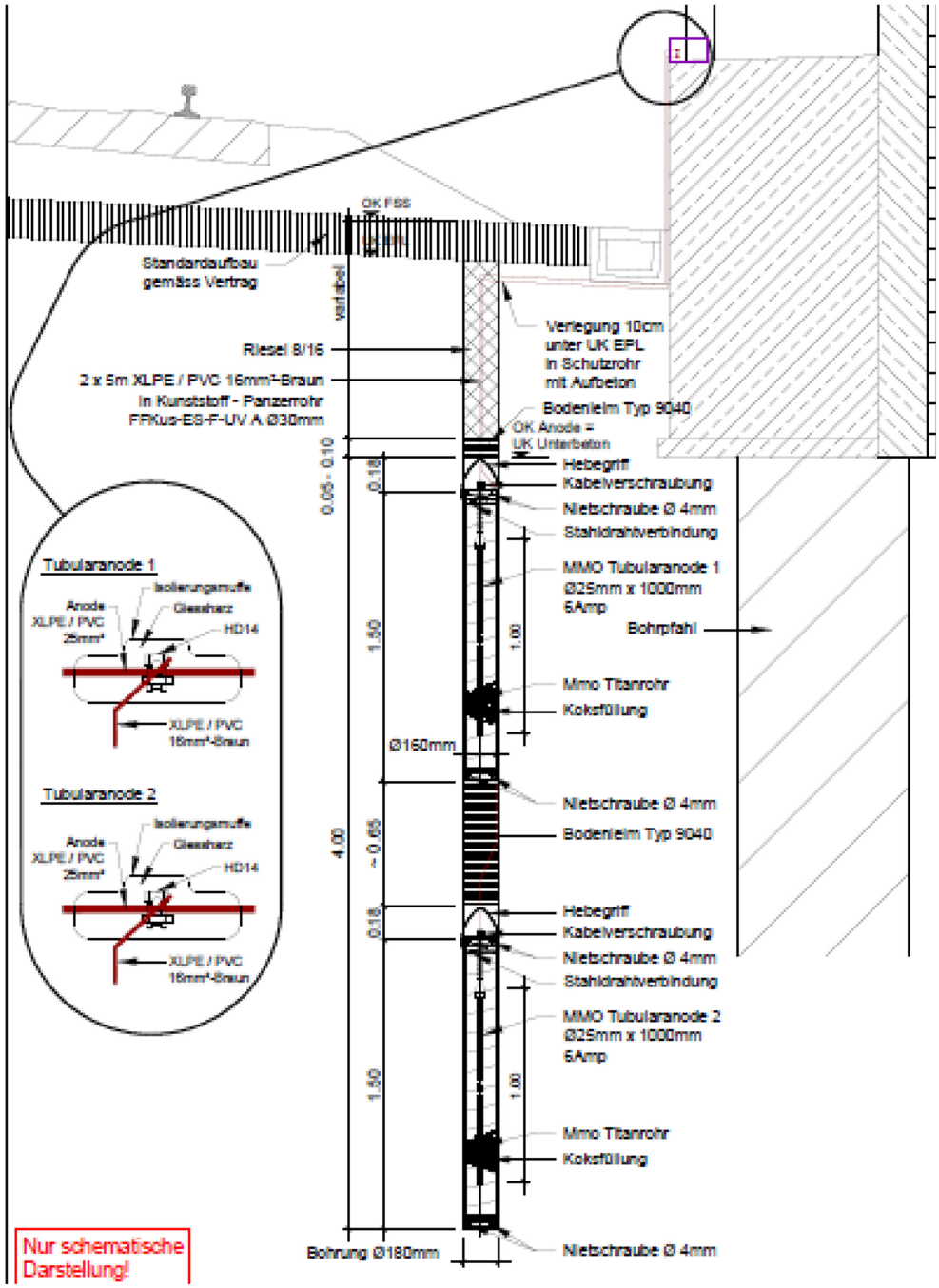

Figure 4. Installation of tubular MMO anodes in batch 31.

places, the holes were not vertical but at an angle and with up to three anodes in one hole. This solution was chosen in areas with no direct access to the pile.

The anodes were embedded in canisters filled with coke to reduce the transfer resistance between anode and soil. Moreover, gases which may be generated at the anodes can escape easily with a backfill of porous coke. In addition, the backfill of coke increases the activated surface of the anode which reduces the spreading resistance of the anode and keeps performance of the anode stable for a long time.

The monitoring system continuously records steel potential versus two different types of reference

electrodes: Mn/MnO_2 reference electrodes were cast into the concrete at the buried sections of the piles, $Cu/CuSO_4$ reference electrodes were placed in soil between the anode and the drilled pile. Furthermore, decay probes and special corrosion sensors will enable current readings in a way specialists can evaluate corrosion behavior at numerous spots.

Even though the soil indicated a low aggressivity milieu for corrosion and the system could have been designed as a preventive solution, the client did not want to bear any risk with respect to a 100 year lifespan and asked for a system layout capable of providing 15 mA/m^2 of steel surface.

3.2 *Power supply and communication*

Due to a stretched CP system with 19 cabinets along a railway route on 2.1 km with only a few options for cable transfer and various other technical equipment in the vicinity above and below the ground, cabling and power supply represented a great challenge. Moreover, all planning had to be in line with standards and guidelines for CP on concrete and buried structures and with a long list of regulations and instructions from Deutsche Bahn. Last but not least, all details had to be robust and durable.

Communication between the cabinets and sensors and power supplies, without interference, was made by fibre-optics.

4 CONCLUSIONS

This paper describes a challenging problem to protect an important structure, which had suffered from low cover to the reinforcement, from corrosion.

The innovative approach taken, using impressed current CP to solve the problem is described. It is well known that projects with Deutsche Bahn are high standard projects. We are proud to provide an innovative solution for a special case with CP.

REFERENCES

Baeckmann, W. V., Schwenk, W.*; Handbuch des kathodischen Korrosionsschutzes*, Wiley-VCH 1999 (in German).

Baeckmann W.V. et al. (1992). Messtechnik beim kathodischen Korrosionsschutz, expert verlag, 3. Auflage

DIN EN ISO 12696: 2912-05 *Cathodic Protection of Reinforced Concrete*

DIN- Handbook 219, *Corrosion and Corrosion Protection.* (2002), Beuth, 3. Edition

DIN EN 14505: 2005-07 – *Cathodic protection of complex structures*

Kompetenz-Center Korrosionsschutz, *Corrosion Protection of buried Pipes* (2002), Vulkan

Concrete Solutions – Grantham et al. (Eds.)
© 2016 Taylor & Francis Group, London, ISBN 978-1-138-03008-4

Assessment of the throwing power generated by a surface applied galvanic cathodic protection system on a light weight concrete bridge deck soffit

R.G. Giorgini
CorrPRE Engineering BV, Reeuwijk, The Netherlands

Hans van den Hondel
Vogel Cathodic Protection BV, The Netherlands

Joost J.W. Gulikers
Dutch Ministry of Infrastructure and the Environment, The Netherlands

ABSTRACT: As part of a triptych this paper will give insight in the research project which was carried out on a prestressed lightweight concrete bridge located in the Netherlands. This project started in the first half of 2013 and measurements are still ongoing on a regular basis.

Years of leakage at the longitudinal joint in between both bridge decks allowed chlorides to penetrate into the bridge deck soffit causing severe corrosion of the mild steel reinforcement eventually resulting in significant cracking and spalling of the concrete cover. As an economic remediation solution it was recommended to apply a Cathodic Protection (CP) system, preferably a galvanic CP system avoiding hydrogen embrittlement in the prestressed tendons.

Generally, it is assumed that only the reinforcing steel located beneath the concrete surface provided with surface applied zinc sacrificial foil will be protected. The objective of these on-site investigations is to have a better indication of the so-called throwing power by measuring the depolarization behavior at 3 different distances from the border of the zinc foil. Since 2013 potential decay values, current output and resistance of each separate zinc layer were monitored of the initial two zones in order to predict the service life of the zinc sacrificial system. The measurement results obtained so far indicate a major influence of the repair mortars used and moisture content of the concrete on the behaviour of the installed GCP system.

1 INTRODUCTION

This paper presents the set-up and the findings of a research project which was carried out on a prestressed lightweight concrete (1650 kg/m^3) bridge "Neerbosschebrug" located in the Netherlands. The investigations started in the first half of 2013 and measurements are still continuing on a regular basis.

Years of leakage at the longitudinal joint in between two parallel bridge decks allowed chlorides originating from the application of de-icing salt in winter periods to penetrate into the bridge deck soffit initiating corrosion of the mild steel reinforcement which eventually resulted into significant cracking and spalling of the concrete cover. As an economic remediation solution it was recommended to apply a Cathodic Protection (CP) system preferably a surface-applied galvanic CP system as this would pose no risk of hydrogen embrittlement in the prestressed tendons.

Generally, it is assumed that only the reinforcing steel located directly beneath the concrete surface provided with surface-applied zinc sacrificial foil will be protected. The objective of these on-site investigations is to have a better indication of the so-called "throwing power" by measuring the depolarization behavior at 3 different distances from the border of the zinc foil. In view of this, since 2013, potential decay, current output and resistance of 22 zinc strips were monitored in two bridge sections, in order to obtain a more reliable estimate of the effective service life of the zinc sacrificial system. The results achieved so far indicate a major influence of the repair mortars used and moisture content of the concrete on the behaviour of the installed GCP system.

2 EXPERIMENTAL PROCEDURE

The ZLA "zinc layer anode" system was applied in long strips over a length of 3.4 m (bridge section length) covering a width of 2 m divided over 2 bridge sections (section 2 and 3 of the northern part of the bridge). The zinc anode was applied on the concrete surface by using 22 strips of 8 cm width with a spacing of 1 cm between the strips.

Prior to application of the zinc strips the spalled and cracked areas of both sections were repaired. In section 2 approximately 2% of the total surface area



Figure 1. Spalled area of section 3.

was repaired and in section 3 a total of 33%. Two types of sprayed concrete mortars were used:

- Weber.tec SBN 170
- Grouttech NSM Multirep

At the soffit in both sections, Ø12 mm and Ø16 mm bars were used with a concrete cover varying between 25 mm and 46 mm. For section 2, the average cover depth amounted to 37 mm and for section 3, an average of 38 mm was detected. According to the design drawings, the distance between the first and second reinforcement mat amounts to 50 mm.

The following listing presents a summary with technical details of the test area of each section.

Section 2

- 2 cathode contacts and on/off K_0-switch for monitoring purposes;
- 22 zinc layer anode strips, width 8 cm, with a distance of 1 cm between neighbouring strips, anode surface area appr. 7 m^2 per section.
- each zinc anode strip is provided with an external electric contact.
- 8 Ti-decay probes (RE):
  - 4 RE's: R1 to R4 located at the depth of the first reinforcement layer,
  - 4 RE's: R5 to R8 located at the depth of the second reinforcement layer,
  - No RE's installed in the patch area.
- 4 Ti-decay probe RE's lined up partly in and beyond the anode area in the first rebar layer in a zone with most negative natural potentials, non patched area:
  - R9 within the anode area,
  - R10 at 20 cm distance from the anode area,
  - R11 at 40 cm distance from the anode area,
  - R12 at 60 cm from the anode area.

Section 3

- 2 cathode contacts and on/off K_0-switch for monitoring purposes;
- 22 zinc layer anode strips, width 8 cm, with a distance of 1 cm between the each strip, anode surface area appr. 7 m^2 per section.



Figure 2. Zinc strips applied on section 2 and 3.

- 22 external anode contacts.
- 8 Ti-decay probes (RE):
  - 4 RE's: R1 to R4 embedded at the depth of the first reinforcement layer,
  - 4 RE's: R5 to R8 located at the level of the second reinforcement layer,
  - 2 RE's: R9 and R10 in the patched area.
- 4 Ti-decay probe RE's lined up partly in and beyond the anode area in the first rebar layer in a zone showing the most negative natural potentials, non patched area:
  - R11 within the anode area,
  - R12 at 20 cm distance from the anode area,
  - R13 at 40 cm distance from the anode area,
  - R14 at 60 cm from the anode area.

All other necessary parameters of the test area were checked and approved, comprising:

- reinforcement steel continuity,
- resistance of each anode strip,
- anode and cathode connections,
- and the resistances and potentials of the reference cells,

3 RESULTS

On July 12, 2013 shortly after the start-up of the system, the resistances, the current outputs and potential decay values were measured. The readings are shown in Tables 1 to 4. The initial current output for section 2 was 28 mA whereas for section 3 an output of 25 mA was measured. These outputs correspond to approximately 3.5–4 mA/m^2 concrete surface area.

The readings of the decay probes R5 to R8 located in section 2 and 3 at the depth of the 2nd rebar layer (approximately 8–9 cm) as given in Table 3 and 4, indicate a good response of the steel on the current output although the surface area was repaired. During approximately 4 months, the response of the decay probes R5 to R8 located in section 2 was relatively poor (between 33–59 mV depolarisation) although they recovered well after that period.

Three Ti-decay probes in section 2, R10 at 20 cm, R11 at 40 cm, and R12 at 60 cm distance from the anode area and 3 Ti-decay probes in section 3, R12 at 20 cm, R13 at 40 cm, and R13 at 60 cm distance from the anode area, show limited response which was not sufficient for full protection according to the protection criteria in the codes. During the first year decay probes R10 in section 2 and R13 in section 3 both at 20 cm distance from the anode showed good response in accordance with the code-based criteria but this gradually reduced in the course of the second year.

4 DISCUSSION

According to the commonly applied international codes for cathodic protection, e.g. ISO12696, reinforcement steel is considered to be sufficiently protected against corrosion when a potential decay values of at least 100 mV from "instant off" is achieved over a maximum period of 24 hours or when a continuous potential decay over an extended period beyond 24 hours of at least 150 mV from "instant off".

Current measurements seem to have minor significance for the evaluation of protection of cathodic protection systems because the potential shift depends

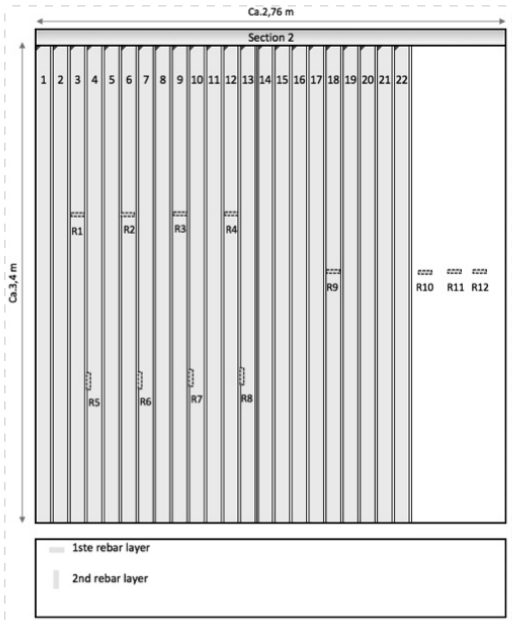

Figure 3. Section 2 : sketch of the anode configuration and decay probes.

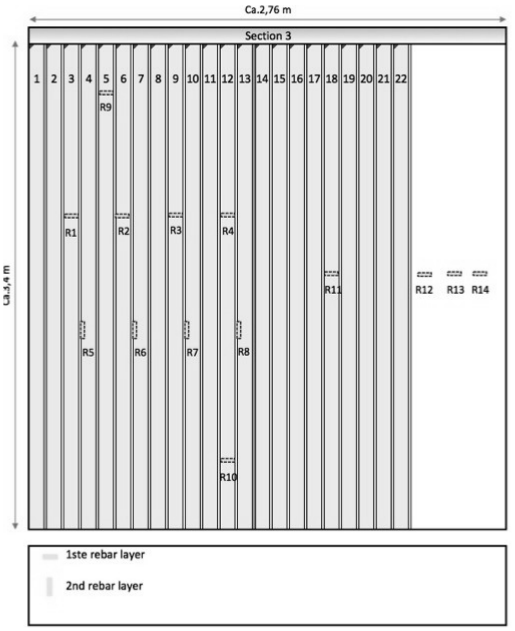

Figure 4. Section 3: sketch of the anode configuration and decay probes.

Table 1. Section 2, Resistances, Potentials and current outputs of each anode strip.

SECTION 2 Strip nr.	Al	A2	A3	A4	A5	A6	A7	A8	A9	A10	A11	A12	A13	A14	A15	Al6	A17	A18	A19	A20	A21	A22
Ohm	217	112	129	136	137	152	128	121	148	126	116	138	112	121	139	122	108	113	105	57	113	105
Potential my	1005	985	960	943	955	923	916	937	910	909	918	896	900	916	895	904	922	904	930	930	927	953
Current mA	3.8	6.3	5.3	5.1	5.1	4.5	5.2	5.4	4.6	5.3	5.8	4.9	5.9	5.9	5	5.7	6.6	6	7	6.8	6.3	6.9

Table 2. Section 3, Resistances, Potentials and current outputs of each anode strip.

SECTION 3 Strip nr.	Al	A2	A3	A4	A5	A6	A7	AS	AS	A10	All	Al2	A13	A14	A15	A16	A17	A18	A19	A20	A21	A22
Ohm	277	216	226	265	297	321	568	546	11.76	1115	960	1368	812	606	229	109	54	43	41.	75	97	108
Potential mV	956	920	921	904	890	881	831.	752	763	769	744	832	696	781	843	774	805	838	808	821	880	860
Current mA	2.2	2.8	2.7	2.3	2.0	1.8	1.1	1.0	0.5	0.5	0.6	0.5	0.5	1.7	2.5	5.5	9.5	11.8	10.0	8.0	6.8	6.1

Table 3. Section 2, potential decay values.

SECTION 2										
28/8/13	27/9/13	22/11/13	28/1/14	28/3/14	10/9/14	4/12/14	2/3/15	16/10/15		
depolarisation										
24 hr	3 hr	24 hr	3 hr	144 hr	26 hr	23 hr	74 hr	240 hr		
mV	mV	mV	mV	mV	mV	mV	mV	mV	RE	
240	151	461	376	148	132	157	263	300	R1	1st layer
337	203	387	452	123	138	183	240	304	R2	
217	108	241	214	64	65	83	109	101	R3	
231	134	225	226	75	79	101	155	123	R4	
146	76	160	131	42	55	61	87	95	R5	2nd Layer
157	92	165	173	66	68	77	130	121	R6	
187	162	237	234	72	78	108	139	141	R7	
224	141	320	271	92	111	116	190	173	R8	
270	314	481	324	182	166	226	289	184	R9	1st Layer
101	64	163	148	48	60	72	104	2	R10	
64	29	90	90	19	34	49	60	31	R11	
47	18	74	69	11	22	37	45	13	R12	

Table 4. Section 3, potential decay values.

SECTION 3										
31/8/13	31/8/13	27/9/13	29/11/13	28/1/14	3/2/14	10/9/14	4/12/14	23/3/15	16/10/15	
depolarisation										
24 hr	**79 hr**	**3 hr**	**24 hr**	**3 hr**	**144 hr**	**26 hr**	**23 hr**	**74 hr**	**240 hr**	
mV	mV	my	mV	mV	mV	mV	mV	mV	mV	**RE**
134	155	99	177	82	152	62	77	210	185	**R1**	1st layer
154	177	128	210	131	219	104	91	268	196	R2	
112	133	73	134	117	231	135	112	293	240	R3	
58	64	31	69	103	149	77	101	320	192	R4	
130	147	105	131	95	141	60	75	313	221	R5	2nd Layer
74	85	60	85	87	144	66	33	310	188	R6	
58	65	42	68	50	89	53	56	247	211	R7	
51	58	36	52	44	76	53	59	193	216	R8	
51	57	35	51	39	74	25	36	202	221	R9	1st Layer
31	39	23	39	45	70	37	38	209	213	R10	
285	333	195	298	453	533	307	192	363	180	R11	
87	102	75	103	87	138	86	82	81	33	**R12**	outside the
56	65	38	57	40	84	57	54	38	21	**R13**	anode area
25	49	22	31	25	60	41	40	26	−1	**R14**	

on the polarisation resistance of the reinforcement steel. It should be noted that the current densities mentioned in these codes are only meant to be used for design purposes and not as protection criteria.

The potential decay values in the tables demonstrate that most reference electrodes located near the first steel mesh layer respond well on the current output of each anode strip in both sections 2 and 3. A similar conclusion applies to the reference electrodes R5, R6, R7 and R8 located at a deeper level near the second steel reinforcement layer, taking into account the potential decay time in hours and seasonal effects which can be seen from the potential variations.

Readings of the reference electrodes R12, R13 and R14 located in section 3 show a gradual decrease of the potential response for a given current output of the anode which reflects the attenuation of the electric field in the concrete. The distance of the reference electrodes R12, R13, and R14 are 20 cm, 40 cm and 60 cm, respectively, from the outermost laying zinc strip.

When considering the results, the following phenomena should be considered which have a strong effect on the readings:

a) Response time of the equipment used to deter mine the "instant off" readings during the poten- tial decay measurements.
b) Resistivities of the concrete and applied repair mortars.
c) Macrocell corrosion currents.
d) Anode to cathode surface areas.

One of the major issues encountered during potential decay measurements when using less appropriate equipment is the exact determination of the true “instant-off” potential reading. When a reference electrode is placed to measure the potential of the cathodically protected structure, this measurement will

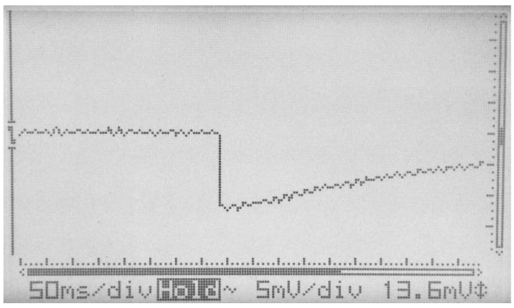

Figure 5. Oscillogram showing the “instant off” potential.

contain two components: (1) the steel-to-electrolyte potential and (2) the so-called IR-drop. The IR-drop error arises from the fact that current is flowing through the electrolyte and thus encounters an electrical resistance between the protected steel and the reference electrode.

This potential must be recorded quickly since the structure will start to depolarise immediately after switching-off the CP-current. According to the international code ISO 12696 measurements of “instant off” are taken typically between 0.1 s and 0.5 s after switching “off” but it is mentioned that the appropriate time will vary from system to system and with the extent/period of polarisation.

Most of the equipment used in the field does not have the possibility to perform quick readings due to the low response time of the devices, like multimeters. A response time is the time required for achieving the accuracy specified for the corresponding range.

Potential readings during this experiment were performed with a Fluke 115 and Metrahit 23S multimeter. The first value appearing on the display of the multimeter immediately after switching off the CP current was considered to be the “instant off” potential.

A simple laboratory test was performed to determine the response time of the equipment so as to have an impression of the error arising from the use of less appropriate equipment for “instant off" readings. A CP system and a reference electrode were installed on a concrete specimen on which the IR-drop could be exactly determined by measuring the impedance of the reference electrode and multiplying the value with the measured CP current. For this particular set-up the IR-drop was determined at 13.3 mV.

An oscilloscope was used to measure the IR-drop value due to the very quick response times of oscilloscopes, however care should be taken because oscilloscopes can be very sensitive to noise.

A total of 20 readings with the oscilloscope showed potential values between 13.6 and 29 mV.

Thereupon 3 multimeters, i.e. a Metrahit 23S, a Fluke 115, and a Fluke 287, were successively used to perform 12 “instant off” readings per device with the same CP lab set-up. Tables 5 to 7 provide an overview of the results.

From these tables it can be seen that the IR-drop (δ mV) calculated from the “instant off” potential

Table 5. “instant off” readings from a Metrahit 23S meter.

Metrahit 23S	on mV	instant-off mV	δmV
1	−625	−607	18
2	−625	−605	20
3	−625	−543	82
4	−625	−570	55
5	−625	−566	59
6	−625	−578	47
7	−625	−505	120
8	−626	−482	144
9	−627	−563	64
10	−627	−616	11
11	−627	−576	51
12	−627	−604	23
		Average=	58 mV
		SD=	41 mV

Table 6. “instant off” readings from a Fluke 115 meter.

FLUKE 115	on mV	instant-off mV	δmV
1	−637	−490	147
2	−637	−537	100
3	−637	−497	140
4	−637	−501	136
5	−637	−490	147
6	−637	−502	135
7	−637	−508	129
8	−637	−504	133
9	−637	−500	137
10	−637	−575	62
11	−637	−496	141
12	−637	−497	140
		Average=	129 mV
		SD=	24 mV

readings significantly differs from the true IR-drop (13.3 mV). It can be concluded that the “instant off“ potential readings obtained with these devices significantly overestimates the IR-drop values used to evaluate the cathodic protection system, which leads to an underestimation of the potential decay values. Despite the underestimation of the potential decay values, it shows that these devices are actually unsuitable for these kind of measurements performed on site.

Tables 1 and 2 show the direct relationship between the anode resistance and the current output. The resistances of each anode strip were measured with an LCR meter to avoid polarisation effects. Section 3 shows anode strips between nr A6 and A15 having relatively high resistances due to the mortar used for concrete repair.

The major part of the overall circuit resistance lies in the area in the immediate vicinity of the anode.

Table 7. "instant off" readings from a Fluke 287 meter.

FLUKE 287	on mV	instant-off mV	δmV
1	−638	−547	91
2	−638	−483	155
3	−638	−613	25
4	−638	−492	146
5	−638	−502	136
6	−638	−583	55
7	−638	−514	124
8	−638	−488	150
9	−638	−493	145
10	−638	−491	147
11	−638	−481	157
12	−638	−497	141
		Average=	123 mV
		SD=	43 mV

The total grounding resistance of an anode, involves 3 components:

1. The resistance of the lead wire and the zinc anode itself, which usually is so small that it can be effectively discarded. However, in case of extended cable connections, the voltage drop in the wiring must be taken into account.
2. The transition resistance between the surface of the anode and the electrolyte is usually low. It can be increased by films of grease, paint, rust or deposits. It contains in addition an electrochemical polarisation resistance which depends on the magnitude of the current.
3. The grounding resistance which depends on both the magnitude of the current and the potential distribution in the electrolyte.

The resistivity of the repair mortar used, i.e. Weber.tc SBN 170, was measured in the laboratory and showed a strong increase of resistivity over time. After 360 days of aging the mortar reached a resistivity of nearly 12.000 Ohm·m. As a comparison: for wet portland cement concrete, resistivities will normally range from 50 to 200 Ohm·m whereas values between 500 and 4000 Ohm·m have been determined for blastfurnace slag concrete and for dry concrete. Usually the resistivities will vary over a wide range, depending on the temperature and moisture content.

An important consideration applies to achieving a uniform current density at the reinforcement steel within each anode zone, as current distribution on the concrete surface is governed by the concrete resistivity or repair mortar resistivity as stated in the RILEM TC154 Report. That is considered one of the reasons why international codes like ISO 12696 provide guidance on how to take into account variations in concrete resistivity. Therefore, for concrete repair the use of repair materials with an electrical resistivity within a range of approximately half to twice that of the parent concrete when measured under the same

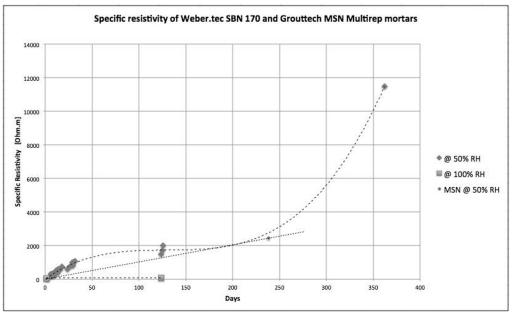

Figure 6. Progress of the resistivity over time of the 2 mortars used.

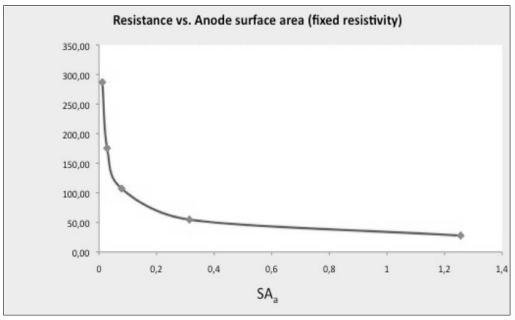

Figure 7. Graphic sketch of the theoretical relation between anode grounding resistance and anode surface area.

conditions as the parent concrete, is recommended. The resistivities of the repair mortars used have been determined and evaluated to identify possible effects by variations in the resistivities. Previous studies with galvanic anodes showed that the position of reference electrodes relative to the location of the anode can be critical when judging whether a system is performing well. These studies showed very clearly that potential decay readings were affected by the actively corroding bars located in close vicinity of the reference electrodes. The results also showed that the combination of passive and active bars embedded in close vicinity may produce a very high macrocell current resulting in such a strong polarisation that erroneous depolarisation readings may be obtained.

In many CP design recommendations and general literature on cathodic protection of steel structures and steel in concrete structures, anode/cathode surface area ratios, and limiting anode current densities are mentioned as points of particular interest due to the effect on the service life of anodes. Figure 7 shows the relationship between anode surface area and anode grounding resistance. It demonstrates that high anode surface areas facilitate higher current outputs.

The relation between anode resistance, current output, steel polarisation and anode/cathode surface area ratios concerning galvanic anodes is complex. This relation can only be explained in a qualitative way by using the "mixed potential theory". Figure 8 shows

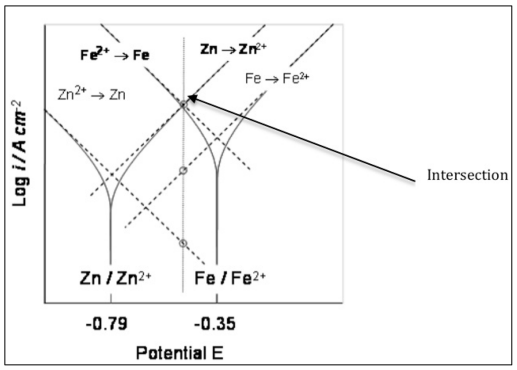

Figure 8. E-Log I polarisation curves of FE vs. Zn by using current densities.

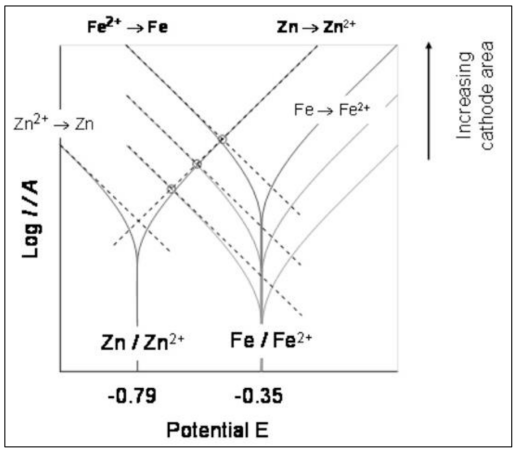

Figure 9. Theoretical E-log I polarisation curves of Fe vs. Zn by using total current output.

E-log I polarisation curves of an iron and a zinc electrode in an electrolyte. When electrically connected, the potential measured will be the point of intersection between the two curves and projected on the potential-axis which is the mixed potential of the two electrodes. This type of diagram is inadequate to reflect all the effects of galvanic coupling, as it deals with current density, and therefore is not able to show the effects of different surface areas between anode and cathode.

Figure 9 is actually re-drawn by not using current density but total current on the log I-axis. This diagram is, however, able to show the effect of changing the area of one electrode relative to the other, and if the cathode area increases, the potential becomes less negative which means less polarisation of the structure, although with an increasing current output.

This phenomenon for sacrificial anodes with small anode dimensions applied on reinforced concrete structures is well noticed in the field. The small surface area of these sacrificial anodes are barely able to polarise the steel reinforcement of the concrete as their surface area is many times smaller than the surface area of the steel reinforcement. A simple solution to overcome this issue is to apply anodes with increased surface area.

5 CONCLUSIONS

- Potential decay measurements show that for this specific situation the surface applied anode strips are able to polarise steel with a distance up to 60cm from the anode. Based on theoretical considerations the anode surface area will play an important role in the electric field distribution (throwing power) of galvanic anodes. Higher anode/cathode surface area ratios will increase the anode's "throwing power".
- Based on code based criteria, a distance of 10–20 cm from the anode will give sufficient corrosion protection, given the fact that for this experiment readings were performed with equipment which strongly underestimates potential decay values.
- The use of repair mortars with low electric resistivities will improve the performance of galvanic anodes by increasing the current output and the anode's "throwing power".

REFERENCES

ISO/FDIS 12696:2011. Cathodic protection of steel in concrete.

Bruns, M. & Raupach, M. 2009. *CP of the rear reinforcement in RC-structures – Numerical modelling of the current distribution.* Concrete Repair, Rehabilitation and Retrofitting. 2nd International Conference on Concrete Repair, ICCRRR-2, Nov. 2008, Cape Town, South Africa, M.G Alexander, H. Beushausen, F.Dehn and P. Moyo (Eds) CRC Press 2008, Pages 301–302

Baeckmann, W. von & Schwenk, W. Handbook of Cathodic Corrosion Protection. *Distribution of current and potential in a stationary electric field*. Elsevier, 1997

Giorgini, R. 2014. *Issues using potential decay techniques to assess a cathodic protection system of steel in concrete caused by macrocell corrosion*. Proceedings of Concrete Solutions 2014, 5th International Conference on Concrete Repair, Belfast. CRC Press, 2014

Giorgini. R. & Papworth, F. 2011. code based protection Galvanic cathodic protection system complying with criteria. Accessed from http://www.srcp.com.au/images/pdf/03-cia-galvanic-anodes.pdf March 2016

Kelly, R.G, Scully, John R., Shoesmith, D and Bucheit Rudolph G. *Electrochemical Techniques in Corrosion Science and Engineering* 2002, CRC Press

RILEM TC154-EMC.2003, *Electrochemical techniques for measuring metallic corrosion*. RILEM Publications Sarl.



Taylor & Francis
Taylor & Francis Group
http://taylorandfrancis.com

Concrete Solutions – Grantham et al. (Eds.)
© 2016 Taylor & Francis Group, London, ISBN 978-1-138-03008-4

The durability of reference electrodes in reinforced concrete applications

P.M. Chess
CPI FORCE Technology, Colchester, UK

O. Klinghoffer & B. Kofoed
FORCE Technology, Brondby, Denmark

ABSTRACT: The use of electrical potentials to judge the likelihood of corrosion by incorporating reference electrodes into the build of a structure has become much more popular in the last twenty years. There has also been a rise in the use of cathodic protection to repair structures which are suffering from premature reinforcement corrosion. In both these cases, an accurate measurement of the electrochemical potential of the steel close to the reference electrode is of great value. In these applications an extremely long life expectancy of the reference electrode is of great benefit both practically and economically.

This paper firstly looks at the concept of how the popular present day reference electrode works and gives a brief description of their construction. A review of the performance of the different types of reference electrodes in published literature is then carried out and consideration is given to why there is an apparent disparity in results between different projects.

1 INTRODUCTION

The concern over reaching the design life of reinforced concrete structures has become more pronounced over the last two decades and owners have started to be prepared to pay for real time corrosion monitoring systems. These systems are installed during construction and are designed so that they can provide real time data over the life of the structure. Normally there will several types of sensor placed at discrete locations considered to be most pertinent in achieving the design life such as at cold joints.

The most common sensors used for these systems are reference electrodes and these are are cast into the concrete during construction and ideally will last as long as the structure's design life, which can be up to 120 years.

The most popular application for reference electrodes in concrete is for monitoring the effectiveness of cathodic protection. This relatively modern technique has examples succesfully operating for more than 25 years and its use is becoming increasingly widespread

For this technique, a precise measurement of the reinforcing steels' electrical potential or changes in potential over a limited time period (typically 24 hours) is required and the reference electrode is the chosen sensor for measuring this.

2 REFERENCE ELECTRODE TYPES (1)

Any piece of metal on which an electrochemical reaction occurs will produce an electrochemical potential when in contact with a water electrolyte with dissolved ions. This potential is reproducible. The actual potential measured is dependent on several factors. The interface is the electrode and the electrochemical reaction is the electrode reaction. This can be seen in practice by the galvanic series. The amount and type of the dissolved ions has a significant effect on the electrochemical potential thus there is an attempt in reference electrodes to control their effect.

The normal laboratory reference electrode is the standard hydrogen electrode (SHE) which gives a very reproducible potential against which all other reference electrodes can be compared. By definition the SHE potential is 0 volts. Unfortunately this electrode type is only suitable for the laboratory as it works by bubbling hydrogen gas over a platinum electrode. Alternative reference electrode types have been developed and used over many years which have been designed to be buried in reinforced concrete.

The ideal reference electrode shall have the following properties:

1) Have a stable potential over a protracted time period of decades

2) Potential is defined by the thermodynamically stable reaction
3) Not be polarised by the measuring circuit but return to its fixed reference potential if accidental polarisation occurs
4) Have a small temperature coefficient
5) Robust design for concrete structures.
6) Immunity to changes in the chemical environment. This is particularly relevant in repaired structures where the anode may be encapsulated with fresh mortar which becomes chloride contaminated over the first few years.

Initially the reference electrodes tried in reinforced concrete structures mirrored those used in the conventional CP industry for pipelines but since the 1960's there has been a substantial evolution. Many types have been tried and found wanting and there are three, which now dominate commercially.

a) Silver/silver chloride/ potassium chloride. This is a metal encapsulated in a sparingly soluble salt which has an interface with a very soluble salt. The reason potassium is used and not the cheaper sodium is this has an ionic diffusion rate which is almost the same as the chloride ion and this minimises the error possible when there are concentration changes at the liquid junctions of the reference electrode. These reference electrodes have a silver core where the outer part has been converted to silver chloride either by dipping the silver foil in a molten salt or with an acid etch. This silver foil is then located in a plastic tube and surrounded by a potassium chloride solution. This solution is often thickened with an agent such as Aqua (a polymer thickening agent). A mortar plug is used to provide the interface to the concrete. In the US these reference electrodes were often placed in bentonite filled cotton bags. This practice was almost never followed in Europe.
b) Manganese dioxide/ sodium hydroxide. This reference electrode is based on proven alkaline battery technology. It is a double junction electrode containing an inner alkaline solution with a pH 13.5. The manganese ion has various valencies depending on which oxidation level is being achieved. In technical terms it is a mixed valency spinel. The various valency states provide the potential difference. By buffering at a high pH, the ratio remains fixed providing a reproducible electrochemical potential. The manganese dioxide is sparingly souble in an aqueous medium. The constant pH of the alkaline solution allows this junction potential to stay constant over many years.The electrode consists of a compacted mass of manganese dioxide in a stainless steel tube. This is interfaced with a solution of sodium hydroxide and a cement plug.
c) Mixed metal oxide (MMO) reference electrodes are used for short term measurements such as potential decay for cathodic protection systems. This MMO reference electrode has largely supplanted graphite which has diminished in popularity in the last two decades. They are not suitable for long term corrosion monitoring systems. They are a ceramic comprised of oxides of ruthenium, iridium and tantalum which are baked onto a titanium substrate. Unlike the two above reference electrode types there is little or no dissolution of the oxide and the electrochemical potential is caused by the presence of oxygen dissolved in the electrolyte. Surprisingly they are not as sensitive to the level of oxygen as was predicted (Myrdal, 2007) but they certainly are partially dependent on oxygen level. There will also be a significant direct effect caused by pH changes of the surrounding concrete on the potential measured.

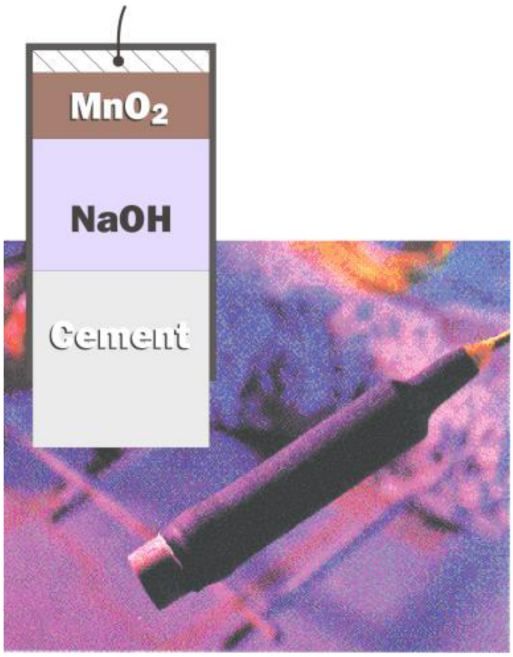

Figure 1. Sketch and photo of a manganese dioxide reference electrode.

A typical construction for these reference electrodes is a 3 mm diameter titanium rod coated with MMO. This is often connected to an insulated titanium wire as these electrodes are thought to have the greatest life expectancy, and the connecting wire is perceived as having a high risk of failure over the decades of service hoped for.

Silver/silver chloride and manganese dioxide reference electrodes have potentials defined by thermodymically stable reactions and therefore can be categorized as true reference electrodes while MMO is a so-called redox reference electrode.

2.1 *Field experiences*

Even though there have been hundreds, if not thousands, of cathodic protection systems in Europe of



Figure 2. Gimsøystraumen Bridge, Norway.

reinforced concrete with automated data logging systems and more around the world, there is a scarcity of data on the reliability of reference electrodes. This is possibly because it is perceived that the greatest risk of failure is with the anode component of the system and this is the item which is concentrated on. We reproduce several items of published data which has detailed the reliability of the electrodes.

2.1.1 *Example 1 – Gimsoystraumen Bridge, Norway (2delete)*

This is an exposed marine bridge which was being assessed as part of a long term corrosion monitoring program. Between 1993 and 1995 64 No reference electrodes of various types were installed and logged by an automatic data logger at 6 hour intervals. The data is given below for this structure in Table 1.

As can be seen, there are dramatic durability differences betweeen the various types of reference electrodes installed. The manganese dioxide and graphite electrodes have performed well while all the conventional (in European terms) silver chloride electrodes have failed. The cotton bag design, which did well, was an American innovation which has subsequently disappeared from view and has not been specified in any installation over the last ten years in Europe. The graphite references performed well while the lead references all failed. The reason for the failure of the silver /silver chloride reference electrodes was speculated on and it was concluded that it was 'probably due to loss of contact between the porous plug and the installation mortar'.

2.1.2 *Example 2 Dutch general survey of reliability of cathodic protection systems ()*

The Dutch looked at the CP systems that had been installed between 1987 and 2010 in the Netherlands and found that were more than one hundred and fifty systems. They had data on 105 of the systems and of these there were 56 more than 10 years old. There was significant reference electrode failures in 5 of these systems.There were 54 systems under 10 years old with electrode failures in two systems. It was not stated in a paper by Polder (2012) which reference electrodes were used but the majority were silver/ silver chloride/potassium chloride with some manganese dioxide.

2.1.3 *Example 3 Runcorn and Widnes viaducts*

Cathodic protection has been applied to various parts of this large series of bridge structures from 1993 to 2013 and reported by Atkins et al 2014. The number and type of references is listed below;

- Phase 1 there were 87 reference electrodes of silver/ silver chloride/ potassium chloride and graphite.
- Phase 2 there were 89 reference electrodes of silver/ silver chloride/ potassium chloride and graphite.
- Phase 3 there were 96 reference electrodes. No type specified
- Phase 4 number and type of reference electrodes not specified
- Phase 5 number and type of reference electrodes not specified
- Phase 6 number and type of reference electrodes not specified
- Phase 7 number and type of reference electrodes not specified
- Phase 8 there were 60 reference electrodes. No type specified

Their conclusions on the reference electrodes was this: 'generally the silver/ silver chloride electrodes were relatively stable and reliable. Approximately 5% of the installed silver /silver chloride electrodes failed. There was no evidence of this being related to age. The graphite probes originally employed as they were to be considered less likely to fail, were more erratic and unreliable. In the later systems mixed metal oxide coated titanium probes were also used and again these proved to be unreliable in service.'

2.1.4 *Example 4 German CP installations*

Esteves et al 2014 reported on a car park called Am Luwigsplatz in Darmstadt. A cathodic protection system was energised in June 2011 with 200 manganese dioxide reference electrodes. All were working two years later. In Germany only the manganese dioxide reference electrodes have approval for use in reinforced concrete structures as there is a system described as the Rili–SIB principle K (K stands for cathodic protection) where for products to be approved they must be laboratory and field tested to the approval of Federal authorities.

2.1.5 *Example 5 United States reference electrode field trials*

An American manufacturer of silver /silver chloride reference electrodes undertook long term field trials over a ten year period with three types of reference electrodes and reported their findings in the NACE conference (Ansuini and Dimond 2001). Tests were performed in both chloride containing and chloride free concrete. They embedded the silver /silver chloride of the cotton bag type (the reference electrode is placed inside this bag which is filled with a conductive backfill) and graphite reference electrodes when

Table 1. Reference Electrode Data Logging for Gimsoystraumen Bridge, Norway.

Type of reference electrode	Installed 1993	Installed 1994	Installed 1995	Total installed	Satisfactory peformance January 2002
MnO2 Ag/AgC1/KC1	16	12	4	32	26
Conventional cotton	–	–	4	4	0
bag' design	–	6	–	6	4
Graphite (C)	11	–	–	11	8
Lead (Pb)	11	–	–	11	1



Figure 3. Photo of Runcorn and Widnes viaducts.

they were constructing the slabs. The manganese dioxide reference electrodes were placed one year later in drilled holes.

It was found that these cotton bag silver / silver chloride reference electrodes showed good stability and durability over the ten years of the trials.

The graphite cells started to deviate 3 months after casting and it was decided that they were only suitable for short term measurements and should not be used to give absolute criteria.

The manganese dioxide reference electrodes were found to have good stability in chloride free concrete but some variability in the chloride contaminated slab. No attempt was made to see if this change was related to the fixing method for these particular reference electrodes which was different to the other two silver chloride reference electrodes.

3 DISCUSSION

Reference electrodes have become increasingly popular as measurement and control instruments for corrosion moitoring and cathodic protection control, indeed it is now very unusal to have any other monitoring devices in CP systems for concrete. As CP and corrosion monitoring have become more popular, the quantities of reference electtrodes used has massively increased and there has been a slow but fairly steady evolution of the types used.

From the examples given above, the lead reference electrodes were in all cases unstable and they are never now specified. Several other types have also been abandoned such as zinc (still popular in seawater) and copper / copper sulphate.

The graphite and now MMO coated reference electrodes were reliable in aggressive conditions but performed significantly worse in more benign conditions. These sensors should have the longest lives as there is a negligible consumption of the oxide but they are unsuitable for use with corrosion monitoring systems as they are probably only stable for days or weeks.

The silver/ silver chloride/ potassium chloride performed well in more benign conditions such as buildings and on land bridges but showed a very high failure rate on a marine structure. This finding is supported on other structures we are unable to quote from. The reason for this occurrence is not clear and could be due to the high levels of chloride contamination and rapid transmission rates by mechanical movement. The bagged silver chloride reference electrodes appear to be significantly more reliable. They are not generally available in the European market.

The manganese dioxide reference electrodes worked well in both benign and aggressive environments and also over long exposure time. Their principal drawback is that they have a significantly higher price then their rivals.

4 CONCLUSIONS

Reference electrodes suitable for placement in concrete have evolved and three types now dominate the market place;

The three types have different strengths and weaknesses

- The MMO reference electrodes are cheap and durable but cannot be used for corrosion monitoring systems and there are concerns over their stability.
- Silver/silver chloride/potassium chloride reference electrodes are popular and reliable in all but aggressive marine environments. Encasing these in a cotton bag with conductive backfill does appear to give significant durability benefits.

- Manganese dioxide reference electrodes are reliable in all environments. Their drawback is their higher price compared to the other electrodes.

REFERENCES

Ansuini F & Dimond J. 2001. *Long term field test of reference electrodes for concrete – ten year results*, NACE conference. Paper No 01296.

European Federation of Corrosion. September 2002. WP1. Task group 5 *Embeddable Reference Electrodes for Concrete.*

Myrdal R. 2007. European Federation of Corrosion. *The electrochemistry and characteristics of embeddable reference electrodes for concrete.* Woodhead Publishing Ltd.

Polder R et al. 2012. Performance and working life of Cathodic protection systems for concrete structures: Concrete Solutions conference, Dresden, 2012, page 157.

Atkins C, Brueckner R & Lambert P. 2014. *Field experience with remote monitored and controlled CP systems*. Concrete Solutions 2014. Michael Grantham, P A Muhammed Basheer, Bryan Magee, and Marios Soutsos (Eds). CRC Press 2014, Pages 147–151.

Esteves H, Meyer S & Stocklein R. 2014. *Cathodic protection of steel in concrete – experiences on parking garages in Germany*: Concrete Solutions 2014. Michael Grantham, P A Muhammed Basheer, Bryan Magee, and Marios Soutsos (Eds). CRC Press 2014, Pages 203–210.



Taylor & Francis
Taylor & Francis Group
http://taylorandfrancis.com

Concrete Solutions – Grantham et al. (Eds.)
© 2016 Taylor & Francis Group, London, ISBN 978-1-138-03008-4

An investigation into impressed current cathodic protection systems in Australian wharfs

P. Nicholls & D.W. Law
School of Engineering, RMIT University, Melbourne, Australia

ABSTRACT: Over the past forty years a significant number of corroding and at risk structures have been maintained using Impressed Current Cathodic Protection (ICCP). Recent studies have shown that steel within a concrete structure protected by ICCP can remain passive for a number of years after the system is discontinued. This indicates that a form of lasting or residual protection is afforded to the structure by the ICCP system.

This study examines this phenomenon of residual protection by suspending the operation of an established ICCP system in a Victorian wharf and monitoring the activity of the steel for a period of 106 days.Residual protection was observed in seven of the test beams located in the splash zone.The results appear to support the hypothesis that residual protection is dependent on the local environment as well as the amount of charge injected over the life of the structure.

1 INTRODUCTION

1.1 *Corrosion of steel in concrete*

The corrosion of reinforced concrete structures represents a significant cost to global economies. A studyconducted in 1999 by the United States Federal Highway Administration estimated the annual direct cost of the corrosion of reinforced concrete bridges in the United States of Americato be over five billion dollars, (Federal Highway Administration, 1999). Effective preventative maintenance and remediation strategies such as ICCP have an important role to play in controlling these costs.

The degradation of steel reinforced concrete structures is driven by the corrosion of the steel within the concrete. This results in the following:

- Delamination of the steel from the concrete matrix which reduces the ability of the concrete to transfer load to the steel (Vidal et al 2007)
- Reduction of the cross sectional area of the steel reinforcement reducing its ability totolerate load.
- The formation of cracks and spalls along the concrete surface. These spalls and cracks offer a pathway for water and contaminants, accelerating corrosion, as well as representing potentialsafety risks depending on the nature of the structure.

The corrosion of steel in concrete is due to the development of macro and micro corrosion cells on the surface of reinforcing steel(Bertolini et al., 2004). These anodic and cathodic areas form due to a variety of factors such as impurities in the steel or differences in the chemistry of the surrounding concrete. As such they are almost impossible to prevent via conventional manufacturing and construction techniques. The corrosion process is exacerbated by the presence of chloride ions. Chloride corrosion of the steel reinforcement is caused the disruption of the steel's protective passive film (Montemor, 2003). The exposed steel at this locationis anodic to the surrounding steel where the passive film is still intact. The resulting small anode to large cathode corrosion cell will cause rapid corrosion at the site of the disruption, known as pitting corrosion (Glass & Buenfeld, 2000; Angst et al., 2009). As a corrosion pit deepens the local environment within will become oxygen depleted favoring the formation of hydrogen ions. As more and more hydrogen ions are formed the interior of the pit becomes increasingly acidic, further increasing the corrosion rate. The result of chloride induced corrosion is both an increase in the likelihood and the severity of corrosion due to the localized nature of the attack. For this reason civil structures exposed to marine environments are at a significantly greater risk of degradation due to corrosion.

1.2 *Impressed current cathodic protection systems*

Impressed Current Cathodic Protection (ICCP) is an electrochemical technique first developed in the 1950s to arrest the corrosion of steel, particularly in aggressive environments. The basis of ICCP is to supply an electrical current to the steel reinforcement. Protection is afforded through a number of mechanismswhich can be considered as primary and secondary (Glass & Chadwick, 1994; Bertolini et al., 1998). The primary mechanism is theshift of the electrochemical potential of the steel to more negative values, reducing the steel's potential. A reduction in the potential of steel decreases the solubility of the iron ion

within the electrolyte which in turn reduces thecorrosionrate (Page & Sergi, 2000). Furthermore if the potential of the steel is shifted below a critical value known as the passive potential or E_{pas}, the steel will become thermodynamically stable (completely insoluble within the electrolyte) and corrosion will be arrested altogether(Pourbaix, 1996).

There are a number of effects which make up thesecondary mechanisms. They are all chemical changes which occur at the steel surface as a result of the applied current (Glass et al., 1991 & Glass & Chadwick, 1994). The first of these secondary effects is the production of hydroxyl ions at the steel surface. This is due to the cathodic reactions taking place at the steel which facilitate the breakdown of oxygen into ions which then react with the surrounding pore water to produce hydroxyl ions. This increases the pH directly surrounding the steel allowing the repair of the passive oxide layer (Bertolini et al., 2012) and returning the steel to the passive state. Reestablishing the pH of the concrete in this way is an electrochemical treatment in its own right known as re-alkalization. The next of the secondary effects is due to the steel becoming negatively polarized. As this occurs the steel will repel negatively charged chloride ions away from its surface (West & Hime, 1985) dropping the chloride concentration below the critical chloride thresholds for corrosion initiation and preparation. This prevents the initiation of new corrosion sites and preventing corrosion within existing sites. The final of the secondary effects is the reduction in concentration of oxygen at the steel surface due to the cathodic reaction occurring at the steel as a result. This will reduce the concentration of oxygen at the steel surface and as oxygen is also a reactant in the anodic reaction, reducing its concentration will reduce the potential corrosion reaction rate (Glass & Chadwick, 1994). The overall result of these secondary effects is to make the microenvironment at the steel surface passive and encourage the formation of protective oxides and hydroxides on the steel surface. This renders the steel itself passive resulting in a pronounced decrease in corrosion rate.

Whilst the operation of an ICCP system is able to reduce the effects of corrosion, there are several risks associated with its use. When the potential of the steel is depressed to sufficiently negative potentials (–1.1V, Ag/AgCl), reactions producing hydrogen gas become more prevalent. Hydrogen gas has the potential to diffuse into the steel and cause embrittlement resulting in brittle failure. This problem is particularly important in high tensile strength steels such as that used in pre and post stressedsystems. Additionally the use of ICCP systems has been linked with changes in the local chemistry of the concrete at the steel causing debondingof the steel from the concrete. These reactions also have the potential toaccelerate the alkali-silica reaction which results in a severe degradation of the concrete matrix (Pedeferri, 1996). Finally, whilst considering the chemical reactions which take place at the cathode, the use of an ICCP system will also cause a cascade of reactions at the anodes. These reactions are known to create hydrogen ions in a similar manner to that which can occur at the steel during corrosion producing an acid product. This causes acidification of the concrete at the anodes leading to dissolution and degradation of the cement paste encapsulating the anode resulting in loss of cohesion between the mesh and the concrete matrix. Hence, whilst the anodes themselves may or may not be affected this will reduce the conductivity of the concrete around the anodes and therefore reduce their ability to transmit current to the steel, reducing the ability of the system as a whole to protect the structure.

The reduction in the corrosivity of the concrete adjacent to the steel due to the secondary effects allows the operating current of the ICCP system to be reduced over time. The reduction of the current will reduce the likelihood of the negative effects discussed above therebypreserving the operational lifetime of the cathodic protection system (Brown & Tinnea; 1991; Pedeferri; 1996).

1.3 *Residual protection*

Research on existing structures with established ICCP systems has indicated that the passivity of the steel can be retained even after the applied current has been discontinued (Glass et al. 1991 & Presuel-Moreno et al. 2005). Initially the research focused on analysing the results of short term interruptions in the current as a result of either short term power outages in the case of unstable or solar power supplies, or inconsistent immersion within the electrolyte as is the case in tidally affected regions of concrete marine structures (Hassanein et al. 1999). However a recent study of ten structures in the United Kingdomwhose ICCP systems had been decommissioned showed that the steel within the structure remained passive, up to three years after the ICCP was decommissioned (Christodoulou et al 2010). This was determined by both potential testing and corrosion rate testing revealing steel potentials which are generally considered passive (consistently less negative than -150mV with respect to silver/silver chloride reference electrodes) as well as corrosion rates below 2μm per year. This indicates that an ICCP system may be able to provide a form of lasting or residual protection to a structure even when its use has been discontinued. It is likely that the ongoing passivity of the steel is due to a culmination of the secondary effects discussed earlier (Hassanein et al 1999 & Glass & Charwick 1994). These same effects are thought to be responsible for the noticeable reduction in the current required to maintain protection levels in newly installed cathodic protection systems (Polder et al. 2011).

Continued protection is not observed within all concrete structures where potential readings after as little as one to three days can indicate that corrosion has re-initiated at the surface of the steel.This may be due to a number of factors including different system design, different levels of exposure, differential oxygenation

of the structure, operating currents, cumulative charge and the local chemistry of the electrolyte.

This study explores this lasting or residual protection effect on established ICCP system installed on wharf infrastructure within the temperate waters of southern Victoria and aims to confirm the existing of residual protection on these structures as well as gain a better understanding of the criticality of the factors discussed above on the protective effect.

2 METHODOLOGY

This study is focused on a wharf with an established ICCP system located in Victoria, Australia.The ICCP system had been operating for eightyears at the time of this study.

An initial desk top review of the wharf was conducted prior to the initiation of the physical works. The review focused on the history of the wharf, ICCP design, commissioning reports and monitoring history. The important details focused on in this review were the length of time the ICCP has been active, exposure environment, deign current densities and charge passed to steel to at the beginning of the study.

Once the operational history of the wharf had been established the system was discontinued for a period of 106 days (approximately 4 months) and the condition of the steel monitored via the embedded silver-silver chloride reference electrodes in line with Australian Standard AS 2832.5 (AS 2832.5 2008). These reference electrodes were embedded into the concrete during the installation of the system eight years prior to the commencement of the study. They were placed at a variety of locations to provide a realistic representation of the potential of the steel throughout the wharf.

AS 2832.5 describes the steel as being protected from corrosion when one of the following criteria are met:

1. A potential decay over a maximum of 24 hours of at least 100 mV from the instantaneous off potential. This is known as the potential decay criterion.
2. A potential decay over a maximum of 72 hours of at least 100 mV from the instantaneous off potential to a continuing decay and the use of reference electrodes for the measurement extended beyond 24 hours. This is known as the extended potential decay.
3. An instantaneous off potential more negative than –720 mV with respect to a silver/silver chloride reference electrode. This is known as the absolute potential criterion.
4. A fully depolarised, or a potential which is continuing to depolarise over 72 hours after the ICCP system has been switched off which is consistently less negative than –150 mV with respect to silver/silver chloride reference electrode. This is known as the absolute passive criterion.

Criteria 3, the absolute potential criterion, is a measure of the thermodynamic stability of the steel in line with the Pourbaix diagram. The remaining criteria are designed to indicate the passivity of the steel. For this study the absolute passive criterion will serve as an indication of the passivity of the steel

In order to generate the required amount of data for a meaningful study of how the potential of the steel changes with time, a data logger wasutilized to measure and record the potential of the steel against the reference electrodes at two hourly intervals. This was to allow for the required granularity in the data whilst still falling within the capacity of the data logger.

2.1 *Structure description*

The wharf was built in the late 1960's with the first ship docking in 1969. The wharf consists of a series of concrete filled steel piles supporting transverse beams, which in turn support a cast insitu concrete deck. The wharf is aligned in a North/South orientation with the southern end more exposed to the elements than the northern. During its years of operation the wharf suffered from chloride induced corrosion of the reinforcement resulting in spalling of the concrete and a reduction in structural capacity. In 2007 the wharf underwent a large scale rehabilitation involving the reinstatement of the corroded elements, the installation of an ICCP system toforty four of the transverse beams at the northern end of the wharf as well as a separate system installed to protect the fender blocks at the southern end of the wharf.

The height of the beams relative to the average water level varies along the beam length, with the western most section of the beams sitting approximately 600mm higher than the easternmost section. This means that the easternmost section of the beams is more susceptible to the effects of the tide than the westernmost section. The beams are protected using internal discrete anodes to maximise cover to the anodes the thereforeminimisethe risk of acidification of the anodes.

Current to the ICCP system is provided via twenty four transformer rectifier units, eighteen of which provide current to the beams, and six of which provide current to the fender elements. This study focuses on the beam system, not the fender elements. These elements are not considered within this study except as a discussion point regarding the potential effects of interference at high tide. The beams have been grouped into cohorts of five, known as a region (regions are labeled i, through to ix). Within each region two zones (zones designated 1-18, matching the controller number) have been defined based on level of exposure, with each zone of beams within a regionreceiving current from a dedicated transformer rectifier unit. Zone two consists of the tidally affected easternmost portion of the beams, while zone one consists of the higher western portion which sits within the splash zone.

A total of 72 silver/silver chloride reference electrodes were installed across the transverse beams. The references were evenly distributed across zones one and two with eight references installed within each

Table 1. showing a summary of the results of the historical current analysis.

	Zone 1	Zone 2
Mean charge passed (MC)	43.15	15.31
Mean charge passed (MC) per sq/m	1.06	1.46
Median charge passed (MC)	43.88	16.39
Median charge passed (MC) per sq/m	1.07	1.56
Max charge passed (MC)	79.82	21.14
Max charge passed (MC) per sq/m	1.96	2.01
Min charge passed (MC)	27.15	7.51
Min charge passed (MC) per sq/m	0.67	0.72

Table 2. Showing the historical charge data for beams which displayed residual protection.

Beam number	Zone	Days passive	Total charge passed (MC)	Total charge passed (MC) per sq/m of steel
193	1	106	58.24	1.44
194	1	89	51.22	1.25
204	1	39	30.27	0.74
215	1	106	53.29	1.31
219	1	106	53.58	1.31
233	1	106	58.03	1.42
235	1	106	56.36	1.38

of the nine regions. All reference electrode potentials, along with the output current and voltage from the transformer rectifier units are monitored using an Aligent 34970A data logger system. The interruption and logging of the system commenced on the tenth of November 2014 and continued until the twenty fourth of February 2015 allowing the trial to run for a total of 106 days.

3 RESULTS

3.1 *Analysis of historical charged passed*

The ICCP system was designed to provide a current density of 20 mA/m^2 of steel reinforcement surface area without exceeding the rated anode output of 110 mA/m^2 of anode surface area. The system was designed to work on an operating voltage of four to five volts to prevent pitting of the titanium conductor bar. Analysis of the original construction drawings from the 1960s shows a steel surface density within transverse beams of approximately 41 m^2 within zone one and 10 m^2 within zone two. When combined with the output currents noted on the regular monitoring reports (reports conducted at approximately six monthly intervals) an approximation of the current injected into each zone, as well as the current injected per square meter of reinforcement surface area was calculated for each individual zone within each beam. A summary of this data is presented below in Table 1.Please note that when gathering data relating to the operating currents of the zones the “as found” currents were used to represent the time period between reports.

3.2 *De-energisation trial*

Of the seventy two reference electrodes installed within the forty four beams,sixty nine showed results indicating that the beams were being protected as per AS 2832.5. Due to equipment error,the potential monitoring data was lost between days zero and four and as such it is not possible to assess the system in line with criteria one and two of AS 2832.5. However the depolarisation achieved by day five is sufficient to indicate protection for the majority of beams. Of the three beams which did not produce results consistent with protection, a known defect in the ICCP system has prevented current flow to these beams for a period of months prior to the initiation of the study. These elements are excluded from this study as they the ICCP system has effectively been decommissioned to these beams for an unknown period of time.

Whilst the majority of the beams were shown to be protected, only seven displayed evidence of residual protection (defined by a potential consistently more positive than –150 mV during the trial) once the ICCP system was de-energised. A plot of beam potential against time elapsed for all seven beams, as well as four typical beams across the structure which were co-located with those that exhibited residual protection but which did not show residual protection themselves, have been included below.

Figures one to eleven show how the potential of the steel varies with time. Each figure shows a significant negative variation across all figures which occurred on the thirtieth of December 2014 which may have been due to a significant event at this time. Beams 233, 234 and 235 also show a significant negative excursion on the twenty fifth of January 2015 which indicates an electrical event at the northern end of the wharf. Figure one shows beam 193 where it is noted that there were a significant number of negative excursions throughout the test period indicating that there is an electrical event at the southern end of the wharf.

Across all figures there is a clear distinction between the amount of noise in the data between zones one and two. This is due to zone two being within the tidal zone. With the exception of the negative excursions (major and minor) the zone one potentials are very stable. The beams which display residual protection (figures one, two, five, six, eight, nine and eleven) the potentials are consistently more positive than -150mV and the beams have stopped depolarizing. The beams which did not display residual protection (figures three, four, seven and ten) also show consistent potentials however they are above the threshold for the steel to be considered passive.

The details of these seven beams are shown below in Table 2.

Across all figures there is a clear distinction between the amount of noise in the data between zones

Table 3. Showing the historical charge data for beams which displayed residual protection.

Beam number	Zone	Days passive	Total charge passed (MC)	Total charge passed (MC) per sq/m of steel
193	1	106	58.24	1.44
194	1	89	51.22	1.25
204	1	39	30.27	0.74
215	1	106	53.29	1.31
219	1	106	53.58	1.31
233	1	106	58.03	1.42
235	1	106	56.36	1.38

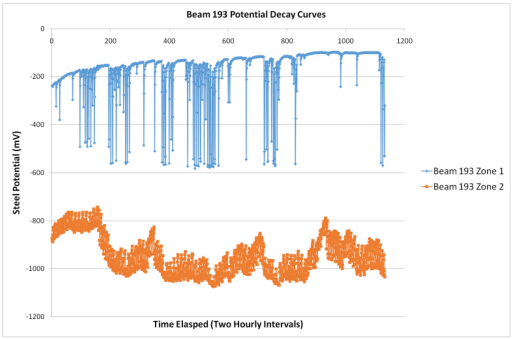

Figure 1. Potential V Time Graph for Beam 193.

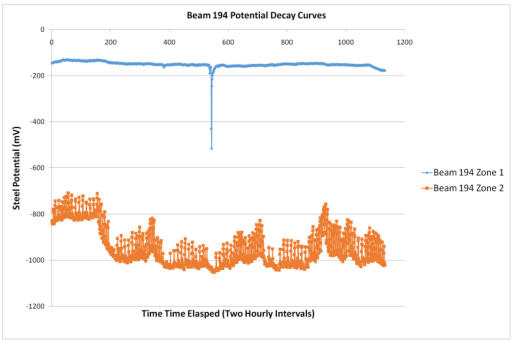

Figure 2. Potential V Time Graph for Beam 194.

one and two. This is due to zone two being within the tidal zone. With the exception of the negative excursions (major and minor) the zone one potentials are very stable. The beams which display residual protection (figures one, two, five, six, eight, nine and eleven) the potentials are consistently more positive than -150mV and the beams have stopped depolarizing. The beams which did not display residual protection (figures three, four, seven and ten) also show consistent potentials however they are above the threshold for the steel to be considered passive.

The details of these seven beams are shown below in Table 2.

4 DISCUSSION

4.1 *Analysis of historical charged passed*

Table 1 shows that a greater amount of charge was injected into zone one than zone two. However when this is normalised to take into account the steel surface area (as zone one extends for the majority of the beam, the quantity of steel within zone one is significantly greater than that within zone two)it is shown that a greater amount of charge per square meter of steel surface area was injected into zone two, the tidal zone. This finding is consistent with the intent of the design and the expectation that zone two will be a more corrosive environment. This expectation is based on the expectation of high moisture content in this region as a result of the twice daily wetting from the action of the tides coupled with the abundant oxygen provided when the front of the beam is exposed to the atmosphere.

It should be noted that the ICCP system for the fender beam, described earlier, will provide some protection to zone two at high tide when the lower elements of this zone and the fender beam are both immersed. This will reduce the current requirements of zone two. Whilst this does go some way to explaining why the current drawn for zone two is less than that for zone one, it is considered to be a minor effect compared to the differences in steel densities.

4.2 *De-energisation trial*

The beams which exhibited residual protection were spread very uniformly across the wharf indicating uniformity to the exposure conditions along the wharf front in line with expectations. All seven of the locations which demonstrated residual protections were located with zone one of the beams. Zone one is at a higher Reduced Tidal Level (RL)(located within the splash zone) of the structure. This is consistent with expectation as the higher zone is anticipated to be a less aggressive environment for the re-trial. Of the seven beams, the beam which became active the fastest was that which had the least amount of charge injected (beam 204) and the beam which became active next had the second lowest amount of charge injected per meter square of steel surface area (beam 194). This supports the assumption of previous works that the residual protection is due to the accumulated localised changes to the concrete environment as a result of the secondary effects of ICCP. The more charge injected into a particular beam, the more prominent these secondary effects will be.

It is clear from the results above that both the location (zone) and historical charge injected into a beam play a role in determining the presence of, and extent of residual protection. In order to explore this further, zone one of each beam was ranked according to the amount of charge per square meter of steel which was historically injected into that zone. The top rankings are shown below in Table 3 with the beams which exhibited residual protection highlighted.

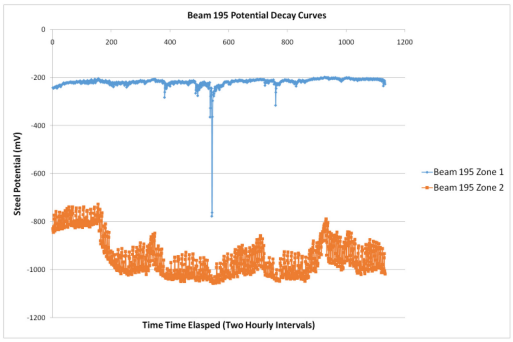

Figure 3. Potential V Time Graph for Beam 195.

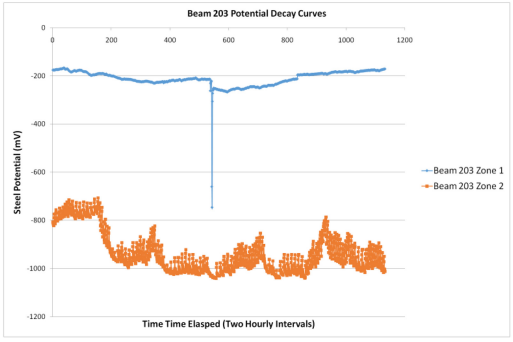

Figure 4. Potential V Time Graph for Beam 203.

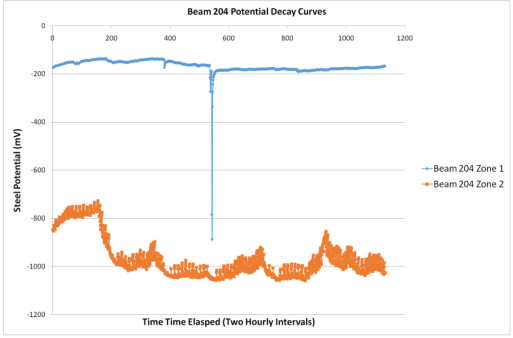

Figure 5. Potential V Time Graph for Beam 204.

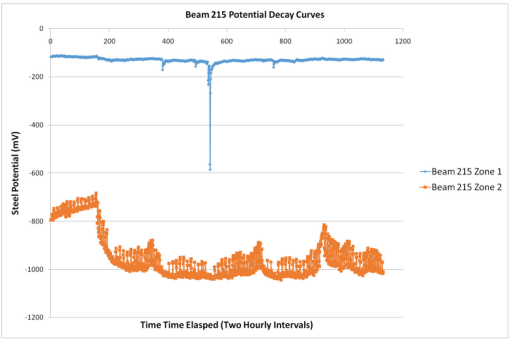

Figure 6. Potential V Time Graph for Beam 215.

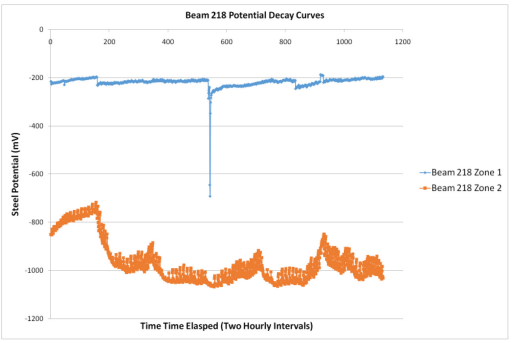

Figure 7. Potential V Time Graph for Beam 218.

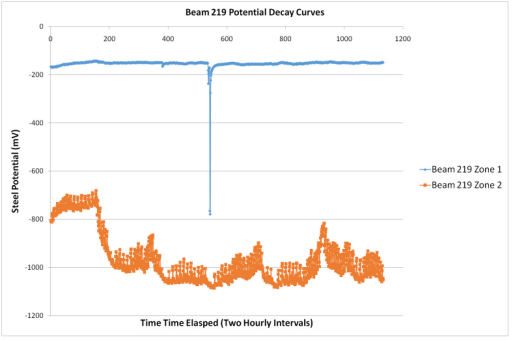

Figure 8. Potential V Time Graph for Beam 219.

It is interesting to note that the five beams which remained passive during the entirety of the 106 day test regime are all located within the top seven ranked beams whilst the eleventh ranked beam was that which remained passive for eighty nine days. It is curious to note however that the zone one of beams 221, 234, 224, 213 and 220 did not show residual protection despite being within the splash zone and having some of the higher levels of injected currents.

Also of note is that beam 204 did show residual protection despite being ranked twenty eighth. The reason for these anomalies may be due to unknown variations in the environment along the length of the wharf resulting in more or less aggressive corrosion environment at these beams

However it is more likely to be due to unrecorded variations in the amount of charge injected into each beam over the operational life of the ICCP system. Data describing the historical currents has been taken from the regular monitoring reports, which, whilst reliable, are only undertaken at six monthly intervals. For the purpose of this study the “as found” current outputs at the time of the monitoring were assumed to be representative of the currents since the previous monitoring. This may not have been the case and fluctuations in the

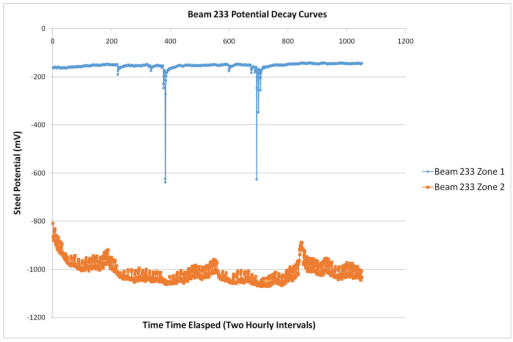

Figure 9. Potential V Time Graph for Beam 233.

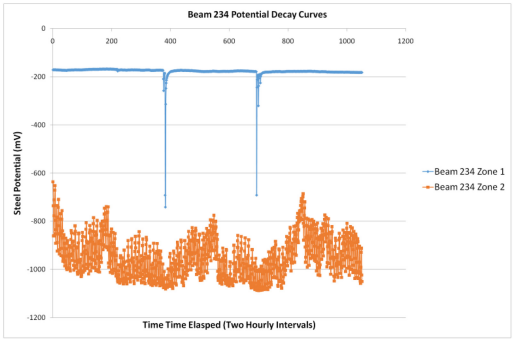

Figure 10. Potential V Time Graph for Beam 234.

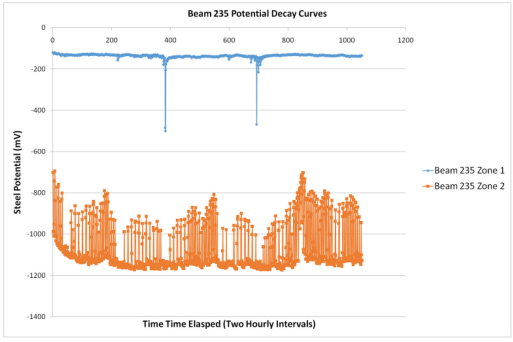

Figure 11. Potential V Time Graph for Beam 235.

level of current may mean that the true rankings differ from those shown in Table 3.

5 CONCLUSIONS

After a period of 106 days with the ICCP system de-energised the zone one portion of five beams out of forty-four were found to have remained in a passive state, while another two beams remained passive for a significant portion of the test period. All beams which showed residual protection were located within zone one which is within the splash zone as opposed to zone two which is in the tidal zone. When comparing the historical charge injected into the beams which showed residual protection to those that did not, a strong trend emerged that the beams which showed residual protection were those which had more charge injected. However there were a number of beams which had relatively high amounts of charge injected which did not show residual protection. This is thought to be due to limitations in the historical current information available.

The results show that residual protection of steel reinforced concrete is heavily dependent on the corrosivity of the local environment and also on the amount of charge injected over the life of the structure. This supports the idea that the residual protection is due to the accumulated secondary effects of ICCP. Further study is needed on structures with a more accurately known historically injected charge to refine the relationship between the amounts of charge injected and the time a structure remains passive.

Table 4. Showing the top ranked beams based on the charge per square meter of steel surface area injected into zone 1.

Rank	Zone	Beam Number	Total charge passed (MA)	Total charge passed (MA) per sq/m of steel
1	1	221	79.82	1.96
2	1	193	58.24	1.43
3	1	233	58.03	1.42
4	1	234	56.54	1.38
5	1	235	56.35	1.38
6	1	219	53.58	1.31
7	1	215	53.29	1.31
8	1	224	52.57	1.29
9	1	213	52.37	1.28
10	1	220	52.25	1.28
11	1	194	51.22	1.25
12	1	214	50.93	1.25
28	1	204	30.26	0.74

REFERENCES

Angst, U., Elsener, B., Larsen, C. & Vennesland, Ø 2009. Critical chloride content in reinforced concrete — A review.*Cement and Concrete Research* 39.

Australian Standard AS 2832.5 Part 5: Steel in concrete structures 2008.

Bertolini, L., Bolzoni, F., Pedeferri, P., Lazzari, L. & Pastore, T. 1998. Cathodic protection and cathodic prevention in concrete: principles and applications. *Journal Of Applied Electrochemistry*.

Bertolini, L., Elsener, B., Perdferri, P. & Polder, R. 2004. Corrosion of steel in concrete, Prevention, diagnosis, repair. John Wiley & Sons.

Bertolini, L., Lupica Spagnolo, S. & Redaelli, E. 2012. Electrochemical Realkalization as a Conservation Technique for Reinforced Concrete.*International Journal of Architectural Heritage* 6: 214–227.

Brown, R. & Tinnea, J. 1991. CP design problems for reinforced concrete.

Christodoulou, C., Glass, G., Webb, J., Austin, S. & Goodier, C. 2010. Assessing the long term benefits of Impressed Current Cathodic Protection. *Corrosion Science* 52.

Federal Highway Administration 1999.*Building More Durable Bridges*. FOCUS Federal Highway Administration, Washington DC, September 1999. p. 6.

Glass, G. & Buenfeld, N. 2000. Chloride-induced corrosion of steel in concrete.*Structural. Engineering*.

Glass, G. & Chadwick, J. 1994. An investigation into the mechanisms of protection afforded by a cathodic current and the implications for advances in the field of cathodic protection.*Corrosion Science*36: 1643.

Glass, G., Green, W. & Chadwick, J. 1991. Long term performance of cathodic protection systems on reinforced concrete structures. *U.K Corrosion* 3.

Glass, G., Hassinein, A. & Buenfeld, N. 2000. CP Criteria for reinforced concrete in marine zones. *.Journal of materials in civil engineering.*

Hassanein, A., Glass, G. & Buenfeld, N. 1999. Chloride Removal by Intermittent Cathodic Protection Applied to reinforced concrete in the tidal zone. *Corrosion* 55.

Montemor, M. 2003. Chloride-induced corrosion on reinforcing steel: from the fundamentals to the monitoring techniques.*Cement & Concrete Composites* 25: 491–502.

Page, C. & Sergi, G. 2000. Developments in CP applied to reinforced concrete. *Journal of materials in civil engineering*.

Pedeferri, P. 1996. Cathodic Protection and Cathodic Prevention.*Construction and Building Materials* 10: 391–402.

Polder, R., Peelen, W., Stoop, B. & Neeft, E. 2011. Early stage beneficial effects of cathodic protection in concrete structures. *Materials and Corrosion* 62 Number 2.

Pourbaix, M. 1996. *Atlas of Electrochemical Equilibrium in Aqueous Solutions*. Houston TX USA. NACE International.

Presuel-Moreno., F Sagüés, A. & Kranc, S. 2005. Steel Activation in Concrete Following Interruption of Long-Term Cathodic Polarization. *CORROSION.*

Vidal, T., Castel, A. & Francois, R. 2007. Corrosion process and structural performance of a 17 year old reinforced concrete beam stored in chloride environment. *Cement and Concrete Research* 37: 1551–1561.

West, R. & Hime, W. 1985. Chloride Profiles in Salty Concrete.*Materials Performance* 24: 29–36.

Concrete Solutions – Grantham et al. (Eds.)
© 2016 Taylor & Francis Group, London, ISBN 978-1-138-03008-4

Prevention of incipient anodes induced by patch repair by a novel type of discrete galvanic zinc anodes

W. Schwarz
CAS Composite Anode Systems GmbH, Vienna, Austria

M. Bakalli
Sika Technology AG, Zurich, Switzerland

M. Donadio
Sika Services AG, Pfäffikon, Switzerland

ABSTRACT: Corrosion of steel reinforcement as a result of repair of concrete damage is a common and well documented result of "patch repairs". The corrosion is caused by the transformation of cathodic areas near the corroding steel reinforcement into "incipient anodes". Cathodic Protection (CP) is one safe method to prevent the formation of incipient anodes. Very often, repairs have to be executed on locally limited areas where CP is not economical. Incipient anodes may be prevented by embedding discrete galvanic anodes into the patch repair close to the interface repair/old concrete, shifting the steel potentials of the passive steel towards sufficiently negative potentials to eliminate or at least minimize macro-cells. Considering the fact that the electrochemical potential of zinc is more negative than even the corrosion potentials of pits on reinforcement, discrete zinc anodes offer a thermodynamically sound possibility to prevent incipient anodes. Reports based on field tests of discrete galvanic anodes yielded mixed results on the durability and reliability of the prevention of corrosion of steel reinforcement adjacent to patch repairs, proving that relying on only the thermodynamics is no guarantee that systems work in reality. The main issues regarding durability and reliability of galvanic zinc anodes are passivation of the zinc anode and the production of anodically formed zinc hydroxide forming an ion-transport barrier. A novel type of discrete galvanic zinc anode will be presented that addresses and solves these issues. The novel discrete galvanic zinc anode system is composed of a novel type of composite zinc mesh embedded into a proprietary matrix that solidifies into an electrolyte with ion exchange properties. The combination of the novel composite zinc anode and the solid matrix containing additives that prevent passivation of the zinc anode assures high and durable galvanic activity of the discrete galvanic zinc anode.

1 INTRODUCTION

Corrosion of the steel reinforcement is one of the major causes for increased maintenance and repair costs and subsequently for the reduction of the service life of concrete structures. The major causes for the corrosion of the steel reinforcement are ingress of chloride into the concrete overlay due to the application of de-icing salts, due to exposure to sea water (Bertolini et al. 2013a, Raupach et al. 2006, Cigna et al. 2003) or due to carbonation of the concrete (decrease of pH). Corrosion initiated by de-icing salts or sea salt is due to the formation of macro cells, coupling corroding anodic sites with passive cathodic sites. Due to the macro cell coupling, corroding zones are acting as a galvanic anode providing a degree of cathodic prevention to the surrounding passive steel (Bertolini et al. 2013, Raupach et al. 2006, Cigna et al. 2003, Broomfield 1997, Dugarte et Sagües 2009). Consequent and lasting repair involves the removal of the macro cells, requiring the replacement of the chloride contaminated concrete entirely with repair mortar or shotcrete, or to apply cathodic corrosion protection on the affected areas of the concrete member. However, in many cases, local corrosion damage is repaired by patch repairs in which only the concrete surrounding the visible corrosion induced damage is removed and replaced. The durability of such repairs is affected by the "halo effect" (Broomfield 1997) wherein the steel within the new repaired area serves as a cathode generating accelerated corrosion of the steel in the surrounding area of the patch repair (Dugarte et Sagües 2009). Formerly anodic zones no longer provide protection, and corrosion can initiate in the areas surrounding the repaired zones (these have been called "incipient anodes" (Sergi & Page 2001, Bertolini et al. 2013b). For the purpose of forestalling the "halo damage", small galvanic anodes ("point anodes", "discrete galvanic anodes") are available commercially and have been applied since 1999 (Dugarte et Sagües 2009,

Sergi & Page 2001, Bennet & McCord 2006). The most comprehensive report on the performance of "galvanic point anodes" – two different types of commercially available anodes were tested over a period of 3 years – was made available in 2009 by the Department of Transportation of Florida (Dugarte & Sagües 2009). The main conclusions of the report were that the activity of the anodes decreased over time significantly and the anodes were estimated to function up to 1/3 to 1/4 of the theoretical consumption limit. Installed in a concrete containing 1.5% chloride/weight of cement, the point anodes tested over 480 days, showed only modest to negligible polarization of the reinforcement bars and were not sufficient for the prevention of initiation of corrosion. The efficiency of galvanic corrosion protection depends on the lasting activity of the zinc anode. Deposition and agglomeration of the anodic products or contact with calcium hydroxide in the pore solution may passivate the zinc anode surface (Schwarz et al. 2014). A novel discrete galvanic zinc anode system, composed of a of composite zinc mesh embedded into a proprietary matrix that solidifies into an electrolyte with ion exchange properties and containing additives that prevent passivation of the zinc anode assuring high and durable galvanic activity of the discrete galvanic zinc anode is presented in this paper.

2 CONCEPT

Incipient anodes in patch repairs are generated by the coupling of the passivated steel reinforcement bars in the patch repair with the reinforcement bars embedded into adjacent concrete with modest chloride contamination. The prevention of the formation of incipient anodes by discrete galvanic point anodes is not achieved by shifting the potentials of the corroding reinforcement bars as in cathodic corrosion protection but by shifting the potential of the passivated reinforcement bars towards potentials equal or more negative than the steel potentials of the reinforcement bars in the adjacent chloride contaminated concrete, eliminating the macro cell formed by the patch repair (Bruns 2015) as shown in figure 1.

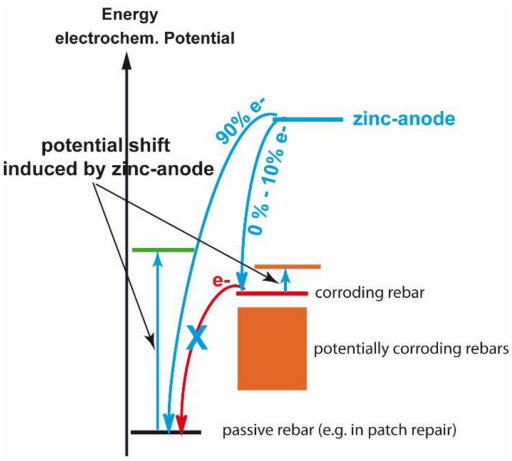

Figure 1. Schematic presentation of the prevention of the formation of incipient anodes by shifting the steel potential of the steel rebar passivated in the patch repair by attached galvanic discrete point anodes.

The activity and efficiency of galvanic anodes depend on the lasting activity of the zinc anode. Zinc tends naturally to passivate by formation of an impermeable zinc oxide/hydroxide layer. Depassivation of zinc is achieved either by embedding the zinc in a high pH matrix (pH > 13) or in a low pH matrix (pH < 6). As a result of the galvanic consumption of zinc in a high alkaline matrix OH^- is consumed and has to be provided either by 170 g KOH/100 g Zinc or by 73 g LiOH/100 g Zinc. If the pH drops below pH 13, the zinc anode will passivate. Depassivation in an acidic environment may lead to further acidification and autocorrosion of the zinc anode. Deposition and agglomeration of the anodic products at the anode surface or contact with calcium hydroxide in the pore solution may also passivate the zinc anode surface.

The anodic products formed need more space than the zinc-metal, e.g. zinc hydroxide consumes 2.34 times more space than zinc metal. Therefore, the anodic products may clog pores and hinder or even block ionic transport to and from the anode surface consequently passivating the zinc anode. The main factors controlling long term activity and durability of discrete galvanic point anodes are: a) prevention of passivation of the zinc anode surface, b) providing enough space for the anodic products formed and c) prevention of auto-corrosion of the zinc anode. The novel discrete galvanic zinc anode system relies on the following basic concepts:

(1) The activity and depassivation of the zinc anode surface is assured by embedding the zinc anode in a proprietary binder matrix described elsewhere in detail (Schwarz et al. 2014). The binder solidifies into a matrix with ion exchange properties containing additives that prevent passivation of the zinc anode assuring high and durable galvanic activity of the discrete galvanic zinc anode.
(2) The zinc anode itself is composed of a zinc-mesh matrix providing a high galvanic available



Figure 2. Sika® FerroGard® ICM discrete galvanic zinc anode (SFG-anode) for the prevention of the formation of incipient anodes induced by patch repairs.

surface from which only part is galvanically active and therefor assuring a nearly constant galvanic active surface over about of 90% of the theoretical service time.

(3) The surface/volume and zinc metal volume/anode volume ratio is such that there is enough space for anodic products formed to be accommodated without impeding ion transport and therefore galvanic activity. Besides the geometric volume ratio this is assured by a volumetric porosity of the binder matrix of at least 35 Vol.%.

(4) The electrochemical environment of the solidified binder matrix contains additives that reduce autocorrosion to negligible values.

(5) Two galvanized wired brackets are integrated into the anode allowing and assuring optimum and quick electrical connection to the steel reinforcement bars (figure 2).

3 EXPERIMENTAL SETUP

To evaluate the performance of galvanic anodes, measurements were performed in galvanic cells that simulate the conditions in a real concrete environment and allow accelerated testing. The set-up of the galvanic cell is shown in figure 3.

The steel electrodes consisted of 4 steel reinforcement bars (Ø 10 mm) connected by welding to a steel rod (Ø 6 mm) with a total steel surface of 200 cm^2. The concrete cell separator was cast with a repair mortar, 1-component CC mortar complying to EN 1504-3 as R4 mortar and having a resistivity similar to the host concrete. The electrolyte in the anode compartment consisted of a simulated concrete pore solution (pH 12.8–13.5), the catholyte consisted of a 1.5–2.0% NaCl solution, initially saturated with calcium hydroxide (CH). The current and steel potentials were measured and recorded online with the CAS MO-DAC monitoring and control system. Data were recorded every 30 min.

The galvanic cell shown schematically in figure 3 simulates the set-up of a patch repair in a concrete member: The SFG anode is connected to the rebar in the passivating environment of the patch repair simulated by the artificial pore solution with a pH of 12.8–13.5, separated by a 3 cm thick mortar slab (made from repair mortar) from the adjacent rebar immersed into a moderately corroding salt solution (1.5% NaCl, satd. CH, pH kept >9) – simulating the "old" concrete. The steel reinforcement bars are intensely aerated in both compartments. This set-up creates an environment that is very harsh in comparison to the real situation with respect to oxygen transport to the steel

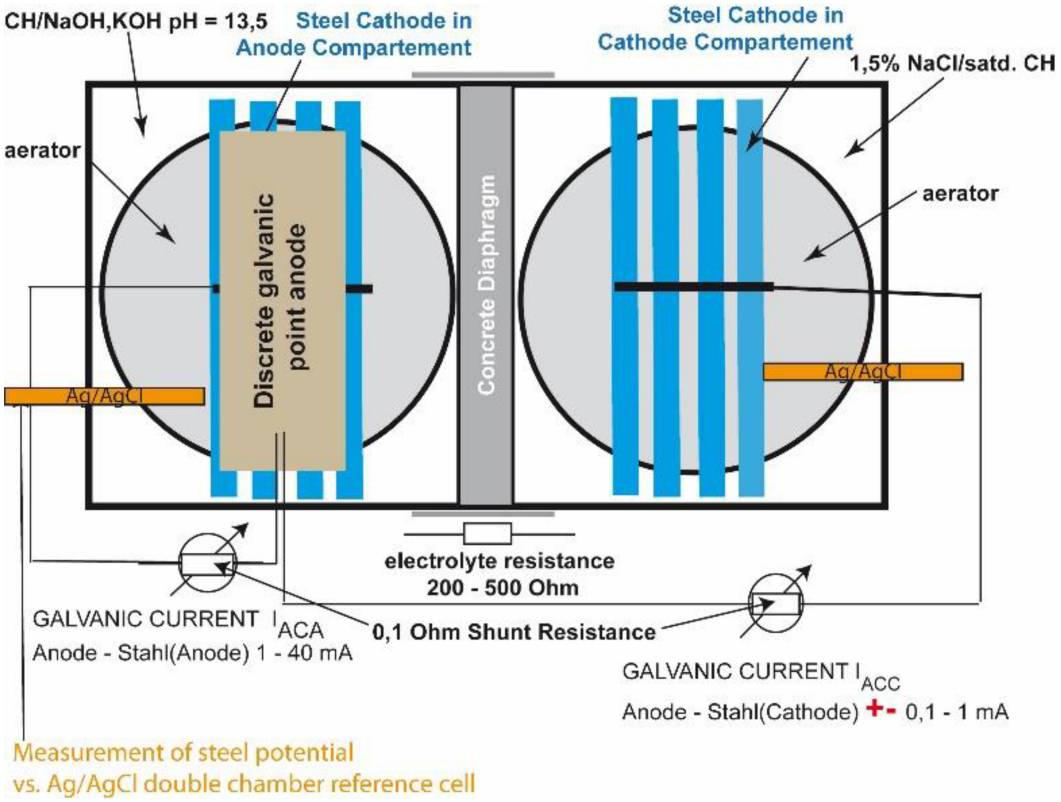

Figure 3. Scheme of the set-up of the galvanic cell simulating a real concrete environment for discrete galvanic point anodes embedded into patch repairs. The concrete diaphragm is prepared from Sika MonoTop®-412 N (Wenk 2013).

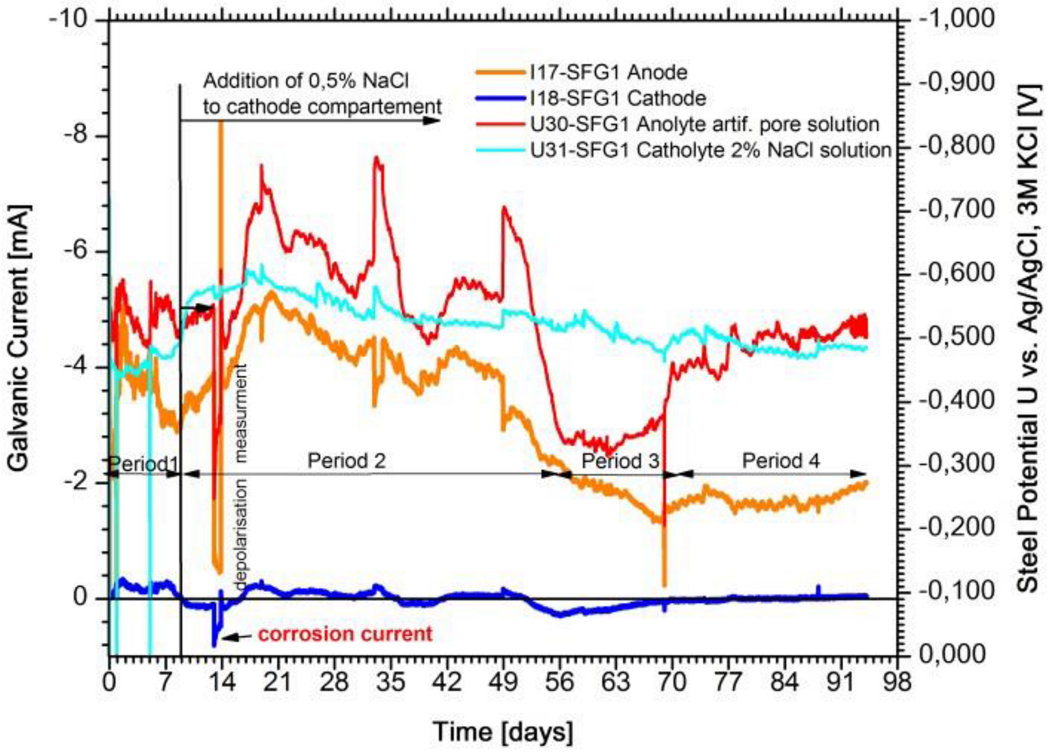

Figure 4. Galvanic performance of Sika® FerroGard® ICM discrete galvanic zinc anode (SFG-anode).

rebar surface and with respect to ion transport which is fast in solution but slow in concrete. Data received so far compared with published data (Dugarte & Sagües) indicate that the time scale in the galvanic cell set-up is about ten times faster than in a concrete environment.

The galvanic performance of the anodes for corrosion protection of steel reinforcement bars in chloride environment (3% NaCl) was evaluated in an electrolytic cell consisting of a 3-litre bucket in which an aerator, steel reinforcement bars and reference cell as shown in figure 3 were immersed in 1.5 litres of 3% NaCl.

4 RESULTS OF GALVANIC CELL MEASUREMENTS

The galvanic performance of an SFG anode (approx. 150 g zinc/anode, 650 cm^2 galvanically available surface, 127 cm^2 galvanically active surface, open circuit potential (OCP) −1160 mV vs. Ag/AgCl) was evaluated in the galvanic cell set-up described above and shown in figure 3. Results are shown in figure 4. The high initial current output of about 6 mA temporarily decreases to about 2 mA (period 1), increases again to currents in the range from 3–5 mA (period 2) which is characteristic for SFG anodes.

After about 1 month, the galvanic current decreases again and stabilizes at about 1.8–2 mA (period 2 & 3). The galvanic current to or from the steel rebars in the cathodic compartment (figure 4, I18 SFG1 Cathode) is in the range of −0.23 to +.0.25 mA. Negative values indicate corrosion protection – current flows towards the steel rebars, while the positive values reveal corrosion. The galvanic current is consumed by about 95% by the rebar in the passive environment of the anode compartment, only 5% is consumed by the reinforcement bars in the moderately corroding environment in the cathode compartment.

The galvanic current shifts the potential of the reinforcement bars in the "patch repair" environment from −240 mV vs. Ag/AgCl by about 300 mV to the level of the potential of the reinforcement bars in the corrosive environment (U31SFG1, about −550 mV vs. Ag/AgCl), efficiently eliminating the "corrosion cell", even slightly cathodically protecting the reinforcement bars by currents of about 1–3 mA/m^2 steel surface. The cathodic protection cedes temporarily by increasing the "corrosivity" of the environment in the cathodic compartment by increasing the NaCl concentration from 1.5% to 2.0% inducing a shift of the steel potentials towards more negative values by about 250 mV. The steel potentials of the reinforcement bars in the patch repair environment shift temporarily to values slightly positive of the potentials of the reinforcement bars in the corrosive environment.

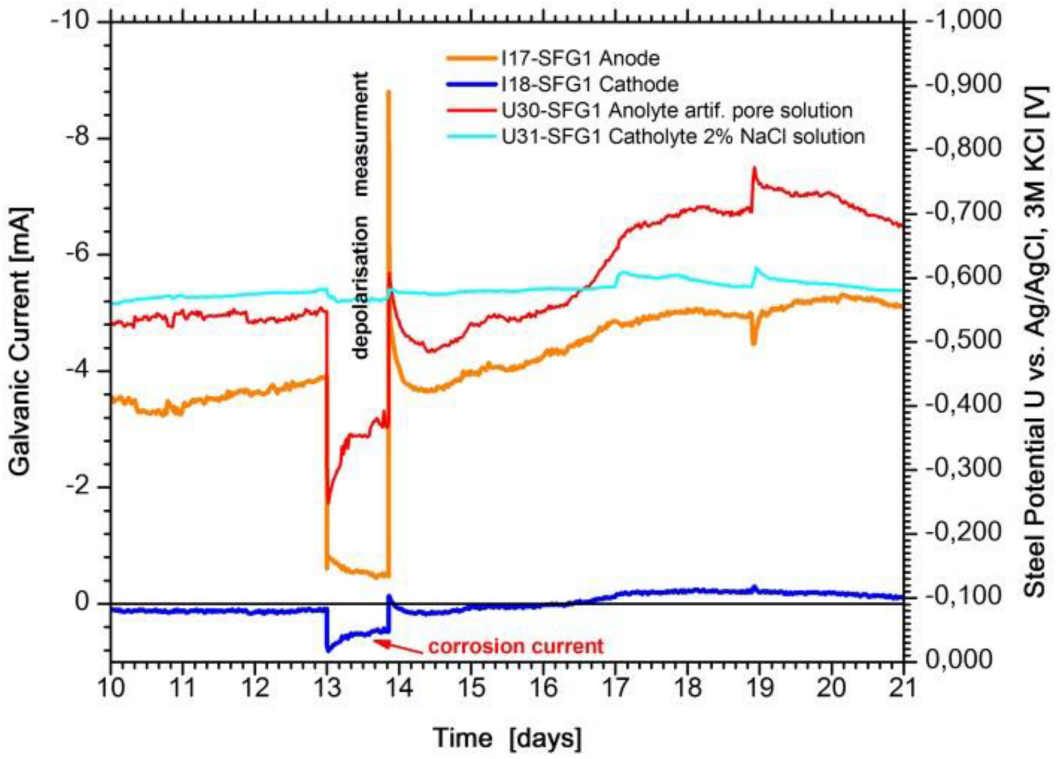

Figure 5. Current and steel potentials during depolarization measurement of a Sika® FerroGard® ICM discrete galvanic zinc anode (SFG-anode) in artificial pore solution.

The performance of the SFG anode in preventing incipient anodes is illustratively shown by the depolarization measurements executed by disconnecting the SFG anode from the system. Complete depolarization in solution is obtained within 3 hours (fig. 5) which is different from concrete where it usually takes 24 hours. The potential of the steel rebar in the patch repair environment shifts by about 300 mV rapidly towards the potential of a steel rebar in a passive environment (−260 mV).

The steel reinforcement bars in the corrosive environment shift by about 20 mV towards positive values, showing that the main effect of the discrete galvanic point anodes is the elimination of the macro cell by shifting the potentials of the passivated reinforcement bars rather than by protecting the reinforcement bars in the adjacent old concrete by cathodic polarization.

Depolarization establishes a macro-cell with a throwing power of about 300 mV and a corrosion current (about 3.5 $\mu A/cm^2$ of steel surface) flows between the steel reinforcement bars in the corrosive and passivating environment. As a consequence, a classic macro-cell is established. The corrosion current shifts the potential of the steel rebar in the patch repair environment towards more negative values as observed in real patch repairs (Wenk 2013). The corrosion current decreases due to that shift stabilizing at values of about 0.5 mA corresponding to 2.5 $\mu A/cm^2$ of steel surface. The currents measured are mirror inverted as the current flows between the steel-rebars.

The macro cell and consequently the corrosion current are immediately eliminated by reconnecting the SFG anode to the steel rebar electrode. The data shown in figure 4 demonstrate illustratively the mode of operation of the SFG discrete galvanic point anodes: Macro cells are eliminated and therefore the formation of incipient anodes is prevented by polarizing the reinforcement bars in the patch repair areas to levels nearly equal to the potentials of the steel reinforcement bars embedded into the concrete adjacent to the patch repair

The course of the potentials of the steel reinforcement in the patch repair environment is not always proportional to the galvanic current flowing to the steel reinforcement, especially during the time period 3 & 4 (figure 4): The steel potential remains nearly constant despite decreasing galvanic current and its value shifts to more negative values during period 4 while the current remains nearly constant. This might indicate passivation of steel rebars during time period 3. The evaluation of the performance of the SFG discrete galvanic anode for corrosion protection of reinforcing steel immersed and aerated in 3% NaCl solution, yielded at the beginning galvanic current of about 25 mA, corresponding to 1.2 A/m^2 steel rebar surface, stabilizing after about 2 month of operation at 3.7 ± 0.7 mA (185 ± 45 mA/m^2) (figure 6). In this

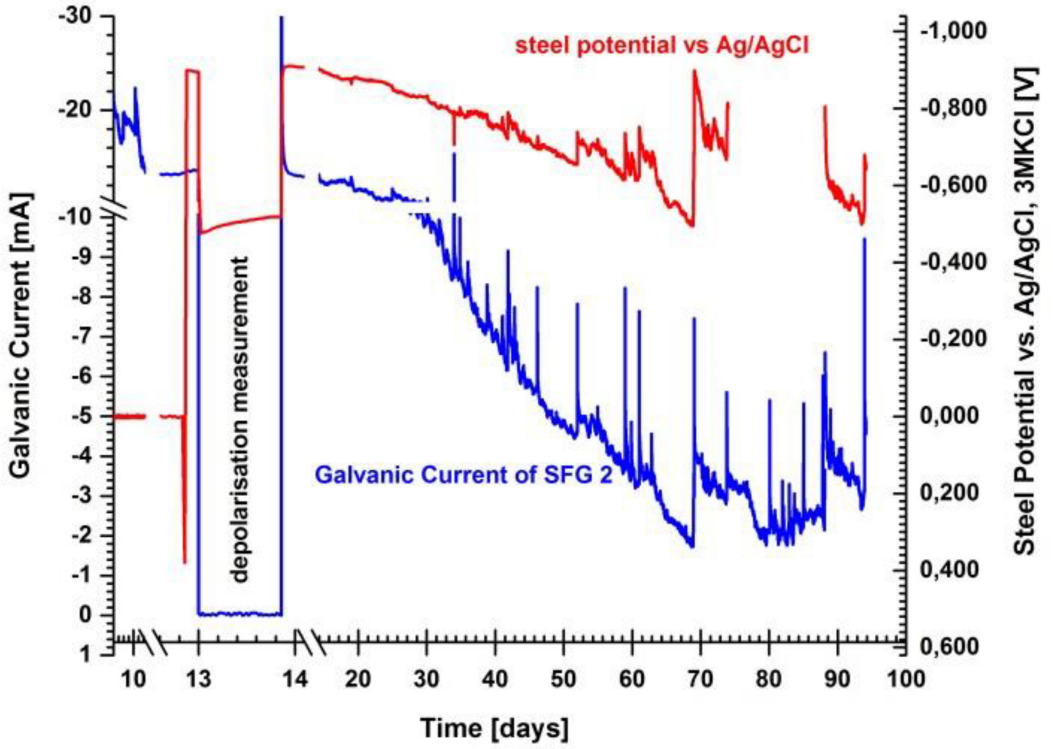

Figure 6. Galvanic performance of Sika® FerroGard® ICM discrete galvanic zinc anode (SFG-anode connected to an aerated reinforcing steel cathode, both immersed into 3% NaCl.

range, current densities depend strongly on the intensity of aeration of the steel rebars – explaining the "current spikes" in figure 6. The steel-reinforcement bars were polarized at the beginning to about −900 mV vs. Ag/AgCl yielding 4 hours depolarization values of 400 mV. The steel potentials are approximately proportional to the galvanic current stabilizing at −600 ± 40 mV vs. Ag/AgCl.

The high galvanic current output is due to the low cell resistance of 4.5 Ohm due to the low resistivity of the binder matrix in which the zinc anode is embedded. However, in a concrete environment, cell resistances between point anodes and steel reinforcement bars in distances up to 30 cm are in the range of several hundred Ohms while the galvanic corrosion protection is effective until about 50 Ohms.

5 CONCLUSIONS AND OUTLOOK

Patch repairs of steel rebar corrosion induced damage to concrete members are a common solution despite the fact that these techniques do not lead to a sustainable solution. Therefore there is a general need to eliminate the incipient anodes generated by the patch repairs. The formation of incipient anodes may be prevented by embedding suitable discrete galvanic point anodes into the mortar of the patch repairs adjacent to the concrete. Numerous galvanic anodes are on the market. However, to offer these galvanic anodes as an essential part of a sustainable concrete repair technique, these anodes have to be reliable in long term performance and durable in current output over a time period of at least 12–15 years.

The novel discrete galvanic zinc anode presented here was developed based on a concept accepted to assure the above defined requirements. The results of the physico-chemical and preliminary accelerated laboratory tests in galvanic cells indicate strongly that the novel galvanic point anodes fulfill the defined requirements. However, the obtained results have to be corroborated and complimented by tests in the field and in pilot test set-ups. These tests are underway covering different environmental conditions and concrete qualities and exposures.

Furthermore, a scientific based criterion may be formulated: Discrete galvanic point anodes should shift the steel potentials of the steel reinforcement bars in the patch repair mortar to potentials nearly equal to the steel potentials of the steel reinforcement bars in the adjacent concrete. Usually, the required potential shifts are in range of 150–250 mV. The effect of galvanic anodes on the passivation of steel rebars should be evaluated.

REFERENCES

Bennet, J. & Mc Cord, W. 2006. Performance of Zinc Anodes Used to Extend the Life of Concrete Patch Repairs, Paper No 06331, Corrosion/2006, NACE International Houston

Bertolini, L., Elsener, B., Pedeferri, P., Redaelli E., Polder, R. 2013. Corrosion of Steel in Concrete, 2nd Edition, Wiley-VCH, Weinheim

Bertolini et al. 2013, pp130

Broomfield, J. P. 1997. Corrosion of Steel in Concrete, Understanding, Investigation and Repair, Taylor & Francis, London

Bruns, M., August 2015. Ingenieurbüro Raupach, Bruns, Wolff GmbH & Co. KG, private communication

Cigna, R., Andrade, C., Nürnberger, U., Polder, R., Weydert, R., Seitz, E. (eds.) 2003. Corrosion of steel in reinforced concrete structures – Final report, *Cost Action 521, European Communities*

Dugarte, M. & Sagües, A. 2009. Galvanic Point Anodes for Extending Service Life of Patched Areas Upon Reinforce Concrete Bridge Members, Contract No BD 544-09, Final Report to the Florida Department of Transportation, 30 September 2009, NTIS Springfield, VA 22161

Raupach, M., Elsener, B., Polder R., and Mietz, J. (eds.) 2006. Corrosion of reinforcement in concrete, Mechanisms, monitoring, inhibitors and rehabilitation techniques, *European Federation of Corrosion Series EFC 38*, Woodhead Publishing Limited, Cambridge, UK.

Schwarz W., Müllner, F., van den Hondel, A. 2014, Maintenance and Repair of Steel Reinforced Concrete Structures by Simultaneous Galvanic Corrosion Protection and Chloride Extraction" in Grantham, M. Muhammed Basheer, P.A., Magee, B., Soutsos, M. (Eds.), *Concrete Solutions*, CRC Press, London, pp 223–228

Sergi, G. & Page, C.L. 2001. Sacrificial anodes for the cathodic prevention of reinforcing steel around patch repairs applied do chloride-contaminated concrete, in Mietz, J., Polder, R., Elsener B. *(eds.) Corrosion of Reinforcement in Concrete, Mechanisms and Corrosion Protection*, The European Federation of Corrosion Publication number 31, The Institute of Materials, London, pp. 93–100

Wenk, F. 2013, "Sika MonoTop-412 N, Measurements of specific electrical resistivity", Report Version 01, 16 October 2013, IBU Institut für Bau und Umwelt, CH 8640 Rapperswil



Taylor & Francis
Taylor & Francis Group
http://taylorandfrancis.com

Concrete Solutions – Grantham et al. (Eds.)
© 2016 Taylor & Francis Group, London, ISBN 978-1-138-03008-4

Application of a surface-applied cathodic protection system on a light weight concrete bridge – Part II: Developments in time of the effectiveness by potential decay values and current densities

A.J. van den Hondel
Vogel Cathodic Protection, Zwijndrecht, The Netherlands

R.G. Giorgini
CorrPRE, Reeuwijk, The Netherlands

J.J.W. Gulikers
Rijkswaterstaat-GPO, Utrecht, The Netherlands

ABSTRACT: As part of a triptych this paper gives insight in the research and investigations which were undertaken on a post tensioned light-weight concrete box girder bridge in the Netherlands. This project started in the first half of 2013 and measurements are still executed regularly. Due to long-term leakage of a longitudinal joint between two parts of the bridge, chlorides had penetrated into the concrete up to the level of the reinforcement and beyond, causing severe corrosion of the steel, spalling of the concrete cover and eventually causing danger for the shipping underneath the bridge due to falling lumps of concrete. To solve this problem, Galvanic Cathodic Protection (GCP) was applied in 2 stages. Firstly, in 2013, zinc based anode strips were applied on the soffit of 2 post tensioned lightweight bridge segments for the purpose of testing and monitoring. After obtaining good results from the test, in 2014/2015 the remaining 29 bridge segments were repaired and protected with the same GCP system as well.

This paper reviews subsequent potential decay measurements, which have provided much more information on GCP performance and throwing power. The results of anode performance at different locations and depths are reviewed. Repair mortars and the moisture content of the concrete have also shown a major influence on the behavior of the installed GCP system.

1 INTRODUCTION

1.1 *The object*

The object concerns the Neerbossche Bridge which spans the Maas-Waal canal at Nijmegen, The Netherlands (Figure 1). The bridge is a post tensioned double box girder bridge from 1982, of which the structure above the canal is constructed with light-weight concrete (1650 kg/m^3). The in-situ cast concrete segments have a length of about 3.4 meters. For each box girder, the part of the bridge located between the piers comprises 33 segments of which the 2 segments above the piers are constructed with conventional normal weight concrete. So each box girder is comprised of 31 light-weight concrete segments above the canal. The soffit of the light-weight concrete sections of the southern box girder showed serious damage and consequently maintenance was required in the short term in view of structural safety as well as possible danger for the shipping underneath the bridge due to falling lumps of concrete.

1.2 *The project*

The damage in the bridge was extensively investigated and reported in a preliminary phase and it was concluded that the damage was limited to the concrete surface at the soffit of the northern cantilever of the span of the southern bridge (Figure 2). Due to long-term leakage in the longitudinal joint between the northern and southern bridge, chlorides originating from the frequent application of de-icing salt during winter periods had penetrated into the concrete up to the level of the reinforcement and beyond. As a consequence, the mild steel reinforcement had started to corrode which eventually resulted in the development of significant tensile stresses in the concrete, leading to cracks, delaminations and spalling at multiple locations. The corrosion induced damage amounted to approximately 44 m^2, which was about 22% of the total surface of the soffit. At other locations, the likelihood of corrosion was demonstrated by corrosion potential measurements which showed values down to −450 mV ($Cu/CuSO_4$) and −350 mV (Ag/AgCl; see Figure 3).

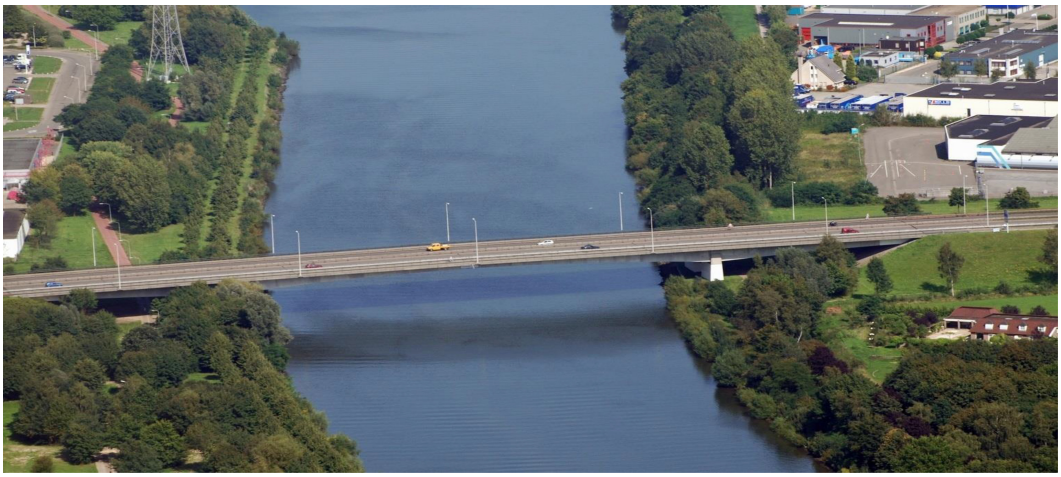

Figure 1. The Neerbossche Bridge over the Maas-Waal canal.



Figure 2. Location of the damaged cantilever (southern bridge).

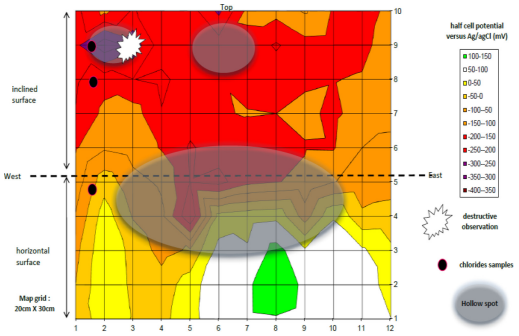

Figure 3. Corrosion potential measurements at the cantilever in the southern bridge. The grey areas denote hollow spots and the white flash a destructive investigation point.

As a long-term solution to this problem, Cathodic Protection (CP) was considered to present a viable and economical option. As the structure was post tensioned, Galvanic Cathodic Protection (GCP) was in favor to be applied in order to avoid the risk of hydrogen embrittlement in the high quality steel tendons. In the summer of 2013 the steel reinforcement in 2 bridge segments was protected with zinc based strip anodes, for testing purposes applied in small size foils which could be connected to the reinforcing steel on and off separately. Also a large number of reference electrodes (titanium decay probes, referred to as RE's) were embedded in the concrete of these 2 segments in order to monitor the effectiveness of the CP system, not only within the protected area but also outside the protected area.

With these 'remote' RE's the so-called throwing power of this CP system could be established. For the same reason RE's were installed at different depths in the concrete cover as well as in repaired areas in order to study the corrosion behavior of the steel in these areas due to the action of the CP system.

In view of the good results that were obtained in this test and the suitability of this GCP system was proven, the full scale project on the remaining 29 bridge segments was executed in the winter of 2014/2015.

1.3 *Scope of the paper*

This paper is part II of a triptych. Part I gives detailed information on the preliminary phase and also on the process of selecting the preferred repair strategy and finally on the results from the test in 2013.

This part II will focus on the highlights of the full scale project in 2014/2015 and will provide results from the still ongoing research and investigation on the effectiveness of the GCP system over time, by measuring potential decay values and current densities.



Figure 4. The access to the soffit at the damaged cantilever.



Figure 5. The workspace created underneath the bridge.

2 THE APPLICATION OF THE GCP SYSTEM

2.1 *Accessibility of the soffits*

The canal underneath the bridge and the location of the cantilever in between the two box girders, at a height of approximately 10 meters above the water level, resulted in poor accessibility. In the past, a vessel with a scaffolding was used for the investigations on this part of the bridge, but due to the busy shipping on the canal and the instability of this kind of construction at a height of 10 meters it was not suitable for the extensive project. A new way for accessibility, developed in the USA, used cables across the canal to create a suspension bridge (Figure 4 & 5). This solution resulted in a good and safe access to the soffit, with no hindrance to the shipping and the possibility to create a closed environment above the water (preventing pollution of the water surface and enabling to work during the winter period).

2.2 *Concrete repair*

The concrete was repaired in accordance with the code based international standards (ISO-EN12696) regarding the surface pretreatment, instead of a full traditional repair with the removal of all chloride-contaminated concrete. Therefore, only the spalled and delaminated concrete parts were removed, the corroded steel bars were sandblasted up to a level of St2 after which a mineral-based mortar was applied to achieve a smooth surface.



Figure 6. Repair of the damaged locations with shotcrete.

The mortar had to be chosen carefully because the light-weight concrete had special features regarding water absorption, aggregates and tensile strength. A good bonding of the repair mortar on to the light-weight concrete had to be achieved, thus the shrinkage of the mortar, the initial absorption of water from the fresh mortar into the old concrete and the water and cement content of the repair mortar had to be adjusted for the two materials. At the same time the mortar had to be suitable for the application of CP, mainly with regard to the electrical resistivity of the mortar. In accordance with the code based CP standards the resistivity of the mortar should not be less than 50% of the resistivity of the original light-weight concrete and should not exceed 200% of this value. Depending on the location, mainly with regard to the moisture conditions, the resistivity measured with a Wenner probe varied between 100 to 500 Ωm in the areas adjacent to the leaking joint and up to 2500 Ωm at the dryer side of the box girder.

Because of the importance of this part of the maintenance, the type of mortar as well as the method of applying the mortar to the surface, was part of the test in 2013 and resulted in the application of shotcrete using a light-weight mortar with a high cement content and no additives (Figure 6). Shotcreting resulted in less shrinkage and better bonding to the original surface (1.3–1.7 N/mm^2). The mortar (Grouttech NSM Multirep) demonstrated resistivity values ranging from 110 to 160 Ωm measured at 100% RH and 7100 to 7500 Ωm at 35% RH and therefore met the requirements.

Before the mortar was applied, the surface at the repair location was treated by drilling in dowels (16 Hilti M8-100 per m^2). This is common practice in the application of shotcrete at pending surfaces in order to withstand the stresses due to shrinkage of the fresh mortar. Also, the light-weight concrete surface was, prior to the spraying of shotcrete, pre-moistened several times to prevent water being adsorbed from the



Figure 7. Application of the zinc anode in strips.

applied fresh mortar. Finally, the shotcrete was applied in 2 successive layers, resulting in a total thickness between 20 and 50 mm. The first layer was sprayed with a thickness of 10 mm in order to achieve a good adhesion with the light-weight concrete substrate. Subsequently, after 2 hours, the second layer was applied to the appropriate thickness. Thereupon, the surface was finished in profile and protected against drying out with polythene sheets for 7 days.

2.3 *Cathodic protection*

After having repaired the concrete, the steel reinforcement was protected with a surface mounted anode, i.e. a Zinc Layer Anode (ZLA; CorrPRE). This anode is applied as a foil on the surface and consists of a 250 μm thick zinc sheet provided with a 750 μm thick ion-conductive adhesive. The adhesive is designed to adhere the zinc strip onto the concrete surface, while simultaneously acting as a zinc activator and conducting electricity.

Based on corrosion potential measurements and the test results on the 2 bridge segments performed in 2013 it was concluded that the complete surface of the soffit should be covered with the zinc anodes (Figure 7). As there was no economic benefit in the application of ZLA in strips with a certain spacing, in order to save material costs, the complete concrete surface was covered with zinc strips using the standard width of 25 cm. The 'protection period' of the ZLA (i.e. material consumption over time) in relation to the cost for accessibility at the moment of an earlier replacement of anode material, made it clear that the application of extra ZLA would have a beneficial impact on the lifetime costs of the CP system.

The 25 cm zinc strips were electrically connected by overlapping each strip slightly and shooting steel nails at a distance of one meter into the overlap (Figure 8). Connections to the steel reinforcement (the cathode) were made at 2 separate locations at each bridge segment. Finally the complete zinc surface, including the edges, was covered with a 2 mm thick layer of BASF 6100FX (a waterproof cement based coating) in order to prevent the zinc from direct contact with moisture due to condensation and the resulting atmospheric corrosion.



Figure 8. Connections at the overlaps of the zinc strips.

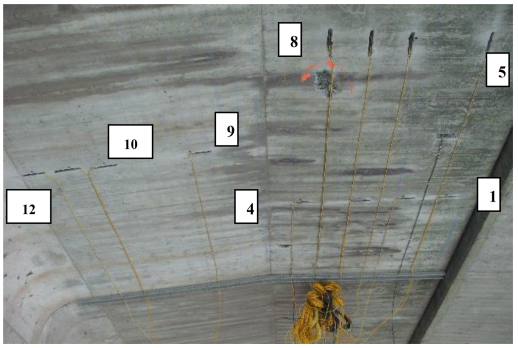

Figure 9. Test location with the embedded RE's in section 2.

3 DEVELOPMENTS IN TIME OF THE EFFECTIVENESS OF THE GCP SYSTEM

3.1 *The test segments*

The original test provisions from 2013 on the 2 segments (Figure 9), with a large amount of RE's and the narrow zinc strips (with a width of 83 mm), were kept unchanged, as much as possible, during the full scale project in 2014/2015 in order to be able to continue the monitoring of the GCP system and to start research of the long-term effects of this type of GCP systems with a surface mounted anode. Since 2013 depolarisation measurements of the CP system in different seasons have been carried out, using all the RE's in and remote from the protected area, as well as in depth. The amount of protection current being generated by each zinc strip was measured and monitored in order to predict the service life of the (sacrificial) anodes. Also other system parameters, such as the resistance in all the components, were monitored. These measurements were carried out during 2.5 years and show interesting results, expanding the knowledge on GCP and the long-term effects on potential decay values, (protective) current densities and the throwing power of galvanic anodes, as well as the influence of repair mortars and the moisture content of the concrete on the behavior of installed GCP systems.

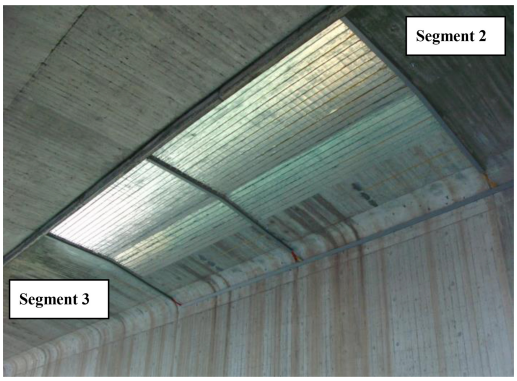

Figure 10. Test locations with the zinc anode material.

3.2 *Data and properties of the test segments*

Two bridge segments were selected in 2013:

1. Segment 2 (of 33) with 4% of concrete damage, a concrete cover between 29 mm and 45 mm ($\mu = 37$ mm) and corrosion potential measurements with values from 0 mV down to −270 mV ($Cu/CuSO_4$)
2. Segment 3 with 33% of concrete damage, a concrete cover between 25 mm and 46 mm ($\mu = 38$ mm) and corrosion potential measurements with values from −30 mV to −350 mV (at the location of the damage)

The reinforcement of the soffit was placed in 2 layers, crosswise, with rebars of Ø12 mm and Ø16 mm in diameter

The carbonation depth as measured in the soffit varied between 2 mm to 11 mm, however high chloride contents were measured, up to 3% on cement weight and up to depths of over 50 mm.

The CP system at the test segments was applied on the horizontal part of the cantilever and the adjacent 50 cm of the inclined segment (thus over a total width of approximately 2 meters). Each test segment was in this way covered with approximately 6,2 m^2 of ZLA (Figure 10).

3.3 *Effectiveness of the installed GCP system*

The measurements were carried out using the titanium decay probes (RE's), embedded in the concrete of the first 2 segments, in and remote from the protected area.

From the start in 2013, the measurements showed that the applied GCP system was effective. The depolarisation (potential decay) values met the code based CP criteria (ISO-EN12696) i.e. a minimum of 100 mV depolarisation after 24 hours or 150 mV after complete depolarisation (Figure 11 and 12), with the exception of 1 RE in segment 3.

Furthermore it was found, from the RE's placed at different depths in the concrete cover, that in segment 2 the second layer of reinforcement was protected as well. However, in segment 3, only 1 of the 4 RE's met

Section 2

Date:	28-8-2013	22-11-2013		28-1-2014	4-12-2014	20-3-2015	16-10-2015	
Session:	1e	3e		4e	7e	8e	9e	
	Depolarization							
	(-mV)	(-mV)	(-mV)	(-mV)	(-mV)	(-mV)	(-mV)	
RE 1	240	255	461	376	157	263	300	First layer of reinforcement
RE 2	337	344	387	452	183	240	304	
RE 3	217	211	241	214	83	109	101	
RE 4	231	217	225	226	101	155	123	
RE 5	146	151	160	131	61	87	95	Second layer of reinforcement
RE 6	157	158	165	173	77	130	121	
RE 7	187	188	237	234	108	139	141	
RE 8	224	229	320	271	116	190	173	
RE 9	270	334	481	324	226	289	184	Most negative potential
RE 10	101	104	163	148	72	104	2	Remote from CP area: 20 / 40 / 60 cm
RE 11	64	69	90	90	49	60	31	
RE 12	47	48	74	69	37	45	13	
Hours of depol:	24	24	168	144	23	74	240	
Threshold value:	100 mV	100 mV	150 mV	150 mV	100 mV	150 mV	150 mV	

Section 3

Date:	28-8-2013	22-11-2013		28-1-2014	10-3-2014	4-12-2014	20-3-2015	16-10-2015	
Session:	1e	3e		4e	5e	7e	8e	9e	
	Depolarization								
	(-mV)	(-mV)	(-mV)	(-mV)	(-mV)	(-mV)	(-mV)	(-mV)	(-mV)	
RE 1	134	155	152	164	152	62	77	210	185	First layer of reinforcement
RE 2	154	177	184	202	219	104	91	268	196	
RE 3	112	133	120	232	231	135	112	293	240	
RE 4	58	64	57	99	149	77	101	320	192	
RE 5	130	147	122	137	141	60	75	313	221	Second layer of reinforcement; partly in repair locations
RE 6	74	85	89	114	144	66	33	310	188	
RE 7	58	65	67	77	89	53	56	247	211	
RE 8	51	58	53	66	76	53	59	193	216	In repair locations
RE 9	51	57	52	73	74	25	36	202	221	Most negative potential
RE 10	31	39	36	46	70	37	38	209	213	
RE 11	285	333	294	309	533	307	192	363	180	Remote from CP area: 20 / 40 / 60 cm
RE 12	87	102	101	150	138	86	82	81	33	
RE 13	56	65	57	85	84	57	54	38	21	
RE 14	25	49	29	72	60	41	40	26	-1	
Hours of depol:	24	79	24	168	144	26	23	74	240	
Threshold value:	100 mV	150 mV	100 mV	150 mV	150 mV	100 mV	100 mV	150 mV	150 mV	

new anode material

Figure 11 & 12. Depolarisation values of segments 2 and 3.

the code based CP criteria, although it should be noted that 2 of the RE's which did not comply with these criteria were placed in repaired locations (RE7 & RE8). In general, the depolarisation values of the second layer were less compared to the ones located in the first layer of reinforcement. In the first 4 months after installation of the CP system, as an average, 70% and 66% of the potential decay values of the first layer were measured at the second layer of reinforcement in segments 2 and 3, respectively.

The best results in segment 3 were clearly obtained for the reinforcement showing the most negative natural potentials prior to installation of the CP system (RE11). In segment 2, the depolarisation values of the similar reference electrode (RE9) were also more than satisfactory with an average of 302 mV in the first 4 months after installation.

The measurements also showed that the CP system was not only effective in the protected area but also at a limited distance from the protected area, at least up to 20 cm.

Finally, RE's placed in repaired areas (segment 3; RE 7–10) showed less depolarisation than similar RE's in non-repaired locations. The depolarisation values did not meet the code based criteria.

3.4 *Developments in time of the potential decay values*

The measured values of the depolarisation in the protected area decreased over time (Figures 13 and 14). At the start in 2013 the measurements showed higher values indicating that the applied GCP system complied with the code based ISO-EN12696 criteria at almost all locations where RE's are installed, resulting in sufficient protection of the reinforcement. More than

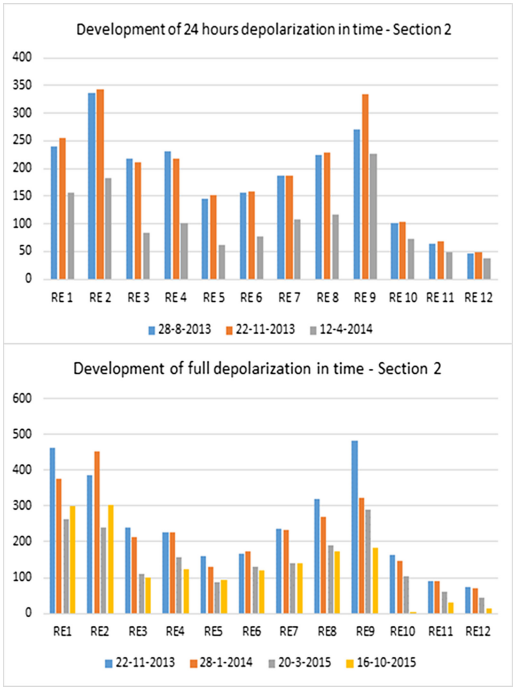

Figure 13 & 14. Development of depolarisation values in time of segment 2.

2 years later (in October 2015) only 3 out of 5 RE's (60%) at the first layer of reinforcement in segment 2 still met the code based protection criteria (compared to 100% compliance in 2013). Drying out of the concrete and polarisation of the steel are considered to be the explanation for this observation.

At segment 3, a part of the zinc anode, as well as some RE's, were replaced during the full scale project in December 2014 due partly to repair mortar disbondment during the test phase. As a consequence, the last measurements with the original anode material dated from December 2014 showing similar results as obtained for segment 2. In segment 3, 17 months after installation, also 3 out of 5 RE's (60%) in the first reinforcement layer met the code based protection criteria (compared to 80% compliance in 2013). The best result in this segment was still coming from the reinforcement with the most negative natural potentials prior to CP installation (RE11).

At the same time, from the RE's placed at the second layer of reinforcement only 1 out of 4 RE's (25%) in segment 2 and none of them in segment 3 (0%) met the code based criteria (compared to 100% and 50% compliance in 2013 respectively).

After replacing a part of the zinc anode and repairing the disbonded areas with the selected type of shotcrete at segment 3 (December 2014), the system reacted immediately and showed good results again. The GCP system (with partly new zinc anode material) met the code based criteria again, indicating sufficient protection of the reinforcement at all locations where RE's are installed i.e. at both the first and second reinforcement layer and in the repaired areas. Moisturizing of the concrete and the new installed anode material can be the explanation for this observation.

At the areas located more remote from the anode, i.e. adjacent to the protected surface, similar observations were found. At the start in 2013 the protected area stretched out at least up to 20 cm adjacent to the anode material. More than 2 years later this positive side effect was no longer measured with the RE's at a distance of 20 cm from the anode material. Drying out of the concrete is considered to be the explanation for this observation.

Finally, the RE's placed in repaired areas (segment 3; RE 7–10) showed, after having replaced the zinc anode and the disbonded areas (December 2014), sufficient depolarisation at all locations. The most probable explanation for the negative outcome of the potential decay values at these RE's during the first 17 months lies in disbondment of the repair mortar.

3.5 *Developments in time of the current density*

The current output readings were carried out for each separate zinc foil (22 strips per segment with a width of 83 mm and a total zinc surface of 0.28 m^2 for each strip) at 3 points in time. The total current output was measured as well for the complete anode system per segment (with a total zinc surface of 6,2 m^2).

The measured current outputs strongly decreased over time (Figures 15 and 16). At the start in 2013 the total current output amounts to 28.6 mA (equal to 4.6 mA/m^2_{anode} and approximately 7.7 mA/m^2_{steel}) and 24.8 mA (equal to 4.0 mA/m^2_{anode} and approximately 6.7 mA/m^2_{steel}) for segment 2 and 3, respectively. After 14 months it was reduced to 5.4 mA (equal to 0.9 mA/m^2_{anode} and approximately 1.5 mA/m^2_{steel}; a reduction of 81%) and 6.8 mA (1,1 mA/m^2_{anode} and approximately 1.8 mA/m^2_{steel}; a reduction of 73%).

The current outputs for each separate zinc foil (22 strips per segment) varied strongly in segment 3. The parts of segment 3 with small patched areas, between zinc strips A5 to A8 and A14 to A16, and the parts of this segment with larger patched areas, between zinc trips A9 to A13 (Figures 17 and 18), showed a lower current output compared to the non-patched areas. Specifically zinc strips A17 to A22 showed much higher current outputs.

The zinc strips applied in segment 2, which has less patched areas, showed more equally distributed current outputs.

Patched areas were shown to have a major influence on the current output of the zinc strips. The observed decrease in the current outputs could be caused by the disbondment of the repair mortar in the test phase, as mentioned before.

To compare the current output of each zinc strip vs the potential reading of respective RE's is complicated due to the fact that the RE is affected by the current output of all neighboring zinc strips.

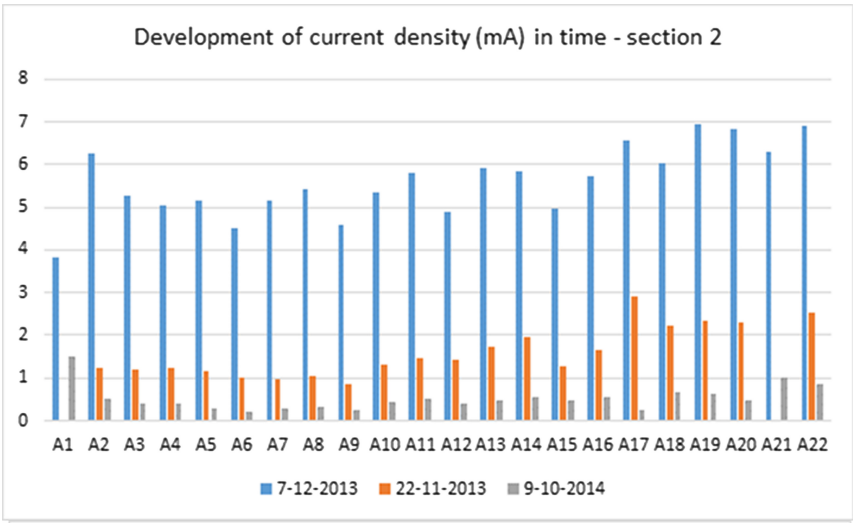

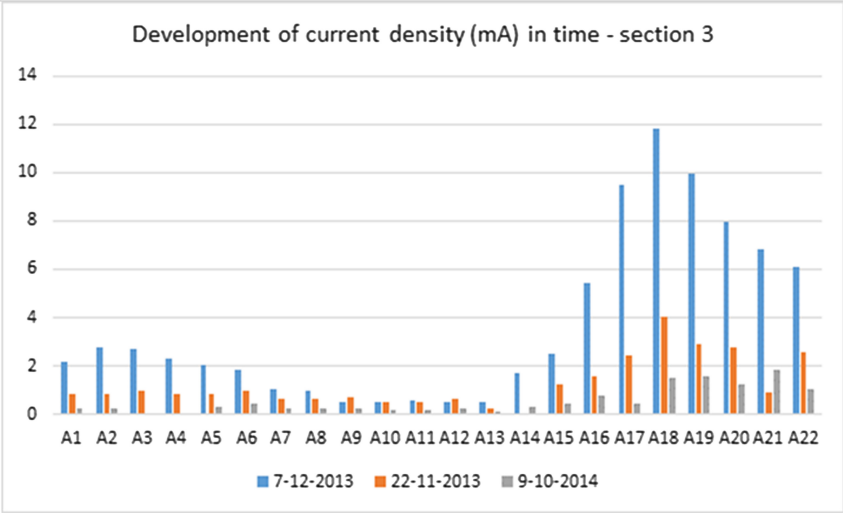

Figure 15 & 16. Development of the total current output in time for segments 2 and 3.



Figure 17. Repair locations and RE's in segment 3.

3.6 *Developments of the concrete resistance in time*

The measurements of the concrete resistance were carried out by measuring the resistance between each individual RE and the reinforcement.

The measured values of the concrete resistance on these specific locations increased strongly over time. At the start in 2013 the measured resistances in segment 2 varied between 1 to 9 kΩ, in segment 3 in the patched areas between 0.4 to 0.7 kΩ and between 1 to 6 kΩ in non-patched areas. After 14 months, it increased substantially and the resistances varied at that moment from 7 to 212 kΩ in segment 2 and in segment 3 from 2 to 5 kΩ in patched areas and from 4 to 130 kΩ in non-patched areas.

4 CONCLUSIONS

4.1 *General*

Since 2013 potential decay values, current outputs and resistances were measured during a period of 2.5 years on 2 selected bridge segments in which a large amount of RE's were installed and on the narrow surface zinc

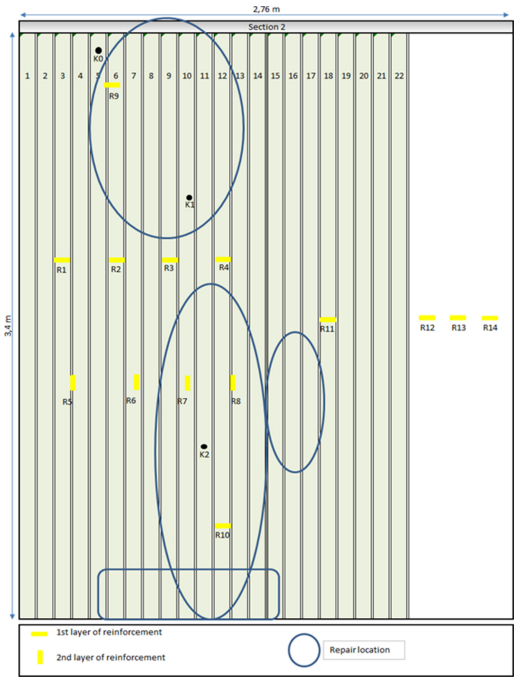

Figure 18. Anode strips, RE's and repair locations in segment 3.

strip anodes. These measurements showed interesting results on the effectiveness of the installed GCP system with surface-mounted zinc strip anodes (ZLA), on the development of the long term potential decay values and (protection) current outputs, and on the throwing power of galvanic anodes. The type and location of repair mortars used and the moisture content of the concrete were identified to have a major influence on the behavior of the installed GCP system.

Monitoring of the installed CP system will continue and will be further reported in the future.

4.2 *Effectiveness of the installed GCP system*

From startup (2013) the measurement results have demonstrated that the applied GCP system resulted in an effective solution. The depolarisation values complied with the code based protection criteria (ISO-EN12696) at almost all of the locations where RE's were installed.

The second reinforcement layer was protected as well (in non-patched areas), however with substantially less potential decay values compared to the first reinforcement layer.

The CP system was not only effective in the anode covered area but also more remote from the covered area, at least up to 20 cm.

RE's located in patched areas showed less depolarisation compared to similar RE's in non-patched areas. The corresponding depolarisation values did not meet the code based protection criteria for CP but this was most probably caused by partial disbondment of the repair mortars during the test phase.

4.3 *Potential decay values over time*

Depolarisation values gradually decreased over time and part of the installed RE's after 1.5–2.5 years showed values which did not comply with the code based protection criteria anymore, predominantly the readings from RE's installed at the depth of the second reinforcement layer. Drying out of the concrete and polarisation of the steel are considered to be the explanation for this observation.

In December 2014, i.e. during the full scale project, some zinc strip anodes needed to be replaced because of the disbondment of repair mortar during the test phase. After replacing the zinc strips and repairing the disbonded areas, the system reacted immediately and showed good results again. Moisturizing of the concrete and the new installed anode material are considered to be the explanation for this observation.

The effectiveness of the CP system to protect steel located at more distance from the protected area decreased over time as well. After more than 2 years this positive side-effect was no longer measured with the RE's placed at a distance of 20 cm from the anode material. Drying out of the concrete is considered to be the explanation for this observation.

4.4 *Current outputs over time*

The current outputs decreased strongly over time. At the start in 2013 the total current output was approximately 4–5 mA/m^2_{anode} (equal to 6.5–8 mA/m^2_{steel}) which was reduced in 14 months to approximately 1 mA/m^2_{anode} (equal to 1,5–2 mA/m^2_{steel})

The current outputs at patched areas were less than at non-patched areas. At spots where no or just minor patched areas were present, the current outputs were more equally distributed.

Patched areas were shown to have a major influence on the current output of the zinc strips. However, this could have been caused by the disbondment of the repair mortar in the test phase and will be investigated in the coming year.

REFERENCES

ISO-EN12696:2012, *Cathodic protection of steel in concrete*. Geneva: ISO.

CUR Aanbeveling 45, 1996. *Cathodic Protection of reinforcement in concrete constructions* (in Dutch, Kathodische bescherming van wapening in betonconstructies). Gouda: CUR.

Van Den Hondel, A.J., 2015. *Execution of concrete repairs with the use of galvanic CP – Neerbosschebrug Nijmegen* (in Dutch, Uitvoering van betonherstel met een galvanisch KB-systeem – Neerbosschebrug Nijmegen). Utrecht: RWS.

NDT and diagnosis of problems



Taylor & Francis
Taylor & Francis Group
http://taylorandfrancis.com

Concrete Solutions – Grantham et al. (Eds.)
© 2016 Taylor & Francis Group, London, ISBN 978-1-138-03008-4

3D localization of the reinforcement in reinforced concrete slab by using GPR

K. Agred, G. Klysz & J.P. Balayssac
Université de Toulouse, UPS Génie Civil, INSA, Laboratoire Matériaux et Durabilité des Constructions (LMDC), Toulouse Cedex 4, France

ABSTRACT: GPR is an inspection technique characterized by a high speed of implementation. It is well adapted for the assessment of reinforced concrete structures. One of the main applications is for the 3D localization of reinforcement. Nevertheless for achieving a good accuracy, the localization in depth needs post processing which requires a good level of expertise.
The objective of this work is to propose a novel measurement procedure and an adapted post processing for 3D localization of the first layer of steel reinforcement in reinforced concrete and for water content assessment of cover concrete. This methodology can be fully done without any processing expertise.
The measurements are done using two GPR antennas with a central frequency of 1.5 GHz, in a bi-static configuration. Both antennas are disposed in a single box equipped with an encoding wheel. The transmitter (T1) – receivers (R1) and (R2) distances are constants, such as (T1)-(R1) is 5.9 cm and (T1)-(R2) is 11.9 cm.
We developed an original algorithm to analyse and process recorded radar signals which provides the position in the plane and depth of the first layer of reinforcement in slabs and walls. This algorithm also allows calculating the velocity of electromagnetic waves in concrete that will be used to quantify the water content. This communication aims to present the performance of this algorithm. The results show that it enables the localization of the reinforcement in depth with an error lower than 4%. Measurement processing is very fast and does not require any knowledge neither of the material nor of the geometry.

Keywords: GPR, location of reinforcement, reinforced concrete, propagation speed, NDT.

1 INTRODUCTION

Nowadays non-destructive techniques with fast implementation used for structure sounding, such as GPR, are very relevant.

GPR (Ground Penetrating Radar) was initially used in geophysics to explore the ground and so it was then adapted for use in civil engineering, in order to inspect the pavement (cavity detection) in airports (Clemena, 2003). Later, radar was used to detect cavities in concrete structures or delamination in bridge decks (Morey, 1998), (Huston et al., 2002), to locate pipes (Cariou et al., 1997) or reinforcements (Shaw et al., 2004), (Hugenschmidt, 2002), to calculate the thicknesses of slabs or wearing course of the roadways (Huston et al., 2002) and to determine the moisture content and chloride contamination in concrete (Balayssac et al., 2007).

Radar is a device that emits an impulse electromagnetic wave which propagates by attenuating in the media, receiving and recording the reflections from the interfaces of different contrasts of electromagnetic property. The recording is done during a predetermined time interval by the operator, and provides a radargram representing the amplitude of the received signal as a function of time (Figure 1).

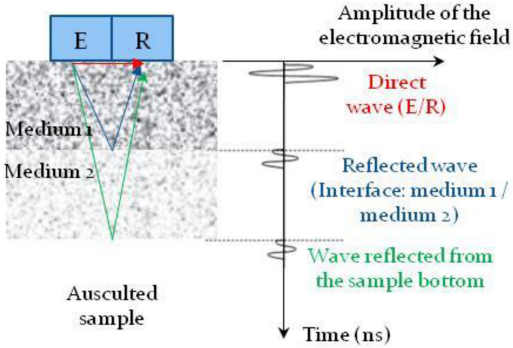

Figure 1. Principle of radar sounding.

The objectives of our work focus on the development of an algorithm for determining the positions, in plan and in depth, of reinforcement in reinforced concrete elements, calculating the electromagnetic wave propagation velocities in the coating layer of the steel, and finally establishing the mapping of wave speed in the material and steel position.

This study is part of the Eco-Industries Atalante project supported by the BPI France. This project

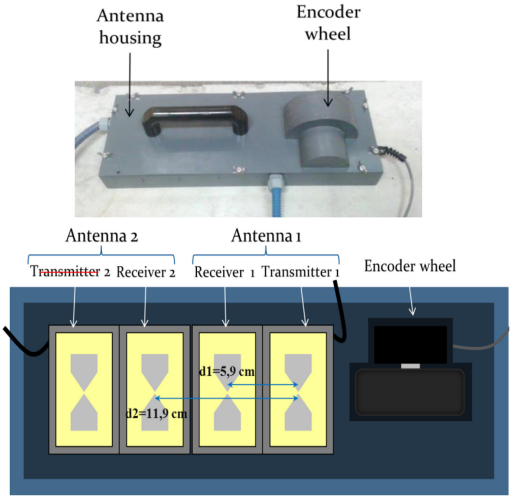

Figure 2. Photo and schema of the box containing the antennas.

consists in developing non-destructive assessment tools which will be adapted on an autonomous robot. These tools focus on the determination of the positions of the first layer of reinforcement in three dimensions in a reinforced concrete structure (the objective of this work) and to quantify the risk of corrosion of the reinforcement (this part is addressed by another study).

2 PRESENTATION EQUIPMENT, TEST AND TREATMENT METHOD

2.1 *Equipment and Measurement Configuration*

For our soundings we used a radar system SIR-30 developed by Geophysical Survey Systems GSSI®, Inc.

The prototype antenna box (Figure 2), proposed for this study, contains two antennas (model 5100 from GSSI®) with a centre frequency in air of 1.5 GHz, in a bi-static configuration. Each antenna has two bowtie type dipoles including one transmitter and one receiver. We used only the transmitter of the antenna 1 (T1) and the receiver of both antenna (R1 and R2). Both antennas are fixed in a compartment designed for this purpose, and the transmitter/receiver distances are maintained constant, such as distance T1-R1 is 5.9 cm and T1-R2 of 11.9 cm.

2.2 *Description of the tested slab*

The tested slab was made with a plain concrete composed of siliceous round aggregates coming from the Garonne river (round siliceous gravel 4/10 mm, and round siliceous sand 0/4 mm having a fineness modulus of 3 and a density 2.68), and a Portland cement CEM I (350 kg/m^3) with a water/cement ratio of 0.55. The concrete had a water porosity measured at 28 days about 14% (Viriyametanont, 2008).

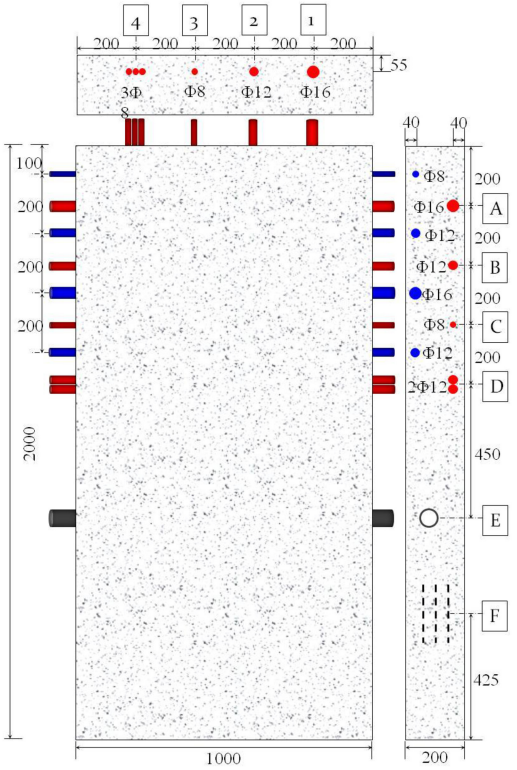

Figure 3. Reinforcement in the slab of reinforced concrete.

The slab had dimensions of $2 \times 1 \times 0.2\,\text{m}^3$. It included three layers of reinforcement, with steel of different diameters (8, 12 and 16 mm). The upper part comprised two crossed layers (in red in Figure 3) located at depths of the order of 3.2 cm to 3.6 cm for the transverse layer, and 4.7 cm to 5.1 cm for the longitudinal. The lower layer (blue) was between 15.2 cm and 15.6 cm deep. PVC pipe (grey) was also embedded in the slab at 7.5 cm deep. And on the right of the pipe, three metal plates were placed at depths of 5, 10 and 15 cm at the end of the slab.

The upper transverse reinforcements are identified by the letters A (Ø16), B (Ø12), C (Ø8) and D (2Ø12). The letter E corresponds to the position of the PVC pipe and the letter F to the position of the three metal plates. The longitudinal rebars are identified by the numbers 1 (Ø16), 2 (Ø12), 3 (Ø8), and 4 (3Ø8).

2.3 *Measurement method*

To make the measurements, the antenna box was placed on the surface of the slab and moved on a linear axis (Figure 4). The parameters of acquisition are reported in Table 1.

Receiving antennas recorded the direct waves Sd signals (transmitter – receiver) and the reflected signals, Sr, by the various interfaces in the reinforced concrete slab having a contrast of electromagnetic properties (concrete/steel, concrete/air that corresponds to

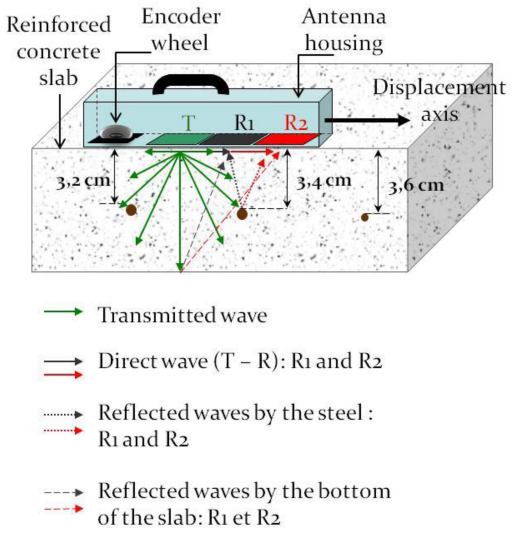

Figure 4. Measuring principle.

Table 1. GPR configurations

Sampling		Gain (dB)		
Horizontal (scans/m)	Vertical (samples/scan)	R1*	R2*	Range (ns)
1000	1024	2	15	8

*R1 and R2, respectively receiver 1 receiver 2.

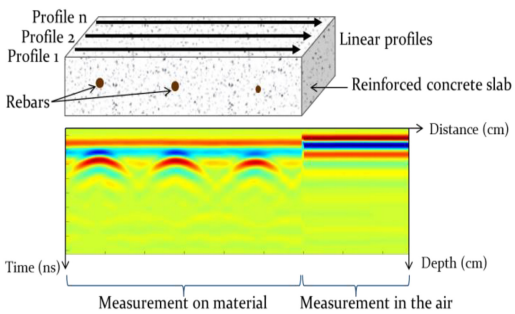

Figure 5. Signals recorded (Bscan) by a receiver in profile.

the bottom of the slab). Once the profile in the material was achieved, a measurement in free space (air) was performed, to determine time zero t_0 in order to reset the received signals on each receiver in time.

Figure 5 shows a Bscan obtained from a measurement profile over three reinforcing bars.

2.4 *Measurement processing*

For the construction of the algorithm that locates surface and deep reinforcement, we supposed that the

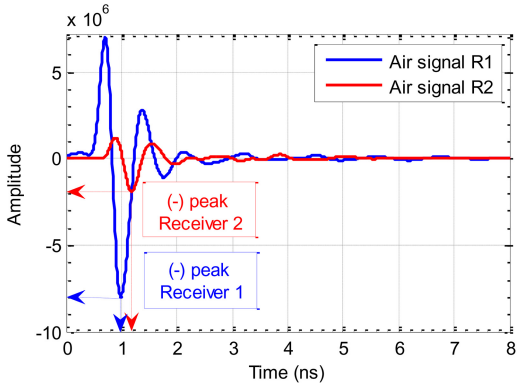

Figure 6. Signals recorded by the two receivers in the air as a function of time.

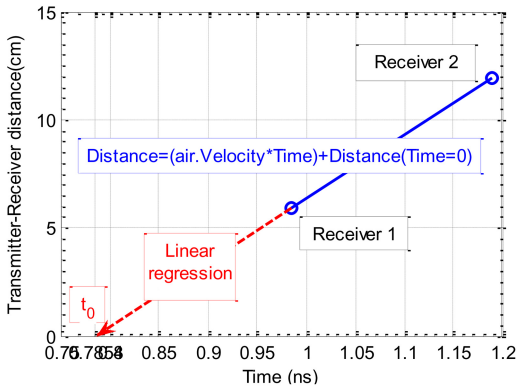

Figure 7. Linear regression.

propagation path of the electromagnetic waves (EM) was linear.

For determining time zero, we noted the arrival time of the first negative peak (the highest absolute value of the amplitude) of the average signal of the direct wave in the air to each receiving antenna (R1 and R2) respectively t1 and t2 (Figure 6). We connected the arrival time t to the corresponding distance d (Figure 7) and plotted the distance versus time (eq. 1). The slope represents the propagation velocity of EM waves in the air which is 30 cm/ns and we determined the time zero t_0 by linear regression.

$$d_i = v_{air} \times t_i + d_0 \quad (1)$$

We thereafter extracted the signals recorded in the material. First we searched automatically for the rebar positions of the first reinforcement layer x_i ($i = 1$ to n), n is the number of steel bars perpendicular to the profile, searching for the apex of each hyperbola corresponding to the B scan.

Secondly, we calculated the depths and velocities for each position of bars in the profile. For that, we used the fact that the received waves in each receiver must arrive coherently depending on the path they follow (transmitter/steel/receiver). Furthermore, we assumed

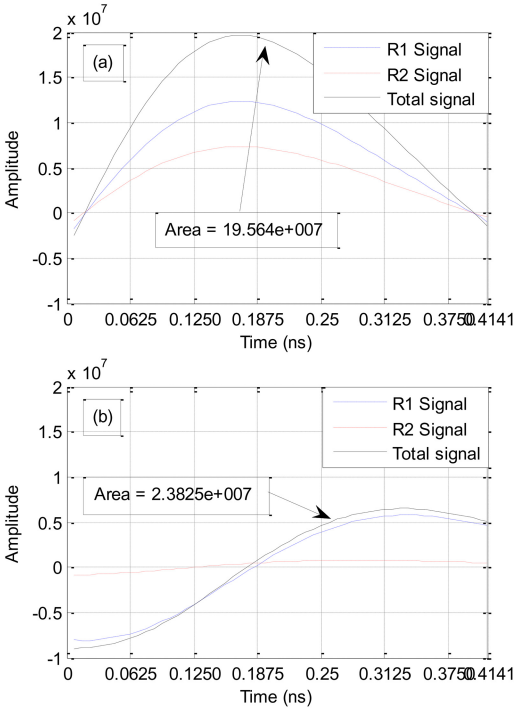

Figure 8. Summation results of temporal windows for a reflector point (a), and non-reflector point (b).

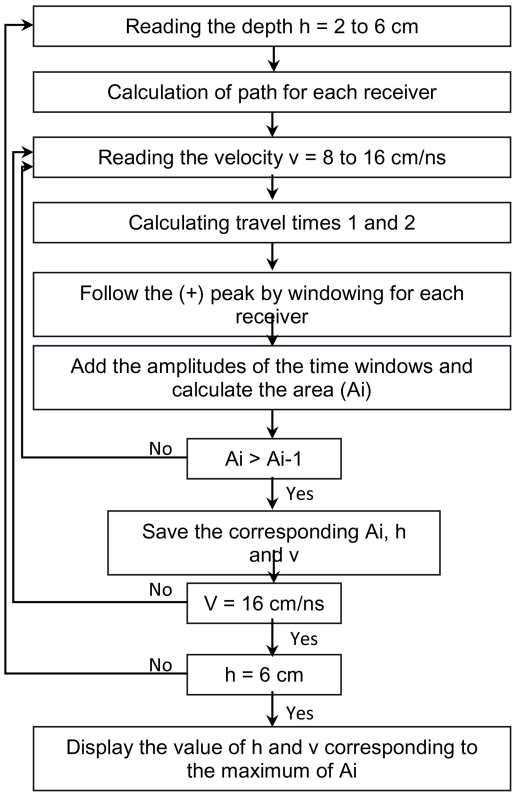

Figure 9. Depth and velocity calculation algorithm.

that the propagation velocity of the waves was constant locally around each steel, and was identical to the waves received at both receivers. We used the range of depths and velocities, respectively (2 cm–6 cm) and (8 cm/ns–16 cm/ns) for calculating the path lengths travelled by the EM wave in the material, from the transmitter to the point in the assumed material located at a depth h, and from this point to the two receivers. At this step, the wave travel time could be calculated for each path. In order to reduce the signal/noise ratio, we took into account several positions of transmitter/receiver in the auscultated space.

We extracted, using temporal windowing, parts of the signal corresponding to the estimated time. The size of the time window was the same time width of the negative peak of the direct wave recorded in free space (highest amplitude). This temporal windowing allowed us to follow the real path of the peak containing the maximum energy of the wave emitted by the transmitter, which would then be reflected on the steel rebar before being registered to the receiver 1 or 2. We added different signals extracted by temporal windowing, and then we computed the area under the curve of the sum of these signals (Hamrouche A., 2011).

For a given depth h and a travel time calculated for a velocity v, the sum of the signals picked up from temporal windowing for each position transmitter – receiver, forms an imposing and dominant area only if this depth, h, corresponds to the position of a real point reflector and if this velocity, v, is the real average velocity of the waves in the material around of this same point (Figure 8.a). In this case, this result indicates the presence of a reflector (the reinforcement in this case) at that depth h, with an average velocity of EM wave's propagation in the coating layer which is v.

Otherwise, if we are not at the right position h of the "real" point reflector (where the reflected waves have the highest amplitude) or if we use a velocity not corresponding to the actual speed in the material, the result of the summation is low (Figure 8.b).

The principle of the developed algorithm is summarized in the flowchart in Figure 9.

3 RESULTS AND DISCUSSION

We conducted a series of measurements on the slab in the longitudinal direction (profile 1) and the transverse direction (profile 2) as shown in Figure 10. The GPR configurations used are reported in Table **1**.

The Bscans obtained for each receiver are presented in Figure 11.

The algorithm described in section 2.4 was tested on these real measurements.

Table 2 shows the positions of bars, their depth and the propagation velocity of the EM waves in the coating layer of concrete above each bar to a longitudinal (N° 01) and a transverse profile (N° 02).

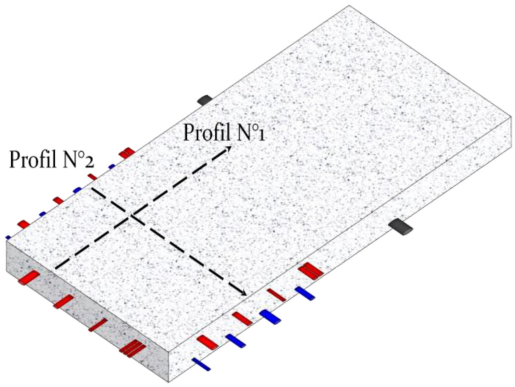

Figure 10. Identification of profiles on the slab.

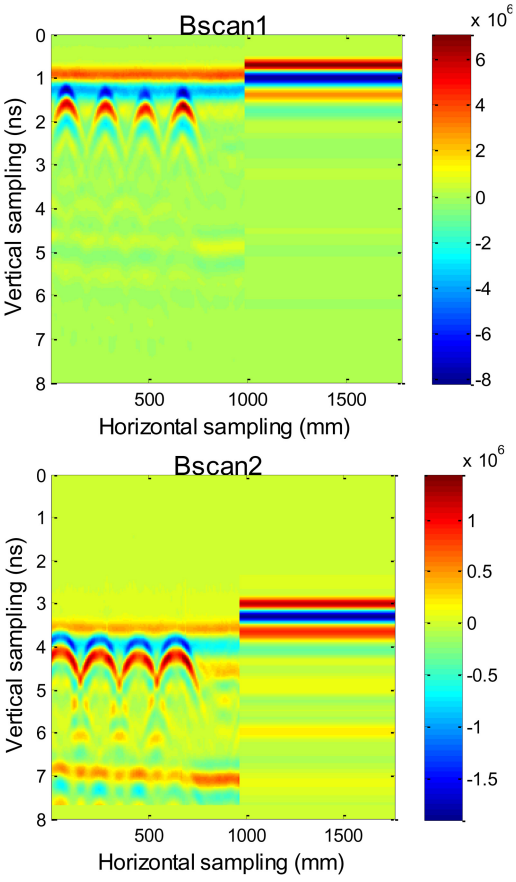

Figure 11. Bscans corresponding to the receivers 1 and 2 for the profile No. 01

The error on the surface positions of the bars A, B, C, 1, 2 and 3 was 3 mm. But it was higher for bar D and 4 because actually, there were two or three juxtaposed bars. However, the error in depth was less than 4% whatever the steel type.

Table 2. Table of results

Direction	N° of rebar	Position × (cm) Real	Position × (cm) Calculated	Error on position (cm)
Longitudinal	A	7.70	7.70	0.0
	B	27.70	27.70	0.0
	C	47.70	47.80	0.1
	D	67.70	66.80	0.9
Transverse	1	7.40	7.40	0.0
	2	27.40	27.30	0.1
	3	47.40	47.70	0.3
	4	67.40	68.10	0.7

Direction	N° of rebar	Depth (cm) Real	Depth (cm) Calculated	Error on depth (mm)	Velocity (cm/ns)
Longitudinal	A	3.2	3.2	0	10.7
	B	3.4	3.36	0.4	10.3
	C	3.6	3.55	0.5	10
	D	3.4	3.46	0.6	10.3
Transverse	1	4.7	4.6	1	10.3
	2	4.9	4.7	2	10.2
	3	5.1	4.9	2	10.5
	4	5.1	5.05	0.5	10.5

4 CONCLUSION

This study was conducted to determine the positions in 3 dimensions of the first reinforcement layer of a reinforced concrete slab, and the propagation velocity of EM waves in the coating layer by means of both a fast measurement procedure and a simple processing of results. The velocity will be used in a subsequent study to estimate the water content of the auscultated medium. The first goal of the study presented in this paper, was to develop an algorithm to achieve both objectives.

The algorithm that we developed does not require prior treatment to estimate the position of the rebars of the first reinforcement layer and the propagation velocity of EM waves in the auscultated material. We get results with errors of about one millimeter, the maximum is 2 mm in depth and less than 3 mm for surface positions for simple rebars.

Our future work will focus on developing mapping of propagation velocity of EM wave in the auscultated field, in order to obtain a map of the water content of the cover concrete. This mapping will be used to identify areas with a high risk of corrosion where it will be possible to apply appropriate characterization techniques for corrosion diagnosis.

ACKNOWLEDGMENTS

The authors wish to thank the Public Investment Bank (BPI France) for supporting the ATALANTE

Eco-Industries Project, which funded this work. The company ETANDEX, ATALANTE project coordinator, is also thanked for its technical support.

REFERENCES

Balayssac J.-P., Kringkaï V., Sbartaï M., Klysz G., Laurens S., Arliguie G., "Contribution au développement du radar pour la caractérisation non-destructive du béton", *25e rencontre de l'AUGC*, 23–25 mai 2007, Bordeaux.

Cariou J., Chevassu G., Cote P., Dérobert X., Le Moal J.Y., "Application du radar géologique en génie civil", *Bulletin des laboratoires des Ponts et Chaussées 211*, Sept-Oct 1997 - RÉF. 4135, p. 117–131.

Clemena G.G., "Short-Pulse Radar Methods", *Handbook on Nondestructive Testing of Concrete Second Edition, V. M. Malhotra and N. J. Carino, CRC Press 2003, Chapter 13.*

Hamrouche R., "Reconnaissance géométrique des structures en maçonnerie ou en béton par imagerie radar multi récepteurs: approche numérique et expérimentale". *Supervision thesis Paul Sabatier University Toulouse 3 and Sherbrooke University*, 2011.

Hugenschmidt J., "Concrete bridge inspection with a mobile GPR system", *Construction and Building Materials 16*, 2002, p. 147–154.

Huston D., Fuhr P., Maser K. and Weedon W., "Nondestructive Testing of Reinforced Concrete Bridges Using Radar Imaging Techniques", *The New England Transportation Consortium Report*, 94–92, 2002, p. 182p.

Morey R., "Ground Penetrating radar for Evaluating Subsurface Conditions for Transportation Facilities", *Synthesis of Highway Practice 255, National Cooperative Highway Research Program, Transportation Research Board. National Academy Press*, 1998.

Shaw M.R., Millard S.G., Molyneaux T.C.K., Taylor M.J., Bungey J.H., "Location of steel reinforcement in concrete using ground penetrating radar and neural networks", *NDT&E International 38*, 2005, p. 203–212.

Viriyametanont K., "Reconnaissance physique et géométrique d'éléments en béton armé par radar et réseaux de neurones artificiels", *Thesis at Institut National des Sciences Appliquées de Toulouse, Université Paul Sabatier de Toulouse, n° d'ordre 926, spécialité Génie Civil*, 2008.

Concrete Solutions – Grantham et al. (Eds.)
© 2016 Taylor & Francis Group, London, ISBN 978-1-138-03008-4

Determination of the electrical resistivity of concrete structures using electrical impedance tomography

Amir Asgharzadeh
Institute of Building Materials Research, RWTH-Aachen University, Germany

Kenji Reichling
The German Committee for Reinforced Concrete, Berlin, Germany

Michael Raupach
Institute of Building Materials Research, RWTH-Aachen University, Germany

ABSTRACT: The electrical resistivity of concrete is an important material parameter for evaluating the current condition of a concrete structure. It can be correlated with different durability related parameters, e. g. the water content, the corrosion rate of the reinforcement and the chloride diffusion coefficient. Usually the determination of the concrete resistivity in existing structures is made by drilling out cores and measuring the resistivity in the laboratory, which goes along with a local destruction of the concrete. Another option is to determine the concrete resistivity non-destructively using a Wenner probe by making the assumption of a homogeneous half-space with a homogeneous resistivity. In practice, however, there are distinctive heterogeneities (e. g. reinforcement or moisture distributions), which can lead to significant misinterpretations. To counteract this problem (see also Asgharzadeh et al, 2014 and Reichling, 2015), the application of Electrical Resistance Tomography (ERT) has been studied. This method is based on the measurement of several apparent resistivity values resulting from different electrode spacings and positions. The actual resistivity distribution in the concrete is calculated by inverse calculations based on iterative numerical methods. This allows the effect of heterogeneities to be considered and to reconstruct the distribution of the actual concrete resistivity. This paper focuses on the applicability of ERT on reinforced concrete structures.

Keywords: reinforced concrete; non-destructive testing; electrical resistivity; electrical resistivity tomography; Wenner; dipole-dipole; sensitivity

1 INTRODUCTION

The electrical resistivity of concrete plays a central role in the evaluation of the condition of reinforced concrete structures. The relationship of the corrosion rate of the reinforcement and the electrical resistivity of concrete was proved by Warkus et al (2010). Other authors demonstrated the correlations with other durability related parameters like water content, porosity and chloride diffusion coefficient (Raupach, 2006; Andrade et al, 2009; Weydert et al, 1999; Castellote et al, 2006), but the physical correlation between the resistivity and these parameters are not yet finally clarified. The electrical resistance (R) is determined by using Ohm's law which states that the current (I) through a conductor between two points is directly proportional to the voltage (V) across the two points.

The electrical resistance depends on the configuration of the measurement electrodes and the geometry of the electric field. Hence the resistivity (ρ), which does not depend on the geometry, is considered as a material specific parameter. The resistivity is obtained from multiplying the measured resistance (R) with a geometry factor (K).

$$R = U / I \quad (1)$$

$$\rho = k * R \quad (2)$$

The measurements can be carried out by using two and four electrode arrays. If the resistivity is determined by a direct current measurement, Ohm's law can be applied. Using a two-electrode array can cause an influence of polarization effects at the electrodes on the results. To counteract this problem a four-electrode array can be used. The current is applied over a different pair of electrodes than the electrical potential is measured, so that the polarization effects can be significantly reduced.

In practice the four-electrode array according to Wenner (1915) is usually applied (see Fig. 1).

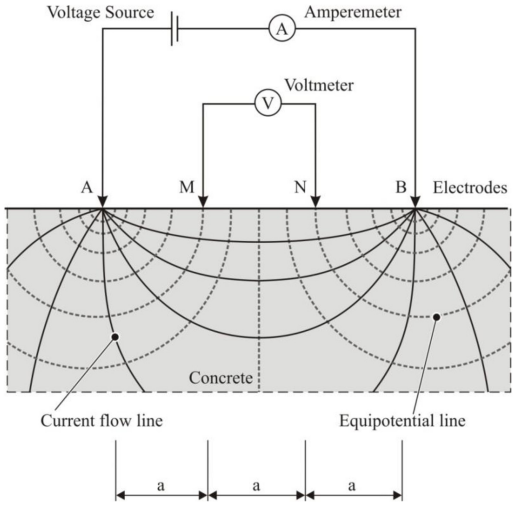

Figure 1. Schematic illustration of the Wenner array showing equipotential and current flow lines for a homogeneous material

The Wenner array consists of four electrodes aligned in a row with an equidistant spacing α. The current is impressed by the outer electrodes (A and B) and the voltage drop is measured by the two inner Electrodes (M and N). The geometry factor arises from the hemispheric potential field propagation between two current electrodes at the surface of the homogeneous half space (Wenner, 1915) and is only dependent on the electrode spacing (see Eq. 3).

$$k = 2 \cdot \pi \cdot a \tag{3}$$

Due to typical heterogeneities in the concrete an application of the Wenner-array on reinforced concrete structures may lead to distinctive deformations of the electric field. These heterogeneities can be attributed to inhomogeneities due to moisture distribution, carbonation or highly conductive reinforcement bars made from black steel. Furthermore, the geometry of small structural elements (e. g. columns) can influence the readings, so that a homogeneous half-space should not generally be taken as a basis. In these cases, the validity of eq. 3 is not given. The values determined on heterogeneous materials, but considering eq. 3 are designated as apparent resistivities.

2 ELECTRODE CONFIGURATION

In order to determine the actual concrete resistivity, the resistivity distribution in the concrete using electrical Resistance Tomography (ERT) has been analysed. The aim has been to identify heterogeneities, e. g. moisture profiles and reinforcement bars, and considering this in the determination of the resistivity distribution. This method is primarily used in geophysics (Friedel, 2000; Viergever et al, 1987; Lines et al, 1984).

The ERT measurements are based on different electrode arrangements and changing electrode spacings in order to map the underground roughly. The actual resistivity distribution in the concrete is calculated by using numerical inversion methods. Information about the distribution of inhomogeneities in the concrete can be gathered by varying the array positions and electrode spacings. By shifting the electrodes laterally, heterogeneities parallel to the concrete surface, such as reinforcement bars, can be localized. Whereas, by changing the electrode spacings, inhomogeneities perpendicular to the concrete surface, such as moisture profiles, can be detected. Beside the Wenner Alpha configuration (see Fig. 1) there also exist other configurations e. g. Wenner Beta, Wenner Gamma, Schlumberger and dipole dipole (see Fig. 2), which imply specific advantages and disadvantages.

The main differences between the arrays can be explained by their sensitivity distributions (Barker, 1979). A sensitivity value includes information about the influence of a specific region in the measuring object on the reading. Typically, the regions near to the current electrodes have the largest sensitivity values and therefore have the most significant influence on the readings. The distribution of the sensitivities in the cross section of the measuring object depends on the array type and the actual resistivity distribution. In Fig. 3 the sensitivity distributions of the Wenner Alpha and the dipole-dipole configuration are exemplarily shown for a homogeneous half space. The dark areas represent the regions with positive values and the dashed lines point out the negative values. If the conductivity in a region with positive sensitivity values is increased, the apparent resistivity would be increased as well. An increase of the resistivity in regions with negative sensitivities would paradoxically cause a decrease in the apparent resistivity. A reinforcement bar situated close to the concrete surface between a current and a potential electrode would theoretically lead to an overestimation of the concrete resistivity, whereas when it is situated between the potential electrodes the concrete resistivity would be underestimated. It is therefore important for interpreting single measurement results to know the specific characteristics of the array types used for a measurement.

Fig. 3 shows that the form of the regions with high sensitivity values is different for the Wenner and the dipole-dipole configuration which reflects the imaging capability of the measuring object. The dipole-dipole configuration leads to a distinctive focused area underneath the array length, which is accompanied by a larger measuring depth compared to other array types. In order to determine the apparent resistivity by using the dipole-dipole configuration the geometry factor from eq. 4 must be included into the analysis. The distance between the electrode dipoles is a multiple (n) of the dipole lengths (α).

$$\mathrm{k} = \pi \cdot \mathrm{n} \cdot (\mathrm{n}+1) \cdot (\mathrm{n}+2) \cdot \mathrm{a} \tag{4}$$

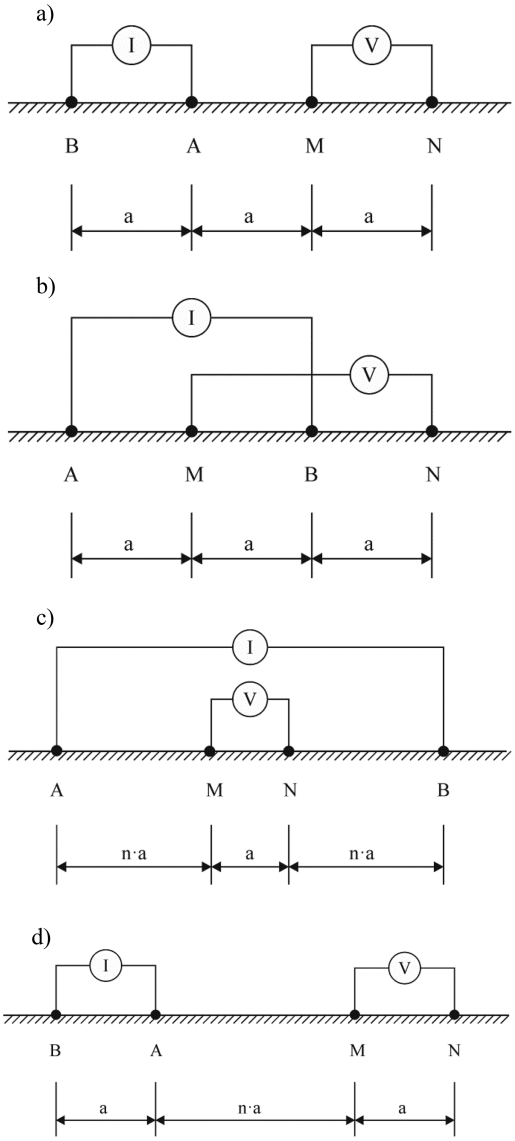

Figure 2. Schematic illustrations of the Wenner Beta (a), Wenner Gamma (b), Schlumberger (c) and dipole-dipole (d) electrode arrays.

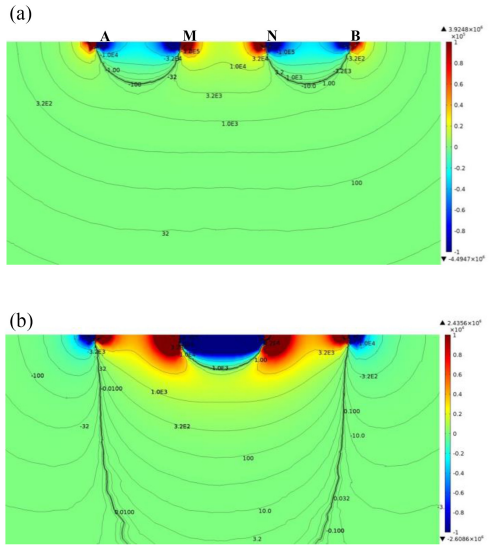

Figure 3. Idealized illustration of the sensitivity distribution of the Wenner Alpha (a) and dipole-dipole (b) arrays for a homogeneous half space.

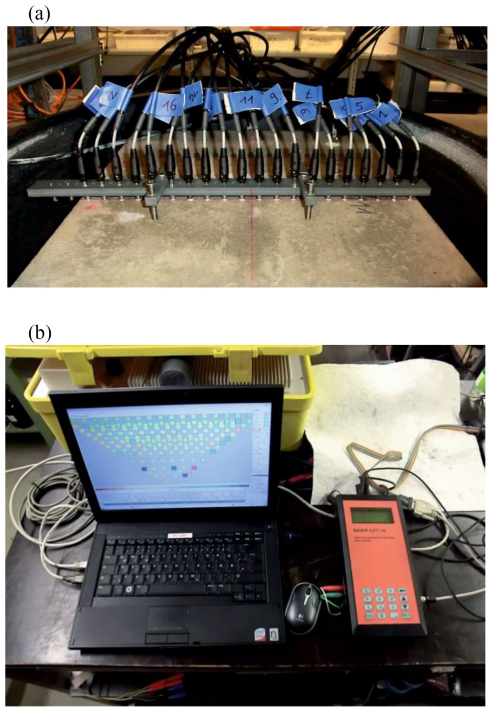

Figure 4. Multi-electrode probe (a) developed for measurements on reinforced concrete specimens and computer controlled measurement system (b).

3 ELECTRICAL RESISTANCE TOMOGRAPHY

In order to study the applicability of ERT for reinforced concrete, a probe with 20 single electrodes with an equidistant spacing (a) of 20 mm is developed. This probe allows a rapid multi-electrode array measurement (see Fig. 4a).

The measurements have been carried out with the device “4point light 10 W” by LGM – Lipmann Geophysical Equipment (Geotest, 2012) (Fig. 4b). The device allows an automated switching of the electrodes individually as current or potential electrodes, so that different array configurations can be measured within a comparably short time.

The measurement process consists of several single measurements, based on a four-electrode setup. Within

one procedure several hundred individual values are typically determined.

Based on the apparent resistivity values, the actual resistivity distribution can be determined by numerical calculations. Starting from an observed (measured) effect (potential distribution) the cause (resistivity distribution) is determined by an inverse analysis. This is done by adjusting stepwise the resistivity distribution of the model and determining synthetic resistivity values by forward calculations, which are compared to the measured resistivities. Based on the deviation the resistivity distribution of the model is updated. This procedure is repeated until a minimal deviation is found. The calculations are based on the Laplace equation (eq. 5) whereas the measurement characteristics are considered by boundary conditions. The current ingress is considered by the Neumann boundary condition (eq. 6) and the potential differences are taken into account the Dirichlet boundary condition (eq. 7) (Friedel, 2000; Viergever et al, 1987; Lines et al, 1984).

$$-\nabla \cdot \sigma \nabla \Phi = 0 \; on \; \Omega \tag{5}$$

$$-\sigma \frac{\partial \Phi_{AB}}{\partial n} = j_{AB} \; on \; \partial\Omega \tag{6}$$

$$\nabla \Phi_{MN} = U_{MN} \; on \; \partial\Omega \tag{7}$$

σ represents the electrical conductivity, Φ the potential distribution, j the current density and U the measured voltage. Within the studies the inversion calculations have been carried out using the software RES2DINV (Geotomo Software, 2012), which has been originally developed for geophysical issues.

4 RESULTS

In order to investigate the influence of the different array types (Wenner and dipole-dipole configuration) on the resistivity distribution comparative measurements have been carried out. For all measurements a frequency of 25 Hz was used. Before starting the measurements the concrete specimens ($40 \times 40 \times 20$ cm^3) have been stored in water. In the center of the specimens a 12 mm reinforcement bar was embedded with a concrete cover depth of 10 mm and the electrode-probe was positioned perpendicularly to the reinforcement bar.

In Figure 5 the resulting resistivity distributions for the reinforced specimen are shown under using different electrode arrays. It can be clearly seen that the Wenner-Alpha configuration leads to an unsatisfactory reproduction of the reinforcement, whereas using the dipole-dipole configuration allows an exact localisation of the rebar. This effect can be explained by the different sensitivity distributions shown in Fig. 3. Due to the significantly focused area with high sensitivity values of the dipole-dipole array, a pronounced lateral resolution can be achieved.

A distinctive gradient in resistivity has been observed at the concrete surface. Supplementary measurements based on Nuclear Magnetic Resonance

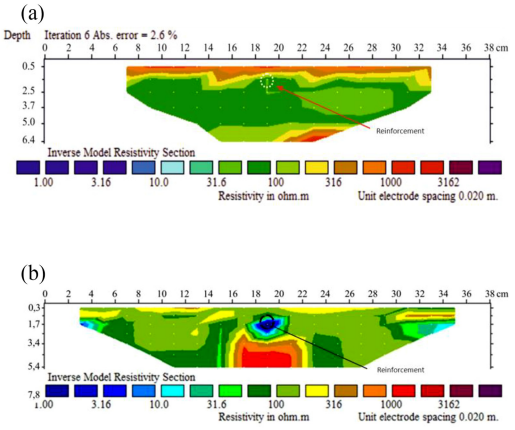

Figure 5. Resistivity distributions measured with the Wenner Alpha (a) and dipole-dipole (b) electrode configuration.

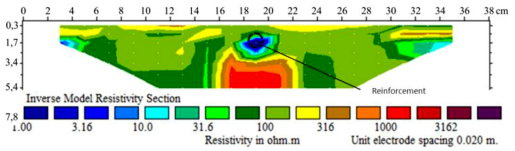

Figure 6. Resistivity distributions measured with the dipole-dipole electrode configuration after grinding the concrete surface.

(NMR) (Antons et al, 2012) allowed detecting an area with an increased porosity close to the surface. This can be traced back to a staggered distribution of the aggregates in the near-surface regions (Stoeckl, 1966). In the case of water-saturation, this results in a decreased resistivity in a small layer close to the surface. By numerical analyses it could be shown that this effect is accompanied with distinctive negative sensitivity values, thus leading to the observed gradient with an increased resistivity. In order to clarify this effect, the surface of the specimen has been ground by approx. 2 mm and the measurements were repeated.

The results in Figure 6 show that the near-surface resistivity gradients are significantly reduced, whereby the effect of negative sensitivity values could be confirmed. Further investigations have shown that the consideration of these near-surface effects within the numerical calculations also lead to adequate results.

5 CONCLUSIONS

The readings taken with a Wenner probe can be significantly influenced by the inhomogeneities in a reinforced concrete structure. ERT is a promising method, to counteract these problems and to allow a precise and reliable determination of the concrete resistivity. It could be shown that it is possible to apply the method on reinforced concrete. By considering

e.g. reinforcement bars an accurate determination of the special resistivity distribution of the surrounding concrete can be achieved non-destructively.

By knowing the spatial distribution of the resistivity, a correlation with durability related properties such as the spatial distribution of e.g. the water saturation, the chloride diffusion resistance, the corrosion rate or the porosity is possible.

ACKNOWLEDGEMENT

The investigations have been carried out at the RWTH-Aachen University in cooperation with Prof. Christoph Clauser and Dr. Norbert Klitzsch "Institute for Applied Geophysics and Geothermal Energy". Great thanks to Mr Udo Antons for help with the NMR measurements.

REFERENCES

Andrade, C.; D'Andrea, R.; Castillo, A.; Castellote, M.: "The Use of Electrical Resistivity as NDT Method for the Specification of the Durability of Reinforced Concrete". Paris: LCPC, (2009). – In: 7th International Symposium on Non Destructive Testing in Civil Engineering: Nantes, France, June 30th to July 3rd 2009, (Abraham, O.; Derobert, X. (Eds.)), S. 497–502

Antons, U.; Raupach, M.: "Zerstörungsfreie Visualisierung von hydrophob wirksamen Schichten in Beton". In: Restoration of Buildings and Monuments 18 (2012), Nr. 5, S. 287–302 ISSN 18647251

Asgharzadeh, A.; Reichling, K.; Raupach, M.; Electrical Resistance Tomography on Reinforced Concrete, 2nd International Congress on Durability of Concrete (2014), New Delhi

Barker, R.D.: "Signal Contribution Sections and their Use in Resistivity Studies". In: Geophysical Journal of Royal Astronomical Society 59 (1979), Nr. 1, S. 123–129

Castellote, M.; Andrade, C.: "Round-Robin Test on Methods for Determining Chloride Transport Parameters in Concrete". In: Materials and Structures (RILEM) 39 (2006), Nr. 10, S. 955–990

Friedel, S. (2000). "Über die Abbildungseigenschaften der geoelektrischen Impedanztomographie unter Berueck-sichtigung von endlicher Anzahl und endlicher Genauigkeit der Messdaten": Shaker.

Geotest v 2.39 (2012), Geophysik Dr. Rauen, http://geophysik-dr-rauen.de

Geotomo Software Sdn. Bhd.; RES2DINV v.3.5 (2011), www.geoelectrical.com

Lines, L. R. & Treitel, S.; "Tutorial- a Review of Least-Squares Inversion and Its Application to Geophysical Problems". Geophysical Prospecting (1984), 32(2), 159–186.

Raupach, M.: "Models for the Propagation Phase of Reinforcement Corrosion" – an Overview. In: Materials and Corrosion 57 (2006), Nr. 8, S. 605–613

Reichling, K. (2015): Bestimmung und Bewertung des elektrischen Widerstands von Beton mit geophysikalischen Verfahren. Berlin 2015, Deutscher Ausschuss für Stahlbeton, Heft 612

Stoeckl, S.; "Das unterschiedliche Verformungsverhalten der Rand- und Kernzone von Beton". Deutscher Ausschuss fuer Stahlbeton (1966), (Heft 185). Berlin.

Viergever, M. A. & Todd-Pokroper, A. E.; "Mathematics and computer science in medical imaging" (1987).

Warkus, J.; Raupach, M.: "Modelling of Reinforcement Corrosion – Geometrical Effects on Macrocell Corrosion". In: Materials and Corrosion 61 (2010), Nr. 6, S. 494-504 ISSN 09475117

Wenner, F.: "A Method of Measuring Earth Resistivity". In: Bulletin of the Bureau of Standards 12 (1915), S. 469–478

Weydert, R.; Gehlen, C.: "Electrolytic Resistivity of Cover Concrete: Relevance, Measurement and Interpretation". Ottowa; NRC Research Press, (1999). – In: Durability of Building Materials and Components, Proceedings of the Eight International Conference, Vancouver, May 30 – June 3,1999, (Lacasse, M.A. ; Vanier, D.J. (Ed.)), Vol 1, S. 409–419



Taylor & Francis
Taylor & Francis Group
http://taylorandfrancis.com

Concrete Solutions – Grantham et al. (Eds.)
© 2016 Taylor & Francis Group, London, ISBN 978-1-138-03008-4

NDT for damage diagnosis in shear-critical concrete beams using external PZTs and a new wireless monitoring system (WiAMS)

M.E. Voutetaki
School of Architectural Engineering, Technical University of Crete, Greece

N.A. Papadopoulos & C.E. Chalioris
Department of Civil Engineering, Democritus University of Thrace, Greece

C.P. Providakis
School of Architectural Engineering, Technical University of Crete, Greece

ABSTRACT: The application of an innovative portable real-time Wireless impedance/Admittance Monitoring System (WiAMS) in damage diagnosis and Non-Destructive Testing (NDT) of shear-critical Reinforced Concrete (RC) beams is experimentally studied. This system is based on an alternative consideration of the electromechanical impedance concept, integrating Piezoelectric lead Zirconate Titanate (PZT) patches that serve as sensors and actuators simultaneously. It uses WiAMS devices and an array of externally bonded PZT patches on the surface of the RC beams in specific locations across the potential diagonal cracking of both shear spans. Voltage signals of the PZTs were measured at the healthy state and at different levels of the applied load and the corresponding damage states. Quantitative assessment of the examined damage levels using statistical damage indices is also presented. Promising results concerning the prediction of the forthcoming final shear failure at early damage stages such as the onset of diagonal cracking were derived.

Keywords: Reinforced Concrete (RC), Non-Destructive Testing (NDT), Structural Health Monitoring (SHM), Shear, Beam, Piezoelectric lead Zirconate Titanate (PZT), Damage assessment.

1 INTRODUCTION

Recent development of various approaches that prevent catastrophic failures and reduce cost of inspection in Reinforced Concrete (RC) structures has emerged from the necessity of real-time damage detection, Non-Destructive Testing (NDT) and Structural Health Monitoring (SHM) techniques. SHM involves NDT and becomes very important in RC members and structures that are governed by shear mechanisms which lead to fragile and abrupt failure modes. A lot of failures in RC structures have been reported over the past two decades that were initiated from local failure of shear-critical members (Divsholi et al. 2009, Tsonos 2014).

Nowadays, the development of SHM techniques is very rapid especially of those based on the use of smart materials such as Piezoelectric lead Zirconate Titanate (PZT). The Electro-Mechanical Impedance (EMI) or its reverse Electro-Mechanical Admittance (EMA) technique is one of the most powerful SHM techniques that is based on piezoelectric materials (Yang & Miao 2008, Wang et al. 2013).

A PZT transducer produces electrical charges when subjected to a strain field and conversely it produces mechanical strain when an electrical field is applied. The SHM and damage detection techniques have been developed based on the coupling properties of the piezoelectric materials. The impedance-based SHM approach utilizes the EMI of these materials that is directly related with the mechanical impedance of the host structural members, a property that is directly affected by the presence of any structural damage. Thus, the impedance and its inverse, the admittance, constitute the properties on which the PZT approach is based for the SHM of structures. The effects produced by structural damage on the PZT electrical signatures are vertical enlargement or/and lateral shifting of the baseline signatures of the initially healthy structure. These effects are the main damage indicators for damage detection and evaluation that much research is based on (Soh et al. 2000, Providakis et al. 2015).

Providakis & Voutetaki (2006) presented a numerical method for structural health monitoring and damage identification of a concrete beam by extracting the electromechanical impedance characteristics of surface bonded self-sensing PZT patches. The damage was firstly quantified conventionally by the root mean square deviation index and then by using a statistical confidence method in system identification advanced routines of a mathematical computational software. Numerical studies that simulate EMA monitoring procedures utilizing PZTs to detect and localize

cracking in concrete beams have also been presented (Providakis & Voutetaki 2007, Voutetaki et al. 2012, Providakis et al. 2014, Karayannis et al. 2015).

Two different installations of PZT transducers have been used to monitor concrete structural elements and specimens; embedded PZTs inside concrete mass as "smart aggregate" and external piezoelectric patches bonded on the surface of concrete. It has been found so far that the surface bonded PZTs are not effective for monitoring a large area or the entire concrete structure due to their small sensing range. On the other hand, the embedded PZT transducers as smart aggregates using the wave transmission technique that is based on electrical wave transmission can be employed to monitor large areas with a reasonably low actuation signal (Divsholi & Yang 2014, Kaur & Bhalla 2015).

Failures in shear-critical RC members and structures are associated with brittle and sudden collapses that might lead to human and material losses. When principal tensile stresses exceed the tensile strength of concrete, diagonal cracking occurs in the shear span and the behaviour of a concrete element under shear stresses is mainly characterised by the tensile strength of the material (Ribas & Cladera 2013, Chalioris 2013).

The Wireless impedance/Admittance Monitoring System (WiAMS) developed was investigated by tests on shear-critical RC beams. This new wireless, portable, lightweight, real-time impedance monitoring system was applied to three large-scale RC beams failing in shear in order to evaluate its ability in damage detection and assessment. Voltage signatures of an array of embedded piezoelectric transducers as "smart aggregates" and externally bonded piezoelectric patches were measured at different levels of applied load and corresponding damage states. Quantitative assessment of the examined damage levels using values of statistical damage index was also attempted. The basic concept of this study was to predict the forthcoming total shear failure at early damage stages using WiAMS in shear-critical RC elements.

2 DAMAGE EVALUATION PROCEDURE USING WIAMS

2.1 *Electro-Mechanical Impedance (EMI)*

The Electro-Mechanical Impedance (EMI) technique uses Piezoelectric lead Zirconate Titanate (PZT) transducers exhibiting their characteristic feature to generate surface electric charge in response to an applied mechanical stress and undergo mechanical deformation in response to an applied electric field. Thus, when a mounted PZT on a structure is actuated, potential damage induces change in the mechanical impedance (or its reverse admittance) of the structure and this change reflects on the electrical signature of the PZT. When a structure is regularly monitored by extracting the signal to the exciting frequency of the installed PZTs, the changes in their signatures become indicative of the presence of structural damage (Naidu & Soh 2004, Providakis et al. 2014, Karayannis et al. 2016).

In the adopted structural health monitoring methodology for the detection of potential damage in RC beams, the PZT transducers were excited for a specific frequency range and their corresponding signals were recorded simultaneously. These measurements were carried out initially on the undamaged RC beam (initial status) in order to record the healthy condition and to be used as a baseline signature. Afterwards, the same measurements were carried out on the damaged RC beam at different levels of damage. More details about the overall concept of the adopted EMI technique can be found in the recent works of Providakis et al. (2014, 2015).

Selection of the excitation frequencies of the mounted PZTs is an important parameter affecting the effectiveness of the method and therefore special attention has been given by Providakis et al. (2014) and Karayannis et al. (2015, 2016). The excitation loading sequence can have a voltage level low enough that the technique may be considered as easily applicable and effective for real structures. In this study analyses were performed for a frequency range of 10 kHz to 260 kHz per step of 10 kHz by using one cycle per 10 kHz. A harmonic excitation voltage of 10 Volts is amplified to the PZT transducers in time domain range at every central frequency, as described by the expression:

$$V_{PZT}(t) = 10\sin(2\pi\omega t) \tag{1}$$

where V_{PZT} is the excitation voltage of the PZT, ω is the angular frequency of the driving voltage and t is the time domain range.

In order to investigate the design of the experimental setup using the developed SHM procedure the following tests were conducted. The shear-critical RC beams were subjected to a typical two-point loading till failure. During testing, the signatures of embedded piezoelectric "smart aggregates" transducers and externally bonded piezoelectric patches were measured at four different loading levels and corresponding damage states.

2.2 *The developed wireless SHM system (WiAMS)*

The overall test setup and the wireless monitoring system of the developed SHM methodology for the in-situ detection of damages in real-scale RC beams is shown in Figure 1. It is a specially implemented wireless monitoring system that is based on the Electro-Mechanical Impedance (EMI) methodology and utilizes the measurements of Piezoelectric lead Zirconate Titanate (PZT) transducers mounted to the structural element which operate as actuators and sensors simultaneously.

WiAMS is a Wireless impedance/Admittance Monitoring System that estimates the impedance magnitude of a PZT transducer that is utilized in order to monitor in situ and in real-time the structural integrity of concrete members and structures. This way, a WiAMS device sends out the interrogating

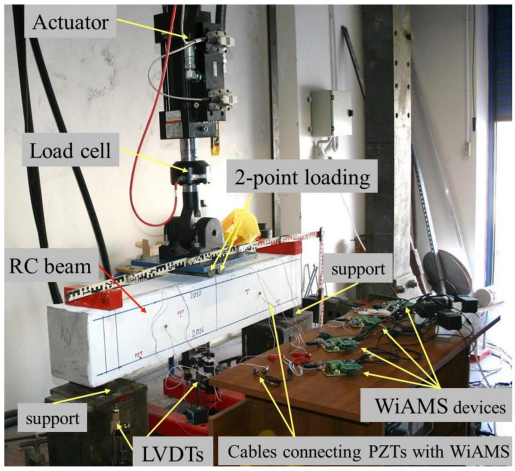

Figure 1. Test setup and wireless monitoring system.

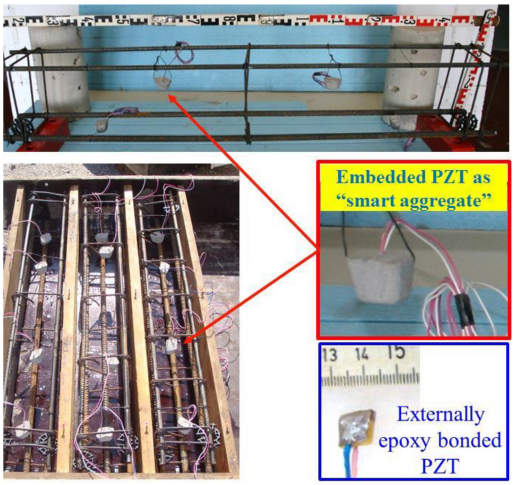

Figure 2. Geometrical, reinforcement and PZT transducers of a typical shear-critical RC beam.

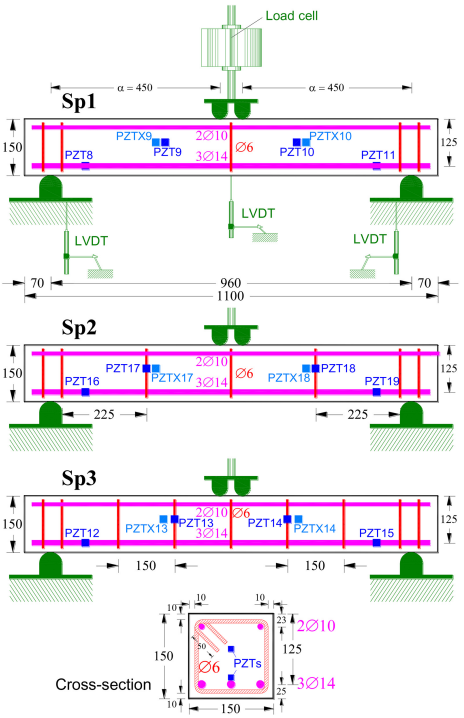

Figure 3. Geometrical and reinforcement characteristics of the tested beams.

waves through a PZT and receives the reflected waves at the same time. The WiAMS device consists of multiple custom-made modules that enable the use of simple and low-cost monitoring topologies compared to the traditional and complex impedance analysers (Chalioris et al. 2015a, 2015b, Voutetaki et al. 2016).

3 EXPERIMENTAL INVESTIGATION

The test program included the application of the developed wireless monitoring platform (WiAMS) to three shear-critical RC beams. The effectiveness of WiAMS to evaluate the damages (cracks) caused on the RC beams during a typical two-point loading test and at different levels of loading – corresponding damage was investigated.

PZTs were mounted to the tested RC beam as (a) embedded PZTs inside the concrete mass of the beams as "smart aggregates" and (b) externally epoxy bonded PZT patches at the surface of the beams. PZT transducers with dimensions 10 mm × 10 mm and material mark designation PIC 255 were used. Characteristics (geometrical, reinforcement and PZT transducers) of a typical tested shear-critical RC beam with embedded "smart aggregates" and externally epoxy bonded PZTs are displayed in Figure 2.

The PZT "smart aggregates" were fixed inside the wooden mould of the RC beams, after the placement of the steel reinforcing bars and stirrups, just before concrete casting. Embedded "smart aggregates" were installed at each shear span and their positions were close to the potential future diagonal cracks. After concrete casting and demoulding the hardened concrete of the beams, PZT transducers with two soldered cables were carefully epoxy bonded on the concrete surface of the RC beams at each shear span, close to the expected location of potential future diagonal cracks. Epoxy adhesive of high shear modulus and very small thickness approximately to one-third of the thickness of the PZT transducer was used to bond each PZT to the concrete surface.

The geometrical and reinforcement characteristics of the tested RC beams are shown in Figure 3. The mean concrete cylinder compressive strength of the beams was 29.1 MPa. The shear spans of beam Sp1 had no transverse web reinforcement in order to control a typical shear failure of a beam without stirrups

(only a few closed stirrups of diameter 6 mm were used just to hold the longitudinal reinforcing bars in place). Beams Sp2 and Sp3 had closed steel stirrups of diameter 6 mm spacing per 225 mm (Ø6/225 mm) and per 150 mm (Ø6/150 mm), respectively.

Twelve PZT transducers were embedded inside the concrete mass of the RC beams as "smart aggregates" (PZT8 to PZT19) and six PZT patches were epoxy bonded externally on the concrete surface of the RC beams (PZTX9, PZTX10, PZTX13, PZTX14, PZTX17 and PZTX18). The exact locations of all PZTs ("smart aggregate" transducers and externally bonded patches) mounted to each beam are displayed in Figure 3.

The test setup and instrumentation of the shear-critical RC beams is shown in Figures 1 and 3. The beams were simply supported on a rigid laboratory frame using two roller supports at a distance of 960 mm. The imposed loading was applied at two points 60 mm apart from each other in the mid-span of each beam using a steel spreader beam. The imposed load was consistently increased with low rate using a pinned-end actuator and was measured by a load cell with accuracy equal to 0.05 kN. The net mid-span deflections of the beams were recorded by three Linear Variable Differential Transducers (LVDTs) with 0.01 mm accuracy. One of them was placed at the middle of the beam span and the other two at the supports, as shown in Figure 3. Measurements for load and deflection were read and recorded continuously during the tests. Further, admittance measurements of the embedded PZT transducers inside concrete mass as "smart aggregates" and the externally epoxy bonded PZTs were recorded at different levels of the applied loading using the WiAMS devices. A harmonic excitation voltage of 10 Volts was amplified to the mounted PZTs in the time domain range at every central frequency, as described by the expression (1).

4 TEST RESULTS AND DISCUSSION

The tested RC beams exhibited typical shear response and brittle diagonal failure, as they were designed and expected. In general, the first flexural cracks formed in the mid-span and perpendicular to the longitudinal axis of the beams. The increase of the applied load caused further flexural cracks that spread and inevitably initial diagonal cracks formed. Consequently, the formation of a critical shear crack on a shear span of each beam caused its brittle failure.

The plots of Figures 4, 5 and 6 present the behaviour of beams Sp1, Sp2 and Sp3, respectively, in terms of the experimental curve of shear load versus mid-span deflection. The cracking patterns of beam Sp2 at different levels of loading and corresponding damage are also displayed in the photographs of Figure 5.

Typical curves of voltage signal measurements of embedded "smart aggregate" transducers are also presented in Figures 7 and 8 for PZT9 of beam Sp1 and PZT18 of beam Sp2, respectively. Further,

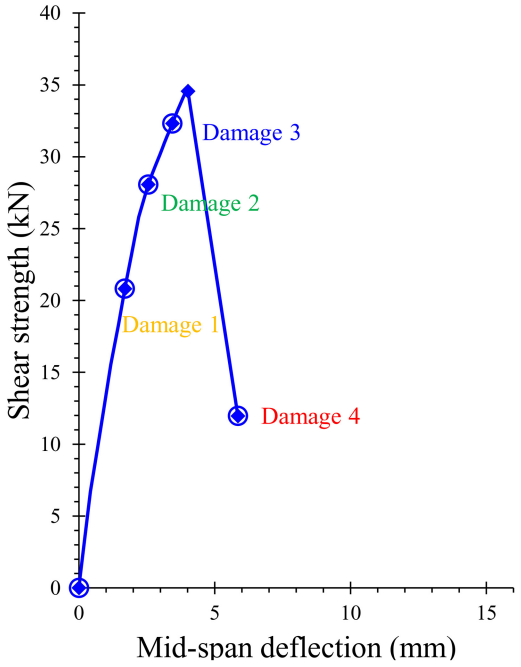

Figure 4. Experimental behaviour of beam Sp1.

Figure 9 shows the voltage signal measurements of the externally bonded PZTX13 on beam Sp3.

It is noted that the discrepancies between the healthy and the damaged levels in the voltage signal curves of the embedded "smart aggregate" transducers PZT9 and PZT18 (Figs. 7 and 8) are clear and higher than the corresponding discrepancies for the voltage signals of the externally bonded piezoelectric patches PZTX13 (Fig. 9) which seem to be rather slight. This indicates that externally bonded PZTs seem to be less sensitive than the embedded ones.

From the comparison of the voltage signal curves between "smart aggregate" transducers PZT9 and PZT18 in Figures 7 and 8, respectively, it is obvious that PZT9 exhibits greater discrepancies between the healthy state and the examined damaged levels with respect to the corresponding discrepancies of PZT18 which are slight and rather negligible for the damage levels 1, 2 and 3. This observation is corresponding to the fact that PZT18 was placed on the right shear span of beam Sp2 where no diagonal cracking occurred (a critical shear crack formed on the left span, as shown in the photographs of Fig. 5).

The quantitative assessment of damage is traditionally made by the use of the statistically scalar damage values of Root Mean Square Deviation index (RMSD) (Hu et al 2014):

$$RMSD = \sqrt{\frac{\sum_{1}^{N}\left(\left|V_p(\omega)\right|_D - \left|V_p(\omega)\right|_0\right)^2}{\sum_{1}^{N}\left(\left|V_p(\omega)\right|_0\right)^2}} \qquad (2)$$

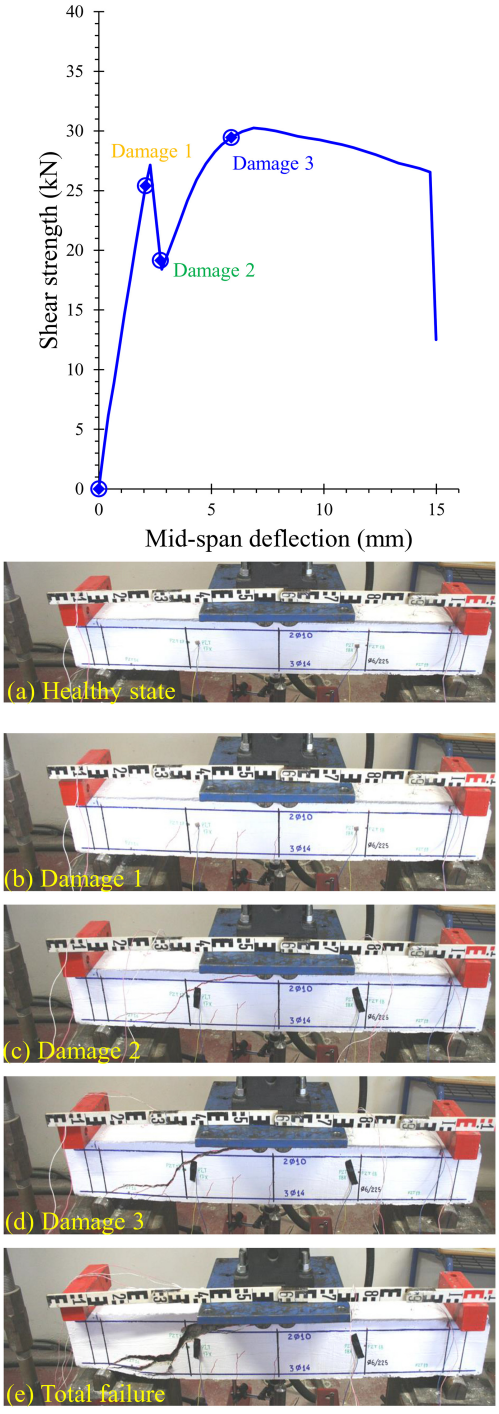

Figure 5. Experimental behaviour and cracking patterns at different damage – loading levels of beam Sp2.

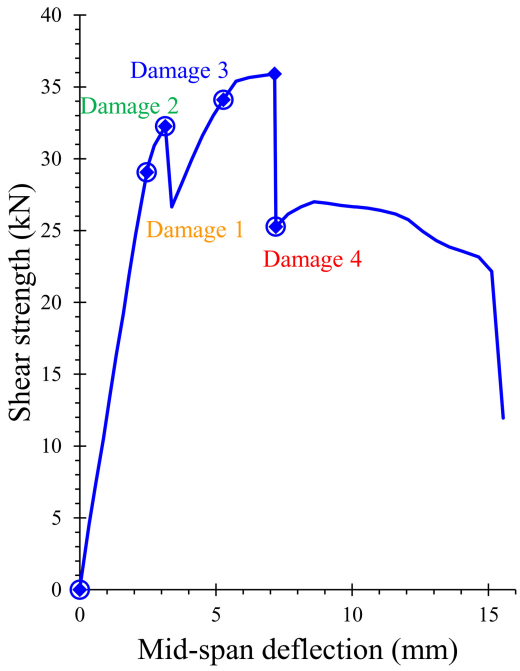

Figure 6. Experimental behaviour of beam Sp3.

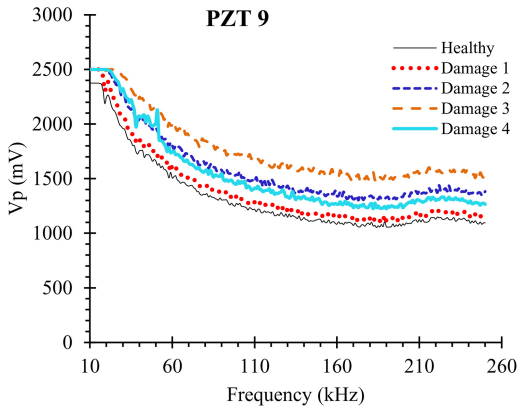

Figure 7. Comparisons of the embedded "smart aggregate" transducer PZT9 measurements of voltage signal between the healthy state and the four damage levels of the beam Sp1.

where $|V_P(\omega)|_0$, $|V_P(\omega)|_D$ are the absolute values of the voltage signal measurements of the examined piezoelectric transducer at the baseline value (subscript 0) of the initial RC beam status ("Healthy" state) and at the examined damage level (subscript D) of the RC beam ("Damage 1", "Damage 2", etc.), respectively, and N is the number of measurements (the frequency index of each sum ranges from 10 kHz to 260 kHz).

Based on the adopted EMA technique principals, when damage occurred in any RC beam, the voltage signal curves measured before damage (initial "Healthy" state) and after damage will change. The greater the damage, the greater the change in the voltage signal curves and, based on expression (2), the greater the absolute value of RMSD. Thus, RMSD index can be used to evaluate the evolvement of damage severity.

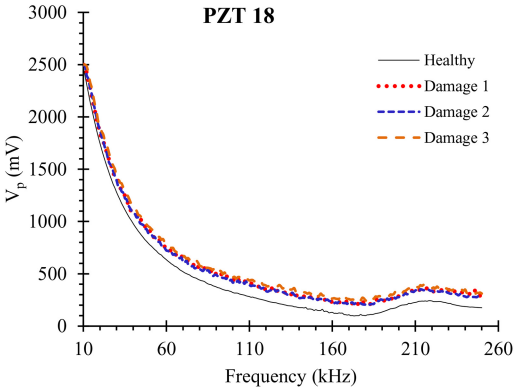

Figure 8. Comparisons of the embedded "smart aggregate" transducer PZT18 measurements of voltage signal between the healthy state and the four damage levels of the beam Sp2.

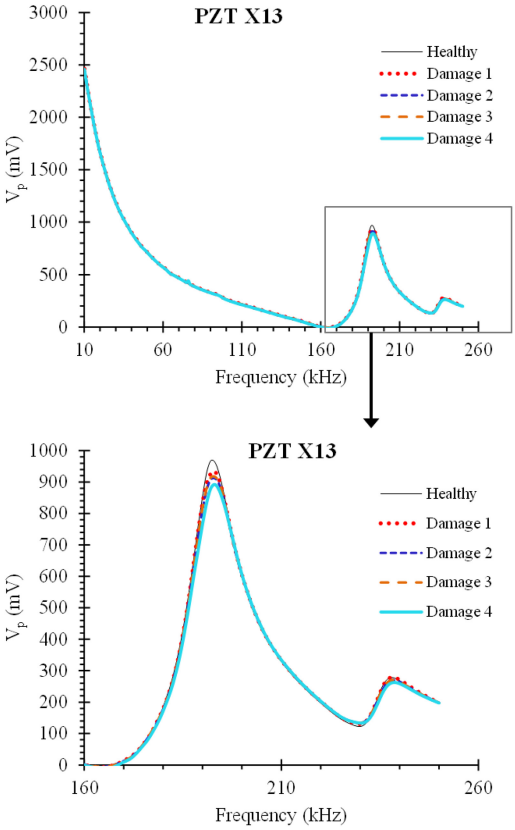

Figure 9. Comparisons of the externally epoxy bonded transducer PZTX13 measurements of voltage signal between the healthy state and the four damage levels of the beam Sp3.

Figures 10, 11 and 12 display the histogram of RMSD index values for the voltage signal measurements of all PZTs mounted to beams Sp1, Sp2 and Sp3, respectively, for the examined damage levels. Figures 10a, 11a and 12a concern the epoxy bonded patches, whereas Figures 10b, 11b and 12b the embedded "smart aggregate" transducers.

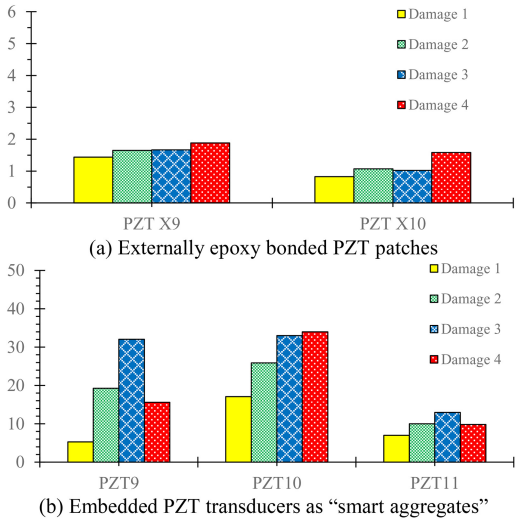

Figure 10. RMSD index values for signal measurements of the PZTs mounted to beam Sp1 for the examined damages.

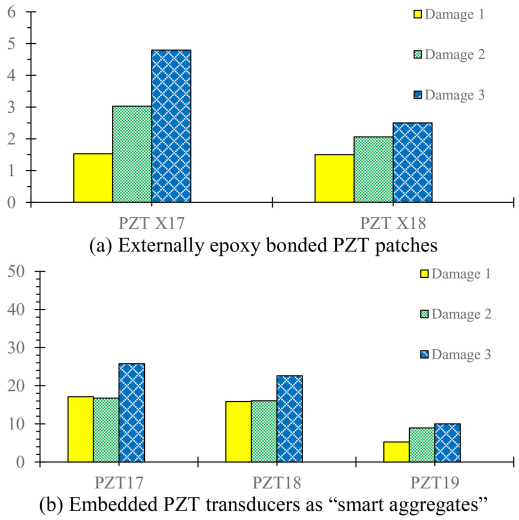

Figure 11. RMSD index values for signal measurements of the PZTs mounted to beam Sp2 for the examined damages.

It is noticeable that, more or less, along with the increase of the damage level, the values of RMSD calculated from the voltage signal measurements were rationally trending upwards in most of the mounted PZTs confirming the increased damage severity. Further, PZTs that exhibited low or decreased RMSD values at high damage levels indicate low or negligible damage severity in the concrete region that they are located. Thus, comparisons of the RMSD values derived from an array of PZTs mounted to specific positions of the examined RC beam can locate the locus and the magnitude of the occurred damage at different loading/damage levels, such as flexural cracking

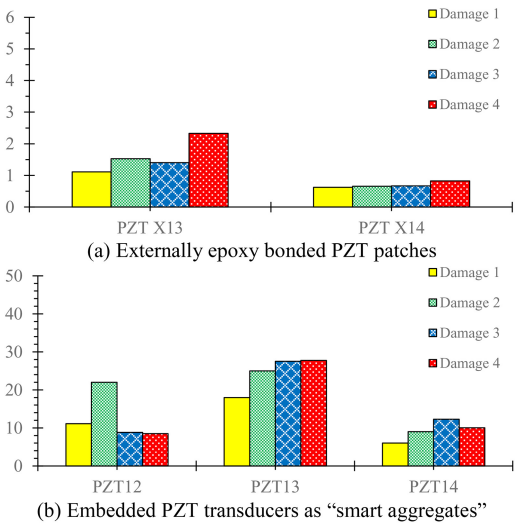

(a) Externally epoxy bonded PZT patches

(b) Embedded PZT transducers as "smart aggregates"

Figure 12. RMSD index values for signal measurements of the PZTs mounted to beam Sp3 for the examined damages.

initiation, onset of diagonal cracking, extended/severe diagonal cracking and final shear failure.

This can be justified from the RMSD values of the externally bonded patches PZTX17 and PZTX18 (Fig. 11a) and the embedded "smart aggregate" transducers PZT17, PZT18 and PZT19 (Fig. 11b) of the beam Sp2 as explained below:

– At Damage "1" (onset of diagonal cracking) PZTX17 and PZT17 mounted to the left shear span of beam Sp2 exhibits slightly higher RMSD values than PZTX18 and PZT18 mounted to the right shear span, where a thin diagonal crack initially occurred on the left shear span of the beam (see also cracking pattern (b) in Fig. 5). It is also noted that PZT19 that was placed near to the right support (right shear span) was far from the first diagonal crack and rationally its RMSD value is significantly low.
– At Damage "2" (extended diagonal cracking) PZT transducers of the left span (PZTX17 and PZT17) exhibits consistently higher RMSD values than PZTs of the right span (PZTX18, PZT18 and PZT19) and diagonal cracking was also extended on the left span of the beam as can be seen in cracking pattern (c) of Figure 5.
– At Damage "3", a severe shear crack developed on the left shear span (see also cracking pattern (d) in Fig. 5) and the RMSD value of PZTX17 on the left span is significantly higher than the RMSD value of PZTX18 on the right span, ensuring (or predicting) this way that the final shear failure would inevitably occurr on the left span as actually happened and it can be observed in cracking pattern (e) of Figure 5. It is emphasized that the RMSD of PZT19 stayed in very low values during the test (see also Fig. 11b) since the region in which it was placed remained undamaged.

5 CONCLUSIONS

The ability of a new integrated wireless structural health monitoring system (WiAMS) to detect and evaluate the damage severity level in shear-critical RC beams using voltage signatures of specially mounted PZTs was experimentally investigated.

Voltage signatures of the PZTs acquired from test measurements using the WiAMS showed obvious discrepancies between the response of the healthy and the examined damage levels for every RC beam. These differences clearly indicated the presence of damage, whereas their gradual character revealed the magnitude of the occurred damage.

Damage assessment was achieved using values of the known statistical RMSD index. It was found that along with the increase of the damage level, the values of RMSD calculated from the voltage signal measurements of the PZTs rationally trended upwards confirming the increase of the damage severity. Both embedded and externally bonded PZT signals exhibited such response. However, the externally bonded PZTs presented significantly lower discrepancies and RMSD values than the embedded ones, indicating that they might be less sensitive.

The test results provide promising indications that the WiAMS measurements of a series of mounted PZTs to specific locations of a shear-critical RC element could help to diagnose damage and to predict the forthcoming total shear failure at early damage stages, such as at the onset of diagonal cracking.

ACKNOWLEDGEMENT

The contribution of the personnel of the Reinforced Concrete Laboratory in Democritus University of Thrace, Greece and especially the support and guidance of Professor C.G. Karayannis is greatly appreciated.

This research has been co-financed by the European Union (European Social Fund-ESF) and Greek National Funds through the Operational Programme "Education and Lifelong Learning" of the National Strategic Reference Framework (NSRF) – Research Funding Program: THALES. Investing in knowledge society through the European Social Fund.

REFERENCES

Chalioris, C.E. 2013. Steel fibrous RC beams subjected to cyclic deformations under predominant shear. *Engineering Structures* 49: 104–118.

Chalioris, C.E., Papadopoulos, N.A., Angeli, G.M., Karayannis, C.G., Liolios, Ast.A. & Providakis, C.P. 2015a. Damage evaluation in shear-critical reinforced concrete beam using piezoelectric transducers as smart aggregates. *Open Engineering* 5(1): 373–384.

Chalioris, C.E., Providakis, C.P., Favvata M.J., Papadopoulos, N.A., Angeli, G.M. & Karayannis, C.G. 2015b. Experimental application of a wireless earthquake damage

monitoring system (WiAMS) using PZT transducers in reinforced concrete beams. *WIT Transactions on The Built Environment* 152: 233–243.

Divsholi, B.S., Yang, Y. & Bing, L. 2009. Monitoring beam-column joint in concrete structures using piezo-impedance sensors. *Advanced Materials Research* 79–82: 59–62.

Divsholi, B.S. & Yang, Y. 2014. Combined embedded and surface-bonded piezoelectric transducers for monitoring of concrete structures. *NDT & E International* 65: 28–34.

Hu, X., Zhu, H. & Wang, D. 2014. A study of concrete slab damage detection based on the electromechanical impedance method. *Sensors* 14(10): 19897–19909.

Karayannis, C.G., Voutetaki, M.E., Chalioris, C.E., Providakis, C.P. & Angeli, G.M. 2015. Detection of flexural damage stages for RC beams using piezoelectric sensors (PZT). *Smart Structures and Systems* 15(4): 997–1018.

Karayannis, C.G., Chalioris, C.E., Angeli, G.M., Papadopoulos, N.A., Favvata M.J. & Providakis, C.P. 2016. Experimental damage evaluation of reinforced concrete steel bars using piezoelectric sensors. *Construction and Building Materials* 105: 227–244.

Kaur, N. & Bhalla, S. 2015. Combined energy harvesting and structural health monitoring potential of embedded piezo-concrete vibration sensors. *Journal of Energy Engineering* 141(4).

Naidu, A.S.K. & Soh, C.K. 2004. Damage severity and propagation characterization with admittance signatures of piezo transducers. *Smart Materials and Structures* 13(2): 393–403.

Providakis, C.P. & Voutetaki, M.E. 2006. Seismic damage detection using smart piezo-transducers and electromechanical impedance signatures. *Earthquake Engineering and Seismology; Proc. europ. conf., Geneva,* Switzerland: Paper Number 307.

Providakis, C.P. & Voutetaki, M.E. 2007. Electromechanical admittance-based damage identification using Box-Behnken design of experiments. *Structural Durability & Health Monitoring* 3(4): 211–27.

Providakis, C.P, Stefanaki, K.D., Voutetaki, M.E., Tsompanakis, J. & Stavroulaki, M.E. 2014. Damage detection in concrete structures using a simultaneously activated multi-mode PZT active sensing system: Numerical modelling. *Structure and Infrastructure Engineering* 10(11):1451–1468.

Providakis, C.P., Karayannis, C.G., Chalioris, C.E., Favvata, M.J., Angeli, G.M. & Papadopoulos, N.A. 2015. Usage of PZTs for damage evaluation of steel reinforcing bar. *Scholars Journal of Engineering and Technology* 3(1B): 80–93.

Ribas, C. & Cladera, A. 2013. Experimental study on shear strength of beam-and-block floors. *Engineering Structures* 57: 428–442.

Soh, C.K., Tseng, K.K.-H., Bhalla, S. & Gupta, A. 2000. Performance of smart piezoceramic patches in health monitoring of a RC bridge. *Smart Materials and Structures* 9(4): 533–542.

Tsonos, A.-D.G. 2014. A new method for earthquake strengthening of old R/C structures without the use of conventional reinforcement. *Structural Engineering and Mechanics* 52(2): 391–403.

Voutetaki, M.E., Providakis, C.P. & Chalioris, C.E. 2012. FRP debonding prevention of strengthened concrete members under dynamic load using smart piezoelectric materials (PZT). *Composite Materials, ECCM 2012, Composites at Venice; Proc. europ. conf., Venice,* Italy: 24–28.

Voutetaki, M.E., Papadopoulos, N.A., Angeli, G.M. & Providakis, C.P. 2016. Investigation of a new experimental method for damage assessment of RC beams failing in shear using piezoelectric transducers. *Engineering Structures* 114: 226–240.

Wang, D., Song, H. & Zhu, H. 2013. Numerical and experimental studies on damage detection of a concrete beam based on PZT admittances and correlation coefficient. *Construction and Building Materials* 49: 564–574.

Yang, Y. & Miao, A. 2008. Effect of external vibration on PZT impedance signature. *Sensors* 8(11): 6846–6859.

Concrete Solutions – Grantham et al. (Eds.)
© 2016 Taylor & Francis Group, London, ISBN 978-1-138-03008-4

Effect of stirrups on reinforcement corrosion measurements in concrete

C.-T. Chen, C.-J. Li & T.-P. Chang
National Taiwan University of Science and Technology, Taipei, Taiwan (ROC)

ABSTRACT: Reinforced concrete is widely used in civil engineering nowadays and its durability is a concern. One of the major durability issues is reinforcement corrosion, which is highly relevant to the mechanical and seismic properties of structures. However, the reinforcement in modern buildings in seismic regions is mostly tightly arranged due to the seismic requirements, thereby leading to the uncertainties during reinforcement corrosion measurements. In view of this issue, this study explores the effects of stirrups on reinforcement corrosion using the galvanostatic and weight loss techniques. During the experiments, mortar specimens with different reinforcement arrangements were continuously charged, and the corrosion rates and weight losses were measured at certain time intervals. Results showed that the corrosion measurements of the main bars were unstable and inaccurate as the spacing between the stirrups and distance between the stirrups and main bars was reduced.

1 INTRODUCTION

Reinforced concrete is one of the most widely used materials in civil engineering and it must have adequate mechanical properties, durability, cost, safety, workability and so on. Among all the properties of reinforced concrete, durability is drawing more and more attentions since many important infrastructures were built in the last century and they are facing problems of aging and deterioration. One of the major durability issues of reinforced concrete is reinforcement corrosion, which is usually associated with ambient carbon dioxide and salt. The reinforcement is protected by concrete due to both physical and chemical mechanisms (Malhotra, V.M. & Carette G.G. 1982). The concrete cover protects the reinforcement from the intrusion of foreign harmful ions. In addition, the pore solution of concrete is highly alkaline (pH = 12–14), which helps reinforcement to form a passive layer at the surface. However, once the reinforcement corrodes, a loose oxide layer is formed at the surface and its volume expands by 2–7 times (Mehta, P.K. 1986). Such expansive oxides induce an expansion force in concrete, leading to tensile cracks in the concrete and loss of bonding between the reinforcement and concrete. Foreign harmful ions further intrude the concrete, leading to more corrosion.

Reinforcement corrosion is not easy to observe until the cover spalls. At that time, it always takes great effort to get the reinforced concrete repaired. Techniques to detect the corrosion at an early stage are important. Among the various techniques, the nondestructive galvanostatic technique is becoming popular nowadays and can be used on site. Not only the corrosion current density but also the resistivity of concrete cover is measured (Klinghoffer O. 1995). During the measurement, a small pulse current is applied so the reinforcement is slightly polarized. The corrosion rate is calculated by the changes of the potential (Newton, C.J. & Sykes, J.M. 1988).

In the literature, the ductility behavior of reinforced concrete is found to be influenced by the location and length of corrosion along the main bar (Ou, Y.C. et al. 2012; Ou, Y.C. et al. 2013; Ou, Y.C. & Chen, H.H. 2014). In addition, the corrosion of stirrups can be also an important factor. Therefore, this study aims to further explore the corrosion of the main bar influenced by the amount of stirrups, spacing between the stirrups and the distance between the stirrups and the main bar. Both the galvanostatic technique and weight loss techniques were used to estimate the amount of corrosion. The corrosion rate measured by galvanostatic technique was integrated with time to obtain the calculated weight of corrosion product, which was compared with the actual weight loss.

2 EXPERIMENTAL

In this study, mortar specimens embedded with a main bar (No.5, 15.9 mm in diameter) and stirrups (No. 3, 9.5 mm in diameter) were prepared. They were divided into three groups: ones without stirrups, ones with a single stirrup and ones with double stirrups, as shown in Figure 1. The water-cement ratio of the mortar was 0.6, as given in Table 1. After the demold, the specimens were cured in saturated lime water for 28 days and immersed in 3.5% salt water. The main bars were charged by a constant current density of 1 mA/cm^2 at the steel surface and their corrosion current densities were measured using galvanostatic technique daily. Such measurements continued until rust was apparent

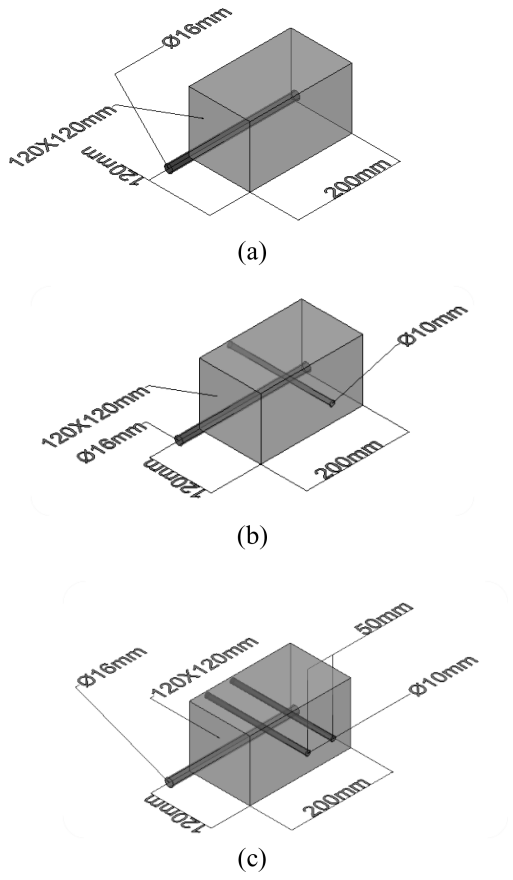

Figure 1. Mortar specimens with (a) single main bar, (b) single main bar and one stirrup, or (c) single main bar and two stirrups.

Table 1. Mix design of mortar specimens.

w/c	cement kg/m^3	water kg/m^3	fine aggregates (SSD) kg/m^3
0.6	358	256	1717

at the surface of specimens. The corroded reinforcement was taken out and weighed to the nearest 0.01 g to calculate the weight loss.

The corrosion rates were calculated by Faraday's law. The calculated amounts of total corrosion were obtained by integrating the fluctuating corrosion rates with time. Such calculated corrosion (calculated weight loss) was compared with the actual weight loss.

The experimental parameters included the amounts of the stirrups and the relative positions of the main bar and stirrups, summarized as follows:

(1) Amounts of stirrups
Specimens with single main bar and one or two stirrups were prepared.

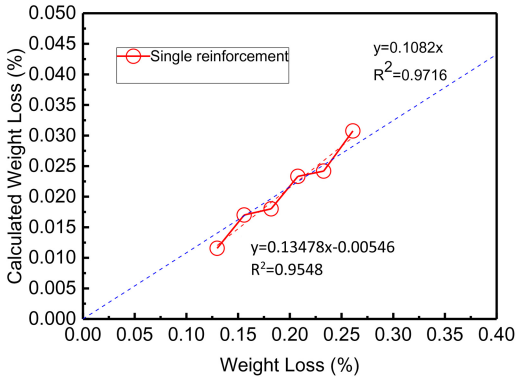

Figure 2. Relationship between the calculated weight loss and the actual weight loss (specimen with single main bar).

(2) Distance between the stirrups and main bar
Specimens with stirrups attached (spacing: 0 mm) or not attached (spacing: 25 mm) on the main bar were prepared to explore the corrosion behavior of the overlapped reinforcement and the influence of the stirrups on the corrosion measurements of the main bar.

(3) Spacing between the two stirrups
The spacing between the two stirrups was 40 mm or 90 mm. Such spacing was determined in reference to current building design code (CPA 2011).

3 RESULTS AND DISCUSSION

3.1 *Specimens with a single main bar*

The results are shown in Figure 2. The calculated amount of corrosion was smaller than the actual weight loss by 8-11 times. The calculated weight loss was around 10.82% of the actual weight loss by the fitting curve. As the charging time increased, the differences between both were reduced, suggesting that the measurements were more accurate as the amount of corrosion was increased. Such differences may result from stray current in the specimen. The galvanostatic current may only pass through the mortar instead of the main bar, leading to errors. As the corrosion was increased, the galvanostatic current probably reached the main bar through microcracks more easily so the measurements were more reliable.

3.2 *Specimens with single main bar and a stirrup*

When the stirrup contacted the main bar, the results are shown in Figure 3. The calculated amount of corrosion was smaller than the weight loss by 4–13 times. As the charging time increased, differences between both were increased, suggesting that the measurements by the galvanostatic technique were less accurate and the corrosion of the main bar was increased rapidly. In addition, the fitting curve in Figure 3 does not pass

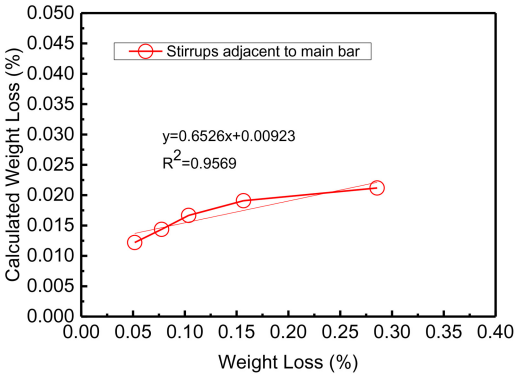

Figure 3. Relationship between the calculated weight loss and the actual weight loss (specimen with single main bar and a stirrup in contact).

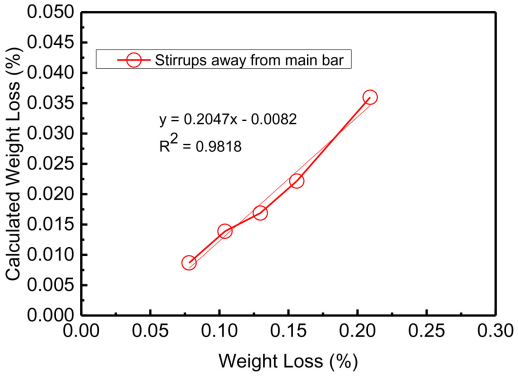

Figure 4. Relationship between the calculated weight loss and the actual weight loss (specimen with single main bar and a stirrup not in contact).

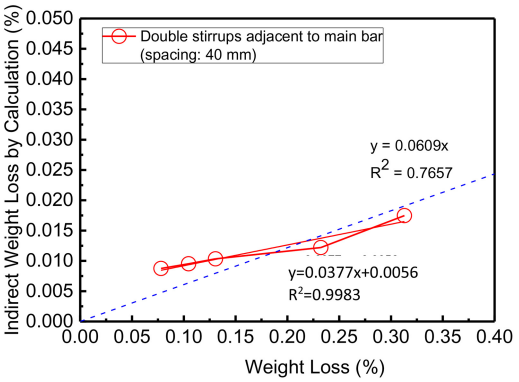

Figure 5. Relationship between the calculated weight loss and the actual weight loss (specimen with single main bar and in contact with double stirrups with spacing of 40 mm).

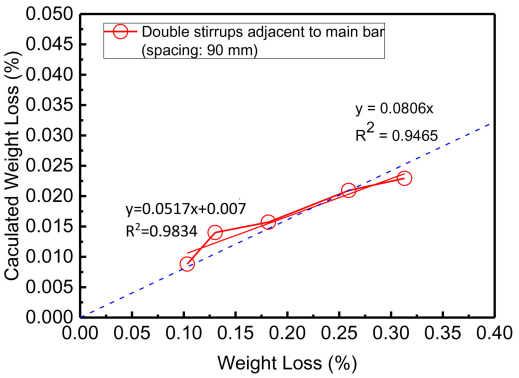

Figure 6. Relationship between the calculated weight loss and the actual weight loss (specimen with single main bar and in contact with double stirrup with spacing of 90 mm).

through the origin, suggesting that the corrosion measured at the early time was due to the corrosion of stirrup rather than the main bar. The calculated corrosion was about 65.26% of the weight loss by the fitting curve.

In contrast to the specimen with a single main bar, the stirrup corroded faster than the main bar and induced many surrounding microcracks, in which the charging current passed through more easily, further leading to accelerated corrosion of main bar. Therefore, the amount of main bar corrosion increased rapidly at later time. Furthermore, the galvanostatic current was obstructed by the stirrups so the measurements were even lower.

When the stirrup did not contact the main bar, the results are shown in Figure 4. The calculated amount of corrosion was less than the weight loss by 5–9 times. As the charging time increased, such differences reduced, suggesting that the measurement by the galvanostatic technique was more accurate and less influenced by the stirrup. Again, the surrounding microcracks due to the corrosion of stirrup helped the transport of galvanostatic current. On the other hand, the fitting curve did not pass the origin. It was likely that the corrosion of the main bar was not measured at early time due to the obstruction by the stirrup near the measuring surface. The calculated corrosion was about 20.5% of the actual weight loss. Although this value was smaller than that of the specimens with the main bar and stirrup in contact, it showed a more linear relationship.

3.3 *Specimens with single main bar and two stirrups*

When the two stirrup (spacing: 40 mm) contacted the main bar, the results are shown in Figure 5. The calculated corrosion was far less than the actual weight loss, only 6.09% by the fitting curve. Such results suggested that the amount of main corrosion increased and the measurements reduced as the amounts of stirrups increased and the spacing between stirrups was reduced.

On the other hand, as the spacing between the stirrups was increased to 90 mm (Figure 6). The corrosion measurement of the main bar was more accurate. The

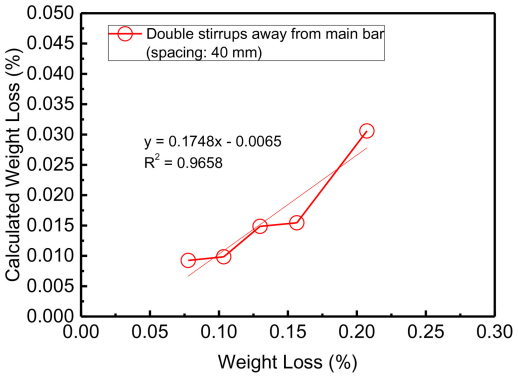

Figure 7. Relationship between the calculated weight loss and the actual weight loss (specimen with single main bar and not in contact with double stirrups with spacing of 40 mm).

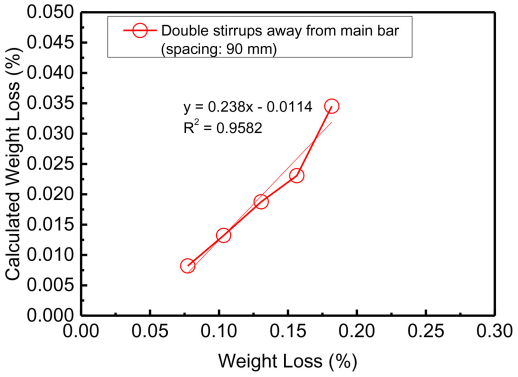

Figure 8. Relationship between the calculated weight loss and the actual weight loss (specimen with single main bar and not in contact with the double stirrups with spacing of 90 mm).

calculated amount of corrosion was around 8.06% of the weight loss by the fitting curve. Although such a calculated weight loss was smaller than those of the specimen with single main bar and a stirrup, the results further suggested that the increased spacing between the stirrups helped to increase the accuracy of the corrosion measurements.

When the main bar was not in contact with the two stirrups (spacing: 40 mm), the results are shown in Figure 7. The calculated amount of corrosion was about 17.48% of the actual weight loss by the fitting curve. When compared with the results in 3.2, it can be found that the close spacing between the stirrups induced deviated measurements even though they were not in contact with the main bar. In addition, when compared with the results in 3.1, the influence of the stirrup on the main bar corrosion measurement was reduced at this time. The actual amount of corrosion was close to that of the specimen with only single main bar.

When the spacing between the two stirrups was further increased (spacing: 90 mm), the results are shown in Figure 8. The calculated amount of corrosion was closer to and more linearly related with the actual weight loss, suggesting that the measurements were more stable and accurate. At this time, the calculated weight loss was around 23.8% of the weight loss by the fitting curve.

Table 2. Ratio of the calculated weight loss to actual weight loss.

Combinations	Spacing between the stirrups	Distance between the stirrup and main bar	Weight loss ratio
Single main bar	–	–	10.82%
Single main bar and one stirrup	–	0 mm	65.26%
		25 mm	20.47%
Single main bar and two stirrups	40 mm	0 mm	6.09%
		25 mm	17.48%
	90 mm	0 mm	8.06%
		25 mm	23.80%

The ratio between the calculated weight loss and the actual weight loss is summarized in Table 2. Such results clearly show that the spacing between the stirrups was an important issue. Accuracies of the measurements were increased with the increased stirrup spacing. Moreover, the presence of the stirrups may influence the corrosion measurements of the main bar and such influence varies with the number of stirrups.

4 CONCLUSIONS

This study explores the effect of the stirrup on the corrosion measurements of the main bar in mortar specimens. The conclusions are summarized as follows:

(1) In specimens with a single main bar but without stirrups, the corrosion was linearly increased by the accelerated current time. The calculated amount of corrosion using the galvanostatic technique was lower than the weight loss by around 8–11 times. With the increase of the charging time, the differences between the two values were reduced, suggesting that the measurements by the galvanostatic technique were more accurate.
(2) When the main bar contacted the two stirrups, the differences between the calculated amount of corrosion and the weight loss were increased with the accelerated current time. On the other hand, when they are not in contact, such differences were reduced with time, suggesting that the galvanostatic technique was more reliable.
(3) When the spacing between the stirrups was reduced, the measurements were not stable and accurate. Increased spacing helps to reduce the influence of the stirrups on the main bar corrosion measurements.

ACKNOWLEGEMENT

The authors would like to thank the financial support from the Ministry of Science and Technology (ROC) under the grant No. 103-2221-E-011 -060 -MY3.

REFERENCES

Construction and Planning Agency (CPA). 2011. Design code for concrete structures. Ministry of the Interior, R.O.C., Taipei, Taiwan

Klinghoffer, O. 1995. In-situ monitoring of reinforcement corrosion by means of electrochemical methods. Nordic Concrete Research 16(1): 1051–1074.

Malhotra, V.M. & Carette G.G. 1982. Silica fume: a Pozzolan of new interest for use in some concretes. Concrete Construction 27(5): 443–446.

Mehta, P.K. 1986. Concrete: Structure, Properties and Materials. Prentice-Hall, New York.

Newton, C.J. & Sykes, J.M. 1988. A galvanostatic pulse technique for investigation of steel corrosion in concrete. Corrosion Science 28(11): 1051–1074.

Ou, Y.C., Tsai, L.L., & Chen, H.H. 2012. Cyclic performance of large-scale corroded reinforced concrete beams. Earthquake Engineering and Structural Dynamics 41(4): 593–604.

Ou, Y.C., Fan, H.D., & Nguyen, D.N. 2013. Long-term seismic performance of reinforced concrete bridges under steel reinforcement corrosion due to chloride attack. Earthquake Engineering and Structural Dynamics 42(14): 2113–2127.

Ou, Y.C., & Chen, H.H. 2014. Cyclic behavior of reinforced concrete beams with corroded transverse steel reinforcement. Journal of Structural Engineering, ASCE. 140(9): 04014050.



Taylor & Francis
Taylor & Francis Group
http://taylorandfrancis.com

Concrete Solutions – Grantham et al. (Eds.)
© 2016 Taylor & Francis Group, London, ISBN 978-1-138-03008-4

Reinforced concrete NDT research and practice in Turkey: A gap analysis

O. Gunes, C. Sengul, C. Colak & M. Asan
Istanbul Technical University, Istanbul, Turkey

ABSTRACT: Use of Nondestructive Testing (NDT) techniques for the assessment of in-situ strength of concrete is an area with high impact potential in condition assessment of existing structures. Such a capability is especially important for Turkey where the majority of the existing building stock is located in high seismicity areas and has questionable quality of materials and workmanship. The Urban Transformation Law recently enacted in Turkey requires identification of all high-risk buildings and their strengthening or renewal within the next couple of decades. Considering that one third of the 20 million occupancy units in Turkey are estimated to be high-risk, their identification is a giant task on its own which requires rapid and reliable condition assessment of existing buildings. Use of NDT, a potentially indispensable tool in this respect, is receiving wider research interest in recent years. This paper makes a review of the current state-of-the-art in NDT research and applications in Turkey and highlights the areas where more intensive and focused research is needed to help develop the urgently needed rapid and reliable condition assessment methodology for existing buildings.

1 INTRODUCTION AND BACKGROUND

Civil Engineering infrastructures constitute the largest investment in every country and their protection against natural and man-made hazards is a priority issue. Turkey is located at the intersection of several tectonic plates and a large proportion of its more than 75 million population live in seismic areas. Since the beginning of the 20th century, earthquakes have been responsible for three out of four damaged or destroyed homes in Turkey, with a death toll in the range of tens of thousands and economic loss in the range of tens of billions of dollars. The contributing factors to this outcome are the improper zoning and settlement, insufficient attention to site and soil conditions, especially the potential of liquefaction and ground failure, poor design and detailing of structures, and poor materials and workmanship stemming from insufficient inspection and supervision. As a result, approximately one third of the 20 million occupancy units in Turkey are estimated to have insufficient seismic resistance and are in need of retrofitting or renewal. This is particularly alarming when considered in conjunction with the knowledge from scientific studies that there is a high probability of another severe earthquake within a couple of decades in the Istanbul area, the most densely populated and most industrialized region in Turkey (Gunes, 2014, 2015, Buyukozturk & Gunes, 2003).

The size of the building stock with insufficient seismic resistance and the urgency of the need for their retrofitting or renewal for timely hazard mitigation make Turkey's grand challenge somewhat unique in nature. Nearly 20 million occupancy units in 9 million buildings must be evaluated within a couple of decades to identify those with seismic risk so that necessary intervention actions can be taken. A massive initiative and an integrated approach were long overdue since the devastating earthquakes of 1999 in Kocaeli and Duzce. The initiative was finally launched in May 2012 with the enactment of Law #6306 entitled 'Transformation of areas under disaster risk,' also known as the Urban Transformation Law, which sets the ground rules and procedures regarding the identification and renewal of high risk buildings as well as high risk areas. The integrated approach, however, has yet to be developed, which is partly the reason why the initiative is already significantly behind schedule.

A possible integrated approach for condition assessment and structural evaluation of a building stock was introduced elsewhere (Gunes, 2015) which involved a geographical information systems (GIS) supported central database that maintains all building and site information and allows a staged assessment and evaluation of buildings with an accompanying quantitative reliability assessment to guide the owner make the decision on whether to invest in further condition assessment and evaluation to obtain more accurate and reliable information, or to initiate a conservative intervention or renewal action (Gunes, 2016).

Since more than half of all buildings in Turkey and more than three quarters of those in Istanbul are reinforced concrete frame buildings, emphasis is placed on this type of construction in this paper. Typical seismic hazard mitigation for buildings begins with condition assessment of the building that includes determination

of geometry, member details and materials quality. Each of these tasks may be a challenge based on the extent of available information and technical documents. Unfortunately, half to three quarters of existing buildings in Turkey lack the design documents and permits required for their construction. Hence, each of above-mentioned tasks is generally a real challenge.

Various exciting technologies can be used to increase the reliability while reducing the duration of condition assessment. Automated modeling of buildings using rapid surveying, image processing and augmented reality can significantly reduce the time to determine building geometry information. The quickly generated structural model is in any case better than having no model to begin with and it lends itself to further improvement and refinement as more detailed information becomes available in later stages of assessment/evaluation. These techniques will be elaborated in detail in future publications.

NDT techniques provide indirect information regarding a member or material without inflicting significant damage. Various NDT techniques show great promise for use in determining member details and materials quality information in a rapid and reliable fashion. Depending on their characteristics NDT techniques may be classified as contact vs. non-contact (remote) techniques, active vs. passive techniques, and based on the type of energy used, mechanical, acoustic, electrical, magnetic, electromagnetic, chemical or electrochemical techniques. NDT combined with imaging techniques may better facilitate obtaining an image of the member or material to determine member details and to detect any anomalies that may be present in the material (Buyukozturk, 1998). Mechanical or acoustic (stress wave) techniques may be better suited for estimating elastic and strength properties. Each technique has advantages and limitations that may be complemented by use of different techniques in combination to improve accuracy and reliability of results.

Use of Nondestructive Testing (NDT) methods in condition assessment of buildings is encouraged in all major codes – including those in Turkey – but the capabilities and reliability of these methods regarding in-situ strength assessment of concrete are not yet sufficient for them to replace destructive methods (Bungey et al, 2006; Maierhofer et al. 2010, Buyukozturk et al. 2011, Breysse, 2012a). For this reason, use of NDT methods is generally allowed in conjunction with destructive methods for in-situ strength assessment so that a reliable correlation can be obtained. TS EN 13791 (2010) standard provides the procedures for use of various NDT techniques for in-situ strength assessment of concrete in conjunction with concrete core sampling as a destructive but relatively more reliable method.

TS EN 13791 requires that at least 18 core samples are obtained from a building to establish a satisfactory correlation between in-situ concrete strength and NDT results. Considering that nearly 9 million buildings are to be evaluated in Turkey, taking core samples alone is a massive task that will require significant time and resources. Strategic development and implementation of improvements prioritized with respect to impact on the speed and reliability of assessment/evaluation appears to be the optimum approach. Developing technologies that can be used to reduce the time of assessment/evaluation requires a time-chain evaluation of the process in order to minimize the most time-taking stages of assessment and evaluation. These technologies include use of nondestructive testing (NDT) techniques to accelerate the condition assessment process and to minimize or ideally eliminate the need for cores (Buyukozturk et al., 2011, Breysse, 2012a,b). The latter seems not possible in the short term due to the need to obtain correlations before reliable estimations can be made, but can be possible in the long term especially when NDT and mildly destructive – but rapid– techniques can be combined to improve the reliability of results.

In this paper, a review of the NDT research and applications in Turkey is provided to determine the current state-of-the-art and to identify the research gaps that need to be addressed for effective use of NDT in rapid and reliable condition assessment of reinforced concrete structures.

2 NDT RESEARCH & APPLICATIONS IN TURKEY

Condition assessment of existing buildings in Turkey is almost exclusively performed in accordance with the provisions in Chapter 7 of ABYBHY (2007), hereafter referred to as the Turkish Seismic Code (TSC). These provisions are summarized elsewhere (Gunes, 2015). This standard makes reference to TS EN 13791 regarding in-situ strength assessment of concrete and use of NDT, but also states less restrictive numbers with respect to the number of cores (minimum 3 per floor and 9 per building) and potential NDT measurements.

In order to enable rapid identification of buildings under high seismic risk, a new specification was recently developed exclusively for use within the urban transformation initiative (RYTEIE 2013). Provisions of RYTEIE are based on those of TSC Ch. 7 with time saving simplifications. For concrete strength, nondestructive tests are required on at least 10 columns or shear walls and a minimum of 5 cores is required from members yielding the lowest NDT results. The in-situ concrete strength is calculated as 85% of the mean concrete strength obtained from compression testing of cores. Steel reinforcement types and layout are to be determined in at least 20% of columns or shear walls, 10% of which are to be performed by exposing steel reinforcement while the remaining 10% can be inspected using covermeter. In-situ yield strength of reinforcing steel is assumed as the minimum characteristic strength required by the code for the identified type of steel.

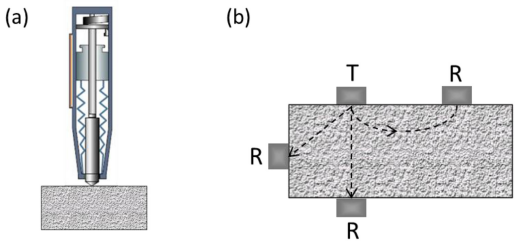

Figure 1. Most frequently used NDT methods for in-situ strength assessment of concrete: (a) Rebound (Schmidt) hammer, (b) Ultrasonic pulse velocity (UPV) in direct, semi-direct, and indirect configurations.

When these specifications are compared from the perspective of time it takes to complete the respective assessment and evaluation procedures, however, the time savings offered by RYTEIE are not substantial. Both specifications inevitably use the essential components of condition assessment and structural evaluation. Since the corresponding techniques and tools are common to the tasks in both specifications, it is unrealistic to expect drastic time savings in their implementation without improving the techniques and tools themselves. In Turkish codes, NDT generally refers to the rebound (Schmidt) hammer technique illustrated in Figure 1a, which is by far the most commonly, and most often wrongly, used technique. To a lesser extent, the ultrasonic pulse velocity (UPV) technique shown in Figure 1b is also among the commonly used NDT methods. Figure 2 shows the potential of both methods in estimating the compressive strength of concrete. Other NDT methods that can be used in condition assessment of reinforced concrete buildings are compiled in an umbrella standard TS 13543 (2013) although their use is relatively much limited.

Simple linear fits were used in Figure 2 due to the preliminary nature of the experimental study. TS EN 13791 uses a bilinear fit for rebound hammer and a parabolic curve fit for UPV. In addition, exponential, power law, and nonlinear curve fits are reported in the literature. Probably the best compilation of existing models in the literature, including those developed in Turkey, was made by Breysse (2012b), who also presented models for combined use of both methods, called the SonReb approach, to improve the accuracy and reliability of estimation. It is demonstrated in this publication that the proposed models may vary significantly based on several factors that include mix proportions, aggregate size and proportion, age, carbonation etc. It was also shown, however, that through calibration using a large data set, the estimation capability can be improved significantly.

The preliminary correlations between NDT results and concrete strength presented in Figure 2 are essentially quite satisfactory considering other variability sources in the structural evaluation process. However, the correlations shown in the figure are not universally applicable to all concrete materials and require

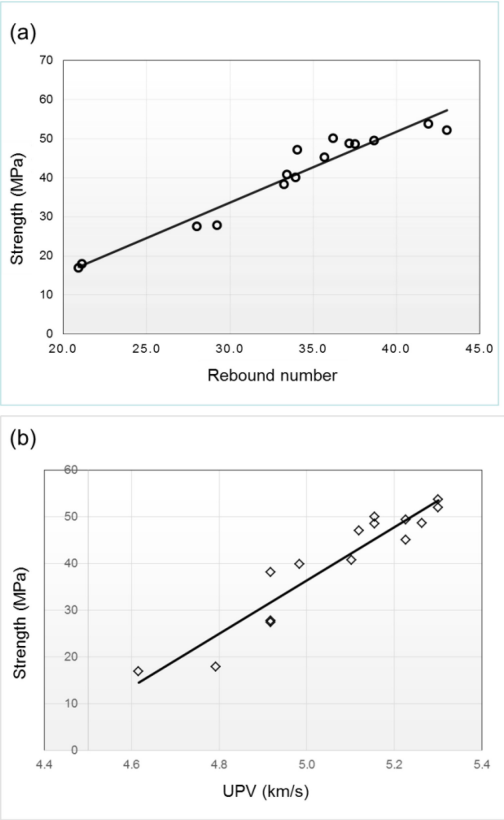

Figure 2. Preliminary experimental results showing the po-tential of estimating in-situ strength of concrete using (a) re-bound hammer, and (b) UPV techniques.

establishment of similar correlations for each structure. Hence, the NDT results cannot be used on their own for concrete strength assessment and need to be correlated with a different and more reliable technique.

In addition to those referenced in Breysse (2012b), several notable research studies were conducted in Turkey that investigated use of rebound hammer and UPV techniques individually or in combination and produced models that are mainly applicable to the concrete mix investigated. A detailed compilation of these studies and the resulting models will be provided in a future report and will be summarized in a publication. Only those that stand out due to their characteristics, methods used, perspective provided, and the original contribution made are listed here for brevity.

Arioz (2004) performed a comprehensive thesis study that investigated destructive, semi-destructive and nondestructive methods including core tests, UPV, rebound hammer, pull-out tests and maturity tests to estimate the compressive strength of concrete. Four different concrete mixtures were tested at different ages using the investigated techniques to achieve correlations between semi/non-destructive and destructive test results. Simple line fits were performed due to the limited number of tests performed using each

Table 1. Models developed by Arioz (2014) for estimation of concrete strength based on NDT results.

Methods	Model
Rebound hammer	fc = 2.25 R – 32.5
UPV	fc = 34.5 UPV – 125.8
Rebound hammer + UPV	fc = 2.09 R – 2.45 UPV – 39.23
Pull-out	fc = 0.987 P + 6.32
Maturity	fc = 5.69 ln(M) – 13.462

Table 2. Models developed by Ozkan et al (2014) for estimation of concrete strength based on NDT results.

Methods	Model
UPV	fc = 275.76 UPV – 984.44
Electrical resistivity	fc = 0.907 R – 117.9

technique. Combinations of different techniques were also considered. The models presented in Table 1 were developed for individual and combined use of different techniques.

Ozkan et al (2004) investigated use of UPV and electrical resistivity tests to estimate the compressive strength obtained from core tests. The resulting models are summarized in Table 2.

Sengul (2014) further used the concept of electrical resistivity as a measure of durability by relating it to the chloride diffusivity of concrete samples. A close correlation (R = 0.98) was obtained between the electrical conductivity and chloride diffusivity, proving its potential for rapid assessment of durability.

Basyigit et al (2012) adopted an interesting approach and attempted to estimate the compressive strength of concrete using image analysis of photos showing the concrete section shown in Figure 3a. Image analysis was combined with rebound hammer and UPV techniques to obtain multivariate correlations that also use the cement matrix ratio obtained from image analysis. The following linear, multilinear, and nonlinear models were developed to predict concrete strength:

$$CS = 1.427Cem - 15.907 \quad (1)$$

$$CS = 0.963Cem - 0.834V + 1.212S - 18.957 \quad (2)$$

$$CS = 0.182V^{0.010}S^{0.680}Cem^{0.902} \quad (3)$$

where *Cem* is cement matrix ratio obtained by image processing technique, *V* is ultrasonic pulse velocity (km/s), *S* is rebound number of Schmidt hammer and the *CS*, is compressive strength of the specimens (MPa). Comparison of experimental and predicted concrete strength values is shown in Figure 3b, which shows promise when image analysis is used in combination with rebound hammer and UPV techniques. It

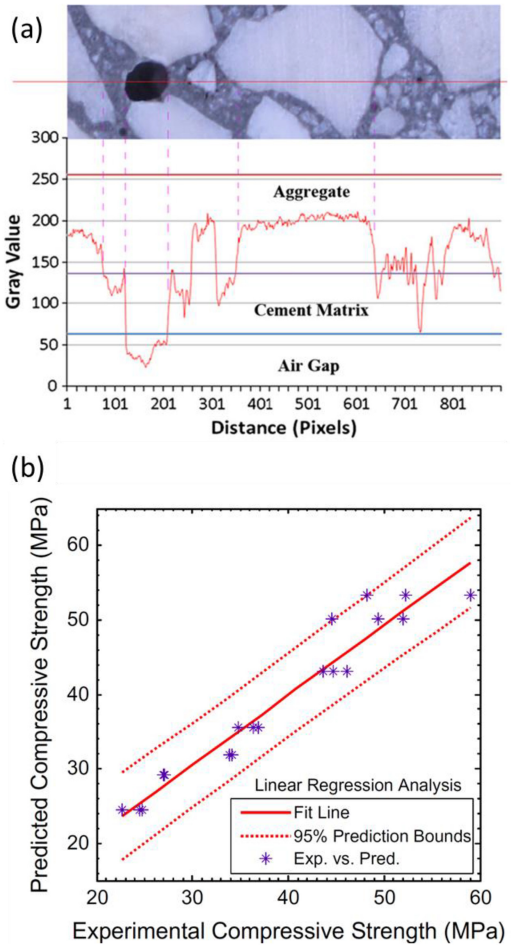

Figure 3. Image analysis of concrete section (a) and estimation of concrete strength in comparison with experimental values (b) (Basyigit et al, 2012).

should be emphasized that a correlation with destructive techniques is still required for different concrete mixtures.

Recognizing the importance of mechanical methods in estimating the strength of concrete, Selcuk et al (2012) made an attempt to develop a practical NDT method based on penetration resistance. The Windsor probe technique is currently the only standardized technique that is based on the penetration resistance of a probe into concrete. However, both the equipment and probes of this system are expensive and it is difficult to acquire since the driver is essentially a powder-actuated gun. Selcuk et al (2012) used a pneumatic nail gun as an inexpensive alternative to the Windsor probe system and calibrated the penetration depth of nails into concrete with the concrete strength. The following empirical relationship between the nail penetration depth *d* and the uniaxial compressive strength of concrete was established:

$$f_c = -2.686d + 120 \quad (4)$$

where f_c is the concrete strength in MPa and d is the nail penetration depth in mm. Figure 4a shows the application of the nail penetration test and in 4b results of this method are compared with those obtained from rebound hammer, UPV and Windsor probe systems. The figure clearly shows the potential of the technique provided that it is properly calibrated with core test results.

3 RESEARCH GAPS

The preceding sections summarize research studies that are characteristically different in their nature and contribution. Naturally, there exist many more studies that may be similar in their approach. The overall number of research studies, however, was found to be less than one hundred, which turned out to be the most significant gap in NDT research in Turkey. Hence, a priority need in this area appears to be to carry out an active promotion of NDT research and introduce more researchers to the area in order to increase the number of researchers, research projects, and publications.

Despite many original and exciting research studies and publications, the existing body of NDT research in Turkey and the resulting publications appear to be disconnected, indicating lack of collaboration and coordination between NDT researchers. Hence, awareness of NDT researchers about other researchers and their ongoing studies is important for developing research collaboration and to display a concerted research effort to reach predetermined goals based on a collective wisdom.

Participation of NDT researchers in Turkey in international NDT research activities and technical committees is vitally important in building research capacity and collaboration.

Commonly used NDT techniques to estimate concrete strength are proven to be successful through numerous studies provided that they are properly precalibrated with destructive methods such as core tests. This necessity limits the potential of such methods to become widely used. There is a need to include semi- or mildly-destructive methods in research studies with the objective for them to replace core testing in the long run to allow rapid condition assessment of buildings.

Accuracy, precision, and reliability of NDT methods in estimating in-situ strength of concrete must be evaluated from a broader perspective in terms of their influence on the outcome of the structural performance evaluation. The expected performance of NDT methods must be proportionate with the influence of their results on the structural evaluation outcome.

Increased numbers of field studies that involve combined use of various destructive, mildly-destructive, and nondestructive methods are urgently needed to develop accurate models based on a large database of experimental and field data.

A greater emphasis needs to be placed on combined use of nondestructive methods in conjunction with mildly destructive mechanical methods to improve the accuracy and reliability of results.

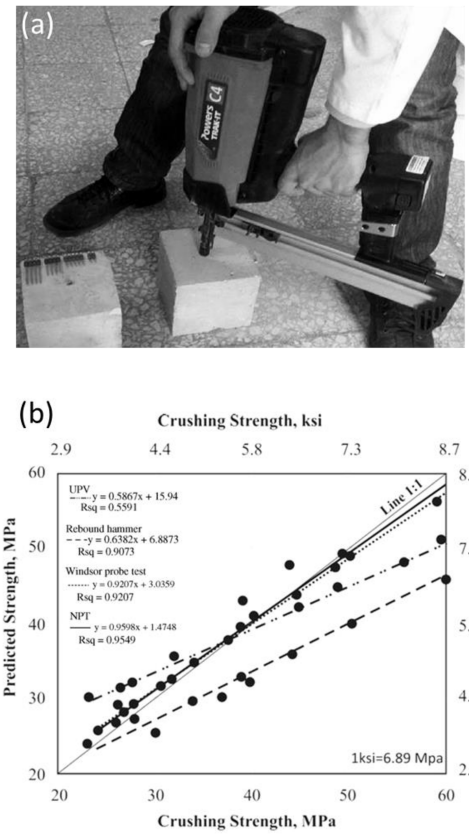

Figure 4. Nail penetration test (a) and its performance in predicting concrete strength in comparison with other NDT techniques (Selcuk et al, 2012).

Planning and development of NDT research studies need to be performed with an integrated approach in mind, where the study complements a part of the overall approach in coordination with other parallel complementary studies.

Experimental and numerical parametric studies as well as benchmark studies participated by multiple researchers need to be performed, investigating the capacity and limitations of individual or combined NDT methods applied to buildings in Turkey.

The research studies presented in this paper focused on estimating the compressive strength of concrete using single or multiple NDT techniques. There are many other aspects of condition assessment applied to existing reinforced concrete structures, such as determining the reinforcement detail, areas, and condition, durability characteristics of materials, and prediction of the building service life as well as the structural performance in order to provide a rational basis for retrofit vs. renewal decisions. Coordinated large scale research studies participated by multiple researchers from different universities and laboratories are needed for development of a collective approach to challenging tasks.

4 CONCLUSION

This paper presents a summary review of NDT research and applications in Turkey to capture the current state-of-the-art, and lists the identified research gaps and needs to collectively address Turkey's grand challenge in an effective and cost efficient manner in the least amount of time. More research and better coordination appear to be the key issues for progress in the right direction.

ACKNOWLEDGEMENT

It is gratefully acknowledged that the work presented in this paper was supported by TUBITAK Project No 214M054.

REFERENCES

ABYBHY 2007. *Specification for Buildings to be built in Disaster Areas* (in Turkish), Ankara: Republic of Turkey, Ministry of Public Works and Settlement.

Arıoz, O. 2004. *Determination of concrete strength by standard, destructive, semi-destructive and nondestructive methods* (in Turkish). Ph.D. Thesis, Anadolu University, Eskisehir, Turkey.

Basyigit, C., Comak, B., Kılıncarslan, S. and Uncu, I.S., 2012. Assessment of concrete compressive strength by image processing technique. *Construction and Building Materials*, 37, pp.526–532.

Breysse, D. (Ed.) 2012a, *Non-destructive assessment of concrete structures: Reliability and limits of single and combined techniques*, State-of-the-Art Report of the RILEM Technical Committee 207-INR, Springer, Dordrecht, The Netherlands.

Breysse, D. 2012b, Nondestructive evaluation of concrete strength: An historical review and a new perspective by combining NDT methods," *Construction and Building Materials*, 33: 139–163.

Bungey, J.H., Millard, S.G. & Grantham, M.G. 2006. *Testing Concrete in Structures*, London: Taylor & Francis.

Buyukozturk, O. & Gunes, O. 2003. Advances in earthquake risk assessment and hazard mitigation for urban ınfrastructures with high characteristic variability, *ARI, The Bulleting of the Istanbul Technical University*, 53(2): 1–20.

Buyukozturk, O., 1998. Imaging of concrete structures. *NDT & E International*, 31(4), pp. 233–243.

Buyukozturk, O., Tasdemir, M.A., Gunes, O. and Akkaya, Y. (Eds.) 2011. *Nondestructive testing of materials and structures*, RILEM Bookseries Vol. 6, Dordrecht: Springer.

Gunes, O. 2014. Turkey's Grand Challenge: Disaster-proof Building Inventory within 20 Years (Keynote paper). *Concrete Solutions 2014*, Grantham, M., Basheer, P.A.M., Magee, B. and Soutsos, M. (Eds.), CRC Press, pp. 11–27.

Gunes, O. 2015. Turkey's grand challenge: Disaster-proof building inventory within 20 years, *Case Studies in Construction Materials*, 2: pp. 18–34.

Gunes, O. 2016. Need for an integrated approach for rapid condition assessment and evaluation of RC building stocks, Structural Faults + Repair – 2016, M.C. Forde (Ed.), 17–19 May 2016, Edinburgh.

Maierhofer, C., Reinhardt, H.-W., Dobmann, G. (Eds.) 2010. *Nondestructive Evaluation of Concrete Structures*, 2 Vol., Cambridge: Woodhead Publishing.

Ozkan, I., Bilim, N., Sezer, R. & Gokay, M.K. 2004. A non-damaging new approach for determining strength values in concrete materials: Electrical conductivity method. *Proc. ROCKMEC 2004-VIIth Regional Rock Mechanics Symposium*, 2004, Sivas, Turkey.

RYTEIE 2013. Principles for Identification of Buildings under Risk (in Turkish), Ankara: Republic of Turkey, Ministry of Public Works and Settlement.

Selcuk, L., Gokce, H.S., Kayabali, K. and Simsek, O. 2012. A nondestructive testing technique: nail penetration test. *ACI Structural Journal*, 109(2), p. 245.

Selcuk, L., Gokce, H.S., Kayabali, K., Simsek, O. 2012. A Nondestructive Testing Technique: Nail Penetration Test, *ACI Structural Journal*, 109(2): 245–252.

Sengul, O., 2014. Use of electrical resistivity as an indicator for durability. *Construction and Building Mater.*, 73: 434–441.

TS 13543 2013, *Nondestructive testing (NDT) methods applicable to Reinforced Concrete Structures* (in Turkish), Ankara: Turkish Standards Institute.

TS EN 13791 2010. *Assessment of in-situ compressive strength in structures and precast concrete components*, Ankara: Turkish Standards Institute.

Concrete Solutions – Grantham et al. (Eds.)
© 2016 Taylor & Francis Group, London, ISBN 978-1-138-03008-4

In-situ methods of detecting steel corrosion using permanent and non-electronic systems

T. Juraschek & O. Weichold
Institute of Building Materials Research, RWTH Aachen University, Aachen, Germany

ABSTRACT: Current systems for insitu monitoring of corrosion of the reinforcement in concrete are realized via highly specialized systems that are commercially not available. Thus, these systems require complete technical support by the installing company. This report shows a cheap, efficient, independent, and reliable method to detect corrosion events in concrete. The detection system is based on an electrochromic device, which changes its colour upon the change of electrochemical potential caused by the corrosion process. The device is realized by a layer-by-layer setup of a transparent electrode, e.g. Indium-doped Tin Oxide (ITO), followed by an electrochromic layer. The system is closed by a metal counter electrode. The electrochromic layer can consist of an electrochromic compound in a conducting polymer system. By connecting such elements to a series of sensors, e.g. an anode ladder, it is possible to monitor the corrosion progress and to verify the service life design of a structure.

1 INTRODUCTION

Life-time analysis of reinforced concrete structures can e.g. be realized by time-resolved monitoring of reinforcement corrosion using anode ladders (Schießl, 1992). The ingress of moisture, Cl^-, or CO_2 causes subsequent corrosion of individual rungs of the anode ladder, which sparks a detectable signal (see figure 1). A basic drawback of these systems are the electronic devices used to monitor the corrosion events, which fail or become outdated long before the end of the designed life-time of the monitored objects (Barclay et al., 1980).

1.1 *Steel corrosion in concrete*

In concrete, steel corrosion is effectively inhibited by passivation due to high pH values causing the formation of inert iron oxide layers (Fe_2O_3/Fe_3O_4) on the steel surface. Upon carbonation, the pH drops resulting in the dissolution of the passivation layer, which enables corrosion of the reinforcement. Another significant problem is chloride-induced corrosion of steel. This process is independent of the state of the passivation layer and even small amounts of Cl^- (around 0.5% by weight of cement, Breit, 1998) are able to cause immediately corrosion. The corrosion process can be described as a chemical reaction, or more precisely: a redox reaction:

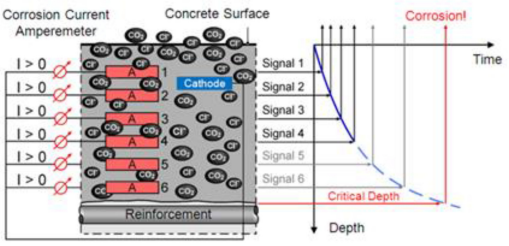

Figure 1. Service-life-time verification based on the extrapolation of reinforcement corrosion as determined by e.g. anode ladders.

$$\text{Oxidation: } Fe \rightarrow Fe^{2+} + 2e^- \qquad E_0 = -0.440\ V \quad (1)$$

$$\text{Red.: } H_2O + \tfrac{1}{2}\,O_2 + 2e^- \rightarrow 2(OH)^- \qquad E_0 = 2.850\ V \quad (2)$$

$$\Sigma\text{: } Fe + H_2O + \tfrac{1}{2}\,O_2 \rightarrow Fe^{2+} + 2(OH)^- \quad (3)$$

The difference in the chemical potential of $\Delta E = 2.410\,V$ represents the voltage that results from this electrochemical system under standard conditions. However, the actually observed potential depends on a number of local factors such as individual concentrations and temperature. Typical values are of the order of approx. $\Delta E = 0.3\,V$.

The exposition of chloride to the iron oxide layer also enforces the depassivation of the reinforcement steel and therefore accelerates the corrosion process enormously. Literature discusses a critical chloride concentration as the main criterion, which corresponds to 0.5 % by weight of cement, which causes corrosion (Breit, 1998).

The current caused by the corrosion event, can be monitored and its change over time can be used to predict further corrosion behaviour as well as providing valuable information on potential restoring concepts. Today, these tasks are usually subcontracted and we

often see frequent changes in the allocation of contracts, which challenges continued data acquisition and processing.

To simplify the process of monitoring and analysis, non-electronic devices offer the possibility of quick and easy read out. The probably simplest device would be an indicator that changes colour upon occurrence of the corrosion event. In chemistry, compounds that change colour when applying a voltage are called electrochromes and these have been tested as displays before the advent of liquid crystal devices. This report presents our first results on employing an electrochromic device to detect corrosion events.

1.2 *The electrochromic system*

Electrochromic compounds are substances that change their colour upon application of an electric current due to an electrochemical reduction (Mortimer, 2011, Monk, 1998). In this study, 1,1'-diheptyl-4,4'-bipyridinium dibromide, a colourless dication, is used as electrochrome, which is reduced to a violet radical cation (equation 4).

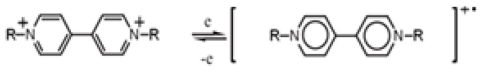

(4)

To establish electrical conductivity within the device, the electrochrome is embedded in a conductive polymer matrix consisting of poly(ethylene glycol) doped with $LiClO_4$. The Li^+ ions coordinate to the ethylene oxide units, which act as weak cross-links and, thus, increase the viscosity (Salomon et al., 1994). Charge transport through this mixture is accomplished by vacancy ion conduction (Haman et al, 2005). As a consequence, the molar ratio of Li^+ to Ethylene Oxide (EO) units plays an important role in the conductivity of the Polyethylene Glycol (PEG) matrix. On the one hand, conductivity can be ensured via high Li^+ concentrations (up to $[Li^+]/[EO] = 1{:}9$). On the other hand ionic conductivity can be also improved by low viscosities, where experimental results show suitable functionality at molar ratios of $[Li^+]/[EO] = 1{:}190$ (Fullerton-Shirey et al., 2009).

2 EXPERIMENTAL

The electrochromic device is realized in a layer-by-layer-setup, consisting of a Polyethylene Teraphthalate (PET) covering sheet coated with indium-doped tin oxide (ITO, Sigma-Aldrich), a transparent, electrically conducting oxide. The counter electrode is a copper or aluminium plate. A 0.4 mm PET distance plate with a 16 mm hole (volume: 80.4 mm^3) was placed between the electrodes to ensure a homogeneous layer of the electrolyte. The electrolyte layer is prepared by dissolving 2.5 mg (4.86 µmol) (1,1'-diheptyl-4,4'-bipyridinium dibromide (Sigma Aldrich) and 0.237 g

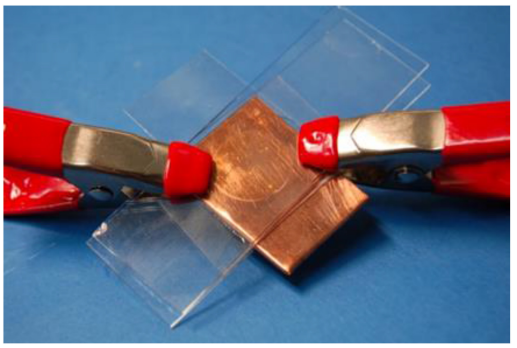

Figure 2. Image of the electrochromic system in its pristine, oxidized state with colourless electrochrome.

(22.3 mmol) $LiClO_4$ (Alfa Aesar) in 10 g poly(ethylene glycol) ($M_w = 400\ g\ mol^{-1}$, Carl Roth GmbH & Co. KG. The ratio of Li^+ to EO unit was 1:190. To ensure a homogeneous layer of the viscous system, a PET distance plate with a punched recess (height: 0.4 mm, diameter: 16 mm, area: 201 mm^2, volume: 80.4 mm^3) was placed between the electrodes. The counter electrode is realized by a copper plate. To ensure a full contact, the setup is placed between two acrylic glass plates that are pressed together by two screw clamps. The ITO-layer and the metal plate are contacted by clip terminals.

Proof-of-principle experiments were run in a beaker containing approx. 400 mL of a saturated $Ca(OH)_2$ solution, a steel rebar ($d = 10$ mm), a titanium oxide mesh electrode, and a MnO_2 (ERE20, Force Technology) reference electrode (figure 3). The solution was gently stirred with a magnetic stir bar. To avoid depassivation due to pH drop by carbonation, solid $Ca(OH)_2$ was added to maintain saturation. The system was monitored with a multimeter until it reached equilibrium, after which the electrochromic device was installed. After passivation, a potential of $U = -0.270$ V was measured. For the corrosion experiment, current and voltage were measured using a PCI4/300 Gamry Potentiostat (C3 Instruments). Corrosion was initiated by adding approx. ten grams of NaCl to the solution.

Cyclovoltammogramms were measured with a PCI4/300 Gamry Potentiostat (C3 Instruments) using a scan rate of 50 mV s^{-1}. To measure the properties within the layer-by-layer-setup, a classic cyclovoltammetry setup was not suitable, due to the lack of a reference electrode. Therefore, the reference electrode was connected to the working electrode. This way, the cyclovoltammetry could be performed *in-situ*. The working electrode was connected to the ITO-layer and the counter electrode to the copper plate.

The impedance of the electrochromic devices was measured with a PCI4/300 Gamry Potentiostat in the range of 10 kHz to 10 Hz with an amplitude of 1.41 V. With respect to the solvent-free layer-by-layer-setup of the electrochromic system, the electrochromic system was attached to the Gamry system in the same way.

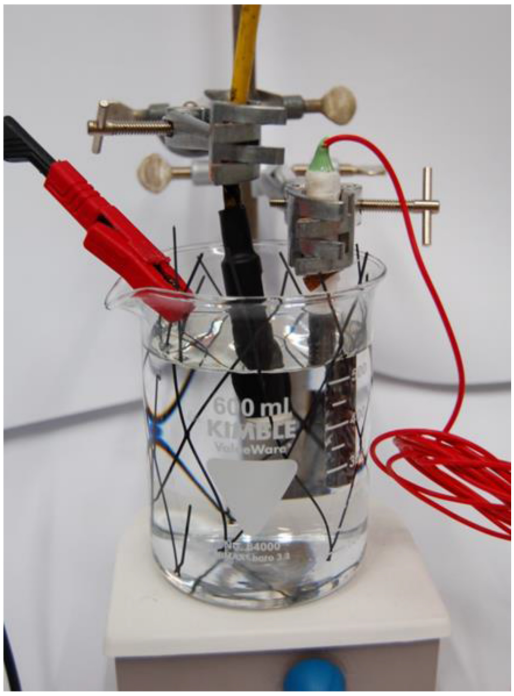

Figure 3. Photograph of the corrosion experiment in the beaker. For the connection of the electrochromic system and the measurement setup, see figure 4.

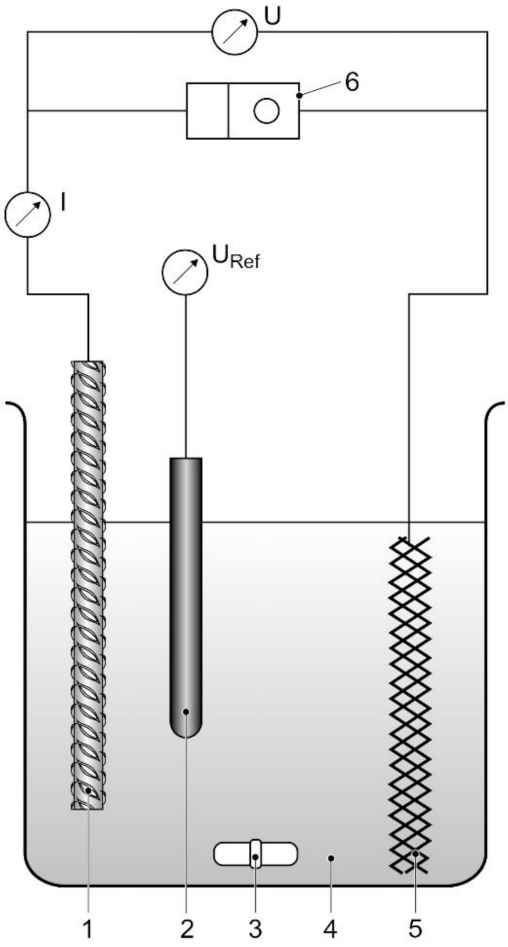

Figure 4. Circuit layout and sketch of the experimental setup for the proof of principle experiment in the beaker. Current and voltage is monitored using the PCI4/300 Gamry system. 1 depicts the corroding rebar, 2 the reference electrode. 3 represents a magnetic stirring bar. 4 shows the saturated $Ca(OH)_2$ solution and 5 the titanium oxide mesh electrode. 6 is given for the electrochromic device.

3 RESULTS AND DISCUSSION

The field of application sets the requirements for the electrochromic system. In contrast to current literature on electrochromic devices, short switching times as well as high switching frequencies and numbers are not required. Instead, a long-term stability is requested for both the oxidized (colourless) and the reduced (coloured) state. In addition, the electrochromic system needs to be stable against environmental influences, which is mainly thermal stability, also against low temperatures and stability against air/oxygen and UV light. This requires the electrochemical reaction to take place under any external condition, or at least react after the conditions are in a suitable range again (e.g. thawing).

Some of these problems can be solved by product design: oxygen and humidity can be excluded when working in a closed system, UV light can be avoided by selecting a suitable location for the installation of the electrochromic sensors.

3.1 *Characterization of the electrochromic device*

The cyclovoltammetric measurement of the electrochromic device shows the proof-of-principle for the electrochromic system: An electrochemical reduction of the 1,1'-diheptyl-4,4'-bipyridinium dibromide within the electrolyte takes place (see equation 4). Also, it can be seen that the electrochemical reaction is entry controlled, since the wave at the lower current curve (reduction) takes place at lower voltages than the peak/shoulder at the upper current curve (oxidation). This behaviour shows also that the electrochemical reaction (see equation 4) is reversible.

This means that the electrochromic system can be switched without any problems using an electric power source. To revert to the original (colourless) state, changing the poles is sufficient.

As can be seen in figure 7, the impedance of the sample is $Z_{real} = 1403\ \Omega$, which is reached at relatively low frequencies of approx. $f = 500$ Hz. According to the geometric parameters (described in chapter 2), the specific resistance of the electrochromic system is $\rho = 68.25\ \Omega$m. This means that the degree of

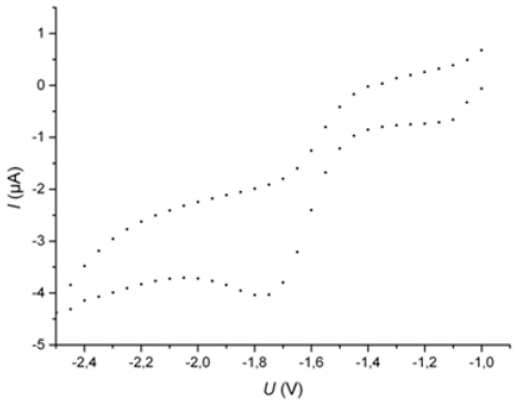

Figure 5. Cyclovoltammetric measurement of 1,1'-diheptyl-4,4'-bipyrridinium dibromide in a conductive EO/Li^+ matrix with a ratio of [EO]/[Li] = 9:1, using a voltage sweep of 50 mV s^{-1}. The curve shows the current reaction of the sample at a given voltage, which is increased (top curve) and decreased (bottom curve) with the given voltage sweep (Haman et al., 2005).

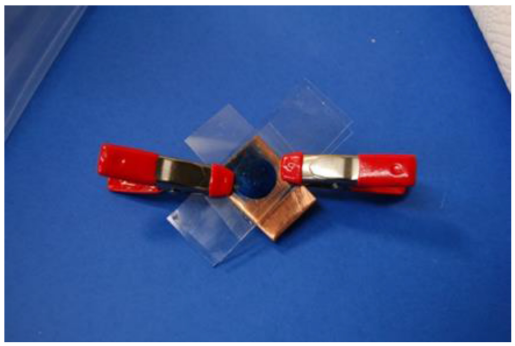

Figure 6. Image of an electrochromic device that has been triggered. The electrochromic compound is now present as a radical cation in its reduced state.

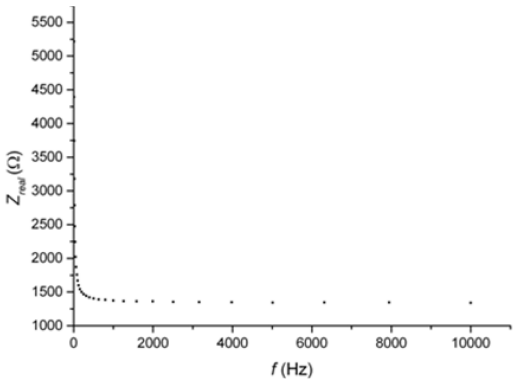

Figure 7. Impedance measurement of the electrochromic device with an amplitude of U = 1.41 V in the frequency range of 10 < f < 10.000 Hz.

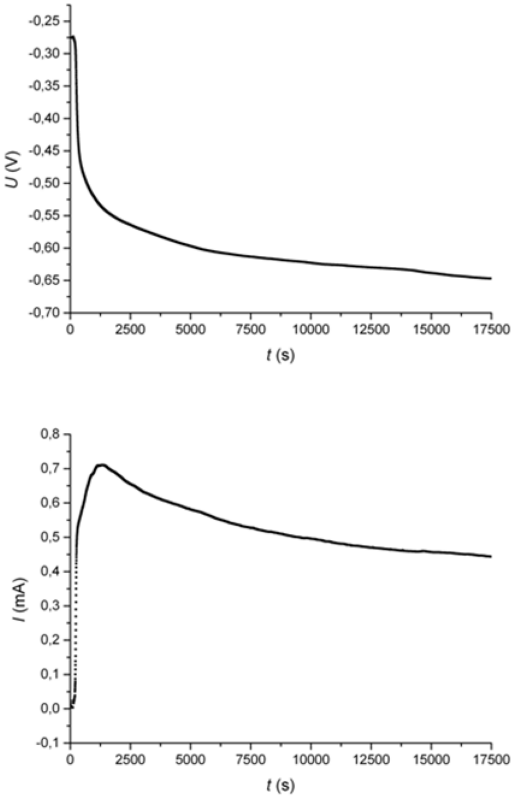

Figure 8. Potential drop over time (top) and current flow over time (bottom) of the beaker corrosion cell.

polarization during the corrosion monitoring process is relatively low. This means that additional resistance due to polarization during application of the electrochromic system can be avoided.

3.2 *Corrosion detection in beaker*

To show the sensitivity of the electrochromic system towards steel corrosion, the electrochromic device was attached to a steel rebar placed in a saturated solution of $Ca(OH)_2$ and a titanium oxide counter electrode. To ensure the presence of a passivation layer, the steel rebar was placed in the solution for two days, during which time, the potential reached −0.270 V. About ten grams of NaCl were added to cause corrosion of the steel rebar, after the experiment was started. Potential and current were recorded over time using the PCI4/300 Gamry Potentiostat setup which is shown in figure 4.

The corrosion process starts approx. 1 min after adding NaCl indicated by a drop in potential from −0.270 V to −0.540 V (Fig 8 top). The decrease in potential slows down after approx. 1300 s. At the same time, the current jumps from 3.251 µA to I_{max} = 0.711 mA after 1300 s (Fig 8 bottom). After

reaching its maximum, the current drops slowly. With an average current of $I_{av} = 0.575\,\mathrm{mA}$ after 1800 s, a charge of $Q = I\ t = 1.034\,\mathrm{C}$ has been transported within the first half hour.

After adding NaCl, it takes approx. 1800 s for the electrochromic device to change its colour extensively. This coincides with the occurrence of the current maximum and indicates that the colour change is triggered by the charge burst. This means that the amount of charge that has flown is representative for the given sample.

4 CONCLUSIONS

The above experiments show that the charge burst accompanying the onset of chloride-induced corrosion events in steel reinforced concrete is sufficient to trigger the electrochromic device under investigation. Using such devices in combination with e.g. anode ladders to monitor steel corrosion in civil engineering structures could potentially provide a simple and economic system that allows assessing the corrosion state during regular inspection intervals.

ACKNOWLEDGEMENT

The authors thank Christian Helm, Rebecca Achenbach, and Nico Seling for their help during this work.

REFERENCES

Barclay D. J., et al.: An integrated electrochromic data display. *SID 80 Digest*, (1980), p. 124 (Abstr. 12.2).

Breit, W.: Kritischer korrosionsauslösender Chloridgehalt. *Beton* 48 (1998), Nr. 7, S. 442-449, Nr. 8, S. 511–514, 516–520.

Fullerton-Shirey, S. et al.: Effect of $LiClO_4$ on the Structure and Mobility of PEO-Based Solid Polymer Electrolytes in *Macromolecules*, (2009) 42, pp. 2142.

Haman, C. et al: Electrochemie, Wiley-VCH, Weinheim, 4th Ed., (2005).

Monk PMS.: The Viologens: Physicochemical Properties, Synthesis and Applications of the Salts of 4,4-Bipyridine. Chichester: J. Wiley & Sons (1998).

Mortimer, R.: Electrochromic Materials, in *Annu. Rev. Mater. Res.* (2011). 41, pp.241–68.

Salomon, M. et al.: Molecular Structure and Dynamics of $LiClO_4$-Polyethylene Oxide-400 (Dimethyl Ether and Diglycol Systems) at 25°C. in *J. Phys. Chem.* (1994) 98, pp. 8234.

Schießl, P. et al.: Monitoring System for the Corrosion Risk for Steel in Concrete in *Concrete International* (1992), 7, pp. 52.



Taylor & Francis
Taylor & Francis Group
http://taylorandfrancis.com

Concrete Solutions – Grantham et al. (Eds.)
© 2016 Taylor & Francis Group, London, ISBN 978-1-138-03008-4

Influence of the reinforcement on concrete resistivity with a new measurement technique

A.Q. Nguyen, G. Klysz, F. Deby & J.-P. Balayssac
LMDC, Université de Toulouse, INSAT, UPS, France

ABSTRACT: Water is a key factor influencing the concrete durability including corrosion of reinforcement. In order to study the water content in concrete the electrical resistivity, due to its sensibility to water, is considered to be one of the most efficient non-destructive solutions. This paper describes a novel method of resistivity measurement developed in laboratory using four-probe array. This technique allows the study of the water content in function of depth in concrete structures. Impacts of reinforcement steels and cover depth on measurement are also studied by measurement over the rebar. Results show that the presence of reinforcement modifies significantly concrete resistivity. This technique also shows the interest of measurement to evaluate the water content gradient in concrete.

Keywords: NDT, resistivity, water content, gradient, concrete, reinforcement

1 INTRODUCTION

In civil engineering, the durability of concrete and the corrosion of the reinforcement are significant problems. The corrosion of the reinforcement, as an electrochemical process, cannot occur without the presence of water. It is the key factor of durability and degradation of concrete. The water content of concrete is studied in this paper by using a non-destructive method.

Electrical resistivity has been used to study the water content of concrete in the literature, thanks to their good correlation. Concrete has a porous structure, which contains an interstitial solution due to the hydration of cement. This is the main source of electrical charges which allows the circulation of ionic current in concrete.

The resistivity measurement on reinforced concrete is influenced by the reinforcement. (Millard, 1991) showed that the presence of the reinforcement near to the position of measurement disturbs the measurement and causes error to the reading. (Polder et al., 2000) recommended some measurement positions to avoid the impact of the rebar.

Despite these recommendations, in this paper, the measurement is performed on the surface of the structure, above the rebar. The aim is to use a short-circuit induced by the rebar to confine the current inside the cover concrete. Unreinforced and reinforced concrete slabs were prepared for the experimental study; the measurements were carried out regularly starting from the saturation state of the concrete and throughout its drying processes. The influence of the reinforcement is studied, along with the cover depth and the effect of moisture content.

Table 1. Concrete mix.

Gravel 4/12.5 mm	970 kg/m^3
Sand 0/4 mm	770 kg/m^3
Cement CEM I 52.5R	280 kg/m^3
Water	198 kg/m^3
W/C ratio	0.71
Porosity	18.79%

2 EXPERIMENTAL TESTS

2.1 *Sample preparation*

Two slabs of exactly the same dimensions were prepared for the research: one with steel reinforcing bars, the other slab without the reinforcement. Plain round steel bars of 10 mm diameter were used in the research with two types of cover depth (2cm and 4cm) in the reinforced slab. There were two layers of steel which allowed the measurement on both sides of the slab. All slabs were cast at the same time with the same batch. For more details, refer to Figure 1.

The concrete mix is presented in Table 1. In order to create a porous concrete, a high W/C ratio was used.

After being cast, all the slabs were conserved in the fog room for 7 days, followed by immersion in tap water saturated with lime to achieve full saturation. The state of saturation was controlled by regular

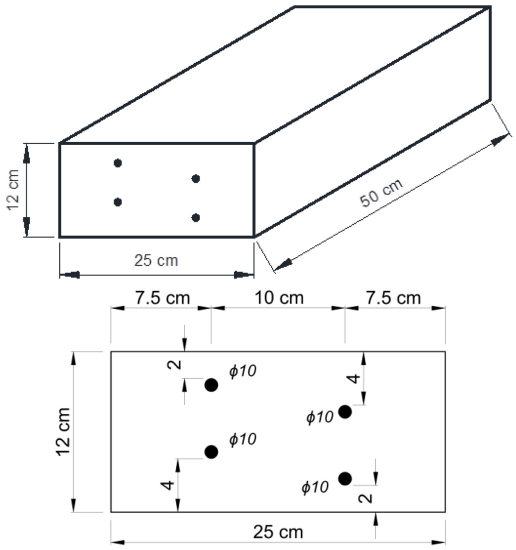

Figure 1. Reinforced concrete slabs (all dimension are in cm).

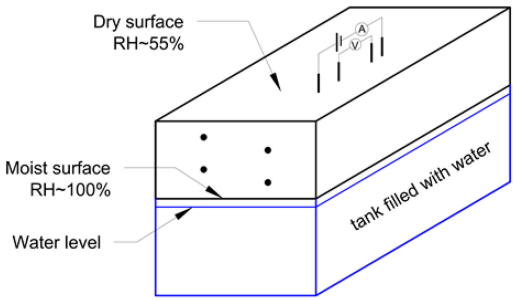

Figure 2. Measurement conditions.

weighing. The process was considered to be complete when the weight ceased to increase. Once fully saturated, they were put in the measurement condition described in Figure 2. The slabs were placed on tanks of exactly the same dimensions, filled with tap water. The top side was in contact with the conditioned medium in which the temperature and the humidity were always controlled at 25°C and 55% respectively. In this installation, the bottom side of the slabs was always moist with relative humidity at around 100% when the top side was kept conditioned. It's also important to note that the slabs were not in contact with water but only had their surface moist. This state is called saturated-surface-dry.

Resin was added to the lateral surfaces of all slabs to make them water-resistant so the water content was considered to be horizontally constant. The goal was to study only the vertical water content gradient. The first day at which the slabs were removed from water was considered as the reference (day 0). Measurement was performed regularly on the surface of the slabs until the gradient was stable.

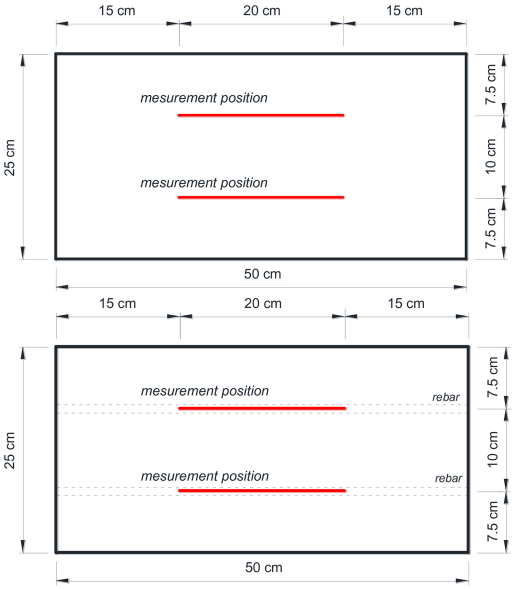

Figure 3. Measurement positions on both reinforced and unreinforced slabs.

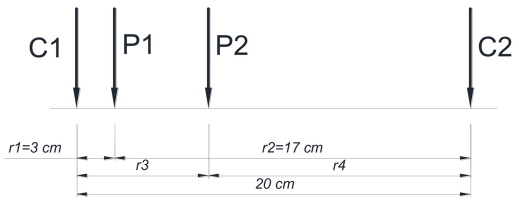

Figure 4. Four point array probe.

2.2 *Measurement positions*

The measurements were performed on both sides of each slab (dry and moist surface, corresponding to drying and humidification gradient). For the reinforced concrete, measurement was carried out above the rebar and for the unreinforced one, it was performed at a similar position (Figure 3).

2.3 *Experimental measurement procedure*

A new procedure of measurement based on the four point array probe was used in the study. It consisted of four electrodes: two current electrodes (C1 and C2) were used for current injection and the two remaining ones measured the potential drop between them.

In this study, the space between the current sources was always kept at 20cm. Three out of four electrodes (C1, C2 and P1) were fixed, in which P1 was located 3cm away from C1 (Figure 4) while the other (P2) was moved every centimeter between P1 and C2. Figure 5 illustrates an example of the curve of the potential variation on the surface of an investigated structure using two point sources in the case of a homogenous and semi-infinite medium (Telford et al., 1990).

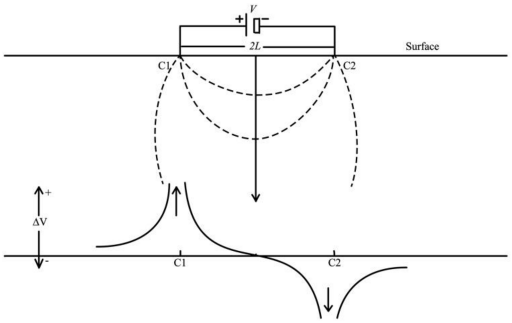

Figure 5. Measurement on surface of a homogenous material with two point sources: Potential variation at the surface. (Telford et al., 1990).

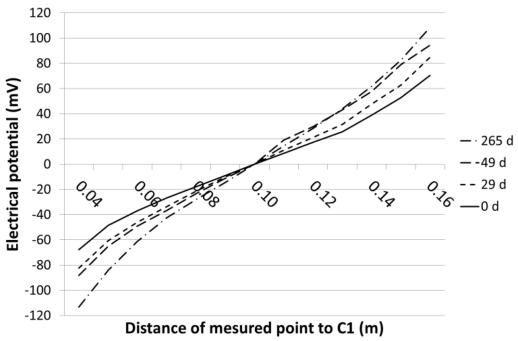

Figure 6. Example of potential measurement curve with the proposed process of measurement.

The figure shows that the potential of a point situated near to current source tends to infinity, causing a high dispersion and showing no interest to investigation. Consequently, the electrode P1 was fixed at 3cm apart from C1 because when potential electrodes (P) are put near the current electrodes (C) the potential differences are too high to exploit the measurement.

The proposed measurement process is interesting because it provides a potential profile which can be exploited in a different manner, as the potential value of every point between C1 and C2 is measured.

The proposed process measures the potential difference between P1 and P2. As P1 is always fixed, the obtained values are potential drop to a pre-defined value. Note that P1 is not a reference electrode so this predefined value isn't well known but supposed to be stable. On the other hand, the middle point is supposed to always have a null potential, as shown in the theory. Hence all the measured potential points are shifted by the same value so that the potential curve passes by 0 at the center point. Figure 6 illustrates electrical potential variation of all points between C1 and C2, in function of its distance to electrode C1 at different times: 0, 29, 49 and 265 days. The shape of these curves is similar to those found in the theory, validating the previous assumptions. The shape changes at different ages as the potential values increase over time which confirms the stabilization of water content gradient.

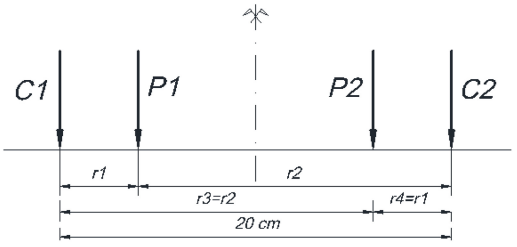

Figure 7. Exploitation layout with symmetric four-point probe.

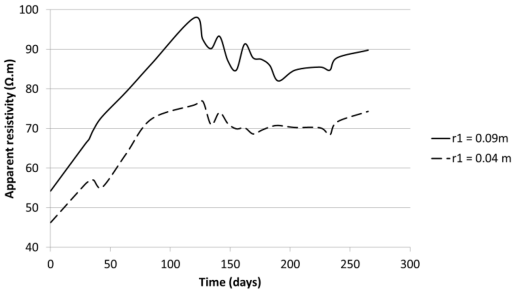

Figure 8. Apparent resistivity at r1 = 4 cm and r1 = 9 cm in function of time.

The method of exploitation is based on a symmetric layout of probes in which the P1 and P2 electrode is always considered to be situated symmetrically compared to the center of the probe. For example, when electrode P1 is r_1 (cm) away from C1 then P2 is also distanced $r_4 = r_1$ (cm) from C2 (Figure 7). The potential values corresponding to r_1 and r_2 are taken from the potential curve, giving ΔV as the potential drop. As the current I is well known the apparent resistivity could be estimated using Eq. 1. The formula is only applicable to a measurement on a homogenous semi-infinite medium. Therefore, the results obtained are not real resistivity of concrete.

$$\rho_{app} = \frac{\pi}{\frac{1}{r_1} - \frac{1}{r_2}} \cdot \frac{\Delta V}{I} \quad (1)$$

r_1; r_2 are respectively the distance from the potential electrode to C1 and C2; ΔV and I are respectively the potential drop between P1 - P2; and the injected current. Together with the resistivity measurement, the slabs were weighed to control the establishment of water gradient over time.

Figure 8 presents measured apparent resistivity at $r_1 = 4$cm and $r_1 = 9$cm, corresponding respectively to apparent resistivity measured on the structure surface and at the core of the slab (presented here the measurement on the moist surface of the unreinforced slab) at different times. As we can notice, the r_1 distance relates to the investigated cover depth: the higher r_1 is, the deeper concrete resistivity is investigated. Therefore we can have different resistivity by changing r_1.

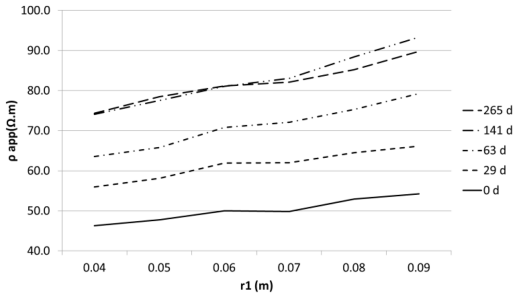

Figure 9. Resistivity measurement on unreinforced concrete slab – moist surface.

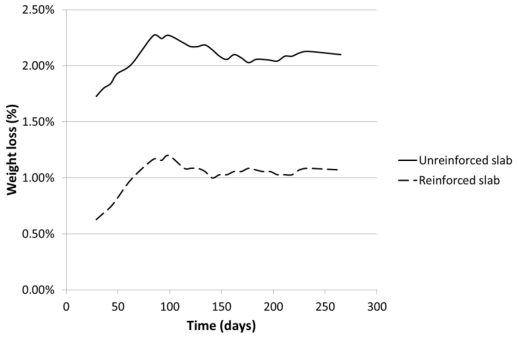

Figure 10. Slab weight in function of time.

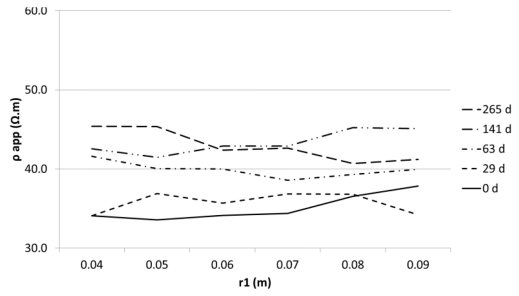

(a)

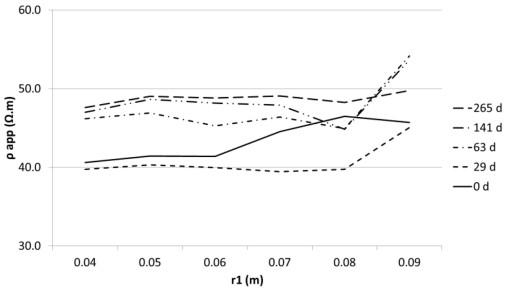

(b)

Figure 11. Resistivity measurement of reinforced concrete slab (a) over 2 cm-rebar and (b) over 4 cm-rebar.

3 RESULTS AND DISCUSSIONS

3.1 *Measurement on moist surface of the slabs*

3.1.1 *Unreinforced slab*

The results in Figure 9 show a good tendency. The low resistivity in the surface (corresponding to small value of r1) refers to the moist material and higher resistivity indicates the drier material at the core of the slab. The curves also show that the moisture gradient is being established in the slab as the resistivity values increased over time.

The stabilization phase of water content gradient started at about 150 days because the variation of resistivity was less significant afterward. At day 265 the water gradient is considered to be stably established. This remark is confirmed by the variation of slab weight in Figure 10 and the measured resistivity at r1 = 4cm and 9cm in Figure 8.

3.1.2 *Reinforced slab*

Figure 11 shows test results of reinforced concrete over a 2cm rebar (Figure 11a) and 4cm rebar (Figure 11b) respectively at different ages.

The presence of rebar seems to disturb the resistivity curves. They are more flat and less organised than in the case of unreinforced concrete. However, the installation of water gradient can be seen clearly with the drying of the slab as the curves rise from time to time. In comparison to the resistivity curves of unreinforced concrete, the variation of the values of the reinforced slab is less significant over time. The resistivity values are also lowered when the rebar is present. This phenomenon is observed in both cases of cover depth studied in this work. The values of resistivity are slightly higher in case of 4cm than in the other case because the cover depth is more important. The remark about the stabilization phase around day 150 is also confirmed here.

3.1.3 *Effect of rebar on reinforced concrete in different time*

The effect of the reinforcing bar is significant on the electrical resistivity measurement. Figure 12 shows test results on unreinforced and reinforced concrete slabs with both types of cover depth in the early stages (day 29) when the gradient is still not stable and at day 265 at the end of the experimental campaign. They show a significant resistivity drop in the presence of rebar: the 2cm and 4cm curves are situated underneath the unreinforced curve. Their shape is also modified: the resistivity curve of unreinforced concrete tend to rise up while they are more flat in the case of reinforced concrete.

This remark demonstrates that measurement on reinforced concrete and over the rebar might lead to a misunderstanding of the water content gradient.

The resistivity drop is also more remarkable at day 265 than day 29. As the concrete is drier and more

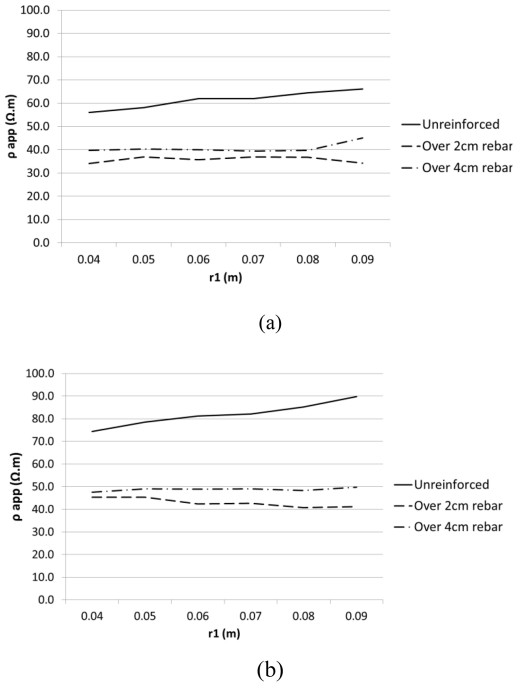

Figure 12. Effect of short circuit in reinforced concrete at (a) day 29 and (b) day 265.

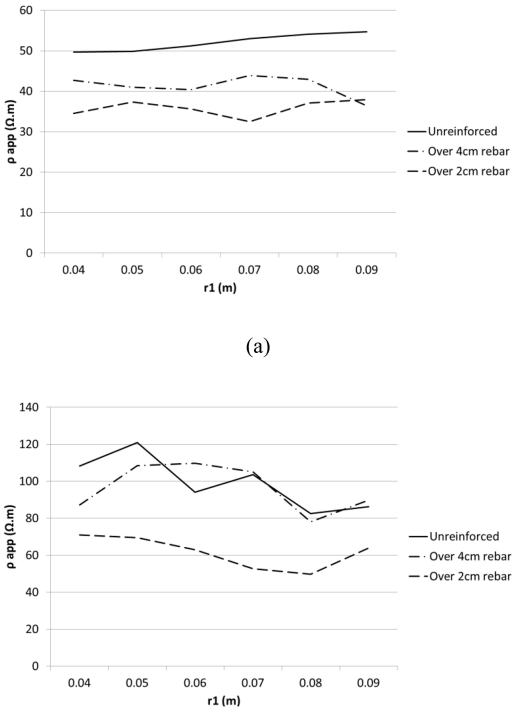

Figure 13. Effect of short circuit on reinforced slab at day 1 (a) and day 84 (b).

electrically resistant, the reinforcing bars become a more preferable path for the electric current.

The resistivity drop can be explained by the effect of short circuit. While concrete is relatively resistive the rebar, as a metal, is electrically conductive. In other words, the high conductivity of steel created an easy route for the current therefore reduces the measured resistivity. This effect is also observed in previous works of (Millard, 1991; Polder, 2001; Bungey et al., 2006; Millard and Sadowski, 2009).

3.2 *Measurement on dry surface*

In this section, only results from the starting day (day 0) until day 84 will be presented. Afterward the upper surface of the slab was too dry causing a high contact resistance and measurement became impossible.

Most of the remarks here are found in the previous section for the moist surface; only the effect of short circuit in the reinforced slab is presented.

The effect of short circuit is confirmed in Figure 13. The presence of the reinforcement decreases significantly the measured resistivity. The effect is also more noticeable in the case of the 2cm rebar than the 4cm rebar. The drying process of concrete is also observed.

At 84 days, no significant drop of resistivity was observed for the 4cm rebar. This remark might be explained by the low moisture content at the surface of concrete which led to a very high resistivity. The presence of water on the surface of the rebar is needed for the exchange of electrical charges between concrete and steel. Therefore, the effect of short circuit cannot be observed in this case.

Table 2. Resistivity drop by averaged values.

Surface Type	Age	2cm rebar	4cm rebar
Dry surface	1 day	16.23 Ω.m (31.00%)	10.85 Ω.m (20.83%)
	84 day	37.65 Ω.m (37.92%)	2.85 Ω.m (2.87%)
Moist surface	29 day	25.73 Ω.m (41.87%)	20.73 Ω.m (33.74%)
	265 day	38.90 Ω.m (47.53%)	33.10 Ω.m (40.44%)

Table 2 shows the resistivity drop by comparing averaged values of all measured points in all the cases. The proportion of drop value was calculated by the ratio of measured resistivity over the rebar and resistivity on concrete slab.

4 INTEREST OF USING REBAR TO ASSESS THE WATER GRADIENT OF CONCRETE

In this section, the interest of exploiting the effect of short circuit is presented numerically by using the finite element software COMSOL Multiphysics. Four models divided into 2 groups were created to simulate the measurement: two big cubes of $1 \times 1 \times 1\ m^3$ and

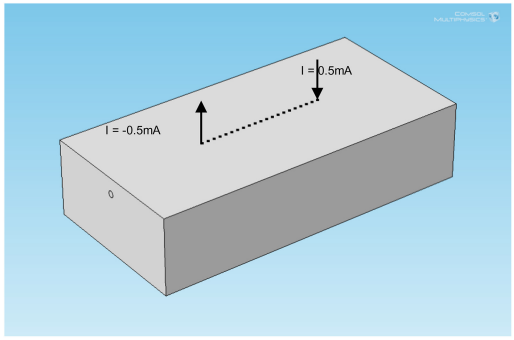

Figure 14. Example of a simulated slab.

Table 3. Numerical modeling incomes.

Big slab dimension	$1 \times 1 \times 1\ m^3$
Small slab dimension	$50 \times 25 \times 12\ cm^3$
Concrete resistivity	200 Ω.m
Steel conductivity	4.032×10^6 S/m
Injected current	0.5 mA
Current source spacing	20 cm

two small ones of exactly the same size to those used in the experimental campaign ($50 \times 25 \times 12\ cm^3$). In each group, there was one unreinforced slab and one reinforced slab with a 10 mm steel bar of 2 cm of cover depth. The current was injected by two source points and the potential was taken at all points between them, as shown in section 1.3. The goal of the numerical study was to show the interest of the measurement above the rebar to reduce the boundary effect.

Table 3 shows different informations conerning the numerical models.

The results from numerical modelling are presented below. Figure 15a shows resistivy curves on unreinforced concrete of both big and small slabs. In the case of the big slab, there is no significant difference between the obtained resistivity and the applied values, while in the other slab, the curve has risen above the real resistivity value. The explication is that in large slabs, the medium is considered to be semi-infinite and there is no boundary effect, which exists in the small slab. It shows that measurement carried out on the small unreinforced slabs has an inevitable error caused by its size, and confirms that the obtained resistivity is only an apparent value.

Figure 15b shows the other case of study on reinforced concrete. There is only a negligible difference between the measurement results, showing that the boundary effect is neutralised by the presence of the steel bar. The latter, which is much more conductive than concrete, has created a favourable path for the external current, and limited the density of current circulated to the bounds of the slab. Since the boundary effect is avoidable when working on a limited medium in the laboratory, using the rebar appears to be a good perspective to study the cover concrete.

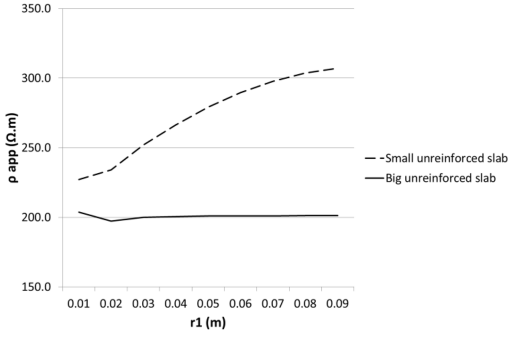

(a)

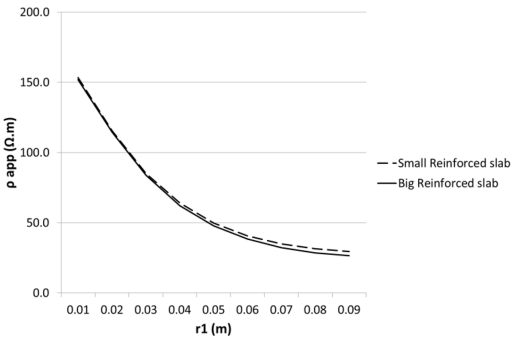

(b)

Figure 15. Resistivity curves obtained by numerical works on unreinforced model (a) and reinforced model (b).

5 CONCLUSION AND PERSPECTIVES

A new way of measurement and exploitation of concrete resistivity is presented in the paper. Two types of water content gradient are studied in the paper: drying and humidification gradient. The influence of the reinforcement is also examined. The presence of reinforcement causes strong reduction of the measured apparent resistivity values, on the reinforced slab due to the high conductivity of rebar and in both cases of moisture gradient. This effect, called the short circuit effect also modifies the shape of the resistivity curves by disturbing the measurement. The cover depth affects also the reading. The more rebar is situated near the surface the more resistivity is lowered.

The measurement process demonstrates also its interest to examine the evolution of water content on both types of concrete and of moisture gradient. Although in the case of a drying gradient it is more difficult to analyze the results than in the other case, it confirms the sensitivity of resistivity to water content.

The measurement above the rebar is a promising perspective in the assessment of cover concrete in the laboratory. The new process of measurement can be used to evaluate the water content gradient by taking advantage of the effect of a short circuit.

REFERENCES

Bungey, J.H., Millard, S.G., Grantham, M.G., 2006. Testing of concrete in structures, 4th ed. Taylor & Francis, London and New York.

Millard, S.G., 1991. Reinforced concrete resistivity measurement techniques. ICE Proc. 91, 71–88. doi:10.1680/iicep.1991.13583

Millard, S., Sadowski, L., 2009. Novel method for linear polarisation resistance corrosion measurement. Presented at the NDTCE'09 Non-Destructive Testing in Civil Engineering, Nantes, France.

Polder, R., Andrade, C., Elsener, B., Vennesland, Ø., Gulikers, J., Weidert, R., Raupach, M., 2000. Test methods for on site measurement of resistivity of concrete. Mater. Struct. 33, 603–611. doi:10.1007/BF02480599

Polder, R.B., 2001. Test methods for on site measurement of resistivity of concrete — a RILEM TC-154 technical recommendation. Constr. Build. Mater. 15, 125–131. doi:10.1016/S0950-0618(00)00061-1

Telford, W.M., Geldart, L.P., Sheriff, R.E., 1990. Applied Geophysics, Cambridge University Press. Cambridge.



Taylor & Francis
Taylor & Francis Group
http://taylorandfrancis.com

Concrete Solutions – Grantham et al. (Eds.)
© 2016 Taylor & Francis Group, London, ISBN 978-1-138-03008-4

Injection quality of steel cable ducts evaluated by NDT

C.G. Petersen
Germann Instruments A/S, Copenhagen, Denmark

ABSTRACT: Injection of steel cable ducts with grout is important for preventing corrosion on the tensioned strands as well as for stress transfer from the strands to the structural concrete. This paper gives experience obtained from Nondestructive Testing (NDT) of the grouting quality of steel cable ducts obtained by testing of a controlled specimen containing a fully injected duct with embedded strands and an empty duct. The test systems used were the DOCter Impact-Echo System and the MIRA Ultrasonic-Echo Tomographer. For verification of the test results, the specimen was subsequently examined by cutting at selected locations. The conclusion is that voided and fully grouted steel ducts can be evaluated by the two NDT systems. Impact-echo can distinguish between reflection from air in the duct and from the steel strands in a fully grouted duct. The ultrasonic-echo tomographer can, with proper color adjustment, also make this distinction. Voids in the grout may be detected by both systems. Verification has to be made by visual inspection of the prestressed strands by opening carefully the ducts without damaging the strands. In an environment with moisture and chlorides it is also necessary to perform chloride analyses of the grout itself and the surrounding concrete.

1 INTRODUCTION

During construction of post-tensioned structures strands are inserted into steel cable ducts (Fig. 1) and tensioned (Fig. 2) after the concrete member has achieved sufficient strength. Subsequently, pressure injection of the protective grout takes place from tubes connected to the ducts until the duct has hopefully been filled completely with grout.

The steel ducts, usually about 100 mm in diameter, typically with 10–12 twisted strands, each 15 mm in diameter inserted into them. The depth of the ducts is typically 100 mm to 150 mm in critical areas, depending on the design.

The injected grout has to encapsulate the strands (Fig. 3) to prevent corrosion of the strands (Fig. 4) and to ensure stress transfer from the strands to the structural concrete member. The examples in Figures 3 and 4 are from a post-tensioned bridge beam in Finland constructed in 1971 (Rapaport 2010).

Consequently, testing for voids in the grout within steel cable ducts is essential, not only at a later stage of a structure's life, but also after setting of the grout for quality assurance purpose.

2 THE NDT METHODS

To minimize destructive invasive testing, selected NDT methods have been used in the past, and are increasingly being used on-site. They are the impact-echo method and ultrasonic-echo tomography; both systems are based on stress-wave propagation.

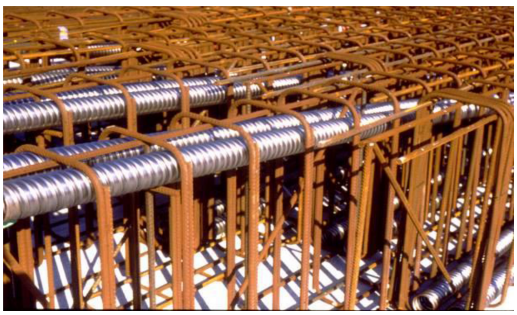

Figure 1. Example of metal ducts.



Figure 2. Post-tensioned strands.



Figure 3. Sound strands in well injected duct.



Figure 4. Corroded strands in an empty steel duct.

In this paper, experience is given with the two systems for testing on a controlled slab containing voided and fully grouted steel cable ducts 100 mm in diameter. The grouted duct contained 10 twisted strands. The ducts were positioned at ~110 mm depth in a 380-mm thick slab

2.1 *Impact-echo principle (Carino 2015)*

Figure 5 is a schematic of the impact-echo test. A short duration mechanical impact is produced on the concrete surface with a small steel sphere. This impact generates three stress waves, an R-wave on the surface and a P-wave and an S-wave that propagate into the concrete. When the P-wave (the longitudinal wave) and the S-wave (the shear wave) reach a boundary with a material having a different acoustic impedance (wave speed × density), they are reflected and travel back to the surface where the impact was generated. By placing the transducer close to the impact point,

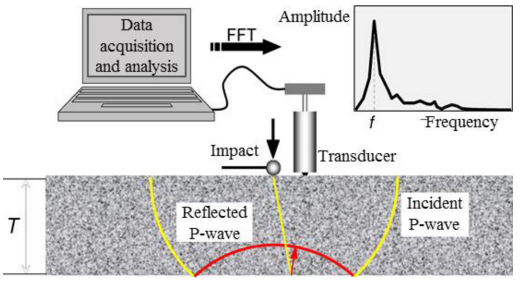

Figure 5. Impact-echo method.

the response from the P-wave is maximized, while the S-wave response is minimized. The transducer is a sensitive broadband displacement transducer.

Upon reflection at a boundary, the P-wave returns into the material and is then reflected back from the surface into the member. The P-wave undergoes, in this manner, multiple reflections between the two surfaces and the recorded waveform of surface displacement has a periodic pattern that is related to the depth of the reflective surface. The displacement waveform is transformed into the frequency domain using the fast Fourier transform (FFT) to produce an amplitude spectrum that shows the predominant frequencies in the waveform.

The analysis of these predominant frequencies is the basis of the impact-echo method, which is governed by the equations shown in Figure 6. The figure shows two conditions (a) a slab with air above and below, and (b) a slab with air above and steel below.

In the first case, the P-wave entering the material will be a compression wave indicated by +. At reflection from a low acoustic impedance surface as air, it will change sign and return to the surface as a tension wave indicated by –. When the tension wave arrives at the surfaces, it causes the surface to move down. At the surface, the P-wave is reflected back into the slab as a compression wave. The process is repeated multiple times. Every time the P-wave arrives at the top surface it will be a tension wave making the surface move downwards. The period in the transducer displacement waveform will be:

$$\Delta t = 2T / C_{plate}, \tag{1}$$

where, C_{plate}, is the P-wave speed in m/s, T is the thickness in m, Δt is the period in s and the predominant frequency in the amplitude spectrum (not shown) is the inverse of this period.

In the second case, the P-wave enters as a compression wave +. Upon reflection from an interface with a higher acoustic impedance material, such as steel, it will not change sign and returns to the surface as a compression wave +. When the reflected compression wave arrives at the surface, it makes the surface move upwards. The wave then returns as a tension wave –, is reflected against steel as a tension wave –, and makes

the surface move down when it arrives at the transducer. This process is repeated. Hence, the period in the transducer displacement waveform will be

$$\Delta t = 4T / C_{plate}, \quad (2)$$

and the frequency in the amplitude spectrum (not shown) is the inverse.

As an example, if the P-wave speed in the slab C_{plate} is 4,000 m/s and the thickness T is 200 mm, for the first case, the peak frequency in the amplitude spectrum will be $f = C_{plate}/(2T) = 4,000$ m/s/$(2 \times 0.2\text{m}) = 10$ kHz. For the second case (air-concrete-steel), the frequency will be $f = C_{plate}/(4T) = 4{,}000$ m/s / $(4 \times 0.2\text{m}) = 5$ kHz.

The information summarized in Figure 6 is of value in being able to distinguish between reflections by air voids in the grout and reflections by the strands surrounded by grout.

2.2 *The ultrasonic-echo tomographer principle (Hoegh et al. 2011)*

Transmitting and receiving transducers are arranged in a "pitch-catch" configuration. One set of transducers sends out a shear wave pulse and all other sets of transducers receive the reflected pulse. The time from the start of the pulse until the arrival of the echo is measured. For a known shear wave speed, C_s, the depth of the reflecting interface can be calculated. The instrument itself measures automatically the shear wave speed.

Figure 7 shows the ultrasonic-echo instrument used in this work. The 4 × 12 transducer array antenna produces many transit time measurements during each test that are analyzed using the synthetic aperture focusing technique (SAFT) in real time to reconstruct a 2D image of the cross section below the instrument. It takes about 3 to 4 seconds to complete data acquisition and data processing at each test location.

Subsequently, the data captured at each test location can be transferred to a computer with dedicated imaging software to create a 3D image of the test region. The software allows views of different slices of the reconstructed internal structure to identify the locations of the reflecting interfaces, which can be the opposite side of the concrete member, reinforcing bars or concrete-air interfaces such as voids, delaminations, honeycombs or other defects.

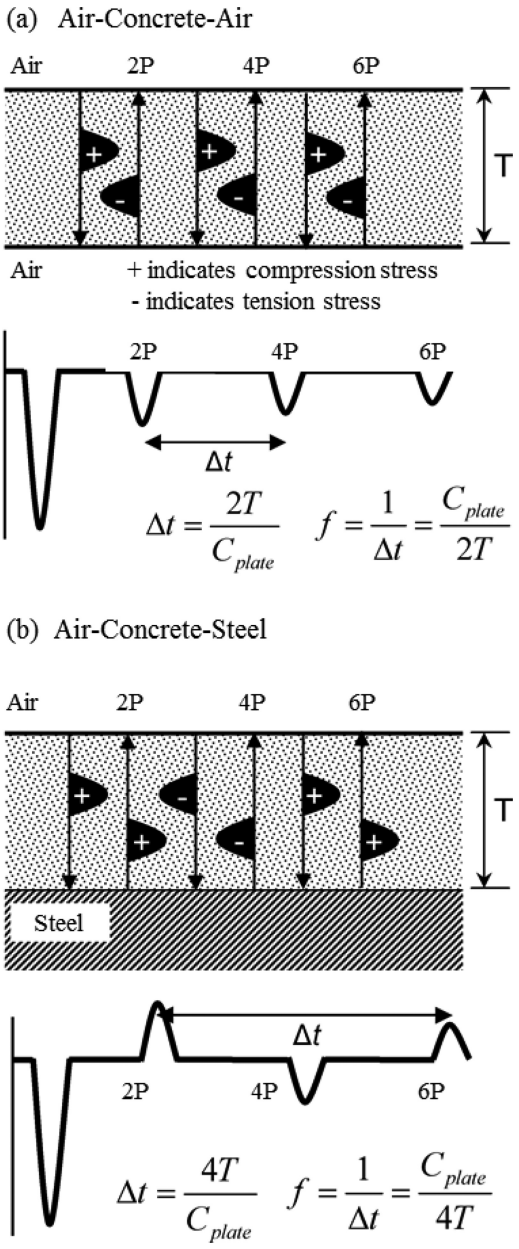

Figure 6. Impact-echo equations for layered systems composed of (a) air-concrete-air and (b) air-concrete-steel (Carino 2015).

3 THE TEST SPECIMEN

3.1 *Slab layout*

Figure 8 shows a cross section and plan view of the 400-mm thick slab. One half of the slab was cast on a polystyrene board and the other half was cast against the soil. The slab was 2 m wide in the N-S direction and 3 m long in the E-W direction. A layer of 16-mm reinforcing bars was placed parallel to the short slab dimension with a cover of 40 mm. Two 100-mm diameter corrugated steel ducts, with 1 mm wall thickness, were cast into the east side of the slab. Duct 1 was empty and Duct 2 contained ten 16-mm post-tensioning strands embedded in non-shrink grout as described in 3.2.

The slab was cast using self-consolidating concrete. Figure 9(a) shows the slab formwork with reinforcement and ducts in place before placing the concrete. Figure 9(b) shows the self-consolidating concrete being pumped into the form.



Figure 7. The ultrasonic-echo tomographer: (top) top face with display showing 2D cross section image; (bottom) the 4 × 12 transducer array antenna.

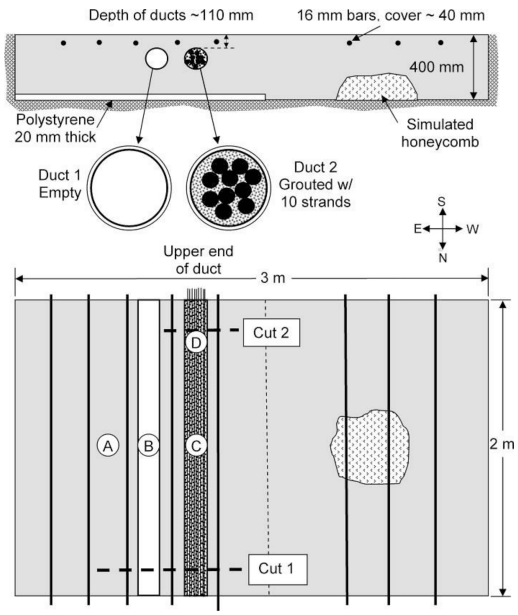

Figure 8. Test specimen.

3.2 *Fabrication of the grouted duct with ten strands*

The 2-meter long corrugated steel duct was kept in a fixed vertical position with the bottom resting firmly against a watertight polystyrene plate. BASF MASTERFLOW 9500 grout (with an autogenous shrinkage of $0.1^0/_{00}$ after 6 days) was mixed in small batches and poured into the duct containing three strands, initially. At a grout height of 200 mm from the bottom, another strand was pushed into the duct, more grout was poured

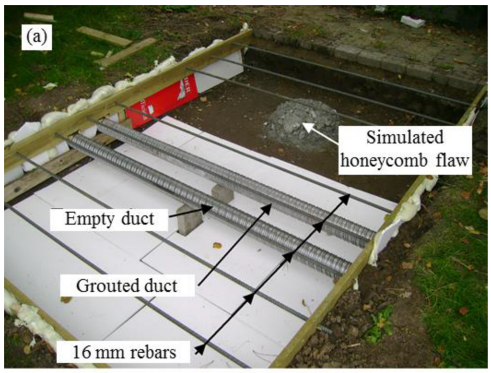



Figure 9. (a) Slab formwork with ducts and bars installed; (b) placing the self-consolidating concrete.

to a height of 400 mm, and another strand was pushed in. The process was repeated until all ten strands were positioned in the duct surrounded by grout to the top. Constantly during casting, the grout was externally vibrated by gently tapping the duct with a rubber mallet to ensure total embedment of the strands in the grout. While filling the upper end of the duct, about 200 mm from the top, the mixer broke down, and another less efficient mixer had to be used.

The cable duct was kept in the same vertical position for 30 days and then placed carefully in the slab formwork (Fig. 9(a)). The upper end of the duct was positioned on the "south" side of the slab, with the strands sticking out of the slab as shown in Figure 8.

4 TESTING

4.1 *Impact-echo*

The impact-echo equipment used is shown in Figure 10.

The plate P-wave speed C_{plate} was determined by thickness measurement and an impact-echo test of the solid slab. For a thickness of 380 mm (slab on polystyrene board) and a measured frequency of 5.37 kHz, the P-wave speed is $C_{plate} = f \times 2 \times \mathrm{T} = 5.37\ \mathrm{kHz} \times 2 \times 0.380\ \mathrm{m} = 4081$ m/s, which is quite reasonable for good quality concrete.

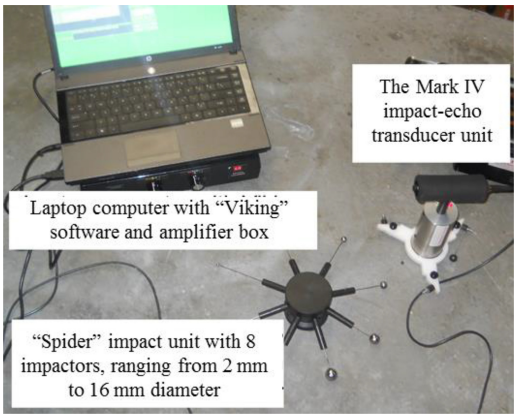

Figure 10. The impact-echo test equipment used.

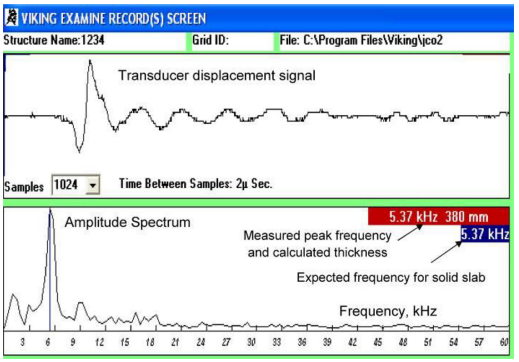

Figure 11. Impact-echo result for solid slab.

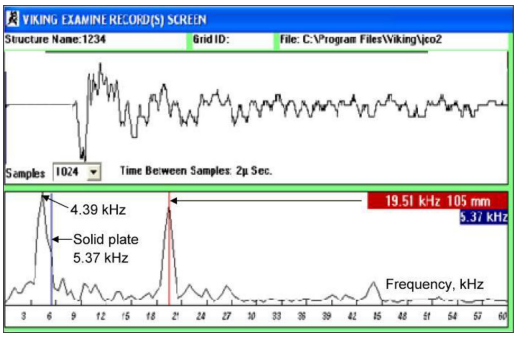

Figure 12. Impact-echo result above empty duct.

For a void at 110 mm depth, the expected frequency will be $f = C_{plate}/(2 \times T_v) = 4081$ m/s / $(2 \times 0.110$ m$) = 18.55$ kHz, and for a steel interface (the strands) at about 115 mm depth, the expected frequency is $f = C_{plate}/(4 \times T_s) = 4081$ m/s / $(4 \times 0.115$ m$) = 8.87$ kHz.

Testing took place along the centerlines of the ducts at a spacing of 50 mm with the impactor positioned 10 to 20 mm from the transducer tip along the centerline of the duct. The selected impactor was primarily an 8-mm steel ball producing a maximum useful frequency of ~20 kHz and, secondarily, a 5-mm impactor with a maximum useful frequency of ~40 kHz (see Carino 2015).

The test results were classified into four categories as follows (see Fig. 8):

1. Category A, solid slab
2. Category B, empty cable duct (40 test results)
3. Category C, fully grouted duct (34 test results)
4. Category D, poorly grouted duct (6 test results)

4.1.1 *Category A–solid slab*

Figure 11 is an example of a test result for the solid slab. The upper window shows the transducer displacement signal in the time domain. The lower window shows the amplitude spectrum, which indicates the frequencies contained in the transducer displacement signal. Two boxes are shown in the upper right hand corner of the amplitude spectrum: an upper box (in red) displaying a frequency and a calculated depth and a lower box (in blue) showing the expected frequency for a solid slab.

For a slab thickness of 380 mm and a plate P-wave speed is 4081 m/s, the expected solid frequency is 5.37 kHz, following the impact-echo equation for air-concrete-air (Fig. 6). This frequency is shown in the lower (blue) box in the amplitude spectrum window. The measured frequency in the upper red box, 5.37 kHz, coincides with this expected frequency and the calculated thickness of 380 mm corresponds to the slab thickness. Thus the test indicates a solid slab.

The amplitude spectrum displays two cursors (vertical lines) that correspond to the frequencies shown in the upper and lower boxes: a blue cursor positioned at the expected frequency for a solid slab and a red cursor positioned at the peak frequency. In Figure 11, the red cursor related to the measured frequency shown in the top (red) box is hidden behind the blue cursor. This red cursor will be positioned automatically at the highest peak, but it can be moved manually to other peaks in the spectrum, and the red box will show the depth corresponding to that frequency.

4.1.2 *Category B–empty duct*

Figure 12 shows a result from a test at a point above the empty duct. The 5.37 kHz solid plate frequency peak in Figure11 has dropped to a lower value of 4.39 kHz, meaning that the apparent travel path of the P-wave is: (4081 m/s / (2 × 4.39 kHz)) = 464 mm, 84 mm longer than 380 mm for the solid plate. Consequently, the P-wave is travelling around the reflection surface, which is the empty cable duct. At the same time, a frequency peak at 19.51 kHz shows up, where the red cursor is positioned. This frequency relates to a depth to the reflection surface of 105 mm, the depth of the empty cable duct indicated in the red box. A 5mm impactor was used to accentuate the high frequency peak.

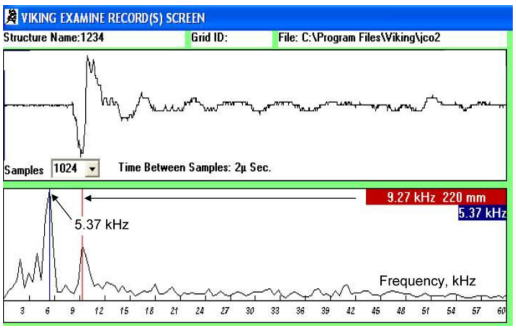

Figure 13. Impact-echo result over fully grouted duct.

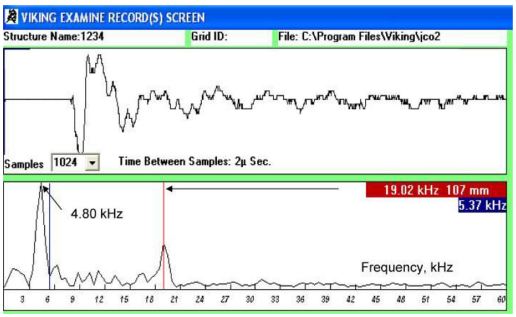

Figure 14. Impact-echo result due to voids in grout.

4.1.3 *Category C–fully grouted duct*

Figure 13 shows the result for a test at a point over the fully grouted duct. The 5.37 kHz frequency measured is the same as the solid frequency in Figure 11, indicating a P-wave travel path of 380 mm. This can only happen if the duct with the strands is fully grouted with no air intrusions, provided the testing is made over the duct. To make sure this is the case, there has to be an additional reflection from the strands inside the grouted duct. This reflection shows up as a peak at 9.27 kHz, equivalent to a depth to the steel strands of $T_s = 4081$ m/s/$(4 \times 9.27$ kHz$) = 110$ mm (half of the 220 mm indicated in the red box), based on the impact-echo equation for air-concrete-steel as shown in Figure 6. An 8 mm impactor was used.

4.1.4 *Category D–poorly grouted duct*

Fig. 14 shows the result for another test at a point above the grouted duct. The P-wave has a travel path of more than 380 mm as the frequency has dropped from 5.37 kHz to 4.80 kHz. This can only happen if there is air in the duct. The air interface is positioned at a depth of 107 mm as indicated by the peak at a frequency of 19.02 kHz. The interpretation is that the duct is poorly grouted and has air voids. An 8 mm impactor was used.

4.2 *Ultrasonic-echo tomographer*

As shown in Figure 15, testing was done along two scan lines above the ducts with 250 mm distance between

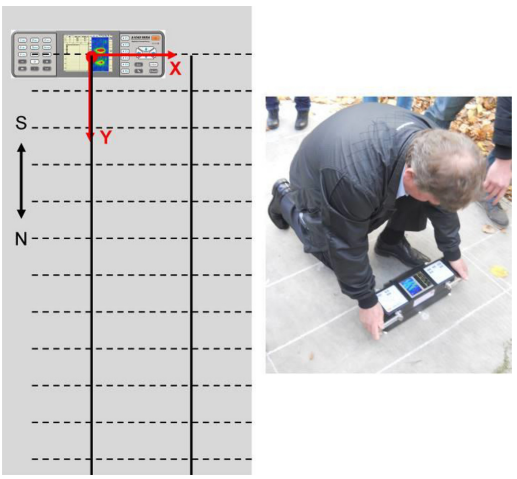

Figure 15. Testing above cable ducts with ultrasonic-echo tomographer.

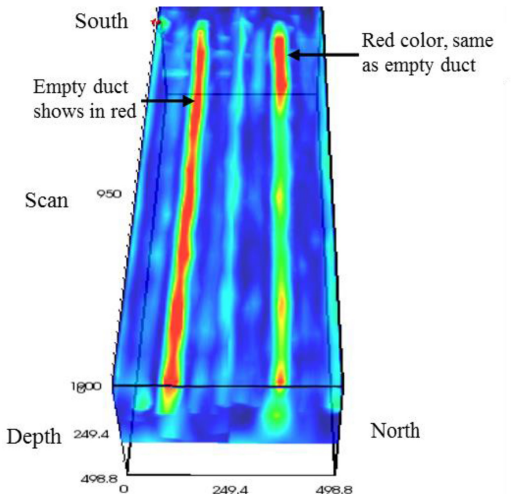

Figure 16. 3D color image of volume tested in vicinity of ducts.

the scan lines and in steps of 100 mm, going from South to North along the 2-meter-wide slab.

The settings of the ultrasonic-echo tomographer were:

- Operating frequency: 25 kHz
- Color option: MIRA
- Color gain: 7 dB
- Analog gain: 30 dB

After transferring the records into the *IdealViewer* software, various images were examined as shown in Figures 16 to 20.

Figure 16 is a 3-D color image of the volume around the ducts. The volume has been clipped so that the back-wall reflection is not shown. The two ducts and the reinforcement bar located between the center lines of the ducts are clearly visible. Note that the south end

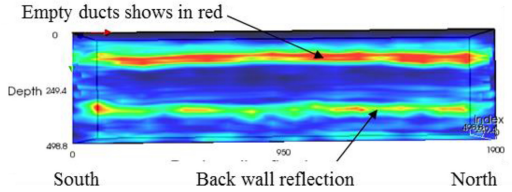

Figure 17. Side view (D-scan) of the reflections from the empty duct and bottom of slab.

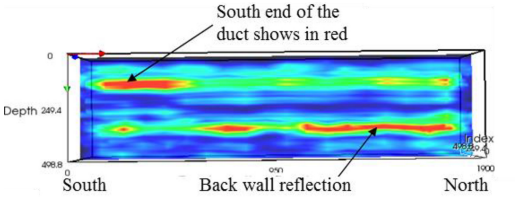

Figure 18. Side view (D-scan) of the reflection from the grouted duct and bottom of slab.

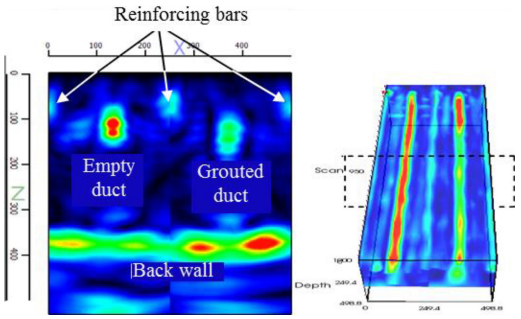

Figure 19. End view (B-scan) at cross section 1.2 m from south face.

of the grouted duct shows the same red color as for the empty duct.

Figure 17 shows a side view of the empty duct (D-Scan). The reflection from the bottom of the slab (back wall) is seen clearly. The empty duct is displayed in red color.

Figure 18 is a side view of the grouted duct. Note the red color near the south end of the duct.

Figure 19 shows an end view (B-Scan) of the slab and ducts at a plane 1200 mm from the south face. Reflections from the reinforcing bars can be seen. Reflections from the empty duct show in red, reflections from the grouted duct show in a blue-green color, and the bottom of the slab is seen clearly.

Figure 20 shows an end view of the slab and ducts at a plane 150 mm from the south face. The similarity in the red colors of the images representing the two ducts indicates that the grouted duct is in fact not fully grouted. Starting from the south face of the specimen and extending about 200 mm along the duct, the red reflection indicates air voids are present in the duct (see also Figs. 16 and 17).

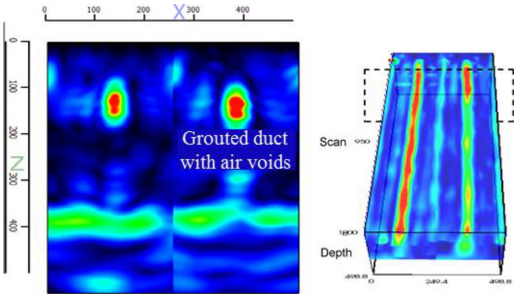

Figure 20. End view (B-scan) at cross section 150 mm from south face.



Figure 21. Cut 1 for verification that duct with the 10 strands was fully grouted.

5 CUTTING SLAB FOR VERIFICATION

The slab was cut at two positions as shown in Figure 8 to verify the interpretations of the impact-echo and ultrasonic-echo test results. Cut 1 was made near the north face, where test results indicated the grouted duct did not have voids in the grout. Figure 21 shows that, in fact, there were no voids in the grout.

Cut 2 was made near the south face as shown in Figure 8. This location was classified as poorly grouted. As shown in Figure 22 there were, in fact, large air voids in the grout, which have been colored black in the photo for better contrast.

Thus the test results were confirmed, and the grouted duct had unplanned voids, which were likely a result of the problems encountered when the last part of the duct was filled with grout.

6 CONCLUSIONS

Both the impact-echo method and the ultrasonic-echo tomographer can detect steel cable ducts without grout.

For practical testing with impact-echo, it is important to test along the longitudinal axis of the duct. Prior to testing, the duct(s) have to be located e.g. by GPR, a deep cover meter, or by the ultrasonic-echo tomographer. During testing, it is important to make sure a reflection frequency is obtained from either the strands in the duct with no drop in the solid frequency,

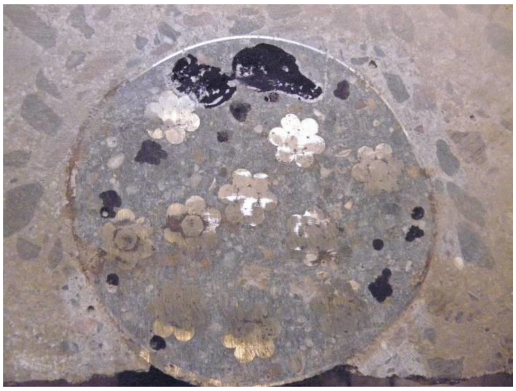

Figure 22. Cut 2 for verification of voids in grouted duct; air voids are enhanced by black marking.

or from a void in the duct accompanied by a drop in the solid frequency. Should the concrete member have changing thickness, the only practical approach is to look for either the frequency associated with reflection from the strands in the grouted duct, or the frequency associated with reflections from voids in the grout.

The ultrasonic-echo tomographer needs adjustment of the image colors for detection of cable ducts without grout.

Partly grouted steel cable ducts can also be detected with both systems. Care should, however, be exercised in interpreting the results. In spite of the presence of voids in the grout, the strands may be fully protected and well bonded to the grout. Only invasive opening will reveal the actual condition of a partially grouted steel cable duct.

Detection of fully grouted steel cable ducts with the ultrasonic-echo tomographer will require proper adjustment of the image colors. For the impact-echo method, the frequency associated with reflections from the strands will be in accord with following the equation $f = C_{plate}/(4 \times T_s)$ with no drop in the solid plate frequency.

Verification of the NDT testing results by invasive probing should be done carefully to prevent damaging the prestressing steel. An additional advantage of the verification (opening of the duct) is that evaluation can be made of the degree of corrosion of the prestressing steel. Samples of the injection grout should be taken for chloride analysis to determine if chlorides have penetrated into the duct, for example from a leaking expansion joint or from corroding regions on the steel cable duct.

As an example, Ramboll Finland Oy (Rapaport 2010) has already successfully applied this kind of testing on more than 50 bridges and has gathered a lot of experience in these types of investigations. One of the important conclusions is that in order to be able to correctly interpret the test results the testing engineer needs to have a lot of experience and understanding of the systems and of the construction of the tested structures.

REFERENCES

Rapaport, Guy: “Scanning by MIRA 3D Tomographer, Test Case, Lieviö Overbridge, Finland”, Ramboll, Kuipio, Finland, 24.10.2010

Carino, N.J.: “Impact Echo: The Fundamentals”, International Symposium on Non-Destructive Testing in Civil Engineering, September 15–17, 2015, Berlin, Germany http://www.ndt.net/article/ndtce2015/papers/257_carino_nicholas.pdf

Hoegh K., Khazanovich L., Yu H.T. “Ultrasonic Tomography Technique for Evaluation of Concrete Pavements.” *Transportation Research Record*: *Journal of the Transportation, Research Board*, No. 2232, pp. 85–94. 2011, Washington, USA

Concrete Solutions – Grantham et al. (Eds.)
© 2016 Taylor & Francis Group, London, ISBN 978-1-138-03008-4

Non-destructive testing of joints in precast element structures

Claus Germann Petersen
Germann Instruments A/S, Denmark

Hugo D. Orozco Recillas
Germann Instruments A/S, Denmark

ABSTRACT: Strength and durability of precast concrete structures are determined to a great extent by the strength and durability of the connections between the precast elements. Most common problems are improper grouting and packing of the filling material in the joints, as well as excess of shrinkage or inadequate bond to the boundaries. Therefore, ensuring a proper filling of joints is a must to avoid undesirable effects such as cracks, steel corrosion, lack of stiffness or loss of load carrying capacity. However, it is not easy to be sure that the workmanship has been done correctly unless coring or drilling of holes are performed. This paper presents a case study carried out on vertical joints of precast concrete wall elements improperly grouted to show fast and reliable non-destructive techniques, for quality control or inspection survey, that require access to only one face of the element: the impact-echo method and an ultrasonic-echo tomographer.

1 INTRODUCTION

In order to form a monolithic structure using precast concrete wall elements, vertical shear connections are usually made as keyed joints reinforced with overlapping U-bars. They form a cylindrical core in which a locking bar is positioned, and all the joints are grouted with mortar. Another alternative is replacing the U-bars with high strength looped wire ropes since their flexibility makes the installation of wall elements easier. The wire ropes are usually pre-installed in "wire boxes" embedded in the precast walls with a rebar in the middle (Jorgensen, 2015).

While these types of joints have proved to be structurally appropriate, sometimes the grouting procedure at the job site is not properly done (Lund et al, 2015). A vertical shear connection joint with defects in the filling mortar can lead to stress concentrations that may induce undesirable plastic deformations in the U-bars or a brittle failure in the looped wire ropes due to their lack of yield plateau in the stress-strain relationship (Jorgensen, 2015). Furthermore, even if the load carrying capacity is not compromised, the service life of the structure might be, because cracks and voids make concrete susceptible to water intrusion and consequently steel corrosion may become a problem or ice can be formed during freezing temperatures, expanding and cracking the surrounding concrete.

A demonstration of quality inspection of joints with looped wire ropes was performed in a multi-story building where precast concrete walls were used extensively. Knowing that the grouting process is very susceptible to human error, looking for possible defects is critical. Two instruments were used, the DOCter, which is based on the Impact-Echo method, and MIRA, an ultrasonic-echo tomographer. The stress wave NDT assessment methods are totally sensitive to these types of defects and fully accomplished the investigation. Results are discussed and compared. Cores were extracted for verification.

1.1 *The DOCter Impact-Echo principle (Carino, 2015)*

A short mechanical impact is produced on the concrete surface with a small steel sphere. This impact generates stress waves that propagate into the concrete. When the P-wave (the longitudinal wave) reaches a material (e.g. air, steel, soil, etc.) with a different acoustic impedance (wave speed x density), it is reflected and travels back to the surface where the impact was generated. The reflective surface is normally the back side of the concrete member but if this concrete has embedded objects or defects such as voids, honeycombs, cracks, etc., they also act as reflective surfaces. A sensitive displacement transducer next to the impact point picks up the displacement of the surface due to the arrival of the P-wave. The P-wave is then reflected back into the member and the cycle begins again. Thus the P-wave undergoes multiple reflections between the two surfaces and the recorded waveform of surface displacement has a periodic pattern that is related to the depth of the reflective surface for a given wave speed. This displacement waveform is transformed into a frequency domain to produce an amplitude spectrum that shows the predominant frequencies in the waveform (see Fig. 1). The analysis of these frequencies is the

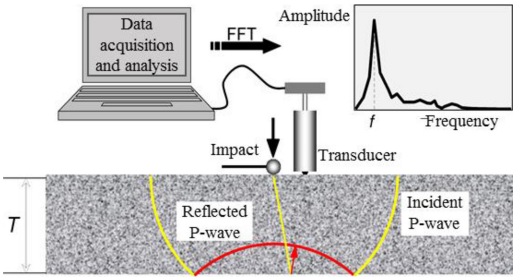

Figure 1. The Impact-Echo method.



Figure 2. DOCter Impact-Echo testing in progress.

basis of the Impact-Echo method which is governed by the equation shown below:

$$f = \frac{C_p}{2\,D} \tag{1}$$

where f = frequency; C_p = P-Wave speed; and D = travel path.

The DOCter instrument is illustrated in operation in Figure 2. Each measurement takes only 1 second.

1.2 *The MIRA ultrasonic-echo tomographer principle (Hoegh et al, 2011)*

MIRA is a portable instrument based on the ultrasonic pulse-echo method using transmitting and receiving transducers in a "pitch-catch" configuration. One set of transducers sends out a shear wave pulse and all other sets of transducers receive the reflected pulse. The time from the start of the pulse until the arrival of the echo is measured. For a known shear wave speed,



Figure 3. The MIRA ultrasonic-echo tomographer. To the left, front face displaying a cross section scan; to the right, the 4 × 12 transducer array antenna; and at the bottom, testing in progress.

Cs, the depth of the reflecting interface can be calculated. The instrument itself measures automatically the shear wave speed.

The 4 × 12 transducer array antenna produces many transit time measurements during each test that are later analyzed using the synthetic aperture focusing technique (SAFT) in real time to reconstruct a 2D image of the cross section below the instrument. It takes about 3 to 4 seconds to complete data acquisition and data processing at each location.

The data captured can later be transferred to a computer with a dedicated software to create a 3D image that allows views of different slices of the reconstructed internal structure to identify the locations of the reflecting interfaces, which can be the opposite side of the concrete member (back wall reflection), reinforcing bars or concrete-air interfaces such as voids, delaminations, honeycombing or other defects alike. Figure 3 shows the instrument.

2 TESTING

Both methods described above were used in a demonstration project that consisted of testing two wire loop joints of precast wall elements during the construction of the Life Science & Bio Engineering Building at the Technical University of Denmark, Campus Lyngby: Joint # 2 in the Ground Level (2GL) and Joint # 2 in the First Level (2FL). The joints were grouted with a fluid mortar, but there were suspicions that a bad procedure of grouting could have been done. The focus of the testing was to find the position and size of possible defects to be repaired.

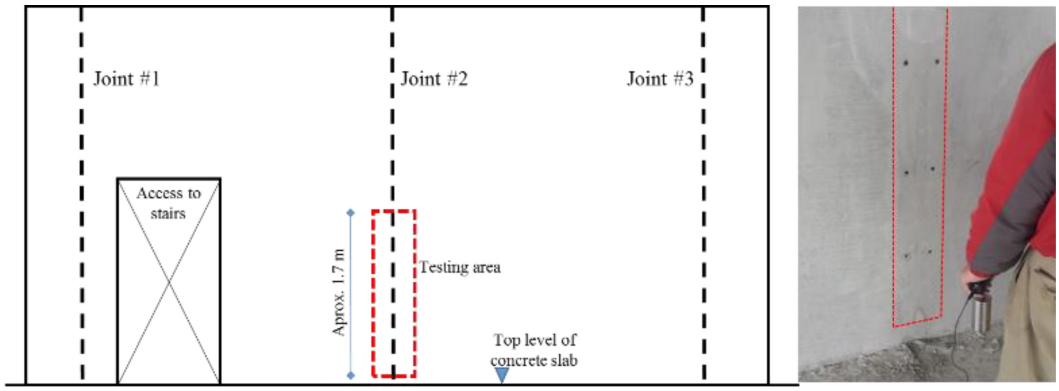

Figure 4. Lateral view of the wall and testing area.

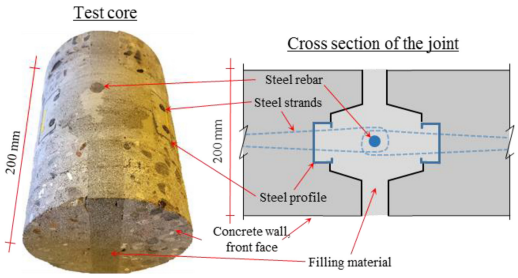

Figure 5. A solid concrete core extracted from the joint for verification together with a drawing of the cross section of the joint.

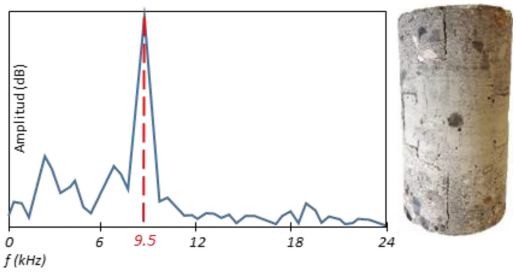

Figure 6. Recorded spectrum of a filled-out joint section. One single main peak is displayed, 9.5 kHz in this case (red line), corresponding to a thickness of 200 mm for a P-wave speed of 3,800 m/s. A 150 mm diameter core was taken from the section for verification, shown adjacent.

A vertical column of 17 testing points, with 100 mm spacing in between, were selected for the joint in the ground floor and 18 points, same spacing, for the joint in the first floor. The tested concrete walls were 200 mm thick (see Fig. 4).

2.1 *Testing with DOCter*

In order to obtain the P-wave wave speed (C_p) of the mortar, the instrument was calibrated in an area of the wall with known good quality filling (see Figure 5) and the wave speed was estimated to be 3,800 m/s (a reasonable P-wave speed for the mortar) from the equation (1):

$$f = \frac{C_p}{2\,D}$$

$$C_p = 2\,D\,f = 2\,(200)(9.5) = 3{,}800\ \text{m/s}$$

with $f = 9.5$ kHz, measured by DOCter from the same well known solid area (see the highest peak in the frequency spectrum from Fig. 6).

2.1.1 *Solid joint*

Figure 6 shows the frequency spectrum of the verification test in joint 2FL which was the reference for comparing the rest of the testing points. It can be seen that the main peak is indicating the 9.5 kHz value used for the calculation of the wave speed velocity and that there are no other major peaks indicating other reflective surfaces than the one from the back side of the wall.

2.1.2 *Joint with a limited defect*

For a limited size of defect, reflections occur mainly from the back side of the member but partly also from the internal small voids. Because the P-wave runs around the defect(s), it will travel longer and the main or solid frequency will drop in the spectrum to a lower frequency value. Yet, the other reflections coming from the defect itself will produce a high amplitude peak on the right side of the frequency spectrum. If this peak is big enough to be clearly identified, the depth of the defect can be estimated using the equation (1).

Figure 7 shows this case with data obtained from joint 2FL. A mixed frequency shows up, partly the solid frequency at 9.5 kHz and partly a frequency at 7.5 kHz related to a longer travel path than the 200 mm thickness of the wall. The interpretation is a partly injected joint with small voids, which was confirmed by the core drilled out shown adjacent to the spectrum. A smaller frequency peak at 22 kHz is also showing up at the right side of the spectrum, however, it is not high enough to identify it clearly in this case.

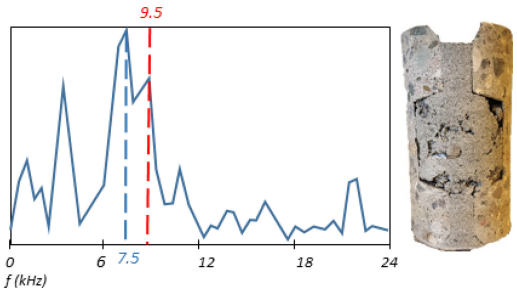

Figure 7. The frequency of the main peak has dropped to 7.5 kHz (blue line). The red line shows the position at 9.5 kHz where the main peak should have been according to Figure 6. The amplitude in this point is still high, meaning that part of the P-wave still runs through solid material. Notice also the 22 kHz frequency peak coming up, related to a larger possible defect. The 150 mm core was taken from the section for verification.

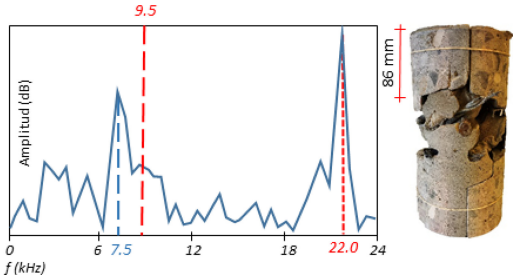

Figure 8. The blue dotted line at 7.5 kHz indicate a longer travel path than the 200 mm related to a frequency of 9.5 kHz. The P-wave runs around a defect. A second main peak in the spectrum shows reflection from a large defect at 22 kHz related to the depth of the defect. A 150 mm core was taken from the section for verification and it can be seen that the depth of the defect was predicted accurately.

It can be also noticed that there are some other peaks on the left side of the spectrum (low frequency region), most certainly caused by e.g. the Rayleigh Wave or flexural displacement. They are not important, keeping a focus only on the main peaks of the solid frequency during the analysis, a drop in this frequency and higher frequency peaks coming up.

2.1.3 *Joint with a large defect*

This time the drop of the main peak of the spectrum is followed by a large second main peak in the higher frequency region, meaning that the defect is big enough to clearly transmit a reflection by itself for the impactor selected. Using this high frequency with the same equation, the depth of the defect can be calculated with equation (1) as follows:

$$D = Cp/2f = 3{,}800/2\,(22) = 86\ \text{mm}$$

Figure 8 shows this case with data obtained from joint 2FL.

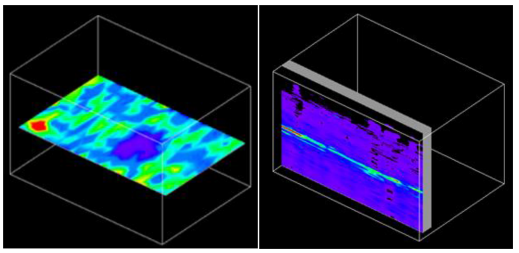

Figure 9. Screenshots of impact-echo representations made by the MIRA d'Or software. On the left, a cross section parallel to the surface at 150 mm depth in a slab. The purple/violet area in the middle shows some honeycombing and the red one shows a void. On the right, a cross section perpendicular to the surface showing the backwall represented by the bright green line.

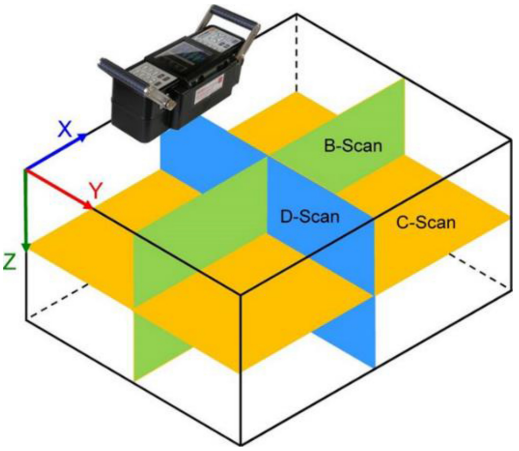

Figure 10. Identification of the 3 orthogonal planes of MIRA according to its position on the surface.

2.1.4 *Summary*

As a summary, the testing points were classified as shown in Figure 12C with 3 colors: blue for solid or filled-out region of the joint, yellow for small voids or defects and red for large voids or defects.

A dedicated software has been developed recently to facilitate the interpretation. The application creates 2D and 3D visual representations of the results obtained from a grid of closely-spaced test points (see Fig. 9).

The technique consists in using the amplitude spectrum to construct a volume model of the test region from which locations of reflecting interfaces can be presented as images where a color coding is used to represent the amplitude of each frequency. This software was however not used in this case as only 1 line of testing points was implemented.

2.2 *Testing with MIRA*

Regarding the use of the MIRA ultrasonic-echo tomographer, one measurement was done at each point that had been previously tested with the Impact-Echo method. However, with MIRA, the coverage of each

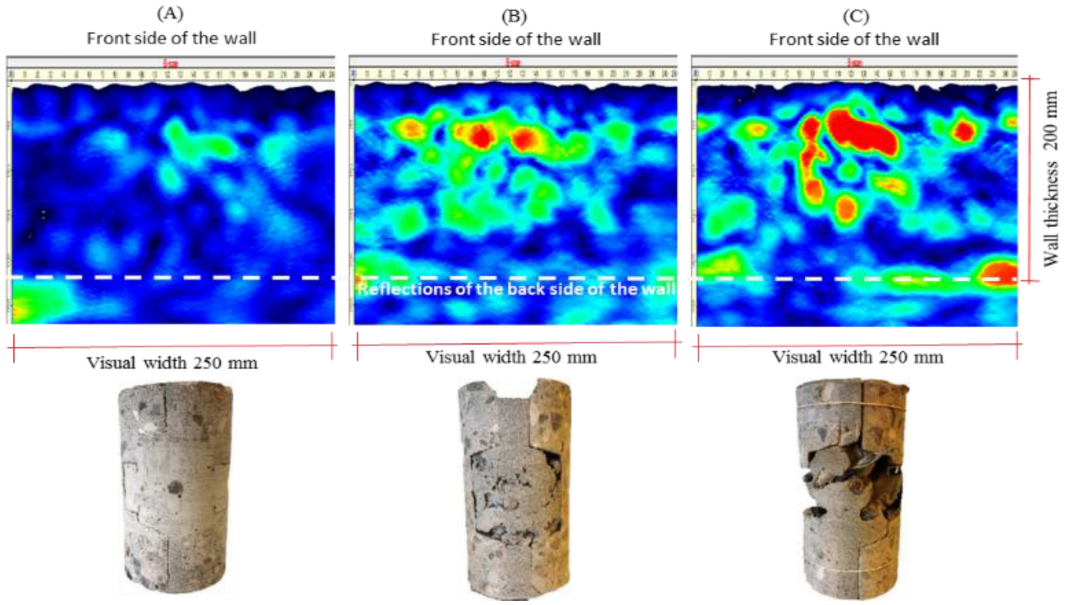

Figure 11. B-scans from the MIRA tomographer. Red zones indicate reflections from voids. (A) fill-out section of the joint. (B) section of the joint with small defects. (C) section of the joint with big defects. Below the verification cores are shown for each case.

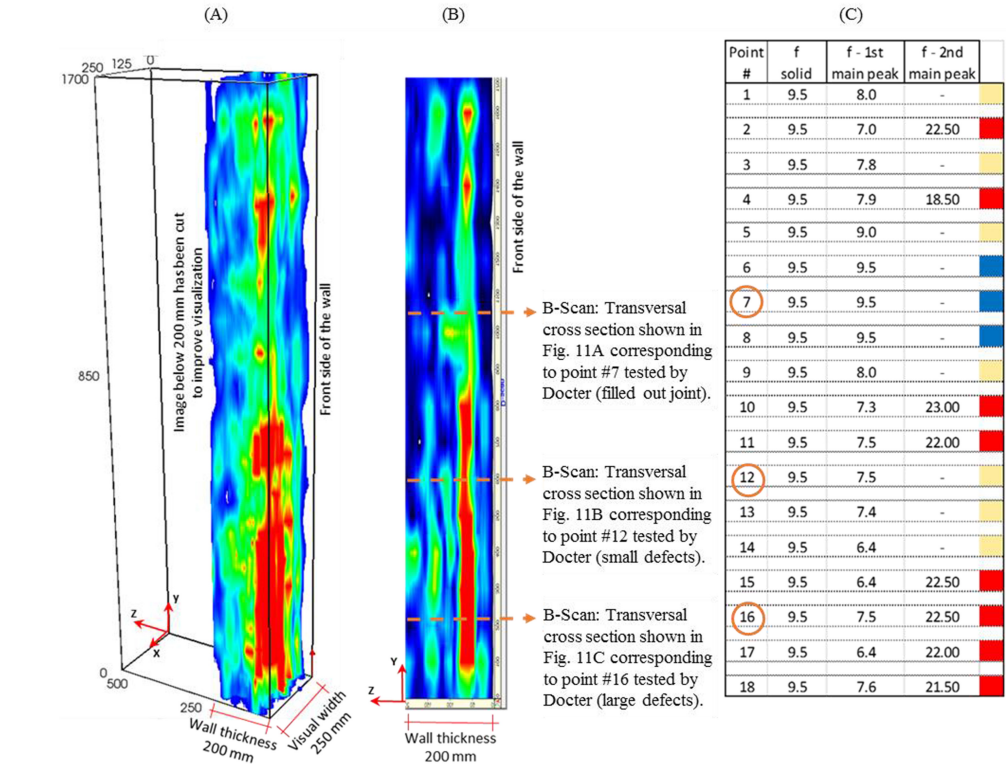

Point #	f solid	f - 1st main peak	f - 2nd main peak
1	9.5	8.0	-
2	9.5	7.0	22.50
3	9.5	7.8	-
4	9.5	7.9	18.50
5	9.5	9.0	-
6	9.5	9.5	-
7	9.5	9.5	-
8	9.5	9.5	-
9	9.5	8.0	-
10	9.5	7.3	23.00
11	9.5	7.5	22.00
12	9.5	7.5	-
13	9.5	7.4	-
14	9.5	6.4	-
15	9.5	6.4	22.50
16	9.5	7.5	22.50
17	9.5	6.4	22.00
18	9.5	7.6	21.50

Figure 12. Final results from joint 2FL and comparison between both testing methods. (A) 3D view of the whole testing area of the joint. (B) D-scan view representing the longitudinal cross section of the joint at its center (x = 125 mm) and the position where the transversal cross sections shown in Figure 11 were taken. (C) Impact-Echo method results with the color classification given.

measurement is about 250 mm width and the image of the plane below the instrument is displayed in 3-4 seconds, the so-called "B-scans" (see Fig. 10).

The instrument was firstly calibrated in an area of the wall with known good quality filling. This was done only once at the beginning where the parameters such as color gain and testing emitting frequency were set.

This calibration should be made carefully before every specific testing job, otherwise the color contours in the images could easily be interpreted erroneously. Furthermore, because reflections could be an indication of other embedded objects, interpretation is recommended to be followed by some testing cores for verification at the beginning before continuing making ample testing.

Figure 11 shows examples of B-scans from 3 different points corresponding, from left to right, to a filled-out joint, a joint with small defects and a joint with big defects. Since the MIRA was placed transversally to the longitudinal direction of the vertical joint as shown in Figure 4, the plane of a B-scan corresponds to the transversal cross section of the joint.

All 2D images obtained from each point were afterwards processed in a laptop with a dedicated software to reconstruct a 3D view of a joint. Figure 13 shows the final results of both instruments, MIRA and DOCter in joint 2FL for comparison.

The table with the Impact-Echo data from the testing points has been positioned to match the height of the images of MIRA and compare the color classification given as explained before. As it will be seen, there is good agreement between both methods.

Some minor differences may be expected because Impact-Echo are point readings below the position of the single transducer whereas MIRA makes a reconstructed map over the whole length of the joint with a width of about 250 mm. However, the general interpretation of both tools for the practical purpose of quality control or quality assurance is equivalent.

3 CONCLUSIONS

Testing from one side only is feasible for checking the quality of injection of joints locking precast elements together. Two such systems are the impact-echo (DOCter) and the ultrasonic-echo method (MIRA). They can help owners or supervisors for quality assurance purposes and contractors by implementing a quick quality control procedure that allows them to change or improve the working conditions or methods to avoid further expense on repairs and delays. The quality of the repair itself can also be tested.

The impact-echo (DOCter) is simple to perform and gives immediate information of the condition of the joint right below the transducer. Once the fundamental frequencies are understood, the testing can take place very quickly, within 1-2 seconds for each test. A newly developed impact-echo software, the MIRA d'OR, allows 2D and 3D images of the joint quality to be produced.

The ultrasonic-echo method performed by means of the MIRA needs careful calibration when starting a testing set, takes a little longer time and it is difficult to perform within confined areas because of the size of the instrument. The advantage is that the 2D color illustration is displayed within 3-4 seconds as a cross section (B-Scan). The 3D reconstruction of the joint condition requires additional time to transfer the 2D data to a laptop with the dedicated 3D software but it is a useful tool to generate friendlier testing reports.

To obtain the full benefits of both systems, the theoretical background should be understood and training in operation of the systems should be received.

ACKNOWLEDGEMENTS

Grateful thanks are extended to the contractor Mr. Jack Pedersen, MT Hoejgaard, Copenhagen, Denmark for core sampling to cross check the findings.

REFERENCES

Carino, N.J. 2015. International Symposium on Non-Destructive Testing in Civil Engineering, *Impact Echo, the Fundamentals*. Berlin, Germany.

Hoegh K., Khazanovich L., Yu H.T. 2011. Transportation Research Record: Journal of the Transportation Research Board, No. 2232, *Ultrasonic Tomography Technique for Evaluation of Concrete Pavement*s, *pp. 85–94*. Washington, USA.

Joergensen, H.B. 2015. (University of Southern Denmark) and Hoang, L.C. (Technical University of Denmark), FIB Symposium Proceedings, *Load carrying capacity of keyed joints reinforced with high strength wire rope loops*. Copenhagen, Denmark.

Lund, Mia. S.M., Arvidsson, M. & Hansen, K.K. 2015. DTU Civil Engineering. FIB Symposium Proceedings 2015, *Homogeneity and strength of mortar joints in Pearl-Chain bridges*. Copenhagen, Denmark.

Concrete Solutions – Grantham et al. (Eds.)
© 2016 Taylor & Francis Group, London, ISBN 978-1-138-03008-4

Development of electrically conductive resins for the on-site fabrication of sensors for corrosion detection and risk assessment in reinforced concrete

P.B. Sassmann & O. Weichold
Institute of Building Materials Research, RWTH Aachen University, Aachen, Germany

ABSTRACT: Assessing the risk of corrosion in steel-reinforced concrete can be accomplished using different types of sensors such as anode ladders or multi-ring electrodes. The former are unsuitable for retrofit installations, while the latter require the use of embedding mortars to achieve conductive connections with the surrounding concrete. However, the porosity of the embedding mortar differs from that of the concrete and the retrofitting action introduces additional moisture. This interferes with resistivity and/or potential measurements and makes interpretations of the actual situation problematic. To circumvent these disadvantages, we have developed a liquid reactive polymer resin with high electrical conductivity that can be used to fabricate sensors directly inside drill holes. The mixture solidifies in a short time and its adhesive properties provide an excellent conductive connection to the concrete walls. The resin contains no water so that reliable values can be obtained immediately after solidification. By changing the additives both resistivity and potential sensors can be obtained. The mixture is cheap so that large sensor networks can be installed at reasonable costs. Such networks are ideal for the precise localization of corrosion events and more importantly for risk assessment in steel-reinforced structures.

1 INTRODUCTION

In 2013 the World Corrosion Organization (WCO) assessed the economic loss caused by corrosion to 2.2 trillion US dollars (WCO 2013). This is why the restoration of residential and infrastructural buildings gains enormous importance. To avoid corrosion continuing unnoticed within structures, monitoring systems can be installed afterwards to assess the actual condition of the reinforcement and to follow the corrosion progress (Raupach 2000). Therefore, timely and minimally invasive recognition of the corrosion conditions is essential. These monitoring systems have to meet requirements such as reliability, precision, and cost efficiency. Furthermore, the post-installation should be simple and should not significantly change the present conditions within the building. Based on these considerations, a sensor system was developed consisting of a liquid, reactive, electrically conductive, polyester resin.

1.1 *Detection of corrosion in reinforced-steel concrete*

The corrosion process in reinforced concrete is supported by the ingress of chlorides and moisture, especially in the form of de-icing salts in winter time. Furthermore, cracks facilitate the transport to the steel reinforcement. In the presence of oxygen, a galvanic cell forms causing the dissolution of steel (anodic reaction, eq. 1) and the formation of hydroxide (cathodic reaction, eq. 2). The overall corrosion process is shown in equation 3.

$$Fe \rightarrow Fe^{2+} + 2\,e^{-} \tag{1}$$

$$O_2 + 2\,H_2O + 4\,e^{-} \rightarrow 4\,OH^{-} \tag{2}$$

$$2\,Fe + 2\,H_2O + O_2 \rightarrow 2\,Fe(OH)_2 \tag{3}$$

The electrochemical potential of the Fe/Fe^{2+} pair under standard condition is -0.44 V (Haynes 2015). Under realistic conditions, the potential depends on a number of factors such as the presence of passive layers, resistance of the electrolyte bridge, and the concentration of chloride, moisture, and oxygen (Reichling 2014).

The change in potential or resistivity can be detected with different types of sensors. However, the post-installation causes problems originating in the use of embedding mortars. Realizing the electrical connection of sensor and old concrete by cementitious systems, changes the moisture distribution and the microstructure in the vicinity of the sensor. As a result, resistivity changes and actual conditions can only be assessed at an unspecified time in the future, when the conditions are equilibrated. In addition, the embedding procedure is complex and the materials processed within the sensors are expensive.

1.2 *Electrically conductive polymers in construction industry*

In civil engineering, plastic materials are not famous for electrical conductivity. However, electrically conductive polymer composites have been known since the early 1950s (Mark, 2013) and intrinsically conductive polymers were first prepared in the early 1970s (Shirakawa, 1977). Nevertheless, these types of materials are not suitable for the intended use as sensors on construction sites because their preparative effort is too high or the synthesis sensitive to external conditions like moisture, temperature fluctuation or oxygen.

Therefore, the sensors systems presented here are based on a newly developed, electrically conductive 2k polymer resin, which is directly injected into drill holes. This way, a close contact between sensor and the concrete walls is automatically realized and since the polymer resin is not aqueous, the moisture balance of the old concrete is not altered. As a result, the system is ready to use as soon as the polymer resin solidifies. The sensor system receives two characteristics: both resistivity and potential sensors can be obtained.

At least, easy implementation and the availability for corrosion monitoring systems at lower cost is of benefit.

2 EXPERIMENTAL

2.1 *Preparation of unsaturated polymer system*

The unsaturated polyesters were prepared by reacting poly(ethylene glycol) ($M_w = 400\,\mathrm{g\,mol^{-1}}$, Carl Roth GmbH & Co.KG) with maleic anhydride (Alfa Aesar) in equimolar quantities in the presence of p-toluenesulfonic acid monohydrate (Carl Roth GmgH & Co.KG), as catalyst. The polycondensation reaction was accomplished in toluene at 160°C for 9 h under atmospheric pressure as described in literature and run until the acid number reached values <20 (Wright 1988). The acid number was determined to be 16.2 by titration with 0.1 M NaOH and is given in mg NaOH/g sample. This corresponds to a molecular weight of $M_w = 2439\,\mathrm{g\,mol^{-1}}$.

2.2 *Curing of electrically conductive polymer resin*

The unsaturated polyester was mixed with 33wt% styrene (MERK), which acts as crosslinking agent, at 80°C. To prevent temperature caused polymerization, the mixture was afterwards rapidly quenched. 2wt% of a low temperature redox initiator system, methyl ethyl ketone peroxide (Mühlheimercomposite) and cobaltoctanate (Shiraz, 2013) was added for the curing reaction. The electrical and ionic conductivity of the polymer resin was established by adding $LiClO_4$ (Alfa Aesar) and different additives such as lead oxide (Sigma-Aldrich), manganese oxide (Fluka Analytics), carbon black (H.C. Carbon) and ferrochrome (Thyssenkrupp). Detailed sample compositions are given in Table 1. Thus, small cylindrical samples with a diameter of 1.2 cm were produced.

Table 1. Sample numbers and composition of the filled polymer resins.

Sample	Styrene wt%	Initiator wt%	Additive 8 wt%	[UP]/[Li^+] wt%
1	33	2	–	–
2	33	2	–	22
3	33	2	MnO_2	22
4	33	2	PbO_2	22
5	33	2	Ferrochrome	22
6	33	2	Carbon Black	22



Figure 1. Two electron potentiostatic measurement of a polymer resin containing MnO_2 using a spacer.

Conductivity measurements were made using the PCI4/300 Gamry Poentiostat (C3 Instruments). Figure 1 shows the experimental setup for the conductivity measurements. The experimental setup was performed using a spacer, to avoid contact between the two electrodes and adjust constant pressure on the sample surface (figure 1).

Potential measurements were carried out by using a standard hydrogen electrode (SHE) in saturated calcium hydroxide. Therefore, the polymer resin sample was contacted by a measuring probe on its surface. Expressing values can only be obtained with a dry sample surface (figure 2).

The curing reaction of an electrically conductive polymer resin was carried out in concrete. Therefore, small holes were drilled into the concrete slab which also contained a reference and a counter electrode.

The desired polymer resin composition was injected inside the holes directly after mixing all ingredients

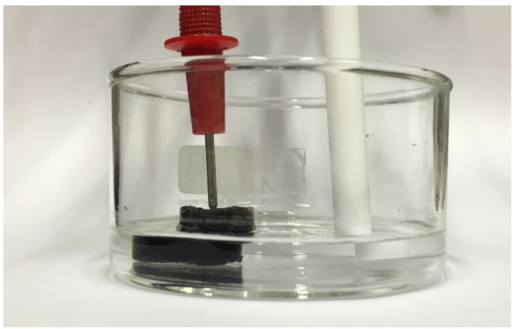

Figure 2. Electric potential measurement of a polymer resin containing MnO_2 using a standard hydrogen electrode in calcium hydroxide solution.

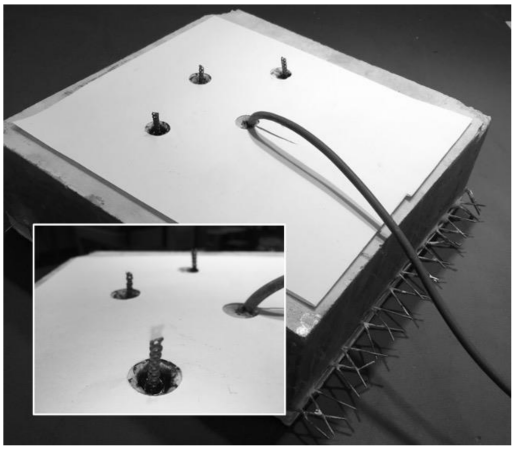

Figure 3. Electrically conductive sensors in concrete containing polymer resins 2(no additive), 3(MnO_2) or 4(PbO_2).

carefully. Afterwards, the titanium mixed metal oxide electrodes were centered inside the drill hole. Figure 3 shows the fabricated sensor system containing the electrode and electrically conductive polymer resin cured inside a drill hole.

3 RESULTS AND DISCUSSION

The sensor system presented here consists of a titanium mixed metal oxide electrode in an ion conducting unsaturated polyester made from maleic anhydride, poly(ethylene glycol), and lithium perchlorate as electrolyte. This type of unsaturated polyester was chosen because similar materials are used in solid lithium ion batteries (Takeoka 1993). To boost the performance of the sensor system, additives with either high electrical conductivity such as carbon black or ferrochrome or with high electrochemical potential such as PbO_2 or MnO_2 were added to the polyester/$LiClO_4$ mixture.

Moreover, the installation of the sensor system must also work at low temperatures and in the presence of moisture. This is why the curing reaction was initiated

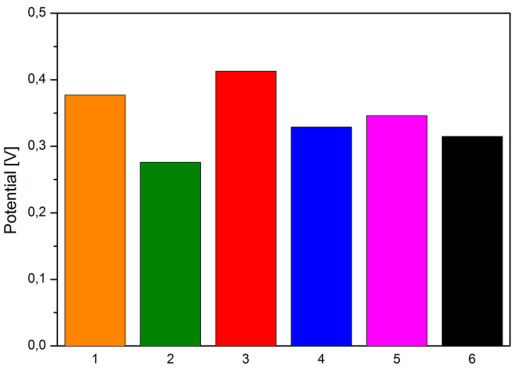

Figure 4. Standard electrode potential of unsaturated polymer resins with various compositions. The numbers refers to the samples in table 1.

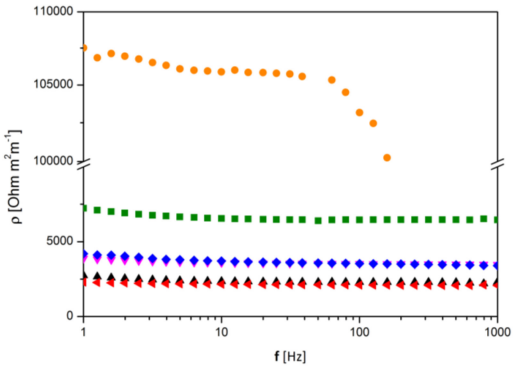

Figure 5. Frequency dependent specific resistivity of circle: sample 1, square: sample 2, arrow: sample 3, hash: sample 4, reverse triangle: sample 5, triangle: sample 6.

a redox initiator system which has an excellent activity also in case of low temperatures.

3.1 *Measurements of the standard electrode potential*

The electrochemical potentials of the composite samples 1-6 were measure against a standard hydrogen electrode in saturated calcium hydroxide solution and were all found to be positive (figure 4).

The values range between 0.25 V and 0.42 V and the highest potential was found for sample 3 containing MnO_2, which by itself has a high standard electrochemical potential of 1.255 against SHE. Interestingly, the pure polyester resin containing no $LiClO_4$ and no additives exhibited a rather high potential.

3.2 *Measurements of the electrical resistance*

Resistivity was measured using a two electrode set-up (cf. figure 1) in a frequency range of 1 to 1000 Hz (figure 5). The spacer prevents contact between the electrodes and ensures an even compression of all samples.

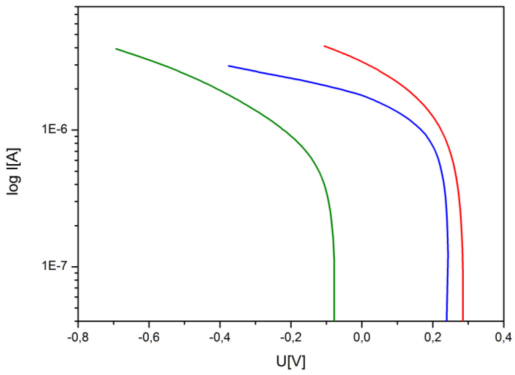

Figure 6. Current-density-potential plot, IR-drop optimized. Red: polymer resin with MnO_2, blue: polymer resin with PbO_2 and green: polymer resin without additives.

As expected, reference sample 1 containing no $LiClO_4$ and no additives has the highest resistivity (107.5 kΩ m), because no ions were able to move through the polymer matrix. Incorporation of a lithium salt reduced the resistivity to 7.5 kΩ m by introducing ion transport in the polymer matrix. A further decrease in resistivity to <5 kΩ m was achieved by incorporating additives, with the best being MnO_2 at a resistivity of 2.45 kΩ m. The reason for this might be the semiconducting properties of MnO_2 (Hofmann 2013).

3.3 *Current-density-potential plot of polymer resins with different additives*

Polymer resins containing ferrochrome and carbon black show good electrical properties and high potentials and can be easily prepared in the lab, but are not suitable for on-site application, since the additive sediments before the resin is fully hardened. This is why only resins with MnO_2 and PbO_2 additives where used in concrete experiments. An unsaturated polymer resin containing only $LiClO_4$ was used as reference.

Figure 6 shows the current-density-potential plot of the polymer resins inside the drill holes in concrete.

The current-density-potential plot shows the current between the working and the counter electrode. Thereby, the potential is traced in the cathodic direction. All samples exhibited a constant potential over a wide region. The order of the samples with the resin containing MnO_2 having the highest and the resin without additives having the lowest potential matches the potentials in figure 4, albeit at lower absolute values. This is an important observation for the application as a sensor material. If the resistivity changes, depending on the level of moisture, the potential is still high enough even if the current varies as well.

4 CONCLUSIONS

Composite unsaturated polyesters containing $LiClO_4$ and potentially additives such as MnO_2 or PbO_2 are excellent materials to prepare conductivity and potential sensor system. The sensor systems are easy to install on site directly inside drill holes. The observed potentials are well in the positive range so that large potential differences can be expected relative to the corroding reinforcement. This allows reliable detection of corrosion events even under dry conditions.

ACKNOWLEDGEMENT

The authors thank Christian Helm for inspiring suggestions as well as Markus Zander and Tim Kurschildgen for their help during this work.

REFERENCES

Chu, P. H. & Wright, P.V., British Polymer Journal, *1989*, 21, 421–427.
Bin, F. & Chun, P. H. & Sheng Kang, Y., Europen Polymer Journal, *1993*, 29, 799–803.
Fenton, D.E. & Parker, J.M. & Wright, P. V., Polymer *1973*,14, 589.
Hofmann, K.A., Anorganische Chemie, Wiesbaden, 21 edition, 2013, 659.
Hynes, M. W., Handbook of Chemistry and Physics, London, 95 edition, *2015*, 79-88.World Corrosion Organisation, Bringing Corrosion Awareness to the Public, *2013*, URL: http://corrosion.org/Corrosion+Resources.html
Mark, H.F., Encyclopedia of Polymer Science & Technology, New Jersey, 3 edition, *2013*, 351.
Wright, P.V., British Polymer Journal, *1975*, 7, 319.
Raupach, M. & Meessen, J., Bautenschutz und Bausanierung 23, *2000*, 2, 18–25.
Reichling, K., Bestimmung und Bewertung des elektrischen Wiederstands von Beton mit Geophysikalischen Verfahren, Dissertation, RWTH Aachen, *2014*.
Shirakawa, H. & Louis, E.J. & MacDiarmid, A.G. & Chiang, C.K. & Heeger, A.J., J Chem Soc Chem Commun, *1977*, 579.
Shiraz, N.Z. & Letafat, B, Inorganic Chemistry, 2013.
Takeoka, S. & Ohno, H. & Tsuchida, E., Polymers for advaced technologies, 1992, 4, 53.

Concrete Solutions – Grantham et al. (Eds.)
© 2016 Taylor & Francis Group, London, ISBN 978-1-138-03008-4

Frequency dependency of concrete resistance measurements

A.-M. Thoresen, K. Hornbostel & M.R. Geiker
Norwegian University of Science and Technology (NTNU), Trondheim, Norway

ABSTRACT: Concrete resistivity is frequently measured in the laboratory and on-site for durability assessment. To avoid polarization effects, measurements with AC (Alternating Current) are commonly recommended. Resistance measurements with AC techniques are frequency dependent. It is assumed that a fixed frequency between 100 Hz to 10 kHz is adequate to allow the determination of the ohmic resistance in concrete. Within the presented study, AC resistance measurements using Electrical Impedance Spectroscopy (EIS) were performed on concrete varying in composition and moisture content. It was found that for concretes with a high resistivity and low moisture content, frequencies below the common recommendations should be applied to obtain the actual ohmic resistance. Within the range of concretes investigated, measurements at 1 kHz resulted in up to 20% underestimation of the actual resistivity of 1-year-old samples which had been stored sealed.

1 INTRODUCTION

Electrical resistivity (ρ) is a material specific property, describing the ability to withstand the flow of electric current. It is dependent on concrete porosity and pore solution conductivity (Spragg et al. 2013) as well as the degree of saturation and temperature (Gjørv et al. 1977). Additions of pozzolans, such as fly ash and silica fume, or ground granulated blastfurnace slag refine the porosity and lower the pore solution conductivity, and consequently increase the electrical resistivity (Bertoloni et al. 2013).

In the present paper, the frequency dependency of resistivity measurements on concrete is investigated, assessing the applicability of measurements undertaken at fixed frequencies. Two resistivity measuring techniques (Electrical Impedance Spectroscopy (EIS) and measurements done with a commercial LCR meter) are compared for concrete prepared with blended cements, stored at different moisture conditions.

1.1 *Measuring electrical resistivity*

Determination of electrical resistance requires at least two electrodes. A current is applied from the electrodes and the corresponding voltage drop is measured (or vice versa). The resistance, R, is given as the voltage drop over applied current:

$$R=\Delta U/I \quad (1)$$

where I is the current and ΔU is the voltage difference (Bertoloni et al. 2013).

A number of different setups for measuring concrete resistivity are available using 2, 4 or multiple electrodes. The electrodes can either be placed on the surface, embedded in the concrete upon casting or be part of the rebar network of an existing structure.

When electrodes are placed on the concrete surface, a conducting liquid is applied on the electrodes to improve contact with the concrete.

The electrical current applied during the measurements may be either direct (DC current) or alternating (AC current), from DC or AC voltage sources respectively. DC is a unidirectional electronic flow, opposed to AC which possesses phase and frequency.

When a DC electric field is applied to an ionic conductor (e.g. concrete), a potential difference is generated. Electrical charge at the electrodes causes mobile ions of opposing charge to move towards the electrode-concrete interface (Keith B. et al. 2011).This results in formation of double layers at the concrete-electrode interface causing polarization of the electrodes. The rate of which polarization occurs is determined by the mobility of the ions and the magnitude of the electric field. Polarization of the electrolyte causes the net electric field to decrease, until steady-state is established (Hansson & Hansson 1983).

Employing AC currents can prevent the polarization and double layer formation (McCarter & Brousseau 1990). Thus, AC techniques are preferred in concrete resistivity measurements. AC electrical resistance measurement principles are implemented in EIS and in an LCR meter.

1.1.1 *Measurements with an LCR meter*

An LCR meter is an electronic device used to measure resistance (R), capacitance (C) and/or inductance (L). The device applies an AC voltage while measuring the current through the material. Depending on the device, fixed frequencies of 100 Hz, 120 Hz, 1 kHz

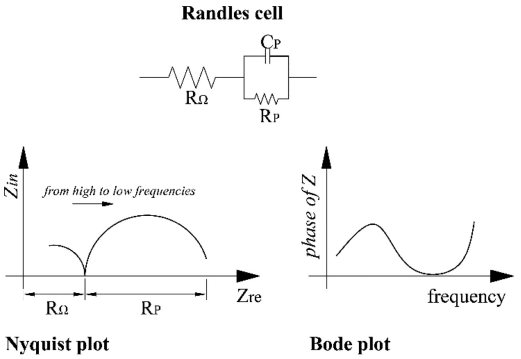

Figure 1. Randles cell and corresponding *Nyquist* and *Bode* plot.

and 10 kHz may be selected. More advanced LCR meters also measure the phase angle (angle between the current and the voltage). Devices may have two- or four terminals for making electrical connection to the electrodes. Calculated parameters are displayed at the screen. The device is easy to use and is applicable for on-site measurements.

1.1.2 *Electrical impedance spectroscopy*

When an electrical field is applied on a material, various microscopic processes take place within the cell, such as transport of electrons through the electronic conductors, transfer of electrons at the electrode-electrolyte interfaces and flow of ions in the electrolyte (Macdonald & Johnson 2005).

During EIS, an AC signal of small amplitude with changing frequencies is applied to the working electrode and the current response is measured. The impedance of the system is studied in different frequency ranges (Lataste 2010).

Impedance is described in a complex form as:

$$Z = Z' + jZ'' \quad (2)$$

where Z' is the real component, Z'' is the imaginary component and j is $\sqrt{-1}$. The phase angle is defined as $\theta = \tan^{-1}(Z''/Z')$ (Macdonald & Johnson 2005).

Impedance data of an electrochemical system are commonly studied in *Nyquist*, *Bode* and/or similar plots. In a *Nyquist* plot, the real and imaginary component are plotted versus each other, with higher frequency data located towards the axis origin (Figure 1) (ASTM Comittee G01 2014). The *Bode* plot gives the frequency on the x-axis (logarithmically) and the negative phase angle on the y-axis (cf. Figure 1) (ASTM Comittee G01 2014).

The model by *Randles* (Randles 1947) is often used to describe simple corroding systems on the bases of impedance data. *Randles* proposed that the electrode and diffusion processes under alternating potential fields are electrically equivalent to a capacity and resistance in parallel, and a resistance in series (*Randles Cell*, Figure 1). The capacitor, C_p, of the system represents the ability to store charge through double layer formation, the polarization resistance is represented by R_p. The electrical resistance of the electrolyte is characterized by R_Ω (Gamry Instruments 2010).

Hence, the ohmic resistance of a material/electrolyte (here: concrete) is retrieved from a *Nyquist* plot by choosing the value of the intersection of the first semicircle with the x-axis (cf. Figure 1). This is equivalent to the resistance at the phase angle equal to zero. The frequency at this point is the adequate measuring frequency to obtain the ohmic resistance (in the following called "ohmic measuring frequency").

2 METHODS

In this study, EIS was used to study the frequency dependence of the electrical resistance of different concretes. A comparison was done between measurements taken on a fixed frequency with an LCR meter and those retrieved from EIS. The concretes studied were all high resistance concrete prepared with different amounts of fly ash, slag and silica fume and cured and stored at different moisture conditions.

2.1 *Concretes*

A total of nine different concretes (A-I) were used. The mix compositions are shown in Table 1. The samples were cubic, measuring $0.1 \times 0.1 \times 0.1$ m^3.

The concrete samples were cast approximately one year before testing as part of a master project (Fossum 2014). The samples were stored at different moisture conditions, after 1 day's curing in moulds: submerged in curing water (SA), sealed in double air-tight bags (SE) and in a laboratory environment (DR). Thus, both the moisture content and the degree of hydration differed between the three sample types (SA, SE, and DR). The moisture contents at the time of measurement were not measured.

2.2 *Methods of investigation*

Concrete resistance was measured using a two-electrode setup. Metal plates were placed on two parallel sides of the cubic samples. As the contact solution, tap water (soft water, pH = 8.11) was used. The applied pressure was 5 kPa. Electrical connections to the potentiostat (EIS) and the LCR meter were done through metallic bolts on the metal plates.

EIS measurements were undertaken, using a potentiostat (*Princeton Parastat2273*). Accompanying software was the *Princeton Applied Research's PowerCorr*. The frequency scanning range was chosen based on the AC response reviewed through *Nyquist* plots. Scanning was performed on a wide range, from 1 MHz–10 mHz.

The resistance corresponding to the lowest phase angle was considered to be the actual ohmic resistance of the concrete, the equivalent ohmic measuring frequency was determined as well (cf. Figure 1 *Bode* plot).

Table 1. Concrete mix compositions.

Cement	Mix ID	w/b	Silica*	Fly Ash*	Vol. Air
Aalborg Portland Rapid	A	0.4	10%	–	2%
Cemex Slag cement, CEM III/B (75% slag)	B	0.35	–	–	2%
	C	0.4	–	–	2%
Norcem Anlegg FA, CEM II/A-V (20% FA)	D	0.35	–	–	2%
	E	0.4	–	–	2%
	F	0.4	10%	–	2%
	G	0.4	–	10%	2%
	H	0.4	10%	10%	2%
	I	0.4	10%	–	5%

*[%] per mass of cement

Table 2. Overview of investigations; number of samples and techniques applied.

Storage	Number of samples	Technique	Pressure [kPa]
SA	18 (2 per mix)	EIS, LCR	5
SE	27 (3 per mix)	EIS, LCR	5
DR	27 (3 per mix)	EIS	5

In plots with interference (e.g. contact interference), a "circle fit" (feature implemented in *PowerCorr)* was applied to approximate the ohmic resistance based on a fit of the first semi cycle shape (cf. Figure 1 *Nyquist* plot).

LCR meter measurements were done using the *Agilent U1732C*. The LCR meter provided the following fixed frequencies: 100 Hz, 120 Hz, 1 kHz and 10 kHz.

Table 2 gives an overview of the samples investigated and measurement techniques applied.

3 RESULTS AND DISCUSSION

The ohmic resistivity of the different concretes in sealed conditions (SE) measured with EIS is presented in Figure 2. Sealed samples are (among SA, SE and DR) assumed to best represent the moisture level and curing conditions for in-situ concrete structures.

3.1 *Frequency*

The 'ohmic measuring frequencies' the measuring frequencies at which the actual ohmic resistance of all samples was found with EIS, are presented in Figure 3.

The ohmic measuring frequency increased with decreasing moisture level. There is a scatter between the mixes within the storage conditions, but the moisture level appears to be the dominating factor in this context. This is in accordance with previous research on the topic where also plain Portland cement concrete was studied (Østvik et al. 2006; Østvik 2004).

Measurements of the samples stored saturated (SA) showed some contact interference in the plots. A distinct third arc in the Nyquist plot was observed

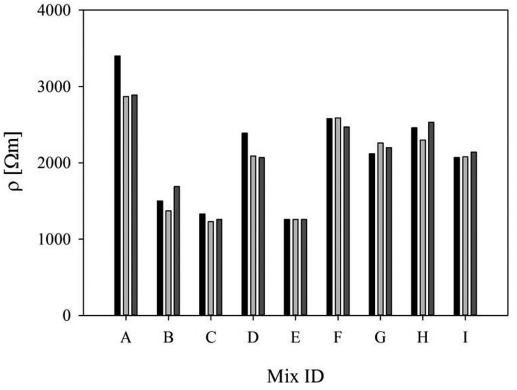

Figure 2. Ohmic resistivity of the concrete samples stored sealed (SE) measured using EIS (3 samples per mix were studied).

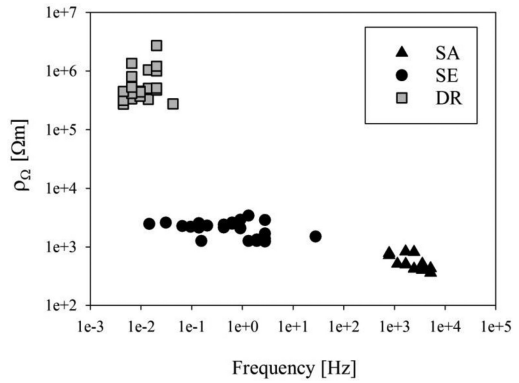

Figure 3. Measuring frequency at which the actual ohmic resistance was measured (storage conditions: SA: saturated, SE: sealed, DR: air exposed in laboratory).

(between the commonly observed first and second arc, cf. Figure 1, *Nyquist* plot). *Gu and Beaudoin* (Gu & Beaudoin 1998) as well as *Ford* (Ford et al. 1998) previously assigned this feature to the electrode-concrete interface. The feature was not apparent for the samples stored at other moisture conditions.

For the dry samples (DR, marked in grey in Figure 3), the ohmic measuring frequencies were much lower (<0.1 Hz) than the recommended range (100 Hz to 10 kHz). In the impedance plots, major disturbances were observed between 1 Hz and 1 kHz. Measurements with the LCR meter confirmed the disturbance by producing unstable results; resistance and phase angle were distorted. The disturbances appeared to be result of the low moisture content as they were not present for samples stored saturated and sealed (SA and SE).

The low measuring frequencies identified to be necessary for the dry samples (DR) might not be applicable for AC measurements. It is the oscillation of the ions, brought about by the impressed AC current that prevents the polarization of the electrodes. However, at such low frequencies, the AC signal holds comparable characteristics to the DC signal where polarization effects may not be avoided. Consequently, for very dry concrete, presumably other techniques should be considered for determining the ohmic resistance.

3.2 *Agreement between EIS and LCR meter*

A comparison was made between EIS and LCR meter measurements to evaluate the applicability of LCR meter measurements. Only SA and SE samples are included in the comparison, due to the unstable results obtained with the DR samples (cf. earlier section). Resistances measured at specific frequencies (100 Hz, 120 Hz, 1000 Hz and 10 kHz) obtained from both EIS and measured with a LCR meter are compared in Figure 4.

The results in Figure 4 demonstrate the potential applicability of an LCR meter. This is expected since the techniques utilize the same principles. EIS measurements take a considerably longer time to perform than the LCR meter measurements. The equipment and knowledge required to perform EIS measurements is also much more advanced compared to measurements undertaken with an LCR meter.

Consequently, as long as it can be assured that the ohmic measuring frequency lies within the range of available frequencies of the LCR meter, the latter is an adequate technique to obtain the ohmic resistance of concrete.

3.2.1 *Validity of measurements performed at fixed frequency (LCR meter) compared to the actual ohmic resistance*

The ohmic resistance measured with EIS was compared to the resistance obtained for LCR meter measurements at fixed frequencies to assess the validity of measurements at fixed frequencies.

Figure 5 presents the ratio between the resistivity determined by EIS (actual ohmic resistivity) and resistivity determined by measurements with the LCR meter at fixed frequencies (LCR: 120 Hz or 1 kHz).

For the samples stored sealed (SE), it is obvious that resistivity measurements taken at a fixed frequency of 120 Hz provided more correct results. Measurements

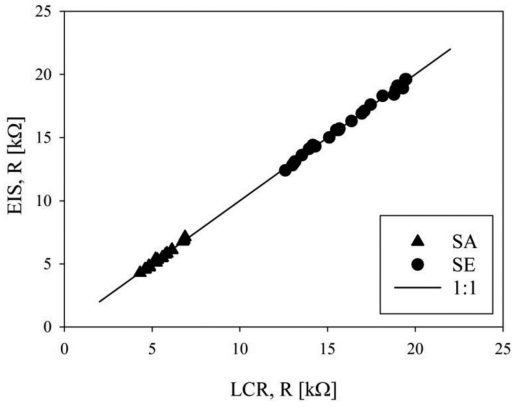

Figure 4. Comparison of resistance measurements with EIS and the LCR meter at 100 Hz, 120 Hz, 1 kHz and 10 kHz (storage conditions: SA: saturated, SE: sealed, DR: air exposed in laboratory).

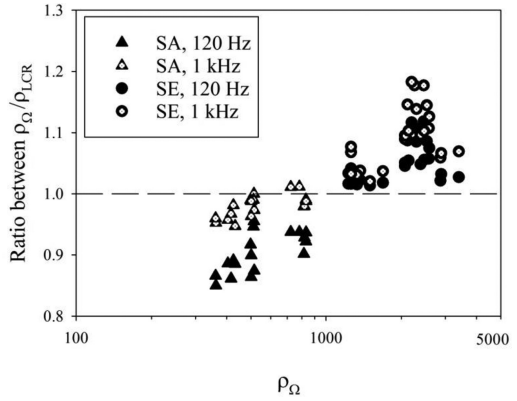

Figure 5. The ratio between actual ohmic resistivity (EIS) and resistivity measured at 120 Hz and 1 kHz (LCR) (storage conditions: SA: saturated, SE: sealed).

undertaken at a fixed frequency of 1kHz tended to underestimate the actual resistivity (by up to 20%).

For saturated samples (SA), the opposite applies. Measurement taken at frequency of 1 kHz gave adequate results, whereas measurements taken at a frequency of 120 Hz overestimated the resistivity.

This underlines that no general measuring frequency can be recommended. The ideal ohmic measuring frequency varies, especially with the moisture condition.

Nevertheless, the results demonstrate that although the actual ohmic measuring frequency may vary up to one order of magnitude from the frequency used in LCR meter measurements, the deviation between the actual resistivity and the resistivity measured using an LCR meter is relatively low (under 20%). In addition, the error can be minimized if the LCR meter provides the phase angle. In this case measurements could be taken at different frequencies and the resistance obtained at the frequency with the lowest phase

angle could be used as an approximation of the actual ohmic resistance.

4 CONCLUSIONS

The 'ohmic measuring frequencies', i.e. the measuring frequencies at which the actual ohmic resistance was found using EIS, were found to decrease with decreasing moisture content of the concrete. For the concretes investigated, the moisture content (saturated vs. laboratory dry) had a larger influence on the ohmic measuring frequency than the mix composition.

The following ohmic measuring frequencies were found; 0.01 Hz–0.1 Hz for laboratory stored concrete (DR), 0.1 Hz–50 Hz for sealed concrete (SE) and 500 Hz–5000 Hz for saturated concrete (SA).

For non-saturated samples (sealed and laboratory stored, SE and DR), frequencies below the commonly recommended range should be applied to obtain the actual ohmic resistance.

As ohmic measuring frequencies for dry concrete samples (DR) were found below 0.1 Hz the applicability of EIS on dry concrete requires further investigation. The measurements undertaken with the LCR meter showed no stable results at all.

Within the range of concretes investigated, measurements with a fixed frequency of 1 kHz (LCR meter) showed a low deviation from the actual resistivity (EIS) of the saturated samples (SA). However, measurements at 1 kHz resulted in up to 20% underestimation of the actual resistivity of the samples stored sealed (SE). Lower frequencies should be applied ($<$120 Hz) to obtain valid results for the sealed samples.

Based on the results, a single measurement frequency cannot be recommended for resistivity measurements on concrete varying in moisture content.

REFERENCES

ASTM Comittee G01, 2014. *Standrard Practice for Conventions Applicable to Electrochemical Measurements in Corrosion Testing (ASTM G57-06)*, West Conshohocken, PA, United States.

Bertoloni, L. et al., 2013. *Corrosion of Steel in Concrete: Prevention, Diagnosis, Repair* 2. ed., Weinheim, Germany: Wiley-VCH.

Ford, S.., Shane, J.. & Mason, T.., 1998. Assignment of features in impedance spectra of the cement-paste/steel system. *Cement and Concrete Research*, 28(12), pp.1737–1751.

Fossum, B., 2014. *Betong i elektrolysehaller for aluminiumsproduksjon*. Norges Teknisk-Naturvitenskapelige Universitet.

Gamry Instruments, 2010. Application Note: Basics of Electrochemical Impedance Spectroscopy. Available at: http://www.gamry.com/application-notes/EIS/.

Gjørv, O.E., Vennesland, Ø.E. & El-Busaidy, A.H.S., 1977. Electrical Resistivity Of Concrete In The Oceans.

Gu, P. & Beaudoin, J.., 1998. Estimation of steel corrosion rate in reinforced concrete by means of equivalent curcuit fittings of impedance spectra. *Advances in Cement Reasearch*, 10(No.2), pp.45–56.

Hansson, I.L.H. & Hansson, C.M., 1983. Electrical resistivity measurements of Portland cement based materials. *Cement and Concrete Research*, 13, pp.675–683.

Keith B., O., Myland, J.C. & Bond, A.M., 2011. *Electrochemical Science and Technology: Fundamentals and Applications*, Wiley-Blackwell.

Lataste, J.-F., 2010. Electrical resistivity for the evaluation of reinforced concrete structures. In *Non-destructive evaluation of reinforced concrete structures*. Woodhead Publishing Limited, pp. 243–275.

Macdonald, J.R. & Johnson, W.B., 2005. Fundamentals of Impedance Spectroscopy. In E. Barsoukov & J. R. Macdonald, eds. *Impedance Spectroscopy*. pp. 1–26.

McCarter, W.J. & Brousseau, R., 1990. The A.C. response of hardened cement paste. *Cement and Concrete Research*, 20, pp.891–900.

Randles, J.E.., 1947. Kinetics of Rapid Electrode Reactions., pp.11–19.

Spragg, R. et al., 2013. Electrical Testing of Cement-Based Materials: Role of Testing Techniques, Sample Conditioning, and Accelerated Curing. , p.23. Available at: http://dx.doi.org/10.5703/1288284315230.

Østvik, J.M. et al., 2006. Electrical Resistivity of Concrete Part I: Frequency Dependence at various moisture contents and temperatures. *2nd International Symposium on Advances in Concrete through Science and Engineering*, (September).

Østvik, J.M., 2004. *Thermal aspects of corrosion of steel in concrete*. Norwegian University of Science and Technology.



Taylor & Francis
Taylor & Francis Group
http://taylorandfrancis.com

Patch repair



Taylor & Francis
Taylor & Francis Group
http://taylorandfrancis.com

Concrete Solutions – Grantham et al. (Eds.)
© 2016 Taylor & Francis Group, London, ISBN 978-1-138-03008-4

An experimental investigation into the effects of water and binder-related parameters on restrained shrinkage cracking in concrete patch repair mortars

P.A. Arito, H. Beushausen & M.G. Alexander
University of Cape Town, Cape Town, Western Cape, South Africa

ABSTRACT: Water and binder-related parameters such as water content, binder content and water:binder ratio are important mix design parameters. They play a critical role in the design and application of concrete Patch Repair Mortars (PRMs). These mix design parameters dictate the durability and cracking resistance of cement-based concrete patch repair materials owing to their influence on important material properties such as shrinkage, tensile strength, elastic and creep deformations and penetrability. This paper presents the experimental results of an ongoing research on the effect of water content, binder content and water:binder ratio on restrained shrinkage cracking in concrete patch repair mortars. The effect of these three mix design parameters on the age at cracking, shrinkage, tensile strength and crack widths in laboratory-made patch repair mortars will be presented.

1 INTRODUCTION

The hydrated cement paste is the major source of shrinkage and relaxation in cement-based concrete patch repair materials. It plays an important role as far as shrinkage-induced cracking is concerned. The water:binder ratio (which will also be referred to as the water:cement ratio interchangeably) is directly related to the pore system of the paste. The porosity of the paste, and its associated interconnectivity, influences important crack-determining material properties such as: tensile strength, elastic modulus and permeability (Yurtdas *et al*., 2006; Abdelkader *et al*., 2010). The water:binder ratio also influences creep and shrinkage; and has been reported by Banthia and Gupta (2009) as one of the most important factors affecting shrinkage-induced cracking. While the relationship between the water:cement ratio and compressive strength is direct and well established, its relationship with cracking is quite complex and incorporates other factors inter alia.

Uys (1983) reports that increasing the water:binder ratio increases the potential for shrinkage; with the effect being more pronounced with a decrease in aggregate content by volume. Banthia and Gupta (2009) – while investigating the effect of water:binder ratio, sand:cement ratio and other parameters on cracking in cementitious materials – further report that increasing the water:binder ratio decreases the total amount of heat evolved, increases the rate of evaporation as well as delays the occurrence of first cracking. They also report that lower water:binder ratios result in low crack areas and small crack widths. The movement of water within the porous paste sets up tensile and hygral stresses which are a function of the water:cement ratio (Beddoe and Lippok, 1999; Yurtdas *et al*., 2006). These stresses result in volumetric changes (e.g., expansion and contraction) within the paste. A reduction in the water:binder ratio, for example, would result in pastes that are characterised with a reduced creep – because they are strong and stiff (Taylor, 1997) – and with a high tensile strength (Kovler *et al*., 1998; Schulze, 1999). A high tensile strength is desirable. Furthermore, pastes with high water:binder ratios contain more free water and are therefore more susceptible to drying shrinkage (He and Li, 2005). The susceptibility of the paste to shrinkage-induced cracking can, thus, be reduced by lowering its water:binder ratio (Neville, 2007). The extent to which the water:binder ratio can be reduced, however, ought to be considered carefully vis-à-vis the susceptibility of a material to undergo autogenous shrinkage that results from mixes with low water:binder ratios (Tazawa and Miyazawa, 1995).

Cement content affects important crack-determining material properties such as shrinkage (Mehta and Monteiro, 2006; Neville, 2007). Increasing the cement content, at a constant water:cement ratio, results in a corresponding increase in shrinkage. However, at a given workability, which approximately means a constant water content, shrinkage is unaffected by an increase in the cement content, or may even decrease, because the water:cement ratio is reduced and the material is, therefore, more capable of resisting shrinkage (Neville, 2007). A reduction in cement content results in a corresponding reduction in heat of hydration and shrinkage (Fowler and Treviño, 2011). Also, an increase in cement content increases flexural strength (Schulze, 1999; Braga *et al*., 2014).

Water content affects shrinkage as far as it reduces the volume of the restraining aggregate. The water

Table 1. Summary of mix designs of laboratory-made PRMs under investigation.

Variable	Mix ID			
	A (control)	B	C	D
BC (kg/m^3)*	250	230	210	225
WC (l/m^3)*	180	165	150	180
a:b*	5.15	5.60	6.13	5.80
w:b *	0.72	0.72	0.72	0.80

* WC denotes water content; BC denotes binder content; w:b denotes water:binder ratio; a:b denotes aggregate binder ratio.

content of a mix would, therefore, indicate the order of drying shrinkage to be expected (Neville, 2007; Alexander and Beushausen, 2009). For given materials and conditions, the higher the water content, the higher the drying shrinkage and the greater the tendency for mortar mixes to crack (Crosswell, 2009). Increasing the free water content above the amount required to achieve the required rheological properties increases the susceptibility of a mix to segregate and bleed. High water contents also increases the porosity of the hardened material, reduces the mechanical properties (e.g., tensile strength, etc.) and durability, reduces resistance to permeation and increases shrinkage and creep deformations (Acker and Ulm, 2001; Mechtcherine, 2012). This paper attempts to elucidate the influence of a combination of three mix design parameters – water content, binder content and water:binder ratio – on the age at cracking, tensile strength, shrinkage and crack width in laboratory-made PRMs.

2 EXPERIMENTAL SETUP

2.1 *Experimental variables and specimen preparation*

The effect of water content, binder content and water:binder ratio on the average age at cracking, crack widths, shrinkage and tensile strength in cement-based concrete patch repair materials was investigated on laboratory-made ring, prism and dog bone specimens made in accordance with various test standards. A summary of the mix designs of the mortars that were developed and tested is shown in Table 1.

Portland cement (PC) CEM II B-M (L), 42.5 N, with a limestone content of 20% and a clinker content of 80% was used throughout this study. The consistence of the trial mortar mixes was tested using the slump test as specified in ASTM C 143. Polycarboxylate superplasticiser was also used in varying dosages, depending on the mix, to achieve the desired slump. The slump of the various mixes ranged from 90 mm to 105 mm. Ring specimens were cured using wet hessian for a period of 7 days in a controlled environmental room that was maintained at a temperature and relative humidity of 23 ± 2°C and 50 ± 4% respectively. Mortar dog bone specimens were water cured in a tank



Figure 1. Mortar rings specimen in mould.

maintained at a temperature of 23 ± 2°C. The duration of curing of dog bone specimens varied with respect to the age at which the tensile strength of the material was required. The shrinkage prism specimens were cast and water cured in a tank that was maintained at a temperature of 23 ± 2°C for a duration of 7 days. Thereafter, the specimens were transferred to an oven whose temperature and relative humidity varied between 50 and 55°C and 15% to 25% respectively. The initial shrinkage measurements were taken after 7 days of water curing and then 7 days after over curing. Shrinkage readings beyond the age of 14 days after casting were taken after every 48 hours for a period of 21 days.

2.2 *Restrained shrinkage tests*

Tests for restrained shrinkage cracking were done in accordance to ASTM C 1581; but with some modifications owing to lack of equipment. The dimensions of the ring specimens used in this study are as follows: outer diameter = 406 mm, inner diameter = 330 mm, height = 150 mm. The thickness of the inner steel ring was 12.5 mm. A sample of freshly mixed mortar was compacted in a circular mould around a steel ring. Figure 1 shows a typical mortar ring in its mould. The resistance of the mortar to cracking was indicated by its age at cracking. The crack width of specimens from each mix was also measured using a crack meter. Three specimens were tested for each mix. The mean of the three different measurements – age at cracking, and crack width – were recorded.

2.3 *Accelerated shrinkage*

Accelerated shrinkage tests were done according to SANS 6085:2006. The test for shrinkage entailed the determination of length changes produced by causes other than externally applied forces and temperature changes in 100 × 100 × 300 mm mortar prisms specimens that are made in the laboratory and exposed to controlled temperature and moisture conditions as described in Section 2.1. The size of the prism specimens were selected such that they ensured that the



Figure 2. Mortar prism specimens for shrinkage tests.

surface area:volume ratio of the rings and prisms were as close as possible. Consistency in the surface area:volume ratio also made it easy to compare various test parameters and properties.

Shrinkage was calculated by dividing the change in length between a set of targets over the duration of measurement by the gauge length of the targets (100 mm). Four specimens were tested for each mix. Shrinkage was monitored over a duration of 45 days from the day of casting. The mean of four shrinkage measurements was reported as the shrinkage of a specific mix. Figure 2 shows a set of mortar prism specimens that were tested for shrinkage.

2.4 *Tensile strength*

Owing to the need for an accurate understanding of the cracking performance of the developed PRMs, as well as the need to overcome the limitations of indirect testing for tensile strength, direct tensile strength tests were undertaken. These tests were done at 3, 7 and 28 days. Uniaxial direct tensile strength was obtained from notched dog-bone specimens. The notches were created by protrusions that were attached to the sides of the mould that was used to cast the specimens. These notches helped to ensure that failure occurred at the same location in all test specimens. Both the dimensions of the notched dog-bone specimens as well as a typical specimen under test are presented in Figure 3.

A Zwick Roell Z020 Universal Testing Machine was used for testing. The remote and flared ends of notched dog-bone specimen were clamped into the cavity within the loading platens of the machine. Thereafter, a direct tensile load was applied on the machine at a constant rate within set limits (0.2 mm/minute or approximately 1.2 microstrain per minute) (Masuku, 2009) until the PRM specimen failed. The loading rates used are also recommended in SANS 863:5-1994 which specifies a time envelope of between three to ten minutes for concrete material tests. The tensile strength of the PRM was calculated as the load

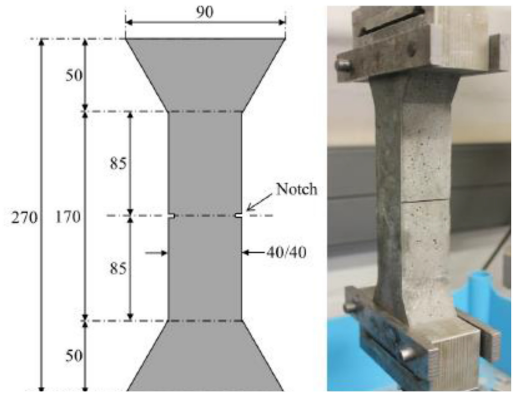

Figure 3. Notched dog bone specimens for direct tensile strength testing.

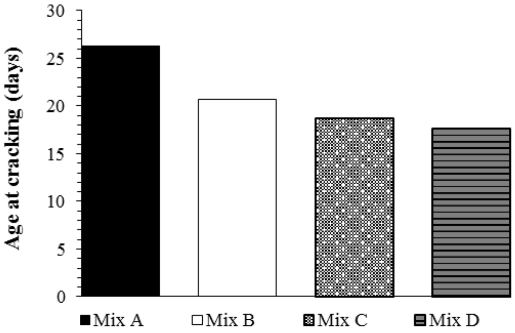

Figure 4. Graph of average crack widths across various mixes.

at failure divided by the cross-sectional area of the specimen. The mean of three tensile strengths measurements was reported as the tensile strength of a particular mix. The environment in which the direct tensile strength tests were done was maintained at a temperature of $21 \pm 1°C$ and relative humidity of $55 \pm 5\%$.

3 RESULTS AND DISCUSSIONS

3.1 *Age at cracking, tensile strength and drying shrinkage*

The effect of the aforementioned experimental variables on the average age at cracking is presented in Figure 4 and summarised in Table 2.

From Table 2, it can be observed that an increase in water:binder ratio – from 0.72 to 0.80 – reduced the average age at cracking by approximately 9 days (33%). More specifically, the slight increase in water:binder ratio changed the potential for cracking, in accordance with the classifications provided in ASTM C 1581 Table X1.1, from 'moderate-low' to 'moderate-high'. Whereas Fowler and Treviño (2011) have reported that reducing the cement content results in a corresponding reduction in the heat of hydrations

Table 2. Average age at cracking in test specimens.

Mix ID	w/b	Average age at cracking (days)			
		Specimen 1	Specimen 2	Specimen 3	Average
A	0.72	31	26	22	26.33
B	0.72	21	21	20	20.67
C	0.72	19	18	19	18.67
D	0.80	17	18	18	17.67

NOTE: The average age at cracking includes the 7 days curing period.

Table 3. Average tensile strength at 3, 7 and 28 days.

Mix ID	w/b	Average tensile strength (MPa)		
		3 days	7 days	28 days
A	0.72	1.211	1.639	2.653
B	0.72	1.096	1.621	1.883
C	0.72	0.788	1.483	1.701
D	0.80	0.794	1.502	1.642

Table 4. Average drying shrinkage of mix specimens.

Mix ID	w/b	Average drying shrinkage (microns)
A	0.72	37400
B	0.72	33250
C	0.72	32750
D	0.80	43500

and shrinkage; which would eventually translate into a delay in the occurrence of first crack, the results from this study contradict this hypothesis. The decrease in the average age at cracking due to an increase in water:binder ratio can be attributed to the interaction between the low tensile strength and high shrinkage (and consequently high shrinkage-induced strains) that was experienced in mix D as shown in Table 3 and Table 4 respectively.

From Table 3, it can be observed that the average tensile strengths of mix D at 3, 7 and 28 days were generally lower than those of mix A at the aforementioned ages despite the fact that it has been reported that increasing the volume of aggregates generally results in an increase in tensile strength. The reduction in tensile strength with an increase in water:binder ratio supports the findings of Kovler *et al* (1998) and Schulze (1999). The slight reduction in the direct tensile strength of mix D relative to that of the control mix (Mix A) would imply that mix D is more susceptible to fail early when specimens made from both mixes (mix A and mix D) are subject to stresses of the same magnitude.

Table 4 reveals that shrinkage in mix D was substantially higher than that of mix A despite the fact that the volume of the restraining aggregates in mix D was slightly higher than that of the control mix (mix A). The increase in shrinkage with an increase in water:binder ratio is consistent with the observations of Uys (1983), He and Li (2005) and Neville (2007). The increased shrinkage in mix D relative to the mix (mix A) could be attributed to the increased porosity that resulted from the increased water:binder ratio. An increase in porosity creates pathways which facilitate the easy loss of moisture from the specimens to the environment, especially in instances where the pores are interconnected. More specifically, the porosity of mix D was higher than that of the control mix (Mix A) by 2%. The increased shrinkage in mix D would have increased the magnitude of tensile stresses that are induced in it. The increased stresses could have significantly contributed to their early failure. Also, the relatively dense and compact microstructure of mix A, owing to its relatively lower water:binder ratio and porosity, implies that this mix can resist shrinkage and shrinkage-induced stresses better.

Furthermore, the reduction in tensile strength – that can be attributed to the increase in water:binder ratio – in conjunction with an increase in free shrinkage implies that specimens cast from mix D are highly susceptible to crack early because their intrinsic low tensile strength is more likely to be exceeded by the extra tensile stresses that are induced by the increased shrinkage.

Also, it can be observed that the simultaneous reduction in both water and binder contents (mixes B and C) at a constant water:binder ratio resulted in a reduction in the average age at cracking when compared to the control mix (Mix A). More specifically, the potential of mortars made using mix B and mix C to cracking, in accordance with ASTM C 1581 Table X1.1 classification, changed from 'moderate-low' to 'moderate-high'. The simultaneous decrease in water and binder contents also translates to an increase in the volume of aggregate. Whereas the increase in the volume of aggregates reduced the magnitude of shrinkage in mix B and Mix C owing to an increase in the restraining action as a result of the additional aggregates (Alexander and Mindess, 2005; Neville, 2007); it was further observed that both mix B and Mix C cracked early. This observation is not consistent with the predominating paradigm that reducing shrinkage would generally translate to a delay in the occurrence of first crack. Furthermore, the reduction in the average age at cracking despite the decrease in shrinkage that results from the increase in aggregate volume implies that there is a high likelihood that there are other more dominant parameters – such as tensile strength, elastic modulus and tensile relaxation – that would dictate the age at cracking. It is, thus, evident that there is a need to understand the interrelationships that exist among the various crack-determining material properties as well as provide a methodology that could be used to rank these properties with respect to cracking.

Table 5. Average crack widths in specimens

Mix ID	w/b	Average crack widths (mm)		
		Specimen 1	Specimen 2	Specimen 3
A	0.72	0.167	0.127	0.063
B	0.72	0.067	0.167	0.073
C	0.72	0.060	0.147	0.113
D	0.80	0.140	0.073	0.087

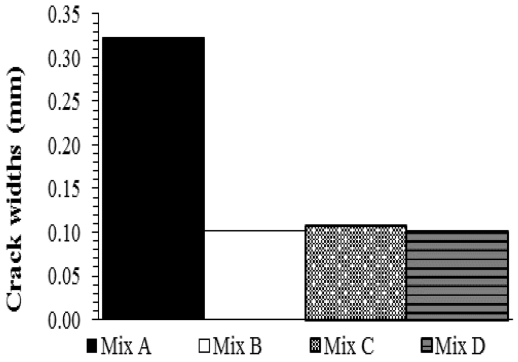

Figure 5. Graph of average crack widths across various mixes.

3.2 *Average crack widths*

The effect of the aforementioned mix design parameters on the average crack width across the mixes under study is presented in Table 5 and Figure 5.

From Figure 5, it can be observed that an increase in water:binder ratio from 0.72 to 0.80 reduced the average crack widths by 69%. The reduction in crack widths with an increase in water binder ratio can be attributed to the lower modulus of elasticity of mix D in comparison to that of the control mix (mix A). The low modulus of elasticity could be attributed to the increased porosity in mixes with high water:binder ratios. Thus, a reduction in elastic modulus, with all other factors held constant, would result in less deformations – in the form of narrow cracks – under a constant stress. The reduction in the average crack widths in mix D could also be attributed to the increase in the volume of aggregates as reported by Banthia and Gupta (2009).

Similarly, from Figure 5, it can be observed that the simultaneous reduction in both binder and water content resulted in a reduction in average crack widths. This reduction in crack widths could also be attributed to the increased volume of aggregates (Banthia and Gupta, 2009) as well as the low modulus of elasticity in mixes B and C as described in the previous paragraph. Also, the increase in the volume of aggregates without a corresponding increase in binder resulted in mixes that were not cohesive. This lack of cohesiveness resulted in mixes that were harsh and difficult to compact well. These mixes were thus prone to have a relatively higher porosity. The increased porosity could have contributed to a reduction in tensile modulus, consequently resulting in a reduction in the magnitude of deformation in the specimens made from mixes B and C, under a constant stress. Also, an increase in aggregate volume, owing to the simultaneous reduction in water and binder contents, translates to an increase in the restraining action of the aggregates within the microstructure of the paste. An increase in the restraining action of the aggregates implies that the magnitude of the shrinkage-induced strains, which would eventually translate into wider cracks, were reduced.

4 CONCLUSIONS

The influence of water:binder ratio, water content and binder content on the average age at cracking, tensile strength, shrinkage and average crack widths have been presented. From the test results that have been presented, the following conclusions can be drawn:

i. Restrained shrinkage cracking in cement-based PRMs is a complex process that is affected by multiple parameters. These parameters are highly coupled to such an extent that they cannot be explained by the simple relationships that are commonly used.
ii. The current methodology that has been used to predict the susceptibility of cement-based PRM mixes to cracking is an oversimplification of an otherwise complex processes; thus rendering it prone to mislead its users in instances where multiple competing parameters are at play.

ACKNOWLEDGEMENTS

The authors wish to acknowledge with gratitude the University of Cape Town and the Carnegie Corporation of New York for their financial support as well as AfriSam for supplying materials for this research. Financial support from the University of Cape Town was in the form of a Research Associateship.

REFERENCES

Abdelkader, S.M., Pozo, E.R., and Terrades, A.M., Evolution of microstructure and mechanical behaviour of concretes utilized in marine environments. *Materials and Design*, 31 (2010), Pp. 3412–3418.

Acker, P., and Ulm, F.-J. Creep and shrinkage of concrete: physical origins and practical measurements. *Nuclear Engineering and Design*, 203 (2001) Pp. 143–158.

Alexander, M., and Beushausen, H. (2009). *Deformation and volume change of concrete. Fulton's concrete technology*, 9th Edition, Midrand South Africa, Gill Owens (Ed), Pp. 111–154.

Alexander, M.G., and Mindess, S. (2005). *Aggregates in concrete*. Taylor and Francis. 435pp.

ASTM C143/C143 M-05a (2005) *Standard test method for Slump of Hydraulic Cement Concrete*. ASTM International, West Conshohocken, PA 19428–2959, USA, 4pp.

ASTM C1581 (2004) *Standard test method for Determining the Age at Cracking and Induced Tensile Stress Characteristics of Mortar and Concrete under Restrained Shrinkage*. ASTM International, West Conshohocken, PA 19428–2959, USA, 6pp.

Banthia, N., and Gupta, R. Plastic shrinkage cracking in cementitious repairs and overlays. *Materials and Structures*, 42 (2009) Pp. 567–579.

Beddoe, R.E., and Lippok, R. Hygral stress in hardened cement paste. *Materials and Structures*, Vol. 32, November (1999) Pp. 627–634.

Braga, M., de Brito, J., and Veiga, R. Reduction of the cement content in mortars made with fine concrete aggregates. *Materials and Structures*, Vol. 47 (2014) Pp. 171–182.

Crosswell, S. (2009). *Sand-cement mixes – mortars, plasters, and screeds. Fulton's concrete technology*, 9th Edition, Midrand South Africa, Gill Owens (Ed), Pp. 381–392.

Fowler D.W., and Treviño, M. (2011). *Overlay Design Process. Bonded cement-based material overlays for the repair, the lining or the strengthening of slabs or pavements*. Bissonnette et al (Eds). State-of-the Art Report of the RILEM Technical Committee 193-RLS. Volume 3. Springer. Pp. 5–16.

He, Z., and Li, Z. Influence of alkali on restrained shrinkage behaviour of cement-based materials. *Cement and Concrete Research*, 35, (2005), Pp. 457–463.

Kovler, K., Schamban, I., Igarashi, S., and Bentur, A. Influence of mix proportions and curing conditions on tensile splitting strength of high strength concretes. *Materials and Structures*, Vol. 32, August-September (1999) Pp. 500–505.

Masuku, C. (2009). *Tensile relaxation of bonded concrete overlays*. MSc Dissertation, University of Cape Town, Department of Civil Engineering, 135pp.

Mechtcherine, V. (2012). *Introduction. Application of Superabsorbent Polymers (SAP) in Concrete Construction*, State of the Art Report Prepared by Technical Committee 225-SAP, Mechtcherine, V., and Reinhardt, R.-W (Eds), Springer, Pp. 1–6.

Mehta, P.K.., and Monteiro, P.J.M. (2006). *Concrete: Microstructure, properties and materials*. Third edition. Tata McGraw Hill, 660pp

Neville, A.M. (2007). *Properties of concrete*, 4th Edition, Pearson Prentice Hall, Pp. 412–481.

SANS 6085:2006. (2006), South African National Standard. *Concrete tests – Initial drying shrinkage and wetting expansion of concrete*. Published by SABS Standards Division, Pretoria, Edition 2.2. ISBN 0-626-18447-9, 6 pp.

Schulze, J. Influence of water-cement ratio and cement content on the properties of polymer-modifies mortars. *Cement and Concrete Research*, 29, (1999), Pp. 909–915.

Taylor, H.F.W. (1997). *Cement chemistry*, 2nd Edition, Thomas Telford, London. 459pp.

Tazawa, E.-I., and Miyazawa, S. Influence of cement and admixture on autogenous shrinkage of cement paste. *Cement and Concrete Research*, Vol. 25, No. 2, (1995), Pp. 281–287.

Uys, A.J. (1983). *The influence of fly ash on the strength, elastic modulus, shrinkage and creep of concrete made with Cape Town aggregates with particular reference to Alkali-aggregate reaction*. University of Cape Town, MSc Thesis. 438 pp.

Yurtdas, I., Peng, H., Burlion, N., and Skoczylas, F. Influences of water by cement ratio on mechanical properties of mortars submitted to drying. *Cement and Concrete Research*, 36, (2006), Pp. 1286–1293.

Concrete Solutions – Grantham et al. (Eds.)
© 2016 Taylor & Francis Group, London, ISBN 978-1-138-03008-4

Strength recovery of concrete repaired using normal and rapid hardening repair mortars

Atef Badr
Head of Civil Engineering Department, Military Technological College, Sultanate of Oman

Sokrates Ioannou
Lecturer, Civil Engineering, Military Technological College, Sultanate of Oman

ABSTRACT: Concrete repair and retrofitting projects are driven by schedule and budget constraints. Therefore, minimizing the time required for repair mortars to achieve adequate service strength is a major concern for repair contractors. Using repair mortars based on Rapid-Hardening Cement (RHC) could accelerate strength gain much faster than repair mortars based on normal Portland cement. However, the cost of Rapid-Hardening Cement (RHC) is significantly higher. This paper reports the results of an experimental programme aiming to compare the strength recovery of concrete repaired using normal and rapid hardening repair mortars. The investigation included repairing concrete produced using virgin and recycled aggregate. The experimental programme involved preparation of damaged concrete specimens, repairing them and finally determining the recovered strength of the repaired specimens after 3, 7 and 28 days from repair. The test results showed that the strength recovered using rapid hardening mortar was superior to the strength recovered using normal repair mortar, regardless of the type of the original concrete or the age at testing. However, this superiority was most significant at 3days and was diminishing with time. Nonetheless, the results proved that concretes made with recycled aggregates could be repaired using normal and rapid hardening repair mortars as successfully as concrete containing virgin coarse aggregate.

1 INTRODUCTION

Repair and retrofitting of concrete structures have become very important activities of the concrete and construction industry. This is reflected in the numerous proprietary repair materials available in the market and the significant increase in the number of repair contractors and consultants offering specialist repair and retrofitting services (Cabrera & Al-Hasan 1997). The Building Research Establishment (2003) reported that the size of the concrete repair industry in the UK is more than 3% of the entire construction industry in the UK. In 2006, the annual concrete repair industry in the US was estimated to be $18–21 billion (Emmons & Sordyl 2006).

The time required for repair mortars and concretes to properly cure and achieve a minimum service strength is a main concern for repair contractors and clients, alike. Rapid strength-gain cement is a special type of cement that can be used in emergency repair works such as a highway repair during traffic, in dams, tanks, airport runways and busy places like pedestrian walkways in order to meet tight schedules of repair projects (Srinivasan et al. 2003). The rapid-setting properties and strength-gain of the Rapid-Hardening Cement (RHC) make it an ideal solution for today's schedule-driven projects. Therefore, concrete and repair contractors are turning to RHC to meet the tight schedules of today's repair projects (Senatore 2010). Along the line of this trend, the use of rapid strength-gain shotcrete emerged as a very attractive solution for emergency repairs in civil applications, where rapid strength-gain materials such as mortars or concretes are necessary to meet shortened construction schedules due to restricted lane closure times on bridges, roadways and restricted access time in tunnels (Ginouse & Clements, 2015).

Although it is possible to accelerate the gain in strength of normal Portland cement, through finer grinding or chemical additives, there is a significant risk of increasing drying shrinkage (Srinivasan et al. 2003).

Rapid-hardening cement, on the other hand, achieves strength much faster than Portland cement. Compared to normal Portland cement, the RHC could develop significant practical compressive strength within few hours (Popovics et al. 1987). Indeed, Reny & Clements (2013) showed that rapid strength-gain dry-mix shotcrete with strength of about 20 MPa after only 2 hours could be effectively produced and placed in mining applications.

In addition, RHC offers superior durability due to improved resistance to chemical attack and reduced susceptibility to shrinkage cracks (Srinivasan et al.

Table 1. Mix proportions (kg/per m^3) of original mixes.

ID	CEM1	LM	RA	Sand	w/c	SP	Slump
RA1	380	515	410	680	0.54	3.80	120
LM1	380	980	–	680	0.54	1.52	140
RA2	407	446	355	895	0.40	6.11	40
LM2	407	892	–	895	0.40	3.26	70

Table 2. Mix proportions (kg/per m^3) of repair mortars.

ID	CEM1 N	CEM1 RH	Sand	PPF	Water	SP
RE1-PC	524	–	1223	9	262	52
RE2-RH	–	524	1223	9	262	52

2003). The cement chemistry and the hydration process controlling the rapid strength development have been the topic of several scientific studies (Juenger et al. 2011, Pelletier et al., 2010).

However, less information is available about the effectiveness of repair of concrete using this type of cement, particularly for concrete containing recycled aggregate. Therefore, this project was conducted to assess the strength recovery of concrete repaired using normal and rapid hardening repair mortars with a particular focus on concrete made with recycled aggregate.

2 MATERIALS AND MIXES

2.1 *Original concrete*

Two types of coarse aggregate were used. Natural Limestone (LM) and Recycled Aggregate (RA). The nominal aggregate size of both types was 100mm. The fine aggregate was Siliceous sand conforming to zone M of BS EN 12620. The only binder used for the original mixes was Portland cement (CEM1) to BS EN 197-1. Superplasticiser (SP) conforming to BS5075 Part 3 was used in all original mixes.

The preliminary phase of the experimental programme involved selecting the types of original concrete. Four mixes were initially optimised from laboratory tests. The compositions of these four mixes are given in Table 1. The ID of every mix indicates the type of the coarse aggregate used in that mix.

2.2 *Repair mortars*

Normal and rapid hardening Portland cement (CEM1) were used in the production of repair mortars. The Rapid Hardening Cement (RHC) has a nominal setting time of 30 minutes and is recommended for typical quick repairs.

Virgin Polypropylene Fiber (PPF) was added at a dosage of 1% by volume to reinforce the repair mortars. Superplasticiser (SP) conforming to BS5075 Part 3 was used for these two mortars at a dosage of 1% of the cement weight.

Two repair mortars, RE1-PC and RE2-RH, were produced using normal and rapid hardening cements, respectively. The mix proportions of these two mortars are given in Table 2.

2.3 *Curing*

All specimens were covered with wet hessian and polyethylene sheets overnight. They were then de-molded after 24 hours and submerged in a water curing tank at a temperature of $20 \pm 2°C$ until they reached the age of testing.

3 REPAIR AND TESTING

3.1 *Preparation and repair of damaged specimens*

Cube specimens were loaded under compression in accordance with BS EN 12390-3 (BSI, 2009) in order to determine the original compressive strength of the specimens, at 28 days. The crushed cubes were then used as damaged specimens to be repaired.

The damaged cubes were repaired by means of 'jacketing' using the repair mortars. More details about the repair process are given elsewhere (Badr 2015).

All repaired specimens were de-molded after 24-hrs and cured in the curing tank until testing. The repaired cubes were then tested to determine the restored compressive strength after 3, 7 and 28 days.

4 RESULTS AND DISCUSSION

4.1 *Effect of type of repair mortar*

Figure 1 presents the compressive strength of concrete specimens repaired with both repair mortars (RE1-PC and RE2-RH) after 3 days from repair. The strength recovered using the RHC (i.e. RE2-RH mortar) was higher than the strength recovered using the normal repair mortar (i.e. RE1-PC) for all types of concrete. On average, specimens recovered 78% of their average original strength when repaired with RE2-RH compared to 64% in the case of specimens repaired using RE1-PC.

The effectiveness of RE2-RH repair mortar in recovering compressive strength of the damaged specimens is also clear at relatively later ages. Figures 2 and 3 presents the compressive strength of concrete specimens repaired using the two repair mortars at 7 and 28 days after repair.

When repaired with RE2-RH, the average recovered strength after 7 days was 85% of the original strength. This corresponds to 73% recovered when repaired using RE1-PC. The same trend continues for the strength recovered after 28 days from repair (Fig. 3). In this case, the percentages of recovered strength were 96% and 88% for RE2-RH and RE1-PC, respectively.

The advantage of RE2-RH repair mortar over RE1-PC repair mortar in terms of its ability to recover higher

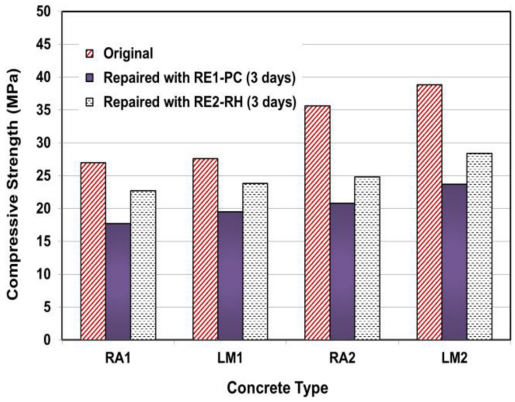

Figure 1. Strength of repaired concrete after 3 days.

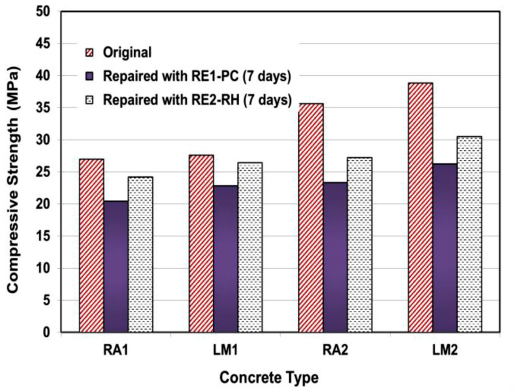

Figure 2. Strength of repaired concrete after 7 days.

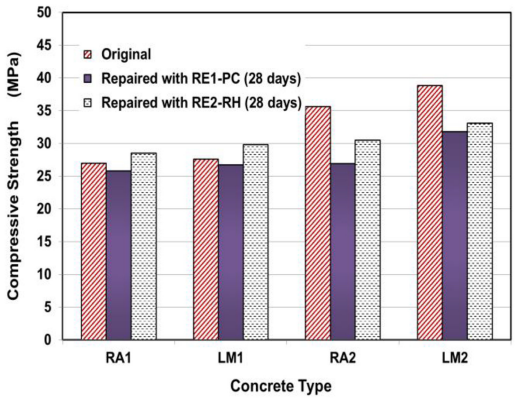

Figure 3. Strength of repaired concrete after 28 days.

strength seems, however, to be fading with time. Figure 4 presents the average recovered strength (as percentage of original strength) of all specimens at different ages after repair.

It can be seen that the gap between the two trend lines, representing the normalized strength recovered using the two repair mortars, is diminishing with time.

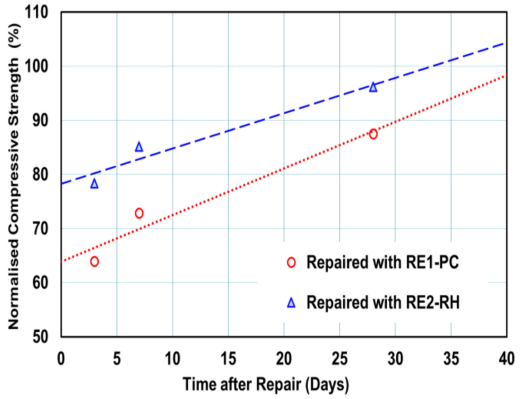

Figure 4. Effect of type of repair mortar at different ages.

Table 3. Improvement of RE2-RH compared to RE1-PC.

Concrete type	3 days	7 days	28 days
RA1	28%	19%	10%
LM1	22%	16%	12%
RA2	19%	17%	13%
LM2	20%	16%	4%
Average	22%	17%	10%

Indeed, this tendency was observed not only for the average values but also for every individual mix, as evident in Table 3, which presents the improvement in the recovered strength obtained using RE2-RH compared to that obtained using RE1-PC.

4.2 *Effect of recycled coarse aggregate*

The use of recycled aggregate did cause a slight reduction in the original compressive strength of mixes RA1 and RA2 compared to mixes produced using virgin LM aggregate; i.e. LM1 and LM2. The average reduction was about 5%. Similar reduction was previously reported (Kwan et al. 2012, Rao et al. 2007, Henry et al. 2011, Rahal 2007), although the extent of reduction is related to many variables such as the replacement level, type of RA, water/cement ratio and the moisture condition (Etxeberria et al. 2007, Mas et al. 2012, Badr 2014).

After repair, the absolute values of the compressive strength of mixes containing recycled aggregate remained inferior to that of the control mix, regardless of the type of the repair mortar or the time lapsed after repair (Figs 1–3). The difference in the recovered strength can be noticed in Figures 1–3 by comparing mix RA1 to LM1 and mix RA2 to LM2. When repaired with RE1-PC, the difference in the average recovered strength between mixes containing RA and those made with virgin LM was 10%. The corresponding value for RE2-PC was 8%.

Further analysis, however, revealed that the recovered strength of individual mixes was, more dependent

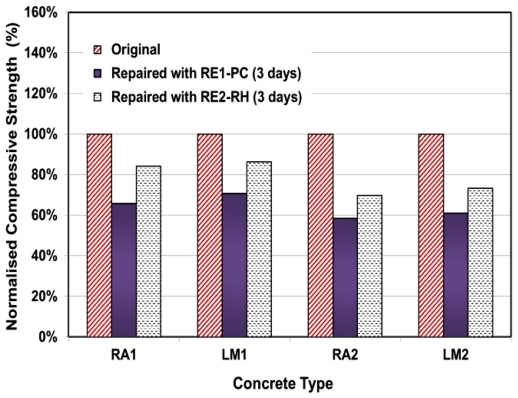

Figure 5. Normalised strength of repaired concrete after 3 days.

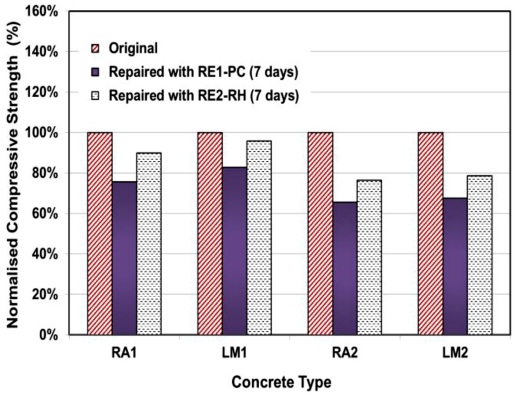

Figure 6. Normalised strength of repaired concrete after 7 days.

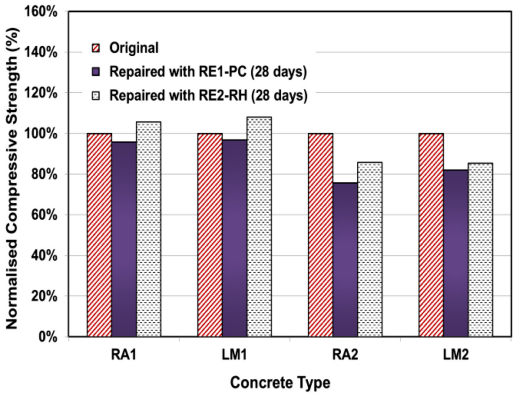

Figure 7. Normalised strength of repaired concrete after 28 days.

on the strength of the original concrete rather than its type. This can be illustrated by presenting the normalized recovered strength of every mix as a percentage of its original strength as shown in Figures 5–7. For example, after 3 days from repair (Fig. 5) the normalized recovered strength of RA1 was about 75% which is so close to the 78% recovered for LM1, although they contain different types of aggregate but have comparable original strength. On the other hand, RA2 recovered a significantly lower normalized strength of 64% compared to the 75% in the case of RA1 although they have the same RA but their original strengths were different. Similarly, LM2 recovered a significantly lower normalized strength of 67% compared to the 78% recovered for LM1 although both mixes were produced using virgin LM without any RA. Similar comparisons could be made for strength recovered after 7 and 28 days from repair. Indeed, the normalized recovered compressive strength, shown in Figures 5-7, revealed a contrariwise relationship between original strength and the percentage of recovered strength. The latter is likely to be lower for concrete of higher original strength, regardless of the type of the repair mortar. When RHC was used, low strength mixes (i.e. RA1 and LM1) recovered 84% and 86% of their original strength after 3 days from repair (Fig. 5). The corresponding values for RA2 and LM2 were 70% and 73%, as they have a relatively higher original strength. Similar observations could be drawn in the case of using RE1-PC. Same trend could be observed in Figures 6 and 7 for the values of recovered strength after 7 and 28 days from repair, respectively.

The values of normalized recovered strength of concrete containing RA and their counterpart concrete containing LM are so close that it can be suggested that the repair of concrete specimens containing RA was as successful as the repair of specimens made with LM. For example, after 3 days of repair using RE2-RH, RA1 recovered 84% compared to 86% for LM1. Similarly, RA2 recovered 70% whereas LM2 recovered 73%. When RE1-PC was used the trend was the same but with lower percentage of recovered strength. For example, RA2 recovered 58% of its original strength, which is not far from the 61% recovered in the case of LM2.

5 CONCLUSIONS

For the concrete, materials and test conditions used in this investigation, the following conclusions could be drawn:

- The normal and rapid hardening repair mortars (RE1-PC and RE2-RH) used in this investigation were successful in restoring significant strength of the damaged specimens, regardless of the concrete type or original strength.
- The strength recovered using the RHC (i.e. RE2-RH mortar) was higher than the strength recovered using the normal repair mortar (i.e. RE1-PC) for the different types of concrete investigated.
- The advantage of RE2-RH repair mortar over RE1-PC repair mortar in terms of its ability to re-cover higher strength seems, however, to be fading with time. The gap between the values of the strength recovered using these two repair mortars appeared to be diminishing with time.

– The values of normalized recovered strength of concrete containing RA and their counterpart concrete containing LM are so close that it can be safely suggested that repairing concrete containing RA could be as successful as repairing concrete made with virgin limestone.

REFERENCES

Badr, A. 2014. Dimensional stability of concrete containing coarse and fine recycled aggregate. *Studies and Researches*, 33(1): 187–199.

Badr, A. 2015. Using standard repair methods on recycled aggregate concrete. *Proceedings of the Institution of Civil Engineers – Construction Materials*, Article in press.

BS EN 12390-3:2009. Testing hardened concrete. Compressive strength of test specimens

Building Research Establishment. 2003. Residual life models for concrete repair: Assessment of the concrete repair process, *BRE Client Report*: Oct02. UK.

Cabrera, J.G. & Al-Hasan, A.S. 1997. Performance properties of concrete repair materials. *Construction and Building Materials*, 11(5): 283–290.

Emmons, P.H. & Sordyl, D.J. 2006. The state of the concrete repair industry and a vision for its future, *Concrete Repair Bulletin*. International Concrete Repair Institute. USA.

Etxeberria, M., Vázquez, E., Marí, A. & Barra, M. 2007. Influence of amount of recycled coarse aggregates and production process on properties of recycled aggregate concrete. *Cement and Concrete Research*, 37(5): 735–742.

Ginouse, N. & Clements, W. 2015. Durability investigation of ultra-rapid strength-gain dry-mix shotcrete. *Shotcrete*, 17(2): 12–15.

Henry, M., Pardo, G., Nishimura, T. & Kato, Y. 2011. Balancing durability and environmental impact in concrete combining low-grade recycled aggregates and mineral admixtures. *Resources, Conservation and Recycling*, 55(11): 1060–1069.

Juenger, M., Winnefeld, F., Provis, F. & Ideker, J. 2011. Advances in alternative cementitious binders. *Cement and Concrete Research*, 41(12):1232–1243.

Kwan, W.H., Ramli, M., Kam, K.J. & Sulieman, M.Z. 2012. Influence of the amount of recycled coarse aggregate in concrete design and durability properties. *Construction and Building Materials*, 26(1):565–573.

Mas, B., Cladera, A., Olmo, K. & Pitarch, F. 2012. Influence of the amount of mixed recycled aggregates on the properties of concrete for non-structural use. *Construction and Building Materials*, 27(1): 612–622.

Pelletier, L., Winnefeld, F. & Lothenbach, B. 2010. The ternary system Portland cement-calcium sulphoaluminate clinker-anhydrite: Hydration mechanism and mortar properties. *Cement and Concrete Composites*, 32(7):497–507.

Popovics, S., Rajendran, N. & Penko, M. 1987. Rapid Hardening Cements for Repair of Concrete. *ACI Materials Journal*, 84(1):64–73.

Rahal, K. 2007. Mechanical properties of concrete with recycled coarse aggregate. *Building and Environment*, 42(1):407–415.

Rao, A., Jha, K.N. & Misra, S. 2007. Use of aggregates from recycled construction and demolition waste in concrete. *Resources, Conservation and Recycling*, 50(1):71–81.

Reny, S. & Clements, W. 2013. Reaching 20 MPa (2900 psi) in 2 hours is Possible. *Shotcrete*, 15(4):26–30.

Senatore, F. 2010. Rapid Hardening Cement: The alternative product for schedule- and budget-driven projects. *Concrete Construction*, (6): 1.

Srinivasan, C.B., Lakshmi Narasimhan, N. & Ilango, S.V. 2003. Development of rapid-set high-strength cement using statistical experimental design. *Cement and Concrete Research*, 33(12): 1287–1292.



Taylor & Francis
Taylor & Francis Group
http://taylorandfrancis.com

Concrete Solutions – Grantham et al. (Eds.)
© 2016 Taylor & Francis Group, London, ISBN 978-1-138-03008-4

Development of new types of repair materials by imparting thixotropic properties

H. Fujiwara, M. Maruoka, T. Kawato, T. Sugawara & K. Yoshikawa
Utsunomiya University, Utsunomiya, Tochigi, Japan

T. Abe
Nittoc Construction Co., Ltd, Tokyo, Japan

S. Takemoto
DPS Bridge Works Co., Ltd, Tokyo, Japan

H. Kasahara
New Tech Co., Ltd, Tokyo Japan

ABSTRACT: New two high performance repair materials were developed by giving them a thixotropic property. Effective repairs require the patches to be thick, which is achieved by increasing the viscosity of the repair material. High viscosity, however, lowers the workability of the repair material. This paper describes new one repair material that has been given a thixotropic property, resulting in a material with greater workability and viscosity. Using this material, sprayed patches can be over 20 cm thick on walls and over 15 cm thick beneath surface of ceilings. Moreover, the another repair material can be force-fed over a distance of more than 1,000 m and sprayed on the walls of headrace tunnels at hydroelectric power plants, which conventionally have small cross sections and long tunnel lengths and are very difficult to repair. This paper describes the properties of these new repair materials.

1 INTRODUCTION

In Japan, materials for repairing cross sections commonly consist of mortar containing an organic polymer. This material has several advantages, including adhesion and waterproofing properties and chemical and wear resistance (Fujiwara et al. 2009). However, this material also has high viscosity. Moreover, as the polymer to cement ratio increases, the compressive strength and flexural strength under high temperature decrease significantly, shrinkage increases, and durability decreases. To avoid these issues, a high thixotropic material without polymer was developed. Thixotropy is a type of rheological property in which, as the shear stress increases, the viscosity reduces reversibly. Newton's law describes a viscous fluid for which the relationship between the shear stress τ and the shear strain rate $\dot{\gamma} = d\gamma/dt$ is as follows.

$$\tau = \eta\dot{\gamma} \tag{1}$$

Here, the constant η is the viscosity. This is a Newtonian fluid. Water is also a Newtonian fluid. Bingham fluids, such as fresh concrete, are non-Newtonian fluids that satisfy Bingham's equation.

$$\tau = \eta\dot{\gamma} + \tau_f \tag{2}$$

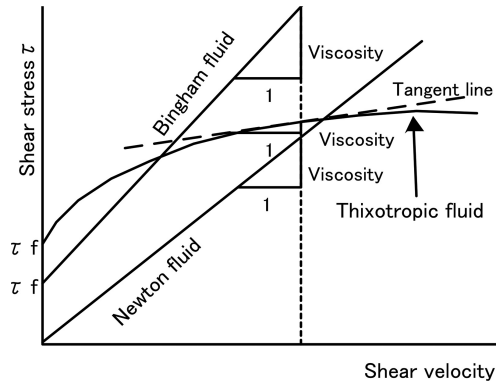

Figure 1. Comparison of Newtonian fluid, Bingham fluid, and thixotropic fluid.

Here, τ_f is the yield value. If the shear stress does not exceed τ_f, the material will not flow. A thixotropic fluid for which the viscosity η in Equation (2) is not constant but decreases as the shear rate increases.

A comparison of these three types of fluids is shown in Figure 1.

For repairing cross sections, a thixotropic mortar has the following advantages. When applied using a

trowel, the pressure of the trowel reduces the viscosity of the mortar, thereby improving workability. When delivered under pressure using a pump, the pressure reduces the viscosity, thereby improving fluidity and allowing the mortar to be easily pumped. When the pressure is released, the viscosity is restored, preventing the mortar from rebounding and reducing mortar loss. Moreover, the mortar does not sag, so it can be applied thickly. Conventional cross-section repair mortar can only be applied to a thickness of about 10 to 40 cm at one time. Mortar with thixotropy, however, can be applied more thickly, thereby reducing construction time.

Conventional headrace tunnels for hydroelectric power plants are long and have a small cross section, which makes them very difficult to repair. Usually, the repair material is force-fed using a pump from the outside to the inside of the tunnel. For long-distance force-feeding, the viscosity of the mortar must be decreased. However, low-viscosity mortar can clog the hose. A mortar with thixotropy, however, can be force-fed more than 1,000 m without clogging the hose and then sprayed on a wall.

This paper evaluates the properties of these repair mortars.

2 PROPERTIES OF THICKENING MORTAR WITH THIXOTROPY

Two types of thixotropic cross-section repair mortar (TCRM) with different strengths have been developed: normal strength (compressive strength: 45 N/mm^2 or higher at 28 days; hereafter referred to as Type-N) and high strength (compressive strength: 75 N/mm^2 or higher at 28 days; hereafter referred to as Type-H). The properties of the fresh and hardened properties of these two types were evaluated.

2.1 *Outline of the tests*

Type-N is a mixture of ordinary Portland cement, cementitious admixtures, and sand (28:24:48 by weight). Synthetic products and other materials are added to achieve specific properties. Organic short fibers are also used to reduce cracking.

Type-H has the same powder composition as Type-N, but some of the cementitious admixtures are finer and the water to binder ratio is lower. This results in greater strength and a slightly greater viscosity.

The workability, strength, adhesion, and shrinkage rate of both materials were confirmed in laboratory tests, and their properties were compared. Outdoor spray tests confirmed that both materials can be applied at a work site.

2.1.1 *Mix proportions*

The mass of the water as a percentage of the mass of the total quantity of premixed powder of Type-N and Type-H were 14.8 and 13.3 respectively.

Table 1. Test items and target values.

Test items	Target values (at 28 days)
Mortar slump test	—
Discharge time of a JP-funnel under pressure	—
Compressive strength test	Type-N : 45 N/mm^2 or higher Type-H : 75 N/mm^2 or higher
Flexural strength test	7 N/mm^2 or higher
Adhesion strength test	1.5 N/mm^2 or higher
Drying shrinkage	0.05% or less

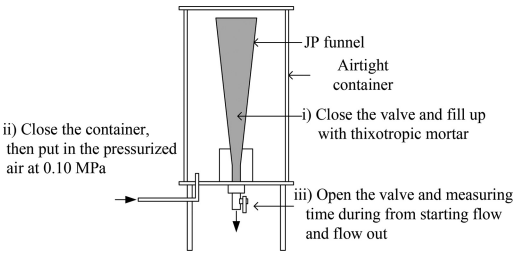

Figure 2. Test device of discharge time from a JP-funnel under pressure.

2.1.2 *Test items*

The test items and target values are shown in Table 1. The target values were set by exceeding the values of conventional products used in Japan.

2.1.3 *Properties of fresh mortar*

A mortar slump test was carried out in accordance with JIS A 1171 (Japanese Industrial Standards Committee, 2000) and the discharge time from a JP- funnel under pressure was measured.

The latter test was previously proposed as a test for evaluating thixotropy (Fujiwara et al. 2005). The test device is shown in Figure 2. The test procedure is as follows.

1. Water is passed under pressure through a JP-funnel, wetting the inside of the device, and the discharge time is measured.
2. The cock is closed, the test sample is placed inside the funnel so that there are no gaps, and the lid is closed. The pressure valve is adjusted so that the pressure within the container is 0.1 MPa.
3. The cock is opened to allow the test sample to flow out, and the time from the start of the flow to the time it ends is measured in units of 1/10th of a second.
4. The inside of the container is depressurized and the lid is opened to confirm that virtually all the test sample within the funnel has been discharged.

In this test, the shorter the discharge time for mortars with the same slump, the higher the thixotropy and the better the workability.

This is because, for the same yield value, the viscosity under pressure is lower and so the workability is

higher. In other words, the thixotropy is higher. If this test were to be carried out using a conventional mortar with an identical slump, the mortar would block the funnel.

2.1.4 *Properties of hardened mortar*

Compressive strength and flexural strength tests were carried out in accordance with JIS A 1108 (Japanese Industrial Standards Committee, 2006) and JIS R 5201 (Japanese Industrial Standards Committee, 1997), respectively. The strength was measured 28 days after curing in water at 20°C. The adhesion strength test was carried out in accordance with JSCE-K 561 (Japan Society of Civil Engineers, 2013). To evaluate the drying shrinkage, the change in length was measured in accordance with JIS A 1129-3 (Japanese Industrial Standards Committee, 2010). The test specimens were prismatic ($40 \times 40 \times 160$ mm). Measurements were started after curing for 7 days in water at 20°C. The drying conditions were temperature of 20°C and relative humidity of 60%.

2.1.5 *Spray tests*

Spray tests were carried out in order to determine whether or not TCRM could be applied at a work site. In these tests, a conventional squeeze-type mortar pump was used. The material was delivered under pressure using a 40 mm diameter hose, and the material was sprayed onto flat concrete slabs placed on a wall and beneath a ceiling. Immediately after spraying, the thickness of the sprayed material was measured.

2.1.6 *Mixing method*

For the spraying test, a 1,000 rpm hand mixer was used for 3.5 min. For other tests, a mortar mixer was used for 3.5 min.2.2 *Test results and discussion*

2.1.7 *Properties of fresh mortar*

The properties of fresh mortar are shown in Table 2, and discharge times from the JP-funnel under pressure are shown in Figure 3. Table 2 and Figure 3 show that the mortar slump was smaller than that of conventional repair mortar.

The discharge time for conventional mortar under pressure in a JP-funnel cannot be measured because of clogging. The discharge time for Type N was shorter than that for Type H. Therefore, Type N has higher thixotropy than Type H. On the other hand, the discharge time of Type H was higher, likely due to the difference in the composition of the powder, which increased the viscosity of the material.

2.1.8 *Properties of hardened mortar*

The results of the hardened mortar property tests are shown in Table 3, those of the compressive strength test in Figure 4, those of the flexural strength test in Figure 5, those of the adhesion strength test in Figure 6, and those of the drying shrinkage test in Figure 7.

Table 3 and Figure 4 show that Type N satisfied the target values for compressive strength and adhesion strength, as well as the target value of 7 N/mm^2 for flexural strength. Therefore, Type N has sufficient strength for repairing cross sections.

The compressive strength of Type H is higher than that of Type N by about 30 N/mm^2 and also satisfies its target value. As can be seen from Figure 5 and Figure 6, the flexural strength and the adhesion strength are higher than those of Type N.

Table 2. Test results of fresh properties.

Type	Temperature of fresh mortar °C	Mortar slump cm	Discharge time from JP-funnel under pressure sec.
Type – N	20.8	3.9	4.9
Type – H	21.5	5.9	11.5

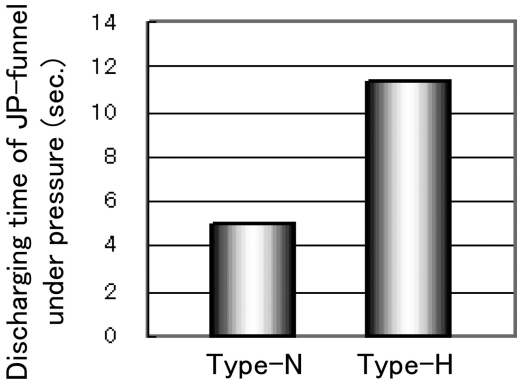

Figure 3. Test results of discharge time from a JP-funnel under pressure.

Table 3. Test results of hardened properties (unit: N/mm^2).

Type	Compressive strength	Flexural Adhesion strength	strength
Type – N	50.8	7.88	3.14
Type – H	79.8	9.90	3.86

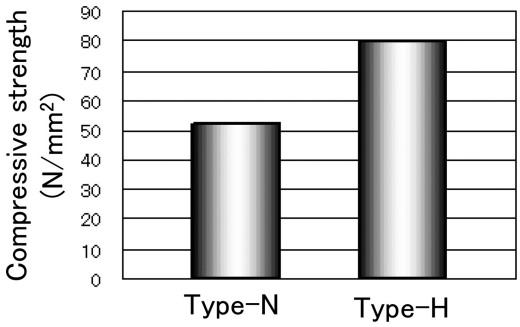

Figure 4. Test results of compressive strength.

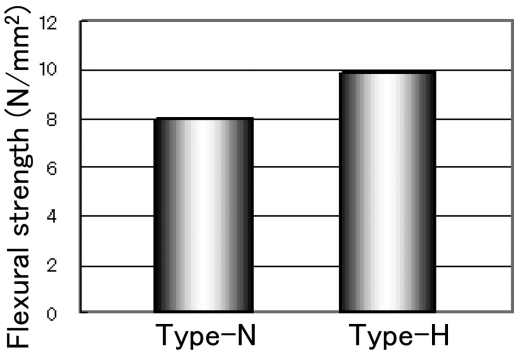

Figure 5. Test results of flexural strength.

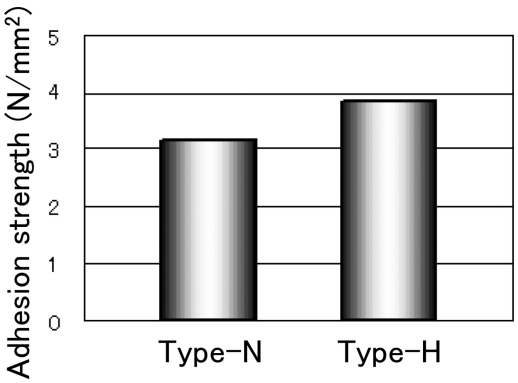

Figure 6. Test results of adhesion strength.

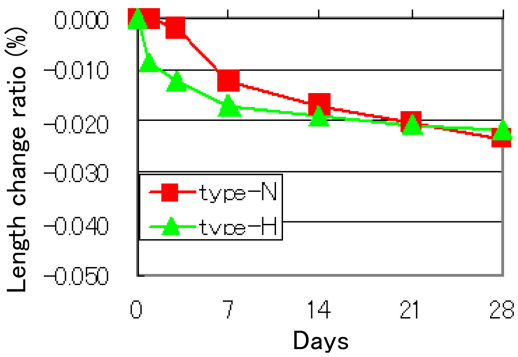

Figure 7. Test results of drying shrinkage.

According to the results shown in Figure 7, the target value of 0.05% for shrinkage rate was satisfied for both Type N and Type H. These TCRM have low drying shrinkage even without using polymer materials.

2.1.9 *Spray test results*

The spray test is shown in Figure 8. The spray test results are shown in Table 4, the sprayed thickness onto the wall surface is shown in Figure 9 and the sprayed thickness beneath the ceiling surface is shown in Figure 10. The workability of Type N was extremely good. The thickness of the material sprayed onto the wall surface was about 150 mm, and that beneath the ceiling surface was about 140 mm.



Figure 8. State of spray test.

Table 4. Spray test results (unit: mm).

	Sprayed thickness	
Type	Wall surface	Ceiling surface
Type – N	150	140
Type – H	150	60



Figure 9. Wall surface after spraying (type-N).

These results show that Type N has extremely good spray performance due to the high thixotropy. When delivered under pressure, the viscosity of TCRM decreases and its fluidity increases. After being sprayed, in the unpressurized state, the viscosity is restored, allowing it to be applied thickly.

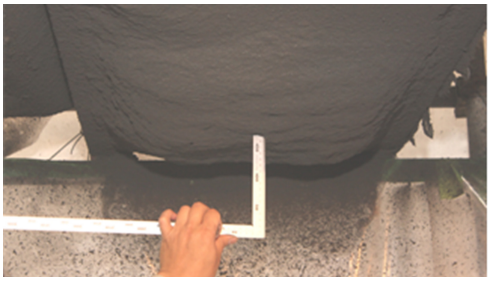

Figure 10. Ceiling surface after spraying (Type-N).



Figure 11. Wall surface after spraying (Type-H).

The state of the wall surface after spraying it with Type H is shown in Figure 11. Regarding its pumpability, about which there had been some concern, Type H was capable of being delivered under pressure without imposing an excessive load on the pump. Also, as shown in Figure 11, the sprayed material was about 150 mm thick on the wall surface, and about 60 mm on the ceiling surface. Thus, Type H can be sprayed to the same thickness on the wall surface as Type N.

Comparing these results with performance of conventional materials, which are capable of a sprayed thickness of about 10 to 40 cm, the spray performance of TCRM clearly greatly exceeds that of conventional materials.

3 PROPERTIES OF SPRAY-TYPE MORTAR THAT CAN BE TRANSPORTED LONG DISTANCE WITH THIXOTROPY

Conventional spray-type mortar is difficult to transport over distances of 1,000 m or greater. The new mortar can be force-fed over distances of more than 1,000 m using a standard pump with a flexible grout hose (38mm inside diameter) and a maximum pumping pressure of 3.0 MPa.

There is a need for a spray-type mortar that can be force-fed over long distances. Such a mortar can be used for repairing long headrace tunnels with small cross sections, which are found at hydroelectric power plants. Conventional technology cannot easily carry spray-type mortar over long distances transporting the mortar and repair instruments. To solve such problems, this new mortar (LDTM) has a thixotropic property that allows the mortar to be force-fed over distances of 1,000 m using a low pumping pressure of less than 3.0 MPa, and sprayed on the wall of a tunnel. This paper evaluates the properties of LDTM.

Table 5. Materials used.

Item	Symbol	Material	Density g/cm^3
Cement	P C	Ordinary Portland cement	3.16
Admixture	T	New admixture	2.49
	—	Quick setting agent	1.08
	SP	Superplasticizer (Poly carboxylic acid)	1.08
Water	W	Tap water	1.00
Aggregate	HS	Fine sand (under 2.5 mm)	2.61

Table 6. Mix proportions.

	Weight ratio		Volume ratio	Weight ratio of SP/P
W/P	C/P	T/P	HS/C	
0.47	0.642	0.358	1.0	0.005 to 0.020

3.1 *Outline of the tests*

The thixotropic property was incorporated into the spraying mortar using a newly developed admixture consisting of mainly inorganic materials, such as fine powders with several grades of fineness. LDTM is made by mixing ordinary Portland cement, fine aggregate, water, the new admixture, and superplasticizer. This paper examined the properties of the fresh and hardened LDTM and its pumpability over long distances.

3.1.1 *Materials and mix proportion*

Tables 5 and 6 show the materials and mix proportion. When LDTM is to be sprayed, a quick setting agent is added at a spray nozzle point using a ratio to total volume of 3–5%.

3.1.2 *Test items*

(1) *Fresh properties*

The test items and target values for the fresh properties are shown in Table 7. The target values were set based on previous test results, which make it possible to force-feed LDTM over a distance greater than 1,000 m (Sasatani et al. 2012).

A mortar flow test was carried out without tapping in accordance with JIS R 5201 and the discharge time under pressure from a JP-funnel was measured using the same method used for TCRM. The bleeding ratio

Table 7. Test items, target values and test results.

Test items	Target values	Test results
Mortar flow	270 to 350 mm	316 mm
Discharge time from a JP-funnel	3.0 sec. or less	2.5 sec.
Schupack bleed test	7.0% or less	3.8%

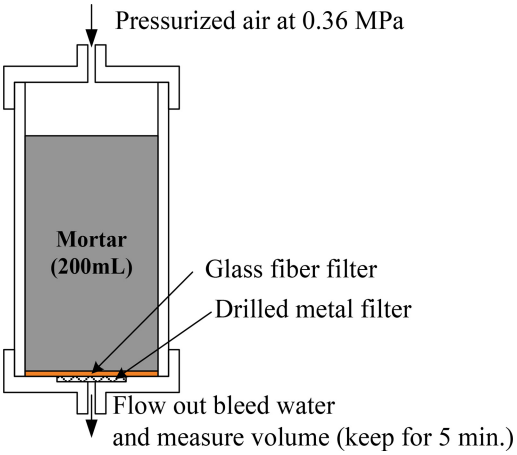

Figure 12. Test device of Schupack pressure bleed test.

under pressure was also measured. This test was carried out in accordance with "Schupack Pressure Bleed Test" (ASTM International, 2012) which is used for evaluating the grout for prestressed concrete. Figure 12 shows the test apparatus. The container is pressurized at 0.36 MPa and kept under pressure for 5 minutes. The volume of the bleeding water is measured. The bleeding ratio is calculated using formula (3).

$$B_p = (B_w / 200) \times 100 \quad (3)$$

Where B_p = Pressurization bleeding ratio (%) and B_w = Bleeding quantity of water (mL).

3.1.3 *Pumpability over long distances*

To evaluate pumpability over long distances, the relationship between the distance and the hose pressure was measured at several flow levels.

A conventional squeeze type pump with a maximum pressure of 3.0 MPa was used. The hose was flexible, 1,000 m in length, and 1.5 inches in inner diameter. A pressure gauge was installed in the hose every 100 m from the pump. The flow varied from 10 to 50 L/min. Figure 13 shows the hose during the test. The hose was coiled up every 25 m.

3.1.4 *Properties of hardened mortar*

The test items and target values for the hardened properties are shown in Table 8. The compressive strength was measured after 7 and 28 days of water curing at 20°C in accordance with JIS A 1107 (Japanese Industrial Standards Committee, 2012). The adhesion strength was measured after atmosphere curing at 20°C and relative humidity of 60% for 28 days in accordance with JIS A 1171.



Figure 13. State of the hose during test.

Table 8. Test items, target value and results.

Test items	Target value	Test results
Compressive Strength	24.0 N/mm^2 or higher (28 days)	28.9 N/mm^2 (7days) 32.6 N/mm^2 (28 days)
Flexural strength	3.4 N/mm^2 or higher	4.62 N/mm^2
Drying shrinkage	0.150 % or less	0.142 %
Accelerated carbonation	—	5.0 mm
Freezing and thawing test	D.F. is over 60% after 300 cycles	65.8%

Drying shrinkage, accelerated carbonation, and frost resistance were evaluated in accordance with JIS A 1106 (Japanese Industrial Standards Committee, 2006), JIS A 1153 (Japanese Industrial Standards Committee, 2012), and JIS A 1148 (Japanese Industrial Standards Committee, 2010), respectively.

These specimens were cured for 28 days in water at 20°C. For the drying shrinkage test, the specimens were placed in an environment with a temperature of 20°C and a relative humidity of 60%. For the accelerated carbonation test, the conditions were a temperature of 20°C, a relative humidity of 60%, and a carbon dioxide concentration of 5%.

3.2 *Test results and discussion*

3.2.1 *Properties of fresh mortar*

The test results for mortar flow, the discharge time under pressure from a JP-funnel, and the bleeding ratio under pressure are shown in Table 7. This table shows that these results satisfied the target values.

3.2.2 *Pumpability over long distances*

Figure 14 shows the relationship between the distance and the hose pressure at several flow levels. At the maximum flow level of 50 L/min, the pressure at the spout of the pump was 2.6 MPa, which is less than the maximum capacity of 3.0 MPa. The pressure at each measuring point decreased as the flow ratio decreased.

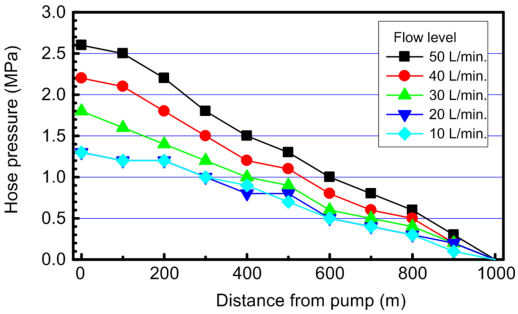

Figure 14. Relationship between the distance and the hose pressure at several flow volume levels.

Table 9. Outlines of the application of LDTM.

	Case 1 Akubetsu power plant	Case 2 Uchinoura power plant
Length of repaired area	532 m	25 m
Cross section size of repaired tunnel	2.5 m width 2.8 m height	2.1 m width 2.3 m height
The shortest distance of repaired area from gate	550 m	830 m
Volume of LDTM used for repairing work	Thickness:40 mm Area size:3633 m^2 Volume:145 m^3	Thickness:50 mm Area size:183 m^2 Volume: 9.1 m^3

The pressure in the hose and the pump depends on the flow ratio and the distance from the pump. Therefore, by controlling the flow level, LDTM can be pumped over a distance greater than 1,000 m.

3.2.3 *Properties of hardened mortar*

Table 8 shows the test result of hardened properties. The compressive strength at the age of 28 days was more than the target value of 24 N/mm^2. The adhesion strength was 2.63 N/mm^2 and exceeded the target value of 1.56 N/mm^2, which is the JIS specified value for repair mortar. The test results for durability are also shown in Table 8. These results show that LDTM has durability equal to that of conventional spray-type mortar.

3.3 *Examples of application for this material*

Table 9 shows two examples of the application of LDTM. These are repairs of deteriorated headrace tunnels at hydroelectric power plants. Figure 15 shows cross sections of these tunnels. The figure shows that the tunnels have small cross sections. Figure 16 shows the mixing plant and pump at Uchinoura power plant. Figure 17 shows the gate of the headrace tunnel at the Uchinoura power plant. Figure 18 shows the deteriorated surface of the tunnel and Figure 19 shows the

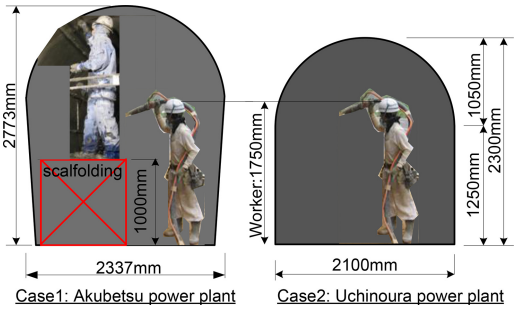

Figure 15. Cross sections of tunnel.



Figure 16. Mixing plant and pump at Uchinoura power plant.



Figure 17. Gate of the headrace tunnel at Uchinoura power plant.



Figure 18. Deteriorated surface of the tunnel at Uchinoura power plant tunnel.



Figure 19. Surface after the repair work at Uchinoura power plant tunnel.



Figure 20. Spraying conditions at Akubetsu power plant tunnel.



Figure 21. Condition before the repairs at Akubetsu power plant tunnel.

surface after the repair work. For this repair work, the surface of LDTM did not require finishing with a trowel. Figure 20 shows the spraying conditions in the Akubetsu power plant tunnelFigure 21 and Figure 22 shows the conditions before and after the repairs. For this repair work, the surface of LDTM required finishing with a trowel. In Japan, now LDTM is used for various types of construction work.

4 CONCLUSION

Two new high performance repair materials, TCRM and LDTM were developed by giving them a thixotropic property.



Figure 22. Condition after the repairs at Akubetsu power plant tunnel.

TCRM has an ability to be sprayed in patches over 20 cm thick on walls and over 15 cm thick on ceiling soffits

LDTM has an ability to be force-fed over a distance of more than 1,000 m and sprayed on the walls.

It was also confirmed that their properties, such as hardened properties and durability, are equal to those of conventional spray-type mortar.

REFERENCES

ASTM C1741-12. Standard Test Method for Bleed Stability of Cementitious Post-Tensioning Tendon Grout.

Fujiwara H., et. al. 2009. Development of Cross Section Repairing Material with High Thixotropy. *SUSTAINABLE INFRASTRUCTURE: Environmental Friendly, Safe and Resource Efficient, IABSE SYMPOSIUM* BANGKOK, 308–309.

Fujiwara H., et al. 2005. Development of high thixotropic grout. *Construction Materials, ConMat '05 and mindess symposium.*

Japanese Industrial Standards Committee, JIS A 1106: 2006. Method of test for flexural strength of concrete.

Japanese Industrial Standards Committee. JIS A 1107: 2012. Method of sampling and testing for compressive strength of drilled cores of concrete.

Japanese Industrial Standards Committee. JIS A 1108:2006. Method of test for compressive strength of concrete.

Japanese Industrial Standards Committee. JIS A 1129-3: 2010. Methods of measurement for length change of mortar and concrete – Part 3 Method with dial gauge.

Japanese Industrial Standards Committee, JIS A 1148: 2010. Method of test for resistance of concrete to freezing and thawing.

Japanese Industrial Standards Committee, JIS A 1153: 2012. Method of accelerated carbonation test for concrete .

Japanese Industrial Standards Committee. JIS A 1171:2000. Test methods for polymer-modified mortar.

Japanese Industrial Standards Committee, JIS R 5201:1997. Physical testing methods for cement.

Japan Society of Civil Engineers, Standard Specifications for Concrete Structures. 2013. Test Methods and Specifications. JSCE-K 561. Test methods of patching repair materials for concrete structure.

Sasatani T., et al. 2012. Shotcrete Method using Thixotropic Mortar for Long-Range Pumping Over 1,000 Meters. *CONCRETE JOURNAL*. Japan concrete institute, Vol.53. No.10. 180–186.

Concrete Solutions – Grantham et al. (Eds.)
© 2016 Taylor & Francis Group, London, ISBN 978-1-138-03008-4

Microwave system for *in-situ* curing of concrete repair

P.S. Mangat, K. Grigoriadis & S. Abubakri
Materials & Engineering Research Institute, Sheffield Hallam University, Sheffield, UK

A. Javaid & C. Zhao
Fraunhofer Institute for Interfacial Engineering & Biotechnology, Stuttgart, Germany

ABSTRACT: This paper presents some results of the FP7 MCure project on the development of a prototype system for microwave curing of concrete and concrete repair. Microwave curing of concrete provides higher early age strength compared to normally cured concrete. A prototype microwave curing system has been developed based on laboratory results on microwave curing of concrete repair materials. Subsequently, field trials were carried out to validate the Pre-Industrial Prototype system by testing elements of four commercial repair materials and a CEM II cement concrete. The prototype control system was used to record data such as surface temperature of concrete, moisture content of concrete and output power of the magnetron. In addition, the relationships between microwave output power, temperature and volume of repair of the field trials were derived and compared with the laboratory results. The prototype microwave system performed effectively. Slabs of dimensions 1 m × 1 m and depths up to 64 mm were microwave cured to temperature up to 45°C for the predetermined time.

1 INTRODUCTION

Patch repair is one of the most common types of repair in concrete structures. It can be classified as non-structural or cosmetic repair in which load carrying capacity is not a major issue and structural repair in which the repair patch is expected to carry load (Plum 1991). Emmons (1992) provides a detailed description of the various stages involved in the execution of a patch repair.

In the case of runway, bridge and car park repairs, high early age strength may be required to minimise delays, disruption and financial costs for the users and owners of the structure. Cold weather repair application is another example in which high early age strength is required to avoid the detrimental effects of low temperatures on long-term compressive strength (Neville 2011). However, under normal curing conditions, it may take 24 hours or more for most cementitious repair materials to harden and it may take several days before sufficient compressive strength is developed to carry the applied loads (Leung & Pheeraphan 1995).

Microwave heating based on dissipation of internal energy due to the excitation of water molecular dipoles when exposed to a rapidly alternating electromagnetic field (Leung & Pheeraphan 1995) can be used to reduce curing time and increase early age strength of cement-based repair materials. This has been shown by various studies performed on cement-based mortars using different types of cement and w/c ratios (Wu et al. 1987, Hutchison et al. 1991 Leung & Pheeraphan 1995, Leung & Pheeraphan 1997, Sohn & Johnson 1999, Lee 2007, Rattanadecho et al. 2008, Makul & Agrawal 2011). Significant reduction in disruption, delays and costs can be achieved by shortening the required curing time of patch repairs in concrete structures and airport runways.

The MCure project funded by the EC FP7 programme has been developed to facilitate rapid and durable patch repairs to concrete structures and pavements. A microwave curing prototype has been developed to accelerate *in-situ* concrete repairs and to enable repair application in cold weather.

2 MCURE PROTOTYPE DESCRIPTION

2.1 *MCure prototype systems*

The MCure prototype (Fig. 1) is comprised of the following six systems:

- Microwave system
- Temperature monitoring system
- Moisture monitoring system
- Remote control system
- Electrical system
- Microwave radiation safety system

2.2 *MCure prototype operating software*

Software based on two different algorithms specifically developed for the MCure system is used to operate the machine. It provides the user with the option of selecting either manual or automatic mode



Figure 1. The MCure prototype.

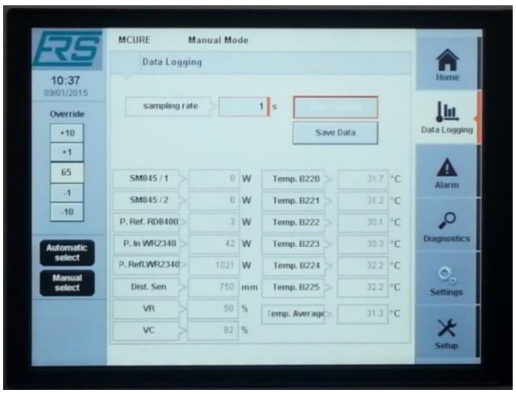

Figure 2. The touch screen display panel.

control for operating the machine. Parameters such as the movement pattern of the antenna over the microwave cured area, microwave power, target temperature and total heating time can be input before the start of operating the machine by using the touch screen panel shown in Fig. 2. The movement of the antenna is subdivided into step by step and continuous movement patterns. The step by step movement pattern means that the antenna will move to the next position only when the temperature of the current position achieves the target temperature. The continuous movement pattern means that the antenna will continuously move over the concrete surface with constant speed/power.

2.2.1 *Manual mode*

Microwave curing parameters such as position of the antenna, microwave power and heating time should be determined by the operator in the manual mode of the machine. The target temperature can be reached using either continuous movement or a step by step approach. In the first case, the antenna moves at a constant speed along a pre-determined path using fixed power and the temperature is recorded. This procedure can be repeated as many times as needed to achieve the target temperature. In the second case, the antenna is positioned above a pre-determined location and remains fixed until the area directly beneath the antenna has reached the target temperature. Once the target temperature is reached, the antenna is moved and positioned at the next area to be microwave cured. By using this approach, it is possible each time to microwave cure an area slightly larger than the projected area of the antenna.

2.2.2 *Automatic mode*

When in automatic mode, only the movement pattern of the antenna is determined by the operator. The target temperature of the microwave cured patch repair is achieved by using either a Proportional Integral Derivative (PID) algorithm or a Fixed Time Power Regulating (FTPR) algorithm specifically developed for the MCure system. The algorithm is used to regulate the required microwave power of the antenna at a specific position. Once the target temperature at this position is achieved, the antenna is moved and positioned over the next area to be microwave cured.

2.2.2.1 PID algorithm

The Proportional Integral Derivative (PID) controller (Minorsky 1922) is a control loop feedback mechanism. It has become the most commonly used closed-loop controller in all types of industrial control systems due to its simplicity and excellent performance (Astrom & Murray 2010). In a PID controller its input signal is the error $e(t)$ between a user defined set point $r(t)$ and a measured plant/process variable $y(t)$ as shown in Equation 1. The terms plant and process refer to the object or the process that is being controlled by the PID controller. In the case of MCure system the process is the microwave heating of the repair patch and the error $e(t)$ is the difference between the measured temperature $y(t)$ and the target temperature $r(t)$ (40 to 45°C) (Mangat et al. 2015, Mangat et al.2016.). The output signal $u(t)$ of the PID controller in time t-domain is given by Equation 2.

$$e(t) = r(t) - y(t) \tag{1}$$

$$u(t) = K_p e(t) + K_i \int_0^t e(\tau)d\tau + K_d \frac{de(t)}{dt} \tag{2}$$

where $e(t)$ = error signal; $r(t)$ = set point value for temperature; $y(t)$ = plant/process variable (measured temperature); $u(t)$ = PID output signal; K_p = proportional gain (a tuning parameter); K_i = integral gain (a tuning parameter); and K_d = derivative gain (a tuning parameter).

In the MCure system, the PID controller continuously measures the error and attempts to minimise it over time by only adjusting the microwave power supplied to the surface of the repair patch. Consequently, the required heating time to reach the target temperature cannot be controlled. Too much microwave power can lead to excessive rates of temperature increase, which in turn can result in plastic shrinkage and cracking, significantly reducing later age strength (Mangat et al. 2015, Mangat et al., 2016). In order to overcome the above limitation, a second algorithm (Fixed

Time Power Regulating (FTPR) algorithm) has been developed for use with the MCure system. In FTPR algorithm the target temperature is achieved at the end of microwave curing (Mangat et al. 2015, Mangat et al. 2016.).

2.2.2.2 FTPR algorithm

The aim of this algorithm is to provide adequate microwave power for reaching the target temperature at the end of a fixed period of microwave curing. Prior to the application of microwave curing the rate of temperature increase for the entire curing cycle is determined based on the initial (ambient) temperature of the repair surface. At the start of the curing cycle an initial microwave power P_1 is applied for an incremental period t_1 and the temperature of the repair surface T_1 is measured at the end of t_1. Next, the rate of temperature increase during period t_1 is compared to that for the entire curing cycle. If the rate of temperature increase during t_1 is higher or lower than the rate of temperature increase for the entire curing cycle the microwave power is either reduced or increased accordingly to a new value P_2.

2.3 *Microwave radiation safety system*

The microwave radiation safety system of MCure prototype consists of a microwave safety enclosure in the form of a rectangular cuboid cage, four microwave leakage sensors and one microwave safety automatic power-off switch. The safety enclosure fully covers the microwave system and is used to confine the emitted and reflected microwave energy within its boundaries (Fig. 3). The walls and roof of the enclosure consist of a semi-transparent stainless steel fabric supported by an aluminum frame. The enclosure is able to provide effective shielding against electromagnetic waves and complies with BS EN 60519-6 (BSI 2011) which limits microwave leakage to 50 W/m^2. It also offers the chance to observe the prototype when in operation. The four microwave leakage sensors are installed on top of each enclosure wall (external face) and continuously monitor the level of microwave leakage. Each sensor is connected to the main control system in such a way that it can individually shut down the whole system by detecting microwave leakage in excess of 50 W/m^2 during its operation. The automatic power-off switch ensures that the whole prototype is automatically switched off once the maintenance door of the enclosure is opened while the prototype is in operation.

2.4 *System integration*

All MCure prototype systems were assembled, integrated and verified as a single operational unit. For this purpose, software developed specifically for the MCure system was used to integrate individual components in the whole system and then verify the whole system as a single unit. In addition, the integrated system was verified for microwave safety. The integrated and verified system was then used to perform trials on large slabs cast using different repair materials.



Figure 3. The microwave safety enclosure.

3 EXPERIMENTAL PROCEDURE

3.1 *Test programme*

A test programme was performed to microwave cure scaled up elements of concrete repair using the MCure prototype system. Tests were carried out to validate the operating and control parameters of the microwave prototype system and to assess their reliability. The results were analysed to validate the basic microwave curing relationships developed for repair patches (Mangat et al. 2015, Mangat et al. 2016.).

3.2 *Repair materials*

The following commercial repair materials were used in this investigation:

- Repair Material 1: A concrete with CEM II/A-LL 32.5 R cement conforming to BS EN 197-1 (BSI 2011), coarse sharp sand (50% passing a 600 μm sieve) and uncrushed river gravel (maximum size of 20 mm) with w/c ratio of 0.45. Density of fresh mix was 2350 kg/m^3.
- Repair Material 2: A low shrinkage polymer modified cement mortar, fibre-reinforced with corrosion inhibitor. Density of the fresh mix was 2100 kg/m^3 (Sika MonoTop-412).
- Repair Material 3: A polymer modified cement mortar. Density of the fresh mix was 2050 kg/m^3 (Sika MonoTop-613).
- Repair Material 4: A polymer modified cement mortar with corrosion inhibitor. Density of the fresh mix was 1900 kg/m^3 (StoCrete GM P).
- Repair Material 5: A polymer modified cement mortar. Density of the fresh mix was 2200 kg/m^3 (StoCrete TG 204).

Table 1. Details of repair material slabs.

Slab	Area (m^2)	Depth (mm)	Repair material	Pre-curing time (min)
S6	1	58	1	43
S7		62	2	40
S8		59	3	46
S9		61	4	38
S10		64	5	41



Figure 4. Compaction of newly cast mix.

3.3 *Details of slabs*

Five slabs were cast in timber moulds of 1000 × 1000 × 105 mm internal dimensions for microwave curing trials of the above repair materials. The mix proportions of each repair material were based on the manufacturer's recommendations. Details of all slabs are shown in Table 1.

3.4 *Mixing and casting of slabs*

The quantity of each repair material (concrete and commercial repair materials of slabs S6 to S10) and water were mixed together in a concrete pan mixer to produce the required volume of mix for the slab element. Each mix was cast in the mould and compacted by hand tamping and trowelled as shown in Figs. 4, 5. The slab specimens were then placed inside the MCure prototype system and microwave cured. Microwave curing was started at 38 to 46 minutes (pre-curing time) after commencing mixing the repair materials, to simulate the typical time taken on construction sites to apply a repair patch.

3.5 *Microwave curing*

Slabs were cast with dimensions of 1 m × 1 m and microwave cured. The surface of each slab was divided into strip areas to heat. The slab surface exposed to microwave power was not covered during curing. The microwave curing was controlled manually. Each strip area was microwave cured for 2.5 minutes at a power of 1700 Watts by locating the microwave antenna above the strip. The projected area of the antenna, with some spread of the microwave energy, was heated at each location. After 2.5 minutes the antenna was moved manually over the next strip. The total microwave curing time of each slab was 50 minutes.



Figure 5. Surface finishing of material.



Figure 6. Thermocouple placed on the base of the mould.

3.6 *Internal temperature monitoring*

The internal temperature of each slab was measured by a single type T thermocouple which was located at the base of the timber mould of the slabs. Fig. 6 shows an installed thermocouple (top right corner) in a typical slab mould. Temperature measurements were taken every 5 seconds using a Data Taker DT85G digital logger.

3.7 *Surface temperature measurement*

In addition to the temperature sensors of the MCure prototype, the surface temperature of the slabs was measured using a FLIR i7 thermal camera (Fig. 7). The accuracy of the camera is 0.2% or ±2°C and gives a resolution of 140 × 140 pixels. The camera provides an image of temperature distribution, maximum and minimum temperature range at a selected area and a spot point temperature.



Figure 7. Thermal camera for monitoring the surface temperature of the slabs.

Table 2. Slab details.

Slabs	Repair material	Volume (l)	Mid-point temperature increase ΔT (°C)
S6	1	58	12.6
S7	2	62	19.1
S8	3	59	16.6
S9	4	61	14.6
S10	5	64	24.4

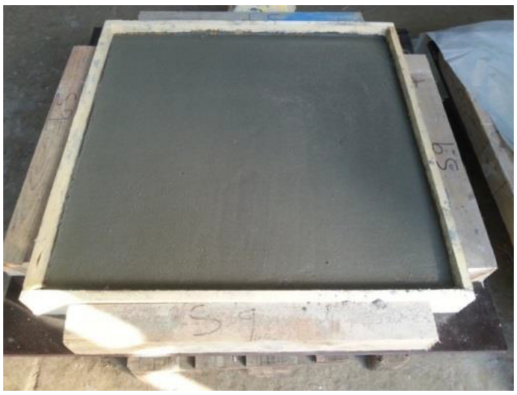

Figure 8. Slab S9 at the end of microwave curing.

4 RESULTS AND DISCUSSION

A significant temperature increase ΔT was achieved at the end of microwave curing in all slabs. The mid-point temperature increase recorded by the thermal camera at the end of microwave curing is shown in Table 2.

The results of slab S9 which are typical of all slabs S6-S10 are described in detail below.

A typical photo of a slab (S9) immediately after the end of microwave curing is provided in Fig. 8, which shows signs of phase change from fluid to solid state. Microwave curing significantly accelerated the setting of the repair slabs and the surfaces were free from plastic shrinkage cracking. Thermal images of slab S9 at the start and at the end of microwave curing are shown in Figs. 9a, b respectively. Finally, details of slab S9 temperature development during successive microwave curing of its strip areas obtained using the embedded thermocouple and the MCure prototype temperature sensors are shown in Table 3.

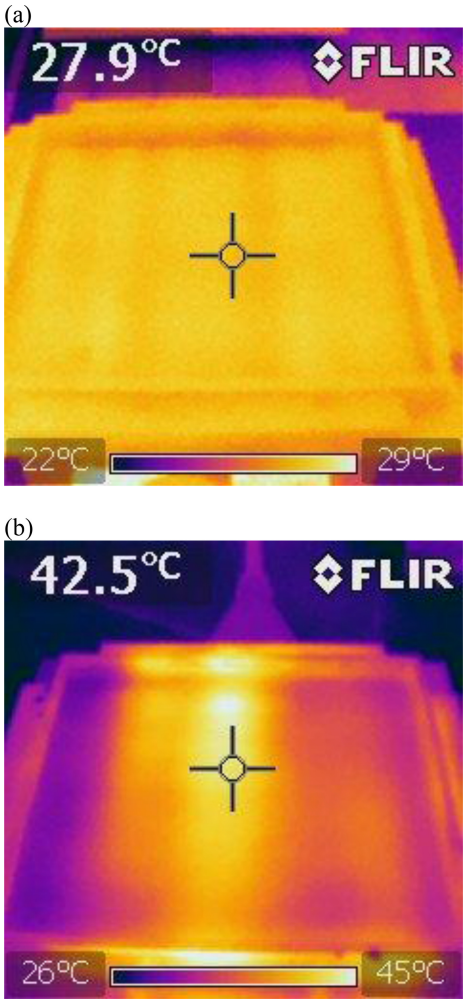

Figure 9. Slab temperature distribution (a) before the start of microwave curing and (b) after the end of microwave curing.

Finally, it should be noted that negligible microwave leakage was detected during curing of all test slabs.

5 CONCLUSIONS

- The microwave prototype system provides sufficient heat to microwave cure concrete repair slabs of dimensions 1 m × 1 m and depths up to 64 mm.
- All systems of the MCure prototype functioned satisfactorily.

Table 3. Slab S9 temperature development.

Microwave curing progress	Thermocouple temperature[1] (°C)	Sensor av. temperature[2] (°C)	Sensor max. temperature[3] (°C)
At the start of the operation	29.5	30.2	30.9
After microwave curing first quarter of slab	34.7	36.5	39.0
After microwave curing second quarter of slab	37.1	38.9	44.0
After microwave curing third quarter of slab	36.8	39.1	44.3
After microwave curing fourth quarter of slab	36.5	40.5	46.2

1-Thermocouple located at mid-point of first quarter of slab, 2-Average temperature reading of the sensors, 3-Maximum temperature of the sensors.

- The prototype enclosure provides satisfactory shielding of microwave radiation (less than 50 W/m^2)
- Microwave curing significantly accelerates the setting of the repair slabs and the surfaces of the repair remain free from plastic shrinkage cracking.

ACKNOWLEDGEMENTS

The authors gratefully acknowledge the European Commission 7th Framework Programme for financing this research for the MCure project (Grant no: 605664).

REFERENCES

Astrom, K.J. & Murray, R. M. 2010. Feedback Systems: An Introduction for Scientists and Engineers. Princeton: Princeton University Press.

BS EN 197-1. 2011. Cement-Part 1: Composition, specifications and conformity criteria for common cements. London: British Standards Institution.

BS EN 60519-6. 2011. Safety in electroheat installations. Part 6: Specifications for safety in industrial microwave heating equipment. London: British Standards Institution.

Emmons, P.H. 1992. Concrete repair maintenance illustrated. 1st ed. New York: John Willey and Sons.

Hutchison, R.G., Chang, J.T., Jennings, H.M. & Brodwin, M.E. 1991. Thermal acceleration of Portland cement mortars with microwave energy. *Cement and Concrete Research* 21(5): 795–799.

Lee, M.G. 2007. Preliminary study for strength and freeze-thaw durability of microwave and steam-cured concrete. *Journal of Materials in Civil Engineering ASCE* 19(11): 972–976.

Leung, C.K.Y. & Pheeraphan, T. 1995. Microwave curing of Portland cement concrete: experimental results and feasibility for practical application. *Construction and Building Materials* 9(2): 67–73.

Leung, C.K.Y. & Pheeraphan, T. 1997. Determination of optimal process for microwave curing of concrete. *Cement and Concrete Research* 27(3): 463–472.

Makul, N. & Agrawal, D.K. 2011. Influence of microwave-accelerated curing procedures on the microstructure and strength characteristics of Type I-Portland cement pastes. *Journal of Ceramic Processing Research* 12(4): 376–381.

Mangat, P., Grigoriadis, K. & Abubakri, S. 2015. Microwave curing of concrete bridge repairs. *In Proceedings of the 16th European Bridge Conference, Edinburgh, 23–25 June 2015.*

Mangat, P., Grigoriadis, K. & Abubakri, S. 2016. Microwave Curing Parameters of In-situ Concrete Repairs. *Construction and Building Materials, 112: 856–866*.

Minorsky, N. 1922. Directional stability of automatically steered bodies. *Journal of American Society of Naval Engineers* 34(2): 280–309.

Neville, A.M. 2011. Properties of concrete, 5th edn. Harlow, Essex: Pearson Education Limited.

Plum D. 1991. Materials-what to specify. *Construction Maintenance and Repair* 6(2): 3–7.

Rattanadecho, P., Suwannapum, N., Chatveera, B., Atong, D. & Makul, N. 2008. Development of compressive strength of cement paste under accelerated curing by using a continuous microwave thermal processor. *Materials Science and Engineering A* 472(1–2): 299–307.

Sohn, D. & Johnson, D.L. 1999. Microwave curing effects on the 28-day strength of cementitious materials. *Cement and Concrete Research* 29(2): 241–247.

Wu, X., Dong, J. & Tang, M. 1987. Microwave curing technique in concrete manufacture. *Cement and Concrete Research* 17(2): 205–210.

Concrete Solutions – Grantham et al. (Eds.)
© 2016 Taylor & Francis Group, London, ISBN 978-1-138-03008-4

Temperature development in microwave cured repair materials

P.S. Mangat, K. Grigoriadis & S. Abubakri
Materials & Engineering Research Institute, Sheffield Hallam University, Sheffield, UK

ABSTRACT: This paper is part of the FP7 MCure project on the development and demonstration of an energy efficient system for accelerated curing during repair of concrete structures. It provides laboratory results on temperature development in microwave cured specimens of six commercial repair materials and a CEM II mortar. Specimens were cast in 100 mm polystyrene moulds and exposed to 60 Watts microwave power to reach approximately 40°C recommended temperature for microwave curing. Temperature development of specimens was monitored for 24 hours after mixing. The results show that microwave curing triggers the peak heat of hydration and brings it forward for all repair materials. In addition, internal temperatures of specimens are higher than the top surface temperatures and the difference increases with increasing temperature. These laboratory based results are backed by the currently confidential data obtained from pre-industry prototype tests which are being used to upgrade the technology to industrial scale.

1 INTRODUCTION

A high rate of compressive strength development of cement based repair materials is often greatly desirable, and can be achieved by higher temperature curing. For instance, high early strength development, makes early removal of formwork possible and accelerates the construction process. Accelerated curing of concrete repair to runways or pavements is another advantage, which prevents traffic disturbance. The Specifications for the Reinstatement of Openings in Highways (RAUC(S) 2015), Manual of Contract Documents for Highway Works (Highways England 2006) and the Design Manual for Roads and Bridges (Highways England 2015) define a compressive strength of 25 N/mm^2 for roads to be reopened and traffic reinstated.

Concrete repair in cold weather is another case where accelerated curing is important to prevent frost attack. If concrete is exposed to the freezing temperature before developing sufficient strength, it suffers a significant loss of performance (Neville 2011). Yi et al. (2014) showed that concrete exposed to 6 hours freezing temperature during the first 12 hours, suffered over 20% reduction in its 28 day strength. The strength reduction exceeds 50%, if exposed to 12 hours freezing temperature. According to ACI306R-10 (ACI 2010) a minimum strength of 3.5 MPa is required for fresh concrete to prevent frost damage. However, according to Koh et al. (2013) even 5 MPa is not adequate to resist the combination of chloride ion penetration and freeze thaw cycles.

In general, 24 hours or more are required for OPC based repair materials to develop sufficient compressive strength under normal ambient temperatures. In some cases, several days are required before safely handling the repair and removing formwork. However, sometimes in order to meet tight construction schedules in cold weather, it is necessary to place concrete in frosty conditions. Developing a technology that can accelerate curing of concrete repair in cold weather is highly desirable.

Curing is the process for promoting the hydration of cement that leads to the development of strength. The curing process affects the strength and durability of concrete in the short and long terms (Bentz & Stutzman 2006) Curing temperature is an important factor in the hydration, microstructure formation and bulk properties of Portland and blended cements. The chemical reaction of hydration is promoted by elevated temperatures and high early strength is achieved (Neville 2011). A high temperature of fresh concrete reduces the length of the dormant period of cement hydration. Conventional heating techniques, such as steam curing, apply heat from the exterior to the interior of concrete through conduction. The result is non-uniform heating and a long heating period – up to 24 hours to attain the required temperature and strength. In general, curing mortar and concrete at high temperature during placing and setting, increases the early strength but it may adversely affect the long-term strength (Neville 2011). However, controlled rise in curing temperature can speed up hydration and result in high early strength of concrete without causing any ill effect on later strength. Microwave curing is one of the recent methods for accelerated development of early age strength of concrete. There are experimental investigations of microwave curing of cement-based mortars using different w/c ratios (Wu et al. 1987, Hutchison et al. 1991 Leung & Pheeraphan 1995,

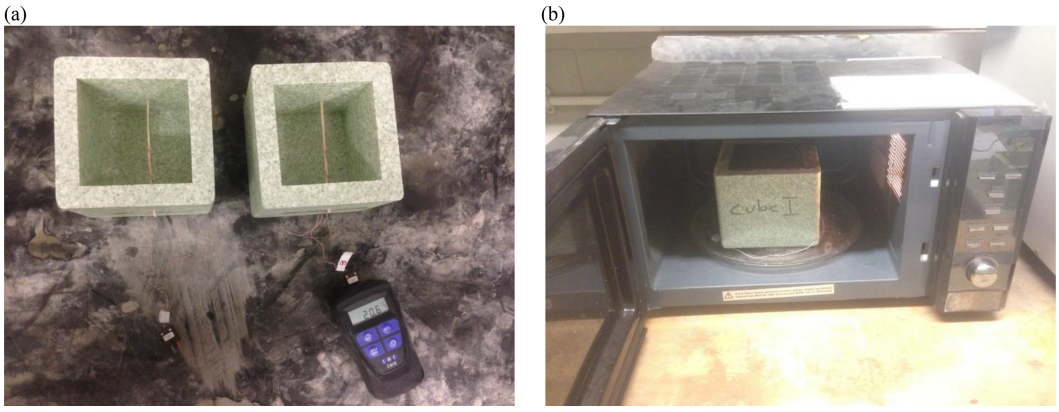

Figure 1. (a) Polystyrene mould with support for T type thermocouple and (b) Specimen placed inside microwave oven.



Figure 2. Set up for monitoring internal temperature.

Leung & Pheeraphan 1997, Sohn & Johnson 1999, Lee 2007, Rattanadecho et al. 2008, Makul & Agrawal 2011, Mangat et al. 2015) which confirm the possibility of its practical application. Microwave curing applies heat to the concrete by dissipation of internal energy due to the excitation of water molecular dipoles when exposed to an electromagnetic field (Leung & Pheeraphan 1995).

2 EXPERIMENTAL STUDY

2.1 *Materials and mix proportions*

The following six commercial repair materials and a CEM II mortar were used for this investigation.

- Repair Material 1: A polymer-modified cement, fibre-reinforced, shrinkage-compensated mortar. Plastic density of mix is 1730 kg/m^3 (Monomix).
- Repair Material 2: A polymer-modified cement, fibre-reinforced, rapid-setting mortar. Plastic density of mix is 2140 kg/m^3(Fastfill).
- Repair Material 3: A polymer-modified cement, fibre-reinforced, shrinkage-compensated mortar. Plastic density of mix is 2280 kg/m^3 (Monopour PC6).
- Repair Material 4: A rapid hardening cement with pulverised fuel ash, shrinkage-compensated concrete. Plastic density of mix is 2260 kg/m^3 (Five Star).
- Repair Material 5: A polymer modified cement, fibre-reinforced mortar with plastic density of 1500 kg/m^3 (HB40).
- Repair Material 6: A polymer-modified, low resistivity, highway agency class M patching mortar and render for cathodic protection. Plastic density of mix is 2200 kg/m^3 (Weber Mortar).
- Repair Material 7: A mortar with CEM II/A-L 32.5 N cement conforming to BS EN 197-1 (BSI 2011), coarse sharp sand (50% passing a 600 μm sieve) with a cement/sand ratio of 1:2, w/c ratio of 0.5, and plastic density of 2200 kg/m^3.

The repair materials were mixed according to the manufacturer's recommendations. The water/powder

ratio, (w/p), for each repair material mix is given in Table 1 along with the 28 day strength given in the manufacturer's data sheet.

A commercial microwave (Logik Model L25MD M13) with maximum nominal output power of 900 watts (manufacture's specification) was used. The microwave oven generated power at incremental levels of 10% up to 100% of its maximum output power. The microwave frequency was 2.45 GHz. The microwave was calibrated according to BS EN 60705 (BSI 2012) to determine the actual output power. For this experimental investigation, 10% of the actual output power was used (60 W).

Table 1. Details of repair materials.

Repair material	w/p ratio	28 Days strength (MPa)*
1	0.14	42
2	0.14	60
3	0.11	65–70
4	0.13	65
5	0.13	≥25
6	0.10	45
7	w/c = 0.5	40

* 28 days strength according to the manufacturer's data sheet.

2.2 *Casting and curing*

Two specimens were cast in 100 mm polystyrene cube moulds for each repair material (mix). A T-type thermocouple (with a welded tip) was located at the centre of each polystyrene mould by securing it to a wooden coffee stirrer stick as shown in Figure 1 (a). The tip of the thermocouple was located approximately 5 mm away from the stirrer stick. The specimens were cast in a laboratory environment (20°C and 60% RH) and cured in the laboratory without any cover.

Thirty minutes after commencing mixing, one cube specimen per mix was placed uncovered in the laboratory environment to cure for 24 hours. This is referred to as the normally cured specimen. The internal temperature of the cube was monitored using a Data Taker DT85G digital logger for 24 hours. The second cube specimen of each mix was exposed to 60 Watts of microwave energy 30 minutes after mixing. Microwave curing was applied until the centre of the cube top surface reached approximately 40 to 45°C (target temperature) recommended by Mangat et al. (2015). The temperature of the top surface was recorded with a Flir i7 Thermal camera before the start of microwave curing, then every 10 minutes. The internal temperature was also measured from the T type thermocouple by using the Data Taker DT85G digital logger. The microwave oven was stopped and the specimen removed from the oven to record the thermocouple data since the data logger could not be placed in the oven. Subsequently, the specimen was moved back for further microwave heating. When the centre of the top surface of the cube reached the target temperature, it was removed from the microwave oven and placed without cover in the laboratory environment (20°C, 60% RH) to cure for 24 hours. This represented the worst possible case of moisture loss during and for 24 hours after microwave curing. The moisture loss was monitored and will be published later. Figure 1 (b) shows the specimen inside the oven during microwave curing.

After the end of microwave curing, the internal temperatures of the specimens were recorded every 30 seconds over 24 hours by using the data logger. These are referred to as microwave cured specimens. Figure 2 shows the experimental set up to monitor internal temperature of cubes during 24 hours after mixing.

Each repair material has a different capacity to absorb microwave energy (Mangat et al. 2015), therefore, different durations of microwave exposure were used to achieve the target temperature with a constant power of 60 W. The period of microwave curing for each mix was estimated from previous research results (Mangat et al. 2015) and is given in Table 2

2.3 *Temperature distribution at top surface*

Figure 3 (a-g) shows the top surface temperature distribution for all repair materials at the end of microwave curing exposed to 60 Watts power for different time durations (Table 2). The temperature at the centre of top surface for repair materials reached 39.9°C (Material 4) to 44.1°C (Material 5) at the end of microwave curing. Temperature variation across the top surface observed in Figure 3 (a-g) is due to the non- uniformity of microwave heating. Figure 4 shows the temperature-time relationship for all tested repair materials. The temperature rises linearly with time for all repair materials (except Material 2). Repair materials experience different rates of temperature rise which is related to their dielectric properties. Dielectric properties of repair materials depend on many parameters such as water/cement ratio (Kharkovsky et al. 2001), temperature, electric field inside microwave cavity and composition of repair material such as admixtures, additives and the fineness of powders (Mangat et al. 2015).

Material 2 is a rapid hardening repair material which hardens after about 10 minutes of microwave curing and its time-temperature relationship becomes much steeper.

2.4 *Development of internal temperature*

Figure 5 presents the temperature-time relationship for Material 7 during 50 minutes of microwave curing. The thermal camera and thermocouple temperatures are plotted. The thermocouple temperature recorded in the normally cured cube, at 20°C, 60% RH, is also plotted. The results show that internal temperatures (thermocouple) for all repair materials were higher than at the centre of the top surface (thermal camera). The differences between top surface and internal temperatures ranged from 5.8°C (Material 2) to 23.8°C (Material 5)

(b) Material 1 at 40 minutes

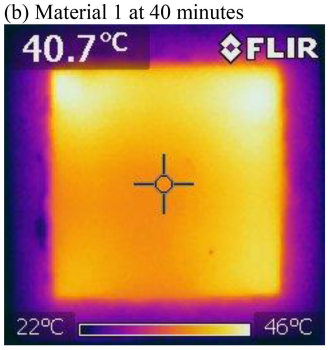

(b) Material 2 at 15 minutes

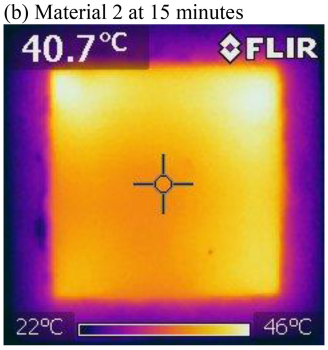

(c) Material 3 at 40 minutes

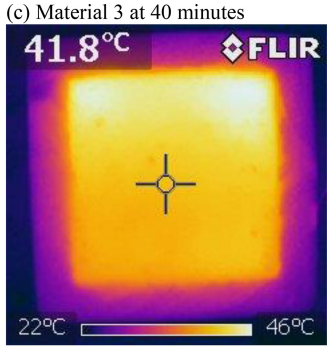

(d) Material 4 at 50 minutes

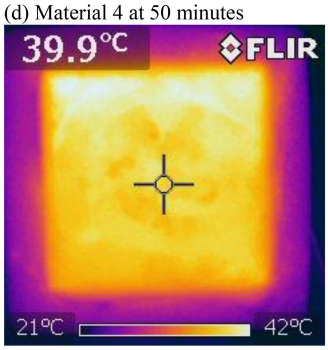

(e) Material 5 at 40 minutes

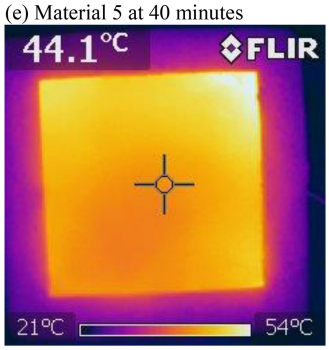

(f) Material 6 at 45 minutes

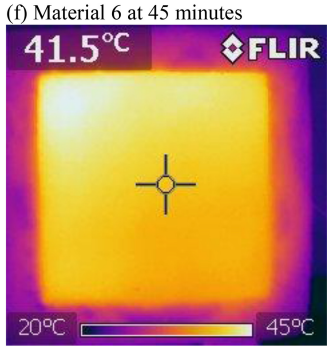

(g) Material 7at 50 minutes

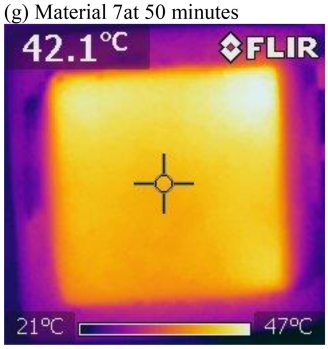

Figure 3(a–g). Top surface temperature distribution of all repair materials exposed to 60 Watts of power at the end of microwave curing (Table 1).

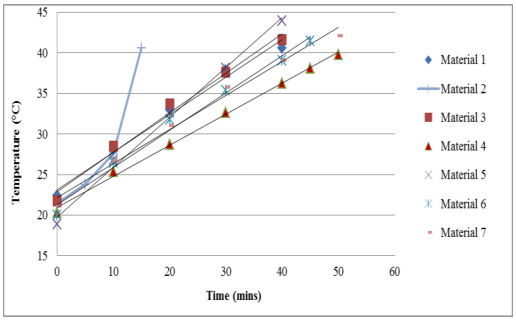

Figure 4. Temperature-time relationship of repair materials exposed to 60 Watts of microwave curing.

for all repair materials at the end of microwave curing. These differences start getting bigger as the microwave curing temperature goes beyond about 35° C. The differences for all repair materials are given in Table 2. These differences can be due to the concentration of microwave energy at the centre of the microwave cavity (Kim et al. 2015) and also due to convective heat loss from the top surface of the specimen. In addition, evaporation of water from the exposed top surface may affect temperature.

2.5 *Effect of microwave curing on peak heat of hydration*

The temperature at the centre of microwave cured and control (normally cured) specimens was monitored for

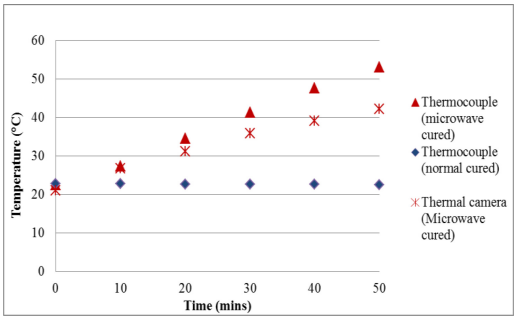

Figure 5. Temperature-time relationship for Material 7.

Table 2. Temperature at the end of microwave curing.

Repair Material	Microwave curing time (mins)	Temperature at the end of microwave curing (°C)		Temperature difference δT (°C)
		Thermal Camera	Thermo-couple	
d1	40	40.6	59.8	19.2
2	15	40.6	46.4	5.8
3	40	41.6	51.8	10.2
4	50	39.9	57.5	17.6
5	40	44.0	67.8	23.8
6	45	41.5	51.5	10.0
7	50	42.1	53.0	10.9

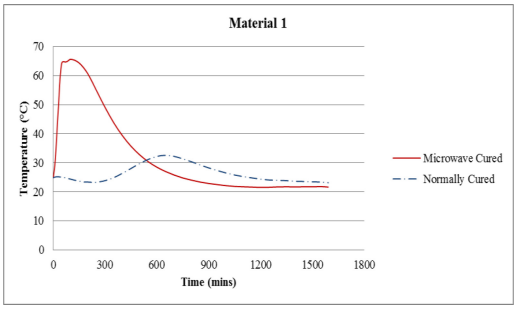

Figure 6. Internal temperature of microwave and normally cured samples for Material 1.

24 hours after commencing mixing. Figures 6 to 12 show the temperature profiles at the centre of normally and microwave cured cube specimens for all repair materials. The maximum temperature occurred after the end of microwave heating within the limits of 4 minutes (Material 6) to 60 minutes (Material 1) for all materials (Table 3). Immediately after the end of microwave curing, the temperature continued to rise for a short period for all materials (Table 3) due to continuing hydration and redistribution of temperature. Variation in temperature distribution occurred during microwave curing, including hot spots, that concurred with previous findings from the food industry

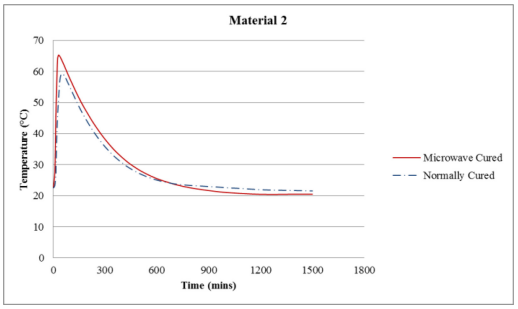

Figure 7. Internal temperature of microwave and normally cured samples for Material 2.

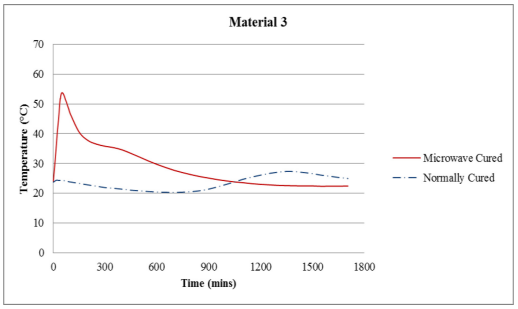

Figure 8. Internal temperature of microwave and normally cured samples for Material 3.

(Vadivambal & Jayas 2010) and also other research on cement based materials (Teo et al. 2002, Mangat et al. 2015, Mangat et al., in prep.). These variations became uniform soon after the end of microwave curing.

The temperature of microwave cured specimens started decreasing gradually after reaching the maximum values at the times given in Table 3. However, a peak of hydration temperature occurred on the falling temperature curve and can be clearly detected for Materials 3, 6 and 7 and less clearly for Material 4 (Figures 6 to 12). The peak of hydration temperature for Materials 1, 2 and 5, on the other hand, occurred before reaching the maximum temperature.

A comparison of the normally cured and microwave cured specimens for each repair material, in Figures 6 to 12, shows that the peak hydration temperature of microwave cured specimens was reached much sooner than the normally cured specimens. This is due to the acceleration of hydration with high temperature (Neville 2011). In some materials such as Material 2 and 5, the peak heat of hydration almost merged with the microwave curing period. For instance, the hydration temperature of the rapid setting Material 2 peaked at about 15 minutes after the end of microwave curing (30 minutes after microwave curing started) whereas for the normally cured specimen of Material 2, the peak heat of hydration occurred at 35 minutes (Figure 7). Other materials, such as 3, 4, 6 and 7, reached their peak heat of hydration during the cooling down period after microwave curing. In each

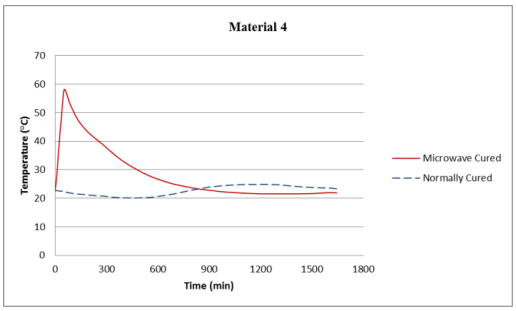

Figure 9. Internal temperature of microwave and normally cured samples for Material 4.

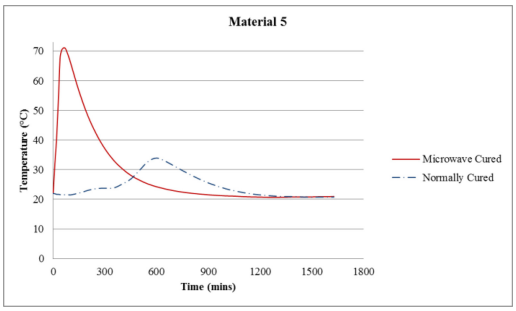

Figure 10. Internal temperature of microwave and normally cured samples for Material 5.

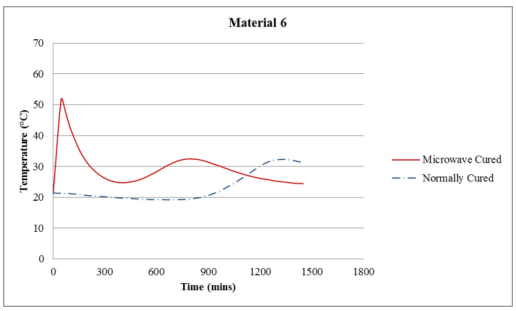

Figure 11. Internal temperature of microwave and normally cured samples for Material 6.

case, the normally cured specimens reached their peak hydration temperature later than the microwave cured specimens.

3 CONCLUSIONS

The following conclusions are drawn from the results presented in the paper:

- The internal temperatures measured with the thermocouple and the surface temperatures monitored by the thermal camera during microwave curing are similar up to about 35°C. Subsequently, the difference between internal and surface temperature increases with increasing temperature.
- The surface temperature of the cube is not uniform. The non-uniformity increases with temperature.
- Different durations of microwave curing at constant power (60 W) are required for different repair materials to reach a common target temperature of curing.
- Microwave curing accelerates the heat of hydration reactions and brings forward the time to reach the peak hydration temperature.

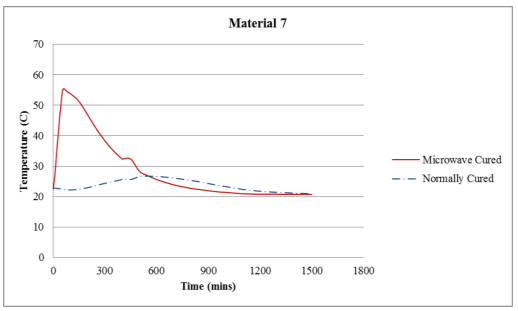

Figure 12. Internal temperature of microwave and normally cured samples for Material 7.

Table 3. Time and maximum temperature after microwave curing.

Repair material	Microwave curing time (mins)	Maximum temperature (°C)	Time* (mins)
1	40	65.5	60
2	15	65.3	15
3	40	53.8	10
4	50	58.2	5
5	40	71.1	20
6	45	52.1	4
7	50	55.4	10

*Time from the end of microwave curing.

ACKNOWLEDGEMENTS

The authors gratefully acknowledge the European Commission 7th Framework Programme for financing this research for the MCure project (Grant no: 605664).

REFERENCES

Guide to Cold Weather Concreting. 2010. Committee 306. American Concrete Institute.

Bentz, D.P. & Stutzman, P.E. 2006. Curing, Hydration, and Microstructure of Cement Paste. *ACI Materials Journal,* 103(5), 348–356.

BS EN 197-1. 2011. Cement-Part 1: Composition, specification and conformity criteria for common cements. London: British Standards Institution.

BS EN 60705. 2012. Household mcirowave ovens. Methods for measuring performance. London: British Standards Institution.

Specification for the Reinstatement of Openings in Roads. 2015. Section 7: Rigid and Modular Roads, 3rd edn. Roads Authorities and Utilities Committee (Scotland).

Design Manual for Roads and Bridges. 2015. Volume 7: Pavement Desing and Maintenance, Section 2: Pavement Design and Construction. Highways England.

Hutchison, R.G., Chang, J.T., Jennings, H.M. & Brodwin, M.E. 1991. Thermal acceleration of Portland cement mortars with microwave energy. Cement and Concrete Research 21(5): 795–799.

Kharkovsky, S.N., Akay, M.F., Hasar, U.C. & Atis, C.D. 2001. Measurement and monitoring of microwave reflection and transmission properties of cement-based specimens. *In Proceedings of the 18th IEEE Instrumentation and Measurement Technology Conference, Budapest, 21–23 May 2001,* vol. 1, 513–518.

Kim, B., Yi, C., & Kang, K. 2015. Microwave curing of alkali-activated binder using hwangtoh without calcination. *Construction and Building Materials,* 98: 465–475.

Koh, K., Park, C., Ryu, G., Park, J., Kim, D. & Lee, J. 2013, An experimental investigation on minimum compressive strength of early age concrete to prevent frost damage for nuclear power plant structures in cold climates, *Nuclear Engineering and Technology,* vol. 45, no. 3, pp. 393–400.

Lee, M.G. 2007. Preliminary study for strength and freeze-thaw durability of microwave and steam-cured concrete. *Journal of Materials in Civil Engineering ASCE* 19(11): 972–976.

Leung, C.K.Y. & Pheeraphan, T. 1995. Microwave curing of Portland cement concrete: experimental results and feasibility for practical application. *Construction and Building Materials* 9(2): 67–73.

Leung, C.K.Y. & Pheeraphan, T. 1997. Determination of optimal process for microwave curing of concrete. *Cement and Concrete Research* 27(3): 463–472.

Makul, N. & Agrawal, D.K. 2011. Influence of microwave-accelerated curing procedures on the microstructure and strength characteristics of Type I-Portland cement pastes. *Journal of Ceramic Processing Research* 12(4): 376–381.

Mangat, P., Grigoriadis, K. & Abubakri, S. 2015. Microwave curing of concrete bridge repairs. *In Proceedings of the 16th European Bridge Conference, Edinburgh, 23–25 June 2015.*

Mangat, P., Grigoriadis, K. & Abubakri, S. 2016. Microwave Curing Parameters of In-situ Concrete Repairs. (in prep.).

Manual of Contract Documents for Highway Works. 2006. Volume 1: Specification for Highway Works, Series 1000: Road Pavements-Concrete Materials. Highways England.

Neville, A. M. 2011. Properties of Concrete, 5th edn. Harlow, Essex: Pearson Education Limited.

Rattanadecho, P., Suwannapum, N., Chatveera, B., Atong, D. & Makul, N. 2008. Development of compressive strength of cement paste under accelerated curing by using a continuous microwave thermal processor. *Materials Science and Engineering A* 472(1–2): 299–307.

Sohn, D. & Johnson, D.L. 1999. Microwave curing effects on the 28-day strength of cementitious materials. *Cement and Concrete Research* 29(2): 241–247.

Teo, C.P, Ong, K.C.G, Shun, C.H., Tan, S.T. 2002. Accelerated heating of precast ferrocement secondary roofing slabs using microwave energy. *Our World in Concrete & Structures.* Singapore.

Vadivambal, R. & Jayas, D.S. 2010. Non-uniform temperature distribution during microwave heating of food materials-a review. *Food Bioprocess Technol, 3*, 161–171.

Wu, X., Dong, J. & Tang, M. 1987. Microwave curing technique in concrete manufacture. *Cement and Concrete Research* 17(2): 205–210.

Yi, S., Pae, S. & Kim, J. 2011, Minimum curing time prediction of early-age concrete to prevent frost damage, *Construction and Building Materials,* vol. 25, no. 3, pp. 1439–1449.



Taylor & Francis
Taylor & Francis Group
http://taylorandfrancis.com

Concrete Solutions – Grantham et al. (Eds.)
© 2016 Taylor & Francis Group, London, ISBN 978-1-138-03008-4

Sustainable and effective self-leveling mortars

I. Papayianni & E. Anastasiou
Laboratory of Building Materials, Department of Civil Engineering, Aristotle University of Thessaloniki (AUTH), Thessaloniki, Greece

P. Avramidis & P. Chatziagorastou
ISOMAT S.A., Thessaloniki, Greece

ABSTRACT: Cement-based self-leveling mortars are dry ready-mixed composite materials mainly for indoor applications for constructing new or renovating hard floors. Their thickness ranges from 10–50 mm and some of their basic requirements are: rapid setting time-but adequate for finishing the application- as well as early strength development, good adhesion to the existing floor pavement, low shrinkage deformations and high resistance to abrasion. In the frame of the SYNERGASIA 2012–15 Program, the Aristotle University of Thessaloniki, in cooperation with ISOMAT S.A. Building Chemicals and Mortars and AEIFOROS Metal Processing S.A., have developed an alternative self-leveling mortar (SLM) by replacing part of the cement in conventional SLM (Self Levelling Mortar) by Ladle Furnace Slag (LFS) at 20 and 30% by mass. Two types of LFS (Stabilag 75 and Stabilag 45), differing in fineness were used. An adequate number of mortar mixtures were prepared and tested in the fresh and hardened state following relevant specifications. As expected, the finer LFS (Stabilag 45) was more effective and may replace up to 30% of cement while the LFS Stabilag 75 may replace up to 20%, with an acceptable reduction in early and 28-d strength. Chemical additives and admixtures were also added in small quantities, in order to finalise the proposed mortar composition which was compared to the conventional control mixture of SLM. It seems that the substitution of cement with LFS increases the initial and final setting time, which is desirable for the rapid hardening cement products and improves significantly resistance to abrasion. The compressive and flexural strength is slightly reduced with the use of LFS, but the shrinkage deformations are remarkably reduced to lower than 0.2mm/m. Restrained shrinkage tests also showed high resistance to cracking. It could be said that the Portland cement replacement by LFS in SLM is not only a sustainable alternative by exploiting an industrial by product but a technically advantageous solution.

1 INTRODUCTION

1.1 *Self-Leveling Mortars (SLMs)*

Self-leveling mortars are principally used to produce a smooth and level floor surface on uneven, rough or unfinished concrete, cement mortar, plywood or ceramic tile floors etc. before the installation of carpets, ceramic tile, linoleum, vinyl tile, marble or wood, or as a final layer hard floor itself. SLMs are typically based on hydraulically active minerals such as cement, lime and calcium sulfates and are also mixed with fillers, resins and admixtures (Patural et al. 2011), while there are also polymer modified SLMs (Nguyen et al. 2013). Calcium aluminate cements have also been used as hydraulically active materials in SLMs due to their rapid hardening properties (Scrivener et al. 1999). An SLM is required to provide a smooth final surface by itself and to harden rapidly without shrinkage and then to allow foot traffic in the shortest time possible after it is placed and finished. Cement based SLMs are expected to be water resistant, to have high strength development, and short curing period. Other desirable properties include rapid set, early strength, rapid drying and shrinkage compensation (Emoto & Bier 2007).

1.2 *Ladle Furnace Slag (LFS)*

Ladle furnace slag is a by-product of the steel industry, produced at the second stage of the production process, after the addition of fluxes. It is produced in granular form and typically shows some latent hydraulic and pozzolanic properties (Shi 2002, Setien et al. 2009). Several researchers have proposed its use in cement-based applications, either as a cement substitute (Manso et al. 2005, Murri et al. 2013) or as filler (Moosberg-Bustnes 2004; Anastasiou et al. 2014). The purpose of this study is to investigate the possibility of using LFS as an additive in Self-Leveling Mortars in order to obtain SLMs of improved characteristics, as well as in order to successfully incorporate an industrial by-product such as LFS into a cement-based final product, which is desirable in terms of sustainability. The final product would be a SLM suitable for indoor use at thicknesses ranging from 10 to 50 mm.

Firstly, the available LFS was tested for fineness and reactivity with cement and lime and then test mortars

were prepared with cement substitution with LFS. The test mortars were tested for their fresh and hardened properties and the results were compared to ordinary cement-based SLM in order to determine possible improvements in the mortar properties with the use of LFS. Finally, a test indoor area was layered partly with the reference and partly with the test mortar in order to assess the SLM performance.

In order to determine the effect of substituting cement with LFS on sustainability, the $CO_{2,eq}$ emissions from the production of 1 m^3 of reference mortar was calculated using Life Cycle Assessment (LCA) methodology and was compared to that of the test mortars.

2 MATERIALS AND METHODS

2.1 *LFS testing*

Two types of LFS were available for testing; Stabilag 75 (S75) and Stabilag 45 (S45), different in granulometry, as S45 was sieved and ground in order to increase its fineness. The cementitious and pozzolanic properties of LFS largely determine its possibility to substitute cement and since these properties are linked with fineness (Papayianni & Anastasiou 2012), the fineness of the two available types of LFS was measured, using a Malvern Laser Particle Size Analyzer.

Also, the Strength Activity Index with cement according to EN 450-1 and the reactivity with lime according to ASTM C593-95 were measured in order to assess the cementitious and pozzolanic properties of the two available types of LFS. The strength activity index with cement was determined by comparing the 7-day and 28-day compressive strength of a reference mortar (450 g CEM I42.5, 1350 g standard sand and 225 g water) with a mortar having 30% of the cement substituted with LFS at equal consistency. The reactivity with lime was determined by measuring the 28-day compressive strength of test mortars prepared with 180 g hydrated lime; 360 g LFS; 1480 g standard sand; and the required water for 160 ± 5 mm consistency, using the flow table.

2.2 *Test SLM mixtures*

An ordinary, commercially available, SLM mixture was selected as reference, containing:

- Cement type CEM I42.5 R
- Gypsum anhydrite
- Carbonate aggregates sized 0–100 μm, 0–0.4 mm and 0.4–1.31 mm
- Admixtures such as methylcellulose in order to improve segregation resistance; set retarder/accelerator in order to control setting time; and superplasticizer in order to control workability

The test mixtures were produced from the reference mortar by substituting either 20% wt. or 30% wt. of the cement with either S75 or S45, resulting in a total of 4 test mixtures.

The 4 test mixtures along with the reference mortar were tested for their fresh and hardened properties. The fresh properties tested were water demand, workability using the Hägermann flow table, bulk density, air content, consistence at various intervals, initial and final setting times. All tests were carried out following the relevant specifications for screed materials (EN 13813).

After mixing, the test mortars were placed in moulds and were cured at 20°C and 95% RH for 28 days until testing. Hardened mortar testing included Shore D hardness, bending and compressive strengths at various ages, BCA abrasion resistance, bond strength, determination of dimensional change and determination of humidity content. Also here, all tests were carried out following the relevant specifications for screed materials (EN 13813).

In addition, in order to determine the long-term durability of the test mortars, some extra testing was performed in the laboratory for the test mortar containing 20% LFS S45. These tests were wetting-drying cycles; a total of 15 cycles with each cycle consisting of 3 days immersion in water and 3 days drying; freeze-thaw resistance according to ASTM C666-03; and restrained shrinkage measurements according to ASTM C1581-09.

2.3 *Sustainability*

Since cement was replaced with LFS in the test mixtures, a reduction in the environmental footprint of the final mortar was expected (Flower & Sanjayan 2007). In order to assess and quantify this reduction in terms of carbon emissions, the LCA methodology as described in EN ISO 14040 and EN ISO 14044 was followed. 1 m^3 was selected as functional unit and the energy inputs for the production and placement of each of the test mortars, as well as the reference mortar were calculated according to IPCC GWP 100a (IPCC 2007), following a cradle-to-gate approach.

3 RESULTS AND DISCUSSION

3.1 *LFS suitability*

The particle size analysis of the two LFS types (Stabilag 75 – S75 and Stabilag 45 – S45), as shown in Figure 1 showed that there was no considerable difference in their granulometry; S45 had ~35% retained at the 45 μm sieve, while S75 had ~40% retained at the 45 μm sieve.

The strength activity tests, on the other hand showed considerable differences between the two slags, as it can be seen in Table 1. It must be noted that EN 450-1 requires strength activity index with cement of at least 75% at 28 days and ASTM C593-95 requires at least 4.10 MPa compressive strength at 28 days.

Therefore, both LFS samples show weak pozzolanic activity, although S45 shows better results, especially regarding strength activity with cement. S45 is produced by crushing LFS, rather than sieving, so the

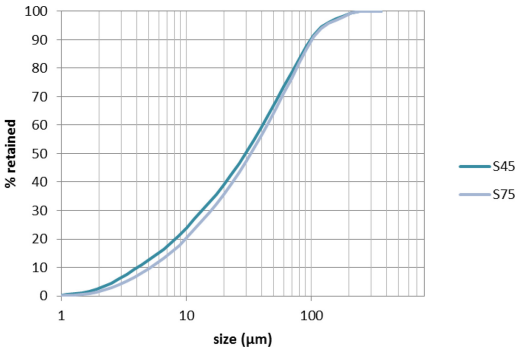

Figure 1. Particle size analysis of LFS S45 and LFS S75.

Table 1. LFS strength activity with cement and with lime.

LFS type	Strength activity index with cement (% of reference mortar compressive strength at 28 days)	Strength activity with lime (compressive strength at 28 days)
S45	86 %	2.30 MPa
S75	73 %	1.70 MPa

difference in reactivity between the two LFS types is probably not based on fineness, but on the increased number of reactive LFS particles, as produced by the crushing process(Papayianni & Anastasiou 2012).

3.2 *Test SLMs at fresh state*

Tables 2 and 3 show the test results of fresh Self-Leveling Mortars at different rates of cement replacement with LFS S45 and S75, respectively. The water content was kept constant for all mixtures in order to determine the effect of LFS replacement in workability at various intervals, as well as setting time.

Regarding the fresh mortar properties, LFS addition does not seem to change initial workability, both according to EN 1015-3 (without drops) and EN 12706. At t = 30′, LFS S45 (and LFS S75 but at lower rate) retained workability to a great extent compared to the reference mortar, which is positive as more time for placement of the fresh mortar would be available. Loss of early workability may lead to setting before compacting and finishing the mortar, which could lead to failures regarding cracking and strength development. The fresh bulk density remained practically unchanged, while air content increased when LFS was used, but remained below the empirical limit of 5% in all cases. Initial and final setting times increased in all cases when LFS was used, but the increase was small in all cases and within acceptable limits (<120 min).The initial and final setting time could be altered, if required, by using different rates of chemical admixtures.

3.3 *Test SLM mortars at hardened state*

Tables 4 and 5 show the test results of fresh Self-Leveling Mortars at different rates of cement replacement with LFS S45 and S75, respectively.

Shore D hardness was used as an indicator of the ability to step on the hardened concrete in order to proceed with construction. The empirical value required after 4 hours of mortar placement is >40, which means that the worker can step on the placed mortar and proceed with construction without producing cracks or other defects on the mortar. All results show Shore D values >50 at 4 hours, which justifies their use as rapid hardening mortars, although with the use of LFS the hardness values are slightly reduced. Also, the 1-day bending and compressive strengths exceed 4 MPa and 12 MPa, respectively, which is considered adequate for rapid hardening mortars.

The target 28-day compressive strength for the SLMs was 25 MPa. The considerably higher value obtained both for the S45 and S75 test mortars indicate that the test mortars could also be used in outdoor conditions, covered with an epoxy resin layer, as well as in indoor pavements and serve for industrial vehicle traffic and similar activities. The substitution of 20% or 30% of cement with LFS reduced 28-day strength only by 7.8% and 14.1%, respectively.

Abrasion resistance, on the other hand, was improved considerably in all cases when LFS was used. This is due to the properties of LFS, as well as due to the production of a smoother final surface, without occluded air and irregularities.

Also, shrinkage results showed improved values for the test mortars, compared to the reference. SLMs in general contain large amounts of Portland cement, which accounts for higher shrinkage values and, therefore, higher risk for cracking. This could be addressed by altering the contents of cement and anhydrite or by lowering the w/c content and increasing the amount of superplasticizer used. These solutions risk the effectiveness of the mortar (workability, strength) or could increase cost considerably. The use of LFS, which is a weak pozzolan, seems to address the problem of shrinkage to a great extent (shrinkage values reduced to less than half of the values for reference mortar), without compromising strength or workability and without increasing cost.

The humidity content (measured by the carbide method) is used in order to determine the time required before covering the floor with wood, tiles or other final layers. The general rule is to have humidity below 4% before covering with a wooden floor and below 2% before covering with ceramic tiles. The results show that these values are achieved within 2–3 days for wooden floors and 7–10 days for ceramic tiles. The use of LFS does not seem to change these values considerably.

3.4 *Durability tests of test SLM mortars*

Both wetting-drying and freezing-thawing cycles were carried out in reference and 20% LFS S45 test mortars.

Table 2. Tests on fresh SLMs with Stabilag S45.

Property	Test method	Cement replacement with LFS		
		0% (Ref.)	20% S45	30% S45
Water content (% wt. of total)	–	23	23	23
Workability at Hägermann table (mm)	EN 1015-3	353	365	358
Flow table workability at t = 0′ (mm)	EN 12706	136	139	134
Flow table workability at t = 15′ (mm)	EN 12706	121	127	129
Flow table workability at t = 30′ (mm)	EN 12706	87	120	121
Fresh bulk density (kg/m^3)	EN 1015-6	2066	2113	2070
Air content (%)	EN 1015-7	2.4	1.2	4.4
Initial setting time (min)	EN 196-3	90	90	120
Final setting time (min)	EN 196-3	100	110	130

Table 3. Tests on fresh SLMs with Stabilag S75.

Property	Test method	Cement replacement with LFS		
		0% (Ref.)	20% S75	30% S75
Water content (% wt. of total)	–	23	23	23
Workability at Hägermann table (mm)	EN 1015-3	353	368	361
Flow table workability at t = 0′ (mm)	EN 12706	136	141	137
Flow table workability at t = 15′ (mm)	EN 12706	121	127	124
Flow table workability at t = 30′ (mm)	EN 12706	87	102	100
Fresh bulk density (kg/m^3)	EN 1015-6	2066	2036	2053
Air content (%)	EN 1015-7	2.4	4.8	4.3
Initial setting time (min)	EN 196-3	90	100	120
Final setting time (min)	EN 196-3	100	110	120

Table 4. Tests on hardened SLMs with Stabilag S45.

Property	Test method	Cement replacement with LFS		
		0% (Ref.)	20% S45	30% S45
Shore D hardness at 4 hours	–	67	54	50
Shore D hardness at 24 hours	–	76	68	65
1-day bending strength (MPa)	EN 196-1	4.4	4.0	4.1
7-day bending strength (MPa)	EN 196-1	6.4	5.4	5.0
28-day bending strength (MPa)	EN 196-1	11.3	11.8	12.2
1-day compressive strength (MPa)	EN 196-1	15.5	13.3	12.7
7-day compressive strength (MPa)	EN 196-1	29.3	26.3	23.4
28-day compressive strength (MPa)	EN 196-1	39.3	36.3	33.8
Resistance to abrasion BCA (μm)	EN 13892-4	407.5	8.75	114.0
Bond strength (MPa)	EN 13892-8	2.4	2.4	2.4
Shrinkage (mm/m)	EN 13872	0.47	0.22	0.15
1-day humidity content at 1 cm width (%)	–	7.4	5.2	6.2
7-day humidity content at 1 cm width (%)	–	2.4	2.8	3.2

A total of 15 cycles were carried out for each test and the results showed no external cracking or change in weight of the test specimens (Fig. 2).

The restrained shrinkage test, as carried out for the reference and the LFS S45 test mortars is shown in Figure 3.

The results of the test, which was carried out for 15 days, showed that the reference and the test mortar performed in a similar way (Fig. 4), and there is at least "moderate-low" potential of cracking.

3.5 *Test production at larger scale*

Finally, the 20% LFS S45 test mortar was selected for production at larger scale. The test mortar was produced and placed at 30 mm thickness, according to

Table 5. Tests on hardened SLMs with Stabilag S75.

Property	Test method	Cement replacement with LFS 0% (Ref.)	20% S75	30% S75
Shore D hardness at 4 hours	–	67	52	50
Shore D hardness at 24 hours	–	76	78	82
1-day bending strength (MPa)	EN 196-1	4.36	4.15	4.17
7-day bending strength (MPa)	EN 196-1	6.41	5.63	5.27
28-day bending strength (MPa)	EN 196-1	11.34	12.49	12.24
1-day compressive strength (MPa)	EN 196-1	15.51	14.68	14.44
7-day compressive strength (MPa)	EN 196-1	29.31	26.41	24.37
28-day compressive strength (MPa)	EN 196-1	39.31	36.25	35.26
Resistance to abrasion BCA (µm)	EN 13892-4	407.5	20.0	11.3
Bond strength (MPa)	EN 13892-8	2.38	2.66	2.80
Shrinkage (mm/m)	EN 13872	0.47	0.19	0.17
1-day humidity content at 1 cm width (%)	–	7.4	4.4	5.8
7-day humidity content at 1 cm width (%)	–	2.4	2.1	2.8



Figure 2. Test SLMs after freeze-thaw cycles.



Figure 3. ASTMC 1581-09 restrained shrinkage test.

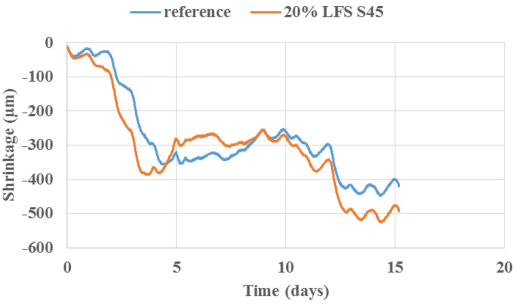

Figure 4. ASTM C1581-09 restrained shrinkage test results.



Figure 5. Test mortar finishing.

standard construction practices (Fig. 5), while a reference area was also placed with reference mortar (Fig. 6).

From the test production, no significant variations in the production process were noticed. The test floors were monitored for surface cracking and irregularities were observed. Also, the color, consistency and self-leveling ability of the two test surfaces did not show any significant differences. These test floors are intended for investigating the long-term behavior of the test mortar and will continue to be monitored in the long run.

3.6 *Life Cycle Assessment*

In order to assess the environmental performance of the test mortars, the total energy and material inputs for the production of 1 m^3 of final product was calculated.



Figure 6. Final surfaces of reference (left) and test mortar (right).

Table 6. Environmental performance of the test SLMs.

Mortar	kg $CO_{2,eq}/m^3$
Reference	455
20% S75	369
30% S75	325
20% S45	384
30% S45	341

These inputs include the energy required for the production of the constituents of the mortars (cement, gypsum, aggregates, etc.) and also energy required for transportation, mixing and placement.

By using the IPCC GWP 100a methodology, the environmental footprint for the production of 1 m^3 of mortar was calculated in kg $CO_{2,eq}$ and the results for all the tested mortars are shown in Table 6.

As can be seen from the results, there is considerable improvement in the environmental performance when substituting cement with LFS in the mortars, ranging from 15% to almost 30%. The improvement is greater when higher amounts of cement are replaced, which is expected because cement is the most energy intensive of the materials used.

4 CONCLUSIONS

From the available LFS types, Stabilag S45 showed better strength activity than Stabilag S75, both with cement and with lime and can be characterized as a weak pozzolan with some hydraulic properties.

The replacement of cement with LFS at 20% and 30%, in the form of either Stabilag S45 or Stabilag S75, led to a small reduction in compressive strength, but on the other hand, improved bending strength, shrinkage and abrasion resistance. The reduction of shrinkage and the increase of abrasion resistance provide a technical benefit for the mortars with LFS, while strength reduction is small and does not alter the possible end uses.

The two LFS types used showed little differences when substituting cement at 20% and 30% rates, but S45 is expected to show increased strength in the long term due to its higher pozzolanicity, so it was decided to direct S45 at 30% cement replacement and S75 at 20% cement replacement.

The laboratory mortar tests were validated with the production of two larger scale surfaces, laid with the reference mortar and the 20% LFS S45 test mortar. The test mortar showed similar workability, color and self-leveling ability with the reference mortar.

Finally, when considering the environmental performance of the various mortars, it seems that the use of LFS as cement substitute adds considerably to the sustainability of the mortars by reducing their environmental footprint.

REFERENCES

Anastasiou, E. K., Papayianni, I., & Papachristoforou, M. 2014. Behavior of self compacting concrete containing ladle furnace slag and steel fiber reinforcement. *Materials & Design* 59: 454–460.

Emoto, T., & Bier, T. A. 2007. Rheological behavior as influenced by plasticizers and hydration kinetics. *Cement and Concrete Research* 37(5): 647–654.

Flower, D. J. & Sanjayan, J. G. 2007. Green house gas emissions due to concrete manufacture. *International Journal of Life Cycle Assessment* 12: 282–288.

IPCC. 2007. IPCC Fourth Assessment Report. Cambridge, UK: Cambridge University Press.

Manso, J. M., Losañez, M., Polanco, J. A., & Gonzalez, J. J. 2005. Ladle furnace slag in construction. *Journal of materials in civil engineering* 17(5): 513–518.

Moosberg-Bustnes, H. 2004. Steel-slag as filler material in concrete. In *VII International Conference on Molten Slags Fluxes and Salts, The South African Institute of Mining and Metallurgy*: 385–391.

Murri, A. N., Rickard, W. D. A., Bignozzi, M. C.& Van Riessen, A. 2013. High temperature behaviour of ambient cured alkali-activated materials based on ladle slag. *Cement and Concrete Research* 43: 51–61.

Nguyen, D. D., Devlin, L. P., Koshy, P. & Sorrell, C. C. 2014. Impact of water-soluble cellulose ethers on polymer-modified mortars. *Journal of Materials Science* 49(3): 923–951.

Papayianni, I. & Anastasiou, E. 2012. Effect of granulometry on cementitious properties of ladle furnace slag. *Cement and Concrete Composites* 34(3): 400–407.

Patural, L., Marchal, P., Govin, A., Grosseau, P., Ruot, B.& Deves, O. 2011. Cellulose ethers influence on water retention and consistency in cement-based mortars. *Cement and Concrete Research* 41(1): 46–55.

Scrivener, K. L., Cabiron, J. L. & Letourneux, R. 1999. High-performance concretes from calcium aluminate cements. *Cement and Concrete Research* 29(8): 1215–1223.

Setién, J., Hernández, D. & González, J. J. 2009. Characterization of ladle furnace basic slag for use as a construction material. *Construction and Building Materials* 23(5): 1788–1794.

Shi, C. 2002. Characteristics and cementitious properties of ladle slag fines from steel production. *Cement and Concrete Research* 32(3): 459–462.

Concrete Solutions – Grantham et al. (Eds.)
© 2016 Taylor & Francis Group, London, ISBN 978-1-138-03008-4

The effect of binding system of mortars on chloride ion penetration

I. Papayianni, M. Papachristoforou & F. Kesikidou
Laboratory of Building Materials, Department of Civil Engineering, Aristotle University of Thessaloniki (AUTH), Thessaloniki, Greece

ABSTRACT: The beneficial effect of pozzolanic materials in reducing chloride ions penetration into cement matrix, has been well known from previous research work. In cement-based repair mortars, even if the cement is partially replaced by pozzolans, it makes a difference in resisting chloride induced corrosion and prolonging the life of the repair. Nowadays, many industrial by-products or other reactive powders are available in local markets after processing. They are of low cost and possess pozzolanic potential. However, their effectiveness in reducing chloride penetration, if used as cementitious materials or fillers in mortar mixtures, has not been valued in comparison with cement types, including pozzolans. In this paper, blended type Portland cements are compared with mixed-type binders, in which cement is partially replaced by local natural pozzolan, zeolith, ladle furnace slag and calcareous fly ash at 20% or 30%. They were used in preparing mortars for repair of concrete suffering from spalling or surface layer detachments due to corrosion. An adequate number of mortar mixtures with the aforementioned binding systems were prepared and tested in the laboratory. Apart from mechanical characteristics, the resistance to chloride penetration was measured by following the ASTM C1202-97 method.

Keywords: chloride ion penetration, rapid test method, mixed-type binders

1 INTRODUCTION

In Greece most buildings are exposed to a marine environment or water-borne chloride and there is much concern about repairing damage from corrosion in concrete structures. The steel cover is one of the most important factors for steel protection (CEB, 1992) and resistance to chloride penetration of repair mortars covering steel, is essential for prolonging the service life of the structure. Chloride ingress depends on mortar characteristics such as water/binder ratio, type of binding system, aggregate content, alkalinity of the mortar mass, temperature and curing time. (Collepardi, 1989) The need for reducing the global carbon footprint makes sustainability a one-way road in construction. Therefore, many blended type cements have been produced by the cement industry incorporating industrial by-products. In addition, mixed-type binding systems with available Supplementary Cementing Materials SCM(s) are favored in concrete construction. As known (Gjorn, 2009), chloride penetration occurs in two ways: water absorption by capillary suction and diffusion of chlorides, through the mortar's saturated capillary pores. It is well established by many researchers and long term experimental and in situ measurements (Gjorn, 1983, Bijen, 1998, Zhang, 1999) that the presence of Supplementary Cementing Materials (SCM(s)) reduces the chloride penetration. This is attributed to the chemical binding potential of SCM(s) because of increased CAH content of the matrix and formation of Friedel's salt, $Ca_3Al_2.CaCl_2.12H_2O$, as well as the increased adsorption of chlorides on C-S-H gel which is increased in pozzolanic cements or concretes with SCM(s). In addition, the pore size distribution refinement which occurs in cement matrices with SCM(s) contributes to the reduction of chloride diffusion (Collepardi, 2006).

Since there are many blended type pozzolanic cements and local SCM(s), it is useful and significant to rate them according to their performance in reducing penetration of chlorides. Therefore, local blended cements and SCM(s) were selected for preparing repair mortars and measuring resistance to chloride penetration. Based on the literature (8)(9), there is a strong controversy about the reliability of the rapid chloride permeability method based on electric conductivity measurement. In particular, in the case of including SCM(s) in the matrix, the results of ASTM C1202 measurements are not accordingly correlated to other properties such as water/binder ratio or permeability. In this paper the results of tests performed to the ASTM C1202 method are presented in relation to other characteristics of mortar compositions such as mechanical characteristics, porosity and capillarity. The experimental research of this investigation contributes to the discussion about the validity of rapid chloride penetration method based on the specific electrical conductivity of pore solution as affected by the addition of SCM(s). Furthermore, the use of SCM(s) in the form of blended cement and separately in the mixer as

additives allow the comparison of their performance on the binding of chlorides, since the SCM(s) potential of retaining chlorides is generally accepted by scientific society.

2 EXPERIMENTAL

To assess the effect of local SCM(s) to chloride penetration twelve mortar mixtures were prepared and after curing for a period of 28 days they were tested in compression and flexure. The Ed (dynamic modulus of elasticity) was also measured by sonometer according to BS 1881-209:1990 (BSI, 1990). The open porosity and capillary absorption were measured after pre-drying at 100° C. For the chloride penetration, the rapid method for chloride penetration, the ASTM C1202-97 test (ASTM, 1997) was followed. The second method of wet-dry cycling in salt solution is still in progress.

For the first mix, cement type CEMI 42.5 was used as control mix for comparison reasons. Another three mixes were prepared by using two blended type cements CEM II 32.5 and "fly ash cement". The latter incorporated 50% calcareous fly ash according to EN 13282. White cement was also used in the WC mortar mix because it is often used for repair purposes. Then another eight mortar mixes were prepared by replacing the control cement CEM I 42.5 by SCM(s) such as:

– Ladle furnace slag (CS20, CS30), – Calcareous fly ash (CFA30, CFA50), – Natural pozzolan (CP20, CP30) and Zeolith (CZ10, CZ20) where the numbers at the end of code names show the percentage of cement replacement by mass.

The amount of water was determined (by using the flow table test (EN 1015-3)) to achieve the required workability 16±1 cm for repair needs. An effort was made to keep the water/binder ratio for all mortars around 0.5. Therefore, a plasticizer dosage of carboxylic basis (aqueous solution of modified polymers), free of sulfates was used occasionally. River sand was used as aggregate and the binder/sand ratio was kept 1:3 for all mixes. The composition of mortar mixes is shown in Table 1 and the granulometric curve of the river sand in Figure 1. The characteristics of the cements and SCM(s) used in the mixed-type binding system are given in Table 2. The fresh mixtures were placed into moulds (four prismatic (40 × 40 × 160 mm) and two cylindrical 100 × 200mm). After demoulding, the specimens were cured in a climatic chamber (RH 95±5%, 25°C).

The determination of the compressive and flexural strength was performed at age 28 days according to (EN196-1). Dynamic modulus of elasticity, Ed, was calculated by using the measurement of the ultrasonic wave velocity according to BS1881. The open porosity was measured according to RILEM CPC 11.3 as well as capillary absorption following the EN method for mortars (EN 1015). For the last two measurements, a pre-drying of specimens took place before testing. For chloride ion penetration, the procedure of ASTM

Table 1. Composition of mortar mixtures.

Code names	Mixture	Binder/ Sand	Water/ Binder	Plast/zer
CEMI42,5	CEMI	1:3	0.56	–
CEMII32,5	CEMII	1:3	0.50	–
fly ash cement	FC	1:3	0.45	0.50%
white cement	WC	1:3	0.50	–
CEMI42,5 + 20% ladle furnace slag	CS20	1:3	0.45	0.40%
CEMI42,5 + 30% ladle furnace slag	CS30	1:3	0.45	0.40%
CEMI42,5 + 30% calcareous fly ash	CFA30	1:3	0.50	1.00%
CEMI42,5 + 50% calcareous fly ash	CFA50	1:3	0.50	1.00%
CEMI42,5 + 20% natural pozzolan	CP20	1:3	0.50	0.50%
CEMI42,5 + 30% natural pozzolan	CP30	1:3	0.50	1.00%
CEMI42,5 + 10% zeolith	CZ10	1:3	0.50	0.50%
CEMI42,5 + 20% zeolith	CZ20	1:3	0.59	2.00%

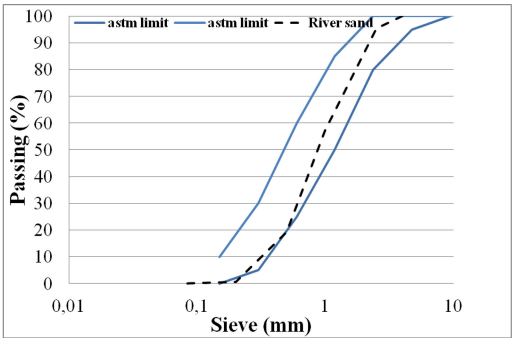

Figure 1. Granulometric curve of river sand.

C1202-97 was followed. The method consists of monitoring the amount of electrical current passed through slices (51 mm thick and of 102 mm diameter). These were cut from cylindrical specimens whose outer surfaces had been previously covered with epoxy resin (in order to seal them) and left for 48 hours for drying. Before testing the cut slices (51 × 102 mm) were put into water for 24 hours. After that, they were placed in rubber gaskets and then into cells containing 3% of NaCl solution from one side and 0.3M NaOH solution from the other side. During the test, the specimens were monitored for 6 hours.

3 RESULTS AND DISCUSSION

The 28-d compressive and flexural strength is given in Figure 2 and Figure 3 for all mixes. The values for compressive strength are the mean values of six specimens of three prismatic specimens.

Table 2. Characteristics of raw materials.

Chemical Com/tion	CEM I42.5	CEM II32.5	WC	FC	LFS	Fly ash	Pozzolan	Zeolite
SiO2	19.60	21.64	22.07	29.90	18.02	34.80	49.57	67.30–68.62
Al2O3	2.40	6.54	3.89	12.65	1.34	14.83	9.79	10.90–11.80
FeO3	8.11	1.01	0.19	3.80	1.68	2.40	1.89	0.8–1.5
CaO	66.84	59.19	58.35	42.90	55.62	31.34	15.25	1.5–4.0
MgO	3.91	3.30	2.74	2.20	6.75	1.39	8.22	0.75
Na2O	0.57	2.10	0.17	–	0.43	4.95	2.78	0.3–0.8
K2O	1.08	1.90	0.08	–	0.29	2.88	4.05	2.5–4.5
L.I.	1.91	4.32	11.07	8.40	15.42	4.55	8.45	12.34
Spec. Gravity (g/cm3)	3.100	2.810	2.811	2.527	2.63	2.380	2.292	2.226
Fineness retained on 45 μm sieve	–	–	–	–	–	43%	–	–
Particle size volume (%)	10–15 μm 6–7%	10–25 μm 5–6%	25–35 μm >6%	10–15 μm 5–6%	60–70 μm >5%	–	4 μm 6–7%	60 μm 4–5%
Poz/city index ASTM C593-95	–	–	–	–	1.7 MPa	9.64 MPa	8.3 MPa	5.23 MPa

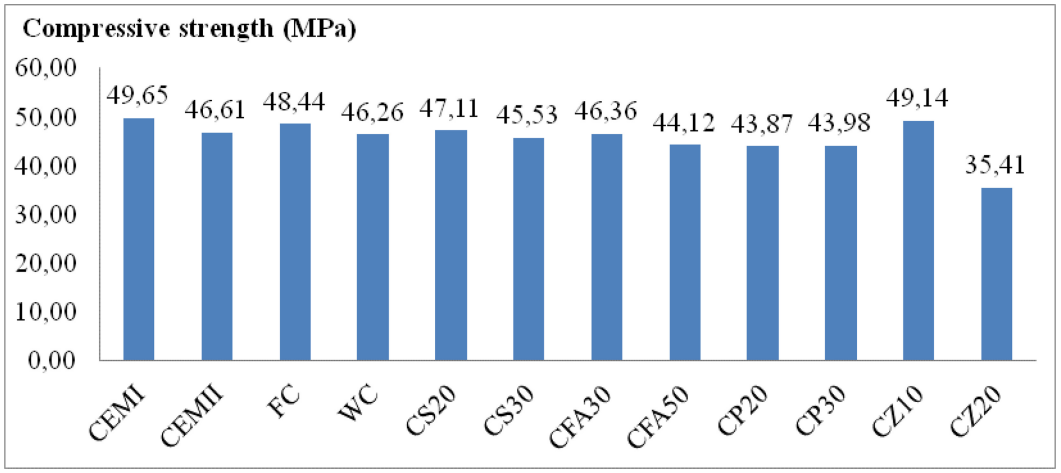

Figure 2. Compressive strength of all mixtures.

As shown in Fig. 2, the highest achieved strength of 50 MPa was developed by the control cement mortar CEMI, although its water/binder ratio was high – 0.56. The lowest strength was developed by CZ20 around 30 MPa, about a 15% reduction in comparison with the control CEMI. The blended cements CEMII, FC and the white cement WC, exhibited a drop in strength of about 5%. All other mixes in which cement was replaced by SCM(s) presented a 10–14% decrease, the higher value corresponding to the greater percentage of cement replacement by SCM(s). Between the two mortar mixes with binders containing 50% calcareous fly ash (FC and CFA50), that with the FC bended binder developed a higher 28-d strength.The CZ10 mortar mixture developed a 28-d strength almost equal to the control mix. For the mortar with zeolith in the binding system, the great demand for water was obvious. To limit this, superplasticizer at the maximum dosage was added. However, the water absorptivity of zeolith remained very high. Therefore, the high strength could be attributed to the reduction of the free water to binder ratio resulting effectively in a lower water/binder ratio and higher strength of the mixture.

Table 3. Limits of chloride ion penetration according to ASTM C1202.

Charge passed (coulombs)	Chloride Ion Penetrability
>4000	High
2000–4000	Moderate
1000–2000	Low
100–1000	Very Low
<100	Negligible

In Fig. 3, it is shown that most of the developed flexural strengths of the mortar mixtures with SCM(s) are around 5.5 MPa. The higher flexural strengths have been exhibited by the control and CP20, CP30 mixtures (around 8.8 MPa). To have an explanation about

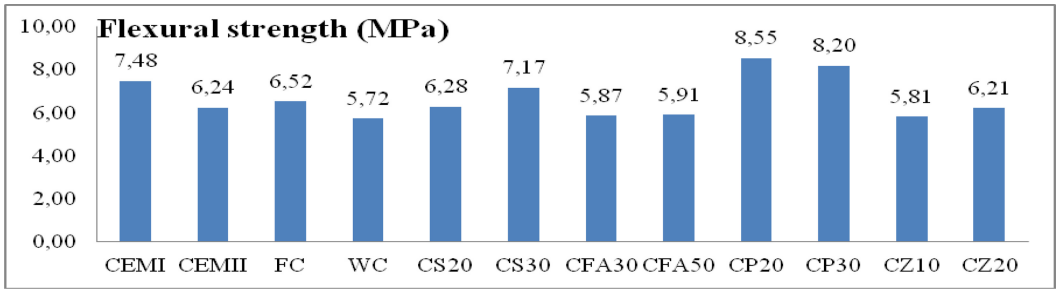

Figure 3. Flexural strength of all mixtures.

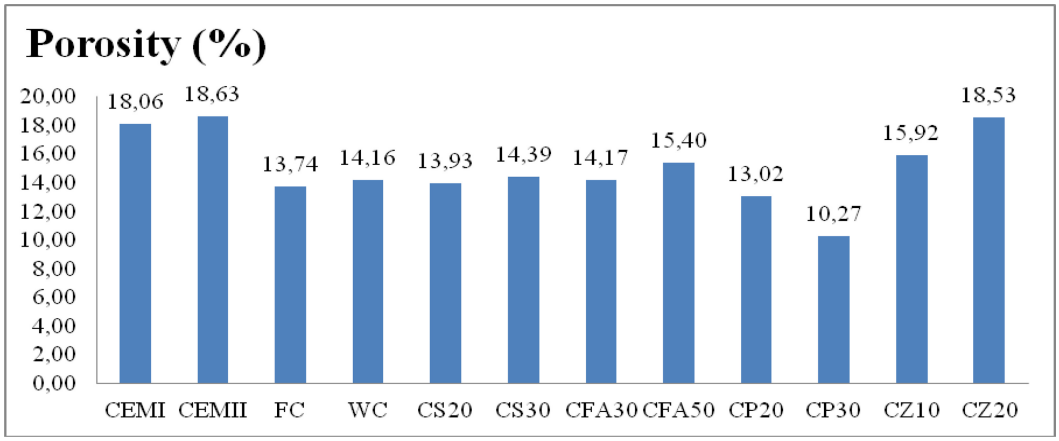

Figure 4. Open porosity.

the high flexural strength of these mortars with natural pozzolan, further investigation is needed. In Table 3, all the mechanical characteristics of the mortar mixes are shown.

Regarding porosity measurements (Fig. 4), it seems that there is no correlation between strength and porosity of the mortars CEMI, CEM II, CZ10 which exhibited the higher porosity. The CZ20 mixture with 20% zeolith also presented high porosity. However, capillary absorption (Fig. 5) seems to be correlated with the porosity.

Based on these remarks it could be said that pre-drying at 100°C in an oven had an effect on enhancing microcracking, contributing to porosity and capillarity.

Anyway, it seems clear that porosity and capillarity of mortars based on cements or binding systems with SCM(s) is generally low (apart from CZ10, CZ20) the lowest values corresponding to those of CP20, CP30 mixtures.

The results of testing chloride penetration are given in Figure 6.

It is obvious that the addition of SCM(s) spectacularly reduces the chloride penetration. Even in the case of CZ10, CZ20 of high porosity and capillarity, the values are much lower than those of the control mixture and can be characterized as moderate penetrability. The best resistance to chloride penetration is

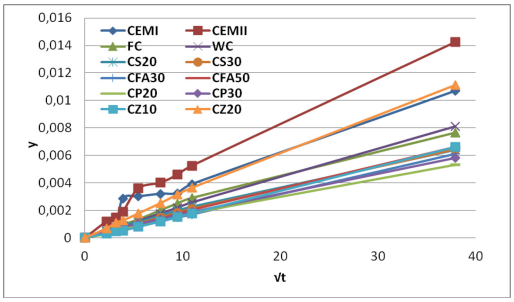

Figure 5. Capillary absorption.

observed in the mixtures with natural pozzolan characterized as a very low class of chloride penetrability. Fly ash as SCM(s) also reduces chloride penetration. The CFA50 and CFA30 are characterized by very low penetrability, while FC shows moderate penetrability. Low to moderate penetrability also characterized the CS30, CS20 mixes with ladle furnace slag. The control mortar mixes belong to the category of high chloride penetrability.

Furthermore, it seems that there is a good relationship between porosity, capillarity and chloride penetration. According to (Glasser, 1988), the mechanism of chloride penetration takes place firstly by capillary

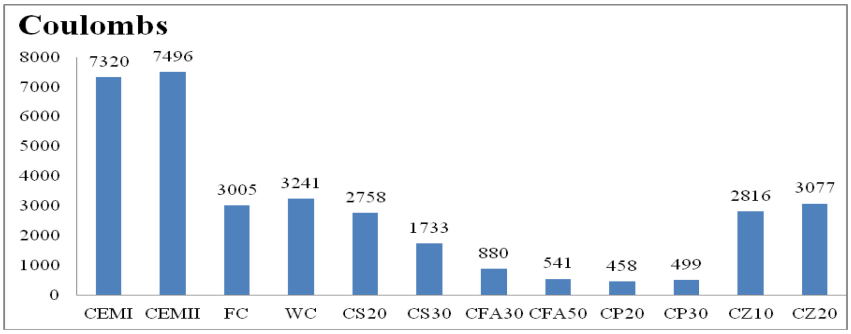

Figure 6. Chloride ion penetration.

absorption (relatively fast stage) and then diffusion starts when accumulation of chloride concentration occurs.

The measurement of chloride penetration results has also shown that apart from capillarity the composition of SCM(s) plays an important role in chloride ion uptake. Calcium aluminate and ferrite phases are considered to impart in the formation of chloroaluminates in which chloride ions are bound. In general, matrices rich in Ca, Al, Mg, SO_{4-2} exhibit enhanced chloride binding capacity (Thomas), (Zihara, 2002). The calcium aluminate hydrates in SCM(s) systems lead to the increase of binding capacity for chlorides. In addition, the SCM(s) increase electrical resistivity of the matrices because they reduce porosity.

4 CONCLUSIONS

The incorporation of significant amounts of SCM(s) (20-50% by mass of cement) in the binding system of a standard mortar either in the form of blended cement (FC) or in a mixed type system has a spectacular reduction in chloride penetration measured by the rapid method of ASTM C1202 in comparison with control Portland cement mortar. In general, the 28-d strength is reduced with addition of SCM(s). The mortars with SCM(s) have also shown a decrease in porosity and capillarity, but the reduction of chloride penetration is greater than expected because of the decrease of porosity and capillarity. This implies that, apart from chloride ion transportation through the capillary pore system, a strong binding capacity is exhibited by the minerals of SCM(s). The greatest chloride ion uptake was showed by the natural pozzolan, followed by calcareous fly ash, ladle furnace slag and zeolith. Among the mortars with 50% calcareous fly ash, the FC in blended form indicated higher chloride penetration in comparison with that of CFA50, in which the fly ash was added in the mixer.

REFERENCES

ASTM C1202-97.

Bijen J. (1998), "Blast Furnace Slag for Durable Marine Structures", *NNC/Beton-Prisma*, Hertogenbosch.

BS 1881-209:1990.

CEB (1992), *Durable Concrete Structures: Design, Guide CEB Bulletin D'Information No 183*, Thomas Telford, London.

Collepardi M. & Biogini S. (1989), "Effect of water/cement ratio , pozzolanic additions and curing time on the chloride penetration", *Proceedings Of International ERMCO Conference Stavanger, Norway*, pp. 606–615.

Collepardi M. (2006), "The New Concrete", edited by Gr. Tintoretto & V. Verdi, pp. 124–139.

EN196-1.

EN 1015-3.

EN 1015-18.

EN 13282-1.

Gjorn O.E. (1983), "Durability of Concrete Containing Condensed Silica Fume", Proceedings Of CANMET/ACI International Conference ACI SP-79, ed. V.M. Malhotra pp. 695–708.

Gjorn O.E. (2009),"*Durability Design of Concrete Structures in Severe Environments*", edition by Taylor and Francis, pp. 60–71.

Glasser F.P., Luke K. & Angus M.J. (1988), " Modification of cement pore fluid composition by pozzolanic additives", *Cement and Concrete Research* 18(1), pp. 165–178.

Hassan Zihara & Kazuo Yamada (2002), "Chloride penetration into concrete. Review of mechanisms and models", *Taiheio Cement Magazine*, pp. 123–138.

RILEM CPC 11.3

Shi Caijun (2004), "Effect of mixing proportions of Concrete on its electrical conductivity and the rapid chloride permeability test (ASTM C1202 or ASSHTO T277) results", *Cement and Concrete Research*, 34, pp. 537–545.

Thomas M.D.A and Bamforth P.B., "Modeling chloride diffusion in concrete. Effect of fly ash and slag", *Cement and Concrete Research* v.29, pp. 487–495.

Torii K., Sasatani T. & Kawamura M. (1998), " Chloride Penetration in Concretes Incorporating Mineral Admixtures in Marine Environment", *Proceedings of 6th CANMET/ACI Conference SP 178-36*, editor V.M. Malhotra, pp. 701–707.

Zhang M.H., Bilodean A., Malhotra V.M., Kim K.S. & Kim J.C. (1999), "Concrete incorporating supplementary cementing materials. Effect on compressive strength and resistance to chloride ion penetration", *ACI Material Journal,* 96(2), pp. 181–189.



Taylor & Francis
Taylor & Francis Group
http://taylorandfrancis.com

Concrete Solutions – Grantham et al. (Eds.)
© 2016 Taylor & Francis Group, London, ISBN 978-1-138-03008-4

Bonding properties of magnesium phosphate cement-based repair materials

Caijun Shi, Nan Yang, Linlin Chong & Zemei Wu
College of Civil Engineering, Hunan University, Changsha, China

Jianming Yang
Department of Civil Engineering, Yancheng Institute of Technology, Yancheng, China

ABSTRACT: Phosphate cement-based materials, produced from dead burnt MgO, KH_2PO_4, and a certain amount of retarders shows exceptional advantages as repair materials due to their quick setting and hardening properties. This paper investigated the effects of bonding agent, curing age and conditions, interfacial moisture conditions and treatments on bonding properties between Magnesium Phosphate Cement (MPC) and Ordinary Portland Cement (OPC) mortars. The bonding mechanisms of MPC from both physical and chemical aspects are discussed as well. The results showed that specimens showed favorable strength under natural conditions, but an over high temperature was detrimental for the strength development. A suitable interfacial saturated surface with brushed treatment demonstrated higher strength. Use of the MPC paste as the bonding agent could improve its bonding properties. Besides, the higher matrix strength indicated higher strength of repaired specimens.

1 INTRODUCTION

With the aging of infrastructure, some environmental factors, such as loading, temperature change and corrosion medium will bring some deterioration and lead to cracking and eventually failure of Portland cement concrete. It becomes more and more important to investigate appropriate methods and materials to repair these failed structures and extend their service life. In this case, complex decisions have to be made in the selection of repair materials. Ideal repair materials are supposed to not only have high mechanical properties and durability, but also good compatibility with the existing substrate (Morgan, 1996).

Magnesia-Phosphate Cement (MPC) composed of dead burnt MgO powders, soluble phosphates and admixtures in certain proportions is a kind of new inorganic cementitious material and can react with water to form phosphate hydrates. As a repairing material, MPC has superior advantages over conventional Portland cement based mortar or paste, which includes short setting and hardening time, high early strength, low drying shrinkage and excellent resistance to bonding, wearing, freezing and thawing. . Much research has been carried out on phosphate cement-based materials and most of them are mainly focused on hydration characteristics (Soudée and Péra, 2000, Chang et al., 2013, Yang et al., 2011, 2013), mechanical properties (Wang, 2006, Jiang and Zhang, 2002) of the materials. However, research on the bonding properties of phosphate cement based materials as repair materials for Portland cement matrices is limited. Tang (Tang, 2006) found that phosphate cement has good compatibility with old concrete, and the repair is effective, but did not provide further explanation. Yang (Yang, 1999) investigated the effects of water to cement ratio, cement to sand ratio and the amount of fly-ash on bonding characteristics of magnesium phosphate cement and Portland cement. The results showed that the bonding strength increased as the ratio of water-cement and cement sand ratio decreased. Ding (Ding, 2005 a, b, c) studied the mechanical properties of magnesium phospho-silicate cement mortar under different curing temperature. They confirmed that the phosphate cement-based material could maintain good strength development rate and bond strength under negative temperature. (Yang et al., 2000) studied the coefficient of thermal expansion and elastic modulus of MKPC and found these values were similar to those of ordinary Portland cement.

The objective of this paper is to study the effect of curing conditions, interfacial moisture conditions and treatments, bonding agent, matrix and strength of repairing materials on bonding properties of Magnesium Phosphate Cement (MPC) with Ordinary Portland Cement (OPC) mortars. The bonding mechanisms from both physical and chemical aspects are discussed.

2 RAW MATERIALS AND TEST METHODS

2.1 *Raw materials*

MPCs prepared with dead burnt magnesia (MgO), monopotassium phosphate (KH_2PO_4, MPP), borax ($Na_2B_4O_7{\cdot}10H_2O$), disodium hydrogen phosphate

Table 1. Chemical composition of dead-burned magnesium oxide (wt/%).

MgO	CaO	SiO_2	Fe_2O_3	Al_2O_3
96.80	1.33	0.92	0.34	0.16

Table 2. Mixture of MPC Paste.

MgO/MPP	Broax/MgO	DHP/MPC	W/S*
2.75	3%	3.5%	0.12

* W/S-water to solid ratio

Table 3. Mixture of MPC Mortar.

Batch	MgO/ MPP	Broax/ MgO	DHP/ MPC	Sand/ binder	W/S
MPC-1	2.75	3%	3.5%	1:1	0.18
MPC-2	2.75	3%	3.5%	1:1	0.24

(DHP, $Na_2HPO_4 \cdot 12H_2O$), and chloride based retarding agent (M) with the mixture showed in Table 2 were used in this study. A MgO/phosphate salt mass ratio of 2.75:1 was employed, Dead-burned magnesium oxide (MgO) powder with a specific surface area of 238 m^2/kg was obtained by grinding magnesia sand. The chemical composition of the magnesia is summarized in Table 1. The potassium dihydrogen phosphate (KH_2PO_4) used in the study was an industrial grade product with particle size of 245–350 μm. The composite retarder (M) was prepared by borax, disodium hydrogen phosphate dodecahydrate, and chloride at a certain percentage. Grade 42.5 ordinary Portland cement was used for substrate OPC mortar with the proportion of C: S: W = 1: 3: 0.5.

2.2 *Specimen preparation and curing*

2.2.1 *Compressive strength substrate OPC mortar*

The substrate OPC mortars were prepared with the proportion of C: S: W = 1: 3: 0.5. Cubic specimens of 40 × 40 × 40 mm^3 were prepared for compressive strength testing. The specimens were demolded after 24 h, then they were cured under room temperature 20 ± 1°C and relative humidity 90% until designed testing ages of 13–14 d. All specimens were cured for 24 h before they were demoulded and put in a room at a temperature of 20 ± 1°C.

2.2.2 *Specimens for compressive strengths test and pullout-out testing*

MPC mortar was prepared according to the designed formulae as shown in Table 3. Borax, DHP, M, and water were poured into the mixer in sequence and mixed for 60 s at low speed. Sand was then added and mixed for another 60 s at low speed and 30 s at high speed. At the end, magnesia was added slowly and mixed for 90 s at low speed and paused for 30 s before mixing at high speed for 90 s. The mortar mixture was then poured into 40 × 40 × 40 mm^3 cubic moulds for compressive strength testing. Two batched of MPC mortars were prepared according to the mixture showed in table 3. Borax, DHP, M, and water were poured into the mixer in sequence and mixed for 60 s at low speed. Sand was then added and mixed for another 60 s at low speed and 30 s at high speed. Magnesia was added slowly and mixed for 90 s at low speed and paused for 30 s before mixing at high speed for 90 s.

A dog bone shape mould, as shown in Figure 1, was used for pullout testing. The mold was divided into two halves by 1 mm thick plates. The substrate was put in the half area of mold, and the MPC mortar was cast into the remaining half and compacted. For each type of mixture, five specimens were prepared. All specimens prepared by were cured at a temperature of 20 ± 5°C and a relative humidity of 50% after1d of casting.

2.2.3 *Interfacial treatments*

The effects of different factors, including curing conditions, interfacial moisture conditions and treatments, bonding agent, matrix, and strength of repairing materials, as shown in Table 4, on bonding properties were studied. In this study, the combination of fixed for A3, S3, C3, M3, and T3 were chose as a control group. For the experiment of influence of interface agent on bonding strength, different interface agent type (A1, A2, and A3), control group for other factors (S3, C3, M3, and T3) were applied.

2.3 *Testing method*

2.3.1 *Compressive strength*

The compressive strength was carried out at 3, 7, 14, and 28 d according to the Chinese Standard GB/T 17671-1999, by a universal testing machine with the vertical load applied axially at a constant rate of 0.375 MPa/min. For each measurement, 4 specimens were used and the average was reported as the result.

2.3.2 *Interfacial bonding strength*

The pullout testing setup is shown in Figure 1. The bonding strength test was conducted on a cupping machine with loading rate 2 mm/min. In order to avoid the effect of eccentricity and torque, the applied pullout force should be kept at the direction of the axial direction of the specimen. The load values and fracture position were recorded and the width and height of cross section were measured with Vernier calipers with an accuracy of 0.02 mm.

The average bonding strength τ was calculated as follows:

$$\tau = F/bh \quad (1)$$

Where F is the maximum pullout load; b is thewidth of the cross section of specimen, mm; and h is the height of the cross section of specimen, mm.

Table 4. Different interfacial treatments for the matrix.

Number	Factors	Treatment name	Detailed information for treatment method
A1	interfacial agent	OPC	Use of the OPC paste with water to cement ratio of 0.3 as the bonding agent with 0.5–1 mm thickness.
A2		MPC	Use of the MPC paste showed in Table 2 as the bonding agent
A3		–	None bonding agent
S1	ages	3 d	3 days standard curing
S2		7 d	7 days standard curing
S3		28 d	28 days standard curing
C1	curing methods	High temperature curing	$40 \pm 2°C$, RH = $50\% \pm 5\%$
C2		Standard curing	$20 \pm 2°C$, RH > 95%
C3		Air curing	$20 \pm 2°C$, RH = $50\% \pm 5\%$
M1	surface moisture state	Dry	Put the specimen into an oven at a temperature about $40 \pm 2°C$ for 1 d after 13 days initial curing in standard condition
M2		Wet	OPC substrates after 14 days in standard curing room was directly used
M3		Half-dry	OPC substrates after 13 d in the standard curing room, followed by 1 d in air to get a half-dry surface
T1	Surface roughness	formed surface	Produced by casting with no further treatment
T2		fractured interface	Tensile rupture interface of substrate
T3		Brushed interface	A steel wire brush was used to further prepare the surface of substrate

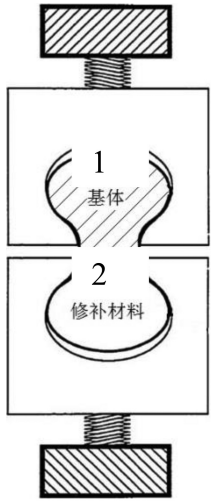

1. Matrix; 2. Repairing Material

Figure 1. Pullout specimen and test setup.

2.3.3 *Drying shrinkage*

For drying shrinkage measurement, OPC and MPC mortars were prepared with the size of $25 \times 25 \times 280$ mm. The initial length was recorded at 3 h after the casting of the specimens (L0), the length changes were measured at age of 1, 3, 7, 14, and 28 days (L_t).

$$\xi_{st} = \frac{L_0 - L_t}{L_b} \times 100\% \quad (2)$$

2.3.4 *Microscopic analysis*

The specimens for microstructural observation were cast and cured in the same condition as that for strength testing. They were dried to constant weight at 60°C. The microstructure of the hardened MPC mortars was examined using a QUANTA200 Environmental Scanning Electron Microscope (SEM) equipped with an energy dispersive spectrometer (EDS). The phase analysis was carried out by a Rigaku D/max-RB X-ray diffraction using Cu-Kα (100 mA, 40 kV) radiation as the source with a step size of 0.05°. Thermal analyzer was used for quantative determination of hydration products in a N_2 atmosphere from room temperature to 600°C at heating rate of 10°C/min.

3 RESULTS AND DISCUSSION

3.1 *Compressive and bonding strengths*

The compressive strength of the OPC and MPC mortars at 3, 7, and 28 d is presented in Fig. 2. The OPC represents the substrate OPC mortars, while the MPC – 1 and the MPC – 2 correspond to the group shown in table 2. As can be seen, the compressive strength of the magnesium phosphate cement is very high at early age but develops slower after seven days than OPC samples. The compressive strength of MPC-2 mortar was higher than that of MPC-1 mortar and OPC mortar at all ages.

The bonding strengths for MPC-1, MPC-2 and OPC mortar at different ages are shown in Figure 3. The bonding strength of MPC paste samples remained almost the same after 14 d, so the 14-day bonding strength was used in this paper. From the figure we can see that the bond strength of MPC repaired samples was larger than that of OPC repaired samples. The OPC strength development was slow at early age. The bonding strength of OPC at 3 d was around 40% of

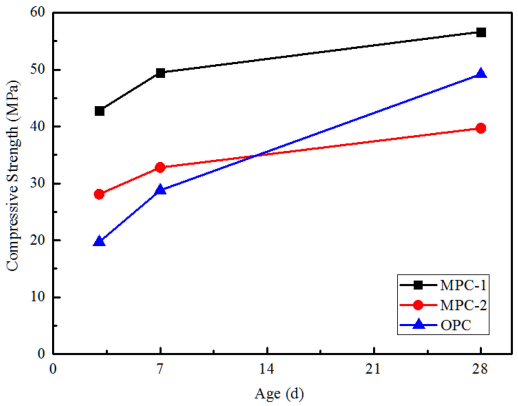

Figure 2. Compressive strength of OPC and MPC motars.

that of MPC repaired specimens. Although the compressive strength of the OPC mortar at later ages was higher, the bonding strength of the MPC repaired samples at 14 d was still 79% greater than that of the OPC repaired samples. The results indicate that MPC repaired samples showed a prominent bond strength which was 69% higher than that of whole casting MPC specimen at 28 days. According to the literature (Ping et al., 2008), the bonding strength of ultra-fine Portland cement with silicon powder, expansive agent, and water reducing agent of net cement slurry as interface agent, was 2.18 MPa. This was lower than that between MPC and OPC mortar in this study. From the experimental results, the fluidity of MPC-1 mortar was lower than the MPC-2 mortar. In order to guarantee the process of molding and full compaction of the substrate interface, MPC-2 was adopted unless otherwise indicated in the following experiments.

3.2 *Mechanism of bonding MPC mortar and OPC mortar*

The good bonding strength of MPC mortar to OPC mortar can be explained from both physical and chemical aspects as follows. Magnesium phosphate cement bond properties are mainly caused by chemical bonding and followed by physical bonding, contrary to Portland cement. Generally, the interface between repairing material and old OPC mortar is the weakest zone and failure always occurs at this zone. Volume compatibility between repairing material and substrate is the key factor that affects interface properties.

The shrinkage of both MPC mortar and reference OPC mortar are shown in Fig. 4. It can be seen that all of the MPC mortars demonstrated less shrinkage than OPC mortar. The shrinkage of OPC sharply increased to 600 microstrain at 7 d, while the shrinkage of MPC-2 mortars was only around 43% of OPC mortar. After that, the shrinkage of both OPC and MPC mortars tended to be stable.The development of shrinkage at early age is considered to be largely due to the chemical reaction and the evaporation or migration of free water determines the shrinkage at later age. The MPC

Table 5. Bonding strength of samples prepared with different cement-based materials.

Batch	Repairing Material	Age	Bonding strength (MPa)	Percentage of the strength of MPC at 14 d (%)	Percentage of the strength of OPC at 28 d (%)
O3	OPC	3 d	0.51	13.6	10.0
O7		7 d	0.82	21.9	16.0
O28		28 d	1.97	52.5	38.5
M1-3	MPC-1	3 d	1.95	52.0	38.1
M1-7		7 d	2.51	66.9	49.0
M1-28		28 d	2.94	78.4	57.4
M2-3	MPC-2	3 d	1.24	33.1	24.2
M2-7		7 d	1.95	52.0	38.1
M2-28		28 d	2.59	69.1	50.6

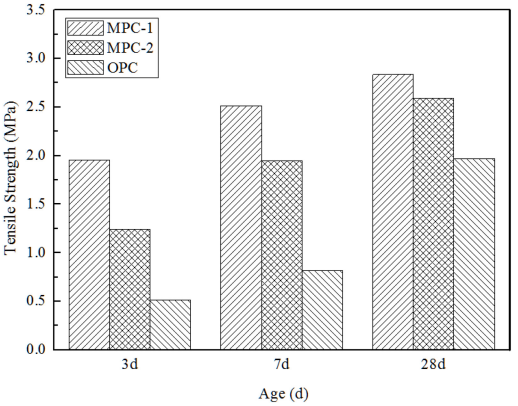

Figure 3. Bonding strength of different materials.

mortars had less shrinkage because of the following reasons: (1) the W/S of MPC mortar (0.18, 0.24) was much lower than that of OPC (0.5), its hydration rate and hydration degree was much higher than those of OPC. Therefore, MPC matrix had less porous microstructure and contained less free moisture, so MPC demonstrated much lower the drying shrinkage; (2) the main reaction products of magnesium phosphate cement are crystalline while that of Portland cement are C-S-H gel. These two hydration products have different thermal expansion coefficients; (3) less chemical shrinkage of magnesium phosphate cement occurred during the hydration process. From the theoretical volumes of individual ingredients as well as the volume of the reaction products in the MPC system given in Table 6, the volume change after reaction can be calculated by the following equation:

$$\text{Estimated volume change} = \frac{155.46 - 10.61 - 58.17 - 90}{10.61 + 58.17 + 90} \times 100\% = -2.09\%$$

In conclusion, larger shrinkage accelerated the formation of microcracks and macroscopic defects at the interface, which leads to lower bonding strength of

Table 6. Properties of reactants and product during MPC hydration.

	MgO	KH_2PO_4	$5H_2O$	$MgKPO_4{\cdot}6H_2O$
Molar mass (g/mol)	40	136	18	266
Density (g/cm^3)	3.77	2.338	1	1.711
Volume (cm^3/mol)	10.61	58.17	90	155.46

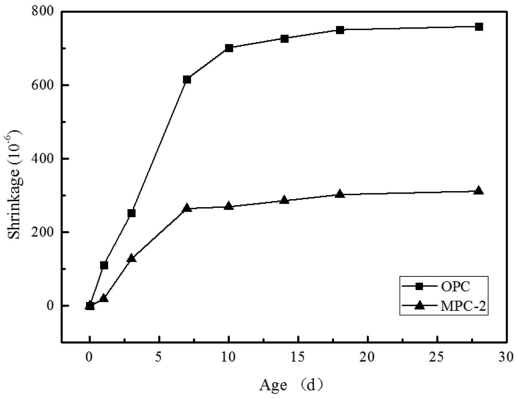

Figure 4. Shrinkage of OPC and MPC-2.

Portland cement than the phosphate cement. Previous studies (Yang Q. et al. 2000, Yang, N. et al.2013) also indicated that the thermal expansion coefficient of MPC is 9.6×10^{-6}/°C, similar to that of ordinary portand cement of 7×10^{-6}/°C, which results in good volume compatibility.

Figure 5 shows the microstructure of the interfacial layer between MPC and OPC mortar. Figure 5(a) shows the backscattered electron of the interfacial layer. High brightness on the left side is Portland cement matrix, and the relatively dark area of right side is MPC mortar matrix with elements, such as Mg, K, and P, etc. The border of the two mortars is evident. Figure 5(b) shows the SEM observation of the interface of the MPC to OPC matrix. As can be seen, the interface between MPC mortar and OPC mortar was dense and continuous without micro-cracks. This confirmed good volume compatibility between MPC mortar and the OPC mortar matrix. Figure 5(c) and 5(d) show the morphology and EDS analyses of the bonding interface area. The acicular colorless crystal is the main hydration product of OPC – ettringite (AFt) and the amorphous hydration product is C-S-H gel. Elemental analysis of bulk crystal (A) confirmed that the elemental composition present was mainly Mg, P, K, and O. Besides, their measured molar ratio was close to the theoretical value of MKP, which indicates that it was the reaction product MKP. It indicated that the two different hydration products of cement were intersecting and overlapping in the ITZ and generating new amorphous hydration products, so the interface bonding strength of MPC improved.

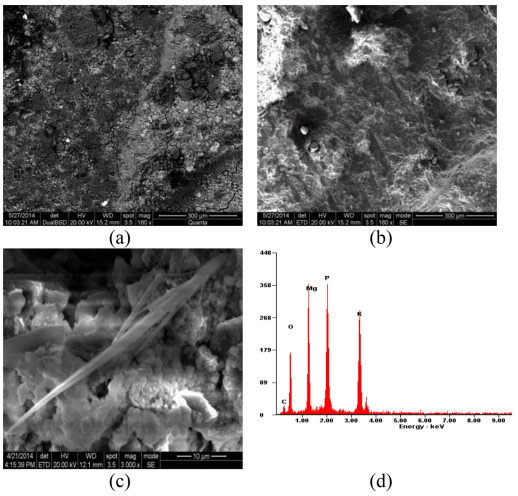

Figure 5. Microstructure of interface between matrix and repairing material ((a) BSE of the interface between OPC and MPC, (b) Microscopic analysis of interfacial zone, (c) Microstructure of hydration products, (d) EDS analysis of area A).

3.3 *Influence of different factors on bonding properties*

3.3.1 *Bonding agent*

The bonding strengths of specimens with different bonding agents are shown in Table 7. The specimens with magnesium phosphate cement paste as bonding agent showed prominent bond strength. When Portland cement paste was used as the bonding agent, the bond strength did not increase but weakened. This is because OPC mixed with magnesium phosphate cement mortar was unfavourable for the two cement's hydration, reducing strength performance and interfacial bond properties.

The interface morphology of specimens with different bonding agents at 28 d are shown in Fig. 6. The upper portion is the repair materials and the lower part is the matrix. The matrix failure surface has a significant difference. Figure 6 (a) shows the specimen fracture morphology without bonding agent. The substrate side interface had some white magnesium phosphate cement, suggesting that repair materials had fully immersed into the matrix. Figure 6 (b) shows the fracture morphology of specimens with OPC paste as bonding agent. Unlike Figure 6 (a), the substrate side interface showed no magnesium phosphate cement repair materials. This indicated that it divided the specimens into two parts as the original instead of promoting the net of magnesium phosphate cement. Figure 6 (c) is the fracture morphology of specimens with MPC paste as bonding agent. The failure mode of both sides is similar; a fracture of fine aggregate caused by tensile fracture had occurred. It indicated that the failures occurred in OPC mortar or in MPC

Table 7. Bonding strength with different agents at different ages.

Batch	Bonding agent	Bond strength (MPa)		
		3 d	7 d	28 d
A1	OPC	1.25	1.58	1.85
A2	MPC-2	2.07	2.41	2.99
A3	–	1.94	2.27	2.52



(a) (b) (c)

Figure 6. Fracture surface of specimens with different bonding agents at 28 d ((a) None bonding agents (b) OPC as bonding agents (c) MPC as bonding agents).

mortar and the actual bond strength between the two kinds of mortar was higher than the flexural strength of either material.

Interface agents can reduce the voidage and gap at the interface to ensure good bond between old and new specimens and increase the adhesive force. In addition, the cement particles of the interfacial agent can penetrate into the cracks and pores on the surface of the specimen and increase the mechanical interaction force to improve the bonding strength. The permeability of the paste is higher than the mortar; it can penetrate into the pores of the substrate and produce hydration products to make the interface agent layer and mortar bond together as a whole, so the bond strength improves. Besides, when the specimens were cured in air, the shrinkage of paste in the interface agent was greater than the mortar. The volume compatibility of old Portland cement mortar specimens and the new casting of magnesium phosphate cement mortar was poor. The shrinkage of the interface agent caused macro cracking in the transition layer and permeable zone, which reduced the bond strength.

3.3.2 *Curing age*

Results on the bonding strength at different curing ages are given in Table 8. The compressivestrength of the substrate OPC mortar developed with hydration time.

Table 8. Bonding strength under different curing age.

Batch	S1	S2	S3
Moisture condition	3	7	28
Compressive strength	19.7	28.8	48.7
Bonding strength (MPa)	1.68	2.31	2.58

Table 9. Bonding strength under different curing conditions.

Batch	C1	C2	C3
Curing condition	High temperature Curing	Standard Curing	Natural Curing
Bonding Strength (MPa)	1.36	1.83	2.31

The higher the strength is, the better the bond strength is. This is because of the high hydration degree of the cement with curing age, resulting in the continual improvement of strength and increase in the interfacial mechanical interaction. Besides, the shrinkage of OPC mainlyoccurredatearly age and basically completed after 7 d. Its volume compatibility under long term curing was high, which further accelerated bond performance.

3.3.3 *Curing condition*

The bond strengths under different curing condition is shown in Table 9. The results indicated that the specimens under natural conditions obtained the largest pullout values, which were 26% and 36% higher than that under standard and high temperature curing, respectively. A higher hydration temperature is good for the strength promotion of cement. The hydration reaction of MPC is usually very fast and a large amount of heat in the hydration is emitted, so the reaction rate speeds up, which gives good strength development at low temperatures. However, when the temperature was too high, water inside the specimens began to evaporate and the hydration products decomposed, leading to change in the structure of the hydration product and thus decreased strength. The bond strength of MPC under dry air conditions was more favorable than standard curing. This was because when the water from the surrounding environment infiltrated material through the surface, some unreacted phosphate was dissolved and the amount of reactant and hydration products was decreased. At the same time, it increased the porosity of the structure.

Therefore, high temperature or high humidity influenced the development of bond strength. No special curing is needed for the phosphate matrix, which enhances its great adaptability.

3.3.4 *Moisture in surface of substrate OPC mortar*

For common repair materials, such as Portland cement, aluminate cement, iron aluminate cement, and alkali

Table 10. Bonding strength of different moisture conditions of the surface.

Batch	M1	M2	M3
Moisture condition	Dry	Wet	Half-dry
Bonding strength (MPa)	1.78	1.52	2.31

-wet surface, the broken surfaces of substrate OPC mortar specimens directly from the standard curing condition; half-dry surface, the broken surfaces of substrate OPC mortar cured in air for1day after13 days standard curing; dry surface, the broken surfaces of substrate OPC mortar dried at $40 \pm 2°C$ for 1 day after water is taken out.

Table 11. Bonding tensile strength with different interfacial treatments.

Batch	T1	T2	T3
Treatments	formed interface	Brushed interface	Fractured interface
Bonding strength (MPa)	1.92	2.31	1.21

slag cement, the moisture conditions usually have an important influence on the interface bond strength. Table 10 shows the bond strength of MPC mortar repair material to OPC mortar substrate with different moisture interfaces. The specimens with dry surfaces showed the highest tensile strength and those with wet surfaces the lowest. This is due to the difference in water content on the interface. The moisture content of the dry substrate interface was much lower than the new mixed magnesium phosphate cement mortar. Water can move to the dry substrate part through the interface, resulting in less hydration products and lower strength. The moist substrate interface has poor bonding strength value caused by excess water in the interface and porous hydrated products, thereby reducing the strength. So there is no need to spray water in the interface or use moist curing for magnesium phosphate cement as repairing material in engineering.

3.3.5 *Surface roughness*

The influence of different interfacial treatments on the bond strength are shown in Table 11. The bonding strength with a brushed interface was 20% higher than that with a formed interface. The rough bond surface increased the effective bond area and led to a higher bond strength. The bonding strength of the specimens with original pull damage-surface was only 52% of those with rough interface treatment. For a fractured interface, micro-cracks can be induced leading to reduction in bond strength. Therefore, in the process of practical engineering of repair, it is necessary to remove the original damage-surface and roughen the surface as well.

4 CONCLUSIONS

Based on the experimental results presented in this study, the following conclusions can be drawn:

(1) The MPC mortar had distinctly higher bond strength than that of OPC mortar. The bonding strength of OPC mortars at 3 d was 26% lower than that of MPC mortar. The MPC mortars exhibited much better volume stability than that of OPC mortar, while the thermal expansion coefficient of MPC was similar to that of ordinary Portland cement. Besides, itis believed the interface exist some chemical interlock between MPC and OPC substrate caused by new amorphous hydration products that improve the bonding performance.

(2) The bond strength of MPC mortar to OPC mortar substrate was higher with the MPC paste as the bonding agent than OPC paste. The higher matrix strength indicated a higher strength of repaired specimens. Specimens under room temperature and humidity was favorable to strength development, but over high temperature was detrimental for the strength development. A wet Interface and handling will also affect the bonding strength, and the most suitable interfacial condition was a saturated surface with brushed treatment, which demonstrated higher strength.

REFERENCES

Chang Y & Shi C.J. et al. 2013. Effect of Fineness of Magnesium Oxide on Properties of Magnesium Potassium Phosphate Cement. *J Chin CeramSoc(in Chinese)* 41(4): 67–74.

Ding Z. &Li Z. 2005. Effect of aggregates and water contents on the properties of magnesium phospho-silicate cement[J]. *Cement and Concrete Composites* 27(1): 11–18.

Ding Z, &Li Z. 2005. High-early-strength magnesium phosphate cement with fly ash. *ACI Materials Journal* 102(6).

Ding Z. 2005. Research of Magnesium Phosphosilicate Cement. *Hong Kong: Hong Kong University of Science and Technology.*

Jiang H.Y. & Zhang L.M. 2002. Investigation on ultra-high early strength phosphate concrete repairing materials, *Highway.* 3.

Morgan, D. R. 1996. Compatibility of concrete repair materials and systems. *Construction and building materials* 10 (1): 57–67.

Ping F& Zhenyu H& Ruiwen Z. et al. 2008. Study on adhesive tensile strengh of cement-based interfacial agents. *Materical Review* 3: 319–321.

Soudée E & Péra J. 2000. Mechanism of setting reaction in magnesia-phosphate cements. *Cement and Concrete Research* 30(2): 315–321.

Wang H.T.2006. Investigation on high performance phosphate cement based materials. (in Chinese, dissertation). Chongqing: Chongqing Unviersity.

Yang Q, Wu X. 1999.Factors influencing properties of phosphate cement-based binder for rapid repair of concrete. *Cement and Concrete Research* 29(3): 389–396.

Yang Q & Zhu B & Zhang S, et al. 2000. Properties and applications of magnesia-phosphate cement mortar for rapid repair of concrete. *Cement and Concrete Research* 30(11): 1807–1813.

Yang, N. & Shi, C. & Yang, J.& Chang, Y. 2013. Research progresses in magnesium – phosphate cement-based materials. *Journal of Materials in Civil Engineering* 26(10): 04014071.

Tang, C.P. 2006. Investigation on ultra high early strength phosphate cementrepairing materials. (in Chinese, dissertation). *Chongqing: Chongqing Unviersity*.

Yang, J.M. & Qian, C.X. & Jiao, B.L., et al. 2011. Effect of $Na_2HPO_4 \cdot 12H_2O$ on hydration and hardening properties of magnesium phosphate cement paste. *Journal of building materials,* 14(3): 299–304.

Yang, J.M. & Shi, C.J & Chang Y, et al. 2013. Hydration and hardening characteristics of magnesium phosphate cement paste ccontaining composite retarders. *Journal of building materials,* 16(1): 43–49.

Concrete Solutions – Grantham et al. (Eds.)
© 2016 Taylor & Francis Group, London, ISBN 978-1-138-03008-4

Effectiveness of different repair materials and methods used for the repair of chloride corroded reinforced concrete structures

Kosmas K. Sideris
Laboratory of Building Materials, Department of Civil Engineering, University of Thrace, Xanthi, Greece

Efstratios Manikas
GEOTEST SA

Athanasios Michalakopoulos
CERS – Structural Rehabilitation

ABSTRACT: Chloride induced corrosion is the main mechanism negatively affecting the durability of reinforced concrete structures. Since corrosion occurs, an extended repair is performed in order to ensure that the structure will meet the initially scheduled service life. The need for durable repairs of chloride damaged concrete structures is significantly increasing during the last years. In the present paper the effectiveness of different repair materials mainly used for patch repairs was experimentally investigated. A total of eighteen reinforced concrete beams were subjected to accelerated chloride corrosion in the laboratory. All of them were repaired after a certain corrosion scenario using different materials covering the requirements of EN 1504 Standard. After the repair was completed, concrete beams were again subjected to the same corrosion scenario in order to investigate the effectiveness of different materials and combinations currently used in the market. The most effective solution found to be the combined use of sacrificial anode with hydrophobic impregnation.

1 INTRODUCTION

Deterioration of concrete structures due to cracking and spalling of surface cover is a major problem in civil engineering. When serviceability of the deteriorated structure becomes an important issue, in comparison with the reconstruction of the concrete elements, the most cost-effective and easily achieved solution is often to perform an extended repair (more than 50% of the structure surface is repaired). Repair and restoration of concrete structures has become an important market during the last decades since there is a considerable amount of aged reinforced concrete structures globally that are, and will continue to, give signs of extended corrosion. The total costs for maintenance of all types of buildings can be assumed to be higher than about 20 billion $ per year. (Raupach, 2006). A significant part of this cost is spent on repair and protection of concrete structures. It is therefore easily understood that the need for durable repair methods and materials is of great importance.

The European Standard EN 1504: Products and systems for the protection and repair of concrete structures provide an integrated framework for the concrete repair industry throughout Europe. Parts 2 to 7 of EN 1504 cover the properties of the materials used in repair works and are the basis for CE marking of the different products and systems to be used for protection and repair of concrete structures. Part 8 regulates the quality control of the products, part 9 describes the principles for the use of the products and part 10 gives a general guideline for site application and quality control of the works.

The effectiveness of different repair materials mainly used for patch repairs is experimentally investigated in the present paper.

2 MATERIALS AND METHODS

A total of sixteen concrete beams were produced. Specimens had a 250 × 150 mm cross-section and length of 100 mm. The concrete used belonged in the strength class C16/20, in order to simulate the poor quality concrete quality used in practice 40 years ago. The main reinforcement consisted of two 12 mm diameter bars on the upper side and two 14 mm diameter bars on the lower side of the beam. Stirrups were 8 mm bars every 10 mm (φ8/10 mm) [Fig. 1].

The concrete specimens were cured under wet burlaps for 28 days. After this age, all specimens were subjected to electrochemical corrosion. They were placed on wooden pedestals in a corrosion basin containing 3% by weight solution of NaCl. The reinforcement cage of each specimen was connecting to an electrical circuit so as to serve as the anode of the

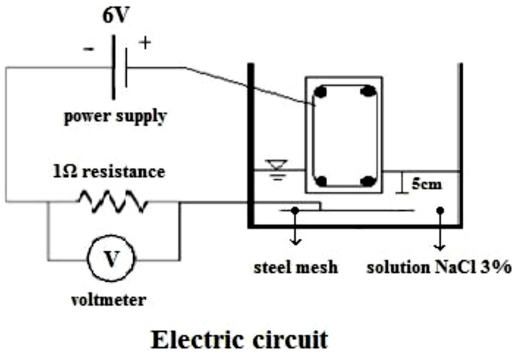

Figure 1. Electric circuit.

corrosion cell. An external steel mesh immersed in the basin was used as the cathode. Both anode and cathode were connected to a constant power supply of 6 V. Ammeters were interpolated between anode and the power supply in order to measure the electric current passing through each specimen in different time intervals. During the first phase of the experiment, all specimens were subjected to 5 wetting and drying cycles. Each cycle had duration of 15 days; 3 days wetting period and 12 days drying period. During the wetting period specimens were immersed in the corrosion basin and connected with the electric circuit. The level of the solution was kept 5cm over the lower surface of the beam. During the drying period, specimens remained in unsheltered outdoor conditions.

The depleted mass of iron ΔMs (g) consumed over the time Δt (s) was estimated from the current Icorr flowing through the cell using Faraday's Law, which assumes a constant rate of iron depletion:

$$\Delta M_s = I_{corr} * \Delta t * A * (n/F) \quad (1)$$

where A is the atomic mass of iron (55.87 g), n is the valency of the reaction usually taken as 2 (assuming the corrosion product is $Fe(OH)_2$) and F is Faraday's constant equal to 96.487 C (g/equivalent). The mass loss ratio ($\Delta M_s/M_{init}$, mass depleted over the initial mass) was calculated using the initial mean value of the weighted cage mass (7.370 g) and the current readings that had been measured every 24 hours during the wetting periods.

After completion of the first phase, all specimens were moved from the corrosion cell. Sixteen beams were repaired, using different methods and materials according to ELOT EN1504 standard. Each method was applied on two corroded beams. All the methods and the materials used are presented in Table 1. Two beams remained unrepaired and subjected to the second phase of the corrosion experiment in order to be used as reference specimens.

After repair, all specimens were subjected again to 5 more wetting and drying cycles, each one having a duration of 15 days, exactly as during the first phase. Half-cell potential and Icorr measurements were performed throughout the second phase as well. Icorr was assessed using an ammeter. The efficiency of the repair work was estimated by calculating the depleted mass of repaired specimens.

Table 1. Repair materials used according to ELOT EN1504.

Repair material	Principle according to ELOT EN1504-9	Method
Repair mortar 627	3	3.1
Repair mortar Dynamic	3	3.1
Repair mortar M [Strobinis et al]	3	3.1
Galvanic anode XP2	10	10.2
Hydrophobic impregnation	2	2.1
Reinforcement paint 910	11	11.1

Table 2. Combinations of different methods and materials used in repair work.

Specimens' code	Materials
R	Reference (no repair)
9M	910, M
96	910, 627
X9D	XP2, 910, D
X96	XP2, 910, 627
XD	XP2, D
X6	XP2, 627
M	M
6	627

3 RESULTS AND DISCUSSION

Weight loss of steel was assessed using Faraday's Law (Eq 1). Icorr was measured twice in all cycles, just after immersion and before removing the specimens to the drying condition. Half-cell potential measurements according to ASTM C876 standard were also used in order to evaluate the condition of steel reinforcement.

After five wetting and drying cycles, all specimens lost about 6% of their steel mass. Half-cell potential values were in any case in the area of −600 mV, indicating that all beams underwent severe corrosion [Fig 2].

Prior to the repair works, concrete was removed from the lower end of the beams and the corroded reinforcement was cleaned [Fig. 3].

After completion of the repair schedule, all specimens remained in outdoor conditions for 14 days [Fig. 4]. After this age, all beams were immersed in the corrosion basin and the second phase of the experiment (five more wetting and drying cycles) was initiated.

Comparative performance of the repair methods used was evaluated by measuring both the half-cell potential and the corrosion current of repaired specimens at different time intervals. All the repair methods



Figure 2. Visible corrosion at the end of the first phase.



Figure 3. Remove of chloride contaminated concrete from the lower end of the beams.



Figure 4. Concrete beams after completion of the repair work.

were found to be effective since the corrosion potential of all repaired specimens increased by more than 50% [Fig. 5] after the repair. During the next weeks of immersion, the half-cell potential of the repaired specimens was decreased with a rate similar to that of the initial phase.

Corrosion current Icorr also decreased; however some differences were noticed among specimens repaired with different materials [Fig. 6]. The most effective repair from the point of view of corrosion current decrease was that of the X9D combination, whilst the least effective one was the 96 and 6 combinations. After completion of the repair Icorr values increased in a way similar to that of the first phase [Fig. 6].

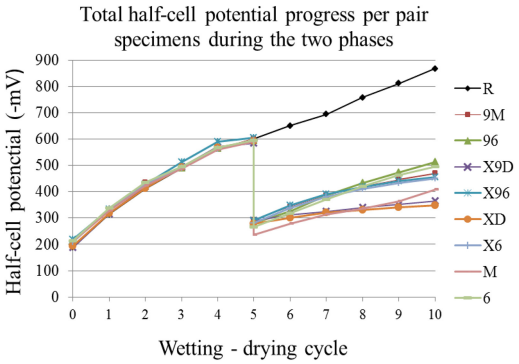

Figure 5. Development of half-cell potential values during the entire exposure period.

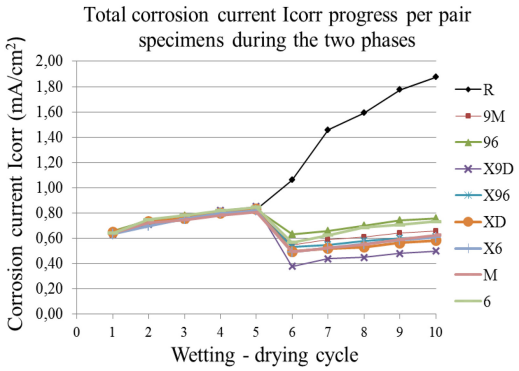

Figure 6. Iccor measurements during the entire exposure period.

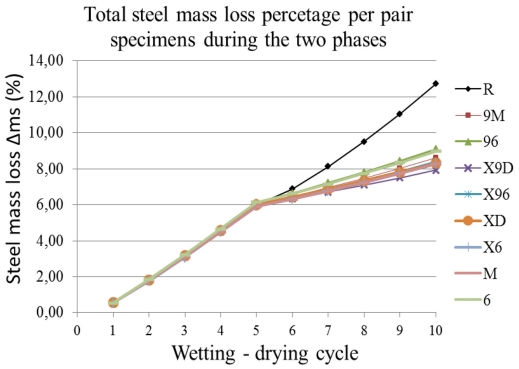

Figure 7. Weight loss of steel rebars during the entire exposure period.

Once the second phase initiated, all specimens underwent further corrosion. Reference beams kept on corroding with an increased rating; Their half-cell potential value decreased down to −900 mV at the end of the exposure period, while their weight loss increased up to 13% [Fig. 7].

All repair combinations were found to be effective since corrosion rate was decreased. The weight loss of

the steel rebars of the repaired specimens measured at the end of the second phase ranged between 9.09% and 7.93%. This is a clear indication that all repair methods offered significant corrosion protection since the steel mass loss decreased between 57% and 72%.

4 CONCLUSIONS

The effectiveness of different repair materials mainly used for patch repairs was experimentally investigated. A total of eighteen reinforced concrete beams were subjected to accelerated chloride corrosion in the laboratory. All of them were repaired after a certain corrosion scenario using different materials covering the requirements of the EN 1504 Standard. All repair combinations tested effectively protected steel from further corrosion since the steel mass loss decreased up to 72%. The combination of galvanic anodes, reinforcement anticorrosive paint and proper repair mortar was found to offer the highest protection under this severe corroding scenario.

ACKNOWLEDGMENTS

Repair materials used in this study were provided by Sika Hellas S.A. This support is greatly acknowledged.

REFERENCES

EN 1504. 2004:. Products and systemsfor the protection and repair of concretestructures – Definitions, requirements, qualitycontrol and evaluation of conformity –

Raupach, M. (2006) Concrete repair according to the New EuropeanStandard EN 1504, in M. Alexander, H.D. Beushausen, F. Dehn andP. Moyo (eds) Concrete Repair, Rehabilitation and Retrofitting -Taylor & Francis Group, London, ISBN 0 415 39654 9, pp.6–8.

Sika Galvashield XP2 Embedded Galvanic Anodes for Corrosion Prevention Downloadable from http://www.epmssupplies.co.uk/Admin/Products/Docments/Sika/Data/Sika%20Galvashield%20XP_XPT_XP2_XP4%20PDS.pdf

Sika MonoTop Dynamic Repair Mortar Downloadable from http://www.technomorfi.gr/UserFiles/file/monotop_dynamic_gr.pdf

Sika MonoTop – 627 Repair Mortar Downloadable from http://www.technomorfi.gr/UserFiles/file/Sika%20MonoTop%20627.pdf

Sika Galvashield XP2 Embedded Galvanic Anodes for Corrosion Prevention, Downloadable from http://www.epmssupplies.co.uk/Admin/Products/Doc ents/Sika/Data/Sika%20Galvashield%20XP_XPT_XP2_XP4%20PDS.pdf

Sika MonoTop – 910N Reinforcement paint Downloadable fromhttp://www.domochemica.com.cy/assets/mainmenu/164/docs/_Sika_Monotop_910___gr.pdf

Strompinis N., Sideris K.K., Douros V-Z, Vitsios I, Zervos I 2014: Self-compacting repair mortars according to BS EN 1504-3. In: *Proceeding of Cocnrete Solutions 5th International Conference on Concrete Repair, Belfast, 1-4 September 2014*: 653–657.

The Concrete Society, 2009. Repair of concrete structures with reference to BS EN 1504. *Technical Report No. 74*. Surrey: The concrete Society.

The Concrete Society, 2011.Cementitious materials. The effect of ggbs, fly ash, silica fume and limestone on the properties of concrete. *Technical Report No. 69*. Surrey: The concrete Society.

Tilly, G. P. & Jacobs, J. 2007.*Concrete repairs.Performance in service and current practice*. UK: IHS BRE Press.

Concrete Solutions – Grantham et al. (Eds.)
© 2016 Taylor & Francis Group, London, ISBN 978-1-138-03008-4

Analytical investigation of bond between ECC matrix and steel reinforcement

S.P. Tastani
Department of Civil Engineering, Democritus University of Thrace, Xanthi, Greece

ABSTRACT: The introduction of Engineered Cementitious Composites (ECC) as a patch repair technique in providing confinement of inadequate anchorages or lap-splices has been studied only lately as one of the applications of ECCs in concrete members and as an alternative to the externally bonded FRP jacketing. This paper analytically investigates the bond – slip relationship and the attained bar strain development capacity of an elastic bar embedded in ECC matrix. In common concrete, the quick exhaustion of tensile strength and strain capacity results in abrupt splitting of the cover concrete. In ECCs with the improved tensile properties as a result of the passive confinement introduced by the mass reinforcement (microfibers), the tensile stresses are resisted at advanced loading stages, thus favorably affecting the bond in terms of strength and toughness. The proposed expression for bond is correlated with published data of bars embedded in ECC matrix and also is used in implementing parametric analyses of important design parameters of the anchorage (geometry, bond strength and bar strain development capacity).

1 INTRODUCTION

In conventional reinforced concrete (r.c.), the interfacial interaction between the surrounding concrete and the reinforcing bar is reflected by the bond stress – slip law of the assembly. In the absence of confinement (i.e. through stirrups) along the embedded length of the bar, the area enclosed by the bond-slip curve and the abscissa of slip (Fig. 1a) -also referred as bond toughness that describes the energy stored in concrete through the rib translation- depends on the poor ability of concrete cover to carry its tensile strength at large deformations imposed by the bar translation. Usually upon small slip values (in the order of 0.2 mm) radial cracking develops in the concrete because the hoop stresses σ_h that balance the radial component of bond σ_r (Fig. 1b), exceed the tensile strength of the material (i.e. f_{ct}). At that point, bar-concrete interaction is released instantaneously and the bar begins to slip uninhibited. This is reflected in the bond-slip law by the steep, post-peak descending branch (Fig. 1a).

In bond tests designed so as the bar and concrete are mobilized in tension (Tastani et al. 2014, Bandelt & Billington 2014, Dagenais & Massicotte 2015), the replacement of concrete (due to its negligible tensile deformation capacity, i.e., 0.015%, Fig. 1c) with an engineered cementitious composite characterized by improved tensile strength and associated strain ductility (Fig. 1c), the cover cracking is postponed to occur at an advanced level of loading (Fischer & Li 2002). (Note: ECC was first introduced by Victor Li in 1993 as a binder with fine-grained ingredients and microfibers

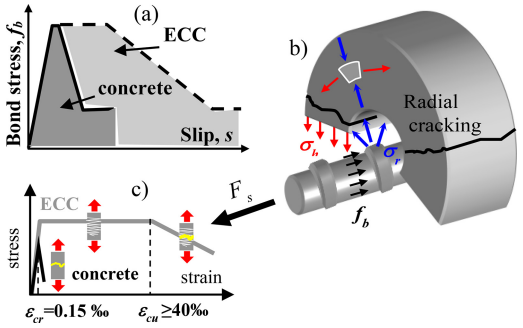

Figure 1. a) Bond stress – slip law of conventional r.c. and reinforced ECC, b) bond stress components (shear f_b and radial σ_r) sustained by concrete hoop stresses σ_h and c) tensile response of ECC versus conventional concrete.

in a dosage as high as 2% per mixture volume). Once cracking initiates, it is sustained firm up to large hoop tensile strains due to the bridging effect provided by the fibers. Upon attainment of the hoop tensile strength in the cover (i.e., $\sigma_h = f_{ct}$ in Fig. 1b), slip of the reinforcement is still negligible due to the compatible elongations of both materials (slip by definition is the relative movement of bar from its surroundings). The elongation compatibility is secured because the ductile ECC has a tensile strain capacity comparable to that of steel reinforcement, in the order of 4–5%. The strong bridging effect provided by the mass reinforcement (i.e. fibers act as an effective confining means in ECC in the hoop direction of the cover) alters the bond

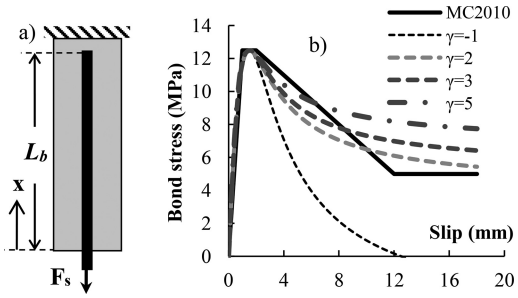

Figure 2. a) The direct tension pullout bond test: both materials are under tension. b)The unified bond-slip law (dashed curves) as compared with the multilinear one of fib MC2010.

failure mechanism from splitting to mixed splitting – pullout (even in the case of very thin cover widths), thus ensuring that the bond strength is sustained up to large values of slip. All the aforementioned response of a bar anchored in an ECC matrix is reflected in the bond law of Fig. 1a by the increased bond toughness denoted by the light grey area.

In the present study, the bond-slip behavior of deformed elastic bars embedded in ECC is analytically investigated (Fig. 2a) regarding the large deformation capacity of the bar cover that enables a much milder descent. For this, a continuous bond-slip relationship (Fig. 2b) is considered in order to approximate the multi-linear bond-slip skeleton curves of Fig. 1a obtained in tests of bars anchored in ECC. The analytical trends are correlated against experimental results (Tastani et al. 2014) and are used to conduct several parametric analyses with parameters of study being:

(i) the anchorage geometry i.e., the length and the bar diameter size, and
(ii) the fracture energy of the ECC matrix surrounding the bar, as quantified by the area under the assumed bond-slip law of Fig. 2a.

The influence of the study variables on the tension strain capacity of the bar anchorage and the associated slip value, both being very critical in determining the deformation capacity and structural performance of ECC members are presented and thoroughly discussed.

2 THE ANALYTICAL INVESTIGATION OF A PULLED BAR EMBEDDED IN ECC

In the direct tension pullout bond test (Fig. 2a, Tastani & Pantazopoulou 2010) the bar is stressed in tension whereas the matrix is forced to carry tensile strains (and thus stresses) as a result of the bond interaction. Thus both materials, with different stiffness, act as parallel springs undertaking in any given cross section mutually complementary forces; the share taken by each material depends on local strain and material stiffness. At any point the total length change of each material phase results from integration of its own strains – thus the total displacement of bar differs from that of concrete. The difference is the relative amount of slip of the bar with respect to the surrounding cementitious matrix.

Derivation of the equations that govern force transfer between reinforcement and the surrounding ECC matrix requires establishing equilibrium of forces, compatibility of deformation and consideration of the constitutive equations of the materials, namely the bar stress-strain behavior and the bond-slip law. In a former work (Tastani & Pantazopoulou 2012) all these equations have been analytically solved for conventional concrete (by neglecting the contribution of concrete in tension), elastic bar (i.e. bar axial stress, $f_s = E_s \varepsilon_s$ where $E_s = 200$ GPa is the Modulus of Elasticity), and for bond law of limited toughness (as per the multilinear curve over the dark grey area of Fig. 1a). In this study the mathematical problem is revisited considering that the tensile strain ductility of the ECC favorably influences the bond law by increasing its toughness. Aiming to simplify the calculations, the assumed bond – slip law (i.e. the f_b-s relation) is a continuous curve (see the dashed curves of Fig. 2b) and it is described by the unified Equation (1).

$$f_b(s) = \frac{\gamma \cdot s + f_b^{max}}{\alpha \cdot s^2 + \beta} \cdot s$$
$$a = \frac{f_b^{max} + 2s^{max}\gamma}{2s^{max} f_b^{max}} \quad \& \quad \beta = 0.5 s^{max} \qquad (1)$$
$$f_b(s^{max}) = f_b^{max}$$

In Equation (1) f_b^{max} and s^{max} are the coordinates of the curve's peak. The advantage of the Eq. (1) is that it provides the ability to modify the slope of the post-peak softening branch through the scalar variable γ. This modification factor actually represents the amount of bond toughness, which is the energy released upon the attainment of anchorage capacity before its failure. The slowly descending branch of the bond curves is a characteristic of the ECC matrices due to the occurrence of multiple cracking instead of crack localization that is observed in conventional concrete; development of cracks and the growth of the crack widths depend on the bridging effect of the embedded fibers in the matrix. Thus, in Fig. 2b, the higher the value of scalar γ (i.e. from $\gamma = -1$ to 5) the milder the slope of the descending branch. The values f_b^{max} and s^{max} are considered known and used for the computation of constants α and β of Eq. (1). They are taken either (i) from the proposed relationships in *fib* MC2010 (*fib*, 2010) for well-confined anchorages and for pullout failure (the case of MC2010 in Fig. 2b), where s^{max} is equal to the arithmetic mean of the values s_1 and s_2, that enclose the horizontal branch of the law or (ii) from published experimental tests (Tastani et al. 2014).

The boundary conditions of the problem (Fig. 2a) are only the incremental slip input at the loaded-end (for $x = 0$ it is $s(0) = s_o$) and the requirement of zero strain at the unloaded-end, (for $x = L_b$ it is $\varepsilon_s(L_b) = 0$).

Table 1. Values for the parametric investigation.

D_b (mm)	L_b/D_b	f_b^{max}(MPa)	γ
10	10	7	−1
12	20	10	2
16	40	12.5	3
20	80	16.5	5
24	100	18.5	

3 PARAMETRIC INVESTIGATION

The influence of the anchorage geometry (in particular the bar size D_b and the embedded length L_b) and the bond law (respecting the bond strength f_b^{max} and the strain energy of ECC that accordingly regulates the descending branch of bond -slip law through the scalar γ) on the overall deformation capacity of a straightly anchored elastic bar is studied in this section by implementing the mathematical framework in MATLAB. Table 1 includes all the investigating parameters and the corresponding assumed values of each one.

The objective of the parametric investigation is to illustrate the sensitivity of the strain development capacity of an anchored bar on the important design parameters of the reinforcement anchorage in ECC matrix. Of particular interest is the strain development capacity since one of the prerequisites for the introduction of high strength reinforcing materials in concrete is the ability to exploit the maximum of their available strain capacity (i.e., the rupture strain of FRP bars ranges between 1.5–2%). Here the bar is assumed elastic (E_s=200GPa) up to rupture strain ε_u. (The strain term ε_u refers to an arbitrary but feasible bar strain at fracture, here taken as 0.025.)

Based on well-established knowledge on bond of bars in conventional concrete (*fib* Bulletin 10, 2000 and Tastani & Pantazopoulou 2006): (i) increasing the available length L_b above a critical threshold L_b^{max}, does not result in a commensurate increase in development capacity of the anchored bar; this is attributed to the finite available fracture energy of conventional concrete which is reflected in the bond law by its limited toughness. Smaller bars are able to develop (ii) higher strains before splitting failure occurs and also (iii) higher average bond strength (this is calculated through the familiar expression $f_m^{ave}=D_b/(4L_b)\cdot f_s$ where f_s is the stress of the bar). However bars of different size but identical rib pattern -thus mobilizing the same frictional resistance- result in the same f_b^{max}, the latter being a characteristic property of the assembly.

These established findings (i)-(iii) for conventional concrete are briefly presented in Fig. 3, where curves of strain versus slip ($\varepsilon_o - s$) at the loaded-end of an anchored bar are depicted. Analytically, for a common bond law ($f_b^{max}=7$ MPa, $s=1.5$ mm and $\gamma=-1$, where splitting rather than pullout failure is anticipated according to *fib* MC2010), and two bar sizes ($D_b=10$ and 20 mm, the black and grey curves respectively)

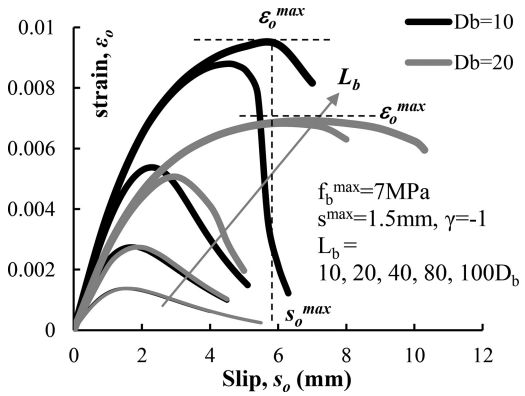

Figure 3. Diagrams of strain versus slip at the loaded-end of an anchored bar with parameters the bar size ($D_b=10$ and 20 mm) and the anchorage length ($L_b/D_b=10$, 20, 40, 80, 100).

incremental strain analysis was implemented for several anchorage lengths (i.e. $L_b/D_b=10$, 20, 40, 80 and 100, where the thicker the curve the larger the anchorage length). It may be concluded that the model accurately predicts the experimental trends, namely the smaller the bar size the higher the attained strain with increasing the available anchorage length (see the black curves in Fig. 3), but for large bar sizes the maximum attained strain (ε_o^{max}) can't further be increased with also increasing the L_b (see the two thicker grey curves in Fig. 3). Based on the verified proposed model, these trends are now re-examined as per their validity in ECC matrix.

3.1 *The effect of the bond toughness, γ*

Let us consider a bar of $D_b=12$ mm anchored in a high strength but zero strain capacity matrix (thus $\gamma=-1$, with bond properties $f_b^{max}=12.5$ MPa and s^{max}=1.5 mm) and alternatively in ECC matrices where only the post-strength toughness is altered: from medium ($\gamma=2$) to higher value ($\gamma=5$), see also Fig. 2b. For several anchorage lengths (i.e. $L_b=5$, 10, 20, 40, 80 and 100*Db*) the overall strain – slip (ε_o-s_o) response of the loaded-end of the anchored bar was analyzed as per Fig. 3; for every anchorage length the maximum attained strain ε_o^{max} and the associated slip s_o^{max} (for their definition see Fig. 3) were isolated aiming to produce diagrams of strain development capacity versus the normalized anchorage length and versus the associated slip (Fig. 4).

Apparently, the longer the available length L_b and the higher the scalar γ the higher the attained strain development capacity of the anchored bar (i.e. see the case of $\gamma=5$ where the ε_o^{max} is almost proportional to the L_b and can approach the rupture limit of ε_u as opposed to the case $\gamma=-1$ where ε_o^{max} is limited to 0.55 ε_u for $L_b>70D_b$). This is because even after the bond mechanism has entered in the descending branch at the anterior part of the anchorage, there is sufficient residual length to support the increased bar force

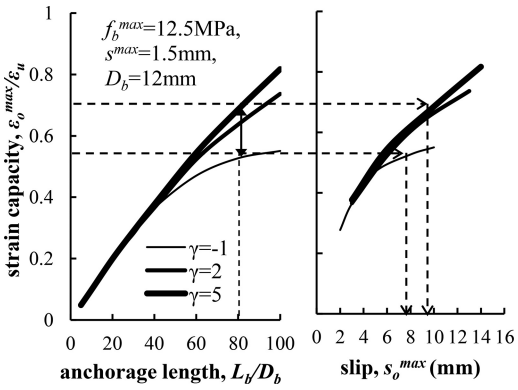

Figure 4. Strain development capacity versus the available anchorage length (to the left) and versus the associated slip (to the right) at the loaded-end ($\varepsilon_u = 0.025$): the influence of γ.

by propagating the bond stress distribution inwards towards the free-end of the anchorage, while satisfying the requirement for force equilibrium.

In the accompanying diagram to the left of Fig. 4 the strain capacity ratio $\varepsilon_o^{max}/\varepsilon_u$ is plotted against the associated maximum slip s_o^{max}. This plot is useful for the calculation of the member's rotation capacity which is the sum of the accumulated flexural curvature and the lumped rotation owing to bar slippage that occurs at the member's critical cross section (i.e., at the connection of a flexural member to its support). Thus, for a given bond-slip law, the available anchorage length results in the attained bar strain development capacity and the associated slip magnitudes s_o^{max}. The latter normalized to the sectional distance of internal forces (i.e. s_o^{max}/jd) is the lumped rotation due to bar pullout of the member. From Figure 4, for sufficient bond length (i.e. L_b=80D_b), the tougher bond – slip law results in a gain in strain capacity of almost 20% (γ from -1 to 5) which on the other hand produces increased slip by 2 mm -an increase of the lumped rotation by 0.65% (3.2% overall lumped rotation) for a member of cross section height 400 mm. Such an increased deformation of the r.c member while load is sustained requires also the compression zone of the section to be able to undertake the extra compression strain without crushing. The ECC compression strain at peak stress is sufficiently large, in the order of 0.005, much higher than of 0.002 of the conventional concrete, thus securing the extreme part of the compression zone from premature failure.

The fact that a ductile ECC matrix is able to increase the strain development capacity of an anchorage has also been experimentally confirmed; for example Tastani et al. 2014 studied short anchorages (i.e. $L_b = 5D_b$) developed in the half of the mid-span of the constant moment region, and also in the tensile region of the cross section. Figure 5 depicts the load – deflection histories of beams reinforced with a steel bar of $D_b = 10$ mm embedded in plain and fiber reinforced cementitious mortars (c.m. and ECC respectively). The

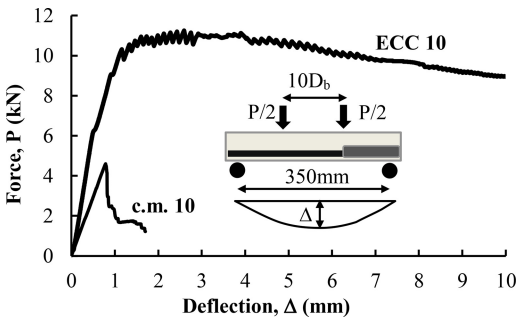

Figure 5. Experimental confirmation that an ECC matrix enables an anchorage to undertake higher strain level as compared with a conventional concrete (from Tastani et al. 2014).

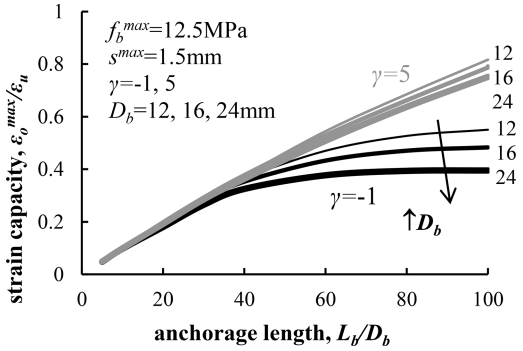

Figure 6. Strain development capacity at the loaded-end versus the available anchorage length: the influence of D_b.

gain in strength -from 4.5 to 11 kN- implies that the bar increased its attained strain from 0.0004 to 0.0009 (strain values have been deduced from sectional analysis) due to the contribution of the fibers. This increased strain is also maintained for large values of deflection, thus attributing ductility to the structural member.

3.2 *The effect of the bar diameter, D_b*

Figure 6 presents the strain development capacity of the anchorage $\varepsilon_o^{max}/\varepsilon_u$ plotted against the available embedded length L_b, normalized by the bar diameter D_b, for bars of $D_b = 12$, 16 and 24 mm. For all cases, the same bond strength was assumed ($f_b^{max} = 12.5$ MPa and $s^{max} = 1.5$ mm). In the case of poor bond toughness (i.e. in Fig. 6 see the curves drawn in black where $\gamma = -1$) it may be concluded that the higher the bar size (from the thinner to the thicker curve in Fig. 6) the lower the developed bar strain, which is not improved with the increase of the embedded length beyond a certain limit (the solid black line curves even out and become horizontal after L_b=60D_b suggesting that there is a cap to the strain development capacity of the reinforcement – i.e. increasing the available development length will not lead to higher developed strain).

The only way to increase the strain development capacity of the anchorage is by enhancing the toughness of the bond law; an effective way to do this is by reducing the slope of the post-peak descending branch through the coefficient γ (in Fig. 6, see the curves drawn in grey, where $\gamma = 5$). This has a physical significance: a milder descent occurs in confined anchorages. Confinement in conventional r.c. is provided through dense stirrups along the L_b whereas in ECC it is provided by the high volume of well dispersed microfibers which are able to bridge cracks in any potential position.

It is interesting to note in Fig. 6 that with increasing the bond toughness bars of larger size are able to develop a higher gain in strain development capacity than smaller ones. For example an anchorage of length $L_b = 100D_b$ implemented with a bar of $D_b = 24$ mm results in a strain increase of $0.36\varepsilon_u$ (from $0.39\varepsilon_u$ to $0.75\varepsilon_u$) whereas for $D_b = 12$ mm the increase is $0.26\varepsilon_u$ (from $0.55\varepsilon_u$ to $0.81\varepsilon_u$). However the strain development capacity of the smaller bars remain higher considering a target L_b (i.e., for $D_b = 12$ mm is $\varepsilon_o^{max} = 0.81\varepsilon_u$ whereas for $D_b = 24$ mm is $\varepsilon_o^{max} = 0.75\varepsilon_u$). In structural elements, this can imply that for the same reinforcement ratio in a cross section, smaller D_b requires a greater number of bars, which mobilize a larger area of the surrounding concrete in tension; if the surrounding media is an ECC then the equivalent matrix area can be mobilized by using larger but fewer bars in the member's section. The benefit in this case is a less dense arrangement of the bar reinforcement in the cross section of the member.

3.3 *The effect of bond strength, f_b^{max}*

If the objective is to develop the bar fracture strain (i.e. to attain a strain ratio $\varepsilon_o^{max}/\varepsilon_u$ as near to the value of 1 as possible) of a straight anchorage of extensive embedded length, not only the stored energy in the assembly (the bond toughness) but also the bond strength need to be adequate. In ECC matrices with high tensile strength sustained up to large strains, the increase in bond strength f_b^{max} may be achieved by increasing the cement content or by adding nano-materials (Tastani et al. 2014).

In Fig. 7, by only altering the bond strength (assumed values for $f_b^{max} = 10$, 12.5, 16.5 and 18.5 MPa, where the thicker the curve the higher the bond strength value) while keeping all other variables constant (i.e. $D_b = 10$ mm and $s^{max} = 1.5$, where $\gamma = 3$ represents a well confined anchorage, see also Fig. 2b) the bar strain development capacity is highly increased even for smaller development lengths (i.e. for $L_b = 40D_b$ the ε_o^{max} is 100% improved -from 30% to almost 60% of ε_u). This has practical use in rehabilitation of short and insufficiently detailed anchorages and lap-splices as a patch repair technique and as an alternative to the externally bonded FRP jacketing because, given the available embedded length, by replacing the surrounding concrete with an ECC matrix by accordingly regulating the bond strength f_b^{max} the anchorage is

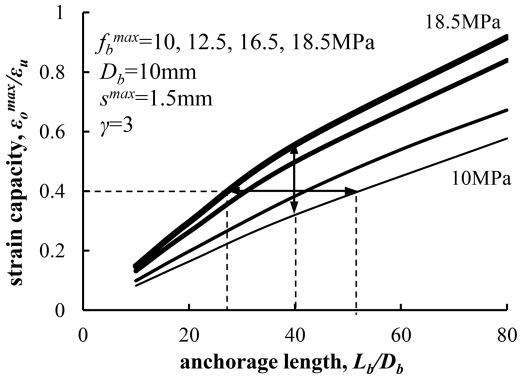

Figure 7. Strain development capacity at the loaded-end versus the available anchorage length: the influence of f_b^{max}.

capable of developing a higher strain thus enabling the structural member to respond in a more ductile manner. Inversely, for a target bar strain ε_o^{max} (i.e. 40%ε_u) the required anchorage length could be reduced from 52 to $27D_b$ resulting in cost-efficient use of reinforcement and also in designing smaller cross sections of the adjacent structural members where the anchorage length is accommodated.

4 CONCLUSIONS

The increased fracture energy of engineered cementitious composites, which are high performance advanced fiber reinforced cementitious materials with increased strain ductility, effectively enhances the development capacity of reinforcing bars enabling significant post-peak energy dissipation prior to anchorage failure. This characteristic resembles the behavior of confined anchorages highlighting the confining role of fibers in the cementitious matrix.

The paper's objective was to analyze straight anchorages of an elastic bar embedded in a ductile matrix possessing large fracture energy reserves by using a simplified equation that describes the entire range of the associated bond-slip law. The paper also includes an extensive parametric study regarding the effect of important design parameters, such as the geometry of the anchorage (length and bar diameter), the bond strength and the bond toughness of the bond-slip law on the strain development capacity and the mode of failure of the anchorage.

REFERENCES

Bandelt M.J., Billington S.L. 2014. Bond behavior of steel reinforcement in high-performance fiber-reinforced cementitious composite flexural members. Materials and Structures, DOI: 10.1617/s11527-014-0475-4.

Dagenais M., Massicotte B. 2014. Tension Lap Splices Strengthened with Ultrahigh-Performance Fiber-Reinforced Concrete. J. of Materials in Civil Engineering 27(7). 10.1061/(ASCE)MT.1943-5533.0001169, 04014206

fib Bulletin 10 (2000). Bond of Reinforcement in Concrete. International Federation for Concrete. Pages: 434, ISBN: 978-2-88394-050-5

fib CEB-FIP, 'fib Model Code 2010 – Final draft, Volume 1', Bulletin No. 65, International Federation for Structural Concrete, Lausanne, Switzerland, 2010.

Fischer G., Li V.C. 2002. Effect of Matrix Ductility on Deformation Behavior of Steel-Reinforced ECC Flexural Members under Reversed Cyclic Loading Conditions. ACI Structural Journal 99(6):781–790

Li, V.C. 1993. From Micromechanics To Structural Engineering – The Design Of Cementitious Composites For Civil Engineering Applications, JSCE J. of Struct. Mechanics and Earthquake Engineering 10(2): 37–48.

Tastani S., Pantazopoulou S. 2010. Direct tension pull-out bond test: Experimental results. ASCE J. Structural Engineering 136(6):731–743.

Tastani S., Pantazopoulou S. 2013. Reinforcement-Concrete Bond: State Determination along the Development Length. ASCE J. Structural Engineering 139(9):1567–1581.

Tastani S.P. and Pantazopoulou S.J. 2006. Bond of G-FRP bars in concrete: experimental study and analytical Interpretation. ASCE J. of Composites for Construction 10(5): 381–391.

Tastani, S.P., Pantazopoulou, S.J., Konsta-Gdoutos, M.S., Balopoulos, V. 2014. Experimental Local Bond of Reinforcing Bars in Cementitious Composites Reinforced with PolypropyleneFibers/CarbonNanoTubes. *3rd International RILEM Conference on Strain Hardening Cementitious Composites (SHCC3-Delft), Dordrecht Netherlands, November 3–5.*

Concrete Solutions – Grantham et al. (Eds.)
© 2016 Taylor & Francis Group, London, ISBN 978-1-138-03008-4

Flexural response of corroded reinforced concrete beams: Experiments and finite element analyses

G.G. Triantafyllou, T.C. Rousakis & A.I. Karabinis
Democritus University of Thrace, Xanthi

ABSTRACT: Deterioration of reinforced concrete structures caused by corrosion of steel bars is one of the major problems that the worldwide use of reinforced concrete is facing. An experimental program was carried out to study the effect of reinforcement corrosion on the load-bearing capacity and ultimate deflection of reinforced concrete beams. The corroded RC beams were exposed to accelerated corrosion by impressing electric current and subjecting to wetting-drying cycles. An analytical model, based on longitudinal cracking of concrete cover, has been developed to estimate the corrosion rate of steel reinforcement and thus to predict the residual flexural strength, using the reduced area of corroded bars. A three-dimensional Finite Element model of RC beams was also constructed using ABAQUS software. Comparisons were made among experimental results and analytical or FE modeling predictions, which were in good agreement.

1 INTRODUCTION

Corrosion of steel reinforcement is very crucial problem, resulting in the deterioration of reinforced-concrete structures. The degree of reinforcement corrosion has a great impact on flexural strength, deflection, ductility, bond strength and failure mode of structures. Numerous studies have been carried out on the influence of structural performance and serviceability of reinforced concrete elements. Most researchers use impressed current to accelerate the corrosion process. Rodriguez et al. (1997) added chlorides into concrete and found that corrosion increased crack widths and deflection at the serviceability limit state and reduced the ultimate strength. Similar methods were used by Azad et al. (2007) and Du et al. (2007) to estimate the mechanical performance in corroded RC beams. Al-Saidy & Al-Jabri (2011) found that corrosion weakened the bond along the corrosion cracks at the interface of steel rebars and concrete. Yuan et al. (2007) made comparison between two accelerated corrosion techniques, with a galvanostatic method and in an artificial climate environment. In the first, the whole surface of the steel bar was corroded, while in the second, corrosion was located on the surface of the steel bar on the side facing the concrete cover. Corrosion can also transfer the failure mode from ductile to brittle. As steel corrodes, there is a loss in cross-sectional area which leads to reduction in flexural strength capacity. El Maaddawy et al. (2005) found that the reduction of the load-carrying capacity was almost proportional to the reduction in steel area. Francois et al. (2013) started a long-term experimental program of -RC beams with corroded steel reinforcement in a natural chloride environment. The corrosion degree strongly affected the mechanical properties of the steel and the ultimate stress and strain. Ultimate elongation is also reduced with increasing corrosion level, with a great impact on structural reliability. Brittle failure mode and depletion of both ultimate load capacity and ductility was also found for a heavily corroded beam which was kept in a non-aggressive environment and under ULS load by Dang & Francois (2013). Zhu et al. (2013) noted that the anchorage of tensile bars was still sufficient to allow bending failure in corroded beams, despite large corrosion cracks and spalling near the support. Thus, natural corrosion, which is not constant all along the bar and around the perimeter, is less detrimental to bond properties than might be assumed from accelerated corrosion by impressed current. The prediction of corrosion degree of steel reinforcement has also been discussed by many researchers, in an attempt to correlate it with the corrosion induced cracks. El Maaddawy & Soudki (2007) proposed a model for the prediction of the time of corrosion initiation (corrosion products fill the porous zone) before corrosion cracking (corrosion products induce expansive pressure on the concrete around the bar).

2 EXPERIMENTAL CONTEXT

2.1 *Test specimen*

Two reinforced concrete beams with 2300 mm length, 300 mm deep and 150 mm width were tested in the Reinforced Concrete Laboratory, D.U.Th. The first beam remained uncorroded in order to be utilized

as reference, while the second beam was subjected to accelerated corrosion. The tension and compression steel reinforcements were three deformed bars of 12 mm diameter at the bottom and two bars of 10 mm diameter at the top of the beams respectively. The shear reinforcement consisted of 8 mm diameter stirrups spaced at 150 mm within the middle span. A clear concrete cover of 20 mm was used. The 28-day cylindrical concrete compressive strength was 34.6 MPa. The mechanical properties of the steel bars were estimated by tensile tests. The yield strength of bars without corrosion was 552.2 MPa, while the ultimate strength was 652.5 MPa.

2.2 *Accelerated corrosion process*

The impressed current technique is widely used to accelerate corrosion of steel in concrete so that corrosion tests can be conducted within a reasonable time frame. To simulate corrosion in the laboratory, an accelerated technique was adopted through the connection of the internal longitudinal steel bars and a dummy external steel rod to a power supply, so as to induce a constant electric current. The tensile steel bars were connected to the positive terminal of the power supply to act as anodes while the steel rod was connected to the negative terminal to act as a cathode. After 28 days curing, the beams were also placed inside a tank with industrial salt solution NaCl of 3% concentration (1 week inside – 1 week outside). They were subjected to 4 wet-dry cycles for a total period of eight weeks.

The mass loss rate of tensile steel was regarded as the corrosion rate so as to evaluate the corrosion level, which can be calculated by considering that the distribution of corrosion within the steel material is uniform. The desired mass loss of tensile bars was achieved using Faraday's law taking into account the corrosion time.

2.3 *Corrosion damage*

At the end of each wetting cycle, crack widths were measured by visual examination and a crack width comparator Corroded beams exhibited rust spots and longitudinal cover cracking parallel to the corroded steel reinforcing bars, on the tensile bottom face and on the two side faces. As the procedure of corrosion progressed, the rate of corrosion crack growth increased and crack widths became even wider. Corrosion exposure for four weeks wetting and four weeks drying resulted in corrosion crack widths of 0.15–0.35 mm on the tensile bottom and of 0.20 mm on the side face of the corroded beam. Figure 1 depicts the bottom of the beam and the crack pattern, while in Figure 2 the crack pattern on the corresponding side face can be illustrated.

After the structural test to failure, steel coupons were extracted from the corroded bars and then cleaned of rust products according to ASTM G1-90 standard.

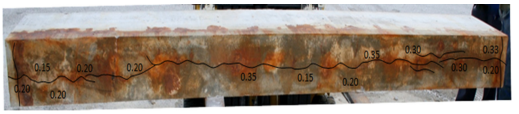

Figure 1. Crack pattern of tensile bottom face of the corroded beam.

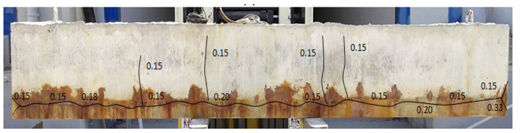

Figure 2. Crack pattern of side face of the corroded beam.



Figure 3. Corroded coupon extracted from the corroded beam without cleaning.



Figure 4. Corroded coupon cleaned of loose rust.

The steel coupons were weighed and the percentage gravimetric mass loss of each coupon m_{grav} was calculated from the relation:

$$m_{grav} = \frac{m_{uncorr} - m_{corr}}{m_{uncorr}} x100(\%) \quad (1)$$

where m_{uncorr} is the average mass per length of an uncorroded steel coupon and m_{corr} is the mass per length of a corroded coupon. The range of mass loss of corroded coupons varies between 3.89–10.01% on the entire length, while the average mass loss of coupons was finally resulted equal to $m_{grav} = 7.56\%$. Typical steel samples that were removed and measured before and after cleaning can be shown in Figures 3 & 4. In figure 3 the rust deposits are obvious, having different colours. In Figure 4, there is a more uniform colouring of the remaining steel with cavities (pitting corrosion etc).

2.4 *Test results and discussion*

The beams were tested under four-point loading to failure, under monotonic loading. Instrumentation included linear variable displacement transducers (LVDTs) to measure displacement and strain gauges installed along the middle of the main longitudinal rebar to measure the steel strain.

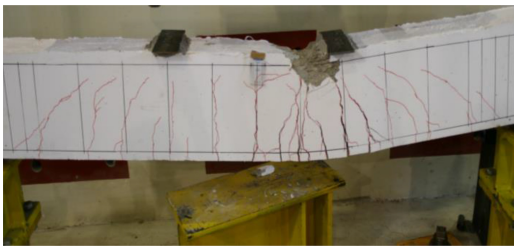

Figure 5. Crack pattern of the uncorroded beam after loading.

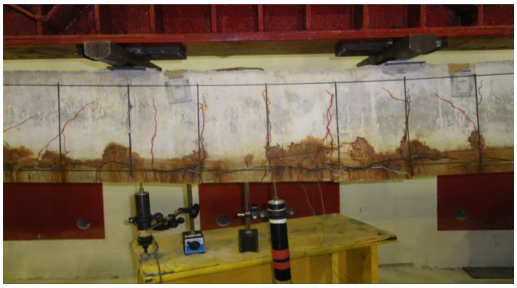

Figure 6. Crack pattern of the corroded beam during loading.

Failure mode of the uncorroded and corroded beam occurred by yielding of tensile steel followed by crushing of concrete in the compression zone. As follows from the test results, corrosion of steel had a small influence on the cracking loading. Regarding the yield load, a slight reduction of 5.55% was measured for the corroded beam with respect to the uncorroded one. The ultimate load of the beam with corroded steel rebars was 4.02% lower when compared to the uncorroded beam. At failure, the corroded beam presented 2.45% higher deflection than the beam without corrosion.

Figure 5 shows the crack pattern of the uncorroded beam after loading up to failure. As loading progressed, more flexural cracks formed and became wider in the middle of the beam and flexural-shear cracks occurred at the shear spans.

Figure 6 depicts the crack pattern of the corroded beam during loading. Further increase of the width of cracks was observed. It is noted that the longitudinal cracks due to corrosion remained almost unaffected.

When the load reached its maximum value, a part of the concrete cover was detached from the middle tensile face of the beam. The maximum corrosion crack width before loading (0.35 mm) increased at maximum load to 0.40 mm. At failure, several concrete cover parts were separated at the middle span area (Figure 7).

2.5 *Model for the assessment of corrosion rate*

In the literature, a number of research works have been carried out on reinforced concrete cracking caused by corrosion. The most crucial approach for estimating structural deterioration and corrosion damage is visual monitoring and drawing of maps of corrosion cracks and of patterns. A new model is presented that relates the steel bar corrosion rate to concrete cover condition (before and after cracking). Relationships for the steel mass loss considering the state of rust formulation to fill the porous zone as well as the state in which the radial pressure overcomes the concrete tensile strength, causing cover cracking are included (Triantafyllou et al. 2015).



Figure 7. Crack pattern of the corroded beam at failure. Separation of concrete cover.

The total percentage mass loss because of corrosion damage after concrete crack initiation is equal to:

$$m_l(\%) = \frac{\frac{w}{\pi}+\delta_c}{\delta_c}\left(m_{l,porous} + m_{l,prad}\right) \quad (2)$$

where w is the crack width, δ_c is the concrete displacement at the steel-concrete boundary, $m_{l,porous}$ is the percentage steel mass loss up to the filling of the porous zone and $m_{l,prad}$ is the percentage steel mass loss up to depletion of the tensile strength of concrete cover.

If corrosion is considered to be uniform as mentioned above, this mass loss corresponds to a residual bar area of steel reinforcement. As a result, the residual yielding and ultimate moment capacity of a corroded beam can be calculated. The analytical predictions of the proposed model have been compared against the experimental results published in the international literature and the performance of the model is satisfactory.

The maximum crack width that was observed on the tensile face of the corroded beam was equal to 0.35 mm. Considering this value, the mass loss of tensile steel reinforcement can be predicted by the proposed analytical model equal to $m_l = 6.31\%$. Thus, the residual diameter of the steel bar can be calculated and subsequently the residual flexural strength of the corroded beam can be estimated. The absolute error between analytical and experimental values is AE = 11.52% for the yielding moment and the ratio of analytical to experimental values is RE = 0.90. The corresponding errors for the ultimate moment are AE = 4.24% and RE = 0.96 respectively.

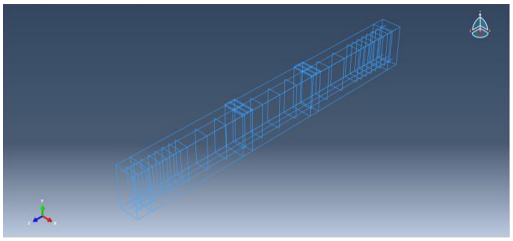

Figure 8. Beam skeleton.

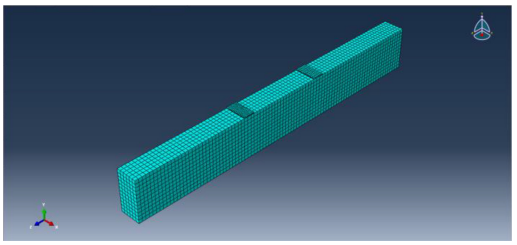

Figure 9. Meshing of beam model.

3 THREE-DIMENSIONAL MODEL FOR RC BEAMS

FE analyses may enable a more accurate consideration of geometrical and material nonlinearity or nonlinear interaction between materials at their contact points or surfaces. Also, the effect of several parameters on mechanical behavior of materials or structural elements can be investigated at a macrostructural or microstructural level, choosing suitable discretization (Rousakis et al. 2007, Karabinis et al. 2008, Rousakis and Karabinis 2009). The objective of this part of the study was to create a three-dimensional model that could accurately predict the load-deflection curve and the global behavior of the beams, using the software ABAQUS. In this model, the concrete material was simulated using a 3-D deformable solid structural element, while a 3-D deformable wire was used to simulate the steel bars and stirrups. The loading plates were also simulated using a 3-D deformable solid element. The skeleton of beams is illustrated in figure 8.

The mechanical behavior of concrete was simulated using the concrete damage plasticity model, proposed by Lubliner et al. (1989) and Lee and Fenves (1998). This model was selected as it can represent complete inelastic behavior of concrete both in tension and in compression including damage characteristics. The concrete damaged plasticity model assumes that the two main failure mechanisms in concrete are the tensile cracking and the compressive cracking. The uniaxial tensile and compressive behavior is modeled utilizing damage plasticity. A post failure stress-strain relationship for concrete subjected to tension is used which accounts for tension stiffening, strain softening and reinforcement interaction with concrete. The stress-strain relation of concrete under compression using stresses, inelastic strains and damage properties was used.

The steel reinforcement bars and stirrups were considered to have linear elastic-plastic behavior. A Poisson's ratio of 0.3 was used and the elastic modulus, the yield and ultimate strength values that resulted from the tensile tests in coupons for uncorroded steel bars were used, as already discussed.

Beams were modeled using boundary conditions similar to the experimental setup and were loaded using a non-linear static procedure. The meshing edge size of 25 mm was used for concrete elements (see figure 9).

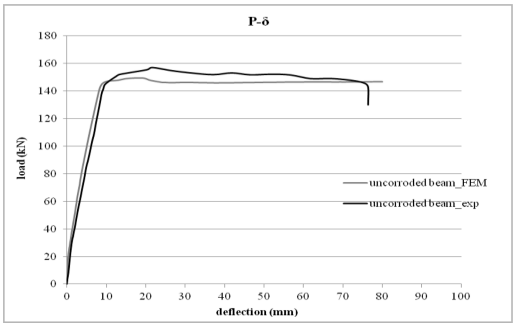

Figure 10. Experimental and FE numerical model load-deflection curves for uncorroded beams.

3.1 *FEM results of 3D models*

Two FEM models were created in ABAQUS. The first one was the RC beam without corrosion, while the second one dealt with the corroded RC beam. The load-deflection curves for both models were drawn at the mid-span point for comparison with the experimental results. Figure 10, shows the load deflection curve. From simulation results of the uncorroded RC beam, it can be concluded that the 3-D model implemented in ABAQUS captures well the yielding load and is in good agreement with the ultimate experimental load. In particular, the FE numerical model led to a slight increase in the yielding load capacity compared with the experimental beam of about 1% (analytical value of 145.3 KN) while a small decrease was observed in the ultimate load capacity of approximately 5.1% (analytical value of 149.3 KN). The FE analysis can capture the degrading load-deflection behavior as well. The FE analysis was terminated at 80.1mm deflection.

Figure 11 shows the stress values at ultimate deflection in the tensile steel reinforcement.

The compressive and tensile stresses that were developed in the concrete of the uncorroded beam at ultimate deflection are shown in figures 12 & 13 respectively.

The FEM model was used again for the corroded beam using the 6.31% mass loss of tensile steel bar cross section as resulted from the analytical model,

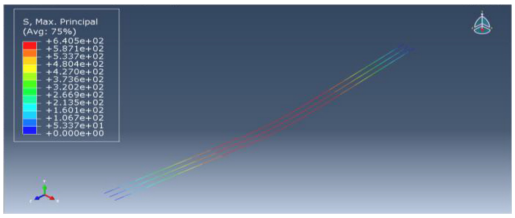

Figure 11. Maximum stress values in the steel for the uncorroded beam.

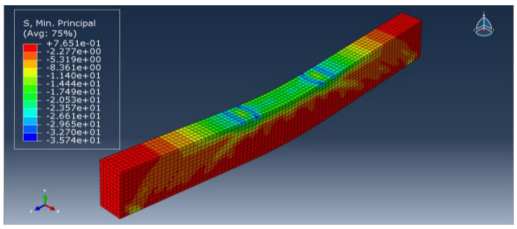

Figure 12. Compressive stresses in uncorroded beam.

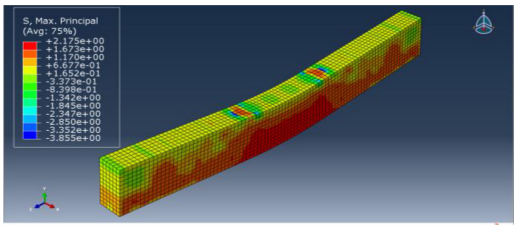

Figure 13. Tensile stresses in an uncorroded beam.

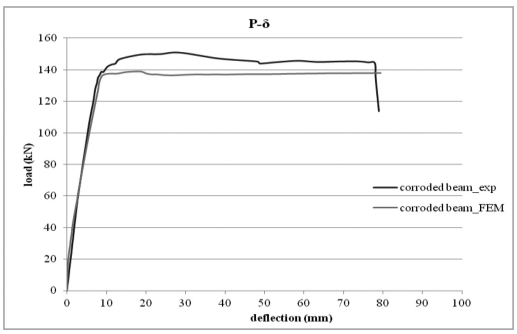

Figure 14. Experimental and FE numerical model load-deflection curves for corroded beams.

proposed for assessment of corrosion rate. The stress-strain values were adopted from the tensile tests of non-corroded steel bars.

Figure 14 shows good agreement between the FE numerical model and experimental results for the load-deflection behavior. It is observed that the predicted yielding load is 0.9% lower than the experimental one, while the ultimate load is 8.5% lower, respectively. Furthermore, the results show that the FE model of the corroded beam gave almost similar deflection values to the experimental value of the corroded beam.

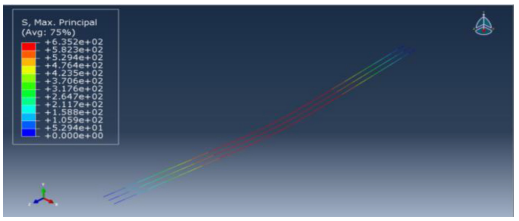

Figure 15. Maximum stress values in the steel for corroded beam.

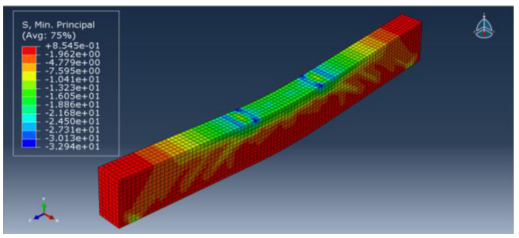

Figure 16. Compressive stresses in corroded beam.

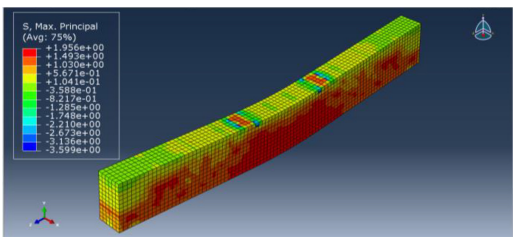

Figure 17. Tensile stresses in corroded beam.

Figure 15 shows the stress values at ultimate in the tensile steel reinforcement.

The compressive and tensile stresses that were developed in the concrete of the corroded beam are shown in figures 16 & 17 respectively.

FE analyses for both uncorroded and corroded beams presented a failure mode similar to the experimental one. The failure of FE models occurred by yielding of tensile steel bars and crushing of the compressive concrete zone.

4 CONCLUSIONS

The structural performance of a corrosion-damaged reinforced concrete beam and an uncorroded beam was investigated. The increase in the corrosion crack width as corrosion progressed was monitored and the steel mass loss was measured at the end of each corrosion phase. Corrosion of steel reinforcement at around 7.5% average mass loss, resulted in a slight reduction of the load carrying capacity and in a slight increase of the ultimate deflection.

An analytical model was proposed for estimating the mass loss of corroded steel reinforcement so as to

estimate the residual flexural capacity of beams from the time that the corrosion process initiates and beyond concrete cover cracking. Given a longitudinal crack width of a corroded beam, the corrosion rate of steel bars can be predicted with satisfactory accuracy.

The main features of the FE numerical models are also developed in order to study further the behavior of both beams. The FE analysis captured the characteristic experimental behavior of the beams, such as load at yield initiation of the steel bars, maximum bearing load of the beams and ultimate deflection with a satisfactory level of accuracy. The constructed FE models may enable further analytical studies of different aspects of the structural behavior of corroded beams and corrosion induced cracking.

REFERENCES

Al-Saidy, A.H. & Al-Jabri K.S. 2011. Effect of damaged concrete cover on the behavior of corroded concrete beams repaired with CFRP sheets. *Composite Structures* 93:1775–1786.

ASTM G1-90. 2002. Standard Practice for Preparing, Cleaning and Evaluating Corrosion Test Specimens. *ASTM International,* West Conshohocken, Pa, 8pp.

Azad, A.K., Ahmad S., Azher S.A. 2007. Residual strength of corrosion-damaged reinforced concrete beams. *ACI Materials Journal* 104 (1):40–47.

Dang, V.H. & Francois, R. 2013. Influence of long-term corrosion in chloride environment on mechanical behavior of RC beam. *Engineering Structures* 48:558–568.

Du, Y., Clark L.A., Chan A.H.C. 2007. Impact of reinforcement corrosion on ductile behavior of reinforced concrete beams. *ACI Structural Journal* 104:285–293.

El Maaddawy, T., Soudki K., Topper T. 2005. Long-term performance of corrosion-damaged reinforced concrete beams. *ACI Structural Journal* 102 (5):649–656

El Maaddawy, T. & Soudki, K. 2007. A model for prediction of time corrosion initiation to corrosion cracking. *Cement & Concrete Composites* 29: 168–175.

Francois, R., Khan, I., Dang V.H. 2013. Impact of corrosion on mechanical properties of steel embedded in 27-year-od corroded reinforced concrete beams. *Materials and Structures* 46:899–910.

Karabinis, A.I., Rousakis T.C., Manolitsi G. (2008): 3D Finite Element Analysis of Substandard Columns Strengthened by Fiber Reinforced Polymer Sheets. ASCE Journal of Composites for Construction, Volume 12, Issue 5, pp. 531–540.

Lee, J. & Fenves, G. 1998. Plastic-damage model for cyclic loading of concrete structures. *Journal of Engineering Mechanics* 124(8):892–900.

Lubliner, J., Oliver, J., Oller, S., Onate, E. 1989. A plastic-damage model for concrete. *International Journal of Solids and Structures* 25(3):299–326.

Rodriguez, J., Ortega, L., Casal, J. 1997. Load carrying capacity of concrete structures with corroded reinforcement. *Construction and Building Materials* 11: 239–248.

Rousakis, T.C., Manolitsi G., Karabinis A.I. (2007): FRP Strengthening of RC Columns – Parametric Finite Element Analyses of Bar Quality Effect. Asia-Pacific Conference on FRP in Structures (APFIS 2007), 12–14 December 2007, Hong Kong.

Rousakis, T.C., Karabinis A.I. (2009): Frp Strengthening of Columns Against Bars Buckling-Parametric Finite Element Analyses. Proceedings of the 9th International Symposium on Fiber-Reinforced Polymer Reinforcement for Concrete Structures (FRPRCS-9), 13–15 July 2009, Sydney – Australia, pp: 91.

SIMULIA, Abaqus Theory Manual (6.12), Dassault Systemes, Providence, RI, USA, 2012.

Triantafyllou, G., Rousakis, T., Karabinis, A. 2015. Coupling of average residual structural section area of corroded steel bars with longitudinal cracking in RC members. *Second Greek-Russian Symposium on Mechanics June 28–July 1 2015.* Greece: Xanthi.

Yuan, Y., Ji, Y., Shah S. 2007. Comparison of two accelerated corrosion techniques for concrete structures. *ACI Structural Journal* 104(3):344–347.

Zhu, W., Francois, R., Coronelli, D., Cleland, D. 2013. Effect of corrosion of reinforcement on the mechanical behaviour of highly corroded RC beams. *Engineering Structures* 56:544–554.

Concrete Solutions – Grantham et al. (Eds.)
© 2016 Taylor & Francis Group, London, ISBN 978-1-138-03008-4

Performance of rapid repair mortars with sulfate aluminium cement and Portland cement

Jie Yuan, Wencui Yang, Xiaoping Cai & Qiaoling Li
Harbin Institute of Technology, Harbin, China

ABSTRACT: Sulfate aluminium cement is usually used as the binder of high early strength mortars due to its fast hydration speed and high early strength. In this study, an ordinary Portland cement was used to replace 20%, 40% and 60% of the sulfate aluminium cement to lower the cost, and the properties of mortars were investigated. Then concrete was cast with the mortars and crushed stone, and the properties of the concrete were tested. The results showed the fluidity of the fresh mortars decreased slightly with the increase of the percentage of ordinary Portland cement. However, the strength of mortars and concrete dropped obviously when the ordinary Portland cement was used, especially at early age. The shrinkage of all mortars was very low. Meanwhile, the impermeability of concrete and the bond strength of concrete and steel were good. The application of a mortar to repair concrete slabs at an airport is also described.

1 INTRODUCTION

As an important building material, concrete has been used for over a hundred years. However, concrete structures suffer from cracks, strength degradation and durability problems due to the internal and environmental factors (Zhang et al. 2014). As a result, many concrete constructions need to be repaired, such as pavements, bridge decks, concrete barriers and wharves, etc. In many cases, to repair concrete structures, fast setting and high early strength materials are demanded, such as when considering airport runways, parking aprons, busy roads, highways or motorways, water tanks and so on.

Cement based repair materials have aroused the attention of many researchers (Srinivasan 2003, Kalagri 2014 & Klisinska-Kopacz 2012). Yang Quanbing investigated the fluidity, mechanical properties and field application of magnesia-phosphate cement (MPB) mortar, and his results showed that MPB mortar is a good material for rapid repair of concrete, and it can be conveniently used (Yang et al 2000). Burak Felekoğlu studied the effect of fly ash and limestone fillers on the viscosity and compressive strength of self-compacting repair mortars. The results showed that all powders increased the initial viscosity when compared with plain cement paste, and the rate of increase depended on the replacement ratio of each mineral or inert admixture. In addition, limestone fillers were more effective than fly ash for improving compressive strength (Felekoğlu et al 2006). G. C. Sang researched the properties of grouting materials composited by Portland and aluminate cement, and the results showed the compressive strength at different ages of the grouts were 27.2 MPa (1 day), 41.5 MPa (3 days), 75.4 MPa (28 days) and 90 MPa (80 days), and one-day expansion ratio was 0.027% (Sang & Liu 2010).

There are a few cements available to meet the requirements to make high early strength repair mortars, like magnesia phosphate cement, jet cement and geopolymeric cement, but most of them are very costly. In this paper, an ordinary Portland cement was used to replace a part of sulfate aluminium cement to lower the cost of rapid repair mortars. And the properties of mortars, including the fluidity, the mechanical properties and the shrinkage, were investigated. Meanwhile, the mortars were cast into crushed stones filling in moulds to produce concrete, and its properties were tested. Furthermore, a mortar based on the experiment results was applied to patch repair concrete slabs at the parking apron of an airport.

2 EXPERIMENTAL WORK

2.1 *Materials and mix proportions*

A Chinese standard P· O 42.5 ordinary Portland cement, produced by Harbin Cement Co. Ltd, Yatai Group, and a sulfate aluminium cement produced by Tangshan 69 Cement Co. Ltd. were used. The oxide composition and the properties of the cements are given in Table 1 and Table 2. Quartz sand with the fineness modulus of 0.95 and the apparent density of 2610 kg/m^3 was used in the experiments. The sieve analysis of the quartz sand was determined, and the fitting curve is shown in Figure 1. A polycarboxylate

Table 1. Oxide composition of the cements.

	Sulfate aluminium cement	Portland cement
SiO_2	10.9	19.9
Al_2O_3	28.93	4.71
Fe_2O_3	3.71	2.9
CaO	45.2	60.5
MgO	1.45	1.41
Na_2O	/	0.2
K_2O	/	1.2
SO_3	8.88	3.2
f-CaO	/	0.86

Table 2. Properties of the cements.

	Sulfate aluminium cement	Portland cement
Water requirement of normal consistency (%)	24	28
Initial Setting time (min)	47	195
Final Setting time (min)	80	320
Compressive strength at 3 days (MPa)	43.3	21.8
Compressive strength at 28 days (MPa)	72	47.1
Flexural strength at 3 days (MPa)	7.1	4.6
Flexural strength at 3 days (MPa)	9.4	7.3

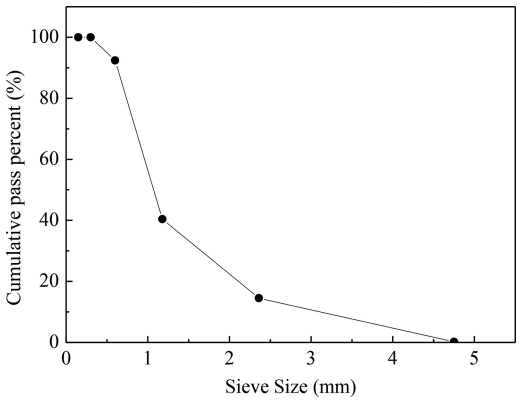

Figure 1. Sieve analysis of the quarts sand.

agent with the water-reducing rate of 20%, a water-retaining agent, an expanding agent, an early-strength agent and a retarder were used.

In this work, Portland cement was used to replace Sulfate aluminium cement at 20%, 40% and 60% to adjust the setting time and lower the cost. And the mix proportions of rapid repair mortars are given in Table 3.

2.2 *Testing programs*

The fluidity of mortar was tested by reference to Chinese National Standards, GB/T 2419-2005. Without vibration, a mortar flowed freely on a glass panel after

Table 3. Mix proportions of mortars (kg/m^3).

Groups	Sulfate aluminium cement	Portland cement	Quartz sand	Water
1	1050	0	1050	294
2	840	210	1050	294
3	630	420	1050	294
4	420	630	1050	294



Figure 2. Casting mortars into crushed stone to produce concrete.

a cone-shape mould was removed. The average value of diameters of the mortar was calculated as the fluidity. The fluidity of fresh mortar and the mortar sat for 30 minutes after being mixed were measured. Prism specimens with the size of 40 mm × 40 mm × 160 mm for strength analysis were prepared, and then they were cured in a condition with the temperature of (20±2)°C and the relative humidity of 95%. The mortar strength was determined according to Chinese National Standards, GB/T 17671-1999. Cube specimens with the size of 70.7 mm × 70.7 mm × 70.7 mm were made to test the vertical expansion of mortars, which was determined according to Chinese National Standards, GB 50119-2003. Prism specimens with the size of 40 mm × 40 mm × 160 mm were prepared for the drying shrinkage test. The test method used was described in JGJ/T 70-2009. And the shrinkage rate could be calculated from equation (1) as follows.

$$S_d = (L_0 - L_d)/160 \times 100\% \quad (1)$$

Where S_d stands for the shrinkage rate of mortar at different age, and L_0 and L_d represents the initial length and length of specimens at different age respectively.

The concrete was cast from the mortars and crushed stones according to the following steps: (1) Coarse aggregates were put into the moulds with the size of 100 mm × 100 mm × 100 mm and 100 mm × 100 mm × 400 mm. (2) Mixing the mortars. (3) Pouring the mortars into moulds, as shown in Figure 2. (4) Curing the concrete samples. The mechanical properties, the permeability, the bond

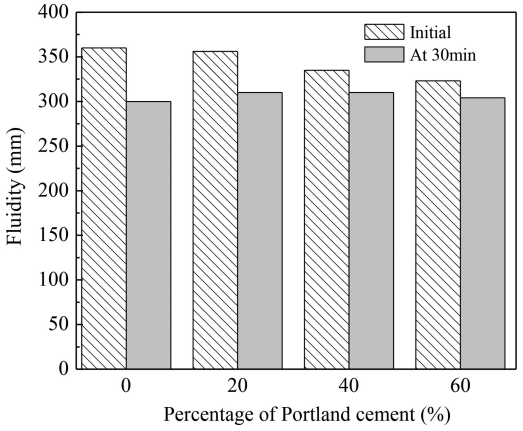

Figure 3. Effect of the percentage of Portland cement on the fluidity of mortars.

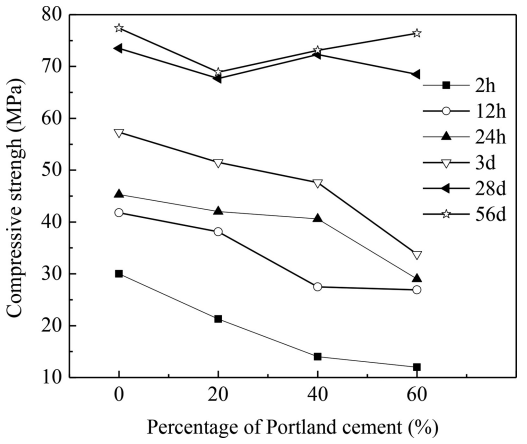

Figure 4. Effect of the percentage of Portland cement on the compressive strength of mortars.

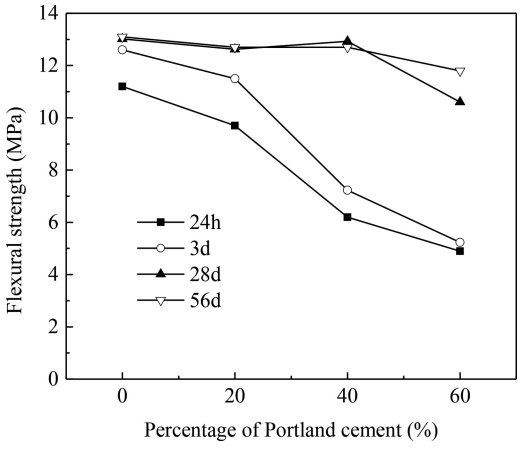

Figure 5. Effect of the percentage of Portland cement on the flexural strength of mortars.

strength between concrete and steel and the condition of reinforcement corrosion were tested. The bond strength of concrete and steel was measured according to DL/T 5150-2001,. The permeability of concrete was evaluated by the electrical conductance of concrete which was tested by ASTM 1202.

3 RESULTS AND DISCUSSION

3.1 *Properties of mortars*

3.1.1 *Fluidity of mortars*

The fluidity of mortar is required to be high when the mortar is poured into the crushed old concrete, as the mortar needs to flow into big voids or gaps between the crushed particles under the action of gravity and bond the discontinued particles into a whole structure.

The fluidity of mortars with sulfate aluminium cement and Portland cement is given in Figure 3. The results showed that the fluidity of four fresh mortars could meet the requirements that should be higher than 320 mm when tested to GB/T 2419-2005. Although the fluidity at 30 min decreased slightly, it was still higher than 240 mm, due to the effect of retarder. With the increase of the Portland cement percentage, the initial fluidity of fresh mortars decreased, since the water requirement of normal consistence for Portland cement was higher, as shown in table 2. And there was no obvious influence of Portland cement replacement on the fluidity at 30 min, as the retarder still had effect after 30 min.

3.1.2 *Mechanical properties of mortars*

The mechanical properties of mortars, including the compressive strength and the flexural strength, are showed in Figure 4 and Figure 5. Figure 4 showed that the compressive strength decreased with the increasing of the content of Portland cement at the curing ages of 2h, 12h, 24h and 3d. For long-age mortars, the effect of percentage of Portland cement on compressive strength was not evident, and at 28d, the compressive strengths with different dosage of Portland cement were all above 68.0 MPa. The hydration rate of sulfate aluminium cement was higher than Portland cement during early ages, especially at the age of 1 day, so the compressive strength of mortar with pure sulfate aluminium cement was much higher than others. With the increasing of curing age, the hydration of Portland cement increased, so the long age strengths of mortars were similar to each other. According tothe technical documents reported by Science and Technology Department of Ministry of Railways of China, [2005] 101, which are shown in Table 4, when the percentages of Portland cement were less than 20%, the compressive strength of mortars could meet the requirements.

From Figure 5, it can be seen that the flexural strength had similar growth tendency to the compressive strength. At the ages of 24h and 3d, the flexural strength dropped sharply with the increasing of the percentage of Portland cement. At 28d and 56d, the

Table 4. Requirements of compressive strength for grouting materials.

Age	Compressive strength (≥,MPa)	Flexural strength (≥,MPa)
8h	20	–
12h	25	–
24h	40	6
28d	50	8
56d	Not reducing	10
90d	Not reducing	–

flexural strength of mortars with different dosage of Portland cement was stable, and most of them were above 12.0 MPa. For the mortars with 0, 20% and 40% of Portland cement, the compressive strengths could meet the requirements. But the 24h flexural strength of mortar with 40% Portland cement was only 0.2 MPa higher than the requirements. Therefore, when the mortars are used in the field, the replacement percentage of Portland cement should be lower than 40%.

3.1.3 *Shrinkage of mortars*

The shrinkages of mortars with different content of Portland cement are given in Figure 6. When the percentage of Portland cement was 60%, the shrinkage was highest during the whole testing period, and it sharply increased at the age of 10 days. For the other three groups, the shrinkage rates were close to each other. When the percentage of Portland cement was 0, 20%, 40% and 60%, the largest shrinkage rates were 0.027%, 0.027%, 0.029% and 0.043% respectively during the testing age. Comparing with results from other researchers (Mindess & Young 1981), the shrinkage rates in this work were much lower. The reason could attribute to more ettringite being produced by the hydration reaction of sulfate aluminium cement, and ettringite can cause the expansion of mortar and compensate the shrinkage.

3.1.4 *Vertical expansivity of mortars*

The vertical expansivity of mortars was shown in table 5. According to the Chinese Industrial Standard JC/T 986-2005, when the contents of Portland cement were 0 and 20%, the vertical expansivity could meet the requirements.

3.2 *Properties of concrete*

3.2.1 *Mechanical properties of concrete*

The compressive strength and the flexural strength of concrete produced by the rapid repair mortars with different percentages of Portland cement are given in Figure 7 and Figure 8 respectively.

The results showed that both the compressive strength and the flexural strength of concrete were decreased with the increasing of the percentage of

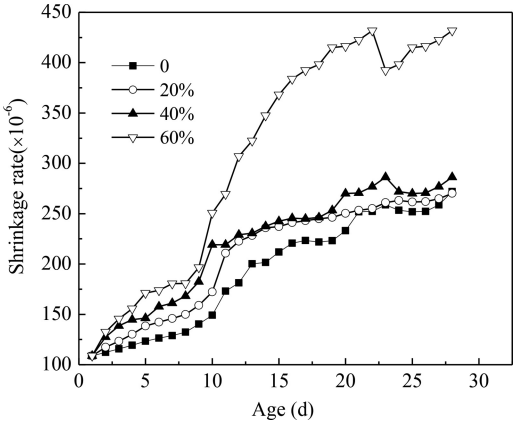

Figure 6. Shrinkage rate of mortars with different percentage of Portland cement.

Table 5. Vertical expansivity of mortars with different percentage of Portland cement.

Percentage of Portland cement (%)	0	20	40	60
Vertical expansivity (1d, %)	0.025	0.021	0.011	−0.007

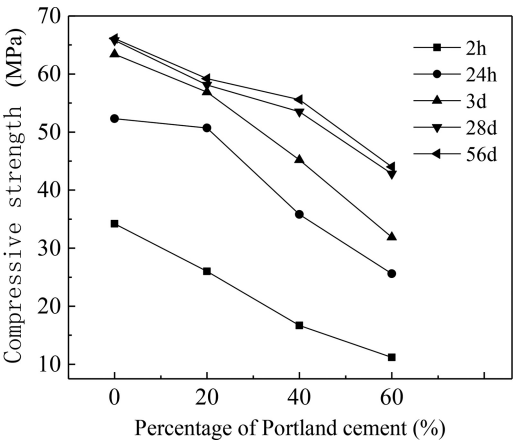

Figure 7. Compressive strength of concrete cast by rapid repair mortar.

Portland cement. Figure 7 shows that the compressive strength of concrete increased rapidly during the first 24 hours. For example, the compressive strength of concrete cast by mortar with and without 20% Portland cement was 50.7 MPa and 52.3 MPa at 1 day. And after 3 days, the growth rate of compressive strengths became slower, as the compressive strength of concrete produced by four mortars was 66.1 MPa, 59.2 MPa, 55.6 MPa and 44.0 MPa respectively at 56 days. Compared with Figure 4, the increment of compressive strength of mortars was higher than that of concrete

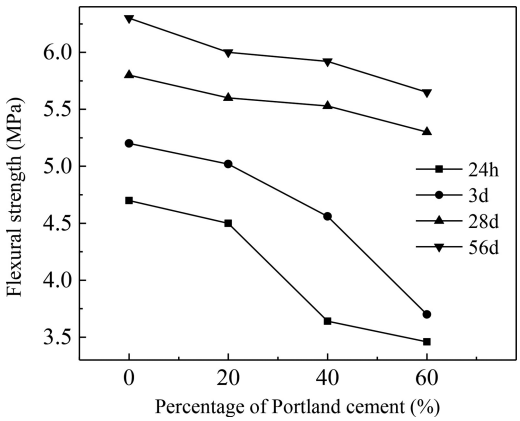

Figure 8. Flexural strength of concrete cast by rapid repair mortar.

Table 6. Permeability of concrete cast by rapid repair mortars.

Groups	Percentage of cement in mortar (%)		Electric flux (C)
	Sulfate aluminium cement	Portland cement	
1	100	0	263.5
2	80	20	617.3
3	60	40	523.3
4	40	60	595.3

after 24h, which was due to the more homogeneous and denser inter structure of mortars, especially for the interface.

Figure 8 shows that with the increasing of the percentage of Portland cement, the early age flexural strength of concrete was decreased, but the effect on flexural strength at greater ages for different concrete was much less apparent.

In order to keep the high early age strength, the percentage of Portland cement should be under 20%. At the same time, with the use of Portland cement, the mortar could be more economical.

3.2.2 *Permeability of concrete*

The test results of electric flux could be seen in table 6, and the results indicated that the permeability of concrete cast by rapid repair mortar was decreased with the addition of Portland cement into the mortar. According to the results in section 3.1.1, the mortars with more sulfate aluminium cement had higher fluidity, so the interface of the mortar and coarse aggregate could be more compact, and the permeability of concrete could be improved.

3.2.3 *Bond strength between concrete and steel*

The bond strength between concrete and steel is given in Table 7, and the results showed that the bond strength

Table 7. Bond strength of concrete and steel.

Groups	Percentage of cement (%)		Bond stress (MPa)
	Sulfate aluminium cement	Portland cement	
1	100	0	7.5
2	80	20	7.0
3	60	40	6.8
4	40	60	5.6



Figure 9. Marked and edge-cut area on concrete for repair.

was decreased with the increase of the percent of Portland cement in mortar. Because the fluidity of fresh mortars decreased with the increase of the percent of Portland cement, more defects would be created at the interface of concrete and steel.

4 FIELD APPLICATION

Based on the above results, a rapid repair mortar with 40% Portland cement was used for the patch repair of serious scaling deterioration of concrete slabs on the parking apron at an airport in Heilong Province of China. The scheme and techniques of the field application were as follows.

(a) Marked square areas on the concrete slabs which were needed to repair, and sawed the edges of the damaged concrete in 8 cm to 10 cm deep along the marks (Figure 9); (b) Crushed and removed the damaged concrete to a solid substrate concrete to form a shallow pit (Figure 10 and Figure 11); (c) Cleaned the small concrete pieces and dust using compressed air (Figure 12); (d) Mixed the rapid repair mortar at the field; (e) Poured the mortar into the pit bottom first and formed a mortar layer to enhance the bond between the old concrete and the repair layer (Figure 13); (f) Filled the pit with crushed stone with the size of 16–31.5 mm and then poured the mortar to produce concrete (Figure 14), and this could be done in two or three layers if the pit was too deep; (g) Smoothed the surface of



Figure 10. Crushing the damaged concrete.



Figure 11. Removing the crushed concrete.



Figure 12. Cleaning the pit with compressed air.

repair layer with a trowel (Figure 15); (h) Cured the repair concrete by covering with plastic films. (i) Cut the repair concrete if it covered the joints between slabs (Figure 16).

The rapid repair mortar performed very satisfactorily in this application. All the patches showed good appearance at the end of application, without cracks or disintegration. So far, the appearance of the repaired concrete slabs is quite good after 1 year.



Figure 13. Rapid repair mortar on the bottom of pit.



Figure 14. Filling the pit with crushed stone rapid repair mortar.



Figure 15. Smoothing the surface of repair layer.

In this application, crushed stone was used with the mortar to make concrete. If the old concrete was crushed and used as coarse aggregate on the repair spot, the repair process could be accelerated and it is better from the aspect of sustainability, which needs more research.



Figure 16. Final surface after joint-cutting.

5 CONCLUSIONS

(1) With the increasing of the percentage of Portland cement, the fluidity, the compressive strength, the flexural strength and the vertical expansivity of mortars were decreased, and the shrinkage rate was increased. And to meet the requirements of Chinese standard, the percentage of Portland cement should be lower than 20%.
(2) The compressive strength, the flexural strength and the permeability of concrete produced by the rapid repair mortar were decreased while the dosage of Portland cement increased. But all concrete with different dosages of Portland cement showed good bond strength with steel.
(3) The application of rapid repair mortar at an airport generally performed well.

REFERENCES

Cementitious grout (JC/T 986-2005). Chinese Industrial Standard. 2005. *China Building Materials Press*.

Code for utility technical of concrete admixture (GB 50119-2003). Chinese National Standards. 2003. *China Standards Press.*

Felekoğlu Burak, Tosun Kamile, Baradan Bülent, Altun Akın & Bahadır Uyulgan. 2006. The effect of fly ash and limestone fillers on the viscosity and compressive strength of self-compacting repair mortars. *Cement and Concrete research*. 36:1719–1726.

Kalagri A., Karatasios I. & Kilikoglou V. 2014. The effect of aggregate size and type of binder on microstructure and mechanical properties of NHL mortars. *Construction and Building Materials*. 53:467–474.

Klisinska-Kopacz Anna & Tilova Renata. 2012. Effect of hydrophobization treatment on the hydration of repair Roman cement mortars. *Construction and Building Materials.* 35:735–740.

Method of testing cements-Determination of strength (GB/T 17671-1999). Chinese National Standards. 1999. *China Standards Press.*

Mindess S & Young J F. 1981. Concrete Prentice-Hall. *Englewood Cliffs. NJ.* 12(5): 45–62.

Sang G. C. & Liu J. P. 2010. Study of properties of Portland and aluminate cementitious composited grouting material. *Materials Research Innovations*. 14(3):200–205.

Srinivasan C.B., Narasimhan N. Lakshmi & Ilango S.V. 2003. Development of rapid-set high-strength cement using statistical experimental design. *Cement and Concrete Research.* 33:1287–1229.

Standard for test method of performance on building mortar (JGJ/T 70-2009). Chinese Industrial Standard. 2009.*China Architecture & Building Press.*

Technical document. Technical requirements of pot type rubber bearing for high-speed rail bridge ([2005] 101). 2005. *Science and Technology Department of Ministry of Railways of China*.

Test method for fluidity of cement mortar (GB/T 2419-2005). Chinese National Standard. 2005. *China Standards Press.*

Test method for hydraulic concrete (DL/T 5150-2001). Chinese Industrial Standard. 2001. *China Electric Power Press*.

Yang Quanbing, Zhu Beirong, Zhang Shuqing & Wu Xueli. Properties and applications of magnesia-phosphate cement mortar for rapid repair of concrete. 2000. *Cement and Concrete Research*. 30: 1807–1813.

Zhang Xiaoping, Sun Changzheng & Zhao Tongfeng. Research on multivariate composite super early strength grouting materials. 2014. *Applied mechanics and materials*. 477–478:990–995.



Taylor & Francis
Taylor & Francis Group
http://taylorandfrancis.com

Concrete Solutions – Grantham et al. (Eds.)
© 2016 Taylor & Francis Group, London, ISBN 978-1-138-03008-4

Early-age cracking resistance of repair cement mortar with copolymer powder and fibers

Wencui Yang, Xiaoping Cai, Yong Ge, Jie Yuan & Dengling Zhou
Harbin Institute of Technology, Harbin, China

ABSTRACT: Cement mortars used for repairing concrete barriers, on which surface scaling deterioration due to deicer salts and freeze-thaw have occurred, are required to have good cracking resistance and durability. In this paper, the effect of dispersible copolymer powder, polyacrylonitrile fibers and basalt fibers on the consistency, strength, cracking resistance of cement mortars at early age and scaling resistance were studied. The results showed that adding copolymer powder and fibers improved the cracking resistance of mortars but decreased the consistency slightly. Copolymer powder reduced the compressive strength but increased the flexural strength at 28 days. The strength of mortars with polyacrylonitrile fibers reduced at early age but increased at 28 days, while basalt fibers or the hybrid of two fibers improved the strength from the early age to 28 days. Adding copolymer powder or polyacrylonitrile fibers improved the scaling resistance of mortars, and they were more effective working with air entrainment.

1 INTRODUCTION

Cement-based materials have been used for concrete repair and have demonstrated acceptable performance due to their compatibility with old concrete (Mirza et al. 2002 & Al-saad et al. 2001). However, cementitious materials are brittle and generate cracks easily because of their relatively low tensile strength and poor resistance to crack opening and propagation. A research showed that the thicker the repair layer, the lower the risk of generating initial defects (Park et al. 2009).

Cracking becomes more obvious when cement based materials are used for repairing damaged concrete surfaces. For example, concrete barriers, along with highways and roads, deteriorated severely due to the action of deicer salts and freeze-thaw cycles. This scaling deterioration started from the base of the barriers where deicer salts accessed first and then progressed and scattered to the whole surface. To smooth the damaged concrete surface and provide additional cover for corrosion protection, a repair overlay could be employed on the barriers, which was usually about 10 mm in depth after a part of surface concrete was removed (Yang et al. 2011). Therefore, this large but thin repair layer easily cracks due to shrinkage stress, particularly at early age.

Polymers and fibers are widely used to improve the cracking resistance of cementitious materials (Fiore 2015, Brandt 2009, Fowler 1999 & Chung 2004). Ramli's study found that the polymer modified ferrocements showed lower crack widths and higher first crack loads, indicating that adding polymer improved the bonding between aggregate, cement and polymer particles, producing a durable matrix and exhibiting higher cracking resistance (Ramli 2012). Another study showed that vinyl acetate and versatate copolymer (VA/VeoVa) powder improved the toughness significantly and reduced the shrinkage of cement mortar when the content was higher than 7%. (Wang & Wang 2011).

In general, the use of any type of fiber in cement-based mortars reduced plastic shrinkage cracking significantly (Juarez 2015). For example, the fibers (steel, mineral and synthetic) restrained the cracking process in concrete under mechanical loading by blocking the propagation and the coalescence of cracks (Hannawi 2016). A research showed that the addition of fibers didn't greatly change the cracking time, but reduced the crack width by about 70% in the case of macrofibers and by almost 90% with microfibers (Passuello 2009).

Controlling cracking of cement based materials at early age is critical to develop durable repair overlays on concrete structures. Some polymer fibers with low-modulus were used to reduce the shrinkage cracking of cement based materials in the few first hours of setting. Some authors recommended use of short fibers to reduce the long-term impact of early age damage and improve the durability of concrete with natural pozzolans cement and silica fume, as polypropylene fibers reduce shrinkage, cracking and permeability (Medina 2015).

In this paper, the effect of a dispersible copolymer powder, polyacrylonitrile fibers and basalt fibers on the cracking behavior of cement mortars at early age

Table 1. Properties of the dispersible copolymer powder.

Properties	
Appearance	White powder
Bulk density (kg/m^3)	470
Ash content (%)	11
Solids content (%)	98∼100
Minimum film forming temperature (°C)	10
Particle size (μm)	<400

Table 2. Properties of the polyacrylonitrile fibers.

Properties	
Length (mm)	6
Fiber number (Denier)	1.9
Density (g/cm^3)	1.18
Tensile strength (MPa)	372
Modulus of Elasticity (GPa)	14.6
Elongation (%)	17

was investigated using slab tests. The consistency, the flexural strength and the compressive strength were also measured. In addition, based on the cracking resistance results, an air entraining agent was used and the scaling resistance of mortars with copolymer powder or fibers was studied.

2 EXPERIMENTAL WORKS

2.1 *Materials*

A Chinese standard P· O 42.5 ordinary Portland cement and river sand with fineness modulus of 2.9 and apparent density of 2600 kg/m^3 were used in the experiments. A polyethylene vinyl acetate dispersible copolymer powder, VINNAPAS® LL 4023N, produced by Wacker Polymer Systems (Nanjing) Co. Ltd was used, and its properties are shown in Table 1, taken from the manufacture's specification sheets. Polyacrylonitrile fibers and basalt fibers, whose properties are given in Table 2 and Table 3 were adopted. A saponin-type air-entraining agent and a naphthalene-type water-reducing agent were used.

Table 3. Properties of the basalt fibers.

Properties	
Length (mm)	12
Density (g/cm^3)	2.80
Tensile strength (MPa)	4150–4800
Modulus of Elasticity (GPa)	93–110
Elongation (%)	3.1

Table 4. Proportion of the control mortar.

	Materials (kg/m^3)			
Series	Cement	Sand	Water-reducing agent	Water
K	572	1430	2.86	260

Table 5. Contents of the copolymer powder & fibers in mortars.

Series	Copolymer powder (% of cement mass)	Polyacrylonitrile fibers (kg/m^3)	Basalt fibers (kg/m^3)
K	0	0	0
J1	1.0	0	0
J2	1.5	0	0
J3	2.0	0	0
X1	0	0.6	0
X2	0	0.8	0
X3	0	1.0	0
X4	0	0	2.4
X5	0	0.5	1.2

2.2 *Mortar proportions*

The control mortar was mixed using cement, sand and water, the proportions of which are given in Table 4. Keeping the main materials constant, the copolymer powder, the polyacrylonitrile fiber and the basalt fiber were added into the mortars respectively. A mortar with two hybrid fibers was also prepared. The dosages of the copolymer powder and fibers of all mortars can be seen in Table 5.

2.3 *Samples and testing programs*

The consistency of mortar was measured according to JGJ/T70-2009, "Standard for test method of basic properties of construction mortar".

Prism mortar specimens with the size of 40 mm × 40 mm × 160 mm for strength tests were prepared, and then they were cured at a temperature of 20 ± 2°C with a relative humidity of 95% after being demoulded. The mortar strengths were determined according to GB/T 17671-1999 "Method of testing cements-Determination of strength".

Cube specimens with the size of 100 mm × 100 mm × 100 mm were made for the scaling resistance test. From the age of 26 days, the cube specimens had been immersed in 3.0 wt.% NaCl solution about 4 mm–6 mm depth from the bottom surface for 2 days. The frost resistance of mortars was tested by a slow freeze-thaw method. One freeze-thaw cycle involved freezing at (−18 ± 2)°C for 16–18 hours, and then thawing at room temperature for 6–8 hours, which simulated a natural freeze-thaw cycle in winter in



Figure 1. Slab mould for testing the cracking resistance of mortars.

the Northeast of China. During the freeze-thaw process, the bottom surface of each specimen was always immersed in 3.0 wt.% NaCl solution about 4 mm–6 mm depth. The scaling per unit area of specimen was used to evaluate the scaling resistance of mortar subjected to the freeze-thaw cycles and deicer salts solution. The scaling of specimens was monitored and recorded each 4 cycles, and three specimens were measured for each mortar and the average value was given in the results. The specimen was considered a failure if its scaling exceeded 1.0 kg/m^2.

The cracking behaviors of mortars were investigated using slabs restrained by external forms and fixed bolts. The slabs had a length of 600 mm, width of 600 mm and a thickness of 10 mm. 5 short bolts with length of 40 mm and 2 longer bolts with length of 100 mm were fixed on each steel edge at intervals of 75 mm to provide restraint in materails. A slab mould is shown in Figure 1.

Three slabs were cast for each mortar and the average value was used in results. Before casting, a Teflon® sheet was placed on the bottom surface of each mould to reduce the restraint force induced. After the mortar had been cast, a plastic film was used to cover the mortar surface for 1 hour. And then a 500W iodine-tungsten lamp was placed at 0.5 m above each slab to keep the temperature of the mortar top surface at 35°C, and a fan was placed aside the slabs to produce wind with a speed of 4m/s on the mortar surface. The lamps and fans were turned off after 4 hours. At the age of 24 h, the length and the width of each crack on the mortar surface were measured using a thread and a crack width microscope. For each mortar, the total length and the maximum width of cracks could be measured. The cracking area, A (mm^2), could be calculated as follows.

$$A = \sum L_i \times W_i \tag{1}$$

Where L_i and W_i are the length (mm) and the width (mm) of crack i for a mortar.

A cracking reduction index was employed to indicate the effect of copolymer powder or fibers on the cracking resistance of mortar, which could be calculated as follows.

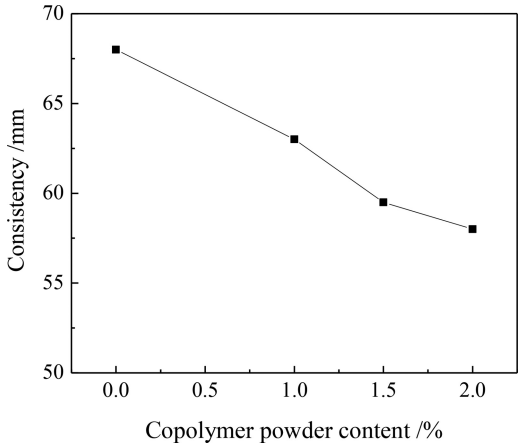

Figure 2. Effect of copolymer powder content on the consistency of mortar.

$$\eta = \frac{A_{mcr} - A_{fcr}}{A_{mcr}} \tag{2}$$

Where A_{mcr} and A_{fcr} are the cracking areas of the control mortar and the mortar with copolymer powder or fiber respectively.

The air content of fresh mortars was measured by an air entrainment meter, according to JGJ/T70-2009, "Standard for test method of basic properties of construction mortar".

3 RESULTS AND DISCUSSION

3.1 *Effects of copolymer powder on the mortar properties*

Althougth the consistency of mortar decreased slightly with increasing copolymer powder content, as shown in Figure 2, it still could meet the flowability requirement for repairing concrete barriers. Research showed that the copolymer had a controversial effect on the consistency of cement paste. On one hand, polymers had a water reducing effect due to the ball-bearing effect provided by the polymer particles and the air entrainment. On the other hand, polymers did not help in enhancing the workability of fresh concrete, since the polymers increased the viscosity (Betioli et al. 2012 & Ismail et al. 2011).

The effects of copolymer powder on the flexural strength and the compressive strength of mortars at different ages can be seen in Figure 3 and Figure 4. At the age of 3 days, the flexural strength of the cement mortar decreased slightly when the copolymer powder was added. This is attributed to the retarding effect of copolymer powder on the hydration of cement as the copolymer particles were adsorbed on the cement surface at early age. However, the flexural

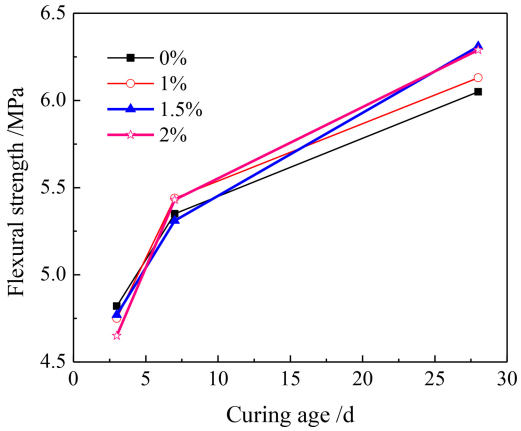

Figure 3. Effect of copolymer powder content on the flexural strength of mortar.

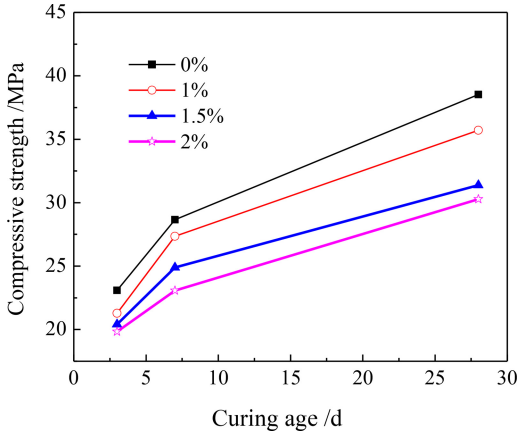

Figure 4. Effect of copolymer powder content on the compressive strength of mortar.

strength of mortar with copolymer powder increased at 28 days, for example, the flexural strength of mortar containing 1.5% copolymer powder increased 4.9% comparing with the control mortar. This is explained by a copolymer network being formed on cracks, capillary surfaces and paste-aggregate interfaces and thus reducing the interfacial defects. In addition, the more the copolymer powder was added, the more completely the copolymer network formed, thus, the flexural strength at 28 days increased with the increasing of copolymer powder content.

However, the addition of copolymer powder decreased the compressive strength of mortars at any age, and the compressive strength reduced with the increasing dosage of copolymer powder. The presence of soft polymer films in voids and around aggregates and cement particles may cause weak bonding between the particles, resulting in the lower compressive strength of mortars.

Under the lamp light and the blowing wind, the mortar slabs cracked due to water loss and shrinkage

Table 6. Number of cracks with different length.

Series	$L_i \geq 200$ mm	200 mm $> L_i \geq 100$ mm	$L_i < 100$ mm
K	1	1	11
J1	2	4	1
J2	1	3	3
J3	1	2	3
X1	0	4	3
X2	0	4	3
X3	0	4	2
X4	0	3	7
X5	0	4	6

Table 7. Number of cracks with different width.

Series	$W_i \geq 1.0$ mm	1.0 mm $> W_i \geq 0.5$ mm	$W_i < 0.5$ mm
K	2	7	4
J1	0	1	6
J2	0	1	6
J3	0	1	5
X1	0	6	1
X2	0	3	4
X3	0	2	4
X4	0	4	6
X5	0	5	5

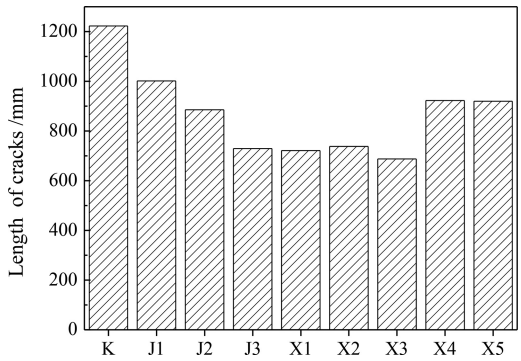

Figure 5. Total length of cracks on the surface of mortars with and without copolymer powder or fibers.

after a few hours of casting. The number of cracks on the mortar surface was counted according to the length and width, and the results are shown in Table 6 and Table 7. Compared with the control mortar, the total cracks number was reduced by adding copolymer powder. Moreover, the number of cracks with a length less than 100 mm or a width more than 0.5 mm decreased remarkably. Therefore, the copolymer powder is not helpful in controlling very long cracks but very effective in reducing wide cracks at early age.

More results of the copolymer powder effect on the cracking behaviors of mortar are given in Figure 5 to Figure 8. And all the results showed that the copolymer powder improved the early-age cracking

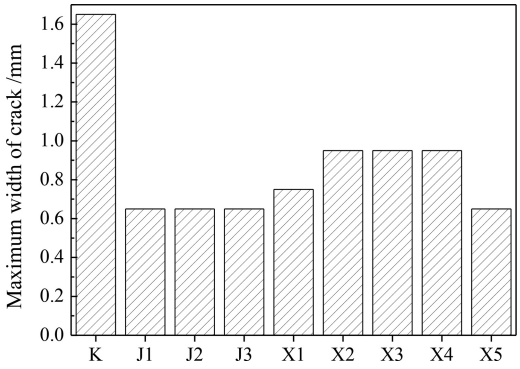

Figure 6. Maximum width of cracks on the surface of mortars with and without copolymer powder or fibers.

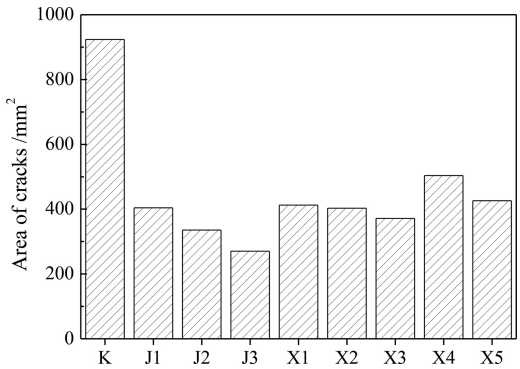

Figure 7. Area of cracks on the surface of mortars with and without copolymer powder or fibers.

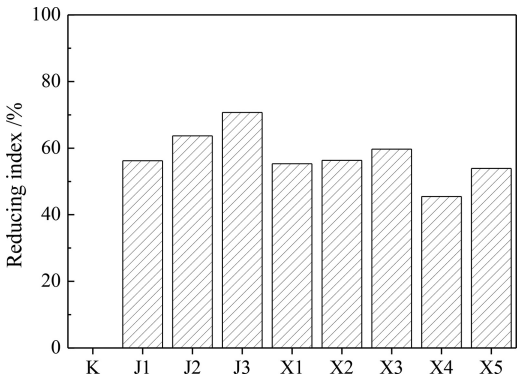

Figure 8. Reducing index of mortars with and without copolymer powder or fibers.

resistance of cement mortars. The total length and the area of cracks were decreased with the increasing of the copolymer powder content. The maximum width was reduced from 1.65 mm to 0.65 mm even when only 1% copolymer was used. The results of the reducing index also showed the improvement from adding copolymer powder on the cracking resistance of mortars. This is

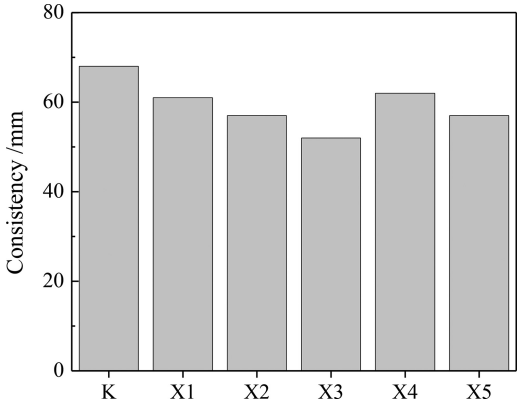

Figure 9. Effect of fibers on the consistency of mortar.

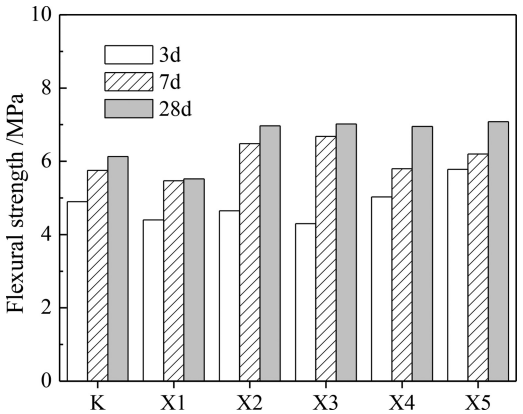

Figure 10. Effect of fibers on the flexural strength of mortar.

probably due to the copolymer network formed by the dispersed copolymer powder in mortars.

3.2 *Effects of fibers on the properties of mortars*

The effect of fibers on the consistency is given in Figure 9. It is can be seen that the consistency of mortar decreased with the increasing of polyacrylonitrile fibers content. In the groups X1 and X4 polyacrylonitrile fibers and basalt fibers were added with the same volume content respectively, and the consistency of X4 was slightly higher than X1, indicating that the basalt fibers had less influence on flowability of mortars. Furthermore, all mortars with fibers could meet the flowability requirement of GB/T 25181-2010.

The flexural strength of mortars with polyacrylonitrile fibers decreased slightly at the age of 3 days, but it increased obviously from 3 days to 7 days, and it exceeded that of the control mortar at 28 days, as shown in Figure 10. The comparison of X4 with K showed that the basalt fibers improved the flexural strength from early age to 28 days. Moreover, the hybrid of two fibers could make the flexural strength of mortars grow at any age.

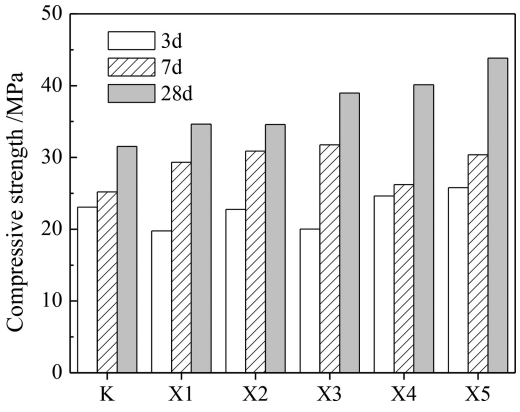

Figure 11. Effect of fibers on the compressive strength of mortar.

From Figure 11, the results of the compressive strength showed that adding polyacrylonitrile fibers into cement mortars reduced the compressive strength at early age but increased it at 28 days. Basalt fibers improved the compressive strength of cement mortar, while the hybrid of two fibers could improve the compressive strength effectively.

As shown in Table 6 and Table 7, and Figure 5 to Figure 8, fibers reduced the total number of cracks compared with the control mortar K, especially, the number of cracks with a length more than 200 mm or the width more than 1.0 mm. Therefore, the fibers are very useful in controlling large cracks. Additionally, the same volume percentage of polyacrylonitrile fibers was more effective than basalt fibers in reducing the early-age cracking of mortars, since more polyacrylonitrile fibers dispersed in a unit mortar. A study showed that increasing the fiber number per unit volume could reduce the total cracking area, the width of the cumulative cracking and the maximum cracking width (Juarez 2015). And Young's modulus of mortars at early age was similar to that of polyacrylonitrile fibers.

3.3 *Scaling resistance of mortars with copolymer powder or fibers*

Based on the results in section 3.1 and 3.2, the group J3 with 2% copolymer powder and the group X3 with 1 kg/m^3 polyacrylonitrile fibers were selected to add air entraining agent, and the air content is given in Table 8. The air content rose when the copolymer powder or polyacrylonitrile fibers were added into the cement mortar.

The scaling of mortars subjected to the salt solution and freeze-thaw cycles is shown in Figure 12. The scaling of non-air entrained mortar specimens increased quickly with the increase of freeze-thaw cycles and reached the limit of 1.0 kg/m^2, which meant failure of mortar. Adding the copolymer powder or polyacrylonitrile fibers improved the scaling resistance remarkably.

Table 8. Air content of mortars with copolymer powder or polyacrylonitrile fibers.

Series	Air entraining agent (%)	Air content (%)
K	0	2.0
J3-3	0	3.0
J3-5	0.015	5.0
X3-2.7	0	2.7
X3-4	0.015	4.0
X3-8	0.03	8.0

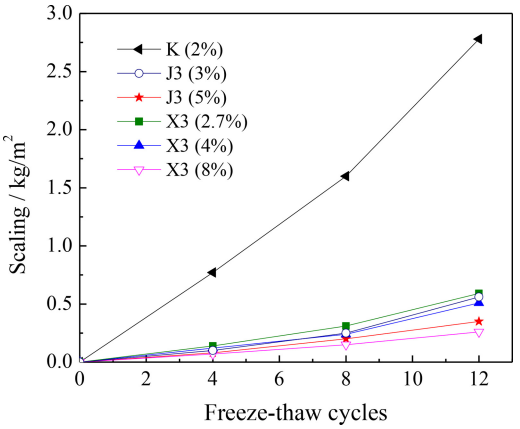

Figure 12. Scaling of air entrained and non-air entrained mortars.

The above results had shown that copolymer powder or polyacrylonitrile fibers improved the early-age cracking resistance of cementitious mortar as well as increasing the air content. Their crack reducing effects at early age could benefit the durability of mortars. In addition, the scaling decreased with increase of air content of mortar, so the copolymer powder or polyacrylonitrile fibers could work with air entraining to improve the scaling resistance of mortars effectively.

4 CONCLUSIONS

The conclusions could be drawn as follows:

(1) Adding copolymer powder, polyacrylonitrile fibers or basalt fibers decreased the consistency of cement mortar slightly, but all mortars could meet the requirement of flowability.
(2) Adding copolymer powder into cement mortar reduced the compressive strength but increased the flexural strength at 28 days. The strength of mortars with polyacrylonitrile fibers reduced at 3 days but increased at 28 days, while basalt fibers or the hybrid of two fibers improved the strength at any age.
(3) The early-age cracking resistance of mortars was improved obviously by adding copolymer powder and fibers. The copolymer powder helped in

controlling wide cracks and the fibers were effective in controlling large cracks. Polyacrylonitrile fibers were more effective than basalt fibers in reducing the early cracking of mortars at the same volume content.

(4) Using copolymer powder or polyacrylonitrile fibers improved the scaling resistance of mortars, and they were more effective working with air entraining.

ACKNOWLEDGMENTS

This work was supported by the National Nature Science Fund (No. 51208152).

REFERENCES

Al-Saad Ziad & Abdel-Halim Mohamed A. H. 2001. Laboratory evaluation of various types of mortars for the conservation of Qasr al-Bint monument, Petra-Jordan. *Engineering Structures*. 23: 926–933.

Betioli A. M, Gleize P. J. P, John V. M & Pileggi R.G. 2012. Effect of EVA on the fresh properties of cement paste. *Cement & Concrete Composites*. 34: 255–260.

Brandt Andrzej M. 2009. Fibre reinforced cement-based (FRC) composites after over 40 years of development in building and civil engineering. *Composite Structures*. 86: 3–9.

Chung D. D. L. 2004. Use of polymers for cement-based structural materials. *Journal of Materials Science*. 39: 2973–2978.

Fiore V, Scalici T, Bella G. Di & Valenza A. 2015. A review on basalt fibre and its composites. *Composites Part B*. 74: 74–94.

Fowler D. W. 1999. Polymers in concrete: a vision for the 21st century. *Cement and Concrete Composites.* 21: 449–452.

Hannawi Kinda, Bian Hui, Prince-Agbodjan William & Raghavan Balaji. 2016. Effect of different types of fibers on the microstructure and the mechanical behavior of Ultra-High Performance Fiber-Reinforced Concretes. *Composites Part B*. 86: 214–220.

Ismail Mohammad, Muhammad Bala, Yatim Jamaluddin Mohd, Noruzman Ainul Haezah & Soon Yong Woo. 2011. Behavior of Concrete with Polymer Additive at Fresh and Hardened States. *Procedia Engineering*. 14: 2230–2237.

Juarez C. A, Fajardo G, Monroy S, Duran-Herrera A, Valdez P, Magniont Camille. 2015. Comparative study between natural and PVA fibers to reduce plastic shrinkage cracking in cement-based composite. *Construction and Building Materials.* 91: 164–170.

Medina N. Flores, Barluenga G & Hernández-Olivares F. 2015. Combined effect of Polypropylene fibers and Silica Fume to improve the durability of concrete with natural Pozzolans blended cement. *Construction and Building Materials*. 96: 556–566.

Mirza J, Mirza M. S & Lapointe R. 2002. Laboratory and field performance of polymer-modified cement-based repair mortars in cold climates. *Construction and Building Materials*. 16: 365–374.

Park DongCheon, Ahn JaeCheol, Oh SangGyun, Song HwaCheol & Noguchi Takafumi. 2009. Drying effect of polymer-modified cement for patch-repaired mortar on constraint stress. *Construction and Building Materials*. 23: 434–447.

Passuello Alexandra, Moriconi Giacomo & Shah Surendra P. 2009. Cracking behavior of concrete with shrinkage reducing admixtures and PVA fibers. *Cement & Concrete Composites*. 31: 699–704.

Ramli Mahyuddin & Tabassi Amin Akhavan. 2012. Mechanical behaviour of polymer-modified ferrocement under different exposure conditions: An experimental study. *Composites: Part B*. 43: 447–456.

Wang Ru & Wang Pei-Ming. 2011. Action of redispersible vinyl acetate and versatate copolymer powder in cement mortar. *Construction and Building Materials*. 25: 4210–4214.

Yang Wencui, Ge Yong, Cai Xiaoping & Chen Xiao. 2011. Scaling Resistance and Application of Cementitious Repair Mortars for Concrete Barriers. *Proceddings of concrete solutions, 4th international conference on concrete repair*, *Dresden, Germany, 26–28 September, 2011*. 479–484.



Taylor & Francis
Taylor & Francis Group
http://taylorandfrancis.com

Repair and preservation of heritage structures, Roman cement



Taylor & Francis
Taylor & Francis Group
http://taylorandfrancis.com

Concrete Solutions – Grantham et al. (Eds.)
© 2016 Taylor & Francis Group, London, ISBN 978-1-138-03008-4

Historical and structural aspects of the durability and maintenance of a reinforced concrete market hall building from the early 20th century

P. Berkowski
Wroclaw University of Technology, Wroclaw, Poland

M. Kosior-Kazberuk
Bialystok University of Technology, Bialystok, Poland

ABSTRACT: The design and construction of the considered reinforced concrete arched frame structure of the market hall in Wroclaw on Piaskowa Street date from the years 1904–1908. This is a three-nave building with a basement and galleries on the first floor that surround the main hall. On plan the object has dimensions of about 39.0 × 86.0 m and the total height reaches nearly 21.0 m. The main load bearing structure consists of parabolic arches with a span of 19.0 m, connected by transversal castellated beams with a length of 12.0 m. Elements of the construction history, a description of the current technical condition and durability, as well as a description of the future maintenance plan of the reinforced concrete structure of the market hall building are presented in the paper. Historical methods used at the beginning of the 20th century for the structural analysis and design of RC structures are also briefly described and analysed.

1 CONSTRUCTION HISTORY AS A PART OF ASSESSMENT OF HERITAGE BUILDINGS

Issues related to the processes of maintenance and assurance of continued and safe exploitation of historic buildings are closely related to the processes of their diagnosis, repair and strengthening. What is more, if a building has heritage value and is on the list of monuments protected by law, various aspects related to conservatory requirements must be taken into account during renovation. Such problems also concern quite new reinforced concrete structures which are already considered to be historical.

The beginning of the twentieth century brought the development of the use of reinforced concrete as a building material that allowed for the construction of many revolutionary engineering structures that were previously impossible to erect (np. Spangenberg 1910a, b, Mändel & Orro 2012, Jasieńko et al. 2013, Crevello et al. 2015). In those days, concrete was considered as a material of extraordinary durability and structures made from it were considered as maintenance free and with no need for protection during their operational life. This was due to the lack of experience in the use of structures made of this material, as well as to the lack of knowledge of the phenomena occurring in it under different environmental impacts. Only from the mid twentieth century did the development of research on issues of durability of concrete and reinforced concrete and related methods of diagnosis begin (eg. Heinemann et al. 2012).

One extremely important element for a proper diagnosis of the technical condition of historic buildings, and also for the adequate design of the process of their refurbishment or of the actions associated with prolonging the time of their use and the processes associated with maintenance, should be the conducting of architectural and structural historical analysis. Such analysis must be related to the following aspects used during the design and construction of the object: design solutions, calculation methods of structural analysis, methods of the dimensioning of structural components, properties of building materials and technologies of their production, and also the technology of construction, including the quality of workmanship (ICOMOS 2003, Heinemann et al. 2012). However, such actions should be taken not only from the point of view of the architectural and conservational needs, but also to gain knowledge of applied historic design solutions and techniques.

Such research, supported of course by the use of the full range of modern material examination techniques and computational simulations, allows a more complete understanding of the analyzed structure. It also provides a possibility to adopt the best technical solutions in the broadly defined actions with an aim to prolong the service life of such heritage structures.

2 OUTLINES FOR THE MAINTENANCE PLAN

Models describing the process of exploitation and maintenance of engineering structures and buildings during their service life are extensively analyzed and described in the literature (ex. NTH 2012). The widest

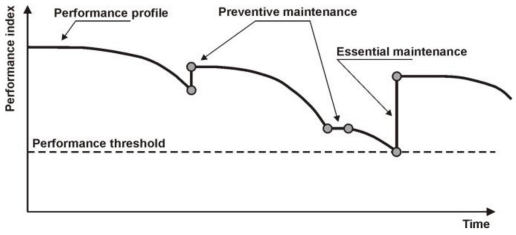

Figure 1. Effect of two main types of maintenance on structural performance (Frangopol & Soliman 2015).

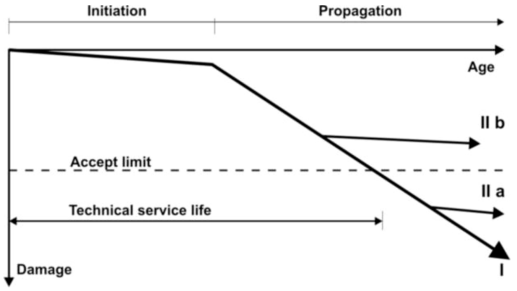

Figure 2. Service life of concrete structures – a two-phase deterioration model (Folič 2009).

analysis of models and methods of life-cycle performance of structural systems were presented in the last period, for example, by Gulvanessian (2012), Sabation et al. (2015) and Frangopol & Soliman (2015). For example, Frangopol and Soliman (2015) described a simple and clear graphical presentation of structural performance taking into consideration the effect of different maintenance types. In Fig. 1, the effects of various maintenance types on the performance of a deteriorating structure are shown. It is very important to define when and what level of maintenance should be introduced: to perform only preventive, essential, or both maintenance types is a difficult question that can be answered through life-cycle management techniques (Frangopol & Soliman, 2015). Considering concrete structures, Folič (2009) described three different types of service life depending on the type of considered performance: *technical service life* (Fig. 2) – the time of exploitation until an acceptable limit state is reached (failure), *functional service life* – the expected time of exploitation until the structure no longer fulfils the functional requirements and also *economic service life* – the time in service until the replacement of the structure is economically justified more than keeping it in service.

Subjects relating to formation and processes of material and structural degradation in structures made of concrete and reinforced concrete (Tang et al. 2015), including historic ones (Bertoloni et al. 2011 Foti 2014 Crevello et al. 2015 Custance-Baker, 2015), are now very well recognized, regularly updated and often codified (EN 1504 2010).

This is done in close connection with the development of research and measurement techniques, allowing the study of the properties of concrete, evaluation of structural durability and development of new repair materials (Budelamann et al. 2012, Kumar Verma et al. 2013, Wachsmann & Budelmann, 2012, EN 1504 2010, Raupach 2009).

The mechanisms of the destruction process of concrete, both contemporary and historical ones, are the same, however, due to many factors relating to the properties of materials or technology used, not to mention the difference in service life, concrete in historic buildings may be more susceptible to the influence of environmental factors. This has, of course, a significant impact on the durability of historical reinforced concrete structures.

In the case of objects made of reinforced concrete and recognized as historical monuments, it is advisable to also take into account aspects resulting from the need to comply with conservation guidelines regarding the process of their maintenance and repair (Heinemann et al. 2012, Heinemann 2016). In practice, however, most historic reinforced concrete structures are repaired in a traditional way due to the fact that they are made of modern concrete. The main aim is to repair damage or strengthen the structures so that they satisfy the functional requirements and that its security is assured. Rarely, at least until recent years, were relevant tests of old concrete carried out which aided the selection of repair materials that would be compatible with the original design material (Valença et al. 2012, Heinemann, 2016).

The discussed reinforced concrete bearing structure of the market hall, despite the passage of over 100 years of use, as well as the survival time of two world wars, is in a quite good technical condition. By far the greatest impact on its state was the fact that it is located inside the building and protected from all external environment influences that affect the durability of concrete. The exceptionally high quality of workmanship for the time when the building was constructed, which was determined during the archival documentation investigation and also by current inspection, was of considerable importance. This was undoubtedly related to the assumption approved in the project that the surface of the concrete structure would remain natural with no additional painting.

However, during service life the discussed building was subjected to various refurbishments and the first major renovation of the concrete structure took place in the early 80s which was about 70 years after the erection of the object. This was therefore after the period of exploitation, when the first signs of destruction of concrete in the normal operation of the structure normally appear and after its exposure to the influence of environmental impacts.

In the case of the presented object, although different repair measures have been conducted, there is no comprehensive program of its maintenance. Listed below are some points of the standard diagnostic process of historic structures, as part of a maintenance program for a discussed structure, taking into account

aspects relating both to ensure its durability and to preserve its historical values.

As was mentioned in section 1, there are recommendations for the reconstruction process of monumental buildings of historical value, defined by ICOMOS (2003). They consist of a set of principles and guidelines for the analysis and restoration of old buildings and define three main phases in the study of historical constructions. They are essential to define the durability related maintenance plan of heritage structures:

- Diagnosis:
  - analysis of archival documentation (construction history),
  - an architectural and structural survey,
  - a conservation opinion,
  - a geotechnical study,
  - material examination,
  - definition of the level of technical deterioration,
  - cause of damage;
- Safety evaluation:
  - structural expertise (structural and strength calculations, etc.);
- Design of intervention:
  - definition of repair technologies,
  - definition of structural safety during repair,
  - monitoring of a structure during repair.

However, to define a proper management schedule for such an iconic structure it would be necessary to additionally include a maintenance plan for the structure related to the creation and implementation of the lifecycle including anticipated costs of all scientific and technical activities.

From all the above points of the assessment process, only the history of the construction of the building (section 3) has currently been recognised. However, it would also require the additional survey of historical sources, despite the presence of the Municipal Building Archive, the library of the University of Wroclaw or even Internet resources.

3 ELEMENTS OF THE CONSTRUCTION HISTORY OF THE MARKET HALL RC STRUCTURE

In the following chapter, based on an example of a reinforced concrete historical market hall, four aspects from the aforementioned elements included in the historical analysis of heritage buildings are outlined, ie.: applied design solutions, methods of structural analysis, methods of dimensioning, and properties of building materials.

3.1 *Applied design solutions*

The original architectural design of the market hall building – Markthalle I – on Piaskowa Street in Wrocław (together with the design of a similar, but not now existing, Markthalle II), was made in the years 1901–1903 by the city architect Richard Plüdemann. Developed on this basis by the city building inspector Richard Friese, the conceptual design of the hall was executed between 1904–1906 and included a construction of the steel structure in the aboveground part, based on the reinforced concrete foundation (Figs. 3 & 4).

Heinrich Küster, a specialist in steel structures, was the author of the execution version of the design which was introduced in 1906 (Küster 1909, 1909b, 1911). Finally, the building was built in the years 1906–1908 (Gryglewska 2008). As early as in 1906, during the execution of works relating to the foundations, the decision to replace the above ground steel structure with the reinforced concrete structure (Figs 5 & 6) was taken at the request of H. Kuster. This resulted, of course, in an increase of the loads on foundations, but was solved by strengthening them. This concept was put forward after analyzing a variety of design solutions of different market hall buildings existing at the time, but primarily due to the properties of concrete structures such as: durability, fire resistance and no need of maintenance. An important factor that also influenced such a decision was the anticipated savings in the cost of the construction, including those arising from the lower costs of maintaining concrete structures as compared with steel structures. Finally, a building with a horizontal projection similar to a rectangle, with a total length of 85.97 m and a width from 38.97 m to 56.33 m was designed and constructed (Fig. 7). The primary load-bearing structure consists of 6 parabolic arches of reinforced concrete (Figs 5, 6 & 8) with a height of 16.95 meters (and with a skylight – 20.80 m) spaced at every 12.00 m.

The arches are connected on two levels (at the windows) by castellated reinforced concrete beams (Figs 6 & 9). Smaller arches were designed in three transverse aisles. In addition, stiffening of the overall structure is ensured by the reinforced concrete gallery, located at first floor level and extending around the entire hall. The roof was made of prefabricated reinforced concrete slabs, with cork as thermal insulation, and covered by ceramic tiles.

Due to the high groundwater level (85 cm above the bottom of the basement), the foundation, as well as the basement part of the building, was made of a reinforced concrete slab of 50 cm in thickness (with a 9 cm layer of base concrete), monolithically connected to the walls of the basement.

As a result of the use of such a solution, these elements created a waterproof basin without dilatation. Its tightness was assured by insulation of 2 bonded layers made of felt and asphalt, derived 20 cm above the maximum level of the groundwater.

3.2 *Methods of structural analysis*

From a structural analysis point of view, reinforced concrete main bearing arches were modelled as flat bi-articulated ones. The calculation of the internal

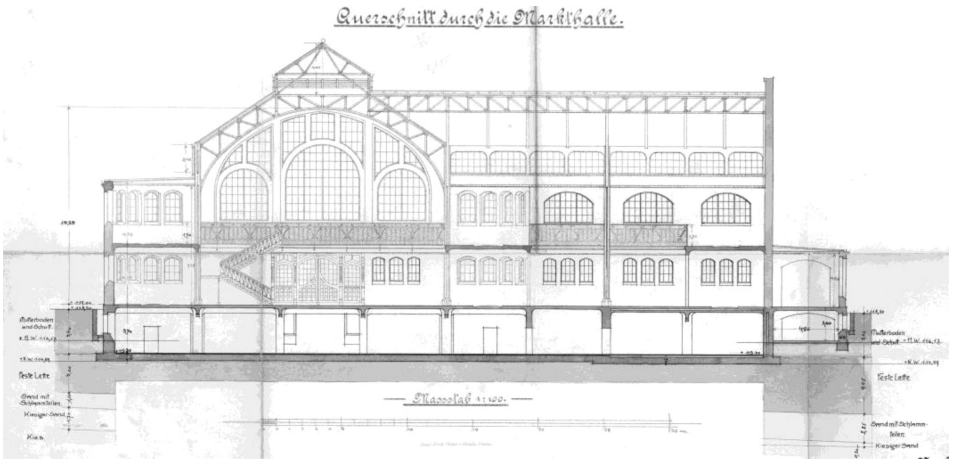

Figure 3. Cross-section of the market hall main nave – steel structure (initial design) 1904 r. (WCBA 1904).

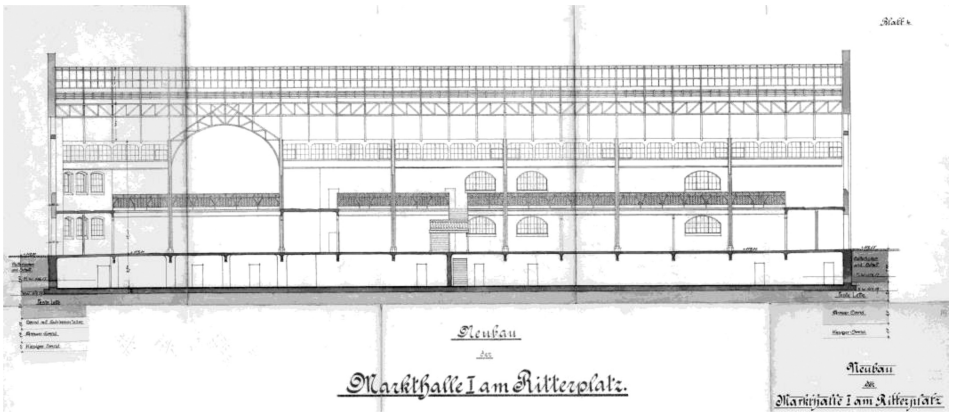

Figure 4. Cross-section along the main nave – steel structure (initial design) 1904 r. (WCBA 1904).

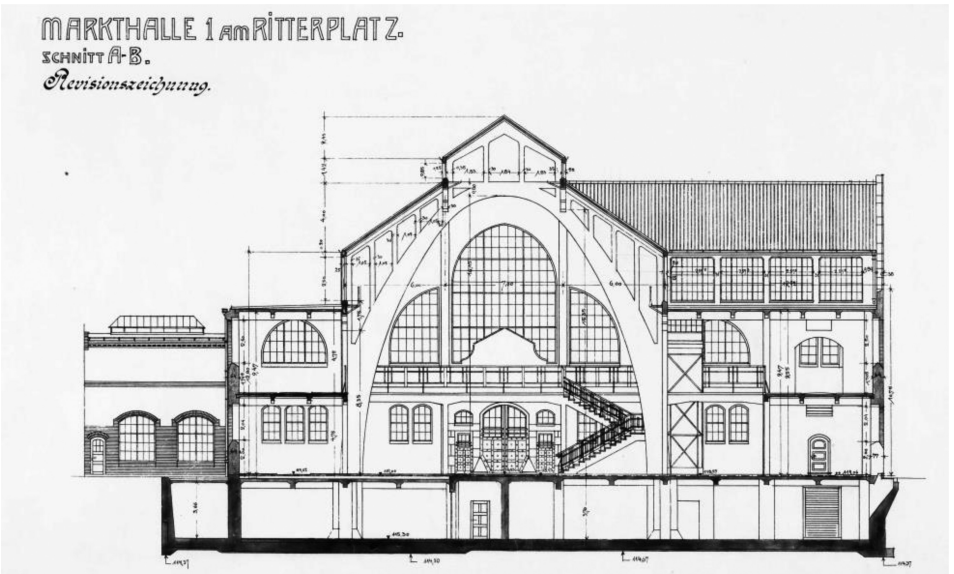

Figure 5. Cross-section of the market hall main nave – RC structure (constructed) (WCBA 1909).

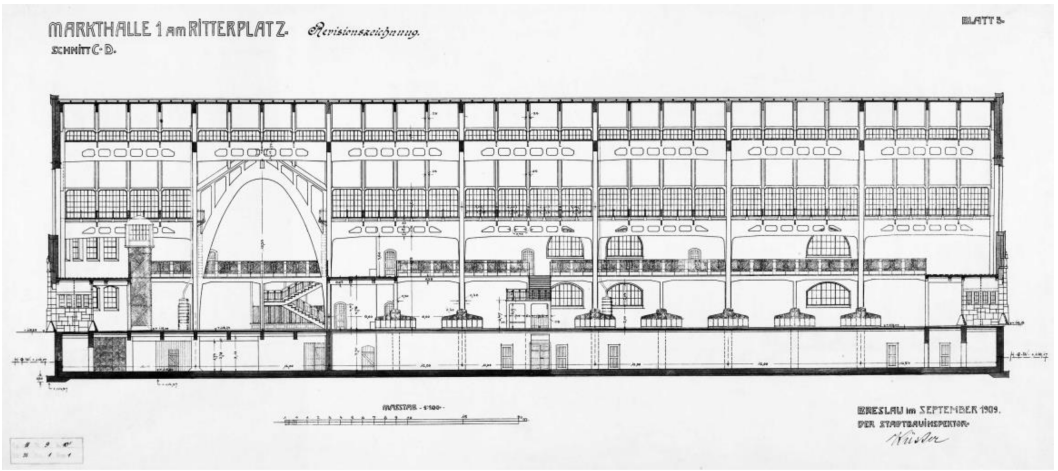

Figure 6. Cross-section along the main nave – RC structure (constructed) (WCBA 1909).

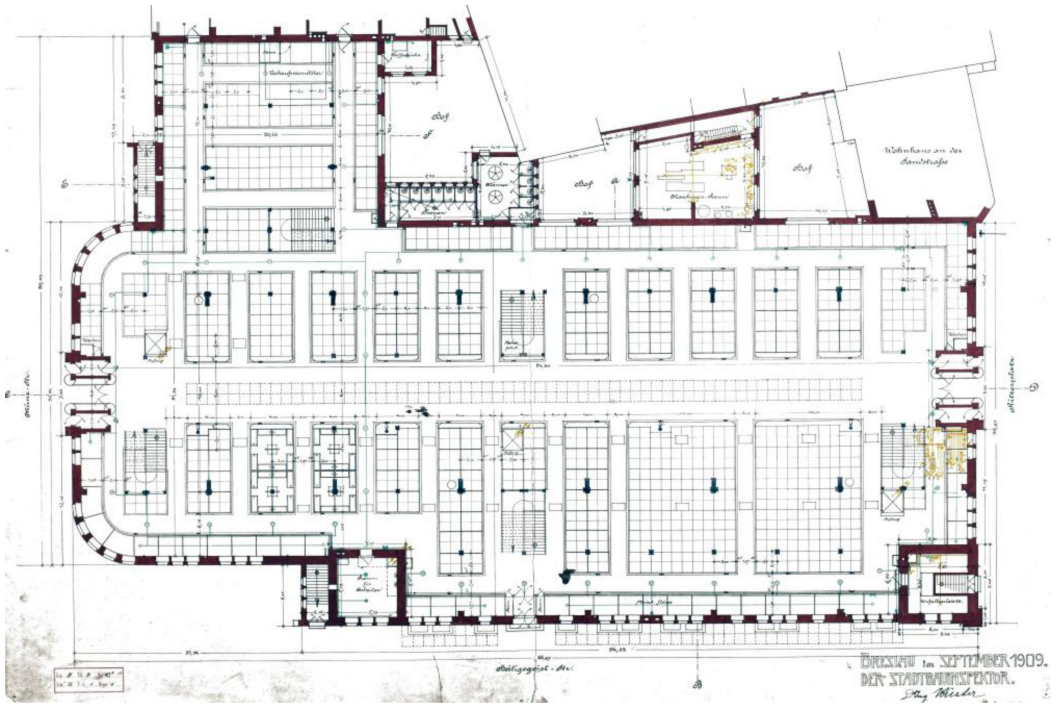

Figure 7. Ground floor plan (constructed) (WCBA 1909).

forces was made graphically (Figs 10 & 11) for each load scheme, including the temperature influence. An applied graphic solution made it possible to determine the position of the joints so that it was possible to centre load on the pillars and walls of the basement (Küchle 1909). Archival technical documentation (WCBA 1907) summarizes the loads and their location, which allows for their verification in the case of the analysis for the current state of loads.

The discussed structure of the market hall undoubtedly requires a spatial scheme and such a model should be assumed for computational verification during structural analysis.

In this case, it would be essential to create an appropriate model using, for example, 3D scanning. However, computational verification for the 2D model used in the historical design can also give valuable information on the stress state of individual load-bearing



Figure 8. View of the main structural arches.



Figure 9. View of the castellated stiffening beams.

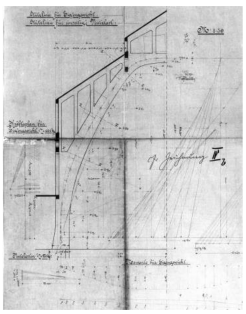

Figure 10. Graphical calculations for the main arch (WCBA 1907).

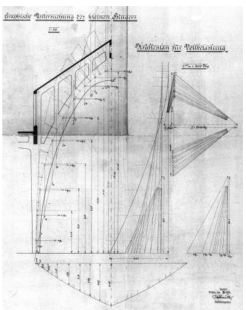

Figure 11. Graphical calculations for the small arch (WCBA 1907).

structural elements and evaluation of the correctness of the adopted static model.

3.3 *Properties of building materials*

Issues relating to the chemical, physical and mechanical properties of materials used to make the structure are crucial in the assessment of the structural strength and the further life time prediction of historical buildings (Hellebois et al. 2010, 2011, Mezzina et al. 2010, Jasieńko et al. 2013). Based on the analysis of archival records (WCBA 1907) and literature (Ahnert & Krause, 1991) it was found that for steel a tensile stress of 100 MPa and a Young's modulus of 210 GPa were adopted. The stress in the concrete did not exceed 5 MPa, and the Young's modulus was determined to be 14 GPa.

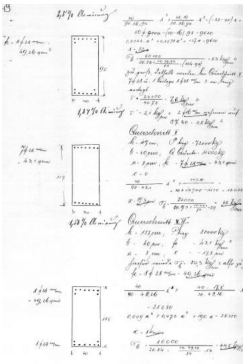

Figure 12. Example of rebar calculation (WCBA 1907).

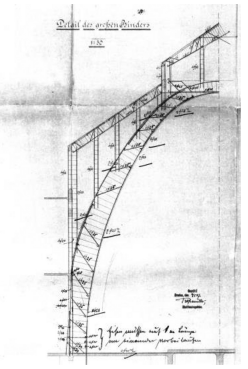

Figure 13. Rebar disposition in the main arch (WCBA 1907).

Of course, one of the key tasks in the process of assessing the discussed structure would be to identify the real material parameters, as well as analysis of the chemical composition of the concrete, using different types of examination, both non-destructive and destructive.

3.4 *Methods of dimensioning*

Calculations (Fig. 12) and reinforcement drawings (Fig. 13) of the main load-bearing components of the hall building are included in the preserved archival documentation (WCBA, 1907). Cross-sectional dimensions of the main arc of the bearing structure are variable, changing from 40 × 80 cm to 40 × 155 cm. For example, in these cross-sections the reinforcement was designed as a symmetrical one, respectively: 5 ϕ 28 mm and 8 ϕ 28 mm, both at the top and bottom.

An extremely important element of the evaluation process is the checking of the cover depth, and also the real diameter and distribution of reinforcement using non-destructive techniques. Experimental determination of the chemical composition and strength of the steel used would require sampling which would require local damage to structural elements. In the case discussed here, however, sampling would even be possible for destructive testing, due to the fact that some elements of the structure are covered, allowing for their temporary destruction.

4 THE CURRENT TECHNICAL CONDITION OF THE STRUCTURE

The considered market hall was built in the first decade of the twentieth century (Fig. 14) and during



Figure 14. View of the front façade in 1909 (A. Pichler, dolny.slask.org.pl).



Figure 15. View of the front façade during repair works in 1980–83 (dolny.slask.org.pl).

its operation time it was subjected to all kinds of minor refurbishment, primarily pertaining to elements of finishing (years 1936–1938).

The first important structural intervention took place after World War II in order to repair some minor damage caused by the war. A fragment of the roof was reconstructed and a section of the reinforced concrete ceiling above the basement was replaced by a segmental ceiling on steel beams. It was only in 1971–73 and 1979–1982 when expert reports and a modernization design were prepared. In the period from 1980 to 1983 the building was subjected to a major repair (Fig. 15).

Regarding the structure, the overhaul mainly consisted of repairing damage, restoring cavities in the concrete and brick walls and protecting the reinforced concrete surface with renovation materials (however, there is no data about what materials were used).

From a structural point of view we are dealing primarily with two construction materials: concrete/reinforced concrete of foundation slabs, the basement and arched supporting structure, and the brick masonry exterior walls.

To date, only a preliminary examination of the whole building has been conducted, designed to identify the basic types of damage and their range. Regarding the reinforced concrete structure, for the components inside the building, the following damage was found:

– local stains with discolouration on the surfaces of the roof panels and reinforced frames (Fig. 16);
– local, multi-directional cracks and honeycombed concrete on the bottom surfaces of the roof panels (Fig. 17);
– a few small cracks on elements of the transversal arch frames at the roof level above the nave (Fig. 18);
– minor cracks in the ceiling slab above the ground floor and over the gallery, as well as on the floors of the front of the tower (Fig. 19),

and in the case of the elements situated on the outside of the building:

– cracks, superficial damage and spalling of fragments of the repaired concrete in window frame elements (Fig. 20).

With respect to the exterior masonry walls made of solid bricks which serve both as a support structure for the concrete floors and beams as well as curtain walls, damage is reduced to local surface corrosion of the bricks, lack of mortar in joints (leaching), and small diagonal scratches, typical for brick walls. Summarizing, both the reinforced concrete structure of the market hall, especially the one situated inside the building, as well as the brick or stone masonry elements, are currently in a quite good technical condition, despite the passage of almost 110 years since the construction of the building. Repair works from the early 80s of the twentieth century certainly had a positive impact on this state. Obviously, conditions of the operational life of the facility were decisive for the lack of serious damage. The whole reinforced concrete structure of the market hall is practically located inside the building and therefore protected against all environmental influences that have a destructive impact on the concrete. Locally occurring stains resulting from penetration of rainwater through leaky roof covering, have been systematically repaired. Existing local cracks in the structural elements, however, do not threaten the overall reliabilty of the structure.

5 FINAL REMARKS

In relation to the presented reinforced concrete structure of the historic market hall, which is undeniably important in the history of reinforced concrete structures, it is necessary to develop a detailed program of its maintenance. It should not only contain a prediction of the development of existing or new damage and degradation of the material, but also guidelines for repair and renovation works in order to ensure its further, safe operation. From the point of view of



Figure 16. Stains on roof slabs and the arch surface.



Figure 17. Cracks and honeycomb concrete in roof slabs.



Figure 18. Local cracks in the main arch roof elements.

the completeness of such a program and with regards to architecture and design, its indispensable elements should be both the historical analysis of the design and the construction of this building, as well as the entire course of its exploitation. Also, conservatory procedures should be taken into account. The historic market hall discussed is undoubtedly an outstanding example of the use of reinforced concrete for the construction of pioneering engineering structures, and due to its



Figure 19. Local cracks in floor slabs.



Figure 20. Local deterioration of concrete on exterior surfaces.



Figure 21. Current view of the market hall – the masonry front façade after renovation.

relatively good technical condition and implemented renovations, should have a strategic plan for continued maintenance. Rapid development of such a plan and implementation of appropriate measures would ensure its continuous safe operation and the preservation of its utility functions and historic value.

REFERENCES

Ahnert, R., Krause, K. H. 1991. *Typische Baukonstruktionen von 1860 bis 1960. Zur Beaurteilung der vorhandenen Baussubstanz, Band 1*. Berlin: Verlag für Bauwesen (in German).

Bertolini, L., Carsana, M., Gastaldi, M., Lollini, F. & Redaelli, E. 2011. Corrosion assessment and restoration strategies of reinforced concrete buildings of the cultural heritage. *Materials and Corrosion*, 62(2): 146–154.

Budelmann, H., Holst, A., Wachsmann, A. 2012. Durability related life-cycle assessment of concrete structures: Mechanisms, models, implementation. In A. Strauss, D.M. Frangopol & K. Bergmeister (eds), *Life-Cycle and Sustainability of Civil Infrastructure Systems; Proc. of Int. Symp., Vienna, 3–6 October 2012*. Leiden: CRC Press/Balkema.

Crevello, G., Hudson, N., Noyce, P. 2015. Corrosion condition evaluations of historic concrete icons. *Case Studies in Construction Materials* 2: 2–10.

Custance-Baker, A., Crevelllo, G., Mcdonald, S. & Normandin, K. (eds). *Conserving Concrete Heritage. An Annotated Bibliography*. Los Angeles: The Getty Conservation Institute.

EN 1504: 2010 *Products and systems for the protection and repair of concrete structures – Definitions, requirements, quality control and evaluation of conformity. Part 1 to 10*. European Committee for Standarization.

Folič, R. 2009. Durability design of concrete structures – part I: Analysis fundamentals. *Facta Universitatis. Architecture and Civil Engineering* 7(1): 1–18.

Foti, D. 2014. Shear Vulnerability of Historical Reinforced-Concrete Structures. *International Journal of Architectural Heritage: Conservation, Analysis, and Restoration* 9(4): 453–467.

Frangopol, D.M, Soliman, M. 2016. Life-cycle of structural systems: recent achievements and future directions. *Structure and Infrastructure Engineering* 1(12): 1–20.

Gryglewska, A. 2008. *Market halls in Wrocław1908–2008*. Wrocław: Wrocław Museum of Architecture & Via Nova (in Polish).

Gulvanessian, H., Calgaro, J-A. & Holický, M. 2012. *Designer's guide to Eurocode: Basis of structural design*. 2nd ed. ICE Publishing Ltd.

Heinemann, H.A. 2016. The development of a new Dutch guideline for the conservation of historic concrete (URL 4005). In F. Dehn et al. (eds), *Concrete Repair, Rehabilitation and Retrofitting IV; Proc. of Int. Conf., Leipzig, 5–7 October 2015.* London: Taylor & Francis Group.

Heinemann, H.A., Zijlstra, H., van Hees, R.P.J. & Nijland, T.G. 2012. From concrete repair to concrete conservation: How to preserve the heritage values of historic concrete. In M. Grantham et al. (eds), *Concrete solutions; Proc. of Int. Conf., Dresden, 26–28 September 2011*. Leiden: CRC Press/Balkema.

Hellebois, A., Germain, O., & Espion, B. 2010. Reinforcement assessment in early reinforced concrete constructions. In Forde, M. (ed.), *Structural Faults and Repair, Proc. of the Int. Conf. Edinburgh*: Engineering Technics Press.

Hellebois, A., Espion, B. 2011. Material properties of reinforced concrete at the turn of the 20th century: a review of primary literature. In *Proc. of the 2nd WTA PhD Symp., Brno, 6–7 October 2011*.

ICOMOS International Council on Monuments and Sites. 2003. *ISCARSAH – Recommendations for the analysis, conservation and structural restoration of architectural heritage*.

Jasieńko, J., Moczko, A., Moczko, M., Dżugaj, R. 2013. Dome of the Centennial Hall in Wrocław. Mechanical and physical properties of hundred years old concrete. In J. Biliszczuk, J. Bień, P. Hawryszków & T. Kamiński (eds), *Concrete Structures in Urban Areas; Proc. of Central European Congress on Concrete Engineering, Wrocław, 4–6 September 2013*. Wrocław: DWE.

Kumar Verma S., Singh Bhadauria, S. & Akhtar, S. 2013. Estimating residual service life of deteriorated reinforced concrete structures. *American Journal of Civil Engineering and Architecture* 1(5): 92–96.

Küchle, F. 1909. Die städtische Markthalle am Ritterplatz in Breslau. *Ostdeutsche Bau-zeitung* 16(7): 93–96.

Küster, H. 1909a. Die städtischen Markthallen in Breslau. *Zentralblatt der Buaverwaltung* 11(29): 74–78.

Küster, H. 1909b. Die Verwendung des Eisenbetons bei den Breslauer Markthallen, *Deutsches Bauzeitung* 8(6): 34–36.

Küster, H. 1911. Markthalle I am Ritterplatz zu Breslau. *Der Industriebau* (2): 281–285.

Mändel, M., Orro, O. 2012. The marvellous reinforced concrete shells of Tallinn seaplane hangars in the context of early concrete architecture in Estonia. *Construction History* 27: 65–85.

NTH. 2012. Niedersächsische Technische Hochschule. http:///www.nth-nau.de.

Raupach, M. 2009. Research in the field of repair – Actual approaches and future needs. In Alexander M. et al (eds), *Concrete Repair, Rehabilitation and Retrofitting II*: 67–72. London: Taylor & Francis Group.

Sabation, S., Frangopol, D.M. & Dong You. 2015. Life cycle utility-informed maintenance planning based on lifetime functions: optimum balancing of cost, failure consequences and performance benefit. *Structure and Infrastructure Engineering* DOI:10.1080/15732479.2015.1064968.

Spangenberg H. 1910a. Zwei monumentale Hallenbauten in Eisenbeton. *Schweizerische Bauzeitung* 55/56(21): 273–278.

Spangenberg H. 1910b. Zwei monumentale Hallenbauten in Eisenbeton. *Schweizerische Bauzeitung* 55/56(22): 293–296.

Tang, S.W., Yao, Y., Andrade, C. & Li, Z.J. 2015. Recent durability studies on concrete structure. *Cement and Concrete Research* 78: 143–154.

Valença, J., Almeida, C., Júlio, E.S. 2012. Concrete heritage: Tentative guidelines for the 'patch restoration method'. In: *Concrete Repair, Rehabilitation and Retrofitting III, Alexander et al. (eds)*. Taylor & Francis Group, London.

Wachsmann, A., Budelmann, H. 2012. Life time prediction for concrete repair measures In A. Strauss, D.M. Frangopol & K. Bergmeister (eds), *Life-Cycle and Sustainability of Civil Infrastructure Systems; Proc. of Int. Symp., Vienna, 3–6 October 2012*. Leiden: CRC Press/Balkema.

WCBA Wrocław City Building Archive. 1907–1909.



Taylor & Francis
Taylor & Francis Group
http://taylorandfrancis.com

Concrete Solutions – Grantham et al. (Eds.)
© 2016 Taylor & Francis Group, London, ISBN 978-1-138-03008-4

Restoration of historical heritage in Russia: The age of architectural concrete

V.R. Falikman
Moscow State University of Civil Engineering, Moscow, Russia

V.V. Deniskin
Scientific Research Center "Construction", Moscow, Russia

ABSTRACT: Russian culture has a rich history and strong traditions, especially when it comes to ancient white-stone architecture. Unfortunately, natural white stone resources are gradually being depleted. Development of the High-Performance Concrete (HPC) concept has revolutionized concrete technology. One of the most promising areas of HPC implementation is manufacture of architectural concrete with improved decorative properties and performance based on mechanically activated composite binders and effective admixtures. Architectural concrete frost resistance reaches 300–600 freezing-thawing cycles and more; the open integral porosity does not exceed 2–4% vol. The values of the prism strength factor and the initial tangent modulus of elasticity of modified concretes meet or exceed regulatory requirements. Durability of architectural concrete may be additionally improved by impregnation with special organic silicate compounds. Some of the most valuable of the white-stone architecture objects reconstructed in Russia with use of architectural concrete in the last decade are presented.

1 INTRODUCTION

Russian culture has a rich history and strong traditions, especially when it comes to ancient white-stone architecture: churches, chapels, ancient country estate complexes, apartment houses and household constructions. White stone was one of the basic building materials in Old Russia and was of great historic importance as an expression of the state's power and imperial ideology in the 11th–15th cc. It played a key role not only in the Old Russian Architecture, but in the history of the Old Russia as well.

Usually the term "white stone" stands for light carboniferous limestone (from the Paleozoic Era), occurring in the central regions of European, part of modern Russia. However, it is also often referred to sandstone, dolomite, and Volga limestone of Permian formation, as well as numerous sorts of limestone, travertine, and alabaster lying in Transdniestria. Consequently, a more general definition of white stone is any treatable white-yellowish matt surfaced stone, which is neither marble nor shell rock. Unfortunately, natural white stone resources are being gradually depleted now. The problem of historical heritage preservation becomes especially acute.

Development of the High-Performance Concrete (HPC) concept has revolutionized concrete technology. By combining high strength with optimum structural characteristics, higher values of physical and mechanical properties and durability, the HPC extends the areas of application of artificial mineral composites (Boyle, 2000).

One of the most promising areas of HPC implementation is manufacture of architectural concrete with improved decorative properties and performance. Application of concrete technology in decorative façade elements, sculptural plaster, and other elements of buildings requires, as a rule, the use of highly workable and fluid mixes. Additionally, plain and colored cements are used to improve decorative properties of the material, while fine aggregates are required to create complex textured and highly detailed surfaces. A combination of these factors leads to increased water requirements for cement mixes, which in turn instigate the growth of shrinkage strains, increase in permeability and reduction in frost resistance of concrete. The features of cement chemical, mineralogical, and material composition (for example, increased content of C_3A, increased content of belite, introduction of bleaching mineral agents during grinding, e.g. diatomite, etc.) contribute to the problem.

Within the framework of implementing the HPC concept, an integrated control system for the structural characteristics, hardening rate and strength of concrete has been developed having in mind to obtain a material with set-up physical and mechanical properties and durability in specific operating conditions. It envisages the use of mechanically activated composite binders with multifunctional chemical modifiers for various applications. Thereby a directional impact is

possible upon the processes of structure formation and hydration, hardening and strength gain, as well as on parameters of concrete structure and durability at all stages of its preparation: from selecting initial materials, specifying material constitution and activation parameters of composite binders, introducing chemical modifiers into a concrete mix at the preparation stage to improve its workability, including efficient superplasticizing admixtures of the new generation, and up to concrete placing and hardening in special forms.

Elimination of the specified contaminating impurities from the front face of ornamental elements, and upgrading of architectural concrete and architectural elements is attained by their treatment with the various compositions reducing permeability to water and water absorption. Among the wide choices of treating and coating compositions and systems (acrylic, urethane, epoxide, silicone, siloxanic, silaned, etc.) those with the greatest technical and economic efficiency include materials such as silicate and organosilicate compositions combining comparative cheapness and accessibility of a raw-material base with a large-scale of decrease of water absorption, and permeability to water, and increase of working life.

2 EXPERIMENTAL PROGRAM

2.1 *Materials*

Portland cement of PCB 1 500 D0 (CEM I 52.5) grade produced by Shchurovo Cement, Russia, and White cement of CEM I 52.5 R grade produced by the Aalborg cement plant, Denmark, were used for the tests (Table 1). For some comparative tests Aalborg White of CEM I 52.5 R grade produced by Aalborg cement plant, Egypt, and Super White Portland Cement produced by Çimsa, Turkey, were used.

Washed crushed granite aplite of 5–20 mm fraction as coarse aggregate and standard siliceous sand were used for concrete preparation.

A superplasticizer based on polymethylene Polynapthalene Sulphonates (PNS) and a retarder based on sodium Tripolyphosphate (TPPh) were used in some tests.

Titanium dioxide produced by DuPont was used as a pigment. Samples of photo catalytic TiO_2 were synthesized according to Falikman et al., 2012.

An organic shrinkage reducing admixture (OSRA) was synthesized on the basis of aliphatic alcohols and their ethers (Falikman & Vajner, 2014).

Table 1. Bogue cement composition.

Cement	C_3S	C_2S	C_3A	C_4AF	R_2O*
PCB 1 500 D0	47.84	29.31	18.5	2.5	0.63
CEM I 52,5 R	77.26	15.52	4.5	1.0	0.25

* alkali content ($Na_2O + 0.658\ K_2O$)

2.2 *Methods*

Fresh concretes and mortars (fine-grained concretes) were tested according to National (Interstate) Standard GOST, 2014, and hardened concretes (mortars) – according to GOST, 1994a-c. Compressive strength of hardened samples was measured in accordance with GOST, 2011.

Shrinkage for concrete samples was measured also starting from the 1-day age (zero reading); 100 mm × 100 mm × 400 mm prisms, prepared according to GOST, 1981, were used for the measurement. Each curve is the average of results obtained for three specimens.

The performance criterion of OSRA was shrinkage strain reduction for three mortar samples (40 mm × 40 mm × 160 mm prisms) as measured using the method described in GOST, 1974. Shrinkage deformations of each specimen were measured using a length comparator, with a sensitivity of 1 μm, and gauge studs on the end sections of the prisms.

The OSRA were incorporated in the mortar mixtures with gauged water (1:3 mixture proportions, 150–170 mm cone flow) in dosage of 2%, 4% and 6% of cement weight. For the first 24 hours after casting the specimens were stored in a normal hardening chamber ($t = 20 \pm 2°C$, $\varphi = 95 \pm 5\%$), then after demolding and throughout the test – in air-dry conditions ($t = 20–25°C$, $\varphi = 60–70\%$). The shrinkage strains were measured starting from the 1-day age (zero reading). To assess the OSRA effect on the hardening rate and mortar strength the appropriate tests were conducted at the age of 1, 2, 3, 7 and 28 days.

To investigate the parameters of the specimen porous structure, the optical method based on the Gallery software was applied.

The efficiency of photocatalysts in cement systems was evaluated in relation to nitrogen oxide degradation according to ISO, 2007 as well as to volatile organic compounds according to ISO, 2011.

3 RESULTS AND DISCUSSION

3.1 *Low water demand binders*

The main principle of low water demand binder is mechanical and chemical activation of a rationally selected raw mix including clinker components, mineral additives, gypsum and an organic modifying agent which contains a water-reducing component. The production of Low Water Demand Binder (LWDB) is carried out under pre-specified conditions in the grinding mills which are traditionally used in the cement industry i.e. tube mills with special ball charges. In such a case, preference is given to closed cycle grinding with the use of separator mills, which are rather widespread. Grinding with modifying agent provides for a variety of advantages which secure certain properties to a ready-made product, including considerable increase in hydraulic activity of the clinker minerals under the simultaneous decrease in water

consumption of the binder. It is achieved due to the additional dispersing of cement grains, change in its fractional structure and its partial mechanical degradation (amorphicity) of the structure, and, apparently, by means of temporary blocking of the most energetically active centers of cement grains by modifying agent molecules, chemosorbing on these centers.

The LWDB technology (Bashlykov et al., 1997) makes it possible to produce binders with a wide range of material composition and properties varying from multicomponent low-clinker binders with 15…25% of clinker consumed (LWDB-15…LWDB-25) to pure clinker binders, the mineral part of which is presented only by the clinker component and gypsum (LWDB-100).

LWDB-100 differs in the increased indicators of physical and mechanical properties and durability. That's why, the use of concrete on its basis when constructing important and unique engineering structures is considered to be technically reasonable and economically viable. The "specific consumption of aggregates" in concrete based on LWDB is so great in comparison with an ordinary Portland cement (max. 13 vs. max. 27) that this allows considering LWDB as a next-generation cement (Ioudovitch et al., 1997).

It should be noted that the organic mineral compounds formed on the clinker grain surface in the activation process determine such technological properties of composite binder-based mixes as resistance to bleeding, a high degree of thixotropic shear thinning and increased reproductive performance, i.e. the ability to reproduce the finest details of the relief or texture without the formation of large air pores and defects on the front surface, which is especially important for decorative elements made from architectural concrete (Bashlykov et al., 1997a, b).

Below the test results are given (Table 2) based on composite binders from LWDB-90 – LWDB-100 test batches that were produced in a ball mill with 0.5 t/h capacity from white cements (for composite binders LWDB designation is used, i.e. the binder having low water demand, the numeral in the designation denotes the content of clinker component in %).

The use of mechanochemical activation provides for a considerable increase in the hardening rate and strength of white cement, which in turn would be used as a basis of composite binders with 60–100 MPa activity (strength quality of cement) depending on the initial cement quality; this corresponds to a strength rise of about 41–53% at 28 days, about 30–70% at 2–7 days and over 2 times at 1 day. Alongside the above, the essential reduction (by 17–25%) of cement paste water demand is provided in spite of the rise in binder dispersivity as compared to initial cements. Introducing at the stage of binder production, mineral additives, such as natural alumina-containing pozzolana to reduce shrinkage or granulated blast furnace slag to control heat release and to increase sulfate resistance, does not result in considerable reduction of binder activity.

Table 2. The impact of binders and admixtures used in concrete mixtures preparation on technological properties and strength of concrete.

No	Quality index, measuring unit	Indicator values								
		White CEM I 52.5R		LWDB-100*				LWDB-90**		
Composition No		1	2	3	4	5	6	7	8	9
1.	Material consumption, kg/m^3									
1.1.	Cement	490	496	480	485	490	472	469	471	487
1.2.	Sand	542	595	710	717	725	698	1641	1649	1705
1.3.	Aggregate	1068	1071	1100	1110	1124	1082	–	–	–
1.4.	Water	226	198	160	162	146	157	159	165	146
2.	Admixture dosage, % cement mass									
2.1.	PNS	–	0,6	–	–	0,5	0,5	–	–	0,6
2.2.	TiO_2	–	–	–	1	1	1	3	3	3
2.3.	Retarder based on sodium tripolyphosphate	–	–	–	–	–	0,07	–	0,07	–
2.4.	OSRA	–	–	–	–	–	–	–	–	6
3.	W/C	0.46	0.4	0.33	0.33	0.3	0.33	0.34	0.35	0.3
4.	Slump, cm	18.5	20	15	5-9	14	20	14	16	18.5
5.	Fresh concrete density, kg/m^3	2326	2360	2450	2475	2490	2410	2288	2295	2338
6.	Air content, %	2.5	3.0	2.7	2.3	2.3	2.5	4.5	5.6	4.7
7.	Compressive strength, MPa, at age									
	1 day	20.5	25.7	55.0	69.7	72.8	16.5	39.8	9.6	8.8
	2 days	36.4	47.4	64.8	70.5	78.4	72.0	55.2	48.4	23.1
	3 days	40.2	51.0	72.1	76.7	83.0	76.1	59.5	68.1	40.9
	7 days	47.6	58.4	83.3	90.0	90.6	84.2	73.4	77.9	73.0
	28 days	55.6	67.3	93.7	103.8	112.6	107.3	81.0	84.0	84.5

* based on white CEM I 52,5R
** based on white CEM I 52,5 R, mineral additive – granulated blast furnace slag

Table 3. Effect of cement whiteness on NO conversion efficiency in concretes with mesoporous TiO_2 nanoparticles (concrete age – 28 days).

Producer	Cement mark	Cement whiteness, %	NO change ratio, %
Aalborg, Denmark	Aalborg White	95	52
Aalborg, Egypt	Aalborg White	87	42
Çimsa, Turkey	Super White Portland Cement	85,5	44
Shchurovo Cement, Russia	PCB 1 500 D0	80	39

3.2 *Fresh concrete and structure formation of concrete*

In accordance with the reduced water demand of binders the making of flowable (or self-compacting) fresh concrete on their basis is achieved at significantly lower – by 20–30% – mixing water consumption (Table 2). At the same time, the specific rheological properties of composite binders associated with mechanochemical activation provide the minimum bleeding, reduction of air entrainment in concrete mixes and increase in their density, suggesting improvements of concrete structural characteristics.

Control of structure formation processes as well as performance and decorative properties of architectural concrete envisages at the stage of concrete mix preparation, first of all, a regulation of their slump loss and introduction of various chemical and mineral admixtures (mineral pigments, shrinkage reducing admixtures, etc.) when mixing. The slump loss of concrete mixes with composite binders, i.e. the rate and time of initial flow reduction, as a rule, corresponds to the slump loss of mixes with ordinary cements.

However, all that may not be sufficient when concreting complex elements, for example, large-scale sculptural reliefs. Besides, the rapid loss of flow is in line with accelerated structure formation of concrete and intensive heat release during the first hours after placement. Introduction of retarding agents can help. The data given in Table 2 and related to the use of the admixture on the basis of sodium tripolyphosphate show that in this case slump loss of concrete mixes essentially decreases, while the beginning of the intensive strength gain occurs at 36–48 hours after molding. This process is accompanied also by the more uniform heat development.

3.3 *Role of titanium dioxide*

Along with admixtures controlling the rate of structure formation, coloring agents, in the first turn, titanium dioxide TiO_2, are introduced when mixing. Even when using binders based on white cement, the introduction of TiO_2 allows neutralizing the color distortion due to contamination of the fillers and aggregates, and makes the mix color more susceptible to the introduction of small doses of mineral pigments for accurate reproduction of colors. Adding small amounts of TiO_2 (up to 3–5% of cement mass) does not actually affect water demand and rheology of concrete mixes, while it affects positively the concrete strength. The data presented in Table 2 show that for all periods of hardening, the strength of concretes increases with the growth of TiO_2 dosage. In combination with PNS the introduction of TiO_2 is accompanied by even greater increase in strength.

Using titanium dioxide sensibilized through nanotechnology gives additional benefits.

It is commonly known that nanodimensional titanium dioxide is widely used as a photocatalyst inphotochemical decomposition reactions of many organic and non-organic pollutants – nitrogen oxides, carbon monoxide, volatile organic substances, etc. The synthesized nanoparticles of mesoporous TiO_2, which are characterized by predominance of the anatase phase, small sizes of crystals and high specific surface area, have demonstrated much higher efficiency of NO transformation (Falikman, 2012). Architectural concrete possessing photocatalytic properties allows self-cleaning surfaces to be made and noticeably reduces the environmental polluting effect, being particularly important in megalopolis conditions.

To improve decorative properties of architectural concrete elements, white and color cements are used, as a rule. In this connection photo catalytic concrete application for architectural finish of building facades as well as landscaping elements and small architectural forms of interest is the assessment of TiO_2 photocatalytic activity in relation to the white cement whiteness (Table 3).

As it is seen from the table, NO conversion is most efficient in white Danish cement matrices characterized by the highest whiteness. The efficiency somewhat decreases with Egyptian and Russian cements; this seems to be explained by "pollution" of these cements with transition metal ions Fe^{3+} and Mn^{3+} (Lin, 2005).

The high photocatalytic activity of synthesized mesoporous TiO_2 nanoparticles was confirmed also in the course of decomposition of volatile organic compounds (VOC), while plastering mortars and cement paints were used as catalyst carriers.

3.4 *Hardened concrete*

The analysis of the data in Table 2 shows that the use of mechanically activated binders is accompanied in all cases by an essential increase of the hardening rate as compared to concretes based on initial cements. Indeed, except for the cases, when a special aim was

Table 4. Main characteristics of architectural concrete depending on binder and admixture types.

No	Quality index, measuring unit	Indicator values			
		White CEM I 52.5R	LWDB-100*	LWDB-90**	
1.	Admixtures and dosage, % cement mass	PNS (0.6%) PNS (0.5%)	TiO_2 (1%) TPPh (0.07%)	TiO_2 (3%) PNS (0.6%)	TiO_2 (3%), OSRA (6%),
2.	Compressive strength, MPa, in age 28 days				
2.1.	Cubic R_c	67.3	112.6	84.0	84.5
2.2.	Prism R_{pr}	48.5	85.6	68.0	65.9
3.	Prism strength factor, R_{pr} / R_c	0.71	0.76	0.81	0.78
4.	Initial tangent modulus of elasticity E x 10^{-3}, MPa				
4.1.	Experimental	38.1	57.7	44.2	46.9
4.2.	Normative	39.0	–	>40.0	>40.0
5.	Volumetric water absorption, %	12.8	7.1	7.8	7.0

* based on white CEM I 52.5R
** based on white CEM I 52.5 R, mineral additive – granulated blast furnace slag

pursued to retard structure formation and hardening by using a retarder (Table 2, compositions 6, 8), the strength of modified concretes reaches 49–67% of the quality class strength as early as 1 day aging, while for concretes based on initial cements this value does not exceed 36–38%. These high hardening rates of concrete cured at ambient air confirm once more a possibility to produce architectural concrete articles without steam curing when used both sand and crushed stone (compositions 1–6) and graded sand mixtures as aggregates (compositions 7–9).

3.5 *Control of shrinkage*

As already noted, at an early hardening stage the important factor of concrete defect-free structure formation is reduction of its shrinkage. A new possibility to control shrinkage of high performance architectural concrete is connecting with the use of OSRA. Being a product of chemical synthesis, this admixture differs from mineral additives on the basis of sulfate and aluminate compounds by stability of its composition and properties. Besides, the OSRA admixture mechanism, based on variation of water bond forms in concrete and regulation of mass-transfer processes, presents a much lesser hazard for the concrete structure formed than appearance of calcium hydrosulfoaluminates, unbalanced conditions of hydration and composition which, together with reduction in shrinkage strains may also lead to structural failures. The reduction of their value is 22–45% by the moment of strain stabilization during hardening under air-dry curing when introducing OSRA in the amount of 2–6% of cement mass.

3.6 *Mechanical properties and durability*

The increased hydraulic activity of mechanically activated binders and efficient mix design of architectural concretes predetermine their high physical and mechanical properties and durability, particularly under favorable conditions of structure formation, e.g. when introducing retarders or OSRA admixture. The data presented in Table 2 shows that the values of physical and mechanical properties of concrete correspond to high values of their strength.

The values of the prism strength factor and the initial tangent modulus of elasticity of modified concretes meet regulatory requirements or exceed them according to National Building Code SP, 2012. A noteworthy increase of prism strength and modulus of elasticity of concrete with OSRA and sodium tripolyphosphate may be associated with reduction of the shrinkable nature microdefects in their structure, on the one hand, and with the absence of structural changes connected with intensive heat development under fast strength gain at an early age, on the other hand.

The value of volumetric water absorption of modified architectural concretes may also serve as an indicator of improvement of their structural characteristics. The data in Table 4 indicates that the mentioned value does not exceed 8%, thus allowing attributing the obtained concretes to materials with a compact structure.

Combination of high density and strength of modified concrete determines, in turn, their high frost-resistance. A frost-resistance factor, $K_{fr,}$ of concretes based on LWDB (i.e. the ratio of strength of key samples after a given number of alternate freezing and thawing cycles to the strength of control samples) is over 1 even after 300–400 test cycles, that indicates to the available reserve of durability and to the predominance of constructive processes in the concrete structure over destructive ones. In contrast, the frost resistance of concrete based on initial white cements does not exceed 100–250 cycles depending on the type of cement.

3.7 *Impregnation with special organic silicate compounds*

In real building practice, ornamental concrete products are exposed to pollution to some extent even prior to the beginning of maintenance – during transportation, warehousing and especially at installation

which is carried out frequently without appropriate protection of exterior surfaces. Surface treatment of architectural concrete with special organic-silicate compounds, which partially or completely seal the pores with high density air-silica-gel, improves performance and durability of material, decreases water absorption up to 20–37% and increases freezing-thawing resistance up to 20–50% (Falikman, 2011). Penetrating sealant systems were developed on the basis of soluble sodium silicate in which the silica modulus SiM varied within 1.98–3.36. It has been found that technological parameters of organosilicate compositions for concrete impregnation can be essentially improved when surface active agents (SAA) of various natures were introduced to soluble silicate, anionic and nonionic surfactants. These additives make a significant impact on the state of soluble silicates in an aqueous solution at low concentration of SAA. The concrete surface treatment by organosilicate composition favors an increase of its working life that is caused by pore structure changes. The effect of formation of aerosilica gel as sealing and additional binding agent in pores and defects of concrete simultaneously revealed above allows the possibility of an increase of compressive strength. This due to the fact of blocking of structural defects by the polymeric buildup contained in the specified sealing systems, and deceleration of structural defect development under load. This view is confirmed by the results of experimental studies of concrete of various compositions with cement content over the range from 180 to 600 kg/m^3, impregnated by the developed organosilicate composition.

With reference to architectural concrete it means also an increase of durability of the surface of ornamental elements to fouling and makes easy the process of their cleaning, and also possibility of protective coating while in service that is confirmed by experience of practical application.

4 CASE STUDY

High performance architectural concrete was used for the manufacture of external decoration with a texture and color simulating a natural white stone in restoration work of many historical monuments and buildings in the City of Moscow and the Moscow Region, including churches, chapels, ancient country estate complexes, apartment houses and household constructions: The Center of Orthodox Heritage in Peredelkino near Moscow where more than 24,000 purpose-made details of outside architectural decoration were installed, Tsaritsino near Moscow (Figure 1), the St. George Church in Romanovo, the Church of the Iveron Icon of the Mother of God, the church tower of the Ascension of Christ at Rogozhky Barrier, etc.

As usual, elements of external decoration had highly rich ornaments of the front surface that reached 3/4 of the total surface of the product. The main objective was to obtain a high quality, defect-free surface with a given



Figure 1. Tsaritsino near Moscow.



Figure 2. High relief of St. Princess Olga, Equal-to-the-Apostles.

texture and color, when the size of individual items was sometimes more than 3.0 × 1.5 m with a thickness not exceeding 80 mm. Elements of architectural decoration were manufactured by vibratory casting method, with the use of vibrators and vibrating table (frequent vibration in the range 10–60 Hz), in a specially designed rigid composite matrix with an outer layer of silicone compounds meeting the requirements of dimensional stability (not more than 0.01 %) that allows producing details with very precise geometric dimensions. At the age of 24 hours after curing in a humid chamber under controlled conditions (T = 40–45°C; RH = 80–95%) the products were demolded and treated by water-repellent composition.

Table 5. The concrete for the St. Princess Olga, Equal-to-the-Apostles high relief.

Properties	Item description	Units	Normative value (TR*)	Index
Aesthetic**	Whiteness	%	Approved model	Reference (dolomite)
	Surface quality	–	A3	A2
Physical & mechanical	Specific gravity	kg/cm^3	2,4	2.503
	Compressive strength	MPa	70	149.8
	Softening index	–	0.9	0.96
	Modulus of elasticity	MPa	$4{,}0 \times 10^4$	$5{,}6 \times 10^4$
	Shrinkage	mm/m	0.3	0.137
Durability	Frost resistance	mark	F300	F800
	Water tightness	mark	W12	W16

* Technical Requirements
** Ordered by Russian Academy of Arts

A unique example of the implementation of the developed architectural concrete was the making of the high relief of St. Princess Olga, Equal-to-the-Apostles for the Cathedral of Christ the Savior with height more than 5 m (Figure 2). The characteristics of the sculpturesque concrete are shown in Table 5.

Calculation of durability of architectural concrete for climatic conditions of Moscow based on fracture mechanics parameters show that the time within which the structural characteristics of the concrete have reached its limit state, is 152 years (Piradov et al., 1998).

5 CONCLUSIONS

Thus, modern concrete technology is able to imitate and replace to the full the natural stones by artificial composites that are not inferior to them in their properties. The above mentioned methods of modifying the architectural concrete provide an opportunity to control its structure and properties as well as concrete mix workability and hardening rate at all stages of its manufacture – from selection of initial materials to surface treatment at the final stage of manufacture or even at the operational stage. Thereby an optimum combination of construction and technical characteristics of concretes and decorative properties of products is achieved that should considerably expand the field of architectural concrete application, solve the problems of historical heritage preservation, and on the whole facilitate the growth of its social significance and attractiveness.

ACKNOWLEDGEMENT

The authors would like to thank Dr. N.F. Bashlykov and recently deceased Dr. Yu.V. Sorokin for their valuable contributions.

REFERENCES

Bashlykov, N.F., Falikman, V.R., Serdyuk, V.N., et al., 1997. Hydraulic Cement, Russian Patent ¹ 2096364, 1996, publ. in Bul. No.32.

Bashlykov, N.F., Falikman, V.R., Serdyuk, V.N., et al., 1997a. Method of Manufacturing of Decorative Binder with Low Water Demand, Russian Patent Np 2085525, 1991, publ. in Bul. No.20.

Bashlykov, N.F., Sorokin, Yu.V., Falikman, V.R., et al., 1997b. Method of Manufacturing of Decorative Building Products and Decorative Coatings, Russian Patent ¹ 2084416, 1992, publ. in Bul. No.20.

Boyle, M.J., 2000. Concrete as a substitute for granite cladding attains high performance concrete consideration as the result of exceptional materials and production control. *International Symposium on High Performance Concrete,* Orlando, Florida, U.S.A., pp 279–293.

Falikman, V., Vajner, A., Zverev I. 2012. New photocatalytic cementitious composites containing modified titanium dioxide nanoparticles. *Proceedings, 3rd Int. Symposium on High Performance Concrete and Nanotechnology for High Performance Construction Materials (Hipermat)*, Kassel, Germany, pp 147–152.

Falikman, V.R., Sorokin, Yu.V., Deniskin, V.V., 2011. Surface protection of high performance architectural concrete. *Proceedings of Concrete Solutions, 4th International Conference on Concrete Repair*, Dresden, Germany, Taylor & Fransis Group, London, UK, pp 813–821.

Falikman, V.R., Vajner, A.Ya., 2014. Hydroxyl Organic Compounds to Reduce Shrinkage Deformations of Concrete. *Proceedings, Application of Superabsorber Polymers and Other New Admixture in Concrete Construction*, Dresden, Germany, RILEM S.A.R.L., pp 159–168.

GOST 10180, 2011. Concretes. Methods for strength determination using reference specimens, GOST.

GOST 10181, 2014. Concrete mixtures. Methods of testing, GOST.

GOST 11052, 1974. Gypsum-alumina expanding cement, GOST.

GOST 12730.0, 1994a. Concretes. General requirements for methods of determination of density, moisture content, water absorption, porosity and impermeability, GOST.

GOST 12730.1, 1994b. Concretes. Methods for determination of density, GOST.

GOST 12730.4, 1994c. Concretes. Methods of determination of porosity parameters, GOST.

GOST 24544, 1981. Concretes. Methods of shrinkage and creep flow determination, GOST.

Ioudovitch, B.E., Dmitriev, A.M., Zoubekhine, S.A., Bashlykov, N.F., Falikman, V.R., and Serdyuk, V.N., 1997. Low Water Requirement Binders as New Generation Cements, *10th International Congress on the Chemistry of Cement*, Goteborg, Sweden, (Pub. No 3iii021).

ISO 22197-1, 2007. Fine ceramics (advanced ceramics, advanced technical ceramics) – Test method for

air-purification performance of semiconducting photocatalytic materials – Part 1: Removal of nitric oxide, ISO.

ISO 22197-3, 2011. Fine ceramics (advanced ceramics, advanced technical ceramics) – Test method for air-purification performance of semiconducting photocatalytic materials – Part 3: Removal of toluene, ISO.

Lin, Z.-H., Tang, X., Zhang, C., Zhou, Q., 2005. A novel TiO_2-pillared microporous manganese oxide. *Chem Letters.* v 34, No10, p.p. 1312–1313.

Piradov, K.A., Guseev, E.A., Falikman, V.R., et al., 1998. The reinforced concrete high reliefs with assured durability more than 100 years for the Cathedral of Christ the Savior. *Beton i zhelezobeton* (*Concrete and Reinforced Concrete*), No 6, p.p. 22–24 (in Russian).

SP 63.13330, 2012. Concrete and reinforced concrete constructions. Design requirements, Standartinform.

Concrete Solutions – Grantham et al. (Eds.)
© 2016 Taylor & Francis Group, London, ISBN 978-1-138-03008-4

The survey of a historical building from the beginning of the previous century. Evaluation of mechanical characteristics of the load bearing system

I. Papayianni, V. Pachta & A. Milosi
Laboratory of Building Materials, Department of Civil Engineering, Aristotle University of Thessaloniki, Thessaloniki, Greece

ABSTRACT: An excellent example of Art Deco style listed building from the interwar period, is the Library of Florina in North Greece. The importance of this building, which is still in operation, is that the bearing system is constructed partly from stone masonry and partly from concrete structural members. It constitutes one of the first constructions in Greece, with the use of concrete as building material. Having completed 90 years of service life, the building presents serious symptoms of deterioration and needs renovation. Before any intervention, a survey was necessary for making architectural design, describing morphological characteristics and mapping damage of the shell and the interior of the building. Since there were not any designs of the skeleton of the building, it was of first priority to recognize and describe the structural members, as well as to determine the residual bearing capacity and the mechanical and elastic characteristics of them. Apart from in situ measurements and small scale excavations for investigating the foundations, a number of samples from the masonry and cores from the concrete members, were taken and analyzed at the Laboratory of Building Materials, AUTH. The rendering mortars of the building are of particular interest and their characteristics were also determined. The crushing strength in compression of the concrete cores showed low values of 13–15 MPa, with a static modulus of elasticity of 12–16 GPa. The concrete pH values were low (9–11) which meant that the concrete had been carbonated. The compressive strength of the bearing masonry was estimated, according to the Eurocode 6 equation, based on the separate strengths of bricks, stones and mortars, which were determined by crushing samples taken from the building. The estimated values for compressive strength of the stone masonry and the fired brick were 14.9 MPa and 2.1 MPa respectively. Based on the survey results, new designs of the structure were made, in which concrete members (and masonry members) are clearly shown. Therefore, the bearing system and residual bearing capacity have been determined in order to proceed to further analysis required for any intervention.

1 INTRODUCTION

The interwar period (1919–1939) was a transition period in Greece for economy, society and architecture, during which urban development started. In the decade of the 1920's, around two million Greek refugees moved to Greekland, causing great demand for labour and housing. After the economic crisis of 1929, a drop in exporting of agricultural products made the State support and motivate national industry and manufacture, such as the cement industry, and brick manufacture (Mazower, 2002). In the same period, modern architecture appeared already in Europe, started to be applied in Greece. Many buildings of this style have been constructed and are still in service (Cholevas, 1988). They are easily recognized by the mosaic floors, beautiful handrails, erkers, artificial renderings and balconies with cast iron railings.

Florina has been the center town of the Western part of North Greece, in which the traditional vernacular architecture prevailed up to the aforementioned period. A number of buildings (private houses, schools and other public structures) were constructed following the Art Nouveau style, such as the house and drugshop of the family Karantza, in which the Library of Florina is now sheltered. However, since this is a transition period, many elements from traditional architecture have been kept in these structures, such as stone masonry foundations, wooden floors, plastered wattle, wooden hipped roofs. Therefore, these buildings, which are now listed, present many particularities and draw special attention of engineers, as they are composed of a mixed type bearing system and testify the history of concrete application in local construction. Firstly, they started using concrete for constructing balconies and floors and after they used concrete for building schools and hospitals. The concrete was prepared outside the house plot by technicians with cement coming from Thessaloniki and aggregates from the nearby river.

Although there are some studies about the architecture of these buildings (Zarkada-Pistioli, 2003), very few are known about the materials used and their properties, especially their mechanical strength. Since most of these buildings need rehabilitation, it is necessary to determine or estimate their materials' strength.

In this paper, the systematic study of materials made with non destructive methods, as well as by analyzing



Figure 1. General view of the Library of Florina.



Figure 2. Architectural design of the W. façade of the building.

laboratory samples taken from the structural members of the library building in Florina are presented. The results of this work could be used as a basic reference for the determination of the strength properties for the materials of similar buildings of the interwar period.

2 ARCHITECTURAL AND MORPHOLOGICAL CHARACTERISTICS

The Library of Florina in North Greece constitutes an excellent example of the Art Deco style listed building, constructed around 1930. Having completed 90 years of service life, it nowadays hosts the municipal library of the town, mainly targeting at young visitors (children and students). It comprises four floors (basement, ground floor, entresol, 1st floor) and it is covered by a wooden hipped roof (Fig. 1).

Regarding the morphological elements of the façades, the ground floor is characterized by large openings framed with pilasters, which are covered at a height of 1 m with a well compacted cement based render, imitating stone revetment. For the protection of the openings, there is a perimetric concrete shelter which bears slots on its underside where luminaires were inserted. Right above, there are the skylights of

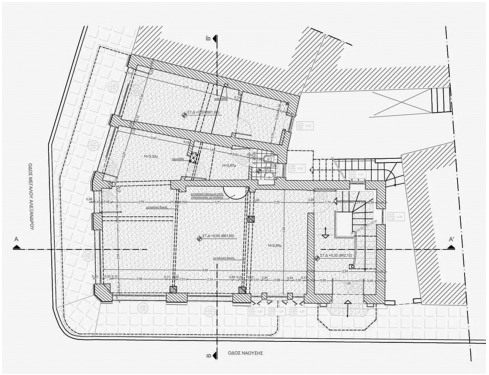

Figure 3. Architectural design of the ground floor of the building.

the entresol and in the first floor, the symmetric openings that are decorated with rectangular frames made of mortar (Fig. 2).

Internally (Fig. 3), there is the stairwell located in the SW part of the building, which concerns precast mosaic block elements, “planted” in the masonry at a depth of about 15 cm. These mosaic block elements were made with cement, sand and angular pebbles at small factories. They were widely used in the buildings of that period. In their contact with the masonry there is perimeter tepi mosaic of 16 cm height and 1 cm thickness. The railing is made of decorated cast iron.

The basement of the building has an auxiliary use and functions as a warehouse. In the ground floor there is an open space of about 55 m^2 where the library is hosted (Fig. 3). In the eastern part, there is a shop which is nowadays closed. The entresol covers almost half of the total open space of the ground floor’s open space and hosts offices for the staff. The 1st floor, due to the severe damage of the wooden floors of specific rooms, functions as a warehouse.

3 CONSTRUCTIONAL MATERIALS AND TECHNIQUES

The building is a mixed structure composed of stone masonry, brick masonry and concrete elements. Since there were no archives regarding the architecture and the constructional materials and techniques applied, the study focused on determining the structural system of the building and the physicomechanical characteristics of the existing building materials (concrete, structural mortars, renders-plasters, stones, bricks).

The method followed concerned the update of the existing architectural designs, the insitu study of the constructional elements by drilling in selected areas in order to define the structural type (concrete or masonry), the application of non-destructive techniques (hammer, pachometer, sonometer) (Fig.4) and the sampling and analysis of an adequate number of building materials.



Figure 4. Non-destructive techniques applied in the building (sonometer, hammer, pachometer).

According to the survey, the walls of the basement, below the level of the outer road pavement, were rubble stone masonry 80 cm thick, covered by thick plasters (∼3 cm). In the front of the stone masonry and in contact with it at places shown in Fig. 3 as pilasters, there were concrete columns without adequate footings on which a low height beam was supported, as well as a concrete slab over. On the next floors, there were brick masonries 30–45 cm thick. The floors were either concrete slabs (15 cm thick) covered with cement based mosaic (ground floor, entresol and 1st floor at the part of the stairwell), or wooden floors with roof plasters on their soffits.

From the preliminary stage of the survey, it was found that the concrete members of the building did not follow a logical pattern to transfer loads, whereas columns and beams were not always consecutive and bonded (Fig. 5). A critical aspect was to define the foundation system of the building, by making short scale excavations in the basement. What resulted was that under the concrete slab of the floor, there was plain concrete (10 cm thick). In the base of the columns there was an enlargement of the column section made from unreinforced concrete of 30 cm. No reinforcement was detected in the floor slabs, while there was much humidity.

Through the comparative evaluation of all insitu and laboratory results, the structural system, as well as the bearing capacity of the building was determined. The designs were therefore updated and all relevant information regarding constructional materials was added.

3.1 *Non-destructive techniques results*

A series of non-destructive techniques were applied to the building, resulting in a total number of 320 hammer, 150 pachometer and 40 sonometer tests. Pachometer tests were realized in order to define the presence, thickness and depth of reinforcement, while hammer and sonometer tests helped in determining the mechanical strength of the structural elements. In tables 1 and 2 the non-destructive tests results are shortly presented.

From the evaluation of the results it was concluded that the corresponding compressive strength of all concrete members and especially of the columns, was very low and could not contribute much to the bearing capacity of the structure. The highest values were given for the slabs of all floors situated near to the stairwell.



Figure 5. Non-connected columns and beams of the ground floor.

Table 1. Hammer test average results of the structural members.

Structural member	Hammer indication	Corresponding Compressive strength (MPa)*
Basement		
Concrete column	19–22	10–12
Concrete beam	30–36	16–26
Concrete slab (roof)	26–30	11–20
Stone masonry	20–22	10–12
Ground floor		
Concrete column	23–30	14–23
Concrete beam	20–22	<10
Concrete slab (floor)	28	25
Brick masonry	16–18	<10
Entresol		
Concrete slab (roof)	36–38	38–42
Concrete beam	22–26	10–11
Brick masonry	14–18	<10
1st floor		
Concrete slab (floor)	48–50	59–64
Brick masonry	16–18	<10

* Hammer indications were previously calibrated to Compressive strength by using proper nomographs.

3.2 *Analysis of building materials*

In total, 35 samples of building materials were taken from the building, comprising 8 samples of renders-plasters, 5 structural mortars, 5 concrete cores, 3 stones, 9 bricks, 4 wooden beams, 1 piece of reinforcement bar. All samples were analyzed according to the holistic methodology developed during the last

Table 2. Sonometer test average results of the structural members.

Structural member	Sonometer indication velocity (km/s)
Concrete column with render (25 cm)	1.28
Beam with render (22 cm)	1.89
Beam with render (24 cm)	1.45
Column with render (35 cm)	1.03
Column with render (33 cm)	1.05

Table 3. Structural mortars' analysis results.

Type	Bind. system L: lime P: pozzolan C:	Aggr. granul. (mm)	Porosity (%) / Ap. spec. clay gravity	Compr. strength (MPa)
A-Basement	L + C	0–4	20/1.85	0.9
B-ground floor	L + P	0–8	28/1.70	1.5

20 years in the Laboratory of Building Materials AUTH (Papayianni et al., 2012).

The tests performed were: Microstructure observation with stereoscope (Leica Wild M10) assisted by image analysis (ProgRes), porosity and apparent specific gravity were performed according to RILEM CPC 11.3, compressive strength (in shaped samples). In mortars (structural, renders) also aggregate granulometry was tested by hand grinding and sieving (EN1015-1:1998), as well as wet chemical analysis assisted by Atomic Absorption and performed in a fine fraction of the sample (<75 μm). All results were comparatively evaluated and additional observations were made, regarding the structure and constituents of samples.

3.2.1 *Structural mortars*

From the evaluation of the results, two main types of structural mortars were apparent (Table 3).

The first type (A, Fig. 6) concerns the mortars taken from the stone masonry of the basement, whose binding system consisted of lime and clay (content of $Ca(OH)_2$: 26%). The aggregates were of physical (river) origin, with gradation 0–4 mm and the Binder/Aggregate (B/A) ratio was approximately 1/1.5. Porosity was around 20%, apparent specific gravity 1.85 and compressive strength 0.9 MPa.

The second type (B, Fig. 7) concerns the mortars taken from the brick masonry of the ground floor, whose binding system consisted of lime and natural pozzolan (content of $Ca(OH)_2$: 31%). The aggregates were of physical (river) origin, with gradation 0–8 mm and the B/A ratio was approximately 1/1.5. Porosity was around 28%, apparent specific gravity 1.7 and compressive strength 1.5 MPa.

3.2.2 *Renders – plasters*

From the evaluation of the results, one type of render and two types of plasters were detected (Table 3).



Figure 6. Insitu, macroscopic and microscopic photo of A' type structural mortar.

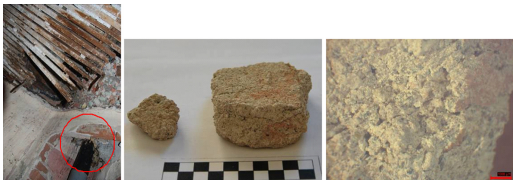

Figure 7. Insitu, macroscopic and microscopic photo of B' type structural mortar.

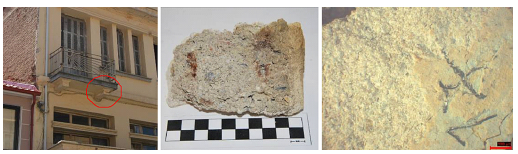

Figure 8. Insitu, macroscopic and microscopic photo of B' type render.

The render (Fig. 8), which covers the facades of the building and creates the decorative corbels and cornices of the openings and the balconies has a thickness of 1–2 cm and internally is in contact with a cement based mortar. It was found to be a lime based mortar (proportion in $Ca(OH)_2$: 30%), with an addition of a clayish material. The aggregates were fine, of physical (river) origin, with gradation 0–1 mm and the B/A ratio was approximately 1/1. Porosity was around 30%, apparent specific gravity 1.7 and compressive strength was 1.6 MPa.

The first type of plasters (type A') were sampled from the stone masonry of the basement, while the second (B') from the wooden roof of the ground floor.

Type A' was found to be cement based of 2 cm thickness and was externally in contact with a thin lime-based layer (0.3 cm thick). The aggregates were of physical (river) origin, with gradation 0–2.5 mm and the B/A ratio was approximately 1/1.5. Porosity was around 25%, apparent specific gravity 1.7 and compressive strength was 3.5–4 MPa.

Type B' consisted of two lime-based layers (external: 0.5 cm, internal: 0.5 cm). The external layer consisted of a low proportion of fine aggregates (0–2.5 mm). The internal, apart from fine aggragates (0–1 mm) had also a proportion (5%ww of binders) of straw. The porosity of the compact sample was 38% and the apparent specific gravity 1.45.

Table 4. Renders' – plasters' analysis results.

Type	Bind. system L: lime C: clay CEM: cement	Aggr. granul. (mm)	Porosity (%) / Ap. spec. clay gravity	Compr. strength (MPa)
Render	L + C	0–1	30/1.70	1.6
Plaster A'	L + CEM	0–2.5	25/1.70	3.5–4.0
Plaster B' (ext)	L	0–2.5	38/1.45	–
Plaster B' (int)	L	0–1	38/1.45	–

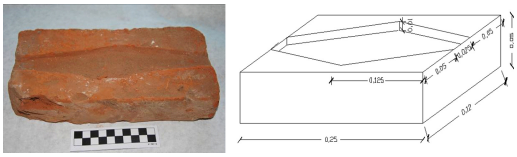

Figure 9. Photo and drawing of a compact brick.



Figure 10. Insitu, macroscopic and microscopic photo of a stone sample.

3.2.3 *Bricks*

The samples of bricks were taken from the masonry of the ground floor and the 1st floor of the building. They were compact, with dimensions 24 × 12 × 5 cm, with a rhombic scarf in the upper side (Fig. 9). Their color was 5YR 6/6 reddish yellow according to the Munsell scale. They consisted of well compacted clay with a low proportion of fine sand. Their porosity was 30%, the apparent specific gravity 1.65, the Modulus of Elasticity ranged from 2.6 to 5.3 GPa, the flexural strength from 1.2 to 2.2 MPa and the compressive strength from 5.2 to 7.7 MPa. The wide range in the analysis results is attributed to the preservation state of the samples.

3.2.4 *Stones*

The samples of stones were taken from the stone masonry of the basement and comprised rubble stones, with approximate dimensions of 20x10cm (Fig. 10). They were characterized as gneiss schists, with color 7.5YR5/1 gray (according to the Munsell scale). Their porosity was around 2–3%, the apparent specific gravity 2.6, while the compressive strength ranged from 100 to 115 MPa.

3.2.5 *Concrete*

The core samples of concrete were taken from the columns of the basement and slab of the ground floor (Fig.11). A Phenolphthalein test (insitu and in the laboratory) showed that they were completely carbonated.



Figure 11. Insitu, macroscopic and microscopic photo of a concrete core.

The column concrete cores consisted of aggregates of heterogeneous origin and granulometry (fine aggregates of natural origin and crushed coarse aggregates) of gradation 0–16 mm. Their porosity was around 13–18%, the apparent specific gravity 2–2.3, while the average compressive strength was 13 MPa. PH (measured in filtered crushed concrete-distilled water solutions 1:5 by mass with pHmeter) ranged from 9.7 to 11.9.

The slab concrete cores also consisted of heterogeneous aggregates of gradation 0–16 mm. Porosity was around 12%, apparent specific gravity 2.2 and compressive strength was 13.5 MPa. A pH test showed pH to be about 9.5.

3.2.6 *Reinforcement bar and wooden beams*

From the analysis of the reinforcement taken from a concrete column of the basement, it was apparent that the oxidization degree was high, resulting in a decrease of 60% of the principal diameter.

In addition, the wooden beams taken from the wooden floor of the 1st floor were also severely deteriorated, suffering from a decrease of 60% of the total volume.

3.3 *Evaluation of the bearing capacity of the building*

Regarding the bearing capacity of the building and taking into account the analysis results of the samples, an approximate evaluation of the preservation state of the building can be conducted.

It is well known that the masonry strength is related to the compressive strength, as well as other properties of the building materials (geometry, joint thickness etc). In the case of a stone masonry under usual loads (lack of earthquakes), the strength can be determined with a series of equations that have been developed (Hendry και Malek, 1986, Tassios, 1988, EN 1996-1 and 2: 2005, Eurocode 6).

In the case of the Library Eurocode 6 was used, concerning the equation:

$$f_{WK} = k \cdot f_b^{0.7} \cdot f_m^{0.3} \ (\text{MPa}) \quad (1)$$

where:

f_{WK} is the characteristic strength of the masonry. It is lower than the compressive strength of the masonry (f_{wc}) and we use it for the determination of

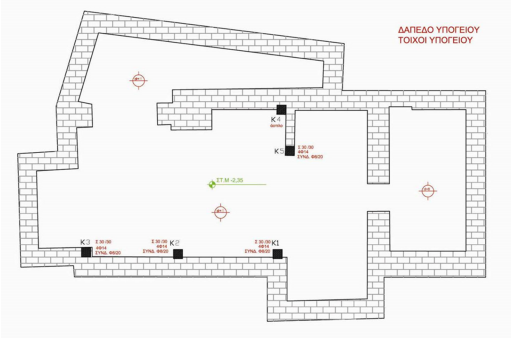

Figure 12. Updated ground plan of the basement indicating constructional materials and types.



Figure 13. Updated ground plan of the ground floor indicating constructional materials and types.

the designing compressive strength, f_{Wd}, from the equation:
$f_{Wd} = f_{WK}/Y_m$ (safety factor).
f_b is the compressive strength of the stone members (MPa)
fm is the compressive strength of the structural mortars (MPa)
Factor k is taken from relevant tables (EC 2) and was determined as 0.50.

In the case of the Library building, the basement is constructed with stone masonry, while the ground floor and the first floor with brick masonry. If the fb value is replaced respectively with the strength of stone and bricks it is possible to calculate the bearing capacity according to the structural system.

3.3.1 *Basement*

The compressive strength of the stone samples ranged from 100 to 115 MPa, while the average value was 108 MPa. The compressive strength of the structural mortar was 1.2 MPa. Following the equation, the bearing capacity of the basement was found to be 14.9 MPa.

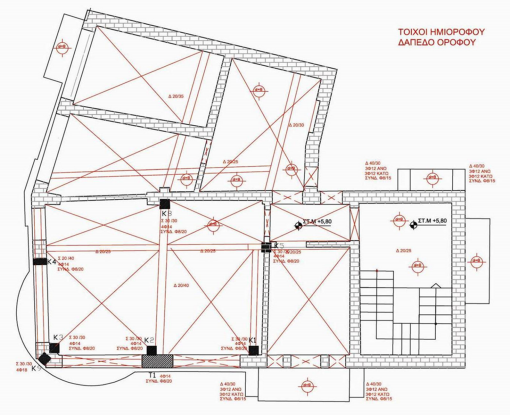

Figure 14. Updated ground plan of the entresol indicating constructional materials and types.

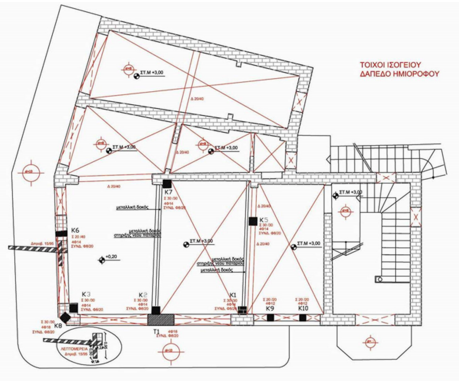

Figure 15. Updated ground plan of the 1st floor indicating constructional materials and types.

3.3.2 *Ground floor – 1st floor*

The average compressive strength of the brick samples was 6.5 MPa. while the compressive strength of the structural mortar was 1.5 MPa. Following the equation, the bearing capacity of the ground and 1st floor was found to be 2.1 MPa.

3.4 *Update of the building architectural designs*

All insitu and laboratory results were comparatively evaluated in order to determine the structural system of the building and recognize the bearing elements. The architectural designs were therefore updated and all relevant information regarding the constructional materials and types of the building were added. Figures 12–15 presents the updated ground plans of all floors.

4 MAPPING OF PATHOLOGY

In order for the survey to be complete and explicit, the pathology symptoms of the building encountered



Figure 16a and b. Mapping of the pathology of the N. façade.

internally and externally were mapped. The architectural designs of the facades were updated with the deterioration problems found, while a list with the type and deterioration degree of the most common pathology symptoms was implemented.

In figures 16–17 the mapping of the pathology of the N. and W. façade is presented.

The main pathology symptoms confronted are summarized as following:

- Severe oxidation of the concrete reinforcement in columns of the basement, resulting in a decrease of 60% of the principal diameter (Fig. 17).
- Cracks in the slab of the balcony (Fig. 18)
- Corrosion and local collapses of the wooden floors of the 1st floor (Fig. 19)
- Detachment and loosening of renders and plasters (Fig. 20)
- Intense moisture concentration
- Corrosion of the openings' wooden frames

5 CONCLUSIONS

Summing up the work done before the rehabilitation of the Library building in Florina, it should be said that the first step is to recognize the elements of the



Figure 17. Severe oxidation of the concrete reinforcement in the basement.



Figure 18. Corrosion and local collapses of the wooden floors of the 1st floor.



Figure 19. Cracks in the slab of the balcony.

bearing system and find the mechanical and elastic properties of their materials. Record and make designs of all architectural details and describe the technology of specific renderings, plasters, mosaics or other materials used for protection or decoration at those times so as to be their reproduction feasible.

Since the technicians and materials used for the construction of the Library in Florina are very possibly the same with those used for the other buildings of the



Figure 20. Detachment and loosening of renders and plasters.

town dated from that period, the strength values and other characteristics of this study could be also considered for estimating the residual bearing capacity of these buildings.

ACKNOWLEDGEMENTS

The study was conducted under the Research Project entitled "Survey of the preservation state and of the listed building of the Library of Florina", sponsored by the Region of Western Macedonia-Regional Unit of Florina.

REFERENCES

Mazowe M. 2002. Greece and the Interwar Economic Crisis. Editions MIET (in Greek).

Cholevas, N.O. 1988. The architecture and Art Nouveau in Greece. Magazine Katoikia Nr 33.

https://www.et.gr/idocs-nph/search/pdfViewerForm.html

https://diavgeia.gov.gr/doc/ΒΛΣΟ4-4ES

https://florina-history.blogspot.com/2013/02/blog-post.html

Zarkada-Pistioli, C. 2003. The architecture of Florina in the interwar period. Dissertation, Aristotle University of Thessaloniki.

Papayianni, I., Pachta, V., Stefanidou, M. 2012. Analysis of ancient mortars and design of compatible repair mortars: the case study of Odeion of the Archaeological site of Dion. *Construction and Building Materials*, Vol. 40, pp. 84–92.

Hendry A.W., Malek M.1986. Characteristic compressive strength of brickwork from collected test results, Mason. Int., Vol. 7, pp. 15–24.

Tassios T.P. 1988. Mechanics of Masonry. Liquori. Napoli.

EN 1996-1 and 2: 2005, Eurocode 6-Design of masonry structures. Part 1-1: – General rules for buildings–reinforced and unreinforced masonry, Design of masonry structures. Design Considerations, Selection of Materials and Execution of Masonry. European Committee for Standardisation CEN,Brussels, 2006.

Repair of fire damage



Taylor & Francis
Taylor & Francis Group
http://taylorandfrancis.com

Concrete Solutions – Grantham et al. (Eds.)
© 2016 Taylor & Francis Group, London, ISBN 978-1-138-03008-4

Study on the effect of firing heating on FRC with various types and content

D. Choumanidis, P. Nomikos & A. Sofianos
School of Mining Engineering, Tunnelling Laboratory, National Technical University of Athens, Greece

E. Badogiannis & E. Papadimitriou
School of Civil Engineering, Laboratory of Reinforced Concrete, National Technical University of Athens, Greece

ABSTRACT: The demand for concrete to withstand heating due to fire resulted in employing various materials such as synthetic fibers. Fibers, despite their enhancing role on the mechanical behavior of concrete, they also contribute to the concrete's coherence, after the fire damage. This paper compares the mechanical behavior of polypropylene FRC, with those of steel FRC and plain concrete, before (20°C) and after exposure at high temperature levels (280°C). Three different testing methods are used for the mechanical assessment of the concrete specimens; bending, compression and double-punching. Ultrasonic pulse velocity is also reported through the ultrasonic pulse wave technique. In total ten concrete mixtures were produced by using at various addition levels, three different types of fibers; one of steel and two of polypropylene. The results showed that the peak and residual strengths of the specimens exposed at high temperature were reduced compared to those under normal temperature.

1 INTRODUCTION

1.1 *Fiber reinforced concrete and high temperatures*

High temperature affects concrete in various ways: porosity increase, thermal expansion, excessive pore pressure, inconsistent heat deformation between mortar and aggregates (Tai et al. 2011, Noumowé et al. 2009, Georgali & Tsakiridis 2005). The use of fibers in concrete mixtures results in all the above mentioned disadvantages. Despite the positive effect of the fibers, it has been found that fiber reinforced concrete structures subjected to high temperature lose a significant part of their compressive strength (Sideris & Manita 2013, Ding et al. 2012, Sideris et al. 2009, Poon et al. 2004) and flexural ductility (Sukontasukkul et al. 2010).

1.2 *Scope*

This work aims to study how different types of fibers in different percentages by volume of concrete, affect the mechanical behavior of fiber reinforced concrete after exposure at high temperature using different testing methods. To this aim, longitudinal compressive stress was used to determine compressive strength, chord modulus of elasticity and Poisson's ratio (ASTM C469-02). A bending test with Crack Mouth Opening Displacement (CMOD) controller was used to measure the flexural tensile strength (EN 14651:2005 + A1:2007). A double-punch test (Barcelona test) with a Total Circumferential Opening Displacement (TCOD) controller was used to measure the indirect tensile strength and compare it with that of the bending test (AENOR UNE 83515:2010). Finally, ultrasonic pulse velocity (UPV) was measured by through transmission technique using two transducers of 54 kHz.

2 EXPERIMENTS

2.1 *Specimen preparation*

In total ten (10) different concrete mixtures were prepared. One type of steel fiber and two different types of polypropylene fibers were used (see Table 1), at 0.5% and 1% content by volume of concrete, either individually or combined in pairs (see Table 2). All cast specimens were water cured (20°C) after demolding and were tested at the age of 28 days.

Each mixture produced 6 cylindrical specimens 100 × 200 mm for compression test, 6 prismatic specimens 100 × 100 × 500 mm for flexure test and 6 cylindrical specimens 150 × 150 mm for the double-punch test. Half of the specimens were tested before heating, at normal temperature (20°C) and the other half after being exposed at a temperature of 280°C.

2.2 *Heating procedure*

The same heating rate and development to Sakkas et al. (2014) was chosen, in order to accomplish comparative results. After 2 h of exposure of the coated



Figure 1. Specimens setup for heating.

Table 1. Fibers' geometrical and mechanical characteristics.

Type	SF	PPF1	PPF2
Material	Steel	Polypropylene	Polypropylene
Length (mm)	30	52	12
Diameter (mm)	0.8	0.46	0.025
Rupturing force (MPa)	1100	613	400
Modulus of elasticity (MPa)	500	5400	1600
l/d	37.5	113	480

concrete specimen to the RWS (RijksWaterStaat) fire load curve (EFNARC 2009), the temperature at the concrete surface was lower than 280°C. In our case the temperature was being increased by 20°C every ten minutes until reaching the maximum temperature of 280°C which was maintained for 30 minutes. Then the specimens were cooled down to ambient temperature in the furnace (Fig. 1).

2.3 *Experimental setup*

A testing machine of 5000 kN capacity with a servo-hydraulic control unit for axial displacement control was used for the compression and Barcelona tests.

2.3.1 *Compression test*

The loading rate was set equal to 2000 N/sec. Two subsequent loadings were carried out until 40% of the peak load, in order to eliminate the effect of any possible instability and to assure repeatability in the conducted tests. The test was over at the failure of the specimen. The longitudinal axial displacement was expressed as the mean value of the values of three transducers placed around the specimen at 120° angle, which were constantly measuring the variation of the distance between the two yokes (Fig.2). The yokes were rigidly attached to the specimen, each one at a distance of 3.75 cm from the mid specimen height. The transverse strain was expressed as the TCOD at half height of the specimen, using a circumferential extensometer (model 3544 EPSILON), fixed to the ends of a chain.

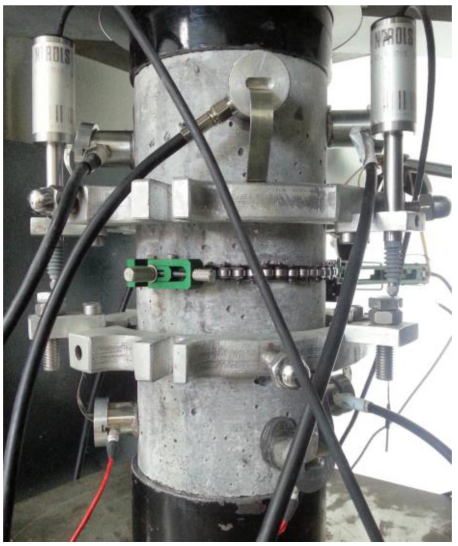

Figure 2. Compression test set up.

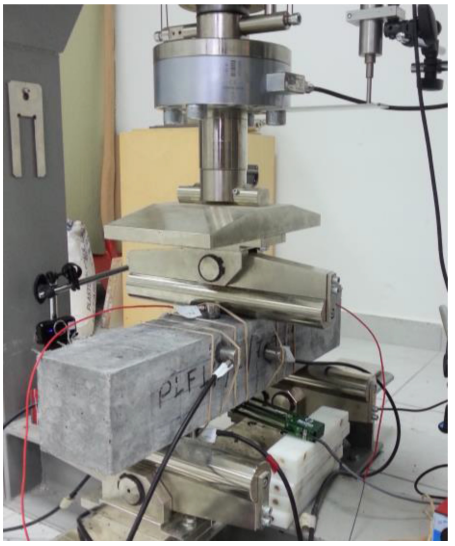

Figure 3. Bending test set up.

2.3.2 *Bending test*

In the present research, the 3-point bending test was used and the standard EN 14651:2005+A1:2007 was followed, on specimens of a smaller scale. The displacement rate (CMOD) was set equal to 0.05 mm/min. Each test lasted until CMOD reached 4 mm, at least. The force and the displacement of the piston were also reported (Fig.3).

2.3.3 *Barcelona test*

The Barcelona test is a double punch test (DPT) performed on a cylindrical FRC specimen with height



Figure 4. Barcelona test set up.

equal to diameter equal to 150 mm (AENOR UNE 83515 2010). The specimen is subjected to compressive loading along its axis, by inserting two cylindrical steel punches with a height of 24 mm and a diameter of 37.5 mm between the loading machine platen and the center of the upper and lower face of the specimen (Fig. 4). An extensometer chain is placed at half-height of the specimen to measure the TCOD. A constant relative displacement rate of 0.5 ± 0.05 mm/min is applied by the press piston. The force and the TCOD are also measured. The test is over when the TCOD is at least 4 mm.

2.3.4 *Ultrasonic pulse velocity*

Using the ultrasonic pulse wave method, the ultrasonic pulse velocity was measured for the different specimens and at different dimensions – width (10 cm, 15 cm, 20 cm and 50 cm) and the mean value for each mixture was calculated. The PUNDIT7 model PC1012 of CNS Farnell with two transducers of 54 kHz was used.

3 RESULTS AND DISCUSSION

All the compared features are average values of experimental measurements of 3 tested specimens.

3.1 *Compressive strength*

The compressive strength is calculated by dividing the maximum load carried by the specimen during the test by the average cross-sectional area (ASTM C39/C39M-03). As it is shown in Figure 5 the minimum decrease occurs to the concrete mixtures that contain PPF2 fibers. The low density of the mixture PPF2-0.5, which also implies an increased percent of entrained air, it is expected to negatively affect the

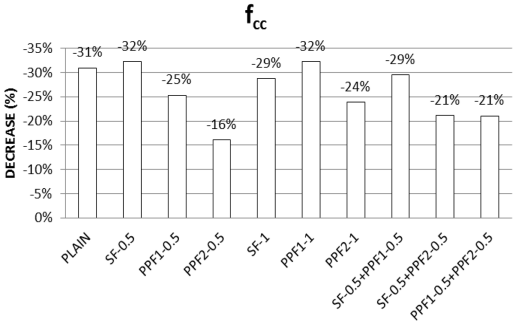

Figure 5. Decrease of compressive strength (f_{cc}) after heating at 280°C.

compressive strength. The existing porosity increases more due to fiber melting as the temperature is developing at higher levels. The increased porosity helps the specimen to redistribute the stresses by ab sorbing strains which would otherwise result in micro cracking and consequently reduced strength.

3.2 *Modulus of elasticity*

The chord modulus of elasticity was calculated as follows:

$$E = (\sigma_2-\sigma_1)/(\varepsilon_2-\varepsilon_1) \quad [1]$$

where σ_1 = stress corresponding to 20% of ultimate load; σ_2 = stress corresponding to 40% of ultimate load; ε_1 = longitudinal strain produced by stress S_1; and ε_2 = longitudinal strain produced by stress S_2.

As Figure 6 shows, the chord modulus of elasticity exhibits the same behavior with the compressive strength.

3.3 *Poisson's ratio*

Poisson's ratio was calculated as follows:

$$\nu = (\varepsilon_{t2}-\varepsilon_{t1})/(\varepsilon_2-\varepsilon_1) \quad [2]$$

where ε_{t1} = transverse strain at mid height of the specimen produced by stress σ_1 ; ε_{t2} = transverse strain at mid height of the specimen produced by stress σ_2. Figure 7 displays the decrease of Poisson's ratio.

3.4 *Flexural tensile strength*

Figure 8 shows the decrease (%) of flexural tensile strength after heating at 280°C. The maximum decrease occurs at concrete mixtures that contain PPF1 fibers and the minimum at concrete mixtures that contain PPF2 fibers. Due to their length, PPF1 fibers offer high flexural tensile strength at normal temperatures unlike to PPF2 fibers whose length doesn't significantly contribute to the flexural strength. At high temperature levels most of the polypropylene fibers are melted and strength's decrease is higher.

Table 2. Concrete mix design characteristics.

Ingredients (kg/m^3)	Plain	SF-0.5	PPF1-0.5	PPF2-0.5	SF-1	PPF1-1	PPF2-1	SF-0.5 + PPF1-0.5	SF-0.5 + PPF2-0.5	PPF1-0.5 + PPF2-0.5
CEM IV/B 32.5R	400	400	400	400	400	400	400	400	400	400
Silica Fume	20	20	20	20	20	20	20	20	20	20
Sand (0/4)	922	922	922	922	922	922	922	922	922	922
Gravel (4/8)	335	335	335	335	335	335	335	335	335	335
Gravel (8/16)	419	419	419	419	419	419	419	419	419	419
Water (w)	219	219	219	219	219	219	219	219	219	219
Steel Fibers		40			80			40	40	
Polypropylene Fibers I			4.55			9.1		4.55		4.55
Polypropylene Fibers II				4.55			9.1		4.55	4.55
Superplasticizer (Sika Viscocrete Techno 40)	1.97	2.33	3.61	3.98	2.33	4.39	5.5	4.69	3.89	4.66
w/(b)	0.48	0.48	0.48	0.48	0.48	0.48	0.48	0.48	0.48	0.48
Slump (cm)	11	13.5	10	11	13	0	13	13	15	13.5
Density (kg/lt)	2.329	2.345	2.28	2.017	2.366	2.299	2.206	2.341	2.036	2.029

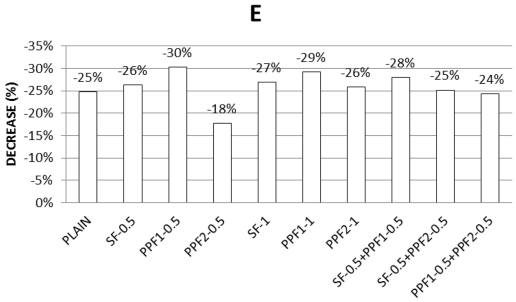

Figure 6. Decrease of modulus of elasticity (E) after heating at 280°C.

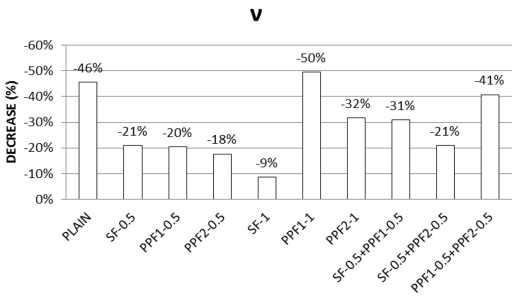

Figure 7. Decrease of Poisson's ratio (v) after heating at 280°C

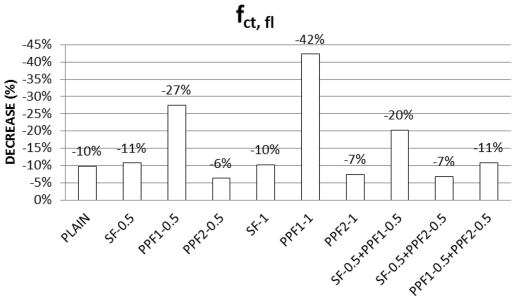

Figure 8. Decrease of flexural tensile strength ($f_{ct,fl}$) after heating at 280°C.

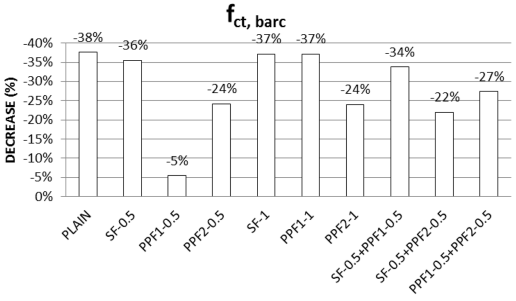

Figure 9. Decrease of indirect tensile strength ($f_{ct,barc}$) in Barcelona test after heating at 280°C.

3.5 *Indirect tensile strength*

The results from the Barcelona test show that indirect tensile strength, follows a similar decreasing trend to that of compressive strength (Fig. 9). Moreover, if PPF1-0.5 mixture is not considered, all the other series exhibit an up to 38% decrease of indirect tensile strength, which is at maximum 8% higher than the decrease of compressive strength. Therefore, it may be assumed that the indirect tensile strength, the compressive strength and the modulus of elasticity show a similar decreasing trend.

3.6 *Pulse velocity*

In Figure 10 the pulse velocity values of the concrete mixtures are reported, together with their percentages of decrease after heating. The lower pulse velocity is

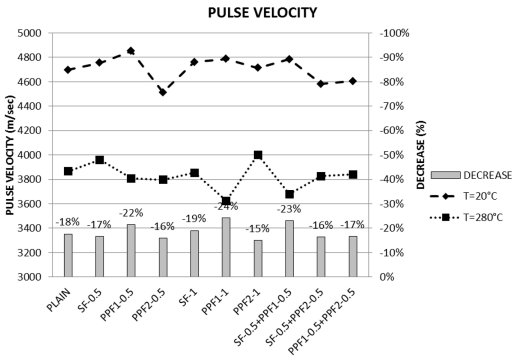

Figure 10. Pulse velocity values before heating and its percentage of decrease after heating.

reported for the PPF2-0.5 concrete mixture at 20°C, confirming the low density and the possibly high percentage of entrained air. After heating, an average reduction of 800 m/sec in the pulse velocity was reported for all concrete mixtures. The percentages of decrease varied from 15% to 24% which is consistent with the decrease percentages of 13% to 26% that were observed by Sideris & Manita (2013). The minimum decrease occurred in the concrete mixtures which contained PPF2 fibers and the minimum values of pulse velocity after heating for the concrete mixtures containing PPF1 fibers. Naturally, due to the absorbed water of the concrete specimens, a variation of +5% in the measured values of the UPV must be considered, according to the constructor instructions (PUNDIT7 MODEL PC1012).

4 CONCLUSIONS

Figures 5–9 indicate that the PPF2-0.5 concrete mixture exhibits the best behavior at high temperature exposure, since it has the lower decrease in the average strength values. However, in respect to their absolute strength values, the PPF2-1 concrete mixture exhibits the highest strength values. Although the addition of the PPF2 fibers in the concrete mixtures didn't offer the expected improvement in the residual strength, PPF2 concrete mixtures showed the best mechanical behavior after heating at 280°C. Finally, steel fibers seem to offer the best improvement in the residual strength, as well as in the compressive, flexural and indirect tensile strength.

ACKNOWLEDGEMENTS

This work was co-funded by IKY, through the Siemens Programme: "IKY Fellowships of Excellence for Postgraduate Studies in Greece – Siemens Program". My father Panagiotis Choumanidis, Andreas Kacapari and Nikos Tzanetis are gratefully acknowledged for their help to the preparation of concrete mixtures. Dr. George Papantonopoulos, scientific staff of the Tunnelling Laboratory of School of Mining Engineering of the National Technical University of Athens are also gratefully acknowledged for their help on the experimental work.

REFERENCES

AENOR. UNE 83515:2010. Hormigones con fibras. Determinación de la resistencia a fisuración, tenacidad y resistencia residual a tracción. Método Barcelona, Asociación Española de Normalización y Certificación Madrid

ASTM C39/C39M-03. Standard test method for compressive strength of cylindrical concrete specimens.

ASTM C469-02. Standard test method for static modulus of elasticity and Poisson's ratio of concrete in compression.

Carmona, S. M. & Aguado de Cea, A. & Molins, C.B. 2012. Generalization of the Barcelona test for the toughness control of FRC. *Materials and Structures* 45: 1053–1069.

Concrix, 2011. Datasheet Concrix ES.

Ding, Y. & Azevedo, C. & Aguiar, J.B. & Jalali, S. 2012. Study on residual behaviour and flexural toughness of fibre cocktail reinforced self -compacting high performance concrete after exposure to high temperature. *Construction and Building Materials* 26: 21–31.

EFNARC, European Federation of National Associations Representing producers and applicators of specialist building products for Concrete, 2009. Specification and guidelines for testing of passive fire protection for concrete Tunnels lining.

EN 14651:2005+A1:2007. Test method for metallic fibre concrete — Measuring the flexural tensile strength (limit of proportionality (LOP), residual)

Georgali, B. & Tsakiridis, P.E. 2005. Microstructure of fire-damaged concrete. A case study. *Cement & Concrete Composites* 27: 255–259.

Poon, C.S. & Shui, Z.H. & Lam, L. 2004. Compressive behaveior of fiber reinforced high-performance concrete subjected to elevated temperatures. *Cement & Concrete Research* 34: 2215–2222.

Pujadas, P. & Blanco, A. & Cavalaro, S.H.P. & de la Fuente, A. & Aguado, A. 2014. Multidirectional double punch test to assess the post-cracking behaviour and fibre orientation of FRC. *Construction and Building Materials* 58: 214–224.

PUNDIT7 MODEL PC1012 Operating Instructions, CNS-FARNELL

Sakkas, K. & Panias, D. & Nomikos, P.P. & Sofianos A.I. 2014. Potassium based geopolymer for passive fire protection of concrete tunnels linings. *Tunnelling and Underground Space Technology 43*: 148–156.

Sideris, K.K. & Manita, P. 2013. Residual mechanical characteristics and spalling resistance of fiber reinforced self-compacting concretes exposed to elevated temperatures. *Construction and Building Materials* 41: 296–302.

Sideris, K.K. & Manita, P. & Chaniotakis, E. 2009. Performance of thermally damaged fibre reinforced concretes. *Construction and Building Materials* 23: 1232–1239.

Sika, 2013. Datasheet Sika®Fiber PP 940-50: Construction.

Sukontasukkul, P. & Pomchiengpin, W. & Songpiriyakij, S. 2010. Post-crack (or post-peak) flexural response and toughness of fiber reinforced concrete after exposure to high temperature. *Construction and Building Materials* 24: 1967–1974.

Taia, Y. & Pan, H. & Kung, Y. 2011. Mechanical properties of steel fiber reinforced reactive powder concrete following exposure to high temperature reaching 800 ?C. *Nuclear Engineering and Design* 241: 2416–2424.



Taylor & Francis
Taylor & Francis Group
http://taylorandfrancis.com

Concrete Solutions – Grantham et al. (Eds.)
© 2016 Taylor & Francis Group, London, ISBN 978-1-138-03008-4

Investigation, assessment and repair of a fire-damaged reinforced concrete structure

A. Elenas & K.K. Sideris
Democritus University of Thrace, Xanthi, Greece

ABSTRACT: This study presents an investigation of a reinforced concrete structure exposed to a fire accident. First, a number of on-site and laboratory-based techniques were conducted for the diagnosis of the post-fire structural material status. Next, the results of a numerical analysis exposed the shortages of the structure, considering the post-fire mechanical and geometrical material properties. Not all the deficiencies found through the visual inspection and the tests, were caused by the fire. Thus, low stirrup amount, significant dispersion of concrete strength and concrete carbonation were detected and were existent before the thermal exposure. Whereas, buckling of longitudinal column reinforcements, material strength reduction and concrete spalling, were produced through the fire impact. Appropriate techniques were adopted for the rehabilitation of the structure. The repair scheme was based on the use of reinforced concrete jackets on structural elements with severe damage, combined with local damage rehabilitation of elements with low damage.

1 INTRODUCTION

Over the years, many fire incidents occur in buildings due to unforeseen circumstances such as the use of explosives, accidents or electrical device failures. The influence of fire on concrete and the embedded reinforcement should not be underestimated, even though concrete cover provides some protection to the latter. Concrete can sustain various degrees of damage depending on the severity of the fire, the temperature levels reached and the time of the structural materials' fire exposure. The effects on concrete components of high temperature fire includes: reduction in compressive strength; micro-cracking within the concrete microstructure; color changes consistent with strength reductions; reduction in the modulus of elasticity; various degrees of spalling; loss of bond between concrete and steel; and possible loss of residual strength of steel reinforcement.

This study investigates a three-story reinforced concrete structure with an underground floor, exposed to a fire and situated in Thasos, which is a Greek island in the North Aegean Sea. The fire broke out in a shop, on the ground floor, after a short-circuit in the electrical installation (Fig. 1). The building was constructed in 1976, according to the design rules of the Greek Codes for building loads (FEK 325/A/31.12.1945), reinforced concrete structures (FEK 160A/26-07-1954) and antiseismic design (FEK 36A/26-02-1959) valid at that time. Thus, the building materials were concrete with quality B 160 and steel reinforcement with quality St I. These qualities correspond to a concrete with $f_{ck,cyl} = 11$ MN/m^2 (C8/10) and a plain steel reinforcement with $f_{yk} = 220$ MN/m^2, in accordance to the design rules of the Eurocode 2.



Figure 1. Fire-damaged ground floor.

For the precise post-fire damage assessment and the valuation of steel and concrete mechanical properties, detailed field observations were performed combined with in-situ and ex-situ experiments. Considering the observed damage and the mechanical material properties, appropriate repair procedures were provided for the rehabilitation of the building.

2 POST-FIRE INSPECTION OF REINFORCED CONCRETE STRUCTURE

2.1 *In-situ visual inspection*

Visual inspection was used to assess apparent damage in the ground floor of the fire affected building, where the fire broke out. Thus, spalling of concrete in several slab, column and beam regions were observed.



Figure 2. Spalling of concrete on a beam.

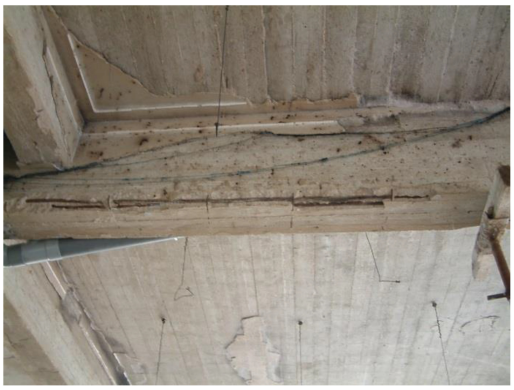

Figure 3. Extended spalling of concrete on a beam.

The spalls (in several places the concrete spalling was severe) exposed the reinforcement in an extremely corrosive and dangerous environment due to the proximity of seawater (Figs 2–3). In addition, specifically in the regions with severe concrete spalling, inadequate (too few) stirrups were exposed (Figs 2–3). Not only in beams (Figs 2–3), but also in columns (Figs 4–5) a low stirrup amount was observed.

Buckling of the longitudinal reinforcement was observed in two columns as shown in Figure 5. The previously described widely spaced stirrups affected the reinforcement buckling. Finally, no significant color change of the concrete from normal to pink/red was observed.

2.2 *Non-destructive in-situ testing*

The concrete's compressive strength was evaluated using a combination of core strength measurements and non-destructive techniques (rebound and pulse velocity measurements) according EN 13791 (CEN 2007). Cores were taken from different locations from the lower third height of six columns. Residual compressive strength of fire damaged elements was assessed using non-destructive tests on a basis



Figure 4. Inadequate amount of stirrups in column.



Figure 5. Buckling of the longitudinal reinforcement in two columns.

of previous research (Ikonomou et al. 1996, Savva et al. 2005) where concrete mixtures with the same constituent materials were produced (Figs 6–7).

The results varied in dependency with the distribution of the damage, the presence of cracks and the distance to a crack. Both procedures indicated that the concrete quality in some structural members was lower than B 160, which was assumed in the original design procedure of the building. In that case the concrete quality belongs to the category B 120 (C8/10 in accordance to recent Eurocode 2). The reason of this dispersion is most probably the in-situ concrete mixing and inadequate consolidation, both characteristics for the time and the region the building was constructed.

The maximum temperature reached in the concrete was evaluated from the velocity of the ultrasound

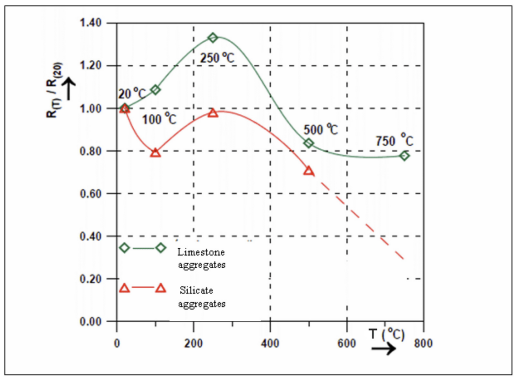

Figure 6. Ratio of the residual rebound number R_T to the initial rebound number R_{20} for concrete mixtures prepared with limestone and silicate aggregates (Ikonomou et al. 1996).

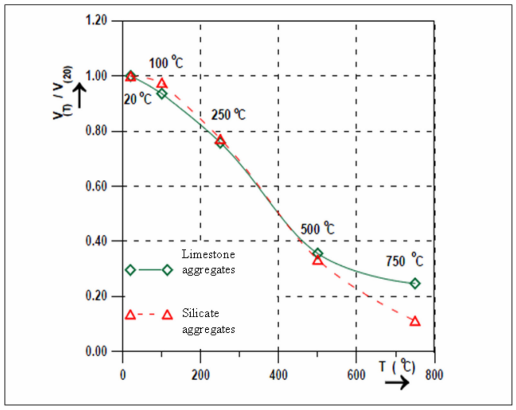

Figure 7. Ratio of the residual pulse velocity V_T to the initial velocity measurement V_{20} for concrete mixtures prepared with limestone and silicate aggregates (Ikonomou et al. 1996).

through the examined structural elements (Fig. 7). Thus, a maximum temperature of 400°C was evaluated through the in-situ tests.

The concrete carbonation tests showed that the carbonation depth was between 1 cm and 3 cm in several structural elements. The results showed that the carbonation depth was at least equal with the concrete cover of the reinforcement bars and thus, steel corrosion protection was not guaranteed.

The calcination test of concrete aggregates showed that, in the top third height of the columns where longitudinal reinforcement buckling was observed and near to that location, calcination was initiated. In addition, calcination initiation was detected in several beams. The reason was the heat concentration at the top of the affected ground floor room. Thus, the maximum temperature reached in that area was estimated to be between 500°C and 600°C.

2.3 *Ex-situ testing*

Cores of concrete in selected zones defined from in-situ inspection should contribute to the final determination of the concrete compression strength besides the non-destructive in-situ tests. Thus, six core specimens were tested. The test result classified the concrete quality to the category B 120. One isolated specimen was classified to the category B 160. Hence, the non-destructive in-situ test results fully confirmed that the concrete quality was not uniform and was partially lower than the assumed quality during the design procedure. In addition, a chemical analysis of the concrete revealed that no considerable amounts of chlorides were detected.

3 EVALUATION OF TEST RESULTS

The inspection and experimental results showed that, in general, the reinforced concrete structure was exposed to a temperature between 400°C and 600°C. The higher temperature (500°C – 600°C) was reached at the regions where concrete calcination was initiated. These regions were beams and columns at the area where buckling of longitudinal reinforcement occurred. At those temperatures the steel St I yielding stress is reduced to 50% (400°C) and 30% (600°C) from its initial value. Further, the steel St I tensile strength is reduced to 95% (400°C) and 50% (600°C) from its initial value. In addition, the steel may have reduced ductility due to rapid cooling from high temperature with the water used during extinguishing the fire. The concrete compression strength is reduced to 80% (400°C) and 55% (600°C) of the initial value at room temperature. The reduction depends on the concrete aggregates. In addition, the concrete quality varied between B 120 and B 160. Although the latter was assumed during the design procedure.

The observed damage was caused due to construction and maintenance deficiencies besides the fire exposure. An inadequate amount of stirrups in beams or columns, concrete carbonation and poor concrete cover are typical construction and maintenance deficiencies. Lower than expected concrete strength is typically caused by inadequate in-situ mixing and, inadequate consolidation in addition to fire exposure. Concrete spalling was caused by fire exposure on the lower part of the beams and the ceiling (Figs 2-4). Buckling of the longitudinal reinforcement was caused by the fire exposure (Fig. 5).

4 REPAIR AND STRENGTHENING

Some observed structural and material deficiencies (e.g. inadequate amount of stirrups, lower concrete category than assumed during the design process and buckling of column reinforcement) affected the static behavior of the whole structure. Therefore, the whole structure was analyzed and designed taking into account the post-fire material and structural status.

The analysis provided the required extent of structural strengthening, in addition to the necessary local repairs. The main repair scheme was based on adding reinforced concrete jackets in columns and beams with reduced bearing capacity. Before carrying out the strengthening work, a temporary support system was needed to carry the vertical loads. Then, removal of damaged concrete and reinforcement, placement of new longitudinal reinforcement with welding, placement of new closely spaced stirrups and concreting could be performed. Deficiencies like poor concrete cover, small concrete cracks and reinforcement corrosion were restored using patch repair procedures.

5 CONCLUSIONS

Fire can affect a structure seriously. The damage grade can be determined by on-site inspection and by in-situ and ex-situ testing. The structural rehabilitation can be local or global depending on the damage level. The present case study investigated a reinforced concrete structure exposed to a fire accident. On-site inspection was carried out in addition to in-situ and ex-situ tests conducted for the diagnosis of the post-fire structural material status. The results of a numerical analysis exposed the shortcomings of the structure, considering the post-fire mechanical and geometrical material properties. The essential global repair scheme was based on adding reinforced concrete jackets in columns and beams with reduced bearing capacity. In addition, secondary deficiencies were restored using local patch repair procedures.

REFERENCES

CEN 2007. EN13791: Assessment of in situ compressive strength of structures and precast concrete components.

FEK 325/A/31.12.1945: Greek code for loads on buildings.

FEK 160A/26-07-1954: Code for the analysis and design of concrete structures.

FEK 36A/26-02-1959: Code for the antiseismic design of structures.

Ikonomou, C., Savva A., Baltzopoulou K., Sideris K.K. & Sideris K. 1996. Assessment of the residual compressive strength of concrete exposed to elevated temperatures using non-destructive techniques. Proceedings of the 12th Greek Concrete Conference, Lemesos, Cyprus, Vol. I, pp. 259–271 (in Greek).

Savva A., Manita P. & Sideris K.K. 2005. Influence of Elevated Temperatures at the Mechanical Properties of Blended Cement Concrete Prepared with Limestone and Silicate Aggregates. Cement and Concrete Composites, 27(2), pp. 239–248.

Concrete Solutions – Grantham et al. (Eds.)
© 2016 Taylor & Francis Group, London, ISBN 978-1-138-03008-4

Innovative materials for passive fire protection of concrete

K.M. Sakkas, P. Nomikos, A. Sofianos & D. Panias
National technical University of Athens, Athens, Greece

ABSTRACT: An essential element of design of concrete structures is to ensure that the structural elements will not fail due to the high temperatures which may be developed during a fire. For this problem, several passive fire protection methods have been developed. However there is always a need for developing a new material with improved fire resistance properties and low cost. Geopolymerization technology seems to be very attractive in developing effective fire resistant materials. The developed materials were tested for their resistance under high temperatures according to E.F.N.A.R.C specifications and guidelines. From the test results it is concluded that the materials perform well under various fire scenarios without yielding or spalling, according to the standard fire temperature curves employed in international norms, and that may occur during a real fire incident. Also as it was shown that they have similar properties to the commercially available materials.

1 INTRODUCTION

Fires in structures can seriously damage concrete structural elements, thus threatening the stability of the structure and rendering it to collapse. The damage is caused particularly by the spontaneous great amount of heat release and aggressive fire gases, resulting in spalling of concrete. Spalling is described as the breaking of layers or pieces of concrete from the surface of a structural element when it is exposed to the high and rapidly rising temperatures experienced in fires. The most severe kind of spalling is so called "explosive spalling" which according to Khoury (2000) is attributed to combined thermal stress and pore pressure. This is described as a violent showering of hot concrete pieces having a detrimental effect on the concrete. Additionally very serious problems may be encountred by the fire fighting service personnel rendering their work substantially more difficult and dangerous. The spalling phenomena are expected at several temperatures depending on the strength of the concrete. However, it is generally accepted that concrete loses part of its strength and carrying capacity when exposed at temperatures higher than 300°C (Khoury, 2000). Then, it is considered as damaged and should be removed and repaired. This temperature is near to the calcium hydroxide dehydration temperature (400°C) which causes significant reduction of the mechanical strength of the concrete (Fletcher et al., 2007). The latter is considered to be significantly reduced at temperatures higher than 300°C (Sakkas et al., 2013a).

In addition to the concrete damage caused by a fire, special attention must also be given to the damage caused to structural steel rebars that often reinforce the concrete members. Structural steel (especially some plain carbon and alloy steels) exhibit both an increase in strength and a substantial decrease in ductility upon their heating at temperatures between 250°C and 300°C. This is known as the "blue brittleness" effect. Above 430°C, steel undergoes significant deformations as well as stress relieving at temperatures ranging from 600°C to 650°C. Its strength is considered to be lost at temperatures between 550°–600°C (Fletcher et al., 2007; Sakkas et al., 2013a; Edwards and Gamble, 1986).

Therefore, both steel and concrete should be viewed as fire sensitive construction elements. They require passive fire protection in order for the concrete to be able to withstand the anticipated temperatures of a serious fire incident, for an appropriate period of time without losing their stability.

Passive fire protection methods are generally divided into two categories: external (insulation) and internal (concrete design). In the external method there are plenty of materials used. In this paper, the development, characterization and passive fire testing of low cost and high performance fire resistant materials, for external passive fire protection of concrete structures, are presented.

1.1 *Geopolymerisation*

Geopolymers are a class of inorganic polymers formed by the reaction between an alkaline solution and an aluminosilicate source. The hardened material has an amorphous to semi-crystalline 3-dimensional structure similar to that of an aluminosilicate glass. The reaction is exothermic and takes place at atmospheric pressure and temperatures below 150°C. Geopolymers possess excellent physicochemical and mechanical properties, like low density, micro or nano-porosity, negligible shrinkage, high mechanical strength, thermal stability, fire as well as chemical resistance and

Table 1. Chemical analysis of Slag

Species	% w/w
SiO_2	41.14
Al_2O_3	13.79
FeO	34.74
Cr_2O_3	5.41
MgO	3.59
CaO	0.71
Ni	0.14

Table 2. Syntheses of the fire resistant materials

	Material I	Material II
Slag (%w.w)	75.758	42.24
Al_2O_3 (%w.w)		25.03
KOH (%w.w)		8.09
NaOH (%w.w)	5.303	
H_2O (%w.w)	18.939	24.64
S/L (g/ml)	4	2.73

notable surface hardness. Due to these properties, geopolymers are viewed as alternatives for certain industrial applications in the areas of construction and building materials, since the geopolymer properties are similar or even better to the conventional construction and fire protection materials. Apart from that, geopolymers seem to be more attractive from the conventional materials due to their low cost production, the lower energetic production requirements and the rational utilization of natural resources (Davidovits 1999).

2 EXPERIMENTAL

2.1 *Materials*

The raw material used in the present study is a slag which was provided by the metallurgical plant of the Greek company LARCO G.M.M.S.A. that treats laterites to produce ferronickel. This slag is generated during the reductive smelting of laterites in electric arc furnaces and is granulated using a flash water cooling process. For the synthesis of inorganic polymers, an adequate quantity of granulated slag was ground to $<90\ \mu m$ and the resulting powder had a mean particle size (d50) of $15.05\ \mu m$. As is shown in Table 1, the FeNi slag is a siliceous material very rich in iron oxides and rich in alumina. It also contains substantial amounts of trivalent chromium, magnesium and calcium oxides, as well as traces of nickel. The mineralogical analysis of the slag showed that it is mainly composed of an X-ray amorphous silicate or aluminosilicate phase.

Also pure alumina, provided by the Aluminum Plant of Greece, was used in the mix design of material ii Alumina has a mean particle size (d50) of $88.61\ \mu m$ measured on a MALVERN Laser Particle Size Analyzer. Except for the aforementioned solid products, sodium hydroxide (Merck, anhydrous pellets), potassium hydroxide, sodium silicate solution (Merck, $Na_2O{:}SiO_2 = 3.4$, $Na_2O = 7.5$–8.5%, $SiO_2 = 25.5$–28.5% and $d = 1.346\ g \cdot l - 1$) and deionized water were used for the synthesis.

2.2 *Design and tests*

Two geopolymeric materials were designed as fire resistant materials which can resist temperatures higher than 1000°C. The compressive strength of the materials according to ASTM C-109 and the cold water absorption according to EN 771-1: 2003 were measured. The thermal conductivity was also evaluated with the HFM 436 Lambda Heat Flow Meter according to ASTM C518 standard test using a specimen of $15 \times 15 \times 2$ cm. In order to test their fire resistance, a $15 \times 15 \times 15$ cm (thickness) composite specimen was prepared, consisting of 5 cm thick geopolymer material on one face and a 10 cm thick concrete slab, based on the EFNARC guidelines. The adhesion of the two materials was enhanced by the use of steel anchors, placed during material preparation. The specimens were subjected to thermal loading by exposing the geopolymer surface to prescribed temperatures according to the ISO-834 or the RWS time-temperature curves. The test was performed 28 days after the production of the specimen. The developed temperature at the interface between the concrete and the geopolymer material was measured by using a "K"-type thermocouple, while the temperature of the back surface of the concrete slab was measured with a high performance infrared thermometer (RAYTEK, Raynger MX4).

2.3 *Syntheses*

The syntheses and curing conditions and times of the two materials are summarized in table 2. The preparation and curing procedures of the inorganic materials are described below. The first material (material I) was a sodium activated geopolymer with S/L ratio equal to 4 g/mL and initial NaOH concentration in the aqueous phase equal to 7 M. The curing of the material took place at ambient conditions. The setting of the material which was evaluated with Vicat apparatus according to according to EN 196-3:2005 standard test was completed after 3 hours . The second material was a potassium activated geopolymer doped with alumina with S/L ratio equal to 2.73 g/ml and initial KOH concentration in the aqueous phase equal to 5.85 M. The curing of the material took place at 70°C for 48 hours.

2.4 *Results*

The first material was tested to the international standard ISO 834 time-temperature curve (shown in Figure 1) that is the most commonly adopted fire curve for simulating a cellulosic fire, or fires in buildings. In

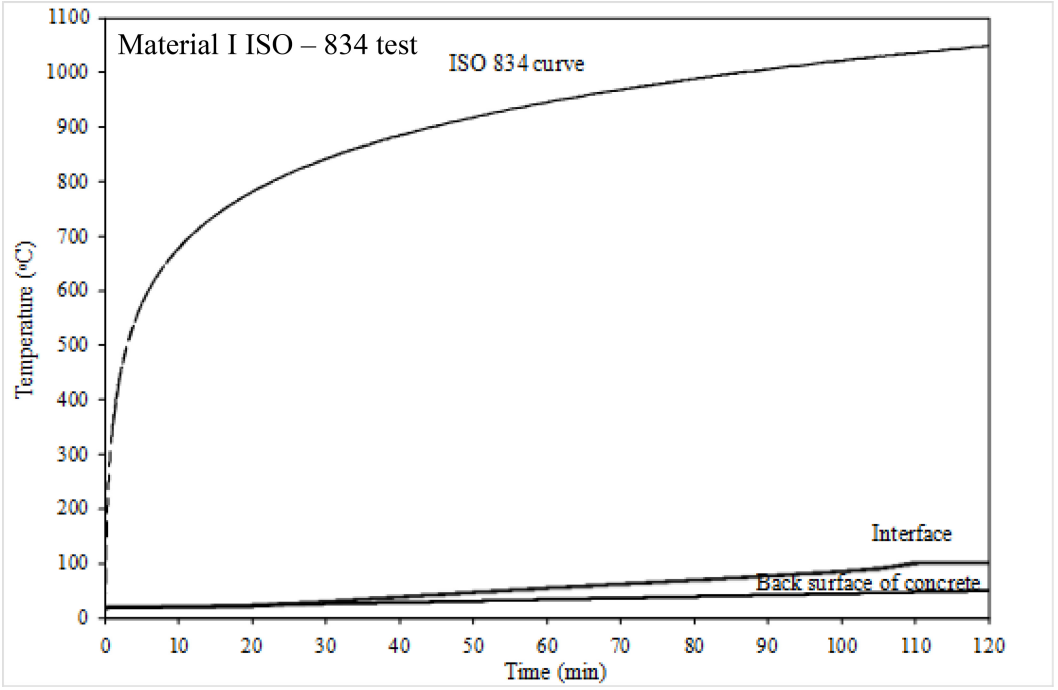

Figure 1. Passive fire protection test of material I exposed to the standard ISO 834 time-temperature curve

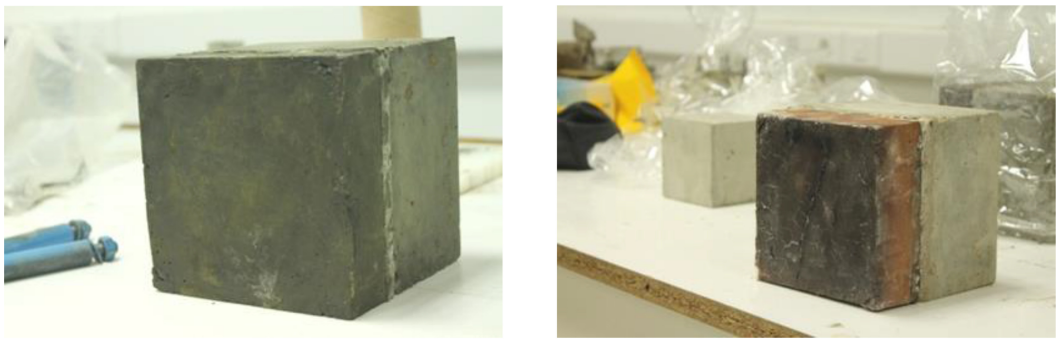

Figure 2. Specimen of material I a) Before the passive fire protection test, b) After the passive fire protection test

figure 1 the temperature development at the concrete-geopolymer interface during time is shown, together with the measured temperature at the unexposed concrete surface and the furnace temperature prescribed by the ISO 834 curve.

As can be seen in Fig. 1, the interface temperature has very low values in the beginning of the experiment for the first 35 minutes (30°C). After that the temperature increases linearly over a period of 75 min and reaches the temperature of 100°C around a time of 110 min. The temperature remains around this temperature until the end of the experiment. This temperature is much lower than the required temperature for maintaining the structural integrity of the concrete. The temperature in the back surface of the concrete specimen increases with a very low rate until 50°C which is close to the ambient temperature (25°C). At the end of the test (120 min) a temperature difference of 950°C was attained between the exposed and unexposed surface of the geopolymer material, creating thus a local thermal gradient of 19°C/mm. Further, as can be clearly observed from the photographs of figure 2, the geopolymer material did not appear to show any creeping or melting phenomena but only a change in colour, which is attributed to mineralogical transformations.

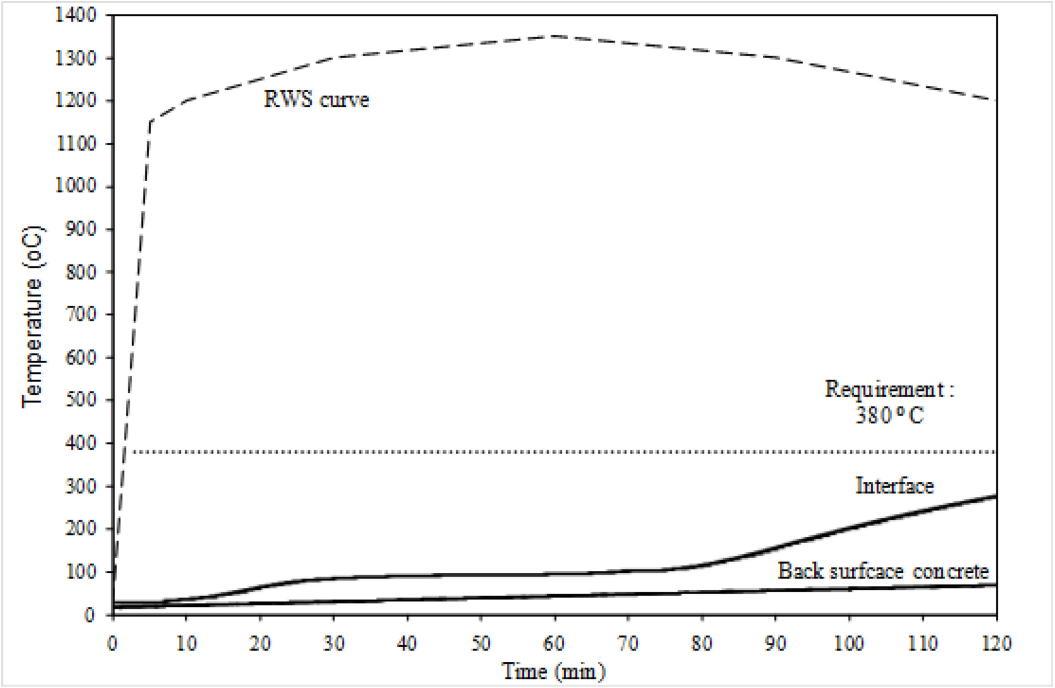

Figure 3. Passive fire protection test of material II exposed to the standard RWS time-temperature curve

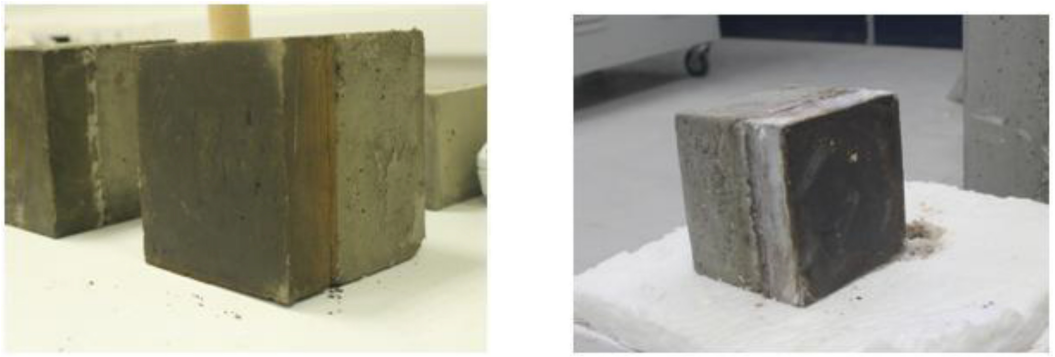

Figure 4. Specimen of material II: a) Before the passive fire protection test, b) After the passive fire protection test

In the front face of the specimen, some cracks were observed (figure 2b) after the test due to the sudden loss of geopolymeric water which however were less than 6 mm wide and 25 mm deep which are the specific performance criteria set by the standard ISO 834-1:1999(E) for the evaluation of integrity of fire resistant materials. The concrete slab protected by the sodium based geopolymer did not appear to show any form of spalling or other mechanical damage. The compressive strength achieved 28 days after the production of the material fluctuated between 11–15 MPa, where the thermal conductivity was measured equal to 0.21 W/m.K. The comparison of the compressive strength and thermal conductivity of the fire resistant geopolymer with those fire resistant materials available on the market shows that the geopolymer's compressive strength was comparable (e.g. to Promatect) or superior (e.g. to Pyrocrete 241) to them. The thermal conductivity of the material was measured to be 0.27 W/m.K at 300°K which is substantially lower than the corresponding ones of the commonly used structural building materials, such as bricks (0.7–1.3 W/m.K), clay tiles (0.5–0.7 W/m.K), normal strength concrete (0.8–1.28–2 W/m.K) and

cement or gypsum plasters (0.2–0.8 W/m.K). The second fire resistant material was tested to the RWS (Rijkswaterstaat) curve which is the most severe fire scenario simulating a 50 m^3 fuel (oil or petrol) tanker fire with a fire load of 300 MW lasting up to 120 minutes. The failure criteria for fire protective materials tested with the standard RWS temperature-time curve is that the temperature at the material/concrete interface should not exceed 380°C and the temperature of reinforcement should not exceed 250°C. In figure 3, the temperature development at the concrete – geopolymer interface during time is shown, together with the measured temperature at the unexposed concrete surface and the furnace temperature prescribed by the RWS curve.

As can be observed in Fig.3, the interface temperature in the first 8 minutes remained low at 30°C . After the first 8 minutes, the temperature increased linearly till 100°C, with the completion of 30 minutes of the test. The temperature remained almost stable for 50 minutes (up to the 80 minutes of the test). During this period the largest part of geopolymeric water in the material was removed. The water removal is an endothermic process consuming a large amount of the incoming heat due to the large evaporation latent heat of water. Because of this, the temperature at the geopolymer/concrete interface in this region remained lower and around 100°C. At that time, a temperature difference of 1250°C was attained between the exposed and unexposed surface of the geopolymer material, creating thus a local thermal gradient of 25°C/mm. With the completion of 80 minutes, the temperature increased again until the end of the test. At the end of the test the temperature at the interface had a value of 280°C, which is 100°C lower than the RWS test requirements and the required temperature for maintaining the structural integrity of the concrete. The thermal gradient in the end of the test was estimated to 21.4°C/mm. The temperature in the back surface of the concrete slab did not exceed 70°C, which means that in the concrete slab the temperature had a range from 70°C – 280°C. Further as can be clearly observed from the photographs of Figure 4, the geopolymer material did not appear to show any creeping or mechanical damage except for change in colour which is attributed to the mineralogical transformations.

This great macroscopical behaviour after the test with no damage and no intense cracking suggests that there is no need to repair the geopolymer material after a fire incident. The concrete slab protected by the potassium based geopolymer did not appear to show any form of spalling and remained stable. The compressive strength achieved 28 days after the production of the material fluctuates around 8.7 MPa, where the thermal conductivity was measured equal to 0.16 W/m.K.

The comparison of the compressive strength and thermal conductivity of the fire resistant geopolymer (material II) with those available fire resistant materials on the market shows that the geopolymer's compressive strength has an intermediate value, since it is higher than PST system's compressive strength, similar to Fire Barrier 135 compressive strength, and lower to Meyco fireshield 1350 compressive strength. The thermal conductivity of the material was measured to be 0.16 W/m.K at 300°K which is substantially lower than the corresponding values of the commonly used structural building materials, such as bricks (0.7–1.3 W/m.K), clay tiles (0.5–0.7 W/m.K), normal Strength Concrete (1.5–2 W/m.K) and cement or gypsum plasters (0.2–0.8 W/m.K) and similar to the commercial available fire resistant materials.

3 CONCLUSIONS

As a conclusion, the sodium based geopolymer from FeNi slag is an appropriate material for passive fire protection systems in ordinary building applications, where cellulosic fire incidents are more widespread. The above test results proved that the potassium based geopolymer from FeNi slag can provide an effective heat flux barrier offering very successful passive fire protection to structural concrete and steel of concrete linings.

ACKNOWLEDGMENT

Greek Scholarship Foundation (IKY) Fellowships of Excellence for postagraduate studies in Greece. Siemens Program

REFERENCES

Alexander Khoury, Yngve Anderberg, 2000, Fire Safety Design, "Concrete spalling review". *Report submitted to the Swedish National Road Administrat*ion, 2000.

Davidovits, J., 1999. Geopolymer '99 2nd international conference, Saint-Quentin, France. 9–39.

Edwards, W.T., Gamble, W.L., 1986. Strength of grade 60 reinforcing bars after exposure to fire temperatures. *Journal of Concrete International*. 8, 17–19

Fletcher, I., Welch, S., Torero, J., Carvel, R., 2007. Usman A. Behaviour of concrete structures in fires. *Journal of Thermal Science.* 11, 37–52.

Sakkas K, Nomikos P, Sofianos A, Panias D (2013) Inorganic polymeric materials for passive fire protection of underground constructions. *Journal of Fire and Materials* 37: 140–150

ASTM C-109: Standard Test Method for Compressive Strength of Hydraulic Cement Mortars (Using 2-in. or [50-mm] Cube Specimens)

EN 771-1 Edition: 2011-06-15 Specification for masonry units, Part 1: Clay masonry units.



Taylor & Francis
Taylor & Francis Group
http://taylorandfrancis.com

Risk management



Taylor & Francis
Taylor & Francis Group
http://taylorandfrancis.com

Concrete Solutions – Grantham et al. (Eds.)
© 2016 Taylor & Francis Group, London, ISBN 978-1-138-03008-4

Application of carbon nanotubes in structural health monitoring of steel-reinforced concrete

P.H.P. Lagason, O.V.M. Antonio & S.A.P. Peñeda
Institute of Civil Engineering, University of the Philippines-Diliman, Quezon City, Philippines

ABSTRACT: Carbon Nanotubes (CNTs) can enhance the mechanical properties of cement composites and can monitor damage due to their piezo-resistive property. While previous studies were focused on the incorporation of CNTs solely into the cement matrix, this paper is aimed at investigating the self-sensing capability of CNTs in steel-reinforced concrete. The beam specimens were subjected simultaneously to a third-point load test, a four-point probe Test, and strain measurement. It was established that the CNT network exhibited conductivity inside the concrete and was able to translate applied stresses to varying resistance readings. An increasing trend in resistivity was found in concrete specimens while fluctuating readings were obtained from steel-reinforced specimens. This is due to the presence of the rebar which requires special detail. Furthermore, a significant increase of 13.6% and 40% in the flexural and compressive strengths, respectively, were observed. Thus, the application of CNTs in new concrete structures, as well as repaired structures, has a significant contribution in the advancement of smart buildings.

1 INTRODUCTION

1.1 *Background of the study*

"Earthquakes don't kill people, buildings do." (Hough and Jones, 2002) With the most recent magnitude 7.8 earthquake that hit Nepal on April 26, 2015, the violent typhoon Haiyan that devastated Tacloban, Philippines back in 2013, the high intensity earthquake that wrecked several structures in Bohol, Philippines and all other natural calamities that come by almost unexpectedly, it is vital that houses, buildings, and other infrastructures are designed or retrofitted to withstand different catastrophic events in order to ensure the safety of the general public. This is where Structural Health Monitoring comes in. The major objective of Structural Health Monitoring is to be able to evaluate the performance of a structure, and to detect possible damage and failure points at an early stage, mitigate risks, and avoid building collapse and other dangerous consequences. Assessment is done by observing structural responses through the use of modern technology in the field of Non-Destructive Testing (NDT). Two examples of NDT techniques are Ultrasonic Pulse Velocity (UPV) testing, and Schmidt Rebound Hammer (SRH) testing.

A more advanced approach in Structural Health Monitoring is the concept of Smart Building. A Smart Building is an ideal structure with self-sensing capabilities that enable its users to evaluate its structural performance directly and instantaneously. Generally, direct testing obtains results of higher accuracy than indirect testing which makes Smart Building an engaging innovation. This technology is made possible through the combination of different non-destructive testing techniques and the idea of a Structural Neural System. This system replicates the function of a human nervous system and its sensing capabilities into a structure. It utilizes smart materials that act as nerve system similar to that of a human body. An example of a smart material is the Carbon Nanotube (CNT).

The piezo-resistive property of a CNT-composite is proven and tested by previous researches. These studies have established optimal CNT content, water content, and other important parameters that highly affect the sensitivity of the CNT network to stress. They, however, focused on cementitious and/or mortar specimens only. Moreover, modern infrastructures are mainly composed of concrete and reinforced concrete structural elements – made of cement, aggregates and reinforcing steel bars. Because of the huge addition of the aggregates' weight and volume to the specimen, the previously determined proportions may not work effectively on a concrete specimen. Other than these mixing parameters, the inclusion of a steel reinforcing bar may notably vary the outcome of the resistance measurement since it is a relatively large conductor inside the concrete matrix. Currently, there are no available published studies on CNT-concrete and CNT-reinforced concrete composites.

The general objective of this research is to be able to apply the CNT-cementitious composite's stress-sensing capabilities to concrete and steel-reinforced concrete elements. Two specific objectives are identified in order to achieve this general objective. The first

is to be able to create a concrete and steel-reinforced concrete composite with carbon nanotubes dispersed in the concrete matrix. The second objective is to be able to determine the effect of the presence of the steel bar inside the matrix to the behavior and performance of the carbon nanotube network in relation to its stress-sensing capabilities.

The significance of the study is to extend the concept of stress-sensing CNT-cementitious composites to concrete and steel-reinforced concrete members in order to utilize these stress-sensing capabilities to different infrastructures such as houses, commercial buildings, etc. In this manner, a direct way of monitoring stress levels of concrete and reinforced concrete structures will be developed. This study also aims to advance the Smart Building Technology.

1.2 *Carbon nanotubes*

In their research paper, the University of Duluth (Yu and Kwon, 2012) described a carbon nanotube as an allotrope of carbon with a tubular structure that can be spread out. It has a very high aspect ratio which makes it an excellent network-generating material. It also has a very high Young's modulus of 1.8TPa which tremendously reduces breakage risk when incorporated into structures. The key property of the carbon nanotube is its piezo-resistivity. This property is the reason behind the linear variation of the CNT network's resistance to the stress applied onto it. Simply put, the change in the electrical resistance of the CNT network subjected to stress is proportional with the applied stress. Because of piezo-resistivity, it is now possible to obtain the stress applied at a certain region of a specimen with incorporated carbon nanotubes by measuring electrical resistances of the CNT.

To better visualize the application of carbon nanotubes in a structural element, consider a mortar mixture. By dispersing carbon nanotubes in this matrix, the mortar becomes a CNT-cementitious composite with the piezo-resistive property of the CNT. In theory, if this composite is subjected to stress, the carbon nanotubes inside vary in terms of interconnection with the applied stress, thus, reducing the resistances of the CNT network inside the mortar. By measuring the change in the electrical resistance at a certain region of the composite, the stress level will be known at that point of the composite. This is particularly effective in cementitious composites since cement is a non-conducting material.

1.3 *Scope and limitations*

The study of the application of carbon nanotubes in the field of Structural Health Monitoring is still relatively new, which accounts for the limited amount of related literature available. Furthermore, published studies focused mainly on cementitious composites only. It is still unknown how the carbon nanotubes will be used with concrete composites and how the carbon nanotube network will react with the presence of a huge conductor, say, a steel reinforcing bar, in terms of resistivity. Because of this, the research will be limited to the proven and tested parameters from previous studies of CNT-cementitious composites that optimize the performance of the carbon nanotube in stress-sensing. Some of these parameters include the CNT content, water content, CNT dispersion method, and resistivity measurement technique.

2 METHODOLOGY

The study was based on the University of Duluth's research (Yu and Kwon, 2012) about carbon nanotube-based self-sensing concrete utilized in pavement structural health monitoring. Fundamentally, stress sensors were created by taking advantage of the piezo-resistive property of the carbon nanotubes. These were mixed into a cement matrix which resulted in a carbon nanotube-cement composite that was embedded on the pavement later on. The composite was subjected to compressive loads by having cars pass over it. The changes in resistivity were measured and translated into stress values by correlating them with the actual values of the applied loadings. In this research, the stress-sensing capabilities of the carbon nanotubes were be applied in concrete structural health monitoring. Concrete specimens with carbon nanotubes were prepared and then subjected to compressive loads through the use of a universal testing machine (UTM). The changes in resistivity were measured together with the actual strains in order to investigate the stress-sensing capabilities of carbon nanotubes in concrete. Furthermore, the behavior of the carbon nanotube network in a steel-reinforced concrete was examined. The testing procedure was divided into four main parts: (1) preparation of specimens, (2) testing setup, (3) actual testing, and (4) data gathering.

2.1 *Preparation of specimens*

The research required the production of concrete and steel-reinforced concrete composites with mixed carbon nanotubes. These were prepared by following several standardized procedures particularly in concrete mixing and carbon nanotube dispersion: the mixing proportions were calculated based on ACI 211.1-91; and the CNT concentration was set to 0.1% by mass of cement since it is the optimum concentration in creating cementitious composites with highly sensitive stress sensors (Yu and Kwon, 2012).

The carbon nanotubes used were obtained from Timesnano, a professional carbon nanotube manufacturer based in China. These are multi-walled carbon nanotubes (MWCNT) with a maximum outer diameter of 8 nm, a length of 10-30 μm, and a purity of 95% or higher. The acquired carbon nanotubes need to undergo a dispersion process in order to minimize agglomeration before they can be used. The dispersion method chosen for this experiment was through

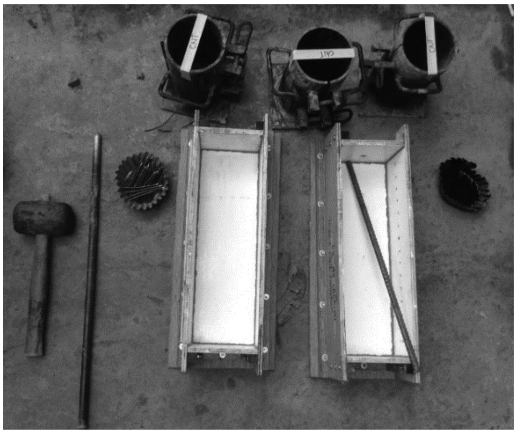

Figure 1. Moulds and other concrete mixing tools.

the addition of a surfactant, a process adapted from the method recommended by Kim et al (2014).

The study consisted of three trials that required two beams and three cylinders each (Figure 1). The cylinders were 20.32 cm (8 in.)tall and had a diameter of 10.16 cm (4 in.). A total of nine cylinders were prepared, three for each trial. As for the beams, a total of six beams were prepared. The dimensions of the beams were 12.7 cm (5 in.) (W) by 12.7 cm (5 in.) (H) by 40.64 cm (16 in.) (L). The beams were modified to suit the requirement of the resistivity testing that will be discussed later on. Type 10 solid copper wires were probed on one surface of every beam that served as electrodes for resistivity readings. A total of 15 wires with a clear spacing of 2.54 cm (1 in.) were embedded on each beam. The probes used were 7.62 cm (3 in.) in length and were embedded at a distance of 4.5 cm from the face of the beam (Figure 2).

Moisture is a key element that directly affects the conductivity of the specimen. For this study, the beams and cylinders were oven-dried to eliminate the effects of moisture. It is important to note that in reality, structures contain moisture, thus a detailed study should be done to take into account the effects on the conductivity/resistivity of the test specimens.

The beams were also categorized into two: concrete beams and steel-reinforced concrete (RC) beams. A 12-mm reinforcing bar was embedded in the three RC beams.

2.2 *Testing set-up*

Several testing set-ups were necessary to thoroughly investigate the behavior of carbon nanotubes in concrete and steel-reinforced concrete structures. The material properties of the concrete mix were obtained by subjecting the cylinders to compressive testing. The loadings were applied to the beams through a standard beam flexure test. The stress sensitivity of the carbon nanotube network was examined through a resistivity test. The soundness of the results gathered from the



Figure 2. Trial 1 beam and cylinder specimens.

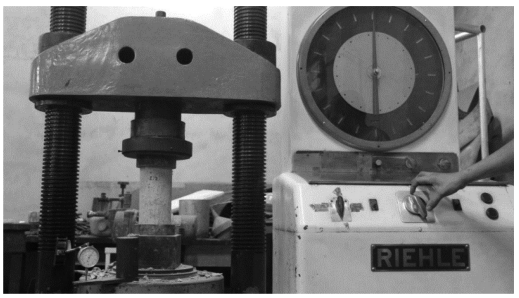

Figure 3. Compressive Strength Test set-up with analog strain gauge.

resistivity test was evaluated by comparing the resistance change patterns with actual strain measurements.

2.2.1 *Compressive test*

A compressive test based on ASTM C140/C140-M – 14a was applied on the concrete cylinders to obtain the actual compressive strength of the concrete mix. Moreover, the strains of each cylinder were collected by using an analog strain gauge on the universal testing machine (UTM) shown in Figure 3.

2.2.2 *Third-point load test*

The flexure test used on the beams was based on ASTM International's Standard Test Method for Flexural Strength of Concrete (Using Simple Beam with Third-Point Loading). This test basically divides the beam into three parts and applies the load on the middle-third segment.

The significance of the Third-Point Load test is to enlarge the area of application of the load, thus increasing the possibility of capturing the critical plane.



Figure 4. Third-Point Load Test set-up utilizing the UTM with additional equipment.



Figure 5. Four-Point Probe Test set-up.

This test utilized the universal testing machine (UTM) with an attached equipment to apply the load on the middle-third segment of the bean as seen in Figure 4.

2.2.3 *Four-point probe test*

The resistivity across the concrete beams was measured through the Four-Point Probe test (Figure 5). This method allows for a more accurate resistivity measurement of highly resistant specimens as compared to the typical two-point probe test. It also neglects the effect of polarity more effectively compared to the two-point probe test according to Konsta-Gdoutos, M. & Aza, C. (2014).

A power supply that is capable of generating 30 V was used together with two digital multimeters for the testing set-up. One of the multimeters was connected to the power supply for current readings. The other multimeter was used to measure the voltage between two probes in order to obtain the resistivity of that segment.

2.2.4 *Strain measurement*

Strain measurements were collected to validate the stress-sensing capability of the carbon nanotube network inside the concrete structures. Actual strain values of the specimens were obtained through the use of strain gauges.

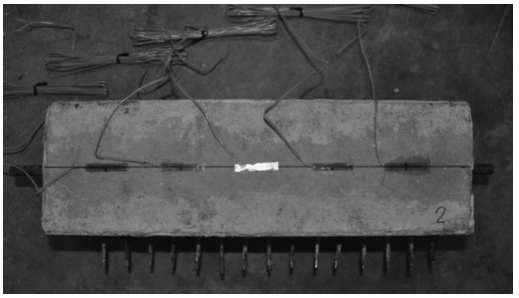

Figure 6. Bottom of the beam with attached strain gauges.

Using the TML Strain Gauge Type PFL-30-11-3LT, five (5) strain gauges were attached at the bottom of every beam (Figure 6). These strain gauges were placed at the centerline, directly below the loading points, and at the points between the loading and the edge of the beam. The locations were strategically chosen to better capture the whole deflection of the specimen. The strains were automatically recorded using an NI data logger (SCXI 1520 with 1314T RJ50 Module).

2.3 *Method of analysis*

2.3.1 *Resistivity measurements*

The resistivity across a segment in the specimen is obtained using the equation $\rho = (R\ S)/L$, where ρ = resistivity of the segment (kΩ.cm); R = resistance obtained by dividing the measured voltage by the current (kΩ); S = cross-section area of the specimen (cm^2); and L = distance between the two probes which is kept constant at 2.54 cm.

The obtained resistivity values were plotted against their corresponding segment to have an overview of the electrical characteristic of the carbon nanotube-concrete composite. They were also plotted against the applied load to observe the effect of the applied load to the resistances. Moreover, each segment was examined closely. The resistivity of each segment was plotted against the applied load to study its behavior.

2.3.2 *Strains*

The strains detected by the strain gauges were presented in graphs to be able to observe trends and establish relationships with other data. Each strain gauge had a segment counterpart that would be used to further analyze the obtained resistivity trends from the four-point probe test.

3 RESULTS AND DISCUSSION

3.1 *Carbon nanotube network conductivity*

In theory, concrete is highly resistive which prevents current from flowing through it. However, a successful dispersion of carbon nanotubes into a concrete matrix will result to a conductive composite through the formation of a carbon nanotube network. This study

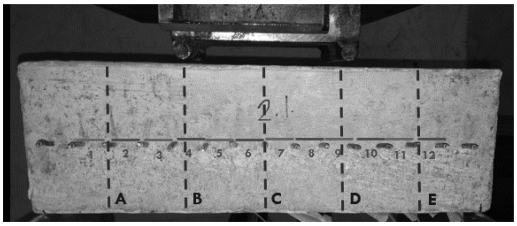

Figure 7. Location of segments and strain gauges.

demonstrated that no current passes through concrete by subjecting an ordinary concrete beam specimen to four-point probe testing. A minimal value of voltage was obtained but the current reading remained 0.0 μA.

The same resistivity measurement method was used on the concrete specimens with carbon nanotubes and yielded different results. With this, it is established that the carbon nanotube network effectively spread across the beam specimens and created a relatively conductive concrete composite.

3.2 *Carbon nanotube in concrete beams*

Each beam was divided into 12 segments for the resistivity measurement. Figure 7 shows the placing of each segment and the relative location of the applied loads, strain gauges labeled from A to E, and the centerline of the beam. The labeling convention used is X.Y., where X is the trial number, and Y is either 1 for concrete beam, or 2 for reinforced beam.

Through the probes embedded at each beam, currents and voltages passing through the specimen were obtained. It is important to note that the currents obtained were steady at 0.7 μA. The resistivities were computed and plotted against the corresponding segments.

The acquired graphs did not reflect the theoretical all-increasing trend for each segment as expected from previous studies. Furthermore, by observing the results from the three trials, they all formed graphs with similar peaks and trends. The highest amplitude of each graph was found between Segment 6 and 7.

Looking closely at Segment 7 of each beam showed that all of the beams had the same increasing trend at the said segment. This trend is similar to the trend of the applied load. This result is in line with the piezoresistive property of the carbon nanotube, although not as linear as expected. A strong point why the resistivities obtained were not all in accordance with the previous studies is that, the test used in this study is a flexure test which include both compressive and tensile stresses while the previous experiments only performed compressive tests.

3.3 *Carbon nanotube in steel-reinforced concrete beams*

The resistivity measurements in reinforced concrete are problematic as compared to the plain concrete beam. It initially detected alternating current (AC) readings as opposed to the required direct current (DC) readings. The graph of Beam 2.2 summarizes the AC Voltage and Current measurements.

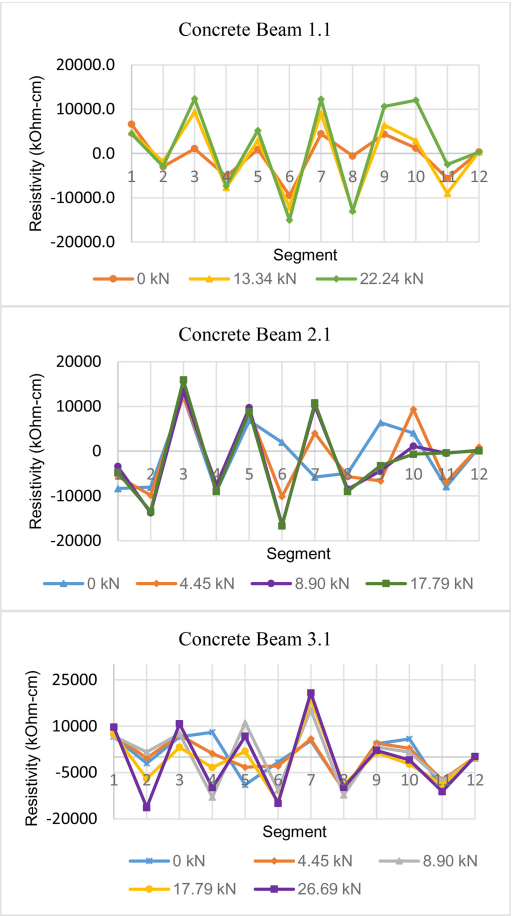

Figure 8. Segment versus Resistivity graph of concrete beams.

The cause of the alternating current is the presence of the steel reinforcing bar which acts as a capacitor in the specimen. A capacitor basically stores up energy and must be filled up first before a steady current can be established. With this, the other reinforced concrete specimens were charged up by connecting the power supply directly to the rebar before testing.

By charging the rebar, a DC reading for each segment was obtained but inconsistently. Once in a while the rebar has to be recharged and it took time before the voltage was stabilized. The graphs of the steel-reinforced concrete beam specimens did not exhibit the same trend as found in the concrete beam specimens. Moreover, the resistivity values at each segment fluctuated such that, their average value is close to zero. This is due to the non-constant charging of the rebar which directly affected the currents and voltages across the beam.

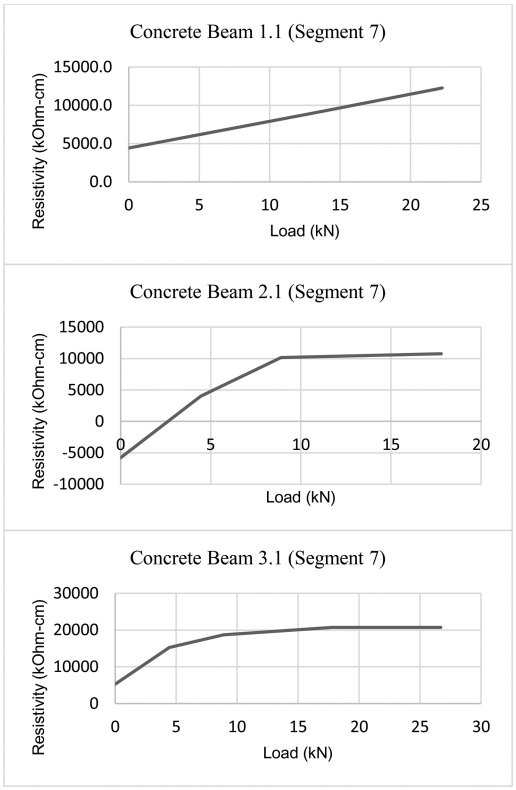

Figure 9. Resistivity versus Load graph of Segment 7 of concrete beams.

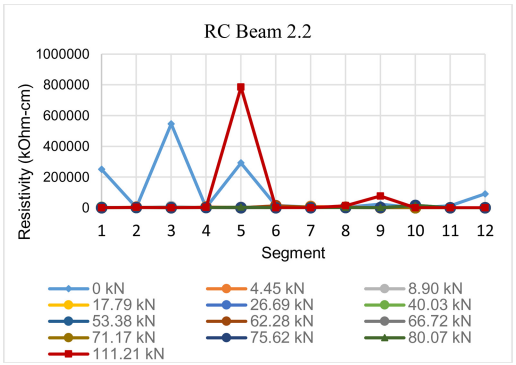

Figure 10. Resistivity versus Segment graph of Trial 2 SteelReinforced Concrete Beam.

3.4 *Strength tests of the specimens*

According to the study of the University of Duluth, carbon nanotubes also cause significant increase in the strengths of the cementitious composites. The compressive strength was increased by 19% and the flexural strength increased by 25% with the addition of 0.5% by weight cement of carbon nanotube. For this research, the target compressive strength calculated was 32.94 MPa. A reinforced beam with the same concrete mix proportions was also tested and

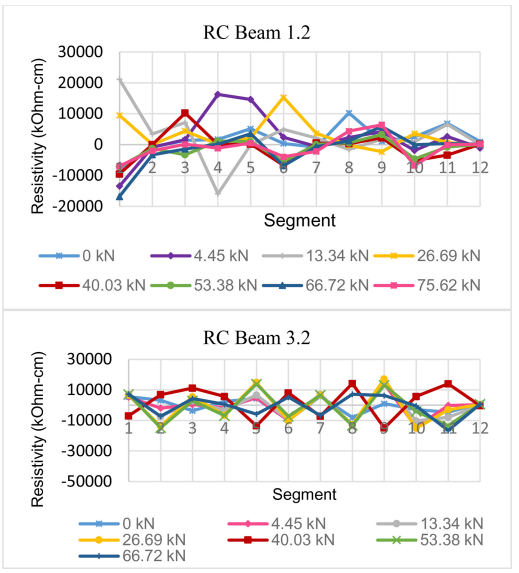

Figure 11. Resistivity versus Segment graph of Trials 1 and 3 steel-reinforced concrete beams.

Table 1. Compressive Strength Test results.

Specimen	Load (kN)	Stress (MPa)
Cylinder 1.1*	358.08	44.17
Cylinder 1.2	467.06	57.61
Cylinder 1.3*	333.62	41.15
Cylinder 2.1	469.29	57.88
Cylinder 2.2	469.29	57.88
Cylinder 2.3	433.70	53.50
Cylinder 3.1*	344.74	42.52
Cylinder 3.2	420.36	50.05
Cylinder 3.3*	358.08	44.17

* Specimens with honeycomb.

obtained a flexural strength of 3.86 MPa. The beams and cylinders were tested accordingly and obtained the following results. The labeling convention used for cylinder specimens is X.Y., where X is the trial number, and Y corresponds for each cylinder per trial.

The concrete mix with carbon nanotubes had a minimum increase of 40% in compressive strength and 13.6% in flexural strength.

3.5 *Stress-strain diagram of concrete cylinders*

During the compression tests of the cylinders, strains were simultaneously measured using the analog strain gauge. The analog strain gauge, together with the universal testing (UTM) dial were video recorded to sync the load applied and the corresponding strain. The strains per applied load were approximated based on the video. It is significant to note that the manner of

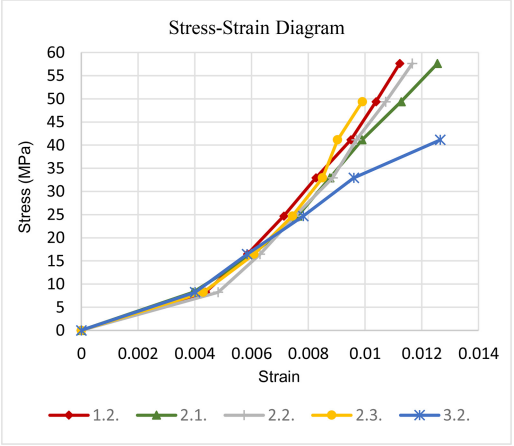

Figure 12. Combined Stress-Strain diagram of cylinders.

collecting strain values was prone to several mechanical and human errors which result to approximate – and not highly accurate – strain values. The stress-strain diagrams of all trials excluding the specimens with honeycombing were combined into one graph as presented in Figure 12.

It could be observed from Figure 12 that the strain is linear with stress up to 0.004 strain. This is a distinct result in comparison to the accepted maximum elastic concrete limit of 0.003 strain. The ultimate strains corresponding to the ultimate strengths of the concrete cylinders fall between 0.01 to 0.012 strains.

4 CONCLUSIONS

The stress-sensing capability of carbon nanotubes can perhaps be extended to concrete and steel-reinforced concrete used in actual structures. It has been demonstrated that the carbon nanotube network was conductive across the concrete matrix. The applied stress on the specimens were translated into changes in resistivity through the carbon nanotubes. Moreover, the change in resistivity of the conductive network had an increasing trend similar to the applied load. The produced carbon nanotube-concrete and steel-reinforced concrete composites had measurable sensors. A linear variation of the resistivity to the stress, however, was not obtained. Furthermore, special detail must be given to the steel-reinforced concrete because of the presence of the steel bar. It acts as a capacitor which stores up energy and blocks the direct currents resulting in alternating current readings. To obtain DC readings, the rebar should initially be charged up. It is also important to note the significant 13.6% and 40% increase in flexural and compressive strength, minimum. Accurate concrete stress-sensor can be achieved by proper adjustments and handling of the carbon nanotubes and specimens. Overall, the objectives were achieved and the research initiated the application of the carbon nanotubes to concrete and steel-reinforced concrete.

REFERENCES

American Concrete Institute (2002). *Standard Practice for Selecting Proportions for Normal, Heavyweight, and Mass Concrete* (ACI 211.1-91).

American Society for Testing and Materials International (2014). *Standard Test Methods for Sampling and Testing Concrete Masonry Units and Related Units* (C140/C140-M – 14a). Retrieved from http://www.astm.org.

Coppola, L., Buoso, A. & Corazza, F. (2011). *Electrical Properties of Carbon Nanotubes Cement Composites for Monitoring Stress Conditions in Concrete Structures.* AMM, 82, pp. 118–123.

Kim, H., Nam, I. & Lee, H. (2014). *Enhanced effect of carbon nanotube on mechanical and electrical properties of cement composites by incorporation of silica fume.* Composite Structures, 107, pp. 60–69.

Konsta-Gdoutos, M. & Aza, C. (2014). *Self-sensing carbon nanotube (CNT) and nanofiber (CNF) cementitious composites for real time damage assessment in smart structures.* Cement and Concrete Composites, 53, pp. 162–169.

Manzur, T. &Yazdani, N. (2014). *Optimum mix ratio for Carbon Nanotubes in cement mortar.* KSCE J Civ Eng.

Meraj, T., Pandey, A. & Rao, B. (2014). *Flexural behaviour of latex modified steel fiber reinforced concrete.* Indian Journal of Engineering & Materials Sciences, 21, pp. 219–226.

Park, I., Kim, H. & Lee, H. (2014). *Preliminary study on piezo-resistivity of CNT/cement mortar composites with different mix proportion.* In: 93rd Annual Meeting of the Transportation Research Board. Washington, D. C., pp. 1–9.

Rehman, A., Abbas, S., Ammad, H., Badshah, A., Ali, Z. & Anjum, D. (2013). *A facile and novel approach towards carboxylic acid functionalization of multiwalled carbon nanotubes and efficient water dispersion.* Materials Letters, 108, pp. 253–256.

Rainieri, C., Fabbrocino, G., Song, Y. & Shanov, V. (2011). *CNT Composites for SHM.* In: Smart Materials, Structures and NDT in Aerospace. pp. 1–10.

Sherbini, K. & Krawczyk, R. (2004). *Overview of Intelligent Architecture.* In: ASCAAD International Conference. pp. 137–152.

Schuetze, A., Lewis, W., Brown, C. & Geerts, W. (2004). *A laboratory on the four-point probe technique.* American Journal of Physics, 72(2), p. 149.

Vemuru, S., Wahi, R., Nagarajaiah, S. & Ajayan, P. (2009). *Strain sensing using a multiwalled carbon nanotube film.* The Journal of Strain Analysis for Engineering Design, 44(7), pp. 555–562.

Yu, X. & Kwon, E. (2012). *Carbon Nanotube Based Self-sensing Concrete for Pavement Structural Health Monitoring.* U.S. Department of Transportation Federal Highway Administration, pp. 1–27.

Yu, X., Rajamani, R., Stelson, K. & Cui, T. (2008). *Fabrication of carbon nanotube based transparent conductive thin films using layer-by-layer technology.* Surface and Coatings Technology, 202(10), pp. 2002–2007.



Taylor & Francis
Taylor & Francis Group
http://taylorandfrancis.com

Service life modelling



Taylor & Francis
Taylor & Francis Group
http://taylorandfrancis.com

Concrete Solutions – Grantham et al. (Eds.)
© 2016 Taylor & Francis Group, London, ISBN 978-1-138-03008-4

Chloride threshold values for corrosion in concrete – a myth?

U.M. Angst
Institute for Building Materials (IfB), ETH Zurich, Switzerland
Swiss Society for Corrosion Protection (SGK), Zurich, Switzerland

B. Elsener
Institute for Building Materials (IfB), ETH Zurich, Switzerland

ABSTRACT: This paper reviews the established conceptual approach of predicting initiation of chloride induced corrosion of reinforcing steel in concrete. The low predictive power of the current approach is illustrated with help of recent field data for the chloride threshold value. Limitations and particular gaps of knowledge are highlighted, and issues urgently needing further research are identified. This includes the production process and the resulting microstructure of the reinforcing steel. Most of our practical long-term experience from real structures relates to systems where cold worked steel and Portland cement were used. During the last few decades, however, a transition to thermomechanically strengthened reinforcing steels and to blended cements occurred. There is indication that this drastically affects the corrosion behaviour

1 INTRODUCTION

In industrialized countries, corrosion of our ageing infrastructure causes high costs to society (Koch et al. 2002). This can be illustrated by Fig. 1 that compares the direct annual costs arising from infrastructure corrosion in the United States of America to some other issues with large economic impact.

Given the societal relevance of medical issues, extensive research efforts were undertaken particularly during the second half of the 20th century and onwards. Thanks to significant advances made through research, it was for instance possible to identify the major risk factors for cardiovascular diseases and to develop evidence-based medical therapies. As a result, the mortality from coronary heart disease has, in the U.S., decreased substantially over the last decades, i.e. approximately by a factor of two (Ford et al. 2007).

Despite the societal relevance of infrastructure corrosion (Fig. 1), particularly corrosion of steel in concrete, relatively little progress has been made over the last decades concerning fundamental understanding about steel corrosion in concrete. Many essential questions remain still open and forecasting the corrosion performance of reinforced concrete structures in their actual exposure environments and over long time spans (e.g. 50–100 years) is still a big challenge for science and engineering.

Roughly 20–30% of the "infrastructure corrosion" costs in Fig. 1 are related to corrosion of reinforced and prestressed concrete (Koch et al. 2002). These structures are exposed to chlorides, e.g. structures in marine environments or structures exposed to deicing road salts. An analysis of degradation cases has revealed

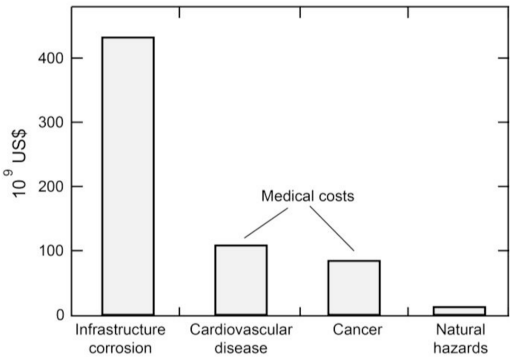

Figure 1. Comparison of the direct annual costs arising from se-lected major issues known to greatly impact the economy of our societies (data from the U.S., from www.corrosion.org, www.cancer.org, and www.heart.org; ca. for the first decade af-ter the turn of the millennium). The costs displayed for infrastruc-ture corrosion include infrastructures such as bridges, airport, gas and oil pipelines, and drinking water reservoirs and utilities.

that chloride-induced corrosion is one of the most important causes for the premature degradation of reinforced and prestressed concrete structures (British Cement Association 1997).

This paper reviews the state-of-the-field and summarizes the established approach of mainstream research that essentially reduces the issue of corrosion initiation in concrete to a mere question of chloride concentrations. Limitations and particular gaps of knowledge are highlighted, and issues urgently needing further research are identified. With help of

selected examples of both well-known facts and recent insight, the concept of the *critical chloride content* (or *chloride threshold value*) is critically discussed.

2 THE CONCEPTUAL APPROACH OF PREDICTING CORROSION INITIATION IN CONCRETE

All efforts made to predict corrosion initiation in concrete are based on the widespread belief that initiation of corrosion is controlled by the concentration of chlorides in the concrete and by the properties of the concrete. This led to the conceptual approach of modeling chloride penetration through concrete in order to predict the chloride concentration over time at the depth of the embedded reinforcing steel and compare it to a threshold value. Corrosion initiation occurs as soon as the chloride concentration at the steel, c_{Cl^-}, exceeds the chloride threshold value:

$$c_{Cl^-} > \text{chloride threshold} \quad (1)$$

This approach of durability design is very similar to the approach of structural design where the maximum stresses arising in a structural member are predicted and compared to the material's strength.

While there is no doubt that mechanical failure can be well described by comparing stresses and strength, it is still unclear if the chloride concentration in the concrete is the best (and only) parameter describing corrosion initiation.

2.1 *Advances in mass-transport modeling*

Over the last decades, extensive research efforts were made to predict transport of chloride through concrete (Tang et al. 2012). These efforts included laborious long-term field experiments, e.g. (Nilsson et al. 1997), committee work (e.g. (RILEM TC 178-TMC)) and led to specific recommendations and model codes to be used by consulting engineers and scientists (DuraCrete 2000, fib 2006). A number of model approaches of varying complexity have been established, ranging from relatively empirical approaches based on Fick's second law of diffusion and the well-known "error-function solution" to more mechanistic mass transport models such as models based on Poisson-Nernst-Planck equations (Samson et al. 1999, Tang et al. 2012, Jensen et al. 2014). However, independent of the underlying equations, predicting chloride penetration through the concrete cover requires characterizing the concrete by means of laboratory testing or by picking tabulated values depending on cement type, mix proportions, age, etc. in order to get the required input parameters for the modeling. Depending on the model approach these may be chloride diffusion/migration coefficients, ageing factors, formation factors, etc. To sum up, the current state-of-the-art permits predicting chloride transport through concrete with reasonable accuracy – at least for some types of concrete and for some exposure conditions.

2.2 *The unanswered question of the chloride threshold for corrosion initiation*

While the current state-of-the-art permits the prediction of chloride transport as a function of concrete mix proportions and exposure conditions, this is not possible for the chloride threshold value for corrosion.

For instance, there is agreement from a number of studies undertaken in alkaline solutions (simulating the concrete pore solution) that the pH plays a major role, i.e. that with decreasing solution pH, the chloride threshold value decreases, e.g. (Hausmann 1967, Gouda 1970). At the same time, it is well known that blended cements or the use of supplementary cementitious materials generally leads to lower concrete pore solution pH values than with Portland cement. Nevertheless, there is no clear literature evidence that cementitious binders leading to lower concrete pore solution pH than Portland cement also have lower chloride threshold values. The results from studies in mortar or concrete regarding the influence of supplementary cementitious materials on the chloride threshold for corrosion initiation are contradictory (Angst et al. 2009). The current state-of-the-art does not permit devising chloride threshold values as a function of cement type.

Even for traditional Portland cement, it was not possible to find a unique chloride threshold value. In a recent review more than 50 publications reporting chloride threshold values were evaluated (Angst et al. 2009). If only laboratory studies dealing with Portland cement are considered, literature chloride threshold values span a range from almost 0 to more than 3% chloride by mass of cement. The variability in data from field exposure sites or from measurements on real structures, on the other hand, is somewhat lower. Different studies published in the 1970s and 1980s reported chloride threshold values in the range 0.1 to 2% chloride by weight of cement (Stratfull et al. 1975, Vassie 1984, Treadaway et al. 1989).

This large scatter in literature data can be explained by the vast diversity in test setups and experimental procedures used to determine chloride threshold values and the unfortunate fact that some of the test conditions have a more dominant influence on the resulting chloride threshold value than the parameters under test (Angst et al. 2009). This became also apparent from the work of RILEM technical committee 235-CTC "Corrosion initiating chloride threshold concentrations in concrete", where a round robin test revealed that issues such as steel surface preparation and concrete specimen pre-conditioning strongly affect the results (RILEM TC 235-CTC).

Moreover, also experimental uncertainties and limited measurement precision contribute to the large variability in literature chloride threshold values. For instance, it is well known that the analysis of the chloride content in the concrete – which is one of the numerous steps in determining the chloride threshold value – can provide significantly different results, depending on the chosen procedure. This is apparent from a number of national and international

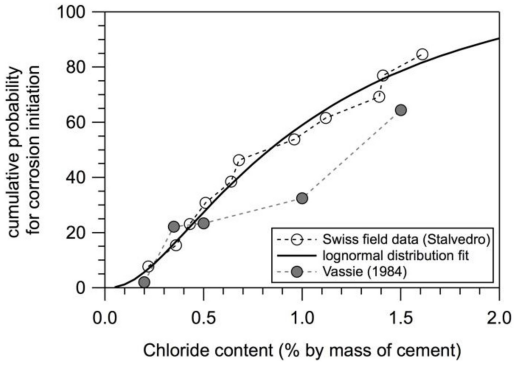

Figure 2. Statistical distribution of field data for the chloride threshold value and lognormal fit to the recent data from the Swiss Stalvedro tunnel (see text for explanations).

round-robin tests, e.g. (Castellote and Andrade 2001).

An additional reason for the large literature scatter in chloride threshold values is the stochastic nature inherent to initiation of pitting corrosion. It is well known that initiation of localized corrosion is governed by local differences at the steel/concrete interface. Examples in this regard are metallurgical features (Li and Sagüés 2004) or voids and gaps in the concrete (Reddy 2001, Soylev and Francois 2003).

Obviously, if local "weaknesses" at the steel surface act as initiation sites, the absence or presence of these within a studied specimen is decisive in determining the chloride threshold value. The smaller the studied specimen, the lower becomes the probability for the presence of such sites of a locally high susceptibility to chloride-induced corrosion initiation (Li and Sagüés 2004). This results in a size effect: On the one hand, the average chloride threshold value of small specimens increases with decreasing specimen size; on the other hand, also the scatter in chloride threshold values increases with decreasing specimen size. Theoretical considerations have indicated that the relatively small dimensions of specimens typically used in laboratory studies are an important reason contributing to the large variability in literature results (Angst et al. 2011a).

3 RECENT INSIGHT

3.1 *Field results from Switzerland*

In a recent study by the Institute for Building Materials at ETH Zurich, the "Stalvedro" tunnel in the Swiss Alps (constructed in the 1970s) was investigated. Based on condition assessment by means of half-cell potential mapping and other non-destructive as well as destructive testing methods, an area was selected at the tunnel ceiling where the reinforcing steel was still in passive condition. Concrete cores (diameter 150 mm) were drilled from within a sampling area of 1–2 m^2. Each concrete core contained a segment of not yet corroding reinforcing steel, passing approximately through the center of the core.

The concrete of the investigated areas of the structure had a chloride resistance of 1.7×10^{-12} m^2/s (migration test) and a compressive strength of 72 MPa. Thin section analyses revealed that the aggregates were primarily silicates, and that Portland cement was used. The carbonation depth was variable, but in the range of a few millimeters, thus far from the reinforcing steel (located at a cover depth of generally more than 50 mm).

The drilled cores were then transferred to the laboratory. Sample preparation included mounting a cable connection to the rebars, a procedure to prevent corrosion initiation at the cut faces of the rebar segments (treating the rebar ends with a dense mortar), and coating of the lateral sides of the cores with an epoxy-resin. The specimens were then exposed to a chloride solution in the laboratory, with stepwise increasing chloride concentrations. Detection of corrosion initiation was based on monitoring the steel potential and on a criterion of a drop in potential as suggested in previous work (RILEM TC 235-CTC , Angst et al. 2011b).

Upon corrosion initiation, the chloride content in the concrete at the steel depth was determined, which is considered the actual chloride threshold value. For a more detailed description of the experimental procedure refer to (Angst et al. in press).

The main advantage of this approach lies in testing real specimens taken from real structures (mature concrete, realistic conditions at the steel/concrete interface, etc.) rather than laboratory made specimens ("labcrete", young concrete, etc.). In combination with the accuracy of laboratory measurement methods for detecting corrosion initiation, the chloride threshold value of each sample can be reliably determined (more accurately than onsite).

The results are shown in Figure 2 together with the well-known field data from bridge structures in the UK reported by Vassie (1984). Apparently, these two data sets are similar, suggesting that steel may be corroding at chloride contents ranging from 0.2% chloride by weight of cement to more than 1.5% chloride by weight of cement. Even at relatively high chloride contents such as 1% chloride by cement weight, these results indicate a probability for corrosion not much higher than 50%.

The data from the Swiss Stalvedro tunnel can be fitted with a lognormal distribution. The parameters of the lognormal distribution are $\lambda = -0.90$ and $\varepsilon = 0.78$. The first two moments of the measured rather than the lognormally transformed data are: $\mu = 0.55$ and $\sigma = 0.50$ (% chloride by cement weight).

Note that the results from the Swiss road tunnel were obtained on samples taken from within a small concrete surface area (<2 m^2). It may thus be assumed that the reinforcing steel and the concrete of all tested cores stem from the same batches, that the concrete was

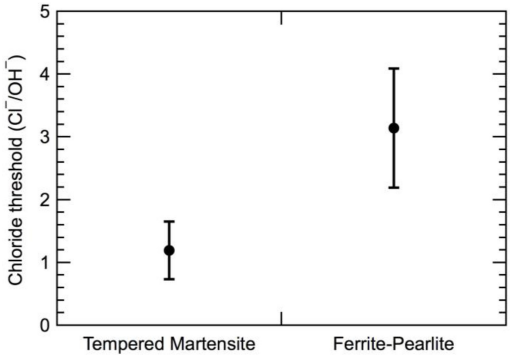

Figure 3. Chloride threshold values for reinforcing steel bars with tempered martensite and ferrite-pearlite microstructures at the surface, resulting from thermomechanical and cold work strengthening, respectively. (Mean and standard deviation) (Angst and Elsener 2015).

placed and compacted by the same workers, and subjected to identical curing conditions. This is in contrast to the data reported by Vassie (1984) that was obtained from a number of different bridges. Despite this, the results from the UK bridges and from the small area in the Swiss road tunnel are comparable.

Additionally, these results confirm the well-known fact that the chloride threshold cannot be expressed by a unique fixed value, but must be described with a statistical distribution. It is important to recognize that this applies even for the case of one small area within one structure.

3.2 *The importance of the steel microstructure*

In a recent laboratory investigation at the Institute for Building Materials at ETH Zurich, the susceptibility to chloride-induced corrosion of reinforcing steel bars (diameter 12 mm) purchased in different countries was tested. The rebars originated from different European countries and from China; in total ten different series were studied.

From selected samples of each series, sections were cut and metallographically analyzed in order to determine the steel microstructure. As expected, the majority of the rebars exhibited a tempered martensite surface layer, which is obtained during a thermomechanical strengthening process such as "Tempcore". On the other hand, two series exhibited a ferrite-pearlite microstructure typical for cold-work hardened steel.

The rebars were tested in their as-received condition. The bar ends were first coated with a duplex corrosion-protection system (a thin layer of polymer modified cement based mortar on the steel, coated with an epoxy resin). The exposed length of the rebar was 6 . The rebars were then exposed in saturated calcium hydroxide solution, initially chloride free, where the chloride concentration was stepwise increased over time. The potential of the rebars was monitored and detection of corrosion initiation was based on a criterion related to a drop in the potential, similar to the experiments described in section 3.1. For a more detailed description of the materials and the experimental procedure, please refer to (Angst and Elsener 2015).

The results are summarized in Fig. 3, which clearly indicates that the process with which these rebars were produced, and most likely their final surface microstructure, strongly affect the tolerable chloride concentration in alkaline solution. Those rebars that underwent cold work strengthening seem to tolerate considerably higher chloride concentrations – by a factor of 2 to 4 – than the rebars with a tempered martensitic microstructure at the surface.

Interestingly, thermomechanical strengthening by processes such as "Tempcore" were developed and introduced in the 1970s–1980s. Up to this time, reinforcing steel was cold worked. This means that virtually all infrastructure reaching a critical age and exhibiting a risk for corrosion damage was built with a different type of reinforcing steel (ferrite-pearlite microstructure) than the majority of younger structures, built after the 1980s, where steel with a tempered martensite surface layer was used. Based on the results summarized here, this may strongly affect the corrosion behavior of these structures.

3.3 *Implications for service life modeling*

The results presented in section 3.1 indicate that the chloride concentration at which corrosion in concrete initiates *in reality* spans over a large range – even in pure Portland cement systems – such as from 0.2% to 2% chloride by cement weight. This large variability inherent to the chloride threshold value has important implications for modelling the time to corrosion initiation according to the established conceptual approach sketched in section 2.

This may be illustrated with a simple chloride ingress model, such as those based on Fick's second law of diffusion, e.g. (DuraCrete 2000, fib 2006). Here, the chloride concentration in the concrete at depth x and at time t, $c(x,t)$, is expressed as follows:

$$c(x,t) = c_o + (c_s - c_o)\left\{1 - erf\frac{x}{2\sqrt{D_{app}\cdot t}}\right\} \qquad (2)$$

The surface chloride concentration c_s is assumed at 3% chloride by weight of cement, the initial chloride content c_o in the concrete is considered negligible, and the apparent diffusion coefficient D_{app} is assumed, independent of time, at 1×10^{-12} m^2/s. Based on this, $c(x,t)$ can be predicted at a certain cover depth over time and together with the statistical distribution of the chloride threshold value shown in Figure 2 (field results from Swiss highway tunnel "Stalvedro"), the probability for corrosion initiation over time can be calculated (Fig. 4). Note that here a simple deterministic model was used, i.e. any variability in the input parameters such as the chloride diffusion coefficient,

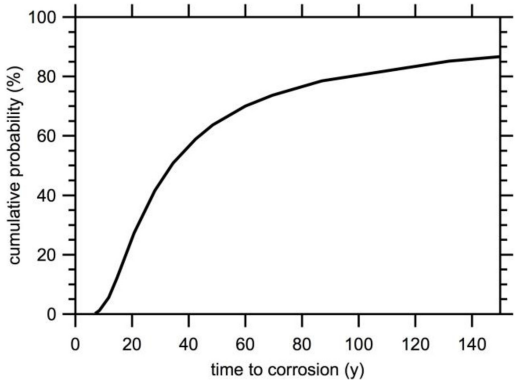

Figure 4. Example of predicted time to corrosion for a cover depth of 50 mm. The plot shows the probability for corrosion in-itiation as a function of years passed, assuming a lognormal dis-tribution for the chloride threshold according to the field data from the Swiss Stalvedro tunnel, presented in Figure 2.

the surface chloride concentration, or the cover depth was neglected.

Nevertheless, Fig. 4 clearly illustrates the large uncertainties inherent to state-of-the-art service life modeling. From the perspective of a consulting engineer or an owner it may be questionable how valuable a prognosis stating that corrosion will initiate sometime between 10 and more than 100 years after construction is and how such a prognosis can assist in decision taking. There is no doubt that the established approach of forecasting the time to corrosion by means of modeling chloride transport and utilizing a chloride threshold has a weak predictive power.

It is important to note that this can hardly be improved by refining chloride transport models. Typically, the chloride concentration at a certain depth in the concrete increases relatively fast initially, but the rate of further increase in chloride concentration diminishes with time. This is well documented from long-term results of different field exposure sites both for marine and road-salt exposure, e.g. in Refs. (Nilsson et al. 1997, Tang and Lindvall 2013). The implication of this is that even small uncertainties in the chloride threshold value are strongly amplified in terms of predicted time to corrosion, i.e. lead to large uncertainties in service life predictions. This in turn means that in order to make accurate service life predictions, the chloride threshold value should ideally be an accurate number or span a very narrow range. Exactly this, however, seems not to be possible. As a result, chloride threshold values in codes of practice are defined in a very conservative manner.

3.4 *Future research*

Obviously, important parameters relevant for corrosion initiation are overlooked in the current concept of predicting chloride-induced corrosion initiation. As corrosion is a system behavior, these parameters might be found at the steel/concrete interface, both related to the steel and to the concrete. RILEM technical committee 262-SCI currently addresses these issues (RILEM TC 262-SCI).

One example might be the steel microstructure, as indicated by recent results. Most of our practical long-term experience from real structures relates to systems, where cold worked steel and Portland cement were used. During the last few decades, however, a transition to thermomechanically strengthened reinforcing steels and to blended cements occurred. There is indication that these modern steel types with a tempered martensite surface layer are more susceptible to chloride-induced corrosion than the cold worked steels used before the 1980s (ferrite-pearlite microstructure). At the same time, there is reason to believe that blended cements are associated with lower chloride threshold values (due to the lower alkalinity in the concrete pore solution), but clear evidence is lacking. These changes in materials may significantly affect the corrosion performance of old, young, and future concrete structures.

Additionally, it is known that environmental parameters such as exposure conditions determining the moisture content in the structure, affect corrosion initiation. The role of macroscopic voids (e.g. entrapped air voids) at the steel/concrete interface in promoting or inhibiting corrosion initiation depends strongly on their moisture state, i.e. whether they are water-saturated or not (Angst et al. 2011b, Hornbostel et al. 2015). For engineering applications, particularly the seasonal variability in moisture conditions introduces large uncertainties that are currently difficult to handle in predictive modeling.

Future research urgently needs to address these issues.

4 CONCLUSIONS

It appears that after now more than 60 years of research attempting to determine chloride threshold values in concrete, the research community failed to provide the input required in engineering to reliably forecast corrosion initiation in concrete exposed to chloride bearing environments. The conceptual approach of reducing the issue of corrosion initiation to a question of chlorides cannot accurately describe reality. This is apparent from the example of the Swiss road tunnel “Stalvedro”, where even for a very small area – with presumably identical concrete, steel (type and previous exposure history), casting conditions, exposure conditions during the service life, age, etc. – the variability in the chloride threshold value was vast. Even for this specific and well-documented case, corrosion predictions can only be made with a low level of confidence.

In summary, clearly more research is needed to finally understand what controls corrosion initiation in concrete. Only this will permit developing a novel conceptual approach capable of more reliably describing reality.

REFERENCES

Angst, U., Elsener, B., Larsen, C. K. and Vennesland, Ø. (2009). "Critical chloride content in reinforced concrete - A review." Cement and Concrete Research 39 (12): 1122–1138.

Angst, U., Rønnquist, A., Elsener, B., Larsen, C. K. and Vennesland, Ø. (2011a). "Probabilistic considerations on the effect of specimen size on the critical chloride content in reinforced concrete." Corrosion Science 53 (1): 177–187.

Angst, U., Wagner, M., Elsener, B., Leemann, A. and Nygaard, P. v. (in press). Research report "Methode zur Bestimmung des kritischen Chloridgehalts an bestehenden Stahlbetonbauwerken" (in German), Swiss Federal Roads Office.

Angst, U. M. and Elsener, B. (2015). Forecasting chloride-induced reinforcement corrosion in concrete - effect of realistic reinforcement steel surface conditions. in: 4th Int. Conf. on Concrete Repair, Rehabilitation and Retrofitting (ICCRRR), Leipzig, Germany. F. Dehn, H.-D. Beushausen, M. G. Alexander and P. Moyo, Eds, CRC Press.

Angst, U. M., Elsener, B., Larsen, C. K. and Vennesland, Ø. (2011b). "Chloride induced reinforcement corrosion: Electrochemical monitoring of initiation stage and chloride threshold values." Corrosion Science 53 (4): 1451–1464.

British Cement Association (1997). Development of an holistic approach to ensure the durability of new concrete construction, Research Report Project 38/13/21 (cc 1031). Crowthorne, UK, British Cement Association.

Castellote, M. and Andrade, C. (2001). "Round-Robin test on chloride analysis in concrete - Part 1: Analysis of total chloride content." Materials and Structures 34 (243): 532–556.

DuraCrete (2000). Final Technical Report, "Brite EuRam III, DuraCrete - Probabilistic performance based durability design of concrete structures".

fib (2006). fib bulletin No. 34: Model code for service life design. Lausanne, Switzerland, International Federation for Structural Concrete (fib).

Ford, E. S., Ajani, U. A., Croft, J. B., Critchley, J. A., Labarthe, D. R., Kottke, T. E., Giles, W. H. and Capewell, S. (2007). "Explaining the decrease in US deaths from coronary disease, 1980–2000." New England Journal of Medicine 356 (23): 2388–2398.

Gouda, V. K. (1970). "Corrosion and corrosion inhibition of reinforcing steel. I. Immersed in alkaline solutions,." British Corrosion Journal 5: 198–203.

Hausmann, D. A. (1967). "Steel corrosion in concrete. How does it occur?" Materials Protection 6: 19–23.

Hornbostel, K., Angst, U., Elsener, B., Larsen, C. and Geiker, M. (2015). "On the limitations of predicting the ohmic resistance in a macro-cell in mortar from bulk resistivity measurements." Cement and Concrete Research 76: 147–158.

Jensen, M. M., Johannesson, B. and Geiker, M. R. (2014). "Framework for reactive mass transport: Phase change modeling of concrete by a coupled mass transport and chemical equilibrium model." Computational Materials Science 92: 213–223.

Koch, G. H., Brongers, M. P. H., Thompson, N. G., Virmani, Y. P. and Payer, J. H. (2002). "Corrosion costs and preventive strategies in the United States." Materials Performance (Supplement) 42.

Li, L. and Sagüés, A. A. (2004). "Chloride corrosion threshold of reinforcing steel in alkaline solutions - Effect of specimen size." Corrosion 60 (2): 195–202.

Nilsson, L.-O., Sandberg, P., Poulsen, E., Tang, L., Andersen, A. and Frederiksen, J. M. (1997). HETEK - A system for estimation of chloride ingress into concrete, theoretical background (report no. 83), Road Directorate, Denmark, Ministry of Transport.

Reddy, B. (2001). Influence of the steel-concrete interface on the chloride threshold level PhD thesis, Imperial College, U.K.

RILEM TC 178-TMC "Testing and modelling chloride penetration in concrete", chair: C. Andrade, 1997–2002.

RILEM TC 235-CTC "Corrosion initiating chloride threshold concentrations in concrete", chair: Luping Tang, 2009–2015.

RILEM TC 262-SCI "Characteristics of the steel/concrete interface and their effect on initiation of chloride-induced reinforcement corrosion", chair: Ueli Angst, started in 2014.

Samson, E., Marchand, J. and Beaudoin, J. J. (1999). "Describing ion diffusion mechanisms in cement-based materials using the homogenization technique." Cement and Concrete Research 29 (8): 1341–1345.

Soylev, T. A. and Francois, R. (2003). "Quality of steel-concrete interface and corrosion of reinforcing steel." Cement and Concrete Research 33 (9): 1407–1415.

Stratfull, R. F., Jurkovich, W. J. and Spellman, D. L. (1975). "Corrosion testing of bridge decks." Transportation Research Records 539: 50–59.

Tang, L. and Lindvall, A. (2013). "Validation of models for prediction of chloride ingress in concrete exposed in deicing salt road environment" Int. Journal of Structural Engineering 4: 86–99.

Tang, L., Nilsson, L.-O. and Basheer, M. P. A. (2012). Resistance of concrete to chloride ingress: testing and modelling. Boca Raton, CRC Press, Taylor & Francis Group.

Treadaway, K. W. J., Cox, R. N. and Brown, B. L. (1989). "Durability of corrosion resisting steels in concrete." Proceedings of the Institution of Civil Engineers Part 1 86: 305–331.

Vassie, P. (1984). "Reinforcement corrosion and the durability of concrete bridges." Proceedings of the Institution of Civil Engineers Part 1 76: 713–723.

Concrete Solutions – Grantham et al. (Eds.)
© 2016 Taylor & Francis Group, London, ISBN 978-1-138-03008-4

Durability design of reinforced concrete structures – service life estimation

S. Demis
Department of Civil Engineering, University of Patras, Patras, Greece

V.G. Papadakis
Department of Environmental and Natural Resources Management, University of Patras, Agrinio, Greece

ABSTRACT: The increased number of premature structural deterioration cases observed on reinforced concrete structures, necessitate the need for a robust durability design. Under this framework, concrete service life estimation models can be a very useful tool. Even though a considerable amount of research has been taken, certain grey areas still remain. Given the different approaches of concrete deterioration, and considering the individualities on the input of each model, results as it is shown in the current study might vary and be difficult to compare. Utilisation of certain service life estimation tools, brings to the surface certain questions. Should a service life estimation model be deterministic or probabilistic? Overall, can a practitioner engineer base its judgment with high confidence on a particular service life estimation tool? Questions that the current study will shed some light on.

1 INTRODUCTION

Even though the definitions of the term durability, in the relevant Standards, might vary in context, ("*ability of the structure to resist weathering action, chemical attack, abrasion, or any other form of deterioration*" in ACI 201.2R-01 (2008), "*ability to maintain a required technical performance throughout the service life under the influence of foreseeable actions*" in *f* ib Model Code (2012] and "*to meet the requirements of serviceability, strength and stability throughout its design working life, without significant loss of utility or excessive unforeseen maintenance*" in EN 1992 (2004)), they all lead to the same conclusion. That, in essence, durability is defined as the "ability of an RC structure to withstand aggressive environmental actions, while at same time be able to maintain its performance well above a minimum acceptable level". Indeed, durability is not a property (as in the sense of a material or section property) but an ability. An ability that is "given" to a reinforced concrete structure, through correct conceptual design, planning, selection of materials, as well as, sound construction and maintenance of the structure. Such an effort should be a part of the preliminary/conceptual design process of any (to be erected) reinforced concrete structure.

Today, more than ever, considering the rare, but also increased number of premature structural deterioration cases observed on Reinforced Concrete (*RC*) structures, the need for a robust durability design is of paramount importance. Why? Because of the end result, the end gain of the durability design process. The aim of the latter is to identify the period of time for which the structure, or a structural element, can be used for its indented purpose without the need for maintenance. In other words to identify the point in time at which the first major repair is needed in order the structure to continue to be able to withstand aggressive environmental agents. Such a time period is noted as service life.

Ideally the processes of structural and durability design should be fully interlinked, especially at the initial design stages, and up to a point they are. Structural (European and National) codes and associated standards (EN 1990 2005, EN 1992 2004, fib Model Code 2012) specify the Ultimate Limit State (ULS) and the Serviceability Limit State (SLS) requirements which need to be met, in terms of structural performance. As far as durability design is concerned, a "deemed-to-satisfy approach" is included in the previously mentioned standards. Such an approach offers prescriptive design rules in tabulated form. The "deemed-to-satisfy" rules related to the different exposure classes defined in EN206:2013 (2014) which provides recommended minimum values of concrete composition and properties (including minimum concrete cover value). According to *f* ib bulletin 53 (2010), these provisions "*may not reflect current best practice measures, because of the time it takes to achieve consensus and to go through the relevant standardisation procedures associated with the*

periodic updating of such guidance". In general, if followed to the letter, they do result in concrete structures durable in most common service environments, up to the pre-assumed (pre-defined) target service life of 50 years, according to Eurocode 2. However, if a service life of more than 50 years is required, or if a more aggressive environment is met, where durability performance requirements are more demanding, a more in-depth procedure is required to be implemented (than a "deemed-to-satisfy" approach).

Such a procedure is allowed under the scope of EN206-1 (2013), where in part 5.3.3 it is stated that "*The requirements related to exposure classes may be established by using performance-related methods (PRMs) for durability*." A PRM considers each relevant deterioration mechanism, the service life of the structure and the criteria which define the end of this service life in a quantitative way. It can be based on data derived from established performance test methods for each relevant deterioration mechanism, or on the use of proven predictive models.

Hence, a "window" for service life estimation techniques is wide open. Bearing in mind that studies on the deterioration of concrete structures conclude that 50% of all cases of deterioration considered were caused by corrosion of reinforcement, due to either chloride penetration or carbonation (*f* ib bulletin 53 2010), emphasis should be paid on utilizing service-life estimation models on these types of deterioration processes. After all, the prospect that a structure is durable can only be assessed via models simulating the deterioration processes to which the structure is likely to be subjected.

The importance of modeling is also followed from the common sense fact that no prediction of future performance can be made without some type of model. Hence from the need of a durability design of an RC structure during the conceptual stage, the need for a forward looking methodology: the service life design process has now emerged.

Service life design is therefore the process by which the designer chooses fundamental properties of the materials and other characteristics of the structure in order to fulfill the functional requirements for the specified period of time (i.e. the design service life). Thus, it is the deterioration mechanisms associated with the service environment, or that it will not be affected by them.

Today, there are a variety of service life estimation models/software tools available, to assist the practitioner engineer on the previously mentioned direction. However, considering the different angles of approaching the same deterioration process and the assumptions included (as illustrated in the following section) a certain level of confusion is evident. Hence the aim of this particular study is twofold. To portray the need (and the basic steps) of durability design and service life estimation, to give characteristic examples of the utilization of representative software tools available, and to critically identify the next research needs in this direction.

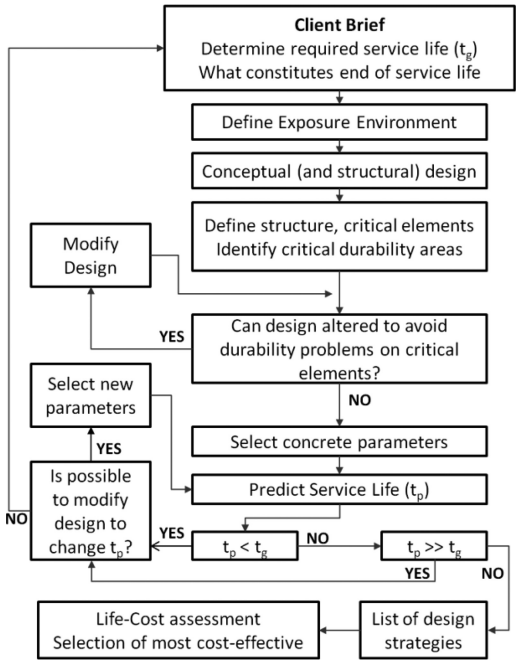

Figure 1. Service life design procedure of an RC structure, after [*f* ib bulletin 53, 2010].

2 SERVICE LIFE ESTIMATION EXPLAINED

A schematic overview of a step-by-step process of service life design is illustrated in Figure 1.

The identification of the end-of-service-life scenarios, together with the establishment of the target service life (in years) of the structure, is the basis of the durability design process. Particular attention has to be paid on what constitutes, and how is defined, the end of the service life. By recognizing the nature and the effects of the relevant degradation process, appropriate scenarios/criteria can be developed based on the various conditions and their consequences which might arise during the life time of the structure. Characteristic conditions can be mentioned as: the point at which corrosion is initiated, the first appearance of a corrosion related crack, or concrete spalling. Ideally, the above have to be defined by, or agreed with the owner of the structure.

In terms of modeling, the end of the service life of an RC structure is defined as the end of the initiation period and the onset of the critical deterioration mechanism. A two-phase conceptual model introduced by Tuuti (1982) is commonly used to represent the inset of corrosion (for both carbonation and chloride ingress) (Figure 2). A distinct initiation period (t_i) is defined, as the period of time where the reinforcement remains in its passive state, followed with the subsequent propagation period (t_p), the time necessary for sufficient corrosion to occur causing damage beyond acceptable limits. Since no damage is assumed to occur during

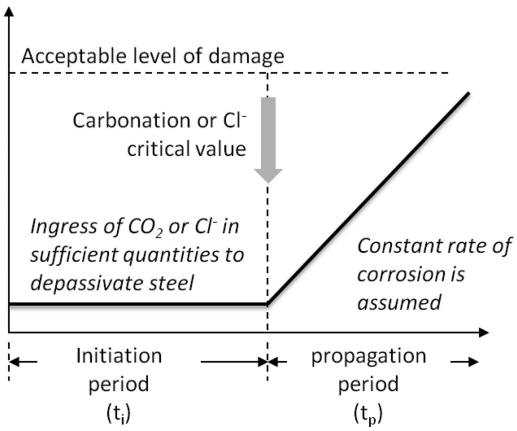

Figure 2. Modeling of service life in corrosive environments.

the buildup of chlorides on the reinforcing steel (or due to the initial ingress of carbon dioxide) during the initiation period, this time phase in the majority of service life models, is considered to be the effective service life of an RC element exposed to such deterioration environments. Its length is strongly influenced, among other factors, by the penetration and transport mechanisms of the aggressive substances in concrete (Tuutti 1982).

Therefore, according to the steps illustrated in Figure 1, by defining the functional and performance requirements of the structure as well as the aggressivity of the service environment, the deemed to satisfy rules are identified and a preliminary mix design is selected. The next step is to estimate the service life of the structure and to compare it with the target service life initially set. Such a prediction is only possible using deterioration models, appropriate to the particular hazards of the service environment, describing the various interactions among environmental conditions, material properties and deterioration mechanisms.

Such physicochemical deterioration models, from a mathematical perspective, can be either deterministic or probabilistic in nature. The latter calculates the probability of reaching a predefined end-of-service life scenario (e.g. the carbonation front to reach the reinforcement). Their utilization and associated analyses can be complicated activities. In most cases there is insufficient amount of data available to fully represent the statistical variability of the input parameters of the deterioration model (*f* ib bulletin 59 2011). The overall effectiveness and ease of use of the service life design options are illustrated in Figure 3. A simpler approach is to utilize a deterministic deterioration model. According to *f* ib Bulletin 53 (2010), the latter type of models "*might be anticipated to give the most accurate prognosis of future behavior*". However, two points have to be mentioned. Firstly, it has been noticed that models for the same deterioration process on the same concrete element give different

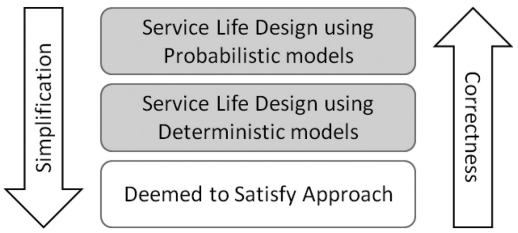

Figure 3. Simplification versus level of correctness of service life design approaches.

predictions. Hence, an issue on the sensitivity of the input parameters of the various models is being raised. Secondly, concerns have also been expressed, on the accuracy of particular models, in connection to the real behaviour of the structure in the actual circumstances and service environment. Hence the need for a systematic validation has been expressed.

Both deterministic and probabilistic service life models are based on a particular input, taking under consideration the actual 'restrictions' and properties of the structure. Via a mathematical process simulating the deterioration mechanism, the end of service life scenario, represented either by carbonation depth or chloride profile terms, is calculated. As far as chloride exposure is concerned, prediction of the chloride profile at a given depth x in time t, and comparison with the critical chloride content for the initiation of corrosion, allows the estimation of the service life of the structure. The same principle applies to carbonation exposure, where the estimated carbonation front at a time t, is compared with the minimum required (or existing) concrete cover.

Let's focus on the action of chlorides. Even though chlorides can also pre-exist in the concrete mix, it is the action of the external chlorides that in a sense define (or limit) the effective service life of the structure. Therefore, the process of chloride penetration into concrete is one of the most important parameters for determining the latter. Chlorides that reach the concrete surface, enter the pore system either by diffusion, or by capillary suction of the surface water in which they are dissolved, or by their combination (Ozbolt et al. 2010). Early work to analyze and extrapolate trends on chloride ingress in concrete based entirely on Fick's 2nd law of diffusion, considered a constant chloride diffusion coefficient with time. Such an approach has been followed in a number of research studies, neglecting however the chloride interaction with the solid phase (Collepardi et al. 1972). It is widely proved that chloride ions are bound from concrete components in a percentage of 30–60% depending on the cementitious materials' composition and content (Glasser et al. 2008, Ozbolt et al. 2010). According to certain case studies (Glasser et al. 2008, Tang et al. 2012) strict use of Fick's 2nd law is not applicable on long term chloride transport in concrete, since it usually leads to the calculation of decreasing chloride

transport coefficient in time. Its strict implementation can be characterized as an oversimplified, underestimating approach resulting in the calculation of the "apparent" chloride diffusivity, not able to explain entirely chloride penetration and binding, in contrast to when chloride binding is taken under consideration in which case the true "intrinsic" diffusion coefficient is calculated, leading to a more accurate service life estimation.

Certain empirical service life estimation models are based on curve fitting equations developed to fit a large quantity of field data, taking the total chloride as driving potential (since it is easier to measure). The latter, being the combined free and bound chlorides, does not give a realistic indication of the risk of corrosion of the reinforcement, since it is the free chloride that has the electrochemical potential for diffusion (CC&AA 2009). In spite of the oversimplified assumptions related to empirical models (based on Fick's 2nd law of diffusion), they are widely used by engineers in practical applications, due to their simple mathematical expressions (Luping 2008). In contrast to the above, physicochemical models are based on the detailed expression of physicochemical processes involved in the chloride transport in concrete. They are usually functioning based on the simulation of chloride penetration (not just diffusion) through the pore solution in concrete using the free chloride as driving potential, and on the calculation of the distribution of the total chloride content in concrete using mass balance equations combined with nonlinear chloride binding.

All of the above are translated into service life estimation tools. Since, a thorough evaluation of every tool available would be a part of a series of research papers, for the scope of this study some of the most documented and widely used service life estimation tools are evaluated. These, with margin for question, can be identified as the Life-365, EUCON and Duracon software packages.

3 THE TOOLS UTILISED

A brief description of the software tools utilized in this study is presented in the current section. Although it is not the scope of this study to compare the different models that each tool is based on but their results from a practitioner's engineer point of view, for reason of completion equations on the calculation of chloride profiles of each tool have been included.

Life-365 (Ehlen et al. 2009) is a service life and life-cycle analysis (LCA) software package. It recognizes diffusion to be the dominant process in chloride ingress in concrete, disregarding the mechanism of chloride binding. The initiation time of corrosion is calculated based on 1-D (for slabs, beams) or 2-D (for columns) finite difference implementation of Fick's 2nd law of diffusion, by taking under consideration that the apparent diffusion coefficient $D(t, T)$ is affected by time (t) and temperature (T), according to the following Equation

$$D(t,T) = D_{ref}\left(\frac{t_{ref}}{t}\right)^{n} \exp\left[\frac{U}{R}\left(\frac{1}{T_{ref}} - \frac{1}{T}\right)\right] \quad (1)$$

where, D_{ref} is the apparent diffusion coefficient at time T_{ref} (usually at 28 days, affected by the w/c ratio of the concrete), m a constant depending on mix proportions, U is the activation energy of the diffusion process, R a gas constant and T is the absolute temperature.

In addition, according to the developers, Life-365 includes a probabilistic prediction of the initiation period of corrosion, although it has been argued to be more of a sensitivity analysis.

Eucon is a software tool, based on proven predictive models, according to performance-related methods for assessing durability, developed and validated by the authors of this study (Demis et al. 2013, Papadakis et al. 1996), for the estimation of concrete service life under harsh environments. The physicochemical processes of Cl^- diffusion in the aqueous phase, their adsorption and binding in the solid phase of concrete, and their desorption, are described by a non-linear partial differential equation. The solution of this allows the calculation of, the chlorides bound in the solid phase $Cl^-(s)$, the adequate concrete cover needed to sustain a corrosion free structure for a given service life and the estimation of the time required for the total chloride concentration surrounding the reinforcement, located at a distance c from surface, to increase over the threshold for depassivation.

$$\frac{\partial[Cl^-(aq)]}{\partial t} = \frac{D_{e,Cl}(1+K_{eq}[Cl^-(aq)])^2}{K_{eq}[Cl^-(s)]_{sat} + \varepsilon(1+K_{eq}[Cl^-(aq)])^2}\frac{\partial^2[Cl^-(aq)]}{\partial x^2} \quad (2)$$

$$[Cl^-(s)] = \frac{K_{eq}[Cl^-(aq)]}{1+K_{eq}[Cl^-(aq)]}[Cl^-(s)]_{sat} \quad (3)$$

where, x is the distance from the concrete surface, K_{eq} the equilibrium constant for Cl^- binding, $[Cl^-(s)]_{sat}$ the saturation concentration of Cl^- in the solid phase, $[Cl^-(aq)]$ the concentration of Cl^- in the aqueous phase, and $D_{e,Cl}-$ is the intrinsic effective diffusivity of Cl^- in concrete.

Duracon (Ferreira 2004) is a software package for probability-based durability analysis of concrete structure, developed under the scope of the DUROCRETE (2000) project. The software is based on a Monte Carlo Simulation of Fick's 2nd law of diffusion, adjusted to allow the time dependency of the chloride diffusivity and the effect of temperature, as it is illustrated in the following equation.

$$C(x,t) = Cs\left[1 - erf\left(\frac{x}{2\sqrt{D(t)t}}\right)\right] \quad (4)$$

Table 1. Main input parameters, in terms of Cl^- exposure, of the software packages investigated.

Life-365	Eucon	Duracon
1. Definition of the Structure and Material Properties		
Type of structure Thickness/ cover, w/c, % FA,SF, Slag, protective systems	Cement type, Concrete constituents, w/c, additions, Air content, Materials oxide analysis, Component thickness	Concrete cover
2. Exposure Conditions		
Surface Cl^- (kg/m^3 conc.) Manual/ profile/ Automatic, Time to max Cl^- surface (years) , Critical Cl^-, Temperature	Surface Cl^- (kg/m^3 sol) Manual, Automatic Cation associated to Cl^- (Na^+/Ca^{2+}) Initial Cl^- (kg/m^3 sol) Critical (total) Cl^- (kg/m^3 conc.)	Surface/critical Cl^- (% wt conc.) Temperature
3. Chloride Diffusion Coefficient		
Apparent diff. coef. D_{28} ($\times 10^{-12}$ m^2/s) Maturity factor *m*	Intrinsic diff. coef. ($\times 10^{-12}$ m^2/s), FA/SF efficiency factor for Cl^- penetration, Equilibrium constant for Cl- binding,	$D_{Apparent,t0}$ ($\times 10^{-12}$ m^2/s) Factor for time dependence of diff. coeff.
4. Time related factor		
Propagation (years) Hydration (years)	Service life (SL) (years)	SL (years) $t_{exposure}$ (days) $t_{testing}$ (days)
5. Probabilistic Aspects		
COV(%) of input	NO	SD/distribution

$$D(t) = \frac{D_0}{1-a}\left[\left(1+\frac{t'}{t}\right)^{1-a} - \left(\frac{t'}{t}\right)^{1-a}\right]\left(\frac{t_0}{t}\right)^{a} k_e \qquad (5)$$

where, $C(x,t)$ is the chloride concentration at depth x after time t, C_s the chloride concentration at the concrete surface, D the apparent chloride diffusion coefficient, D_0 the diffusion coefficient after the reference time t_0, α a parameter representing the time dependence of the diffusion coefficient, t' is the age of the concrete at time of chloride exposure and k_e a parameter taking into account the effect of temperature. The model also incorporates the stochastic nature of the individual durability parameters.

An analytical overview of the input parameters of the software tools and their individual outputs is given in Tables 1 and 2.

On each of the previously mentioned tools a common input, in terms of structure and exposure location, was given from structures indentified in the literature (Ferreira 2004).

Structural elements from field studies from two different concrete harbour structures exposed to a chloride rich environment (environmental exposure class XS3; tidal splash and spray zone), were selected as case studies for the models. On structure A, an 8 year old structure comprised of an OPC cement mix with a w/c of 0.45 and 5% addition of silica fume, two distinct beam elements were identified. The first element (sample A-1) is directly exposed to atmospheric agents as wind and rain, therefore subjected to a periodic wash-off, while the second (sample A-2) is not subjected to rain, with therefore higher chloride concentrations. On structure B (7 years old), comprised of a plane OPC cement mix of a 0.45 w/c ratio, a beam element 3.8 m above sea level was chosen (sample B-1). The service life, of these structures, according to the preliminary design was defined as 50 years. A value of 10% of probability of failure, not to be exceeded, was chosen for probability-based durability analysis, according the recommendations of *f*ib Model Code (2012) and *f*ib bulletin 34 (2006). The various parameters obtained from measurements and data collected on these structures including the corresponding Standard Deviations, are given in Table 3.

4 RESULTS AND DISCUSSION

The service life of the structural elements, as estimated by the models previously described, is illustrated in

Table 2. Output parameters, in terms of Cl^- exposure, of the software packages investigated

Life-365	Eucon	Duracon
1. Chloride Profiles		
Total Cl^- (kg/m^3 conc.) profile Level of total Cl^- at steel up to initiation time of corrosion Change of Cl^- diffusion coefficient with time	Free Cl^- (kg/m^3 sol) profile Bound Cl^- (kg/m^3 conc.) profile Total Cl^- (kg/m^3 conc.) profile	NO
2. Service Life Estimation		
Corrosion initiation time (years) Service life (years)	Concrete Service life as a function of adequate concrete cover to sustain a chlorides free element	Probability of corrosion initiation Change of reliability index with time (years)
3. Other parameters		
Change of dif. coef. with time of exposure Uncertainty in concrete mix design initial times	NO	Can by utilized for parametric analysis of the influence of concrete composition factors

Table 3. Mix design and durability parameters of the structural elements.

	A-1	A-2	B-1
Concrete Cover (mm)	48.3 (5.9)		60.8 (1.8)
Cement /SF (kg/m^3)/w/c	380/19.2/0.45		400/ 0/ 0.45
Apparent Cl^- Diffusion Coeff. ($\times 10^{-12}$ m^2/s)	0.948 (0.166)	1.140 (0.162)	1.589 (0.432)
Surface Cl^- (% wt. conc.)	0.555 (0.158)	0.828 (0.079)	0.518 (0.070)
Critical Cl^- (% wt. conc.)	0.080 (0.010)	0.080 (0.010)	0.070 (0.010)
Age at testing (days)	2920		2555
Service life (years)	50		50

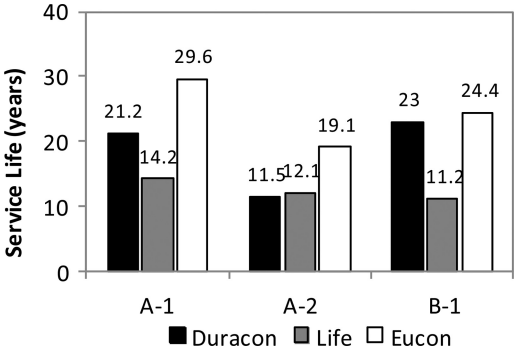

Figure 4. Service life of the structural elements under chloride exposure.

Figure 4. At first view results seem to vary and might promote a certain level of confusion.

Analysis of statistical importance of the differences of the service life estimates of each tool utilized (Table 4), revealed that comparison of the values

Table 4. Analysis of significance of statistical difference of service life estimates.

Comparison	Significant difference	F_{value}	$F_{critical}$
Duracon-Life 365	No	2.72	7.71
Duracon-Eucon	No	1.53	7.71
Life 365Eucon	Yes	14.1	7.71

derived between Duracon and either Life-365, or Eucon do not have a statistically significant difference, while between Life-365 and Eucon they do.

Statistically speaking this might be a valid argument, but from a practical engineering point of view is not. A practitioner engineer needs to know with a high level of confidence what is the service life of a particular structure. In the current case on element A1 is it 21 or almost 30 years, which according to the previous do not differ substantially from a statistical point of view?

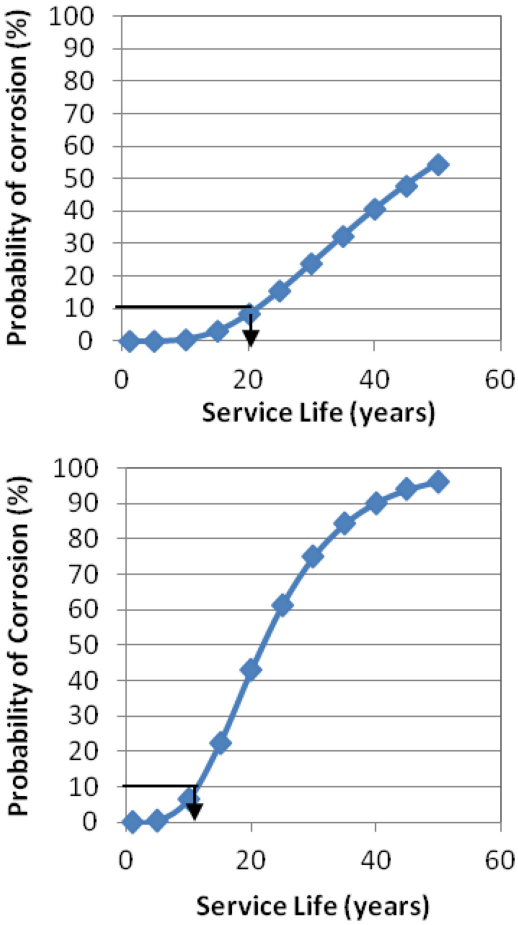

Figure 5. Probability of corrosion on elements A-1 (top) and A-2 (bottom) according to Duracon.

A closer look of the service life values derived reveals the following. Probability-based analysis, according to Duracon software (Figure 5), suggests that a 10% probability of failure would be exceeded at 21, 11 and 23 years for elements A-1, A-2 and B-1, respectively.

Service life estimation according to Life-365, of similar input to Duracon in terms of definition of chloride exposure, of the apparent diffusion coefficient at 28 days and on the incorporation of time-reduction factors, yielded lower service life values on elements A-1 and B-1, by 33% and 51% (14 and 11 years) respectively. Comparing the chloride profiles estimated from Life-365 to the measured actual chloride profile of the elements, it was seen (Figure 6) that their concentration was overestimated from 26.2% on average in element A-2, to 36.8% on element B-1. In general, this overestimation of chloride ingress (up to 36.8%), leading to an underestimation of the service-life up to 51.3% (on sample B-1; 11.2 years according to Life-365 and 23 years according to Duracon), has also been reported elsewhere (Oslakovic et al. 2010).

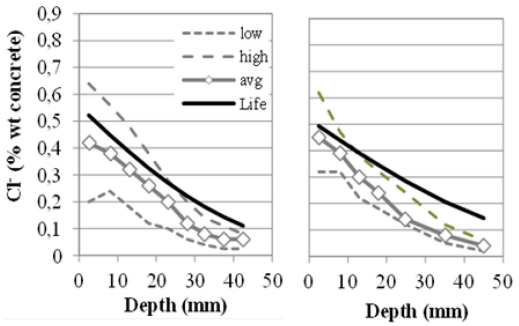

Figure 6. Comparison of predicted Cl^- profile according to Life-365, with experimental on elements A-1 (left) and B-1 (right).

Such a behavior can be attributed to certain restrictions that the Life model entails on the way chloride ingress is taken under consideration, as:

- the oversimplification that concrete remains saturated and that chloride ingress occurs only by ionic diffusion,
- the dependence of the diffusion coefficient on just the w/c ratio,
- the reduction coefficient of chloride diffusion in Life-365 is more conservative (than the one in Duracon).

It should be noted however, that even though Life-365 is based on the previously mentioned assumptions, the user can also input the experimentally derived value of the chloride diffusion coefficient. In that case, based on the diffusion coefficient experimentally derived (e.g. 1.589×10^{-12} m^2/s for element B-1, instead of the one calculated: 1.047×10^{-11} m^2/s) no underestimation of service life was estimated (24.3 years on element B-1, 25.7 years on A-1, compared to 23 and 21.2 years according to Duracon).

Utilisation of the Eucon software tool gave considerable higher service life values on elements A-1 and A-2 (29.6 and 19.1 years respectively), but not on element B-1. Let us consider for a moment, how this particular model approaches service life. The Eucon model by taking into account the processes leading to concrete deterioration, including the chloride binding process, it can estimate the chloride profile of the structure at different service-life periods. Based on the calculated chloride profile for a given service life (at depth x) and according to the set value of critical chloride content for the initiation of corrosion, the service life of a structure with a concrete cover c can be estimated. Comparing the chloride profiles estimated by Eucon to the experimental profile, it can be seen (Figure 7) that although, especially close to the external surface, the profile follows a trend closer to the real situation, overall lower estimates (up to 23.2%) were produced, up to the depth of 25 mm.

Considering that the Eucon software tool is based on a very detailed physicochemical model, such an underestimation raises concerns. Perhaps a detailed

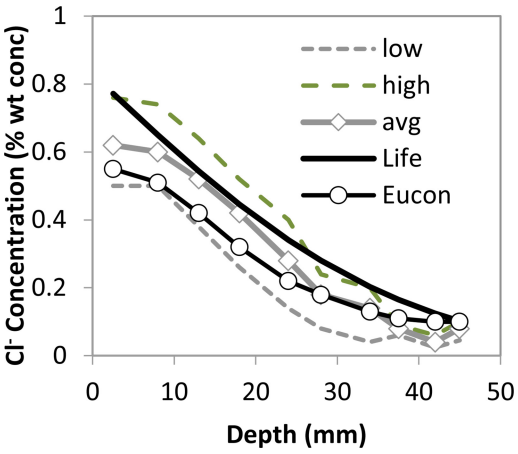

Figure 7. Chloride profile from Eucon model on element A-2.

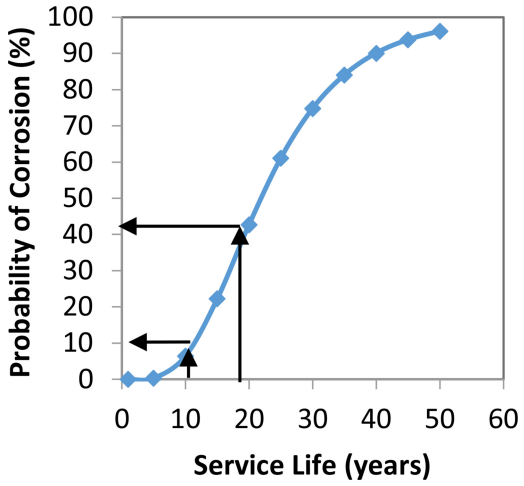

Figure 8. Correlation of service life according to Eucon to a probability of corrosion.

review of all the parameters contributing to the estimation of the chloride ingress and a more comprehensive validation scheme with results should be enforced. It should be noted at this point that Eucon is based on the calculation of the actual "intrinsic" diffusion coefficient, completely different from the apparent one, in which only diffusion of chlorides is taken under consideration as in the case of Life-365 or Duracon. Even if the intrinsic diffusion coefficient is assumed to be constant, in contrast to Duracon where the effect of time or temperature on the reduction of this factor is taken under consideration, the detailed physicochemical modeling of every Cl^- interaction (adsorption, binding in the solid phase of concrete, and desorption) affords a certain level of confidence on service life estimation.

In addition, the relationship between the deterministic and probabilistic approach, from the results point of view, should also be examined. Although in theory outputs of these process are not directly comparable, from a practitioner's engineer point of view which he is only interested on the validity of the end result of the service life estimation, one might state the following.

It has been suggested (*f* ib bulletin 53, 2010) that a deterministic approach, based upon the mean depth of cover, provides a larger probability (up, or close, to 50%) of achieving the required 50 years service life. When a 10% risk of having corrosion initiated after 50 years is considered acceptable, as in the case of a probabilistic approach, then larger covers are required. In other words, the adequate concrete cover calculated from a deterministic model c_d, would be smaller than the concrete cover $c_{p,10}$ calculated with a 10% accepted probability of failure, for the same service life. Hence on an existing structure, based on the existing cover of the concrete element examined, the remaining service life calculated based on a deterministic software tool would be higher than the one derived from a probabilistic tool. This appears to be the case in the current study (Figure 8), considering the fact that the 19.1 years

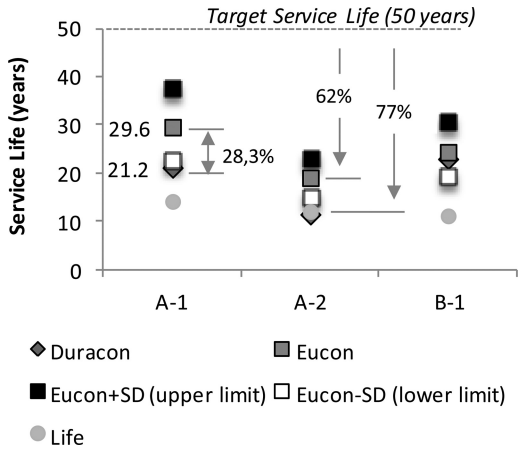

Figure 9. Incorporation of standard deviation of concrete in Eucon estimated service life values.

service life of element A-2, corresponds to a 40% probability of corrosion, according to a probability based analysis (with 10% PoF).

Based on the above, the fact that the service life values of element B-1, according to Eucon and Duracon seem to be quite close (23 and 24.4 years respectively) it can be safely assumed to be a case specific situation (and should be neglected from any overall conclusions).

When the standard deviation of the measured cover values of the structural elements was indirectly taken under consideration in the deterministic physicochemical software tool Eucon, as in the case of Duracon or Life-365, the software yielded a range of service life values, as illustrated in Figure 9. It is evident, that although the actual service life estimated on elements A-1 and A-2, are up to 39.8% higher than the ones calculated with Duracon, lower service life estimates have been produced.

Table 5. Remaining Corrosion-free service life of structural elements evaluated.

	Life-365	Duracon	Eucon
A-1	6.2	13.2	21.6
A-2	4.1	3.5	11.1
B-1	4.2	16	17.4

Overall, each tool utilized in this study produced a unique (different) service life value, on each structural element, with the same environmental aggressive actions and properties. Hence every service life estimation tool should be used (on its own) with extreme caution and deep understanding on its principles and limitations is essential. A common observation, however, is that indeed the structural elements examined face a serious durability problem, due to the action of chlorides. Their estimated service lives seem in certain cases to be more than 70% smaller than the initially assumed target service life of 50 years, during the design stages. Just to emphasize this fact, element A-1 of 8 years old when evaluated, has at the best case scenario 21.6 corrosion-free years according to Eucon (29.6 years service life estimation), while at the worst case scenario 6.2 years according to Life-365 (1 14.2 years estimation), or 13.2 years before corrosion will occur (with a 10% probability of occurrence), according to Duracon which produced an estimation of 21.2 years, as illustrated in Table 5.

According to the above it can be safely stated that given the variety of service life estimation tools and their individualities in terms of modeling principles/limitations, definition of environmental aggression and structure, as well as results, a certain level of confusion has risen. Is possible to give a single answer on which is the service life of the structural elements identified?

At the end of the day, on which type of service life estimation tool should a practitioner engineer base its preliminary design? Should he follow a deterministic or a probabilistic approach?

The answer to all of the above valid concerns is not univocal. By all means the overestimation of service life, is equally as dangerous as its underestimation, especially under the scope of a life-cycle analysis, based on which service life values a calculated judgment will be made, for the time of the first major repair?

All of the above are valid concerns which have halted the wide acceptance of a single particular type of service life estimation tool. Some might argue that perhaps it is better that way. The designer has a range of tools at his or her disposal, which can be utilized according to their needs. To do this effectively, however, the designer needs to study the literature of the model behind each tool and know how and when to utilize it.

However, what is actually needed is a widely accepted process on service life estimation. In other words, we should be able to make the end-result, the process of estimating service life, more standardized, more universal and easier to be enforced. It seems that the latest research efforts in terms of service life estimation and durability design, aid in this direction.

5 DESIGN APPROACH FOR ENVIRONMENTAL LOADS

Emphasis has been paid to mould the concept of service life estimation into a design approach similar to the structural design philosophy currently used in modern structural design codes (EN 1990 2005, EN 1992 2004, fib Model Code 2012).

In structural design, such an approach is based on the definition of limit states (LS), conditions beyond which the structure infringes an accepted performance, for a target level of reliability. A distinction is made between ultimate limit state (ULS) that refers to irreversible adverse effects and serviceability and serviceability limit state (SLS) which refers to effects that restrict the normal use of the structure. Under these LS, in structural design, a load or an action (S_d) acting on a structural member should be smaller than its associated resistance (R_d) or capacity.

The same principle can be applied in terms of environmental actions and of concrete resistance to withstand these actions. Suitable LSs have to be defined and utilization of models on the load side (S_d) and on the resistance side (R_d) have to be implemented. In the case of chloride induced corrosion the resistance parameter is the critical chloride content, while the load parameter is the chloride concentration at the depth of the reinforcement.

On this note, depassivation of reinforcement caused either by carbonation or the action of chlorides can be defined as a SLS (since there is no immediate consequence to structural safety), while spalling/cracking of the concrete cover, or collapse due to the loss of cross-sectional area of the reinforcement can by defined as ULS.

Having defined the LSs, the performance under environmental actions of a particular structure or element, is prescribed and safeguarded by meeting certain requirements in terms of resistance, serviceability, durability and robustness. Taking under consideration the causes and nature of degradation, the associated limit state and the consequences (defined as classes, CC1, CC2, CC3) of achieving this limit state, certain reliability levels (RC1, RC2, RC3) are defined (*f*ib bulletin 34 2006, *f*ib bulletin 53 2010). Each reliability class can be expressed via the reliability index β. Depending on the type of limit state and the consequences of failure, appropriate values of the reliability index are chosen, which correspond to a particular probability of achieving this particular limit state (noted as probability of failure, PoF). A process of reliability differentiation based on the concepts of robustness, on design supervision and on the quality of execution has also been proposed to further fine

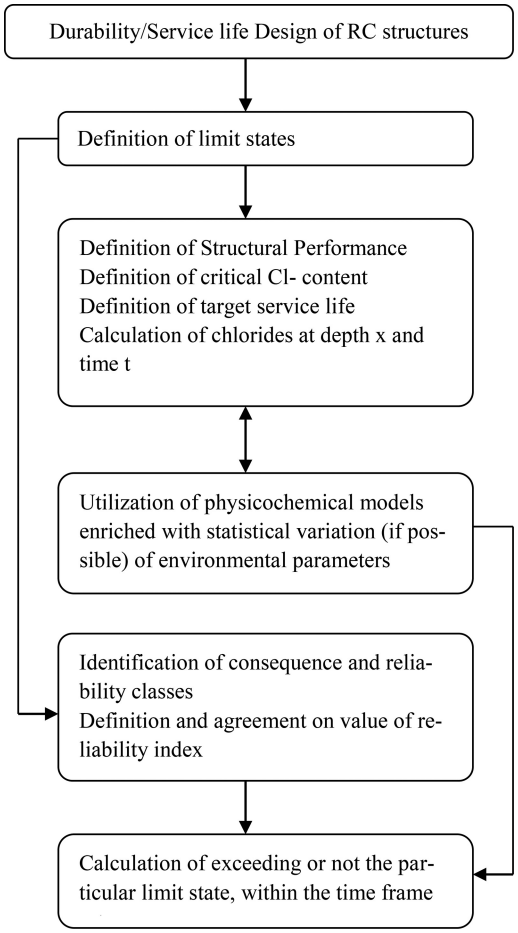

Figure 10. Principles of service life estimation according to the design process of the structural codes.

tune the β values. Usually for SLS a reliability index β is defined in the range of 1.0 to 1.5, with the value of 1.3 being commonly used (corresponding to a 10% probability of failure).

Overall, as illustrated in Figure 10, the service life of a reinforced concrete element, is defined via:

- definition of the relevant limit state,
- definition of the target service life,
- definition of the a required level of reliability for not passing the limit state defined, during the target service life.
- quantification of the deterioration process with appropriate deterioration physicochemical models (if possible enriched with statistically quantified environmental parameters).

In this way the service life of a structure or of a structural element is not a single deterministic value, but a value of time directly related apart of the nature of the structure and its properties, to the predefined client's needs, to the consequences of corrosion and to a certain level of reliability, hence to direct economic constraints.

6 NEXT STEPS ON SERVICE LIFE DESIGN

Having emphasized the need for a robust durability design of reinforced concrete structures, the requirement on that extent for service life estimation, and the associated level of confusion, certain areas according to the author's opinion still have to be improved.

A thorough review and validation of the current deterministic physicochemical estimation tools has to take place. Such an effort can be initiated under the scope of a task group of an International body (e.g. *f* ib, BCA) or as an action of a relative European research project. Agreement on the input per aggressive environmental factor, in terms of importance of parameters and units, on defining the structure/element properties and the environmental loads is a necessity. On this direction a database of the major environmental parameters per location (level of CO_2, RH, annual and monthly average temperatures, average level of concentration of chlorides on the external surface of buildings) would be extremely helpful, especially for countries as the Greek region in which such types of data are not easily accessible.

Having accomplished the previous a wide validation scheme of the service life estimation tools should then take place, under the umbrella of the previous mentioned bodies/actions. A common input should be given to a range of service life estimation tools (including Eucon in which an underestimation of chloride profile was noticed), as it took place in this study, in order to validate their estimations and adjust appropriately their calculation steps. In this way the practitioner engineer will be able to utilize a deterministic service life estimation tool, if appropriate to his case study, with a higher level of confidence than today.

Furthermore, in terms of the durability design based on limit states, as it was described in the previous section, the following needs seem to be appropriate.

- Incorporation of the durability design approach according to *f* ib, to the next level Eurocodes or relative European Standards. These recommendations, for example, could easily be adopted on the next version of EN 206 (2013) Standard for concrete.
- Universal and crystal clear definition of limit states for durability (on a European level)
- Although the existing reliability differentiation tool should be up to the National bodies to be further defined (when adopted to the Eurocodes), a more easy to follow from the practitioner's engineer point of view approach should be developed.

Overall, in terms of the necessity of a valid reinforced concrete durability design it is the author's view that it should be implemented at the early stages of conceptual structural design and that especially for actions that induce reinforcement corrosion, aggressive environmental agents (as the action of chlorides or carbon

dioxide from the atmosphere) should be included as loads on structural design software packages.

7 CONCLUSIONS

The need for a durability design, more advanced than the "Deemed-to-Satisfy" method currently available in the standards, especially during the initial design stages of a RC structure has been strongly emphasized. Under this scope the importance of modeling of the concrete deterioration process and service life estimation has strongly emerged.

The currently available service life estimation tools are often prone to debate, due to their sometimes conflicting results. Representative deterministic and probabilistic tools utilized in this study on the evaluation of 7 and 8 year old structural elements (under the action of chlorides) produced varying remaining service life estimates, all of them however smaller than the 50 years assumed service life. Issues such as the assumptions that each tool is based on (especially on the ingress of chlorides in concrete) and differences in quantification of the input parameters are responsible for the deviations exhibited in this study.

The importance of the intrinsic chloride diffusion coefficient was emphasized, as well as the dependence of the former on time and temperature on both deterministic and probabilistic models.

According to the latest research and standardization attempts, durability design is shaped according the principles of structural design, based on the utilization of validated physicochemical models.

Society demands sustainable and environmentally friendly solutions and owners demand reliable service lives of structures. Using a performance based methodology, the performance of the structure, defined by the limit state, can be evaluated for the service life.

REFERENCES

ACI 201.2R-01. 2008. *Guide to durable concrete*. American Concrete Institute, USA.

CC&AA. 2009. *Chloride Resistance of Concrete.* Cement Concrete & Aggregates Australia, Australia.

Collepardi, M. Marcialis, A. & Turriziani, R. 1972. Penetration of chloride ions into cement pastes and concrete, *J. A. Ceram. Soc.* 55 (10):534–535.

Demis, S. Efstathiou, M.P. & Papadakis, V.G. 2014. Computer-aided modeling of concrete service life. Cement & Concrete Composites 47:9–18.

DUROCRETE. 2000. Brite-Euram Project BE95-1347: Duracrete – Probabilistic performance based design of concrete structures.

Ehlen, M.E. Thomas, M.D.A. & Bentz, E.C. 2009. Life-365 service life prediction model. *Concrete International*.

EN 1992-1-1. 2004. *Eurocode 2: Design of concrete structures – part 1-1: General rules and rules for buildings*, European Committee for Standardization, Brussels.

EN 1990:2002+A1. 2005. *Eurocode – Basis of structural design*, European Committee for Standardization, Brussels.

EN 206:2013. 2014. *Concrete – Specification, Performance, Production and Conformity* European Committee for Standardization, Brussels.

Ferreira, R.M. 2004. *Probability based durability analysis of concrete structures in marine environment*. Ph.D. Thesis, University of Minho, Guimarães, Portugal.

f ib Model Code. 2012. *Model Code 2010 Final Draft*. International Federation for Structural Concrete (*f* ib).

f ib Bulletin 34. 2006. *Model Code for Service Life Design*. International Federation for Structural Concrete (*f* ib).

f ib Bulletin 53. 2010. *Structural Concrete – Textbook on behavior, design and performance Volume 3*. International Federation for Structural Concrete (*f* ib).

f ib bulletin 59. 2011. *Condition control and assessment of reinforced concrete structures*. International Federation for Structural Concrete (*f* ib).

Glasser, F.P. Marchand, J. & Samson, E. 2008. Durability of concrete- Degradation phenomena involving detrimental chemical reactions', *Cement and Concrete Research*. 38(2):226–246.

Luping, T. 2008. Engineering Expression of the ClinConc model for prediction of free and total chloride ingress in submerged marine concrete. *Cement and Concrete Research*. 38:1092–1097.

Oslakovic, I.S, Bjegovic, D. & Mikulic, D. 2010. Evaluation of service life design models on concrete structures exposed to marine environment', *Materials and Structures.* 43:1397–1412.

Ozbolt, J. Balabanic, G. Periskic, G. & Kuster, M. 2010. Modelling the effect of damage on transport processes in concrete. *Construction and Building Materials*. 24:1638–48.

Papadakis, V.G. Fardis, M.N. & Vayenas, C.G. 1996. Physicochemical Processes and Mathematical Modeling of Concrete Chlorination", *Chem. Engng Sci.*, 51(4):505.

Tang, L. Nilsson, L.O. & Basheer, P.A.M. 2012. *Resistance of Concrete to Chloride Ingress: Testing and modeling*. Spon Press, New York, USA.

Tuutti, K. 1982. *Corrosion of steel in concrete*. CBI Forskning.



Taylor & Francis
Taylor & Francis Group
http://taylorandfrancis.com

Concrete Solutions – Grantham et al. (Eds.)
© 2016 Taylor & Francis Group, London, ISBN 978-1-138-03008-4

Service life estimation of cracked and healed concrete in marine environment

M. Maes & N. De Belie
Magnel Laboratory for Concrete Research, Ghent University, Belgium

ABSTRACT: In the aggressive seawater environment, the durability of concrete is strongly influenced by the presence of chlorides and sulfates. Marine structures mostly have an important social function with a high economic impact, which makes durability a key issue. In addition, early-age cracks are a common problem, specifically for massive structural components. Repair of cracks is expensive and often impossible due to inaccessibility. Self-healing concrete is a promising solution to make marine structures more durable. In this study, capsules containing Polyurethane (PU) prepolymers were embedded in the concrete to release their contents when cracks appear. In cracked mortar, the chloride diffusion coefficients in the zone immediately around the crack significantly increased compared to uncracked mortar. The crack width dependency could be introduced into the service life model using a crack effect function. For crack widths in the range of 100 μm to 300 μm a service life decrease of around 80% was calculated. Autonomous crack healing had a beneficial influence on the resistance against chloride diffusion. However, for about one third of the cracks the healing mechanism failed, probably due to shifting of the tubes, tubes not rupturing properly, too high capillary forces in the tubes, etc. Nevertheless, on average, the service life of autonomously healed structures by means of encapsulated polyurethane increased with around 100% compared to cracked, unhealed structures. Moreover, in the most beneficial situation of proper healing, a service life increase of 150–550% was obtained, reaching values similar as for sound structures.

1 INTRODUCTION

A lot of deterioration is reported for constructions in marine environments. In this aggressive environment, the durability of concrete is strongly influenced by the presence of chlorides and sulfates, the main components of sea water. On the one hand, sulfate attack will degrade the concrete directly by forming expansive reaction products as well as strength decreasing products. On the other hand, chlorides will attack the concrete indirectly, by initiating corrosion of the reinforcement steel. In addition, concrete has a high sensitivity to crack formation because of its low tensile strength. That is why reinforcement is used in concrete to carry the tensile loads. Reinforced concrete has an increased resistance to cracking but does not eliminate it. This means that when cracks appear in concrete structures, aggressive substances like chlorides and sulfates may penetrate faster into the concrete and as a consequence faster deterioration can result. According to the standard NBN EN 1992-1-1 (2010), the allowable crack width in reinforced concrete structures depends on the environmental class and is in the range of 300 μm to 400 μm. However, according to Ismail et al. (2008) crack widths of 200 μm and wider allow unlimited chloride diffusion perpendicular to the crack faces. Djerbi et al. (2008) and Audenaert et al. (2009) found a bilinear relation between the chloride migration coefficient and the crack width. For crack widths between 0 μm and 100 μm, the migration coefficient increased with increasing crack width, and for crack widths between 100 μm and 200 μm this increase was less clear and the migration was rather constant. On the other hand, Sahmaran (2007) concluded that when the crack width increases, the diffusion coefficient increases as well, and this effect was even more distinct when the crack width was larger than 135 μm. Similarly, Kwon et al. (2009) found for on-site drilled cores that chloride diffusion coefficients kept increasing with crack widths up to 300 μm. Furthermore, apparent diffusion coefficients calculated by Mu (2012) show rising values with increasing crack width from 0 μm to 450 μm, and only when the crack width exceeded 450 μm, did the diffusion coefficient remain constant. In addition, his results indicate that concrete cracking accelerates chloride diffusion and steeply reduces the time to de-passivation of the reinforcement. Besides, the crack density had more significant influences on the de-passivation time of rebars than the crack depth, which was in turn more important than the crack width.

A possible solution to prevent maintenance and repair is self-healing of cracks in concrete (Van Tittelboom and De Belie, 2013, Van Tittelboom et al., 2011). Self-healing concrete has the ability to recover without external intervention. Nevertheless, specific data on degradation of self-healing concrete in aggressive environments are only sparsely available. These

data are important to prove that an important service life extension of structures and concomitantly reduced repair and maintenance can be achieved by applying self-healing concrete.

2 MATERIALS AND METHODS

2.1 *Healing agent*

A commercially available polyurethane healing agent from BASF was used. One component of the two component agent consisted of a prepolymer of polyurethane (PU) which starts foaming in moist surroundings. The second component consisted of a mixture of 10% accelerator and distilled water. The expanding reaction of this healing agent may lead to an increase in volume of 25 to 30 times. This reaction is the driving force for the healing agent to flow out of the capsules. So, the additional volume created by the cracks may be filled up.

2.2 *Capsules with healing agent*

In order to carry the healing agent and to trigger the healing action upon crack appearance, tubular glass capsules were used for proof-of-concept, similar to the capsules used by (Van Tittelboom et al., 2011). Due to their high brittleness, the tubes will easily break whenever cracks appear in the mortar matrix. Borosilicate glass tubes with an internal diameter of 3 mm, an outer diameter of 3.35 mm and a length of 35 mm were used. It should be noted that polymeric tubes that can survive concrete mixing and yet release their contents upon crack formation, are currently under development.

First, the tubes were sealed with polymethylmethacrylate at one end. Then half of the tubes were filled with the prepolymer and the other half was filled with a mixture of accelerator and water, through injection by means of a syringe. Afterwards, the open ends were sealed as well.

2.3 *Samples with(out) self-healing properties*

Cylindrical PVC moulds with a height of 50 mm and an inner diameter of 100 mm were used to produce all of the specimens. These moulds were clamped on a wooden plate in order to prevent leakage of concrete and mortar at the bottom. For the self-healing mortar samples (coded PU), nylon wires were attached to the PVC moulds and the capsules were glued on them by means of a droplet of MMA in order to prevent the capsules from floating during casting. Six capsules were equally divided along the diameter over two layers, at 12.5 mm and 37.5 mm height. First, a 20 mm mortar layer was brought into the moulds. When this layer was compacted on a vibration table, the moulds were completely filled with mortar and vibrated again. The mortar was prepared with Ordinary Portland Cement CEM I 52.5 N, a sand 0/4 over cement ratio of 3/1 and a water/cement ratio of 0.45. The reference samples without self-healing properties (uncracked – coded REF; cracked – coded CR) were prepared in the same way as described above, however, samples belonging to these series contained no glass tubes. After casting, the specimens were placed in an air-conditioned room with a temperature of 20°C and a relative humidity of at least 95%. Demoulding took place the next day whereupon the specimens were stored again under the same conditions until the age of 21 days. Then, the specimens were coated with epoxy at the sides. This coating acted as a kind of reinforcement during crack formation. The coating was allowed to harden for 3 days under laboratory conditions.

2.4 *Crack formation and healing*

Realistic cracks of 100, 200 or 300 μm were produced by means of a crack width controlled splitting test. The embedded tubes broke during crack formation and both components of the healing agent were released into the crack due to capillary forces. Upon contact of both components, PU foam was formed, resulting in crack healing. The polymerization reaction is usually complete within one day. After crack formation, the outermost 5 mm (casting surface) was cut off. Then, the specimens were coated again except for the test surface. Before immersion in the test solutions, the crack widths were measured microscopically.

2.5 *Chloride diffusion tests*

The resistance to chloride penetration of reference and autonomously healed mortar samples, was evaluated experimentally using the diffusion test as described in (NT Build 443, 1995). For every test series, at least 9 specimens were tested of which at least 3 were used for obtaining chloride profiles. At the age of 28 days, the coated specimens were placed in a 4 g/l $Ca(OH)_2$ solution for 7 days. Afterwards, the specimens were placed in a closed container with a 165 g/l NaCl solution.

After 7 weeks storage in the test solution, the specimens were split orthogonal to the crack and the chloride penetration was visualized by spraying 0.1 Mol/l $AgNO_3$ on both halves of the split specimens. Next, total chloride profiles were obtained by means of potentiometric titration (Maes, 2015). To do so, powder was collected by grinding layers of 2 mm thickness up to a depth of 20 mm. Powder was first collected in a zone of 18×75 mm^2 with the crack in the middle (coded C); afterwards, powder was collected from separated zones of 28.5×75 mm^2 both 9 mm away from the crack (coded R) (Figure 1). As such, the total ground surface had a diameter of 75 mm.

Non-steady-state diffusion coefficients and chloride surface concentrations were obtained by fitting Equation 1.

$$C(x,t) = C_s - (C_s - C_i)\mathrm{erf}\left(\frac{x}{\sqrt{4D_{nssd}t}}\right) \quad (1)$$

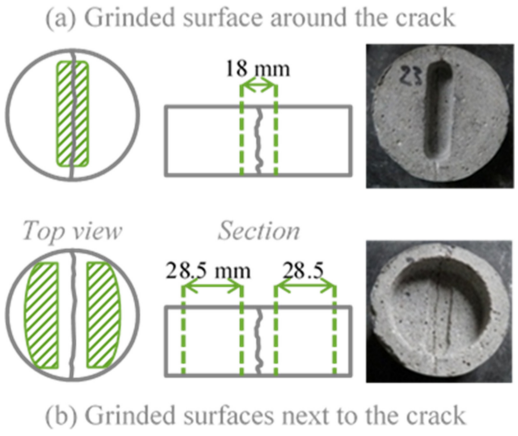

Figure 1. Grinding method to collect powder around the crack (a) and next to the crack (b).

where $C(x,t)$ is the chloride concentration at depth x and time t (mass % concrete), C_i the initial chloride concentration (mass % concrete), C_s the chloride concentration at the surface (mass % concrete), D_{nssd} the non-steady-state diffusion coefficient (m^2/s), x the distance from the surface until the middle of the considered layer (m) and t the exposure time (s).

It is reasonable to assume that the initial chloride concentration C_i equaled 0% (in reality, this value can differ from 0% and in current research an average concentration of 0.15 ± 0.05 wt.% binder was found). The first layer was excluded from the regression analysis, since the measured chloride concentration in this layer is generally considered not representative.

3 RESULTS AND DISCUSSION

3.1 *Chloride penetration profiles*

Figure 2 shows the total chloride profiles for specimens with initial crack widths of 100 μm and 300 μm, respectively. Each profile is the average of three individual profiles and refitted with the obtained diffusion coefficient.

It is clear that the highest chloride concentrations at every depth are found in the 18 mm wide zone with the crack in the middle, regardless of the crack width. Next, it can be seen that in the zones further away from the healed cracks the profiles are comparable to chloride profiles obtained for uncracked mortar specimens (REF) which implies a limited chloride penetration perpendicular to the crack wall. In between these two profiles, the profiles obtained in the zone around the healed cracks are situated. So, based on these chloride profiles it seems that autonomous crack healing has a beneficial influence on the resistance against chloride penetration compared to cracked mortar. Note that the PU polymerization reaction occurs very fast (within one day) and the healing action could be considered as completed, before immersion of the

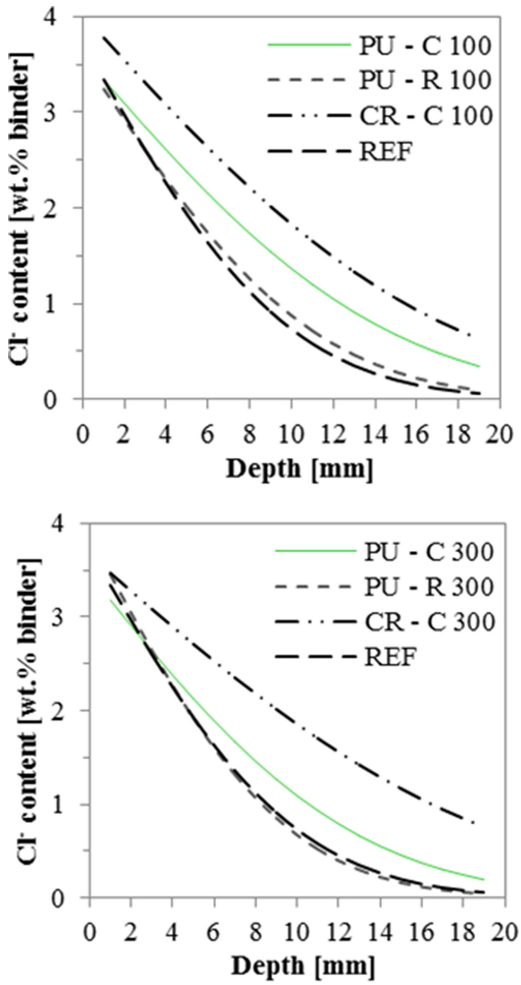

Figure 2. Average total chloride profiles around (C) and further away from (R) the cracks for healed (PU) and unhealed (CR) mortar specimens with an initial crack width of 100 μm (top) and 300 μm (bottom) and an uncracked reference (REF), obtained after 7 weeks immersion in NaCl solution.

specimens in the chloride solution. Nevertheless, the chloride concentrations are higher than in uncracked mortar.

To study the efficiency of the healing mechanism itself the individual chloride profiles per specimen are shown in figure 3.

It can be seen that for none of the three tested specimens was a similar profile measured. For specimens with a 100 μm crack only one of the three tested specimens was (almost) totally healed (PU – C 3) while one showed no healing at all (PU – C 1). The other specimen (PU – C 2) showed a chloride profile similar to the average profile in Figure 2, namely in between healed and unhealed. The same trends were found for initial crack widths of 200 μm and 300 μm.

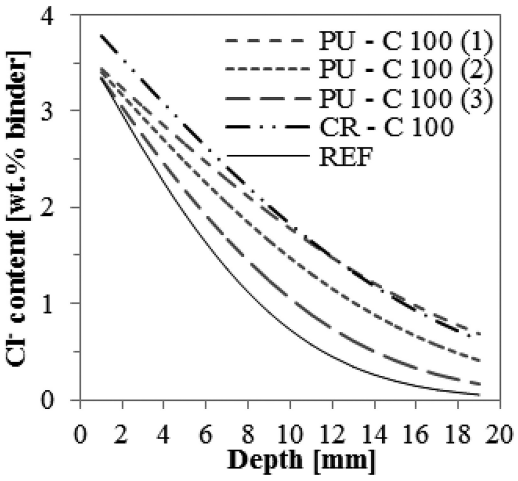

Figure 3. Individual total chloride profiles around the crack for autonomously healed mortar specimens with an initial crack width of 100 μm, after 7 weeks immersion in NaCl solution.

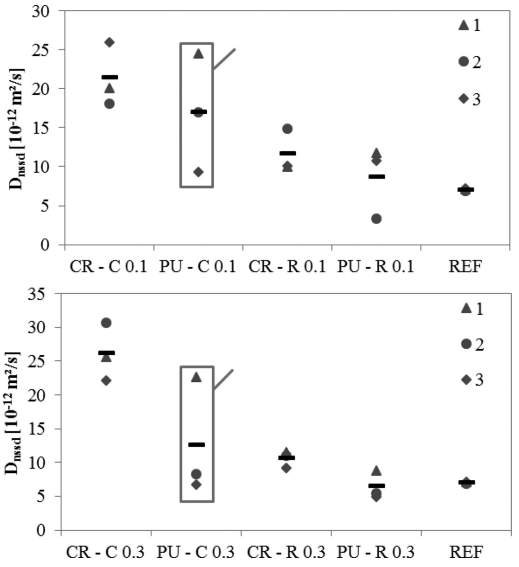

Figure 4. Total chloride diffusion coefficients in different zones around (C) or further away from (R) a 100 μm (top) or 300 μm (bottom) crack, after 7 weeks immersion in a 165 g/l NaCl solution. With indication of individual and mean values.

3.2 *Chloride diffusion coefficients*

Figure 4 gives the individual total chloride diffusion coefficients with an indication of the mean value per test series.

In general, regardless of the crack widths, the average diffusion coefficients in the zone around a PU-healed crack are lower than the diffusion coefficients in the zone around an unhealed crack, indicating the beneficial influence of PU-crack healing. In addition, based on the statistical analysis (Student-Newman-Keuls test with level of significance = 0.05), it seems that the diffusion coefficients obtained for healed mortar with initial crack widths of 100 μm are not significantly different from the diffusion coefficients obtained for healed mortar with initial crack widths of 300 μm. Furthermore, it is clear from the statistical analysis that none of the chloride diffusion coefficients measured around a 100 μm healed crack or a 300 μm healed crack are significantly different from the reference diffusion coefficients in uncracked mortar.

From Figure 4, it can also be observed that the scatter on the diffusion coefficients measured around the PU-healed cracks is clearly larger than those on the other diffusion coefficients. This was also clear from the individual chloride profiles and can be explained by the fact that only a part of the PU-healed cracks are really sealed. The latter is probably due to falling short of the healing mechanism rather than the fact that chlorides penetrate through the PU-foam which should fill up the crack. During a visual inspection of the specimens and the glass tubes after splitting, it was observed that in the autonomously healed specimens without improved resistance against chloride penetration, the healing agents were still (partially) in the tubes, maybe due to the higher capillary forces in the capsules than in the cracks. Furthermore, some tubes may have shifted if not properly fixed, which could explain why the PU-prepolymer did not react with the accelerator causing a fast foaming reaction. Also in some cases, crack formation may not trigger the healing mechanism.

4 SERVICE LIFE ESTIMATION

To evaluate the influence of autonomous crack healing in concrete/mortar in a quantitative way, the service life prolongation is estimated with regard of the service life for cracked structures. To do so, a full probabilistic design approach is used.

4.1 *Apparent chloride diffusion coefficient*

The apparent chloride diffusion coefficient is calculated starting from the diffusion coefficient obtained by means of curve fitting based on Equation 1. These coefficients are tabulated in Table 1. Remark that the unit of the calculated diffusion coefficients is mm^2/year ($=31.54 \times 10^{-12}$ m^2/s).

Concerning the chloride diffusion coefficient for autonomously healed mortar in the zone around the crack (PU-C), a mean value can be calculated regardless of the crack width. This mean chloride diffusion coefficient amounts to 447 ± 219 mm^2/year. Furthermore, the influence of autonomous crack healing will also be taken into account by means of the minimum and maximum calculated values per initial crack width.

On the other hand, the chloride diffusion coefficient for unhealed samples (CR-C) changes (to a limited

Table 1. Chloride diffusion coefficients for cracked (CR-C) and autonomously healed (PU-C) OPC mortar, after 7 weeks immersion in a 165 g/l solution.

D_{nssd}	100 μm		200 μm		300 μm		
[mm²/yr]	CR-C	PU-C	CR-C	PU-C	CR-C	PU-C	REF
Min.	572	327	662	189	762	213	215
Max.	758	776	757	599	903	716	226
Mean	654	546	704	400	824	396	222
St dev	95	224	48	205	72	278	5

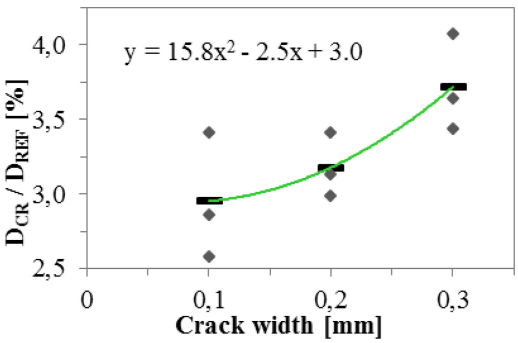

Figure 5. Relation between chloride diffusion ratio (coefficient for cracked mortar/coefficient for uncracked mortar) and crack width.

extent) in function of the crack width '*w*'. So, a crack effect function is suggested based on a regression analysis as shown in Figure 5.

This crack effect function is implemented in the equation to calculate the apparent chloride diffusion coefficient by means of the parameter k_{cr}. So in this particular case, the apparent chloride diffusion coefficient can be calculated from equations (2) to (5).

$$D_{app,C} = k_e \cdot D_{nssd,REF} \cdot k_t \cdot W(t) \cdot k_{CR} \quad (2)$$

$$k_e = \left(b_e \left(\frac{1}{T_{ref}} - \frac{1}{T_{real}} \right) \right) \quad (3)$$

$$W(t) = \left(\frac{t_0}{t} \right)^a \quad (4)$$

$$k_{CR} = 15.8\, w^2 - 2.5\, w + 3.0 \quad (0.1\ \text{mm} \le w \le 0.3\ \text{mm}) \quad (5)$$

with the apparent chloride diffusion coefficient D_{app} (mm²/years) calculated starting from the chloride diffusion coefficient for uncracked mortar $D_{nssd,REF}$ (mm²/years) taking into account a transfer parameter k_t (–), an ageing function W(t) with the ageing exponent a (–), the reference point of time t_0 (years) and the time t (years), an environmental factor k_e (–) including a regression variable b_e (K) as well as the standard test temperature T_{ref} (K), the temperature of the structural element or the ambient temperature T_{real} (K), and at last a crack effect function k_{CR} (–) with the crack width w (mm).

Table 2. Default input parameters for service life prediction.

Parameter		Mean	St. Dev.	Lower bound	Upper bound
C_{crit} [wt%]	Beta	1.90	0.15	0.2	3
C_0 [wt%]	Normal	0.10	0.025	–	–
$C_{s,\Delta x}$ [wt%]	Normal	3.0	0.8	–	–
d [mm]	Lognorm	60	8	–	–
Δx [mm]	Constant	0	–	–	–
b_e [K]	Normal	4800	700	–	–
T_{ref} [K]	Constant	293		–	–
T_{real} [K]	Normal	293	5	–	–
$D_{nssd,REF}$ [mm²/year]	Normal	Table 1 (REF)			
k_t [–]	Constant	1	–	–	–
t_0 [year]	Constant	0.211 (28 days curing + 49 days immersion)			
a [–]	Beta	0.40	0.12	0	1
w [mm]	Constant	[0.1–0.3]	–	–	–

4.2 *Effect of crack width on service life*

The results of the service life prediction can vary a lot depending on the assumed values for the concrete cover, the critical chloride content, etc. In this paper the influence of these parameters on the specific service life is not discussed since the aim is to evaluate the effect of cracks in cementitious materials and the autonomous healing.

The default parameters as described in fib Bulletin 34, Duracrete or the CUR guideline VC 81 are taken into account, see Table 2, however some of them are adapted in order to have a reference service life of about 100 years. This is obtained by changing the concrete cover and the ageing factor in accordance with acceptable values found in literature (Van den Heede et al., 2014), 60 ± 8 mm and 0.40 ± 0.12, respectively. In addition, the crack effect function parameter k_{cr} is introduced in the model taking the crack width w into account.

The results considering the influence of crack widths between 100 and 300 μm (CR – xx) are shown in Figure 6. The curves indicating the probability of failure P_f in function of time for cracked cementitious materials are plotted against the same curve for sound material (REF). The end of service life corresponds to a probability of failure of 0.10. It is clear that the presence of cracks induces a significant service life reduction. The service life for structures decreases from 103 years for the uncracked situation to 23 years in case of cracks with a width of 100 μm, and 20 and 16 years for 200 and 300 μm wide cracks. The obtained values are in reasonable agreement with the results obtained by Kwon et al. (2009) for in-situ cracked concrete of port wharves which had been operated for 8 and 11 years.

It is furthermore described in literature that microcracks caused by service loads should be taken into

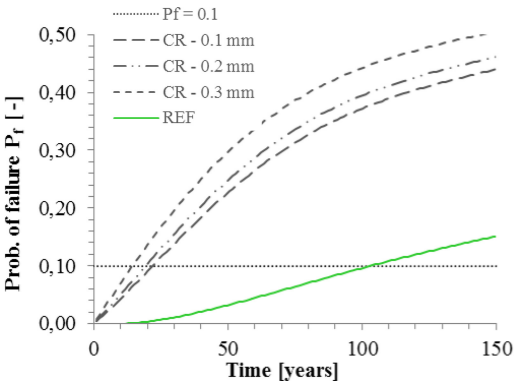

Figure 6. Service life prediction for cracked OPC mortar.

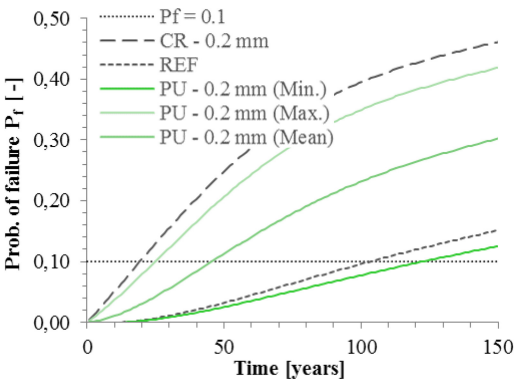

Figure 7. Service life of healed OPC mortar with initial crack width 200 μm.

account during service life prediction. The chloride migration coefficient of concrete under loading is different and can be significantly higher than that without loading. Concrete in aggressive environments with service loading of over 50% of the ultimate compressive stress can have a 2–4 times higher chloride migration coefficient compared to concrete without loading (Wang et al., 2016). However, when a permanent compressive load of 30% of the ultimate load is applied, the average diffusion coefficient decreased to about 70% of the diffusion coefficient for an non-loaded concrete at the same age (Egüez Alava et al., 2015).

4.3 *Effect of autonomous crack healing*

In order to report the effect of autonomous crack healing, different points of view are possible. Firstly, the averaged effect is studied based on the mean chloride diffusion coefficient for autonomously healed mortar, regardless of the initial crack width. This coefficient is used as an input parameter in the model without k_{CR}. Based on the averaged effect of autonomous healing, the service life is higher than for cracked mortar (Figure 7). Nevertheless, it is still clearly lower than the time to reinforcement depassivation in sound mortar. More specifically, the service life of healed mortar amounts to 32 years. This is an increase of 39%, 60% or 100% when compared to the service life for cracked mortar with crack widths of 100 μm, 200 μm and 300 μm, respectively.

So the averaged effect of autonomous crack healing by means of encapsulated PU is rather positive. To take the non-constant efficiency of autonomous crack healing into account, service lives were predicted for every initial crack width individually based on the maximum, minimum and mean measured chloride diffusion coefficient for healed mortar. Since the input parameter in the estimation of the service life for cracked mortar is an average value, it is possible that an estimation of healed mortar based on a single value results in a slightly lower service life. This is the case when the maximum measured value for the chloride diffusion coefficient in autonomously healed mortar with initial crack width 100 μm is considered, which leads to a service life of 17 years. On the other hand, the prediction based on the mean and the minimum observed value for autonomously healed mortar with initial crack width 100 μm results in a service life increase to 28 and 58 years respectively. In Figure 7 the probability of failure in function of the time for healed mortar with initial crack widths of 200 μm is visualised. The service life predicted based on the maximum measured chloride diffusion coefficient for autonomously healed mortar is equal to the service life for cracked mortar, namely 25 years. On the opposite, the calculation with the minimum measured coefficient leads to a service life of 122 years, equal to the one for sound mortar. In addition, the mean diffusion coefficient leads to 44 years.

Table 3. Increase of the service life for autonomously healed mortar predicted by means of the maximum, mean and minimum measured chloride diffusion coefficient and compared to cracked mortar.

Crack width [mm]	Service life increase compared to cracked mortar [%]			
	PU – Max.	PU – Mean	PU – Min.	REF
0.1	–26	22	154	348
0.2	25	120	510	415
0.3	19	181	550	544
Mean	6	108	405	436
St. Error	16	46	126	57

For autonomously healed mortar with initial crack widths of 300 μm, similar observations can be made. The predicted service lives amount to 19 years, 45 years and 104 years based on the maximum, the mean and the minimum measured chloride diffusion coefficients. Starting from the aforementioned results, relative differences are calculated compared to the cracked mortar. These increases and decreases are tabulated in Table 3.

It can be observed that almost all samples benefit from a service life increase through self-healing.

Except for the samples with initial crack widths of 100 μm, this relative increase seems independent of the initial crack width. In general, it can be concluded that in the worst case scenario, an average increase of 6% is obtained, assigned to autonomous healing. In the most beneficial situation an increase of 405% is obtained. On average, autonomous crack healing induces a service life increase of 108% compared to the case without healing. In practice, the effect of self-healing will have to be weighed against other options, such as the use of stainless steel in XS3 environments.

5 CONCLUSIONS

Chloride penetration increases when a mortar is cracked and there is a limited effect of the crack width (for cracks of 100 μm to 300 μm).

The chloride diffusion coefficients in the zone immediately around the crack (9 mm at each side) significantly increase compared to uncracked mortar. For crack widths in the range of 100 μm to 300 μm, the relation between the chloride diffusion coefficient ratio and the crack width can be expressed through a crack effect function (equation 5). Service life of mortar/concrete structures containing cracks decreases with 81% compared to sound structures. These conclusions indicate the need for a proper crack repair mechanism. One of the solutions is self-healing concrete/mortar by means of encapsulated polyurethane.

Autonomous crack healing of mortar by means of encapsulated polyurethane has a beneficial influence on the resistance against chloride diffusion. In the most beneficial situation, a service life increase of 154% up to 550% can be obtained by autonomous crack healing compared to cracked unhealed structures, leading to a service life similar to the one for sound structures. On average, the service life of autonomously healed structures by means of encapsulated polyurethane increases 108 ± 46% compared to the service life of a cracked, unhealed structure.

If the healing mechanism works properly and the crack is sealed well, (almost) no chlorides will penetrate along the crack. So, autonomous crack healing by means of encapsulated polyurethane is able to improve the durability and increase the service life of mortar/concrete structures in chloride-containing environments.

ACKNOWLEDGEMENTS

This research was funded by a Ph.D. grant for Mathias Maes of the Agency for Innovation by Science and Technology (IWT). Support by the Korea Agency for Infrastructure Technology Advancement is also gratefully acknowledged.

REFERENCES

Audenaert, K., De Schutter, G. & Marsavina, L. 2009. Influence of cracks and crack width on penetration depth of chlorides in concrete. *European Journal of Environmental and Civil Engineering*, 13: 561–572.

Djerbi, A., Bonnet, S., Khelidj, A. & Baroghel-Bouny, V. 2008. Influence of traversing crack on chloride diffusion into concrete. *Cement and Concrete Research*, 38: 877–883.

Egüez Alava, H., De Belie, N., De Schutter, G. 2015. The ingress of chlorides in concrete under compressive or tensile loads. *Proceedings of the 14th international congress on Chemistry of Cement (ICCC), 13-16 October 2015, Beijing.* p. 438 in abstract book, 7 p. paper on Proceedings CD.

Ismail, M., Toumi, A., Francois, R. & Gagne, R. 2008. Effect of crack opening on the local diffusion of chloride in cracked mortar samples. *Cement and Concrete Research*, 38: 1106–1111.

Kwon, S. J., Na, U. J., Park, S. S. & Jung, S. H. 2009. Service life prediction of concrete wharves with early-aged crack: Probabilistic approach for chloride diffusion. *Structural Safety*, 31: 75–83.

Maes, M. 2015. Combined effects of chlorides and sulfates on cracked and self-healing concrete in marine environments, PhD in Civil Engineering, Ghent University. ISBN: 978-90-8578-786-0.

Mu, S. 2012. Chloride Penetration and Service-Life Prediction of Cracked Self-Compacting Concrete. PhD Thesis, Ghent University.

Sahmaran, M. 2007. Effect of flexure induced transverse crack and self-healing on chloride diffusivity of reinforced mortar. *Journal of Materials Science*, 42: 9131–9136.

Van den Heede, P., Maes, M., De Belie, N. 2014. Influence of active crack width control on the chloride penetration resistance and global warming potential of slabs made with fly ash + silica fume concrete. *Construction and Building Materials*, 67: 74–80.

Van Tittelboom, K. & De Belie, N. 2013. Self-Healing in Cementitious Materials-A Review. *Materials*, 6: 2182–2217.

Van Tittelboom, K., De Belie, N., Van Loo, D. & Jacobs, P. 2011. Self-healing efficiency of cementitious materials containing tubular capsules filled with healing agent. *Cement & Concrete Composites*, 33: 497–505.

Wang, J., Basheer, P.A.M., Nanukuttan, S.V., Long, A.E., Bai, Y. 2016. Influence of service loading and the resulting micro-cracks on chloride resistance of concrete. *Construction and Building Materials*, 108: 56–66.



Taylor & Francis
Taylor & Francis Group
http://taylorandfrancis.com

Concrete Solutions – Grantham et al. (Eds.)
© 2016 Taylor & Francis Group, London, ISBN 978-1-138-03008-4

Propagation of pitting corrosion of steel in concrete: Conceptual models for local cross section loss

Rob B. Polder
TNO Technical Sciences, Delft, The Netherlands
Delft University of Technology, Civil Engineering and Geosciences, Delft, The Netherlands

Ueli M. Angst
ETH Zurich, Switzerland

Jose Pacheco
CTLgroup, Chicago, USA

Willy H.A. Peelen
TNO Technical Sciences, Delft, The Netherlands

ABSTRACT: Where exposed to an aggressive environment, concrete structures will develop reinforcement corrosion at some point in their life. Chloride ions from de-icing salt or sea water induce pitting corrosion. Local cross section reduction may occur relatively quickly and expansion due to corrosion products precipitating may crack and spall concrete cover and reduce steel-concrete bond. With the aging of the existing stock, questions arise about the effects of corrosion on their structural behaviour, safety and reliability. TNO has started a four-year programme to investigate this subject. One project concerns modelling of pitting corrosion from electrochemical principles, aimed at prediction of cross section loss with time and, in a next stage, corrosion product formation. Existing models for pitting corrosion are highly simplified and essentially two-dimensional, while pitting is clearly a three-dimensional phenomenon. The difference may have serious consequences for structural safety. New approaches are needed, including new conceptual models and addressing uncertainties on several levels. The paper presents some conceptual models for pitting corrosion and reports preliminary results of numerical (finite element) modelling of pitting corrosion, based on solving potential and current distributions and resulting in cross section loss as a function of time. Further work including experimental validation is foreseen.

Keywords: reinforcement corrosion, pitting, model, propagation

1 INTRODUCTION

Concrete structures exposed to aggressive environments may develop reinforcement corrosion at some point in their life. Chloride ions from de-icing salt use or sea water induce pitting corrosion (Bertolini et al. 2013). Local cross section reduction may occur relatively quickly after initiation and, at later stages, expansion due to precipitation of corrosion products may crack and spall the concrete cover and reduce steel-concrete bond. With the aging of the existing stock of e.g. bridges (Polder et al. 2012), questions arise about the effects of corrosion on structural behaviour, safety and reliability. TNO has started a four-year programme to investigate this subject. One project concerns modelling of pitting corrosion from electrochemical principles, aimed at prediction of cross section loss with time and, in a next stage, corrosion product formation. Existing models for pitting corrosion (Andrade & Alonso 2001, Andrade et al. 2001, Rodriguez et al. 1996) are highly simplified and essentially two-dimensional, while pitting corrosion is clearly a three-dimensional phenomenon; they also generally neglect time dependencies. These differences may have serious consequences for structural safety of corroding structures. New approaches are needed, including new conceptual models and addressing uncertainties on several levels. This paper intends to discuss conceptual models for pitting corrosion as a basis for numerical modelling in particular of cross section loss as a function of time. It draws amongst other things from studies on the early stages of pitting (Angst et al. 2011). However, the emphasis here is on well-developed pitting. In engineering practice, 10% diameter loss (20% cross section loss) is considered a "rule of thumb" boundary value for structural effects. Consequently, macroscopic pits of at least 1 mm in size will be considered.

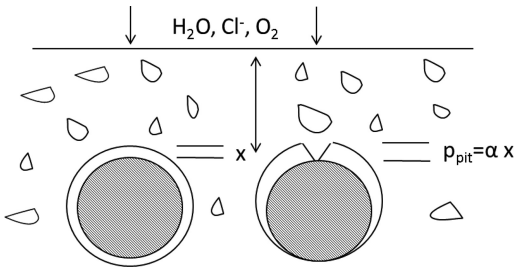

Figure 1. Essence of existing models for corrosion, left uniform, right localised (after Andrade & Alonso 2001, Andrade et al. 2001).

2 EXISTING MODELS FOR STEEL SECTIONAL LOSS DUE TO PITTING CORROSION IN CONCRETE

Existing models for pitting corrosion of steel reinforcement in concrete usually consider a cross section of a bar with a (V-shaped) pit, that becomes deeper over time proportional to the corrosion current (density), Figure 1 (right). Conceptually, this approach assumes that the metal loss has the form of a V- shaped groove along the bar (of undefined length). For a given amount of metal dissolved, a three-dimensional pit would be much deeper than the V-shape. Cross section (V-shape, 2D) models would underestimate local cross section loss and loss of structural capacity. This problem was recently addressed by Cao (2014), who suggested to model in 3D, Figure 2.

In addition, existing models use the concept of pitting factor, expressing the localised nature of corrosion. Essentially the pitting factor is the ratio of local penetration to uniform corrosion penetration across the entire metal surface, Figure 1 (right, α). The basis for pitting corrosion is the electrochemical process itself, providing some level of protection to cathodic areas surrounding an anodic site (pit). 2D (cross section) models only consider the circumference, so the pitting factor is limited to the ratio between the non-corroding and the corroding part of the perimeter, Figure 1 (right) and Figure 2 (top). In reality, much more cathodic surface along the rebar may sustain the anodic process, as shown in Figure 2 (bottom). As above, this simplification may underestimate the actual (local) corrosion penetration. Finally, none of the existing models for the prediction of the local loss of steel sectional area over time due to pitting corrosion are based on electrochemical mechanisms.

3 CONCEPTUAL APPROACH

3.1 *General considerations*

Pit growth rate in a rebar in concrete is determined by a 3D current and ion transport distribution. No symmetry planes or axis apply to this problem. Simplifying to 2D models therefore will lead to loss of geometric features which will affect calculated growth

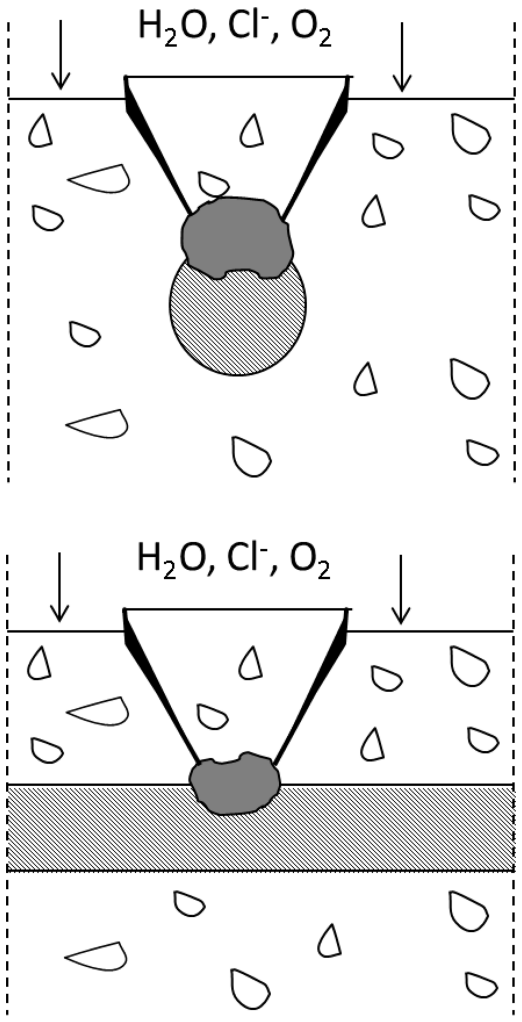

Figure 2. Views of localised corrosion in cross section (top) and along the bar (bottom) (after Cao 2014).

rates. Therefore, ideal models for pit growth of steel in concrete should be 3D; moreover, they should take into account (at least) polarisations (reaction kinetics), transport of Cl^-, OH^- and O_2 through the concrete cover, resistive effects and environmental influences (temperature, spatial and temporal moisture distribution) on all of these. Recent attempts in the TNO project showed that this was too ambitious to be incorporated in one go, and that different model setups should be devised to support a staged implementation from simple to elaborate. In the following, the approach is setting up a (small) series of models from simple to more complicated in order to determine which components are essential (and at what level of sophistication) and which can be simplified or missed.

3.2 *Basic model*

A very basic one-dimensional model is shown in Figure 3. In this model, the line A+C represents the metal

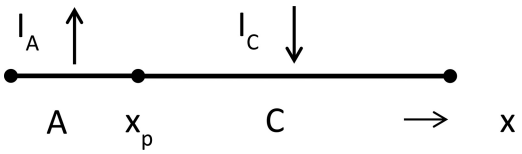

Figure 3. Conceptual model (1) for pitting corrosion of steel in concrete.

surface, A is the anodic part and C is the cathodic part; I_A the anodic current and I_C the cathodic current (which have equal magnitude but opposite sign). Here x_p is the "corrosion penetration" which is defined as the length of the line A divided by the total length of the line (A + C); x_p increases as a function of time, proportional to I_A.

Some rules can be thought to apply: $I_A = -I_C = I_{corr}$. If this current is assumed to be fully used to further oxidise the metal, x_p moves to the right proportional with I_{corr} according to $\Delta\, x_p = K^* I_A$. K expresses the relation between current and metal dissolution (some form of Faraday's law). If we assume that no cathodic process takes place in the anodic area, then corrosion will stop when it has extended over the complete surface because no more cathodic area is available. This is obviously oversimplified, as in real structures there will always be cathodic area available. Consequently, it is important to include cathodic surfaces in a realistic manner (e.g. depending on geometry and resistive effects). In addition, this model is certainly not fitting for uniform corrosion, e.g. due to carbonation, where anodic and cathodic processes take place with an equal distribution over the surface area. Summarising, this "first stage" model contains essential elements, but using it will produce unrealistic results. A more sophisticated model is needed.

3.3 *2D model*

In a next stage the model is set up in 2 dimensions and some more parameters are introduced, as shown in Figure 4. Domains are electrolyte E, pit P and metal M. A few observations can be made.

1. The pit domain P can grow in the x or (negative) y directions or both, producing either a shallow or a bell shaped pit, forms which both appear to occur in the field. As a side note, the difference between shallow or deep pitting will have consequences for structural behaviour. Proper documentation of pitting forms and understanding of the factors involved seems to be lacking and requires further study. Here, the simplest assumption would be to allow pit growth in both x and y directions. For a more sophisticated approach see item 6.
2. Spatial effects can be introduced by assigning a conductivity ó less than infinite or a resistivity above zero to domain E for ohmic control; generally the conductivity of steel can be assumed infinite. As the current through E experiences ohmic drop, the local cathodic current density will depend on x. Realistic resistivity values are available (COST 509 1997, Polder et al. 2000, Polder 2001), that depend on concrete composition (cement type) and environmental influences (temperature, wetting).
3. The spatial current distribution along C will also be affected electrochemically by the voltage drop across the steel/concrete interface, i.e. electrode polarisation. This may be represented by a linear polarisation resistance (Raupach & Gulikers 2006) or using a non-linear Butler-Volmer type approach (Redaelli et al. 2006, Angst et al. 2011, Isgor & Razaqpur 2006, Kranc & Sagues 1997, Brem 2004, Warkus 2012). Non-linear modelling should be preferred as potentials will likely be outside the linear range. With input values from literature, spatial effects and electrochemical kinetics can be modelled realistically.
4. Kinetics can also be introduced by realising that I_A is carried by ions, in particular ferrous, chloride, and hydroxyl ions (sodium and potassium can be neglected). The total ionic flow may control the current, which is one aspect of resistive control, either overall or specifically in the anodic region (Glass et al. 1991). The relative transport rates of chloride and hydroxyl affect the pH in the pit, and decide on its continued growth or extinction (repassivation) (Angst et al. 2011, Polder 2009). In addition, it should be realised that hydroxyl ions entering the pit will be consumed by reaction with Fe^{2+}, while chloride ions accumulate and may build up high concentrations (Isgor 2015, Polder & Geiker 2015). These mass transport related influences on the corrosion kinetics may be modelled with sets of Nernst-Planck or similar equations that account for diffusion and migration processes.
5. Another factor regarding kinetics is that oxygen should enter the system as cathodic reactant. Oxygen transport from outside through E and/or its activation polarisation may control the cathodic process. Realistic modelling of this effect would require reliable data on oxygen transport and reaction rate as a function of moisture content, which do not seem to be abundant (Papadakis et al. 1991).
6. Realistic pit form modelling would have its shape controlled by transport inside the pit, e.g. diffusion of dissolved metal ions from the reactive surface to the interface with the electrolyte E (Scheiner & Hellmich 2007, Galvele 1967).

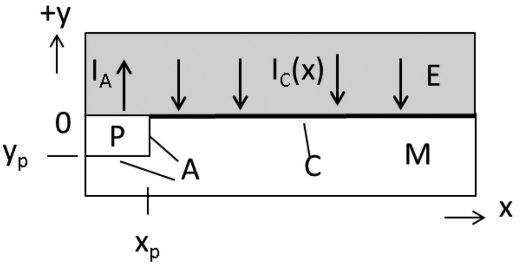

Figure 4. Conceptual model (2) for pitting corrosion of steel in concrete.

Time dependency deserves some attention here. As the pit grows, the effective anode/cathode ratio will become smaller, because the effective cathode surface area is controlled by resistive effects (roughly remaining constant) while the anodic areas grows (though depending on pit shape, see item 6). The anodic current density will decrease (as anode surface area increases). However, the total anodic current and thus the overall metal dissolution rate will roughly remain constant. This may provide a basis for model validation based on "corrosion rate" measurement, e.g. by linear polarisation resistance.

In fact, this model contains many of the parameters that are believed to control corrosion in reality. Others have previously modelled localised corrosion based on similar parameters (Kranc and Sagüés 1997). However, even less parameters than the ones mentioned appeared to be a challenge for our first attempts at 3D modelling. Consequently, it is proposed to use this 2D model. Geometrically, the 2D geometry can be "rotated" along the lower boundary of Figure 4 to form a 3D shape (utilizing radial symmetry); the "pit" will appear like a ring shaped notch cut out of a steel cylinder, with the remaining surface acting as cathode. Although not highly simplified and less than perfect, this seems more correct than a V-shaped groove along the bar that results from the 2D cross section model in Figure 1. For a given amount of metal loss, predicting the effect on structural capacity using the "ring notch" model will be more representative of actual behaviour than using the "cross section V shape" model. It may be useful to start using this model, including resistive and polarisation effects (items 2 and 3), and for the time being neglecting other effects (items 4, 5 and 6).

4 PRELIMINARY RESULTS

In the 2015 work carried out, a 2D cross section model was simulated in finite element package COMSOL Multphysics. In a first attempt, anodic and cathodic potentials were fixed. In 2D, calculations were made up to 80 years. Figure 5 gives an impression of pit development from 1 to 80 years. The Figure should be taken indicatively; colours indicate potentials (see explanation in caption). The small tip in the centre of the pit bottom is a numerical artefact. Calculated pit depths and approximate corrosion rates are shown in Table 1. The corrosion rate appears to be relatively stable, which is as expected when the driving voltage is held constant and only the geometrical influence can play a role.

5 CONCLUSIONS AND OUTLOOK

Realistic modelling of local steel sectional loss over time due to pitting corrosion for assessing structural effects requires at least a realistic approach to pit geometry. Presently existing models seem to lack that quality. Their cross section approach produces a

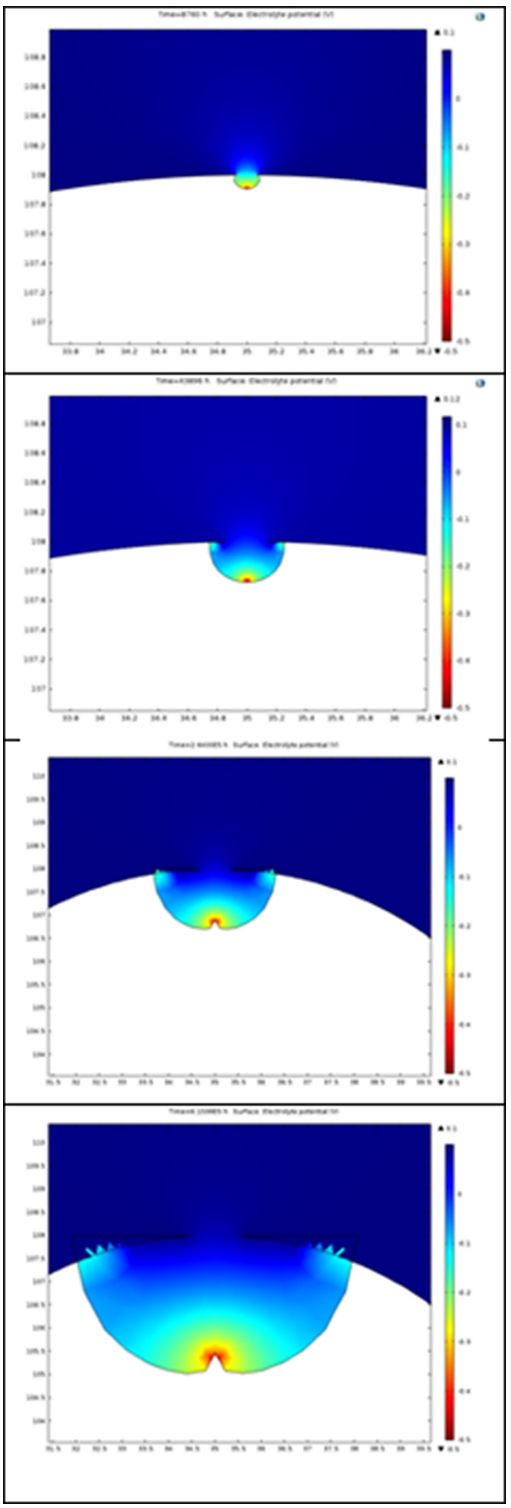

Figure 5. 2D pit growth simulations over time, from top to bottom: 1 year, 5 year, 30 year, 80 year; field of view 5 by 8 mm, colours indicate potentials: dark blue (top of figure) c. + 0,.1 V, deep red (bottom of pit) c. −0.5 V.

Table 1. Pit depths and approximate corrosion rates calculated by 2D modelling.

Simulation time, years	Pit depth (mm)	Approximate corrosion rate (μm/year)
5	0.2	40
30	1.1	36
80	2.5	32

V-shaped groove along a rebar, which may result in underestimation of loss of structural capacity. As a first attempt at 2D modelling it is proposed to implement radial symmetry along the long rebar axis, producing a pit in the form of a ring shaped notch. Numerical modelling based on electrochemical principles appears a promising approach. Factors involved have been identified, with most required parameters being available from literature. Future work will be directed at including the essential parameters and validation from experimental work.

REFERENCES

Andrade, C & Alonso M.C., 2001. On-site measurements of corrosion rate of reinforcements, Construction and Building Materials 15, 141–145.

Andrade, C., Rodriguez, J., Ortega, L., Casal, J. 2001. CONTECVET IN309021 A validated users manual for assessing the residual life of concrete structures, IETcc, GEOCISA.

Angst, U., Elsener, B., Larsen, C.K., Vennesland, Ø. 2011. Chloride induced reinforcement corrosion: Rate limiting step of early pitting corrosion. Electrochimica Acta, 56, 5877–5889.

Bertolini, L., Elsener, B., Pedeferri, P., Redaelli, E., Polder, R.B. 2013. Corrosion of Steel in Concrete: Prevention, Diagnosis, Repair, 2nd Edition, Wiley-VCH Verlag GmbH & Co. KGaA, Weinheim, ISBN 3-527-33146-8, 414 pp.

Brem, M. 2004. PhD thesis, ETH Zurich.

Cao, C. & Cheung, M.M. 2014. Non-uniform rust expansion for chloride-induced pitting corrosion in RC structures. *Construction and Building Materials*, *51*, 75–81.

Cao, C. 2014. 3D simulation of localized steel corrosion in chloride contaminated reinforced concrete. *Construction and Building Materials*,*72*, 434–443.

COST 509 1997. Corrosion and protection of metals in contact with concrete, Final report, Eds. R.N. Cox, R. Cigna, O. Vennesland, T. Valente, European Commission, Directorate General Science, Research and Development, Brussels, EUR 17608 EN, ISBN 92-828-0252-3, 148 pp.

Galvele J.R. 1967. Transport processes and the Mechanism of Pitting of Metals, J. Electrochem. Soc. 123, 464–474.

Glass, G.K., Page, C.L., Short, N.R. 1991. Factors affecting the corrosion rate of steel in carbonated mortars, Corrosion Science, 32, 1283–1294.

Gulikers, J. & Raupach, M. 2006. Numerical models for the propagation period of reinforcement corrosion – Comparison of a case study calculated by different researchers, Materials and Corrosion, 57 (8), 618–627.

Isgor, B. 2015. Personal communication in RILEM TC SCI, November 26, Zurich

Isgor O.B. & Razaqpur A.G. 2006. Modelling steel corrosion in concrete structures, Materials and Structures, 39, 291–302.

Kranc S.C. & Sagüés A.A. 1997. Modeling the time-dependent response to external polarization of a corrosion macrocell on steel in concrete, J. Electrochem. Soc. 144, 2643–2652.

Papadakis, V., Vayenas, C.G., Fardis, M.N. 1991. Fundamental modeling and experimental investigation of concrete carbonation, ACI Materials Journal 88(4) 363–373.

Polder, R.B., Geiker, M.R.. 2015., Electro Active Repair of concrete for improved durability of conventional repair, Proc. 4th Int. Conf. Concrete Repair, Rehabilitation and Retrofitting (ICCRRR), Eds. F. Dehn, H.-D. Beushausen, M.G. Alexander, P. Moyo

Polder, R.B., Peelen, W.H.A., Courage, W.M.G. 2012. Non-traditional assessment and maintenance methods for aging concrete structures – Technical and non-technical issues, Materials and Corrosion, Vol. 63 (12), 1147–1153

Polder, R., Andrade, C., Elsener, B., Vennesland. Ø., Gulikers, J., Weidert, R., Raupach, M. 2000. Draft RILEM Technical Recommendation Test methods for on site measurement of resistivity of concrete, Materials and Structures, Vol. 33, 603–611.

Polder, R.B. 2001. Test methods for on site measurement of resistivity of concrete – A RILEM TC-154 Technical Recommendation, Construction and Building Materials, Vol. 15, no. 2–3, 125–132.

Redaelli, E., Bertolini, L., Peelen, W., Polder, R. 2006. FEM-models for the propagation of chloride induced reinforcement corrosion, Materials and Corrosion, Vol. 57, (8), 628–635.

Rodriguez, J., Ortega, L.M., Casal, J., Diez, J.M. 1996. Corrosion of reinforcement and service life of concrete structures, 7th Int. Conf. Durability of Building Materials and Components, Stockholm.

Scheiner, S. & Hellmich C. 2007. Stable pitting corrosion of stainless steel as diffusion-controlled dissolution process with a sharp moving electrode boundary, Corrosion Science, 49, 319–346.

Warkus J. 2012. Einfluss der Bauteilgeometrie auf die Korrosionsgeschwindigkeit von Stahl in Beton bei Makroelementbildung, PhD thesis, RWTH Aachen, Germany, 2012.



Taylor & Francis
Taylor & Francis Group
http://taylorandfrancis.com

Concrete Solutions – Grantham et al. (Eds.)
© 2016 Taylor & Francis Group, London, ISBN 978-1-138-03008-4

Influence of crack width on the initial corrosion of surfaces exposed to high chloride

M. Schneider, E. Baumgartner & P. Druml
Carintian University of Applied Sciences, Spittal d.D., Austria

F. Pruckner
Korupp GmbH, Twist, Germany

ABSTRACT: Civil engineers are faced with the problem of defining the limit of the crack widths in concrete structures, which should be as small as possible. Even more important is the durability of the concrete matrix, which is affected by the environmental influence. A limitation of the crack widths in reinforced concrete structures is given in EC 2. There, the maximum crack width for common exposure classes is set to 0.3 mm. For XC 1 a limitation of 0.4 mm crack width is accepted because in this case the crack width has no influence on the durability of the matrix. In structures with requirements for water impermeability (white tank), the limitation of the crack width is 0.1 – 0.2 mm. It seems that, according to this Standardization, a summary is allowed. "Crack widths from 0.1 – 0.2 mm may be visible for the human eye, but are in most cases completely harmless." In some fieldwork on a multi-storey car park, the measurement of the potential field shows important information about the correlation between crack width and contamination of chloride anions and the initial corrosion. Another example is an underground parking garage with very thin cracks, where the corrosion started one year after construction. For a well-adapted restoration of those damaged structures, analyzing and estimation of the corrosion potential inside the cracks are an important foundation. Using nondestructive measurement methods of potential field in the area of cracks is more and more important to understand the influence of crack width for highly exposed reinforced concrete structures. This paper develops the work with the non-destructive potential field method in the area of cracks and summarizes the influence of corrosion inside the cracks on the structure and the durability.

1 INTRODUCTION

1.1 *General overview about the topic*

One of the most discussed topics in the last years on the field of corrosion of reinforcement due to chloride contamination of concrete was the allowed crack width. The official literature is orientated by Standardization (Eurocode 2, 2010) and guidelines (Fingerloos & Mayer, 2010). Otherwise a hidden discussion paper is available; where the focus on the durability of a multi-storey car park is preferred (Raesch, 2013). For cracks in reinforced concrete structures, the European Standard Specification Eurocode 2 limits the maximum permissible crack widths to 0.3 mm, which is set for the most common exposure classes (DAfStb Guideline 525, 2010). For XC 1, the crack width limitation is set to 0.4 mm because in this case the crack width has no influence on the durability of the structure. In structures with requirements for water impermeability (white tank), the limitation of the crack width is 0.1 – 0.2 mm (DAfStb Guideline 555, 2006). According to Eurocode 2 the crack width is a mathematic function of probability. It depends on the crack width. During the design of reinforced structures, a valid crack size is calculated. Small cracks with a crack width lower than 0.1 mm have a probability of approximately 70 % quantile and cracks with a crack width of 0.3 mm have a probability of some 80-90 % quantile (Budnik, 2006), see figure 1 (Roos, 2009).

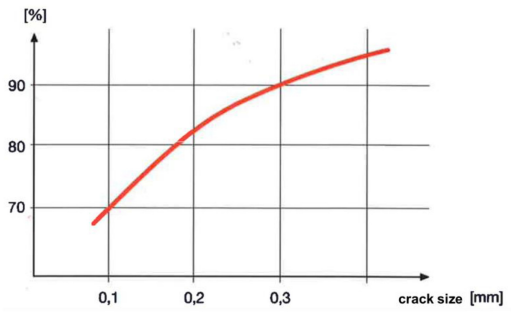

Figure 1. Frequency of occurrence during the estimation of the crack width.

The calculation of the crack sizes is not performed by the designer of the load bearing capacity, but is considered in the design for durability. At this point, it

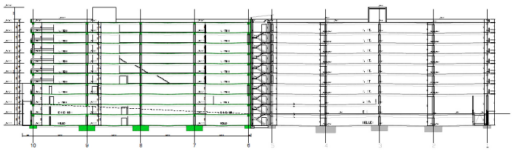

Figure 2. Levels of the car park.



Figure 3. Surface of one level.

should be noted that multi-storey car decks and ground bearing slabs are more or less influenced by early restraint during hydration of cement or late restraint during temperature change between winter and summer. The assumption of the type of restraint influences the amount of reinforcement (Meier, 2012).

The crack width is important for durability because once the crack appears, fluids can penetrate more easily. These fluids can be polluted by chloride. The penetration of fluids is relatively independent of the crack width before a naturally self-healing effect is started (Nikolaus, 2011). In multi-storey car park buildings and garages, the cracks should be covered with surface protection systems, which are based on acrylate, polyurethane or epoxy resin (Fingerloos & Mayer, 2010). But usually no cover is applied when the crack opening begins. Otherwise the repair of open cracks is very late or the structure is not in maintenance. For this situation it is important to know the influence of the crack width on the corrosion rate to understand the effects of an injection with resin to close the crack. Some current research shows a decrease of the corrosion rate when polyurethane resin is injected (Kosalla, 2014). The corrosion process does not stop completely and because of that, the present publication has a focus on the real corrosion situation in a common multi-storey car park building.

1.2 *Description of the practical analyzed project*

During an investigation of a multi-storey car park building some effects of corrosion could be measured on the surface, beams and columns of the decks and the ground bearing slab with different methods. One method was the ordinary measurement of chloride pollution due to multi- layer analysis in different drilled profiles. Adapted on this, a potential field measurement was used to find all zones of corrosion on the surface, beams and columns. The following pictures

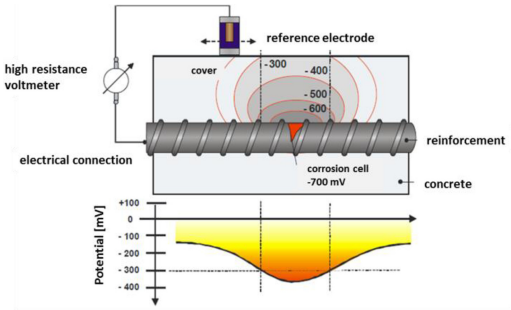

Figure 4. Schematic of the principle of potential field measurement.

are giving an overview about the dimensions of the multi-storey car park.

The surfaces, which should be tested, were level 0 (ground bearing slab), level 1, 3, 5 and 7. The examination was a part of an investigation for preparing and planning of the whole structure for a cathodic corrosion protection system.

2 ANALYSING THE STRUCTURE

2.1 *Theoretical background of the examination*

The structure was about 15 years old and the corrosion process had already started. The destruction of the reinforcement is different and it depends on the pollution with chloride anions. Parts of the structure also have corrosion processes due to carbonation of the portlandite in the cement paste. The pH value decreases to less than 11. From this point the passivation of the steel inside the concrete matrix is no longer provided. But the more important pollution of the structure was the contamination with chloride. The corrosion due to the influence of chloride starts normally by getting a corrosion initiating concentration. This value is interpreted very differently by a lot of experts. That is why the corrosion process is analyzed with a measurement of the half-cell potential field. With this method it is possible to analyze the corrosion development of the reinforcement in reinforced concrete members. It is possible to localize areas with high risk of corrosion due to a measuring of the chemical potential difference. During the measurement of the current electro-chemical potential on the contact zone of steel and concrete of the reinforcement, the potentials at the surface can be measured. The equipment is a high resistance voltmeter with a connection to the reinforcement and a reference electrode, see the following figure (Sodeikat, 2013).

During the continuous moving of the reference electrode on the surface of the structure, corrosion cells can be detected. In these areas high negative potentials are measured.

The electro-chemical potential can be measured by different kinds of electrodes. Usually a $Cu/CuSO_4$-electrode or Ag/AgCl-electrode are used. For this

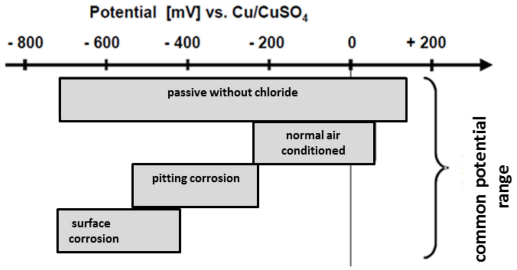

Figure 5. Common potential range.

Table 1. Areas of corrosion probability.

$Cu/CuSO_4$	corrosion probability
>-200 mV	low
>-200 mV to -350 mV	middle
<-350 mV	high
>-500 mV	very high

electrode a standard electrode potential is given which is then compared to the steel of the reinforcement. In those areas with high potential gradients the probability of corrosion is very high. But it is not successful to use a fixed parameter, see figure 5 (Kosalla, 2015).

In the passive state the potential areas of the reinforcement are different because it depends on a wide range of parameters. Because of that it is not possible to localize activated corrosion zones and passive corrosion zones. It is only possible to find probabilistic information of the real situation, see table 1.

The results are only probabilistic values about the corrosion. One method of supplementing this information to provide additional evidence for the risk of corrosion is an analysis of the chloride contamination at different depths of the concrete together with breaking out the concrete cover to allow visual inspection of the steel.

2.2 *Preparation of the potential field measurement*

Before the measurement starts, a lot of preparation work has to be done, e.g.:

- connection to the reinforcement
- remove all remains of surface protection systems and pollutions
- wetting of the surface
- check the continuity of the reinforcement

For common use, stick electrodes or wheel electrodes are usual.

2.3 *Adaption with measurement of chloride content*

The preparation of the samples for the analysis of chloride profiles is done by drilling powder samples or by slices of drilled cores from the structures, which are then powdered. For the homogenization of the depth of

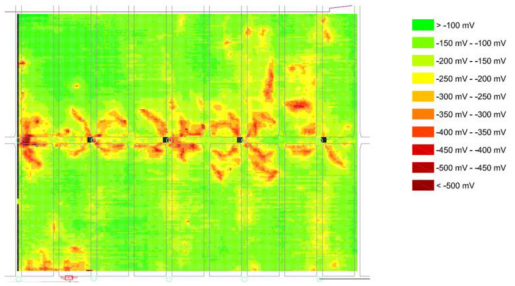

Figure 6. Result of the potential field measurement of the slab surface.

the profiles the separation is important. In this case an average of chloride content is measured in the area of the depth from the surface of the structure. The powder is typically extracted with dilute nitric acid. This is normally taken to indicate total chloride content. The quantification of the chloride content can be done by titration or photometric analysis. The validation of the chloride content differs in Standards and guidelines. The following list is giving a validation according to (OEBV Guideline, 2014):

- chloride content less than 0.6 % by mass related to the cement content of the concrete, no action is necessary, if it is possible to save the structure for furthermore pollution with chloride. But in this case no corrosion should be observed.
- between 0.6 and 1.0 % by mass of the cement content of the concrete and no corrosion is observed, monitoring can be installed in a period of 1 to 3 years
- chloride content more than 1.0 % by mass of the cement of the concrete and no corrosion is observed, a monitoring can be installed in a period of 1 year
- when the structure is built using pre-stressed concrete, the maximum chloride content should be less than 0.2 % by mass of cement of the concrete
- when the pH-value is less than 9.5, carbonation has occurred, the maximum chloride content is 0.2 % by mass of cement of the concrete and no corrosion is observed, monitoring can be installed in a period of 1 year

From this point of view, the real corrosion situation of the reinforcement is important. For a validation the surface has to be opened to examine the condition of the reinforcement.

3 RESULTS

3.1 *Potential field measurement*

In the present examination only selected areas of the structure were measured. The following figure shows the measurement of the surface on level 1.

It is observable that the most affected areas are around the columns and at the wall. The potential measured was between -300 mV up to -500 mV. The

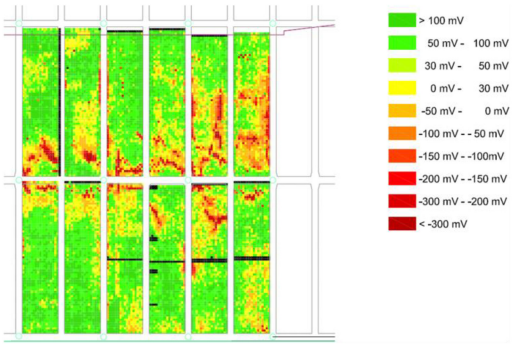

Figure 7. Result of the potential field measurement of the slab soffit.

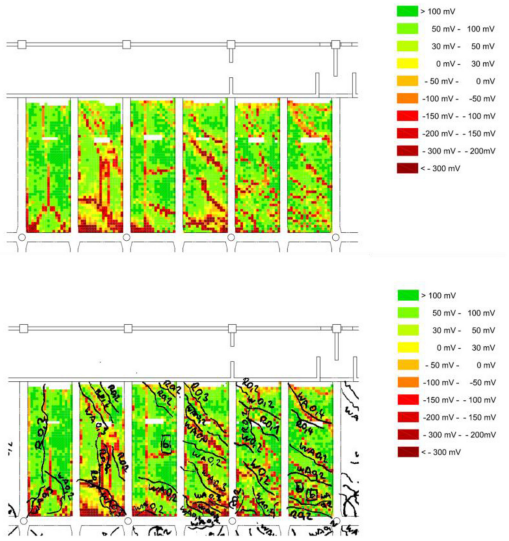

Figure 8. Result (exemplary) of the potential field measurement of the soffit with marks of cracks.

corrosion probability is very high in these zones. In the next figure the soffit area is shown.

The highest corrosion potential is also in the zones of the column between the beams. The next figure shows the potential field results with marks of the cracks in the area with the highest corrosion probability.

The correlation of the cracks to the zones with the highest corrosion probability is given. The measured crack widths were 0.1 mm to 0.3 mm. The measurement was in June 2013.

3.2 *Chloride content*

Table 2 shows the results of the chloride tests from level 1, where the results of potential field measurement were given in section 3.1. This adaption is important for analyzing the corrosion process inside the structure and for the interpretation of the corrosion probability

Table 2. Results of chloride content in % by mass of the cement content of the concrete.

Nom.	Depth 0 to 2 cm	Depth 2 to 4 cm	Depth 4 to 6 cm
P1 E1 B	0.31	0.09	0.03
P2 E1 B	0.08	0.02	0.01
P3 E1 B	0.12	0.08	0.05
P4 E1 B	0.87	0.42	0.52
P5 E1 B	0.93	0.69	0.23

according to the results of the potential field measurement. The results are given by mass % related to the cement content of the concrete. Often this information is not given by the tender documents. Because of that a factor by 10 usually is used for considering the worst case of the different cement contents if mass % related to concrete weight was measured.

Most of the chloride contents on the surface are in a critical range. In deeper layers the corrosion probability decreases.

The corrosion probability is usually very well related to the content of chloride. The next step is the analysis of the real situation of the reinforcement in the areas where a high potential of corrosion exists. During the examination some cores were drilled for analyzing the status of the corrosion and for determining the compressive strength. The cores were drilled in areas without cracks to get intact samples to measure the compressive strength. According to the results of chloride analysis and potential field measurements a high potential of corrosion was found but the corrosion status at the drilled cores was not extremely high. This behavior correlated very well with the information from the potential field, because in the intact zones of the deck a lower potential of corrosion was detected. The behavior in the cracked zones seems more interesting. In the zones of high potential differences, cracks occurred. In these areas corrosion was found by opening the surface.

4 EXAMPLE OF INITIAL CORROSION WITH THIN CRACKS

That the crack width is relatively independent for the corrosion of the reinforcement shows another example of an underground parking garage. The building was only 1 year in use. The ramp to the different levels has a high axial force during winter times. The inside temperature differences in the building between summer and winter are round about 30 K. The garage has 3 levels underground and the problems are in the first level near the gateway. The crack width was only 0.1 mm as maximum and the surface protection layer was made of epoxy resin.

Inside the cracks, the chloride content was examined in 3 cracks of the ramp, see Table 3.

Table 3. Results of chloride content in % by mass of the cement content of the concrete.

Nom.	Depth 0 to 2 cm	Depth 2 to 4 cm	Depth 4 to 6 cm
Crack 1	0.53	0.27	0.15
Crack 2	1.50	1.31	1.07
Crack 3	1.71	1.54	1.08



Figure 9. Exposed rebar showing local corrosion.

The chloride content is very high and the penetration is relatively deep. The crack size more than 0.1 mm doesn't lead to a significant reduction of the pollution. The results were higher than a maximum chloride content of 0.6 mass % of cement. The concrete was removed in the area, where the chloride is tested. The result of one example of excavation is shown in figure 9.

It seems that the pitting corrosion starts extremely fast when the maximum chloride content is met. The cross section of the reinforcement is not reduced but the change of the color at the surface of the reinforcement show an active corrosion zone.

5 ANALYSIS OF THE RESULTS

In cracks, the upper layer of reinforcement and the lower layer of reinforcement acting as cathode. Both corrosion cells must be eliminated. It was observed, that the potential results did not seem to vary with crack size, see figure 8. It seems that it is necessary to repair all cracks. As indicated by the potential results and that self healing of the crack had not completed.

One of the usual solutions is the covering of the surface by a surface protection system and to close the cracks with resin. The first results of (Kosalla, 2014) show, that a reduction of the corrosion process was observed. Another usual refurbishment is the application of a cathodic protection system. In this case it must be considered, that the most effect of the

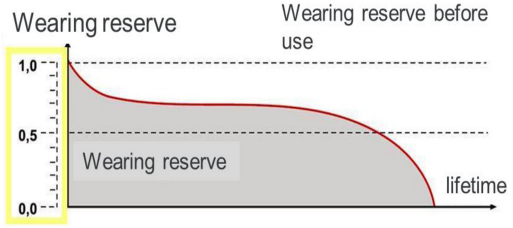

Figure 10. Function and substance of technical properties.

cathodic protection is to reach the upper layer of the reinforcement. This layer takes round about 85% of the protective current if the anode is on the surface. This is only a practical experience but it leads to a special handling for the protection of the lower layer of reinforcement. A cathodic protection coating can be used from the deck soffit or a separate cathodic protection system can be applied. The next possibility of refurbishment is the conservative method of replacement of the concrete; cleaning the reinforcement and patch repairing the area. This method can be used if the reinforcement has a high corrosion rate, which leads to a lower load bearing capacity level because of the reduced reinforcement cross section. By using that method of replacement, the area around the crack also has to be replaced. It is possible that the reinforcement is not bonded completely. Often the polluted water penetrated the crack and flowed longitudinal the reinforcement. A good solution to get the recommended bonding is the replacement of 50 cm right and left from the crack too. During the refurbishment the load bearing capacity of the structure is extremely reduced. An estimated support of the structure is necessary.

6 CONCLUSION

The examination and the discussion of the possibilities of the refurbishment of chloride initialized corrosion should open the focus on the situation of structures with high crack potential. In case of cracks the refurbishment is often more complex than in the areas without cracks. The Eurocode has a very good system to protect the structure by exposition classes of the concrete. The highest classes are XD3 (chloride ions taken from deicing salt) and XS3 (chloride ions taken from seewater), which are used when chloride is considered. The design codes define a valid crack width for such exposition classes. But in the reality the cracks need an additional protection system. The concrete without cracks has a high resistance against the pollution of chloride according to expositions classes XD3 and XS3. The cement paste is dense enough to meet the end of the lifetime. Figure 10 shows the common wearing during the lifetime of a non-cracked concrete (Kochs, 2010). But this design is not really representative when cracks occur in a reinforced concrete structure, e.g. decks, columns, ground bearing

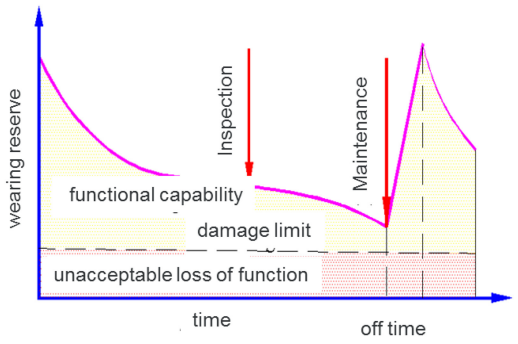

Figure 11. Function and substance of technical properties of structures with high potential of cracks.

slabs and beams in multi-storey and underground car parks.

For reinforced structures with high potential of cracks the following behavior has to be considered, see figure 11 (Kochs, 2010).

During the examination of the multi-storey car park, see capture 3, it seems that the crack width is relatively independent to the corrosion of the reinforcement, if chloride polluted water penetrated. This result correlates with other researchers (Arya, 2016).

7 ONGOING RESEARCH

The influence of the crack width on the corrosion activity on reinforcement of specimens with restraint will be the focus of our next research activities. A number of specimens with different cracks will be polluted over a period of some months with water and chloride. The potential differences from the beginning till the end of the tests will be examined. Some effects will be considered e.g. self-healing of concrete and dynamic loading during exposition.

REFERENCES

Arya, C. 2016. An examination of the crack control provision in BS EN 1992-2; *Structures and Buildings, Vol. 169 Issue SB4.*

Budnik et al. 2006. DBV Guideline Crack control in reinforced and prestressed structures

DAfStb Guideline 525 – Eraeuterungen zu den Normen DIN 1045-1. 2010.

DAfStb Guideline 555 – Erlaeuterungen zur DAfStb-Richtlinie Wasserundurchlaessige Bauwerke aus Beton. 2006.

Eurocode 2: Design of concrete structures – Part 1–2: General rules – Structural fire design. 2010.

Fingerloos, F. & Mayer, L. 2010. DBV Guideline – Multi-storey and Underground Car Parks.

Kochs, A. M. 2010. 4. Symposium Infrastruktur-Daten-Management fuer Verkehrsunternehmen IDMVU. Darmstadt.

Kosalla, M. 2014. Korrosion der Bewehrung im Bereich von Trennrissen nach kurzzeitiger Chlorideinwirkung; *Presentation on the BUEV qualification Workshop Frankfurt*.

Kosalla, M. 2015. Untersuchungen zum kritischen korrosionsausloesenden Chloridgehalt von Stahl. *Presentation on the 50. Aachener Baustofftage*. Aachen.

Meier, A. 2012. Der spaete Zwang als unterschätzter – aber maßgebender – Lastfall für die Bemessung. *Beton- und Stahlbetonbau 107, Heft 4*.

Nikolaus, C. 2011. Effekt einer verminderten Selbstheilung von Beton in Massenbetonbauteilen und Betonbauteilen unter Zwang - Regionalstudie München. *Präsentation on the DBV Regional Conference 2011*. Munich.

OEBV Guideline – Erhaltung und Instandsetzung von Bauten aus Beton und Stahlbeton 2014.

Raesch et al. 2013. Muenchner Runde – Tiefgaragenbauwerke und Parkgaragen.

Roos, F. 2009. Die Beurteilung von Rissen im Stahlbetonbau; *Beton-Informationen 3. Verlag Bau+Technik,* Duesseldorf.

Sodeikat et al. 2013. Auffinden von Bewehrungskorrosion mit Hilfe der Potentialfeldmessung. *Beton- und Stahlbetonbau 97, Heft 9*.

Concrete Solutions – Grantham et al. (Eds.)
© 2016 Taylor & Francis Group, London, ISBN 978-1-138-03008-4

The "Predicted Performance Curve" (PPC): A new structural performance deterioration model for concrete infrastructure

Nabil Semaan
University Of Balamand, Lebanon

Tarek Zayed
Concordia University, Canada

ABSTRACT: This paper develops a "Predicted Performance Curve" (PPC), a structural performance deterioration curve for concrete infrastructure. The PPC utilizes a reliability-based cumulative Weibull function in order to construct the structural performance curve. The PPC curve starts by constructing an Ideal Performance Curve (IPC) using the Weibull function. Then, an Updated Performance Curve (UPC) is constructed, by introducing at least one piece of available inspection data to the IPC. Finally, after the last inspection, a Predicted Performance Curve (PPC) is constructed. The PPC shows a predicted concrete deterioration curve, and predicts the useful service life. It also can easily consider Maintenance and Rehabilitation (M&R) plans for the structural component. The PPC model is the closest model to represent concrete deterioration, and can be easily developed using scarce inspection (condition assessment) data. In addition, the PPC can also be developed to model a deterioration curve for several structural components as a parallel and series system, hence be extended for the whole infrastructure. The PPC model is applied to transit infrastructure for the *Société de Transport de Montréal* (STM). The inspection of subway structures is difficult and expensive, hence the PPC proved to be the best method to model the deterioration of the structural components.

Keywords: Concrete Infrastructure, Concrete Deterioration Model, Service Life, Concrete Inspection, Maintenance and Rehabilitation.

1 INTRODUCTION

Civil public transportation infrastructure is crucial for economic growth and prosperity. Among the various civil public transportation infrastructure systems, subway networks represent a great challenge since they are the complex city's essential means of transportation.

Subway networks deteriorate in time due to a continuous increase in loading frequency and severity, and due to harsh environmental conditions. STM estimated an amount of 5.1 Billion CAD for its subway system infrastructure maintenance for the next ten years, starting in 2010. With the deteriorating condition of subway infrastructure and huge backlog of expenditures, public transit authorities have been under increasing pressure to develop strategies that manage the subway assets with a limited budget in a manner to ensure long term sustainable performance. Thus, there is an urgent need for developing a structural performance assessment tool for subway systems. Thus, performance curves of subway network components, and lines are crucial in developing a sustainable maintenance strategy and plan.

Existing research works on deterioration modeling utilizing techniques such as regression curves, Markov chains and reliability failure curves. These mathematical models cannot be applied to subway networks because they (a) require a huge amount of inspection reports, which are not available for subway networks; (b) entail high statistical analysis, which is intricate for a regular transit authority manager; (c) involve complex mathematical calculation and thus cannot be applied to a high number of structural components in a subway system; and (d) are difficult to use in order to evaluate network performance.

2 EXISTING INFRASTRUCTURE DETERIORATION METHODOLOGIES

Deterioration models are essential for asset management because they can predict the future deterioration of an asset or its components (Madanat 1993; Madanat *et al.,* 1997). Deterioration is by definition the gradual decrease in performance over time. Therefore, it can be understood as the opposite or inverse of performance. Thus, performance is generally understood as behavior related to use (Sarja and Vesikari, 1996). In principle the performance can be related to stability, safety, serviceability, integrity and other characteristics. Performance is always a function of time and is

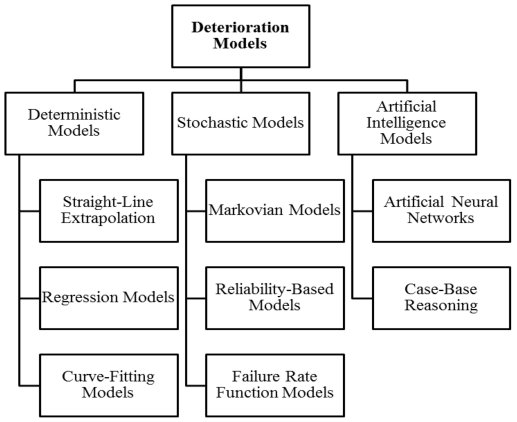

Figure 1. Deterioration Modeling Techniques.

always measured 'over time' or 'with time'. Prediction of service life is an important and fundamental aspect of performance modeling. Service life is the period of time from the completion of the facility to when the facility or any of its components reaches a state where the facility cannot provide acceptable service because of physical deterioration, poor performance, functional obsolescence, or unacceptably high operating costs (Hudson et al. 1997).

Service life can be estimated from: (1) empirical experience; (2) a historical database using survivor techniques; (3) established performance models; (4) laboratory testing; and (5) accelerated field testing (Hudson *et al.,* 1997). This section investigates the most important techniques used for modeling and predicting the deterioration, or inversely, the performance of infrastructure. Mathematical presentations that show decreased performance (or increased deterioration) as a function of time and appropriate design parameters are called performance models (Sarja and Vesikari, 1996). Performance modeling is an important part of infrastructure management on both project and network levels.

According to Hudson *et al.* (1997), performance models can be developed by a variety of techniques, including the following: (i) an expert system incorporating a knowledge base of empirical experience, (ii) a regression analysis, (iii) Markov transition probabilities, (iv) artificial neural network analysis, (v) Bayesian methodology, and (vi) econometrics methods. Elhakkem (2005) defines three categories of evaluating major deterioration techniques: (1) deterministic, (2) stochastic, and (3) artificial intelligence models. Figure 1 illustrates the different techniques used in performance modeling by combining those of Hudson and Elhakkem.

2.1 *Deterministic straight-line extrapolation models*

In the simple case, the model is established by stretching a line between two points with known conditions; it is possible to extrapolate the future condition at any time to a third point. The straight-line extrapolation models are too simplistic for the modeling of the probabilistic nature of failures. In addition, these models fail to relate the rate of deterioration with time. Hence the rate of deterioration and time are considered independent (Tran, 2007).

2.2 *Deterministic regression models*

Regression analysis provides a more accurate representation of future deterioration than simple straight-line extrapolation. Regression is a statistical tool that can be used to investigate relationships between variables. There exist various types of regression analysis such as linear, non-linear, stepwise and multiple regression.

Typical functions could be in the following forms:

$Y = a_0 + a_1.x$ Linear
$Y = a_0 + a_1.x + a_2.x^2 + \ldots + a_j.x^j$ Polynomial
$Y = a.\ x^b$ Exponential

The main drawbacks of regression modeling are as follows:

- Regression modeling has three major limitations: i) if the scatter diagram does not show a known model shape, ii) if many different independent variables influence the dependent variable, and iii) if the goodness of fit is low (Hudson *et al.,* 1997).
- Regression models fail to consider probabilistic behavior of deterioration, and assume that the deterioration rate is independent of time (Tran, 2007).
- According to Madanat and Ibrahim (1995) and Madanat *et al.*, (1997), it is not appropriate to model discrete condition states using regression models (especially the linear regression model).
- Furthermore, the fitting of multi-linear (polynomial) regression models is mathematically difficult to assess. Hence, the polynomial deterioration model is a hard task that requires significant computational effort.

2.3 *Stochastic Markov chain models*

Markovian models are the most common stochastic techniques that have been used extensively in modeling the deterioration of infrastructure facilities (Elhakeem, 2005). Many research efforts are based on Markov Chains (MC), for instance Morcous (2006) used this model for Bridge Management Systems. Wirahadikusumah (1999) and Baik *et al.,* (2006) developed sewer management models using Markov Chain (MC) modeling. Butt *et al.,* (1987), Yang *et al.,* (2005), Ortiz-Garcia *et al.,* (2006), and Hong and Prozzi (2006) used it for pavement deterioration modeling.

Markov Chain (MC) modeling considers the deterioration profile of the infrastructure as a stochastic process that evolves with time into a probabilistic process. The stochastic process is represented by an

indexed collection of random variables and it describes the deterioration degree or state at a particular point in the service life of the deteriorated element (Hillier and Lieberman, 2005). Markov Chain modeling is a stochastic process characterized by the Markovian property, or lack-of-memory property. This Markovian property means that the probability of any future state, given any past and present state, is independent of the past state and only depends upon the present state (Farran, 2006). These models use the Markov Decision Process (MDP) that predicts the deterioration of a component by defining discrete states and accumulating the probability of transition from one condition state to another over a multiple discrete time interval (Lounis *et al.,* 1998).

Transition probabilities are represented by a matrix of order ($n \times n$) called the Transition Probability Matrix (TPM), where (n) is the number of possible condition states.

State *1* represents an excellent condition; state *2* represents a deteriorated condition and so on up to state *n* which represents the critical condition. Each element of the matrix $p_{i,j}$represents the probability to move from state *i* to state *j* during a certain time interval called the transition period *'t'*. The sum of the probabilities in each row is unity. Since infrastructure deteriorates with time, the bottom triangle of the TPM is made of zero probabilities. Also reasonably assuming that deterioration happens gradually, the infrastructure component deteriorates only to the next state; hence two probabilities only appear on each row.

Markov transition probability models are particularly useful where a historical database does not exist. They capture the experience of engineers or technologists in a structured way by utilizing different classes or combinations of situations and condition states (Hudson *et al.,* 1997).

The Markov Chain approach captures the uncertainty in the deterioration process and evaluates the future condition based on the current condition. However, a few drawbacks of the Markov Chain Model must be considered:

- It assumes fixed transition probabilities, in addition to discrete transition time intervals, a constant population and stationary transition probabilities (Collins, 1972).
- For simplicity, it assumes that each state is independent. (DeStephano and Grivas 1998, Madanat *et al.,* 1997), thus past condition has no effect on predicted ones (Madanat *et al.,* 1997).
- The transition probabilities are estimated in terms of subjective engineering judgment and require frequent updating when new data are obtained (Tokdemin *et al.,* 2000).
- It does not predict the condition improvement after repair, i.e. maintenance done at a specific time (Madanat and Ibrahim, 1995).

Finally, it is difficult to consider the interaction among different components (Sianipar and Adams, 1997) and therefore cannot consider network deterioration (Van Noortwijk and Frangopol, 2004a).

2.4 *Stochastic reliability-based models*

Reliability-based methods of modeling infrastructure' deterioration have gained increasing acceptance in academic circles. Reliability methods take a probabilistic approach that results in a reliability index or an inverse of the probability of failure. In structural assessment and design, critical factors such as the loads, resistances, and deterioration models are highly random. The associated uncertainties must be quantified in order to ensure the public safety (Estes and Frangopol, 2005). The reliability methods are computationally more difficult and complex than traditional deterministic methods. Reliability methods involve complex convolution integrals that have no closed form solution. Simplified methods use first and second order approximations in order to reduce the complexity of computation. Monte Carlo simulation is a crude method to solve the reliability problem, although it requires a large number of simulations to obtain good results.

The biggest drawback of Monte Carlo simulation is the large number of simulations required to obtain a valid result (Estes and Frangopol, 2005).

When attempting to make decisions about a structure over its useful life, time becomes an important variable. If the Load (L) and Resistance (R) of the structure can be projected for the future, the simplest approach is a point-in-time method in which the reliability is computed at various specific times in the future. A trend is established and the structure is scheduled for a repair when the reliability falls below an acceptable threshold level. The problems of this approach are: i) the difficulty of predicting the future load and resistance of the structure, and ii) the failure to account for previous structural performance. A better time-dependent reliability approach is to compute the probability that a structure will perform satisfactorily for a specific period of time. Thus, a survivor function is defined as the probability that an element is safe at any time t.

Some researches assume this survivor function in the shape of a cumulative Weibull distribution (Grussing *et al.,* 2006) or a Gamma distribution.

One big advantage of reliability-based deterioration modeling is the flexibility of this method for the analysis of one component as well as a system of components. Many advantages are gained by quantifying the interrelationship between these components and by analyzing a structure as an entire system. A system analysis, for instance, may reveal that some repairs are more important than others. It also may reveal that while each individual component of a structure is safe, the whole system may be unsafe. A general structural system is usually made up of a combination of components in series and parallel. The most important drawback to reliability methods is the amount of

input data needed to perform a valid analysis. Furthermore, the reliability results are only as good (or bad) as the input data that support them.

2.5 *Stochastic failure rate functions models*

Failure rate functions representing deterioration have been used since the 1960's. A failure rate function is defined as a lifetime distribution representing the uncertainty in the time of failure of a component or structure.

A useful probabilistic interpretation of the failure rate function is that it represents the probability that a component of age '*t'* will fail in the time interval *[t,t+dt]* (Van Noortwijk and Frangopol, 2004b). Failure rate increases as the deterioration increases over time. Failure rate functions are especially useful in mechanical and electrical engineering fields, where equipment assume two states: a functioning state and a failed state. On the other hand, a degrading structure can be in a range of states. Thus a serious disadvantage of failure rates is that they cannot be measured for structural components (Van Noortwijk and Frangopol, 2004b).

2.6 *Summary*

Deterioration models are developed for most types of infrastructure, such as bridges, buildings, sewers and water mains. The methods used to model deterioration are either deterministic, such as regression analysis or stochastic methods, such as Markovian models, reliability-based models or failure-rate functions analysis. Reliability-based models may take linear forms or Weibull cumulative function shapes. These existing methods show considerable limitations.

Markov Chain, for example, assumes fixed transition probabilities, in addition to discrete transition time intervals, a constant population, and stationary transition probabilities. This method also assumes, for simplicity, that the states are independent, thus past condition has no effect on predicted ones. In addition, the transition probabilities are estimated in terms of subjective engineering judgment and require frequent updating when new data are obtained. Furthermore, Markov Chain does not predict the condition improvement after repair, i.e. maintenance done at a specific time. Finally, it is difficult to consider the interaction among different components using Markov Chain, i.e. network deterioration cannot be considered.

On the other hand, reliability-based deterioration modeling is more flexible in analyzing one component as well as a system of components. However, the most important drawback to reliability methods is the amount of input data needed to perform a valid analysis. Furthermore, the reliability results are only good or bad as the input data that support them.

Deterministic models such as regression models fail to consider probabilistic behavior of deterioration and assume that deterioration rate is independent of time. Furthermore, the fitting of multi-linear (polynomial) regression models is mathematically difficult to assess. Hence, the polynomial deterioration model is a time-consuming task that requires a great deal of calculation, which is data hungry technique.

3 THE PREDICTED PERFORMANCE CURVE (PPC) MODEL

3.1 *The PPC methodology*

The Predicted Performance Curve model develops a structural performance curve for concrete infrastructure components. The PPC utilizes a reliability-based cumulative Weibull function in order to construct the structural performance curve. The PPC curve starts by constructing an Ideal Performance Curve (IPC) using the Weibull function. Then, an Updated Performance Curve (UPC) is constructed, by introducing at least one available inspection data to the IPC. Finally, after the last inspection, a Predicted Performance Curve (PPC) is constructed. The PPC shows a predicted concrete deterioration curve, and predicts the useful service life. It also can easily consider Maintenance and Rehabilitation (M&R) plans for the structural component. The PPC model is the closest that represent concrete deterioration, and can be easily developed using scarce inspection (condition assessment) data. In addition, the PPC can also be developed to model a deterioration curve for several structural components as a parallel and series system, hence be extended for the whole infrastructure. The PPC model flow chart is illustrated in Figure 2.

The PPC model evaluates the structural performance curve of a concrete component based on a structural performance assessment index. Semaan and Zayed (2014) developed a structural performance assessment index model. Their model combines a physical condition (based on condition defects) performance index, and a functional (based on structural functional cracks) performance index. Then, this model combines these two indices into a single one, the "Integrated Performance Index" P_I. Although the PI index is applied to subway components, it can be generically used to any infrastructure structural concrete component. The PPC model may use the PI index, or any other index related to condition and/or functionality.

3.2 *The ideal performance curve*

Utilizing the structural Integrated Performance Index (P_I) for each concrete component, the PPC model develops the curve of the performance (P_I) over time, as the inverse cumulative Weibull probability distribution function.

The Weibull reliability function has many advantages in which it is the most appropriate technique for modeling the performance of the structural components within subway networks.

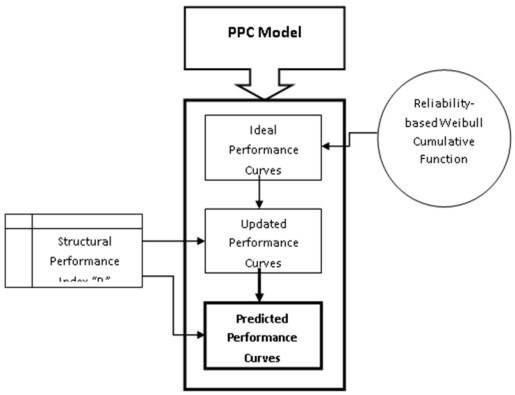

Figure 2. The PPC Model Flow Chart.

- The Weibull reliability function has proven to be one of the best functions to represent concrete deterioration. Depending on its parameters, the function starts at the maximum performance level and remains constant for a certain time (slope equals zero). This is true, since concrete structures remain functional and typically have an excellent condition for a certain time after construction. However, after this 'stable' time (steady state), concrete structural performance starts decreasing, (i.e. deterioration occurs); the Weibull reliability function similarly starts decreasing (negative slope). The concrete deterioration speed decreases near the end of its service life. Similarly the slope of the Weibull reliability function decreases and the function passes through an inflection point.
- The second advantage enforces the justification of the usage of the Weibull reliability function. Subway network inspection reports are few and the deterioration model must consider this fact. The Weibull reliability function, while modeling the deterioration, uses a few number of inspections. The Weibull reliability function does not need a lot of historical inspection data. Third, the Weibull reliability function can be easily used to model the components up to network performance, in contrast to other methods. Finally, the Weibull reliability function parameters are easily calculated and are also significant figures.

The main drawback of the Weibull function is the evaluation of its parameters. The PPC model overcomes this difficulty by adding important conditions that helps determining the parameters easily and without difficulty. It is difficult to obtain a Weibull reliability shape performance function that considers the history of inspection for components and their maintenance history, if applicable. The PPC model overcomes this difficulty by first modeling an Ideal Performance Curve. It subsequently updates the performance curve for each inspection. At the end, the updated performance curve or the predicted performance curve is constructed after considering the last inspection.

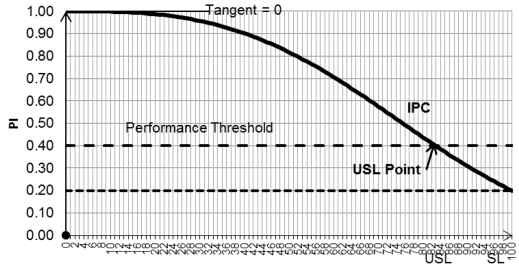

Figure 3. The Ideal Performance Curve.

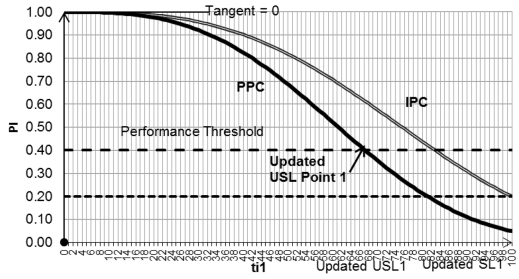

Figure 4. The Predicted Performance Curve.

The IPC is defined in the following Equation 1.

$$P_I(t)^{IPC} = 1 \cdot e^{\left[\frac{\ln(0.2)t^3}{100^3}\right]} \quad (1)$$

Where t = time.

The IPC equation assumes that at time equals zero, the P_I is maximum and equals 1.0. The service life of the components is 100 years, thus for t = 100, $P_I = 0.2$ (minimum performance). The Useful Service Life is defined as the year where $P_I = 0.4$ (performance threshold). The IPC has the shape illustrated in Figure 3:

3.3 *The predicted performance curve*

The Predicted Performance Curve is an update of the IPC after each inspection. At each specific inspection, an integrated performance index is evaluated. Then the performance curve must pass through this point. The curve must have a slope of zero at time zero. The PPC is defined in Equation 2:

$$P_I(t)^{PPC} = 1 \cdot e^{\ln(P_{Ii})\left(t/t_i\right)^3} \quad (2)$$

Where $P_{Ii} = P_I$ at the inspected year t_i.

The PPC shape is illustrated in Figure 4:

The Predicted Performance Curve (PPC) with a Maintenance and Repair (M&R) action done on a component is shown in Figure 5:

Where t_m = time of M&R action, $t_m + 1$ = Time of improved performance, M&R action assumed

to take 1 complete year, ΔM = M&R action performance improvement, P_{Im} = Performance directly before the M&R action, P_{IM} = Performance after the M&R action, $P_{IM} = P_{Im} + \Delta M$, P_{Ii} = Performance at year of inspection t_i.

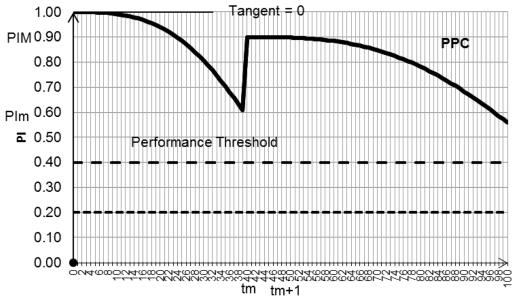

Figure 5. The Predicted Performance Curve with M&R.

Table 1. Case Study Subway Systems.

Systems Designation	Components	Construction Year	Inspection Year
STA 1	– Platform Level slabs, walls and stairs. – 1st Floor slabs, walls and stairs – 2nd Floor slabs, walls and stairs	1966	2005
AS 1	– Top and Bottom slab – Side Walls	1966	1995
TUN 1	– Dome – Side walls – Bottom slab	1966	2004

It should be noted that in subway networks, and due to the high number of components in stations, tunnels and auxiliary structures on one hand, and the few number of inspection reports on the other, lot of components do not have an inspection record (or never been inspected). In this case the ideal performance curve applies to such components. It should also be stressed that for components that have more than two inspection records, the predicted performance curve depends on the last inspection. In case at the last inspection an M&R action is applied (i.e., no inspection record after the M&R action), the PPC model assumes the performance curve after the M&R to be the ideal performance curve. Also, if an M&R action is applied and the transit authority did not assess the improvement of performance due to this action, the PPC model assumes that this improvement leads to an integrated performance of 0.9 (90%); assuming that no M&R action improves the performance to a 100% level.

4 THE PPC APPLICATION TO SOCIETE DE TRANSPORT DE MONTREAL

The PPC model is applied to real life in order to prove its functionality in a case study from the Societe de Transport de Montreal (STM). The case study consists of selecting an STM station, a tunnel, and an auxiliary structure, and assessing the integrated performance index, and constructing the performance curves of the components. The components of the following different systems defined in Table 1, are analyzed.

The different components PPC are evaluated. Figure 6. Illustrates the station STA1 components performance curves.

Figure 6 shows that the stations' components WE1, WI1, WE2 and SE2, the respective P_I in 2005 is 0.9. This means that after 39 years the performance drops

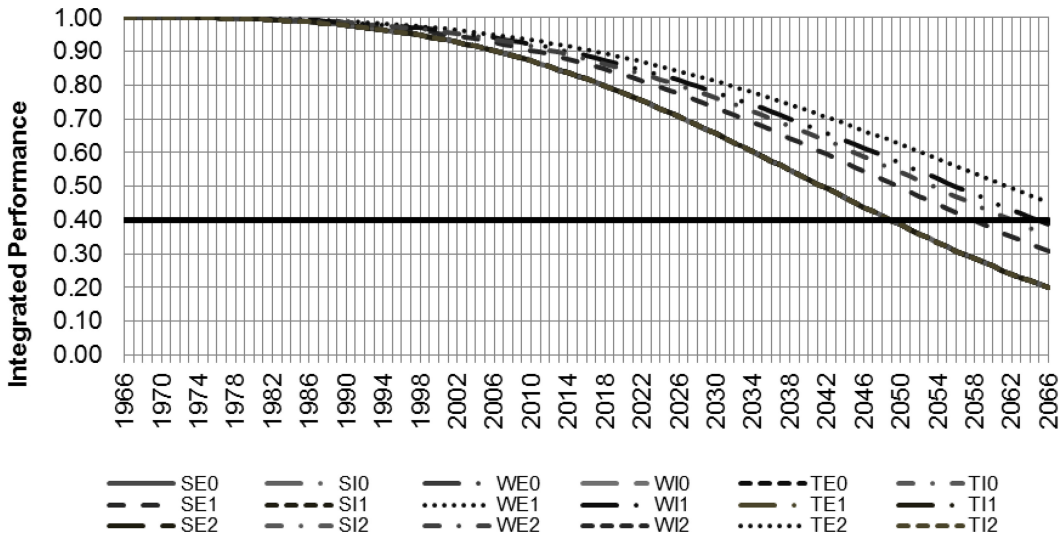

Figure 6. STA1 Components Performance Curves.

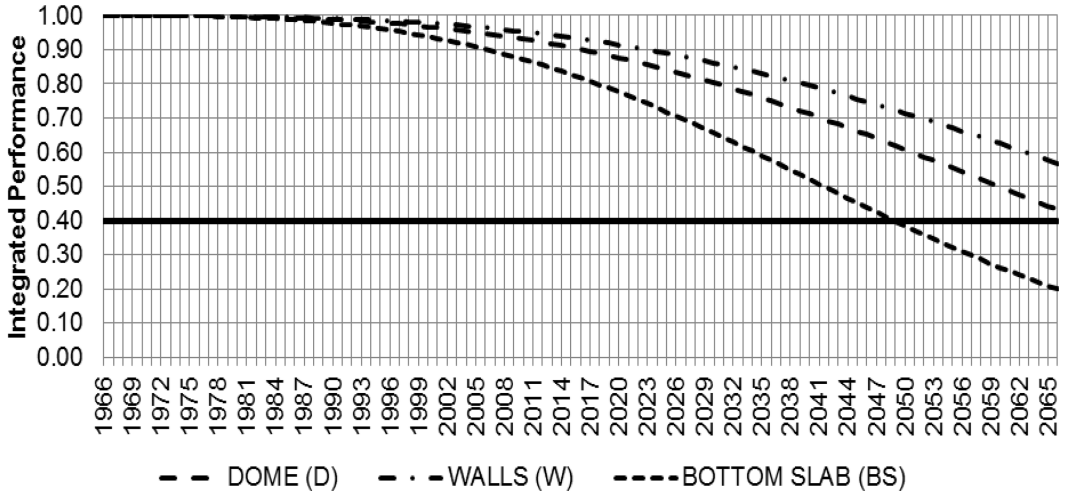

Figure 7. TUN1 Components Performance Curves.

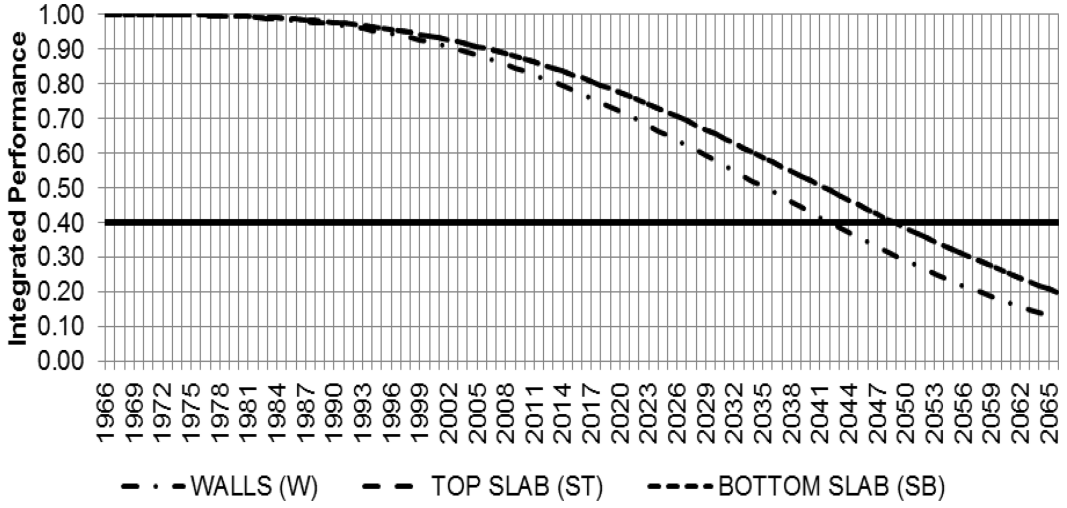

Figure 8. AS1 Components Performance Curves.

from 1.0 to 0.95, thus the slop of the curve is lower than that of the IPC.

Figure 7 illustrates the TUN1 components performance curves.

Figure 6 shows that the stations' components WE1, WI1, WE2 and SE2, the respective P_I in 2005 is 0.9. This means that after 39 years the performance drops from 1.0 to 0.95, thus the slop of the curve is lower than that of the IPC.

Figure 7 illustrates the TUN1 components performance curves.

Figure 7 shows that the tunnel bottom slab component follows an IPC, while the walls and dome components show a drop of performance of 0.97, and 0.96 respectively in 38 years and follow a PPC, higher than the IPC.

Figure 8 illustrates the AS1 components performance curves.

Both the auxiliary structure top slab and bottom slab follow an IPC. But here, the wall's performance drop to 0.95 in 29 years. Thus, the wall's PPC is lower than the IPC.

The average useful service life of the systems' components is 83 years; i.e. the performance reaches the threshold (0.4) in year 2050. Moreover, the average deterioration rate of the components ranges between 1% and 2%.

5 CONCLUSION

A model for developing the structural performance curves of concrete components is developed, entitled the 'Predicted Performance Curve' (PPC). The PPC model works when no or very few inspection

reports are available. Hence, it overcomes the limitations of the existing traditional deterministic and stochastic models. The PPC model follows the inverted Weibul cumulative distribution curve, and applies to it characteristics of the structural concrete performance.

The PPC is applied to a case study for the Societé de Transport de Montreal (STM). This case study has proven that PPC model is easy to apply, and the performance curves were easily developed, without complex mathematical calculation. Also, the PPC can be interpreted significantly, where the steady state number of years, the deterioration rate per years, the useful service life and the service life are read.

REFERENCES

Baik H., Jeong H. S., and Abraham D., (2006), "Estimating Transition Probabilities in Markov-Chain-Based Deterioration Models for Management of Wastewater Systems", *Journal of Water Resources Planning and Management*, Vol. 23, No. 1, pp. 15–24.

Butt A.A., Shahin M.Y., Feighan K.J., and Carpenter S.H., (1987), "Pavement Performance Prediction Model Using the Markov Process", Transportation Research Record: *Journal of the Transportation Research Board*, No. 1123, TRB, Washington, D.C., pp. 12–19.

Collins L., (1972), *An Introduction to Markov Chain Analysis*, CATMOG, Geo Abstracts Ltd., University of East Anglia, Norwich, U.K.

DeStephano P.D., and Grivas D.A., (1998), "Method for Estimating Transition Probability in Bridge Deterioration Models", *Journal of Infrastructure Systems*, Vol. 4, No. 2, pp. 56–62.

Elhakeem A., *An Asset Management Framework for Educational Buildings with Life-Cycle Cost Analysis*, (2005), PhD Thesis, Waterloo University, Civil Engineering, Canada.

Farran M*., Life Cycle Cost for Rehabilitation of Public Infrastructure: Application to Montreal Metro System*, (2006), MaSc. Thesis, Concordia University, Faculty of Civil, Environmental and Computer Engineering, Department of Building, Civil and Environmental Engineering, Canada.

Estes A., and Frangopol D., "Reliability-Based Condition Assessment", In Ratay T. (2005), Structural Condition Assessment, John Wiley and sons, The University of Michigan, pp. 1–66.

Grussing M.N., Uzarski D.R., and Marrano L.R., (2006), "Condition and Reliability Models using the Weibull Probability Distribution", *Proceedings of the 9th Application of Advanced Technology in Transportation (AATT) Conference*, August 13–16, Chicago, IL.

Hillier, F. S., and Lieberman, G. J., (1967). *Introduction to Operation Research*, Holden-Day, London.

Hong F., and Prozzi J., (2006), "Estimation of Pavement Performance Deterioration Using Bayesian Approach", *Journal of Infrastructure Management*, Vol. 12, No. 2, pp. 77–86.

Hudson W.R., Hass R., and Uddin W., (1997), *Infrastructure Management*, McGraw Hill, New York, USA.

Lounis Z., Lactase M.A., Vanier D. J., and Kyle B.R., (1998), "Towards Standardization of Service Life Prediction of Roofing Membranes". *Roofing Research and Standards Development: 4th Volume.* ASTM, STP 1349, PA, USA.

Madanat S., (1993), "Optimal Infrastructure Management Decisions under Uncertainty", Transportation Research, Part C, Vol. 1, No. 1, pp. 77–88.

Madanat, S. and Ibrahim, W. H. W., (1995), "Poisson Regression Models of Infrastructure Transition Probabilities", *Journal of Transportation Engineering,* ASCE, Vol. 121, No. 3, pp. 267–272.

Morcous G., (2006), "Performance Prediction of Bridge Deck Systems Using Markov Chains", *Journal of Performance of Constructed Facilities*, Vol. 20, No. 2, pp. 146-155.

Ortiz-Garcia J., Costello S.B., and Snaith M.S., (2006), "Derivation of Transition Probability Matrices for Pavement Deterioration Modeling", *Journal of Transportation Engineering*, Vol. 132, Issue 2, pp. 141–161.

Sarja A., and Vesikari E., *Durability Design of Concrete Structures*, (1996), RILEM Report 14, Technical Research Center of Finland, E & FN Spon.

Semaan N., *Subway Station Diagnosis Index (SSDI): A Condition Assessment Model*, (2006), MaSc. Thesis, Concordia University, Faculty of Civil, Environmental and Computer Engineering, Department of Building, Civil and Environmental Engineering, Canada.

Semaan N., & Zayed T., (2014), "An Assessment Model For Structural Performance of Subway Systems", *International Journal of Sciences, Environment and Technology*, Vol. 3, No. 6, pp. 1943–1968.

Société de Transport de Montreal (1992), "*Evaluation of structural deterioration Guide*", Report No. 890725, Montreal.

Tran H. D., *Investigation of Deterioration Models for Storm Water Pipe Systems*, (2000), PHD Thesis, Victoria University, School of Architectural, Civil and Mechanical Engineering, Faculty of Health, Engineering and Science, Australia.

Van Noortwijk J., and Frangopol D., (2004a), "*Deterioration and Maintenance Models for Insuring Safety of Civil Infrastructure at Lowest Life-Cycle Cost*", Published in Frangopol D., Brühwiler E., Faber M.H., and Adey B., editors, *Life-Cycle Performance of Deteriorating Structures: Assessment, Design, and Management*, pp. 384–391, Reston, Virginia, ASCE.

Van Noortwijk, J. M., and Frangopol, D. M. (2004b). "Two probabilistic life-cycle maintenance models for deteriorating civil infrastructure." *Probabilistic Engineering Mechanics*, Vol. 19, Issue 4, pp. 345–359.

Wirahadikusumah R., (1999), "Sewer Management Life Cycle Cost Approach", PHD Thesis, Department of Civil Engineering, Purdue University, USA.

Yang J., Gunaratne M., Lu J.J., and Dietrich B., (2005), "Use of Recurrent Markov Chains for Modeling the Crack Performance of Flexible Pavements", *Journal of Transportation Engineering*, Vol. 131, Issue 11, pp. 861–872.

Concrete Solutions – Grantham et al. (Eds.)
© 2016 Taylor & Francis Group, London, ISBN 978-1-138-03008-4

Service life design of concrete structures using probabilistic modelling tools: Statistical analysis of input parameters

I.P. Sfikas & J.P. Ingham
Mott MacDonald Ltd., Special Services Division, UK

ABSTRACT: Probabilistic modelling tools are increasingly being used to predict the service life of concrete structures, both as part of durability design for new build projects and residual life assessment of existing structures. An important aspect of the modelling process is the correct selection of the model input parameters, in terms of their statistical variation and type of probabilistic distribution. This paper reviews previous published scientific research, case studies and on-site investigations of actual structures and dedicated field studies from around the world regarding chloride-induced reinforcement corrosion. It provides potential ranges and general distribution trends for the most significant model input parameters, such as surface chloride concentration, chloride migration coefficient, critical threshold for corrosion and age factor. Different concrete mix properties (type of cement, type and quantity of mineral additions, water-to-binder ratio), age and exposure conditions of the reviewed studies are statistically analysed and discussed. Guidance is provided for prospective users of probabilistic modelling tools regarding the selection process of input parameters for different situations. Recommendations for standardisation and research to enhance the current level of knowledge are made with the aim of unlocking the full potential that concrete durability modelling tools have for improving sustainability, durability, climate change resilience and reducing the whole-life cost of concrete infrastructure.

1 INTRODUCTION

Durability design of concrete structures offers benefits for both asset owners and society. By understanding the deterioration processes affecting structures, design and asset management can be optimised to ensure that service life aspirations are met without unnecessary use of resources during construction and maintenance. This offers improvements in sustainability, climate change resilience and potentially the whole-life cost. Consequently, durability modelling tools for determining service life of concrete structures are being increasingly used on global infrastructure projects.

Chloride-induced reinforcement corrosion is arguably the most important deterioration mechanism affecting concrete structures. Predictive tools for determining chloride ingress for reinforced concrete structures and estimating the time taken to reach critical levels have become an important part of the tender and/or detailed design stages of new build structures, as well as of the condition assessment of existing structures and of asset management planning for deteriorating concrete structures, especially:

- in particularly aggressive environments (e.g. marine conditions, arid climates, etc.);
- for extended service life requirements (greater than 100 years; up to 120 or even 150 years); and
- for critical infrastructure (bridges, tunnels, power facilities, etc.).

2 SERVICE LIFE DESIGN

A range of limit state functions that can be used to assess the effects of the environmental exposure on a designed concrete mix and, thus, estimate the service life of a concrete structure (or structural element) have been developed over the previous decades, through extended laboratory and field studies. These established limit state functions have been further adopted by design code developers for the preparation of commercial deterministic modelling tools for Service Life Design (SLD), which allow the estimation of the service life of a concrete structure on the basis of simple input parameters.

By using these modelling tools, the service life of a structure is estimated by assessing the capacity of the examined concrete (i.e. durability that is associated with a specific mix design and specified concrete cover to reinforcement) against certain environmental and special exposure conditions (e.g. temperature, humidity, chloride-ion exposure, carbonation, freeze/thaw mechanisms, etc.) on the basis of a desired limit state, such as the initiation of attack or the partial or full deterioration of the structure or element under consideration. Specifically, a time-dependent load or action (S) is compared to the corresponding time-dependent resistance (R) of the structure. As shown in Figure 1, the intersection of the $S(t)$ and $R(t)$ curves gives the deterministic solution for the mean service life, t, of the examined structure or element.

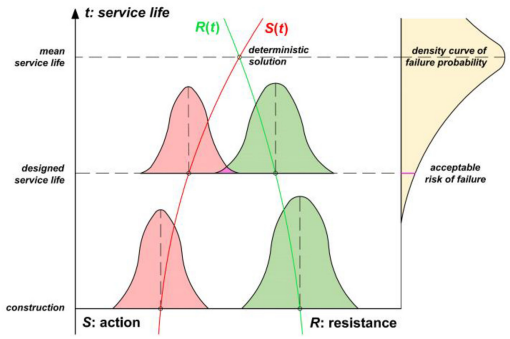

Figure 1. Estimation of service life.

The deterministic approach is based on the analysis of a defined set of input parameters (e.g. concrete cover depth, chloride penetration resistance of concrete mix, exposure conditions), which by being fed into a model, gives a unique, consistent output that is certain (occurrence risk: 100%), neglecting any risk that is associated with the variation of these parameters.

Conversely, the probabilistic approach aims to associate the deterministic solution with a level of risk. The major assumption of this approach is that part of (or all) of the input parameters may vary within probabilistic distributions, which are or can be statistically quantified (by assigning a type of distribution, a mean value, a standard deviation and/ or an upper/ lower bound value). Multiple runs of the limit state function with varying input parameters, using computational algorithms (Monte Carlo methods) that obtain numerical results by performing random sampling within the predefined statistical distributions for each individual parameter, are used to estimate a probability distribution for the output parameter, i.e. the service life up to the desired limit state. In other words, the probabilistic approach is a statistical way to analyse deterministic models and comprises the estimation of the probability that the predefined limit state will not be exceeded during the service life of a structure.

3 ASSOCIATED CODES & STATE-OF-THE-ART REPORTS

There are numerous scientific publications regarding the theoretical background of probabilistic SLD of concrete structures or elements. The most important codes, standards and state-of-the-art reports include:

- ISO 2394:1998. General Principles on Reliability of Structures;
- Duracrete. 2000. Probabilistic Performance based Durability Design of Concrete Structures;
- JCSS PMC. 2000. Probabilistic Model Code (Technical University of Denmark);
- *fib* 34:2006. Model Code for Service Life Design;
- BS EN 1990:2002 + A1:2005. Basis of Structural Design; and
- Concrete Society Technical Report No. 61 (2004). Enhancing reinforced concrete durability.

Table 1. Input parameters for the *fib* model limit state function for chloride-induced corrosion.

Symbol		Description	Comments (suggested source)
t or t_{SL}		Service life	Sensitivity analysis
C_{crit}		Critical chloride threshold	Concrete Society TR 61 (2004) or other literature
$C_{s,\Delta x}$		Chloride level at depth Δx	Analysis of exposure
$C0$		Initial chloride level	Mix design
Δx		Depth of convection zone	Analysis of mix design versus exposure
d_c		Cover depth	Sensitivity analysis
$A(t)$	a	Age factor/ ageing exponent	Concrete Society TR 61 (2004) or other literature
	t_0	Reference age	28 days (standard)
$D_{RCM,0}$		Chloride migration coefficient	Laboratory methods
k_e	b_e	Regression variable	Model assumption
	T_{ref}	Standard test temperature	293 K (20°C)
	T_{real}	Ambient temperature	Weather station data

4 INPUT PARAMETERS

This paper focuses on the limit state function for chloride-induced corrosion of reinforced concrete, as proposed by the *fib* Model Code for SLD (2006). A list of the required input parameters to be assumed by the designer for solving the associated limit state function is shown in Table 1. Most of these parameters can be assumed as varying parameters following statistical distributions, such as the normal, the lognormal and the beta or Pert distribution. The distribution parameters can normally be assessed through:

- available project data (ground investigation reports, environmental studies, concrete mix designs, etc.)
- a targeted laboratory testing regime (chloride diffusion using accelerated methods, age factor, etc.)
- measurements in adjacent structures built with similar materials and/or concrete mixes and that are exposed to similar conditions.

However, the currently available probabilistic models generally do not provide sufficient guidelines for the determination of most of their input parameters, a fact that was recently highlighted in a research study by Lollini et al. (2015). The aforementioned methods for determining statistical distributions of the various

input parameters cannot usually provide the required level of confidence, owing to the limited number of tests that are usually performed for a particular project. In addition, the prediction of long term effects cannot be confidently performed due to the associated uncertainties that are unknown at the time of design.

Therefore, a thorough review of published literature is required beforehand, to develop an extended database on durability behaviour of different structures or dedicated field studies under different environments and conditions, which can be then used as a basis for reference and aid for parameter selection.

5 SCOPE OF STUDY

This paper is a result of an extended review of previous literature and research studies and aims at statistically analysing and quantifying the parameters that are needed for the *fib* model limit state function for chloride-induced corrosion and providing recommendations for further research.

For the purposes of this study, various research studies have been reviewed and a large database has been created. It is intended that the database will be further developed with the aim of providing a powerful tool for assuming realistic distribution for input parameters of probabilistic modelling tools for SLD. This will allow a realistic estimation of service life in both new and existing structures with a higher level of confidence.

6 REVIEW OF PREVIOUS STUDIES

In total, 1477 database entries have been extracted so far from available literature (over 40 research studies, as listed in Section 9). Each entry represents one set of parameters and includes any available information on the structure (type, location), the mix design (origin and quantities of component materials), the fresh, mechanical and durability properties, as well as on the exposure duration and conditions and *in situ* measurements (chloride concentrations, carbonation, etc.). These entries do not always include all required data (e.g. strengths are only mentioned in almost half of the entries). Table 2 includes the number of entries for each major parameter, along with the minimum and maximum value reported. In the following sections, a more detailed description of the extracted data is provided.

6.1 *Types of examined structures*

Almost 80% of the 1477 database entries originate from test specimens (either exposed to field conditions or under controlled conditions to replicate in-service conditions), so that a significant lack of measurements on actual structures is apparent. Out of the remainder (20% of the database entries), the majority come from bridges, jetties and coastal structures, whereas about 6% do not explicitly refer to the type of concrete examined.

Table 2. Statistical data of concrete mix parameters.

Parameter	Number of entries	Min.	Max.	Units
Duration of exposure	1402	0.03	696	Months
Cement[1] (*c*)	1060	84	650	kg/m^3 concrete
	1090	20	100	% *w/w* binder
Silica fume (*sf*)	438	1.9	33.3	% *w/w* binder
Fly ash (*fa*)	387	4.3	75	% *w/w* binder
Ground granulated blast-furnace slag (*ggbs*)	95	9.9	80	% *w/w* binder
Metakaolin (*mk*)	12	5	15	% *w/w* binder
Other mineral admixtures	34	10	30	% *w/w* binder
Binder (*b*)	1322	230	796	kg/m^3 concrete
Water-to-binder ratio (*w/b*)	1253	0.18	0.84	–
Compressive strength ($f_{cc,28}$)	751	16.6	132	N/mm^2

[1]In the referenced studies, cement is either reported as quantity in kg per m^3 of concrete and/or as percentage by weight of total binder

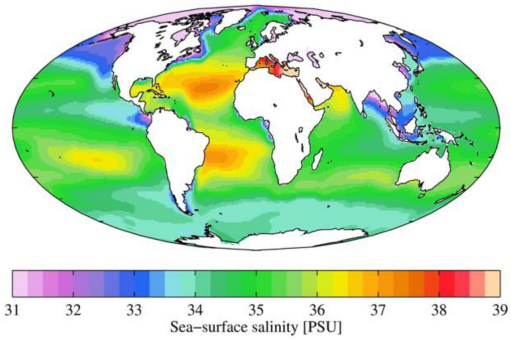

Figure 2. Annual mean salinity of sea surface (source: Wikipedia, http://en.wikipedia.org/wiki/File:WOA09_sea surf_SAL_ AYool.png, accessed 23/3/14 – original figure, licensed under the Creative Commons Attribution-Share Alike 3.0 Unported license].

6.2 *Geographical location*

Data from literature studies were analysed in terms of the geographical location of the examined structures, which is a very significant parameter for estimating service life (on account of the influence of different climatological and environmental conditions). For example, the sea-surface salinity can vary significantly, depending on open-ocean or closed gulf conditions, as can be seen in Figure 2.

When analysed by continent, it was found (Fig. 3) that more than half of the studies (57%) originated from Europe, whereas another 35% came from across Asia. America represented 7% of the total, out of which the vast majority originated from the USA (Fig. 4).

Most of the studies originate from Northern Europe (Sweden, Denmark, Norway), followed by countries

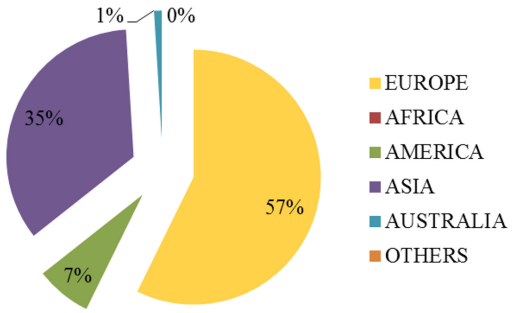

Figure 3. Locations of structures by continent.

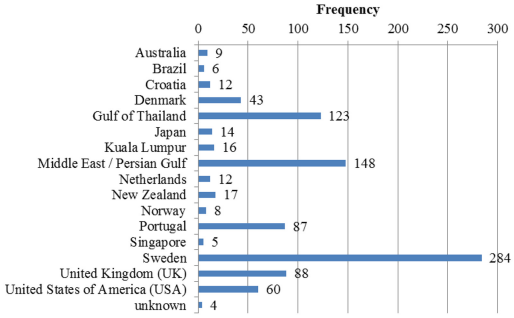

Figure 4. Locations of structures by country or region.

in the Middle East and the Gulf of Thailand. It was observed that the very high-salinity Mediterranean sea has poor background information, e.g. structures in the southern parts of Europe (Greece, Italy, France, Spain, Malta, Cyprus), western Asia (Turkey, Lebanon, Israel) or northern Africa (Egypt, Libya, Tunis, Algeria, Morocco, etc.) were either not substantially or not at all supported with data.

6.3 *Exposure conditions*

A major finding from reviewing literature studies was that the type of exposure conditions were either not clearly mentioned or not mentioned at all (Fig. 5). The terminology used was also not always univocally defined. These facts create an urgent need for the both academics and industry to work towards standardising methods for declaring and grouping exposure conditions, so that the results of different studies can be directly compared. A few studies avoided generic ambiguous descriptions by instead clearly mentioning the vertical and/ or horizontal distance from sea or salt concentration, which in the authors' opinion is more useful.

Concerning the duration of exposure, this ranged from one day to sixty years (Fig. 6). Specifically, out of 1477 database entries, 18.5% referred to results from exposure up to 3 months, 25.5% from exposure between 3 and 12 months, 40% from exposure between 1 and 10 years and 14% from exposure between 10 to 60 years. In about 2% of the studies the duration of

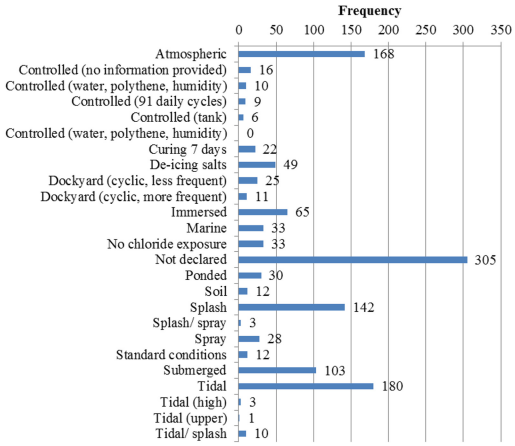

Figure 5. Exposure conditions of structures.

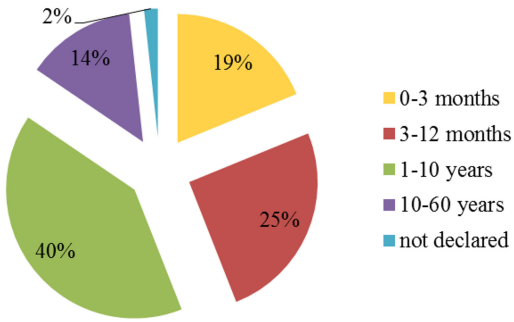

Figure 6. Exposure duration of structures.

exposure was not mentioned at all. There is an apparent lack of results in the long term (over 10 years), which is the most important in-service period for the durability design. For future research, the investigation of concrete structures with ages of at least 100 years should be considered.

6.4 *Concrete ingredients*

The behaviour of concrete under specific exposure conditions is related to mix design. When designing a new-build project or investigating an existing structure, some of the input parameters will be known (e.g. minimum cement content, type of mineral addition or target 28-day compressive strength). In order to predict the behaviour of concrete, similar mixes to the ones that are used in probabilistic SLD should be selected from the database. In order to have an adequate data sample (i.e. sufficient entries to extract a satisfactory statistical distribution of the desired parameter, such as the surface chloride concentration or the chloride diffusion coefficient), the initial number of entries for each mix design parameter in the database should be 'high'. An actual number cannot possibly be specified, as depending on the combinations of input parameters even a very big number of initial entries can lead

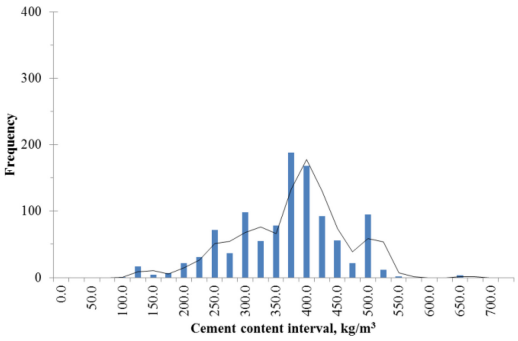

Figure 7. Histogram for cement content, *c*.

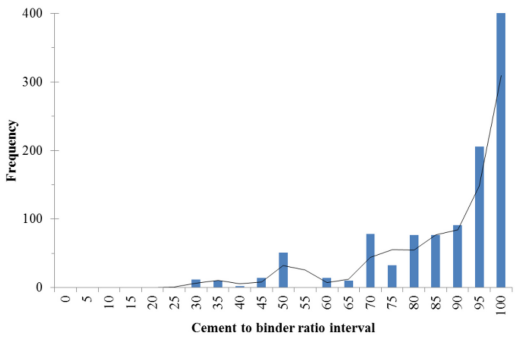

Figure 8. Histogram for cement to binder ratio, *c/b*.

to a limited sample that is inadequate to produce a satisfactory statistical distribution. Further engineering judgement and previous experience is required to group different entries and increase the initial sample without reducing the level of confidence. For the full number of entries currently included in the developed database, histograms of the several concrete mix design parameters are prepared in the figures that follow.

6.4.1 *Cement content*

Figure 7 shows the distribution of cement (*c*) content, where it appears that most of the examined structures used mix designs with the content of Portland cement varying between 300 and 450 kg/m^3. This range appears to be reasonable. However, it may not be suitable for mixes with very low or very high cement contents. For example, mixes with mineral additions where the cement content may be toward the lower end of the scale (e.g. 200–300 kg/m^3) or mixes with high cement content (e.g. 450–550 kg/m^3) aiming to achieve high strengths had a very limited statistical population. This is illustrated in Figure 8 where the cement-to-binder (*c/b*) ratio is shown. It is evident that the great majority of the studies examined mixes with a total binder content with either low or no content of mineral admixtures (cement content is higher than 85% *w/w* binder in more than 50% of the mixes).

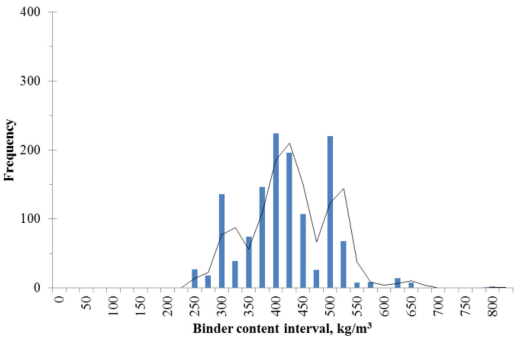

Figure 9. Histogram for binder content, *b*.

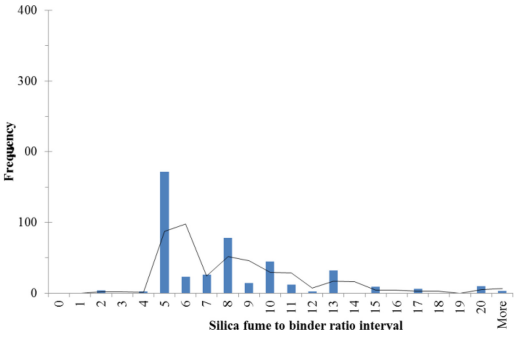

Figure 10. Histogram for silica fume to binder ratio, *sf/b*.

6.4.2 *Binder content*

When binder content (cement plus mineral additions) (*b*) was considered (Fig. 9), an improved population of mixes was evident in the range between 300 and 500 kg/m^3. This range is quite representative of standard mixes commonly used in contemporary design and construction. As it is now common to incorporate mineral additions in concrete, so that the total binder content can be up to 550 (or sometimes even 600) kg/m^3, future studies should focus on higher binder contents.

6.4.3 *Silica fume content*

So far, relatively few studies have been reviewed where silica fume (*sf*) had been used in the mix design. Only 30% of the examined mixes include silica fume. As shown in Figure 10, the typical contents used appear to be concentrated around distinct values: 5, 8, 10 and 13%. The number of entries for intermediate addition levels or silica fume contents higher than 10% was very low.

6.4.4 *Fly ash content*

Approximately 25% of the examined studies included fly ash (*fa*) in the mix design, with addition rates of up to about 60% of the total binder content. The frequency distribution curve of fly ash contents (Fig. 11) appears to be relatively flat, but mainly for contents between 10 and 35%, which is a common range for fly ash in the mix. However, the number of entries for each of the

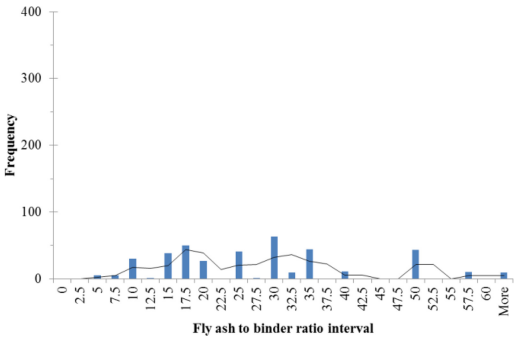

Figure 11. Histogram for fly ash to binder ratio, *fa/b*.

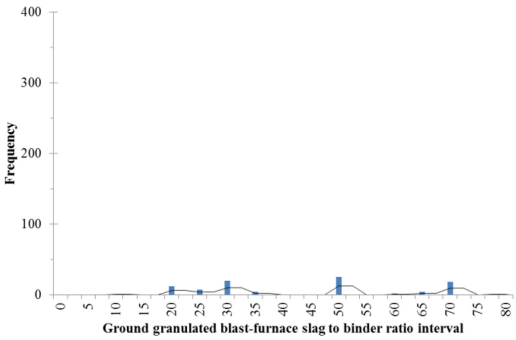

Figure 12. Histogram for ggbs to binder ratio, *ggbs/b*.

peak content is relatively small, not exceeding 40–50 concrete mixes.

6.4.5 *Ground granulated blast-furnace slag content*

Studies including ground granulated blast-furnace slag (*ggbs*) was surprisingly limited; less than 6.5% of the total mixes examined. Peak contents (expressed as a percentage of the total binder) in the histogram shown in Figure 12 are evident in 20, 30, 50 and 70%, but with less than 20 mixes for each.

6.4.6 *Water content*

The water content, expressed as water-to-binder (*w/b*) ratio in Figure 13, had a good distribution between the examined studies. The distribution almost resembles a normal distribution curve with a peak (average) of around 0.40–0.45. Reported w/b ratios are as low as 0.25 and as high as 0.75. For future studies, a focus on lower w/b ratios (up to 0.40–0.45) is needed to reflect current practice in significant projects. Conversely, a focus on higher w/b ratios (between 0.50 and 0.70) would also be beneficial to reflect common practice in older structures, where excessive non-conforming water contents were sometimes used to achieve a better workability during construction. Data from such mixes could be useful in condition surveys and forensic engineering investigations to help estimate the remaining service life of (older) existing structures.

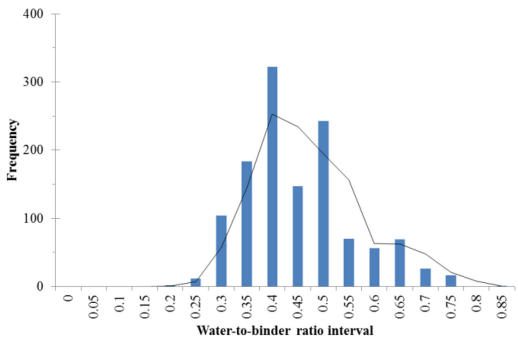

Figure 13. Histogram for water-to-binder ratio, *w/b*.

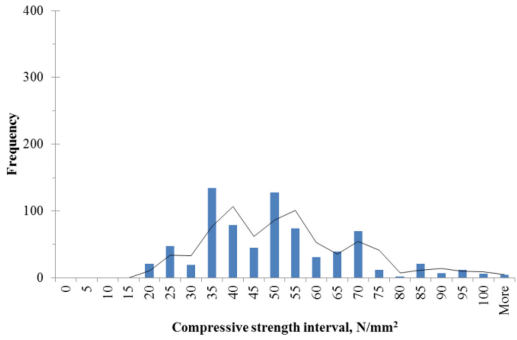

Figure 14. Histogram for compressive strength, $f_{cm,28}$.

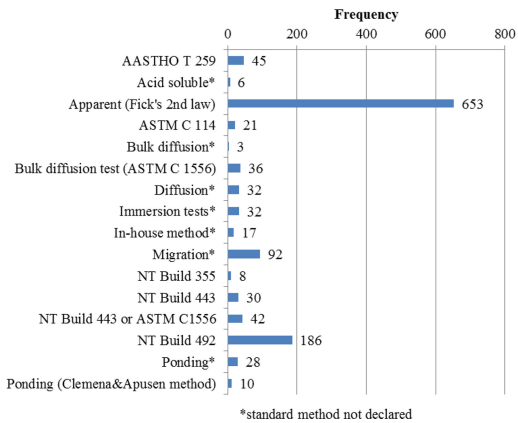

Figure 15. Methods of determination for chloride diffusion.

6.5 *Compressive strength*

The compressive strength was only reported in approximately half of the studies reviewed (751 out of 1477). Compressive strength was typically expressed as 28-day mean cube strength and this varied between 16.6 and 100 N/mm^2, with some *in situ* results from bridge structures in Denmark being as high as 132 N/mm^2. As seen in Figure 14, the majority of the mixes fall within the 30 to 60 N/mm^2 range and there appeared to be a relative lack of higher strengths commonly achieved in construction projects today.

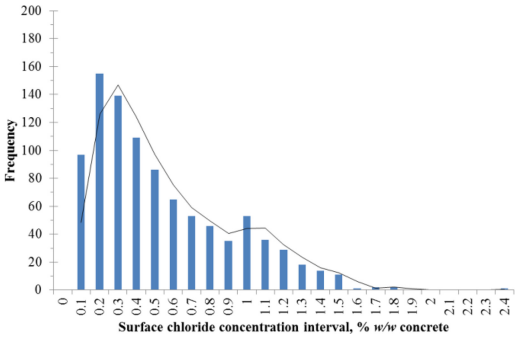

Figure 16. Histogram for surface chloride concentration, *C*s.

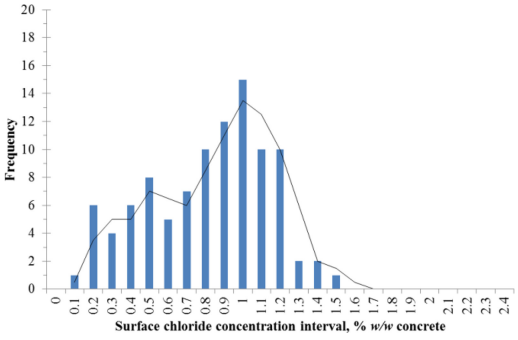

Figure 17. Histogram for surface chloride concentration, *C*s, for group of concrete mixes exposed to tidal/splash conditions.

6.6 *Diffusion coefficient*

A series of different standard or non-standard methods have been used (Fig. 15) for the determination of the salt concentration in concrete and/ or the coefficient representing the rate of chloride ingress. There exists an incompatibility between the methods used, which limits the reliability of the comparison between different studies. The uncertainties, which are associated with inherent bias, errors, repeatability and reproducibility of each method, along with the limited background research on the correlation between different methods for various concretes and exposures make this assessment more difficult. Going forward, the authors recommend that all studies should include the use of a single standard method to allow comparison.

7 GENERIC DISTRIBUTIONS FOR INPUT PARAMETERS FROM REVIEWED STUDIES

7.1 *Surface chloride concentration*

Figure 16 shows the distribution of the surface chloride concentration, *C*s (% *w/w* concrete), regardless of the concrete mix design, the exposure conditions, and the method used for its determination. It appeared that the distribution was quite smooth, without significant peaks or discontinuities. The average and median concentrations are calculated as 0.49% and 0.38% *w/w* concrete, whereas 95% of the measured values did not exceed 1.22% *w/w* concrete in a total of 952 values.

If the database entries are filtered, so that only mixes with a w/b ratio varying between 0.40 and 0.50 that are exposed to splash/ tidal (marine) conditions for over one year are included in the sample, then the number of entries is significantly reduced down to only 26 (out of the initial 952 entries). Figure 17 shows the corresponding distribution of *C*s (% *w/w* concrete). The average and median values under such conditions are increased to 0.77% and 0.84% *w/w* concrete, whereas 95% of the values do not exceed 1.19% *w/w* concrete.

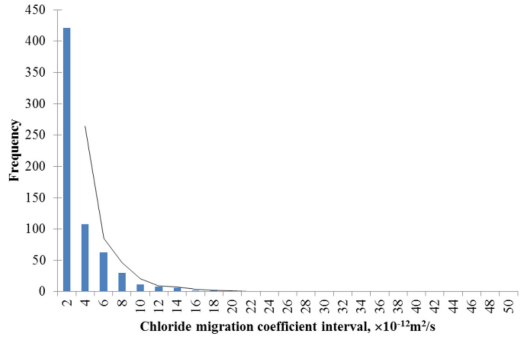

Figure 18. Histogram for chloride migration coefficient, $D_{RCM,0}$, by Fick's 2nd law.

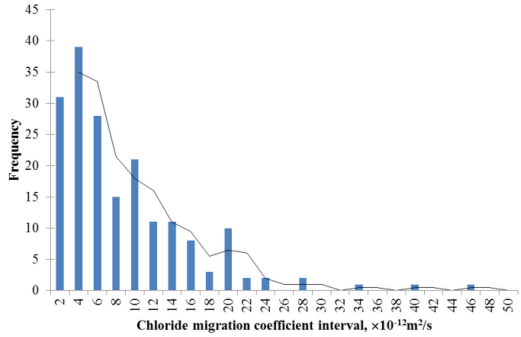

Figure 19. Histogram for chloride migration coefficient, $D_{RCM,0}$, by NT Build 492 test method.

7.2 *Chloride migration coefficient*

The distribution of chloride migration coefficient could only be analysed per method of determination. Figure 18 shows the distribution of the apparent diffusion coefficient, as measured by the Fick's 2nd law in 653 entries of the database. The average and median values are 2.47×10^{-12} and 1.46×10^{-12} m^2/s, whereas 95% of the entries are below 7.92×10^{-12} m^2/s. Similarly, Figure 19 shows the distribution of the chloride diffusion coefficient, as measured by the NT Build 492 (1999) test method in 186 database entries. The average and median values are 7.92×10^{-12} and 5.62×10^{-12} m^2/s, whereas 95% of the entries do not exceed 19.9×10^{-12} m^2/s.

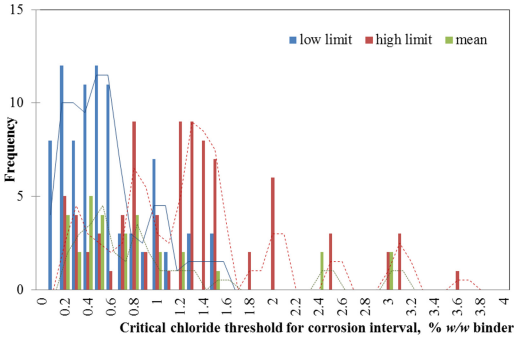

Figure 20. Histograms for critical chloride threshold for corrosion, C_{crit}.

7.3 *Critical threshold for corrosion*

From analysing the findings for the critical threshold for chloride-induced corrosion of embedded reinforcement by various research studies, it appeared that the limiting value depended on the reinforcement bar type (smooth, ribbed, deformed), steel condition (polished, cleaned, sandblasted) and the method used for corrosion detection. The reported values for total chloride concentration on corroded steel varies between 0.02% and 3.6% *w/w* binder. Approximately three-quarters of the database entries (85 out of 116) provided a range of threshold values (low and high concentrations), whereas other entries (31 out of 116) give a single mean value. The average of lower-limit value was calculated as 0.62% *w/w* binder, which should be compared with recommended standard values above which the corrosion is expected to initiate (e.g. 0.4% *w/w* binder limit of BS 8110-1:1997).

All corresponding distributions are shown in Figure 20, where it is evident that corrosion has been detected in a great range of concentrations. It is considered that further research is required to understand the affecting factors and their significance.

It is important to note that the inherent accuracy and precision of the laboratory test methods used to determine chloride content of concrete has an influence on the values for critical threshold for corrosion and also, those for surface chloride concentration. For example, a recent laboratory trial of the BS 1881-124:1988 (British Standards Institution, 1988) method indicated repeatability and reproducibility standard deviation of 0.006 – 0.011 and 0.013 – 0.035 respectively (% by mass of sample). In addition, the trial results typically overestimated the chloride content in the samples so that (in a 'real world' situation) they could potentially result in overly conservative risk classification. This serves to emphasise the importance of engineering judgement in the interpretation of chloride content test results (Concrete Society Technical Report No. 32, 2nd Edition, 2014).

7.4 *Age factor*

The studies reviewed made almost no reference to the age factor (or ageing exponent), which is related to the reduction in diffusivity, i.e. the ability of chlorides to be transferred through the concrete matrix over time due to continuing hydration of the concrete. In most cases, this was only theoretically approached and no measurements were provided.

As this parameter may significantly affect the risk of corrosion, it is very important for future studies to report all results on chloride diffusivity: (i) at an early age of the structure (at 28 days or at higher ages, e.g. 90 days, if mineral additions are included in the concrete mix design), (ii) at various times of intermediate measurements while monitoring the structure throughout its service life, and/ or (iii) at the time of ultimate inspection (at the time of corrosion initiation or developed corrosion). Thus, it will be possible for the effect of age on chloride diffusion to be quantified and fed into the model to acquire more realistic results for any remaining service life.

8 CONCLUSIONS

From our literature review to date, we have found that there is a need for the following research to be undertaken, in order to improve confidence in the selection of input parameters for probabilistic modelling of concrete structures:

- standardising testing and reporting procedures to allow data to be comparable. Every study or structure should include a clear report the on concrete ingredients used (type, origin and quantities), vertical and horizontal distance from the source of chlorides, duration of exposure, etc.;
- planning and conducting additional research regarding the correlation between different methods used for the determination of chloride migration into concrete and, preferably, standardising a single test method to be used in future;
- conducting further *in situ* studies of real structures while in-service, in a range different locations and exposure conditions. The increased uncertainty that is associated with the selection of frequency distribution curves for input parameters may be reduced by conducting further tests in different types of structures, with a great range of different concretes that are exposed to various conditions for different durations; and
- monitoring new build and existing (older) structures and systematically recording their behaviour under real (in service) conditions over long durations.
- recent trials of a test method (BS 1881-124:1988) used for determining chloride content of concrete for surface chloride concentration and critical chloride threshold indicated that it may be less accurate than commonly thought. Chloride content test methods with improved accuracy need to be developed.

Specialist engineering advice will always be needed for the interpretation and assessment of all parameters to be used in solving probabilistic service life design

(SLD) models, but further research of the type identified above will allow for a more justified selection of these parameters, reduce risks and uncertainties and increase of the associated level of confidence.

The potential benefits of improving the quality of input data for probabilistic modelling of concrete infrastructure are considerable. Given that concrete durability modelling is well aligned with current/rising global engineering imperatives such as sustainability, carbon reduction, climate change resilience and whole-life cost reduction, there is a strong case for undertaking further research in this area.

LIST OF REVIEWED PAPERS

Angst, U. & Vennesland, Ø. 2007. SINTEF Report: *Critical chloride content – State of the art*. SINTEF/COIN.

Angst, U. & Vennesland, Ø. 2009. *Critical chloride content in reinforced concrete – State of the art*. Concrete Repair, Rehabilitation and Retrofitting II – Alexander et al (eds), Taylor & Francis Group, London, ISBN 978-0-415-46850-3.

Ashrafi, H.R. & Ramezanianpour, A.A. 2007. Service Life Prediction of Silica Fume Concretes. *International Journal of Civil Engineering*: 5(3):182–197. Iran University of Science & Technology.

Bamforth, P.B., Price, W.F., Emerson, M. 1997. *An international review of chloride ingress into structural concrete*. Contractor Report 359, Transport Research Laboratory.

Bertolini, L, Lollini, F., Redaelli, E. 2008. *Concrete composition and service life of reinforced concrete structures exposed to chloride bearing environments*. Proceedings of the First International Symposium on Life-Cycle Civil Engineering, F. Biondini and D.M. Frangopol (Eds.), 10-14 June 2008, Varenna, Italy, pp. 113–118, Taylor & Francis Group, London, ISBN: 978-0-415-46857-2.

British Cement Association. 1998. *Minimum requirements for durable concrete: Carbonation- and chloride-induced corrosion, freeze-thaw attack and chemical attack*. Ed. Hobbs DW , Camberley, UK. ISBN 0721015247.

Chalee, W., Jaturapitakkul, C., Chinaprasirt, P. 2009. Predicting the chloride penetration of fly ash concrete in seawater. *Marine Structures*: 22:341–353. Elsevier.

Chalee,W. & Jaturapitakkul, C. 2009. Effects of w/b ratios and fly ash finenesses on chloride diffusion coefficient of concrete in marine environment. *Materials and Structures*: 42:505-514. Springer.

Cheewaket, T, Jaturapitakkul, C, Chalee, W. 2014. Concrete durability presented by acceptable chloride level and chloride diffusion coefficient in concrete: 10-year results in marine site. *Materials and Structures*: 47:1501–1511. Springer.

Costa, A. & Appleton., J. 1999. Chloride penetration into concrete in marine environment – Part I: Main parameters affecting chloride penetration. *Materials and Structures*: 32:252-259. Springer.

Cramer, S.D., Covino, Jr B.S., Bullard, S.J., Holcomb, G.R., Russell, J.H., Nelson, F.J., Laylor, H.M., Soltesz, S.M. 2002. Corrosion prevention and remediation strategies for reinforced concrete coastal bridges. *Cement and Concrete Composites*: 24:101–117. Elsevier.

Detwiler, R.J., Whiting, D.A., Lagergren, E.S. 1999. Statistical approach to ingress of chloride ions in silica fume concrete for bridge decks. *ACI Materials Journal*: November/December.

Dhir, R.K & Byars, E.A. 1993. PFA concrete: chloride diffusion rates. *Magazine of Concrete Research*: 45(162): 1–9.

Dusti, A., Moradian, M., Taheri, S.R., Rashetnia, R., Shekarchi, M. 2013. Corrosion Assessment of RC Deck in a Jetty Structure Damaged by Chloride Attack. *Journal of Performance of Constructed Facilities*: 27:519–528. ASCE.

Dusti, A., Rashetnia, R., Almotahari, A., Shekarchi, M. 2012. *Effect of different marine exposure conditions on chloride diffusion in concrete*. 2nd International Conference on Microstructural-related Durability of Cementitious Composites, Amsterdam, The Netherlands.

Fidjestøl, P. & Justnes, H. 2001. *Long term experience with microsilica concrete in a marine environment*. Workshop proceeding no. 3: Durability of Workshop proceeding no. 3: Durability of Exposed Concrete Containing Secondary Cementitious Materials, Nordic Miniseminar.

Ghods, P., Chini, M., Hoseini, M., Alizadeh, R. 2005. Evaluating the chloride diffusion of concrete by measuring electrical resistivity. *ICE Young Researchers' Forum*: January:191–199.

Hassan, Z.F.A. 2012. *Rapid assessment of the potential chloride resistance of structural concrete*. PhD Thesis, University of Dundee.

Heiyantuduwa, R. & Alexander, M.G. 2009. *Studies on prediction models for concrete durability*. Concrete Repair, Rehabilitation and Retrofitting II – Alexander et al (eds), Taylor & Francis Group, London, ISBN 978-0-415-46850-3.

Hooton, R.D., Betz, E., Kojundic, T. 2010. *Long-term chloride penetration resistance of silica fume concretes based on field exposure*. Proceedings: Service Life Design for Infrastructure RILEM PRO 70(1):503–512. RILEM.

Kumar, S., Rao, B.K., Misra, S. 2002. Chloride penetration resistance of concrete containing blast furnace slag. *The Indian Concrete Journal*: 76(12):745–751.

Larsen, E.S., Buhr, B., Eriksen, K. 2001. *Long term performance of micro silica concrete – edge beams of the Fiskebæk Bridge*. Workshop proceeding no. 3: Durability of Workshop proceeding no. 3: Durability of Exposed Concrete Containing Secondary Cementitious Materials, Nordic Miniseminar.

Lee, N.P. & Chisholm, D.H. 2005. *Durability of Reinforced Concrete Structures under Marine Exposure in New Zealand*. Study Report No.145, BRANZ Ltd, Judgeford, New Zealand.

Lindvall, A. & Nilsson, L-O. 2001. *Studies on the effect of secondary cementitious materials on chloride ingress.* Workshop proceeding no. 3: Durability of Workshop proceeding no. 3: Durability of Exposed Concrete Containing Secondary Cementitious Materials, Nordic Miniseminar.

Lizarazo-Marriaga, J. & Claisse, P. 2010. Determination of the transport properties of a blended concrete from its electrical properties measured during a migration test. *Magazine of Concrete Research*: 62(3):163–175. Thomas Telford Ltd.

Luping, T. & Nilsson, L-O. 1992. Chloride diffusivity in high strength concrete at different ages. *Nordic Concrete Research*: No.11:162–171.

McNally, C., Richardson, M., Evans, C., Callanan, T. 2005. *Chloride diffusion coefficient determination for specifications*. Proceedings of the 6th International Congress on Global Construction, Dhir, R. K. (ed.), Thomas Telford.

Meira, G.R., Andrade, C., Padaratz, I.J., Alonso, C., Borba, Jr J.C. 2007. Chloride penetration into concrete structures in the marine atmosphere zone – Relationship between deposition of chlorides on the wet candle and chlorides

accumulated into concrete. *Cement and Concrete Composites*: 29:667–676. Elsevier.

Meira, G.R., Andrade, C., Vilar, E.O., Nery, K.D. 2014. Analysis of chloride threshold from laboratory and field experiments in marine atmosphere zone. *Construction and Building Materials*: 55:289–298. Elsevier.

Mustafa, M.A. & Yusof, K.M. 1994. Atmosperic chloride penetration into concrete in semi-tropical marine environment. *Cement and Concrete Research*: 24(4):661–670. Elsevier.

Nielsen, E.P., Thrysøe, J., Herfort D., Geiker M. 2003. *Performance of white Portland cement in aggressive environment*. Proceedings of the 7th International Conference on Concrete in Hot and Aggressive Environments.

Otsuki, N., Yodsudjai, W., Nishida, T., Yamane, H. 2004. New test methods for measuring strength and chloride ion diffusion coefficient of minute regions in concrete. *ACI Materials Journal*: March–April.

Pargar, F., Valipour, M., Shekarchi, M. 2010. *Comparison of chloride diffusion in nine months concrete specimens containing metakaoline and silica fume pozzolans*. Fracture Mechanics of Concrete and Concrete Structures – Assessment, Durability, Monitoring and Retrofitting of Concrete Structures- B. H. Oh, et al. (eds), Korea Concrete Institute, Seoul.

Poulsen, S.L. & Sørensen, H.E. 2012. *Chloride threshold values: state of the art*. Danish Expert Centre for Infrastructure Constructions.

Ryan, P.C. & O'Connor, A.J. 2011. Probabilistic Modelling of Marine Bridge Deterioration. *International Scholarly and Scientific Research & Innovation:* 5(12):548–554, World Academy of Science, Engineering and Technology.

Safehian, M. & Ramezanianpour, AA. 2013. Assessment of service life models for determination of chloride penetration into silica fume concrete in the severe marine environmental condition. *Construction and Building Materials*: 48:287–294. Elsevier.

Stipanovic-Oslakovic, I., Bjegovic, D., Mikulic, D. 2010. Evaluation of service life design models on concrete structures exposed to marine environment. *Materials and Structures*: 43:1397–1412. Springer.

Tang, L. & Andersen, A. 2001. *Chloride ingress data from five years field exposure in a Swedish marine environment.* PRO 19: 2nd International RILEM Workshop on Testing and Modelling the Chloride Ingress into Concrete by C Andrade and J Kropp (eds.), 487p, RILEM.

Tang, L. & Sørensen, H.E. 2001. Precision of the Nordic test methods for measuring the chloride diffusion/migration coefficients of concrete. *Materials and Structures*: 34:479–485. RILEM.

Thomas, M.D.A. & Bamforth, P.B. 1999. Modelling chloride diffusion in concrete – Effect of fly ash and slag. *Cement and Concrete Research:* 29:487–495. Elsevier.

Thomas, M.D.A. & Matthews, J.D. 2004. Performance of pfa concrete in a marine environment – 10-year results. *Cement and Concrete Composites*: 26:5–20. Elsevier.

Valipour, M., Pargar, G., Shekarchi, M., Khani, S., Moradian, M. 2013. In situ study of chloride ingress in concretes containing natural zeolite, metakaolin and silica fume exposed to various exposure conditions in a harsh marine environment. *Construction and Building Materials*: 46:63–70. Elsevier.

Visser, J. 2009. *Predicting the durability of marine structures in the Netherlands: assessing the migration coefficient*. 2nd International RILEM Workshop on Concrete Durability and Service Life Planning (ConcreteLife '09), 7–9 September 2009, Haifa, Israel, RILEM.

Wood, J.G.M. & Crerar, J. 1997. Tay Road Bridge: Analysis of chloride ingress variability & prediction of long term deterioration. *Construction and Building Materials*: 11(4):249–254. Elsevier.

Yoon, C.S., Kim, K.H., Yang, W.Y., Cha, S.W. 2012. Chloride diffusion coefficient at reference time for high performance concrete for bridge pylons in marine environment. *Journal of the Korea Concrete Institute*: 24(4):435–444.

Zeng, J.J., Wang, S.N., Lv, W.Q., Su, Q.K., Shui, Z.H. 2014. *Water-binder ratio monitoring as a quality control tool for the high-performance concrete used in the construction of the submerged tunnel*. 4th International Conference on the Durability of Concrete Structures, Purdue University, West Lafayette, IN, USA.

OTHER REFERENCES

AASTHO T 259. 2006. *Standard Method of Test for Resistance of Concrete to Chloride Ion Penetration*. AASHTO.

ASTM C 114. 2015. *Standard Test Methods for Chemical Analysis of Hydraulic Cement*. ASTM International.

ASTM C 1556. *Standard Test Method for Determining the Apparent Chloride Diffusion Coefficient of Cementitious Mixtures by Bulk Diffusion*. ASTM International.

British Standards Institution. 1988. BS 1881-124: *Testing concrete – Part 124: Methods for analysis of hardened concrete*, BSI, London, UK.

British Standards Institution. 1997. BS 1881-1: *Structural use of concrete – Part 1: Code of practice for design and construction*. BSI, London, UK.

British Standards Institution. 2002+A1:2005. BS EN 1990: *Basis of Structural Design*. BSI, London, UK.

Concrete Society. 2004. *Enhancing reinforced concrete durability: Guidance on selecting measures for minimising the risk of corrosion of reinforcement in concrete*. Technical Report No. 61. The Concrete Society, Camberley, UK.

Concrete Society. 2014. *Analysis of Hardened Concrete: A guide to tests, procedures and interpretation of results.* Technical Report No. 32, 2nd edition. The Concrete Society, Camberley, UK.

Duracrete. 2000. *Probabilistic Performance based Durability Design of Concrete Structures,* Final Technical Report, The European Union – Brite EuRam III.

fib 2006. Model Code 34: *Model Code for Service Life Design,* Sprint-Digital-Druck, Stuttgart, Germany.

International Organization for Standardization. 1998. ISO 2394: General Principles on Reliability of Structures. ISO, Switzerland.

JCSS PMC:2000. Probabilistic Model Code. Technical University of Denmark.

Lollini, F., Carsana, M., Gastaldi, M., Redaelli, E., Bertolini, L. 2015. The challenge of the performance-based approach for the design of reinforced concrete structures in chloride bearing environment. *Construction and Building Materials:* 79:245–254.

NT Build 355. 1997. *Concrete, mortar and cement based repair materials: Chloride diffusion coefficient from migration cell experiments* (Ed.2). Nordtest: Nordic cooperation.

NT Build 443. 1995. *Concrete, hardened: Accelerated chloride penetration. Concrete, hardened: Accelerated chloride penetration.* Nordtest: Nordic cooperation.

NT Build 492. 1999. *Concrete, mortar and cement-based repair materials: Chloride migration coefficient from non-steady-state migration experiment.* Nordtest: Nordic cooperation.

Strengthening materials and techniques/Repair with composites



Taylor & Francis
Taylor & Francis Group
http://taylorandfrancis.com

Concrete Solutions – Grantham et al. (Eds.)
© 2016 Taylor & Francis Group, London, ISBN 978-1-138-03008-4

Assessment of strengthening techniques of reinforced concrete elements rehabilitated with composites

Dimitra V. Achillopoulou, Alexandra N. Kiziridou,
Georgios A. Papachatzakis & Athanasios I. Karabinis
Democritus University of Thrace, Greece

ABSTRACT: The current study focuses on the assessment of strengthening techniques of reinforced concrete elements with composite materials (carbon fiber reinforced polymers-CFRPs, glass fiber reinforced polymers-GFRPs, textile reinforced mortars-TRM's, near surface mounted bars-NSMs) and the description of the transfer mechanisms from concrete elements to the strengthening materials through analytical models based on failure modes: plate end interfacial debonding and intermediate flexural crack induced interfacial debonding. A database of 55 in total reinforced concrete columns (scale 1:1) is presented containing elements rehabilitated with various techniques (29 wrapped with CFRP's, 5 wrapped with GFRP's, 4 containing NSM and 4 strengthened with TRM). The failure modes are discussed together with the performance level of each technique as well as the efficiency level in terms of ductility and bearing/ bending capacity. The analytical models' results are in acceptable agreement with the experimental data and can predict the failure modes. Despite the heterogeneity of the elements contained in the aforementioned database the results are of high interest and point out the need to incorporate the analytical expressions in design codes in order to predict the failure mechanisms and the limit states of bearing capacities of each technique.

1 INTRODUCTION

Composites over the past years are proved to play an important role on the strengthening of existing structures especially under the prism of modern ductile regulations. Many investigations have been conducted considering the kind of composite used (GFRP, CFRP), the type of the added element (jacket, NSM rods, laminates, TRM) and above all its efficiency to enhance the response of the rehabilitated structural element made of reinforced concrete.

Even though modern codes internationally have incorporated various expressions in order to help the new practitioners to perform safe design, there is a lack of instructions considering which method is more appropriate for every different scenario. In fact, many standards and codes describe techniques and response without emphasizing on the failure modes of each rehabilitation system.

Previous studies have focused on the investigation of various variables which affect the overall response of structural elements such as: confinement, flexural and torsional response, axial load capacity, cross-section shape, kind of loading, lap-splices existence, bar buckling phenomena, contribution of others structural elements, etc (Chalioris 2008, Karabinis 2002, Karabinis & Rousakis 2002, Karayannis & Sirkelis 2008, Rousakis et al. 2007).

The approach of this study aims primarily to the investigation of the interface performance and effectiveness of each technique. As it is world widely admitted to be the key element of safe design and chained to failure modes, a deeper understanding of every failure mode and the divergence of codes' provisions is fundamental. Within this ambit, a cautious collection of experimental data and analytical expressions have been gathered. A wide dataset with results of various researchers (Bournas et al. 2009, Realfonzo & Napoli 2009, 2012, Sadone et al. 2012, Sarafraz & Danesh 2010, Wu et al. 2008) on strengthened full scale concrete columns with composite elements subjected to horizontal cyclic loading with constant axial load is collected and statistical tools are used to evaluate and discuss the results

By looking at the interface study there is a gap of knowledge considering interfacial forces and transferring. Especially, a description that can predict the type of the upcoming failure with the desired response. Analytical research is limited mainly to concrete beams (Smith & Teng 2001, Wang 2006, 2007, 2008). These studies describe mainly two kind of failures: a) plate end debonding, b) intermediate crack induced by external loading.

The conclusions of this research are presented after analyzing and processing the results. Furthermore, provisions of design codes (CNR 2004, Eurocode 8 1998, FIB Bulletin No. 56. 2010) were used in order to be evaluated, based on statistical comparison of displacement ductility of the aforementioned elements.

Finally, a simple algorithm, based on previous research, implementing non-linear slip-stress law for the calculation of internal stresses (shear and normal) along the interface of the column for a certain load level were developed for calculating the ultimate load in which debonding occurs. This helps describe the effectiveness of an FRP jacket wrapped to a concrete column in order to understand better the slip phenomena and the effective zone of the jacket-substrate system and the failure of interface. Relative slippage at the interface occurs at the point where bending cracks are created (due to the high moment caused at the base of the columns by the horizontal load imposed on the top), resulting in risk of debonding.

2 EXPERIMENTAL RESULTS

2.1 *Database*

A database containing results of 55 experimental tests performed on square and rectangular, full scale elements subjected to cyclic loading and a constant axial load was assembled from the scientific literature (Bournas et al. 2009, Realfonzo & Napoli 2009, 2012, Sadone et al. 2012, Sarafraz & Danesh 2010, Wu et al. 2008). Of these, 42 columns were retrofitted with composite materials; 33 were reinforced with CFRP, 2 with GFRP, 2 with NSM, 1 with transverse embedded GFRP bars placed in the middle of each side of the column, 3 with carbon textile reinforced mortar (TRM C) and 1 with glass textile reinforced mortar (TRM G). Some of the specimens with CFRP sheet reinforcement were designed with additional retrofitting; 2 included NSM bars, 2 included embedded GFRP bars and 1 included CFRP laminates. The columns were designed either with smooth (18 specimens) either with deformed (37 specimens) longitudinal reinforcement. Furthermore, 38 of the experiments included lap-splices.

Relevant details about the experiments collected in the database are listed in Tables 1–6 (ANNEX A).

2.2 *Codes*

Provisions of design codes (CNR 2004, Eurocode 8 1998, FIB Bulletin No. 56. 2010) were evaluated using the database regarding ductility accomplished through each strengthening technique. Displacement ductility was calculated according to each design code's provision, using the equations listed below.

For every code displacement ductility μ_δ was considered equal to chord rotation ductility, which is calculated by the following equation:

$$\mu_\delta = \mu_\theta = \left(\frac{\theta_u}{\theta_y} \right) \tag{1}$$

where θ_u is the ultimate chord rotation and θ_y is the chord rotation at yielding.

The ultimate chord rotation for EC8 part 3 (Eurocode 8 1998) is estimated according to equations in §A.3.2.2 and the chord rotation at yielding according to equations in §A.3.2.4.

Respectively, θ_u and θ_y is calculated by equations (4.54) and (4.55) in §4.7.3.1.2 for Italian design code CNR (CNR 2004).

As for chord rotations according to FIB's provisions (FIB Bulletin No. 56. 2010), θ_u is estimated by equation (7.4–40) in §7.4.3.4 and θ_y by provisions in §7.4.3.2.1.

3 EVALUATION OF STRENGTHENING METHOD

3.1 E*valuation indexes*

Several indexed were formed in order to evaluate the results with more accuracy.

The normalized bending moment is given by:

$$\mu_{max} = \left(\frac{F_{max} * H}{b * h^2 * f_{cm}} \right) \tag{2}$$

In cases in which there were data for the lateral load in pull and push direction (F^+_{max}, F^-_{max}), the average value ($F^+_{max} + F^-_{max}$)/2 was used.

The improvement in terms of flexural strength and deformation capacity has been evaluated by means of the following two indexes.

The flexural strength index I_μ:

$$I_\mu = \left(\frac{\mu_{max}}{\mu_{max,un}} \right) \tag{3}$$

and the maximum displacement index I_δ:

$$I_\delta = \left(\frac{\delta_{max}}{\delta_{max,un}} \right) \tag{4}$$

where un indicates the corresponding value for the unstrengthened column.

Furthermore, the displacement index, in which the first failure is noted I^1_δ, is used in order to understand the level of displacement developed when the column is retrofitted (Eq. 5). The first failure corresponds to the first noticeable failure (FRP failure, concrete crush, concrete spalling, bar buckling, NSM and concrete crush, NSM debonding, slippage or pullout of steel connectors) of each specimen.

$$I_\delta{}^1 = \left(\frac{\delta_1}{\delta_{1,un}} \right) \tag{5}$$

The increase in terms of confined concrete strength is represented by the index f'_{cc}/f_{cc}, where f_{cc} is the confined concrete's compressive strength due to transverse steel reinforcement confinement and f'_{cc} is the confined concrete's compressive strength due to

transverse steel and composite material reinforcement confinement.

Drift ratio (Eq. 6) is also a useful index since it shows the displacement capacity regardless the column's height.

$$dr = \left(\frac{\delta_1}{H} \right) \tag{6}$$

3.2 *Statistical indexes*

In statistics, the coefficient of determination, denoted R^2, is a number that indicates how well data fit a statistical model. In regression, the coefficient of determination R^2 (Eq. 7) is a statistical measure of how well the regression line approximates real data points. An R^2 equal to 1 indicates that the regression line perfectly fits the data, while an R^2 of 0 indicates that the line does not fit the data at all. This latter can be because the data is non-linear or because it is random.

$$R^2 = \left(\frac{Cov(\exp, d)}{S(\exp) * S(d)} \right)^2 \tag{7}$$

where d is the corresponding design code's value.

The root of the mean squared error RMSE (Eq. 8) is a measure of the dispersion of the distribution of predicted results' errors. In other words, it calculates the root of the mean squared deviations of the predicted values from the respective experimental. Root mean squared error (RMSE) and data are of same scale and its' main characteristic is that it is more sensitive to extreme values, values that are far from the mean of errors. The smaller the value of RMSE index, the more reliable the results of prediction of ductility from provisions of the design codes used.

$$RMSE = \sqrt{\frac{\sum (\mu\delta, \exp - \mu\delta, d)^2}{n}} \tag{8}$$

Due to lack of data for certain type of failures, conclusions from R^2 and RMSE were drawn for FRP fracture and concrete spalling failures that the majority of specimens noted.

3.3 *Analytical investigation, assumptions and approach*

Both columns and the fiber reinforced polymers are modeled as linear elastic members, which are connected by a thin layer of binding material. The flexural crack introduces local flexibility at the crack location (at the bottom of the column) and is conventionally modeled as a rotational spring with infinitesimal thickness at the crack location. The basic assumption in all of these solutions is that the adhesive layer is subjected to shear and normal stresses that are constant across the thickness of the adhesive layer.

A series of focused experiments (Bizindavyi & Neale 1999, Chajes et al. 1996) show that local interfacial shear stress distribution (mode II fracture behavior), effective bond length, and initiation and propagation of an interfacial crack between the bonded FRP and concrete can be described fairly accurately by using a bilinear shear stress-slip relation, consisting of a linear ascending branch followed by one descending softening branch. Bond stress increases linearly with an increase in relative shear displacement till the local bond strength, τ_f, is reached (Stage I: Linearly elastic stage), after which softening response is triggered (Stage II: Elastic-softening stage), until complete loss of bond (Stage III: Elastic-softening-debonding stage).

Debonding is considered to occur when no stress can be transferred, or the energy required to create a unit area of debond is available. The area under the curve determines the interfacial fracture energy, G_i^f.

In view of the fact that the tensile strength of adhesive is significantly greater than the concrete tensile strength, and that debonding often occurs within the cover concrete, mode I fracture behavior at the interface can be assumed to follow that of concrete. It should be noticed that no account is taken of the coupling effect between mode I and mode II behavior other than the assumption that no shear transfer occurs along the interface once the magnitude of peeling stress attains the level of the tensile strength, f_t, or enters the softening branch. Thus loss of shear transfer capacity can occur if either mode II fracture energy G_i^f is met, or if the normal tensile stress, f_t is attained.

3.4 *Calculation of internal stresses along the concrete interface and debonding failure mechanism*

An iterative process that predicts the maximum external load P_u in which debonding occurs is described by the algorithm in ANNEX B. By inserting the geometrical and mechanical parameters of the column and the FRP used for the retrofitting together with the required values to describe the interfacial shear stress/normal stress–slip relationship, the load in which the specimen loses shear transfer capacity and concrete is separated from FRP in the interface leading to failure (Stage III: Elastic-softening-debonding stage) is derived. After calculating interface capacity, the internal stresses (shear and normal) along the column-FRP interface can be obtained, by using the analytical equations for a certain external load. Finally, using the values of the force transfer mechanism, any other failures related to the interface behavior (concrete's substrate failure, FRP fracture), can be observed.

3.5 *Experimental verification*

A second database consisting of 15 specimens (RC column) from the aforementioned database was assembled in order to verify the analytical equations. All were strengthened with FRP jackets (carbon or glass) with different mechanical characteristics and thickness

and all of them failed due to FRP fracture. Thereafter, for each specimen analytical calculations were conducted to find the shear and normal stresses of the interface and the normalized strain of the FRP along the columns, for the ultimate load each column suffered and the ultimate load in which the debonding occurred.

Group C is consisted of four specimens from the database with 2200 mm height and square section 300 × 300 m retrofitted with CFRP sheets (total thickness $t_{tot} = 0.44$ mm and volumetric ratio $\rho_f = 0{,}00587$) and also strengthened with steel angles with anchorage to the concrete foundation (Type "A1") or without (Type "A2"). The compressive strength and tension strength of the concrete varied from $f_{ck} = 14.9$–27.3 MPa and $f_t = 1.1.8$–2.7 MPa respectively. The Young's Modulus of the CFRP is $E_f = 390$ GPa. For the two utmost examples the experimental results show that for specimen C6-S-A2 the maximum horizontal force is $F_{max} = 63.32$ kN while on C11-S-A1 is $F_{max} = 97.53$ kN. According to the analytical solutions (neglecting steel connectors influence), the maximum external force in which debonding in the Column-FRP interface occurs (Stage III: Elastic-softening-debonding stage) is $P_u = 93$ kN. This verifies that the experiments failure was not caused by loss of function of the force transfer mechanisms between concrete and FRP sheets for all specimens except C11-S-A1. Figures 1(a) and 1(b) give the interfacial shear and normal stress distributions, respectively, for the maximum experimental recorded load F_{max}, measured from the base of the column to the top. It can be observed that for three experiments the interface is in Elastic-softening stage (Stage II) with the maximum shear stress ($\tau_f = 8$ MPa) recorded at a distance 21 mm to 90 mm from the base. For C11-S-A1, though, a debonding zone of approximately 15 mm occurs. In the experimental process, no failure due to Concrete-FRP interface is observed. So, from the algorithm's results it can be assumed that steel profiles placed on the column's base help by shifting the effective length in which debonding may occur over the profiles' length. Finally, no failure of concrete's substrate was observed as seen in Figure 1(b) as the maximum normal stresses $\sigma(x)$ are significantly smaller from concrete's tension strength.

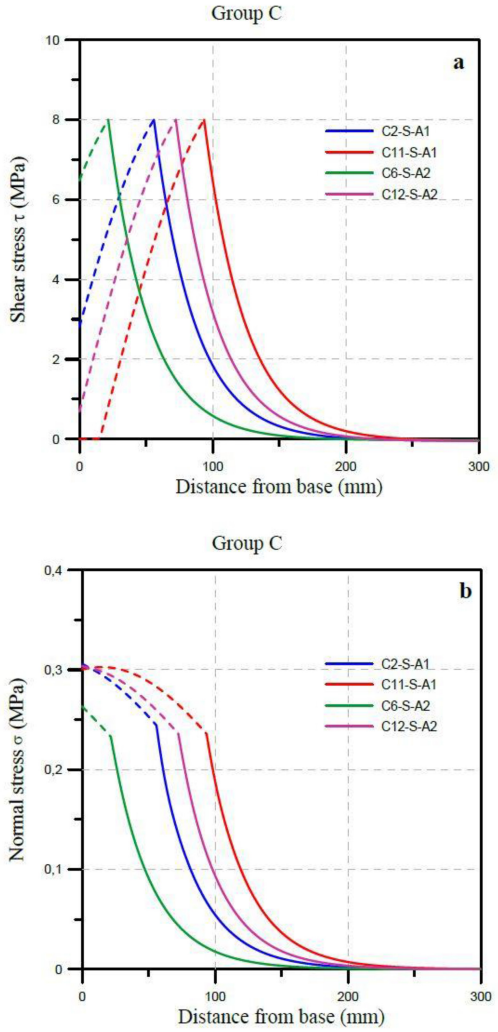

Figure 1. Interfacial stress distributions along FRP–concrete interface: (a) interfacial shear stress–slip relationship, (b) interfacial normal stress–displacement relationship.

4 RESULTS AND DISCUSSION

The investigation's conclusions are summarized in a rather qualitative manner as follows:

Firstly, it was observed that strengthening with fiber reinforced sheets leads to increased confined concrete strength. Also, increasing the confinement causes an increase of the maximum lateral load that the column can bear. The result indicate that by increasing the characteristic strength f_{ck}, a decrease of the maximum normalized horizontal load ρ_{hor}^{max} is appeared.

Since CFRP's strength is higher, in order to obtain the same results in terms of flexural retrofitting with GFRP strengthening a higher amount of sheet is needed, fact that is confirmed by results (Fig. 2(a)). Regarding the maximum displacement and the displacement index I_δ^1, the glass fibers (GFRP) contribute more (16–40% and 27–48%, respectively), since the material has higher failure strain $\varepsilon_{f,u}$. Concerning displacement ductility (μ_δ), columns retrofitted with GFRP developed greater values than the ones with CFRP (increase of 26–35%) (Fig. 2(b)).

Aiming at flexural strengthening carbon textile reinforced mortar (TRM C) and glass textile reinforced mortar (TRM G) produced almost the same results (Fig. 2(c))). Regarding the increase of the compressive concrete strength, TRM C proved to be more efficient (20%) compared to glass textile reinforced mortar TRM G (Fig. 2(a))). In order to increase the ultimate displacement, TRM C was considered more

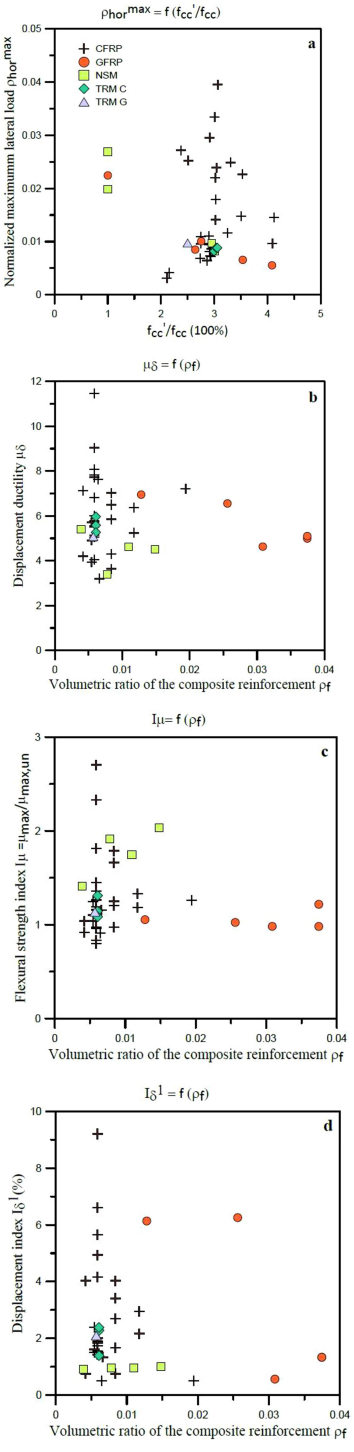

Figure 2. a) maximum normalized lateral load dependence on f'_{cc}/f_{cc}, b) displacement ductility dependence on volumetric ratio of the composite reinforcement, c) flexural strength index I_μ dependence on volumetric ratio of the composite reinforcement, d) displacement index I_δ^1 dependence on volumetric ratio of the composite reinforcement.

effective since it noted the same ultimate displacement ($\delta_{max} = 124$ mm) but no failure compared to the columns containing TRM G. Since the column with TRM G failed, the corresponding column with TRM C developed higher displacement ductility (10% higher).

By comparing the results of columns strengthened with CFRP and columns with TRMC, it was proved that the TRMC exhibited greater flexural strength index I_μ (3.6–5.6% more) (Fig. 2(c)). Regarding the increase in displacement corresponding to the first failure, it seems that in specimens without lap-splices the TRMC develops higher contribution than CFRP (52% higher), while in specimens with lap-splices the CFRP contributed more (16%) (Fig. 2(d))). Examining the maximum displacement, it seems that in specimens without lap-splices the TRMC develops higher contribution (48%), while in specimens with lap-splices both materials demonstrated similar behavior, so the main mechanism that defined the behavior are the lap-splices (Table 7). Overall, TRM C exhibited greater values of displacement ductility than CFRP (Fig. 2(b)) and similar results were recorded between the two materials for enhancing the concrete's compressive strength (Fig. 2(a)).

Columns with glass fiber composites (GFRP) exhibited three times higher increase in displacement index I_δ^1 and 29% increase in displacement ductility compared to columns strengthened with glass textile reinforced mortar (TRMG), since the material corresponds to higher failure strain $\varepsilon_{f,u}$.

Near surface mounted FRP bars (NSM) did not contribute in increasing the displacement in which the first failure is developed and in displacement ductility (Fig. 2(b, d)), but contributed in increasing the maximum lateral load and maximum moment that the column can undertake (40–90%) (Fig. 2(a,c)), making them an effective flexural strengthening technique.

Composite laminates did not help in increasing the displacement index I_δ^1, the maximum displacement and the displacement ductility. However, they proved capable of increasing the maximum moment achieved (Table 8).

Transverse embedded bars placed in the middle of each side of the column led to increased maximum displacement and ductility, but did not increase the strength for confined concrete and maximum moment (Fig. 2(a, b, c)).

Steel profiles placed along the corners at the base of each column are proved not to help in terms of confinement and ductility and prevent the full development of maximum displacement and displacement in which the first failure is formed. However, (they work favorably in obtaining a higher level of maximum moment (49% increase). The reason of this notation is attributed to the increased elements' stiffness caused by the installation of steel profiles.

By analysing the provisions of international standards and codes (CNR 2004, Eurocode 8 1998, FIB Bulletin No. 56. 2010) R^2 coefficient is extracted. Results show (Fig. 3) that for FRP fracture type of failure, the Italian CNR provides more accurate outcomes,

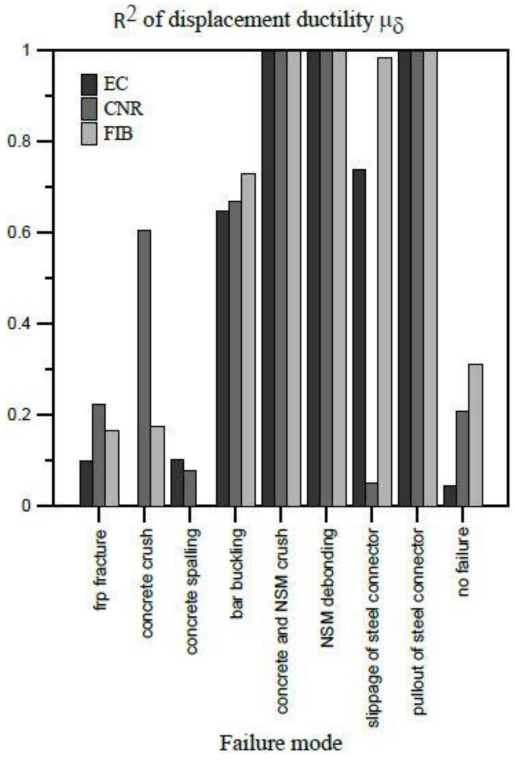

Figure 3. Bar chart of R^2 (EC, CNR, FIB) for every type of failure.

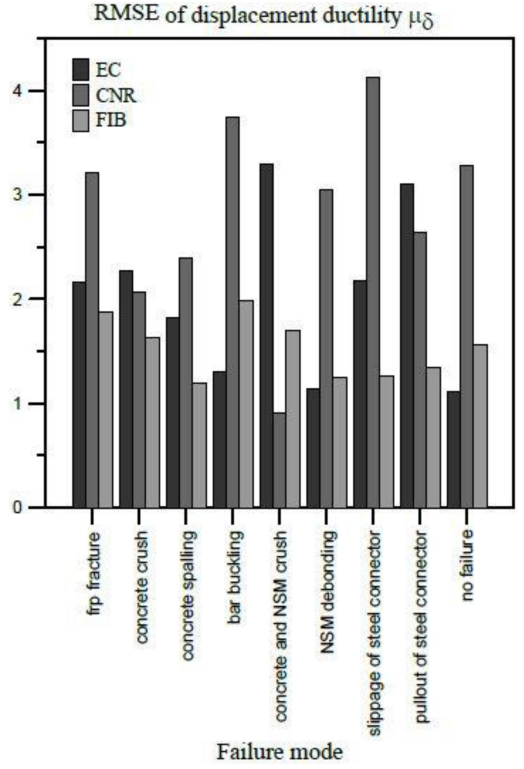

Figure 4. Bar chart of RMSE (EC, CNR, FIB) for every type of failure.

followed by the European FIB and Eurocode (EC). Furthermore, for a concrete spalling type of failure the respective ranking arose differently, where Eurocode (EC) fits better to the experimental results, followed by the Italian CNR and European FIB codes.

The distribution of errors between the results of codes and experiments were examined by using the coefficient RMSE. RMSE values and the corresponding bar charts (Fig. 4) showed that for FRP fracture and concrete spalling type of failures, the European FIB code delivers less distribution of errors, followed by Eurocode (EC) and the Italian CNR.

According to the estimators' plots for codes, regarding every type of failure, it is concluded that the Italian CNR code was the most conservative and European FIB the most immoderate. The reason for this is attributed to the fact that in general the estimators between experimental and CNR values of ductility is located above the ideal estimator (identity line, slope of 1:1) (Fig. 5(b)). Respectively, the estimator between experiments' and FIB's ductility results appear under the ideal estimator more often than the other codes' results (Fig. 5(c)). In general, all the codes studied are considered conservative due to the data positions in the charts. The data correspond to a value of ductility predicted by the design codes on the horizontal axis and the respective experimental value of ductility. The ideal estimator is constructed in order to represent the identity line, which notes a slope of 1. If the data appear to be above the ideal estimator, the code predicts lower ductility than the experimental, which means that the code is conservative. In contrast, if the data emerge below the ideal estimator, the miscalculation according to the design code can result to unexpected failure. Such conclusions may be drawn from Figure 5. EC and FIB did not effectively predict ductility in columns that were retrofitted with NSM bars and failed due to NSM and concrete crushing. Furthermore, displacement ductility in columns that failed due to FRP fracture and concrete crushing was in some cases calculated successfully by EC and FIB. The same results arose for a concrete spalling failure in FIB's predictions. Regarding CNR's estimations, the results showed that in almost every case, the predictions surpass the experimental values, which indicates safer but not necessarily more accurate results. Figure 5 confirms and depicts all the above, especially for displacement ductility levels surpassing a value $\mu_\delta = 4$. Practically, the scatters emerging below the ideal estimator state the divergence of codes' predictions in terms of failure modes. That is to say, codes in cases overestimate or underestimate displacement ductility, though they are specific on the kind of failure the interface is expected to exhibit with the strengthening performance chosen. Especially in the case of EC code, there is a strong tendency after a specific level of performance to note failures of all FRP

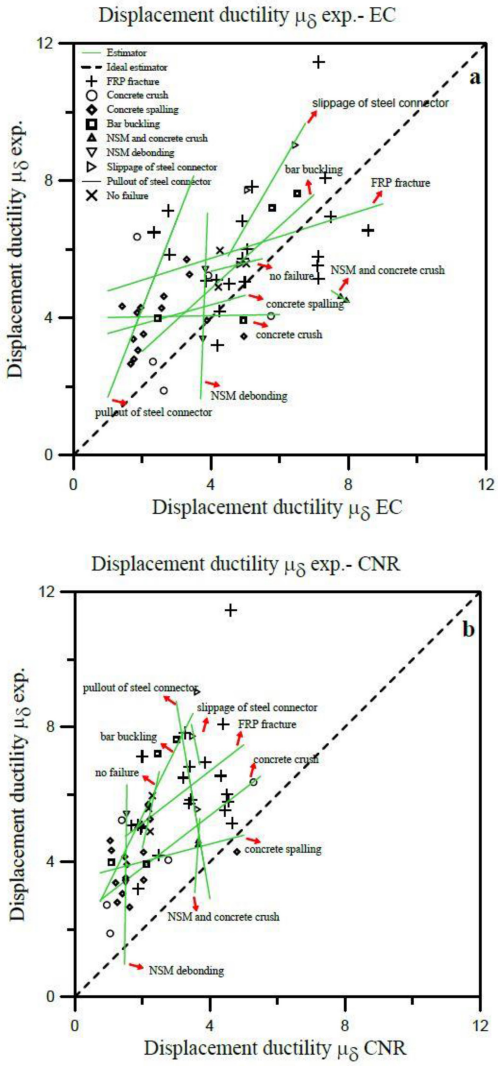

Figure 5a, b. Estimator charts for every type of failure for a) EC and b) CNR.

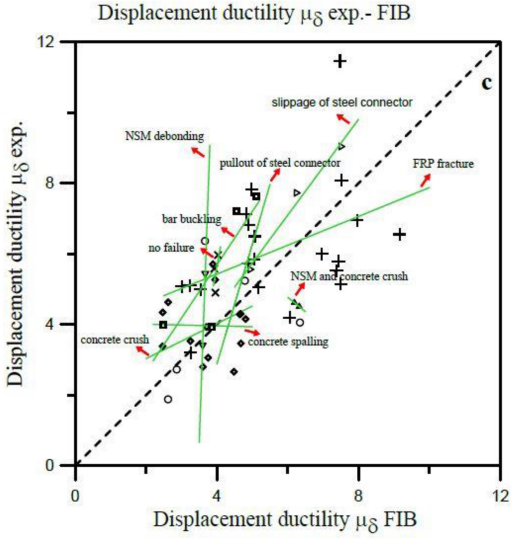

Figure 5c. Estimator chart for every type of failure for FIB.

strengthening systems. Given the opportunity, further information regarding failures correlated to performance level should be incorporated into modern codes with simple tools.

In the current analytical model, the force transfer mechanism between concrete and FRP is analyzed. Shear and normal stresses that are created along the interface at every loading phase can be obtained and examined. It is also possible to predict the ultimate external load in which debonding occurs or concrete's surface fails.

From the exported results, using the aforementioned experimental database, it is concluded that the use of steel connectors in the base of columns apart from strengthening purposes, it also helps preventing debonding of FRP sheets and eventually premature failure. As in the experimental process only FRP fracture is observed, it is proven that steel connectors helped to shift the maximum stress concentration range in the interface above them and prevent the debonding area that was observed from the analytical solution.

5 CONCLUSIONS

A comparison between composite materials and retrofitting systems is conducted. It is noted that design codes do not provide recommendations regarding the most suitable technique for each desired retrofit. Moreover, there are no regulations and distinctions regarding failure modes among different performance levels and strengthening system.

In every retrofitting system the composite material used is found to be a very important factor with regard to the efficiency of the retrofitting element.

The effect of confinement was distinctively significant in the response and behavior of retrofitted concrete columns when subjected to seismic loading in terms of strength, ductility and load and deformation capacity as found in previous research. The new element emphasized by this study is the failure every retrofitting system exhibits depending on the different performance level.

Finally, an algorithm based on non-linear slip-stress law is transformed for cases of RC columns strengthened with FRP sheets. This investigation results in defining the region in which the failure mode initiates and the length of the phenomenon.

It is noted that usage of steel profiles at the column's base can contribute in terms of shifting the length of the zone in which debonding of the FRP may be developed. Consequently the length in which stress concentration may occur is eventually located above

the profiles. Nevertheless, in all the cases which did not include steel profile retrofitting, the algorithm's results were in good agreement with the experimental observations.

REFERENCES

Bizindavyi, B. & Neale, K. (1999). Transfer Lengths and bond strengths for composites bonded to concrete. Journal of Composites for Construction. 3(4):153–160.

Bournas, D. et al. (2009). Textile-Reinforced Mortar versus FRP Jacketing in Seismic Retrofitting of RC Columns with Continuous or Lap-Spliced Deformed Bars. Journal of Composites for Construction. 13(5):360–371.

Chajes, M. et al. (1996). Bond and force transfer of composites materials plates bonded to concrete. Structural Journal. 93(2): 209–217.

Chalioris, C. (2008). Torsional Strengthening of Rectangular and Flanged Beams using carbon fibre-reinforced-polymers – Experimental Study. Construction and Building Materials. 22(1): 21–29.

CNR. (2004). Guide for the design and construction of externally bonded FRP systems for strengthening existing structures (materials, RC and PC structures, masonry structures), CNR-DT 200/2004. Italian National Research Council, Advisory Committee on Technical Recommendations for Constructions. Rome.

Eurocode 8. (1998). Design of structures for earthquake resistance, Part 3: Assessment and retrofitting of Buildings.

FIB Bulletin No. 56. (2010). Model Code 2010 – First complete draft, Volume 2. International Federation for Structural Concrete.

Karabinis, A. (2002). Reinforced concrete beam-column joints with lap splices under cyclic loading. Structural Engineering and Mechanics. 14(6).

Karabinis, A. & Rousakis, T. (2002). Concrete confined by FRP material: A plasticity approach. Engineering Structures. 24(7): 923–932.

Karayannis, C. & Sirkelis, G. (2008). Strengthening and rehabilitation of RC beam–column joints using carbon-FRP jacketing and epoxy resin injection. Earthquake Engineering & Structural Dynamics. 37(5):769–790.

Realfonzo, R. & Napoli, A. (2009). Cyclic Behavior of RC Columns Strengthened by FRP and Steel Devices. Journal of Structural Engineering. 135(10): 1164–1176.

Realfonzo, R. & Napoli, A. (2012). Results from cyclic tests on high aspect ratio RC columns strengthened with FRP systems. Construction and Building Materials. 37: 606–620.

Rousakis, T. et al. (2007). FRP-confined concrete members: Axial compression experiments and plasticity modelling. Engineering Structures. 29(7): 1343–1353.

Sadone, R. et al. (2012). Experimental study on RC columns retrofitted by FRP and subjected to seismic loading. Conference on FRP Composites in Civil Engineering, CICE. Rome.

Sarafraz, M. & Danesh, F. (2010). Experimental Study on Flexural Strengthening of RC Columns with Near Surface Mounted FRP Bars. Journal of Seismology and Earthquake Engineering. 12(1–2).

Smith, J. & Teng, J. (2001). Interfacial stresses in plated beams. Engineering Structures. 23(7):857–871.

Wang, J. (2006). Cohesive zone model of intermediate crack-induced debonding of FRP-plated concrete beam. International Journal of Solids and Structures. 43(21): 6630–6648.

Wang, J. (2007). Cohesive zone model of FRP-concrete interface debonding under mixed-mode loading. International Journal of Solids and Structures. 44(20): 6551–6568.

Wang, J. & Zhang, C. (2008). Nonlinear fracture mechanics of flexural–shear crack induced debonding of FRP strengthened concrete beams. International Journal of Solids and Structures. 45(10): 2916–2936.

Wu, Y. et al. (2008). Experimental Investigation on Seismic Retrofitting of Square RC Columns by Carbon FRP Sheet Confinement Combined with Transverse Short Glass FRP Bars in Bored Holes. Journal of Composites for Construction. 12(1):53–60.

ANNEX A – TABLES

Table 1. Experimental data.

Source	Specimen	h (mm)	b (mm)	H (mm)	r_f (mm)	c (mm)	h′ (mm)	b′ (mm)	A_g (mm^2)
Realfonzo &	C3-S	300	300	2200	–	27	–	–	
Napoli	C4-S-G	300	300	2200	30	27	240	240	89016
2009	C1-S-G	300	300	2200	30	27	240	240	89016
	C10-S-C	300	300	2200	30	27	240	240	89016
	C13-S-C	300	300	2200	30	27	240	240	89016
	C2-S-A1	300	300	2200	30	27	240	240	89016
	C11-S-A1	300	300	2200	30	27	240	240	89016
	C6-S-A2	300	300	2200	30	27	240	240	89016
	C16-S	300	300	2200	–	27	–	–	
	C18-S	300	300	2200	–	27	–	–	
	C17-S-C	300	300	2200	30	27	240	240	89016
	C19-S-C	300	300	2200	30	27	240	240	89016
	C20-S-A2	300	300	2200	30	27	240	240	89016
	C12-S-A2	300	300	2200	30	27	240	240	89016
	C9-D	300	300	2200	–	27	–	–	
	C7-D-C	300	300	2200	30	27	240	240	89016
	C8-D-C	300	300	2200	30	27	240	240	89016
	C14-D-C	300	300	2200	30	27	240	240	89016
	C15-D-A1	300	300	2200	30	27	240	240	89016
	C21-D	300	300	2200	–	27	–	–	
	C22-D-C	300	300	2200	30	27	240	240	89016
	C23-D-C	300	300	2200	30	27	240	240	89016
	C24-D-A1	300	300	2200	30	27	240	240	89016
Realfonzo &	C25-S	700	300	2500	–	30	–	–	
Napoli	C26-S-C	700	300	2500	30	30	640	240	209046
2012	C27-S-C	700	300	2500	30	30	640	240	209046
	C28-S-A1	700	300	2500	30	30	640	240	209046
	C29-D	700	300	2500	–	30	–	–	
	C30-D-C	700	300	2500	30	30	640	240	209046
	C31-D-C	700	300	2500	30	30	640	240	209046
	C32-D-A1	700	300	2500	30	30	640	240	209046
	C33D-C	700	300	2500	30	30	640	240	209046
Wu et al.	C2	200	200	1320	–	25	–		
2008	C3	200	200	1320	–	25	170	170	39823
	C4	200	200	1320	15	25	170	170	39823
	C5	200	200	1320	15	25	170	170	39823
	C6	200	200	1320	15	25	170	170	39823
Sarafraz &	C1	200	200	1000	–	18	–	–	
Danesh	C2	200	200	1000	20	18	160	160	39632
2010	C3	200	200	1000	20	18	160	160	39632
	C4	200	200	1000	20	18	160	160	39632
	C5	200	200	1000	20	18	160	160	39632
Bournas et al.	L0_C	250	250	1600	–	10	–	–	
2009	L0_R2	250	250	1600	25	10	200	200	61868
	L0_M4	250	250	1600	25	10	200	200	61868
	L0_M4G	250	250	1600	25	10	200	200	61868
	L20d_C	250	250	1600	–	10	–	–	
	L20d_R2	250	250	1600	25	10	200	200	61868
	L20d_M4	250	250	1600	25	10	200	200	61868
	L40d_C	250	250	1600	–	10	–		
	L40d_R2	250	250	1600	25	10	200	200	61868
	L40d_M4	250	250	1600	25	10	200	200	61868
Sadone et al.	Pref-1	370	250	2500	–	18	–	–	
2012	PC-1	370	250	2500	18	18	334	214	92220
	PCL-1	370	250	2500	18	18	334	214	92220

Table 2. Experimental data.

Source	Specimen	Steel bar type	n	$Ø_l$ (mm)	ρ_l (%*)	$f_{y,l}$ (MPa)	$Ø_s$ (mm)	s (mm)	ρ_s (%*)	$f_{y,s}$ (MPa)
Realfonzo & Napoli 2009	C3-S	Smooth	6	14	10.0	346	8	200	1.67	346
	C4-S-G	Smooth	6	14	10.0	346	8	200	1.67	346
	C1-S-G	Smooth	6	14	10.0	346	8	200	1.67	346
	C10-S-C	Smooth	6	14	10.0	346	8	200	1.67	346
	C13-S-C	Smooth	6	14	10.0	346	8	200	1.67	346
	C2-S-A1	Smooth	6	14	10.0	346	8	200	1.67	346
	C11-S-A1	Smooth	6	14	10.0	346	8	200	1.67	346
	C6-S-A2	Smooth	6	14	10.0	346	8	200	1.67	346
	C16-S	Smooth	6	14	10.0	346	8	200	1.67	346
	C18-S	Smooth	6	14	10.0	346	8	200	1.67	346
	C17-S-C	Smooth	6	14	10.0	346	8	200	1.67	346
	C19-S-C	Smooth	6	14	10.0	346	8	200	1.67	346
	C20-S-A2	Smooth	6	14	10.0	346	8	200	1.67	346
	C12-S-A2	Smooth	6	14	10.0	346	8	200	1.67	346
	C9-D	Deformed	6	14	10.0	556	8	200	1.67	556
	C7-D-C	Deformed	6	14	10.0	556	8	200	1.67	556
	C8-D-C	Deformed	6	14	10.0	556	8	200	1.67	556
	C14-D-C	Deformed	6	14	10.0	556	8	200	1.67	556
	C15-D-A1	Deformed	6	14	10.0	556	8	200	1.67	556
	C21-D	Deformed	6	14	10.0	556	8	200	1.67	556
	C22-D-C	Deformed	6	14	10.0	556	8	200	1.67	556
	C23-D-C	Deformed	6	14	10.0	556	8	200	1.67	556
	C24-D-A1	Deformed	6	14	10.0	556	8	200	1.67	556
Realfonzo & Napoli 2012	C25-S	Smooth	14	14	10.0	346	8	200	1.20	346
	C26-S-C	Smooth	14	14	10.0	346	8	200	1.20	346
	C27-S-C	Smooth	14	14	10.0	346	8	200	1.20	346
	C28-S-A1	Smooth	14	14	10.0	346	8	200	1.20	346
	C29-D	Deformed	14	14	10.0	556	8	200	1.20	556
	C30-D-C	Deformed	14	14	10.0	556	8	200	1.20	556
	C31-D-C	Deformed	14	14	10.0	556	8	200	1.20	556
	C32-D-A1	Deformed	14	14	10.0	556	8	200	1.20	556
	C33D-C	Deformed	14	14	10.0	556	8	200	1.20	556
Wu et al. 2008	C2	Deformed	4	16	30.2	507.6	6	100	2.83	419.3
	C3	Deformed	4	16	30.2	507.6	6	100	2.83	419.3
	C4	Deformed	4	16	30.2	507.6	6	100	2.83	419.3
	C5	Deformed	4	16	30.2	507.6	6	100	2.83	419.3
	C6	Deformed	4	16	30.2	507.6	6	100	2.83	419.3
Sarafraz & Danesh 2010	C1	Deformed	4	14	15.3	410	10	100	7.85	380
	C2	Deformed	4	14	15.3	410	10	100	7.85	380
	C3	Deformed	4	14	15.3	410	10	100	7.85	380
	C4	Deformed	4	14	15.3	410	10	100	7.85	380
	C5	Deformed	4	14	15.3	410	10	100	7.85	380
Bournas et al. 2009	L0_C	Deformed	4	14	9.9	523	8	200	2.01	351
	L0_R2	Deformed	4	14	9.9	523	8	200	2.01	351
	L0_M4	Deformed	4	14	9.9	523	8	200	2.01	351
	L0_M4G	Deformed	4	14	9.9	523	8	200	2.01	351
	L20d_C	Deformed	4	14	9.9	523	8	200	2.01	351
	L20d_R2	Deformed	4	14	9.9	523	8	200	2.01	351
	L20d_M4	Deformed	4	14	9.9	523	8	200	2.01	351
	L40d_C	Deformed	4	14	9.9	523	8	200	2.01	351
	L40d_R2	Deformed	4	14	9.9	523	8	200	2.01	351
	L40d_M4	Deformed	4	14	9.9	523	8	200	2.01	351
Sadone et al. 2012	Pref-1	Deformed	6	10	5.1	603.5	6	150	1.26	613.7
	PC-1	Deformed	6	10	5.1	603.5	6	150	1.26	613.7
	PCL-1	Deformed	6	10	5.1	603.5	6	150	1.26	613.7

Table 3. Experimental data.

Source	Specimen	Retroffiting technique	$E_{f,sh}$ (GPa)	$\varepsilon_{f,u,sh}$ (%)	$f_{f,u,sh}$ (MPa)	t_j (mm)	$t_{j,tot}$ (mm)	$\rho_{f,sh}$ (%*)
Realfonzo	C3-S	–	–	–	–	–	–	–
& Napoli	C4-S-G	GFRP sheets	80.7	3.5	2560	0.48	0.96	12.80
2009	C1-S-G	GFRP sheets	80.7	3.5	2560	0.48	1.92	25.60
	C10-S-C	CFRP sheets	390	0.8	3000	0.22	0.44	5.87
	C13-S-C	CFRP sheets	390	0.8	3000	0.22	0.44	5.87
	C2-S-A1	CFRP sheets	390	0.8	3000	0.22	0.44	5.87
	C11-S-A1	CFRP sheets	390	0.8	3000	0.22	0.44	5.87
	C6-S-A2	CFRP sheets	390	0.8	3000	0.22	0.44	5.87
	C16-S	–	–	–	–	–	–	–
	C18-S	–	–	–	–	–	–	–
	C17-S-C	CFRP sheets	390	0.8	3000	0.22	0.44	5.87
	C19-S-C	CFRP sheets	390	0.8	3000	0.22	0.88	11.73
	C20-S-A2	CFRP sheets	390	0.8	3000	0.22	0.44	5.87
	C12-S-A2	CFRP sheets	390	0.8	3000	0.22	0.44	5.87
	C9-D	–	–	–	–	–	–	–
	C7-D-C	CFRP sheets	390	0.8	3000	0.22	0.44	5.87
	C8-D-C	CFRP sheets	390	0.8	3000	0.22	0.44	5.87
	C14-D-C	CFRP sheets	390	0.8	3000	0.22	0.44	5.87
	C15-D-A1	CFRP sheets	390	0.8	3000	0.22	0.44	5.87
	C21-D	–	–	–	–	–	–	–
	C22-D-C	CFRP sheets	390	0.8	3000	0.22	0.44	5.87
	C23-D-C	CFRP sheets	390	0.8	3000	0.22	0.88	11.73
	C24-D-A1	CFRP sheets	390	0.8	3000	0.22	0.44	5.87
Realfonzo	C25-S	–	–	–	–	–	–	–
& Napoli	C26-S-C	CFRP sheets	390	0.8	3000	0.22	0.44	4.19
2012	C27-S-C	CFRP sheets	390	0.8	3000	0.22	0.88	8.38
	C28-S-A1	CFRP sheets	390	0.8	3000	0.22	0.88	8.38
	C29-D	–	–	–	–	–	–	–
	C30-D-C	CFRP sheets	390	0.8	3000	0.22	0.44	4.19
	C31-D-C	CFRP sheets	390	0.8	3000	0.22	0.88	8.38
	C32-D-A1	CFRP sheets	390	0.8	3000	0.22	0.88	8.38
	C33D-C	CFRP sheets	390	0.8	3000	0.22	0.88	8.38
Wu et al.	C2	–	–	–	–	–	–	–
2008	C3	GFRP bars	–	–	–	–	–	–
	C4	GFRP bars+CFRP sheets	230	1.78	4049	0.165	0.33	6.60
	C5	GFRP bars+CFRP sheets	230	1.78	4049	0.165	0.33	6.60
	C6	CFRP sheets	230	1.78	4049	0.165	0.33	6.60
Sarafraz &	C1	–	–	–	–	–	–	–
Danesh	C2	NSM bars	–	–	–	–	–	–
2010	C3	NSM bars	–	–	–	–	–	–
	C4	NSM bars+CFRP sheets	240	1.55	3800	0.176	0.352	7.04
	C5	NSM bars+CFRP sheets	240	1.55	3800	0.176	0.352	7.04
Bournas	L0_C	–	–	–	–	–	–	–
et al.	L0_R2	CFRP sheets	230	1.65	3800	0.17	0.34	5.44
2009	L0_M4	TRM Carbon sheets	225	1.69	3800	0.095	0.38	6.08
	L0_M4G	TRM Glass sheets	70	2.43	1700	0.089	0.356	5.70
	L20d_C	–	–	–	–	–	–	–
	L20d_R2	CFRP sheets	230	1.65	3800	0.17	0.34	5.44
	L20d_M4	TRM Carbon sheets	225	1.69	3800	0.095	0.38	6.08
	L40d_C	–	–	–	–	–	–	–
	L40d_R2	CFRP sheets	230	1.65	3800	0.17	0.34	–5.44
	L40d_M4	TRM Carbon sheets	225	1.69	3800	0.095	0.38	6.08
Sadone	Pref-1	–	–	–	–	–	–	–
et al.	PC-1	CFRP sheets	105	1	1050	0.48	0.48	6.43
2012	PCL-1	CFRP sheets+ Laminates	105	1	1050	0.48	0.48	6.43

Table 4. Experimental data.

Source	Specimen	D_{bar} (mm)	l_{bar} (mm)	$E_{f,bar}$ (GPa)	$\varepsilon_{f,u,bar}$ (%)	$f_{u,bar}$ (MPa)	$\rho_{f,bar}$ (%)	$E_{f,lam}$ (GPa)	$\varepsilon_{f,u,lam}$ (%*)	$f_{u,lam}$ (MPa)	$\rho_{f,lam}$ (%*)
Realfonzo	C3-S	–	–	–	–	–	–	–	–	–	–
& Napoli	C4-S-G	–	–	–	–	–	–	–	–	–	–
2009	C1-S-G	–	–	–	–	–	–	–	–	–	–
	C10-S-C	–	–	–	–	–	–	–	–	–	–
	C13-S-C	–	–	–	–	–	–	–	–	–	–
	C2-S-A1	–	–	–	–	–	–	–	–	–	–
	C11-S-A1	–	–	–	–	–	–	–	–	–	–
	C6-S-A2	–	–	–	–	–	–	–	–	–	–
	C16-S	–	–	–	–	–	–	–	–	–	–
	C18-S	–	–	–	–	–	–	–	–	–	–
	C17-S-C	–	–	–	–	–	–	–	–	–	–
	C19-S-C	–	–	–	–	–	–	–	–	–	–
	C20-S-A2	–	–	–	–	–	–	–	–	–	–
	C12-S-A2	–	–	–	–	–	–	–	–	–	–
	C9-D	–	–	–	–	–	–	–	–	–	–
	C7-D-C	–	–	–	–	–	–	–	–	–	–
	C8-D-C	–	–	–	–	–	–	–	–	–	–
	C14-D-C	–	–	–	–	–	–	–	–	–	–
	C15-D-A1	–	–	–	–	–	–	–	–	–	–
	C21-D	–	–	–	–	–	–	–	–	–	–
	C22-D-C	–	–	–	–	–	–	–	–	–	–
	C23-D-C	–	–	–	–	–	–	–	–	–	–
	C24-D-A1	–	–	–	–	–	–	–	–	–	–
Realfonzo	C25-S	–	–	–	–	–	–	–	–	–	–
& Napoli	C26-S-C	–	–	–	–	–	–	–	–	–	–
2012	C27-S-C	–	–	–	–	–	–	–	–	–	–
	C28-S-A1	–	–	–	–	–	–	–	–	–	–
	C29-D	–	–	–	–	–	–	–	–	–	–
	C30-D-C	–	–	–	–	–	–	–	–	–	–
	C31-D-C	–	–	–	–	–	–	–	–	–	–
	C32-D-A1	–	–	–	–	–	–	–	–	–	–
	C33D-C	–	–	–	–	–	–	–	–	–	–
Wu et al.	C2	–	–	–	–	–	–	–	–	–	–
2008	C3	6	100	58.62	1.45	850	30.8	–	–	–	–
	C4	6	100	58.62	1.45	850	30.8	–	–	–	–
	C5	6	100	58.62	1.45	850	30.8	–	–	–	–
	C6	–	–	–	–	–	–	–	–	–	–
arafraz	C1	–	–	–	–	–	–	–	–	–	–
& Danesh	C2	10	700	40.8	1.6	760	3.9	–	–	–	–
2010	C3	10	700	40.8	1.6	760	7.8	–	–	–	–
	C4	10	700	40.8	1.6	760	3.9	–	–	–	–
	C5	10	700	40.8	1.6	760	7.8	–	–	–	–
Bournas	L0_C	–	–	–	–	–	–	–	–	–	–
et al.	L0_R2	–	–	–	–	–	–	–	–	–	–
2009	L0_M4	–	–	–	–	–	–	–	–	–	–
	L0_M4G	–	–	–	–	–	–	–	–	–	–
	L20d_C	–	–	–	–	–	–	–	–	–	–
	L20d_R2	–	–	–	–	–	–	–	–	–	–
	L20d_M4	–	–	–	–	–	–	–	–	–	–
	L40d_C	–	–	–	–	–	–	–	–	–	–
	L40d_R2	–	–	–	–	–	–	–	–	–	–
	L40d_M4	–	–	–	–	–	–	–	–	–	–
Sadone	Pref-1	–	–	–	–	–	–	–	–	–	–
et al.	PC-1	–	–	–	–	–	–	–	–	–	–
2012	PCL-1	–	–	–	–	–	–	160	7	11200	12.9

Table 5. Experimental data.

Source	Specimen	N (KN)	v	f_{ck} (MPa)	f_{cm} (MPa)	Bar distance from section edge
Realfonzo & Napoli 2009	C3-S	323.82	0.140	17.7	25.7	–
	C4-S-G	312.48	0.140	16.8	24.8	–
	C1-S-G	362.88	0.140	20.8	28.8	–
	C10-S-C	327.60	0.140	18.0	26	–
	C13-S-C	364.14	0.140	20.9	28.9	–
	C2-S-A1	346.50	0.140	19.5	27.5	–
	C11-S-A1	381.24	0.120	27.3	35.3	–
	C6-S-A2	333.90	0.140	18.5	26.5	–
	C16-S	990.00	0.400	19.5	27.5	–
	C18-S	486.00	0.400	5.5	13.5	–
	C17-S-C	612.00	0.400	9.0	17	–
	C19-S-C	496.80	0.400	5.8	13.8	–
	C20-S-A2	435.60	0.400	4.1	12.1	–
	C12-S-A2	824.40	0.400	14.9	22.9	–
	C9-D	372.06	0.130	23.8	31.8	–
	C7-D-C	328.86	0.140	18.1	26.1	–
	C8-D-C	333.90	0.140	18.5	26.5	–
	C14-D-C	381.24	0.120	27.3	35.3	–
	C15-D-A1	277.20	0.140	14.0	22	–
	C21-D	421.20	0.400	3.7	11.7	–
	C22-D-C	421.20	0.400	3.7	11.7	–
	C23-D-C	450.00	0.400	4.5	12.5	–
	C24-D-A1	540.00	0.400	7.0	15	–
Realfonzo & Napoli 2012	C25-S	635.25	0.250	4.1	12.1	–
	C26-S-C	855.75	0.250	8.3	16.3	–
	C27-S-C	687.75	0.250	5.1	13.1	–
	C28-S-A1	724.50	0.250	5.8	13.8	–
	C29-D	614.25	0.250	3.7	11.7	–
	C30-D-C	1186.5	0.250	14.6	22.6	–
	C31-D-C	787.50	0.250	7.0	15	–
	C32-D-A1	614.25	0.250	3.7	11.7	–
	C33D-C	370.44	0.140	4.6	12.6	–
Wu et al. 2008	C2	440.00	0.201	46.6	54.6	–
	C3	440.00	0.201	46.7	54.7	60/70
	C4	440.00	0.200	46.9	54.9	60/70
	C5	440.00	0.248	36.4	44.4	60/70
	C6	440.00	0.244	37.0	45	–
Sarafraz & Danesh 2010	C1	200.00	0.160	23.3	31.3	–
	C2	200.00	0.163	22.7	30.7	100
	C3	200.00	0.169	21.6	29.6	47
	C4	200.00	0.177	20.3	28.3	100
	C5	200.00	0.161	23.1	31.1	47
Bournas et.al 2009	L0_C	534.88	0.275	23.1	31.12	–
	L0_R2	530.75	0.275	22.9	30.88	–
	L0_M4	528.00	0.275	22.7	30.72	–
	L0_M4G	526.63	0.275	22.6	30.64	–
	L20d_C	519.75	0.275	22.2	30.24	–
	L20d_R2	501.88	0.275	21.2	29.2	–
	L20d_M4	499.13	0.275	21.0	29.04	–
	L40d_C	492.25	0.275	20.6	28.64	–
	L40d_R2	488.13	0.275	20.4	28.4	–
	L40d_M4	485.38	0.275	20.2	28.24	–
Sadone et al. 2012	Pref-1	700.00	0.107	63.0	71.04	–
	PC-1	700.00	0.097	70.2	78.23	–
	PCL-1	700.00	0.137	47.3	55.32	18

Table 6. Experimental data.

Source	Specimen	First failure type	δ_1 (mm)	l_b (mm)
Realfonzo & Napoli 2009	C3-S	concrete spalling	20.00	600
	C4-S-G	FRP fracture	122.74	600
	C1-S-G	FRP fracture	125.12	600
	C10-S-C	FRP fracture	83.13	600
	C13-S-C	FRP fracture	98.77	600
	C2-S-A1	FRP fracture	113.05	600
	C11-S-A1	FRP fracture	132.09	600
	C6-S-A2	FRP fracture	184.11	600
	C16-S	concrete crush	52.02	600
	C18-S	concrete spalling	41.99	600
	C17-S-C	concrete crush	79.90	600
	C19-S-C	concrete crush	90.95	600
	C20-S-A2	slippage of steel connector	98.60	600
	C12-S-A2	FRP fracture	73.10	600
	C9-D	concrete spalling	59.67	600
	C7-D-C	FRP fracture	118.83	600
	C8-D-C	FRP fracture	109.48	600
	C14-D-C	FRP fracture	109.82	600
	C15-D-A1	slippage of steel connector	85.00	600
	C21-D	concrete spalling	47.43	600
	C22-D-C	FRP fracture	95.03	600
	C23-D-C	concrete crush	140.08	600
	C24-D-A1	slippage of steel connector	71.91	600
Realfonzo & Napoli 2012	C25-S	concrete spalling	60.00	600
	C26-S-C	FRP fracture	45.00	600
	C27-S-C	FRP fracture	45.00	600
	C28-S-A1	pullout of the steel connectors	100.00	600
	C29-D	concrete spalling	22.33	600
	C30-D-C	FRP fracture	90.00	600
	C31-D-C	FRP fracture	90.00	600
	C32-D-A1	pullout of the steel connectors	60.00	600
	C33D-C	concrete spalling	76.10	600
Wu et al. 2008	C2	concrete crush	49.14	–
	C3	concrete spalling	27.72	–
	C4	FRP fracture	65.52	–
	C5	FRP fracture	65.52	–
	C6	FRP fracture	65.52	–
Sarafraz & Danesh 2010	C1	concrete spalling	23.00	–
	C2	NSM debonding	21.00	–
	C3	NSM debonding	22.00	–
	C4	NSM and concrete crush	22.00	–
	C5	NSM and concrete crush	23.00	–
Bournas et.al 2009	L0_C	bar buckling	54.88	–
	L0_R2	bar buckling	82.48	–
	L0_M4	no failure	124.96	–
	L0_M4G	FRP fracture	115.20	–
	L20d_C	concrete spalling	57.44	280
	L20d_R2	concrete spalling	92.48	280
	L20d_M4	concrete spalling	80.00	280
	L40d_C	concrete spalling	52.40	560
	L40d_R2	no failure	124.96	560
	L40d_M4	no failure	124.96	560
Sadone et al. 2012	Pref-1	concrete spalling	70.00	–
	PC-1	bar buckling	35.00	–
	PCL-1	bar buckling	35.00	–

Table 7. Results.

Source	Specimen	F_y (KN)	δ_{Fy} (mm)	F_{max+} (kN)	δ_{Fmax+} (mm)	F_{max-} (kN)	δ_{Fmax-} (mm)	δ_{max} (mm)
Realfonzo & Napoli 2009	C3-S	49	16	52.73	47.33	50.91	30	68.6
	C4-S-G	48	17.7	55.07	60.36	50.31	42.6	123
	C1-S-G	53	17.7	62.45	115.98	56.51	35.5	116
	C10-S-C	45	17	49.71	35	51.02	35.5	87.5
	C13-S-C	45	18	49.08	49	48.14	27	99.4
	C2-S-A1	70	18.8	83.75	58	76.89	49.7	108.8
	C11-S-A1	80	18	97.53	99.5	95.69	48	145.5
	C6-S-A2	28.2	16	40.64	49.7	63.32	50.88	183.4
	C16-S	73	20	81.51	36	69.82	30.6	54.5
	C18-S	36	17	42.33	27	41.21	24.8	52
	C17-S-C	52	18	61.95	72.2	56.26	42.6	73
	C19-S-C	45	18.9	50.27	32.7	50.81	39.6	99
	C20-S-A2	93	19.8	100.47	49.5	79.57	39	179
	C12-S-A2	84.5	19.8	91.67	29.7	87.53	29.7	100
	C9-D	56	17	71.08	42	66.32	41	60
	C7-D-C	58	17	65.33	52	69.1	102.28	116
	C8-D-C	61	17	69.74	42.6	63.51	46.16	97.5
	C14-D-C	54	17	62.87	35	58.65	33.3	133
	C15-D-A1	104	17.9	110.74	50.38	110.81	49.21	99.5
	C21-D	48	20	52.83	37.5	47.05	32	56
	C22-D-C	47	20	55.74	40	59.54	30	120
	C23-D-C	61	22	72.94	100	69.03	60	140
	C24-D-A1	112	22	119.82	52	112.35	42	170
Realfonzo & Napoli 2012	C25-S	134	14	161.67	29.43	158.08	22.25	58.14
	C26-S-C	158	15.3	229.31	44.31	218.63	43.3	64.24
	C27-S-C	166	15.3	202.09	52.29	215.49	59.29	89.5
	C28-S-A1	231	16.8	302.04	89.76	303.9	89.79	118
	C29-D	147	15.3	177.62	22.32	180.54	22.33	40.7
	C30-D-C	131	15.3	317.57	89.57	317.95	74.65	109
	C31-D-C	266	14.8	293.27	89.32	280.56	66.51	96.15
	C32-D-A1	269	20	319.33	66.75	320.9	66.83	72.8
	C33D-C	282	17.7	204.52	47.81	171.45	71.79	76.1
Wu et al. 2008	C2	40	17.14	48.7	30.24	52.86	30.24	32.22
	C3	41	15.75	51.35	30.24	48.57	28.98	72.92
	C4	38	16.25	47.06	36.54	53.17	30.24	81.09
	C5	45	17.77	52.14	34.02	48.41	32.76	90.62
	C6	42	15.5	50.16	28.98	46.67	26.46	49.6
Sarafraz & Danesh 2010	C1	17	7	18.8	19	19.2	19.6	27.5
	C2	20	7	26.4	23	26.1	22.8	37.9
	C3	28	11.2	34.6	23.5	34.2	23.1	37.9
	C4	25	9.4	30.2	23.5	29.8	23.2	43.4
	C5	30	9.7	37.8	24	38.9	23.6	43.7
Bournas et al. 2009	L0_C	36	17.3	41.63	40	42.48	40	68.96
	L0_R2	36	21.5	43.46	44	48.7	49.6	84.48
	L0_M4	40	21.5	45.77	44	49.19	44	124.96
	L0_M4G	42	24.5	48.82	64	45.28	44	124.32
	L20d_C	39	18.5	41.5	29.92	36.62	29.92	80.32
	L20d_R2	36	18.5	41.26	44.96	52.86	49.92	105.6
	L20d_M4	43	19.9	48.46	49.92	49.8	34.88	104.8
	L40d_C	42	22	46.26	40	43.82	34.88	74.4
	L40d_R2	40	25	42.97	74.88	49.93	80	122.56
	L40d_M4	42	21	45.9	29.92	50.48	60	125.28
Sadone et al. 2012	Pref-1	42.4	22.4	51	70	44	55	77.6
	PC-1	48	22.4	49.7	74.6	45.6	41	171
	PCL-1	46.4	23.7	48.31	40.6	44.8	41	171

Table 8. Results.

Source	Specimen	ρ_{hor}^{max}	M_{max} (kNm)	μ_{max}	I_μ	I'_δ	μ	dr
Realfonzo	C3-S	0.0224	89.64	0.1643	–	–	–	1.18
& Napoli	C4-S-G	0.0069	93.62	0.1731	1.054	1.793	6.137	7.22
2009	C1-S-G	0.0058	106.17	0.1683	1.024	1.691	6.256	7.36
	C10-S-C	0.0073	86.73	0.1578	0.961	1.276	4.157	4.89
	C13-S-C	.0065	83.44	0.1371	0.834	1.449	4.939	5.81
	C2-S-A1	0.0115	142.38	0.2380	1.449	1.586	5.653	6.65
	C11-S-A1	0.0110	165.80	0.2230	1.357	2.121	6.605	7.77
	C6-S-A2	0.0089	107.64	0.1598	0.973	2.673	9.206	10.83
	C16-S	0.0324	138.57	0.2242	–	–	–	3.06
	C18-S	0.0338	71.96	0.2521	–	–	–	2.47
	C17-S-C	0.0122	105.32	0.2833	1.264	1.339	1.536	4.70
	C19-S-C	0.0097	86.38	0.2984	1.184	1.904	2.166	5.35
	C20-S-A2	0.0253	170.80	0.6062	2.704	3.284	1.895	5.80
	C12-S-A2	0.0144	155.84	0.3188	1.265	1.923	1.741	4.30
	C9-D	0.0243	120.84	0.1760	–	–	–	3.51
	C7-D-C	0.0098	117.47	0.2098	1.192	1.933	1.991	6.99
	C8-D-C	0.0098	118.56	0.2049	1.164	1.625	1.835	6.44
	C14-D-C	0.0071	106.88	0.1402	0.797	2.217	1.840	6.46
	C15-D-A1	0.0179	188.38	0.4103	2.331	1.658	1.425	5.00
	C21-D	0.0474	89.81	0.3478	–	–	–	2.79
	C22-D-C	0.0153	101.22	0.4014	1.154	2.143	2.004	5.59
	C23-D-C	0.0149	124.00	0.4627	1.330	2.500	2.953	8.24
	C24-D-A1	0.0257	203.69	0.6306	1.813	3.036	1.516	4.23
Realfonzo	C25-S	0.0609	331.42	0.2247	–	–	–	2.93
& Napoli	C26-S-C	0.0258	470.09	0.2337	1.040	1.105	0.75	2.20
2012	C27-S-C	0.0247	441.75	0.2711	1.206	1.539	0.75	2.20
	C28-S-A1	0.0335	623.00	0.3734	1.662	2.030	1.667	4.88
	C29-D	0.0684	370.11	0.2603	–	–	–	1.09
	C30-D-C	0.0272	651.80	0.2391	0.918	2.678	4.030	4.39
	C31-D-C	0.0302	601.20	0.3253	1.250	2.362	4.030	4.39
	C32-D-A1	0.0396	657.85	0.4653	1.788	1.789	2.687	2.93
	C33D-C	0.0239	419.27	0.2537	0.975	1.870	3.408	3.71
Wu et al.	C2	0.0238	66.60	0.1535	–	–	–	3.72
2008	C3	0.0231	64.70	0.1507	0.982	2.263	0.56	2.10
	C4	0.0090	66.99	0.1506	0.982	2.516	1.333	4.96
	C5	0.0104	65.70	0.1868	1.218	2.812	1.333	4.96
	C6	0.0099	63.20	0.1775	1.157	1.539	1.333	4.96
Sarafraz	C1	0.0143	19.20	0.0759	–	–	–	2.30
& Danesh	C2	0.0200	26.40	0.1069	1.409	1.378	0.91	2.10
2010	C3	0.0271	34.60	0.1453	1.915	1.378	0.96	2.20
	C4	0.0082	30.20	0.1325	1.746	1.578	0.96	2.20
	C5	0.0099	38.90	0.1541	2.031	1.589	1.000	2.30
Bournas	L0_C	0.0216	67.97	0.1384	–	–	–	3.43
et al.	L0_R2	0.0086	77.92	0.1528	1.104	1.225	1.503	5.16
2009	L0_M4	0.0085	78.70	0.1583	1.144	1.740	2.277	7.81
	L0_M4G	0.0101	78.11	0.1572	1.136	1.803	2.099	7.20
	L20d_C	0.0217	66.40	0.1323	–	–	–	3.59
	L20d_R2	0.0097	84.58	0.1650	1.248	1.315	1.610	5.78
	L20d_M4	0.0089	79.68	0.1732	1.310	1.305	1.393	5.00
	L40d_C	0.0256	74.02	0.1610	–	–	–	3.28
	L40d_R2	0.0094	79.89	0.1675	1.040	1.647	2.385	7.81
	L40d_M4	0.0093	80.77	0.1747	1.085	1.684	2.385	7.81
Sadone	Pref-1	0.0077	127.50	0.0488	–	–	–	2.80
et al.	PC-1	0.0032	124.25	0.0445	0.911	2.204	0.5	1.40
2012	PCL-1	0.0043	120.78	0.0615	1.259	2.204	0.5	1.40

Table 9. Results.

Source	Specimen	f_{cc} (MPa)	f'_{cc} (MPa)	f'_{cc}/f_{cc}	μ_δ	$\mu_{\delta,EC}$	$\mu_{\delta,CNR}$	$\mu_{\delta,FIB}$
Realfonzo & Napoli 2009	C3-S	26.125	26.125	100.00	4.29	2.56	2.03	4.65
	C4-S-G	25.225	89.177	353.53	6.95	7.48	3.85	7.96
	C1-S-G	29.225	119.385	408.50	6.55	8.57	4.33	9.16
	C10-S-C	26.425	77.570	293.55	5.15	7.14	4.66	7.50
	C13-S-C	29.325	84.066	286.67	5.52	7.10	4.44	7.38
	C2-S-A1	27.925	80.942	289.86	5.79	7.12	4.54	7.43
	C11-S-A1	35.725	98.111	274.63	8.08	7.33	4.39	7.52
	C6-S-A2	26.925	78.698	292.29	11.46	7.13	4.62	7.48
	C16-S	27.925	27.925	100.00	2.73	2.31	0.95	2.86
	C18-S	13.922	13.922	100.00	3.06	1.88	1.41	3.75
	C17-S-C	17.423	56.556	324.60	4.06	5.75	2.77	6.34
	C19-S-C	14.223	58.219	409.34	5.24	3.92	1.39	4.79
	C20-S-A2	12.522	44.156	352.63	9.04	6.46	3.63	7.53
	C12-S-A2	23.324	70.504	302.28	5.05	4.99	1.97	5.17
	C9-D	32.481	32.481	100.00	3.53	2.04	1.51	3.25
	C7-D-C	26.780	78.052	291.45	6.82	4.92	3.40	4.89
	C8-D-C	27.180	78.953	290.48	5.74	4.92	3.38	4.89
	C14-D-C	35.982	98.368	273.38	7.82	5.20	3.26	4.98
	C15-D-A1	22.679	68.679	302.83	5.56	4.84	3.64	4.96
	C21-D	12.372	12.372	100.00	2.80	1.76	1.26	3.61
	C22-D-C	12.372	43.344	350.33	6.00	5.06	4.50	6.96
	C23-D-C	13.173	54.313	412.30	6.36	1.85	5.29	3.66
	C24-D-A1	15.675	51.866	330.87	7.73	5.06	3.49	6.27
Realfonzo & Napoli 2012	C25-S	12.651	12.651	100.00	4.15	1.85	1.48	4.81
	C26-S-C	16.853	42.307	251.03	4.20	4.25	2.48	6.06
	C27-S-C	13.652	41.565	304.47	5.85	2.80	3.43	5.05
	C28-S-A1	14.352	43.195	300.97	7.02	3.07	3.30	5.22
	C29-D	12.576	12.576	100.00	2.66	1.67	1.62	4.48
	C30-D-C	23.487	55.707	237.18	7.12	2.75	1.99	4.82
	C31-D-C	15.881	46.287	291.46	6.50	2.34	3.22	5.07
	C32-D-A1	12.576	38.578	306.76	3.64	1.76	3.88	4.22
	C33D-C	13.477	40.716	302.10	4.30	1.96	4.80	4.67
Wu et al. 2008	C2	55.552	55.552	100.00	1.88	2.63	1.05	2.62
	C3	55.652	55.652	100.00	4.63	2.63	1.05	2.62
	C4	55.852	147.554	264.19	4.99	4.53	1.95	3.53
	C5	45.350	124.933	275.48	5.10	4.17	1.87	3.24
	C6	45.950	126.240	274.73	3.20	4.19	1.88	3.26
Sarafraz & Danesh 2010	C1	33.672	33.672	100.00	3.93	3.88	1.54	3.71
	C2	33.071	33.071	100.00	5.41	3.84	1.53	3.67
	C3	31.969	31.969	100.00	3.38	3.76	1.50	3.60
	C4	30.666	92.156	300.52	4.62	7.77	3.65	6.19
	C5	33.472	98.722	294.94	4.51	7.94	3.65	6.32
Bournas et al. 2009	L0_C	31.413	31.413	100.00	3.99	2.45	1.08	2.48
	L0_R2	31.173	90.816	291.33	3.93	4.94	2.12	3.86
	L0_M4	31.013	92.940	299.68	5.58	5.03	2.19	3.92
	L0_M4G	30.933	77.321	249.96	5.07	3.86	1.68	3.01
	L20d_C	30.533	30.533	100.00	4.34	1.42	1.08	2.47
	L20d_R2	29.493	87.037	295.11	5.71	3.29	2.18	3.89
	L20d_M4	29.333	89.091	303.72	5.27	3.37	2.23	3.95
	L40d_C	28.933	28.933	100.00	3.38	1.74	1.21	2.47
	L40d_R2	28.693	85.226	297.03	4.90	4.22	2.23	3.96
	L40d_M4	28.533	87.245	305.77	5.97	4.26	2.29	4.03
Sadone et al. 2012	Pref-1	71.799	71.799	100.00	3.46	4.96	2.04	4.68
	PC-1	78.990	166.830	211.21	7.63	6.52	3.00	5.12
	PCL-1	56.078	120.842	215.49	7.22	5.77	2.45	4.55

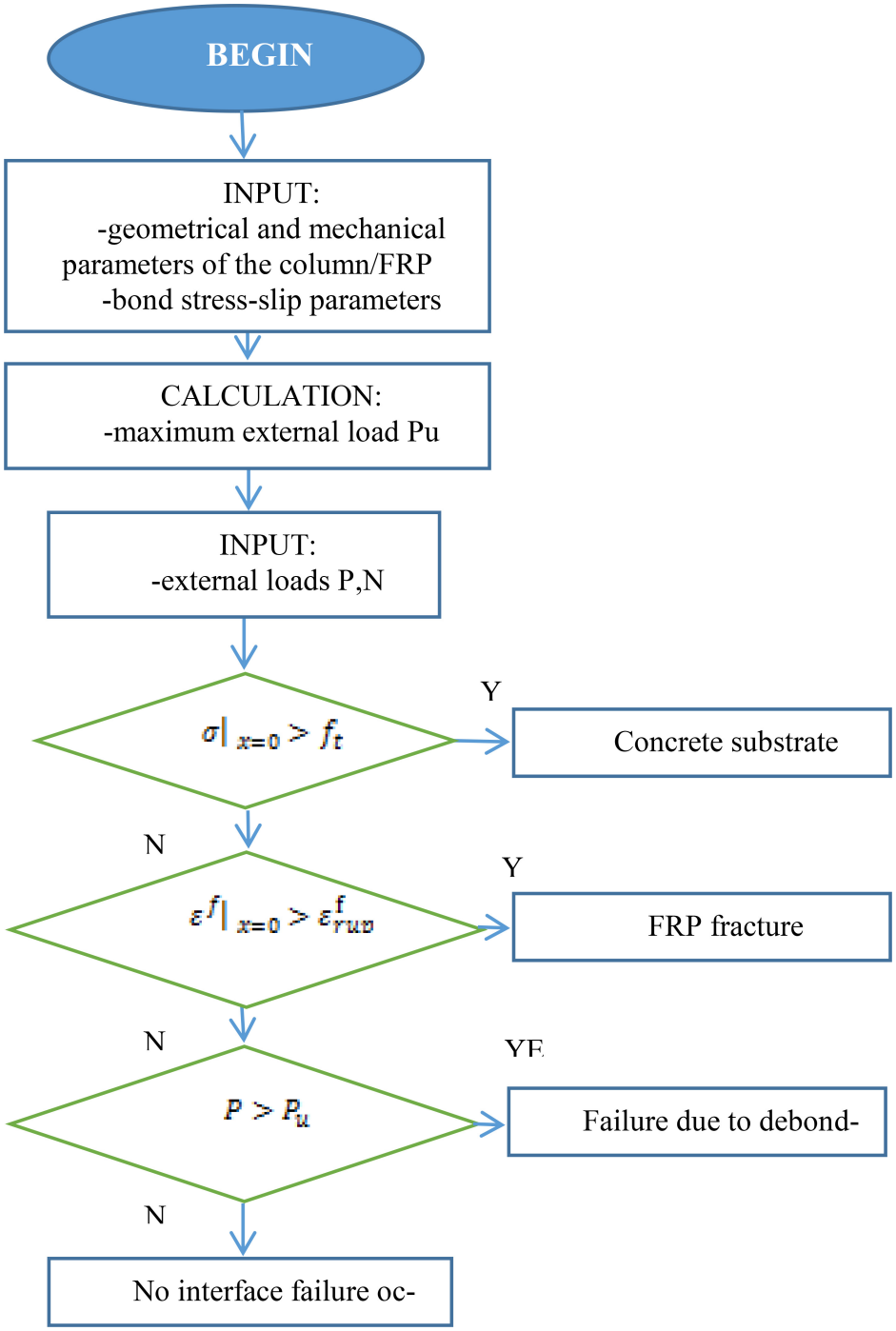
BEGIN
INPUT:
-geometrical and mechanical parameters of the column/FRP
-bond stress-slip parameters
CALCULATION:
-maximum external load Pu
INPUT:
-external loads P,N
$\sigma|_{x=0} > f_t$
Y
Concrete substrate
N
$\varepsilon^f|_{x=0} > \varepsilon^f_{ruv}$
Y
FRP fracture
N
$P > P_u$
YE
Failure due to debond-
N
No interface failure oc-

Concrete Solutions – Grantham et al. (Eds.)
© 2016 Taylor & Francis Group, London, ISBN 978-1-138-03008-4

Experimental analysis for the development of an Ultra High Performance Fiber Reinforced Concrete (UHPFRC)

A.L. Mina
National Technical University of Athens, Greece
University of Cyprus, Cyprus

M.F. Petrou
University of Cyprus, Cyprus

K.G. Trezos
National Technical University of Athens, Greece

ABSTRACT: One of the important recent innovations in concrete technology is Ultra High Performance Fiber Reinforced Concrete (UHPFRC) which constitutes a remarkable type of cement based material with incomparable mechanical properties. This paper presents the findings of an experimental study aiming to develop an UHPFRC composed of materials produced in Cyprus in addition to micro silica, super plasticizer and steel fibers coming from abroad. Different mixtures were tested, in order to investigate the influence of w/b ratio and steel fibers on the mechanical properties of UHPFRC. Five mixtures were examined, two with w/b = 0.2 with and without steel fibers, another two with w/b = 0.24 also with and without fibers and one with w/b = 0.32 which included steel fibers. The 2% by volume steel fibers were 13 mm long with 0.16 mm diameter. UHPFRC composed of local materials exhibit high compressive and tensile strength. Steel fibers improved significantly its flexural strength.

1 INTRODUCTION

In the last few decades, concrete technology has made significant improvements leading to new types of concrete such as Ultra High Performance Concrete (UHPC). UHPC demonstrates significantly higher compressive strength compared to normal concrete. The disadvantage of high strength concrete is that it becomes more brittle. During uniaxial compression testing, a linear elastic region is developed until the formation of micro cracks signaling the transition to a sudden and explosive failure. To overcome this disadvantage, steel fibers with high tensile strength were added, which control cracking and offer a clear warning before failure. Ultra High Performance Fiber Reinforced Concrete (hereinafter designated as UHPFRC) is formed when steel fibers are included in UHPC. Significant experimentation has been conducted on UHPFRC in order to improve its composition and properties (Nicolaides et al. 2013, Benson & Karihaloo 2005, Yang et al. 2009, Song & Hwang 2004).

In Cyprus, a series of experiments, recently completed, helped to develop a mix design of an UHPFRC with the use of materials available in Cyprus (Nicolaides et al. 2013). Thereby, the scope of this manuscript is to present the results of a further investigation on UHPC and UHPFRC. In order to investigate the influence of water to binder ratio and steel fibers, five mixtures were tested, two with w/b = 0.2, with and without steel fibers, another two with w/b = 0.24 again with and without steel fibers and one with w/b = 0.32 which included steel fibers. The 2% by volume steel fibers were 13 mm long and 0.16 mm diameter. For these five mixtures, the ultimate compressive and tensile strength with their corresponding strains, the modulus of elasticity and Poisson's ratio were determined.

2 EXPERIMENTAL PROCEDURE

2.1 *Mix design and specimens*

Table 1 features details of the mix proportions with w/b = 0.16 on which the present study was based (Nicolaides et al. 2013).

This mix design was the first UHPFRC mixture in Cyprus and it was developed on an extensive experimental investigation (Nicolaides et al. 2013) based on a previous study (Benson & Karihaloo 2005).

Specifically, Nicolaides et al. investigated the different potential variations of the mix design in order to improve its workability and mechanical properties. The variables examined were water/binder ratio, the time of curing under different temperatures, the optimum percentage of silica fume, and the volume of steel fibers.

Table 1. Mix design w/b = 0.16.

Materials	Kg/m^3
Cement	880
Microsilica	220
Quartz sand 125–250 μm	475
Quartz sand 250–500 μm	358
Water	176
Super plasticizer	67
Fibers 6 mm	401
Fibers 13 mm	80

Table 2. Mix designs tested in this study.

Materials Kg/m^3	UHPC		UHPFRC		
w/b	0.2	0.24	0.2	0.24	0.32
Cement	880	880	880	880	880
Microsilica	220	220	220	220	220
Sand 125–250 μm	475	475	475	475	475
Sand 250–500 μm	358	358	358	358	358
Water	220	264	220	264	352
Super plasticizer	67	67	67	67	67
Fibers 13 mm	0	0	160	160	160

The mix designs used in this study are presented in Table 2. As mentioned before steel fibers were 13 mm long and 0.16 mm diameter.

The following mixing procedure was implemented based on the studies by Benson and Karihaloo (Benson & Karihaloo 2005). Silica sand, silica fume and portland cement were mixed first. Afterwards, steel fibers were added in three different dosages with 2 minutes of mixing time in each dosage while they passed from a vibrating sieve. Then, two-thirds of the super plasticizer was added in the water. The created liquid was divided in three parts of one half, one quarter and one quarter respectively. These proportions were added continuously in the dry mixture with 2 minutes stirring time for each dosage. Finally, the remaining one-third of the super plasticizer was added directly in the mixture. All of the specimens were cast into moulds while they were compacted on a vibrating table. They were created based on the CYS EN 12390 – 1 (2009) standard specifications.

Specimens were composed of cubes 100 × 100 × 100 mm, cylinders with a 100 mm diameter and 200 mm height, beams of 100 mm height, 100 mm width and 500 mm length and beams of 100 mm height, 50 mm width and 500 mm length. Specimens were left 24 hours in the moulds covered with damp hessian sheets. Afterwards, they were removed from the moulds and placed in a hot curing tank of 90°C, where they remained for eleven days. Later on, the specimens were moved into a standard curing water-tank for future testing.

Cubes were tested under uniaxial compression in order to determine ultimate compressive strength, cylinders were evaluated at 28 days in order to measure ultimate compressive strength and corresponding strain, modulus of elasticity and Poisson's ratio, beams 100 × 100 × 500 mm were tested under three point bending (indirect tension) in order to determine flexural strength and beams 100 × 50 × 500 mm were tested under direct tension in order to measure tensile strength along with corresponding strain.

It is necessary to mention that only one batch was used to create all specimens for each mix design. Also the five different mixtures were made using the same equipment in order to reduce the variability in the results.

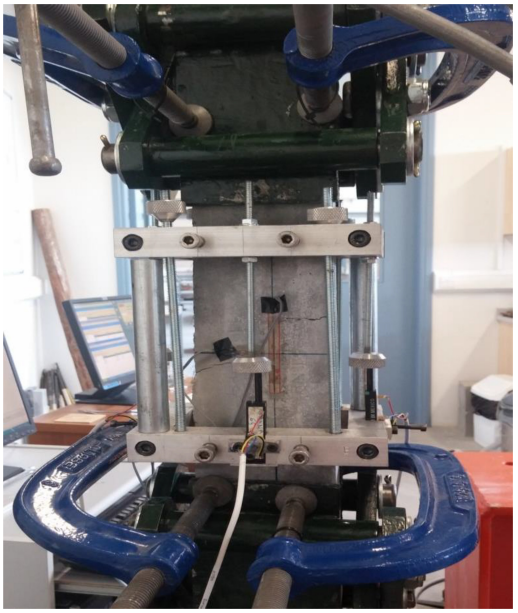

Figure 1. Setup for uniaxial tension test.

2.2 *Tension test*

The aim of the investigation was to avoid using a dog-bone specimen due to its preclusive mold and casting difficulties and measure the direct tensile strength in a different way. Subsequently, a technique based on Stelios Kolias and R. I.T. Williams prototype was utilized (Kolias & Williams 1978). A double scissor friction grid system and plain geometrical specimens like beams composed the technique which had the same efficacy as the dog-bone procedure. Since fiber distribution depends on the shape and size of the specimens (Benson et al. 2005), the width of beams for a tensile test was selected to be more than two times the length of the fiber. Longitudinal strain gauges placed on the beam's surface were used to measure strains. Additionally, three Linear Variable Displacement Transducers (LVDTs) were placed on a system of 2 rings which were screwed on the beam specimen. The above experimental setup is shown in Figure 1.



Figure 2. Setup for uniaxial compression test.

2.3 *Compression test*

Cylinders were capped according to ASTM C 617-98 (2003) standard. Displacement control was used for the compression test. Two circular rings were mounted around the cylinder specimen and then they were tight fastened with four screws at 90° to maintain the rings' stability. A major concern was the need for the rings to be horizontal with 70cm space between them, symmetrically to the specimen's midheight. On the top of the rings, three LVDTs were placed at 120° angles to be able to measure the occurring displacements. Another four LVDTs were placed on the machine's loading plates in order to measure the plate's displacement. This technique was adopted from Hassan et al. study as a backup system in case there were any deviations and instabilities with the two rings (Hassan et al. 2012). One longitudinal and one transverse strain gauges were placed next to each other in order to determine the Poisson's ratio and the modulus of elasticity. The longitudinal strain gauge was placed at the mid-height of the specimen. The displacement rate for the compression tests of cylinders was 0.015 mm/min. Cubes were evaluated under compression at a rate of 0.5 MPa/s according to CYS EN 12390 – 3 (2009). The above experimental setup is shown in Figure 2.

3 RESULTS

3.1 *Discussion*

Table 3 presents the cubes' compressive strength, the elastic modulus of elasticity and Poisson's ratio results. The ultimate compressive strength remained almost the same when w/b ratio was increased from 0.20 to 0.24. A significant increase of compressive strength was observed when steel fibers were added in the concrete mixtures. Specifically, the compressive strength was increased by 28% and 18% when fibers were included in the mixtures with w/b ratio of 0.20 and 0.24 respectively. A 30% decrease of the compressive strength was observed when the w/b ratio was increased to 0.32. It is important to mention that there is no corresponding mixture with w/b of 0.32 and no fibers.

Table 3. Compressive strength (cubes), modulus of elasticity and Poisson's ratio.

Mixtures	Compressive Strength MPa	Modulus of elasticity GPa	Poisson's ratio
UHPC w/b = 0.20	104.42	28.34	0.3
UHPC w/b = 0.24	109.86	29.80	0.3
UHPFRC w/b = 0.20	134.13	30.45	0.3
UHPFRC w/b = 0.24	129.86	31.31	0.3
UHPFRC w/b = 0.32	99.09	28.75	0.3

The Modulus of elasticity was much lower than expected and close to 30 GPa for all mixtures. It did not improve despite the use of steel fibers and lowering the amount of water in the mix. The above findings, however, need further investigation due to the fact that UHPFRC generally exhibits high modulus of elasticity values (Hassan et al. 2012). This could be associated with the local materials, geometrical characteristics of steel fibers and the mix design.

UHPC and UHPFRC mixtures had higher values of Poisson's ratio, 0.3, compared to the normal concrete, 0.15–0.20. Steel fibers and water to binder ratio had no effect on the results.

From the results presented in Tables 4, 5, 6 the following observations can be made:

The compressive strength measured from cylinder testing, excluding UHPC with w/b ratio of 0.24, was on the average, 75% of the compressive strength of the corresponding cubes. UHPC cylinders with w/b ratio of 0.24 exhibited much lower strength (52%) than the corresponding cubes. This mix has to be repeated. The strain values corresponding to the ultimate compressive strength increased with the reduction of the w/b ratio and the addition of steel fibers (54%, on average).

Ultimate tensile strength was increased when steel fibers were added in the mix and when w/b ratio was decreased. Specifically, the mix ultimate tensile strength was increased by 70% for w/b = 0.20 when steel fibers were added. Also, for UHPFRC when w/b decreased from 0.32 to 0.24 and from 0.24 to 0.20, tensile strength increased 16% and 40% respectively. For the UHPC mix with w/b = 0.24 the tensile

Table 4. Compressive strength and corresponding strain.

Mixtures	Compressive Strength From cylinders MPa	Corresponding strain microstrain
UHPC w/b = 0.20	70.78	2610
UHPC w/b = 0.24	57.17	2000
UHPFRC w/b = 0.20	107.66	3587
UHPFRC w/b = 0.24	95.89	3980
UHPFRC w/b = 0.32	75.40	3080

Table 5. Tensile strength and corresponding strain.

Mixtures	Tensile Strength MPa	Corresponding strain microstrain
UHPC w/b = 0.20	3.67	110
UHPC w/b = 0.24	1.13	40
UHPFRC w/b = 0.20	6.25	163
UHPFRC w/b = 0.24	4.44	157
UHPFRC w/b = 0.32	3.82	140

Table 6. Flexural strength.

Mixtures	Flexural Strength MPa
UHPC w/b = 0.20	7.62
UHPC w/b = 0.24	8.70
UHPFRC w/b = 0.20	28.97
UHPFRC w/b = 0.24	24.22

strength is very low, only 1.13 MPa, which needs further investigation.

The strain corresponding to the ultimate tensile strength was increased considerably, by 104% on average, with the addition of fibers. They were also increased with the reduction of w/b ratio. The average modulus of elasticity in tension, based on these results, was around 31 GPa, very similar to the one measured in compression.

Steel fibers had also great influence on the flexural strength (indirect tension). Steel fibers contributed to a significant increase of flexural strength up to 280% and 178% for w/b = 0.2 and w/b = 0.24 respectively. On the other hand, water to binder ratio had limited effect on flexural strength. UHPFRC with w/b=0.32 was not tested on three point bending.

4 CONCLUSIONS

The incorporation of fibers in the UHPFRC matrix improved the compressive strength, tensile strength and especially flexural strength significantly.

When water to binder ratio was decreased in UHPFRC mixtures, the compressive and tensile strength improved considerably.

The strains corresponding to the cylinder compressive strength increased substantially when steel fibers were added in the mix.

Water to binder ratio and steel fibers appeared to have no effect on the modulus of elasticity and Poisson's ratio. The modulus of elasticity was lower than expected and the Poisson's ratio was higher than expected.

REFERENCES

Benson, D.S.D.P. & Karihaloo, L. 2005. CARDIFRC – Development and mechanical properties Part I: Development and workability, *Magazine of concrete research 57(6):347–352.*

Benson, D.S.D.P. et al. 2005. CARDIFRC – Development and mechanical properties Part II: Fibre distribution, *Magazine of concrete research 57(7):421–432.*

Hassan, A.M.T. et al. 2012. Experimental test methods to determine the uniaxial tensile and compressive behavior of ultra high performance fibre reinforced concrete (UHPFRC), *Construction and Building Materials 37:874–882.*

Kolias, S. & Williams, R.I.T. 1978. Uniaxial Tension Tests on Cement-Stabilized Granular Materials, *Geotechnical Testing Journal 1 (4):190–198.*

Nicolaides, D. et al. 2013. Mix design and Mechanical properties of Ultra High Performance Fibre Reinforced Cementious Compocites (UHPFRCCs), *Proc. intern. RILEM con. on rheology and processing of construction materials 2013.* Paris.

Song, P. S. & Hwang, S. 2004. Mechanical properties of high-strength steel fiber-reinforced concrete, *Construction and Building Materials 18:669–673.*

Yang et al. 2009.Influense of aggregate and curing regime on the mechanical properties of ultra-high performance febre reinforced concrete (UHPFRC), *Construction and Building Materials 23:2291–2298.*

Concrete Solutions – Grantham et al. (Eds.)
© 2016 Taylor & Francis Group, London, ISBN 978-1-138-03008-4

Bond performance of the deep embedment shear strengthening method

M. Caro
University of Birmingham, Birmingham, UK

Y. Jemaa
Shire Structures, Bromsgrove, UK

S. Dirar & A. Quinn
University of Birmingham, Birmingham, UK

ABSTRACT: The Deep Embedment (DE) technique is a recently developed method for concrete shear strengthening. In this method, vertical holes are drilled upwards from the soffit in the shear spans of existing concrete beams. High viscosity epoxy resin is then injected into the drilled holes and Fibre Reinforced Polymer (FRP) or steel bars are embedded into the concrete core. The bond performance of DE FRP bars has not been fully investigated. This study provides further insight into the bond behaviour of glass FRP (GFRP) and carbon FRP (CFRP) bars embedded into concrete prisms using an epoxy adhesive. The experimentally investigated parameters include the embedment length, type of FRP bar, bar diameter and hole diameter. The experimental results show that the maximum average bond stress decreases with the increase in embedded length or bar diameter. Using a hole diameter of 1.5 times the bar diameter enhances the bond behaviour of the DE technique Specimens with CFRP bars achieved higher bond strength than those with GFRP bars.

1 INTRODUCTION

Various strengthening techniques utilising Fibre Reinforced Polymer (FRP) composites have been adopted to achieve shear strength enhancement of deficient Reinforced Concrete (RC) structures. Non-corrodible FRP composites can effectively enhance the shear capacity of RC structures due to their high strength-to-weight ratios, durability and good impact resistance. A new method referred to as the Deep Embedment (DE), or Embedded Through-Section (ETS), technique was proposed by Valerio and Ibell (2003). In this method, vertical or inclined holes are drilled upwards from the soffit in the shear spans of existing RC beams or girders and high viscosity epoxy resin is injected into the drilled holes to bond FRP or steel bars to the concrete core. A number of experimental and numerical studies (Valerio and Ibell 2003; Valerio et al. 2009; Chaallal et al. 2011; Mofidi et al. 2012; Breveglieri et al. 2015) proved superiority of the DE method over other techniques in terms of the confinement conditions, bond performance and shear strengthening effectiveness. For example, Chaallal et al. (2011) compared the shear strengthening effectiveness among DE FRP bars, near-surface mounted (NSM) FRP rods and externally bonded (EB) FRP sheets concluding that the shear strength capacity of the strengthened RC beams was increased by 61 %, 31% and 23 %, respectively.

The DE method provides higher strengthening effectiveness because unlike the EB and NSM techniques, in the DE method, the concrete core transfers the stresses to the bars. Thus, the DE technique enhances the RC shear capacity and avoids the de-bonding failure mechanism and de-lamination of concrete cover associated with external shear strengthening techniques (Chaallal et al. 2011).

Pull-out tests have been commonly adopted by researchers as a practical approach to assessing the bond performance for both steel and FRP bars embedded in concrete blocks. The most comprehensive pull-out test studies on the bond behaviour of the deep embedment technique have been published by Valerio et al. (2009) and Godat et al. (2012). Valerio et al. (2009) performed sixty-five pull-out tests using aramid FRP (AFRP), glass FRP (GFRP), carbon FRP (CFRP) and steel bars. These bars were epoxy-bonded into 150 mm × 150 mm × 150 mm concrete cubes with a cube compressive strength of 60 MPa. Five embedment lengths ranging from 15 to 75 mm and hole diameters of 1.2 and 1.3 times that of the bar diameter were considered. Godat et al. (2012) performed 13 pull-out tests on DE CFRP bars. The CFRP bars were epoxy-bonded into 190 mm × 190 mm × 190 mm concrete cubes. The key studied parameters were embedment length (48 to 285 mm) and hole diameter (1.25 to 2 times that of

the bar diameter) but the concrete cylinder compressive strength (21 and 43 MPa) and bar diameter (9.5 and 12.7 mm) were very limitedly considered.

Godat et al. (2012) confirmed that as the concrete strength increased, the maximum average bond stress also increased and a change in the failure mode of the specimens was also observed. Specimens with low concrete compressive strength failed due to concrete splitting, while specimens with high concrete strength experienced bar pull-out at the bar/adhesive interface.

Both research studies concluded that, for all bar types, as the embedded length increased the average bond stress decreased. Valerio et al. (2009) found that the average bond stress values for the DE strengthening combination of non-sag epoxy with steel and CFRP bars were higher than those achieved by the GFRP and AFRP bars. This is due to a better bond performance and a more ductile bond stress-slip response achieved by the steel and CFRP bars which have an elastic modulus considerably higher than that of GFRP and AFRP bars. Godat et al. (2012) also confirmed a tendency of embedded CFRP bar to fail by rupture if a sufficient bond length is provided. In addition, the bond capacity is higher for FRP bars of greater diameter due to a larger contact area thus higher bond force. Also, the average bond stress is greater for bars of smaller diameters. An adequate amount of high-viscosity, high-strength epoxy adhesive is crucial to prevent de-bonding failure and to achieve a good bond contact between the bar and concrete along its full embedded length. The effect of quantity of adhesive on the bond behaviour of deep embedment technique was investigated only by Godat et al.(2012). They recommended an optimum hole diameter of about 1.5 times that of the bar diameter (1.5 d_b).

However, the DE bond behaviour is not fully understood and additional tests are required to examine more in depth the effect of FRP bar type and diameter on the bond performance. The results will enable development of a more accurate bond-slip model for the FRP/concrete interfacial behaviour of the deep embedment technique.

The objectives of this research study are:

a) To investigate the bond behaviour of the DE FRP bar/concrete interface by performing twelve pull-out tests on both CFRP and GFRP bars epoxy-bonded into 200 mm × 200 mm × 200 mm concrete cubes.
b) To carry out a comprehensive assessment of the main parameters (e.g., embedment length, bar diameter and hole diameter) that affect the bond behaviour of epoxy-bonded DE bars in concrete.

2 EXPERIMENTAL PROGRAMME

The experimental program is based on the recommendations provided by ACI 440.2R-08 (ACI 2008) and the experimental pull-out test studies performed previously by Achillides and Pilakoutas (2004) and Godat et al. (2012). A total of twelve concrete cube specimens with embedded GFRP or CFRP bars were tested as reported in Table 1. A pull-out load was applied on such bars in order to obtain the average bond-slip relationships at the loaded end of the tested bars. The effect of various parameters on the bond behaviour of the DE strengthening method was examined. The following sections provide a detailed description of the material properties, test specimens, installation of FRP bars and the pull-out test setup.

2.1 *Materials*

Two batches of concrete were cast. The concrete mixes were designed according to the BRE (1997) guidelines. Portland cement (class 32.5) and aggregates (gravel) with a maximum size of 10 mm were used in both concrete batches. Each concrete batch was used to cast six pull-out concrete cubes (200 mm × 200 mm × 200 mm) and seven ancillary control samples (four cubes (100 mm × 100 mm × 100 mm) and three cylinders (100 mm diameter × 200 mm height)). The control specimens were used to characterise the concrete compressive strength according to ASTM (2011a) recommendations. The average measured cylinder compressive strengths on the day of pull-out testing were 26.1 MPa (referred to as C26) and 24.8 MPa (referred to as C25).

Two types of sand-coated FRP bars (CFRP and GFRP) were used in this study. The sand-coated FRP bars had diameters of either 10 mm or 12 mm. The GFRP bars had an elastic modulus, tensile strength and ultimate strain of 40 GPa, 973 MPa and 2.43 %, respectively, as tested by the manufacturer. The CFRP bars had an elastic modulus, tensile strength and ultimate strain of 130 GPa, 2300 MPa and 1.76 %, respectively, as tested by the manufacturer.

A commercially available high viscosity epoxy resin (Hilti 500) was used to bond the DE FRP bars to the concrete. This epoxy resin had a compressive strength, compressive modulus, tensile strength, bond strength and ultimate strain at failure of 82.7 MPa, 1493 MPa, 43.5 MPa, 12.4 MPa and 2%, respectively, as tested by the manufacturer.

2.2 *Test specimens*

Table 1 provides a summary of the pull-out test specimens. Each specimen had a four-part designation. The first part (either C25 or C26) specifies the concrete compressive strength. The second part identifies the embedded length of the FRP bar ($5d_b$, $10d_b$ or $15d_b$ where d_b is the nominal bar diameter). The third part denotes the FRP bar type and diameter (CFRP 10/12 or GFRP 10/12). The last part represents the hole diameter (either 1.5 d_b or 1.8 d_b). Hence C26-15d_b-CFRP12-1.5d_b refers to a specimen with a concrete cylinder compressive strength of 26.1 MPa, embedment length of 15 d_b (180 mm), 12 mm diameter CFRP bar and a central hole with a diameter of 1.5 d_b (18 mm).

Table 1. Test specimens

Specimens	Pull-out load kN	Bond stress MPa	Failure mode
C26-15d_b-CFRP12-1.5d_b	73.3	10.8	Concrete splitting
C26-15d_b-GFRP12-1.5d_b	48.8	7.2	Bar rupture
C26-15d_b-GFRP12-1.5d_b	61.8	9.1	Bar rupture
C26-15d_b-GFRP10-1.5d_b	58.2	12.4	Bar rupture
C26-15d_b-GFRP10-1.8d_b	54.7	11.6	Bar rupture
C26-15d_b-CFRP10-1.5d_b	56.2	11.9	Bar pullout
C25-5d_b-GFRP12-1.5d_b	22.8	10.1	Bar pullout
C25-5d_b-CFRP12-1.5d_b	31.6	14.0	Bar pullout
C25-5d_b-GFRP12-1.5d_b	27.1	12.0	Bar pullout
C25-5d_b-CFRP12-1.5d_b	30.1	13.3	Bar pullout
C25-10d_b-GFRP12-1.5d_b	36.3	8.1	Bar pullout
C25-10d_b-CFRP12-1.5d_b	49.6	10.9	Bar pullout

2.3 *Installation of FRP bars*

In order to install the CFRP and GFRP bars, vertical holes were cast along the centreline of the 200 mm concrete cubes using polyvinyl chloride (PVC) rods with diameters (d) of either 15 mm or 18 mm (d = epoxy thickness + d_b). The PVC rods were positioned vertically at the centres of the moulds prior to concrete casting. To control the embedded length of the FRP bar in a given pull-out specimen, a square (40 mm × 40 mm) polystyrene block with a central hole equal to the PVC rod diameter was glued with waterproof silicon around the PVC rod. The length of the polystyrene blocks varied from 10 to 130 mm depending upon the required value of the embedded length. This approach was selected for simplicity and also to prevent any cracking or local damage that may occur if a drilling machine was used. De-moulding of all the concrete specimens and the removal of the PVC rods were carried out 24 hours after casting. Following de-moulding, the concrete specimens were marked and cured at room temperature (about 20°C) for at least 28 days. Before installing the GFRP and CFRP bars, a wire brush was used to roughen the internal walls of the holes. This was followed by using compressed air to clean the holes from any cement and aggregate residues. The bottom ends of the holes were blocked to prevent leakage and high viscosity epoxy resin (Hilti 500) was used to fill two-thirds of the holes. A thin layer of epoxy was also applied along the embedded length of the FRP bars and then the bars were twisted as they were being inserted into the holes in a vertical position. This step was deemed necessary in order to ensure that no air pockets were formed or left inside the hole. The excess epoxy was removed from the top surface of the hole. The specimens were then cured for a week before testing.

2.4 *Test setup*

Figure 1 illustrates the pull-out test setup.

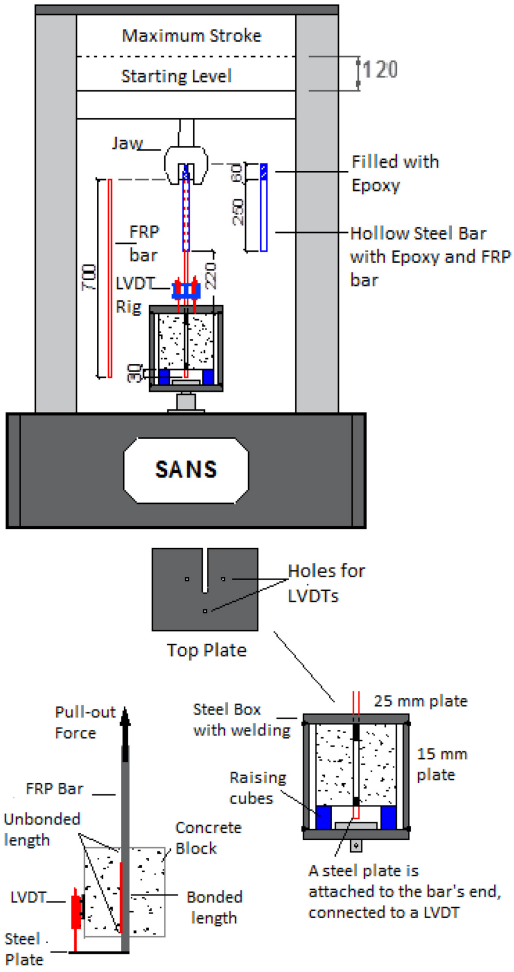

Figure 1. Pull-out test setup.

The FRP bars were cut into 700 mm lengths to meet the recommendations of the CSA/S806-02 (2007) and to ensure that the test specimens fitted properly within the testing machine. The concrete cube, with the epoxy-embedded FRP bar, was placed inside a steel box as shown in Figure 1. The upper bar end was gripped by the testing machine. To ensure that the FRP bar remained undamaged during testing, a 310 mm long hollow steel tube with 42 mm external diameter and 4.8 mm wall thickness was bonded to the upper end of the FRP bar using Hilti 500 epoxy resin.

Linear variable differential transducers (LVDTs) were mounted on a PVC rig to measure the slip between the FRP bar and the concrete cube at the upper side of the cube (see Figure 1). The FRP bar was extended by 30 mm at the lower end of the concrete cube and a steel plate was attached to the lower bar end. An LVDT mounted on one of the external faces of the concrete block was placed on the lower steel plate to measure the slip at the lower end (see Figure 1).



(a) (b)

Figure 2. Failure modes of duplicate specimens: (a) bar pull-out; (b) bar rupture.

A displacement-controlled testing machine was used to apply the pull-out load at a rate of 0.03 mm/s. This arrangement is similar to that used by Godat et al. (2012).

3 EXPERIMENTAL RESULTS

This section provides a comprehensive analysis of the pull-out test results which are presented in terms of average bond stress-slip relationships. The effect of embedded length, bar diameter and quantity of epoxy on the bond strength and failure mode are explained.

The correlation between the average bond stress (τ) and pull-out force (P) is expressed by ACI 440.1R-06 (2006) as in Equation 1:

$$\tau = P / \pi d_b l_b \quad (1)$$

where l_b = embedded length of the bar, d_b = bar diameter. Equation 1 assumes the average bond stress to be constant along the embedded length. This assumption allows comparison of the average bond stress-slip curves.

Three sets of specimens were tested twice to ensure repeatability of the results. The bond strength and failure mode for each set were comparable. The duplicate specimens C25-5d_b-GFRP12-1.5d_b failed due to bar pull-out (slip) at the adhesive/concrete interface without developing cracks on the concrete surface (Fig. 2a). The difference in the bond strength was 1.9 MPa. The failure mode of the second set of specimens, C26-15d_b-GFRP12-1.5d_b, was rupture of the GFRP bar (Fig. 2b). The difference in the bond strength was also 1.9 MPa. The last set of specimens, C25-5d_b-CFRP12-1.5d_b, experienced bar pull-out and the difference in bond strength was 0.7 MPa.

3.1 *Bond stress-slip curves and failure modes*

Figures 3 and 4 illustrate the average bond stress-slip curves for the specimens with 12 mm and 10 mm FRP bars, respectively. The overall behaviour of these

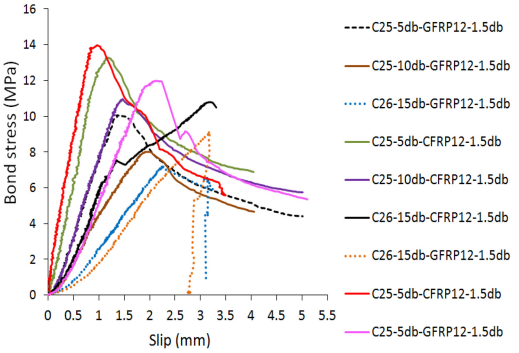

Figure 3. Bond stress-slip relations for the specimens with 12 mm FRP bars.

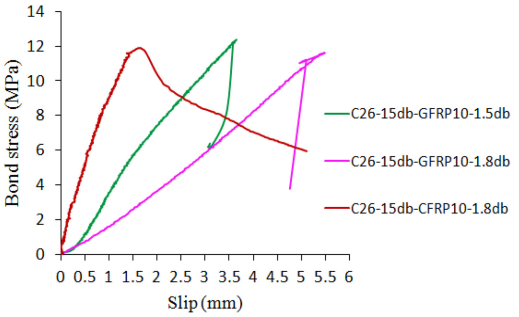

Figure 4. Bond stress-slip relations for the specimens with 10 mm FRP bars.

curves is characterised by an initial, almost linear, increase in the average bond stress with slip (ascending branch), followed by a descending branch once the maximum average bond stress has been achieved.

Figure 3 demonstrates that as the embedment length increased from 5 d_b to 15 d_b in the specimens with GFRP and CFRP bars, the initial stiffness (i.e. the stiffness of the ascending branch) was reduced. As a consequence, the slip values corresponding to the peak bond strength increased for both types of bar. The highest slip value was for specimens with CFRP bar and an embedment length of 15 d_b. The impact of embedment length on the peak bond stress in the specimens with GFRP bars was less compared to those with CFRP bars. For the same embedment length, the initial stiffness was higher in the specimens with CFRP bar than GFRP bars. In addition, the slip corresponding to the peak bond stress was lower in the specimens with CFRP bars, confirming a better bond performance.

It can be seen in Figure 4 that as the hole diameter was increased from 1.5d_b to 1.8d_b in the specimens with GFRP bars, the initial stiffness (i.e. the stiffness of the ascending branch) reduced dramatically. As a result, the slip corresponding to the peak bond strength was higher for the specimen with GFRP bar and a hole diameter of 1.8d_b. Yet, the mode of failure was not affected by the increase in quantity of adhesive (i.e. hole diameter) as both specimens experienced rupture of the GFRP bars. Moreover, the specimen with

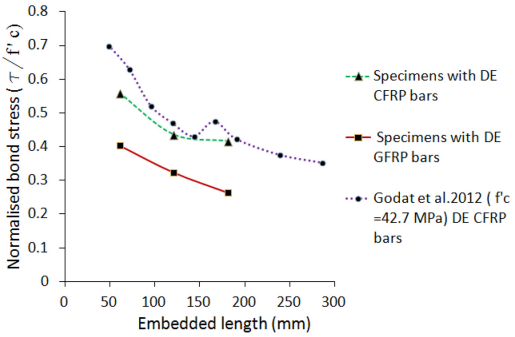

Figure 5. Effect of embedded length on the normalised bond stress.

10 mm CFRP bar and hole diameter of $1.8d_b$ had the highest initial stiffness and the least slip at peak bond strength. This specimen experienced bar pull-out at the adhesive/concrete interface.

C26-$15d_b$-CFRP12-$1.5d_b$ failed suddenly due to concrete splitting where cracks initiated at the central hole and extended toward the edges of the concrete block. These cracks reduced the confinement action, which caused the bar, together with the attached adhesive layer, to pull out of the concrete. This brittle failure mode explains the lack of a descending branch for this specimen.

Except for C26-$15d_b$-CFRP10-$1.8d_b$, the mode of failure for the remaining specimens with an embedded length of $15d_b$ was bar rupture (Fig. 2b). C26-$15d_b$-CFRP10-$1.8d_b$ and the specimens with shorter embedded lengths ($5d_b$ and $10d_b$) experienced pull-out at the adhesive/concrete interface along the embedded length (Fig. 2a).

3.2 *Effect of embedment length*

In this study, the impact of three different embedded lengths ranging from $5d_b$ (60 mm) to $15d_b$ (180 mm) was considered. The assessed specimens included either CFRP or GFRP bars of 12 mm diameter. Tepfers et al. (2003) and Baena et al. (2009) explained the dependence of bond stress on the embedded length as a result of stress transfer along the bar during pull-out testing where the maximum bond stress migrates gradually from the loaded end toward the unloaded end of the bar, leading to a nonlinear stress distribution along the bar. The impact of the embedded length is discussed in terms of normalised bond stress (Fig. 5) and failure modes.

It can be observed that, for all specimens, as the embedded length increased, the bond stress decreased (Fig. 5), which is in agreement with Equation 1. An increase of three times in the embedded length for the specimens with 12 mm GFRP or CFRP bars led to a decrease in the bond stress of 1.53 and 1.35, respectively. The majority of these specimens experienced pull-out at the adhesive/concrete interface (Fig. 2a). It was also observed that a thin adhesive layer was attached to the GFRP bars during pull-out. However, specimen C26-$15d_b$-GFRP12-$1.5d_b$ with a longer embedded length of $15d_b$ (180 mm) failed due to GFRP bar rupture. The bar remained well attached to the concrete surface until the end of the test (Fig. 2b). In addition, cracks were not induced during either mode of failure. Thus, the test results for the effect of embedded length on the bond stress clearly indicate that as the embedded length increases, the applied load approaches the tensile strength of the bar. This observation is in agreement with the results by Nanni et al. (1995) for FRP reinforced concrete.

For the same embedded length, the specimens with 12 mm CFRP bars achieved higher bond stress values. This is due to a better bond performance achieved by the CFRP bars which have an elastic modulus considerably higher than that of GFRP bars. As the embedded length increased three times, the increase in bond force for the specimens with CFRP and GFRP bars was 2.3 and 2.1, respectively. Figure 5 extends the comparison of the test results of this study with those of Godat et al. (2012). They studied the effect of embedded lengths ranging from $5d_b$ up to $30d_b$ for 9.5 mm CFRP bars embedded in concrete using high-viscosity epoxy. Similar to the observations of this study as the embedded length increased, the bond stress decreased. The increase in the embedded length of about 6 times led to a decrease in the bond stress of almost 3 times. In addition, it was observed that pull-out failure was the governing failure mode for embedded lengths ranging from $5d_b$ to $20d_b$, while for greater embedded lengths ($25d_b$ and $30d_b$) bar tensile failure occurred with the FRP bar remaining well attached to the concrete core. Therefore, as the embedded length increased, the applied load reaches the tensile strength of the DE FRP bars.

3.3 *Effect of bar diameter*

The impact of bar diameter on the bond behaviour was studied by comparing two sets of specimens: (i) C26-$15d_b$-GFRP12-$1.5d_b$ and C26-$15d_b$-GFRP10-$1.5d_b$, and (ii) C26-$15d_b$-CFRP12-$1.5d_b$ and C26-$15d_b$-CFRP10-$1.5d_b$. The observed failure mode for the specimens with GFRP bars was bar rupture (Fig. 2b). The specimen with 10 mm CFRP bar failed due to bar pull-out (Fig. 2a) without developing cracks on the concrete surface. The failure mode for the other specimen with 12 mm CFRP bar was concrete splitting where the cracks initiated at the central hole and extended toward the edges of the concrete block.

Theoretically, for a larger bar diameter, the contact area between the bar and the adhesive is greater, and hence a higher bond force is expected. As can be seen in Equation 1, for a given applied load increasing the bar diameter would decrease the bond stress. A comparison of the normalised bond stress for the two sets of specimens and two additional specimens tested by Godat et al. (2012), with CFRP bars of 9.5 mm and 12.7 mm diameter, is presented in Figure 6. As expected, for all specimens the bond stress decreased with the increase in the bar diameter, in agreement

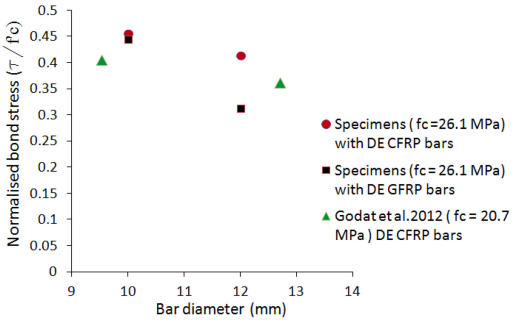

Figure 6. Effect of bar diameter on the normalised bond stress.

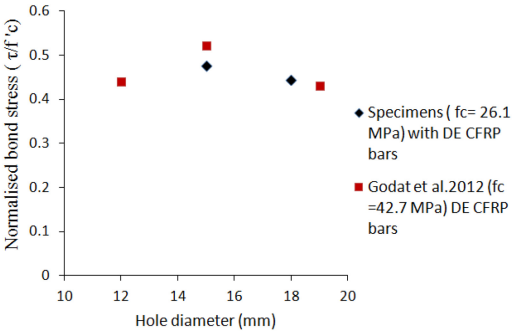

Figure 7. Effect of quantity of adhesive on the normalised bond stress.

with Equation 1. As the bar diameter increased from 10 mm to 12 mm, the bond stress for the specimens with CFRP bars and GFRP bars decreased by about 10% and 34%, respectively. For the same bar diameter, the bond stress values achieved by the specimens with CFRP bars were higher than those achieved by the specimens with GFRP bars (Table 1). This is attributed to a better bond performance of CFRP bars compared to GFRP bars.

In addition, an increase in CFRP bar diameter from 9.5 mm to 12.7 mm led to a decrease in bond stress for the specimens tested by Godat et al. (2012) by about 11%. This result is quite comparable to that of the CFRP specimens tested in this study. It is also in agreement with the findings of Baena et al. (2009) who stated that, for geometrically similar FRP reinforced concrete specimens, the larger the bar diameter, the lower the bond strength. This was attributed to the greater amount of elastic energy available in larger diameter bars. For a given bond stress, increasing the bar diameter would increase the bond stress that causes failure, and this in turn would increase the area up to the bond stress under the bond stress-strain curve, which is a measure of elastic energy.

3.4 *Effect of quantity of adhesive*

The impact of quantity of adhesive (hole diameter) on the bond behaviour of the DE technique was investigated by considering two specimens with different hole diameters: C26-15d_b-GFRP10-1.5d_b and C26-15d_b-GFRP10-1.8d_b. Figure 7 displays the influence of the increase in adhesive quantity on normalised bond stress for the above two specimens as well as comparable specimens tested by Godat et al. (2012).

Increasing the hole diameter from 1.5d_b (15 mm) to 1.8d_b (18 mm) led to a decrease in the bond stress from 12.4 MPa to 11.6 MPa. The effect of confinement was reduced due to possible greater shrinkage that occurs in larger holes compared to smaller ones. This result agrees well with the results of the research study conducted by Godat et al. (2012) who studied the impact of the quantity of adhesive by considering three different hole diameters (1.25d_b, 1.5d_b and 2.0d_b). They concluded that as the hole diameter increased from 1.25d_b to 1.5d_b, the bond performance was enhanced leading to better confinement and greater bond strength. The same behaviour was not exhibited for larger holes sizes ranging from 1.5d_b to 2.0d_b where the bond stress was reduced. Thus, the results of the current study combined with those of Godat et al. (2012) indicate that the optimum hole diameter is about 1.5d_b. This conclusion agrees well with the recommendations of ACI 440.2R-08 (ACI 2008) for the NSM strengthening technique.

4 CONCLUSIONS

This research study has expanded the experimental results and has provided further insight into the bond performance of the DE method by conducting pull-out tests on both CFRP and GFRP bars epoxy-bonded into 200 mm × 200 mm × 200 mm concrete cubes. The impact of embedment length, bar diameter and quantity of adhesive on the bond strength was examined. Based on the results of this study, the following conclusions can be made:

An increase in embedded length led to a decrease in bond stress and a change in the failure mode of the tested specimens. There was a tendency for the bar to fail by rupture rather than pull-out when the embedded length was sufficient (about 15db).

The bond strength reduced when larger diameter (i.e. 12 mm) embedded FRP bars were used. The average bond stress was greater for smaller diameter (i.e. 10 mm) bars, comfirming an inversely proportional relationship between the bond stress and bar diameter.

An adequate amount of high-viscosity adhesive is crucial to prevent de-bonding failure and to achieve a good bond contact between the bar and concrete along its full embedded length. The results of this research study suggest that using a hole diameter of 1.5db enhances the bond behaviour of the DE technique.

In general, specimens with CFRP bars achieved higher bond strength than those with GFRP bars. This is due to a better bond performance achieved by the CFRP bars which have an elastic modulus considerably higher than that of GFRP bars.

ACKNOWLEDGEMENTS

The financial support of the Engineering and Physical Sciences Research Council (EPSRC) through Grant EP/L010364/1 is gratefully acknowledged. The authors are grateful to the staff of the Civil Engineering Laboratory at the University of Birmingham for their help and support. Additional data related to this publication is available at http://rab.bham.ac.uk/pubs.asp?id=17d02f0b-4df1-4a0e-a1f1-e8aa64f2134f or may be accessed via http://findit.bham.ac.uk.

REFERENCES

Achillides, Z., and Pilakoutas, K. 2004. Bond behaviour of fiber reinforced polymer bars under direct pullout conditions. *J. Compos. Constr., 8(2), 173–181*.

American Concrete Institute (ACI). 2006. Guide test methods for fiber reinforced polymers (FRPs) for reinforcing or strengthening concrete structures. *Rep.No.4403R-04, Farmington Hills MI.*

American Concrete Institute (ACI). 2008. Guide for the design and construction of externally bonded FRP systems for strengthening concrete structures. *Rep. No. 440 2R-08, Framington Hills, MI.*

ASTM. 2011a. Standard test method for compressive strength of cylindrical concrete specimens. *C39/C39M, West Conshohoken, PA*

Baena, M., Torres, L., Turon, A., and Barris, C. 2009. Experimental study of bond behaviour between concrete and FRP bars using a pull-out test. *Compos.: Part B, 40(8), 784–797.*

Breveglieri, M., Aprile, A., Barros, J.A.O. 2015. Embedded Through-Section shear strengthening technique using steel and CFRP bars in RC beams of different percentage of existing stirrups. *Compos. Struct., 126 (2015) 101–113. http://dx.doi.org/10.1016/j.compstruct.2015.02.025*

Building Research Establishment (BRE). 1997. Design of normal concrete mixes. *Building Research Establishment Ltd Garston, Watford, BR 331, ISBN 86081 172*

Chaallal, O., Mofidi, A., Benmokrane, B., and Neale, K. 2011. Embedded through-section FRP rod method for shear strengthening of RC beams: performance and comparison with existing techniques. *Compos. Constr., 15(3), 374–383*.

Concrete Society, 2012. Design guidance for strengthening concrete structures using fibre composite materials. *Tech. Rep. 55, Crowthorne, UK*.

Canadian Standards Association.(CSA). 2007. Design and Construction of Building Components with Fibre-Reinforced Polymers. *S806-02, CAN/CSA, Rexdale, Ontario, Canada.*

Dalfre G., Barros J. Machado D.2012. Embedded through-section bars for the shear strengthening of RC beams. In Monti, G, editor. *Proceedings of sixth international conference on FRP composites in civil engineering (CICE 2012), Rome, Italy*.

Fib – Bulletin 40.2007.FRP reinforcement in RC structures. Technical report by Task Group TG 9.3 *FRP Int. Federation for Structural Concrete, Lausanne, Switzerland*

Godat A, L'Hady A, Chaallal O, Neale KW., Chaallal O. 2012. Bond behaviour of the embedded through -section FRP bar shear strengthening method. *Comput Struct; 16 (5):529–539.*

Mofidi, A., Chaallal, O., Benmokrane, B., and Neale, K. 2012. Experimental tests and design model for RC beams strengthened in shear using the embedded through-section FRP method. *Compost. Constr., 16 (5), 540–550*.

Nanni, A, AI-Zaharani, M. M., AI-Dulaijan. S. U., Bakis, C. E., and Boothby, T. E. 1995. Bond of FRP reinforcement to concrete experimental results. *Proc., 2nd Int. RILEM Symp. (FRPRCS-2J, L.Taerwe, ed.*

Tepfers, R., and De Lorenzis, L. 2003. Bond FRP reinforcement in concrete - A challenge. Mech. *Compos. Mater., 39(4), 315–328.*

Valerio P, Ibell TJ. 2003. Shear strengthening of existing concrete bridges. *Proc Inst Civil Eng Struct Build*. 156, No.1, 75–84.

Valerio P, Ibell TJ, Darby AP. 2009. Deep embedment of FRP for concrete shear strengthening. *Proc Inst Civil Eng Struct Build 2009; 162(5):311-321.*



Taylor & Francis
Taylor & Francis Group
http://taylorandfrancis.com

Concrete Solutions – Grantham et al. (Eds.)
© 2016 Taylor & Francis Group, London, ISBN 978-1-138-03008-4

Shear strengthening of reinforced concrete T-beams with EB-FRP sheets

C.E. Chalioris & C.A. Argiriou
Department of Civil Engineering, Democritus University of Thrace, Greece

ABSTRACT: The full jacketing application of externally Epoxy-Bonded Fibre-Reinforced-Polymer (EB-FRP) materials for the strengthening of shear-deficient Reinforced Concrete (RC) beams with rectangular cross-section has been proved to be a promising strengthening method. However, T-beams are usually shear strengthened using EB-FRP sheets (continuous jackets or strips) on the three sides of the web of the beam (U-shaped retrofitting) and premature debonding failures are obtained. The present study deals with the shear strengthening of RC beams with T-shaped cross-section using U-shaped EB-FRP jackets or strips. Provisions of three different Code Standards (Greek Code of Interventions, Eurocode 8 and ACI) for the design of EB-FRP shear strengthened concrete beams are extensively examined. The design predictions of these Code Standards are checked against 109 available test data of T-shaped RC beams that have been strengthened for shear using EB-FRP jackets or strips with U-shaped configuration. The ability of the Code provisions to generate safe design estimations is discussed. The calculated values of the EB-FRP effective strain are also examined and estimated based on the experimental results.

Keywords: Reinforced Concrete (RC), T-shaped beams, Epoxy-Bonded Fibre-Reinforced-Polymer (EB-FRP), Shear, U-shaped retrofitting.

1 INTRODUCTION

Strengthening of deficient Reinforced Concrete (RC) structures using externally Epoxy-Bonded Fibre-Reinforced-Polymers (EB-FRP) has become very popular because of the advantages of these materials such as their superior strength-to-weight ratio, their easy-to-apply character, their durability and their chemical and corrosion resistance. Especially for shear-critical RC elements with rectangular cross-section, full jacketing application of EB-FRP sheets around the cross-section and along their entire length provides increased strength and enhanced structural performance since it alters the shear brittle response to a ductile one. However, common constructional limitations, such as the existence of a slab, usually prevent the wrapping of EB-FRP sheets around the cross-section. Thus, most RC beams with T-shaped cross-section are shear strengthened using EB-FRP sheets (jackets or strips) on the three sides of the web of the beam (U-shaped retrofitting). A significant deficiency of this technique is the premature failure of the strengthened member due to the debonding of the EB-FRP at the adhesive composite and concrete interface (Karayannis & Chalioris 2003a, 2003b, Chalioris 2003, 2007, 2008, Bousias et al. 2004).

Several experimental studies have demonstrated the effectiveness of the use of EB-FRP sheets in strengthening works of shear-deficient RC members. Chaallal et al. (1998) proposed one of the first models for predicting the shear contribution of the EB-FRP based on the assumption that the composite fibres contribute to the shear capacity similar to internal transverse reinforcement. It further assumes that the limiting EB-FRP tensile strength is reached when the composite is intersected by the shear failure crack if the bond length is sufficient. Triantafillou (1998) used the truss theory to estimate the effective strain on FRPs, which developed from regression of experimental data. This model disregards the different strengthening schemes and failure modes. Triantafillou & Antonopoulos (2000) proposed an extension of Triantafillou's model, in which different effective strain expressions and coefficients were adopted for carbon FRP wrapping and other schemes, based on regression of a larger database (75 tests).

Khalifa et al. (1998) and Khalifa & Nanni (2000) amended the previous models by introducing coefficients to take into account reduced strain developed due to increase of shear crack width and loss of aggregate interlock. Deniaud & Cheng (2001, 2003) proposed a model assuming a uniform strain distribution among the composite fibres crossing the concrete shear crack. Pellegrino & Modena (2002) assuming the EB-FRP strains were equal to those of internal stirrups, introduced a reduction factor for Khalifa's model (1998) considering the interaction between the EB-FRP and the internal shear steel reinforcement according to experimental results. Chen & Teng (2003a, 2003b) analysed shear failure in RC beams strengthened with EB-FRP and concluded that the

stress distribution of the fibres along the crack is non-uniform. They proposed an analytical model for failure by EB-FRP rupture (Chen & Teng 2003a) and another for failure by EB-FRP debonding (Chen & Teng 2003b), in which the limiting stresses are determined by the effective bond length and the width coefficients of the applied EB-FRP. Carolin & Täljsten (2005) presented an expression to predict the contribution of the EB-FRP based on a refinement of the truss model theory. Strain limitations are prescribed for the principal strain in the concrete instead of the fibre strain. Monti & Liotta (2007) proposed a debonding model for EB-FRP shear strengthened RC beams. This model has three core components: a generalized constitutive mode for the EB-FRP concrete bond, boundary limitation and shear crack opening provision. It also introduced a generalized criterion for EB-FRP failure. The design proposal described in this model has been incorporated into the Italian design Code.

EB-FRP sheets have also been applied in RC beams and beam-column joints that suffer shear stresses. Constructional difficulties and limitations in beam-column joints are also caused undesirable shear failure in the joint specimens retrofitted with EB-FRPs (Ghobarah & Said 2002, Tsonos 2007, 2008, Karayannis & Sirkelis 2008,).

This paper aims to evaluate the results of the design provisions of three different Code Standards; Greek Code of Interventions (2013), Eurocode 8 part 3 (2004) and ACI Committee 440 (2008) for the design of shear strengthened RC T-beams with EB-FRP materials using 109 test data available in the literature.

2 DESIGN PROVISIONS

A number of guidelines and design provisions for the shear strengthening of RC beams using EB-FRP materials have been proposed. Based on them, the nominal shear strength of an EB-FRP retrofitted RC beam, V_n, is calculated by adding the contribution of the EB-FRP to the shear resistance, V_f, with the corresponding resistance of the concrete, V_c, and the steel shear reinforcement (stirrups or/and bent-up bars), V_s:

$$V_n = V_c + V_s + V_f \tag{1}$$

The strength components of V_c and V_s are usually calculated according to the provisions of the existing design codes for non-strengthened RC members. The contribution of the EB-FRP materials to the shear resistance is usually obtained by multiplying the ultimate vertical stress developed in the EB-FRP by the area of the fibres that crosses a potential shear crack. Thus, the EB-FRPs that are intersected by this diagonal shear crack are assumed to contribute the same effective strain. Most of the design guidelines and models use a similar design relationship with different definitions or estimations of the EB-FRP effective design strain or/and the corresponding stress.

2.1 *Greek Code of Interventions (KAN.EPE.)*

The Greek Code of Interventions, also known as KAN.EPE. (2013) adopts the model proposed by Chen & Teng (2003a, 2003b) and estimates the EB-FRP contribution using the following expression:

$$V_{jd} = \sigma_{jd}\rho_j b_w h_{j.ef}\left(\cot\theta + \cot a\right)\sin^2 a \tag{2}$$

where ρ_j is the reinforcement ratio of the EB-FRPs; b_w is the width of the web of the RC beam; $h_{j,ef}$ is the effective depth of EB-FRP that can be assumed to be equal to $h_{j,ef} = 2/3d$; d is the effective depth of the beam; θ is the strut inclination angle that can be taken as $\theta = 45°$; α is the angle between the fibre direction and the longitudinal axis of the member; σ_{jd} is the EB-FRP effective design stress at failure:

$$\sigma_{jd} \le \frac{f_{jk}}{\gamma_m} \qquad \text{for fibre rupture failure} \tag{3}$$

where $f_{jk} = E_j\ \varepsilon_{j,crit}$ is the design tensional strength of the EB-FRP; E_j is the modulus of elasticity of EB-FRP; $\varepsilon_{j,crit} = k_v\varepsilon_{j,max}$ is the design (critical) strain of the EB-FRP; $k_v = 0.5$; $\varepsilon_{j,max} = \varepsilon_{ju}\psi \le 1.5\%$ is the ultimate strain of the EB-FRP; $\psi = k^{-1/4}$ if $k \ge 4$ and $\psi = 1$ if $k < 4$ is a degrease coefficient of multiple EB-FRP plies; k is the number of the EB-FRP plies; $\gamma_m = 1.2$ is the partial safety factor.

$$\sigma_{jd} \le \frac{\sigma_{j,crit}}{\gamma_{Rd}} \qquad \text{for debonding failure} \tag{4}$$

where $\sigma_{j,crit} = k_v\sigma_{j,max}$ is the design (critical) stress of the EB-FRP; $k_v = 0.4 + 0.25\lambda \le 0.65$; $\lambda = L_{av}/L_e \le 1$; $\sigma_{j,max}$ is the ultimate stress of the EB-FRP as calculated by the following expression; $L_{av} = h_{j,ef}$ is the available bond length of the EB-FRP; L_e is the effective bond length of the EB-FRP as calculated by the following expression; $\gamma_{Rd} = 1.2$ is the safety factor for modeling uncertainty.

$$\sigma_{\mathrm{j,max}} = \beta_w\beta_L\frac{f_{ctm}}{t_j}L_e \text{ and } L_e = \sqrt{\frac{E_j t_j}{2f_{ctm}}} \text{ where:}$$

$$\beta_w = \sqrt{\frac{2 - w_j/s_j\sin a}{1 + w_j/s_j\sin a}},\ \beta_L = \sin\left(\frac{\pi\lambda}{2}\right) \cong \lambda(2-\lambda)$$

where f_{ctm} is the mean compressive strength of concrete; $t_j = \psi k t_{j1}$ is the thickness of the EB-FRP; t_{j1} is the thickness of one EB-FRP ply; w_j and s_j are the width and the spacing of the EB-FRP strips, respectively, that in the case of jackets $s_j = w_j$.

It is noted that the ratio of the applied EB-FRP is calculated based on the following expression:

$$\rho_j = \frac{2t_j w_j}{s_j b_w \sin a} \tag{5}$$

Thus, equation (2) can be written in the form of:

$$V_{jd} = h_{j.ef}\sigma_{jd}2t_j\left(\frac{w_j}{s_j}\right)\left(\cot\theta+\cot a\right)\sin a \qquad (6)$$

2.2 *Eurocode 8 part 3*

Eurocode 8 part 3 (2004) adopts the model proposed by Monti & Liotta (2007) and estimates the EB-FRP contribution by the following expression:

$$V_{Rd,f} = 0.9d f_{fdd,e}2t_f\left(\frac{w_f}{s_f}\right)^2\left(\cot\theta+\cot\beta\right)\sin\beta \qquad (7)$$

where d is the effective depth of the beam;t_f is the total thickness of the EB-FRP; w_f is the width of the EB-FRP strips that in the case of EB-FRP jackets it is equal to $w_f = \min(0.9d,\ h_w)\ \sin(\theta+\beta)/\sin\theta$; s_f is the axial spacing of the EB-FRP strips that in the case of jackets $s_f = w_f$,h_w is the height of the web of the beam; θ is the strut inclination angle; β is the angle between the fibre direction and the longitudinal axis of the member; $f_{fdd,e}$ is the effective design stress of the EB-FRP that depends on the type of the retrofitting scheme (fully wrapped, U-shaped and side bonded) and in the examined case of U-shaped retrofitting it is calculated:

$$f_{fdd,e,U} = f_{fdd}\left[1-k\frac{L_e\sin\beta}{z}\right] \qquad (8)$$

where f_{fdd} is the design debonding strength of the case of U-shaped EB-FRP that equals to:

$$f_{fdd} = \frac{1}{\gamma_{fd}}\sqrt{\frac{0.6E_f f_{ctm}k_b}{t_f}} \qquad (9)$$

where f_{ctm} is the mean compressive strength of concrete; E_f is the modulus of elasticity of EB-FRP; $k = (1-2/\pi)$; $z = 0.9d$; k_b is the covering coefficient as calculated by the following expression; L_e is the effective bond length of the EB-FRP as calculated by the following expression; $\gamma_{fd} = 1.5$ is the partial safety factor for EB-FRP debonding.

$$k_b = \sqrt{1.5\left(2-w_f/s_f\right)\left(1+w_f/100mm\right)} \text{ and}$$

$$L_e = \sqrt{\frac{E_f t_f}{\sqrt{4\tau_{\max}}}} \text{ where:}$$

$\tau_{max} = 1.8f_{ctm}k_b$ is the maximum bond strength.

2.3 *ACI Committee 440*

ACI Committee 440 (2008) is based on the design equations derived by Khalifa et al. (1998) and estimates the EB-FRP contribution by the following expression:

$$V_f = \frac{A_{fv}f_{fe}(\sin a\ +\ \cos a)d_f}{s_f} \qquad (10)$$

where $A_{fv} = 2nt_f w_f$ is the area of the EB-FRP; d_f is the effective depth of the EB-FRP;n is the number of the EB-FRP plies; t_f is the thickness of one EB-FRP ply; w_f and s_f are the width and the spacing of the EB-FRP strips, respectively, that in the case of continuous jackets $s_f = w_f$; a is the angle between the fibre direction and the longitudinal axis of the member; $f_{fe} = E_f\varepsilon_{fe}$ is the effective design stress of the EB-FRP; E_f is the modulus of elasticity of the EB-FRP; $\varepsilon_{fe} = k_v\varepsilon_{fu} \le 0.4\%$ is the EB-FRP effective strain; ε_{fu} is the ultimate rupture strain of the EB-FRP; k_v is a bond-reduction coefficient that depends on the specified concrete compressive strength, f_c, the type of the retrofitting scheme and the stiffness of the EB-FRP:

$$k_v = \frac{k_1k_2L_e}{11{,}900\varepsilon_{fu}} \le 0.75 \text{ where:}$$

$$k_1 = \left(\frac{f_c}{27}\right)^{2/3},\ k_2 = \frac{d_f - L_e}{d_f} \text{ (for U-wraps) and}$$

$$L_e = \frac{23{,}300}{(nt_fE_f)^{0.58}}$$

Thus, equation (10) can be written in the form of:

$$V_f = d_f f_{fe}2\left(nt_f\right)\left(\frac{w_f}{s_f}\right)(\sin a\ +\ \cos a) \qquad (11)$$

and the design value of the EB-FRP contribution to shear is $\phi\psi_f V_f$ (reduction factors: $\phi = \psi_f = 0.85$).

3 DATABASE RESULTS AND DISCUSSION

The database used consists of 109 shear-critical RC beams with T-shaped cross-section that have been externally strengthened with U-shaped EB-FRP continuous and discontinuous sheets (jackets and strips, respectively). Test results are used to compare the analytical predictions of the design provisions concerning the EB-FRP contribution to the shear capacity with the experimentally obtained values. The 109 tested beams were collected from the following 19 existing works around the world: Chajes et al. (1995), Sato et al. (1997), Khalifa et al. (1999), Khalifa & Nanni (2000), Annaiah et al. (2001), Deniaud & Cheng

(2001), Park et al. (2001), Chaallal et al. (2002), Karayannis & Chalioris (2003a), Deniaud & Cheng (2003), Dias & Barros (2006), Bousselham & Chaallal (2006a, 2006b), Jayaprakash et al. (2007), Altin et al. (2010), Gamino et al. (2010), Panda et al. (2011), Panigrahi et al. (2014) and Mofidi & Chaallal (2014).

The beams of the database are sorted in the two groups; "jackets" and "strips". The first group consists of 71 RC beams strengthened with EB-FRP jackets, in which 23 have an anchorage system. The second one consists of 38 RC beams strengthened with EB-FRP strips.

Externally EB-FRP sheets with fibres from Carbon, Glass and Aramid are examined. The EB-FRP thickness varies from 0.063 mm to 2.10 mm. The minimum values of the concrete compressive and the tensile strength are 20.6 MPa and 1.64 MPa, respectively.

In the first group (jackets) 32 beams have also steel transverse reinforcement (stirrups) from which 27 have EB-FRP from Carbon fibres and 5 from Glass fibres. Further, 39 beams have no steel shear reinforcement (without stirrups) from which 29 have EB-FRP from Carbon fibres, 6 from Glass fibres and 4 from Aramid fibres. In the second group (strips), 28 beams have also steel transverse reinforcement (stirrups) from which 27 have EB-FRP from Carbon fibres and 1 from Glass fibres. Further, 10 beams have no steel shear reinforcement (without stirrups) from which 8 have EB-FRP from Carbon fibres and 2 from Glass fibres.

In Figures 1, 2 and 3 the analytical predictions derived from the provisions of the Greek Code of Interventions (2013), the Eurocode 8 part 3 (2004) and the ACI Committee 440 (2008), respectively (denoted as V_{jd} in "KAN.EPE.", $V_{Rd,f}$ in "EC8" and $\phi\psi_f V_f$ in "ACI", respectively) are compared with the test results ($V_{f,exp}$) of the EB-FRP contribution to the shear resistance of the examined RC T-beams retrofitted with U-shaped EB-FRP jackets and strips. The diagonal lines signify the design datum (tests results are equal to the analytical ones). The design values have been calculated with the safety factors and the area above these lines denotes the safe side.

Table 1 summarizes the minimum and the maximum values of the main features of the shear-critical T-shaped RC beams of the database such as the cross-sectional dimensions $b_s/b_w/h/h_s$ (slab width / web width / height / slab depth), the mean concrete compressive strength f_{cm}, the ratio of the steel tensional longitudinal reinforcement ρ_{sl}, the ratio of the steel transverse web reinforcement (stirrups) ρ_{sw}, the modulus of elasticity of the EB-FRP E_f, the ratio of the EB-FRP ρ_f and the contribution of the EB-FRP to the shear resistance $V_{f,exp}$.

The comparisons between the test results and the design predictions of the examined Code provisions in Figures 1, 2 and 3 indicate a rather large scatter between the predicted values and the experimental results. Further, unsafe estimations (points below the diagonal line of the design datum) of all three Codes

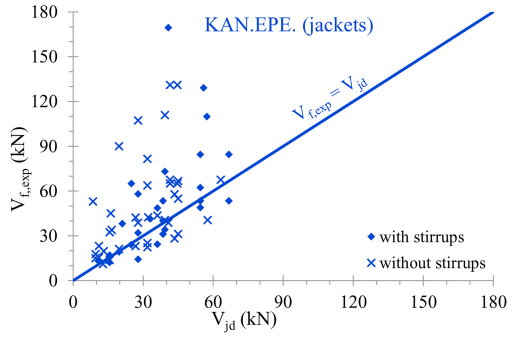

(a) U-shaped retrofitted T-beams with EB-FRP jackets

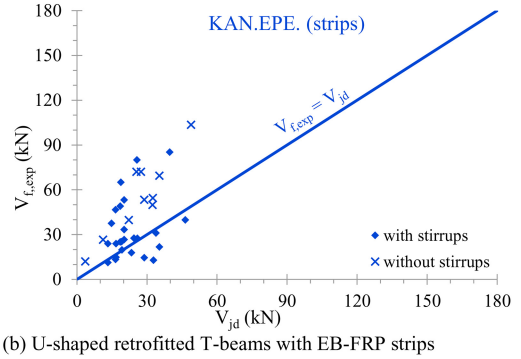

(b) U-shaped retrofitted T-beams with EB-FRP strips

Figure 1. Results of the Greek Code of Interventions.

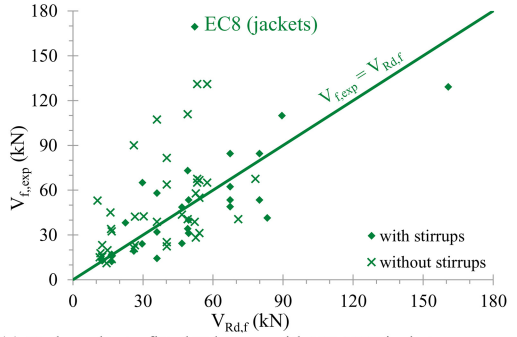

(a) U-shaped retrofitted T-beams with EB-FRP jackets

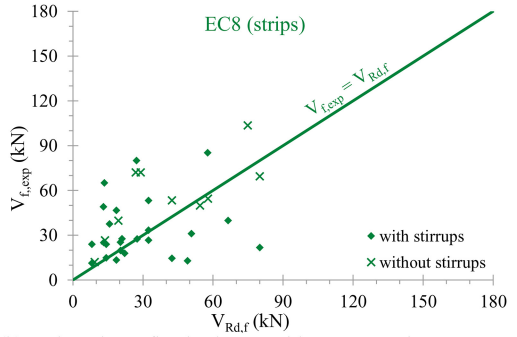

(b) U-shaped retrofitted T-beams with EB-FRP strips

Figure 2. Results of the Eurocode 8 part 3.

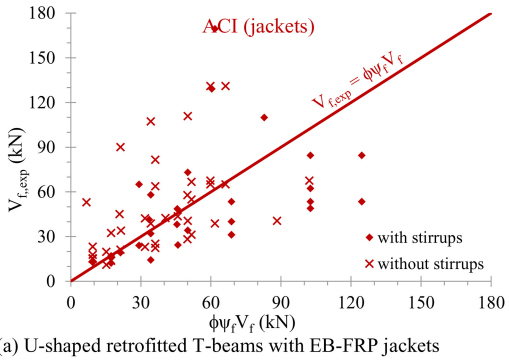

(a) U-shaped retrofitted T-beams with EB-FRP jackets

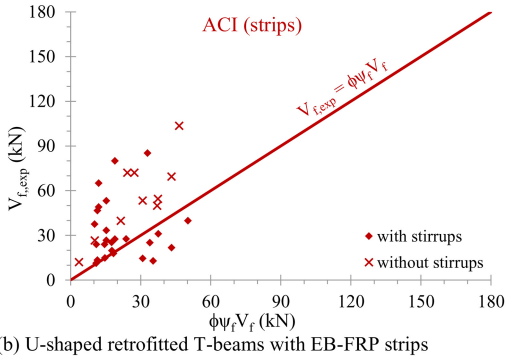

(b) U-shaped retrofitted T-beams with EB-FRP strips

Figure 3. Results of the ACI Committee 440.

Figure 3. Results of the ACI Committee 440.

Table 1. Experimental database characteristics.

$b_s/b_w/h/h_s$ (mm)	f_{cm} (MPa)	ρ_{sl} (%)	ρ_{sw} (%)	E_f (GPa)	ρ_f (%)	$V_{f,exp}$ (kN)
T-beams with stirrups and U-jackets (32 specimens)						
min: 270/95/220/50	25.0	2.1	0.10	8.1	0.07	12.2
max: 584/152/600/150	44.1	5.5	0.83	240	3.46	169.4
T-beams without stirrups and U-jackets (39 specimens)						
min: 140/64/175/50	20.6	0.5	–	12.8	0.07	11.0
max: 660/152/406/150	59.6	3.8	–	231	3.28	131.0
T-beams with stirrups and U-strips (28 specimens)						
min: 300/100/300/50	32.8	1.7	0.10	155	0.05	11.3
max: 508/180/600/150	68.5	3.8	0.79	240	0.80	80.0
T-beams without stirrups and U-strips (10 specimens)						
min: 250/100/175/50	26.3	2.3	–	13.2	0.07	12.0
max: 508/152/600/150	44.1	3.8	–	230	0.67	103.5

can be observed for certain specimens. The unsafe predictions are less in the case of beams with EB-FRP strips than in the case of beams with jackets. Nevertheless, for the majority of the collected beams the Code provisions provide safe estimations and satisfactory correlation (see also Table 2).

The observed discrepancies could be justified by the following facts. The analysis and the prediction of the shear resistance of shear-critical RC beams is a difficult task due to the influence of complex interacting phenomena involved (Karayannis & Chalioris 2013).

Table 2. Code provisions predictions.

	KAN.EPE.	EC8-3	ACI-440
Safe factor:	1.20	1.50	1.38
T-beams with stirrups and U-jackets (32 specimens)			
mean value:	1.36	1.04	0.99
standard deviation:	0.75	0.59	0.60
T-beams without stirrups and U-jackets (39 specimens)			
mean value:	1.78	1.49	1.57
standard deviation:	1.17	0.93	1.31
T-beams with stirrups and U-strips (28 specimens)			
mean value:	1.52	1.54	1.93
standard deviation:	0.88	1.13	1.41
T-beams without stirrups and U-strips (10 specimens)			
mean value:	2.21*	1.58*	2.17*
standard deviation:	0.57	0.66	0.69

* *Uncertain results due to the limited database (10 specimens)*

This complexity is even augmented by the application of EB-FRP to increase the shear capacity of RC beams. Code provisions are based on analytical models for the prediction of the EB-FRP contribution to the shear resistance of RC beams, which, in general, were calibrated from (a) a reduced amount of experimental results, (b) rather unrealistic geometric conditions (laboratory beams) and (c) test programs of only rectangular cross-section beams. Further, most theoretical approaches for the case of T-shaped beams are treated as a special case of the rectangular beams with bonded fibers over a fraction of the cross section and in some cases they have been validated with experimental data obtained from rectangular cross sections (Sas et al. 2009).

The evaluation of the effective strain in fibres is an important parameter that, in most analytical models, determines the contribution of the EB-FRP to the shear resistance of the RC beams. Further, the ratio of the strains $\varepsilon_{fe}/\varepsilon_{fu}$ (effective strain to the ultimate strain of the EB-FRP) indicates the effectiveness of the EB-FRP in the basis that cases of premature debonding failures exhibit low ratio values whereas cases of fibre rupture failures exhibit high ratio values. It is known that the majority of the strengthened T-shaped RC beams with U-wraps of EB-FRP materials fail due to debonding.

Figures 4, 5 and 6 display the diagrams of the ratio $\varepsilon_{fe}/\varepsilon_{fu}$ versus the amount of the applied EB-FRP in terms of the ratio $E_f\,\rho_f/f_{ctm}$. It is noted that the values of the effective strain have been calculated based on the provisions of the Greek Code of Interventions (2013), the Eurocode 8 part 3 (2004) and the ACI Committee 440 (2008), respectively. The values of the mean compressive strength of concrete, the ultimate strain, the modulus of elasticity and the reinforcement ratio of the EB-FRPs have been taken from the experimental data of the examined beams.

A simple regression analysis using polynomials has been applied to the results shown in Figures 4-6 (see the trend-lines of the data points in these Figures).

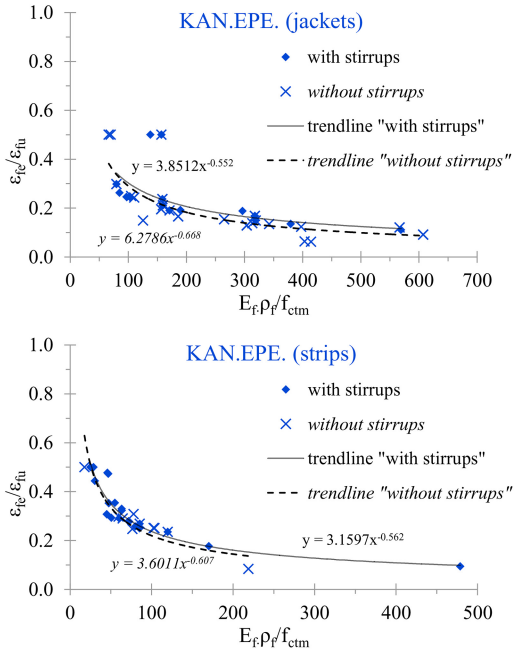

Figure 4. Effectiveness of the EB-FRP retrofitting based on the Greek Code of Interventions provisions.

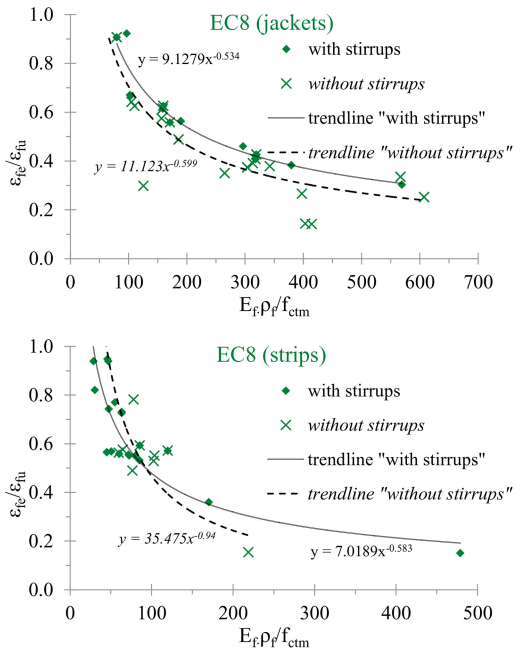

Figure 5. Effectiveness of the EB-FRP retrofitting based on the Eurocode 8 part 3 provisions.

In the same way and for comparison reasons the diagrams of Figures 7 and 8 present the ratio $\varepsilon_{fe}/\varepsilon_{fu}$ versus the ratio $E_f\,\rho_f/f_{ctm}$ where the effective strain ε_{fe} has been evaluated using the experimental results and

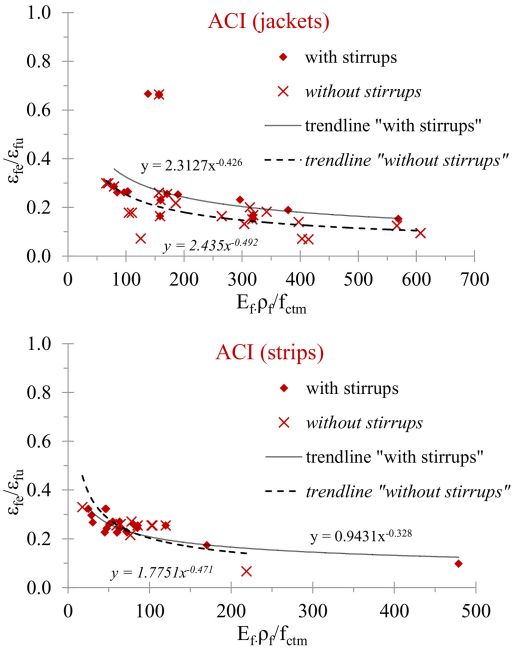

Figure 6. Effectiveness of the EB-FRP retrofitting based on the ACI Committee 440 provisions.

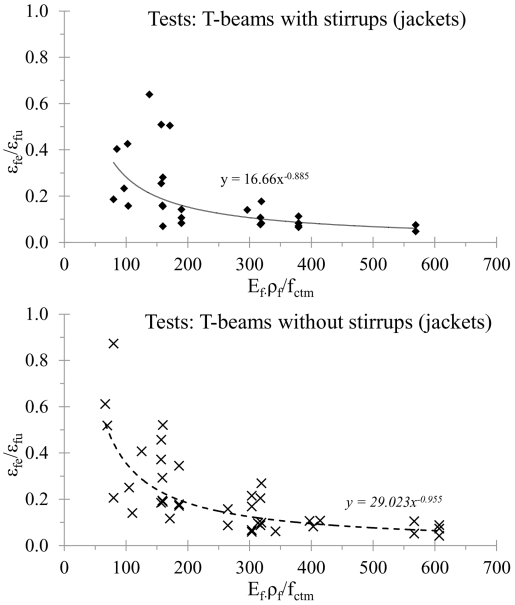

Figure 7. Effectiveness of the EB-FRP retrofitting based on the test results of T-beams strengthened with U-shaped EB-FRP jackets.

especially the contribution of the EB-FRP to the shear resistance $V_{f,exp}$ as follows:

$$\varepsilon_{fe} = \frac{\sigma_f}{E_f} = \frac{V_{f,\exp}}{E_f \rho_f b_w d_f \left(\cot\theta + \cot a\right)\sin^2 a} \qquad (12a)$$

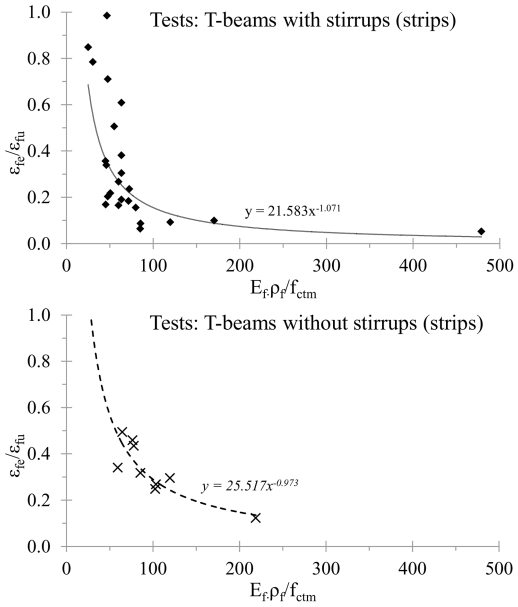

Figure 8. Effectiveness of the EB-FRP retrofitting based on the test results of T-beams strengthened with U-shaped EB-FRP strips.

$$\varepsilon_{fe} = \frac{V_{f,\exp}}{E_f 2t_j d_f \left(\cot\theta + \cot a\right)\sin a}\left(\frac{s_f}{w_f}\right) \qquad (12b)$$

The diagrams of Figures 7 and 8 demonstrate the effectiveness of the EB-FRP retrofitting based on the test results of T-beams strengthened with U-shaped EB-FRP jackets and strips, respectively. It is obvious that the test data in Figures 7 and 8 results to quite different polynomial expressions than the analytical in Figures 4, 5 and 6. Therefore, a more thorough understanding of the behaviour of EB-FRP shear strengthened T-shaped beams is rather needed.

4 CONCLUSIONS

U-shaped retrofitting is an open-form strengthening technique with inadequate anchorage at the edges of the externally applied EB-FRP sheet.The lack of any special anchorage system at these edges significantly affects the shear capacity and the overall behavior of the U-shaped retrofitted RC T-beams. Substantial reductions of the potential shear strength and low values of the effective strain of the applied EB-FRP materials are reported due to the occurrence of premature debonding failures.

The provisions and consequently the predictions of the Greek Code of Interventions (KAN.EPE.), Eurocode 8 part 3 and the ACI Committee 440 for shear strengthened RC T-beams using U-shaped EB-FRP jackets or strips vary. Different expressions for the estimation of the effective design strain or/and the corresponding stress are used. Comparisons between 109 test data of T-beams from existing studies and analytical design predictions derived from these provisions indicate that for the majority of the examined beams the Codes provide safe estimations. However, unsafe estimations of all three Codes are observed for certain specimens.

REFERENCES

Altin, S., Anil, Ö., Kopraman, Y., Mertoğlu, Ç., & Kara, M.E. 2010. Improving shear capacity and ductility of shear deficient RC beams using CFRP strips. *Journal of Reinforced Plastics and Composites* 29(19): 2975–2991.

American Committee 440. 2008. *Guide for the design and construction of externally bonded FRP systems for strengthening concrete structures*. Rep. No. 440 2R-08, Farmington Hills, Michigan: American Concrete Institute.

Annaiah, R.H., Micelli, F. & Nanni, A. 2001. Shear performances of RC beams strengthened in situ with FRP composites. *Composites in Construction; Proc. intern. conf., Porto,* Portugal.

Bousias, S.N., Triantafillou, T.C., Fardis, M.N., Spathis, L. & O'Regan, B.A. 2004. Fiber-Reinforced Polymer retrofitting of rectangular reinforced concrete columns with or without corrosion. *ACI Structural Journal* 101(4): 512–520.

Bousselham, A. & Chaallal, O. 2006a. Behavior of reinforced concrete T beams strengthened in shear with carbon fiber reinforced polymer An experimental study. *ACI Structural Journal* 103(3): 339–347.

Bousselham, A. & Chaallal, O. 2006b. Effect of α transverse steel and shear span on the performance of RC beams strengthened in shear with CFRP. *Composites Part B: Engineering* 37(1): 37–46.

Carolin, A. & Täljsten, B. 2005. Theoretical study of strengthening for increased shear bearing capacity. *Journal of Composites for Construction ASCE* 9(4): 497–506.

CEN. Eurocode 8. 2004. *Design of structures for earthquake resistance – Part 3: Assessment and Retrofitting of buildings*. EN 1998-3: Brussels.

Chaallal, O, Nollet, M.J. & Perraton, D. 1998. Shear strengthening of RC beams by externally bonded side CFRP strips. *Journal of Composites for Construction ASCE* 2(2): 111–113.

Chaallal, O., Shahawy, M. & Hassan, M. 2002. Performance of reinforced concrete T-girders strengthened in shear with carbon Fiber-Reinforced Polymer fabric. *ACI Structural Journal* 99(3): 335–343.

Chajes, M.J., Januszka, T.F., Mertz, D.R., Thomson, T.A. & Finch, W.W. 1995. Shear strengthening of reinforced concrete beams using externally applied composite fabrics. *ACI Structural Journal* 92(3): 295–303.

Chalioris, C.E. 2003. Shear performance of RC beams using FRP sheets covering part of the shear span. *Concrete Repair; Proc. intern. conf., St-* Malo, Brittany, France: 809–816.

Chalioris, C.E. 2007. Analytical model for the torsional behaviour of reinforced concrete beams retrofitted with FRP materials. *Engineering Structures* 29(12): 3263–3276.

Chalioris, C.E. 2008. Torsional strengthening of rectangular and flanged beams using carbon fibre-reinforced-polymers. *Construction and Building Materials* 22(1): 21–29.

Chen, J.F. & Teng, J.G. 2003a. Shear capacity of Fiber-Reinforced Polymer-strengthened reinforced concrete beams: Fiber Reinforced Polymer rupture. *Journal of Structural Engineering ASCE* 129(5): 615–625.

Chen, J.F. & Teng, J.G. 2003b. Shear capacity of FRP-strengthened RC beams: FRP debonding. *Construction and Building Materials* 17(1): 27–41.

Deniaud, C. & Cheng, J.J.R. 2001. Shear behavior of reinforced concrete T-beams with externally bonded fiber-reinforced polymer sheets. *ACI Structural Journal* 98(3): 386–394.

Deniaud, C. & Cheng, J.J.R. 2003. Reinforced concrete T-beams strengthened in shear with fiber reinforced polymer sheets. *Journal of Composites for Construction ASCE* 7(4): 302–310.

Dias, S. & Barros, J. 2006. Influência da percentagem e orientação de laminados de CFRP no reforço ao corte de vigas de betão armado. *Anais do VI° Simpósio EPUSP sobre Estruturas de Concreto*, São Paulo, Brasil.

Gamino, A.L., Sousa, J.L.A.O., Manzoli, O.L. & Bittencourt, T.N. 2010. R/C structures strengthened with CFRP part II: Analysis of shear models, *IBRACON Structures and Materials Journal* 3(1): 24–49.

Ghobarah, A. & Said, A. 2002. Shear strengthening of beam-column joints. *Engineering Structures* 24(5): 881–888.

Jayaprakash, J., Samad, A.A.A., Abbasovich, A.A. & Ali, A.A.A. 2007. Repair of precracked RC rectangular shear beams using CFRP strip technique. *Structural Engineering and Mechanics* 26(4): 427–439.

KAN.EE 2013. *Greek Code of Interventions*. Team for development of code of interventions on reinforced concrete buildings, Harmonization team of code of interventions to Eurocodes: Council of Europe, European Centre on Prevention and Forecasting of Earthquakes (E.C.P.F.E.), Earthquake Planning and Protection Organization (E.P.P.O.): Athens.

Karayannis, C.G. & Chalioris, C.E. 2003a. Strengthening of shear T-beams using carbon FRP. *Concrete Repair; Proc. intern. conf., St-Malo, Brittany*, France: 775–782.

Karayannis, C.G. & Chalioris, C.E. 2003b. Experimental investigation of the contribution of bonded C-FRP jackets to shear capacity of RC beams. *Celebrating Concrete: People and Practice; Proc. intern. symp., University of Dundee, Scotland*, UK: 689–696.

Karayannis, C.G. & Sirkelis, G.M. 2008. Strengthening and rehabilitation of RC beam-column joints using carbon-FRP jacketing and epoxy resin injection. *Earthquake Engineering and Structural Dynamics* 37(5):769–790.

Karayannis, C.G. & Chalioris, C.E. 2013. Shear tests of reinforced concrete beams with continuous rectangular spiral reinforcement. *Construction and Building Materials* 46:86–97.

Khalifa, A., Gold, W.J., Nanni, A. & Aziz, A.M. 1998. Contribution of externally bonded FRP to shear capacity of RC flexural members. *Journal of Composites for Construction ASCE* 2(4): 195–202.

Khalifa, A. & Nanni, A. 2000. Improving shear capacity of existing RC T-section beams using CFRP composites. *Cement and Concrete Composites* 22(3): 165–174.

Khalifa, A., Tumialan, G., Nanni, A. & Belarbi, A. 1999. Shear strengthening of continuous RC beams using externally bonded CFRP sheets. *FRP for Reinforcement of Concrete Structures (FRPRCS4); Proc. intern. symp., American Concrete Institute, Baltimore,* USA: 995–1008.

Mofidi, A. & Chaallal, O. 2014. Tests and design provisions for reinforced-concrete beams strengthened in shear using FRP sheets and strips. *International Journal of Concrete Structures and Materials* 8(2): 117–128.

Monti, G. & Liotta, M.A. 2007. Pretension of externally bonded FRP fabrics for flexural reinforcement of RC beams: Methods and design equations. In Smith S.T. (ed). *FRP in Structures (APFIS 2007); Proc. intern. conf., Hong Kong*, Republic of China: 379–385.

Panda, K.C., Bhattacharyya, S.K. & Barai, S.V. 2011. Strengthening of RC T-beams with shear deficiencies using GFRP strips. *Journal of Civil Engineering and Architecture* 5(1): 56–67.

Panigrahi, A.K., Biswal, K.C. & Barik, M.R. 2014. Strengthening of shear deficient RC T-beams with externaly bonded FRP sheets. *Construction and Building Materials* 57: 81–91.

Park, S.Y., Namaan, A.E., Lopez, M.M. & Till, R.D. 2001. Shear strengthening effect of RC beams using glued CFRP sheets. *FRP Composites in Civil Engineering; Proc. intern. conf., Hong Kong*, China: 669–676.

Pellegrino, C. & Modena, C. 2002. Fiber reinforced polymer shear strengthening of reinforced concrete beams with transverse steel reinforcement. *Journal of Composites for Construction ASCE* 6(2): 104–111.

Sas, G., Täljsten, B., Barros, J., Lima, J. & Carolin, A. 2009. Are available models reliable for predicting the FRP contribution to the shear resistance of RC beams? *Journal of Composites for Construction ASCE* 13(5): 514–534.

Sato, Y., Ueda, T., Kakuta, Y. & Ono, S. 1997. Ultimate shear force capacity of reinforced concrete beams with carbon fibre sheet. *Non-Metalic (FRP) Reinforcement for Concrete Structures; Proc. intern. Symp., Saporo,* Japan: 499–505.

Triantafillou, T.C. 1998. Shear strengthening of reinforced concrete beams using epoxy-bonded FRP composites. *ACI Structural Jourbal* 95(2): 107–115.

Triantafillou, T.C. & Antonopoulos, C.P. 2000. Design of concrete flexural members strengthened in shear with FRP. *Journal of Composites for Construction ASCE* 4(4): 198–205.

Tsonos, A.G. 2007. Effectiveness of CFRP-jackets in post-earthquake and pre-earthquake retrofitting of beam-column subassemblages. *Structural Engineering and Mechanics* 27(4): 393–408.

Tsonos, A.G. 2008. Effectiveness of CFRP-jackets and RC-jackets in post-earthquake and pre-earthquake retrofitting of beam-column subassemblages. *Engineering Structures* 30(3): 777–793.

Concrete Solutions – Grantham et al. (Eds.)
© 2016 Taylor & Francis Group, London, ISBN 978-1-138-03008-4

Flexural and cracking behaviour of concrete beams reinforced with FRP bars

C.E. Chalioris, P.K. Kosmidou, T.A. Panagiotopoulos & C.G. Karayannis
Department of Civil Engineering, Democritus University of Thrace, Greece

ABSTRACT: The experimental behaviour of three large-scale concrete slender beams reinforced with tensional carbon FRP bars and subjected to flexural loading is presented. The effectiveness of a special anchorage configuration of the FRP bars using mild steel spiral reinforcement is also examined. The applied steel spirals have circular shape and installed at the transverse direction around each anchorage end of the FRP bars. Potential enhance of the bonding properties between FRP and concrete due to the confinement provided by the spirals is discussed through the flexural and cracking performance of the tested beams. Although all the examined beams reinforced with FRP bars exhibited flexural response with significant load and satisfactory deflection capacities, the lack of ductility revealed one of the main disadvantages of the application of FRP bars in concrete elements with respect to the use of common steel bars.

Keywords: RC beams, CFRP bars, Flexure, Spiral, Tests.

1 INTRODUCTION

Corrosion of steel reinforcing bars embedded in concrete beams and girders has been the cause of severe structural damages and of high costs in repair and maintenance. Several researchers investigated the harmful effects of corrosion in Reinforced Concrete (RC) elements and especially in their durability properties (Malumbela et al. 2009, Sideris & Anagnostopoulos 2013, Zeris et al. 2014). Because of that, there has been recent interest in the potential use of new reinforcing materials that can prevent or minimize corrosion-related issues. The application of Fibre Reinforced Polymer (FRP) bars instead of conventional steel bars is a promising alternative reinforcement technique in RC elements (Konsta-Gdoutos & Karayannis 1998).

FRP bars exhibit excellent corrosion resistance, reliable durability, high tensile strength, non-magnetization properties and light weight (ACI-440.1R 2006, Fib bulletin 40 2007). However, the low modulus of elasticity and the non-yielding characteristics of the FRP materials results in large deflection and wide cracks in flexural concrete members reinforced with FRP bars (Wang & Belarbi 2013, Rafi et al. 2006). Further, significant lower bond characteristics between the FRP bars and the surrounding concrete have been reported with respect to the traditional deformed steel reinforcing bars. Furthermore, the observed problematic service behaviour of the concrete members reinforced with FRP bars could be responsible for the tensile stresses that allow cracking formation in the radial direction of the tensional bars endangering the bond between FRP and concrete (Achillides & Pilakoutas 2006).

Bond conditions between the interface of the provided FRP bars and the surrounding concrete greatly influences the flexural performance of the structural elements. Sufficient FRP-concrete bond should be mobilised in order to exploit the superior strength characteristics of the composite bar and to ensure the successful transfer of the developed tensional forces between bar and concrete.

Several experimental and analytical studies that investigate the bond properties of various FRP bars and concrete have been reported in the literature (Achillides & Pilakoutas 2004, 2006, Muñoz 2010, Vilanova et al. 2015). Most of these comprehensive researches aim to understand the force transfer mechanism between the concrete and the FRP bars activated in pull-out tests and to determine bond stress-slip constitutive laws. The influence of the anchorage type of the FRP bar to the bond behaviour and to the required bonded length of the FRP bars has also been examined (Vint & Sheikh 2015).

Nevertheless, it has been proved that the application of steel spiral reinforcement provides increased confinement compared to the equal quantity of common steel stirrups and enhances the concrete compressive strength. Thus, the capacity of concrete for shear transfer and subsequently its bond properties are expected to be improved (Karayannis & Chalioris 2013, Chalioris & Karayannis 2013). Based on this aspect, the flexural behaviour of slender

RC beams with special spiral reinforcement configurations installed at the anchorage of the provided tensional FRP bars is experimentally investigated herein.

2 EXPERIMENTAL PROGRAM

The test program of this research includes three (3) RC beams with carbon FRP bars subjected to flexural monotonic loading (see also Fig 1). Two beams have extra anchorage configurations of the tensional FRP bars using steel spiral reinforcement with circular shape at the transverse direction and around each end of each FRP bar (beams "F5.5-c1" and "F5.5-c1.5"). The flexural and cracking behaviour of these beams is studied and compared with the baseline performance of a reference specimen (beam "F5.5") in order to examine any potential improvement of the FRP-concrete bond properties due to the installed spirals.

2.1 *Characteristics of the tested beams*

Geometrical and reinforced characteristics of the RC beams are shown in Figure 1. All three beams have the same rectangular cross-section and dimensions. Their total length is 2.7 m, the height to the width ratio is $h/b = 250/200$ mm, the shear span is $\alpha = 1$ m and the span-to-depth ratio is $\alpha/d = 5$.

The longitudinal reinforcement of all beams is two carbon FRP bars of diameter 5.5 mm as tensional reinforcement (2HD5.5 bottom) and four common deformed steel bars of diameter 14 mm as compressional reinforcement (4Ø14 top).

The ratio of the top compressional reinforcement of all beams is high in order to prevent brittle failure of the compression zone. The tensional FRP ratio, ρ_f, and the compressional steel reinforcement ratio, ρ_s are:

$$\rho_f = \frac{A_f}{bd} = 0.12\% \quad (1)$$

$$\rho_s = \frac{A_s}{bd} = 1.54\% \quad (2)$$

where b, d = the width and the effective depth of the cross-section, respectively; A_f = the area of the tensional FRP bars; and A_s = the area of the compressional steel bars.

According to the design provisions of ACI Building Code (2006) the balanced FRP ratio, ρ_{fd}, can be calculated as follows:

$$\rho_{fb} = 0.85\beta_1 \frac{f_{cm}}{f_{fu}} \frac{E_f \varepsilon_c}{E_f \varepsilon_c + f_{fu}} \quad (3)$$

where f_{cm} = the mean cylinder compressive strength of concrete (MPa); f_{fu} = the design ultimate tensile strength of FRP (MPa); ε_c = the maximum compressive strain of concrete; E_f = the modulus of elasticity of the FRP bars (MPa); and β_1 = the factor of the compressive strength of concrete that can be taken as 0.85 for concrete strength up to 28 MPa (for strength above 28 MPa this factor is reduced continuously at a rate of 0.05 per each 7 MPa of strength in excess of 28 MPa, but should not be less than 0.65).

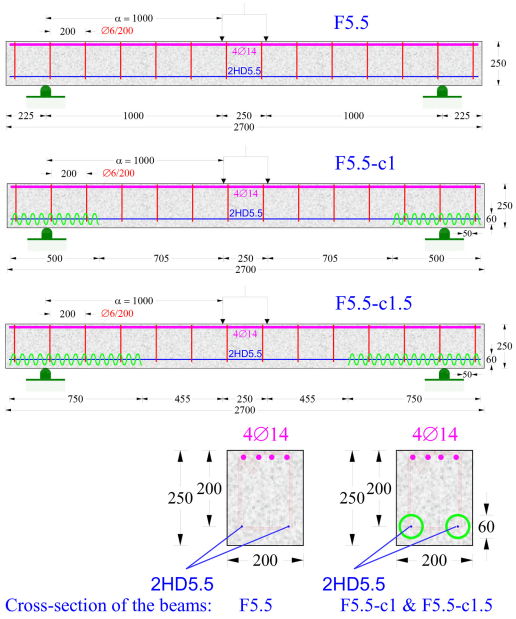

Figure 1. Geometry and reinforcements of the tested beams.

Further, the FRP bars ratio, ρ_f, is compared to the balanced FRP ratio, ρ_{fd}, to define the expected failure mode. If $\rho_f < \rho_{fd}$ the beam is under-reinforced and FRP rupture failure mode governs. If $\rho_f > \rho_{fd}$ the beam is over-reinforced and the failure is expected to occur due to concrete crushing. The reinforcement ratio of FRP bars for all tested beams is 0.12% and the balanced ratio is 0.23%. Thus, according to the design provisions of ACI Building Code (2006) the tested beams are alleged as under-reinforced and the expected failure mode is FRP rupture.

Common mild steel closed stirrups of diameter 6 mm spacing at 200 mm (Ø6/200 mm) consist the adequate transverse reinforcement of all the flexural RC beams in order to prevent shear failure.

In beams "F5.5-c1" and "F5.5-c1.5" continuous steel spiral transverse reinforcements with circular shape have been installed around each FRP bar at both anchorage ends, as shown in Figures 2 and 3, respectively. The length of these spirals is 500 mm and 750 mm, respectively (see also Figs 1–3).

2.2 *Material properties*

The used carbon FRP bars (HD5.5) were produced by the pultrusion process. Continuous carbon fibres with a volume fraction of 57% by volume were used. The

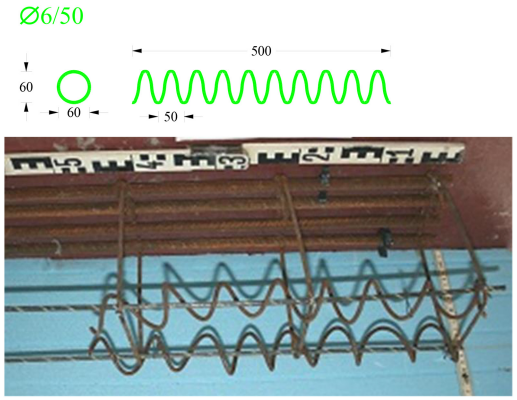

Figure 2. The applied circular shaped steel spiral reinforcement around each FRP bar at the anchorage of beam "F5.5-c1".

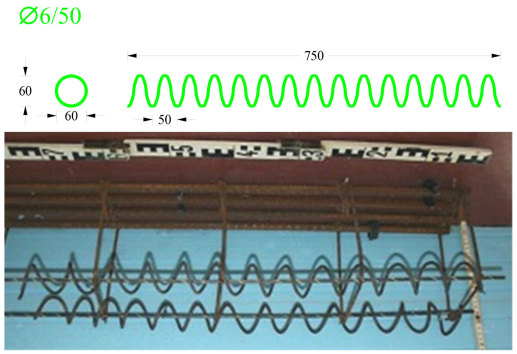

Figure 3. The applied circular shaped steel spiral reinforcement around each FRP bar at the anchorage of beam "F5.5-c1.5".

nominal tensile strength and the elastic modulus of the carbon fibres were greater than 4 GPa and 230 GPa, respectively. The resin used to bond fibres was epoxy vinyl ester. These carbon FRP bars have a relatively rough external surface produced by special surface treatment with quartz-sand. The nominal ultimate tensile strength and the elastic modulus of CFRP bars are 1.8 GPa and 130 GPa, respectively.

The mean cylinder compressive strength of the used concrete is $f_{cm} = 33$ MPa and the mean axial tensile strength is $f_{ctm} = 2.57$ MPa. The yield tensile strength of the compressional deformed steel bars (Ø14) and the transverse mild steel stirrups (Ø6) is $f_{yl} = 550$ MPa and $f_{yt} = 310$ MPa, respectively.

2.3 *Test setup and instrumentation*

A typical four-point bending scheme and setup is adopted for the flexural monotonic testing of the RC beams, as in Figures 4 and 5. Tested beams were simply edge-supported on roller supports 2.25 m apart using a rigid laboratory. The imposed load was applied in two points 250 mm apart in the mid-span of the beams using a steel spreader beam. The length of the shear

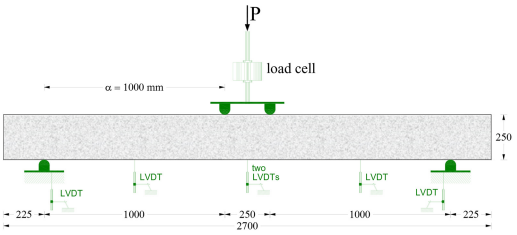

Figure 4. Dimensions of the test apparatus.

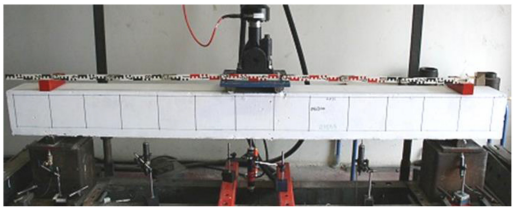

Figure 5. Test rig and instumentation.

span of the beams is $\alpha = 1$ m and the span-to-depth ratio is $\alpha/d = 5$ (typical slender beam).

The imposed load was consistently increased with low rate using a pinned-end actuator and was measured by a load cell with accuracy equal to 0.05 kN. The deflections of the tested beams were recorded using six Linear Variable Differential Transducers (LVDTs); four of them with 0.01 mm and two with 0.005 mm accuracy. Two of the installed LVDTs were placed at the mid-span of the beams (one at the front side and one at the back side to increase accuracy), one at the middle of the left shear span, one at the middle of the right shear span and two at the supports (see also Figs 4 and 5). This way, the net deflections at the mid-span and at the middle of the left-span and of the right-span of the beams were accurately estimated.

Further, the width of the flexural cracks was measured using crack transducers that were installed on the front side of the beams whenever each crack initially appeared. Measurements for load, deflection and crack width were read and recorded continuously during tests until the ultimate bearing capacity and the total failure of the beams.

3 TEST RESULTS

Test results of the beams are presented in Figures 6, 7 and 8 for specimens "F5.5", "F5.5-c1" and "F5.5-c1.5", respectively. The flexural and the cracking behaviour of the beams is demonstrated in terms of bending moment versus deflection curves (Figs 6a, 7a and 8a) and bending moment versus crack width curves (Figures 6b, 7b and 8b), respectively. Deflections of the mid-span, left-span and right-span of the beams are displayed and compared in Figures 6a, 7a and 8a.

All tested beams exhibited flexural behaviour as expected. First cracking initiated approximately at the

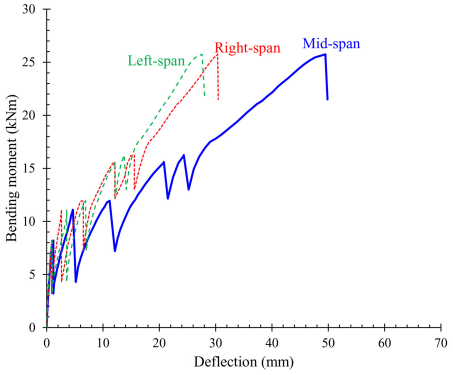

(a) Bending moment versus deflection curves.

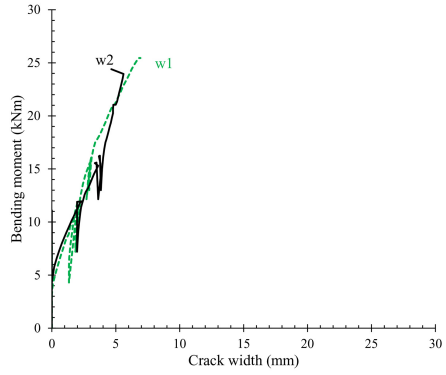

(b) Bending moment versus crack width curves.

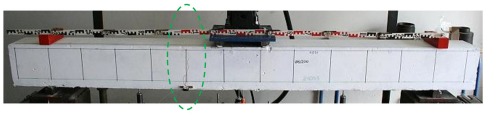

(c) Cracking pattern at the onset of flexural cracking.

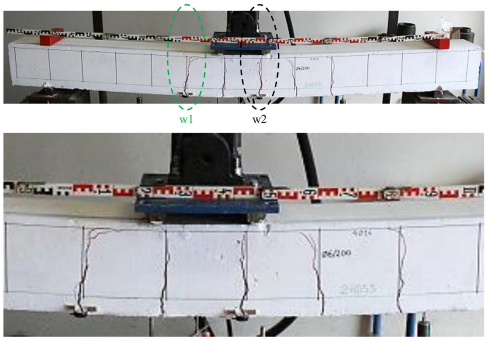

(d) Cracking pattern at failure.

Figure 6. Experimental results of the beam “F5.5”.

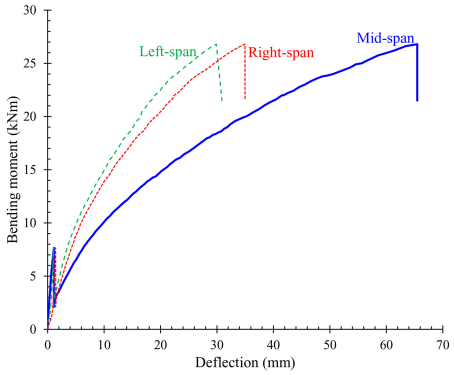

(a) Bending moment versus deflection curves.

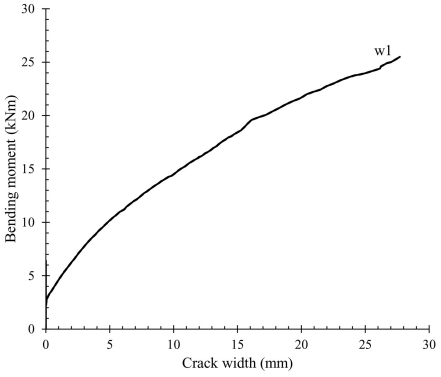

(b) Bending moment versus crack width curve.

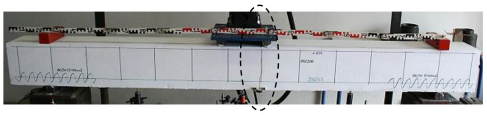

(c) Cracking pattern at the onset of flexural cracking.

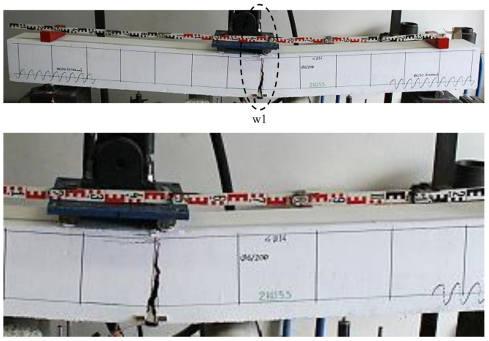

(d) Cracking pattern at failure.

Figure 7. Experimental results of the beam “F5.5-c1”.

same loading level and close to the mid-span for all beams. These flexural cracks were formed perpendicular to the longitudinal axis of the beam at the region of the constant maximum moment or nearby this region, where the shear stresses are zero or almost zero (see also the cracking patterns at the onset of flexural cracking for the specimens “F5.5”, “F5.5-c1” and “F5.5-c1.5” in Figs 6c, 7c and 8c, respectively).

After first cracking, all beams suffered reduced stiffness and increased deflections as indicated from

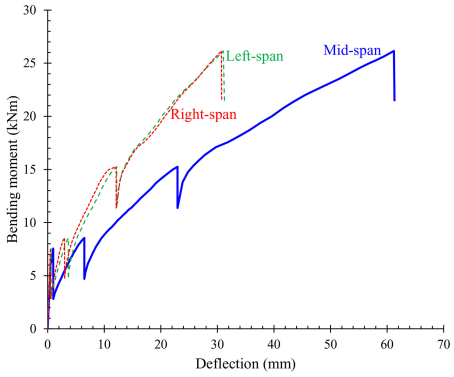

(a) Bending moment versus deflection curves.

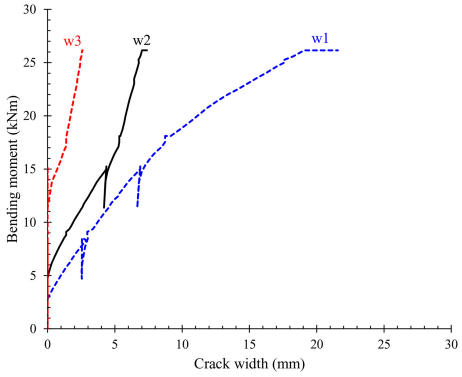

(b) Bending moment versus crack width curves.

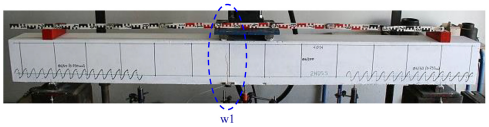

(c) Cracking pattern at the onset of flexural cracking.

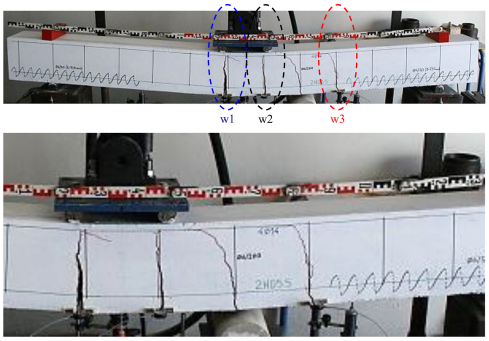

(d) Cracking pattern at failure.

Figure 8. Experimental results of the beam "F5.5-c1.5".

the reduced slope of the bending moment versus deflection curves. As the applied load increased, the developed cracks traversed towards the compression zone of the beam and a few more flexural cracks appeared in beams "F5.5" and "F5.5-c1.5" until the ultimate load capacity and the total failure of the beams. Beam "F5.5-c1" exhibited only one crack that propagated deeply into the compression zone of the beam till the total failure of the specimen. All beams failed due to the rapture of the carbon FRP bars. The cracking patterns of the beams at failure are demonstrated in the photographs of Figures 6d, 7d and 8d.

Table 1. Test results.

Beam	P_{max} (kN)	P_{cr} (kN)	δ_{peak} (mm)	M_{ult} (kNm)
F5.5	51.5	16.4	49.49	25.8
F5.5-c1	53.6	15.3	65.47	26.8
F5.5-c1.5	52.3	15.1	61.20	26.2

The measured values of the peak applied load (ultimate bearing capacity), P_{max}, the applied load of the first crack formation, P_{cr}, the deformation at the maximum (peak) applied load, δ_{peak}, and the ultimate bending moment of all tested beams are presented and compared in Table 1. The values of the bending moment capacity of the beams, M_{ult}, are calculated using the following expression:

$$M_{ult} = \frac{P_{\max}}{2} a \tag{4}$$

4 CONCLUDING REMARKS

Test results of the experimental program presented herein indicated that concrete slender beams reinforced with carbon FRP bars exhibited flexural response with significant load and satisfactory deflection capacities. The lack of yielding and adequate ductility in the observed flexural behaviour of the beams reveals one of the main weaknesses of the application of FRP bars in RC elements with respect to the use of common steel bars. This is attributed to the linear elastic tensile stress-strain behaviour of the FRPs up to ultimate load and to their brittle failure.

The effectiveness of a special anchorage system of the FRP bars using common mild steel spiral reinforcement is also examined. The applied steel spirals have circular shape and placed at the transverse direction around each anchorage end of the tensional FRP bars. Although the ultimate bending moment capacities of the tested beams with this extra anchorage configuration were more or less the same with the corresponding bending moment of the reference beam (specimen without spirals), the cracking behaviour of these beams has been ameliorated. Beams with steel spirals exhibited substantial higher crack width values and increased deformations at the maximum load with respect to the baseline behaviour of the beam without spirals. This effort to improve the bond conditions between the interface of the FRP bars and the concrete would further be investigated.

Tested beams failed suddenly at ultimate load due to the rupture of the carbon fibres of the FRP bars. This experimentally observed failure mode of the beams agrees with the prediction of the design provisions of ACI Building Code (2006) for flexural under-reinforced concrete elements with tensional FRP bars.

REFERENCES

Achillides, Z. & Pilakoutas, K. 2004. Bond Behavior of Fiber Reinforced Polymer Bars under Direct Pullout Conditions. *ASCE Journal of Composites for Construction* 8 (2): 173–181.

Achillides, Z. & Pilakoutas, K. 2006. FE modelling of bond interaction of FRP bars to concrete. *Structural Concrete* 7 (1): 7–16.

American Committee 440 2006. *Guide for the Design and Construction of Structural Concrete Reinforced with FRP Bars.* Michigan: American Concrete Institute.

Chalioris, C.E. & Karayannis, C.G. 2013. Experimental investigation of RC beams with rectangular spiral reinforcement in torsion. *Engineering Structures* 56: 286–297.

Fib bulletin 40 2007. *FRP reinforcement in RC structures*. Lausanne: International Federation for Structural Concrete.

Karayannis, C.G. & Chalioris, C.E. 2013. Shear tests of reinforced concrete beams with continuous rectangular spiral reinforcement. *Construction and Building Materials* 46: 86–97.

Konsta-Gdoutos, M. & Karayannis, C.G. 1998. Document Flexural behaviour of concrete beams reinforced with FRP bars. *Advanced Composites Letters* 7 (5): 133–137.

Malumbela, G., Moyo, P. & Alexander, M. 2009. Behavior of RC beams corroded under sustained service loads. *Construction and Building Materials* 23(11): 3346–3351.

Muñoz, M.B. 2010. *Study of Bond Behavior between FRP reinforcement and Concrete*. PhD Thesis, Girona: University of Girona.

Rafi, M.M., Nadjai, A., Ali, F. & Talamona, D. 2006. Aspects of behavior of CFRP reinforced concrete beams in bending. *Construction and Building Materials* 22: 277–285.

Sideris, K.K. & Anagnostopoulos, N.S. 2013. Durability of normal strength self-compacting concretes and their impact on service life of reinforced concrete structures. *Construction and Building Materials* 41: 491–497.

Vilanova, I., Baena, M., Torres, L. & Barris, C. 2015. Experimental study of bond-slip of GFRP bars in concrete under sustained loads. *Composites Part B: Engineering* 74: 42–52.

Vint, L.M. & Sheikh, S. 2015. Investigation of bond properties of alternate anchorage schemes for glass Fiber-Reinforced Polymer bars. *ACI Structural Journal* 112 (1): 59–68.

Wang, H. & Belarbi, A. 2013. Flexural durability of FRP bars embedded in fiber-reinforced-concrete. *Construction and Building Materials* 44: 541–550.

Zeris, C., Batis, G., Mouloudakis, V. & Marakis, J. 2014. Accelerated corrosion investigation of axially loaded reinforced concrete elements. *Anti-Corrosion Methods and Materials* 61 (4): 215–223.

Concrete Solutions – Grantham et al. (Eds.)
© 2016 Taylor & Francis Group, London, ISBN 978-1-138-03008-4

Fatigue design of RC beams strengthened in flexure with FRP laminates

B. Charalambidi, T.C. Rousakis & A.I. Karabinis
Laboratory of Reinforced Concrete, Department of Civil Engineering,
Democritus University of Thrace (DUTh), Xanthi, Greece

ABSTRACT: The aim of the present research is the experimental and analytical investigation of the response of fiber reinforced polymer strengthened reinforced concrete beams, of large scale, under fatigue loading. For that purpose, reinforced concrete beams were cast, both of rectangular and T cross sections, with web dimensions 200 × 500 mm and 3050 mm long. Beams were strengthened in flexure with externally bonded CFRP laminate or with CFRP laminates bonded into slits on the concrete cover surface. The different fatigue life and modes of failures are discussed. Moreover, an analytical design equation is proposed, based on the existing experimental results available in the international literature. The analytical model takes into account the effect of the external FRP strengthening reinforcement on the fatigue response of the beams.

1 INTRODUCTION

Externally bonded fiber reinforced polymers (FRP) are very popular in retrofit of reinforced concrete beams. They have high strength to weight ratio and geometric versatility while the most recent research, has confirmed the upgraded response of carbon FRP (CFRP) strengthened reinforced concrete beams, both in flexure and shear. Recently, considerable interest has been attracted by the fatigue behavior of reinforced concrete members, especially beams and bridge girders. Fatigue experiments are very demanding as they are time and energy consuming, require thoroughly designed experimental setup and equipment, to resist millions of cycles of loading. Therefore, the beams are usually of small scale and the studied parameters limited. The presented study focuses on large scale RC beams of 200 mm wide, 500 mm high and 3050 mm in length. Two different flexural strengthening techniques with FRP laminates were investigated: EBR or NSM. The research included also rectangular or T-shaped beams with different concrete cover. The FRP strengthened beams (EBR or NSM) were designed according to ACI Committee 440.2R-08, in order to exhibit 30% higher ultimate flexural strength than unstrengthened ones. Thus, two different ratios of the relative axial tensile rigidity of tensile steel reinforcement to the tensile rigidity of FRP strengthening were examined that were close to applications of practice: a ratio of 6.09 for the EBR case and 12.18 for the NSM case.

2 EXPERIMENTAL PRORAM

2.1 *Specimens description and test setup*

The experiments presented in this paper involved seven reinforced concrete beams, measuring 200 mm wide × 500 mm deep × 3050 mm in length. Normal strength, ready-mixed concrete was used of 24.8 MPa average compressive. All beams had the same reinforcement configuration. The internal reinforcement consisted of three bottom bars of 16 mm diameter and two top bars of 12 mm diameter. Stirrups of 8 mm diameter were placed in the beam as shear reinforcement, at a spacing of 290 mm. At the support regions, and for a length of 450 mm, stirrups were spaced at a distance of 50 mm (Fig. 1).

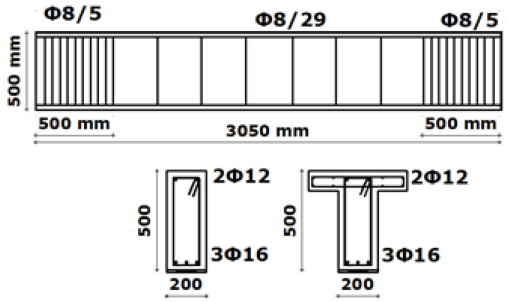

Figure 1. Concrete beam geometry, detailing of reinforcements.

The longitudinal rebars and the shear stirrups of the specimens had a nominal yield stress of 500 MPa. The specimens were strengthened for both shear and flexure. The shear strengthening was accomplished with U shaped CFRP sheets with unidirectional fibers, wrapped at the shear spans of the beams. Sheets had a reported tensile strength of 4100 MPa, modulus of elasticity of 231 GPa and 0.12 mm thickness. The flexural strengthening included two different strengthening schemes. Four out of the seven beams were externally bonded with one carbon fiber laminate of 2805 MPa strength, 165 GPa modulus of elasticity,

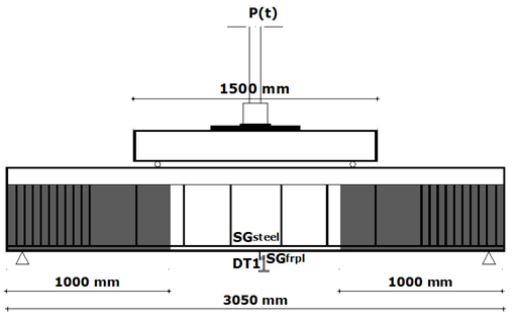

Figure 2. Test setup and instrumentation.

100 mm width and 1.2 mm thickness. The remaining beams were strengthened with 2 NSM CFRP laminates of 3100 MPa, 165 GPa modulus of elasticity, 10 mm height and 3.0 mm thickness.

The beams were tested under four-point bending, at a constant loading frequency of 2 Hz. Two different loading amplitudes were performed with different upper load limit. The low amplitude loading, denoted as series L (low), ranged from 20% to 60% of the design ultimate strength of the beams. This amplitude represents the ratio of live to dead design loads of a common bridge girder. The high load amplitude, denoted as series H (high), ranged from 20% of the design ultimate strength of the beam to 80% of the strength corresponding to the nominal yield stress of the longitudinal reinforcement. A peak reinforcing bar stress of 80% of yield represents the upper limit recommended by ACI Committee 440 (2008).

3 TEST RESULTS

3.1 *Fatigue life and failure mode*

The L series beams (REX20-L and TEX20-L) accomplished the fatigue loading reaching 2 million cycles and 1.3 million cycles and then the testing was stopped. It seems that both beams can successfully sustain fatigue loading during their service life. On the contrary, the specimens of the H series failed at less than 2 million cycles. These beams exhibited a similar primary mode of failure. Failure was due to tensile fracture of the steel reinforcement. No prior fatigue failure of the concrete cover in between the steel bar and the FRP strengthening was recorded in any case. Table 1 cites the number of performed cycles, the maximum recorded load and the corresponding deflection during the fatigue tests.

In all cases, a main crack was formed at the midspan region of the beam, between the two vertical loads. As the number of fatigue loading cycles increased, an increase of the number of cracks and of their width was observed. During the last cycles, one particular crack was much wider than the rest of the recorded cracks. This main crack indicated the region where the steel fracture occurred. Figure 3, depicts the main crack for beam REX20-H.

Table 1. Test results, fatigue lives.

Fatigue loading				
Series	Specimen	Cycles	P_{max} (kN)	δ_{Pmax} (mm)
Series L	REX20-L	2,000,000	125.96	5.75
	TEX20-L	1,300,000	126.92	9.01
Series H	REX20-H	990,147	153.07	21.65
	REX40-H	1,450,105	159.13	21.18
	RNSM20-H	807,437	146.80	26.79
	RNSM40-H	696,500	148.11	22.46
	TNSM20-H	774,411	152.69	22.75

* L and H correspond to low and high fatigue load amplitude
*P_{max} and δ_{Pmax} correspond to the last cycle before fatigue failure
* R, T correspond to the cross sectional geometry of the beams: Rectangular and T-section
* EX indicates the external FRP reinforcement
* NSM indicates the NSM FRP reinforcement
* 20, 40 correspond to the concrete cover of the specimen

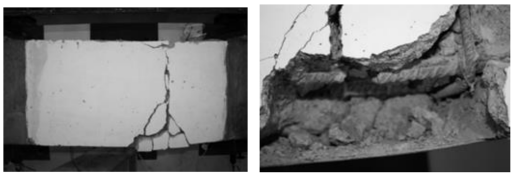

Figure 3. Crack pattern (above) and steel fracture (below), after fatigue loading of beam with rectangular section, external FRP laminate, 20 mm concrete cover, under high amplitude loading, REX20-H.



Figure 4. Bottom side view of the soffit of beam RNSM20-H, after fatigue loading. The NSM laminates did not debond.

Debonding of the externally bonded FRP laminate was a secondary failure mechanism of the strengthened beams in the H series, that occurred after the fatigue failure of the bar reinforcement. The debonding of the laminate initiated at the place where the wider crack occurred and expanded towards almost the whole midspan of the beam. In the cases of beams strengthened with NSMs, there was no laminate debonding observed and the laminates were kept in place, even after the fracture of the steel bars (Fig. 4).

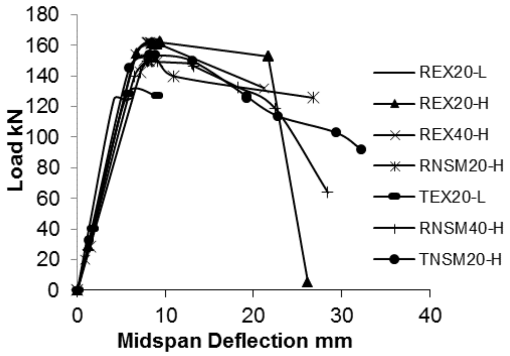

Figure 5. Load vs deflection envelops for all specimens under fatigue loading.

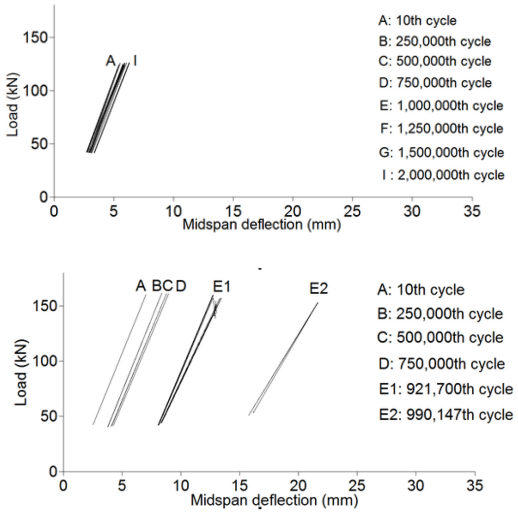

Figure 6. Load vs deflection curve for specimens REX20-L (above) and REX20-H (below).

3.2 *Load – deflection curves*

The mechanical behavior of beams is assessed through their load – deflection diagrams and diagrams of deflection vs number of cycles.

The specimens of the H series achieved an ultimate deflection almost three times higher than the specimens of the L series (Fig. 5 and Table 1). More detailed, Figure 6 illustrates the load vs deflection diagrams at every 250,000 cycle groups of data for beams REX20-L and REX20-H.

During the first 250,000 cycles there was an initial increase of the midspan deflection, followed by a region where the deflections remained relatively constant for the next 1,500,000 cycles for the REX20-L and 500.000 cycles for the REX20-H. At the end of the fatigue loading, during the last 250.000 cycles, beam REX20-H exhibited an abrupt increase of deflections (curve at points D-E1-E2 in Fig. 6) and failed. The described response of the beams REX20-L and REX20-h is typical for the rest of the specimens in this study. The effect of the EBR or the NSM strengthening or of the concrete cover or of the shape of the section in the P-δ curves was negligible. The variable behavior of the beams under high amplitude fatigue loading may be attributed to the decrease of the secant axial rigidity of the steel rebars during the fatigue cycles within the elastic range. This assumed decrease is expected to be more pronounced for a higher amplitude of load and number of cycles. As concluded above, the only mechanism to restrict the axial strain evolution due to fatigue in the steel reinforcement was the elastic axial stiffness of the FRP that remained constant throughout loading (no debonding was reported).

4 ANALYTICAL MODEL

4.1 *Effect of the maximum applied steel stress to steel yielding ratio*

The effect of the maximum stress and the stress range of the steel reinforcement to the fatigue behavior of the reinforced concrete beams, has already been investigated by several authors (Papakonstantinou et al. 2001, Kim and Heffernan 2008 among others). ACI Committee 440.2R-08 guide, recommends stress limits for FRP strengthening under tension and concrete under compression as well as a peak reinforcing bar stress of 80% of yield strength to estimate the upper limit of fatigue loading in Serviceability Limit State (SLS). It is acknowledged by the existing literature that the critical material vulnerable to fatigue failure is steel and that stresses on steel about 60% of its yielding strength practically do not lead to fatigue failure (Papakonstantinou et al. 2001, Heffernan and Erki 2004, Gussenhoven et al. 2005, Gheorgiu et al. 2007). The available fatigue prediction models provide the number of cycles to failure with respect to the steel stress range (Helgason and Hanson 1974, Moss 1982, CEB 1990, Mallet 1991, Papakonstantinou et al. 2001, Diab and Wu 2008 among others) assuming indirectly a sustained load between a minimum and maximum level. Given the SLS design approach for steel stress limitation, the present research aims to introduce directly the ratio of maximum steel stress to the yielding strength of steel σ_{max}/f_y into the fatigue design.

There is a beneficial effect from the restrictive action of the elastic strengthening material (FRP laminate) while other critical parameters remain that are not adequately addressed. In general, strengthening of the tension zone with an elastic material that does not yield, such as the FRP materials, may enhance the restrictive mechanism through constant FRP stiffness that may delay fatigue failure in steel. Therefore, besides σ_{max}/f_y, a second variable that should be taken into consideration, is the ratio of axial rigidity of the steel bars to that of the FRP reinforcement k_s/k_f, as it affects the fatigue life of RC beams.

The present analytical study proposes a fatigue model that includes the effect of the yielding strength

of steel as well as the effect of FRP strengthening restrictive mechanism. The proposed model is a $y = a \cdot x^b$ equation type. Two sets of parameters a, b are proposed to account for the effectiveness of maximum stress and yielding strength. For the determination of parameters a and b regression analysis was carried out, taking into account the yielding stress of specimens in literature. The proposed model has the following expression:

$$\frac{\sigma_{max}}{f_y} = (0.00336 \cdot f_y + 2.383) \cdot N'^{(-0.00019 \cdot f_y - 0.04967)}_{an} \quad (1)$$

where σ_{max} is the maximum stress of steel, f_y is the yielding stress of steel and N is the number of cycles.

4.2 *Effect of steel to FRP axial rigidity k_s/k_f*

In order to include the effect of the FRP strengthening to the proposed fatigue model, a new regression analysis was designed and further improved equations are proposed that involve the ratio of axial rigidity of steel to FRP reinforcement and depend on the value of σ_{max}/f_y ratio. The model requires the calculation of the analytical number of cycles N'_{an}, of Equation 1. Then the k_s/k_f effect is included according to the different σ_{max}/f_y and the final theoretical number of cycles N_{theor} is estimated. The model is modified for various σ_{max}/f_y ratios according to regression analysis of the experimental data of literature that correspond to different σ_{max}/f_y values. The final model for the estimation of N cycles to fatigue failure is cited below ($N = N_{theor}$):

$$N_{theor} = [(\frac{\sigma_{max}/f_y}{(0.00336 \cdot f_y + 2.383)})^{(1/(-0.00019 \cdot f_y - 0.04967))}] / (0.0125 \frac{k_s}{k_f} + 1.2983) \quad (2)$$

for $\sigma_{max}/f_y > 0.78$,

$$N_{theor} = [(\frac{\sigma_{max}/f_y}{(0.00336 \cdot f_y + 2.383)})^{(1/(-0.00019 \cdot f_y - 0.04967))}] / (-0.0349 \frac{k_s}{k_f} + 1.1814) \quad (3)$$

for $0.68 \leq \sigma_{max}/f_y \leq 0.78$,

$$N_{theor} = [(\frac{\sigma_{max}/f_y}{(0.00336 \cdot f_y + 2.383)})^{(1/(-0.00019 \cdot f_y - 0.04967))}] / (0.1192 \frac{k_s}{k_f} + 0.4798) \quad (4)$$

for $0.60 \leq \sigma_{max}/f_y < 0.68$,

For the evaluation of the theoretical models available in the literature and of the model proposed in this paper, the criterion of the average absolute errors of the predictions for each model of the experimental data of the literature were used (Eq. 5).

$$AAE = \frac{\sum_{i=1}^{N} E_i}{N} \quad (5)$$

Table 2. Assessment of the proposed prediction model.

	Proposed model	CEB 1990	Helgason & Hanson	Moss 1982	Diab & Wu
AAE (%)	24.7	58.1	43.38	229.8	50.19
Average	0.88	1.02	0.90	2.74	1.12

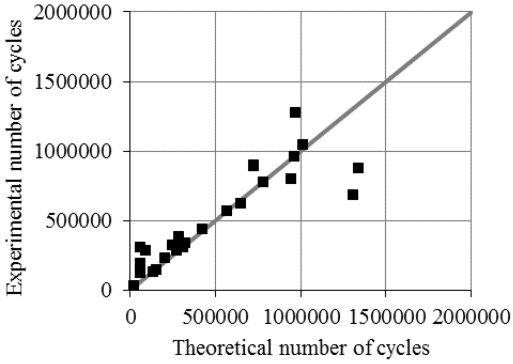

Figure 7. Performance of the proposed model

where the error of each theoretical prediction N_{theor} over the experimental values N_{exp} is calculated as E as follows:

$$E(N)\% = \frac{N_{theor} - N_{exp}}{N_{exp}} \cdot 100 \quad (6)$$

The proposed model shows an average absolute error equal to 24.7% and an average ratio of 0.88compared to the models provided in the literature (Table 2). The performance of the proposed model is assessed in Figure 7.

The model attempts to identify the effects of the ratio of maximum steel stress to the yielding strength of the steel and of the ratio of axial rigidity of steel to that of FRP reinforcement. In practical applications of strengthening, the previous fatigue loading and corresponding remaining fatigue life of steel bars of such beams should be appropriately assessed and considered in redesign. Further improvement of the accuracy of the proposed model may allow for the rational prediction of such remaining fatigue life in order to design suitable FRP strengthening for advanced fatigue performance.

5 DISCUSSION AND CONCLUSIONS

The present study concerns the experimental and analytical investigation of reinforced concrete beams strengthened through FRP configurations.

Seven reinforced concrete beams were tested both of rectangular and T cross-section, strengthened with two different FRP techniques: externally bonded

CFRP laminates and NSM CFRP laminates. The specimens were subjected to fatigue loading up to failure. In all cases of fatigue loading:

- The failure of the beams was due to tensile fracture of the steel bar reinforcement under fatigue loading.
- In the case of the externally strengthened beams with FRP laminates, the steel fracture was followed by the FRP laminate debonding.
- No debonding occurred in the cases of NSM laminate strengthening.
- An increase in deflections with the number of cycles was recorded. All specimens experienced an abrupt increase of the deflections during the last cycles of before failure.

A fatigue design model is proposed in this study. The model estimates the number of cycles with respect to the maximum stress of the tensile steel reinforcement, the steel yielding strength and the axial rigidity of steel and FRP. The proposed model provides improved predictions compared to other existing models in the literature. It provides an absolute average error prediction equal to 27.3% and an average ratio of 0.9. Beams of steel reinforcement alone, show a variably and gradually weakened restrictive mechanism in the tension zone, under cyclic loading. Strengthening with an elastic material that does not yield, such as the FRP, may enhance the combined restrictive mechanism through constant stiffness and suppress fatigue failure of steel under service loading. Incorporation of f_y as a significant parameter for fatigue design should be further refined to better address the different post-yielding restrictive action of the steel, depending on the characteristics of its yielding plateau and of its hardening modulus. Also, previous static and fatigue loading history of the beams should be properly assessed and considered in the design.

ACKNOWLEDGMENTS

The authors wish to thank Sika Hellas S.A. for providing the FRP materials and resins, DUTh RC Laboratory staff for the assistance in the construction, casting and preparation of the specimens and DUTh RC Laboratory and Sika Hellas S.A. staff for the assistance in the FRP implementation.

REFERENCES

AASHTO (2007). LRFD Bridge Design Specifications, 4th edition and 2008–2009 interims, American Association of State Highway and Transportation Officials, Washington, D.C.

American Concrete Institute (ACI) Committee 215. (1997). "Considerations for design of concrete structures subjected to fatigue loading." 215R-92, Farmington Hills, MI.

American Concrete Institute (ACI) Committee 440.2R-08 (2008). "Guide for the Design and Construction of Externally Bonded FRP Systems for Strengthening Concrete Structures." American Concrete Institute, Michigan.

Aidoo, J., Harries, K. a., & Petrou, M. F. (2004). Fatigue Behavior of Carbon Fiber Reinforced Polymer-Strengthened Reinforced Concrete Bridge Girders. Journal of Composites for Construction, Vol.8, No 6, 501–509

Barros J.A.O., Fortes A.S. (2005). Flexural strengthening of concrete beams with CFRP laminates bonded into slits. Cement and Concrete Composites 27,471–480

Bizindavyi L., Neale K.W., Erki M.A. (2003). Experimental investigation of bonded fiber reinforced polymer-concrete joints under cyclic loading. Journal of Composites for Construction. Vol.7, No 2, 127–134

Brown J., Kunnath S. (2000). Low Cycle Fatigue behavior of Longitudinal Reinforcement in Reinforced Concrete Beam Columns. Technical Report MCEER-00-0007. University of Central Florida

Canadian Standards Association (CSA) (2006). "Canadian Highway Bridge design code." CAN/CSA S6-06, Mississauga, ON, Canada.

Charalambidi B., Rousakis T., Karabinis A. Fatigue behavior of large scale reinforced concrete beams strengthened in flexure with fiber reinforced polymer laminates. Journal of Composites for Construction 2016; paper accepted for publication.

De Lorenzis L., Nanni A. (2002). Bond between Near-Surface Mounted FRP rods and concrete in structural strengthening. ACI Structures Journal, Vol. 99, No 2, pp. 123–133

Diab H.M., Wu Z. (2008). Review of existing fatigue results of beams externally strengthened with FRP laminates. Fourth International Conference on FRP Composites in Civil Engineering (CICE2008), 22–24 July 2008, Zurich, Switzerland

Ekenel M., Rizzo A., Myers J.J., Nanni A. (2006). Flexural fatigue behavior of reinforced concrete beams strengthened with FRP fabric and procured laminate systems. Journal of Composites for Construction. Vol.10, No 5, 433–442

Ferrier E., Bigaud D., Clément J.C., Hamelin P. (2011). Fatigue-loading effect on RC beams strengthened with externally bonded FRP. Construction and Building Materials 25, 539–546

Gheorgiu C., Labossiere P., Proulx J. (2007). Response of CFRP strengthened beams under fatigue with different load amplitudes. Construction and Building Materials 21, 756–763

Gussenhoven R., Brena S.F. (2005). Fatigue Behavior of Reinforced Concrete Beams Strengthened with Different FRP Laminate Configurations. Proceedings of the Seventh Fiber Reinforced Polymers for Reinforced Concrete Structures (FRPRCS7) Conference, New Orleans, November 2005

Heffernan P.J., Erki M.A. (2004). Fatigue Behavior of Reinforced Concrete Beams Strengthened with Carbon Fiber reinforced plastic laminates. Journal of Composites for Construction. Vol.8, No 2, 132–140

Kim Y., Heffernan P. (2008). Fatigue Behavior of Externally Strengthened Concrete Beams with Fiber-Reinforced Polymers: State of the Art. Journal of Composites for Construction. Vol.12, No 3, 246–256

NCRP Report 679 (2011). Design of Concrete Structures using High-Strength Steel Reinforcement. Transportation Research Board

Papakonstantinou C.G., Petrou M.F., Harries K.A. (2001). Fatigue behavior of RC beams strengthened with GFRP sheets. Journal of Composites for Construction. Vol. 5, No 4, 246–253

Sena Cruz J., Barros J.A.O. (2004). Modeling of bond between near surface mounted CFRP laminate strips and concrete. Computers and Structures 82, 1513–1521

Soltani A. (2010). Bond and serviceability characterization of concrete reinforcement with high strength steel. PhD Thesis, Swanson School of Engineering, University of Pittsburgh

Teng J.G., De Lorenzis L., Wang Bo, Li Rong, Wong T.N., Lam Lik (2006). Debonding failures of RC beams strengthened with Near Surface Mounted CFRP strips. Journal of Composites for Construction, Vol. 10, No 2, 82–105

Tilly G.P. (1979). Fatigue of steel reinforcement bars in concrete: a review. Fatigue of Engineering Materials and Structures Vol. 2, pp. 251–268

Toutanji H., Zhao L., Deng Y., Zhang Y., Balaguru P. (2006). Cyclic behavior of RC beams strengthened with carbon fiber sheets bonded by inorganic matrix. Journal of Materials in Civil Engineering. Vol.18, No1, 28–35

Wahab N., Soudki K.A., Topper T. (2011). Mechanics of bond fatigue behavior of concrete beams strengthened with NSM CFRP rods. Journal of Composites for Construction. Vol.15, No 6, 934–942

Wang Y.C., Lee M.G., Chen B.C. (2007). Experimental study of FRP-strengthened RC bridge girders subjected to fatigue loading. Composite Structures 81, 491–498

Williams G., Higgins C. (2008). Fatigue of diagonally cracked RC girders repaired with CFRP. Journal of Bridge Engineering. Vol.13, No1, 24–33.

Concrete Solutions – Grantham et al. (Eds.)
© 2016 Taylor & Francis Group, London, ISBN 978-1-138-03008-4

Evaluation of the mechanical behavior of FRC with different types of fibre, through Barcelona and bending testing

D. Choumanidis, P. Nomikos & A. Sofianos
School of Mining Engineering, Tunnelling Laboratory, National Technical University of Athens, Greece

E. Badogiannis & E. Papadimitriou
School of Civil Engineering, Laboratory of Reinforced Concrete, National Technical University of Athens, Greece

ABSTRACT: The paper focuses on the post-cracking behavior of FRC and discusses the effectiveness of two different testing methods. Three different fibre types (steel and polypropylene) were added in concrete at two percentages (0.5 and 1.0%) and by their type combination (hybridization), ten concrete mixtures were produced. Two testing methods have been employed in order to characterize the mechanical behavior of FRC after the fracture; the bending test and the double-punch test (Barcelona test). The fibre reinforcement of concrete, especially in the hybrid mixtures, resulted in the development of residual tensile strength and of improved toughness. Also it has been validated the main advantages of the Barcelona test, that it is a convenient compressive test which offers rapid and compact results.

1 INTRODUCTION

1.1 *Fibre reinforced concrete*

Concrete has characteristic mechanical properties such as compressive strength, modulus of elasticity, Poisson's ratio, shear strength and tensile strength. The latter is significant due to the fragility that characterizes the tensile failure, but its direct measurement demands complicated testing procedures. The splitting tensile test is an alternative testing method that indirectly measures the tensile strength of concrete. Unfortunately the splitting tensile test cannot offer data about the post crack behavior of fibre reinforced concrete. On the contrary, the bending test provides not only the value of the flexural strength but also the information needed to characterize fibre reinforced concrete in respect to the post-cracking behavior. All bending tests regardless of their experimental set-up have some main drawbacks; big scatter of results and large sized specimens (Chen & Yuan 1980, Chen 1973). The double punching test (Barcelona test) is a method that uses significantly smaller specimens and offers less scattered results (Blanco et al. 2014, Carmona et al. 2012, Molins et al. 2009, Pujadas et al. 2014).

1.2 *Scope*

This work aims to study how different types of fibres in different volume fractions affect the post-cracking mechanical behavior of fibre reinforced concrete and what influence the hybridization of steel and polypropylene fibres has. Researchers have shown that hybridization increases the flexural strength and toughness significantly (Dawood & Ramli 2012, Hsie et al. 2008). Additional advantages of hybridization are the weight reduction due to the lower weight that the polypropylene fibres have, the lower production cost of FRC and the increased strength and toughness that they offer to FRC, properties that remain at high level, even after exposure to high temperatures.

For the characterization of the mechanical behavior of FRC, an axial compressive test was used to determine compressive strength, chord modulus of elasticity and Poisson's ratio (ASTM C469-02). A bending test with crack mouth opening displacement (CMOD) controller was also used, in order to measure the flexural tensile strength (EN 14651:2005 + A1:2007). Finally, a double-punch test (Barcelona test) with total circumferential opening displacement (TCOD) controller was used to measure and compare the indirect tensile strength with that of the bending test (AENOR UNE 83515:2010).

2 EXPERIMENTS

2.1 *Specimen preparation*

In total ten (10) different concrete mixtures were prepared. One type of steel fibres and two different types of polypropylene fibres were used (see Table 1), at 0.5% and 1% content by volume of concrete, either individually or combined in pairs (see Table 2). All the cast specimens were water cured

(20°C) after the demoulding and they were tested at the age of 28 days. From each mixture, 3 cylindrical specimens 100 × 200 mm for compression test, 3 prismatic specimens 100 × 100 × 500 mm for flexure test and 3 cylindrical specimens 150 × 150 mm for double-punch test were produced.

2.2 *Experimental setup*

A testing machine of 5000 kN capacity with a servo-hydraulic control unit for axial displacement control was used for the compression and Barcelona tests. A testing machine of 150 kN capacity was used for the bending tests.

2.2.1 *Compression test*

The loading rate was set equal to 2000 N/sec. Two subsequent loadings were carried out until 40% of the peak load, in order to eliminate the effect of any possible instability and to assure repeatability in the conducted tests. The test was over at the failure of the specimen. The longitudinal axial displacement was expressed as the mean value of the values of three transducers placed around the specimen at 120° angle, which were constantly measuring the variation of the distance between the two yokes (Fig. 1a). The yokes were rigidly attached to the specimen, each at a distance of 3.75 cm from the mid specimen height. The transverse strain was expressed as the TCOD at half height of the specimen, using a circumferential extensometer (model 3544 EPSILON), which was fixed to the ends of a chain.

2.2.2 *Bending test*

In the present research, the 3-point bending test was used and the standard EN 14651:2005 + A1:2007 was followed, on specimens of a smaller scale. The displacement rate (CMOD) was set equal to 0.05 mm/min from the start till the end of the testing except for some series of tests where the rate was increased at 0.10 mm/min when CMOD reached 500 μm. Each test lasted until CMOD reached at minimum 4 mm. The force and the displacement of the piston were also reported (Fig.1b).

2.2.3 *Barcelona test*

The Barcelona test is a double punch test (DPT) performed on a cylindrical FRC specimen with height of 150 mm, equal to its diameter, (AENOR UNE 83515, 2010). The specimen is subjected to compressive loading along to its axis, by inserting two cylindrical steel punches with a height of 24 mm and a diameter of 37.5 mm between the loading machine platen and the center of the upper and lower face of the specimen (Fig. 1c). An extensometer chain is placed at half-height of the specimen to measure the

TCOD. A constant relative displacement rate of 0.5 ± 0.05 mm/min is applied by the press piston. The force and the TCOD are also measured. The test is over when the TCOD is at least 4 mm.

Table 1. Geometrical and mechanical characteristics of fibres.

Type	SF	PPF1	PPF2
Material	Steel	Polypropylene	Polypropylene
Length (mm)	30	52	12
Diameter (mm)	0.8	0.46	0.025
Rupturing force (MPa)	1100	613	400
Modulus of elasticity (MPa)	500	5400	1600
l/d	37.5	113	480

3 RESULTS AND DISCUSSION

3.1 *Compressive strength*

The compressive strength is calculated by dividing the maximum load carried by the specimen during the test by the average cross-sectional area (ASTM C39/C39M-03). The results are presented in Table 3 and illustrated in Figure 2, comparatively to the compressive strength of plain concrete. The compressive strength is in general higher than that of the plain concrete. Lower compressive strength is reported for the PPF2-0.5, SF-0.5 + PPF2-0.5 and PPF1-0.5 + PPF2-0.5 concrete mixtures. The respectively lower density of the mixture (Table 2), which also implies an increased percent of entrained air, it is considered that it negatively affected the development of the compressive strength.

3.2 *Flexural tensile strength*

The flexural tensile strength is calculated from equation [1] according to EN 14651:2005 + A1:2007:

$$f_{ct,B}=3F_Pl/2bh_{sp}^2 \quad [1]$$

where F_P: is the peak load or the load corresponding to 0.05 mm of CMOD whatever comes first (N),
l: is the span length (mm),
b: is the width of the specimen (mm) and h_{sp}: is the distance between the top of the notch and the top of the specimen (mm).

Figure 3 shows the variation (%) of flexural tensile strength of FRC compared to plain concrete. The flexural strength of all the mixtures is presented raised, compared to the plain concrete. A significant decrease is reported only for the PPF2-0.5 concrete mixture, which is in accordance to the reported decrease of the compressive strength.

3.3 *Double-punch tensile strength*

Indirect tensile strength in the Barcelona test is calculated using the expression [2] provided by the UNE 83–515:

$$f_{ct,BC}=4F_p/9\pi ah \quad [2]$$

Table 2. Concrete mixtures' details and properties of fresh concrete.

Ingredients (kg/m^3)	Plain	SF-0.5	PPF1-0.5	PPF2-0.5	SF-1	PPF1-1	PPF2-1	SF-0.5 + PPF1-0.5	SF-0.5 + PPF2-0.5	PPF1-0.5 + PPF2-0.5
CEM IV/B 32.5R	400	400	400	400	400	400	400	400	400	400
Silica Fume	20	20	20	20	20	20	20	20	20	20
Sand (0/4)	922	922	922	922	922	922	922	922	922	922
Gravel (4/8)	335	335	335	335	335	335	335	335	335	335
Gravel (8/16)	419	419	419	419	419	419	419	419	419	419
Water (w)	219	219	219	219	219	219	219	219	219	219
Steel Fibres		40			80			40	40	
Polypropylene Fibres I			4.55			9.1		4.55		4.55
Polypropylene Fibres II				4.55			9.1		4.55	4.55
Superplasticizer (%p.w.)	0.65	0.63	0.86	1.02	0.61	1.05	1.31	0.93	1.12	1.11
w/(b)	0.48	0.48	0.48	0.48	0.48	0.48	0.48	0.48	0.48	0.48
Slump (cm)	11*	11.5*	10	12.5**	14**	0	13	13	15	13.5
Density (kg/lt)	2.313*	2.339*	2.28	2.001**	2.347**	2.299	2.206	2.341	2.036	2.029

*mean value of 3 concrete batches of the same properties
**mean value of 2 concrete batches of the same properties

Table 3. Mechanical properties of FRC.

Strength (MPa)*	Plain	SF-0.5	PPF1-0.5	PPF2-0.5	SF-1	PPF1-1	PPF2-1	SF-0.5 + PPF1-0.5	SF-0.5 + PPF2-0.5	PPF1-0.5 + PPF2-0.5
Compressive	48.1	51.3	50.7	38.11	49.2	51.7	52.3	50.1	47.5	44.3
COV (%)**	3.43%	4.95%	4.73%	3.29%	3.49%	2.43%	1.27%	2.21%	1.81%	0.90%
Flexural	5.3	5.4	5.4	4.8	5.6	6.1	5.7	5.6	5.6	5.2
COV (%)	3.96%	4.75%	2.37%	4.16%	4.65%	2.59%	1.06%	2.20%	3.89%	3.26%
Barcelona	7.7	8.0	7.6	5.6	7.8	7.9	8.1	7.8	6.6	7.1
COV (%)	2.82%	3.49%	1.84%	5.64%	1.07%	1.66%	2.45%	1.49%	4.94%	2.86%

* mean values of 3 to 9 experimental measurements
** COV = Coefficient of Variation

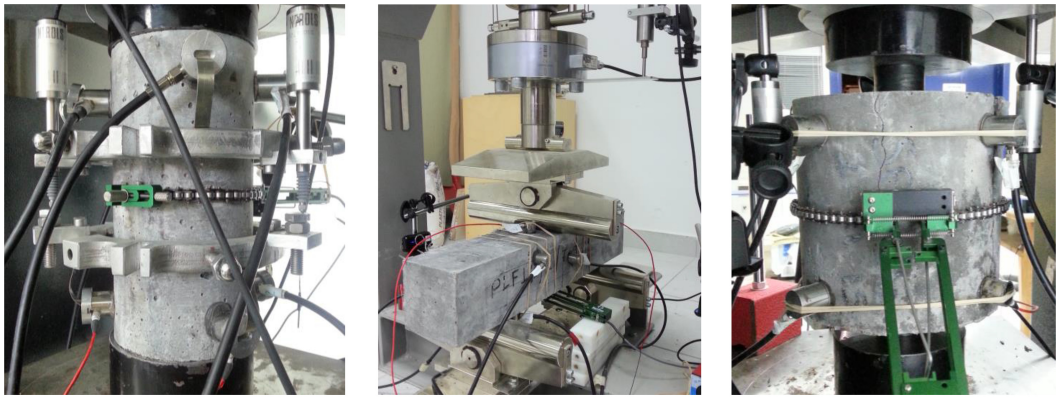

(a) (b) (c)

Figure 1. (a) Compressive test set up, (b) Bending test set up, (c) Barcelona test set up.

where F_P: is the peak load or the load corresponding to 0.05 mm of TCOD whichever comes first (N),
a: is the loading platen diameter (mm) and
h: is the specimen height (mm).

The indirect tensile strength results from Barcelona testing are shown in Figure 4. The tensile strength is slightly improved compared to that of plain concrete. Similarly, in the mixtures PPF2-0.5 and

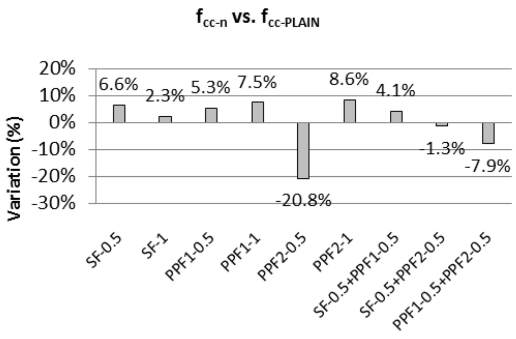

Figure 2. Variation of compressive strength of FRC compared to the compressive strength of plain concrete.

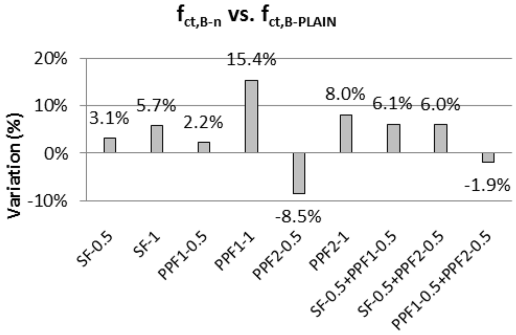

Figure 3. Variation of flexural tensile strength of FRC compared to flexural tensile strength of plain concrete.

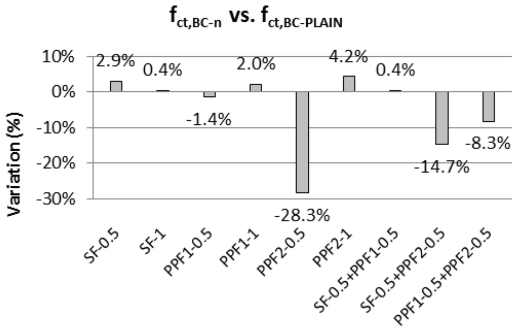

Figure 4. Variation of double-punch tensile strength of FRC compared to double-punch tensile strength of plain concrete.

SF-0.5+PPF2-0.5 and PPF1-0.5+PPF2-0.5, decreased tensile strength is reported, in accordance to the compressive and flexural tensile strength results.

Figures 5a, 6a exhibit the effect of content and type of fibres on both the flexural and double-punch indirect tensile strength. In both tests, the tensile strength increases with the increase of the fibre content. However, this improvement is better illustrated in the Barcelona testing results, than in the bending testing. It seems that Barcelona specimens are more susceptive

Table 4. Strength's values variation (%), after the doubling of the fibre content.

Test	SF	PPF1	PPF2
Compression	−4.1%	2.0%	37.1%
Bending	−2.4%	3.5%	45.4%
Barcelona	2.6%	12.9%	18.1%

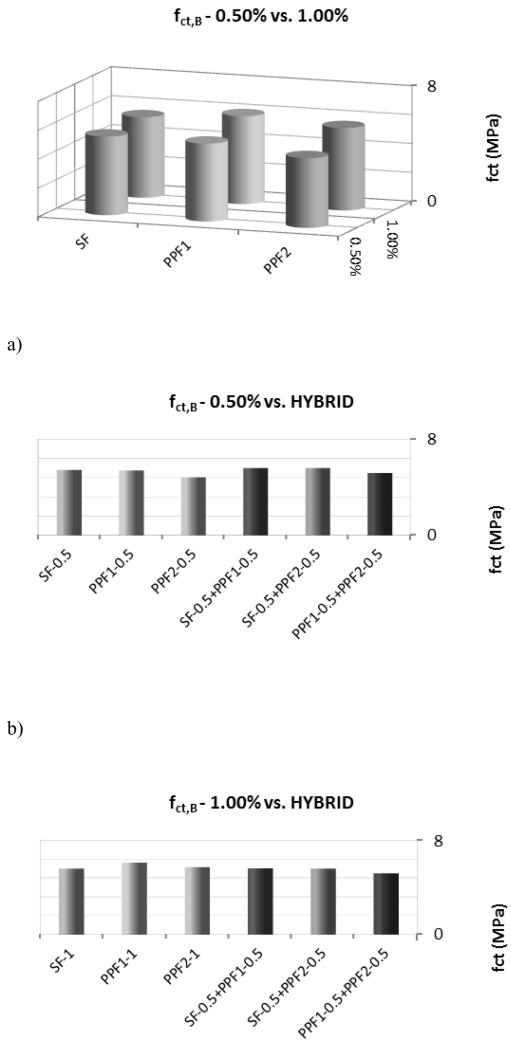

Figure 5. Flexural tensile strength: a) 0.5% compared to 1% b) 0.5% compared to hybrid and c) 1% compared to hybrid.

and sensitive to the fibre content percentage, probably due to the fact that a more extended failure surface is involved in the double-punch testing. As far as the type of fibres is concerned, in the case of PPF2 fibres, the

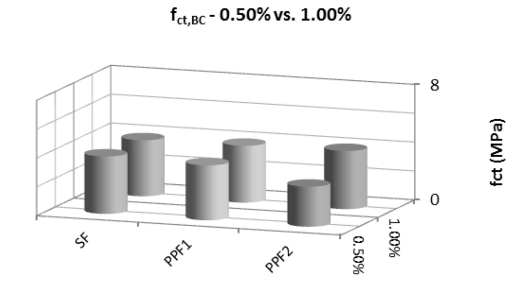

a)

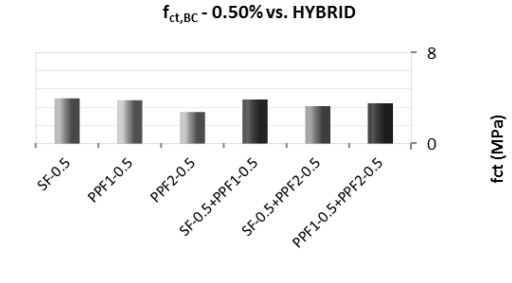

b)

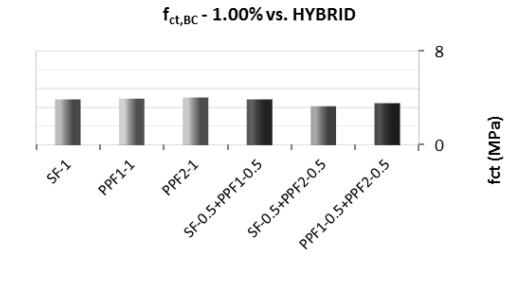

c)

Figure 6. Barcelona tensile strength: a) 0.5% compared to 1% b) 0.5% compared to hybrid and c) 1% compared to hybrid.

doubling of their volume fraction (%) has a positive influence on the mechanical properties. However, the reported high percentage of strength gain, occurs only because the comparative strength of the PPF2-0.5 was very low.

In the case of PPF1, the increase of the fibre content to 1% v/v, has an insignificant contribution to the mechanical properties of the concrete, while in the case of the SF fibres, it has a negative effect (Table 4).

Figures 5b, c and 6b, c, show that the hybridization hasn't a significant effect on the strength development.

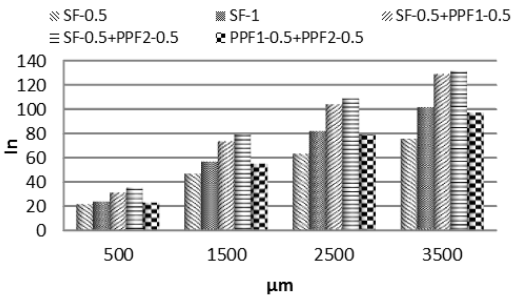

Figure 7. Toughness indices evaluated by the Barcelona test.

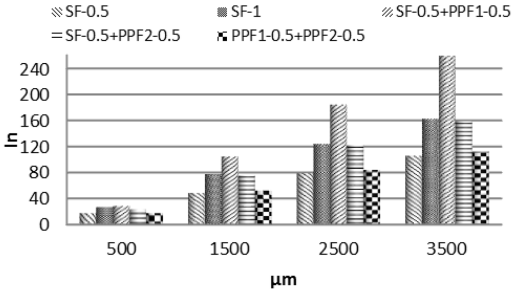

Figure 8. Toughness indices, evaluated by the bending test.

3.4 *Toughness*

Toughness is used to estimate, in terms of rupture energy, the ductility of FRC beams. Toughness indices are usually determined according to ASTM C1018 and EN 14651:2005 + A1:2007. In this paper, the toughness indices were determined according to EN 14651, at CMOD = 0.5/ 1.5/ 2.5/ 3.5 mm. Barcelona testing results were also used for the toughness evaluation and the toughness indices were calculated at TCOD values of 0.5/ 1.5/ 2.5/ 3.5 mm.

Figures 7 and 8 illustrate the effect of either the increase of fibre content or the hybridization, on toughness, evaluated by both tensile strength tests. The comparison is made to the steel FRC, since the steel fibres exhibit the higher values of toughness compared to all the concrete mixtures, reported by both testing methods.

As far as the influence of the volume fraction is concerned, Barcelona testing results show that an increase of the fibre content, leads correspondingly to an increase of all the toughness indices (Fig. 7). Similarly, the results obtained from the bending tests, showed an increase of all the toughness indices (Fig. 8).

As far as the influence of the hybridization is concerned, Barcelona testing results show that a significant increase of toughness is achieved by the hybridization, compared to the SF0.5 and SF1.0 FRC. Only in the mixture PPF1-0.5 + PPF2-0.5, is a limited increase reported; though it is notable. Bending testing results also show a positive effect of

the hybridization on all the toughness indices. Similarly, the mixture PPF1-0.5 + PPF2-0.5, showed an insignificant increase in toughness.

It is worth's noticing that, although in the case of SF the increase of the fibre content didn't positively affect the tensile strength, it had a great positive influence on its toughness.

4 CONCLUSIONS

Even though tensile strength, estimated by both tests of flexural and double-punch, is reported improved, the ductility is the feature that characterizes the post-cracking mechanical behavior of fibre reinforced concrete. Steel fibres seem to be the best choice in order to achieve adequate ductility. Hybridization can contribute to the increase of the ductility and also to provide additional features in the FRC, that are of great interest for specific applications.

More specific, it can be concluded that hybridization offers an increase of toughness at least similar to the increase that the doubling of the fibre content offers.

Finally, it can be said that the double-punch test, which is a more stable and easy to use test than bending, provides equivalent information regarding the post-crack mechanical behavior of fibre reinforced concrete.

ACKNOWLEDGEMENTS

This work was co-funded by IKY, through the Siemens Programme: "IKY Fellowships of Excellence for Postgraduate Studies in Greece – Siemens Program".

The first author's father Panagiotis Choumanidis, Andreas Kacapari and Nikos Tzanetis are gratefully acknowledged for their help in the preparation of concrete mixtures.

Dr. George Papantonopoulos, scientific staff of the Tunnelling Laboratory of School of Mining Engineering of the National Technical University of Athens is also gratefully acknowledged for his help on the experimental work.

REFERENCES

AENOR. UNE 83515:2010. Hormigones con fibras. Determinación de la resistencia a fisuración, tenacidad y resistencia residual a tracción. Método Barcelona, Asociación Española de Normalización y Certificación Madrid

ASTM C39/C39M-03. Standard test method for compressive strength of cylindrical concrete specimens.

ASTM C469-02. Standard test method for static modulus of elasticity and Poisson's ratio of concrete in compression.

ASTM C1018-97. Standard Test Method for Flexural Toughness and First-Crack Strength of Fibre-Reinforced Concrete (Using Beam With Third-Point Loading).

Blanco, A. & Pujadas, P. & Cavalaro, S. & de la Fuente, A. & Aguado, A. 2014. Constitutive model for fibre reinforced concrete based on the Barcelona. *Cement & Concrete Composites 53*: 327–340.

Caggiano, A. & Cremona, M. & Faella, C. & Lima, C. & Martinelli, E. 2012. Fracture behavior of concrete beams reinforced with mixed long/short steel fibres. *Construction and Building Materials* 37:832–840.

Carmona, S. M. & Aguado de Cea, A. & Molins, C.B. 2012. Generalization of the Barcelona test for the toughness control of FRC. *Materials and Structures* 45: 1053–1069.

Chen, W.F. 1972. Double-punch test for tensile strength of concrete. *Journal of Materials, American Society of Testing and Materials* 7 (2),148–154.

Chen, W.F. &Yuan, R.L. 1980. Tensile strength of concrete: double punch test. *Journal of Structural Divisions* 106: 1673–1693.

Concrix, 2011. Datasheet Concrix ES.

Dawood, E.T. & Ramli, M. 2012. Mechanical properties of high strength flowing concrete with hybrid fibres. *Construction and Building Materials* 28: 193–200.

EN 14651:2005+A1:2007. Test method for metallic fibre concrete — Measuring the flexural tensile strength (limit of proportionality (LOP), residual)

Hsie, M. & Tu, C. & Song, P.S. 2008. Mechanical properties of polypropylene hybrid fibre-reinforced concrete. *Materials Science and Engineering A* 494:153–157

Molins, C. & Aguado, A. & Saludes, S. 2009. Douple Punch Test to control the energy dissipation in tension of FRRC (Barcelona Test). *Materials and Structures* 42: 415–425.

Pujadas, P. & Blanco, A. & Cavalaro, S.H.P. & de la Fuente, A. & Aguado, A. 2014. Multidirectional double punch test to assess the post-cracking behaviour and fibre orientation of FRC. *Construction and Building Materials* 58: 214–224.

Sika, 2013. Datasheet Sika®Fibre PP 940-50: Construction.

Concrete Solutions – Grantham et al. (Eds.)
© 2016 Taylor & Francis Group, London, ISBN 978-1-138-03008-4

Improving the ductility of FRP strengthened unidirectional RC slabs via hybrid CFRP/BFRP reinforcing

T. Donchev, D. Petkova & A. Pavlovic
Faculty of Science, Engineering and Computing, Kingston University, London, UK

ABSTRACT: The excellent strength to weight ratio, lack of corrosion and aesthetic appearance of Fibre Reinforced Polymer (FRP) materials gives them advantage over more traditional materials, especially for structural strengthening. Nonetheless, elements strengthened using FRP materials typically have brittle failure, which is highly undesirable. This research is aiming to investigate an innovative approach via usage of a combination of different FRP materials (hybrid reinforcement) to overcome this problem. The experimental investigation include the preparation and testing of 4 reinforced concrete slabs with different amounts and proportions of externally bonded carbon FRP (EB CFRP) laminates and near-surface-mounted basalt FRP (NSM BFRP) bars. It was aimed at investigating their effect towards developing more ductile behaviour of the strengthened slabs. After thorough analysis of the acquired data, the initial hypothesis was successfully confirmed. The strengthened samples with hybrid CFRP/BFRP reinforcement achieved higher ultimate capacity and much more ductile behaviour than the CFRP only sample.

1 INTRODUCTION

The existing research has confirmed the advantages of FRP strengthening, such as durability, effectiveness, speed of installation and aesthetic appearance. Some disadvantages have been pointed out as well, in the first place, the mode of failure is most commonly brittle, although actual failure can occur due to a number of reasons. In structural strengthening of RC members, brittle failure should be avoided by all means, as it presents a safety hazard due to absence of sufficient warning before destruction. The danger of such sudden failure is the main reason for the widely accepted rule increased capacity of EB CFRP strengthened elements to be no more than two times their capacity before strengthening.

While some authors have been attempting to resolve this issue, insufficient published research has looked into the possibility of combining two techniques/materials in order to join their benefits, and reduce the brittleness of destruction. This paper is focuses on experimental testing of unidirectional reinforced concrete slabs strengthened using both externally bonded CFRP laminates and near surface mounted BFRP bars. A four point bending test was conducted on four samples: one control RC slab with no FRP strengthening, one strengthened using only EB CFRP and two strengthened using EB CFRP and varying percentage of NSM BFRP reinforcement. The main aim is to clarify, by comparing the results obtained from the experiment, whether additional NSM BFRP bars can contribute towards more ductile behaviour of RC slabs strengthened using EB CFRP laminates.

2 BACKGROUND

FRP materials have been in use in the automotive, aerospace and marine industries for a longer period of time, but have only been introduced for construction application in the late 1980s (Balaguru, Nanni and Giancaspro, 2009).

The use of externally bonded FRP for strengthening can constrain or decrease the ductility of the strengthened structure. This decrease of ductility varies for different failure modes and other factors, such as strain in all components. (GangaRao et al., 2007). The brittle behaviour of FRP has implications for their structural application, as it limits the stress redistribution (Teng et al., 2002). American Concrete Institute's EB FRP design guide takes this into account by introducing a strength reduction factor (φ). This factor takes a value of 0.70 for brittle sections, and 0.90 for ductile sections.

Experimental research has been conducted with the intent of resolving these issues and to enable a higher level of utilisation of FRP's structural capacity. Some of the work is based on combining different types of FRP strengthening. The main idea is to make use of one techniques/material's strength to compensate for other technique's/material's weakness, and vice versa.

Hybrid reinforcing with different FRP materials (CFRP laminates in vertical direction and BFRP bars between the layers of bricks) has been applied by Sayari and Donchev (2012) for strengthening of masonry walls against out-of-plane loading. The results obtained indicated achieving both high capacity and more gradual destruction due to the application of hybrid reinforcement.

A group of researchers from University of Timisoara has investigated the application of hybrid FRP strengthening technique for retrofitting two-way slabs, with and without cut outs. In one direction, the slabs were strengthened with NSM CFRP laminates, and in the other direction, using externally bonded CFRP. The results confirmed that it is possible to restore and increase capacity of slabs by strengthening them in such a manner (Floruț et al., 2013).

A publication by Rezazadeh and Barros (2014) looks into benefits of a hybrid strengthening system in terms of increase of deflections, while simultaneously achieving high ultimate capacity. The experimental study was conducted using six RC beams strengthened using non-prestressed CFRP laminates, prestressed CFRP laminates and a combination of both non-prestressed and prestressed laminates. The authors concluded that the proposed hybrid technique via combining prestressed and non-prestressed laminates may contribute towards higher energy dissipation values and more ductile behaviour at high levels of loading.

The research conducted by Tavallaee et al. (2014) provides insight into the advantages of combining different FRP materials for bi-directional strengthening of RC slabs. This experimental study has investigated the use of FRP materials for flexural strengthening including combined usage of EB CFRP and NSM BFRP. As a conclusion, the authors have noted that hybrid strengthening system results in more ductile behaviour of the samples with less brittle failure.

The results of the aforementioned studies are encouraging in terms of the possibility of preventing brittle failure by combining FRP materials with different Young's modulus such as carbon and basalt fibre polymers.

3 METHODOLOGY

3.1 *Preparation of the samples*

Laboratory testing of four samples was conducted. All four samples were one-way slabs 1100 mm long, 500 mm wide and 80 mm thick. The same concrete mixture was used for all four slabs, designed for C30/35 type of concrete. Standard concrete cubes (a = 150 mm) and cylinders (d = 150 mm, h = 300 mm) were cast to verify the strength of the concrete. All slabs had the same internal steel reinforcement, as shown in figure 1. The longitudinal reinforcement was 6 no. N10 bars top and bottom and the links were R6 mild steel reinforcement at 250 mm c/c. All samples were cured for 28 days in a curing room at 20°C temperature and 95% humidity.

After drying at normal room conditions for at least 3 additional days, samples were further prepared according to the following specification:

- Sample 1 was used as the control sample and thus was not strengthened.
- Sample 2 was strengthened using two CFRP laminates, 900 mm long, 50 mm wide and 1.2 mm thick. CFRP laminates were bonded to the bottom surface of the slab using EpoxyPlus (SBD Weber) adhesive. They were positioned symmetrically, with distance of 300 mm c/c between them.
- Samples 3 and 4 were strengthened using externally bonded CFRP in the same way as sample 2. They were additionally strengthened using 6 mm diameter NSM BRFP bars between the laminates – one bar for sample 3 and two bars for sample 4. The bars were 1000 mm long, installed in grooves preformed during the casting of the samples with size 8 × 8 mm and using the same adhesive as for the laminates.

3.2 *Experimental setup*

A four point bending test was conducted on each sample. Slabs were loaded with two uniformly distributed linear loads, perpendicular to the axis of the strip, 300 mm from each other and with 350 mm shear span on both sides.

The total load was increased at a rate of 2 kN per 5 min. During the testing, the load, the deflections and the strains were measured and the appearance and development of the cracks was recorded. Strain gauges were affixed to the BFRP bars prior to casting of the

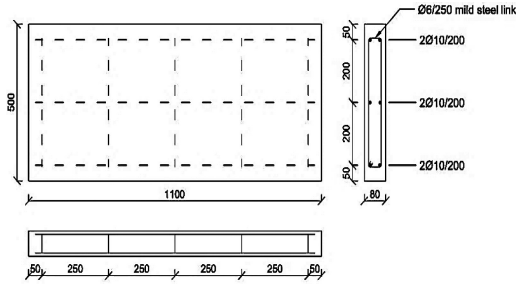

Figure 1. Internal steel reinforcement.

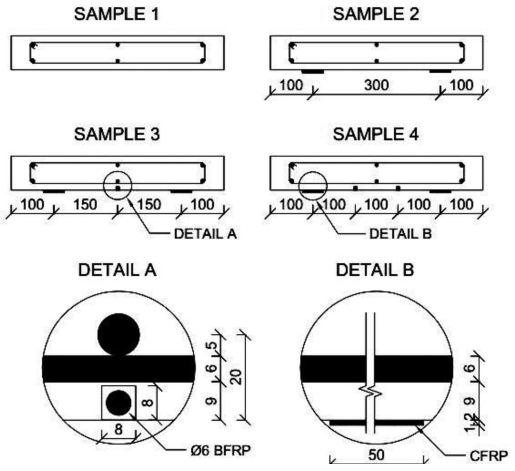

Figure 2. Cross section of samples.

samples and on CFRP laminates after their installation. The ambient temperature of the air during the testing of all samples was 23.5 ± 1°C.

The vertical displacements for all samples were measured via LVDTs at midspan, quarter spans and at the supports. Linear strain gauges both for BFRP bars and CFRP laminates were installed at midspan and quarter spans.

4 EXPERIMENTAL RESULTS

4.1 *Deflections and mode of failure*

Sample 1 (without strengthening) showed very limited deflections until the first crack was formed, at around 0.52 mm of deflection at midspan and about 5 kN load. After that, gradual increase of deflections with load increase was observed, at a constant rate. At approximately 40.0 kN (around 9.5 mm deflection at midspan), the rate of increase of deflection became more rapid. From this point, the deflections rose by an increased rate until an ultimate load of 44.9 kN had been reached. After that, as expected, the deflections continued to increase, while the load dropped. The adopted criterion for failure was when the load was not able to be increased above a certain level, so the test was terminated soon after reaching ultimate capacity. The sample slab exhibited some ductility at stage C of the graph (Figure 3) due to the yielding of steel reinforcement.

Sample 2 showed similar behaviour in the beginning of the bending test, i.e. until the first crack appeared at about 6 kN load, altering the rate of change of deflection. From that point, the deflection continued to grow with increase of load, at a steady rate. It can be observed that the graph tangent was much steeper than for Sample 1 due to the increased stiffness of the sample after applying the CFRP laminates. The ultimate load was reached immediately after reaching [F]_ult = 54.5 kN when delamination at one end of one of the CFRP laminates occurred. Delamination was instantaneous, without previous warning signs, such as cracking of adhesive. This occurrence was followed by a sudden drop of load. The diagram is interrupted after the delamination of the first of the CFRP laminates, due to problems with measuring equipment. However, the testing was continued and an approximation was made based on manually recorded data at the end of the testing period (dashed line on the graph). After the second delamination, the observed change in the force was not connected with any significant increase.

After the delamination of the CFRP, the load was uninterruptedly applied, at a rate of 1 kN/5 min. Following the initial immediate drop, the load began to rise again slightly, until 49.6 kN was reached. Subsequently, the failure of the other CFRP laminate occurred in the same way as the first one, by instantaneous delamination. The second CFRP laminate delaminated at the opposite end of the slab and as in the previous case, the load also dropped. The application of pressure in the jack was continued and, when it was observed that the load was continuously decreasing, at 35 mm deflection the testing was stopped.

The behaviour of sample 3 until delamination of CFRP strips was similar to that of sample 2. Deflection increase was comparatively slow, and there was a slight change in rate after formation of the first crack at 11.2 kN. Similarly, the delamination of both strips was instantaneous, and followed by a sudden drop in load. The first delamination appeared at 60.2 kN and 6.5 mm deflection. After the first delamination, the load dropped down to 52 kN and started to increase quickly again. The second delamination happened at a level of loading of 58.2 kN and 7.4 mm deflection. The load dropped down to 42 kN. It can be noticed that the drop in load was much larger after the second delamination −16.2 kN versus 8.5 kN after the first delamination.

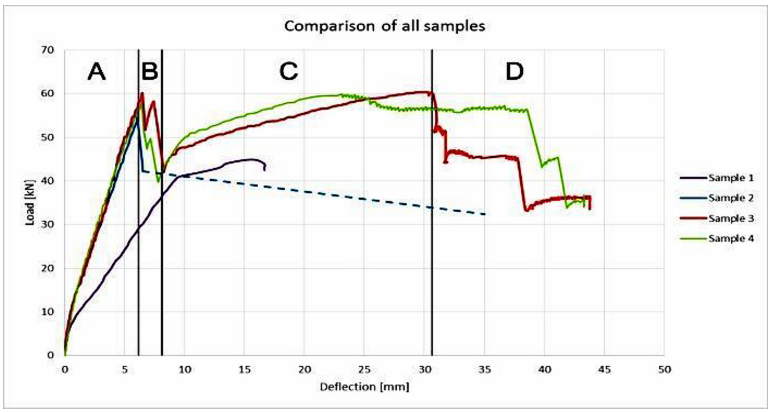

Figure 3. Comparative Load-Midspan deflection diagram.

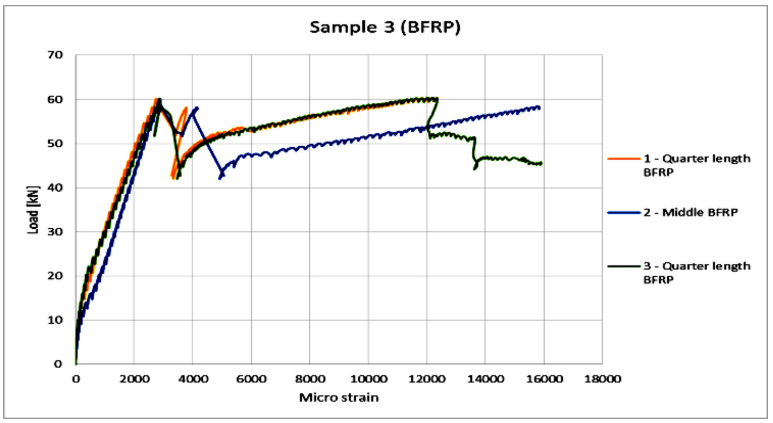

Figure 4. Load – Strain (all gauges on BFRP) graph (Sample 3).

After the delamination of the CFRP, the load began to increase at a steady rate, accompanied by a very large increase of deflection. This ductile behaviour continued until a maximum load of 60.4 kN was reached at 29.9 mm deflection, when BFRP failure occurred by fracture of the surrounding concrete, and subsequently by bond failure on the epoxy – concrete interface at the anchoring zone of the BFRP bar. Testing was terminated after no further increase of load was observed.

Sample 4 behaved in a similar manner to Sample 3 during testing. The beginning was characterised by a slight change of tangent of the Load – Deflection diagram, approximately along with appearance of the first crack at about 10 kN level of loading. The continual load increase was interrupted by the first delamination of CFRP at 57.6 kN and 6.4 mm deflection. This damage was followed by an abrupt drop of load down to 48 kN. After that, the load increased again, until the other CFRP laminate failed at 49.6 kN and 7.2 mm deflection, causing another drop of the load down to 40 kN.

The subsequent steady load growth, along with a large increase of deflection, was more significant than in sample 3. The failure of BFRP did not occur immediately after reaching the maximum load of 59.8 kN and 23.1 mm deflection. There was a long period of further deflection increase up to 38.5 mm with load, going gradually down to 56.5 mm before the failure. Complete debonding at the FRP-epoxy interface occurred at the ends of both BFRP bars. The BFRP bars failed independently one after the other, causing corresponding drops in the applied loads. Testing was terminated shortly after failure of the second of the BFRP bars.

4.2 *Strain values*

The strain gauges, installed on the CFRP laminates on sample 2, confirmed the achievement of maximum load before the first delamination of 54 kN with obtained strains at the middle of both laminates close to 3 K micro strain. The change in the strain corresponded to the shape of load-deflection diagram until first delamination, when the strain for one of the laminates fell back to zero. The strain gauge on the other laminate registered the decrease of the stress after the first delamination and the beginning of their increase before the second stage of delamination. The strain gauges at quarter span and the end of the laminates showed correspondingly lower values as expected.

Sample 3 was equipped with seven strain gauges in total. As for Sample 2, the change of the recorded strains on the surface of the CFRP laminates was consistent with the load-deflection diagram until first delamination at load of 60 kN, the reduction of the strain immediately after the delamination down to load level of 52 kN and the following increase of the strain up to load of 58 kN before the second delamination. The maximum strain at the time of first delamination reached 3.4 K microstrain at midspan and 4 K microstrain for the point when the second delamination appeared.

The data from the three strain gauges installed on the BFRP bar (one in the middle and two at quarter spans on both sides) was collected for a longer period of time due to the lack of delamination. The strain readings from these gauges are shown in Figure 4. The strain values for the BFRP were approximately the same as the ones measured on CFRP laminates for the same level of loading as expected. The data from the BFRP installed gauges was acquired for the whole duration of the experiment, clearly illustrating the secondary stiffening effect after the delamination of CFRP. The strains in midspan continued to increase reaching up to 16 K microstrain when the failure of the BFRP bar started. Corresponding values from the gauges at the quarter spans at this point of loading exceeded 12 K.

In sample 4, the data from gauges installed on CFRP laminates was consistent in shape with the load-deflection diagram for the same sample until delamination. Further readings of all strain gauges mounted on CFRP laminates were ignored as the level of delamination influenced the strain in the laminates significantly. The difference in the positioning of the

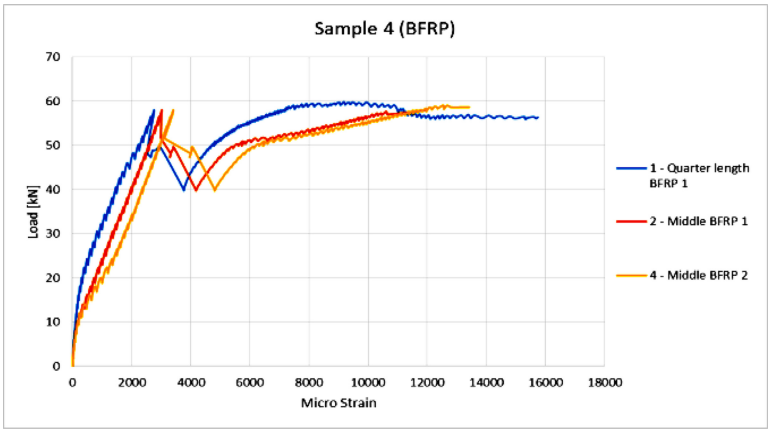

Figure 5. Load – Strain (all gauges on BFRP) graph (Sample 4).

gauges on the BFRP rebars in comparison with sample 3 was an addition of a strain gauge in the middle of the second rebar. One of the gauges installed at quarter length of one bar malfunctioned and did not record data properly. Other gauges remained undamaged throughout the testing process and the data from them is presented in Figure 4.

The shape of the diagram is concurrent with the shape of the load/deflection diagram (see previous subsection). Strain values recorded at the end of testing were similar to those recorded on Sample 3. The evolution of the strains at the middle of the BFRP bars was very similar, clearly indicating developing of secondary stiffening via gradual increase of the loading with increase of the deformation. The lower levels of strain for the bar at the quarter span compared with midspan values at the same levels of loading was as expected. At the same time, the gradual reduction of the levels of loading with the increase of the deformations, visible for the quarter span gauge was in good correspondence with the registered gradual decrease of the load with increased deflections, recorded in Figure 5.

5 ANALYSIS OF RESULTS

The following figure represents a comparative midspan load-deflection diagram for all samples. The diagram for sample 3 was divided into four stages, namely A, B, C and D, to illustrate the behaviour of hybrid reinforced samples (Figure 3).

Stage A spans from beginning of testing until initial delamination of the first CFRP laminate for strengthened samples. It is characterised by approximately linear-elastic behaviour of all samples. The diagrams peaked at load levels of 54.5 kN, 60.2 kN and 57.6 kN for Samples 2, 3 and 4 respectively. The difference between these values was not significant, which is an indication that the addition of BFRP bars

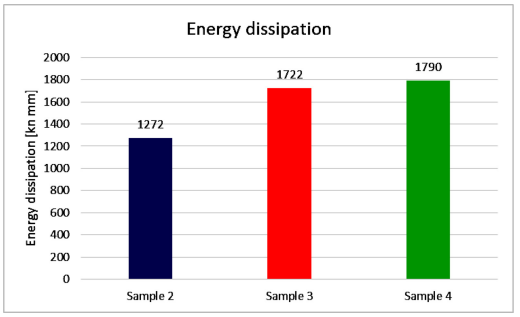

Figure 6. Estimation of energy dissipation.

doesn't influence significantly the initial delamination level of loading.

The behaviour of all three strengthened samples was similar in Stage B as well. An immediate drop in load after delamination of the first CFRP strip was followed by a slight increase in load before delamination of the second laminate, connected with another steep drop in the recorded load values.

The shape of the curve of the un-strengthened control sample (sample 1) during stage C corresponds approximately to the so called plastic plateau, with significant increase of deflections with limited increase in loads. For sample 2 (EB CFRP only) continuous decrease in load level and rapid increase of deflections was monitored.

Stage C was drastically different for Samples 3 and 4 in comparison with Sample 2. This stage for samples 3 and 4 was characterized by secondary stiffening for the two samples strengthened via the hybrid CFRP/BFRP system and corresponding increase of the load with gradual and significant increase of the deformations.

Stage D mainly describes the destruction of Samples 3 and 4. The final destruction of Sample 3 initiated

right after reaching the ultimate capacity of 60.4 kN (at 30.7 mm deflection), with continuously decreasing load values. Sample 4, however, exhibited even more ductile behaviour after reaching its ultimate capacity with deflections increasing more than for Sample 3, with loads remaining at the approximately same level, until final destruction, which occurred at 38.5 mm.

The effectiveness of strengthening using EB CFRP laminates for all strengthened samples and NSM BFRP bars for Samples 3 and 4 can be judged by the ultimate load capacity achieved. As expected, the strengthening effect was slightly better for samples with hybrid CFRP/BFRP reinforcement than for the CFRP only sample.

The much more significant effect of adding BFRP reinforcement was the gradual destruction of the hybrid samples, which could be assessed via the energy dissipation as measurement of the ductility of the samples. Areas under the load deflection curves up to 35 mm deflection were calculated and these values are presented in Figure 6, representing estimated values of energy dissipation. The addition of BFRP reinforcement resulted in 35% and 41% increase in energy dissipation for Samples 3 and 4 respectively, in comparison with Sample 2.

6 CONCLUSIONS

After consideration and analysis of acquired data, the following conclusions can be made:

- The achieved load level before initial delamination depends mainly on CFRP reinforcement.
- The effect of additional NSM BFRP reinforcement was exhibited via increase of the stiffness of the samples after initial delamination, up to significantly higher deflections, in comparison with the CFRP only sample.
- The ultimate capacity for hybrid reinforced samples 3 and 4 was achieved after initial delamination of CFRP laminates and secondary stiffening.
- The range of deflections before final failure due to the secondary stiffening effect was significant – more than 30 mm for sample 3 and more than 38 mm for sample 4.
- The energy dissipation for NSM BFRP strengthened samples was significantly higher than for the sample strengthened using only EB CFRP only – 35% for Sample 3 and 41% for Sample 4 and the destruction of these samples was less brittle.
- The aforementioned conclusions show clearly the positive effect of using hybrid FRP reinforcement for obtaining increased ductility and less brittle failure of the strengthened RC elements.

ACKNOWLEDGEMENTS

The authors would like to express their gratitude to MagmaTech for sponsoring with BFRP bars and to the technicians in laboratories in Kingston University – London.

REFERENCES

Balaguru, P., Nanni, A., Giancaspro, J. (2009) FRP Composites for Reinforced and Prestressed Concrete Structures. New York and London: Taylor & Francis.

Floruț, S., Stoian, V., Nagy-György, T., Dan, D., Diaconu, D. (2013) Assessment of hybrid EBR-NSMR strengthening technique applicable to RC slabs, 11th International Symposium on Fiber-Reinforced Polymer Reinforcement for Concrete Structures (FRPRCS-11), June 26–28, 2013, Guimarães, Portugal.

GangaRao, H.V.S., Taly, N. and Vijay, P.V. (2007) Reinforced Concrete Design with FRP Composites. Boca Raton: Taylor & Francis Group

Rezazadeh, M. and Barros, J. (2014) A new hybrid methodology according to near surface mounted carbon fiber reinforced polymer technique for the flexural strengthening of reinforced concrete beams, Journal of Reinforced Plastics and Composites. Vol. 33(21) pp. 1993–2009. DOI: 10.1177/0731684414551374

Sayari, A. and Donchev, T. (2012) Factors influencing the out-of-plane behaviour of FRP strengthened masonry walls. Proc. 6th International Conference CICE 2012, Rome, Italy, 13–15 June 2012.

Tavallaee, M., Donchev, T., Petkova, D., Hadavinia, H., Mirshekari, M. (2014) Bi-directional strengthening of two-way concrete slabs using fiber reinforced polymer. The 7th International Conference on FRP Composites in Civil Engineering (CICE). August 20–22, 2014, Vancouver, Canada.

Teng, J.G., Chen, J.F., Smith, S.T. and Lam, L. (2002) FRP-strengthened RC Structures. Chichester: John Wiley & Sons, Ltd

Concrete Solutions – Grantham et al. (Eds.)
© 2016 Taylor & Francis Group, London, ISBN 978-1-138-03008-4

Stress field analysis of reinforced concrete slab with central cutout strengthened using FRP laminates

L. Vasiliadis, I. Kavvadias, I. Litina & K. Bantilas
Department of Civil Engineering, Institute of Structural Mechanics and Earthquake Engineering, Democritus University of Thrace, Greece

ABSTRACT: Strengthening reinforced concrete slabs with a central cutout using FRP composites is analytically investigated in this paper. Introducing an opening in existing slabs in RC buildings due to functional changes is commonly required. In comparison to traditional strengthening methods, the application of FRP laminates is very suitable not only because of their mechanical properties, but also due to their ease of application. One simply supported two-way reinforced concrete slab measuring 600 × 600 × 16 cm with a central cutout dimensioning 150 × 150 cm was studied. Three different strengthening arrangements with FRP laminates were examined. In the first one, the FRP laminate was placed in parallel with the opening edges, in the second, the laminate was placed at the corners of the cutout at a 45° angle and in the third, a combination of the two above arrangements was used. Great care was drawn to the sufficient and suitable anchorage of the FRP laminates suggested by the relevant provisions. For the purposes of this study a finite element model for the simulation of the members was adopted where, a damage plasticity model was used for the concrete. The steel reinforcement was modelled as elasto-plastic and the CFRP as a linear elastic material until failure. The distribution of the stresses around the cutout, strains on the concrete, and the FRP's, as well as deflections on the slab surfaces are reported in order to provide useful conclusions about the effectiveness of the use of FRP laminates in existing reinforced concrete slabs with central cutouts.

1 INTRODUCTION

Currently, reconstruction of existing buildings has becoming quite common due to functional requirements from the users. Functional requirements such as staircases, elevators and escalators lead to the introduction of cutouts, openings or penetrations in existing reinforced concrete slabs. Thus, there exists a need for strengthening the existing slabs, particularly as regards the introduction of large openings. Traditional methods of strengthening existing slabs with cutouts, such as the embedding of reinforcing bars, the addition of beams or the addition of columns at the edges of the cutout can be expensive and generally difficult to apply.

The application of Fiber-Reinforced-Polymers (FRPs') has been proved to be a competitive strengthening technique compared with traditional ones. Their relatively high strength to weight ratio and their easy-to-apply character, make them promising candidates for repair and retrofitting of deficient RC structures. In the last decade, several experimental and theoretical studies have been carried out, to the repairing and strengthening of RC members in flexure (Plevris et al. 1995), shear (Triantafillou 1998), confinement (Tastani et al. 2006) and even in torsion (Chalioris 2006 and 2007) using FRP.

Strengthening of slabs with cutouts could be carried out by bonding Fiber Reinforced Polymer (FRP) laminates to the tension face of the slab in the vicinity of the cutout where the FRP-strengthening essentially provides 'strong' bands around the cutout. Although several studies have been published on the strengthening of RC slabs with FRP (Mossalam & Mosalam, 2003), less research has been presented on the strengthening of RC slabs with cutouts using externally bonded FRP composites which are intended to replace the internal steel reinforcement lost when the cutout is made.

Comprehensive investigations on one-way spanning FRP strengthened slabs with cutouts have been reported by Vasquez & Karbhari (2003), Tan & Zhao (2004) and Smith & Kim (2009). The outcome of these studies was that the FRP laminates can be used to restore the original load carrying capacity of slabs weakened by cutouts while the failure of the slab has occurred by intermediate crack debonding of the FRP. Studies on the strengthening of two way slabs with cutouts using externally bonded FRPs' have been presented by Enochsson et al (2007) and Casadei et al. (2003). The increased load capacity of the retrofitted slabs were highlighted in both studies.

In this paper, an analytical study of a two-way simply supported reinforced concrete slab with a central cutout subjected to a uniformly distributed load has

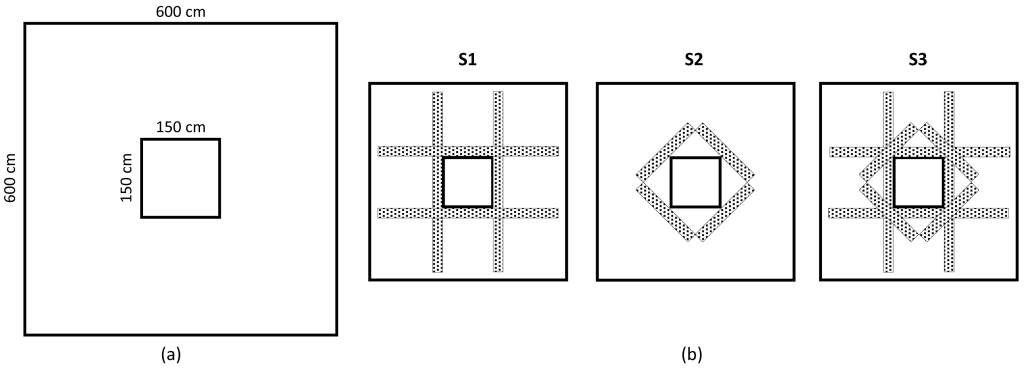

Figure 1. (a) Examined slab dimensions, (b) FRP arrangements.

been performed. Three different patterns of FRP laminates were examined. In the first one, the FRP laminate was placed in parallel with the opening edges, in the second, the laminate was placed at the corners of the cutout at a 45° angle and in the third, a combination of the two above arrangements was used.

2 NUMERICAL MODELING

2.1 *Properties of the examined slab*

One simply supported two-way reinforced concrete slab measuring $600 \times 600 \times 16$ cm with a central cutout dimensioning 150×150 cm was studied (Figure 1a). The slab was reinforced at the inferior (tension) side with 8 mm diameter rebars with spacing 100 mm. The concrete was assumed as C16/20 with mean compressive strength $f_{cm} = 24$ MPa, and the rebars as S400 with tensile strength at yielding $f_y = 400$ MPa. The selection of the materials was made in order to correspond to a reinforced concrete building aged about 30 years old, which comprise the majority of the building structures in Greece. FRP laminates with Young's modulus 165 GPa, tensile strength 3.1 GPa and rupture strain 1.7% were considered.

The FRP strengthening sheets were placed around the cutout on the tension side of the slab. Three different strengthening arrangements with FRP laminates were examined (Figure 1b). In the first (S1) FRP sheets were placed along the opening. In the second (S2) FRP sheets were placed at the corner of the openings with a 45° angle and finally, in the third (S3) a combination of the two above arrangements was used.

The sheet length was calculated according to ACI 440.2R-02 (ACI 2002) provisions in order to provide the required anchorage, to reduce the stress concentration effect at the laminate terminations and avoid premature peeling.

2.2 *FRP estimation*

A simplified method to estimate the necessary amount of the FRP was adopted. The amount of FRP used to strengthen the slab was computed under the premise that the loss of steel reinforcement caused by the cutout would be replaced by an equivalent amount of FRP by accounting for the differences in the lever arms and the effective widths of the compression zone.

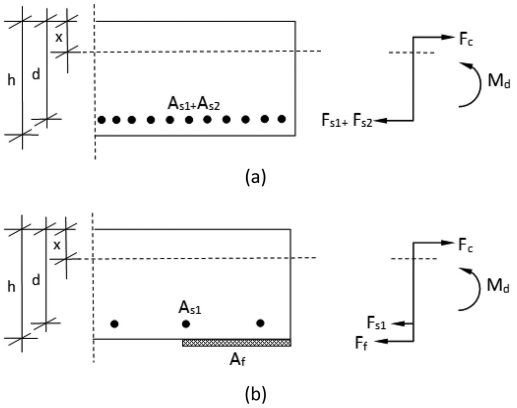

Figure 2. Cross section analysis (a) with the lost reinforcement, (b) with the FRP.

The amount of the lost reinforcement in each direction was $A_{s2} = 1507\,mm^2$ of which half had to be placed along each edge of the cutout. The required area of the FRP sheets was computed using the simplified method by a cross-section analysis (Figure 2). So the estimated amount of the FRP sheets was $A_f = 1427\,mm^2$ at each edge.

2.3 *FEM modeling*

The numerical modeling of the problem was performed using the finite element method (FEM). Due to the geometrical symmetry of the model it was assumed that a quarter of the structure was adequate to give the response of the whole structure with sufficient accuracy.

The complex, nonlinear material behavior of concrete is described by the elasto-plastic damage model "concrete damaged plasticity" (ABAQUS 2012) that was developed by (Lubliner et al. 1989) and elaborated

by (Lee & Fenves 1998). This model is thoroughly investigated for the simulation of reinforced concrete slabs by Genikomsou & Polak (2015). Non-associated flow is assumed where the flow potential G is the Drucker–Prager hyperbolic function. The parameters that have to be determined are the dilation angle (ψ), the ratio of the second stress invariant on the tensile meridian (Kc), the plastic potential eccentricity (ε) and the ratio of the strength in the biaxial state to the strength in the uniaxial state (σ_{bo}/σ_{co}).

The stress-strain behavior under sustained compressive loading is modelled by the expressions of the Model Code (CEB-FIB 1993) recommendations. Furthermore, regarding the modeling of the tension strength of the concrete, the post-failure behavior is specified in terms of the stress–strain response using the proper relationship, proposed by Wang and Hsu (2001).

The rebars were simulated as a truss element and the steel model was assumed to be ideal elasto-plastic with an equal behavior in tension and compression. All the steel bars were embedded within the concrete element.

The FRP material of the laminates was considered as linear elastic until failure. The interaction between the concrete slab and the FRP was modelled without considering debonding.

3 RESULTS

3.1 *Overall response*

The load versus deflection relationship could be a first indicator to estimate the effect of the FRP implementation. Comparative load-deflection diagrams are displayed in Figure 3. The deflection was measured at the mid side of the opening. The contribution of all the FRP arrangements to the response of the slab could be easily observed.

Between the different applied patterns that with the FRP sheets placed at the corners of the cutout in 45° angle (S2) contributed the least. That could be noticed also comparing the S1 with the S3 model in which the FRP sheets placed at the corners of the cutout did not considerably ameliorate the total response. Hence the pattern with the FRP laminates placed in parallel with the opening edges improved the response of the slab the most.

Despite the enhanced load capacity of the retrofitted slab, all the examined slabs had an elastic response under the design load ($F_{Design} = 15\,kN/m^2$).

3.2 *Reinforcement and concrete stress results*

In order to evaluate the strengthening method of the slab, the demanded stresses of the initial materials are presented.

In Figure 4 the required principal stresses of a reinforcement rebar in the middle of the opening is depicted. The developing stresses of all the

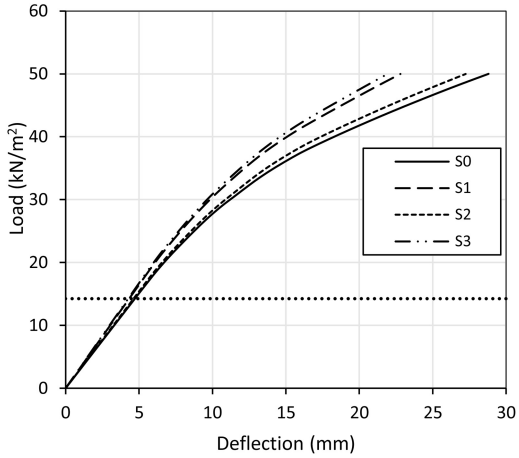

Figure 3. Load – Deflection curves.

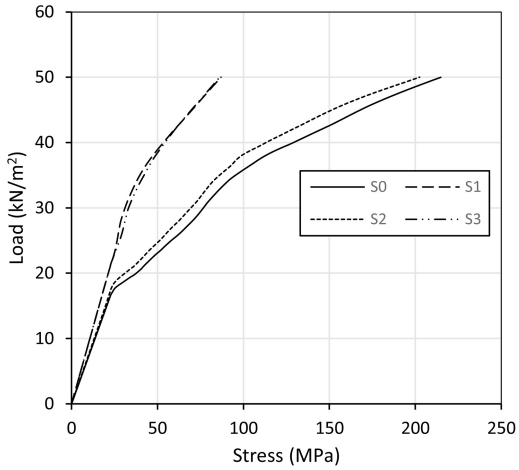

Figure 4. Load – Reinforcement Stresses curves.

retrofitting patterns are lower comparing with the initial unstrengthen slab.

The pattern with the FRP sheets implemented in parallel with the cutout edges (S1) considerably alleviates the stress of the reinforcement. Particularly the demanded stress was reduced by approximately 22% under the design load. For the maximum load the decrease of the required stresses is about 59%.

In Figure 5 the stress field of the concrete's tension side is presented. Specifically, this display corresponds to the demanded stress of the concrete part of the slab under the design load. From the tension stress field of the concrete, the cracking pattern of the slab could be obvious. So the cracking propagation is mainly from the corner of the opening to the corner of the plate.

The mean tensile strength of the concrete is $f_{ctm} = 2.51$ MPa, so it can be observed for the initial slab that the concrete has developed 94% of the mean

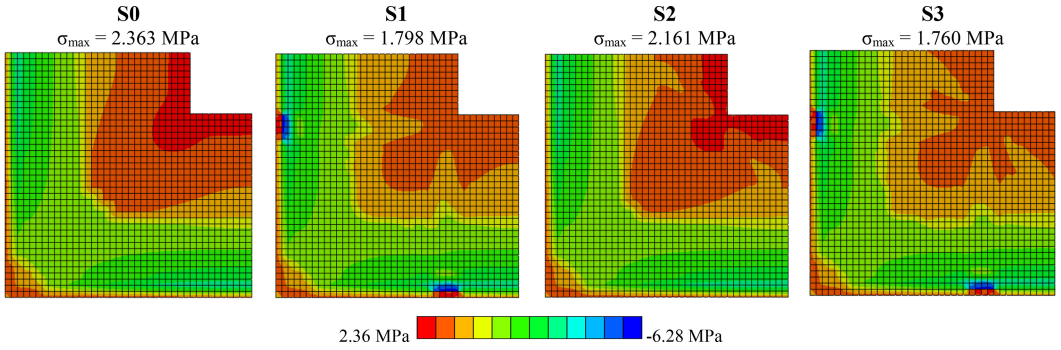

Figure 5. Concrete tension stress field.

tensile strength. Furthermore, the increasing stress values are concentrated next to the opening edges and mainly around the corner of the cutout.

As from the above results, the enhancements of the FRP implementation is observed also by the concrete developing stresses. The appliance of the FRP along the opening edges (S1) is beneficial primarily for the concrete part. On the other hand the appliance of the FRP at the corner of the opening at a 45° angle (S2) does not significantly contribute. The better response is observed for the case of the implementation of the FRP both along the edges and at the corner of the opening (S3). However the improved behavior of the S3 arrangement is almost similar with the S1, as the FRP implemented at the corners of the cutout, slightly affects the response.

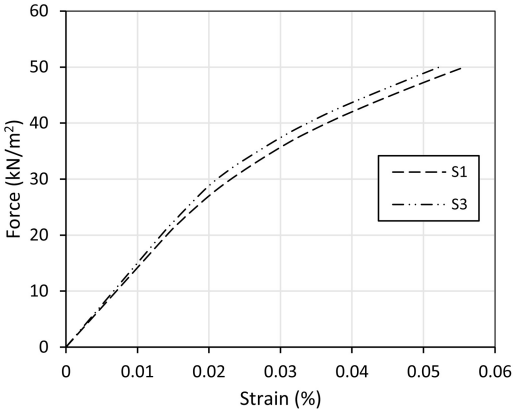

Figure 6. FRP strains.

3.3 *FRP strain results*

The developing strain in the FRP laminate which is placed in parallel to the cutout edge is presented in Figure 6. The measurement of the strain is made at the mid side of the opening. At the same point the deflection and the reinforcements stress were measured too. In both studied cases the ultimate limit strain of the FRP sheets (1.7%) was not reached.

In Figure 6, the comparison of the strains between the retrofitted pattern without (S1) and with (S3) the FRP sheet applied at the corner of the opening is made. In respect with the results above, the strain of the FRP is slightly reduced (6%) when the FRP laminate at the corner is considered.

Figure 7 shows the development of the FRP sheet strains lengthwise. The highest FRP strain is observed at the corner of the opening as expected. This region is also where the maximum tensile stresses on the concrete are localized. The required strains correspond to the slab under the design load. The maximum developing strain is not even close to the ultimate rupture strain of the FRP sheet.

The interaction between the concrete slab and the FRP is modelled without considering debonding. Although, the strain of the FRP did not reach the rupture strain, the flexural cracking of the concrete that occurred in the maximum bending moment region

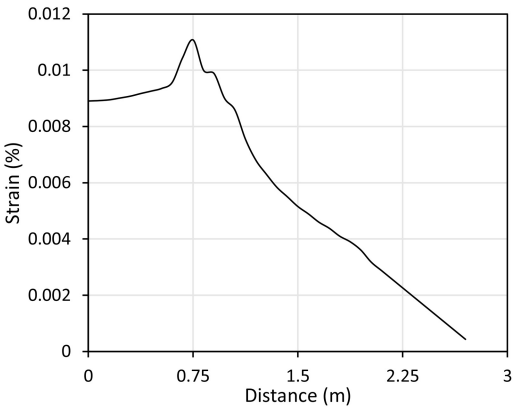

Figure 7. Developing strains along a FRP sheet.

around the cutout may lead to debonding of the FRP laminates from the concrete.

4 CONCLUSIONS

Strengthening reinforced concrete slabs with a central cutout using FRP composites is analytically investigated in this paper. Introducing an opening

in existing slabs in RC buildings due to functional changes are commonly required. In comparison to traditional strengthening methods, the application of FRP laminates is very suitable not only because of their mechanical properties, but also due to their ease of application.

One simply supported two-way reinforced concrete slab measuring 600 × 600 × 16 cm with a central cutout dimensioning 150 × 150 cm was studied. Three different strengthening arrangements with appliance of FRP sheets were examined. In the first one (S1) the FRP laminates were placed along the opening edges, in the second (S2) they were placed at the corners of the cutout at a 45° angle and in the third (S3) a combination of the two above patterns was used.

A damage plasticity model was used for the simulation of the concrete. The steel reinforcement was modelled as elasto-plastic and the CFRP as a linear elastic material until failure. The interaction between the concrete slab and the FRP is modelled without considering debonding.

The evaluation of the proposed strengthening methods was made by results in terms of slab deflection, the reinforcement and the concrete developing stresses, and the strains of the FRP sheet.

From the Load versus Deflection diagram, the increase of the load capacity for all the strengthening patterns is noticed. Furthermore, the the pattern with the FRP laminates placed in parallel with the opening edges increased the carrying load the most (−20%). Despite this, under the design load even the initial slab responded elastically.

From the results of the developing stresses of the reinforcement and the concrete of the slab, the profitable effect of the FRP sheets can be seen. For the arrangement where the sheets were placed in parallel with the opening edges, the required stresses of the reinforcement decreased 60%, whilst the concrete stresses were reduced 24%. The pattern where the FRP sheets were placed at the corners of the cutout at a 45° angle did not significantly ameliorate the slab response. Finally, the third arrangement slightly improved the already improved response of the retrofitted slab with the first pattern.

From the illustration of the tension stress field of the concrete, the cracking propagation from the corner of the opening to the corner of the slab can be obviously noticed.

By the strain results of the FRP, it can be seen that the FRP sheet exhibited the maximum strain at the corner of the opening without reaching the rupture strain.

Generally the usage of FRP sheets for the strengthening of a two way slab with a central cutout seemed to be very efficient. An accurate simulation of the interface between the concrete and the FRP was made in order to include in the numerical model the intermediate cracking/debonding failure which is the main failure observed in the literature.

REFERENCES

ACI 440.2R-02 2002. *Guide for the Design and Construction of* Externally *Bonded FRP Systems for Strengthening Concrete Structures*. Farmington Hills, MI: American Concrete Institute.

Casadei, P., Nanni, A., Ibell, T.J. 2003. *Experiments on two-way RC slabs with openings strengthened with CFRP laminates.* Proceedings, *Advancing* with Composites, PLAST, Milan, Italy, 7–9 May 2003.

Chalioris, C.E. 2007. *Analytical Model for the Torsional Behaviour of Reinforced Concrete Beams Retrofitted with FRP Materials*. Engineering Structures, 29 (12): 3263–3276.

Chalioris, C.E. 2008. *Torsional Strengthening of Rectangular and Flanged Beams using Carbon Fibre-Reinforced-Polymers – Experimental Study.* Construction and Building Materials 22(1): 21–29.

Comité Euro-International du Béton. 1993. *CEB-FIP Model Code 1990*. *Thomas* Telford Services Ltd.

Dassault Systems Simulia Corp. 2012. *ABAQUS Analysis user's manual Version 6.12.*

Enochsson, O., Lundqvist, J., Täljsten, B., Rusinowski, P., Olofsson, T. 2007. *CFRP strengthened openings in two-way concrete slabs – An experimental and numerical study.* Construction and Building Materials 21(4):810–26.

Genikomsou, A. S., & Polak, M. A., 2015. *Finite element analysis of punching shear of concrete slabs using damaged plasticity model in ABAQUS.* Engineering Structures, 98, 38–48.

Lee, J., and G. L. Fenves, 1998. *Plastic-damage model for cyclic loading of concrete structures*. Journal of Engineering Mechanics 124(8): 892–900.

Lubliner, J., Oliver, J., Oller S., & Onate E. 1989. *A plastic-damage model for concrete.* International Journal of Solids and Structures 25(3): 299–326.

Plevris, N., Triantafillou, T.C., and Veneziano, D. 1995. *Reliability of RC members strengthened with CFRP laminates.* Journal of Structural Engineering 121(7): 1037–1044.

Smith, S.T., Kim, S.J. 2009. *Strengthening of one-way spanning RC slabs with cutouts using FRP composites.* Construction and Building Materials 23(4):1578–1590.

Tan, K.H., Zhao, H.D. 2004. *Strengthening of openings in one-way reinforced concrete slabs using carbon fiber-reinforced polymer systems.* Journal of Composites for Construction, ASCE 8(5):393–402.

Tastani, S. P., Pantazopoulou, S. J., Zdoumba, D., Plakantaras, V., & Akritidis, E. (2006). Limitations of FRP jacketing in confining old-type reinforced concrete members in axial compression. Journal of Composites for Construction, 10(1), 13–25.

Triantafillou, TC. 1998. *Shear strengthening of reinforced concrete beams using epoxy-bonded FRP composites*. ACI Structural Journal 95(2): 107–15.

Vasquez, A., Karbhari, V.M. 2003. *Fiber-reinforced polymer composite strengthening of concrete slabs with cutouts.* ACI Structural Journal 100(5):665–73.

Wang, T., Hsu T.T.C. 2001. *Nonlinear finite element analysis of concrete structures using new constitutive models*. Computers and Structures 79(32): 2781–2791.



Taylor & Francis
Taylor & Francis Group
http://taylorandfrancis.com

Concrete Solutions – Grantham et al. (Eds.)
© 2016 Taylor & Francis Group, London, ISBN 978-1-138-03008-4

Pullout behavior of single steel fiber with different strengths of concrete

M. Iqbal Khan & Wasim Abbass
Center of Excellence for Concrete Research and Testing, Department of Civil Engineering, King Saudi University, Saudi Arabia

ABSTRACT: Addition of fibers in concrete significantly enhances the tensile and flexural properties of concrete. It is due to a bridging mechanism by the fibers over the crack width. Performance of fiber-reinforced concrete is significantly affected by fiber/matrix interface properties. Behavior of fibers with different concrete strengths should be well understood to achieve better performance of fiber reinforced concrete. The influence of various matrix strengths on hook ended single steel fiber is reported in this paper. Concretes with different strengths were prepared to execute the pullout test program. Test results revealed that pullout behavior is influenced by the strength of the matrix and the embedment length of fiber. Results showed that increase in total pullout energy is more prominent in increased embedment length and larger diameters of steel fibers.

1 INTRODUCTION

Concrete is one of the most commonly used construction materials. It has quasi-brittle behavior with low fracture toughness and tensile strength. Steel bars are used to improve its tensile behavior as reinforcement in structural elements in concrete. Another common way to improve tensile behavior of concrete is to add steel fibers in concrete (Naaman 1985). Addition of fibers enhances the post-cracking behavior of material, since stresses are transferred across the crack through fiber bridging and resists crack opening and propagation which leads to smaller crack opening widths. Fiber reinforced concrete also has an advantage with regard to its durability, therefore, addition of fiber to conventional reinforced structures also enhance the ductility and durability of the concrete (Breitenbücher et al. 2014). Total fibers intercepting the crack is a controlling parameter of the crack bridging effect across the opening. The efficiency of bridging of fiber largely depends upon fiber-matrix bond characteristics (Mandel et al. 1987). Therefore; it is important to study the mechanism of bond to comprehend the behavior of steel fiber reinforced concrete at a structural level. Measurement of reaction forces during pullout of single fibers embedded in the matrix for different types of fiber and concrete mixes is crucial (Robins et al. 2002).

One of most commonly used type of fiber in steel fiber reinforced concrete is hook ended fiber. The total pullout force considerably increases during pullout of hook ended fiber due to resistance of the hook to straightening (Alwan et al. 1999, Chanvillard 1999, Van 1999). The behavior of fiber pull out depends on the fiber characteristics and the matrix. Increased matrix strength is reported to have a positive effect on the bond strength of fiber and matrix (Tuyan & Yazici 2012 Abu-Lebdeh et al. 2011 Shannag et al. 1997). It has also been reported that the peak pull-out load of hook ended steel fibers was considerably higher than smooth steel fibers. The effect of end condition of fibers on pull out behavior of the fiber-matrix interface was also reported by some researchers and similar results were reported (Banthia & Trottier 1994, Shannag et al. 1997, Silva et al. 2011).

Interfacial bond strength has been enhanced by many researchers with various methods. These methods include densification of interfacial transition zone with fine fillers and grains, and mechanical bond application of deformed steel fibers (Alwan et al. 1999, Igarashi et al. 1996, Bentur & Alexander 2000 Gurrero & Naaman 2000). The effect of grain size of sand and sand to cement ratio on interfacial bond strength of steel fiber in mortar was reported. It was reported that a higher sand to cement ratio and finer sand had a stronger bond with steel fiber and variation in strength was also reported with type of fiber (Kang et al. 2013). The effect of water cement ratio has been investigated. With lowering water cement ratio, the bond strength of fiber and matrix increases and it also reduces the role of embedment length of hooked end fibers. Debonding toughness and the pullout peak load also increased with lowering water cement ratio in all curing conditions in reactive powdered concrete and ordinary mortar (Beglarigale & Yazici 2015).

Deformed fiber without rupture has shown increase in maximum pull-out load and total pullout energy with increase in matrix strength. Total pullout energy more significantly increased than peak load (Taher et al. 2011). It is also reported that fibers aligned along with the direction of loading showed higher peak load than fibers inclined with respect to loading. Inclined

Table 1. Physical and chemical properties of cementitious materials.

Oxide Composition (%)	Ordinary Portland Cement
SiO_2	20.2
Al_2O_3	5.49
Fe_2O_3	4.12
CaO	65.4
MgO	0.71
Loss on ignition (%)	1.38
Fineness	373
Specific Gravity	3.14

fibers have also shown more slips at peak load than aligned fibers. Premature failure in the form of matrix splitting or fiber fracture has been observed in case of high strength matrices therefore provoking a brittle failure (Banthia & Trottier 1994).

Geometry of te fiber has a significant effect on the peak load and energy absorption capacity. Total work has increased up to 100% for some fibers. Increase in embedment length also increases peak load and total pullout work for different fibers (Hamoush et al. 2010). Deformed fibers are severely stressed during pullout and fiber fracture is more often observed as compared to straight fiber. Material and fiber geometrical properties are more crucial to understand fiber matrix interaction.

In this research an attempt has been made to formalize fiber pullout with respect to different matrix strength, embedment length and different diameter of hooked end fibers. Two different diameters of fibers were chosen for investigation. Three different matrix strengths have been investigated for pullout behavior of hook ended steel fibers.

2 MATERIAL AND METHOD

2.1 *Fine powder*

Type I ordinary Portland cement (OPC) was used as binder material as per ASTM C150. The average grain size of the OPC was 13 μm. The physical and chemical properties of the OPC are shown in Table 1. The particle size distribution of th OPC is shown in Figure 1.

2.2 *Fine and coarse aggregates*

Two types of sands with different particle sizes were used for preparation of mixes named as crushed sand and fine sand. Fineness moduli were 1.47 and 4.66 for fine and crushed sand, respectively. Fine and crushed sand were combined as 65% and 35%, respectively to achieve a fineness modulus of 2.54. Coarse aggregate with maximum size of 10 mm was used for mix preparation. Physical properties of the fine and coarse

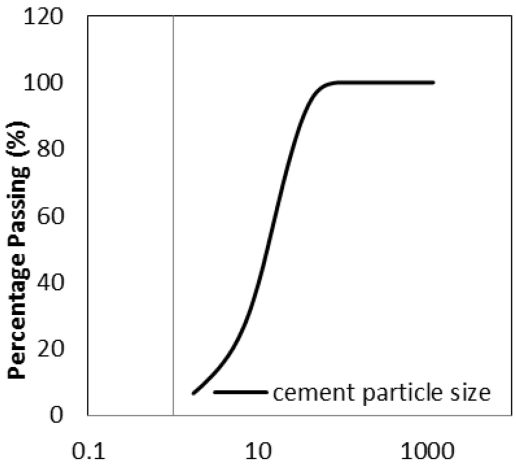

Figure 1. Particle size distribution of cement.

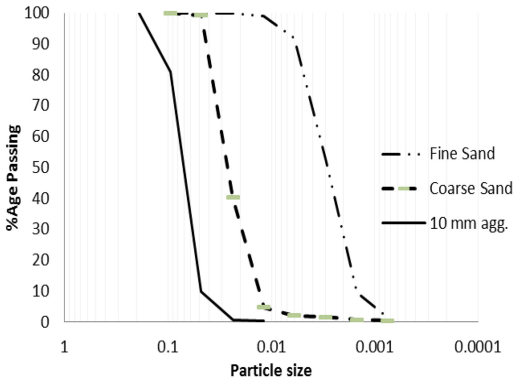

Figure 2. Particle size distributions of fine and coarse aggregate.

Table 2. Physical properties of fine and coarse aggregate.

Properties/ Material	Specific Gravity	Absorption (%)	Unit Weight Kg/m^3
White Sand	2.63	0.45	1725
Crushed Sand	2.68	1.52	1552
Coarse Aggregate (10mm)	2.65	1.45	1570

aggregate are summarized in Table 2. Particle size distributions of sands and coarse aggregate are shown in Figure 2.

2.3 *Chemical admixtures*

A modified polycarboxylic ether (PE) polymer (Glenium 51) was used for production of the required mixture. It has a specific gravity of 1.1 and dry extract of 36%. The dosage of PE is expressed as a dry extract (D.E.) per cement weight. Optimized PE dosages were determined.

Table 3. Properties of steel fibers.

S. No.	Length (mm)	Diameter (mm)	Aspect Ratio	Young's Modulus GPa	Tensile Str. (MPa)
1	≈60.54	0.72	84	210	1250
2	≈51.42	0.58	88	210	1250



Figure 3. Steel fibers.

2.4 *Fibers*

Hook ended steel fibers with two different diameters and length were used in this study. The properties of pthe fibers are summarized in Table 3. The Physical appearances of fiber are shown in Figure 3.

2.5 *Methods*

The experimental plan was performed on a single fiber embedded in concrete. A cylindrical specimen size of 50 mm diameter and 100 mm length was used for testing. A steel bar of 10 mm was embedded in one side of cylinder to hold the specimen whereas steel fiber was fcast into the other end. A circular plate of 50 mm was cut with an exactly concentric hole of 1 mm to pass through fiber in to the concrete. The fiber was embedded with different lengths in the concrete to study the effect of embedment length. A special set up was prepared to ensure alignment of fiber and steel bar for testing fiber pullout as shown in Figure 4. Samples were cast in two equal layers. Once samples were cast, the top plate with fiber in the center was placed at the top of cylinder to make sure of embedment of fiber inside the concrete specimen. The fiber was held vertical with the help of tape and samples were demolded after 24 hours. Three samples were cast for each matrix strength, embedment length and diameter of fiber.

2.6 *Mixing procedure and testing*

Mixtures with different strength concrete were prepared by dry mixing all coarse and fine aggregates until homogenizing. Then absorption water was added to the dry mix and mixed for one minute. Water along with the superplasticizer (SP) dosage was added to the mixer and mixed for three minutes and then a further three-minute wait. After stopping for three minutes, material was mixed for a further two minutes. The concrete was poured in cylindrical moulds followed by insertion of fibers according to different length.

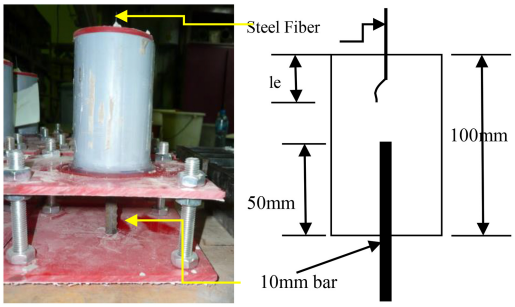

Figure 4. Single fiber pullout specimen.

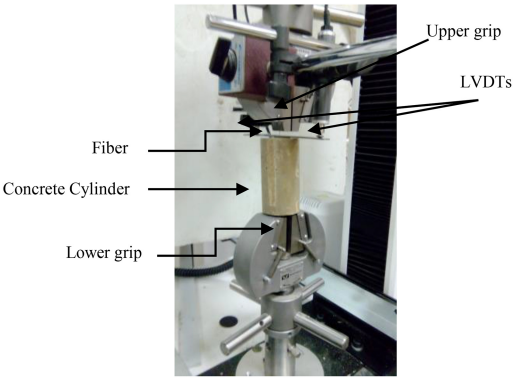

Figure 5. Pullout specimen Set up in direct tension testing machine.

Each single fiber pullout specimen was tested using an INSTRON 3360 machine. Two different grips were used to test specimens. Each cylindrical specimen in the direct tension testing machine was tested at a speed of 1 mm/min as shown in Figure 5.

Two LVDTs on two opposite sides of the fiber were used for the measurement of slip of fiber and a data acquisition system was used to record the slip data. The compressive strength for the different strength concretes was measured by using a cylinder of size 100 × 200 mm at a loading rate of 0.25 MPa/s. Three mixes with different strengths were designated as M-1, M-2 and M-3 as shown in Table 4, fiber embedment length was designated as E10 and E20 where 10 and 20 is embedment length of fiber in matrix in millimeters, and fiber diameter as D58 and D72 where 58 and 72 are designated for 0.58 mm and 0.72 mm diameters of two fibers embedded in the matrix. The mix design for three different strength of concrete is shown in Table 4.

3 RESULTS AND DISCUSSION

3.1 *Mechanical properties of matrices*

The concrete compressive strength at 28 days is shown in Table 5. A compressive strength of 52, 62 and 85 MPa was achieved for the three mixes (Table 5).

Table 4. Mix design.

Mix ID	Cement (kg/m^3)	Sand (kg/m^3) White sand	Sand (kg/m^3) Crushed Sand	Coarse Aggregate (kg/m^3)	Water (kg/m^3)
M-1	350	523	280	1056	187
M-2	450	468	252	1056	185
M-3	550	447	241	1056	165

Table 5. Compressive strength of mixtures.

Mix Designation	Compressive Strength (MPa)
M-1	52.4
M-2	61.7
M-3	85.5

3.2 *Effect of matrix strength on pullout of fiber*

The influence of strength of matrix on pull-out behavior of single steel fibers is shown in Figure 6. It is clear from the figures that matrix strength has a direct influence on the pull out response of fibers. Results reveal that higher strength of matrix has higher pull-out response which indicates that as strength of matrix increase pullout response of fiber increases proportionally. The peak load for fiber pullout increased with increase in matrix strength. Figures 6 (a) & (b) represent the effect of matrix strength on fiber with embedment length of 10mm and diameters of 0.58 mm and 0.72 mm and Figure 6 (c) & (d) shows the influence of matrix strength with embedment length of 20 mm. It indicates that matrix strength had a more pronounced effect on the 20 mm embedment length. The energy absorption capacity increased with increase in matrix strength. The post-peak behavior for the single fiber pullout of higher strength matrix had significantly increased with respected to the lesser strength matrix due to straightening of the hook end as shown in Figure 6.

3.3 *Effect of diameter on pullout strength of fiber*

The effect of diameter on pullout response is shown in figure 7. The effect of two different diameters on the pullout response of the single steel fiber has been shown in Figure 8. Results revealed that with an increase in fiber diameter, peak load significantly increased with respect to the smaller diameter. It can also be seen that the pullout response of the lesser embedment length had almost no effect on the peak load of the fiber. Figures 7 a, b & c shows that peak load significantly increased with larger diameter. Whereas Figure 7 d, e & f show almost the same peak load for two different diameters of the fibers.

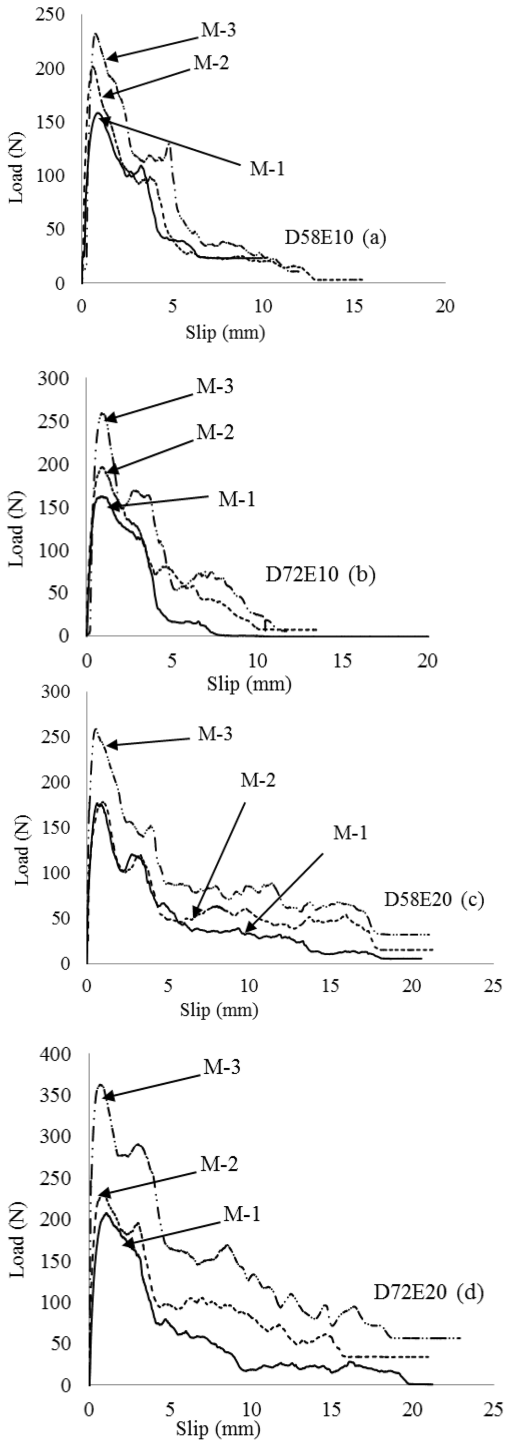

Figure 6. Load vs slip for different strength of mixtures.

Figure 7 reveals that the larger diameter showed more pullout response with respect to the smaller diameter of fiber and this effect is more pronounced with increase in matrix strength. With an

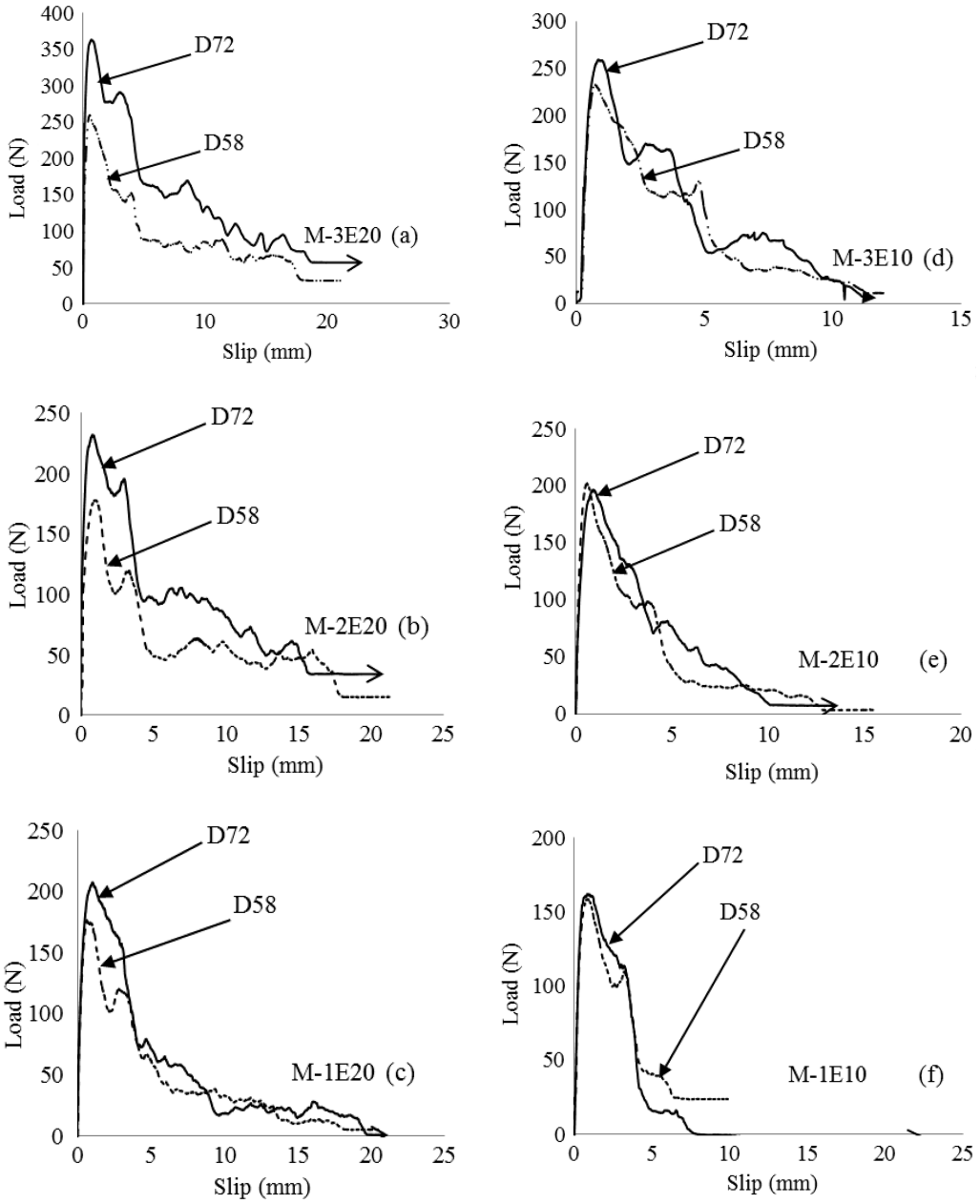

Figure 7. Pullout load vs slip of single fiber for different diameters of fiber.

increase in strength of matrix the effect of diameter is more pronounced with respect to lower strength matrices.

3.4 *Effect of embedment length on bond strength of fiber and matrix*

The bond strength of matrix was greatly influenced with embedment length of fiber. With an increase in embedment length of the fiber, the peak load and total pullout response of fiber significantly increased with respect to lower embedment length. Results revealed that peak load increased with increase in embedment length and total energy absorption capacity significantly increased with increase in embedment length.

Figure 8 shows that peak pullout load is a function of embedment length of the fiber. The effect of embedment length is significant in higher strength matrices, embedment length is also critical for larger diameter while energy absorption capacity increased for greater embedment length.

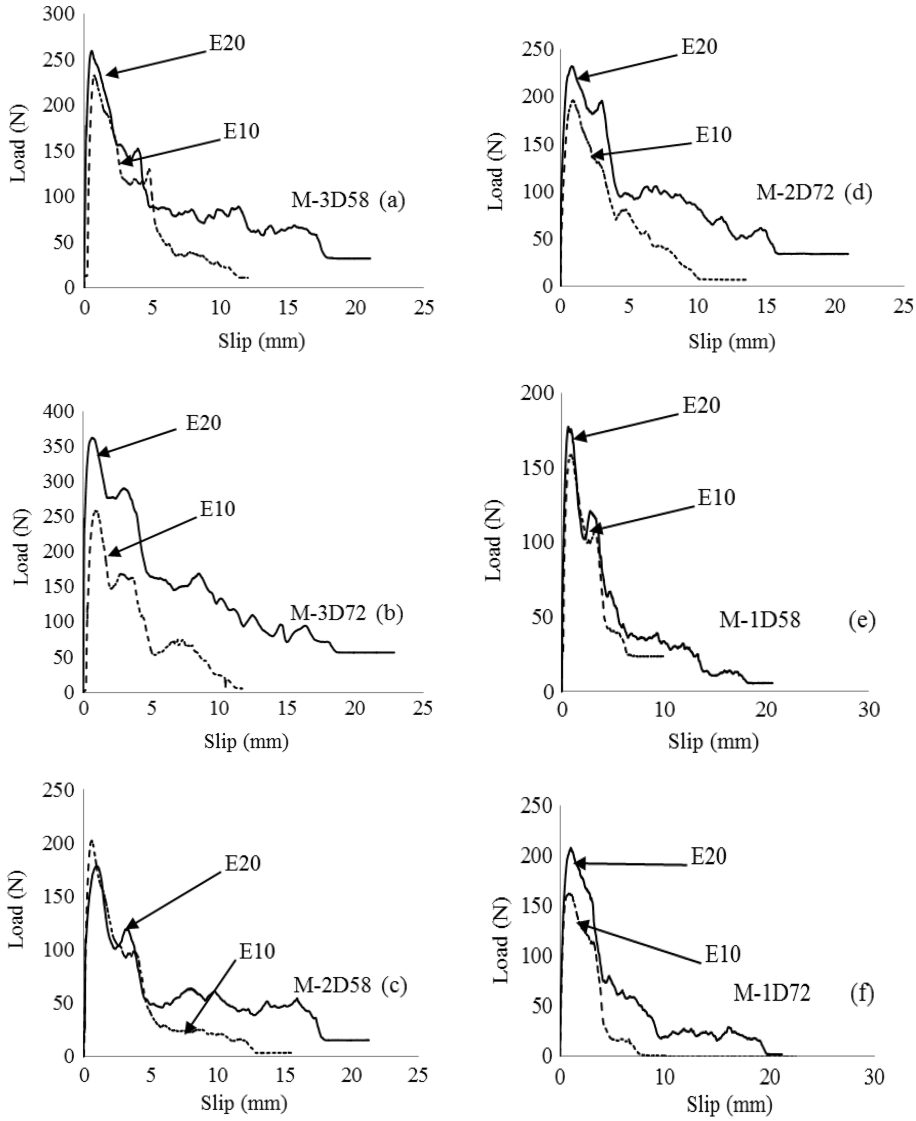

Figure 8. Pullout load vs slip for different embedment lengths of fiber.

4 CONCLUSIONS

The behavior of a single fiber in different strength matrices is summarized in the following conclusions:

Fiber pullout response with hook ended fibers was significantly influenced by the strength of matrix. With an increase in strength of matrix, peak pullout load increased and post peak load also increased significantly. Post peak load increased due to straightening of the hook end because it is pulled out of the matrix.

Pullout response of fiber in the concrete matrix was also a function of fiber diameter which increased the peak load of the single fiber in the concrete matrix. An increase in peak load from 22% to 44% was achieved with increased fiber diameter from lower strength matrix to higher strength matrix, respectively.

Embedment length was also a key parameter for pullout response of single fibers. Embedment length increased peak load from 11% to 39% for smaller and larger diameter fibers, respectively.

REFERENCES

Abu-Lebdeh, T., Hamoush, S., Heard, W., Zornig, B. 2011. Effect of matrix strength on pullout behavior of steel fiber reinforced very-high strength concrete composites. Construction and Building Materials 25: 39–46.

Alwan, J., Naaman, A. E., Guerrero, P. 1999. Effect of mechanical clamping on the pullout response of hooked steel fibers embedded in cementitious matrices. Concrete Science and Engineering 1: 15–25.

Banthia, N. & Trottier, J.F. 1994. Concrete Reinforced with Deformed Steel Fibers, Part I: Bond-Slip Mechanisms. ACI Materials Journal 91(5): 435–446.

Beglarigale, A., Yazıcı, H. 2015. Pull-out behavior of steel fiber embedded in flowable RPC and ordinary mortar. Construction and Building Materials 75: 255–265.

Bentur, A., Alexander, M.G. 2000. A review on the work of the RILEM TC159-ETC: engineering of the interfacial transition zone in cementitious composites. Materials and Structures 33(2): 82–7.

Breitenbücher R., Meschke G.,Fanbing Song F., Zhan Y. 2014. Experimental, analytical and numerical analysis of the pullout behaviour of steel fibres considering different fibre types, inclinations and concrete strengths. Structural Concrete 15(2): 126–135.

Chanvillard, G. 1999. Modeling the pullout of wire-drawn steel fibers. Cement and Concrete Research 29: 1027–1037.

Gurrero, P., Naaman, A.E. 2000. Effect of mortar fineness and adhesive agents on pullout response of steel fibers. ACI Materials Journal 97(1): 12–20.

Hamoush, S., Abu-Lebdeh, T., Cummins, T. & Zornig, B. 2010. Pullout Characterizations of Various Steel Fibers Embedded in Very High-Strength Concrete. American Journal of Engineering and Applied Sciences 3 (2): 418–426.

Igarashi, S., Bentur, A., Mindess, S. 1996. The effect of processing on the bond and interfaces in steel reinforced cement composites. Cement and Concrete Composites 18(5): 312–22.

Kang, S.H., Kim, J.J., Kim, D.J., Chung, Y.S. 2013. Effect of sand grain size and sand-to-cement ratio on the interfacial bond strength of steel fibers embedded in mortars. Construction and Building Materials 47: 1421–1430.

Mandel J., Wei S., Said, S. 1987. Studies of the properties of the fiber-matrix interface in steel fiber reinforced mortar. ACI Materials Journal 84: 101–109.

Naaman, A. E. 1985. Fibre reinforcement for concretes. Concrete International: Design and Construction 7: 21–25.

Robins, P., Austin, S., Jones, P. 2002. Pullout behavior of hooked end steel fibres. Materials and Structures 35: 434–442.

Shannag, M.J., Brincker, R., Hansen, W. 1997. Pullout behavior of steel fibers from cement-based composites. Cement and Concrete Research 27: 925–36.

Silva, F.A., Mobasher, B., Soranakom, C., Filho, RD.T. 2011. Effect of fiber shape and morphology on interfacial bond and cracking behaviors of sisal fiber cement based composites. Cement and Concrete Composites 33: 814–23.

Tuyan M., Yazici H. 2012. Pull-out behavior of single steel fiber from SIFCON matrix. Construction and Building Materials 35: 571–7.

Van Gysel, A. 1999. A pullout model for hooked end steel fibres. High Performance Fiber Reinforced Cement Composites (HPFRCC 3), RILEM Publications S.A.R.L.



Taylor & Francis
Taylor & Francis Group
http://taylorandfrancis.com

Concrete Solutions – Grantham et al. (Eds.)
© 2016 Taylor & Francis Group, London, ISBN 978-1-138-03008-4

FRP confinement of high-aspect ratio concrete columns

C.S. Kolyvas
FYFE EUROPE S.A., Greece

T.C. Triantafillou
University of Patras, Greece

A.I. Bernakos
FYFE EUROPE S.A., Greece

ABSTRACT: An important limitation in the majority of the globally available guidelines, with regard to concrete strengthening, is the confinement of vertical members of high-aspect ratio cross-sections by means of externally applied FRP. For that matter, the paper investigates FRP confinement of wall-like reinforced concrete columns, by examining a number of parameters, namely the effectiveness of different types of carbon FRP anchors, the role of different cross-section aspect-ratios (3 and 4), the number of externally applied FRP layers, local strengthening at the corners and the reduction of aspect-ratio by cross-section enlargement. It is concluded that properly dimensioned anchoring system, nearly doubles the confining effectiveness of FRP. Moreover, the use of additional FRP layers near the edges of the cross-section increases the confining effectiveness of the jacket by approximately 50%, and shape enlargement of the cross section with mortar is practically as effective as the use of FRP anchors.

Keywords: concrete, confinement, fibre-reinforced polymers, shape enlargement, FRP anchors, high-aspect ratio columns

1 INTRODUCTION

Confinement of reinforced concrete (RC) columns with FRP has become a common technique for increasing the axial load capacity of columns in non-seismic areas as well as for increasing the ductility and for preventing lap-splice failures and delaying rebar buckling of columns under seismic actions. External confinement with FRP materials is typically applied on circular or rectangular columns, wrapped with epoxy-bonded sheets made of unidirectional fibres in the circumferential direction.

The confining action of FRP wrapping is more effective on circular columns, where fibres are equally stressed on the entire cross section. On the contrary, at square or rectangular columns the parts of the cross section near the corners are confined effectively, but the intermediate parts remain unconfined. This loss of effectiveness is generally modelled with parabolic areas defined by the corners. FRP jackets in rectangular cross sections are less effective than in a circular one and their effectiveness depends heavily on the aspect ratio of the cross section (ratio of largest to smallest side). Depending on the radius at the corners of the cross section, the effectiveness of FRP jackets reduces significantly as the aspect ratio of the cross section approaches values in the order of 2–3 (e.g. Harajli et al. 2006).

In the case of wall-like columns, with aspect ratios of cross sections higher than 3, both experimental and analytical studies highlight that the effectiveness of FRP jackets is limited. Hosny et al. (2001) tested 12 rectangular reinforced concrete columns with cross section of 150x450 mm and height equal to 1.5 m. The axially loaded columns were confined using carbon fibre reinforced polymer (CFRP) strips. A key conclusion in this study was that the low effectiveness of CFRP could increase by transforming the shape of the cross section to elliptical or by adding longitudinal steel plates along the wide sides, fixed with anchor bolts. Tan (2002) performed compression tests on 52 RC columns with cross section of 115 × 420 mm and height equal to 1.2 or 1.5 m. The jackets comprised CFRP or glass FRP (GFRP) in the circumferential direction, occasionally combined with longitudinal plies near the corners or in the middle of the long sides. In two of the columns, the jackets were anchored on the long faces of the columns, but no further information is provided on the type, spacing etc. of the anchors. One last parameter in this investigation was the combination of FRP jackets with or without plaster finishes. This study demonstrated that circumferentially applied

FRP has increased effectiveness if combined with longitudinal sheets or anchors.

Tanwongsval et al. (2003) tested five RC columns with cross section of 115 × 420 mm and height equal to 1.5 m. The columns were strengthened with both circumferentially and longitudinally applied GFRP and were tested in uniaxial compression. The possibility of installing the FRP after enlarging the cross section with two semi-cylindrical parts made of high strength mortar was explored and the effect of strengthening under sustained loading was investigated. A key conclusion in this investigation was that the use of semi-cylindrical attachments in contact with the short faces of the columns was quite effective in increasing the load capacity of columns, by reducing stress concentrations near the corners. Prota et al. (2006) performed uniaxial compression tests on 9 columns with the geometry as in Tan (2002) and Tanwongsval et al. (2003). Parameters under investigation in this study included the use of quadri-directional GFRP and the combination of wrapping with longitudinally applied C-shaped plies around the corners, as a means of delaying buckling of the longitudinal steel rebars. Experimental findings were compared with existing analytical models for FRP confined concrete and it was concluded that reasonably good agreement was found with the model of Lam and Teng (2003).

From the literature survey presented above it is clear that confinement of wall-like RC columns with FRP has received very limited attention. Even less attention, if any at all, has been paid to the important aspect of anchoring the FRP along the wide faces. One promising technique to achieve this involves the use of fibre anchors, which comprise resin-impregnated fibre rovings. In the field of confinement, fibre anchors have been used in columns with L-shaped cross sections (Karantzikis et al. 2005) and in columns with circular or rectangular sections with aspect ratio equal to 2 (Ilki et al. 2008, Kim et al. 2011).

In this paper, FRP confinement of wall-like columns is investigated. The study examines a number of parameters not addressed before: the effectiveness of different types of anchors, the role of different cross section aspect ratios (3 and 4), the number of layers, local strengthening at the corners and the reduction of cross section aspect ratio by increasing the dimension of the columns' small side.

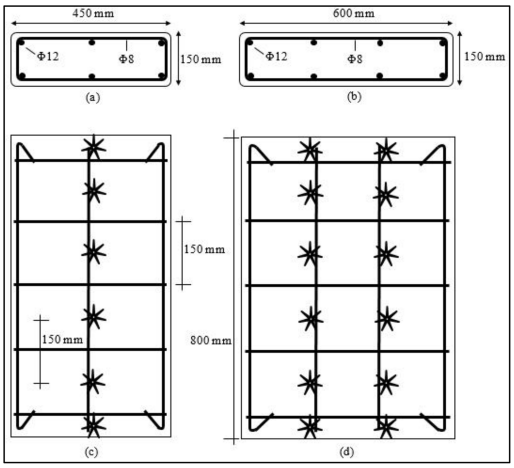

Figure 1. Column geometry and reinforcement: (a) cross section with aspect ratio 3; (b) cross section with aspect ratio 4; (c) side view of columns with aspect ratio 3, illustrating the locations of fibre anchors in specimens with one anchor in the middle of the long side; (d) side view of columns with aspect ratio 4, illustrating the locations of fibre anchors in specimens with anchors placed in pairs.

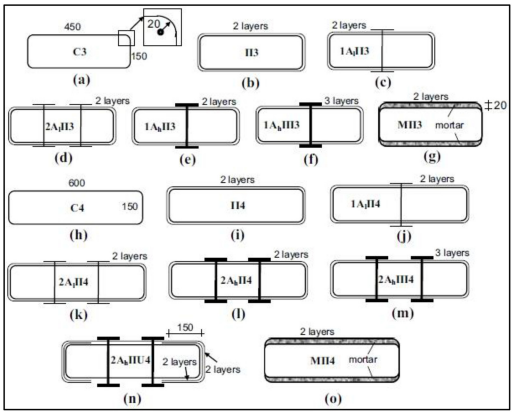

Figure 2. Configuration of strengthening schemes: (a) C3; (b) II3; (c) 1AlII3; (d) 2AlII3; (e) 1AhII3; (f) 1AhIII3; (g) MII3; (h) C4; (i) II4; (j) 1AlII4; (k) 2AlII4; (l) 2AhII4; (m) AhIII4; (n) 2AhIIU4; (o) MII4 (all dimensions in mm).

2 TEST SPECIMENS AND PARAMETERS

A total of 45 identical rectangular reinforced concrete columns were constructed, and tested in uniaxial compression. A group of 7 column designs had a cross section measuring 150 mm by 450 mm, with an aspect ratio of 3, and a second group of 8 column designs had a cross section of 150 mm by 600 mm, with an aspect ratio of 4. To facilitate FRP wrapping, the four corners were chamfered to a radius of 20 mm. All columns measured 800 mm in height. Longitudinal reinforcement comprised of 6 and 8 deformed re-bars – in columns with aspect ratio 3 and 4, respectively – of diameter equal to 12 mm. Thus, the longitudinal steel ratio was 1%. Transverse reinforcement consisted of 8 mm diameter stirrups at a spacing of 150 mm. The reinforcement was placed with a clear concrete cover of 15 mm. Details of column geometries and reinforcements are given in Fig. 1.

A description of the specimens is presented in Fig. 2.

Columns C3, II3, 1AlII3, 2AlII3, 1AhII3, 1AhIII3 and MII3 were of a cross sectional aspect ratio equal to 3.

Columns C4, II4, 1AlII4, 2AlII4, 2AhII4, 2AhIII4, 2AhIIU4 and MII4 were of a cross-sectional aspect ratio equal to 4.

In the notation of all specimens, C denotes a control specimen, II or III denotes the use of two or three CFRP layers, nA_i denotes the use of fibre anchors ($n = 1$ or 2 for one or two anchors, $i = l$ or h for light or heavy anchors), M denotes the use of mortar to enlarge the cross section, U denotes the use of U-shaped CFRP inserts near the corners and the number at the end, 3 or 4, denotes the cross sectional aspect ratio.

3 MATERIALS AND STRENGTHENING PROCEDURES

The average compressive strength at the time of testing of the columns (a few months after casting), measured on 150×300 mm cylinders was 18 MPa (average value from six specimens). Strength properties (average values from three specimens) for the steel used for longitudinal and transverse reinforcement were as follows: yield stress 570 MPa, tensile strength 680 MPa. A few days before testing, all specimens were capped with a special self-levelling high-strength mortar.

The carbon fibre sheet used for confinement was a unidirectional Carbon Fabric (TYFO® SCH-41). The carbon fibre sheet was impregnated with TYFO® S Epoxy with tensile strength of 72.4 MPa and an elastic modulus of 3.2 GPa (cured three days at 60°C). Mean values of tensile strength and elastic modulus for one layer of the Carbon Composite System was equal to 986 MPa and 95.8 GPa, respectively, corresponding to a nominal thickness equal to 1 mm. These values were confirmed by testing five coupons in uniaxial tension according to EN 2561 (1995). The test results gave an average tensile strength equal to 1046 MPa and an elastic modulus equal to 93.7 GPa.

The anchors used (TYFO® SCH Carbon Composite Anchors) had a length equal to 350 mm, mean tensile strength equal to 986 MPa and mean tensile modulus equal to 95.8 GPa. The diameter was 6.35 mm and 12.70 mm for the light (A_l) and the heavy (A_h) anchors, respectively. Impregnation and bonding of fibre anchors was done using the same epoxy adhesive used for the impregnation of the carbon sheets, namely TYFO® S Epoxy.

For the columns receiving mortar to enlarge the dimension of the short side, a TYFO® C-Matrix plastering was used, with a binder to water ratio equal to 5:1. The flexural and compressive strength of the mortar was obtained according to EN-1015-11 (1993), as average of 6 specimens. The compressive and flexural strength at the time of testing the columns were 20 MPa and 6.2 MPa, respectively.

The surfaces of the columns to be strengthened were ground mechanically to remove any laitance. Small cavities were filled with epoxy resin (Fig. 3a). Application of the CFRP took place a few months after concrete casting, by pre-wetting each sheet manually

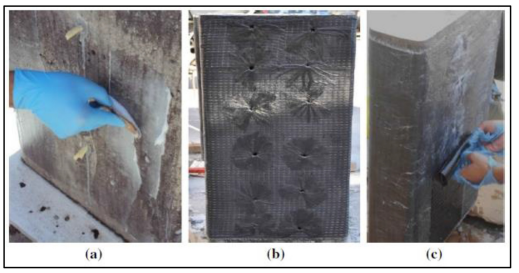

Figure 3. Photographs illustrating: (a) filling of cavities with epoxy resin, plastic inserts covering the holes; (b) side view of column with fibre anchors placed in pairs; and (c) coverage of anchors with longitudinal CFRP.

(using a roller brush) with the epoxy adhesive. Each of the (two or three) consecutive layers was bonded on each column so that the starting and finishing edges of the wraps overlapped by 200 mm on the wide face of the column. The extra U-shaped CFRP inserts in column 2AhIIU4 were placed under the two continuous CFRP layers, starting at a distance of 150 mm from each corner of the cross section (Fig. 2n).

Fibre anchors were formed by impregnating dry fibres with epoxy. Before applying the CFRP layers, 12 mm diameter holes were drilled through the thickness of the columns. To facilitate wrapping with CFRP, the holes were temporarily covered with protruding plastic inserts (Fig. 3a), which were removed prior to application of the anchors. Each fibre anchor was inserted into the holes after applying all layers of the CFRP around the columns, and the protruding fibres were fanned out radially over the last layer, at a distance equal to 100 mm (Fig. 3b). Finally, the anchors were covered with a 200 mm wide strip of CFRP in the central part of each wide face of the column, applied longitudinally, that is with the fibres in vertical orientation (Fig. 3c).

4 EXPERIMENTAL RESULTS AND DISCUSSION

Testing was performed approximately one month after application of the strengthening system. All columns were tested in uniaxial compression through the application of monotonic loading at a rate of 0.01 mm/sec in displacement control, using a 4000 kN compression testing machine. Loads were measured from a load cell and displacements were obtained using external linear variable differential transducers (LVDT) mounted on the two long sides, at a gauge length of 300 mm, in the middle part of each specimen.

Average values for peak forces, ultimate strains (defined at the point where either the FRP jacket ruptures or the load has dropped by 20% of the peak value) and the corresponding increase for each jacketing system with respect to values for unconfined columns are given in Table 1.

Failure of the control specimens (C3, C4) was typical of not properly confined reinforced concrete, due to buckling of the longitudinal rebars, which led to crushing of the concrete (Fig. 4a). All the other specimens failed when the FRP jacket ruptured in the circumferential direction at one of the four rounded corners (Fig. 4b), due to stress concentrations. Column 2AhIIU4, with the two extra layers of CFRP around the corners, was the only one where the jacket ruptured in its straight part, near the middle of the long side (Fig. 4c). In all columns with light anchors (1AlII3, 2AlII3, 1AlII4, 2AlII4), rupture of the jacket was preceded by gradual rupture of the anchors, implying that at failure the jacket acted as if no anchors were in place (Fig. 4d). This fact explains why the capacity of columns without anchors was similar to that of columns with light anchors. On the contrary, the heavy anchors remained intact (Fig. 4e), thereby increasing the effectiveness of the CFRP jacket all the way to failure.

The results for specimens II3, 1AlII3 and 2AlII3 indicate that in columns with aspect ratio equal to 3, two layers of CFRP with no anchors or with the light anchors (which failed prematurely) increased the strength by 30–40%. As expected, the corresponding increase in columns with aspect ratio equal to 4 (II4, 1AlII4 and 2AlII4) was lower, in the order of 25%. The strength of columns 1AhII3 and 2AhII4 was 57.4% and 45.2% higher than that of C3 and C4, respectively, indicating that the use of heavy anchors nearly doubled the effectiveness of jackets with two layers. Jackets with three CFRP layers combined with (heavy) anchors performed extremely well too, increasing the strength by nearly 80% and 70%, for columns with aspect ratio 3 (1AhIII3) and 4(2AhIII4), respectively. The use of additional CFRP near the edges (column 2AhIIU4) was also quite effective, by suppressing premature failure of the jacket at the corners; the respective increase in strength was 67%. Finally, shape enlargement of the cross sections with mortar (columns MII3 and MII4) was practically as effective as the use of (heavy) anchors (1AhII3 and 2AhII4). In this case the strength increased by approximately 60% and 40% in columns with aspect ratio 3 (MII3) and 4 (MII4), respectively, which is comparable to approximately 57% and 45% corresponding to columns 1AhII3 and 2AhII4.

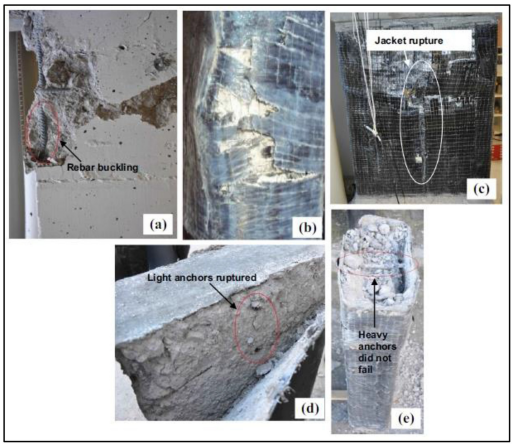

Figure 4. Typical photographs of failed columns: (a) rebar buckling and concrete crushing in control specimens; (b) jacket rupture at the corner; (c) jacket rupture in the middle of the long side; (d) premature rupture of anchors in columns with light anchors; and (e) no failure of the heavy anchors.

5 NOTES FOR DESIGN

In order the findings of the current research project to be applied to actual design cases, appropriate scale factor shall be implemented. The FRP strengthening scheme shall be scaled according to the dimensions of the cross section of the tested columns. Specifically, the amount of FRP as well as the configuration of the fibre anchors shall be adjusted accordingly. In any case the fibre anchors shall be applied along the height of the column at a maximum spacing of 200 mm.

The findings can be used for designing an FRP strengthening scheme, as long as, partial material safety factors and/or overall capacity safety factors are considered following the general design code/guideline that is applicable.

Apart from the increased confined concrete compressive strength, the FRP strengthening scheme contributes in preventing the longitudinal reinforcement from premature buckling and thus allowing the steel to contribute to the axial capacity of the columns. It is noted that the longitudinal steel shall not contribute to the axial capacity of under-reinforced columns in terms of transverse steel reinforcement, namely sparse stirrups, unless appropriate FRP strengthening scheme is applied. Further increase of the axial column capacity can be achieved by adding U-wraps around the short sides of the section prior to the main FRP strengthening scheme (see Fig. 2-n). The U-wraps shall consist of the same FRP amount as the main scheme and extend along the long sides of the section at a length equal to the short side of the section. The additional increase of the axial capacity is due to the enhanced concrete confinement at the ends of the column. In cases of U-wrap further increase of the calculated upgraded axial capacity of 15% shall be considered.

Enlarging the cross section along its short side and thus reducing the aspect ratio results in further increase of the axial column capacity. This is implemented by application of repair mortar at both long sides of the section prior to applying the FRP strengthening scheme (see Fig. 2-o). The additional increase is due to the more effective confinement of the lower aspect ratio section and partially due to the direct compressive force contribution of the added repair mortar area. In designing an FRP strengthening scheme the shape modification parameter shall be calculated following the enlarged dimensions of the section and a transformed sectional area shall be considered for the calculation of the axial capacity, where a portion of the

Table 1. Specimen notation and summary of test results.

Notation	Strengthening scheme	Peak force (kN)	Average peak force (kN)	Failure mode	Strength increase (%)	Ultimate strain ε_{cu} (–)	Average ε_{cu} (–)	Increase in ε_{cu} (%)
C3	–	1198.5	1149.4	RB[1]+	–	0.0026	0.0030	–
		1125.3		CC[2]		0.0027		
		1124.3				0.0038		
II3	2 layers of CFRP	1548.5	1601.4	JRc[3]	39.3	0.0099	0.0153	410
		1603.2				0.0202		
		1652.4				0.0159		
$1A_lII3$	2 layers of CFRP,	1608.8	1556.4	AR[4], JRc	35.4	0.0075	0.0112	273
	1 light anchor	1540.3				0.0142		
		1520.2				0.0120		
$2A_lII3$	2 layers of CFRP,	1470.5	1477.3	AR[4], JRc	28.5	0.0141	0.0145	383
	2 light anchors	1426.6				0.0150		
		1534.7				0.0145		
$1A_hII3$	2 layers of CFRP,	1764.3	1809.2	JRc	57.4	0.0105	0.0083	177
	1 heavy anchor	1846.8				0.0057		
		1816.5				0.0086		
$1A_hIII3$	3 layers of CFRP,	2114.2	2043.8	JRc	77.8	0.0422	0.0305	917
	1 heavy anchor	1881.3				0.0297		
		2135.9				0.0198		
MII3	Section enlargement,	1911.6	1830.3	JRc	59.2	0.0143	0.0181	503
	2 layers of CFRP	1743.2				0.0215		
		1836.2				0.0185		
C4	—	1403.8	1509.0	RB+CC	—	0.0037	0.0044	—
		1604.4				0.0048		
		1518.9				0.0046		
II4	2 layers of CFRP	1877.7	1907.6	JRc	26.4	0.0105	0.0147	234
		1934.7				0.0126		
		1910.4				0.0209		
$1A_lII4$	2 layers of CFRP,	1987.5	1934.4	AR, JRc	28.2	0.0114	0.0119	170
	1 light anchor	1899.9				0.0125		
		1915.8				0.0118		
$2A_lII4$	2 layers of CFRP,	1901.4	1870.7	AR, JRc	24.0	0.0130	0.0101	130
	2 light anchors	1820.5				0.0082		
		1890.3				0.0090		
$2A_hII4$	2 layers of CFRP,	2118.8	2191.5	JRc	45.2	0.0103	0.0163	270
	2 heavy anchors	2259.3				0.0065		
		2196.5				0.0081		
$2A_hIII4$	3 layers of CFRP,	2708.3	2598.0	JRc	72.2	0.0132	0.0126	186
	2 heavy anchors	2410.0				0.0122		
		2675.6				0.0125		
$2A_hIIU4$	2 layers of CFRP,	2457.1	2518.1	JRm[5]	67.0	0.0142	0.0131	198
	2 layers of U,	2631.8				0.0127		
	2 heavy anchors	2465.3				0.0125		
MII4	Section enlargement,	2103.5	2102.2	JRc	39.3	0.0131	0.0109	148
	2 layers of CFRP	2092.7				0.0085		
		2110.4				0.0110		

[1]Rebar Buckling; [2]Concrete Crushing; [3]Jacket Rupture at corner; [4]Anchor Rupture; [5]Jacket Rupture near the middle of the long side.

repair mortar area will be taken into account, according to the ratio of moduli of elasticity between existing concrete and mortar.

6 CONCLUSIONS

A total of 45 reinforced concrete columns measuring 150 by 450 mm or 150 by 600 mm in the cross sectional dimension, that is with aspect ratio 3 or 4, were tested to failure to examine the effectiveness of different CFRP jacket solutions with or without anchors as well as with section enlargement. From the work carried out herein it is concluded that:

- CFRP jackets without anchors give moderate increase in axial strength, in the order of 40% or 25% for columns with aspect ratio 3 or 4, respectively.
- Light anchors fail prematurely and the columns behave as if no anchors are used.
- Heavy anchors nearly double the confining effectiveness of CFRP jackets.

- If CFRP jackets are combined with heavy anchors, their effectiveness increases almost linearly with the number of layers. Jackets with three layers increase the strength by nearly 80% or 70% for columns with aspect ratio 3 or 4, respectively, whereas the corresponding values for two layers are about 55% and 45%.
- The use of additional CFRP in the circumferential direction near the edges suppresses failure of the jacket near the corners, thereby increasing the confining effectiveness of the jacket by approximately 50%.
- Shape enlargement of the cross section with mortar is practically as effective as the use of (heavy) anchors.

Despite the large number of parameters examined in the present study, further investigation is needed to study other FRP materials, long-term effects, response under cyclic loading and jacket-steel reinforcement interactions.

REFERENCES

EN 1015-11 (1993). Methods of test for mortar for masonry – Part 11: Determination of flexural and compressive strength of hardened mortar, European Committee for Standardization, Brussels.

EN 2561 (1995). Carbon fibre reinforced plastics – Unidirectional laminates – Tensile test parallel to the fibre direction, European Committee for Standardization, Brussels.

Harajli, M., Hantouche, E. and Soudki, K. (2006). "Stress-strain model for fibre-reinforced polymer jacketed concrete columns." ACI Structural Journal, 103(5), 672–682.

Hosny, A., Shahin, H., Abdelrahman, A. and El-Afandy, T. (2001). "Strengthening of rectangular RC columns using CFRP." Proc. 5th Intern. Conference on Fibre-Reinforced Plastics for Reinforced Concrete Structures, C. Burgoyne ed., 773–782.

Ilki, A., Peker, O., Karamuk, E., Demir, C. and Kumbasar, N. (2008). "FRP retrofit of low and medium strength circular and rectangular reinforced concrete columns." Journal of Materials in Civil Engineering, 20(2), 169–188.

Karantzikis, M., Papanicolaou, C. G., Antonopoulos, C. and Triantafillou, T. C. (2005). "Experimental investigation of non-conventional confinement for concrete using FRP." Journal of Composites for Construction, 9(6), 480–487.

Kim, I., Jirsa, J. O., and Bayrak, O. (2011). "Use of carbon fibre-reinforced polymer anchors to repair and strengthen lap splices of reinforced concrete columns." ACI Structural Journal, 108(5), September-October, 630–640.

Lam, L. and Teng, J. G. (2003). "Design-oriented stress-strain model for FRP-confined concrete in rectangular columns." Journal of Reinforced Plastics and Composites, 22(13), 1149–1186.

Prota, A., Manfredi, G. and Cosenza, E. (2006). "Ultimate behaviour of axially loaded RC wall-like columns confined with GFRP." Composites: Part B, 37 (670–678).

Tan, K. H. (2002). "Strength enhancement of rectangular reinforced concrete columns using fibre-reinforced polymer." Journal of Composites for Construction, 6(3), 175–183.

Tanwongsval, S., Maalej, M. and Paramasivam, P. (2003). "Strengthneing of RC wall-like columns with FRP under sustained loading." Materials and Structures, 36, 282–290.

Concrete Solutions – Grantham et al. (Eds.)
© 2016 Taylor & Francis Group, London, ISBN 978-1-138-03008-4

Durability restoration of cementitious composites via micro encapsulated mineral repair agents

C. Litina, A. Kanellopoulos & A. Al-Tabbaa
Department of Engineering, University of Cambridge, Cambridge, UK

ABSTRACT: This research proposes and evaluates an embedded self-sustained restoration system based on the trigger-release of microencapsulated repair agents within the concrete matrix. Micron-sized polymeric capsules carrying a mineral based repair agent were designed to rupture upon stress build-up, releasing the enclosed compound that set and bridged the formed cracks. Cementitious prisms incorporating microcapsules were subjected to controlled cracking and subsequently submerged in water to facilitate the self-repair process. Compressive, flexural strength and permeability tests were performed to evaluate crack width restoration and durability recovery. Two different mass fractions, i.e. 1% and 5% microcapsules/cement ratios were investigated to assess the effects on repair efficiency. The effect of age at crack onset was also considered. The healing products were isolated and characterised through SEM, TGA and XRD. Results were promising on the use of colloidal silica as a repair material for durability restoration of cementitious composites.

1 INTRODUCTION

Cracking is an intrinsic property of concrete and the main cause of service life reduction. Therefore, addressing and restricting the development of early age small cracks at their onset is favourable and could significantly improve long-term durability of concrete structures. A promising concept is the embedment of functional healing agents in the concrete to repair damage and micro-cracks when they appear. Thus repair is achieved not through external post-damage application of appropriate repair agents but through the internal triggered release of these materials in the damaged location.

This can be achieved by the application of microcapsules. This was first introduced in the field of self-healing materials by the groups of White and Sottos (White et al. 2001; Youngblood & Sottos 2008). The principle of the concept is that the cracks cause the rupture of the capsule triggering the release of the healing agent into the crack void under capillary suction.

For cementitious applications, urea-formaldehyde shells have been suggested as potential shell materials for microencapsulation aided healing. In preliminary investigations by Mihashi et al. (2000), urea-formaldehyde microcapsules (20–70 μm) were used filled with epoxy resin as part of a two-component system. The researchers however, reported poor results concluding that the quantity of repair agent was insufficient to allow adequate mixing. Wang et al. (2013) employed similar microcapsules with an epoxy core at two different contents (3% and 6%) dispersing the catalyst within the mortar matrix. This approach allowed efficient activation of the epoxy, yielding an increased healing effect exceeding 20% for higher microcapsule content.

In an effort to provide the cementitious matrix with a healing compound structurally similar or identical to the host matrix and ensure better interfacial compatibility between the healing material and the substrate, alkali-silica solutions have been introduced. Previous work by Mihashi et al. (2000), Pelletier et al. (2011) and Gilford et al. (2013) have reported on the use of such solutions as repair materials implying a potential for strength recovery.

It has been contended that these solutions react with calcium hydroxide, available during cement hydration yielding a calcium-silica-hydrate (C-S-H) gel with low Ca/Si ratio (Pelletier et al. 2011; Kendrick et al. 1998) similar to the main hydration phase of cement (Lea 1956; Neville 1996) as follows:

$$Na_2O \cdot SiO_3 + Ca(OH)_2 \xrightarrow{\rightarrow H_2O} x(CaO \cdot SiO_2) \cdot H_2O + Na_2O \quad (1)$$

$$(CaO \cdot SiO_s) \cdot H_2O + Na_2O + CO_2 \rightarrow CaCO_3 + SiO_2 + 2NaOH \quad (2)$$

This gel expands and hardens in the crack void sealing it and allowing a partial recovery of strength (Pelletier et al. 2011). Pelletier et al. and Gilford et al. introduced this alkali-silica healing agent in the matrix through a discrete system of polyurethane and urea-formaldehyde microcapsules respectively. Pelletier et al. (2011) reported a relative 20–26% recovery in flexural strength for concrete specimens after one week of curing compared to 10–14% observed for control mixes. Microcapsules were incorporated at 2% vol.

On the other hand Gilford et al. (2013) considered a higher content of microcapsules (∼5%) for autonomic healing of concrete. They considered the relative change of modulus of elasticity before and after healing to quantify the potential of the microencapsulated system. Although elastic moduli values reported an improvement compared to the control specimen, where no recovery was observed, the actual mechanical regain was limited to 11%. Moreover, an investigation on the overall durability of such a composite system has not been conducted. Concurrently data is still scarce on the use of other silica and mineral compounds.

Our research reports on the development and performance of a discrete system of polymeric microscopic carriers, namely microcapsules (MCs) to deliver and release a silica-precursor repair solution. Microcapsules were synthesised in situ through a simple one-step interfacial polymerisation process. Colloidal silica, an aqueous suspension of fine silica particles introduced in cementitious compositions for enhanced durability and mechanical performance (Green 2012), was investigated as a potential repair agent. The synthesised microcapsules were embedded in cement prisms and tested for recovery against mechanical and environmental actions. The crack width and durability recovery were assessed using optical and scanning electron microscopy (SEM), X-ray diffraction (XRD) and thermal analysis (TGA).

2 MATERIALS AND METHODS

2.1 *Microcapsule materials*

Commercially available monomers: diphenyl methylene diisocyanate (MDI) and 1,4-butanediol (BD), gum arabic (GA), polyethylene glycol (PEG400), colloidal silica (CS) Ludox®AS-40 and toluene were obtained from Sigma Aldrich, UK. These products were used without further purification. Solvents (ethanol and acetone) were of analytical grade and were used as received. Deionised water was used for all experiments.

2.2 *Preparation of the MCs*

The overall preparation procedure of the microcapsules is illustrated in Figure 1. At room temperature, 120 ml of deionised water and 13.5 g of GA as surfactant were mixed in a 500 ml beaker. The solution was agitated at 500 rpm for 3 hrs on a magnetic stirrer, with a 40 mm magnetic stub before beginning encapsulation. MDI (9 g) and 0.9 g of BD were completely dissolved in 10 ml toluene. Once the prepolymer was completely dissolved, CS was added and mixed well for 30 min. The mixture was then slowly poured into the GA solution. Then the latter was heated at 50°C and 8.2 g of PEG400 (as a crosslinker) were slowly added to the emulsion. The beaker was covered and heated at 70°C for 2 hrs. Once cooled to ambient temperature, the suspension of microcapsules was separated from the mother liquor and left in water overnight.

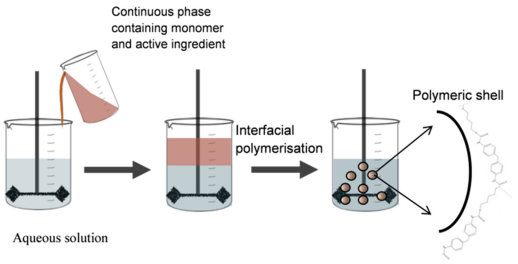

Figure 1. Schematic representation of the microcapsule preparation process via interfacial polymerisation.

The microcapsules were washed with deionised water and ethanol several times, separated by decantation, filtered and dried in air for 24–48 hrs and collected finally as a free-flowing powder.

2.3 *Preparation of cement specimens*

The studied cement paste mixtures were composed of ordinary Portland cement (CEM I 52.5 N), water and a varying amount, i.e. 1 and 5% of microcapsules expressed as mass% (m%) of cement weight. The water to binder (total solids) ratio adopted in this design was kept constant (w/c = 0.6 by weight). The mixing sequence was the following: the cement and the microcapsules introduced as a dry powder were first mixed to ensure uniform distribution and then the water was added to form the paste. For the control specimens, microcapsules were not incorporated into the mixing.

When the mixture was consistent and uniform, it was cast into moulds. The series used for three-point-bending and compressive strength tests consisted of six, $160 \times 40 \times 40\,mm^3$ prism and $50 \times 100\,mm^2$ cylindrical samples respectively. Cylindrical discs were used in the permeability tests and were 50 mm in diameter and 15 mm high. All specimens were demoulded after 24 hrs and then either tested directly or cured under water for an additional 27 days prior to testing; the former to establish the early age effect while the latter the later age effect on the properties. The studied mixtures with their composition and curing conditions are listed in Table 1.

2.4 *Characterisation and testing of materials*

2.4.1 *Optical and SEM imaging of the MCs*

Images of dried microcapsules were obtained using scanning electron microscopy (SEM, EVO LS 15, Carl Zeiss). Capsule diameter measurements and size distribution was estimated using ImageJ analysis software. Samples were prepared by dropping an aliquot (ca. 40 µl) of the particle suspension onto an SEM stub (12.5 mm diameter) and oven drying at 40°C for 30 min. The resulting powder sample was sputter coated with a thin layer of gold (∼10 nm).

Table 1. Studied paste samples with their code, m% of MCs, method of cracking, curing conditions and number of specimens tested.

Specimen	Reference	m% of MCs	Cracking	Curing regime	Number
Prism	CI	0	3-point bending test	Water curing	6
	CIMC1	1			6
	CIMC5	5			6
Cylinders	CI	0	Compressive Splitting	Water curing	6
	CIMC1	1			6
	CIMC5	5			6

2.4.2 *Influence of microcapsules on cement properties*

The effect of microcapsules on both fresh and hardened cement properties was investigated. Viscometric studies were conducted to explore the rheological changes due to variant composition. The viscometric studies of the pastes were conducted on a Brookfield DV3T Rheometer adopting a shearing profile to emulate typical cementing applications; like pumping, pouring and spreading of the material, between 0 and 100 s^{-1} (Banfill 2006; Saak et al. 2001). Moreover, the setting time of the compositions was estimated to isolate any adverse effects of uncontrolled release of healing material. The test was performed following BS EN196:3/2005 and using an automated Vicat apparatus with different attachments for the determination of the initial and final setting time.

Finally, compressive strength tests were performed on cylindrical specimens to assess the effects of microcapsule content on cement hydration and strength development. This latter further provided an indication of the survivability of the microcapsule through the mixing process and within the matrix. crack width reduction and durability recovery.

By means of a displacement-controlled three-point-bending test, cracking was induced on the composite prisms at two different ages; 1 day and 28 days after demoulding, ensuring a displacement-controlled quasi-static loading (0.002 mm/s). The displacement was increased until the maximum flexural capacity was reached. A large final crack was formed. To control the cracking and avoid abruption of the fragments, external lateral support was in place. Cracked samples were then placed in high moisture conditions for a set period of 28 days to impart healing. Specimens containing encapsulated healing agent were autonomously healed when allowed to cure. The healing efficiency (H_{eff}) was estimated as the ratio of the recovered ultimate strength over the initial capacity. In between both loading periods, microscopic observations were performed.

For the determination and quantification of the sealing recovery, the gas permeability method and apparatus proposed by Alshamsi and Imran (2002) were adopted. According to the method the permeability coefficient can be calculated as follows:

$$k = \frac{2L\eta P_2 Q}{A(P_1^2 - P_2^2)} \quad (3)$$

where η = the dynamic viscosity (Ns/m^2); Q = the volumetric flow rate (m^3/s); L = the length of the sample (m); P_1 = the inlet pressure (N/m^2); P_2 = the outlet pressure (N/m^2) and A = the cross-sectional area perpendicular to the flow direction (m^2). The apparent intrinsic permeability coefficients calculated with the described method had to be corrected to obtain proper permeability coefficient values. For that purpose, Darcy's law was assumed:

$$K = \frac{k\rho g}{\mu} \quad (4)$$

where k = the estimated intrinsic permeability coefficient; g = the gravitational acceleration (m/s^2) and ρ = the density (kg/m^3), and μ = the viscosity of the fluid properties (Pa.s); in this case methanol gas.

For each composition, samples were tested at 1 day and 28 days respectively. Permeability tests were carried out after cracking the specimens by means of a laterally confined compressive test. Half were loaded to their respective ultimate compressive strength and then set aside for 28 days in water to allow the healing process to take place. The rest of the same batch was used to benchmark the healing efficacy. Before testing, the disk specimens were vacuum-dried for 24 hrs to remove the moisture within specimens and then placed and sealed on the top of a cell with silica gel sealer to avoid leakage of methanol vapor (Figure 2).

2.4.3 *Microscopic observation of microcracks and SEM/XRD analyses*

A microscopic analysis was performed to examine the cracks and measure the crack width variation with time due to healing. After cracking, the crack planes were analysed using a stereomicroscope with a camera and crack widths were determined at equally spaced locations along the crack length. The ImageJ (NIH) image analysis computer package was used to measure the crack width (Van Tittelboom et al. 2012). A quantitative comparison between the different compositions was calculated according to the following equation, similar to γ adopted by Jiang et al. (2015):

$$\zeta(t) = \left(1 - \frac{A(t)}{A_o}\right) \times 100 \quad (5)$$

where A_o = the area of the crack-opening at the time of the cracking (μm^2) and A(t) = the area of the

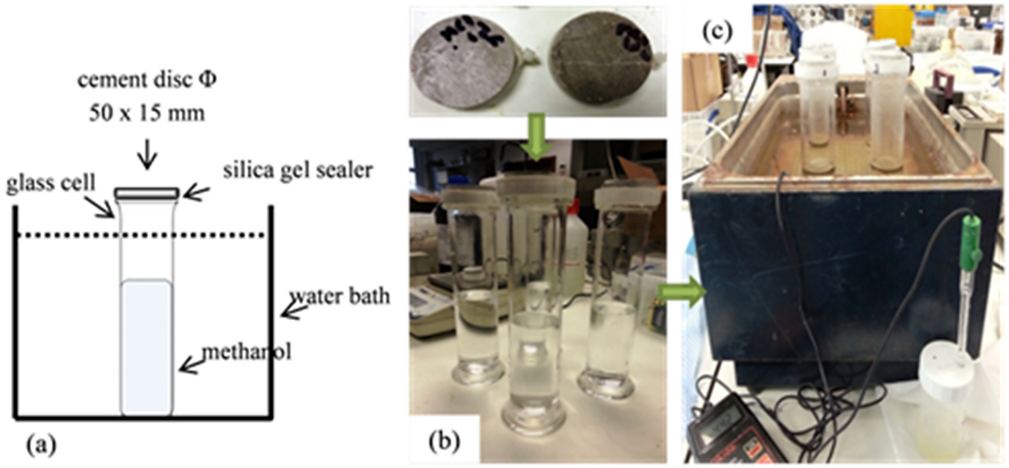

Figure 2. (a) Schematic illustration of experimental setup for the gas permeability test; (b) sample preparation and (c) configuration adopted for research needs.

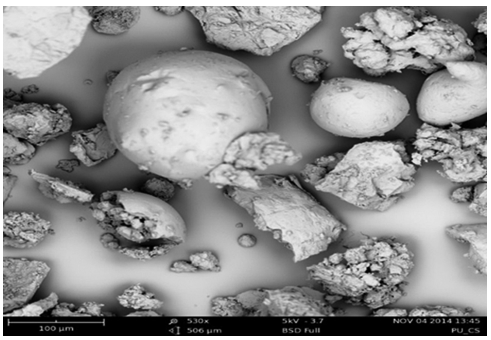

Figure 3. SEM images of produced polyurethane microcapsules.

crack-opening obtained after t days of crack healing (μm^2). Subsequently a value of ζ close to zero means that no crack healing occurred while a value of 100% means that complete crack healing has been achieved. To further examine the distribution of microcapsules within the composite cement material and the localised morphology at the crack at the microscopic level, samples were extracted from the crack flanks and subjected to scanning electron microscopy.

A thermogravimetric analysis (TGA) was performed with a Perkin Elmer STA 6000 instrument to determine the composition of the white crystallisation residue found on the crack planes and to identify the healing materials. To further analyse and identify the mineralogy of the extracted healing products X-ray diffraction (XRD) was used.

3 RESULTS AND DISCUSSION

3.1 *Morphology of the MCs*

The surface and shell morphology of the developed microcapsules are shown in Figure 3. Microcapsules appeared to retain a spherical structure. SEM images of PU microcapsules revealed capsules with maximal diameter of 55.6 μm and relatively smooth and non-porous walls. They appeared individually distributed with no visible conglomeration. Microcapsule yield, shown in Table 2, was measured by the mass of capsules collected as a solid residue at the end of the experimental process compared to the mass of solids used in the encapsulation (i.e. shell wall forming materials and core).

Table 2. Characteristics of produced microcapsules.

Yield	Diameter	Wall thickness
(%)	(μm)	(μm)
52 ± 30	40.6 ± 15	4.4 ± 2.6

This percentage is higher compared to previous results for polyurethane microencapsulation (Saihi et al. 2006; Bouchemal et al. 2004; Frére et al. 1998) and remained consistent during the production process.

3.2 *Durability enhancement of the cement speciments*

The effect of microcapsules on the fresh material properties is presented collectively in Table 3. A close examination of the results reveals that an increase in microcapsule content from 1% to 5% significantly affects the viscosity. Microcapsules seem to behave like chemical admixtures. Organic admixtures have functional charged groups and when added in cement adsorb on the surfaces of cement particles and hydration products via electrostatic forces. Thus adsorption can alter the surface properties of cement particles and

Table 3. Effect of microcapsule content on fresh material proeprties.

Mix ref	Plastic viscosity (cP)	Setting time (hrs)	Density (kg/m^3)
CI	77	7.95	1739
CIMC1	68	6.67	1742
CIMC5	89	6.98	1757

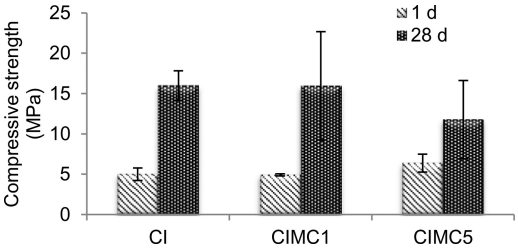

Figure 4. Effect of microcapsule content on 1 day and 28 day compressive strength.

thus the interparticle relationship of the suspension (Jolicoeur & Simard 1998).

Moreover, one cannot dismiss the effect of potential free colloidal silica powder in the system. That can be introduced either via unexpected release during mixing process or as unbound core material leftover from microcapsule processing.

The initial and final setting time of microcapsule-doped mixes confirm a relative acceleration in setting time. Indicatively, CIMC1 reported a 16% reduction, compared to the neat cement paste whereas sample prepared with highest microcapsule content (CIMC5) a 12% reduction in final setting time. Although no clear pattern can be discerned concerning the variation of microcapsule content, the results do confirm implications on presence of core material. The available CS could have acted as an accelerator of the cement hydration process either by providing a reactive siliceous surface for early C-S-H precipitation or through direct pozzolanic reaction with free calcium hydroxide. Similar findings on the behaviour of nano silica on cement hydration have been reported (Senff et al. 2009).

The effect of microcapsule content on the strength development is reflected in Figure 4. This corresponds well to the accelerated setting time values discussed previously; Thus identifying the contribution of free available core material to the higher strength development. Nonetheless the fluctuation in the results could account for gravitational forces imposing segregation; but more importantly infer a potential uneven distribution of microcapsules within the samples.

Figure 5 illustrates the typical response at 3-point bending for mixes initially tested at two different ages; 1 day and 28 days and again retested after a 28 day healing period. The recovery of mechanical properties is indicative of self-recovery. As expected the

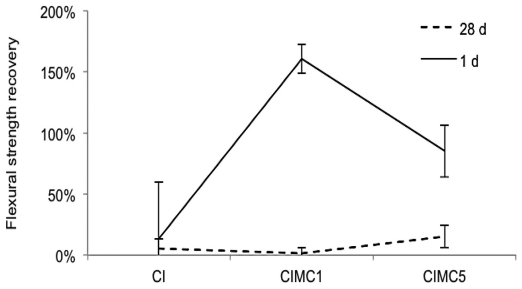

Figure 5. Relative flexural strength recovery for healed sspecimens. Samples had been initially tested either at 1 day or 28 days, respectively and then retested after a 28 day healing period.

addition of microcapsules does initially impair the flexural strength. Nevertheless, it is accountable for an almost complete strength recovery. Results revealed that even for low microcapsule concentration, the healing efficiency more than doubled compared to the control specimen. Thus it can be inferred that the recovery potential compensates for the initial strength reduction. However, a concern is raised by the result variability as it may reflect an inefficient distribution of microcapsules within the pastes, in particular for lower microcapsule concentrations. Moreover, the lack of reinforcement and aggregates and overall internal support enhanced the deviation of the results. Yet the consistency of the recovery was much improved with an increase of microcapsule content.

3.3 *Gas permeability of cement specimen*

Figure 6 illustrates permeability recovery values for samples cracked at 1 and 28 days respectively for variant microcapsule content. After the cracking occurs, the relative recovery of permeability appears higher in cementitious mixes enhanced with microcapsules. Not only do the microcapsules allow the formation of denser structures but also a recovery exceeding even 100%. However, confirming strength recovery results, this relies on the mass of microcapsules added. A similar trend can be observed at a later age. Mature mixes produce denser structures due to the evolution of the hydration process. It could be assumed that if the mineral precursor was added from the start or released directly the material would have been already consumed towards a denser structure and wouldn't be able to exhibit any significant sealing recovery. Although there were implications for the microcapsule enhanced specimen, there was sufficient agent available to allow for a better recovery.

3.4 *Microscopic analyses*

Macroscopic results from strength and permeability recovery imply that the behaviour of microcapsule-doped pastes emulates plain cement specimens. Still results are improved as the crack closing ratio demonstrates (Fig. 7). The latter supports the initial

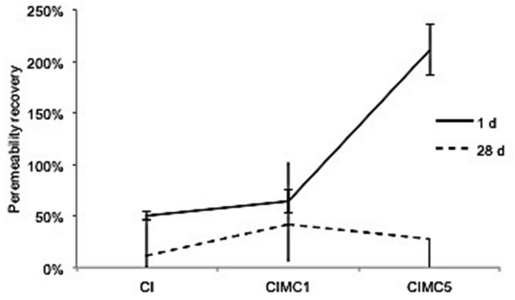

Figure 6. Permeability reduction achieved for healed samples prepared with microcapsules. Samples were tested at 1 day and 28 days respectively and then retested after a 28 day healing period.

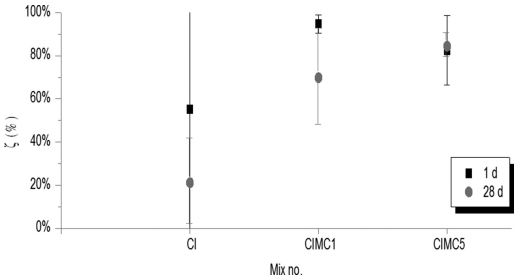

Figure 7. Surface crack-closing ratio (ζ%) for each of the mix compositions under investigation.

hypothesis that silica precursors participate in autogenic healing patterns, enhancing and improving them nonetheless.

A suggested mechanism would imply the reaction of colloidal silica with available portlandite stimulating further cement hydration as follows:

$$SiO_2 + Ca(OH)_2 \rightarrow x(CaO \cdot SiO_2) \cdot H_2O \qquad (5)$$

However, whether this is the case *in situ* remains in question. Therefore, to compliment microscopic investigations, clarify the recovery mechanism and establish the contribution of the encapsulated agents, microstructural analyses were performed. SEM micrographs of samples extracted from the crack planes can be viewed in Figure 8.

Images confirm literature findings about the structural nature of healing products; ettringite formation and calcite can be discerned, together with an amorphous structure of hydrates. However, for samples prepared with higher microcapsule addition, more distinct products are formed, whereas for lower contents, no distinct contribution to the hardened cement matrix can be observed. Microcapsules can be distinguished, some intact, others ruptured allowing release and reaction of healing agent. Nonetheless, in either case they seem integrated and encompassed in the surround matrix of healing material, thus, suggesting that they could behave as nucleation sites for particle precipitation. Moreover, a three dimensional mesh-like structure formed of nanoparticles appears implying



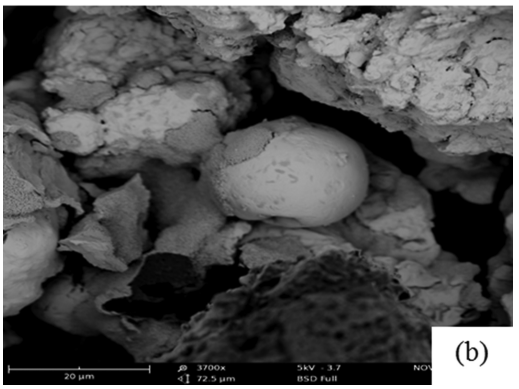

Figure 8. SEM micrographs of samples extracted from crack planes. (a) Surface characteristics and morphology of healing material extracted from CIMC1; Broken microcapsules entangled in ettringite needles. Calcite crystals visible; (b) Morphology of healing product extracted from CIMC5, crystalline structure generated from the microcapsule.

a thin C-S-H network. This confirms the suggested mechanism of CS reaction.

The reduced permeability can be attributed to the self-healing effect of the microcapsules. The observations under XRD and TGA (Fig. 9 and 10) confirm that the microcracks in specimens incorporating microcapsules were healed mainly with calcium carbonate and portlandite (Van Tittelboom et al. 2012; Yang et al. 2009; Snoeck et al. 2012). The characterisation by TGA gave indication of the components of healing materials formed in cracks. Although the gel-like material lacks the crystalline orientation and may not be clearly identified, the mineral phases intertwined can be elucidated through XRD analysis. Overall, diffractograms presented similar trends to the healing products extracted from plain CI samples mainly calcite and portlandite.

Moreover, there was indication of the contribution of hydration products; gennite and tobermorite-like phases identified attest to further hydration products both at early age and in mature specimens. Ettringite was only observed as part of the cementitious matrix

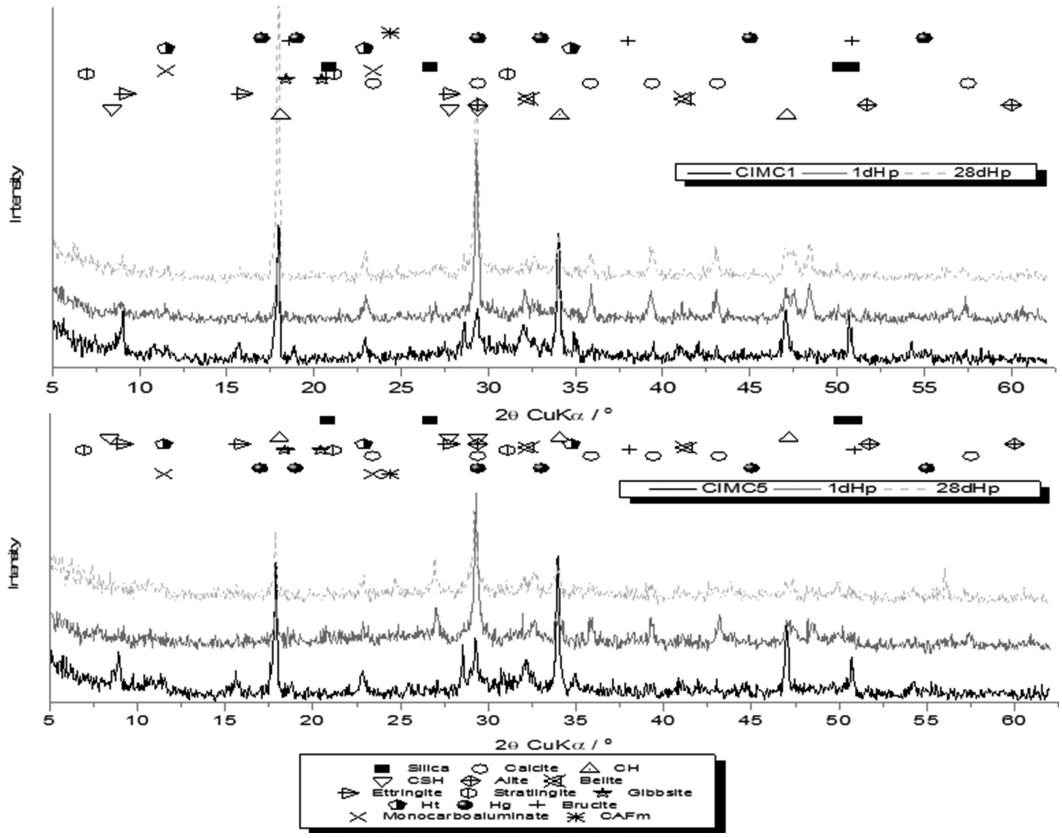

Figure 9. XRD diffraction peaks of bulk paste and healing material produced by early (1 day) and mature cracking (28 days) for (top) CIMC1 and (bottom) CIMC5.

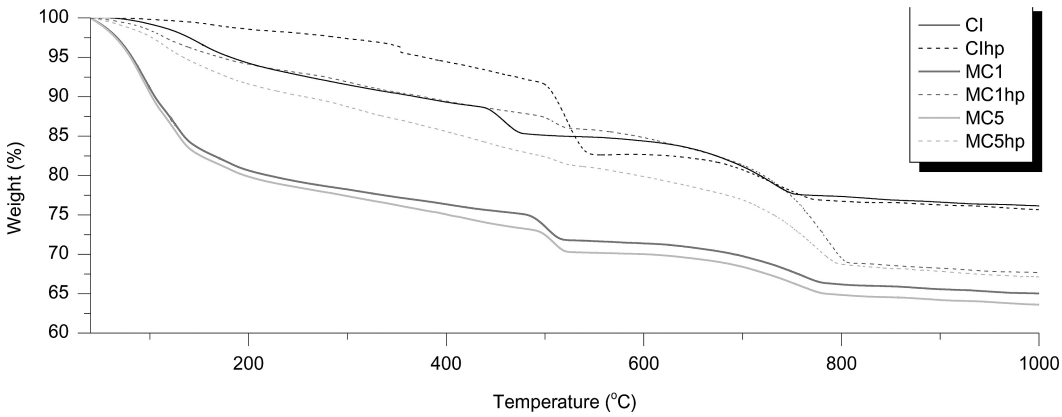

Figure 10. Comparative TG curves of reaction products (denoted as hp) formed in cracks and bulk paste. Initial crack onset is at the age of 1 day and 28 days, respectively and healing time is 28 days.

and not included in the healing products, confirming the SEM images. There is no strong evidence of extended carbonation. Thus it could be assumed that the increased silica content provided by the microcapsule system, bound excessive portlandite levels decelerating calcium carbonate yield.

4 CONCLUSION

This work detailed the investigation of the performance of the proposed composite-microcapsule/binder-system. The addition of a 'foreign' material in the cementitious matrix can have adverse effects on

the development of physical and mechanical properties of the latter. However, that is dependent on the microcapsule content.

However, the real contribution of the microcapsule system is demonstrated in the recovery of material properties after induced micro cracking:

- The inclusion of micro particles was demonstrated to reduce the gas permeability of hydrated cement composites. The reduced permeability can be attributed to the self-healing effect of the microcapsules;
- A gel-like material was observed in the cracks bridging the crack flanks and protecting from intrusion of environmental compounds. This material was considered to behave as a scaffold for the precipitation/interlocking/interaction of autogenic healing materials;
- XRD and TGA results confirmed the mineral phases products. Healing products typical for neat cement were identified implying a complementary support mechanism by the microencapsulated system;
- The age of crack onset affected the overall efficiency of the healing mechanism but not the mechanism of microcapsule contribution. Material released gelates, reacting with portlandite to form a C-S-H network, underpinning the precipitation of other healing materials;
- Thus strength recovery still primarily relies on the nature of healing materials precipitated;
- Despite implied survivability concerns, the self-healing pattern confirmed sufficient material still in place for recovery after processing.

These quantitative and qualitative observations constitute a proof of concept that the proposed microcapsule system works. Investigation is under way to assess the efficiency of the proposed system under variant curing regimes and environmental conditions.

ACKNOWLEDGEMENTS

Financial support from the Engineering and Physical Sciences Research Council (EPSRC) and the Hellenic States Scholarship Foundation for the PhD study of the first is gratefully acknowledged. Support from EPSRC for the Materials for Life project (EP/K06631/1) is also gratefully acknowledged.

REFERENCES

Alshamsi, A.M. & Imran, H.D.A. 2002. Development of a permeability apparatus for concrete and mortar. *Cement and Concrete Research*, 32(6), pp. 923–929.

Banfill, P.F.G. 2006. Rheology of Fresh Cement and Concrete. *Rheology Reviews*, pp. 61–130.

Bouchemal, K. et al. 2004. Synthesis and characterization of polyurethane and poly(ether urethane) nanocapsules using a new technique of interfacial polycondensation combined to spontaneous emulsification. *International Journal of Pharmaceutics*, 269(1), pp. 89–100.

Frére, Y., Danicher, L. & Gramain, P. 1998. Preparation of polyurethane microcapsules by interfacial polycondensation. *European Polymer Journal*, 34(2), pp. 193–199.

Gilford, J. et al. 2013. Dicyclopentadiene (DCPD) and Sodium Silicate Microencapsulation for Self-Healing of Concrete. *Journal of Materials in Civil Engineering*, pp. 886–896.

Green, B.H. 2012. Development of a High-Density, High-Strength, Cementitious Grout Using Colloidal Silica Nano-Particles (ASCE). In *Grouting and Deep Mixing*. pp. 1850–1858.

Jiang, Z., Li, W. & Yuan, Z. 2015. Influence of mineral additives and environmental conditions on the self-healing capabilities of cementitious materials. *Cement and Concrete Composites*, 57, pp. 116–127.

Jolicoeur, C. & Simard, M.-A. 1998. Chemical admixture-cement interactions: Phenomenology and physico-chemical concepts. *Cement and Concrete Composites*, 20(2–3), pp. 87–101.

Kendrick, D., Parsonage, J. & Vazifdar, R. 1998. Interaction of alkali and alkali earth metal hydroxides with microsilica. *Cement and Concrete Research*, 28(11), pp. 1537–1544.

Lea, F.M. 1956. *The chemistry of cement and concrete* 2nd ed., London: Edward Arnold ltd.

Mihashi, H. et al. 2000. Fundamental Study on Development of Intelligent Concrete Characterized by Self-Healing Capability for Strength. *Concrete Research and Technology*, 11(2), pp. 21–28.

Neville, A.M. 1996. *Properties of concrete* 4th and Fi., New York: Wiley and Sons, Inc.

Pelletier, M. et al. 2011. *Self-healing concrete with a microencapsulated healing agent*, Kingston, USA.

Saak, A.W., Jennings, H.M. & Shah, S.P. 2001. New Methodology for Designing Self-Compacting Concrete. *Materials Journal*, 98(6), pp. 429–439.

Saihi, D. et al. 2006. Microencapsulation of ammonium phosphate with a polyurethane shell. Part II. Interfacial polymerization technique. *Reactive and Functional Polymers*, 66(10), pp. 1118–1125.

Senff, L. et al. 2009. Effect of nano-silica on rheology and fresh properties of cement pastes and mortars. *Construction and Building Materials*, 23(7), pp. 2487–2491.

Snoeck, D. et al. 2012. Self-healing cementitious materials by the combination of microfibres and superabsorbent polymers. *Journal of Intelligent Material Systems and Structures*, 25(1), pp. 13–24.

Van Tittelboom, K. et al. 2012. Influence of mix composition on the extent of autogenous crack healing by continued hydration or calcium carbonate formation. *Construction and Building Materials*, 37(null), pp. 349–359.

Wang, X. et al. 2013. Experimental Study on Cementitious Composites Embedded with Organic Microcapsules. *Materials*, 6(9), pp. 4064–4081.

White, S.R. et al. 2001. Autonomic healing of polymer composites. *Nature*, 409(6822), pp. 794–7.

Yang, Y. et al. 2009. Autogenous healing of engineered cementitious composites under wet–dry cycles. *Cement and Concrete Research*, 39(5), pp. 382–390.

Youngblood, J.P. & Sottos, N.R. 2008. Bioinspired Materials for Self-Cleaning and Self-Healing Self-Cleaning Surfaces?: *MRS Bulletin*, 33(August), pp. 732–741.

Concrete Solutions – Grantham et al. (Eds.)
© 2016 Taylor & Francis Group, London, ISBN 978-1-138-03008-4

Cyclic response of large lightly reinforced concrete walls made of plain and fibre concrete

C.G.R. Mircea & A. Faur
Technical University of Cluj-Napoca, Romania

A. Harcsa & M. Mulea
Artifex Engineering Ltd. Cluj-Napoca, Romania

C. Baera
NIRD Urban-Incerc Cluj-Napoca Branch, Romania

ABSTRACT: Large lightly reinforced concrete walls performed very well during numerous earthquakes after 1950. Two full scale specimens were tested to cyclic loading. The specimens were made of plain concrete and polypropylene Fiber Reinforced Concrete (FRC). The paper refers to the structural performance of the specimens, focusing on the energy dissipation capacity, aiming to find out if such solutions may provide an adequate seismic response for low rise buildings.

The results prove that FRC shear walls can ensure behavior factors with values corresponding even for medium ductility members. Even a low fiber content has the ability to double the failure drift of a plain concrete wall. A higher fiber content is expected to provide an adequate failure warning, similar to the flexural failure.

1 INTRODUCTION

1.1 *Basics of force based seismic design of shear walls*

The shear wall density (i.e., the ratio between the walls' cross-sectional area and the floor area) has values of 3–4 % at current collective multistory shear wall structures (e.g., cellular and comb type). When dealing with very low rise buildings (e.g., one or two stories), the wall density may decrease even below 2.0 %, depending on the severity of the seismic hazard. Such structures are defined by EN 1998-1:2004 as structures with large lightly reinforced concrete walls, because there is no need for a large quantity of reinforcement, and confining of the wall ends is not necessary. However, the inelastic response of such structures is still in debate due to the lack of traditional flexural ductility.

Seismic design philosophy implies the inelastic response of the structures when analyzed to the Ultimate Limit State, usually ensured by the yielding of the tensioned reinforcement. Hence, for slender/flexible structures, the traditional force based design considers the elastic shear base (F_{be} – associated to the fully elastic response) reduced by the behavior factor q

$$F_{by} = F_{be}/q \tag{1}$$

that actually is equal to the displacement ductility factor when considering the equal displacement of the structural system (Fig. 1), as introduced by Newmark & Hall (1973):

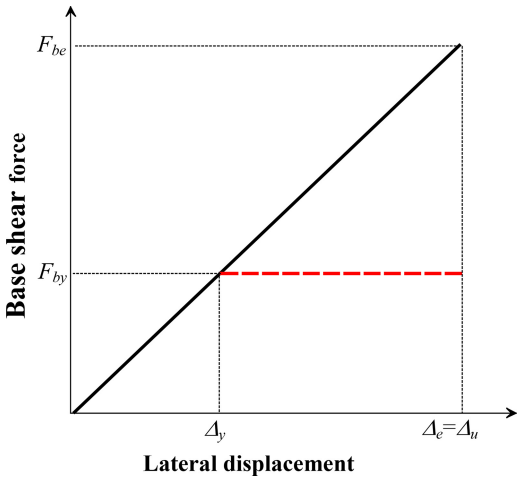

Figure 1. Equal displacement approach in determining the behaviour factor.

$$q = \mu_\Delta = \Delta_u/\Delta_y \tag{2}$$

However, such a ductile inelastic response is not probable when dealing with squat shear walls and large lightly reinforced concrete walls. For such structures,

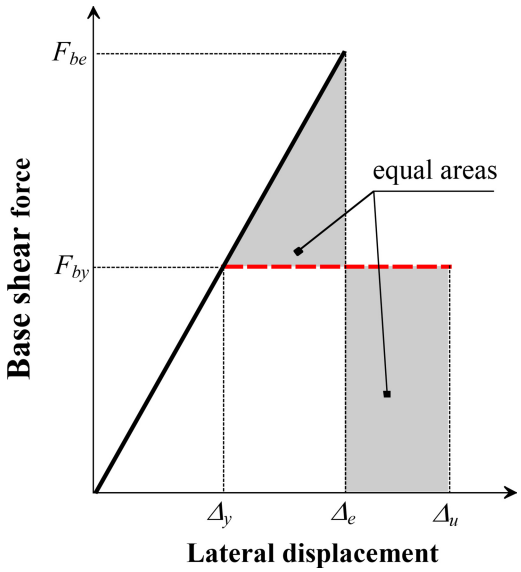

Figure 2. Equal energy approach in determining the behavior factor.

the behavior factor results applying the equal energy principle are shown in Figure 2 (Como & Lanni, 1979):

$$q = \sqrt{2\mu_\Delta - 1} \tag{3}$$

By the definition given in EN 1998-1, a large lightly reinforced concrete wall is a *"wall with large cross-sectional dimensions (horizontal dimension l_w at least equal to 4.0 m or two-thirds of the height h_w of the wall, whichever is less) due to which it is expected to develop limited cracking and inelastic behavior in the seismic design situation"*. A note mentions that that *"such a wall is expected to transform seismic energy to potential energy (through temporary uplift of structural masses) and to energy dissipated in the soil through rigid-body rocking, etc. Due to its dimensions, or to lack-of-fixity at the base, or to connectivity with large transverse walls preventing plastic hinge rotation at the base, it cannot be designed effectively for energy dissipation through plastic hinging at the base."*

While significant research has been done on ductile shear walls, less scientific evidence is available with respect to the seismic behavior of large lightly reinforced walls.

Even the previous definition does not provide clear information. Despite the definition and associated notes, EN 1998-1 frames large lightly reinforced concrete walls as medium ductility (i.e., ductile walls) and low ductility members (Fig. 3). For the medium ductility class, which can be designed even in important seismic zones, flexural ductility is intrinsically associated. For the low ductility class, gravitational design rules may be applied and the solution may be considered for the design in low seismic activity zones.

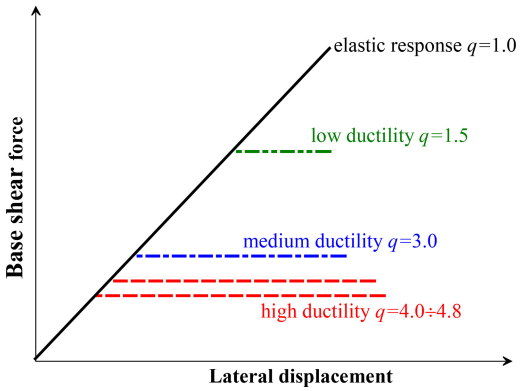

Figure 3. Ductility classes and behavior factors for shear wall structures according to EN 1998-1:2004.

1.2 *Concrete toughness and inelastic response*

After the 1960's, important research was done to improve the properties of plain concrete. Disperse fiber reinforced concrete (FRC) is a significant option. Since than, even if important results were obtained, practical application of those findings is limited. In general, toughness is a very important characteristic of structural materials in all fields of engineering. However, when dealing with concrete it was neglected even in the research prior to the mid 1970's. Even today, codes do not address clear specifications to the use of this property in structural design. Nevertheless, as can be expected, toughness of concrete can dramatically influence the inelastic response of a structure. An increased toughness of concrete should result in a higher fracturing energy, even in shear failure. Various fiber types (e.g., steel, polypropylene, glass, aramid etc.), in a variety of shapes, contents and mixed compositions may be used in order to increase the toughness of concrete.

Up to the present, several proposals have been made to quantify the toughness of concrete through bending tests performed on notch or unnotched beams, in various loading arrangements. Figure 4 presents the most significant proposals for the quantification of the dimensionless toughness index, a measure of the energy adsorption capacity of concrete. Heneger (1978) defined the toughness index as the ratio of the amount of energy required to deflect a fiber concrete specimen up to 1.9 mm, to the energy corresponding to bring the specimen to the point of the first crack (Fig. 4a). Johnson (1982) suggested that toughness indices are related to a number of prescribed deflections corresponding to multiples of the first-crack deflection (Fig. 4b). A more general formulation (i.e., applicable both to notched and unnotched specimens and various loading arrangements) is given by Barr & Hasso (1985), which introduced the toughness index as the ratio of two areas under the load-deflection curve up to two-times the deflection at first-crack (Fig. 4c).

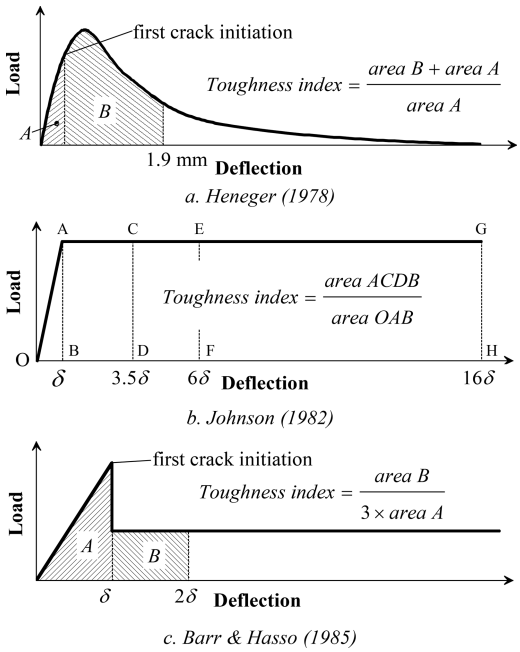

Figure 4. Main proposals for the quantification of the dimensionless bending toughness index of concrete.

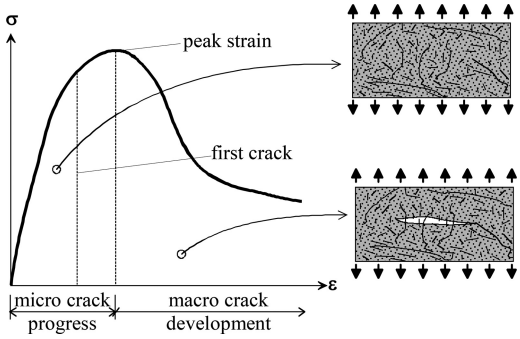

Figure 5. The use of the first peak instead of the first crack in determining toughness parameters.

To avoid the ambiguity and subjectivism in determining the first crack, strongly influenced by the size of the specimen, Gopalaratnam & Gettu (1995) proposed to use the first peak instead of the first crack, as shown in Figure 5.

More recently, based on shear tests, Rao & Rao (2010) showed that the shear toughness indices are up to fifteen times higher than the bending toughness indices. Such a conclusion is explained through the different crack propagation mechanism, which is dominated by the combined action of shear, compression and aggregate interlocking.

Therefore, it is an obvious conclusion that such a material seems to satisfy the codes' provisions with regard to the seismic performance, even when shear failure is assumed. Such a failure is usually associated with a rigid behavior, characteristic to the small cantilevers vulnerability of low rise buildings.

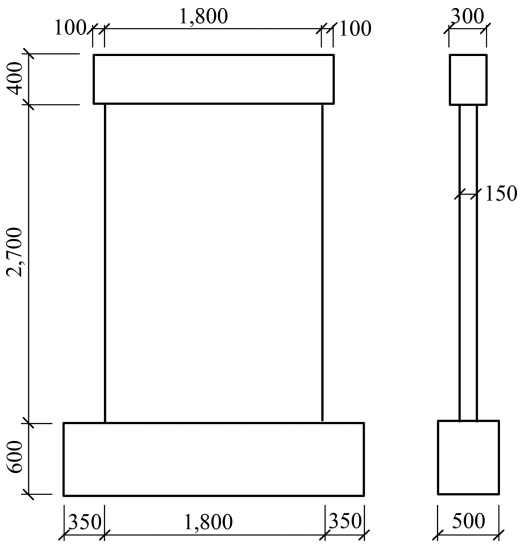

Figure 6. Geometric parameters of the experimental specimens.

1.3 *Research significance*

Some experimental research was performed with regard to the energy dissipation mechanism and inelastic behavior of large lightly reinforced/plain concrete walls. Two static-cyclic tests were performed on a wall specimen made of plain concrete, and polypropylene FRC respectively. The aim of the tests was to provide information if such walls (e.g., FRC, discrete/discontinuous reinforced concrete) may be considered in the seismic design of one/two floor shear wall structures. In order to increase the economical potential, polypropylene fibers were considered in a low content mix composition, currently available on the concrete manufacturing market.

The results prove that FRC shear walls can ensure behavior factors with values corresponding even for medium ductility members and are a valuable solution for the structure of low rise buildings.

2 EXPERIMENTAL PROGRAM

2.1 *Test set-up*

Two experimental specimens (Fig. 6) were subjected to static-cyclic loading. The shear wall panels were connected to the head beam and bottom anchored footing by reinforced concrete belts. The first wall specimen was made of plain concrete, while the second one was made by FRC, by adding polypropylene fibers to the same fresh plain concrete mix.

Table 1. Strength of concrete.

Specimen	f_{cm} MPa	f_{ctm} MPa	f_{ck} MPa	f_{ctk} MPa	f_{cd} MPa	f_{ctd} MPa
plain concrete	18.07	1.62	12.07	1.13	10.06	0.95
FRC	17.76	2.52	11.76	1.76	9.80	1.47

Table 2. Polypropylene fibers properties.

Density kg/cm^3	Tensile strength MPa	Tensile modulus GPa	Length mm
0.91	620–758	4.70	38/54

Table 3. Johnson's toughness indices.

Specimen	I_5	I_{10}	I_{30}
plain concrete	1.00	1.00	1.00
FRC	1.86	2.82	8.54

The properties of concrete, determined by standard compressive and flexure tests at the age of testing, are shown in Table 1. The characteristic and design strengths were calculated according EN 1992-1-1, with a partial safety factor of 1.20.

A low polyethylene fiber (monofilament/ fibrillated type) content of 0.5 % in volume (i.e., 4.5 kg/m^3 of concrete) was considered. The properties of the fibers are shown in Table 2. Table 3 shows the Johnson's toughness indices obtained through standard flexural tests.

The tests were performed without axial force, which is a reasonable assumption for low rise buildings. Thus, the bending capacity was found considering a fully plasticized tensioned area:

$$M_u = \gamma W_{cr} f_{ct} \tag{4}$$

where γ = correction factor, W_{cr} = cracking resistance modulus and f_{ct} = the tensile strength of concrete (e.g., f_{ctm}, f_{ctk} and f_{ctd}, upon case). Then, the associated shear forces V_u were found by dividing the bending capacity with a lever of arm of 2.90 m. The ultimate shear force V_R was calculated considering only the compressed concrete section:

$$V_R = f_{cv} A_{cc} / k \tag{5}$$

with f_{cv} = the shear strength of concrete (equal with the tensile strength), A_{cc} = area of compressed concrete at the bending capacity and k = shear distribution factor. The significant values are shown in Table 4.

Table 4. Estimated bending and shear capacities.

Specimen	Reference strength	M_u kNm	V_u kN	V_R kN
plain concrete	f_{ctm}	153.9	56.0	153.4
	f_{ctk}	107.3	39.0	107.0
	f_{ctd}	90.2	32.8	90.0
FRC	f_{ctm}	239.3	87.0	238.6
	f_{ctk}	167.2	60.8	166.7
	f_{ctd}	139.6	50.8	139.2

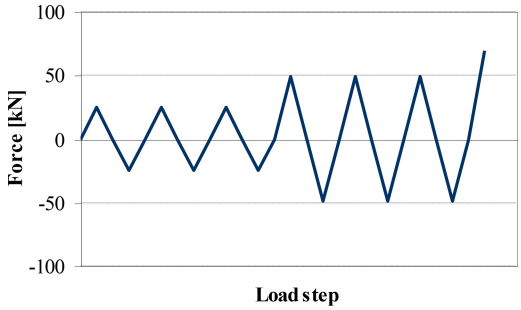

a. plain concrete model

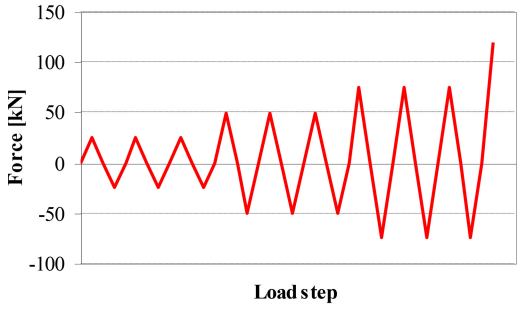

b. FRC model

Figure 7. Loading programs.

As results from Table 4, a bending failure was expected in both cases. The associated loading programs are shown in Figure 7. After several alternate loading cycles, the loads were gradually increased up to failure.

The testing stand is shown in Figure 8. The instrumentation of the experimental specimenss with force transducers, displacement transducers and strain gauges permitted monitoring loads, lateral displacements and strains on the concrete surface. The load was quasi-statically applied in small increments up to the target values.

2.2 *Results*

Figure 9 presents the cyclic behavior of the tested specimens, Figure 10 the comparative base shear – drift envelopes and Figure 11 the failure fractures.



Figure 8. Testing stand.

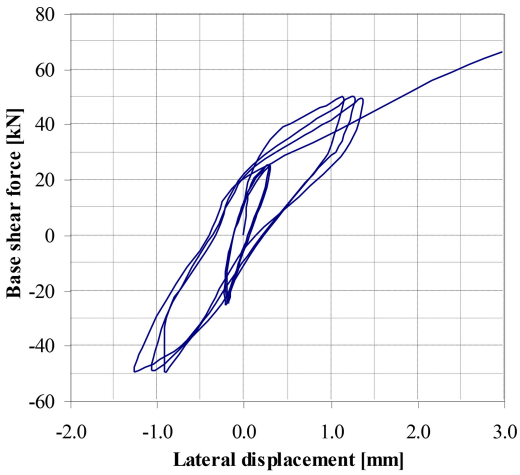

a. plain concrete model

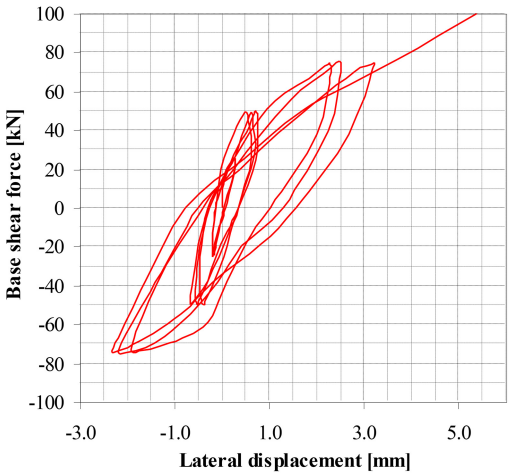

b. FRC model

Figure 9. Registered cyclic behavior.

Despite the appearance of two sliding shear failures, both failures are flexural failures which are explained by the unstable propagation of the normal flexural crack. Such fractures are typical for plain concrete,

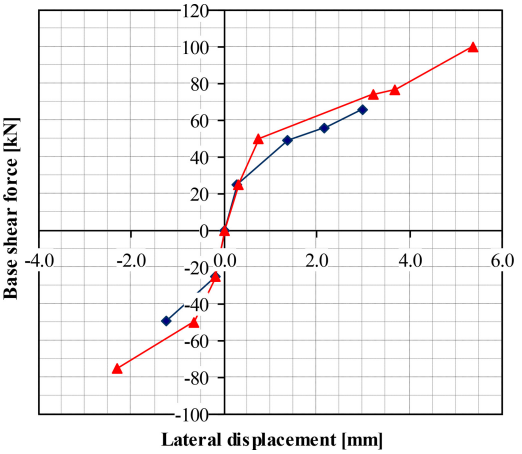

Figure 10. Cycling envelopes.



a. plain concrete model



b. FRC model

Figure 11. Failure fractures.

while more cracks develop in the case of reinforced concrete. The failure shear forces were 66.0 kN for the plain concrete specimen and 99.7 kN for the FRC specimen, respectively. The associated drifts were of 3.0 mm (i.e., relative drift of meaning 0.11 %), and 5.4 mm (i.e., relative drift of meaning 0.20 %) respectively. The fracture of the FRC specimen occurred above the reinforced belt (Fig. 11.b), while the fracture of the plain concrete specimen occurred at 0.67 m above the base.

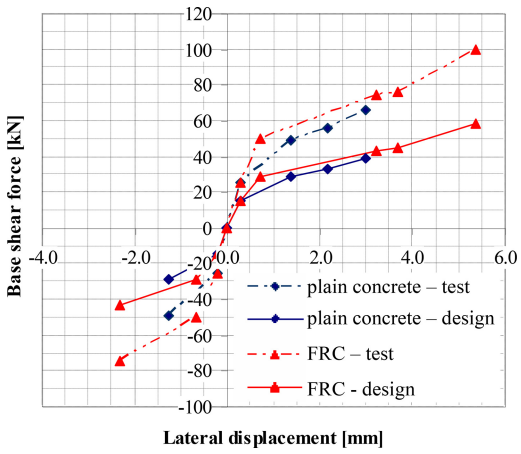

Figure 12. Comparative cycling envelopes translated to the design assumption.

3 ANALYSIS AND DISCUSSION

Next, reference will be made to the results obtained by tests and their translation in the terms of the design assumption. Figure 12 presents the cycling envelopes derived for the design situations.

Both failures had a brittle nature, specific to the bending failure of plain concrete. However, even if low, the fiber content of 0.5 % enabled the drift practically to double, but a relative drift of 0.20 % at failure is still far from the limit target of 2.5–3.5 % considered by the codes, and by the experimental shear failure values reported for reinforced concrete walls, raising up to 0.80 % (Hidalgo et al. 2002). A higher fiber content it is expected to ensure higher ultimate drifts. Unfortunately, the current market provides such concrete mixes with difficulties and future technological progress is necessary.

Figures 13 and 14 emphasize the energy balance complying with the minimum and maximum behavior factors when dealing with the equal energy approach. As shown in Figure 13, the minimum of value 1.50, imposed by EN 1998-1:2004 is easily satisfied, even if practically now warning with regard to failure exists. As can be seen in the results from Figure 14, the maximum values in the ULS conditions are 2.57 for plain concrete and 2.68 for FRC. Such values suggest that a higher fiber content and/or traditional reinforcing of the boundaries of the wall can ensure the compliance with the requirements of medium ductility walls, with a minimum target value of 3.0. Moreover, reinforcing of the boundaries will ensure a flexural ductile behavior even if it may guide the failure of the wall to the shear specific modes (e.g., diagonal tension, sliding shear).

Table 5 presents the energy balance when determining the behavior factors. The design scenarios (i.e., Ultimate Limit State – ULS) present a conservative assumption in respect with the tests, the behavior factors being reduced with 37.7 % in the case of the plain concrete specimen, and 39.6 % in the case of the FRC specimen.

Table 6 shows the total fracture energy corresponding to the failure envelope neglecting the opposite

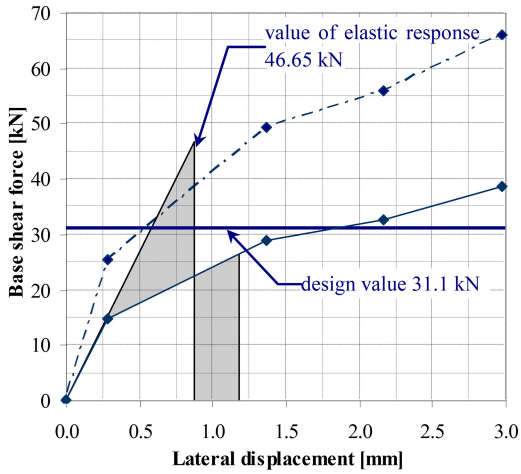

a. plain concrete model

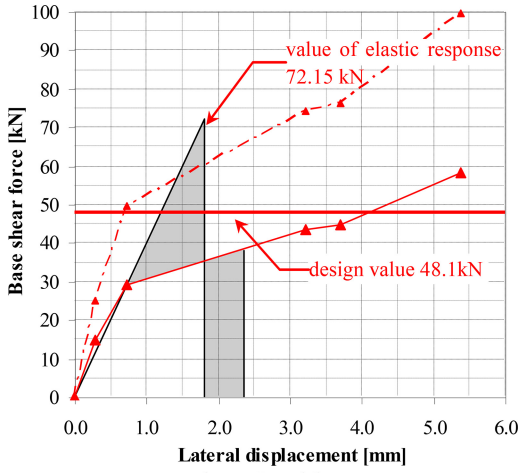

b. FRC model

Figure 13. Equal minimum energy (q =1.5) approach in design.

Table 5. Balanced energy at ULS and testing.

		Potential energy	
		Design	Test
Specimen	q	J	J
plain concrete	1.50	7.1	22.3
FRC	1.50	20.3	64.4
plain concrete	2.57	40.2	–
FRC	2.68	107.6	–
plain concrete	4.12	–	74.2
FRC	4.44	–	183.4

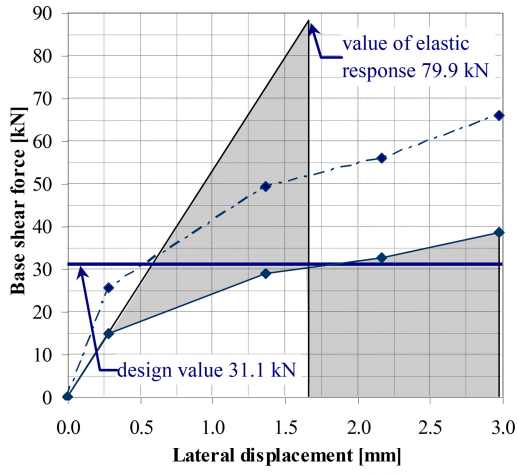

a. plain concrete model q_{max}=2.57

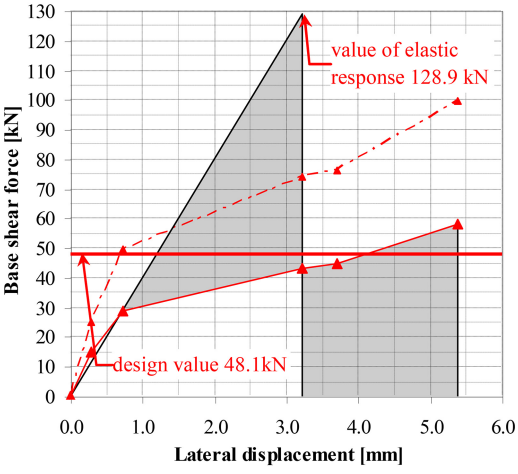

b. FRC model q_{max}=2.68

Figure 14. Equal maximum energy approach in design.

Table 6. Failure unidirectional deformation energy.

	Potential energy	
	Design	Test
Specimen	*J*	*J*
plain concrete	79.3	135.9
FRC	209.1	358.4

Table 7. Dissipated energy on the alternant loading cycles.

		Deformation energy	
		Plain concrete	FRC
Cycle	Source	*J*	*J*
C1	test	18.6	17.9
C2	test	18.1	17.2
C3	test	17.9	14.3
C4	test	154.3	74.9
C5	test	174.7	83.8
C6	test	171.3	109.9
C7	test	–	467.7
C8	test	–	513.9
C9	test	–	605.9

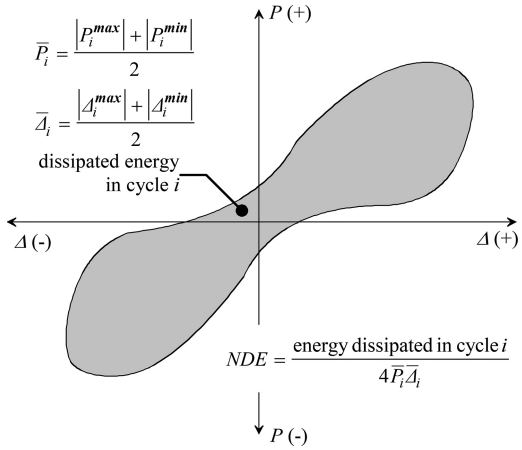

Figure 15. Definition of the normalized dissipated energy *NDE* (Hidalgo et al. 2002).

Table 8. Normalized dissipated energy *NDE* by cycle.

		Normalized deformation energy	
		Plain concrete	FRC
Cycle	Source	%	%
C1	test	79.9	80.0
C3	test	75.1	76.2
C3	test	72.3	72.4
C4	test	70.6	81.5
C5	test	68.5	76.2
C6	test	66.1	71.9
C7	test	–	75.2
C8	test	–	73.7
C9	test	–	71.3
Prior to failure	estimation	24.9	21.8

alternant cycles, while Table 7 presents the cycle's dissipated energy and Table 8 the normalized cycle's dissipated energy (see Figure 15).

Such energy values confirm the behavior factors, by comparison with the values given in the literature (e.g., Hidalgo et al. 2002). On the other hand, the behavior factors are similar to the ones stipulated by EN 1998-1:2004 for unreinforced masonry, which are acceptable up to two stories for the design earthquake acceleration $a_g = 0.15\,g$ for wall densities of

5%. If a 250 mm thick wall is similar to a 150 mm plain concrete wall with regard to out of plane capacity and stability, the approximate wall density for the presented specimens, is conservative and approximately appreciated for a one floor building to 1.0 % in the case of the plain concrete specimen, and 0.6% in the case of the FRC specimen.

Reviewing the failure mechanisms (see Fig. 11), a substantial difference between the two specimens can be noticed. The fracture, with the appearance of a sliding shear, occurred at different levels. In the case of the plain concrete speciment, the fracture is placed at 0.67 m above the top of the footing, while in the case of the FRC specimen the fracture is placed near the bottom reinforced brace. The difference in respect to the level of arm can be explained only through the existence of a weak zone. At the failure of the plain concrete specimen, the bending moment just above the reinforced concrete brace was of 181.5 kNm, while at fracture level was of 147.2 kNm, while the predicted failure value (see Table 4) was 153.9 kNm. In the case of the FRC specimen, failure occurred at a bending moment above the brace of 274.2 kNm, while the predicted value (see Table 4) was 239.3 kNm. In this case, the superior resistance can be explained by the superior toughness of the concrete.

4 CONCLUSIONS

The tests on a plain concrete and FRC specimens emphasized a brittle failure in bending. A small content of fiber (i.e., 0.5% in volume) practically doubled the failure drift, and a higher content is expected to provide an adequate warning of structural failure by large inelastic deformations.

In the terms of the energy balance, both specimens fulfilled the minimum requirement of EN 1998-1:2004 with regard to the behavior factor. Even if such walls may be designed only according to the gravitational design rules, medium ductility performance may be expected.

A high fiber content and/or ends reinforc with mild steel reinforcement seems to provide an adequate inelastic response, even without specific horizontal and vertical shear reinforcement. On another hand, such a solution it is far to be recommended when the value of the axial compressive force translate the behavior of the wall in the domain of eccentric compression.

ACKNOWLEDGEMENTS

The testing facility was provided by the NIRD Urban-Incerc, Cluj-Napoca branch. The help of this institution is gratefully acknowledged by the authors.

REFERENCES

Appa Rao, G. & Rao, A.S. 2010. Toughness indices of fiber reinforced concrete subjected to mode II loading. In B.H. Oh et al. (eds), *Recent Advances in Fracture Mechanics of Concrete, Proceedings of FraMCoS-7, May 23–28, 2010.* Seoul, Korea Concrete Institute: 112–117.

Barr, B.I.G. & Hasso, E.B.D. 1985. A Study of Toughness Indices. *Magazine of Concrete Research*, 37 (1985): 162–173.

EN 1992-1-1:2004. Eurocode 2: Design of concrete structures – Part 1-1: General rules and rules for buildings.

EN 1998-1:2004. Eurocode 8: Design of structures for earthquake resistance – Part 1 : General rules, seismic actions and rules for buildings.

Gopalaratnam, V.S. & Gettu, R. 1995. On the characterisation of flexural toughness in FRC. *Cement & Concrete Composites*, 17 (1995): 239–254.

Henegar, C.H. 1978. Toughness Index of Fibre Concrete. *Testing and Test Method of Fibre Cement Composites (RILEM Symposium 1978)*, Construction Press Ltd., Lancaster: 79–86.

Hidalgo, P.A., Ledezma, C.A. & Jordan, R.M. 2002. Seismic Behavior of Squat Reinforced Concrete Shear Walls. *Earthquake Spectra*, 18(2) (2002): 287–308.

Johnson, C.D. 1982. Definition and measurement of flexural toughness parameters for fiber reinforced concrete. *Cement, Concrete & Aggregates*, 4 (1982): 53–60.

Concrete Solutions – Grantham et al. (Eds.)
© 2016 Taylor & Francis Group, London, ISBN 978-1-138-03008-4

Differences in losses of prestress between steel and FRP reinforcement

M. Mirshekari, T. Donchev, D. Petkova & M. Limbachiya
Faculty of Science, Engineering and Computing, Kingston University, London, UK

ABSTRACT: Materials like Glass FRP (GFRP) and Basalt FRP (BFRP) possess high tensile strength, but relatively low modulus of elasticity. Due to this the BFRP and GFRP reinforced structural elements develop significant deformations when are loaded under working loading. One of the possible approaches to reduce the deformability of BFRP or GFRP reinforced elements with more effective damage control is via introducing initial pre-stress in the reinforcement. This research focuses on gaining an insight into the behaviour of concrete beams reinforced with BFRP bars and investigating the effect of prestressing of the reinforcement. The intention is to overview existing research and to investigate FRP pre-stressed elements behaviour, focusing specifically on the losses of pre-stress at normal temperatures.

1 INTRODUCTION

A low tensile capacity of concrete can result in development of flexural cracks and significant deflection at an early stage of loading. Those effects are more significant in the case of using BFRP and GFRP reinforcement,which possess relatively low Young's modulus and allow for faster development of the deformations. One of the widely used possible approaches to reduce or prevent such effects from developing is via application of an eccentric or concentric force, imposed in the longitudinal direction of a structural element, called a prestressing force.

There are two methods for prestressing concrete members through reinforcement – prestressing and post-tensioning.In both cases, the initial tensile stress applied in the prestressed or post-tensioned reinforcement decreases during and after process of production of the RC elements through several ways. The theory of loss of prestress for steel reinforced prestressed elements is well developed. Prestressing with FRP reinforcement is a relatively new approach and proper analytical tools for estimation of losses in such cases are in process of development.

2 BACKGROUND

Fibre Reinforced Polymers (FRPs) are attractive for use as external or internal reinforcement of concrete structure due to their non-corrosive nature, light weight and high strength. They can increase the service life and the load carrying capacities of reinforced and prestressed concrete structures, as they exhibit low relaxation losses and good fatigue properties (ISIS Canada, 2007).

A significant research milestone in developing of FRP prestressed concrete was achieved in 1998 during construction of the Taylor Bridge in Headingley, Manitoba. Two types of carbon FRP (CFRP) reinforcements were used in the project. The girders were pretensioned by using Leadline (Mitsubishi Chemical Co.) CFRP bars. The bridge is remotely monitored to estimate the effects of the long-term behaviour and durability of the FRP materials comparative to conventional steel reinforcement (Shehata at al., 1999).

Between the first publications in the area of prestressing with FRP materials are a wide range of publications by Burgoyne (Burgoyne and Chambers, 1985) etc. In Burgoyne's study on prestressing via polyaramid tendons, he obtained very positive results for such a type of prestressing (1992). Balafas and Burgoyne (2012) Suggested innovative method of optimal design of beams reinforced with usual and prestressing FRP reinforcement. The method is based on developed diagrams reflecting the ratio of depth of the beam to the area of the reinforcement.

Braimah (2000) investigated beams pre-tensioned with CFRP rods and with steel prestressing strands. He pointed out that at the sustained load level the steel pre-tensioned beam shows higher mid-span deflection in comparison with the CFRP pre-tensioned beams.

Between the first attempts for using BFRP bars as prestressing reinforcement Jonsson (2011) states that ultimate bearing resistance of a beam with prestressed BFRP tendons is not significantly higher than without prestressed, on other hand serviceability limit state(SLS) bearing resistance is significantly higher and the deflection is smaller to comparison with un-prestressed beams. Guðmundsson (2012) investigated concrete beams, prestressed with BFRP tendons and commented that BFRP prestressed beams without shear reinforcement are weak to transverse loading

even if the shear span to depth(a/d) ratio is high. Pearson and Donchev (2013) pointed out that for elements reinforced with post-tensioned internal BFRP bars a higher level of prestressing significantly reduces the deformation at the same level of loading. Grouting has a beneficial effect on increasing the ultimate capacity and decreasing the deformability of BFRP reinforced beams.

The above indicated initial research clearly defines the opportunity to use relatively deformable BFRP and GFRP reinforcement for prestressing purposes, in this way achieving reduction of the deformability of the beams. At the same time certain limitations about prestressing with BFRP and GFRP reinforcing bars, such as creep rupture (ACI, 2006) and difficulties connected with construction of appropriate anchoring devices have to be kept in mind. According to an ACI (2006) review of available information about GFRP creep rupture, the results for 50 years lifespan are varying between 29% and 55% of the ultimate load. Similar results are indicated in (Banibayat, 2011) for BFRP reinforcement under relatively high temperature and alkaline environments. Indicating the same limits for GFRP reinforcement. ISIS (2006) are noting that laboratory testing is not necessarily representative of field performance. Some information from conducted experiments with BFRP reinforcing bars (Pearson & Jonsson) are in support of this view and give initial indication that the laboratory conditions for such estimation could be quite conservative.

For the purposes of this publication, attention is focused on relatively short term behaviour of prestressed FRP elements, when creep rupture effects are not governing. Possible solutions for mitigating the effects of creep rupture are outside the scope of this work as well.

3 MAIN SOURCES OF PRESTRESS LOSSES

Prestress loss for design of PC element in concrete structures is an important design parameter which must be taken into consideration with FRP reinforcement. ACI Committee 318 (2011) states that prestress losses have little effect on ultimate design strength of steel reinforced members, but can affect service conditions such as deflections, cracking load and camber. Overestimation on prestress losses at service loads can be nearly as detrimental as underestimation.

Prestressing losses can be determined analytically or experimentally. Analytical methods to estimate prestressing losses are divided into the following levels (NCHRP REPORT 496, 2003);

(1) Lump-sum method to estimate total prestressing losses (TPL) (oversimplified methods for preliminary design);
(2) Detailed methods to estimate prestress losses separately due to each particular source; and
(3) Accurate determination of cumulative losses by time-step methods.

For the purpose of this publication the application of the second type of estimation is adopted. To determine prestress losses from experimental techniques requires a back-calculation from the test data by using the theory of mechanics concepts.

A summary of the sources of the separate prestressing losses and the stage of their occurrence is given in table 1. From this table, the total loss in prestress can be calculated for post-tensioned and pretensioned members as follows (Nawy, 2006):

Pretensioned members:

$$\Delta f_{pT} = \Delta f_{pES} + \Delta f_{pR} + \Delta f_{pCR} + \Delta f_{pSH} \quad (1)$$

Post-tensioned members:

$$\Delta f_{pT} = \Delta f_{pES} + \Delta f_{pR} + \Delta f_{pCR} + \Delta f_{pSH} + \Delta f_{pF} + \Delta f_{pA} \quad (2)$$

where Δf_{pES} is applicable only when tendons are jacked sequentially, and not simultaneously.

3.1 *Elastic shortening of concrete (ES)*

When pre-tensioned tendons are released from the anchorage or post-tensioning is applied, this can cause an elastic deformation of the concrete. The loss of force in each group of steel tendons of area AP varies along its length and based on BS EN 1992-1-1 (2004) can be approximately estimated from the formula below:
for pretensioned members:

$$\Delta P_{el}(x) = A_p \frac{E_p}{E_{cm}(t)} \sigma_c(x) \quad (3)$$

where: A_p = cross-sectional area of tendon; E_p = modulus of elasticity of prestressing steel; E_{cm} = modulus of elasticity of concrete at time t; $\sigma_c(x)$ = is the stress in the concrete adjacent to the bar at transfer; $E_P/E_{cm}(t)$ = the modular ratio, with the modulus for concrete based on its age at transfer.
for post-tensioned members:

$$\Delta P_{el} = A_p E_p \sum [\frac{j\Delta\sigma_c(t)}{E_{cm}(t)}] \quad (4)$$

where: $\Delta\sigma_c(t)$ = variation of stress at the centre of gravity of the tendons applied at time t; j = is a coefficient equal to $(n-1)/2n$ where n is the number of identical tendon successively prestressed. As an approximation j may be taken as $1/2$ for the variations due to permanent actions applied after prestressing.

This loss of prestress for FRP reinforcement is expected to be the same as for steel reinforcement.

3.2 *Relaxation losses (REL)*

After the concrete member is cast around the pretensioned bars, additional factors such as time and temperature applied in accordance with the corresponding curing method influence relaxation prestress losses. EN 1992-1-1 (2004) states that the starting point is the relaxation loss at 1000 hours from an initial

Table 1. Types of prestress loss (after Nawy, 2006).

	Stage of occurrence		Tendons stress loss	
Type of prestress loss	Pretensioned members	Post-tensioned members	During time interval (t_i, t_j)	Total or during life
Elastic shortening of concrete (ES)	At transfer	At sequential jacking	–	Δf_{pES}
Relaxation of tendons (REL)	Before and after transfer	After transfer	$\Delta f_{pR}(t_i, t_j)$	Δf_{pR}
Shrinking of concrete (SH)	After transfer	After transfer	$\Delta f_{pS}(t_i, t_j)$	Δf_{pSH}
Creep of concrete (CR)	After transfer	After transfer	$\Delta f_{pC}(t_i, t_j)$	Δf_{pCR}
Anchorage seating loss (A)	–	At transfer	–	Δf_{pA}
Total	Life	Life	$\Delta f_{pT}(t_i, t_j)$	Δf_{pT}

stress of 70% of the actual tensile strength of the steel tendons. To determine the long-term relaxation loss, a duration of 5000 h can be used.

According to ISIS Canada, (2007) the losses due to relaxation for CFRP are negligible when the initial stress is equal to 50% of the ultimate tensile stress. However, relaxation losses for different types of FRPs vary. The relaxation losses in FRP tendons are a combination of three sources and the total relaxation loss (REL) can be calculated by assessing these three effects separately. ACI (2004) defines these three effects as follows:

$$REL = REL1 + REL2 + REL3 \quad (5)$$

REL1 – Relaxation of polymer

When stress is applied to the tendons, a portion of the load is carried in the resin matrix. The matrix, which is a visco-elastic material, relaxes and loses its contribution to the load carrying capacity. This relaxation can be obtained by:

$$n_r = \frac{E_r}{E_f} \quad (6)$$

where, n_r is the modular ratio of the resin. E_r is the elastic modulus of the resin, E_f is the modulus of the fibre. The volume of fibres in the tendon can be determined from $\nu_f + \nu_r = 1.0$, where ν_f and ν_r are the volume fractions of fibre and resin, respectively. REL1 can be expressed as follow:

$$REL1 = n_r \times \nu_r \quad (7)$$

REL2 – Straightening of Fibres

The fibres in a pultruded section are nearly but not completely parallel. Therefore, stressed fibres flow through the matrix and straighten, and this straightening appears as a relaxation loss in typical applications. An assumed 1% to 2% relaxation of the transfer stress is adequate to predict this portion of the relaxation loss calculation.

REL3 – Relaxation of Fibres

The CAN/CSA-S806-02 (2004) report indicates that the fibre relaxation is dependent upon the fibre type. According to this report, in the absence of specific information, the following values of relaxation may be used (with t = time in days), expressed as a percentage of the transfer stress. for CFRP:

$$\text{Relaxation (\%)} = 0.231 + 0.345 \log(t) \quad (8)$$

forAramid FRP(AFRP):

$$\text{Relaxation (\%)} = 3.38 + 2.88 \log(t) \quad (9)$$

The behaviour of BFRP and GFRP reinforced elements in this aspect is not sufficiently investigated.

3.3 *Shrinkage loss (SH)*

Shrinkage of concrete is affected by several factors such as mix properties, type of cement, type of aggregate, curing time, size of the member, time between the end of external curing, application of prestressing and the environmental conditions. Narayanan and Beeby, (2005) mentioned that as the concrete shrinks, the prestressing steel must compress by the same strain which causes a loss of prestress and a change in the concrete stress. According to BS EN 1992-1-1 (Canadian Standards Association, 2004) the prestress loss due to concrete shrinkage can be determined as:

$$\varepsilon_{cs} - \frac{\Delta_{\sigma c}}{E_{ce}} = \frac{\Delta_{\sigma p}}{E_p} \quad (10)$$

where: ε_{cs} = shrinkage strain; E_{cs} = effective concrete modulus; E_p = modulus of elasticity of the prestressing steel; z_{cp} = eccentricity of the tendons; I_c = second moment of area of the concrete section; A_c = area of the concrete section.

According to ACI Committee 209 (1997) the average value of ultimate shrinkage strain in both steam-cured and moist-cured concrete is given as $\varepsilon_{SH} = 780 \times 10^{-6}$ m/m.The Prestressed Concrete Institute, (1999) stipulates for standard conditions an average value for nominal ultimate shrinkage strain $(\varepsilon_{SH})_u = 820 \times 10^{-6}$ m/m. This average value is affected by temperature, length of initial moist curing, concrete composition and ambient relative humidity. To take such effects into account, ε_{SH} should be multiplied by a correction γ_{SH} as follow:

$$\varepsilon_{SH} = 780 \times 10^{-6} \times \gamma_{SH} \quad (11)$$

Table 2. Values of K_{SH} for Post-Tensioned Members (after Prestressed Concrete Institute, 1999).

Time from end of moist curing to application of prestress, days	1	3	5	7	10	20	30
K_{SH}	0.92	0.85	0.80	0.77	0.73	0.64	0.58

the loss in prestressing in pretensioned members is

$$\Delta f_{pSH} = \varepsilon_{SH} \times E_{ps} \quad (12)$$

where Δf_{pSH} is shrinkage of concrete. E_{ps} is modulus of elasticity of prestressing reinforcement.

For post-tensioned members, shrinkage loss is slightly less than pretensioning since some shrinkage has already taken place before post-tensioning. The general formula for loss in prestressing due to shrinkage becomes:

$$\Delta f_{pSH} = 8.2\times10^{-6} \text{ x } K_{SH}\ E_{ps}(1–0.06V/S)(100–RH) \quad (13)$$

where, RH is relative humidity and V/S is volume to surface ratio. $K_{SH} = 1.0$ for pretensioned members and table 2 gives the values of K_{SH} for post-tensioned members.

According to CAN/CSA S6-06 Prestress losses due to shrinkage of concrete (SH) may be calculated, using empirically-derived equations, as follows.
for pretensioned members:

$$SH = 117 – 1.5RH \quad (14)$$

for post-tensioned members:

$$SH = 94 – 0.85RH \quad (15)$$

3.4 *Creep loss (CR)*

Creep is the deformation in the concrete due to the longitudinal stress. It depends on the ambient humidity, the dimensions of the element and the composition of the concrete. BSI (2008) states that creep is also influenced by the maturity of the concrete when the load is first applied and depends on the duration and magnitude of the loading. From BS EN 1992-1-1 (2008) the prestress loss due to creep is:

$$\frac{\sigma_c}{E_c}\phi(t,t0) - \frac{\Delta_{\sigma c}}{E_{ce}} = \frac{\Delta_\sigma}{E_p} \quad (16)$$

$$\Delta\sigma_{p,c} = \frac{\frac{E_p}{E_c}\phi(t,t0)\sigma_c}{1+\frac{E_p}{E_{ce}}\frac{A_p}{A_c}(1+\frac{A_c}{I_c}z^2_{cp})} \quad (17)$$

where, σ_c is the initial concrete stress adjacent to the steel tendons.

$$\Delta f_{pCR} = K_{CR}\frac{E_{ps}}{E_c}(\bar{f}_{cs} - \bar{f}_{csd}) \quad (18)$$

$$\Delta f_{pCR} = n\ K_{CR}\ (\bar{f}_{cs} - \bar{f}_{csd}) \quad (19)$$

where: $K_{CR} = 2.0$ for pretensioned members & 1.60 for post-tensioned members (both for normal concrete); $\bar{f}cs$ = stress in concrete at level of centre of gravity of steel (CGS) immediately after transfer; $\bar{f}csd$ = stress in concrete at level of CGS due to all superimposed dead loads applied after prestressing is accomplished; n = modular ratio. Note that K_{CR} should be reduced by 20% for light weight concrete.

Since modulus of elasticity of steel tendons is generally higher than a corresponding FRP tendon, losses for prestressed FRP tendons due to elastic shortening, shrinkage and creep of concrete will be less than for prestressed steel tendons (ISIS, 2007).

When the elements are pretensioned, losses of prestressdue to anchorage seating and friction are not applicable and will not be subject of this research.

4 CONCLUSIONS

As a result of this critical overview for prestressing via pretensioning with FRP reinforcing bars the main losses of prestress to be considered are as follows:

- Elastic shortening of concrete (ES) – similar to steel, but their further development is getting gradually less than for steel reinforcement, due to the difference in Young's modulus.
- Anchorage seating loss (A) & Friction (F) are not applicable for pretensioning.
- Shrinkage loss (SH) – modification due to difference in modulus of elasticity is needed.
- Creep loss (CR) – similar tosteel, but for FRP reinforcement is less than for steel reinforcement.
- Relaxation losses (REL)–is the most dramatic difference in comparison with streel, both theoretical and experimental investigations are needed especially for BFRP and GFRP reinforcement. The long term deformability of different types of FRP reinforcement with varying load conditions have to be kept in mind.

The overviewed data indicates the need fordeveloping precise methodology for calculating losses of prestress in FRP reinforced elements.

REFERENCES

ACI Committee 209, 1997. *Prediction of Creep, Shrinkage, and Temperature Effects in Concrete Structures*. ACI 209R-92. American Concrete Institute.

ACI Committee 440, 2006. *Guide for the Design and Construction of Structural Concrete Reinforced with FRP Bars*. ACI 440-1R-06. American Concrete Institute.

ACI Committee 318, 2011. *Building code requirements for Structural Concrete*. Farmington Hills: American Concrete Institute.

Balafas I. and Burgoyne C.J., 2012, Economic design of beams with FRP rebar or prestress, Mag. Concrete Res, 64/10, 885-898, Oct 2012. DOI: 10.1680/macr.11.00099.

Banibayat, P., 2011, *Experimental Investigation of the Mechanical and Creep Rupture Properties of Basalt Fiber Reinforced Polymer (BFRP) Bars*. Ph.D. thesis, University of Akron, Akron, U.S.A.

Braimah, A. 2000, *Long-Term and Fatigue Behaviour of Carbon Fibre Reinforced Polymer Prestressed Concrete Beams*, Ph.D. thesis, Queen's University Kingston, Ontario, Canada.

BSI. 2008. *Eurocode 2 : design of concrete structures: British standard (BS EN 1992-1-1)*. London, British Standards Institution.

Burgoyne C.J., 1992 Tests on beams prestressed with polyaramid tendons, Procs 1st Int. Conf. on *Advanced Composite Materials in Bridges and Structures*, Sherbrooke, Quebec.

CAN/CSA-S806-02, 2004, Design and Construction of Building components with Fibre Reinforced Polymers". Canadian Standards Association, Ottawa, Ontario, Canada.

Guðmundsson, S.H., 2012, *Capacity of Concrete Beams Prestressed with BFRP Tendons*. MSc. Thesis, Reykjavík University, Iceland.

ISIS Canada, 2006. *ISIS Educational Module 8: Durability of FRP Composite for Construction*. Manitoba, Canada.

ISIS Canada, 2007. *ISIS Educational Module 9: Prestressing Concrete Structures with Fibre Reinforced Polymers*. Manitoba, Canada.

Jonsson, B.S., 2011, *Prestressed BFRP tendons in concrete beams*. MSc. Thesis, Reykjavík University, Iceland.

Narayanan, R. and Beeby, A. 2005. *Designers' guide to EN 1992-1-1 and EN 1992-1-2. Eurocode 2: design of concrete structures*. London: Thomas Telford.

Nawy, E. 2006. *Prestressed concrete*. Upper Saddle River, N.J.: Pearson/Prentice Hall.

NCHRP Report 496, 2003. *Prestress Losses in Pretensioned High-Strength Concrete Bridge Girders*. Washington: National Cooperative Highway Research Program.

Pearson, M. and Donchev, T., 2013, Experimental Study on the Behavior of Prestressed Concrete Beams with Internal BFRP Reinforcement, Conference*: 11th International Symposium On Fiber Reinforced Polymers For Reinforced Concrete Structures*. June 26–28, 2013. Guimarães, Portugal.

Prestressed Concrete Institute., 1999. *PCI Design Handbook*. 5th ed. Chicago: PCI.

ShehataI, E., Haldane-Wilsone, R., Stewart, D., Tadros, G. and Rizkalla, S. 1999, *Taylor Bridge – A Bridge For the 21st Century*. In: WORLD WISE'99.

Wu, C., Zhao, W., Beck, T. and Peterman, R. 2011, Optical Sensor Developments for Measuring the Surface Strains in Prestressed Concrete Members. *strain*, pp.e376–e386.



Taylor & Francis
Taylor & Francis Group
http://taylorandfrancis.com

Concrete Solutions – Grantham et al. (Eds.)
© 2016 Taylor & Francis Group, London, ISBN 978-1-138-03008-4

Use of 3D microscopy in the analysis of FRP strengthened concrete

D. Petkova, T. Donchev & D. Wertheim
Kingston University London, UK

ABSTRACT: The development of methods and techniques for the strengthening of Reinforced Concrete (RC) structural elements with Fibre Reinforced Polymers (FRP) has grown markedly over the past two decades. The wide range of beneficial properties of FRP, such as high strength, lack of corrosion and quick installation has contributed to the high popularity of such design approaches. However, it would be useful to improve some properties of FRP, such as susceptibility to degradation at elevated temperatures. This is an important area for investigation and development of appropriate techniques should help gain knowledge about effects of elevated temperatures on different FRP materials.

This study uses confocal microscopy to study in 3D, the effects of heating of FRP materials. Carbon FRP (CFRP) plates were attached to reinforced concrete RC prisms and heated to 50°C, 150°C and 250°C and then cooled. The samples were subsequently inspected with a confocal microscope to determine the level of surface deformation at three different temperatures. Confocal microscopy showed clear differences in 3D surface appearance associated with heating with the most significant variation in surface level found in the sample heated to 250°C. This study suggests that confocal microscopy can help in the evaluation of the effects of elevated temperatures of FRP.

1 INTRODUCTION

Due to high population densities in urban areas and the ever increasing traffic, the maintenance and inspection of the existing infrastructure has become an important part of any successful economy. Thus there is a necessity for a fast and reliable method of strengthening of structures such as buildings and bridges. In the last two decades FRPs have become a viable option to tackle such a demand.

Among the benefits of using FRP are their excellent mechanical properties, light weight and lack of corrosion which makes them a better alternative to steel plates. FRPs on the other hand can be affected significantly by exposure to elevated temperatures and fire and their glass transition temperature Tg is quoted as the critical temperature for service under such conditions. The presented research shows the effect of heating to 50°C, 150°C and 250°C on the surface layers of the FRP and the possible physical changes, using a 3D microscope. Such an approach could be used as a non-destructive test to determine the level of heating after high temperatures and fire exposure of the FRP and the corresponding effect on the mechanical properties of the strengthening material which could affect the capacity of the strengthened specimens.

2 BACKGROUND

The roughness of the surface has been studied to find a relationship between the bond strength and the roughness parameters of the substrate using various non- destructive techniques.

Santos et al. (2007) investigated the effect of surface treatment on the bond of concrete-to-concrete joints based on pull-off and slant shear tests combined with digital image analysis of the contact surface. The typical parameters considered in such a study were the average roughness, the mean or maximum peak-to-valley height and the mean or maximum peak height or valley depth. The authors concluded that, for smooth surfaces, a more accurate technique was required in order to study the profile of the substrate.

Sadowski et al. (2016) summarized the most common methods used in surface morphology analysis. Those included mechanical profilometry, laser profilometry, vertical scanning interferometry, scanning electron microscopy and laser scanning. Apart from the first method, all techniques were based on non-contact analysis and offered a good level of accuracy for the analysis of a concrete surface.

Hola et al. (2015) found that 3D scanner analysis is good to be combined with other non-destructive methods such as the impulse response method and the impact-echo method in order to determine the pull-off adhesion of the concrete layer.

As the roughness of the concrete surface would reflect the bond characteristics of the concrete-to-FRP joints such studies present important information about the surface treatment and the adhesion to the substrate. On the other hand little information is available on the bond between the FRP and the epoxy adhesive and the physical changes which occur at

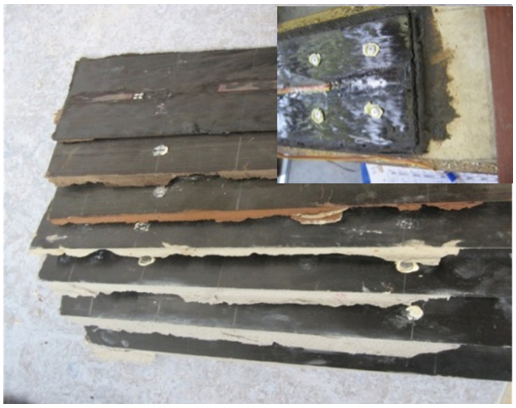

Figure 1. CFRP plates after heating between 50°C and 300°C and volume change at 300°C.

elevated temperatures. Donchev et al (2009) presented the microscopic changes in CFRP laminate, adhesive and concrete after heating the CFRP-to-concrete joints to a target temperature within the range of 50 to 300°C. Observations were made using an optical, laser scanning confocal and a scanning electron microscope. Colour changes of the adhesive layer and the concrete were observed at elevated temperatures. Cracking and discontinuities were observed in the CFRP later and in the adhesive layer at the interface between the adhesive and the CFRP plate. Petkova (2010) also studied the effects of elevated temperatures on CFRP strengthened RC specimens and observed colour changes in the adhesive from grey to light and dark brown for the temperature range of 20°C to 300°C. Some physical changes such as a volume change of the CFRP plate could also occur which could indicate the maximum level of heating the specimens (Petkova et al., 2014).

This study is based on 3D microscope observations of CFRP samples used for strengthening of RC beams.

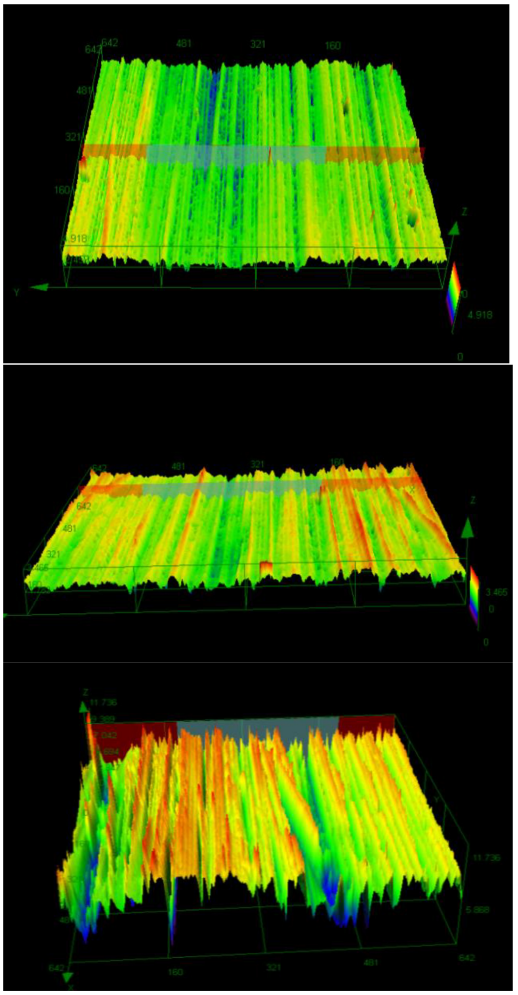

Figure 2. a, b and c. 3D microscopic views of CFRP after heating to 50°C, 150°C and 250°.

3 METHODOLOGY

A LEXT OLS4100 laser scanning confocal microscope (Olympus Corporation, Japan) was used to acquire 3D surface images on FRP samples using a x20 objective lens.

The CFRP laminates as a material consist of unidirectional carbon fibres held in an epoxy resin. The surface changes of the sample would depend on the properties of the resin and the temperatures. Three different samples of CFRP laminates were studied under the microscope at the same magnification. Those had been heated to 50°C, 150°C and 250°C and cooled. When subjected to elevated temperatures the CFRP materials exhibit a transition between a solid and rubber-like state denoted as a glass transition temperature (Tg). Above that, the mechanical characteristics show a significant drop and the strengthening effect is lost.

In this study, for the materials used, the Tg is quoted between 60°C and 80°C which indicated that such samples might suffer significant chemical and physical changes as the temperatures increase. Upon cooling, depending on the level of heating, some of the properties might recover or even improve due to the curing of the resin. Heating between 20°C and 250°C proved to cause little physical damage to the plates not detectable with a naked eye but at 300°C the effect was visible as the CFRP expanded with some individual fibres detaching from its surface (Figure 1).

The temperatures would affect the bond strength of CFRP-to-concrete joints below 250°C. Therefore the study of the surface condition of the samples could reveal the extent of changes which will occur at elevated temperatures and the possible effect on the bond between the CFRP and the adhesive used in the joints.

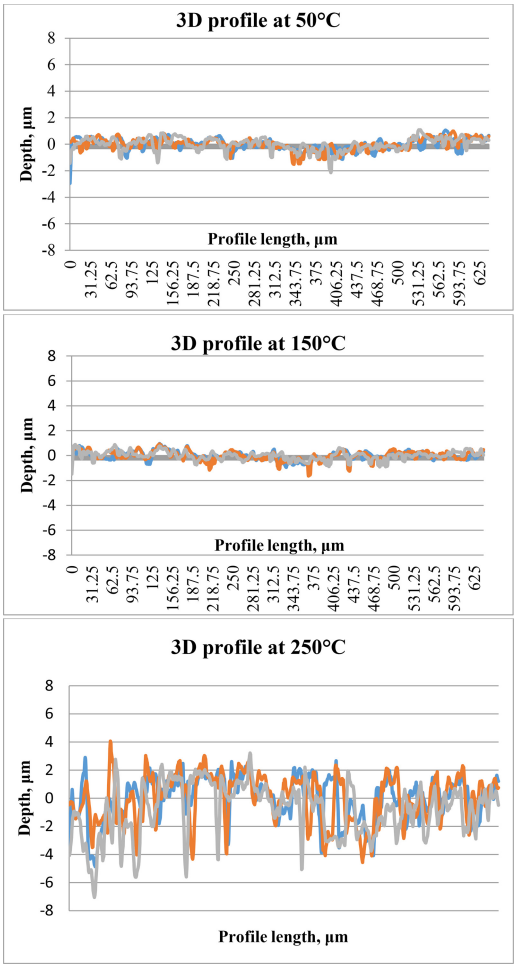

Figure 3. a, b and c. Profiles of CFRP after heating to 50°C, 150°C and 250°C.

4 RESULTS

The 3D images of the CFRP samples are given in figures 2a, b, and c. As can be seen, at 50°C the surface is regular with small peak and valley values throughout the 3D image of the surface layer.

The image at 150°C shows a similar trend, however when comparing the peak and valley values, the difference between them increases. At 250°C the surface profile shows a significant rise in the peak-to-valley values indicating that at this temperature the condition of the CFRP plate is affected and as the roughness of the surface changes this effect has to be considered when estimating the capacity of the strengthened samples.

5 ANALYSIS AND CONCLUSIONS

Figures 3 a, b and c show the profile of the CFRP samples at three different positions relative to the average level of the profile. At 50°C the maximum peak and valley values appear between −1 and 1 µm about the average level as can be observed at 150°C as well. At 250°C the difference increases with maximum peak and valley values between 2 and −4 µm about the average level.

When comparing the absolute differences between the peak and valley values considering adjacent sections of the profile the 50°C specimens vary within 1 µm, at 150 the range is 1.4 µm and at 250°C the range shows a dramatic increase to 6 µm. Such a trend agrees with the decrease in the capacity of CFRP strengthened minibeams subjected to temperatures between 20 and 300°C (Petkova et al, 2014). Based on the presented results the following conclusions about the use of 3D microscope in the assessment of CFRP plates after heating to elevated temperatures and cooling can be drawn:

- The application of a 3D imaging microscope to assess the changes of the surface roughness of visually smooth surfaces is successful.
- 3D imaging could be used for the evaluation of the range of heating of CFRP laminates
- For temperatures between 150°C and 250°C, the changes in the roughness of the surface of the laminates is significant which allows the use of 3D microscopy for estimation of temperatures of heating above 150 C.
- The obtained information is a clear indication about the change in the capacity of the CFRP strengthening above 150°C.

REFERENCES

Donchev, T.D., Abouamer, S. & Wertheim, D. 2009. Microscopic analysis of the connection between CFRP laminates and concrete at elevated temperatures. In Grantham, Majorana & Salomoni (ed) *Concrete solutions 2009; Proc. Intern. Conf. Padova, 2009*. London: Taylor & Francis.

Hoła, J., Sadowski, Ł., Reiner, J. & Stach, S. 2015. Usefulness of 3D surface roughness parameters for nondestructive evaluation of pull-off adhesion of concrete layers, *Construction and Building Materials* 84: 111–120.

Pedro M.D., Santos, Eduardo N.B.S., Julio, Vıtor D. Silva 2007. Correlation between concrete-to-concrete bond strength and the roughness of the substrate surface, *Construction and Building Materials* 21:1688–1695.

Petkova, D. 2010. Behaviour of RC beams strengthened with CFRP laminates at elevated temperatures. PhD thesis, Kingston University.

Petkova, D., Donchev, T. & Wen, J. 2014. Experimental study of the performance of CFRP strengthened small scale beams after heating to high temperatures. *Construction and Building Materials* 68: 55–61.

Sadowski, Ł., Czarnecki, S. & Hoła, J. 2016. Evaluation of the height 3D roughness parameters of concrete substrate and the adhesion to epoxy resin. *International Journal of Adhesion & Adhesives 67: 3–13.*



Taylor & Francis
Taylor & Francis Group
http://taylorandfrancis.com

Concrete Solutions – Grantham et al. (Eds.)
© 2016 Taylor & Francis Group, London, ISBN 978-1-138-03008-4

CFRP-steel hybrid retrofitting of steel-concrete composite structures

M. Subhani, R. Al-Ameri & M.I. Kabir
School of Engineering, Deakin University, Victoria, Australia

ABSTRACT: Carbon Fiber Reinforced Polymer (CFRP) is found to be an effective material for the retrofitting of both Reinforced Concrete (RC) and steel structures. However, retrofitting such structures using CFRP alone is shown to exhibit a premature failure due to early de-bonding of the CFRP laminates from the hosting surfaces. On the other hand, steel plates are also used separately for the steel and RC structures. However, steel plates usually add to the self-weight of the structures whereas CFRP is known for its high strength to weight ratio. In the present study, the advantages of both steel plates and CFRP are used to form a hybrid retrofitting system that is able to withstand the existing load to prevent the failure of the structures. In order to improve the retrofitting efficiency of steel-concrete composite structures, an experimental investigation is carried out to examine the use and effectiveness of a CFRP-steel hybrid retrofitting system.

1 INTRODUCTION

1.1 *Preamble*

Application of Fibre Reinforced Polymer (FRP) composites has becoming widespread to strengthen or repair deficient Reinforced Concrete (RC) members where the use of conventional techniques such as epoxy-bonded steel plates, steel-jacketting, etc. can be problemetic. Improvement of strength by bonding FRP to RC members can significantly improve the strength without excessive change of stiffness (Bakis et al., 2002). Flexural strengthening of RC beams is conducted by applying FRP to beam soffits by epoxy based adhesive. RC slabs can also be retrofitted with FRP. In the case of one way, simply-supported slabs, FRP is bonded to the soffit with the alignment of fibre to the required directions whereas for two way slabs, FRP is bonded in both directions (Heiza et al., 2014).

Although application of FRP in reinforced concrete structures has proven its suitability, research on the retrofitting of steel-concrete composite structures with FRP composites is still limited. Steel-concrete composite beams are used as main structural elements in flexure in the construction of bridges and buildings. The deterioration of steel-concrete composite girders in bridges can be caused by corrosion of steel beams due to environmental attack and poor maintenance (Al-Saidy et al., 2004) and require repair with suitable techniques. In addition, to meet the increased traffic density, the strength capacity may need to be upgraded. FRP composites can be a suitable option to upgrade and repair steel-conrete composite girders due to their light weight, corrosion resistance and easy application. Among available FRPs, Glass Fibre Reinforced Polymer (GFRP) is inexpensive and easily available, and has been used in concrete and masonry ructures. However, its low modulus of elasticity makes it ineffective for repair of steel girders. CFRP, on the other hand, has a higher modulus of elasticity than GFRP and can be applied to the tension face of steel girder to improve the flexural performance (Tavakkolizadeh and Saadatmanesh, 2003b).

1.2 *Literature review*

Mertz and Gillespie (1996) strengthened small scale and large scale steel beams with CFRP plates. Six mm thick CFRP plates were applied to the tension flanges for the strengthening of small scale specimens (W8 × 10 rolled beams of 1.52 m length). Beams were tested with four-point bending and showed more than 50% increase in flexural strength before the termination of tests due to buckling of the top cover plate. Two full scale beams (0.61 m deep I-beams, of 6.4 m length) were taken from a demolished bridge which had severely corroded bottom flanges with about 40% loss of tension flange. These beams were strengthed with 6 mm thick plates bonded to both faces of the bottom flange. A signifcant increase in strength was reported.

Sen et al. (2001) investigated the suitability of CFRP epoxy laminates for the repair of steel composite bridge members. They used six specimens consisting of 6.1 m long W8 × 24 wide flange steel beam composite with a 0.114 m thick by 0.71 m wide reinforced concrete slab. The composite beams were initially loaded by four-point bending to yielding of tension flanges of steel beams and then repaired with 3.65 m lengths of 2 mm or 5 mm thick CFRP plates. They reported 21 and 52% strength gains of 310 MPa (yield strength) steel beams for 2 and 5 mm thick CFRP, respectively. The corresponding strength gains for 370 MPa (yield strength) steel beam were 9 and 32%, respectively.

Miller et al. (2001) applied CFRP strengthening in the field to upgrade a steel girder in a slab-on-girder bridge in Delaware. In order to retrofit the girder, 5.3 mm thick CFRP plate was bonded to the tension flange. Diagnostic load tests were conducted before and after strengthening and strain comparison on the inner face of the tension flange revealed that an 11.6% strain reduction (11.6% increase in flexural stiffness) could be achieved due to the strengthening technique.

Tavakkholizadeh and Saadatmanesh (2003a) investigated the behaviour of damaged steel-concrete composite beams repaired with CFRP sheets. A total of three large-scale composite girders were fabricated of W355 × 13.6 A36 steel sections and 75-mm-thick by 910-mm-wide concrete slabs. Specimens with 25, 50, and 100% loss of the cross-sectional area of the tension flange of steel beams were repaired with one, three, and five layers of CFRP sheet, respectively. The ultimate load-carrying capacity could be restored to 20, 80 and 10% for the beams with 25, 50 and 100% damage, respectively. Also, on a different study, Tavakkholizadeh and Saadatmanesh (2003b) reported results of a study on the behaviour of steel-concrete composie girders strengthened with CFRP sheets under static loading using pultruded CFRP sheets on the girders with the same geometrical properties of their previous study. Constant 1.27 mm thick pultruded CFRP sheets but with varying numbers of layers (1, 3 and 5) were applied to retrofit the steel beams. Then the beams were tested by four-point bending under monotonic load. Experimental results showed an increase in load-carrying capacity by 44, 51 and 76% for one, three and five layers of CFRP sheets, respectively.

Al-Saidy et al. (2004) investigated the behaviour of damaged steel composite beams after being repaired with CFRP plates. They induced damage to the steel beams by removing part of the bottom flange and varied the degree of damage between no damage and 75% loss of the bottom flange to simulate the effect of corrosion of steel. Six steel-concrete composite beams were fabricated consisting of W8×15 grade A572 structural steel and concrete slab of 812 mm wide by 76 mm thick. Shear studs of 12.7 mm diameter and 50.8 mm long were used to provide shear connection between steel and concrete. The length of each beam was 3.4 m (both steel beam and concrete slab) with 3.05 m clear span. Among the six beams, two steel beams were used as undamaged controls, one was a control with 50% damage, and the remaining three were repaired with different CFRP dimensions and placements depending on the degree of damage (50% and 75%). Two beams with 50% damage were repaired with CFRP on the steel web and CFRP on both the web and flange whereas the beam with 75% damage was repaired with CFRP on the web.

Al-Saidy et al. (2008) conducted a parametric study on the behavior of short span composite bridge girders strengthened with CFRP plates following a successful experimental study by the authors on strengthening steel-concrete composite girders using Carbon Fiber Reinforced Polymer (CFRP) plates. The parametric study investigated the influence of some of the important parameters, namely, the concrete compressive strength, the yield strength of steel, the CFRP plate stiffness, the CFRP plate thickness, the ultimate strain of the CFRP plate, and the steel beam bottom flange area on the behavior of the section. In addition, they investigated the effect of girder damage on the overall load distribution of a typical short span composite bridge for various load cases.

Fam et al. (2009) conducted research on the strengthening of intact steel-concrete composite girders and the repair of notched steel beams applying CFRP materials with Young's modulus varying from 150 to 400 GPa. They tested three large-scale (6100 mm long) steel-concrete girders scaled down (4:1) with accurate proportional dimensions from a bridge. The cross section of the girders consisted of W250 × 25 hot-rolled steel sections with a 65 mm thick and 500 mm wide concrete slab. Two composite beams were strengthened with CFRP sheets of two types. In addition, 15 small-scale (1000 mm long) W100 × 19 sections with various levels and configurations of loss (50% and 100% loss) in the tension flange, induced by notching, were repaired with CFRP sheets. The increase in flexural strength of the strengthened composite girders was reported as 51%. Complete cutting of tension flanges in W-sections reduced the ultimate capacity of the beams by 62%, whereas there was negligible reduction due to 50% loss of the flanges. CFRP repair schemes restored the strength up to 79% for the former whereas insignificant gains were observed for the latter.

Sallam et al. (2010) studied the effect of pre-intermediate separation on the behaviour of CFRP flexural strengthening of steel-concrete beams either by CFRP sheet bonding to steel beams or by welded/bonded steel plate to steel beams. They fabricated eight steel-concrete composite beams consisting of a standard steel I beam of size 16 (web thickness of 6.3 mm, flange thickness of 9.5 mm, flange width of 74 mm and height of 160 mm) composite with a concrete deck slab of 500 mm width by 100 mm thickness. The composite beams had a clear span of 1800 mm. In the first group, three beams were strengthened with steel plates attached to the tension flange of I beams with three different patterns: discontinuous welding, U-shape welding at both ends, and bonding with adhesive together with U-shape welding at both ends. In the second group, two beams were strengthened either by bonding of two layers of CFRP wet lay-up sheets to the tension flange of an I beam or by bonding of CFRP sheets (two layers) to the tension flange together with wrapping around the part of the web on both sides of the I beam. In the same group, two beams were strengthened with the similar patterns except for the inclusion of artificial debonding (50 mm × flange width) between the bottom of the steel flange and the first layer of CFRP sheet at mid-span. One beam was used as an unstrengthen beam for comparison. Test results showed that there was no

growth of intermediate debonding before the yielding of the lower flange for all CFRP strengthened beams. The beams with pre-debonding showed lower flexural capacity than those with full bonding after yielding. In the case of steel plate bonding, no difference in yield load was observed between three patterns except a negligible difference in the elastic stiffness.

Based on the literature review and according to the authors' best knowledge, no studies considered strengthening the tension face of concrete slabs together with the bottom flange of the steel beam in composite girder systems. Considering this research gap, the current study aims to investigate the effectiveness of six different strengthening schemes for scaled down steel-concrete composite bridge girders under static load, employing strengthening of the concrete slab soffit only, the steel bottom flange only and the steel beam flange together with the concrete slab soffit using CFRP only, steel plate only and a combination of both.

2 EXPERIMENTAL PROGRAM

2.1 *Fabrication of specimen*

A total of seven composite beams were fabricated consisting of a 2 m long, 500 mm wide by 50 mm thick concrete slab composite with 2.2 m long 150UB18.0 steel beam (overall depth of 155 mm, flange width of 75 mm, flange thickness of 9.5 mm and web thickness of 6.5 mm). Ten mm thick steel plates were welded to the both ends of the steel beam covering the full cross-section (155 mm height and 75 mm width). Two more steel plates with the same thickness (136 mm height and 34.5 mm width) were welded on both sides of the steel web at 95 mm clear distance from each end of steel beam in order to stiffen the support regions. Table 1 provides the material properties of the steel beam and stiffener plates. Concrete slabs were fabricated from seven batches with same mix ratio. Wire mesh (N10 bars with 100 mm spacing in both direction) was used as longitudinal and transverse reinforcement for the concrete slab. A maximum coarse aggregate size of 9.5 mm was used due to the small slab thickness. The properties of concrete related to each beam are given in Table 2 which were obtained from the cylindrical test based on Australian Standard (AS 1012). A total of 18 M8 grade 8.8 bolts (spacing = 100 mm) were welded to the top flange of the steel beam in one row to provide shear connection between the steel beam and concrete. The mechanical properties of the shear connectors are as listed in Table 3. The cross-section of composite beams can be seen in Figure 1.

2.2 *Strengthening scheme*

After curing of concrete for 28 days in humid air (covered with wet hessian), sand blasting of the tension flange of the steel beams was conducted. Sand blasting of the concrete slab soffits was also conducted for bonding of steel plate/CFRP to the concrete. Beam 1 was used as a control beam which was not strengthened with any technique. Beam 2 was strengthened with the application of one layer of high tensile CFRP sheet with the dimension of 1 m length, 50 mm width and 0.17 mm thickness on both sides of the concrete slab soffit (middle of each soffit) by two part-epoxy resin primer and epoxy resin saturant. Beam 3 was strengthened with one layer of CFRP sheet (the same dimension as used for the concrete slab) bonded to the steel beam tension flange. In the case of beams 4, 5 and 7, a steel plate with 1 m length, 50 mm width and 10 mm thickness was welded to the steel bottom flange. The only difference among these three beams was in the concrete strengthening. In beam 4, no concrete retrofitting was applied. Beam 5 had steel plates (1 m length, 50 mm width and 10 mm thickness) bonded to both sides of the concrete bottom surface with MasterBrace 1444 epoxy binder (two parts). Both sides of the concrete bottom surface in Beam 7 were retrofitted with CFRP sheets. In case of Beam 6, both steel and concrete was strengthened with one layer of CFRP sheet with the same dimension used for Beam 2, 3 and 7. Some of these repairing techniques are shown in Appendix. Before bonding of CFRP sheets to concrete, a primer layer (MasterBrace P 3500) was applied to the concrete or steel surface where CFRP needs to be bonded. After curing of primer for 24 hours, CFRP sheets were applied with epoxy saturant (MasterBrace 4500). The mechanical properties of CFRP and steel plate are provided in Table 4. The CFRP sheets bonded to concrete and steel beam and steel plates bonded to concrete were cured for at least two days before testing.

Table 1. Mechanical properties of steel beam and stiffener.

Yield strength (MPa)	Tensile modulus of elasticity (GPa)	Ultimate strength (MPa)
320	210	440

Table 2. Mechanical properties of concrete for composite beams.

Beam ID	W/C ratio	Mean compressive strength (MPa)
1	0.38	60.4
2	0.38	62.3
3	0.38	66.3
4	0.38	54.5
5	0.38	50.9
6	0.38	54.4
7	0.38	52.5

Table 3. Mechanical properties of shear connector.

Min. tensile strength (MPa)	Min. yield stress (MPa)
830	660

Table 4. Mechanical properties of CFRP and steel plate.

Material	CFRP (Mbrace CF 230/4900)	Steel plate
Thickness (mm)	0.17	10
Yield strength (MPa)	N/A	320
Ultimate tensile strength (MPa)	4900	440
Tensile modulus of elasticity (GPa)	230	210

2.3 *Test setup and instrumentation*

All beams were tested under three point bending with load control at a speed of 0.05 kN/sec up to 60 kN followed by displacement control at a speed of 0.6 mm/min until the beam failed. The test set-up of the beam is shown in Figure 2. The mid-span deflection was also measured using a 100 mm capacity LASER.

3 RESULT AND DISCUSSION

3.1 *Load vs mid-span deflection and failure mode*

Load vs. mid-span deflection curves were plotted for all composite beams in order to compare the behaviour of retrofitted beams (Beams 2–7) to that of the control beam (Beam 1).

From the load-deflection plots (Figure 3), it is clearly visible that, when comparing against Beam 1, Beams 2, 3 and 6 behaved almost similarly whereas Beam 4, 5 and 7 have higher values in terms of yield load and maximum load. Thus, the analysis of the load-deflection curve can be discussed in two groups. Group A – consisted of Beam 2, 3 and 6 which are related to CFRP, and Group B which includes Beam 4, 5 and 7 that had steel plates attached to the soffit of the steel beam.

Beam 1 yielded at about 172 kN. The large drop of load after reaching maximum load of 216.7 kN indicates initiation of shear connector failures at both ends of the composite beams which can also be seen at Figure 4(b). The beam was unloaded at about 60 mm deflection after cracks extended to the concrete top fibre. In addition to the major flexural crack at mid-span there were several minor cracks. Yield loads for Beams 2, 3 and 6 was 175 kN, respectively, whereas maximum loads for the same were 216.1, 215.7 and 219.3 kN, respectively. For beam 2, the CFRP on the concrete started to debond after the load reached the maximum value with consecutive load drops which represent extension of the debonded zone (Figure 5).

Unlike Beam 1, Beam 2 showed progressive flexural cracks from mid-span to both ends of the CFRP reinforcement because of debonding propagation in the concrete layer.

Although a gap between the steel beam and concrete at both ends and a longitudinal crack along the shear connector on the top of the concrete slab was seen in Beam 2, there was no indication of failure in the shear connector unlike Beam 1. CFRP on both sides completely debonded from the same end while the top concrete fibre was crushed.

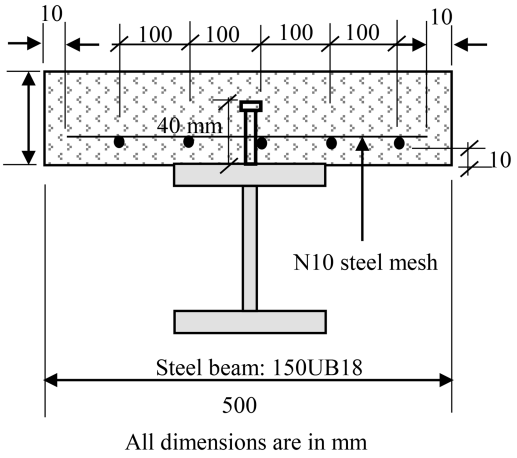

Figure 1. Cross-section of the composite beam (not to scale).



Figure 2. Test set up of three point bending loading.

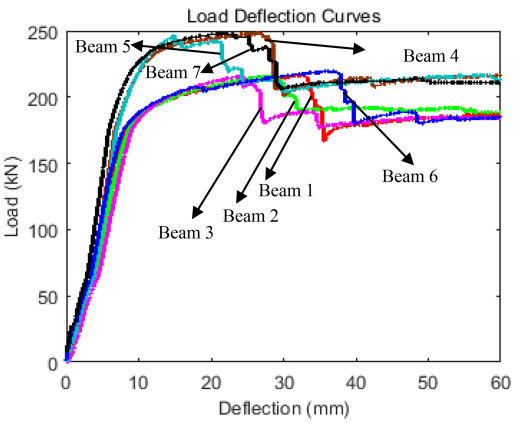

Figure 3. Load-deflection plots of all beams.

Beam 3 showed slightly higher post-elastic sfiffness than beam 1, 2 and 6 after yielding of the steel beam due to the contribution of CFRP bonded to the steel beam. Then, at about 25 mm deflection, it showed a small drop of load indicating initiation of debonding followed by a large drop to 175 kN due to separation of the connection between the concrete and steel beam at both ends. The CFRP debonded completely after a



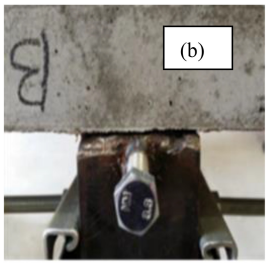

Figure 4. Failure modes of Beam 1: (a) cracks in concrete and (b) separation of shear connection.

slight increase in load to 180 kN at a deflection level of 33 mm. The beam failed by crushing of concrete at a deflection close to 60 mm (Figure 6). In beam 6, after steel yielding at 175 kN, the CFRP debonded from the steel beam at 210 kN when the deflection was only 18 mm. A small drop of load was observed at this point of loading. A large drop in load to about 170 kN after maximum load indicates failure in the shear connector (at about 40 mm deflection). Then the load slightly increased followed by few small drops indicating CFRP debonding from concrete. The beam failed by crushing of concrete as soon as the CFRP debonded from the concrete (Figure 7). It can be noted that the CFRP failed in the primer layer from the steel beam, the steel surface was complete smooth and clean without any epoxy attached to it. Whereas, theCFRP debonded from the concrete had some concrete debris as well as epoxy attached.

Group B beams (beams 4, 5 and 7) which had steel plate welded to the steel beam in common, showed almost similar load-deflection behaviour in terms of maximum load. In beam 4, non-linearity started at 175 kN due to the steel plate yielding. Then at about 235 kN, the deflection became more pronounced with a very small increase in load, possibly because of yielding of the web of the steel beam as well as at other locations far from mid-span. After reaching a maximum load of 248.1 kN a large drop in load to less than 200 kN indicates failure of the shear connector at both ends, which was followed by several drops (load increased slightly after the first shear connector failure) of load representing gradual failure of the shear connectors. Finally, the concrete crushed at about 68 mm deflection with continuous decrease in load carrying capacity. Figure 8 shows the mode of failure of beam 4. Beam 5, showed non-linearity at 175 kN like beam 4. However, the non-linearity was not due to yielding of steel; a large slip in the shear connector was

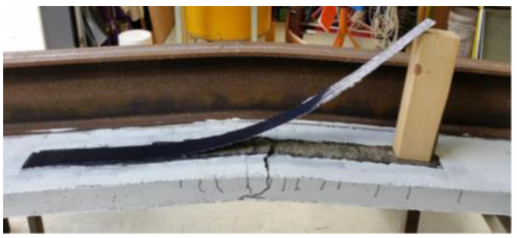

Figure 5. Failure modes of Beam 2.

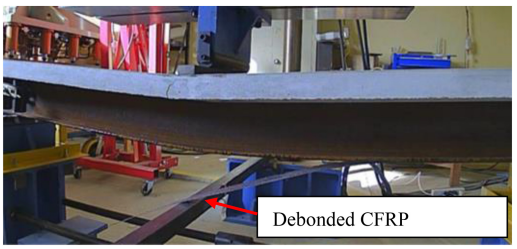

Figure 6. Failure modes of Beam 3.



Figure 7. Failure modes of Beam 6.

the contributing factor for the non-linearity. The steel plate bonded to the concrete debonded very early in the loading regime at about 50 kN when the first flexural crack appeared. After reaching a maximum load of 246.2 kN, there are several load drops representing shear connector failures (Figure 9).

The crack in the concrete slabs (of Beam 5) propagated diagonally upward parallel to the direction of the debonded steel plate and coincided with another major flexural crack (forming a wedge shape). The significant crack widening induced by the self-weight of the debonded steel plate from the concrete can be the reason for the loss of composite action and failure of the shear connectors. The large deflection without significant increase in load represents a high slip between steel and concrete. The steel yielded just before failure of the beam by concrete crushing at about 58 mm deflection. Beam 7 reached a plastic stage with the yielding of the steel plate at 175 kN indicated by the non-linearity of the load-deflection curve. At about 240 kN (deflection of 15 mm), there is slight drop of load when the debonding of CFRP from concrete initiated. After reaching a maximum load of 248.2 kN, there were several load-drops due to both initiation of

Table 5. Comparison of maximum load with Beam 1.

Beam ID	2	3	4	5	6	7
%increase in maximum load	−0.3	−0.4	+14.5	+13.6	+1.2	+14.5

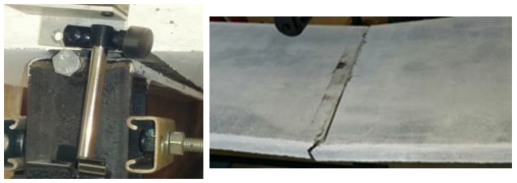

Figure 8. Failure modes of Beam 4.

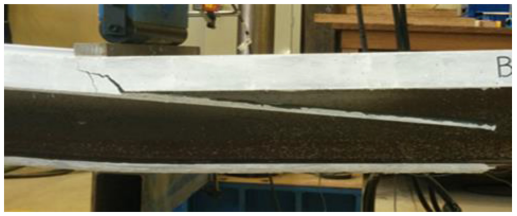

Figure 9. Failure modes of Beam 5.

shear connector failures and debonding crack propagation of concrete. Load dropped to about 206 KN at a deflection level of 28 mm. This is due to failure of the shear connector at both ends (Figure 10). Immdiately, after failure of the shear connector, the FRP completely debonded on both sides of the concrete slab with no noticeable increase in load. Then gradual failures of the shear connector occurred until the beam failed by concrete crushing. Figure 10 shows the failure modes of Beam 7.

3.2 *Maximum load*

In terms of maximum loads (Figure 11) of the retrofitted beams with CFRP only, beam 2 (CFRP on concrete), beam 3 (CFRP on steel) and beam 6 (CFRP on concrete and steel) did not show any significant improvement. In fact, beam 2 and beam 3 reached maximum loads slightly lower than the control beam (Beam 1).

Beams 4, 5 and 7, which were retrofitted with steel plate welded to the steel beam soffit only, steel plate glued to concrete in addition to a steel plate welded to the steel beam soffit and CFRP bonded to concrete in addition to steel plate at the steel beam soffit, respectively, showed significant improvement in load-carrying capacity. The percent increases were 14.5, 13.6 and 14.5, respectively (Table 5). However, the increased load-carrying capacity can be mainly attributed to steel beam retrofitting not to concrete retrofitting, since, Beam 4 and Beam 7 showed exactly



Figure 10. Failure modes of Beam 7.

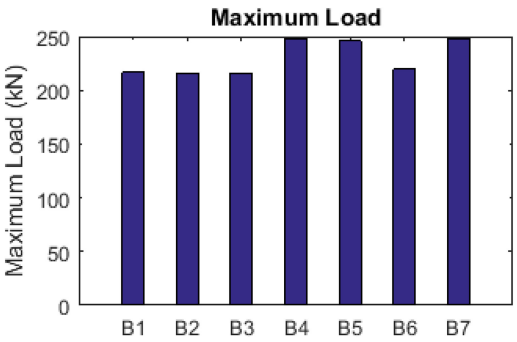

Figure 11. Comparison of maximum load capacity.

the same increase in load-carrying capacity whereas beam 5 showed slightly lower capacity. It is evident from the observations that steel plate welded to the steel beam is the main contributing factor to the strength increase, since beam 4 retrofitted with steel plate welding at the steel beam soffit showed a similar strength improvement to beams 5 and 7. CFRP attached to the steel plate did not show any improvement and debonded very early in the load regime probably in the primer layer, as there was no glue attached to the steel beam. The glue layer was seen only on the debonded CFRP sheet which did not allow the CFRP to participate much in resisting the tensile stress at the extreme bottom fiber of any cross section.

Hence, it can be concluded that steel plate welded to steel beam compared to CFRP attached to steel beam is the better technique.

4 CONCLUSIONS

This study aimed to investigate six techniques to strengthen steel-concrete composite beams incorporating retrofitting of the concrete slab soffit only, retrofitting of the steel beam only and a combination of both applying CFRP wet lay-up sheets and steel plate. Based on the experimental results of the load-deflection behavior of retrofitted steel-concrete composite beams, the following conclusions can be drawn-

- There was no significant effect of CFRP on the retrofitting of steel-concrete beams in terms of load-carrying capacity. The beams retrofitted with

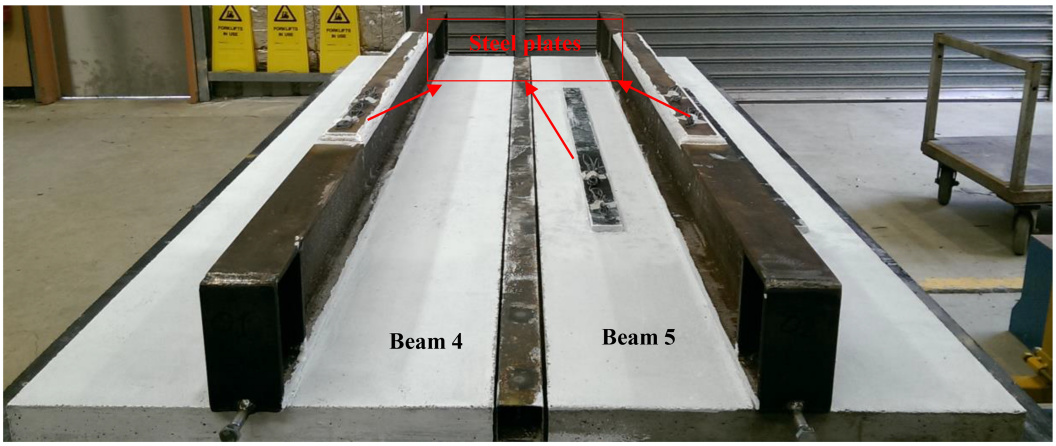

Figure 12. Retrofitting technique of beam 4 and 5

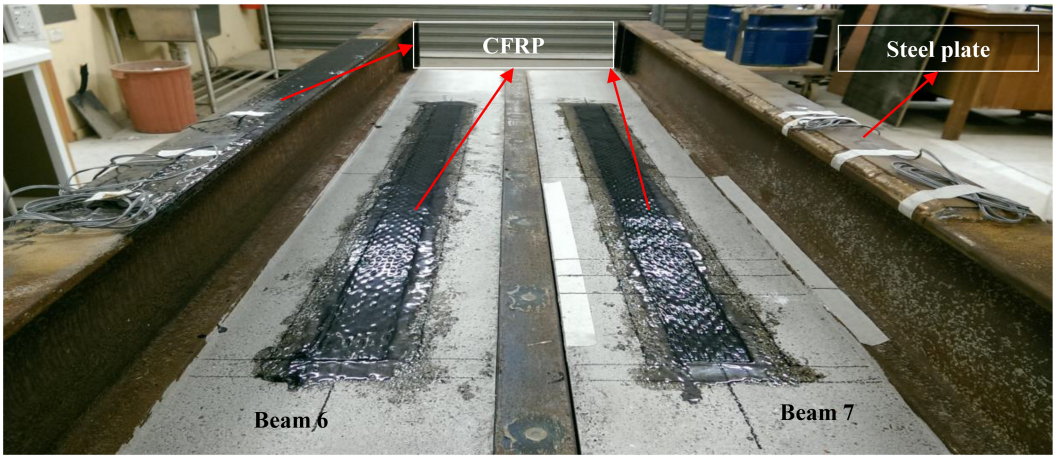

Figure 13. Retrofitting technique of beam 6 and 7

CFRP on concrete, CFRP on steel beam and CFRP on concrete and steel showed almost the same load-carrying capacity as unstrengthened beams.

- The beams which were retrofitted with steel plate welded to steel beam in common showed an almost similar increase in load-carrying capacity (13.6 to 14.5 %) regardless of the retrofitting of the concrete slab. Hence, the hybrid retrofitting is the most suitable one in terms of improvement of load capacity.
- Although all beams except one yielded first, gradual failure of shear connectors followed the steel yielding before complete failure by crushing of concrete. Further investigation needs to be carried out on how to increase the performance of shear connections in existing composite beams.

APPENDIX

Appendix – Repair layouts of different beams

REFERENCES

Al-Saidy, A., Klaiber, F., Wipf, T., Al-Jabri, K. & Al-Nuaimi, A. 2008. Parametric study on the behavior of short span composite bridge girders strengthened with carbon fiber reinforced polymer plates. *Construction and Building Materials*, 22, 729–737.

Al-Saidy, A. H., Klaiber, F. & Wipf, T. 2004. Repair of steel composite beams with carbon fiber-reinforced polymer plates. *Journal of Composites for Construction*, 8, 163–172.

Bakis, C., Bank, L. C., Brown, V., Cosenza, E., Davalos, J., Lesko, J., Machida, A., Rizkalla, S. & Triantafillou, T. 2002. Fiber-reinforced polymer composites for construction-state-of-the-art review. *Journal of Composites for Construction*, 6, 73–87.

Fam, A., Macdougall, C. & Shaat, A. 2009. Upgrading steel-concrete composite girders and repair of damaged steel beams using bonded CFRP laminates. *Thin-Walled Structures*, 47, 1122–1135.

Heiza, K., Nabil, A., Meleka, N. & Tayel, M. 2014. State-of-the Art Review: Strengthening of Reinforced Concrete Structures-Different Strengthening Techniques.

Sixth International Conference on Nano-Technology in Construction, 22–24 March 2014. Cairo-Egypt.

Mertz, D. & Gillespie, J. 1996. Rehabilitation of steel bridge members through the application of advanced composites. Final Report. *NCHRP-93-ID01*.

Miller, T. C., Chajes, M. J., Mertz, D. R. & Hastings, J. N. 2001. Strengthening of a steel bridge girder using CFRP plates. *Journal of Bridge Engineering*, 6, 514–522.

Nie, J., Cai, C. & Wang, T. 2005. Stiffness and capacity of steel-concrete composite beams with profiled sheeting. *Engineering structures*, 27, 1074–1085.

Nie, J. & Cai, C. S. 2003. Steel-concrete composite beams considering shear slip effects. *Journal of Structural Engineering*, 129, 495–506.

Sallam, H. E. M., Badawy, A. A. M., Saba, A. M. & Mikhail, F. A. 2010. Flexural behavior of strengthened steel-concrete composite beams by various plating methods. *Journal of Constructional Steel Research*, 66, 1081–1087.

Sen, R., Liby, L. & Mullins, G. 2001. Strengthening steel bridge sections using CFRP laminates. *Composites Part B: Engineering*, 32, 309–322.

Tavakkolizadeh, M. & Saadatmanesh, H. 2003a. Repair of damaged steel-concrete composite girders using carbon fiber-reinforced polymer sheets. *Journal of Composites for Construction*, 7, 311–322.

Tavakkolizadeh, M. & Saadatmanesh, H. 2003b. Strengthening of steel-concrete composite girders using carbon fiber reinforced polymers sheets. *Journal of Structural Engineering*, 129, 30–40.

Concrete Solutions – Grantham et al. (Eds.)
© 2016 Taylor & Francis Group, London, ISBN 978-1-138-03008-4

Bacteria-based self-healing mortar: A comparison of two studies

E. Tziviloglou, V. Wiktor, H.M. Jonkers & E. Schlangen
Delft University of Technology, The Netherlands

ABSTRACT: Self-healing concrete has drawn a lot of attention in recent years. There are numerous projects worldwide that work on the development of self-healing agents. Among those, bacteria-based self-healing concrete is a very promising solution to prevent durability problems in concrete that are related with cracking. Bacteria-based self-healing concrete not only provides sealing of open micro-cracks that endanger the structure's health, but it also has economical and environmental benefits, since it will extend the lifetime of the structure and reduce repair costs. In this study, the bacteria-based self-healing agent consists of alkaliphilic bacterial spores, organic mineral precursor compounds and Light Weight Aggregates (LWA). Although the success of the concept has been proven in previous research, in this study an optimized method for the incorporation of the organic compounds into the LWA has been developed. The method allows more of the organic compounds to be stored into the LWA. This paper focuses on comparing performance on mechanical properties and sealing efficiency of cracks of mortar samples from past and current research. The initial hypothesis of the study was that the lightweight mortar with the higher amount of healing agent will show faster and more efficient crack sealing capacity. The comparison revealed different results than expected. In fact, the sealing efficiency trend proved to be similar for the two studies which was speculated to be due to oxygen limitation rather than healing agent limitation in permanently water submersed specimens.

1 INTRODUCTION

Self-healing concrete has drawn a lot of interest in recent years. The main reason is that self-healing concrete has given promising results for preventing durability problems caused by cracking (Schlangen et al.), without external intervention. Therefore, the lifespan of a structure can be prolonged and repair costs can substantially decrease. After studying the "built-in" ability of concrete to repair cracks with limited crack width in the presence of water, scientists tried to enhance this property by creating self-healing concrete. Numerous projects worldwide may work with different self-healing concepts (De Rooij et al., 2012), but they have one common target; to improve the performance of concrete after cracking. Improving the performance lies in two aspects: the recovery of water-tightness (sealing) and/or the regain of strength and stiffness (healing).

The incorporation of bacterial spores in concrete is a relatively newly developed concept. Spores and organic compounds are incorporated into the concrete during mixing. At a later age, when cracking occurs the healing agent is exposed to the atmosphere. Then, the bacterial spores are activated due to the presence of nutrients, moisture and oxygen inside the crack. Subsequently, active bacteria degrade the organic compounds, resulting in the formation of calcium carbonate ($CaCO_3$) crystals that eventually bridge the open cracks.

In this study, bacterial spores and their nutrients are embedded in lightweight aggregates (LWA) for protection and immobilization during mixing and setting of concrete. The original idea was conceived by Jonkers (Jonkers, 2011) and was further developed by Wiktor and Jonkers (Wiktor and Jonkers, 2011). Those previous studies have shown that by introducing the bacteria-based healing agent in the concrete or mortar matrix, sealing of cracks of 0.15 to 0.46 mm can occur. In the present study, a comparison in crack sealing capacity is made between two mortar mixtures. The first mixture, based on the mix design and the impregnation method given in (Wiktor and Jonkers, 2011), has a relatively low amount of nutrients. The second mixture has an increased amount of nutrients due to a more efficient loading of the LWA. This study investigated the compressive strength of mortar prisms, the type of minerals formed inside the healed cracks and the recovery of water-tightness of cracked mortar prisms.

2 MATERIALS AND METHODS

2.1 *Preparation of the healing agent*

The bio-based healing agent consisted of spores derived from alkaliphilic bacteria of the genus *Bacillus*, nutrients (calcium lactate and yeast extract) and

LWA (Expanded clay particles, Liapor 1/4 mm, Liapor GmbH Germany). In the preceding study (S1), the spores and organics were loaded in the LWA in two steps. First, via impregnation under vacuum, with a calcium lactate (80 g/L) and yeast extract (1 g/L) solution, followed by a second impregnation with a bacterial spore suspension (10^8 spores/L), as described by Wiktor and Jonkers (Wiktor and Jonkers, 2011). After the two subsequent impregnations, the LWA were left to dry in a ventilated oven at 36°C for 7 days. In the present study (S2), the organic compound solution applied was more concentrated (calcium lactate 200 g/L; yeast extract 4 g/L) and also contained the bacteria spores (10^8 spores/L). This suspension was loaded in the LWA through only one vacuum impregnation action. The higher concentration of organics in the solution was obtained by increasing the solution temperature from 15°C (in S1) to 75°C (in S2). Following the impregnation procedure, the LWA were left to dry at room temperature 20°C for 7 days.

2.2 *Preparation of the mortar prisms*

In both studies three types of mortar mixtures were investigated: one reference mixture (REF) with normal weight aggregates, one control mixture (CTRL) with non-impregnated LWA and one mixture (B) with impregnated LWA. The mixtures were based on ordinary Portland cement (CEM I 42.5 N, ENCI, The Netherlands) and 0/4 mm sand or 0.125/1 mm sand and 1/4 mm LWA. The detailed mix proportions are presented in Table 1. For testing flexural and compressive strength of the hardened mix, 3 prisms (40 mm × 40 mm × 160 mm) were cast per mixture. In addition, for the investigation of sealing efficiency (SE) of cracked mortars, specific reinforced (steel wire ø1 mm) mortar prisms (40 mm × 40 mm × 160 mm) featuring a 5 mm diameter hollow tube in the centre were cast. All prisms were demoulded 24 h after casting and kept in a room with standard temperature (20 ± 2°C) and >95% RH for 28 days.

2.3 *Crack introduction on mortar prisms and healing regime*

Cracks were introduced in the specifically prepared reinforced hollow tube-containing 28-days-old mortar prisms by means of 3-point bending. In this procedure, the reinforced prisms were placed on the testing machine, where a vertical load was applied at their middle span, so that the crack opening increased constantly by 0.5 μm/s. When a crack opening of approximately 400 μm was reached, the samples were slowly unloaded. Following the crack creation, the samples were submerged horizontally in a plastic bucket filled with tap water in order to heal. The bucket was kept open to the atmosphere at standard room temperature (20 ± 2°C). Extra water was added (on a weekly basis), to compensate for evaporation to keep a constant liquid-to-solid ratio. In S1 healing (sealing) at 28 and 72 days, and in S2 healing at 28 and 56 days was determined.

Table 1. Mixing proportions of mortar specimens.

Mixture	CEM I (kg/m^3)	Water (kg/m^3)	0/1 mm Sand (kg/m^3)	1/4 mm Sand (kg/m^3)	LWA 1/4 mm (kg/m^3)
REF1&2	463	231.5	810	810	0
CTRL1&2	463	231.5	810	0	257
B1	463	231.5	810	0	270*
B2	463	231.5	810	0	283**

*weight of impregnated LWA after S1 impregnation, assuming weight increase of 5% **weight of impregnated LWA after S2 impregnation, assuming weight increase of 10%

2.4 *Assessment of sealing efficiency via crack permeability test*

A crack permeability test via water flow was used in both studies to evaluate the crack sealing efficiency (Tziviloglou et al., 2015) after cracking and healing. The test was performed before and after the water submersion periods. During the test, water pressurized from a water column of 0.5 m passed through the hollow tube in the middle of the specimen. The water dripping from the crack located in the mid-section of the prism was collected in a container placed on an electronic scale. The test data (weight of water in time) was recorded by a computer connected to the electronic scale. The SE of a specimen after cracking and healing of the specimen was calculated according to Equation 1.

$$SE = 1 - \frac{S_{unhealed}}{S_{healed}} \quad (1)$$

Where S_{healed} = the average (out of three specimens) slope derived from permeability data of the healed specimens; and $S_{unhealed}$ = the average (out of three specimens) slope derived from permeability data of the unhealed specimens.

2.5 *Investigation of healing product*

For the investigation of the healing product formed inside the crack during water submersion, the prisms were separated in two parts after the healing treatment. The morphology of the precipitates exposed on the crack surface was investigated by Environmental Scanning Electron Microscope (ESEM) equipped with Energy Dispersive X-ray spectrometer (EDS).

3 RESULTS

Weight measurements on impregnated and dried LWA used in S1 and S2 revealed that the latter contained substantially higher amounts of organics (see Table 2).

The compressive strength tests on 28-days-old mortar prisms for both S1 and S2 showed that the REF specimens exhibited the highest strength: 49 MPa and

Table 2. Weight increase in LWA due to loading with organics and bacterial spores in S1 and S2.

Study	Organic compound content in LWA (% per dry weight)	Estimated organic compound content in the mortar (% per cement weight)
S1	5.7	3.16
S2	11.2	9.76

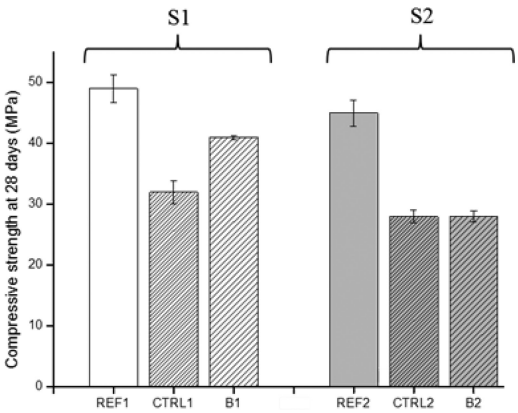

Figure 1. Average 28-days compressive strength of REF, CTRL and B specimens for S1 and S2.

45 MPa respectively (Figure 2). It was also observed that the substitution of normal weight sand with LWA (CTRL specimens) caused a substantial decrease in compressive strength (35% for the S1 and 37% for S2). On the other hand, B specimens (based on LWA loaded with bacterial spores and organic compounds) revealed different compressive strength behaviour in S1 and S2, when compared with the CTRL specimens. In S1, B specimens showed, on average, increased strength (26%) compared with the CTRL, while the compressive strength of B- and CTRL- specimens in S2 was similar (Figure 1).

Cracks obtained in reinforced prisms of specimens used for the permeability test varied between 295 and 370 μm. Figure 2 shows the frequency of the crack width values before healing. As can be derived from Figure 2, the average crack width value was 335 μm and the most frequently occurring values ranged from 335 to 365 μm.

Following the crack creation, 3 prisms from each of the three series were subjected to the crack permeability test. The rest of the specimens were tested for crack permeability after the healing period ended (28, 56 or 72 days of water immersion). Figure 3 shows the calculated SE of specimens (for S1 and S2) immersed in water for 28 days. The results showed an increased performance of the B specimens compared to the CTRL (more than 20%) specimens.

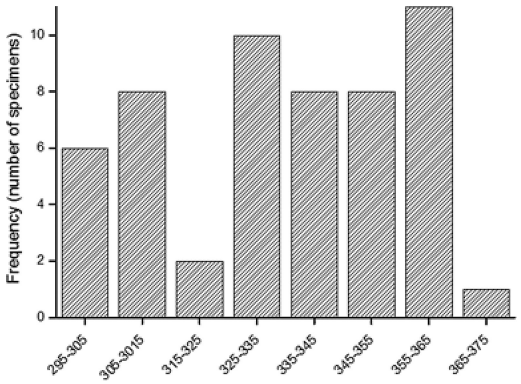

Figure 2. Frequencies of crack width values as obtained by 3-point-bending on prisms prior to crack permeability tests.

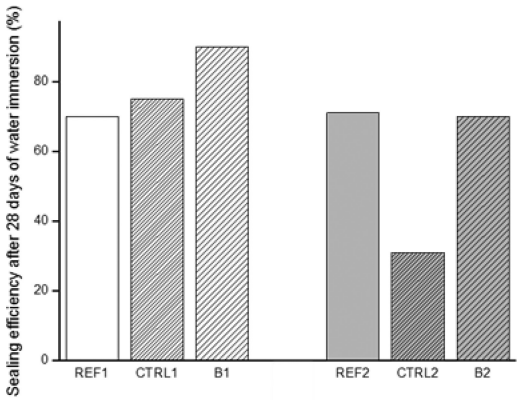

Figure 3. SE of specimens subjected to water immersion for 28 days. Left results of the previous study 1 (S1), right of the present study (S2).

Additionally, specimens of both S1 and S2 showed a similar trend after 72 and 56 days of continuous water immersion. The specimens without healing agent (REF and CTRL) exhibited SE values of approximately 80–85%, while the specimens with the healing agent (B) revealed a SE over 90% (see Figure 4).

The EDS analysis of formed minerals on crack surfaces indicated high peaks of calcium, carbon and oxygen atoms, suggesting minerals were $CaCO_3$ based. ESEM images (Figure 5) showed that the main crystal shapes occurring on crack surfaces of the three different types of mortar specimens were clustered sharp-edged formations or asymmetric rhombohedral polymorphs of probably $CaCO_3$.

4 DISCUSSION

4.1 *Compressive strength*

The compressive strength of the REF and CTRL prisms produced in S1 and S2 revealed comparable values. In fact, the values obtained in the present

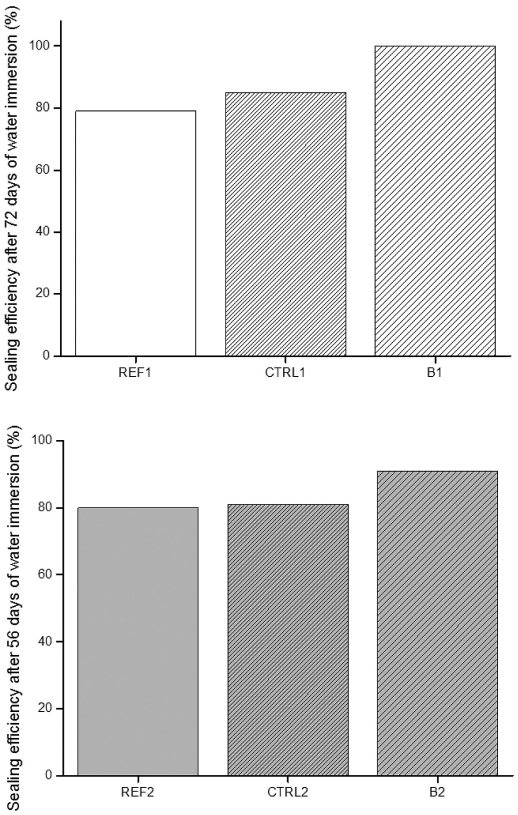

Figure 4. SE of specimens subjected to water immersion for 72 days (above) and water immersion for 56 days (below).

study S2 showed a small strength decrease of about 8% for the REF and 12% for the CTRL specimens respectively. The values, however, fell within the range of standard deviations. On the other hand, the compressive strength of B1 and B2 differed significantly (approximately 30%). It was assumed that the decrease in compressive strength of B2 was caused by the higher organic compound content in the incorporated LWA.

4.2 *Sealing efficiency*

The initial hypothesis of the current study was that the mortar with the higher content of healing agent (S2) would result in better sealing after cracking and healing treatment. However, the sealing efficiency of the bacteria-based specimens in both studies did not differ substantially (both were ranging at about 95%) and the hypothesis must therefore be rejected. However, in both studies, significantly higher self-healing (crack sealing) was found in the healing agent-containing than the non- healing agent containing specimens. SE appeared more profound in 56 and 72 days of healing treatment. The possible reasons for lack of significant difference in self-healing efficiency between healing agent-based specimens in S1 and S2 are summarized below.

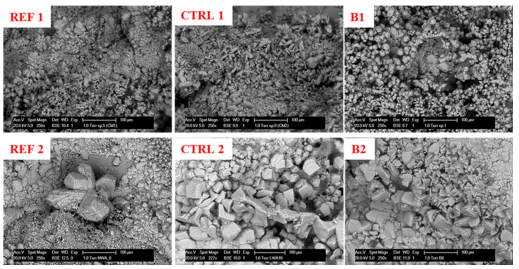

Figure 5. ESEM observations of crystalline formations found on the edges of the cracks after healing.

The final crack widths created through 3-point-bending were not equal in most of the reinforced specimens (see Figure 2). These varying crack widths led also to varying crack volumes. Taking into account that the tests before and after healing were carried out on different sets of triplicate specimens can at least partly explain why hardly different SE values of healing agent-based specimens were found between the first and the second study. Another, and probably quantitatively more important, reason for lack of significant differences in SE results is probably due to continuous submersion of specimens in water during the healing period resulting in oxygen limitation for the metabolically active bacteria. Lack of oxygen results in decreased metabolic activity and thus in decreased conversion of organic compounds to crack-sealing inorganic minerals. Oxygen limitation, and not healing agent amount, might thus be the determining factor for crack-sealing efficiency in continually water submersed specimens.

Finally, the sealing performance of the B specimens in S1 was already rather efficient. Consequently, there was only a small room for improvement in S2 where a higher amount of healing agent was used to seal the same crack width.

5 CONCLUSIONS

In conclusion, the recovery of water tightness proved to be higher in healing agent containing specimens than in specimens without. Although a higher quantity of healing agent was applied in specimens of the second study, no substantial further improvement of the already efficient self-healing capacity as in the first study was observed. The reason for this apparent lack of healing improvement might primarily be due to limitation of oxygen diffusion in permanently submersed specimens. Limited oxygen availability reduces the capacity of crack sealing due to decreased bacterial metabolic activity and concomitant reduced calcium carbonate based mineral production. The application of higher amounts of healing agent might thus be only effective in non-permanently submersed specimens where oxygen limitation does not play a major role.

ACKNOWLEDGEMENTS

The authors acknowledge the financial support of the European Union Seventh Framework Programme (FP7/2007-2013) under grant agreement n° 309451 (HEALCON), and Mr Arjan Thijssen for the ESEM images.

REFERENCES

De Rooij, M., Van Tittelboom, K., & Schlangen, E. 2012. Self-healing phenomena in cement-based materials, State-of-the-art Report of RILEM Technical Committee.

Jonkers, H.M. 2011. Bacteria-based self-healing concrete. HERON, 56, 1–11.

Schlangen, E. & Josef, C. 2009. Self-healing materials: fundamentals, design strategies, and applications, VCH verlag GmbH and Co KGaA, pp. 141–182.

Tziviloglou, E., Wiktor, V., Jonkers, H. M., & Schlangen, E. 2015. Development of bio-based self-healing concrete to increase durability of structures, In Construction in the 21st Century.

Wiktor, V. & Jonkers, H.M. 2011. Quantification of crack-healing in novel bacteria-based self-healing concrete. Cement and Concrete Composites, 33, 763–770.



Taylor & Francis
Taylor & Francis Group
http://taylorandfrancis.com

Concrete Solutions – Grantham et al. (Eds.)
© 2016 Taylor & Francis Group, London, ISBN 978-1-138-03008-4

Some considerations on precipitation rate of calcium carbonate in bio-based materials used for concrete repair

K. Kawaai, I. Ujike, S. Yamamoto & P.Y. Putri
Ehime University, Matsuyama, Japan

ABSTRACT: This paper presents some considerations on repair methods using bio-based materials comprising yeast, glucose or sucrose and calcium acetate mixed in Tris buffer solution. The investigation revealed that calcium carbonate can precipitate as crystals within 24 hours depending on the concentrations of these materials used in the mixture and pH levels. The results suggested that reaction rate at early stages e.g. 6 hours later and resulting precipitates up to 24 hours after mixing may have a significant effect on the effectiveness of sealing cracks in concrete.

1 INTRODUCTION

Reinforced Concrete (RC) structures have been commonly used in infrastructure facilities including highways, bridges, and marine structures. Although quality control of concrete used in these structures is strictly required, initial defects are likely to occur owing to structural constraints and poor workmanship. For example, construction-joints or gaps tend to form especially at joints between structural members used in bridge structures. When it rains, it may cause leakage from the gap leading to a decrease in serviceability and should be aesthetically unacceptable. Difficulties associated with repair techniques for such defects as shown in Figure 1 are that conventional repair materials are less effective in sealing the gap formed spatially distributed in large areas, especially deeper zones in concrete structures.

For example, organic materials e.g. epoxy resin and inorganic materials e.g. cement-based grout materials with higher viscosity are less practical in repairing deeper zones of cracks or gaps in large areas. In addition, they may cause adverse effect on the natural environment if they flow out through the gaps or cracks which are not completely repaired. Therefore, it is advantageous if the material is not based on such materials, however, it should have similar materials properties to concrete.

Recently, liquid-based repair techniques in the field of self-healing through the use of microbial induced precipitation (MIP) have been intensively investigated (Kawasaki et al., 2006; Wiktor and Jonkers, 2010, 2015; Kubo et al., 2013; Ujike et al., 2014). The mixtures are comprised of a microorganism, an organic carbon source and a calcium source which is readily available in concrete. When dry yeast is selected as the microorganism, carbon dioxide produced through the microbial metabolic processes consuming an organic

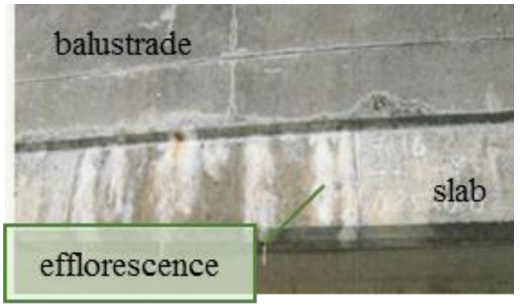

Figure 1. Leakage observed in existing bridge structure.

carbon source such as glucose and/or sucrose provides carbonate ions. The carbonate ions react with calcium ions present in the mixture, leading to the precipitation of calcium carbonate depending on the pH levels in the alkali environment. The reactions with respect to the fermentation are summarized as following:

$$\begin{aligned} &C_6H_{12}O_6 \rightarrow 2CO_2 + 2C_2H_5OH \\ &CO_2 + H_2O \rightarrow CO_3^{2-} + 2H^+ \\ &Ca^{2+} + CO_3^{2-} \rightarrow CaCO_3 \downarrow \end{aligned} \quad (1)$$

It should be noted that the material produced through the reactions is not harmful to concrete materials because the precipitates are mainly comprised of calcium carbonate which is one of reaction products formed by carbonation of hydration products. Besides the material properties, the mixture is a less viscous material compared to However, the precipitation rate through MIP processes is largely affected by the concentrations of each constituent used and the pH levels. Therefore, this study examined the precipitation rate especially at early stages depending on the

concentrations and initial pH levels. In addition, the application method, taking into consideration the precipitation rate, was explored to obtain a better effect on the leakage repair.

2 METHODOLOGY

2.1 *Selection of basic constituents of mixtures*

Mixtures used in this study need calcium and carbonate ions for producing calcium carbonate as shown in Figure 2. In addition to the reaction, it is essential to control the pH levels in mixtures to facilitate the precipitation of calcium carbonate. Tris (tris hydroxymethyl aminomethane) buffer solution with an alkali buffering function was used in this study. The solution is adjustable with respect to pH when mixed with hydrochloric acid. The use of hydrochloric acid should be minimized in adjusting pH levels for ensuring no adverse effect on the integrity of hardened concrete and preventing chloride-induced corrosion.

The source of calcium ions used for mixtures was chosen taking into consideration higher solubility and no adverse effect on concrete materials. The material should be also commercially available and cost-effective. Based on the considerations above mentioned, calcium acetate was chosen in this study.

In addition, commercially available dry yeast was used as a microorganism, which is anaerobic and active in the absence of free oxygen. Organic carbon sources are necessary for the metabolism of the microorganism. Through anaerobic fermentation, the yeast converts carbohydrates to carbon dioxide and alcohols in the presence of glucose ($C_6H_{12}O_6$) or sucrose ($C_{12}H_{12}O_{11}$) which was selected as an organic carbon source.

It is known that the highly alkaline environment which the pore solution in concrete exhibits is a severe condition for the yeast. It is crucial for the microorganism to exist in the mixtures with relatively lower pH, which is adjusted as low as possible initially. According to past research, it has been reported that the precipitation of calcium carbonate could not be sustained when pH decreased less than 7.5 (Ujike et al., 2014). In order to maintain the appropriate pH levels in the mixtures tested, Tris buffer solution was used for all the mixtures tested. The pH was initially adjusted as 9.0 or 8.0 in room conditions controlled at 20°C. With the above materials, 13 combinations of mixtures were tested in this study. Table 1 shows the mix proportion of each material tested in this study.

2.2 *Testing procedure for determining the amount of precipitates in mixtures*

In order to measure the concentration of calcium ions present and the pH in mixtures after the reaction had started, each mixture was prepared in a test tube. First, each material, based on the mix proportion specified as shown in Table 1, was prepared and they were mixed with Tris buffer solution in a beaker. The mixture in the beaker was subsequently stirred until each material was dissolved into the solution. And then further Tris buffer solution was added to make the solution 40 mL totally. The test tubes were placed in room conditions controlled at 20°C for the measurement. The concentration of calcium ions and pH were measured in filtered mixtures using commercially available meters. Each test was carried out using two test tubes to confirm the consistency of results obtained.

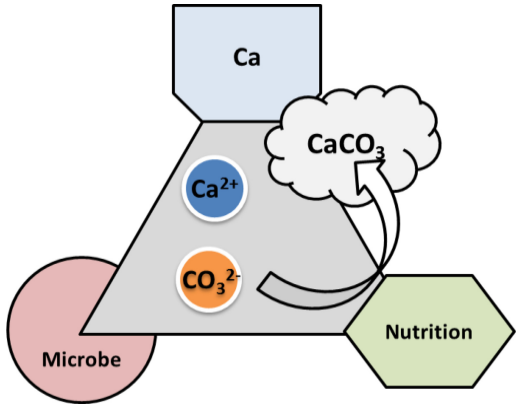

Figure 2. Basic constituents of bio-based repair material.

Based on the results of calcium ions measured, precipitated calcium carbonate was estimated using the following formula:

$$CaCO_3 = Q(\text{mol/L}) \times m(\text{L}) \times M(\text{g/mol}) \times \frac{C_0 - Ca}{C_0} \quad (2)$$

where $CaCO_3$: the amount of precipitates (g), Q: concentration of calcium acetate (mol/L), m: amount of solution (L), M: molar mass of calcium carbonate (100.09), C_0: Initial concentration of calcium ion and Ca: concentration of calcium ion measured.

The precipitates were also tested for X-ray powder diffraction analysis to examine the crystals formed though the MIP processes in mixtures.

2.3 *Water permeability test*

A water permeability test, when cracked concrete specimens were subjected to water flowing at a pressure of 15 kPa, was carried out to evaluate the effectiveness of the selected mixtures for sealing cracks in concrete specimens. Concrete specimens enclosed in PVC pipe were first cast with a water to cement ratio of 0.5. The concrete specimens with cracks which were induced by splitting were subsequently sealed with waterproof tape in order to prevent repair mixtures from leaking through the side of specimens as shown in Figure 3. The crack width was about 0.3 mm at most in each specimen. Before the selected mixtures were poured into the crack, water permeability tests were carried out as benchmarks. The quantity of water flowing through the crack was measured for 5 minutes. And then, selected mixtures were poured into the crack via

Table 1. Mix proportion of dry yeast, glucose/sucrose and calcium acetate.

Cases	Dry yeast (g/L)	Glucose/Sucrose	(mol/L)	Calcium acetate (mol/L)	Tris buffer solution pH	Tris buffer solution (mol/L)
A1	3.0	Sucrose	0.10	0.05	9.0	0.10
A2	3.0	Glucose	0.10	0.05	9.0	0.10, 0.25, 0.50
A3	6.0					
A4	9.0					
A5	3.0	Glucose	0.10	0.05	8.0	0.10, 0.25, 0.50
A6	6.0					
A7	9.0					
B1	12.0	Glucose	0.20	0.10	9.0	0.10, 0.25, 0.50
B2	18.0		0.30	0.15		0.75, 1.0
B3	24.0		0.40	0.20		
C1	18.0	Glucose	0.20	0.10	8.0	0.50, 0.75
C2	27.0		0.30	0.15		1.0, 1.25
C3	36.0		0.40	0.20		

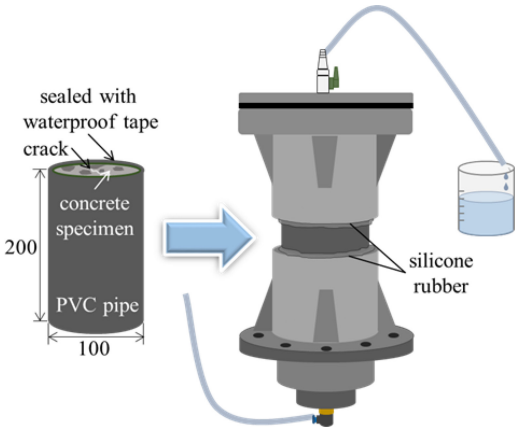

Figure 3. Experimental set-up for water permeability test.

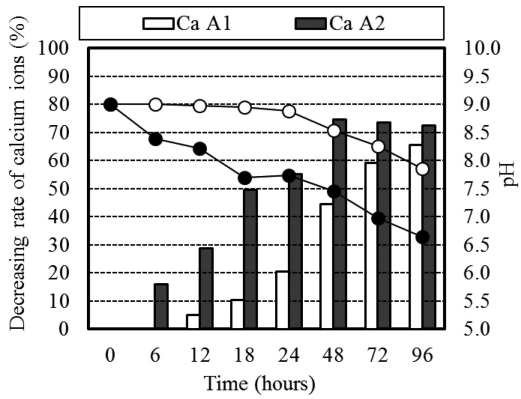

Figure 4. Concentrations of calcium ions and pH (A1&A2).

ponding using a PVC pipe fixed with epoxy resin on the specimen. It was removed prior to the water permeability tests which were finally carried out using the specimens in which cracks were supposed to be sealed with precipitated calcium carbonate. It should be noted that the pressure was applied to the plane on the side of the repaired surface.

3 RESULTS AND DISCUSSION

3.1 *Influence of organic carbon source*

The effect of an organic carbon source given to the yeast was examined with respect to the precipitation rate up to 96 hours after they were mixed. The mixtures tested were the A1 and A2 cases as shown in Table 1. They were comprised of glucose or sucrose as an organic carbon source. Figure 4 shows the decreasing rate of calcium ions and changes of pH measured in the mixtures tested. As can be seen, the concentration of calcium ions in the A1 mixture mixed with sucrose was decreased by 20% after 24 hours and the decreasing rate reached about 65% some 96 hours later. On the other hand, the decrease in the concentration of calcium ions in the A2 mixture were notably observed in 6 hours of the monitoring after mixing. Besides the faster reactions observed in the A2 mixture, the decreasing rate reached about 70% up to 48 hours of elapsed time. For the changes of pH in those mixtures, the pH was observed to decrease from the early stages of precipitation processes in the case of the A2 mixture.

It is known that sucrose as disaccharide can be converted into glucose though glycolysis, which can be subsequently consumed by the metabolic processes of the yeast. Thus, the use of monosaccharide led to higher generation rate of carbon dioxide through the fermentation of the yeast. It was found that the A2 mixture comprising glucose and the yeast showed a higher precipitation rate of calcium carbonate owing to the use of monosaccharide as the organic carbon source. It is noted that the decreasing rate of calcium ions was comparable after 48 hours of monitoring in the case of A1 and A2 mixtures tested, which could be

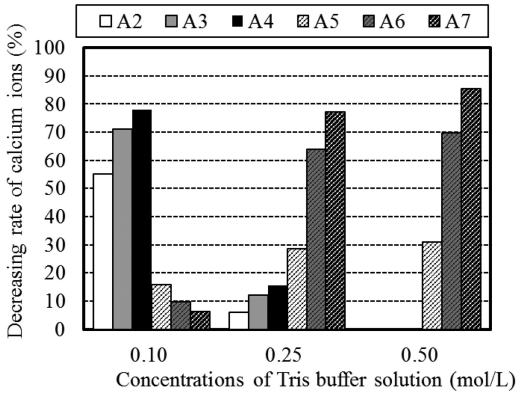

Figure 5. Decreasing rate of calcium ions after 24 hours (A2 to A7 mixtures).

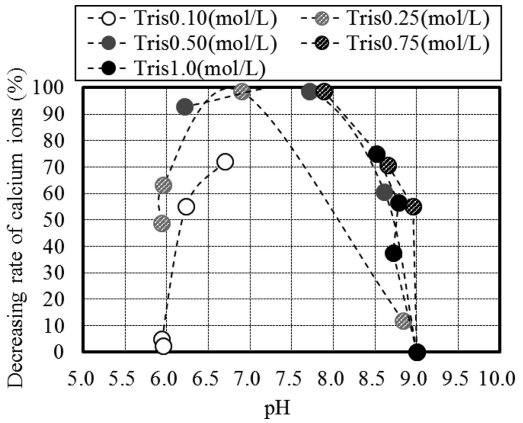

Figure 6. Decreasing rate of calcium ions and pH (A3, B series).

attributed to the pH drop below 7.5 especially after 48 hours of monitoring.

3.2 *Concentrations and initial pH of Tris buffer solution*

In order to determine appropriate concentrations of Tris buffer solution depending on the initial pH, A3 to A7 mixtures were tested based on the results of the A2 mixture comprising glucose as an organic carbon source. They were basically comprised of higher concentrations of the yeast mixed in two series of Tris buffer solution with an initial pH of 8.0 or 9.0. Figure 5 shows that the decreasing rate of calcium ions measured at 24 hours of elapsed time after the materials were mixed in each Tris buffer solution. In the case of A3 and A4 mixtures mixed in Tris buffer solution with an initial pH of 9.0, the precipitation seemed to be faster in the cases of the solution adjusted with concentration of 0.10 mol/L, which reached greater than 70% of the decreasing rate at the time. The pH measured in each mixture after 24 hours was 7.69, 6.97 and 6.91 for A2, A3 and A4 mixtures respectively. The results suggested that the use of larger amount of the yeast led to faster generation of carbonate ions, which is beneficial for the precipitation of calcium carbonate. The rate of generation with respect to carbonate ions will be further discussed in Section 3.4.

On the other hand, the precipitation processes of A5, A6 and A7 mixtures mixed in Tris buffer solution adjusted with an initial pH of 8.0 were not similar to those observed in the A2 to A4 mixtures with an initial pH of 9.0. The concentration of Tris buffer solution seemed to be adequate in the case of a concentration of 0.50 mol/L, which is illustrated by the higher decreasing rate observed up to 24 hours later. The pH measured in the A7 mixture which showed the highest decreasing rate of calcium ions tested was 6.26 (Tris: 0.10 mol/L) and 7.58 (Tris: 0.50 mol/L). Thus, pH levels in the region of alkali environment were maintained for the latter case. The highest decreasing rate can be explained by the fact that the precipitation process could be prolonged owing to the use of the solution with higher alkali buffering effect.

Although a higher decreasing rate was observed in most of the mixtures tested when mixed with larger amounts of yeast, the results suggested that the concentration of Tris buffer solution needed to be adjusted depending on the initial pH for facilitating the precipitation processes. Thus, the use of a lower pH i.e. 8.0 needed a relatively higher concentration of Tris buffer solution especially for the cases of mixtures comprising larger amount of yeast. In contrast, a decrease in the concentration of calcium ions was not observed in the case of Tris buffer solution with a concentration of 0.50 mol/L when the initial pH was adjusted with 9.0. Section 3.3 reports on testing results for mixtures with higher concentrations of each constituent.

3.3 *Mixtures with higher concentrations of each constituent*

As mentioned in Section 3.2, calcium ions present in the mixtures were mostly converted into calcium carbonate which precipitated well before 24 hours in the mixtures comprising glucose when adjusted with adequate concentrations for each initial pH. The precipitation was clearly observed in the test tubes, and the XRD pattern obtained for the precipitates is shown in section 4 (Figure 11). Section 3.3 deals with mixtures with higher concentrations specified based on the results of A3 and A7 mixtures. In order to determine the appropriate concentration of Tris buffer solution for the mixtures of the B and C series as shown in Table 1, precipitation processes at early stages accompanied by pH drop through microbial metabolic processes occurring up to 24 hours after mixing was central to this investigation.

Figures 6 and 7 show the results of the decreasing rate of calcium ions and pH after 24 hours for the mixtures of B and C series. As can be seen, the mixtures with the highest concentration of Tris buffer solution i.e. 1.0 mol/L or 1.25 mol/L in each mixture,

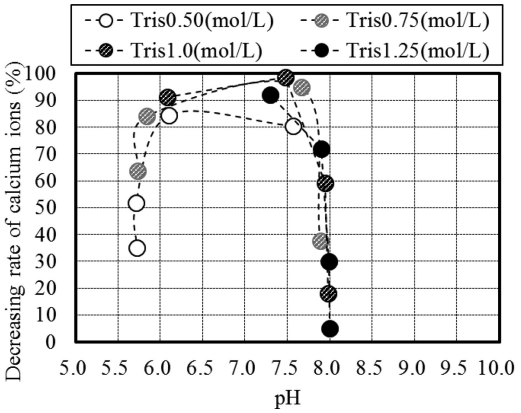

Figure 7. Decreasing rate of calcium ions and pH (A7, C series).

the changes of pH in the mixtures after 24 hours were marginal.

In contrast, the mixtures with relatively lower concentrations of Tris buffer solution led to rapid drop of pH below 7.5, resulting in lower decreasing rate of calcium ions.

In addition, the pH in mixtures which reached almost 100% of the decreasing rate of calcium ions seemed to be maintained at around 7.5 at 24 hours of elapsed time after mixing. This could be explained by the fact that the generation of carbonate ions through metabolic processes leading to calcium carbonate precipitation accompanied by pH drop and alkali buffering effect of Tris buffer solution especially at these pH levels can be better balanced. Thus, the calcium ions present mostly resulted in precipitation in those mixtures. In this study, the concentrations of Tris buffer solution were found to be adequate in the range of 0.5 to 0.75 (mol/L) in the case of an initial pH of 9.0 and 0.75 to 1.0 (mol/L) in the case of an initial pH of 8.0.

3.4 *Alkali buffering function and precipitation rate*

Section 3.4 reports on how the precipitation processes involved with generation of carbonate ions and changes of pH occurs simultaneously in mixtures. Mixtures selected in this investigation were B2 (Tris: 0.50 mol/L) and C1 (Tris: 0.75 mol/L) mixtures which showed higher decreasing rate of calcium ions. It was confirmed that the pH levels were maintained above 7.5 in each mixture up to 24 hours later. Figure 8 shows the precipitates left in tubes after filtering, which was evidently observed to be densely distributed compared to those tested in Section 3.1 and 3.2. It should be noted that there is a need to find the best combinations contributing to larger amount of precipitates as crystals as well as faster reaction rate especially at early stages, which could be more effective in sealing the leakage parts in concrete. Figure 9 shows estimated concentrations of carbonate ions using the following

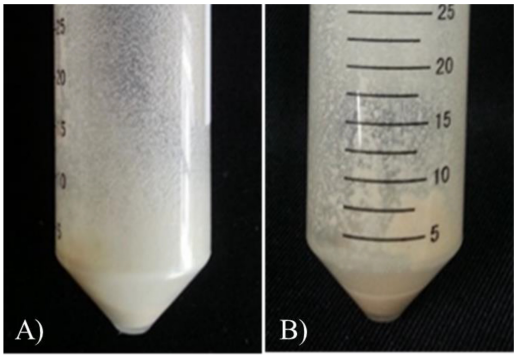

Figure 8. Precipitates left: A) B2 mixture & B) C1 mixture.

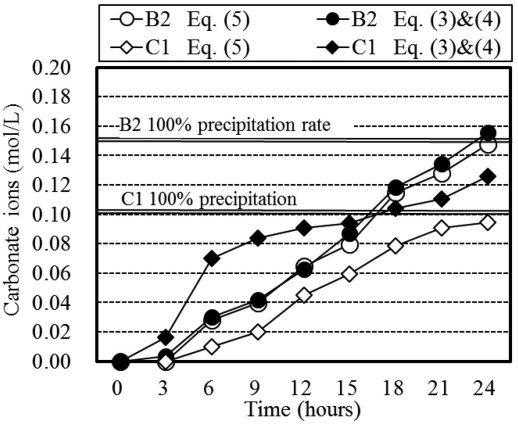

Figure 9. Estimated carbonate ions up to 24 hours: B2 (pH: 9.0, 0.50 mol/L) and C1 (pH: 8.0, 0.75 mol/L).

equations based on concentrations of calcium ions and pH measured.

$$[CO_3^{2-}] = \frac{[C_0] - [Ca^{2+}]}{M} \quad (3)$$

$$pH = pK_a + \log\frac{[B] - [H^+]}{[BH^+] + [H^+]} \quad (4)$$

$$[CO_3^{2-}] = 1/2[H^+] \quad (5)$$

where pK_a: acid dissociation constant (8.2, 20°C), [B]: the concentration of base (mol/L), $[BH^+]$: the concentration of acid (mol/L), $[H^+]$: the concentration of hydrogen ion (mol/L), $[CO_3^{2-}]$: the concentration of carbonate ion estimated (mol/L), $[C_0]$: initial concentration of calcium ion (g/L), $[Ca^{2+}]$: the concentration of calcium ion measured (g/L) and M: molar mass of calcium (40.08).

From Figure 9, the concentrations of carbonate ions calculated based on Eqs. (3), (4) and (5) for the B2 mixture were comparable up to 24 hours. The results seemed to suggest that the calcium carbonate is combined simultaneously when the pH changes owing to carbonate ions produced through the microbial

metabolic processes. In contrast, differences observed in the concentrations calculated for the case of C1 mixture were significant especially for the times between 6 to 9 hours after the mixing. The difference tended to decrease with time up to 24 hours later. This seems to imply that the calcium ions in the mixture were not necessarily combined with carbonate ions although the pH was notably decreased. It was found that the generation of carbonate ions was faster in the mixture with relatively lower pH i.e. 8.0 adjusted initially. However, this was not the case for the precipitation of calcium carbonate illustrated by the results obtained by the C1 mixture. It is noted that the precipitation of calcium carbonate seemed to be completed slightly earlier in the case of C1 mixture

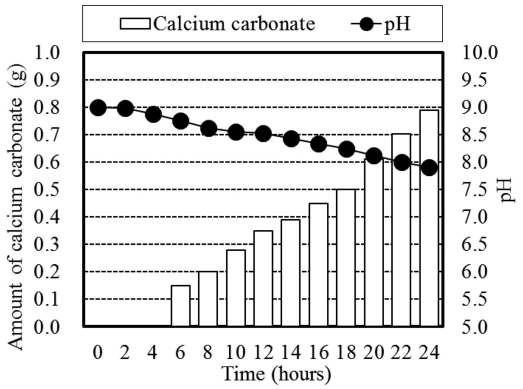

Figure 10. Estimated calcium carbonate precipitated (B3).

4 APPLICATION TO REPAIR FOR CRACKED CONCRETE SPECIMEN

4.1 *Selection of mixtures*

Chapter 3 examined influencing factors on MIP processes associated with calcium carbonate. Based on the results obtained, an initial reaction rate with respect to the precipitation of calcium carbonate and the amount of calcium carbonate which could be produced via prolonged reactions should be taken into consideration in selecting the effective mixture used for sealing cracks in concrete specimen. Thus, B3 mixture comprising yeast: 24.0 g/L, glucose: 0.40 mol/L and calcium acetate: 0.20 mol/L mixed in Tris buffer solution with an initial pH of 9.0 and a concentration of 0.75 mol/L was selected in this examination. Based on Eq. (2), the amount of precipitates mainly comprising calcium carbonate was calculated as shown in Figure 10. From this figure, a decrease in the concentration of calcium ions was clearly observed after 6 hours in the mixture, which was decreased with time during the monitoring. Precipitates were substantially formed in the test tube up to 24 hours after they were mixed, which seemed to reach about 0.8 g in the mixture. It is noted that the pH was maintained above 7.5, indicating that the precipitation process could be prolonged and the source of calcium ions provided can be mostly consumed by the reactions in the mixture adjusted with an initial pH of 9.0. This could be attributed to the higher concentration of Tris buffer solution which was suitable to the mixture with higher concentrations of each constituent.

Figure 11 shows the results of X-Ray diffraction analysis carried out using the residue left in test tube after 24 hours. As can be seen, the results showed peaks at 23°, 29°, 36° and 39° for the B3 mixture, thus suggesting that the crystals were mainly comprised of calcite.

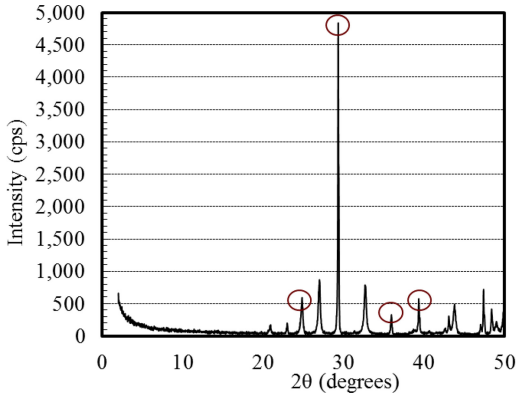

Figure 11. XRD pattern of precipitates in B3 mixture.

4.2 *Testing procedure*

Before mixtures were poured into specimens, PVC pipe was fixed with epoxy resin on the specimens. The application of the B mixture to cracked concrete specimens was carried out from the top surface of concrete specimens via ponding. First, 500 mL of the mixture was poured into the specimen in each application. And it was carried out once a day for 3 days, thus 1500 mL in total was applied before the water permeability test was conducted. Based on the results obtained in Section 4.1, the application time after the materials were mixed in Tris buffer solution was selected as summarized in Table 2. Also shown is the precipitated calcium carbonate estimated using the results as discussed in Section 4.1.

It is noted that the bottom surface was not sealed when the mixture was poured. Thus, the less viscous mixture essentially flowed out through the cracked specimen unless bonding between cracked surface and precipitates was formed immediately after they flowed. After 24 hours from the time when the last pouring was carried out, the application surface on the cracked concrete specimens were observed using a portable microscope.

A water permeability test was carried out before and after the mixture was poured into the cracked specimen to evaluate the effectiveness of the liquid based repair mixture for leakage in concrete.

Table 2. Application time of B3 mixture.

Case	Application time	Precipitated calcium carbonate (g)
X1	After mixed	0
X2	After 6 hours	1.9
X3	After 12 hours	4.4

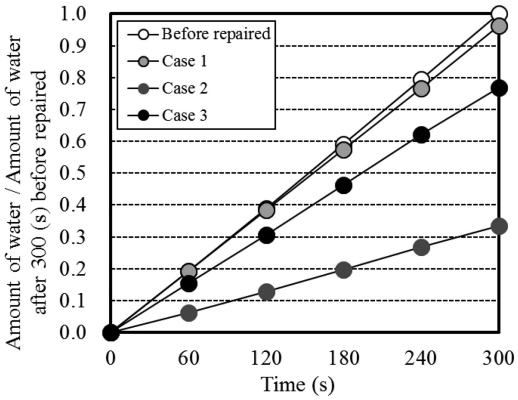

Figure 12. Results of water permeability test (X1-X3).

4.3 *Results of water permeability test*

The quantity of water flowing through the cracks in the concrete specimens was measured at predetermined intervals up to 300 s as shown in Figure 12. As can be seen, the water flowing through the cracked section was substantially decreased, which was prominent in the case of the mixture poured into the specimen after the mixture was left in room conditions for 6 hours (X2). The amount of water flowing out up to 300 s was decreased by about 70% compared to that measured in the concrete specimen before the mixture was poured into the cracked specimen. Precipitation comprising calcium carbonate was visually confirmed in the vicinity of the cracked surface after 3-day pouring of the mixture, some of which was observed using a microscope as shown in Figure 13. It is worth noting that the precipitated calcium carbonate could be clearly present in the cracked parts even after water permeability tests were carried out, which led to the significant decrease in the water permeability.

Figure 14 shows the split surface of concrete specimens after water permeability tests were carried out. The repair mixtures were applied from the top surface of the concrete specimens as shown in the figures. The changed color on the surfaces was noticeable owing to the precipitation especially in the specimens of X2 and X3. In contrast, there was no observable difference on the surface of the concrete specimen (X1). The precipitation left on the cracked surface was observed to be distributed in relatively deeper zones of the cracked section when the mixture was poured after 6 hours (X2) as shown in Figure 14(B). Besides, the cracked

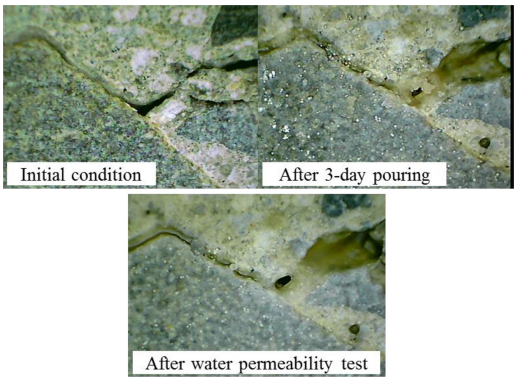

Figure 13. Cracked surface before/after repaired and after water permeability test was carried out.

surface almost sealed with precipitated calcium carbonate, the widespread precipitates in the specimen led to the significant decrease in the water permeability. The results suggested that precipitated calcium carbonate in cracked parts concomitant with seeping into deeper zones of concrete specimens was crucial to seal the crack effectively. In addition to the precipitation processes occurring, during which the mixture penetrated into deeper zones, a certain amount of precipitates initially formed are essential as a filler in sealing the cracked section. However, a large amount of precipitation as a filler before being applied may not necessarily lead to better sealing effect as illustrated by the case of X3. This may have an adverse effect in the precipitation taking place in deeper zones of cracked specimens, which led to lesser amount of precipitation left and distributed in relatively smaller areas. Thus, the water permeability was not improved compared to that observed in the case of X2.

5 CONCLUSIONS

The investigation revealed that calcium carbonate precipitates as crystals depending on the types of constituents used in the mixtures and the pH levels within 24 hours after mixing. In the case of mixtures mixed with an initial pH of 9.0, the rate of initial reaction tended to be faster, which could be attributed to lower concentration of Tris buffer solution adjusted with a relatively higher pH in the mixture. The precipitates, mainly comprising calcium carbonate, were clearly observed even at 6 hours later in those mixtures. Based on results obtained via water permeability tests carried out using cracked specimens, substantial calcium carbonate initially precipitated (i.e. 6 hours later) was crucial for the liquid based system in sealing cracks, which could exist even after the tests were carried out. Besides the precipitation distributed in relatively larger areas on the cracked surfaces, water permeability was substantially lower compared to that measured before the mixtures were cast into the specimens. And it is postulated that the viscosity adequately provided in the

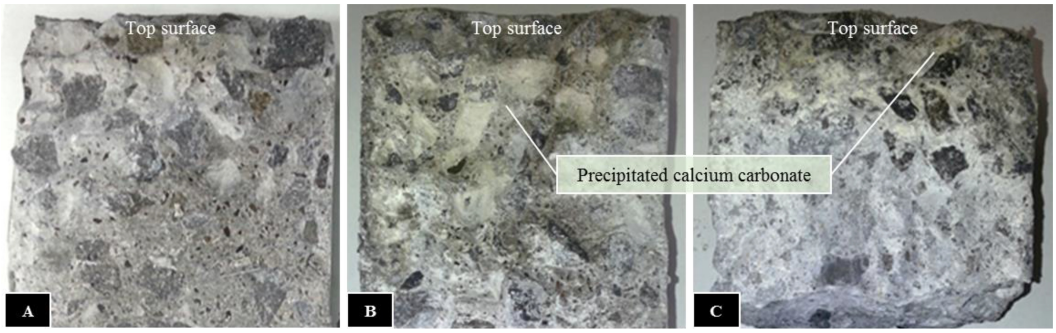

Figure 14. Precipitation distributed on cracked surface in the top half of concrete specimens: A) X1; B) X2; and C) X3.

liquid based repair mixture could improve the effectiveness in sealing cracks, especially in deeper zones of cracked section in concrete specimens.

ACKNOWLEDGEMENTS

Financial support from Japan Society for the Promotion of Science under the Grant-in-Aid for Scientific Research (B), Grant Number: 15H04025 is gratefully acknowledged.

REFERENCES

Kawasaki, S., Murano, A., Hiroyoshi, N., Tsunekawa, M., and Kaneko, K., 2006. Fundamental Study on Novel Grout Cementing Due to Microbial Metabolism, Journal of Japan Society of Engineering Geology, Vol. 47, No. 1, pp. 2–12

Kubo, K., Okazaki, S., and Ujike, I., 2013. Development of Microbial Metabolic Processes to Repair Concrete Joint Leakage, Advanced Materials Research, Vol. 845, pp. 158–162.

Ujike, I., Kubo, F., Kawaai, K., and Okazaki, S., 2014 Influencing factors affecting microbial metabolic processes of bio materials used for leakage repairs, Concrete Solutions, pp. 127–133.

Wiktor, V. and Jonkers, H.M., 2010. Quantification of crack healing in novel bacteria-based self-healing concrete, Cement & Concrete Composites (33): pp. 763–770.

Wiktor, V. and Jonkers, H.M., 2015. Field performance of bacteria-based repair system: Pilot study in a parking garage, Case Studies in Construction Materials, Vol. 2, pp. 11–17.

Concrete Solutions – Grantham et al. (Eds.)
© 2016 Taylor & Francis Group, London, ISBN 978-1-138-03008-4

Study on tensile bearing behavior of nodes in CFRP grid

B. Wang, K. Uji, V.D. Tran, A. Ueno & K. Ohno
Department of Civil and Environmental Engineering, Tokyo Metropolitan University, Japan

ABSTRACT: Carbon Fiber Reinforced Plastic (CFRP) grid is used for strengthening of existing concrete structures. The number of nodes in the CFRP grid influences the anchorage effect of the grid in mortar. In order to make full use of the tensile strength of CFRP grid, the number of nodes should be enough to generate the reliable anchorage action. In this study, pull-out specimens with different types of CFRP grids (CR5@50, CR5@100, CR8@50, CR8@100 and CR13@100) and different number of nodes (one node, two nodes and three nodes) were conducted to analyze the tensile bearing behavior of nodes in CFRP grid. The ultimate tensile load of the single node, tensile bearing process and bearing mode were analyzed. In addition, the calculation formula of maximum tensile load of CFRP grid with multiple nodes was established. Analysis results show that: if only considering the resistant action of the node, in order to make full use of the tensile strength of CFRP grid, it needs 2 nodes at least for CR5@50 and CR5@100; it needs 3 nodes at least for CR8@100; it needs 4 nodes at least for CR8@50 and CR13@100.

Keywords: CFRP grid, nodes, tensile bearing behaviour, pull-out test

1 INTRODUCTION

It is known that more and more existing concrete structures have been deteriorated by aging or natural disasters. In order to extend the service life of these structures, strengthening is necessary. Recently, a new strengthening method, using the combination of sprayed polymer cement mortar (PCM) and carbon fiber reinforced plastic (CFRP) grid has been applied in Japan. CFRP grid is a mesh-type structural material, which is manufactured by several layers of CFRP vertical and horizontal bars by pressing and adhesion. It has high tensile strength and good corrosion resistance. The principle of this strengthening method is fastening the CFRP grid on a suitable surface of an existing concrete structure by using sprayed mortar according to the requirements in practical engineering. Past research results show that it could increase the shear and flexural capacity of RC beams effectively (Uji et al. 2007, Liang et al. 2008, Kikuchi et al. 2013) as well as the seismic performance of RC columns (Sugiyama et al. 2011, Miyauchi et al. 2011) by using this strengthening method. For shear strengthened RC beams, the CFRP grid is fastened on the side of the beam; while for flexural strengthened RC beams, the CFRP grid is fastened on the bottom of the beam. A sketch of the construction method is shown in Figure 1.

It is clear that making full use of the tensile strength of the CFRP grid is key to improving the strengthening effect. In order to make full use of the tensile strength of the CFRP grid, it should have a reliable anchorage in the mortar. It has been clarified that the anchorage

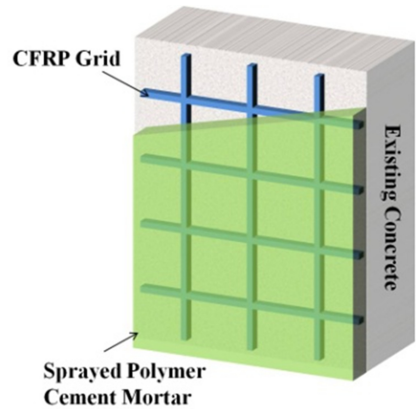

Figure 1. Sketch of construction method by using CFRP grid.

action of the CFRP grid in mortar is composed of two parts: the resistant action of the horizontal bar in the node and the bond action of the vertical bar (Wang et al. 2015): the resistant action is the dominant part of the anchorage action. As shown in Figure 2, the node in the CFRP grid would generate the resistant action when the vertical bars bear the tensile load. To reveal the anchorage mechanism of CFRP grid in mortar, it is necessary to first ascertain the bearing behavior of nodes. However, it hasn't been clarified yet. In this paper, pull-out tests were conducted to solve this problem. The ultimate tensile load of the single

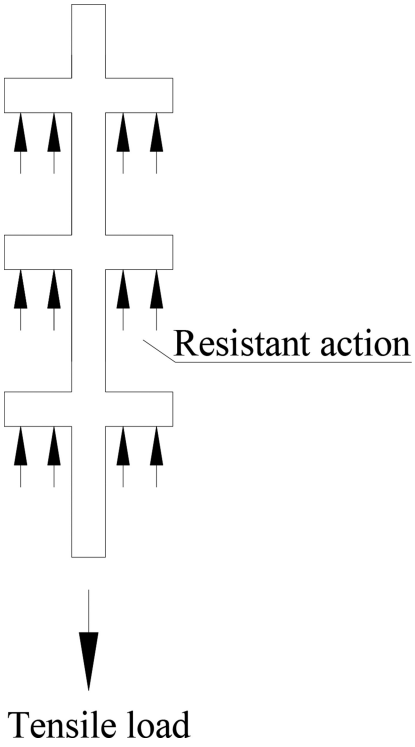

Figure 2. Resistant action of the horizontal bar in the node.

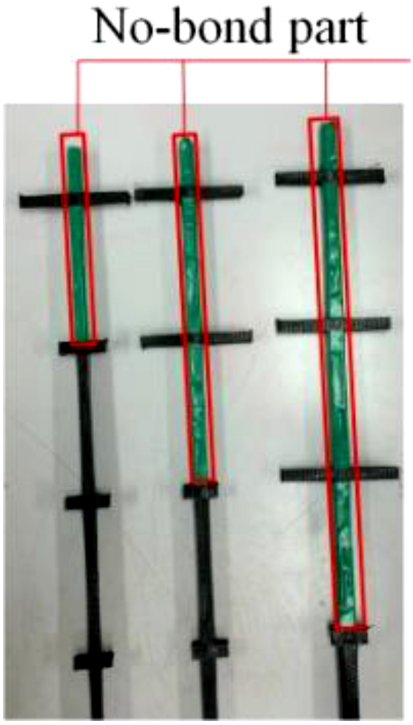

Figure 3. Fabricated CFRP grids.

node, failure mechanism and bearing mode of multiple nodes in CFRP grid were analyzed. Finally, the calculation method of minimum number of nodes in CFRP grid for full use of tensile strength of CFRP grid was established.

2 EXPERIMENTAL PROGRAMS

2.1 *Design of specimens*

In order to construct the bearing condition of nodes in CFRP grid (as shown in Figure 2), the bond action of the vertical bar should be eliminated. In this experiment, the smooth tape was wrapped around the vertical bar to construct a no-bond condition. The type of CFRP grid and the number of nodes were selected as the changing parameters. Five types of CFRP grids (CR5@50, CR5@100, CR8@50, CR8@100 and CR13@100) with different numbers of nodes (one node, two nodes and three nodes) were fabricated, as shown in Figure 3.

To avoid the failure of the mortar before the CFRP grid, high strength mortar and steel pipe were used in this experiment. Figure 4 shows the pouring mould and a representative specimen. The specimen with one node is used to attain the ultimate tensile load of the node in the CFRP grid. For specimens with two nodes and three nodes, they are used to analyze the bearing mode of multiple nodes in the CFRP grid.



(a) Pouring mould. (b) Representative specimen.

Figure 4. Pouring mould and representative specimen.

For each specimen design, three identical specimens were manufactured. The total number of specimens was 5 (grid type and interval) × 3 (number of nodes) × 3 (samples), which is Equal to 45. The dimensions of the specimen are shown in Figure 5. Where i = the grid interval (50 mm and 100 mm); h = the distance from the side of the node to the end of the horizontal bar (when the grid interval is 50 mm and 100 mm, this value is taken as 15 mm and 30 mm respectively); v = the distance from the side of node to the end of vertical bar (when grid interval is 50 mm and 100 mm, this value is taken as 20 mm and 30 mm respectively).

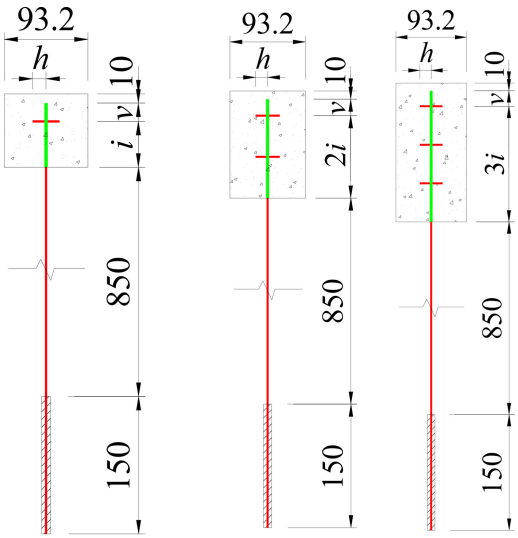

(a) one node (b) two nodes (c) three nodes

Figure 5. Dimensions of specimens.

Table 1. Mix proportions of mortar (kg/m^3).

Cement	Water	Sand	Expanding material	Water reducer
1000	309	1000	50	2

2.2 *Mix proportions of the mortar*

Table 1 shows the mix proportions of the mortar. The test results show that the compressive strength of the mortar was about 106 MPa.

2.3 *Loading program*

According to the "Test method for bond strength between reinforcing steel and concrete by pull-out test (JSCE-G503)", the pull-out test has been developed to investigate the tensile bearing behavior of nodes in the CFRP grid. Figure 6 (a) shows the experimental device with 1000 kN load capacity. Figure 6(b) shows the experimental loading method. Displacement-control loading method was applied and the loading rate was set as 1.5 mm/min. Load and displacement data are acquired during the loading process.

3 EXPERIMENTAL RESULTS

3.1 *Maximum tensile load*

Average maximum tensile loads of all specimens are shown in Table 2.

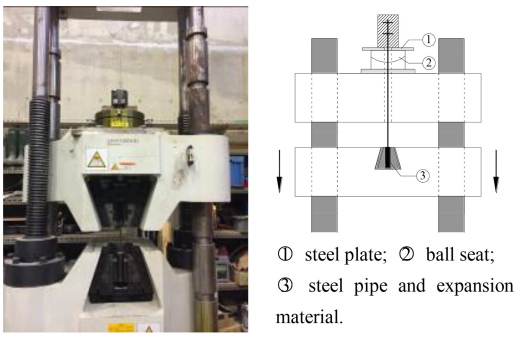

(a) Experiment device

① steel plate; ② ball seat; ③ steel pipe and expansion material.

(b) Loading method

Figure 6. Experiment device and loading method.

Table 2. Average maximum loads of specimens (kN).

Type	One node	Two nodes	Three nodes
CR5@50	11.2	18.1	19.1
CR5@100	12.0	18.5	21.4
CR8@50	17.0	28.3	31.3
CR8@100	18.6	30.9	35.9
CR13@100	48.5	67.9	79.9

Table 3. Failure mode of the external CFRP grid.

Type	One node	Two nodes	Three nodes
CR5@50	A	A	A + B
CR5@100	A	A	C
CR8@50	A	A	B
CR8@100	A	A	B
CR13@100	A	A	C

3.2 *Failure modes*

Failure modes of all specimens could be divided into three types, which were called A-mode, B-mode and C-mode for short, as shown in Table 3.

A—stands for the vertical CFRP bar being pulled out to a certain distance;
B—stands for the breaking of the CFRP grid;
C—stands for the explosive rupture of the CFRP grid.

Representative failure photos are shown in Figure 7.

3.3 *Load-displacement curves*

Statistical analysis of 45 load-displacement curves shows that the resistant action-displacement relationship could be reflected by lineal model, as shown in Figure 8. Figure 9 shows the load-displacement curves of CR5@100 with two nodes and CR13@100 with one node.

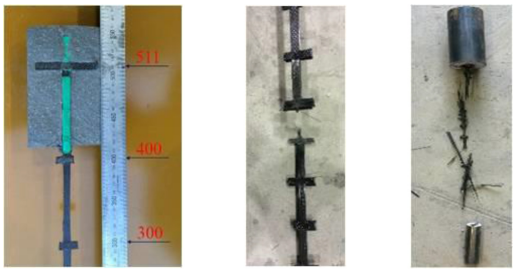

A-mode: pulled out to a certain distance

B-mode: break

C-mode: smash

Figure 7. Representative failure photos.

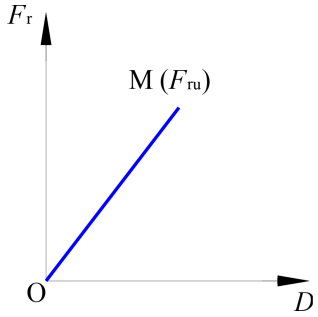

Figure 8. Load-displacement relationship.

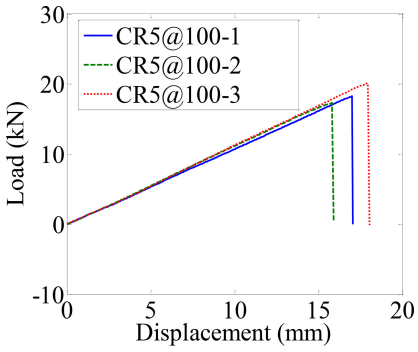

(a) CR5@100 with two nodes

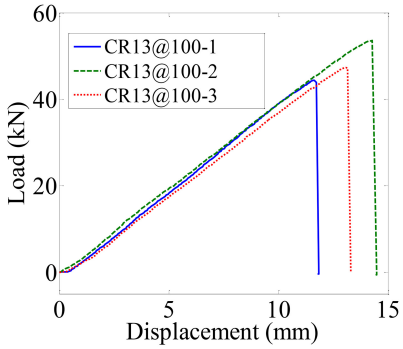

(b) CR13@100 with one node

Figure 9. Representative load-displacement curves.

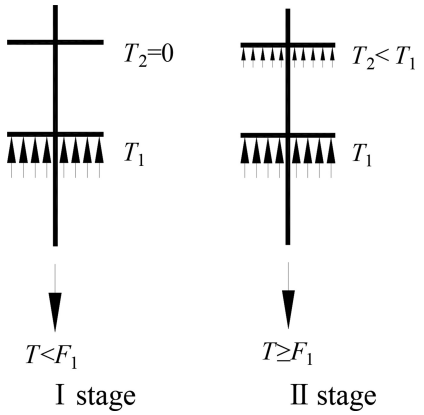

Figure 10. Bearing process of CFRP grid with two nodes.

4 TENSILE BEARING PROCESS AND MODE OF CFRP GRID WITH TWO NODES

4.1 *Bearing process of CFRP grid with two nodes*

The bearing process of CFRP grid with two nodes could be divided into two stages, as shown in Figure 10.

(1) Single node bearing stage (I stage)

In this stage, the single node near the loading part bears all the tensile load. For the grid interval, the transmission of tensile load from the first node to the second node would take a certain time. When the tensile load increases to a certain value F_1, the second node begins to bear the load.

(2) Two nodes bearing together (II stage)

With the increasing of the tensile load, the second node begins to bear the load. In this stage, two nodes bear the tensile load together, but the borne load of the first node T_1 is much larger than for the second node T_2 all the time. Finally, when the borne load of the first node is Equal to the ultimate tensile load of the single node in CFRP grid, the specimen will break.

4.2 *Bearing mode of CFRP grid with two nodes*

As in the analysis above, the ultimate tensile load of the CFRP with two nodes is equal to the ultimate tensile load of the single node plus the borne tensile load of the second node. As shown in Equation (1).

$$T_u = T_{1u} + T_{2u} = P_0 + T_{2u} \tag{1}$$

where T_u = ultimate tensile load of the CFRP grid with two nodes, as shown in Table 2; T_{1u} = the borne tensile load of the first node at ultimate point; T_{2u} = the borne tensile load of the second node at ultimate point; P_0 = ultimate tensile load of the single node, as shown in Table 2.

Table 4. Tensile bearing ratio.

Type	Bearing ratio (r)
CR5@50	0.62
CR5@100	0.54
CR8@50	0.66
CR8@100	0.61
CR13@100	0.40

The tensile bearing ratio between the first node and the second node could be calculated by Equation (2). The calculation results are shown in Table 4.

$$r = \frac{T_{2u}}{T_{1u}} = \frac{T_u - P_0}{P_0} \tag{2}$$

5 TENSILE BEARING MODE OF CFRP GRID WITH MULTIPLE NODES

5.1 *Tensile bearing mode of CFRP grid with three nodes*

As analysis above, the bearing ratio is only relative to the type of CFRP grid and grid interval. Accordingly, it is reasonable to suppose that the bearing ratio is constant between the adjacent two nodes corresponding to the specific CFRP grid. So the ultimate tensile load of CFRP grid with three nodes could be calculated by Equation (3).

$$T_u = T_{1u} + T_{2u} + T_{3u} = P_0 + rP_0 + r^2P_0 = (1 + r + r^2)P_0 \tag{3}$$

where T_{1u}, T_{2u}, T_{3u} = the borne tensile load of the first node, the second node and the third node at the ultimate point respectively.

In order to testify the reasonability of the calculation method, the calculation results can be compared with the experimental results, as shown in Table 5. It shows that the difference is acceptable, which indicates that the proposed tensile bearing mode is reasonable. And the reason for the difference is that it's not a perfect no-bond condition by wrapping tape around the vertical bar, so there must be residual bond action along the vertical bar which will increase the ultimate tensile load of the single node in the CFRP grid (P_0). Moreover, this would influence the accuracy of the bearing ratio (r).

5.2 *Tensile bearing mode of CFRP grid with multiple nodes*

Suppose the number of nodes in the CFRP grid is n. Based on the analysis above, the ultimate tensile load could be calculated by Equation (4).

$$T_u = \sum_{i=1}^{n} T_i = P_0 + rP_0 + r^2P_0 + \ldots + r^{n-1}P_0 = \frac{1 - r^n}{1 - r}P_0 \tag{4}$$

Table 5. Calculation of maximum tensile load of the CFRP grid with three nodes (kN).

Type	T_{1u}	T_{2u}	T_{3u}	T_{uc}*	T_{ut}**
CR5@50	11.2	6.9	4.3	22.4	19.1
CR5@100	12.0	6.5	3.5	22.0	21.4
CR8@50	17.0	11.3	7.5	35.8	31.3
CR8@100	18.6	11.3	6.9	36.8	35.9
CR13@100	48.5	19.4	7.8	75.7	79.9

* Calculation results of maximum tensile load.
** Test results of maximum tensile load.

Table 6. Calculation of minimum nodes.

Type	Bearing ratio (r)	P_0(kN)	f_t(MPa)	A_c(mm^2)	n_m
CR5@50	0.62	11.2	1400	13.2	2
CR5@100	0.54	12.0	1400	13.2	2
CR8@50	0.66	17.0	1400	26.4	4
CR8@100	0.61	18.6	1400	26.4	3
CR13@100	0.40	48.5	1400	65	4

where T_i = the borne tensile load of each node in the CFRP grid at the ultimate point respectively.

Specially, when $n = 3$, $T_u = \frac{1-r^3}{1-r}P_0 = (1 + r + r^2)P_0$. This is same with Equation (3).

6 THE MINIMUM NUMBER OF NODES IN THE CFRP GRID FOR FULL USE OF TENSILE STRENGTH

In order to make full use of the tensile strength of the CFRP grid in practical engineering, the number of nodes in the CFRP grid should be enough to generate the anchorage action. Based on Equation (4), the minimum number of nodes in the CFRP grid could be calculated by Equation (5). And the calculation results are shown in Table 6.

$$\frac{1 - r^{n_m}}{1 - r} \approx \frac{f_t A_c}{P_0} \tag{5}$$

where f_t = tensile strength of the CFRP grid, which is 1400 MPa; A_c = cross sectional area of the CFRP grid, for CR5, CR8, CR13, it is 13.2 mm^2, 26.4 mm^2 and 65 mm^2 respectively.

The calculation results show that: in order to make full use of tensile strength of CFRP grid, it needs 2 nodes at least for CR5@50 and CR5@100; it needs 3 nodes at least for CR8@100; it needs 4 nodes at least for CR8@50 and CR13@100.

In order to estimate the reasonability of the calculation method, define the tensile strength utilization β by Equation (5).

$$\beta = \frac{T_u}{G_u} \times 100\% \tag{5}$$

Table 7. Tensile strength utilization (%).

Type	One node	Two nodes	Three nodes
CR5@50	60.5	97.8	103.2
CR5@100	64.9	100	115.7
CR8@50	45.9	76.5	84.6
CR8@100	50.3	83.5	97.0
CR13@100	53.3	74.6	87.8

where T_u = average maximum pull-out load of specimen, as shown in Table 2; G_u = maximum tensile load of CFRP grid, for CR5, CR8 and CR13, it is 18.5 kN, 37.0 kN and 91.0 kN respectively. It is the product of theoretical tensile strength of CFRP grid (1400 MPa) and the average cross sectional area (13.2 mm^2, 26.4 mm^2, 65 mm^2 corresponding to CR5, CR8, CR13 respectively).

Calculation results of tensile strength utilization are shown in Table 7.

It shows that: for CR5@50 with two nodes, CR5@100 with two nodes and CR8@100 with three nodes, the tensile strength utilization is approximately equal to 100%, it means that: in order to make full use of the tensile strength of the CFRP grid, for CR5@50 and CR5@100, the minimum number of nodes is 2; for CR8@100, the minimum number of nodes is 3. This is same with the calculation results by equation (5), as shown in Table 6. Accordingly, the bearing mode of nodes in the CFRP grid proposed in this paper is reasonable and it could be applied in the analysis of the anchorage behavior of CFRP grid in mortar.

7 CONCLUSIONS

In order to analyze the tensile bearing behavior of nodes in CFRP grids, 45 pieces of pull-out specimens were conducted. The following conclusions can be attained in this study:

(1) Based on the pull-out specimens with one node, the ultimate tensile load of a single node in a CFRP grid has been attained. It shows that the crossing point is the weak part of CFRP grid.
(2) The bearing mode of the CFRP grid with multiple nodes could be illustrated by the Equation with the ultimate tensile load of the single node and the bearing ratio. The bearing ratio could be regarded as the constant between the adjacent two nodes corresponding to the specific CFRP grid.
(3) If only considering the resistant action of nodes in CFRP grid, in order to make full use of the tensile strength of CFRP grid, the minimum number of nodes in CFRP grid was obtained: for CR5@50 and CR5@100, it needs 2 nodes at least; for CR8@100, it needs 3 nodes at least; for CR8@50 and CR13@100, it needs 4 nodes at least.

ACKNOWLEDGEMENT

Thanks are due to J. Zhang for assistance with the experiment. And this research was supported by the Asian Human Resources Fund from the Tokyo Metropolitan government.

REFERENCES

Kikuchi R., Ohno K., Zhang J., Uji K. & Ueno A. 2013. Shear failure process of RC beam strengthened by CFRP grids and sprayed mortar. *Proceedings of Retrofitting and Strengthening of Concrete Structures*, 13:585–592.

Liang J., Uji K., Matsumura S. & Sato K. 2008. Shear strengthening of RC beam with CFRP grid and sprayed mortar. *Proceeding of the Japan Concrete Institute*, 30(2):607–612.

Miyauchi K., Akita M., Shimoeda H. & Minami K. 2011. Seismic strengthening of existing RC columns with ploymer cement mortar sprayed by dry system. *Concrete Research and Techanology*, 22(1):43–55.

Sugiyama K., Yamaguchi K., Nakamura S. & Hino S. 2011. Stress transfer mechanism of the reinforced interface and seismic retrofit existing RC Pier by ploymer cement mortar for shotcrete with CFRP grid. *Proceeding of Construction Structures*, 57A:1042–1051.

Uji K., Satoh K. & Kobayashi A. 2007. Effects of retrofitting method using CFRP grid on the shear behavior of existing concrete members. *Proceedings of FRPRCS-8*, CD-ROM, Greece

Wang B., Uj K., Zhang J., Ueno A., Ohno K. & Tran V.D. 2015. Experimental study on anchorage behavior of the CFRP grid in mortar, *Concrete 2015*, CD-ROM, Melbourne, Australia.

Concrete Solutions – Grantham et al. (Eds.)
© 2016 Taylor & Francis Group, London, ISBN 978-1-138-03008-4

Resistance to fatigue of self-healed concrete based on encapsulated polymer precursors

J. Feiteira, V. Couvreur, E. Gruyaert & N. De Belie
Magnel Laboratory for Concrete Research, Department of Structural Engineering, Faculty of Engineering and Architecture, Ghent University, Belgium

ABSTRACT: Moving cracks are often present in concrete structures and in those circumstances any self-healing technique for concrete must satisfy specific performance requirements, to guarantee its increased durability. These requirements include the capability of withstanding multiple cycles of crack movement without failing to keep healed cracks sealed. This paper shows early results from a testing protocol suggested by the authors to assess the performance of polymers as healing materials for moving cracks. Ultrasound (US) shear waves were used for continuous monitoring of small prismatic mortar specimens containing a single healed crack under a cyclic load. The maximum amplitude of US waves transmitted across healed cracks was correlated to the area effectively healed and the magnitude of crack movement. A decreasing trend of the maximum amplitude during cyclic loading was observed for strain levels on the polymer corresponding to 70% of its strain limit, but soundness at lower strain levels was confirmed after 300 cycles.

1 INTRODUCTION

As with other emerging concrete technologies, self-healing concrete currently lacks straightforward test methods to assess its performance. This is particularly true for test methods simulating realistic conditions that are similar to those found in field structures. One such condition is the occurrence of moving cracks in concrete elements, often present in structures subjected to traffic loads or extreme daily temperature variation.

Under increasing load, self-healed cracks only remain sealed if a flexible polymer is used as healing material. Mineral materials would result in the reopening of the healed crack while a new crack would form if very stiff polymers were used. This issue has been addressed by the authors in previous publications (e.g. Feiteira et al. 2016) where the strain limit of several flexible polymers bridging moving cracks was determined. There, the strain limit was defined as the strain after which failure occurs due to rupturing of the polymer or its detachment from the crack walls, resulting in considerable increase of the water uptake through the healed crack.

If the load on a healed concrete element is cyclic, however, the strain limit of the healing material may be reduced due to fatigue. This is of great importance, but not studied to date. Even in related research areas, such as injection products for concrete repair, this topic is seldom studied, e.g. Shin et al. (2011). Regarding the research on self-healing concrete involving fatigue performance, only one study by Yang et al. (2011) was found. The differences between the two research areas are essentially limited to the fact that for injection products there is the possibility for surface preparation before introducing the liquid polymer into the crack, which is done under pressure. On self-healing concrete, the polymer precursor is released from embedded capsules immediately upon cracking of the concrete element, flowing into the crack due to capillary tension.

This paper presents early stage data of a testing setup developed to assess the fatigue resistance of a polymer precursor used as an encapsulated healing agent for self-healing concrete. The proposed test is performed at a small scale on mortar specimens and includes a continuous monitoring technique based on the transmission of ultrasound (US) waves. The use of ultrasound as a monitoring technique in this context is built upon previous results published by Malm and Große (2015). US waves are affected by changes in the propagation medium and are affected by any potential loss of continuity across the faces of healed cracks. Thus, they have been used to detect fatigue-related failure due to changes in the matrix of the polymer filling the crack or its detachment at the interface.

2 MATERIALS

A moisture-curing polyurethane precursor of low viscosity (200 mPa.s) was used in this study. From a previous study (Feiteira et al. 2016) it was known that this precursor leads to very effective sealing of cracks

when used as an encapsulated healing agent and had showed also good strain capability for this application (approximately 50%). The precursor was encapsulated in Ø3 mm glass tubes cut to a 50 mm length and sealed with Poly(methyl methacrylate) glue. Although not fit for bulk addition during mixing of concrete, the brittleness and barrier properties of glass tubes make them ideal carriers for laboratory work, where they can be pre-placed into moulds and careful pouring of concrete or mortar can take place.

3 PROCEDURE

3.1 *Specimen preparation*

A pair of glass capsules was pre-placed in each mould for $40 \times 40 \times 150\,mm^3$ prisms, held by nylon wires, and mortar was poured over them. The mortar mix design consisted of cement CEM I 52.5 N, 0/4 mm sand, a cement to sand ratio of 1:3 and a water to cement ratio of 0.5. Mixing and moulding were carried out according to the procedure described in EN 196-1 and the specimens were cured in sealed conditions at 20°C for at least 14 days. After the curing period, a $7 \times 150\,mm^2$ wide strip of fibre reinforced polymer (FRP) was glued with a structural epoxy glue along two opposing sides of the specimen (see Figure 1). The specimens were then cracked under 3-point bending, with the FRP strips at the compression side. They were then used not as conventional reinforcement, but as a way to avoid complete separation of the two halves of the specimen after cracking. A crack approximately 300 μm wide at the crack mouth remained after unloading. The final configuration of the specimens is shown in Figure 1. After a period of 3 days, to allow the healing agent to flow and harden, mortar specimens with a single healed crack were ready to be tested.

3.2 *Protocol for cyclic loading*

An LVDT was placed across the crack mouth to control the crack movement during testing. Cyclic loading occurred under bending, with each cycle defined as a crack width increase from a starting displacement of 0.05 mm to the desired maximum displacement, corresponding to a certain strain on the polymer filling the crack. After each cycle, a waiting period of 5 s was introduced at the starting displacement of 0.05 mm, so that the monitoring equipment could acquire data in stable and well defined conditions. A visual representation of these cycles is shown later in this document, in Figure 5. A loading speed of 0.013 mm/s was used, resulting in a frequency of approximately 0.07 Hz, but depending on the maximum displacement level set for the test.

3.3 *Monitoring with ultrasound transmission equipment*

A FreshCon system from Smartmote was used to generate, trigger and acquire ultrasonic pulses of 800 V and a pulse width of 5 μs. Olympus V150-RB shear wave sensors were used and monitoring took place at 2 s intervals during cyclic loading. The sensors were coupled to opposing tops of the specimens (Figure 1) with silicone gel and were kept in place with a system of small supporting metal plates and an elastic band pressing them against the specimen. The maximum amplitude of the US waves was used as the monitoring parameter.



Figure 1. Specimen configuration with a single crack at mid-span and a reinforcing FRP strip; US shear sensors are attached at opposite tops.

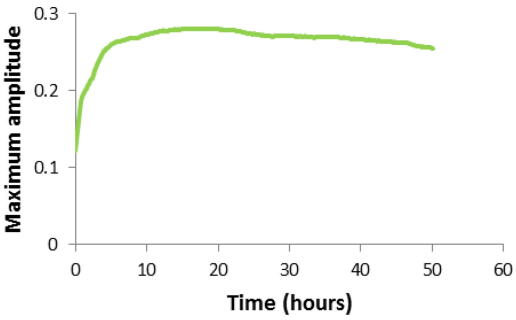

Figure 2. Increase of maximum amplitude of US wave during the healing period.

4 RESULTS

4.1 *Monitoring of the healing process*

As shear waves don't propagate well through liquid phases, the ultrasound shear waves were used to monitor the progressive dispersion and hardening of the polymer precursor inside the crack on one of the specimens, after flowing out of the ruptured glass carriers. As shown in Figure 2, while the precursor turns from a liquid compound into a solid polymer, the maximum US wave amplitude increases progressively.

Most of the hardening occurs during the first 24 h after contact with the moisture present in the mortar matrix. The slight decrease in maximum amplitude after this period could have been due to absorption of the silicone gel (used to couple the sensors) into the mortar matrix, otherwise, a slow rate of increase is expected.

The final maximum amplitude after healing is dependent on the area of the crack effectively healed. Figure 3 shows the crack faces of two split specimens

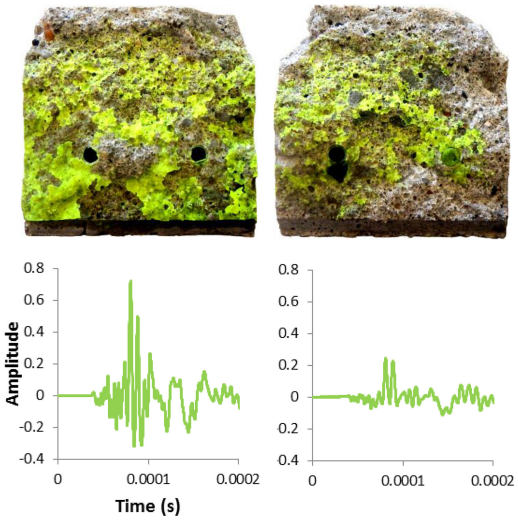

Figure 3. Crack faces of split specimens, showing a particularly well healed crack (left) and crack with a smaller area effectively healed (right); the respective waves transmitted across the cracks are shown below.

with considerably different sizes of the crack surface effectively healed. For these specimens, a fluorescent dye was added to the precursor for easy detection of the surface covered with polymer. Although there is a correlation between area healed and the maximum amplitude of the US wave transmitted across the healed crack, the amplitude is also slightly dependent on the consistency of coupling between the sensors and the specimen.

4.2 *Evolution of US wave amplitude with increasing polymer strain*

As mentioned, the transmission of ultrasonic waves is affected by changes in the continuity of the propagation medium. As a healed crack gets increasingly larger and the strain on the polymer increases, failure due to detachment or rupturing of the polymer matrix eventually occurs and a decrease of the maximum amplitude of the US wave is thus expected. This is shown in Figure 4 for several specimens.

4.3 *Fatigue assessment: combined cyclic loading and monitoring based on US wave transmission*

As US wave data was acquired constantly, at 2 s intervals, post processing of the data was required to select only the data points corresponding to the 5 s waiting period introduced in the protocol, at 0.05 mm displacement. Only this data, acquired in stable conditions, was used to monitor the continuity across crack faces. The data points of higher wave amplitude occur naturally at the moments of lower LVDT displacement, corresponding to the waiting period, as shown in Figure 5.

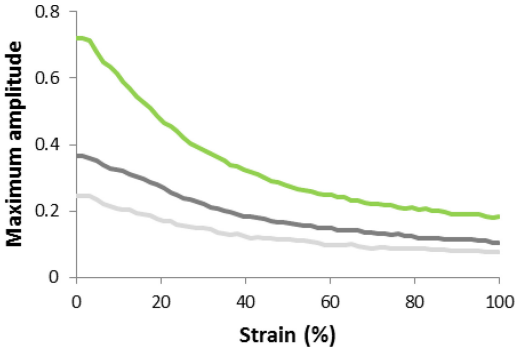

Figure 4. Progressive reduction of maximum US wave amplitude with increasing crack widening and strain on the polymer.

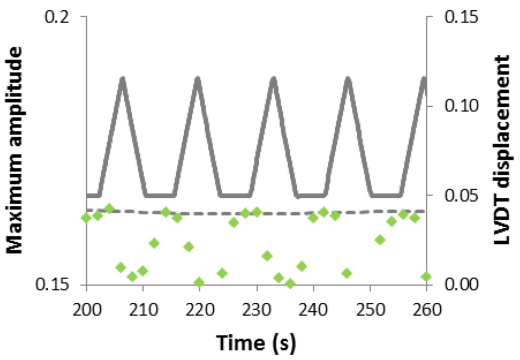

Figure 5. Approximately 5 cycles of the cyclic loading protocol showing displacement (solid line), amplitude (green) data points and upper envelope of amplitude data (dotted line).

The upper envelope of the amplitude data (line crossing data peaks) could then be used as the monitoring parameter.

Assuming the strain limit of the polymer to be 50%, after which detachment from the crack faces occurs, early tests were performed at different levels of the strain limit, i.e. 40% of the strain limit and 70% of the strain limit. The evolution of the maximum wave amplitude (upper envelope of US wave data acquired) is shown in Figure 6 for specimens at the two strain levels tested, as a function of the number of cycles performed.

For a tested strain level of 70% of the strain limit, the maximum amplitude shows a decreasing trend, suggesting that progressive failure may be occurring, which previous results show to be due to detachment of the polymer from the crack faces. For a lower strain level of 40% of the strain limit, there is no considerable change in the maximum amplitude after 300 cycles, suggesting a sound healed crack and no susceptibility to fatigue failure. A micrograph of a section of the crack mouth, where polymer could be seen at the surface (Figure 7), confirms these results and shows the polymer still attached to the crack faces.

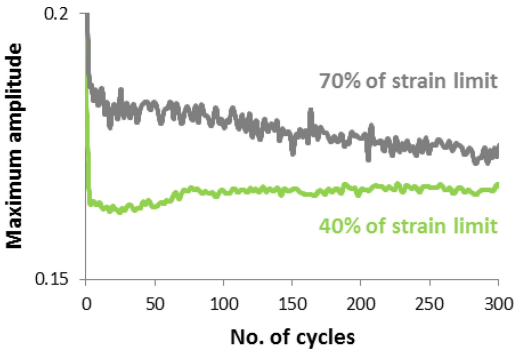

Figure 6. Evolution of maximum amplitude of US waves acquired at a stable deformation of 0.05 mm.

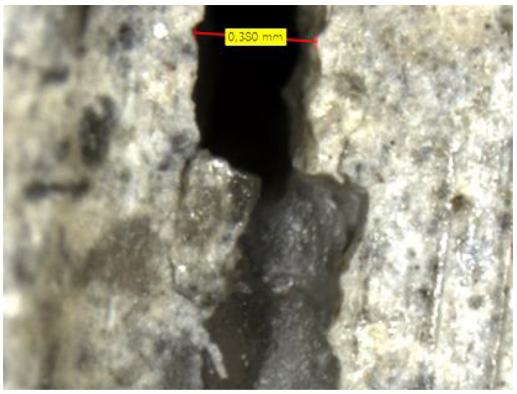

Figure 7. Section of 0.38 mm crack mouth where stretched polymer could still be seen attached to the crack walls after more than 300 cycles.

After these early results, the testing protocol was confirmed to be accurate and useful for monitoring the soundness of self-healing cementitious material. A larger number of tests still needs to be performed, with the inclusion of water uptake tests after a fixed number of cycles as additional confirmation of soundness or failure due to fatigue.

5 CONCLUSIONS

The maximum amplitude of US waves transmitted across healed cracks is a simple parameter that was successfully correlated with both the surface of the crack that was effectively healed with an encapsulated polymer precursor and the strain on the polymer, i.e. the amount of crack movement. Changes in maximum amplitude at stable levels of crack movement were also successfully used to monitor the soundness of healed specimens when subjected to multiple cycles of crack movement. When tested at a maximum strain level of 40% of the strain limit, after which detachment of the polymer from the crack faces is known to occur, the amplitude of the US waves was stable after 300 cycles. This suggests that at levels much below the strain limit, the self-healing technique is resistant to fatigue, which was confirmed by microscopic observation of a section of the crack mouth. At higher strain levels of 70% of the strain limit, there was however a decreasing trend of the maximum amplitude, suggesting that the strain limits of the self-healing system should be corrected to consider failure due to fatigue.

ACKNOWLEDGEMENTS

The research leading to these results has received funding from the European Union Seventh Framework Programme (FP7/2007-2013) under grant agreement n° 309451 (HEALCON). The kind help of Fabian Malm (TUM) is also acknowledged.

REFERENCES

Feiteira, J.; Gruyaert, E.; De Belie, N. 2016. Self-healing of moving cracks in concrete by means of encapsulated polymer precursors. *Construction and Building Materials* 102: 671–678.

Malm, F.; Große, C. 2015. Proof of efficiency: Examination of concrete beams with self-healing properties by non-destructive testing methods. Fifth International Conference on Self-Healing Materials (ICSHM2015). Durham, U.S.A..

Shin, H.; Miyauchi, H.; Tanaka, K. 2011. An experimental study of fatigue resistance in epoxy injection for cracked mortar and concrete considering the temperature effect. *Construction and Building Materials* 25: 1316–1324.

Yang, Z.; Hollar, J.; He, X. 2011. A self-healing cementitious composite using oil core/silica gel shell microcapsules. *Cement and Concrete Composites* 33: 506–512.

Surface protection methods and materials



Taylor & Francis
Taylor & Francis Group
http://taylorandfrancis.com

Concrete Solutions – Grantham et al. (Eds.)
© 2016 Taylor & Francis Group, London, ISBN 978-1-138-03008-4

Concrete protection with hydrophobic impregnation – importance of correct specifications

M. Donadio
Sika Services AG, Switzerland

N. Anagnostopoulos
Sika Hellas SA, Greece

ABSTRACT: Hydrophobic impregnations are a potentially effective method to prevent water and any soluble aggressive elements entering into a concrete structure. The paper will highlight the importance of conducting penetration depth measurement on the targeted concrete quality in order to specify properly the right product with the appropriate consumption.

1 INTRODUCTION

Hydrophobic impregnations are used to prevent water and water soluble deleterious materials from penetrating mineral substrates. These hydrophobic impregnation treatments change the surface tension of the mineral substrates including concrete, render and brickwork.

They render the surface water repellent and prevent water absorption (reducing the penetration of soluble substances such as chlorides or sulphate) while allowing the substrate to breathe.

The purpose of this paper is to compare the performances of different products versus standards such as EN 1504-2 or American methods/standards and to understand the importance of penetration depth in order to classify correctly the different products

2 STANDARDS

2.1 *EN 1504-2*

In Europe, the use of hydrophobic impregnation is regulated via the global standard for repair and protection of concrete substrate, EN 1504. They shall comply with the relevant criteria of Part 2.

While items 1 through 3 relate to performance criteria which the products must comply to, items 4 & 5 classify the products in different levels.

Products complying with Class I of the drying rate test have little to no incidence to the vapor transmission ability of the substrate. Class I is preferred when it is desired to have some drying effects (e.g. to fight against the alkali silica reaction or to reduce corrosion rate of the reinforced bars).

Products complying with Class II of the penetration depth have the ability to penetrate dense substrates, although works done by Johannsson and Wittmann have shown hydrophobic impregnation hardly penetrate in very high performance concrete (W/C $\leq$ 0.35).

Generally, only high performing products (silane with a high concentration of solid content) can be classified as Class II for the penetration depth.

Lower performing products (e.g. diluted silane, either in water or solvent, or siloxane material), although compliant with the EN 1504-2, cannot achieve this classification.

EN 1504-2 does not require a specific test for chloride penetration to be performed so this is left to the national regulations. It is also said that if a product demonstrates a water capillary uptake lower than 0.01 $kg/m^2.h^{0.5}$, it is deemed that diffusion of chlorides is not to be expected

2.2 *American standards*

In the United States, hydrophobic sealers shall comply with various standards according to the relevant DOT (Department of Transport). The most commonly used test methods are from NCHRP (National Cooperative Highway Research Program) Series II & IV. Although these tests are only for comparative study, they are often used as the basis for DOT's specifications.

The Series II program require hydrophobic sealers to be tested for water capillary uptake, chloride penetration, water vapour transmission and for the Series IV program, accelerated weathering for the Southern and Northern climate is taken into consideration.

There is a test method to measure penetration depth of the hydrophobic sealers applied on the structure (OHD L-34 & 35) but only a limited number of DOT's have included penetration depth as part of their specifications. The DOT from Oklahoma and South Carolina

Table 1. EN 1504-2 performance criteria for hydrophobic impregnation.

Item	Performance characteristic	Criteria
1	Initial water absorption	<7.5% to the untreated specimen
2	Water absorption after alkali stress	<10% to the untreated specimen
3	Loss of mass after freeze-thaw-salt stress	Loss of material must occur at least 20 cycles later than the untreated specimen
4	Drying rate	Class I: >30% Class II: >10%
5	Penetration depth	Class I: <10 mm Class II: ≥10 mm

Table 2. Comparison of products.

Product type	Description	Active content
Ia	Solvent based siloxane	<10%
Ib	Solvent based siloxane	~15%
II	Water emulsion silane	~40%
III	Solvent based silane/siloxane	~30%
IV	Silane liquid	~99%
V	Silane cream	~80%

Table 3. Water absorption and alkali resistance as per EN 13580.

Product type	Water absorption	Alkali resistance
Ia	2.5%	8.2%
II	5.2%	9.1%
III	1.0%	2.7%
IV	3.8%	5.1%
V	5.1%	8.3%

Table 4. NCHRP 224 Report Series IV Southern exposure.

Product type	Resistance to UV light	Reduction to soluble chloride
Ib	Very slight scaling	97.6%
II	No discoloration	79%
III	–	–
IV	No discoloration	98%
V	No discoloration	93%

Table 5. NCHRP 224 Report Series II.

Product type	Reduction to water absorption	Reduction in chloride ion content
Ib	87%	95%
II	–	96%
III	–	–
IV	–	92%
V	81%	86%

require 0.15" (~4 mm) minimum penetration depth while the one from Texas requires 0.25" (~6 mm).

2.3 *Products compared*

Different hydrophobic impregnations are compared.

3 DISCUSSION

Tests such as water absorption, chloride penetration, alkali resistance, etc. are performed in conditions where the treated specimens are placed in a situation to promote capillary uptake or under immersed conditions with very low pressure (water bath). These conditions do not apply severe stress on the sealers as they only need be present at the surface to be effective.

Table 3 shows the results of 5 products (all complying with EN 1504-2) with regards to their water absorption and resistance to alkali. If only these tests were to be considered, it seems obvious that product III or even product Ia show the best results. These results are confirmed when we compare these products (Product Ib has the same molecule as product Ia but with slightly higher active content) when tested to NCHRP 224 test methods (refer to table 4 & 5).

The product Ib, when exposed to UV shows some level of degradation but it does not seem to affect the performance in term of soluble chloride reduction or water absorption. Despite this light deterioration, there are no significant differences between the different products presented, and if we assume the cost of the materials are directly related to the active content, then these two products (Ia & Ib) seem to have the best performance/cost ratio.

So based on these test methods, either from the European standard or from the American Highway Research Program, the ranking would be as follows in Table 6.

Now if we compared these products to their ability to penetrate the concrete, then the picture will look completely different. The same products (Ia, II, III, IV & V) were applied at different consumption rates with two different types of artificially carbonated concrete.

The penetration depth clearly shows the importance of the active content because for a similar consumption rate, the active content is directly proportional.

Table 6. Ranking of product.

Product type	Active content	Ranking	
		EN 1504-2	NCHRP IV & II
Ia	<10%	2nd	–
Ib	~15%	–	1st
II	~40%	6th	3rd
III	~30%	1st	–
IV	~99%	4th	2nd
V	~80%	5th	4th

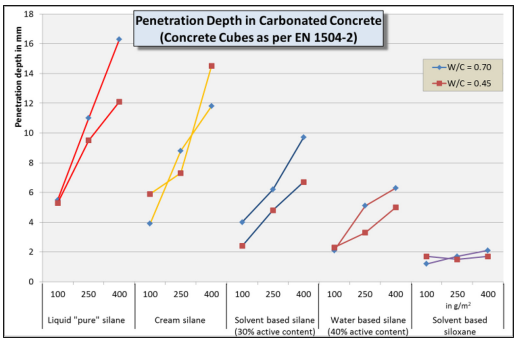

Figure 1. Penetration depth of different hydrophobic impregnation according to consumption rate.

Actually, product III (solvent based 30%active content) penetrates better than the water based silane due to its solvent carrier even if its active content is lower.

Various authors: Wittman (2001), Freitag (2010) and Dai (2008) have highlighted the need for a proper penetration depth to ensure durability of the treatment with hydrophobic sealers.

Wittmann (2001), in his investigation of the use of hydrophobic impregnations in marine structures, has shown that to be effective against the actions of waves or tides, the hydrophobic sealers should penetrate at least 4 to 6 mm into the substrate.

Freitag and Bruce (2010) presented a detailed review for the New Zealand bridge authorities where they stressed the need to differentiate product performances based on their ability to penetrate.

Dai (2008) presented a study where different hydrophobic sealers were used with various consumption rates. He demonstrated that low active content siloxane material (similar to the products Ia or Ib presented in the table 2 & 3 above) were not effective in preventing chlorides from penetrating or to arrest corrosion in cracked concrete (refer to figure 2).

The study also shows that if a good product (high active content similar to product IV presented in table 2 & 3 above) was used at a low consumption rate yielding an insufficient penetration, then its effectiveness is reduced when applied before the cracks occur. Finally, the study shows that if a good product (cream or gel type) is applied correctly with a high penetration

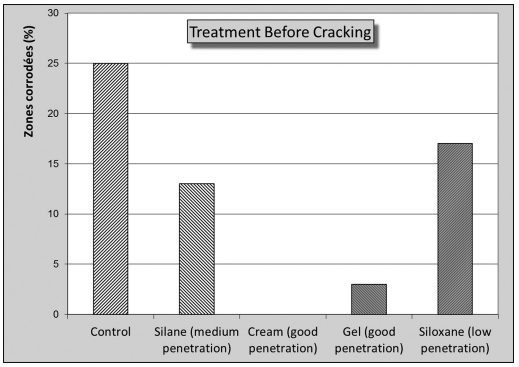

Figure 2. Corrosion of cracked reinforced concrete after 1 year of accelerated cycles with sea water.

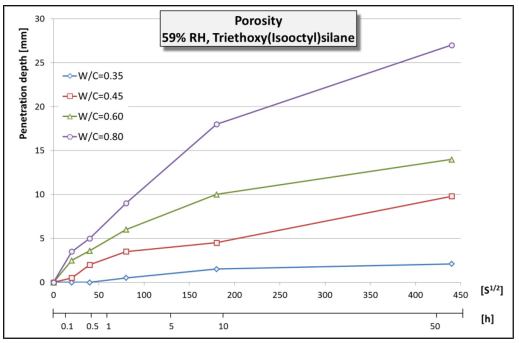

Figure 3. The influence of porosity on the effective penetration depth. The time on the x-axis is the duration of contact for the treatment. The penetration depth is measured four months later.

depth, then their effectiveness remains high to prevent corrosion of the reinforcement even when applied before the cracks occur.

3.1 *Consumption dilemma*

Johansson (2007) has shown that penetration depth of various silane molecules available in the market is dependent on different parameters such as porosity, time of contact, and degree of saturation into the concrete. The time of contact for the treatment is directly related to the consumption.

Figure 3 shows the penetration depth of a silane (similar to the product IV mentioned earlier in the paper) applied on different quality concretes with variable contact time (equivalent to variable consumption rate).

Figure 4 shows that even with a very porous concrete (W/C = 0.80), a pure silane cannot migrate easily into a moisture saturated substrate. Johannson (2007) clearly proves that due to the variation of site conditions (age of concrete, its porosity and moisture saturation), a given consumption rate cannot cater to all situations.

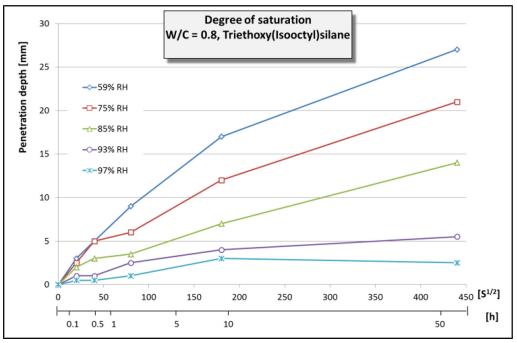

Figure 4. The influence of the conditioning environment around the specimen. The time on the x-axis is the duration of contact for the treatment. The penetration depth is measured four months later.

If durability of the treatment is of concern, it is then necessary to conduct some preliminary investigation in order to assess the relevant consumption rate required to achieve the targeted penetration depth.

An example of penetration depth versus consumption rate was given previously in Figure 1. Using this example, if the penetration depth target for the carbonated concrete with W/C 0.45 was more than 5 mm, the graph shows that when using the cream silane, only 100 g/m^2 was necessary to achieve that target (3 times lower than the typical consumption recommended by the manufacturer). This shows that by optimizing the consumption rate, not only will durability be achieved but a substantial cost saving as well.

This preliminary test will also allow users to determine the optimized surface preparation in order to remove the surface pollution that might prevent the hydrophobic sealer from migrating properly.

4 CONCLUSION

The above information shows that to give only performance testing criteria such as water uptake or chloride reduction is not enough to achieve the highest performance required.

It is important to specify the penetration in order to select the relevant product.

It is also crucial, as highlighted by many authors, that this penetration depth shall be asserted directly using similar concrete quality to the one planned for the project as penetration depth will heavily depend on porosity, quality, saturation level etc. Hence the consumption rate shall be adapted to suit the project conditions.

REFERENCES

Dai J. et al, 2008. Investigation of Chloride Ingress in Cracked Concrete Treated with Water Repellent Agents. 1Ufe Cycle Management Research Centre, Port and Airport Research Institute, Japan. *Hydrophobe V, 5th International Conference on Water Repellent Treatment of Building Materials. Aedificatio Publishers, 299–310*. Brussels, Belgium

Freitag, SA and Bruce S.M. (2010). The influence of surface treatments on the service lives of concrete bridges. NZ Transport Agency research report 403. 91pp

Johansson A. et al, 2007. Penetration Depth for Water Repellent Agents in Concrete as a Function of Humidity, Porosity and Time. Swedish Cement and Concrete Research Institute, Sweden. *Restoration of Buildings and Monuments Vol. 13, No. 1, 3–16*.

Sika Technologies AG, Internal tests by MPL, April 2012

Wittmann, M. et al. 2001. Application of Water Repellent Treatments for the Protection of "Offshore" Constructions. *Hydrophobe III – 3rd International Conference on Surface Technology with Water Repellent Agents. Aedificatio Publishers, 1–1* Hannover, Germany

Concrete Solutions – Grantham et al. (Eds.)
© 2016 Taylor & Francis Group, London, ISBN 978-1-138-03008-4

Development of chloride induced reinforcement corrosion in cracked concrete after application of a surface protection system

F. Hiemer, S. Keßler & C. Gehlen
Centre for Building Materials, Technische Universität München, Munich, Germany

ABSTRACT: Crack formation is inherent for Reinforced Concrete (RC) structures. The reduction of the concrete's barrier property against chlorides often leads to a local depassivation of the reinforcement. A macro-cell corrosion element is formed in the cracked area. To protect direct driven concrete surfaces such as in multi-storey car parks, German Standards demand the application of surface coatings.

In a research project, basic electrochemical parameters of reinforcement corrosion are measured on cracked RC beams to investigate the influence of an applied surface coating on the corrosion process. The paper presents results of the short-time chloride exposure and discusses the development of these parameters throughout the coating period. Furthermore first findings from the destructive investigation are presented. Chloride contamination led to active corrosion whereas after the coating macro-cell corrosion mostly decreased.

1 MOTIVATION

Crack formation is an inherent characteristic of reinforced concrete structures as it enables the load transfer between concrete and reinforcement. Considering the durability of RC structures, cracks impair the structure's resistance against corrosion promoting agents, such as e.g. chlorides (Šavija & Schlangen 2010). Although cracks enable only a locally limited path, the accumulation of chlorides in the crack area can exceed the critical corrosion-initiating chloride content of the reinforcement very quickly. Therefore RC traffic structures which are highly exposed to de-icing salts (e.g. parking decks) have a significant risk of reinforcement corrosion, since the discrete depassivation of the steel surface can promote the formation of macro-cell corrosion with high corrosion rates (Raupach 1992).

In this form of corrosion, anodic and cathodic subprocesses are spatially separated. The depassivated steel surface in the crack area forms the anode, leading to a potential difference to the surrounding cathodic areas. This electrochemical process was transferred into Equation 1 (Beck 2010) to assess the corrosion current. The sub-processes are expressed into resistances and a driving potential ΔE resulting from the potential difference of the electrodes.

$$I_{corr} = I_{macro} + I_{micro} = \frac{\Delta E}{R_{P,A} + R_{P,C} + R_e} + I_{micro} \qquad (1)$$

The overall corrosion current I_{corr} contains the macrocell corrosion current I_{macro} and the microcell corrosion current I_{micro}. Of the last named, the cathodic process takes place in close vicinity to the anodic reaction and therefore contributes inseparably to the corrosion process

I_{macro} is described by the potential difference ΔE and the sum of all system resistances, such as anodic polarization resistance $R_{P,A}$, cathodic polarization resistance $R_{P,C}$ and the electrolytic resistivity of concrete $R_{E,}$. Herein, especially R_E is considered a major factor influencing active corrosion (Hunkeler 1995; Warkus & Raupach 2008, Hornbostel 2015).

Regarding the repair of cracks this relation is used to protect direct driven concrete surfaces in Germany (DIN EN 19921-1/NA 2013). The German bulletin "multi-storey or underground car parks" (DBV 2010) recommends the application of a crack-bridging coating for new, cracked concrete structures. The coating avoids further intake of water and corrosion promoting agents, minimizing the risk of depassivation as well as reducing the moisture content of the concrete (DAfStb 2001). Due to the increasing resistances, the corrosion rate is expected to be reduced to technically tolerable extents. An already initiated corrosion process due to a short-time chloride exposure is not considered hazardous for the structure's load bearing capacity.

Therefore, it is important to clarify the effects of an applied coating, since the reinforcement corrosion behavior in cracked and afterwards sealed concrete has not yet been scientifically analyzed.

2 EXPERIMENTAL

The aim of the research project was to investigate the effect of an applied surface protection system on the

corrosion process in cracked concrete after a short-term chloride exposure, with respect to the provided design principles given in (DBV 2010). Especially in cracked concrete, the decisively influencing factors (e.g. moisture content, critical chloride content) on chloride corrosion can scatter widely.

In the course of the project, reinforced concrete beams were fabricated in which defined bending cracks were initiated. Initially the basic electrochemical parameters of reinforcement corrosion were monitored during a short-term chloride exposure of one winter season. Subsequently a surface protection system was applied in order to specify the corrosion situation after the repair measure.

In the following sections, a brief presentation of the specimen setup as well as the exposure and measuring schedule is given. Further information on these topics can be found in (Hiemer et al. 2015).

2.1 *Specimens*

Nineteen reinforced concrete specimens with bending cracks orthogonal to the depassivated anode bar, as shown in Figure 1, were produced. Two "cathode cages" were positioned outside the crack area to exclude their depassivation. Anode bar and cathode cages were electrically separated to assess all electrochemical parameters on each half cell individually.

In order to reproduce the structural situation of a multi-storey car park, the concrete composition was chosen in accordance with DIN 10452 (2008) and the requirements resulting for a concrete component in the corresponding exposure condition XD3 (DIN EN 199211 2011). As binder a Portland cement (CEM I) was used.

28 days after concreting, the cracks were initiated by three-point bending, adjusting the crack width to 0.3 mm, the permitted width in exposure class XD3. Afterwards the lateral areas were sealed diffusion-proof in order to simulate a slab structure.

2.2 *Exposure & measuring schedule*

During the chloride exposure and afterwards, all specimens were stored in a climate of 20° C / 85% RH. The concrete surface in the central 10 cm of the specimen was wetted with a 1.5 M sodium chloride solution. To ensure even moistening, the outer areas were loaded with tap water only. The specimens were loaded once a week for 12 weeks, to reproduce the chloride intensity of one winter period. Figure 2 shows the finally prepared specimens.

Afterwards the surface was allowed to dry for around 5 weeks before the surface coating could be applied.

The electrochemical parameters were regularly recorded, beginning before the first exposure. The macrocell corrosion current I_{macro} was logged periodically every 3 hours with a low-resistance ammeter. Once a week, the circuit was disconnected resulting in a depolarization of the electrodes. By using the MnO_2 reference electrode, the open circuit potentials (OCP) of anode (E_A) and cathode (E_C) were then determined. Hence, the driving potential ΔE of the corrosion cell could be derived from the difference of these potentials ($E_C - E_A$). As shown in Equation 1 both of these parameters, I_{macro} and ΔE represent a basic parameter to assess the reinforcements' corrosion state.

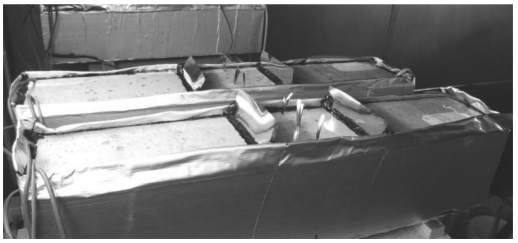

Figure 2. Specimens exposure (Hiemer et al 2015).

Afterwards the polarization resistance of the anode $R_{P,A}$ was determined. While shifting the anodic potential gradually from $-20\,\mathrm{mV_{OCP}}$ to $+20\,\mathrm{mV_{OCP}}$ (ΔE) the resulting current ΔI of the system was recorded. Since the gradient of the potential-current relationship is almost linear around the close vicinity of the OCP, the polarization resistance is defined as the quotient of imposed potential ΔE and resulting current ΔI. Furthermore Angst & Büchler (2015) showed that an inverse proportionality between the polarization resistance and the corrosion current I_{corr} exists. Therefore the time dependent recording of $R_{P,A}$ allowed the qualitative evaluation of the corrosion state throughout the whole exposure and coating period.

In the last step, the alternating current resistance, or impedance, was determined via Electrochemical Impedance Spectroscopy (EIS). It was measured using a small sinusoidal excitation voltage to which the systems current response had the same frequency, but was shifted in phase. During variation of the voltage frequency over a large range, the systems response was recorded, from which the system impedance could be derived. By using equivalent circuit diagrams, system specific parameters, such as the electrolytical resistance R_e, were determined. The continuous detection of EIS data allowed a qualitative evaluation of the resistance development between the electrodes throughout the exposure as well as after the application of the coating. Due to the interrelation of electrolytic resistance and changes in moisture distribution, drying effects of the sealing and an eventual variation of the corrosion process could be detected.

Finally, after their lifespan was reached, depth dependent chloride profiles were taken from each specimen via direct removal of concrete powder. The chloride content was then quantified relative to the weight of cement [m-%/c] using the photometry method according to (DAfStb 1989).

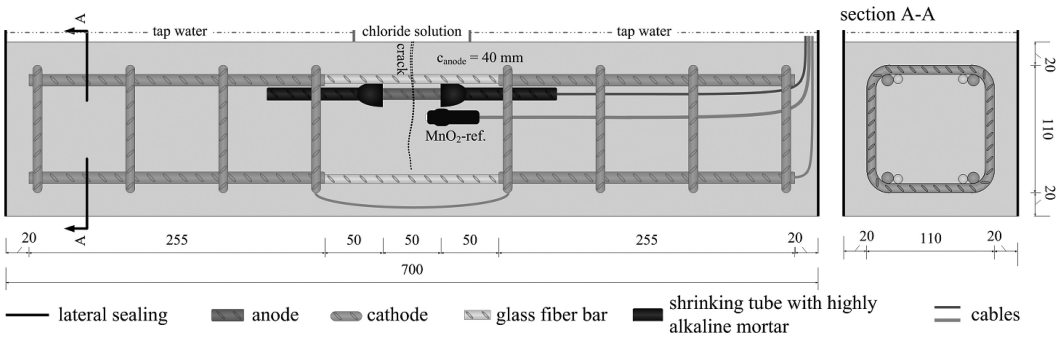

Figure 1. Geometry and reinforcement setup of the specimens, all dimensions in [mm] (Hiemer et al. 2015)

3 RESULTS

3.1 *Overview*

In Table 1, all 19 specimens are classified by their state of corrosion activity which occurred during the whole time of investigation: no depassivation, active corrosion only during chloride exposure, active corrosion throughout the application of the coating and so on. For each specimen, the relevant electrochemical parameters to determine their state of corrosion throughout the complete investigation period are provided. The classification of the specimen was based on the three parameters: driving potential ΔE, macro-cell corrosion current I_{macro}, and the anodic polarization resistance $R_{P,A}$. Furthermore the chloride contents $c(Cl^-)$ from destructive investigations are given. These represent the mean value obtained in the crack area at a depth of 40 to 45 mm, the same level as the anode bar.

On eight of the 19 specimens, no indicators of corrosion activity could be found. On these specimens the anode bar mostly had a very constant OCP indicating that the steel surface in the crack area was not depassivated. The electrodes were not polarized and no macro corrosion current was measured. A qualitative consideration of the rather high minimal polarization resistances confirms this state. In most cases the $R_{P,A}$ values descended only slightly from their initial values during the whole exposition. Regarding the chloride content at the depth of the anode, one can see that in comparison to the values of actively corroding specimens, passive samples had lower contents with a mean value of 0.69 m%/c.

On the remaining eleven specimens active corrosion could be identified during the twelve weeks of cyclic wetting. However two different scenarios have to be considered.

On seven samples the corrosion activity halted before the concrete surface coating could be applied. Either it subsided during the exposure or right afterwards, during the surface drying time before the coating could be applied. Specimen PC-12 serves as an example for this kind of specimen. Its electrochemical parameters are extensively discussed in section 3.2 in order to describe the average corrosion behavior of all active samples during the short-time chloride exposure. The average chloride contents of these specimens (mean value: 0.96 m-%/c) mostly exceeded the values of the passive specimens, however specimen PC-11 and PC-12 ranged in the same region.

Even though four other samples showed the same diminishing current response to the ongoing cyclic

Table 1. Selected electrochemical parameters of all specimens, separated by corrosion activity.

	max. ΔE [mV]	max. I_{macro} [µA]	times active [d]	min. $R_{P,A}$ [kΩ]	$c(Cl^-)$ [%/c]
No depassivation					
PC-01	0	0	0	27	0.51
PC-06	30	0	0	23	0.61
PC-09	20	0	0	34	0.44
PC-10	20	0	0	36	0.90
PC-13	0	0	0	30	1.00
PC-15	0	0	0	27	0.54
PC-16	100	2	1	15	0.79
PC-18	70	2	1	20	0.84
Active corrosion only during chloride exposure					
	max. ΔE [mV]	max. I_{macro} [µA]	times active [d]	min. $R_{P,A}$ [kΩ]	$c(Cl^-)$ [%/c]
PC-02	240	25	100	3	1.25
PC-04	290	31	90	3	1.30
PC-08	170	12	40	7	0.91
PC-11	165	26	85	4	0.49
PC-12	265	41	115	2	0.60
PC-14	260	46	105	3	1.20
PC-17	150	16	55	8	0.95
Active corrosion throughout coating					
	max. ΔE [mV]	max. I_{macro} [µA]	times active [d]	min. $R_{P,A}$ [kΩ]	$c(Cl^-)$ [%/c]
PC-03	270	45	410	3	n.a.
PC-05	275	51	190	3	0.94
PC-07	295	70	415	2	n.a.
PC-20	305	50	370	3	n.a.

wetting, the processes did not stop completely or it resumed after the coating was applied. In section 3.3 the electrochemical parameters of specimen PC-7 are presented in order to discuss the long term corrosion behavior after sealing the concrete surface. At present, the chloride profile was only obtained from specimen PC-05, which had a chloride content at the depth of the anode comparable to other active specimens.

3.2 *Corrosion behavior during short-time chloride exposure*

To evaluate the corrosion state of the crack crossing anode in the specimens, the data of the corrosion current I_{macro} (black line, top), the driving potential ΔE (grey dashed line, top) between their electrodes, the anodic polarization resistance $R_{P,A}$ (black dashed line, bottom) as well as the electrolytic resistance from EIS R_E (grey line, bottom) are regarded. Figure 3 contains these parameters from a characteristic specimen (PC-12) representing a case of active corrosion throughout the exposure.

After crack initiation and before the beginning of exposure the anodic and cathodic potentials were in the same range, leaving the driving potential at values around 0 and therefore indicating the passivity of the steel surface. Since no corrosion current is measured the assumption of passivity before the exposure is assured. In this passive state, the values of the polarization resistance range around 47 kΩ. Before the first exposure, the electrolytic resistivity is approximately 450 Ω.

Only a few days after the first moistening, a significant increase of the driving potential ($\Delta E \approx 240$ mV) indicates an immediate depassivation. This potential drop of the anode was accompanied with an instant increase of the macro-cell corrosion current. With the continuing chloride loading, the driving potential increased to a maximum of 260 mV after around 42 days. The corrosion current reached its maximum of 41 µA after 28 days, when it started to decline during the ongoing cyclic loading. The descent in corrosion current was accompanied by a positive development of the anodic potential, lowering the overall driving potential ΔE.

The development of polarization resistance and electrolytic resistance provides further information about the reason of the corrosion onset. On the one hand the first moistening of the specimen reduces the concrete's resistance to nearly half. During further wetting cycles, the concrete stayed rather moist, but due to ongoing hydration of the quite young concrete, its overall resistance slowly rose to values of its initial state. On the other hand the polarization resistance of the anode dropped from 47 kΩ to 3 kΩ after the first contact with chloride solution. This indicates a sufficient supply of chlorides to depassivate the steel surface from the beginning. This provision stayed intact until day 42. Oxidation products that are formed during the corrosion process can shield the area of active corrosion, which in this case lead to

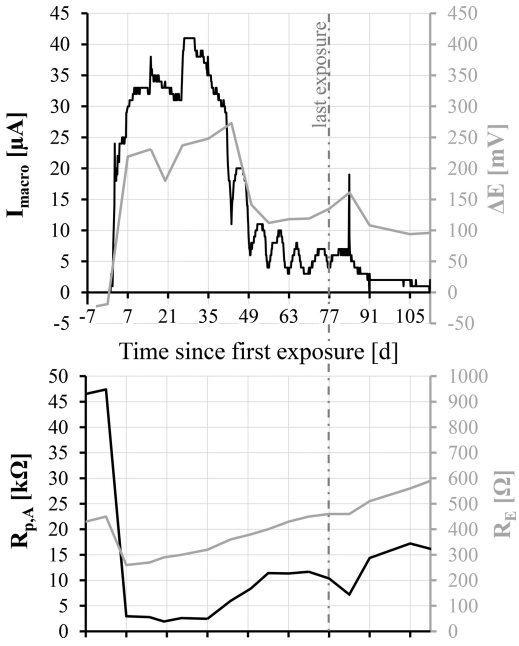

Figure 3. Electrochemical parameters of specimen PC-12 during the short-time chloride exposure.

an increase of $R_{P,A}$ by a factor of 4 (Raupach 1992). This obstruction decreases the macro element current significantly as can be seen between days 42 and 77.

After the last exposure (vertical dotted line in Figure 3) and before the application of the surface coating, the polarization resistance increased even further, which might have been due to the lack of chloride supply in the corroding area. A slight drying effect could also be identified regarding the electrolytic resistance, which increased minimally steeper than before. These circumstances lead to a further reduction of the overall macro corrosion current, which in the presented case results in a complete halt of corrosion activity 115 days after the first exposure.

3.3 *Influence of a concrete surface coating on chloride induced corrosion*

As mentioned before on four of the eleven active specimens the corrosion process did not stop before sealing the concrete. The electrochemical parameters obtained from specimens PC7 in the time after the surface coating are shown in Figure 4 representatively for all four specimen.

As mentioned before, this specimen was also subject to decreasing corrosion activity after the last exposure, happening 35 days before the coating of the specimen. The corrosion current was declining although the driving potential of the system fluctuated continually at around 190 mV during the drying period. The attenuation of the processes can rather be led back to the anodic polarization resistance which doubled its value in those 5 weeks from 5 kΩ to around

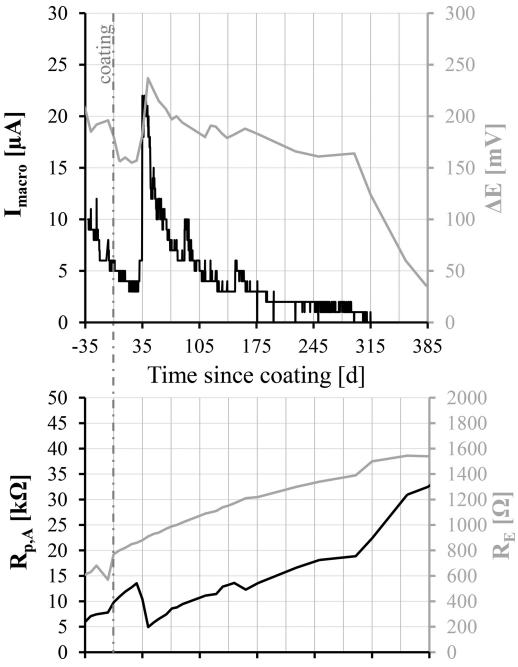

Figure 4. Electrochemical Parameters of specimen PC-07 after the application of the coating

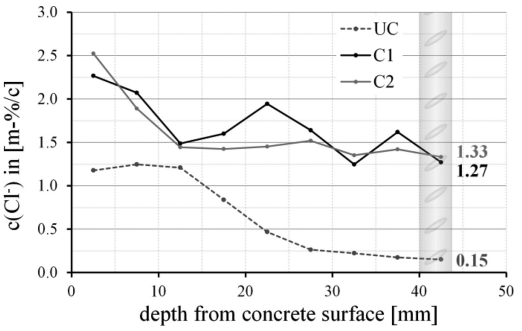

Figure 5. Chloride profile of specimen PC-04.

10 kΩ. A significant drying effect wasn't indicated by the electrolytic resistance.

Initially, the coating of specimen PC-7 resulted in a further decrease of corrosion current. All electrochemical parameters indicated declining corrosion activity. The anodic potential drop occurred after five weeks under sealed conditions and resulted in a sharp increase of the macro-cell corrosion current of about 20 µA. The driving potential rose immediately by 100 mV whereas the polarization resistance dropped down to 5 kΩ. A change in electrolytic resistance is not detectable. These parameters lead to the assumption that after the coating was applied to the specimen, a redistribution of chlorides in the corroding area took place, which led to a further depassivation of the steel surface, resulting in very high corrosion activity.

Nonetheless, the current afterwards slowly declined and did come to a complete halt, indicating a standstill of corrosion activity 315 days after the specimen was coated. The driving potential was initially only falling slightly, when it sharply dropped down after 300 days. However the polarization resistance seemed again to be the limiting factor, increasing by a factor of four to nearly 20 kΩ until day 300.

All four active specimens showed this steep increase of macro-element current immediately when their surface was coated or, as in specimen PC-07, a few weeks later. Since the increase of current varied significantly between the active specimens (PC-05: 10 µA; PC-03: 30 µA; PC-20: 33 µA) their development afterwards was different.

The corrosion activity of specimen PC-05 had already halted 60 days after the coating application. On the contrary specimen PC-03 showed very active corrosion ($I_{macro} = 35$ µA; $R_{P,A} = 3$ kΩ) until 120 days after sealing. Its corrosion current then dropped within two weeks to only 5 µA and subsided completely 270 days after coating.

Nevertheless, specimen PC-20 is still actively corroding, even one year after sealing. The corrosion current set in 3 weeks after coating and rose to values of 33 µA, accompanied by a drop of the polarization resistance to 3 kΩ. The current afterwards decreased to a mean value of 15 µA where it stayed consistently to the time of preparing this paper.

3.4 *Chloride profiles from destructive investigations*

As already mentioned, depth dependent chloride profiles of each specimen were taken after the electrochemical measurements were finished. Due to the tight reinforcement situation, two profiles from the crack area of each sample were drilled with a 20 mm drill bit (C1, C2). Continuing from the crack on the surface of the specimen, the probes were taken stepwise in depths of 5 mm each, oriented orthogonal to the concrete surface. Therefore in specimens with a very uneven crack path, the chloride profiles might vary. On each sample a reference profile from the "uncracked" area (UC) was taken.

In Figure 5 the profile of active specimen PC-04 is presented. The profile in the crack area shows a high, quite constant development in the deeper areas. This aligns well with the assumption that cracks enable a rapid ingress of chlorides. Only in the areas closer to the surface, chloride contents are even higher. Due to the glass fiber reinforcement at a depth of 20 mm, the crack could be narrowed down, reducing the chloride content in deeper areas. Nevertheless, the chloride content at the steel surface exceeded most values (>0.5 m-%/c) which were identified to be the critical chloride content in different investigations (Angst et al. 2009; Breit et al. 2011).

In Figure 6 the profile of the non depassivated sample PC-15 is shown.

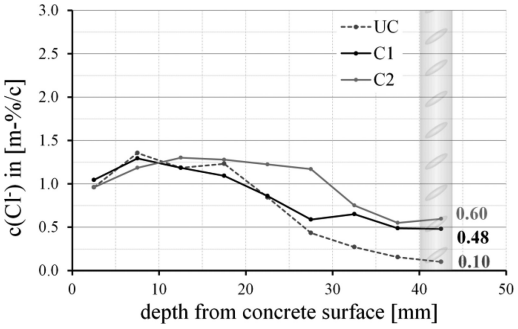

Figure 6. Chloride profile of specimen PC-15.

One can see that near the concrete surface, all values range in same order. Only at the depth of 32.5 mm did the values begin to differ, reaching values in the cracked area around of 0.48 to 0.60 m-%/c. It can be assumed that in this specimen the critical chloride content was not surpassed.

Both quite similar uncracked profiles show that an intact concrete cover of 40 mm would provide a sufficient barrier against depassivation by chlorides during the short-term chloride attack.

4 DISCUSSION, CONCLUSION AND OUTLOOK

The results of the corrosion behavior in cracked concrete after a short-term chloride exposure show that a depassivation of the crack crossing reinforcement is quite likely to occur.

In 11 out of 19 specimen after 12 weeks of exposure to a 1.5 M. sodium chloride solution, the anodic potentials dropped significantly, leading to potential differences ΔE between anode bar and cathode cages of approximately 250–300 mV. These drops were accompanied by increasing macro-cell corrosion currents from 12 up to 70 µA, which afterwards mostly showed a degressive progress. Since the exact size of the corroding area is not yet known, the assumption of the whole exposed steel surface of the anode bar as the corroding surface can give an impression about the current densities. Even with an assumed area of 15.70 cm^2, the current densities reach from 0.76 $\mu A/cm^2$ up to 4.46 $\mu A/cm^2$, which classifies the rate of corrosion, according to the recognized rules of technology (e.g. RILEM TC 154EMC) to moderate and even high corrosion rates.

As further investigations on the resistivity confirmed the degressive process of corrosion activity could be traced back to an increasing electrolytic resistance resulting from the continuously hydrating cement paste. On the other hand, during the corrosion process, oxidation products are formed that can shield the area of active corrosion. This can lead to a shortage of corrosion promoting agents such as chlorides, reducing their overall concentration and therefore increasing the anodic polarization resistance in the corrosion system. Periodical measurements of the linear polarization resistances of the active anode bar confirmed that increasing polarization resistances were the decisive parameter to lower the overall macro element currents.

Nevertheless, eight of the 19 specimens showed no indication for corrosion activity. Chloride analysis confirmed that most chloride contents of the passive specimens were significantly lower than those specimens which showed active corrosion. However, some of the passive samples exceeded the chloride contents of active specimens, which confirms that the critical chloride threshold depends on various factors and can't be seen as a constant value. Furthermore, it may be possible that the crack path was not identical in all specimens, so that the crack in these specimens did not cross the anode bar.

As already mentioned, the corrosion currents tended to decrease throughout the exposure, stopping the corrosion activity in seven of the eleven depassivated specimens. In the four remaining specimens the corrosion processes continued until the application of the crack-bridging surface protection system. The coating of these concrete specimens resulted in a spontaneous sharp increase of macro-cell current, which in some of those specimens decreased afterwards. This sharp rise could be explained due to time dependent diffusion effects, which have led to a repeated accumulation of chlorides on the steel surface. These provoked further depassivation of the reinforcement which occurred coincidently at the same time when the coating was applied or a few weeks later. In three actively corroding specimens the process was still halted, from a few weeks up to half a year after the coating was applied. In one specimen however it remained constant over the observed period of one year after the sealing of the concrete surface.

To finally clarify the corrosion behavior of the last coated specimen the measurements will be continued.

As mentioned in the beginning, micro-cell corrosion is an inherent characteristic of reinforcement corrosion. Furthermore during the corrosion process oxidation products are formed, which can shield the corroding area and therefore can significantly affect the formation of micro-cell corrosion (Beck 2010). Therefore the effects of micro-cell corrosion should not be ignored. Additionally the surface coating can maintain a micro climate in the crack area, which could maintain micro-cell corrosion endangering the load bearing capacity of the structure.

Hence, at the end of the exposure, anode bars from three specimens are removed. Every three months further anodes are dismounted and the corrosion products are removed from the surface. By calculating the gravimetric mass loss, differences between gravimetric and coulometric mass loss, calculated from the accumulated corrosion current I_{macro}, enables the quantification of the micro-cell corrosion. The time dependent development of the micro-cell corrosion can be assessed due to the ongoing destructive investigations of the specimens.

Therefore further investigation is carried out to assess the effectiveness of a subsequently applied surface protection system.

ACKNOWLEDGEMENTS

The authors wish to thank the German Research Foundation (DFG) for supporting this project. Furthermore we would like to sincerely thank Schöck Bauteile GmbH, Badische Stahlwerke GmbH and SCHWENK Zement KG, who provided some of the materials used in this project.

REFERENCES

Angst, U. & Büchler, M. 2015. Optimierung und Validierung von Verfahren zur Bestimmung der Korrosionsgeschwindigkeit in Stahlbeton. *Forschungsprojekt AGB 2012/013 auf Antrag der Arbeitsgrupper Brückenforschung (AGB).*

Angst U, Elsener B, Larsen CK, and Vennesland Ø. Critical chloride content in reinforced concrete – A review. 2009. *Cement and Concrete Research 39 1122–1138.*

Beck, M. F. 2010. Zur Entwicklung der Eigenkorrosion von Stahl in Beton. *Dissertation, RWTH Aachen, Germany*

Breit, W., Dauberschmidt, C., Gehlen, C., Sodeikat, C., Taffe, A., Wiens, U. 2011. Zum Ansatz eines kritischen Chloridgehaltes bei Stahlbetonbauwerken. *Beton- und Stahlbetonbau, 106, Heft 5, Berlin.*

DAfStb Deutscher Ausschuss für Stahlbeton e. V, 1989. DAfStb Heft 401 – Anleitung zur Bestimmung des Chloridgehaltes von Beton, Berlin: Beuth Verlag.

DAfStb Deutscher Ausschuss für Stahlbeton e. V, 2001. DAfStb Richtlinie – Schutz und Instandsetzung von Betonbauteilen (Instandsetzungsrichtlinie), Part 1–4. Berlin: Beuth Verlag.

DBV German Society for Concrete and Construction Technology 2010. DBVBulletin: Multi-storey and Underground Car Parks.

DIN Deutsches Institut für Normung e.V. 2008. DIN 10452, Concrete, reinforced and prestressed concrete structures – Part 2: Concrete – Specification, properties, production and conformity – Application rules for DIN EN 206-1, Berlin: Beuth Verlag.

DIN Deutsches Institut für Normung e.V. 2011. DIN EN 199211, Eurocode 2: Design of concrete structures – Part 1-1: General rules and rules for buildings; *German version EN 1992-1-1:2004 + AC:2010.* Berlin: Beuth Verlag.

DIN Deutsches Institut für Normung e.V. 2013. DIN EN 1992-1-1/NA, National Annex – Nationally determined parameters – Eurocode 2: Design of concrete structures – Part 1-1: General rules and rules for buildings. Berlin: Beuth Verlag.

Hiemer, F., Keßler, S., Gehlen, C., 2015. Reinforcement corrosion behavior in bending cracks after short-time chloride exposure, *Proceedings of 4th International Conference on Concrete Repair, Rehabilitation and retrofitting, Leipzig, Germany, 5–7 October 2015.*

Hornbostel, K., 2015. The role of concrete resistivity in chloride-induced macro-cell corrosion. *Dissertation, NTNU, Trondheim, Norway.*

Hunkeler, F. 1995. The resistivity of pore water solution – a decisive parameter of rebar corrosion and repair methods. *Construction and building materials, Vol. 10, No. 5, pp.381–389, 1996.*

Raupach, M. 1992. Zur chloridinduzierten Makroelementkorrosion von Stahl in Beton. *Deutscher Ausschuss für Stahlbeton*, *Issue 433,* Berlin: Beuth-Verlag.

RILEM TC 154-EMC, Electrochemical Techniques for Measuring Metallic Corrosion, Test methods for on-site corrosion measurement of steel reinforcement in concrete by means of the polarization resistance method. *Materials and structures, Vol. 37, pp. 246–258, November 2004*

Šavija, B. & Schlangen, E. 2012. Chloride ingress in cracked concrete- a literature review. In C. Andrade and J. Gulikers (eds.), *Advances in Modeling Concrete Service life: Proceedings of 4th International RILEM PhD Workshop held in Madrid, Spain, 19 November 2010.*

Warkus, J. & Raupach, M. 2008. Numerical modelling of macrocells occurring during corrosion of steel in concrete. *Materials and corrosion, 59, No. 2, pp. 122–130.*



Taylor & Francis
Taylor & Francis Group
http://taylorandfrancis.com

Concrete Solutions – Grantham et al. (Eds.)
© 2016 Taylor & Francis Group, London, ISBN 978-1-138-03008-4

An investigation of the surface properties of air-cured microconcretes developed with controlled permeability formwork liners using destructive and non-destructive methods

A.S. Marinos, M.S. Katsiotis, G. Batis & M. Beazi-Katsioti
School of Chemical Engineering, National Technical University of Athens, Greece

J.L. Gallias
Laboratoire de Mécanique et Matériaux du Génie Civil, Université de Cergy-Pontoise, France

V. Kaloidas
"Heracles" General Cement Co, Greece

ABSTRACT: This paper reports the results of an investigation carried out to study the influence of Controlled Permeability Formwork (CPF) liners on the surface properties of air cured microconcretes, using destructive and non- destructive methods. For the development of the specimens, two cement types were used (CEM I and CEM II/B – M (PW). The specimens were developed in wooden moulds with and without CPF. For each specimen, destructive (chloride migration according to NT Build 492, carbonation depth) and non-destructive measurements (surface water absorption, ultrasonic pulse velocity, rebound number) were conducted. Experimental results confirm the beneficial effects of CPF liners on concrete surface properties, which have a significant impact on service life. A strong correlation between destructive and non-destructive methods is revealed, a fact that allows for in situ estimation of concrete durability against chlorides.

1 INTRODUCTION

Due to the many environmental factors that can cause severe deterioration problems to reinforced concrete structures, service life is directly dependent on concrete permeability. A number of methods and materials have been developed in order to create an almost impermeable bulk concrete microstructure, increasing the durability and service life of the concrete structures. The need for an impermeable concrete microstructure is essential for structural elements and important from an economical point of view, since the cost of repair for concrete structures is in most cases very high. One of the few materials usually employed for directly improving the concrete surface zone is Controlled Permeability Formwork (CPF) [Wilson 1994, Duggan 1992, Sousa 1998, Sousa 2003]. CPF consists of a textile liner set on the formwork, allowing air bubbles and surplus water to drain out, but retaining cement particles (Figure 1).

CPF enables the water-cement ratio (w/c) of the outer layer to become very low and the concrete to hydrate to a very dense surface skin, as an adequate amount of water is made available at initial stages to activate optimum hydration. The reduction of the outer layer w/c results in increased surface strength and resistance to abrasion, minimizes blowholes and reduces water and air permeability, water absorption,

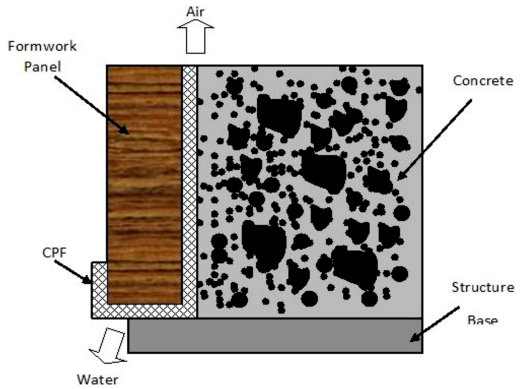

Figure 1. Controlled Permeability Formwork – Schematic Representation.

depth of carbonation and chloride and oxygen diffusion [Price 1991, Reddi 1992, Suryavanshi 1997, Cairns 1999, Coutinho 2001, McCarthy 2001, Philip 2005].

In this work we present how the use of CPF liners beneficially affects the properties of microconcretes' surface compared to plain formwork, under laboratory environment conditions. Microconcrete containing sand as aggregate can emulate the structure

and properties of concrete. Also, the estimation of the non-steady-state migration coefficient using non-destructive methods and statistical analysis tools was examined.

2 EXPERIMENTAL WORK

2.1 *Materials*

The materials used in this study were two commercially available cement types (CEM I 52.5 N and CEM II/B – M (P-W) 42.5 N), potable water according to EN 1008, fine aggregate (crushed calcareous sand) and two types of CPF (Zemdrain® MD and Zemdrain® Classic). The two cement types conformed to European Standard EN 197-1. A chloride free, polycarboxylate based superplasticizer (Viscocrete® 300) was employed to achieve the desired workability of the microconcretes. Table 1 contains the chemical analysis and the physical properties of the cements and sand. The particle size distribution of sand was acquired according to ASTM C 136- 06 and found to conform to required standards (not shown here).

2.1.1 *Mix design*

Nine different microconcretes were prepared in a 50lt rotary mixer, all having the same w/c ratio (w/c = 0.5). The microconcrete mix design is presented in Table 2 for all samples.

Air content and flow table spread of the fresh microconcrete were measured according EN 459-2 and EN 1015-3:1999 respectively. The superplasticizer was added at the time of mixing in order to keep flow table values in the range 175 ± 10 mm for all mixes. For each mix, $250 \times 250 \times 150$ mm specimens (Fig. 2) were cast in wooden moulds with and without CPF and compacted with a vibrating table. Where applicable, Zemdrain was placed to all four vertical sides of the specimens, as shown in Figure 3. After casting, the

Table 1. Properties of CEM I 52.5 N, CEM II 42.5 N and Calcareous Sand.

	II 42.5 N	I 52.5 N	Sand
SiO_2	22.10	20.93	0
Al_2O_3	6.27	5.80	0
Fe_2O_3	3.55	3.51	0.02
CaO	55.97	60.07	55.50
MgO	2.0	2.03	0.72
K_2O	0.71	0.67	0.01
Na_2O	0.30	0.20	0
SO_3	3.10	2.99	0
TiO_3	0.31	0.3	0
Loss on Ignition	5.23	3.3	43.52
Blaine (g/cm^2)	44461	4176	
Specific Gravity (g/cm^3)	2.96	3.06	2.70
Strength			
2 days	28.9	31.1	
7 days	40.4	43.2	
28 days	50.7	53.7	

Table 2. Composition of microconcrete mixtures in kg/m^3.

Cement Type/ Age (days)	Mould type	Cement	Water	Sand	SP	Flow table	Air Content
CEM II 42.5 N/28	Formwork+ Classic	496	248	1489	2	178	3.1
	Formwork+ MD Plain Formwork	497	248	1491	2	182	3.0
		497	249	1492	2	176	2.9
CEM II 42.5 N/90	Formwork+ Classic	497	249	1492	2	174	2.9
	Formwork+ MD Plain Formwork	496	248	1487	2	170	3.2
		497	248	1491	2	169	3.0
CEM I 52.5 N/28	Formwork+ Classic	498	249	1495	1	176	3.3
	Formwork+ MD Plain Formwork	499	250	1498	1	181	3.1
		498	249	1493	1	179	3.4



Figure 2. Wooden mould (Plain Formwork) and $250 \times 250 \times 150$ mm microconcrete specimen.



Figure 3. Wooden mould with Zemdrain Classic on the sides (Formwork + Classic) after specimen compaction.

specimens were covered with a wet blanket and left in the laboratory for 24 h. All specimens were demoulded 24 hours after casting.

2.1.2 *Curing*

All specimens were left to cure continuously in the laboratory under ambient conditions until the test age. The top and the bottom sides of the 250 × 250 × 150 mm specimens were hermetically sealed, in order to allow the air curing of the specimens happen through the CPF formed sides. The temperature was maintained in the range 20 ± 2°C and the relative humidity generally ranged between 55% and 70%. The CEM I 52.5 N specimens were cured for 28 days and the CEM II 42.5 N specimens were cured for 28 and 90 days, in order to study how CPF affects the surface properties of concretes developed with cements containing pozzolanic materials.

2.2 *Methods*

2.2.1 *Estimation of non – steady state chloride migration coefficient according to NT Build 492.*

The 250 × 250 × 150 mm specimens were used for the determination of non – steady state migration coefficient according to NT Build 492 "Concrete, mortar and cement-based repair materials: Chloride migration coefficient from non-steady-state migration experiments" (Nordtest Method, 1999, pp. 10). After Ø100 × 150 mm cores taken from 250 × 250 × 150 mm specimens, two discs 50 mm thick were cut from the central part of each core and prepared according to the NT Build 492 standard procedure for testing. Due to the applied electrical field on each disc, chloride ions migrated from NaCl solution (catholyte) to NaOH solution (anolyte) through the specimens. The voltage applied to each specimen and the duration of the measurement were as defined by the standard. The apparatus used and the principle of operation are shown in Figure 4 and Figure 5.

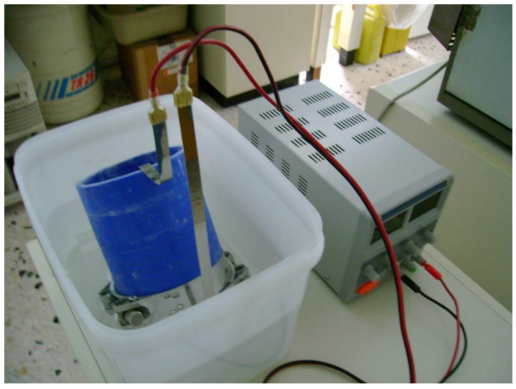

Figure 4. Apparatus for non- steady state migration coefficient measurements according to NT Build 492.

Once the measurement was over, the discs were split axially and sprayed with 0.1M $AgNO_3$ solution. $AgNO_3$ reacts with chlorides and produce AgCl, a white precipitate. The production of AgCl indicates the depth that chloride ions migrate up to a concentration of about 0.07 N into the specimen porosities. For each mixture, two discs were tested, the non-steady state migration coefficient (D_{nssm}) calculated from Equation 1 for each specimen and the mean value of the migration coefficients is reported.

Equation 1.

$$D_{nssm} = \frac{RT}{xFE} * \frac{x_d - a\sqrt{x_d}}{t},$$

where $E = \frac{U-2}{L}$, $a = 2\sqrt{\frac{RT}{xFE}} * erf^{-1}(1 - \frac{2c_d}{c_0})$

where D_{nssm}: Non-steady state migration coefficient (m^2/sec), z: Absolute value of ion valence, for chloride, z = 1, F: Faraday constant, F = 9.648 × 104 J/(V ∗ mol), U: Absolute value of the applied voltage, V, R: Gas constant, R = 8.314 J/(K ∗ mol), T: Average value of the Initial and Final Temperatures in the anolyte solution, K, L: Thickness of the specimen, m, xd: Average value of the penetration depths, t: Test duration, seconds erf^{-1}: Inverse of error function, cd: Chloride concentration at which the colour changes (about 0.07 N), c0: Chloride concentration in the catholyte solution (about 2 N).

2.2.2 *Determination of Surface Water Absorption.*

Measurements of surface water absorption were conducted on 250 × 250 × 150 mm specimens. The surface water absorption results were expressed in ml/m^2/sec according to BS EN 1881 Part 208:1996 "Recommendations for the determination of the surface absorption of concrete".

2.2.3 *Carbonation depth measurements.*

A carbonation chamber with constant conditions (% CO_2: 22–23%, % RH: 55–70%) was used for testing microconcrete durability to carbonation. The carbonation test was conducted on cylindrical core specimens

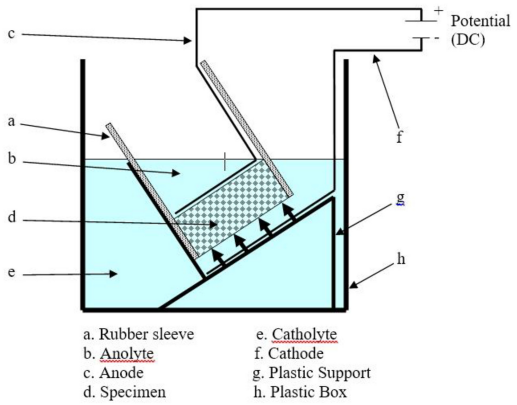

Figure 5. Principle of operation for NT Build 492.

taken from 250 × 250 × 150 mm specimens. The carbonation depth was measured by splitting the specimens axially and spraying them with phenolphthalein, which indicates the depth that mortar has carbonated, as shown in Figure 6.

2.2.4 *Determination of the velocity of Ultrasonic pulse propagation.*

Ultrasonic Pulse Velocity (UPV) measurements were conducted according to EN 12504-4:2004 "Determination of ultrasonic pulse velocity"; the transducers were set on the opposite faces of both the long (250 mm) and short (150 mm) dimension of concrete specimens to measure direct transmission (specimen dimensions: 250 × 250 × 150 mm); the equipment used included a Cooper Technology UPV tester with 54KHz transducers.

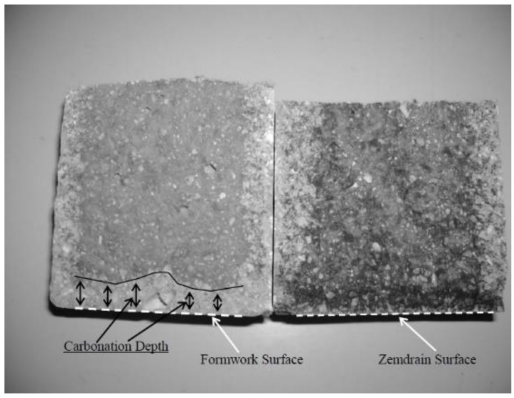

Figure 6. Indication of carbonation depth of microconcretes with and without CPF.

2.2.5 *Surface Hardness*

The surface hardness was measured with a conventional Schmidt rebound hammer. Fifteen hits were made on a small area on the 250 × 250 mm surface of the microconcrete specimens and the average value of the measurements obtained from the hammer's scale divisions (rebound number) is reported [Klieger 1994, Malhotra 2004].

3 RESULTS & DISCUSSION

3.1 *Estimation of non–steady state migration coefficient (NT Build 492)*

The non – steady state migration coefficients estimated from the measurements conducted according NT Build 492 presented in Figure 7.

From the above presented results it is obvious that the lower w/c ratio surface that it is developed due to the use of CPF liners leads to a significantly lower surface absorption (50% and lower) compared to the absorption of the microconcrete surface produced by plain wooden formwork.

3.2 *Carbonation Depth*

The results of carbonation depth measurements (% CO_2: 22–23%, % RH: 55–70%) conducted for various formwork and cement types are presented in Figure 8. Carbonation of concrete is a procedure that can be strongly affected by w/c ratio. The outer layer

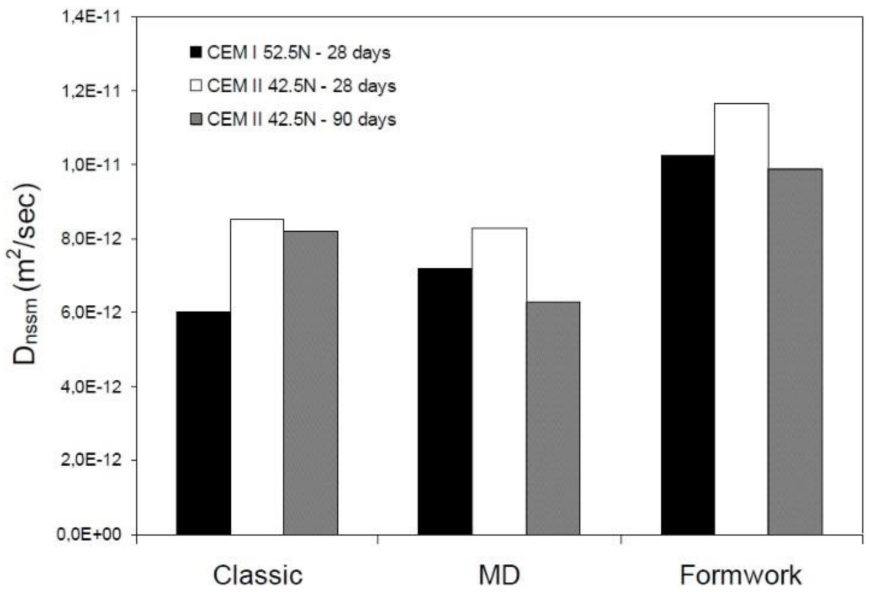

Figure 7. Non – steady state chloride ion diffusion coefficient.

of microconcretes formed with CPF has a lower w/c, which leads to a lower surface porosity. Therefore, as can be observed, microconcretes prepared with CPF showed zero or negligible carbonation depth compared to microconcretes without CPF, which showed high carbonation depth (see Figure 10).

3.3 *Ultrasonic Pulse Velocity (UPV)*

Ultrasonic Pulse Velocity (UPV) is a non-destructive evaluation test to qualitatively asses the uniformity and integrity of mortar and concrete. Water content and any discontinuity in cross section like cracks, cover concrete deterioration and large air voids can be assessed with UPV test. In our experiments, the microconcrete specimens with CPF on their surface developed a denser (lower w/c ratio) outer layer than the mortar specimens produced in plain formwork moulds. This outer layer is able to prevent the inside of the specimens drying fast during air curing, a fact that allowed microconcrete specimens to continue their hydration in time. Due to this, microconcrete specimens with CPF developed a more solid structure. The results of UPV measurements conducted on 250 × 250 × 150 mm specimens are presented in Figure 11. It is observed that the specimens with a CPF formed surface show a higher UPV for both types of cement and for all the curing ages.

3.4 *Surface Hardness*

The test results of the surface hardness measurements conducted with a Schmidt Rebound Hammer for various types of formwork are presented in Figure 12.

The rebound number indicates the surface's uniformity and stiffness. It is observed that an increased rebound number was found for the specimens with a CPF formed surface for both types of cement and for all the curing ages. The low w/c ratio outer layer (about 10–20 mm) that was formed by the use of CPF increased the surface hardness of the specimens leading to a denser and more durable surface for the microconcrete.

3.5 *Correlation between D_{nssm} and Surface Water Absorption results*

The linear correlation between D_{nssm} and 30 min Surface Water Absorption results from our study is presented in Figure 13. It is observed from our results that the linear correlation between D_{nssm} and 30 min Surface Water Absorption results shows for all the cement types and curing ages a very high correlation coefficient ($R^2 > 95\%$), something that is not happening with the correlation coefficients of the other time intervals (10, 60 and 120 min).

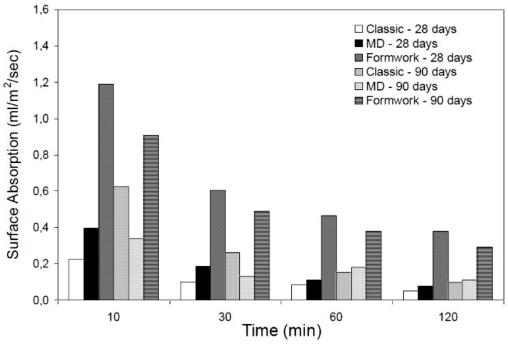

Figure 9. Surface Water Absorption for CEM II 42.5 after 28 and 90 days of curing.

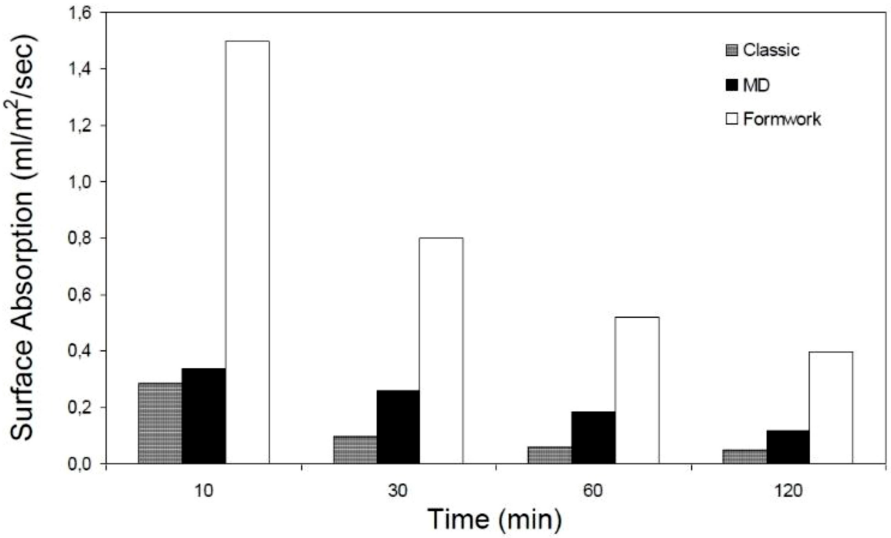

Figure 8. Surface Water Absorption for CEM I 52.5 after 28 days of curing.

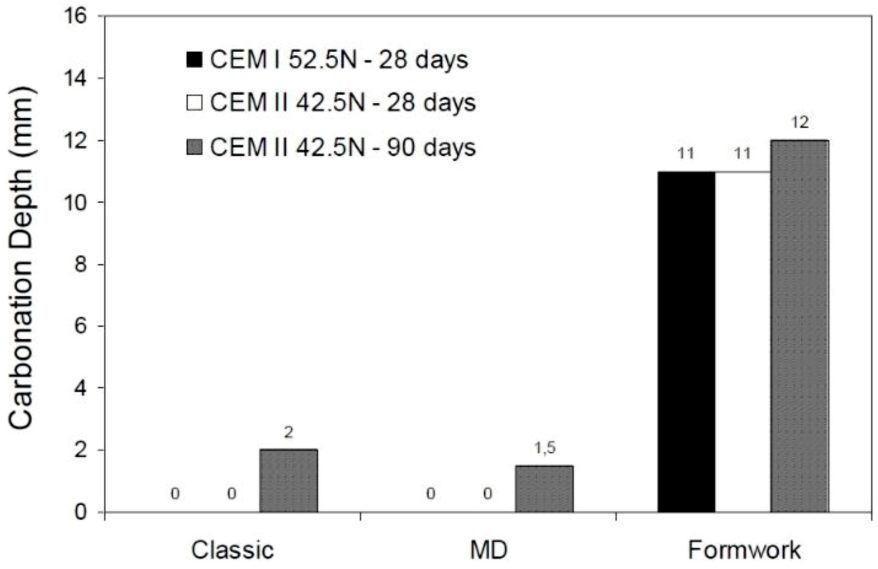

Figure 10. Carbonation depth measurements for microncrete specimens prepared in formwork with and without Zemdrain lining.

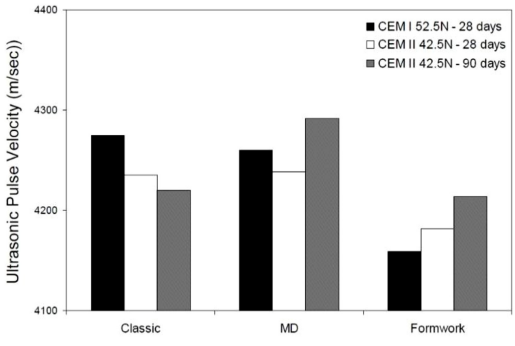

Figure 11. Ultrasonic pulse velocity measurements.

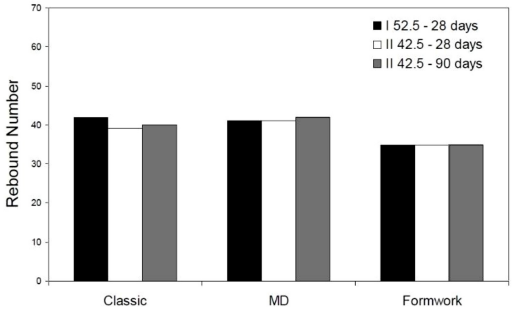

Figure 12. Rebound Hammer test results.

3.6 *Correlation between D_{nssm} and Ultrasonic pulse velocity results*

The linear correlation between D_{nssm} and Ultrasonic Pulse Velocity results from our study is presented in Figure 14. It is observed that a very strong correlation exists between the results of these two methods.

3.7 *Electrical Conductivity Calculation*

It has been reported in literature that the chloride permeability of concrete can be predicted from electrical conductivity measurements, which is a rapid and non-destructive method [Whittington 1981, Lu 1997, Zhao 1998, Snyder 2000, Lizarazo-Marriaga 2009, Ghosh 2011, Yildirim 2011]. The electrical conductivity of a concrete specimen can be calculated from Equation 2: Equation 2.

$$\sigma = \frac{I_0 * L}{A * V}$$

where σ = conductivity (S/m), I_0 = Initial Current (Ampere) measured immediately after specific Voltage applied, L = Specimen Length (m), V = Applied Voltage (Volts) and A = Exposure Area (m^2).

In this study, electrical conductivity of microconcretes was measured according to NT Build 492, thus the parameter values for Equation 2 were set as follows:

I0 = The current measured immediately after we applied 30V at the beginning of the measurement (NT Build 492 procedure).
A = Exposure Area (0.00785 m^2)
L = Specimen Length
V = 30 V (Initial Voltage according NT Build 492)

Using the parameters we mentioned above for each specimen, the calculated conductivity is presented in Table 3. As shown in Figure 15, a high linear correlation between D_{nssm} and conductivity exists.

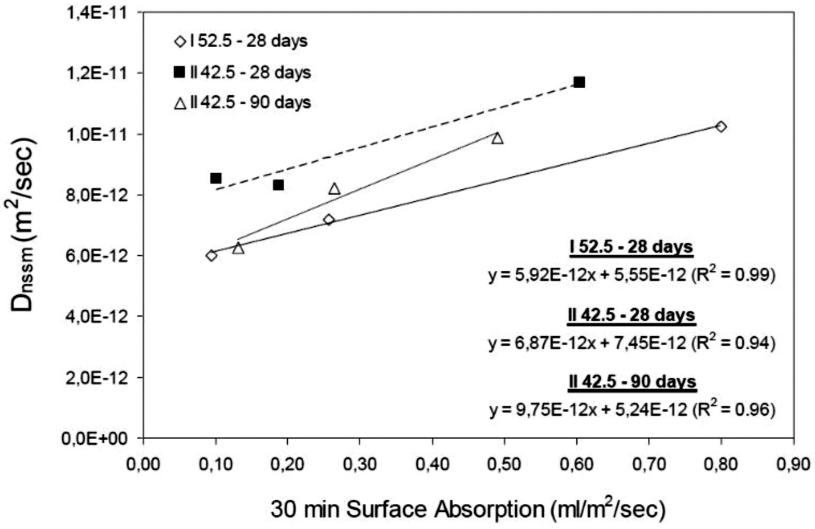

Figure 13. Correlation between D_{nssm} and 30 min Surface Absorption results.

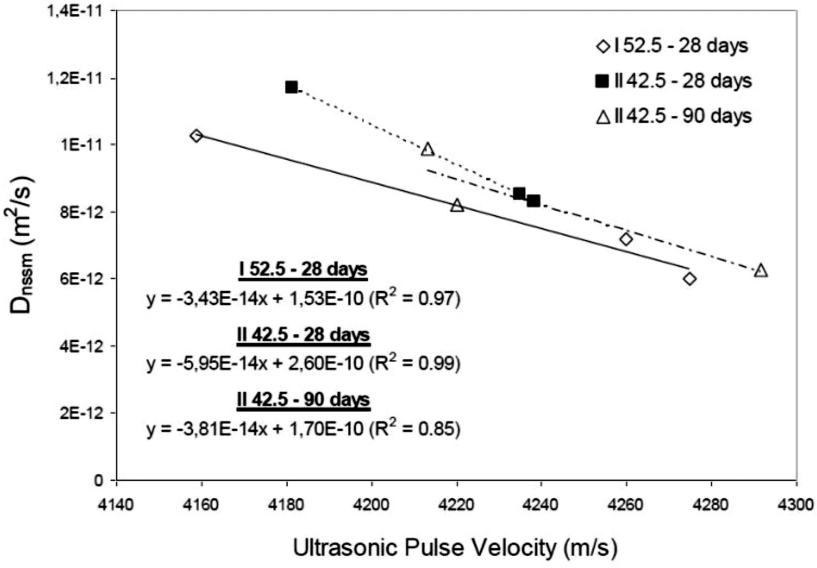

Figure 14. Correlation between D_{nssm} and Ultrasonic Pulse Velocity results.

3.8 *Correlation between D_{nssm}, age and non-destructive methods using Multiple Regression Analysis*

Using Multiple Regression Analysis, the non-steady state diffusion coefficient (D_{nssm}) can be predicted from the microconcrete age and the results of non-destructive methods (Equation 3):

D_{nssm} = X1*Age + X2*30min Surface Water Absorption + X3 *UPV + X4*Rebound Number + X5*Electrical Conductivity + X6

The values of coefficient X, t-test and p-value of each variable are presented in Table 4:

The linear regression between the measured and the predicted values for D_{nssm} from Eq.3 are shown in Figure 16.

The regression coefficient R^2 between measured and predicted D_{nssm} is equal to 0.99. From Table 4 and R^2 value we can conclude that D_{nssm} can be predicted with great precision from the results of non-destructive methods.

4 CONCLUSIONS

The effects of using CPF liners in microconcrete hydration were studied; the following conclusions can be made:

- The use of CPF liners results in significantly lower chloride permeability and carbonation of microconcrete surfaces, for both types of cement at all ages that were studied.
- From the results of Surface Water Absorption, Ultrasonic Pulse Velocity and Rebound Hammer measurements, which are non-destructive methods, we can conclude that the use of CPF dramatically decreases surface water absorption while increasing ultrasonic pulse velocity and surface hardness. These results occurred due to the lower w/c ratio that developed in the near surface layers (10–20 mm), which lowers surface's porosity and enhances cements paste stiffness and uniformity.

Table 3. Electrical conductivity of microconcretes.

Age	Specimen	Σ (S/m)
28	CEM I + Classic	0.0320
28	CEM I + MD	0.0325
28	CEM I + Formwork	0.0425
28	CEM II + Classic	0.0301
28	CEM II + MD	0.0294
28	CEM II + Formwork	0.0316
90	CEM II + Classic	0.0240
90	CEM II + MD	0.0227
90	CEM II + Formwork	0.0271

Table 4. Values of t-test, p-value and coefficients obtained from Multiple Regression Analysis.

	Coefficient X	t-test	P-value
Age	−3.01283E-14	−7.86086	0.004289
60 min Surface Water Absorption	3.14943E-12	3.315004	0.045223
UPV	−2.61885E-14	−7.18121	0.005564
Rebound Number	−2.61704E-13	−4.176	0.025008
Electrical Conductivity	−2.13178E-10	−8.64852	0.003252
Intercept	1.36625E-10	9.69168	0.002333

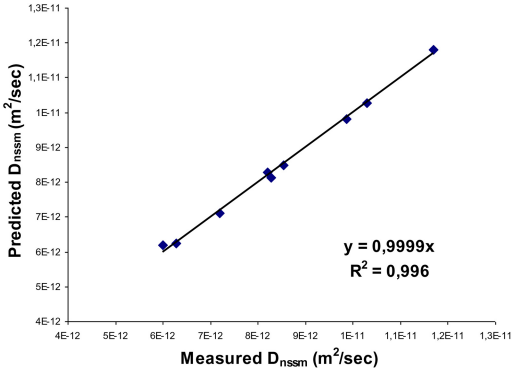

Figure 16. Correlation of predicted and measured D_{nssm}.

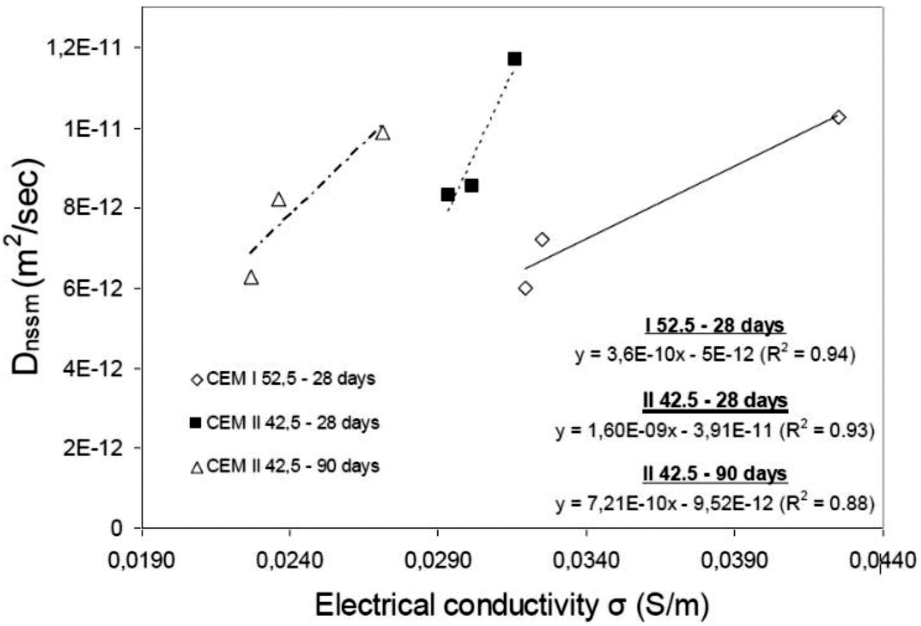

Figure 15. Correlation between D_{nssm} and Electrical Conductivity.

- In general we can say that the use of CPF liners develops a stronger and more durable surface than plain formwork. A more durable surface can lead to less repairs of the structure and an increased service life.
- Electrical conductivity and non-steady state diffusion coefficient show a high linear regression coefficient. Therefore, electrical conductivity of concrete can be used as an indicator of concrete chloride permeability.
- Comparison between experimental non-steady state diffusion coefficients and theoretical non-steady state diffusion coefficients which were obtained from multiple regression of non-destructive methods' experimental results shows a very high regression coefficient ($R2 = 0.99$). Therefore, we can predict the diffusion coefficient of concrete using non-destructive measurements, which can be conducted easily on existing structures.

REFERENCES

Cairns J. 1999. Enhancements in surface quality of concrete through use of controlled permeability formwork liners. *Magazine of Concrete Research*, 51, 73–86.

Duggan T. 1992. Enhancing Concrete Durability Using Controlled Permeability Formworks in 17th Conference on "Our World in Concrete and Structures", Singapore, August, 1992. pp. 57–62.

Ghosh P. 2011. Computation of diffusion coefficients and prediction of corrosion initiation in concrete structures, Doctorate Thesis, The University of Utah, Department of civil and Environmental Engineering (site: http://content.lib.utah.edu/utils/getfile/collection/etd3/id/449/filename/198.pdf, accessed 1st of April, 2016).

Klieger P., Lamond J.F. 1994. *Significance of tests and properties of concrete and concrete-making materials*. ASTM International.

Lizarazo-Marriaga J., Claisse P. 2009. Determination of the concrete chloride diffusion coefficient based on an electrochemical test and an optimization model. *Materials Chemistry and Physics,* 117, 536–543.

Lu X. 1997. Application of the Nernst-Einstein equation to concrete, *Cement and Concrete Research*, 27, 293–302.

Malhotra V.M., Carino N.J. 2004. *Handbook on nondestructive testing of concrete,* CRC Press.

McCarthy M.J., Giannakou A., Jones M.R. 2001. Specifying concrete for chloride environments using controlled permeability formwork, *Mat Struct*, 34, 566–576.

Philip M. 2005. Controlled permeability formwork, *Concrete,* 39, 28–31.

Price W., Widdows S. 1991. The effects of permeable formwork on the surface properties of concrete, *Magazine of Concrete Research,* 43, 93–104.

Reddi S. 1992. Permeable formwork for impermeable concrete, *The Indian Concrete Journal,* 66, 31–35.

Snyder K., Ferraris C., Martys N., Garboczi E. 2000. Using impedance spectroscopy to assess the viability of the rapid chloride test for determining concrete conductivity, *Journal of Research-National Institute of Standards and Technology,* 105, 497–510.

Sousa-Coutinho J. 2001. Effect of controlled permeability formwork (CPF) on white concrete. *ACI Materials Journal*, 98.

Sousa-Coutinho J. 1998. Melhoria da durabilidade dos betões por tratamento da cofragem, FEUP edições, Porto, Portugal.

Sousa-Coutinho J. 2003. The combined benefits of CPF and RHA in improving the durability of concrete structures, *Cement and Concrete Composites*, 255, 51–59.

Suryavanshi A.K., Swamy R.N. 1997. An evaluation of controlled permeability formwork for long-term durability of structural concrete elements. *Cement and Concrete Research,* 27, 1047–1060.

Whittington H., McCarter J., Forde M. 1981.The conduction of electricity through concrete. *Magazine of Concrete Research,* 33 48–60.

Wilson, D. 1994. Controlled permeability formwork (CPF), *Concrete*, pp 20–21.

Yildirim H., Ilica T., Sengul O. 2011. Effect of cement type on the resistance of concrete against chloride penetration, *Construction and Building Materials,* 25, 1282–1288.

Zhao T.J., Zhou Z.H., Zhu J.Q., Feng N.Q. 1998. An Alternating Test Method for Concrete Permeability, *Cement and Concrete Research*, 28, 7–12.



Taylor & Francis
Taylor & Francis Group
http://taylorandfrancis.com

Concrete Solutions – Grantham et al. (Eds.)
© 2016 Taylor & Francis Group, London, ISBN 978-1-138-03008-4

Durable surface repair of waterway engineering structures with sprayed textile reinforced concrete

C. Morales Cruz & M. Raupach
Institute of Building Materials Research (ibac) of the RWTH Aachen University, Germany

ABSTRACT: Many existing waterway structures are currently in need of maintenance and repair. The current surface repair methods include anchored, steel reinforced concrete or sprayed concrete procedures but are at least 90 mm thick due to the concrete cover. Alternatively, thinner, non- (steel) reinforced, non-anchored layers using sprayed polymer modified mortar or concrete can be used. However, a snap-through of the cracks into the protection layer and thus a reduction of the intended service life cannot be ruled out. Therefore, at the Institute of Building Materials Research (ibac) of the RWTH Aachen, DURTEX, a durable, water-impermeable and crack-spreading protective textile reinforced concrete layer was developed for the surface repair of waterway engineering structures. This paper introduces the proposed principle for the surface repair of waterway engineering structures with a low concrete compressive strength as well as a low surface strength, crack widths ranging from 0.1 to 3.0 mm and cyclically opening cracks and construction joints up to 0.5 mm. Furthermore the components of the developed DURTEX-protective layers within the framework of the transfer project T09 funded by the German Research Foundation (DFG) "Textile Reinforced Sprayed Mortar Layers for the Surface Repair of Waterway Engineering Structures" for the surface protection of the old concrete classes "A2" and "A3", without hydrostatic water pressure, with which a crack bridging up to 0.5 mm has been achieved are presented.

1 INTRODUCTION

Inspection results of hydraulic structures carried out by the Federal Office of Hydraulic Engineering (BAW), in Germany, show that many existing waterway structures are currently in need of maintenance and repair [Morales Cruz & Raupach, 2014]. In most cases, unreinforced tamped concrete hydraulic structures present cyclic opening movement joints and cracks [Orlowsky et al, 2011]. Additionally, older hydraulic structures also present low strength concrete substrates (<40 MPa). In 2004, a study on over 140 constructions and construction elements to identify a large range of concrete properties especially compressive strength and adhesive tensile strength was carried out [Maultzsch, 2004]. For example, on 35% of the examined concrete substrates the compressive strength constituted between 20 and 30 N/mm^2 whereas the adhesive tensile strength was between 1.2 and 1.4 N/mm^2 [Maultzsch, 2004]. Considering the upcoming repair measures and taking the different concrete properties of the existing waterway engineering structures into consideration, four "old concrete" classes were created (A1 – A4) in the German guideline ZTV-W LB 219, 2013 [ZTV, 2013]. These classes take the compressive and surface strength of the concrete substrates into account (see Table 1).

Table 1. Classification of the concrete substrates according to the ZTV-W LB 219 [ZTV, 2013].

Characteristic values	unit	Old concrete class			
		A1	A2	A3	A4
Compressive strength	N/mm^2	≤10	>10	>20	>30
Surface strength (arithmetic mean)		–	≥0.8	≥1.2	≥1.5
Surface strength (lowest single value)		–	≥0.5	≥0.8	≥1.0

The permissible methods for surface repair are limited. However, these include the use of concrete, polymer-modified mortars, sprayed mortars/concrete as well as various surface protection systems. The choices of concrete and sprayed mortar/concrete procedures both require steel reinforcement, anchorage and must be at least 90 mm thick [ZTV, 2013]. This leads to an increase in the component cross-section, which can be problematic for the repair of hydraulic structures such as floodgates and weir structures, where the inside space is often limited.

For the low strength old concrete classes A2-A4 (concrete strengths between 10 and 40 MPa), thinner (20–60 mm), non-reinforced and non-anchored layers are also allowed [ZTV, 2013]. However, there are currently only a few suitable solutions for the old concrete classes A2 and A3. Due to the characteristics of unreinforced sprayed mortar/concrete layers, the risk of

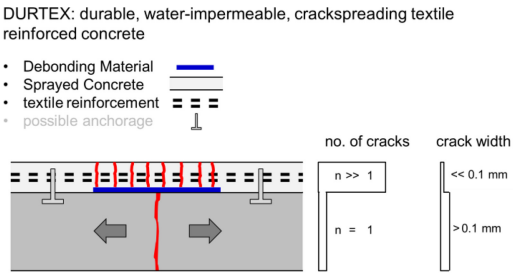

Figure 1. Schematic drawing of the textile reinforced concrete DURTEX-layer. The crack width and the number of cracks on the DURTEX-layer and supporting surface are presented – the thickness of the de-bonding are is exaggerated on purpose.

snap-through of cracks into the protection layer cannot be avoided. And therefore, reducing of the intended service life by failing to accomplish the goal ofsealing the cracks(width < 0.1 mm) to prevent water penetration, possibly resulting in spalling of the repair layer due to frost [Orlowsky & Raupach, 2012, Morales Cruz & Raupach, 2014].

For this purpose "DURTEX" was developed at the Institute of Building Materials Research (ibac) of RWTH Aachen, for the repair of concrete and steel concrete structures (see figure 1) [Morales Cruz & Raupach, 2014]. DURTEX is a textile reinforced protective layer whose strength and deformation is fitted to their respective substrate concretes. It distinguishes itself by its durable, water-impermeable and crack-spreading characteristics. "DURTEX" is an acronym for German words meaning "durable", "water-impermeable" "crack-spreading" and "textile reinforced concrete". It consists of several components: the sprayed on polymer modified concrete, the textile reinforcement, a delamination area and, if necessary, an anchorage [Morales Cruz & Raupach, 2015]. In a pilot application at Weir Horkheim the general suitability of DURTEX-layers was tested and in a subsequent project T09,a deeper analysis of the materials and composite system was carried out [Orlowsky et al, 2011], [Morales Cruz& Raupach, 2014c].

The goal of the recently finalized research projectT09 was to expand the existing systems surface maintenance of hydraulic structures, for the old concrete classes A2 and A3, via protective layers of textile reinforced, sprayed polymer modified concrete for a durable protection of low strength concretes by using thin layers with a cross section between 20 and 60 mm according to [ZTV, 2013]. Thereby the enhancement of serviceability is in superior focus to strengthening the system. A subdivision of the project was created for the event of hydrostatic water pressure (5 meter water column). However, this paper describes the results of the part of the project without hydrostatic water pressure.

In order to reduce the thickness of a concrete based reinforced protective layer, so-called technical textiles were used as reinforcement material. Technical textiles are biaxial fabrics made from AR-Glass-fiber or Carbon rovings and have mesh sizes from 5 to 38 mm. These textile reinforcements are essential components to achieve a fine crack distribution. These allow single cyclically opening cracks (>>1 mm) in the substrate are to be converted into multiple small cracks (<<0.1 mm), which leads to an extended sustainability of the maintenance repair [Orlowsky et al, 2011], [Büttner et al, 2013], [Morales Cruz & Raupach, 2014b] (see Figure 1).

In addition to the textile reinforcement, a so called de-bonding area must be created along the sides of the joint or crack in the supporting surface in order to achieve a fine crack distribution with sufficiently small crack widths. The de-bonded area creates a free expansion length in the protective layer. The number and width of the resulting cracks in the protective layer depends mostly on the type of textile reinforcement and the bonding behavior between the cement matrix and textile reinforcement. Since the de-bonded area is much smaller than the total bonded area, it can be assumed that the durability of the protective layer is not negatively influenced by any local delamination between the supporting surface and the protective layer. [Morales Cruz & Raupach, 2014]

2 MATERIALS

Within the framework of this project, a base cement compound with normal polymer content based on the weight of the cement for concrete categories A2 called StoCrete TS 126 and A3 called StoCrete TS 136 were developed for the dry sprayed process by the company StoCretec [Morales Cruz & Raupach, 2015]. A largest grain size of 6 mm was used to achieve the project-given thickness of 20 to 60 mm and to preferably produce a product with low shrinkage. Therefore the mesh size of the textile layers have to be adapted to the largest grain size of 6 mm to ensure a sufficient penetration of the reinforcement layers and to produce specimens without defects and so called "injection shadows".

In the course of this project, different textile structures were tested. Since the goal of this project was to find materials that would increase the durability of the surface repair and not strengthen a component, the focus was not set on finding textile reinforcements with the highest bearing capacity. In fact during the development of the technical textiles, amongst others, the focus was on adhesive behaviour in combination with the sprayed concrete [Morales Cruz & Raupach, 2014]. The greatest improvement of the composition between textile reinforcement and shotcrete was achieved by a surface modification consisting of a combination of hot curing epoxy resin (EP) and quartz sand (grain size 0.3–0.8 mm) after the end of the project (see Figure 2) [Morales Cruz & Raupach, 2015].

The de-bonding area is necessary to ensure a fine crack distribution while still maintaining the sealing effect. In comparison to the total area, the de-bonding

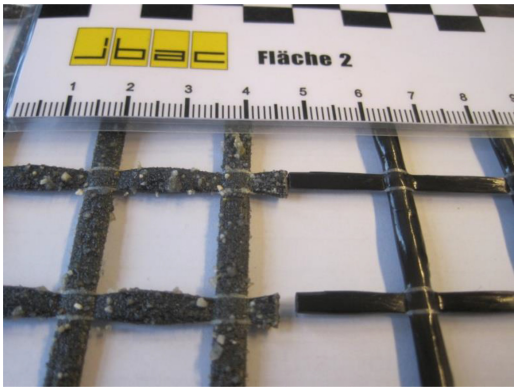

Figure 2. EP impregnated carbon structure Q90-CEP-21 from the company Solidian. Left: with a subsequent sand dusted hot curing epoxy-coat; right: untreated.

area is relatively small. There, the protective layer does not or only slightly adheres to the surface and so can elongate freely. The effect has been confirmed through crack-bridging tests [Orlowsky et al, 2011], [Büttner et al, 2013], [Morales Cruz & Raupach, 2014], [Morales Cruz & Raupach, 2014b], [Morales Cruz & Raupach, 2015]. Two materials for anti-adherence were favourably selected. One is an adhesive tape with an acrylate adhesive made by the Biolink company and a thickness of 1200 µm and the other is a crack bridging cement bound coating from StoCrete FB. The adhesive tape has the advantage that there is no waiting time necessary between the anti-adherence of the moving cracks and the application of the sprayed polymer modified concrete. However StoCrete FB is able to be applied on damp substrates.

3 TESTING

In order to evaluate the interaction between the sprayed concrete, textile reinforcement and substrate, lengthy studies on the composite system were performed. In additional to determining the adhesive strength, the crack-bridging ability of the textile reinforced protective layer was also examined. Therefore, two different experimental set-ups were required. Adhesive tensile tests for verifying the bonding behavior were conducted between substrate/sprayed concrete and sprayed concrete/textiles according to DIN EN 1542:1999 on drill cores with a 50 mm diameter.

To test the crack-spreading abilities of the composite system, uniaxial tensile tests were carried out on a crack bridging specimen as seen in Figure 3 in a so called “crack bridging test”. The length of the specimens is 700 mm and a width of 100 mm.

Starting from a cracked supporting system, i.e. the substrate concrete, a crack-bridging specimen was produced (see Figure 3).The substrate concrete of the crack bridging specimen is recreated by a concrete with low strength as well as a low adhesive strength

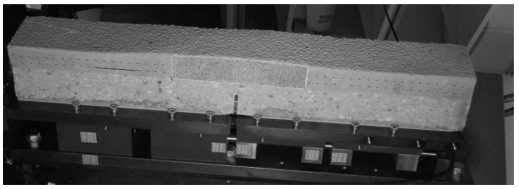

Figure 3. Crack-bridging specimen for examining the DURTEX-layers (laying down position) with display of the stochastic pattern on the testing surface.

according to Table 1. To provide a free elongated length, a de-bonded area with a 20 cm width along the crack of the supporting system was created with either an acrylic-adhesive with HDPE-film (Biolink) for dry and up to moist surfaces or a cement-based StoCrete FBcoat for moist or damp surfaces (see [Morales Cruz & Raupach, 2015]). Subsequently there is no adhesion between the textile reinforced concrete layers along the de-bonded area.

The crack bridging test was developed in [Orlowsky et al, 2011] with the purpose to enable a realistic reproduction of the crack movement on the construction. The latest test results and developments were introduced in [Büttner et al, 2013], [Morales Cruz & Raupach, 2014], [Morales Cruz & Raupach, 2014b], [Morales Cruz & Raupach, 2015]. The main goal of the crack-bridging experiment is the quantification of crack-distributing properties of the DURTEX-layer with a defined crack opening of the supporting surface. By converting the crack opening of the supporting surface into much smaller cracks in the protection layer (goal: w $\leq$0.1 mm), it is possible to achieve water tightness (in a technical sense) [Morales Cruz & Raupach, 2015]. Therefore it is very important to be able to identify the effectiveness of crack distribution of the DURTEX-layers. The temporal evolution of the cracks and their widths were observed with the optical 3D deformation measurement system ARAMIS® because cracks with widths of <0.1 mm are not clearly visible to the naked eye (see Figure 4) [Morales Cruz & Raupach, 2015]. The coordinate accuracy of ARAMIS®is at maximum 20 µm per meter [Morales Cruz & Raupach, 2014b]. More information about ARAMIS®, the requirements and preparation of the specimen are described in [Morales Cruz & Raupach, 2014b]. In addition to that, the description of the evaluation of the time-dependent crack development is to be found there.

In the framework of the project T09 and moreover, the present experimental setup regarding manageability and the necessary bending stiffness of the connection between specimen and testing machine was put to further development. In the current setup the testing of crack-bridging is at the side of the specimen (see Figure 5). The bottom side of the specimen is glued to plates of steel which lay on a rolling cage that serves as a friction bearing. This setup is again connected rigidly to the testing machine. The load application is realized via a massive angle bracket in

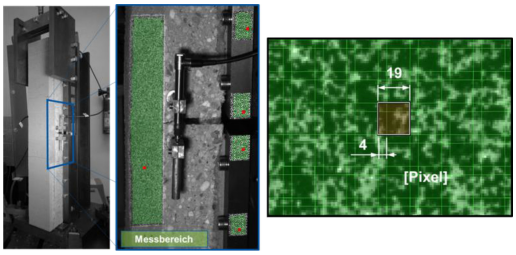

Figure 4. Crack-bridging specimen for examining textile reinforced sprayed concrete layers, with illustration of the measuring range.

the middle of the reinforced layer to provide a resistant environment to bending in the specimen during the tensile strength test. [Morales Cruz & Raupach, 2014b].

During testing the substrate crack is opened up to at least 0.5 mm with a rate of load application of 0.05 mm/min. The crack opening in the concrete is determined by inductive travel sensors on both sides of the specimen. [Morales Cruz & Raupach, 2014b] In the previous publications the measuring area was set on the surface of the smoothed down surface of the sprayed polymer modified concrete layer. The new measuring area is on the side of the crack-bridging specimen and is at least as long as the delamination area of the protective layer as shown in Figure 3 and 4. This lateral measurement of the cross-section of the protective layer provides for a significantly more accurate analysis of the crack pattern over the entire depth of the DURTEX protective layer. Additionally, the surface of the specimen does not have to be altered.

4 RESULTS

The best adhesive strength results for the A2 and A3 substrate and the corresponding sprayed polymer modified concretes S-A2 or S-A3 were achieved when using the sand dusted epoxy-coated carbon textiles Q90-CEP-21. For example, the failure of the composite specimen consisting of A2 substrate, the sprayed polymer modified concrete StoCrete TS 126 and the sanded reinforcement Q90-CEP-21 occurred at about 1.6 N/mm^2 always in the substrate (see Figure 6 left).

In order to determine the adhesion between the sprayed polymer modified concrete and textiles, the maximum breaking load was identified in an additional test consisting of only the TRC-Layer. This happened at an average load of 2.0 N/mm^2 in the sprayed concrete layer due to failure of cohesion (see Figure 6 right). Consequently the substrate concrete is the weak point of the composite specimen.

Extensive studies have proven that the crack-distributing ability of the protective layer is mostly influenced by the type of textile reinforcement, the cement matrix strength as well as by the de-bonding width as well from the bonding behavior of the textile

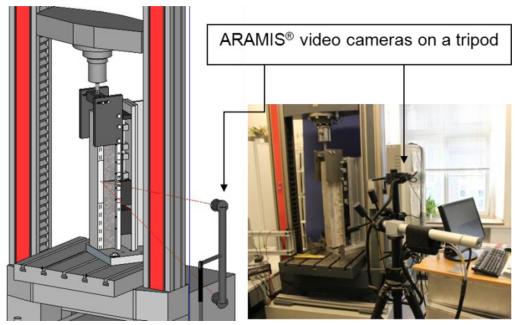

Figure 5. Test setup including the image recording and analysis ARAMIS® System.

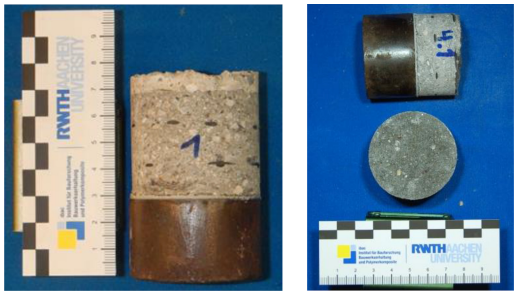

Figure 6. Fracture pattern of adhesive tensile strength test. Left: cohesion failure in the substrate; right: cohesion failure in the sprayed polymer modified concrete.

reinforcement and the cement matrix. The requirements on the crack distribution as well as the maximum crack widths from section 1were achieved for the A2 and A3 substrates with the Q90-CEP-21 sanded textile reinforcement. Figure 7 shows an exemplary analysis of the crack-bridging test done with ARAMIS®for a DURTEX protection developed during this project. The following materials were tested:

- two 2D layers of an EP impregnated with a subsequent sand dusted epoxy-coatcarbon textile reinforcement – Q90-CEP-21,
- a sprayed polymer-modified concrete mixture – StoCrete TS 126 (S-A2)
- and a 20 cm wide de-bonding acrylic-adhesive with HDPE-film (Biolink)

The evaluation of the crack-bridging ability of the developed DURTEX protective layer for an A2 substrate shows, for a crack opening of the substrate crack of 0.5 mm, a total of 11 cracks inside the 20 cm de-bonding area. The single crack widths above the substrate crack are shown in the left part of Figure 7. The average crack width is 0.05 mm. All crack widths are significantly smaller than the target of 0.1 mm. The location of the cracks alongside the main direction of deformation (x-axis) as well as the chronological formation is seen in the right part of figure 7.

With the exception of the sprayed polymer modified concrete an equally successful material combination

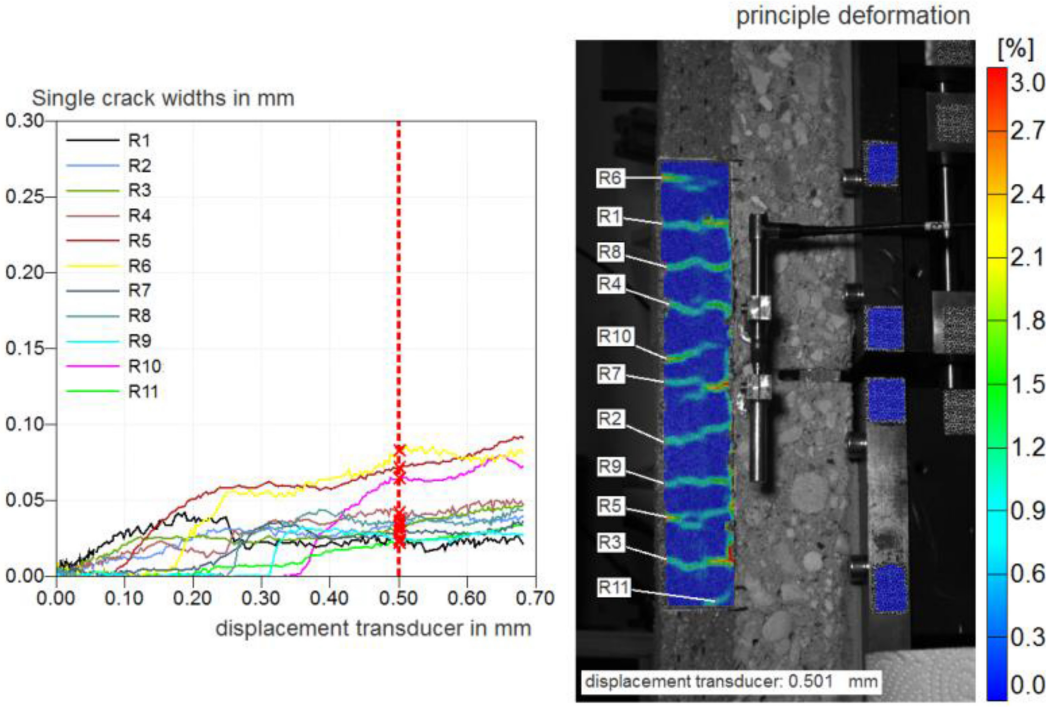

Figure 7. Analysis of the crack-bridging test with ARAMIS®, substrate: A2, textile reinforcement: Q90-CEP-21 sanded, sprayed polymer modified concrete: StoCrete TS 126, de-bonding material: Biolink 20 cm. Top left: individual cracks over the crack opening of the concrete body; bottom left: sum of the cracks in the protective layer over the crack opening of the concrete body; right: visualization of individual cracks in the measuring field.

was tested for an A3 subtract. In this case the sprayed polymer modified concrete StoCrete TS 136 was used.

The crack width opening of 0.5 mm of the substrate which was selected and examined during the transfer project is on the safe side. This is supported by the deformation measurements in [Orlowsky et al, 2011, Morales Cruz & Raupach, 2014c] from the BAW and ibac of a pillar of the hydraulic structure (Weir Horkheim), which faced natural weathering conditions for more than two and a half years. In this case a maximum crack opening of the substrate of 0.28 mm was measured. Furthermore, the reports for e.g. in Figure 7, show that even with a crack width opening of 0.7 mm of the substrate the associated crack widths on the DURTEX-layer smaller than 0.1 mm were achieved.

Table 2. Proposed material combination for the surface repair of the old concrete classes A2 and A3 with a crack width opening of 0.5 mm.

		Old concrete class	
Components		A2	A3
De-bonding Material	dry	acrylic-adhesive with HDPE-film, 20 cm wide	
	damp	StoCrete FB, 20 cm wide	
Textile Reinforcement		Q90-CEP-21, subsequent sand dusted epoxy-coat	
Dry sprayed polymer modified concrete		StoCrete TS 126	StoCrete TS 136

5 CONCLUSIONS

As part of the recently concluded transfer project T09, solutions for both low strength A2 and A3 substrates of hydraulic structures with a crack with opening of the substrate of up to 0.5 mm were developed. These, however, only apply if no hydrostatic water pressure is present.

The proposed materials according to the substrate class are given in Table 2.

As part of a more advanced task, the influence of the crack-bridging properties of the DURTEX-layer under cyclic load is currently being investigated. Additionally the possibility of a self-healing of the cracks is being investigated

REFERENCES

BAW Merkblatt 2012, Spritzmörtel/Spritzbeton nach ZTV-W LB 219, Abschnitt 5.

Büttner, T. & Morales Cruz, C. & Raupach, M. 2013.Dauerhafte Schutzschichten aus Textilbeton für Bauwerksoberflächen im Wasserbau. *Bautechnik,* Volume 90, Issue 8, pages 485–490.

Maultzsch, M.: Dünnschichtige Spritzmörtel – Materialien für geringer feste Untergründe. Karlsruhe, Hamburg, Ilmenau: Bundesanstalt für Wasserbau, BAW, 2004. – In: BAW-Kolloquium der Abteilung Bautechnik, Instandsetzen von Wasserbauwerken ZTV-W LB 219 (2004), Hannover, 17. Oktober 2004, S. 41–46.

Morales Cruz, C. & Raupach, M. 2014. Textile Reinforced Sprayed Mortar for the Repair of Hydraulic Engineering Structures. In: Structural Faults and Repair, Issue 2014.

Morales Cruz, C. & Raupach, M. 2014b. Untersuchungen zur kontrollierten Rissverteilung textilbewehrter Schutzschichten.Studies for a Controlled Crack Distribution on Textile Reinforced Protective Layers with an Optical 3D Deformation Analysis System. In:*Restoration of Building and Monuments*, Issue 20, Nr. 6, pages 405–412.

Morales Cruz, C. & Raupach, M. & Westendarp, A. & Bruder, S. 2014c. Untersuchungen an einer vier Jahre alten Schutzschicht aus textilbewehrtem Spritzbeton am Wehr Horkheim. *Beton 64,* Nr. 10, pages 390–395.

Morales Cruz, C. & Raupach, M. 2015. Sprayed Textile Reinforced Concrete Layers for a Durable Protection of Waterway Engineering Structures. ICCRRR 2015.

Orlowsky, J. & Raupach, M. & Westendarp, A. 2011. Textilbewehrte Spritzmörtel zur Instandsetzung von Wasserbauwerke. *Beton 61*, Nr. 12:pages 486–490.

Orlowsky, J. & Raupach, M. 2012. Textile reinforced sprayed mortar for the repair of hydraulic engineering structures. Concrete Repair, Rehabilitation and Retrofitting III, pages 1065–1070.

ZTV-W LB 219, 2013. Zusätzliche Technische Vertragsbedingungen – Wasserbau für Schutz und Instandsetzung der Betonbauteile von Wasserbauwerken.

Sustainable repair



Taylor & Francis
Taylor & Francis Group
http://taylorandfrancis.com

Concrete Solutions – Grantham et al. (Eds.)
© 2016 Taylor & Francis Group, London, ISBN 978-1-138-03008-4

An engineering example of energy saving renovation of external wall of original building with lightweight insulation composite panel

Yunxing Shi, Yangang Zhang, Jingbin Shi, Shaolin Yang & Wei Liu
Technical Centre, China State Construction Engineering Corporation, Beijing, China

ABSTRACT: This paper presents an engineering application of lightweight insulation composite panel in energy saving renovation of two original buildings. The composite panels were made of Reinforced Concrete (RC) and ceramsite cellular concrete (CCC – a type of lightweight aggregate concrete) with integrative method, namely CCC was poured following closely the placing finish of Normal Concrete (NC), the interface of the two layers integrated into a whole as concrete hardening. The RC layer was for load bearing, and the CCC layer for thermal insulation. A satisfactory insulation effect was fulfilled in the building by using the composite panel as external wall, and indoor environment became more comfortable and suitable for people to live in.

In this paper, the manufacture process and properties of the composite panel, mounting construction process and main joints of the structure, etc., are introduced.

1 INTRODUCTION

Energy saving of buildings has been regarded as an important issue in China, because of a serious challenge from an enormous population and a low per capita energy resource level. Energy saving of building envelopes by adoption of effective thermal insulation materials and structure optimization of the walls are currently technical measures at present in China.

The lightweight insulation composite panel for external walls, developed by the Technical Center of CSCEC, is an energy saving product for building envelopes. It has been certificated with China Invention Patent (Number CHINA: ZL201210489 490.7). The panel, as a novel material of external walls, was characterized by its function of thermal insulation together with the effect of decoration, in other words, in addition to thermal insulation of CCC layer, its outside was formed into an architectural concrete.

Two original wing buildings of the Technical Center of CSCEC next to the main building were built in 2002, and they were both RC frame structures with architectural concrete external mounting pane. The appearance of the existing western wing building, one of the two buildings to be renovated, is shown in Fig. 1.

In the two original wing buildings, inside the panel there was a layer of rock wool felt about 5 cm mounted as a thermal insulation material. However, after use for many years, the structures became obsolete. At beginning of reconstruction, as the external wall panels were removed, it was apparent that the layer of rock wool had deteriorated and actually, its thermal insulation effect had been lost to a great extent. As shown in Fig. 2.



Figure 1. Existing western wing building.



Figure 2. Layer of deteriorated rock wool.



Figure 3. Partial keel steel system.

A design of the solution scheme for the renovation of the building envelope was by using the lightweight insulation composite panel as an external wall, to realize effects of both thermal insulation and external elevation decoration.

2 STRUCTURE OF THE PANEL AND BRACING SYSTEM

In accordance with the renovation design, the existing RC frame structure would be strengthened as the new main structure, but the envelope will be completely reformed with the composite panel.

Against the new main structure there was an external keel steel erection system, on which self-heat insulation composite panel was to be mounted instead of the RC panel and layer of rock wool layer used in the original building. The appearance of the partial keel steel system installed is shown in Fig. 3.

The structure of the composite panel is shown in Fig. 4. Total thickness of the panel was 110 mm, which was constituted of reinforced concrete (RC) and ceramsite cellular concrete (CCC), the thickness of former and latter was 50 mm and 60 mm respectively. Steel bars of diameter Φ8 mm used as reinforcement was embed in the NC layer. The metal connectors marked MJ1 was preset, and also in the normal concrete (NC) layer, as shown in Fig. 4.

RC layer was for load bearing, and CCC layer for heat-insulation.

3 MANUFACTURE OF COMPOSITE PANEL AND ITS PROPERTIES

The design strength grade of the normal concrete was C30, and the compressive strength design of the CCC was 5MPa, with a bulk density of 650 kg/m^3.

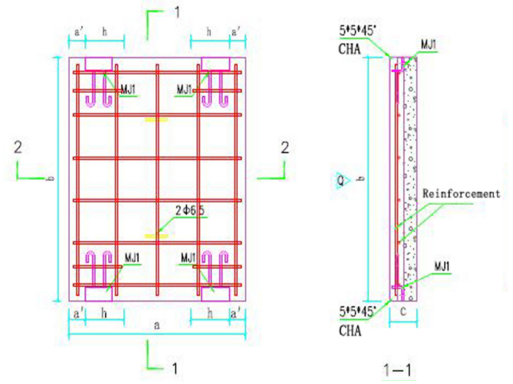

Figure 4. Structure of the composite panel.

Table 1. Mix proportion of CCC (kg/m^3).

Cement	310
Fly ash	50
Ceramsite* bulk volume (m^3)	0.4
Foam volume (m^3)**	0.55
Water	109
Superplasticizer	2.5

*Light weight expanded clay aggregate by sintering;
**There were some losses of foam volume with mixing

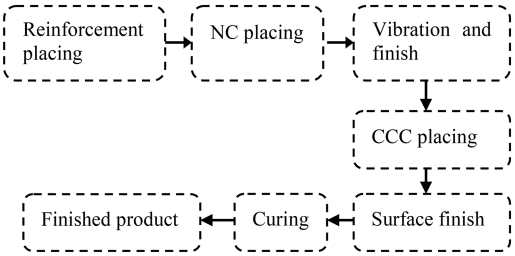

Figure 5. Main manufacture process of the composite panel.

The mix proportions of the CCC are shown in Table 1, and the composite panels were manufactured following the main technical process as shown in Fig. 5. In the manufacture process, CCC was placed closely following by pouring a finish of NC, then with hardening, the two types of concretes at the interface became an integral. The cross section of the panel and micro-structure of the CCC are shown in Fig. 6.

From the appearance of CCC shown in Fig. 6, an enormous quantity of small closed pores in uniform distribution including that in both a ceramsite and cellular matrix are visible: it is these closed pores that gave the panel a good thermal insulation.

The heat transfer coefficients in table 2 were practical measured data, which were comprehensive effects of RC and CCC layer theoretically.

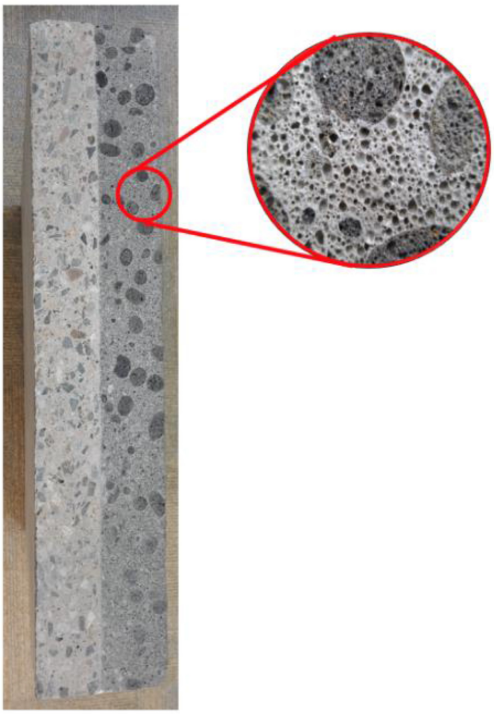

Figure 6. Cross section of the composite.

Table 2. Heat transfer coefficient of the composite panel.

Thickness of RC (mm)	Thickness of CCC (mm)	Heat transfer coefficient ($W/m^2 \cdot k$)
50	60	1.18
60	100	1.0
60	150	0.737

4 MOUNTING CONSTRUCTION

The main keels system was made of square steel with cross section of 80 mm × 40 mm × 5 mm, and angle steel with cross section of 60 mm × 60 mm × 5 mm for sub-keels. Joints of the main and sub-keels were connected by a welding process, and all welding points were given a rust-proofing with anti-corrosive paint. The situation of composite panels installing on the keels is shown in Fig. 7.

For the panel to be fixed accurately, preliminarily, the panel was attached on the keels, then checking each of the items were conducted according to requirements listed in Table 3, as shown in Fig. 8.

The location of the panel being attached to the keels might have minor adjustments before being fixed completely, if necessary.

Table 3. Allowable deviation.

Items	Allowable deviation (mm)	Check method
Joint width between panels	±2	Check with steel ruler
Straightness of full-length joint	2	Drawing a wire line
Height difference at joint	1	With guiding rule and running rule
Total verticality	0.5 H/1000	With theodolite
Planeness of wall	2	With guiding rule and running rule



Figure 7. Composite panel installation.



Figure 8. Planeness adjustment.



Figure 9. Western wing building just completed.

5 THE RESULTS OF THE ENGINEERING CONSTRUCTION AND CONCLUSIONS

The energy saving renovation of two wing buildings was well completed after construction for one year and the total area of composite panel mounted was over 7000 m^2. The appearance of the western wing building just completed is shown in Fig. 9.

The engineering practice showed that the building envelope formed by utilizing the composite panel made of RC and CCC was a comprehensive solution to energy saving of the building envelope, which achieved both good effect of energy saving and decoration, and, in addition, improved the efficiency of construction as well.

REFERENCES

Shi, Y., Song, Z., Zhang, Y., et al, A new type of integrative composite panel with energy saving and decoration, Cina Invention Patent (Number China: ZL201210489490.7) 2012 (in Chinese).

Wang, Q., Shi, Y., et al, A testing and analysis on thermal performance of ceramsite celluar concrete block wall, New Building Materials, 2014(12) (in Chinese).

Zhang, Y., Shi, Y., Li, J., et al, Mounting technology of composite external wall panels with light weight concrete, Construction Technology, 2015(5) (in Chinese)

Concrete Solutions – Grantham et al. (Eds.)
© 2016 Taylor & Francis Group, London, ISBN 978-1-138-03008-4

Production of durable concretes using EAF slag aggregates

K.K. Sideris, A. Chatzopoulos & Ch. Tassos
Democritus University of Thrace, Xanthi, Greece

ABSTRACT: Electric Arc Furnace slag (EAF) is a by-product of the steel making industry. In this research EAF fine (0–5 mm) aggregates were used for the production of C25/30 and C30/37 concrete mixtures. EAF slag aggregates replaced ordinary limestone crushed sand at percentages of 10%, 20%, 30%, 50%, 75% and 100% by volume. The hardened properties measured were the compressive strength at different ages as well as their resistance against carbonation, freeze thaw attack and chloride ingress. The preliminary results of this study revealed the fact that fine EAF slag may be replace part of the total volume of limestone sand without compromising the strength or the durability of the so produced concretes. On the contrary durability of EAF slag concretes was increased up to 30% as compared with reference limestone concretes.

1 INTRODUCTION

Steel production is performed in Basic Oxygen Furnaces (BOF) and in Electric Arc Furnaces (EAF). Electric arc furnaces are used for more than 40% of the world steel production as, due to their lower cost, more and more steel industries are adopting their use.

Furthermore, because of the ability of steel production to recycle scrap, the use of EAF contributes to sustainable construction. The slag produced by Electric Furnaces (EFS) is the main industrial by-product of steel production and the quantity produced in Europe is estimated at around 20 million tons annually (Pelegrino et al 2013).

The possibility to use electric furnace slag in concrete has been the subject of many pieces of research. Pelegrino et al (2013) prepared concretes where the EFS used as an aggregate (sand and coarse aggregate). The researchers found that replacing conventional coarse aggregates with EFS coarse aggregate is possible without causing a reduction in the compressive strength of concrete. On the other hand, they observed that in the case of exclusive use, sand from EFS caused at least a 7% reduction of 28day strength. For this purpose they suggest replacing conventional sand with EFS sand in smaller percentages.

Polanco et al (2011) studied the properties of the concrete prepared by EFS fine and coarse aggregates. The researchers found that both the mechanical and resistance properties measured were satisfactory for concretes with EFS aggregates.

Pellegrino & Caldo (2009) concluded that EFS fine (2–4 mm) aggregates can replace conventional aggregates without adverse effect on long-term properties of the concrete on condition that the EFS will have previously been exposed to air for long periods in order to be stabilized.

Manso et al (2004) prepared six concretes produced using EFS as coarse aggregate and/or fines. The EAF slag had previously been exposed to the air for several weeks. The researchers concluded that concretes prepared with EAF slag aggregates developed a compressive strength similar to conventional mixtures and slightly lower durability characteristics.

In contrast, Maslehuddin et al (2003) concluded that the durability of concrete produced exclusively with EFS aggregates was superior to that of concrete produced with crushed limestone aggregates. But, since the specific weight of the concrete was increased, they suggest replacing conventional aggregates with EFS at 50% for both sand and coarse aggregates.

The same conclusion regarding the increased resilience of the mixtures produced by complete replacement of aggregates with EFS was reached by Arriba et al (2014). These researchers, however noted that the resistance of the mixtures against chloride penetration was increased and the likelihood of corrosion of the reinforcement was reduced to the concrete produced with EFS aggregates compared with the conventional mix.

The EFS has been used successfully in Greece for preparing special concretes (Anastasiou 2009, Papachristoforou 2013). These mixtures showed very good characteristics. The use of EFS as aggregates in concrete is safe to the environment: Papayianni & Anastasiou (2003, 2011) concluded that the amount of heavy metals emitted by concrete prepared with EFS aggregates is lower than the quantities specified in Directive 80/778/EEC (1980).

In this paper, the possibility of preparing conventional concrete C25/30 and C30/37 with partial and total replacement of conventional limestone sand with electric furnace slag sand is experimentally investigated.

Table 1. Chemical analysis of cements and slag.

	CEM II 32.5N	CEM II 42.5R	EFS
SiO_2	28	23.85	10.89
AI_2O_3	9	5.22	7.71
Fe_2O_3	5.5	4.13	29.19
CaO	48	58.2	33.52
MgO	2.2	3.2	4.03
SO_3	3.2	3.3	–
K_2O	1.5	0.68	0.03
Na_2O	0.5	0.32	0.1
TiO_2	–	0.24	0.43
P_2O_5	–	0.06	–
SrO	–	0.03	–
Cr_2O_3	–	0.02	0.34
ZnO	–	0.01	–
MnO	–	–	4.77
Specific weight	3.15	3.1	3.35

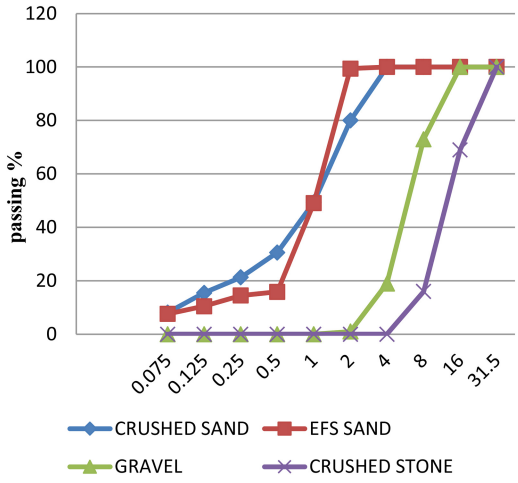

Figure 1. Grading curve of the aggregate.

2 EXPERIMENTAL PROGRAMME

Fourteen different conventional concrete mixtures were produced. The mixtures belonged to strength classes C25/30 and C30/37, according to EN206-1 Standard (2000). All mixtures were prepared using the same cement types CEM II A-M/32.5N and CEM II A-M/42.5R. The coarse aggregate consisted of crushed granite with a maximum size of 32mm. The fine aggregate used was crushed limestone sand. The electric furnace slag was used as an alternative material, replacing the fine aggregates in six mixtures for each class of strength by 10%, 20%, 30% 50%, 75% and 100% per volume. Superplasticizer was added at different dosages in order to achieve the desired workability.

The chemical analysis of the cement and EFS used appear in Table 1.

The gravel (2–16 mm) and chippings (8–32 mm) used, came from natural rock crushing into the crusher. In some mixtures, the limestone sand was replaced by electric furnace slag sand (0–4 mm).

The gradation of limestone sand, EFS sand, gravel and crushed stone are presented in Figure 1.

The proportions and the properties of fresh mixtures are shown for all concretes prepared in Tables 2 and 3.

The specimens prepared were 150 mm edge cubes, 100 mm edge cubes and cylinders 60 × 100 mm and 100 × 200 mm. All samples were stored for 28 days in the maintenance chamber (T = 20°C, RH > 98%). The cubes of 150 mm were used to measure the compressive strength at different ages. The cubes of 100 mm were used for testing the freeze-thaw resistance. Once cut in half, placed in a solution of 3% NaCl and subjected to 15 freeze-thaw cycles (24 hours freezing at −14°C and 24 hours at +20°C). Resistance to carbonation was measured on cylindrical specimens 60 × 100 mm. These small cylinders were initially maintained for 3 days in the maintenance chamber and then placed in a laboratory environment (relative humidity = 50–60%, and temperature = 20 ± 2°C). At the age of 28 days they were transferred to an accelerated carbonating chamber (T = 20°C, relative humidity = 55%, CO_2 = 1%). The specimens remained in this chamber for 60 days.

The resistance to chloride penetration of concrete was measured on cylindrical specimens with 100 mm diameter and 50 mm in height formed from 100 × 200 mm cylinders. These specimens were maintained as above until the age of 28 days. Then estimated the apparent chloride diffusion coefficient in accordance with the procedure described in the NT Build 492 model (Figure 2).

Table 2. Mix design and characteristics of the C25/30 strength class concretes.

Mix design	Ref	10% EFS	20% EFS	30% EFS	50% EFS	75% EFS	100% EFS
kg/m³	M1	M2–10	M3–20	M4–30	M5–50	M6–75	M7–100
CEM II 32.5	300	300	300	300	300	300	300
CEM II 42.5	50	50	50	50	50	50	50
Gravel	270	270	270	270	270	270	270
Crush Stone	630	630	630	630	630	630	630
Crush Sand	900	810	720	630	450	270	0
EFS Sand	0	108	216	324	539	809	1079
Water	180	180	180	180	180	180	180
Sup/zer	1.42	1.08	1.83	1.92	2.00	1.83	1.87
W/C	0.51	0.51	0.51	0.51	0.51	0.51	0.51
Slump (cm)	20	19	19.5	17.5	18	19	17.5
Air Cont. (%)	2.5	2.3	3.0	2.4	2.4	2.2	2.1

Table 3. Mix design and characteristics of the C30/37 strength class concretes.

Mix design	Ref	10% EFS	20% EFS	30% EFS	50% EFS	75% EFS	100% EFS
kg/m^3	M8	M9 10	M10 20	M11 30	M12 50	M13 75	M14 100
CEM II 32.5	150	150	150	150	150	150	150
CEM II 42.5	200	200	200	200	200	200	200
Gravel	270	270	270	270	270	270	270
Crush Stone	630	630	630	630	630	630	630
Crush Sand	900	810	720	630	450	225	0
EFS Sand	0	108	216	324	539	809	1079
Water	180	180	180	180	180	180	180
Sup/zer	1.67	1.37	1.75	2.08	1.83	2.00	2.00
W/C	0.51	0.51	0.51	0.51	0.51	0.51	0.51
Slump (mm)	19	18.5	18.5	17.5	18	18	18
Air Cont. (%)	2.2	2.3	2.8	2.2	2.2	2.1	2.2

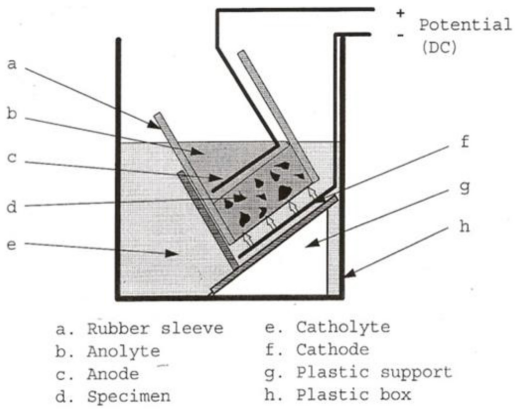

Figure 2. Test device used to calculate the chloride diffusion coefficient De. (NT Build 492, 1999).

Table 4. Compressive strength of C25/30 mixtures.

(MPa)	M1	M2–10	M3–20	M4–30	M5–50	M6–75	M7–100
fc_2	25.2	21.0	22.7	22.8	22.8	23.3	26.8
fc_7	30.1	31.0	29.9	30.9	32.5	33.1	36.9
fc_{28}	39.1	40.2	41.0	45.0	43.9	46.3	46.8
fc_{90}	44.6	45.5	46.4	51.3	50.5	53.0	53.5

Table 5. Compressive strength of C30/37 mixtures.

MPa	M8	M9–10	M10–20	M11–30	M12–50	M13–75	M14–100
fc_2	28.7	25.0	24.9	25.5	24.4	24.9	26.4
fc_7	30.2	32.9	32.6	39.7	34.8	35.1	36.7
fc_{28}	46.4	45.6	46.8	51.8	46.8	49.2	49.5
fc_{90}	50.3	49.0	50.4	58.5	52.1	53.0	54.5

Table 6. Carbonation depth of C25/30 mixtures.

(mm)	M1	M2–10	M3–20	M4–30	M5–50	M6–75	M7–100
Accelerated	8.3	8	6.2	5.2	7.8	7.8	5.3

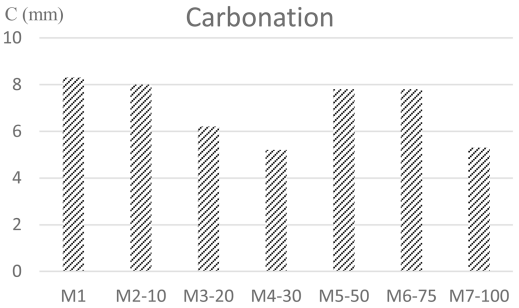

Figure 3. Carbonation depth of C25/30 mixtures.

From the values of the above tables, it appears that the use of EAF slag as fine aggregate causes a reduction in compressive strength at two days, regardless of the rate used to replace the limestone sand. This condition seemed to change at later ages. So at the age of 28 days, mixtures in which EFS has been used as a partial or total replacement of limestone sand at 10–100% in concrete C25/30 (M2–10 to M7–100) and 20–100% in concrete C30/37 (M9 to M14) showed a higher strength than the reference concrete by 20% (M7–100). In fact it seems that in both strength categories, the maximum strength occurs in mixtures where limestone sand was replaced by the EFS sand at 30% and 100% percentages. The increased compressive strength relative to the reference mixture is continued at the age of 90 days for all mixtures of C25/30 and most of the C30/37 mixtures.

3 EXPERIMENTAL RESULTS AND DISCUSSION

3.1 *Compressive strength*

The compressive strength was measured for all mixtures at the ages of 2, 7, 28 and 90 days. These values are presented in Tables 4 and 5.

3.2 *Carbonation depth*

The carbonation depth was measured by spraying the freshly broken surface of the samples with phenolphthalein in accordance with the procedure described in the EN 14630 standard. The carbonation depth of all mixtures is presented in Tables 6 and 7 and Figures 3 and 4.

Table 7. Carbonation depth of C30/37 mixtures.

(mm)	M8	M9 10	M10 20	M11 30	M12 50	M13 75	M14 100
Acc/ted	5.3	5.2	4.4	3.9	5.1	4.8	4.1

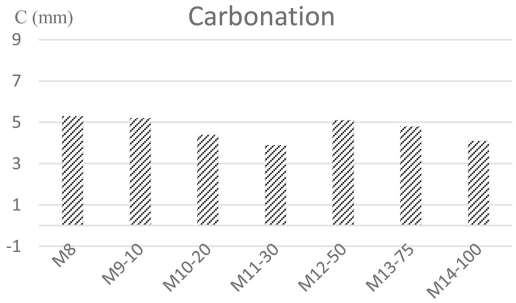



Figure 4. Carbonation depth of C30/37 mixtures.

These figures show the positive effect of the replacement of limestone sand with EAF sand in mixtures. The carbonation depth of all mixtures remains constant (M2–10, M5–50, M9–10, M12–50) or decreased by up to 37%. (M4–30). In both strength classes the largest decrease was noticed at the 30% and 100% replacement rate.

3.3 *Diffusion coefficient of chlorides*

The values of chloride diffusion coefficient De that measured according to NT Build 492 Standard presented for all mixtures in Tables 8 and 9.

The chloride penetration rate is reduced in all the mixtures which were prepared by using EAF aggregates. It is noteworthy also the fact that in mixtures M2–10, M3–20, M4–30 and M7–100 coefficient De was lower than the value of the M8 concrete which

Table 8. Diffusion coefficient of chloride De ($\times 10^{-12}$ m^2/s) of C25/30 mixtures.

$\times 10^{-12}$ m^2/s	M1	M2–10	M3–20	M4–30	M5–50	M6–75	M7–100
De	14.3	11.3	10.9	11.9	12.9	14.0	12.0

Table 9. Diffusion coefficient of chloride De ($\times 10^{-12}$ m^2/s) of C30/37 mixtures.

$\times 10^{-12}$ m^2/s	M8	M9 10	M10 20	M11 30	M12 50	M13 75	M14 100
De	12.5	11.3	9.5	9.8	11.9	11.4	10.2

Table 10. Percentage weight loss of C25/30 mixtures.

	M1	M2–10	M3–20	M4–30	M5–50	M6–75	M7–100
% mass loss	28.0	24.7	22.4	20.0	21.8	18.6	18.2

Table 11. Percentage weight loss of C30/37 mixtures.

	M8	M9 10	M10 20	M11 30	M12 50	M13 75	M14 100
% mass loss	18.0	16.8	16.2	10.9	15.7	15.0	13.2

belongs to the higher strength class. The lowest De values were measured in mixtures M3–20, M4–30, M10–20 and M11–30 where EAF slag replaced crushed limestone sand in 20% and 30% replacement rate.

3.4 *Freezing-Thawing*

The mass loss percentage of the test specimens after 15 daily freeze-thaw cycles for all concretes are presented in Tables 10 and 11.

The mass loss of specimens produced with EAF slag was improved in both strength classes and for all replacement rates. However the weight loss was more reduced in mixtures M6–75, M7–100, M14–100 and M11–30. This improvement was found to be equal to 33.6%, 35%, 26.7% and 39.4% respectively for the above mentioned concretes.

4 CONCLUSIONS

Replacing limestone sand by recycled electric arc furnace slag resulted in the preparation of concrete with slightly increased strength at the age of 28 and 90 days.



Figure 5. Comparison of M1 (left) and M7-100 (right) specimens after 15 freeze-thaw cycles.

Mixtures with EAF sand developed at least the same behavior with reference mixtures regarding durability indicators tested in this research. Resistance against carbonation, resistance against chloride penetration and resistance to freeze-thaw cycles were all found to be improved in all mixtures with recycled aggregates in both tested strength classes.

The optimum rate of replacement of the limestone sand by EAF sand appears to be 30%. The mixtures obtained showed increased compressive strength and improved durability characteristics up to 37% compared with the reference mixtures of the same strength class.

It may be concluded therefore that EAF slag sand may be used to replace limestone crushed sand at replacement levels up to 50% by volume without compromising the strength or the durability of the produced concretes.

Further research is underway to investigate the long-term behavior of mixtures with recycled aggregates and estimate accurately the benefits-environmental and economic- from the use of EFS aggregates as a replacement of conventional aggregates.

ACKNOWLEDGMENTS

EAF steel aggregates, cement and chemical admixtures used in this study were provided by AEIFOROS SA, TITAN Cement Industry and Sika Hellas S.A. respectively. Their support is greatly acknowledged.

REFERENCES

Anastasiou, E. 2009. Utilization of steel slags and lignite fly ashes in the production of concrete for special aplications. PhD thesis. Department of Civil Engineering AUTH.

Arribas, I., Vegas, I., San-Jose, J.T. & Manso, J.M. 2014. Durability studies on steelmaking concretes. Materials and Design 63: 168–176.

Manso, J. M., González, J. J. & Polanco, J. A. 2004. Electric Arc Furnace in Concrete. Journal of Materials in Civil Engineering 16(6): 639–645.

Maslehuddin, M., Sharif, A. M., Shameem, M., Ibrahim, M. & Barry, M. S. 2003. Comparison of Properties of Steel Slag and Crushed Limestone Aggregate Concretes. Construction and Building Materials 17(2): 105–112.

Papachristoforou, M. 2013. Development of concrete with EAF steel slag aggregates for shielding against radiation and high temperatures exposure. PhD thesis. Department of Civil Engineering AUTH.

Papayianni, I. & Anastasiou, E. 2003. Concrete incorporating high volumes of industrial by-products. In R.K. Dhir, M.D. Newlands & K.A. Paine (eds.), Role of Concrete in Sustainable Development, Proceedings of the International Conference on Celebrating Concrete: People and Practice: 595–604. Dundee.

Papayianni, I. & Anastasiou, E. 2011. Concrete incorporating high calcium fly ash and EAF slag aggregates. Magazine of Concrete Research 63(8): 597–604.

Pellegrino, C., Cavagnis, P., Faleschini, F. & Brunelli, K. 2013. Properties of concretes with Black/Oxidizing Electric Arc Furnace slag aggregate. Cement & Concrete Composites 37: 232–240.

Pellegrino, C. & Gaddo, V. 2009. Mechanical and Durability Characteristics of Concrete Containing EAF Slag as Aggregate. Cement and Concrete Composites 31(9): 663–671.

Polanco, J., Manso J.M., Setién J. & González J.J. 2011. Strength and Durability of Concrete Made with Electric Steelmaking Slag. ACI Materials Journal 108(2): 196–203.



Taylor & Francis
Taylor & Francis Group
http://taylorandfrancis.com

Concrete Solutions – Grantham et al. (Eds.)
© 2016 Taylor & Francis Group, London, ISBN 978-1-138-03008-4

Author index

Abbass, W. 517
Abe, T. 259
Abubakri, S. 267, 273
Achillopoulou, D.V. 449
Adarsh Kumar, N.S. 87
Agred, K. 175
Al-Ameri, R. 557
Al-Tabbaa, A. 531
Alexander, M.G. 247
Alonso, M. 65
Álvarez, F. 65
Anagnostopoulos, N. 591
Anastasiou, E. 281
Angst, U.M. 391, 417
Antonio, O.V.M. 381
Argiriou, C.A. 479
Arito, P.A. 247
Asan, M. 201
Asgharzadeh, A. 181
Atkins, C. 3
Avramidis, P. 281

Badogiannis, E. 363, 499
Badr, A. 253
Baera, C. 539
Bakalli, M. 157
Balayssac, J.P. 175, 213
Banfill, P.F.G. 113
Bantilas, K. 511
Batis, G. 603
Baumgartner, E. 423
Beazi-Katsioti, M. 603
Belichenko, O.A. 99
Berkowski, P. 9, 335
Bernakos, A.I. 525
Beushausen, H. 247
Brazhnyk, H.V. 99
Brueckner, R. 3

Cai, X. 317, 325
Caro, M. 471
Chalioris, C.E. 187, 479, 487
Chang, T.-P. 195
Charalambidi, B. 493
Chatziagorastou, P. 281
Chatzopoulos, A. 625
Chen, C.-T. 195
Chess, P.M. 121, 125, 143
Chong, L. 293
Choumanidis, D. 363, 499
Colak, C. 201
Corbett, P. 73
Couvreur, V. 585

De Belie, N. 409, 585
Deby, F. 213
Del Coz, J.J. 65
Demis, S. 397
Deniskin, V.V. 345
Dirar, S. 471
Dmochowski, G. 9
Donadio, M. 157, 591
Donchev, T. 505, 547, 553
Druml, P. 423

Elenas, A. 369
Elsener, B. 391
Esteves, H. 131

Falikman, V.R. 345
Faur, A. 539
Feiteira, J. 585
Fujiwara, H. 259

Gallias, J.L. 603
Ge, Y. 325
Gehlen, C. 595
Geiker, M.R. 239
Giorgini, R.G. 13, 135, 165
Grigoriadis, K. 267, 273
Gruyaert, E. 585
Gulikers, J.J.W. 13, 19, 135, 165
Gunes, O. 201

Harcsa, A. 539
Hiemer, F. 595
Hold, S. 25, 33
Hornbostel, K. 239
Husaini, D. 61

Ingham, J.P. 437
Ioannou, S. 253

Javaid, A. 267
Jemaa, Y. 471
Jin, H. 105
Jonkers, H.M. 565
Jurado Cabañes, C. 43
Juraschek, T. 207

Kabir, M.I. 557
Kaloidas, V. 603
Kanellopoulos, A. 531
Karabinis, A.I. 311, 449, 493
Karayannis, C.G. 487
Kasahara, H. 259
Katsiotis, M.S. 603
Kavvadias, I. 511
Kawaai, K. 571
Kawato, T. 259
Kesikidou, F. 287
Keßler, S. 595
Khan, M.I. 517
Kiziridou, A.N. 449
Klinghoffer, O. 143
Klysz, G. 175, 213
Kofoed, B. 143
Kokkalis, A. 49
Köliö, A. 55, 61
Kolyvas, C.S. 525
Kosior-Kazberuk, M. 335
Kosmidou, P.K. 487

Lagason, P.H.P. 381
Lahdensivu, J. 55, 61
Lambert, P. 3
Law, D.W. 149
Li, C.-J. 195
Li, H. 105
Li, Q. 317
Limbachiya, M. 547
Litina, C. 531
Litina, I. 511
Liu, W. 621
Lozano, A. 65

Maes, M. 409
Mangat, P.S. 267, 273
Manikas, E. 301
Marinos, A.S. 603
Maruoka, M. 259
Mayer, S. 131
Merola, R. 3
Michalakopoulos, A. 301
Milosi, A. 353
Mina, A.L. 467
Mircea, C.G.R. 539
Mirshekari, M. 547
Morales Cruz, C. 613
Mulea, M. 539

Nguyen, A.Q. 213
Nicholls, P. 149
Nomikos, P. 363, 373, 499

Ohno, K. 579

Pacheco, J. 417
Pachta, V. 353
Pahuja, A. 87
Panagiotopoulos, T.A. 487
Panetsos, P. 49
Panias, D. 373
Papachatzakis, G.A. 449
Papachristoforou, M. 287
Papadakis, V.G. 397
Papadimitriou, E. 363, 499
Papadopoulos, N.A. 187
Papanikolas, P. 73
Papantoniou, I.C. 73
Papayianni, I. 281, 287, 353
Pavlovic, A. 505
Peelen, W.H.A. 417
Peñeda, S.A.P. 381
Petersen, C.G. 221, 229
Petkova, D. 505, 547, 553
Petrou, M.F. 467
Polder, R.B. 417
Providakis, C.P. 187
Pruckner, F. 423
Putri, P.Y. 571

Quinn, A. 471

Rao, B.S. 87
Raupach, M. 181, 613
Recillas, H.D.O. 229
Reichling, K. 181
Rousakis, T.C. 311, 493

Sakkas, K.M. 373
Sassmann, P.B. 235
Schlangen, E. 565
Schneck, U. 81
Schneider, M. 423
Schukina, A. 95
Schwarz, W. 157
Semaan, N. 429
Sengul, C. 201
Sfikas, I.P. 437
Sharma, A. 87
Sharma, S. 87
Shi, C. 293
Shi, J. 621
Shi, Y. 621
Shilin, A. 95
Sideris, K.K. 301, 369, 625
Sofianos, A. 363, 373, 499
Stathopoulos-Vlamis, A. 73
Subhani, M. 557
Sugawara, T. 259

Takemoto, S. 259
Tassos, Ch. 625
Tastani, S.P. 305
Thoresen, A.-M. 239
Tolmachov, S.N. 99
Tran, V.D. 579
Trezos, K.G. 467
Triantafillou, T.C. 525
Triantafyllou, G.G. 311
Tziviloglou, E. 565

Ueno, A. 579
Uji, K. 579
Ujike, I. 571

van den Hondel, A.J. 13, 165
van den Hondel, H. 135
Vasiliadis, L. 511
Voutetaki, M.E. 187

Wang, B. 579
Weichold, O. 207, 235
Wertheim, D. 553
Wiktor, V. 565
Wu, Z. 293

Xie, Y. 105

Yamamoto, S. 571
Yang, J. 293
Yang, N. 293
Yang, S. 621
Yang, W. 317, 325
Yi, Z. 105
Yoshikawa, K. 259
Yuan, J. 317, 325

Zayed, T. 429
Zhang, Y. 621
Zhao, C. 267
Zhou, D. 325